CODEN: JASMAN

The Journal of the Acoustical Society of America

ISSN: 0001-4966

Vol. 112, No. 4 October 2002

ACOUSTICAL NEWS—USA 1215

USA Meetings Calendar 1219

ACOUSTICAL NEWS—INTERNATIONAL 1223

International Meetings Calendar 1223

TECHNICAL PROGRAM SUMMARY 1225

ABSTRACTS FROM ACOUSTICS RESEARCH LETTERS ONLINE 1227

BOOK REVIEWS 1229

REVIEWS OF ACOUSTICAL PATENTS 1233

LETTERS TO THE EDITOR

Influence of velocity profile nonuniformity on minor losses for flow exiting thermoacoustic heat exchangers (L) — Ray Scott Wakeland, Robert M. Keolian — 1249

Intraglottal pressure distributions for a symmetric and oblique glottis with a uniform duct (L) — Ronald C. Scherer, Daoud Shinwari, Kenneth J. De Witt, Chao Zhang, Bogdan R. Kucinschi, Abdollah A. Afjeh — 1253

Innate phonetic boundaries revisited (L) — Richard N. Aslin, Janet F. Werker, James L. Morgan — 1257

A reply to "Innate phonetic boundaries revisited" [J. Acoust. Soc. Am. 112, 1257–1260 (2002)] (L) — Susan Nittrouer — 1261

BegoStone—a new stone phantom for shock wave lithotripsy research (L) — Yunbo Liu, Pei Zhong — 1265

GENERAL LINEAR ACOUSTICS [20]

An effective quiescent medium for sound propagating through an inhomogeneous, moving fluid — Oleg A. Godin — 1269

A functional equation for the specular reflection of rays — A. Le Bot — 1276

Acoustic diffraction by a half-plane in a viscous fluid medium — Anthony M. J. Davis, Raymond J. Nagem — 1288

Field induced in inhomogeneous spheres by external sources. I. The scalar case — Gerassimos C. Kokkorakis, John G. Fikioris, George Fikioris — 1297

(Continued)

THE JOURNAL OF THE ACOUSTICAL SOCIETY OF AMERICA VOL. 112, NO. 4, OCTOBER 2002

CONTENTS—*Continued from preceding page*

A boundary integral equation method using auxiliary interior surface approach for acoustic radiation and scattering in two dimensions	S. A. Yang	1307
Meridional ray backscattering enhancements for empty truncated tilted cylindrical shells: Measurements, ray model, and effects of a mode threshold	Scot F. Morse, Philip L. Marston	1318
Free field measurements of the absorption coefficient for nonlocally reacting sound absorbing porous layers	G. Jansens, W. Lauriks, G. Vermeir, J. F. Allard	1327
The complex phase gradient method applied to leaky Lamb waves	O. Lenoir, J. M. Conoir, J. L. Izbicki	1335

NONLINEAR ACOUSTICS [25]

Coupled dynamics of translation and collapse of acoustically driven microbubbles	Anil J. Reddy, Andrew J. Szeri	1346

AEROACOUSTICS, ATMOSPHERIC SOUND [28]

Band gaps and defect modes in periodically structured waveguides	J. N. Munday, C. Brad Bennett, W. M. Robertson	1353

UNDERWATER SOUND [30]

Internal-wave time evolution effect on ocean acoustic rays	Stanley M. Flatté, Michael D. Vera	1359
The effect of reverberation on the damping of bubbles	T. G. Leighton, P. R. White, C. L. Morfey, J. W. L. Clarke, G. J. Heald, H. A. Dumbrell, K. R. Holland	1366
Geoacoustic inversion of ambient noise: A simple method	C. H. Harrison, D. G. Simons	1377
Effects of incoherent and coherent source spectral information in geoacoustic inversion	Stan E. Dosso, Michael J. Wilmut	1390

ULTRASONICS, QUANTUM ACOUSTICS, AND PHYSICAL EFFECTS OF SOUND [35]

A new 1-D integral representation for dynamic response of anisotropic elastic solids due to a point force	Kuang-Chong Wu	1399
Influence of ultrasonic frequency on multibubble sonoluminescence	Kyuichi Yasui	1405
Theory of inert gas-condensing vapor thermoacoustics: Propagation equation	Richard Raspet, William V. Slaton, Craig J. Hickey, Robert A. Hiller	1414
Theory of inert gas-condensing vapor thermoacoustics: Transport equations	William V. Slaton, Richard Raspet, Craig J. Hickey, Robert A. Hiller	1423
A nonlinear model of thermoacoustic devices	Sergey Karpov, Andrea Prosperetti	1431

STRUCTURAL ACOUSTICS AND VIBRATION [40]

Dynamics of two-dimensional composites of elastic and viscoelastic layers	Michael El-Raheb	1445
Flexural vibration of perforated plates and porous elastic materials under acoustic loading	D. Takahashi, M. Tanaka	1456
Diffuse wavefields in cylindrical coordinates	R. S. Langley, P. J. Shorter	1465

NOISE: ITS EFFECTS AND CONTROL [50]

Novel active noise-reducing headset using earshell vibration control	Boaz Rafaely, Joao Carrilho, Paolo Gardonio	1471
Theoretical and experimental investigations on coherence of traffic noise transmission through an open window into a rectangular room in high-rise buildings	Jiping Zhang, Weikang Jiang, Ningrong Li	1482

(Continued)

THE JOURNAL OF THE ACOUSTICAL SOCIETY OF AMERICA VOL. 112, NO. 4, OCTOBER 2002

CONTENTS—*Continued from preceding page*

Fuzzy models for accumulation of reported community noise annoyance from combined sources — Dick Botteldooren, Andy Verkeyn — 1496

ACOUSTIC SIGNAL PROCESSING [60]

Statistically stable ultrasonic imaging in random media — James G. Berryman, Liliana Borcea, George C. Papanicolaou, Chrysoula Tsogka — 1509

Range-dependent seabed characterization by inversion of acoustic data from a towed receiver array — Martin Siderius, Peter L. Nielsen, Peter Gerstoft — 1523

Iterative reconstruction algorithm for optoacoustic imaging — G. Paltauf, J. A. Viator, S. A. Prahl, S. L. Jacques — 1536

PHYSIOLOGICAL ACOUSTICS [64]

Interpretation of standard distortion product otoacoustic emission measurements in light of the complete parametric response — David M. Mills — 1545

Modifications of a single saturating non-linearity account for post-onset changes in $2f_1-f_2$ distortion product otoacoustic emission — Andrei N. Lukashkin, Ian J. Russell — 1561

Place specificity of multiple auditory steady-state responses — Anthony T. Herdman, Terence W. Picton, David R. Stapells — 1569

PSYCHOLOGICAL ACOUSTICS [66]

Contribution of spectral cues to human sound localization — Erno H. A. Langendijk, Adelbert W. Bronkhorst — 1583

An adaptive procedure for categorical loudness scaling — Thomas Brand, Volker Hohmann — 1597

Lateralization and detection of pulse trains with alternating interaural time delays — Uma Balakrishnan, Richard L. Freyman — 1605

Detection of static and dynamic changes in interaural correlation — Susan E. Boehnke, Susan E. Hall, Torsten Marquardt — 1617

SPEECH PRODUCTION [70]

Economy of effort in different speaking conditions. I. A preliminary study of intersubject differences and modeling issues — Joseph S. Perkell, Majid Zandipour, Melanie L. Matthies, Harlan Lane — 1627

Economy of effort in different speaking conditions. II. Kinematic performance spaces for cyclical and speech movements — Joseph S. Perkell, Majid Zandipour — 1642

Experimental verification of the quasi-steady approximation for aerodynamic sound generation by pulsating jets in tubes — Zhaoyan Zhang, Luc Mongeau, Steven H. Frankel — 1652

SPEECH PERCEPTION [71]

Perceptual learning following changes in the frequency-to-electrode assignment with the Nucleus-22 cochlear implant — Qian-Jie Fu, Robert V. Shannon, John J. Galvin III — 1664

Benefits of amplification for speech recognition in background noise — Christopher W. Turner, Belinda A. Henry — 1675

MUSIC AND MUSICAL INSTRUMENTS [75]

Acoustical analysis and model-based sound synthesis of the kantele — Cumhur Erkut, Matti Karjalainen, Patty Huang, Vesa Välimäki — 1681

BIOACOUSTICS [80]

Linking the sounds of dolphins to their locations and behavior using video and multichannel acoustic recordings — Rebecca E. Thomas, Kurt M. Fristrup, Peter L. Tyack — 1692

(Continued)

THE JOURNAL OF THE ACOUSTICAL SOCIETY OF AMERICA VOL. 112, NO. 4, OCTOBER 2002

CONTENTS—*Continued from preceding page*

Discrimination of amplitude-modulated synthetic echo trains by an echolocating bottlenose dolphin — Lois A. Dankiewicz, David A. Helweg, Patrick W. Moore, Justine M. Zafran — 1702

CUMULATIVE AUTHOR INDEX — 1709

ACOUSTICAL NEWS—USA

Elaine Moran
Acoustical Society of America, Suite 1NO1, 2 Huntington Quadrangle, Melville, NY 11747-4502

Editor's Note: *Readers of this Journal are encouraged to submit news items on awards, appointments, and other activities about themselves or their colleagues. Deadline dates for news items and notices are 2 months prior to publication.*

New Fellows of the Acoustical Society of America

William C. Moss—For contributions to numerical modeling of single bubble sonoluminescence.

Marshall H. Orr—For application of high-frequency acoustics in imaging small-scale ocean processes.

Ning Xiang—For contributions to signal processing, architectural acoustics, and acoustic detection.

143rd Meeting of the Acoustical Society of America held in Pittsburgh, Pennsylvania

The 143rd meeting of the Acoustical Society of America was held 3–7 June 2002 at the Pittsburgh Hilton Hotel in Pittsburgh, Pennsylvania. This was the second time that the Society has met in this city, the first time being in 1934.

The meeting drew a total of 1069 registrants, including 115 nonmembers and 296 students. Attesting to the international ties of our organization, 93 of the registrants (that is, about 12%) were from outside North America. There were 13 registrants from the United Kingdom, 14 from Japan, 9 from Korea, 8 from France, 7 each from Germany and the Netherlands, 4 each from Italy, Poland and Sweden, 3 each from Australia and Russia, 2 each

FIG. 1. Bruce D. Cornuelle (1), recipient of the 2002 Medwin Prize in Acoustical Oceanography is congratulated by ASA President William Hartmann (r).

FIG. 2. William Hartmann (1) congratulates James J. Finneran, recipient of the 2002 R. Bruce Lindsay Award.

 0001-4966/2002/112(4)/1215/6/$19.00

FIG. 3. William Hartmann (1) congratulates Thomas J. Royston, recipient of the 2002 R. Bruce Lindsay Award.

from China, Croatia, Denmark, Finland, India, and Norway, and 1 each from Belgium, Brazil, Romania, Spain, and Ukraine. North American countries, the United States, Canada, and Mexico, accounted for 943, 30, and 3, respectively.

A total of 715 papers, organized into 72 sessions, covered the areas of interest of all 13 Technical Committees. The meeting also included five meetings dealing with standards. The Monday evening tutorial lecture series was continued by James A. Simmons of Brown University, Providence, Rhode Island. His tutorial ''Keep Your Ear on the Ball: Display of Targets in the Bat's Sonar Receiver'' was presented to an audience of about 100.

The Short Course on Conversational Systems was held on Sunday and Monday, 2–3 June, at Carnegie Mellon University (CMU). The course was given by Alan W. Black, Ronald Rosenfeld, Alexander I. Rudnicky, and Richard M. Stern, faculty members at CMU. The Technical Committee on Architectural Acoustics and the National Council of Acoustical Consultants sponsored a student design competition which was professionally judged at the meeting. Winners received $1000 and $500 prizes.

Technical tours were arranged by the local meeting committee to the

FIG. 4. Neal F. Viemeister (1) receives the Silver Medal in Psychological and Physiological Acoustics from ASA President William Hartmann.

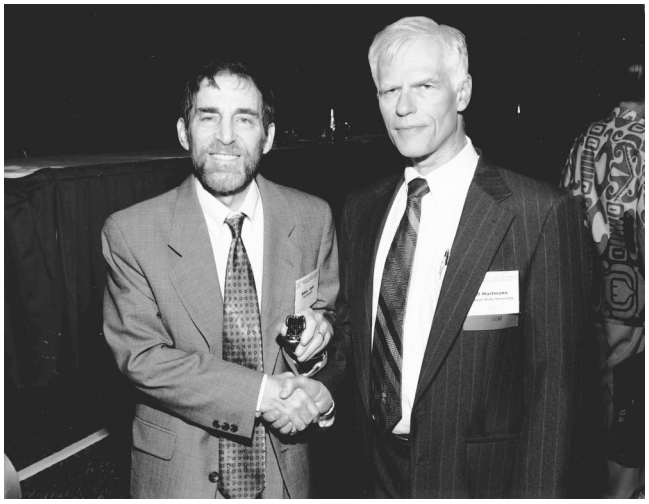

FIG. 5. Robert E. Apfel (1) receives the 2002 Gold Medal from ASA President William Hartmann.

FIG. 6. Tony F. W. Embleton (1) recipient of the 2002 Gold Medal is congratulated by President William Hartmann.

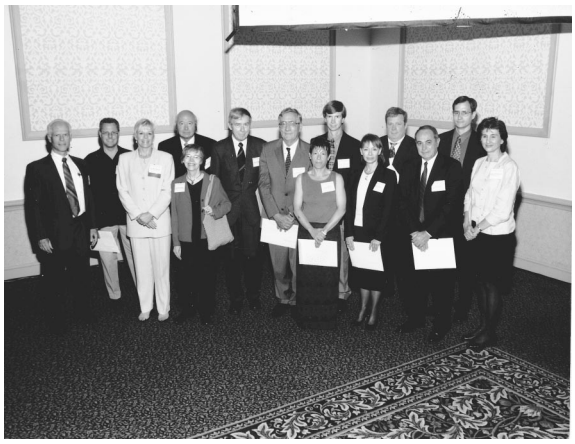

FIG. 7. New Fellows of the Acoustical Society of America receive their certificates from ASA President William Hartmann (far left) and ASA Vice President Janet Weisenberger (third from left).

FIG. 8. Courtney B. Burroughs, Chair of the Pittsburgh meeting, addresses the meeting attenders.

Mine Safety and Hearing Administration and National Institute of Occupational Safety and Health and to Heinz Hall and the Benedum Center.

Other events included the two social hours held on Tuesday and Thursday, receptions for students in various areas of acoustics, and a Fellows Suite. These events provided the settings for participants to meet in relaxed settings to encourage social exchange and informal discussions. The Women in Acoustics Luncheon was held on Wednesday afternoon and was attended by over 60 people. The Fellows Luncheon was held on Thursday afternoon and was attended by over 115 people who heard a presentation by ARTEC's Russell Johnson on concert hall acoustics.

The National Council of Acoustical Consultants (NCAC) celebrated its 40th anniversary during the Pittsburgh meeting. At their banquet, the ASA President presented the NCAC with a certificate of congratulations and noted the substantial benefits to both the NCAC and the ASA as a result of their close association.

The plenary session included the presentation of awards and a prize. The Medwin Prize in Acoustical Oceanography was presented to Bruce D. Cornuelle ''for the effective use of sound in the discovery and understanding of physical and biological parameters and processes in the sea.'' Earlier in the day Dr. Cornuelle gave the Acoustical Oceanography Lecture, as part of the prize program. (See Fig. 1.)

Two R. Bruce Lindsay Awards were presented. James J. Finneran received the award ''for contributions to the understanding of auditory mechanics and transduction to teleost fish and of hearing by dolphins.'' (See Fig. 2.) Thomas D. Royston received the award ''for contributions to the nonlinear characterization and control of vibration and acoustical outreach to inner city youth.'' (See Fig. 3.) The Silver Medal in Psychological and Physiological Acoustics, the presentation of which was delayed from the Fall 2001 meeting, was presented to Neal F. Viemeister ''for contributions to the understanding of temporal and intensive aspects of hearing.'' (See Fig. 4.) Two Gold Medals were awarded. Robert E. Apfel received the medal ''for fundamental contributions to physical acoustics and biomedical ultrasound, and innovative leadership in electronic publishing.'' (See Fig. 5.) Tony F. W. Embleton received the medal ''for fundamental contributions to understanding outdoor sound propagation and noise control and for leadership in the Society.'' (See Fig. 6.)

Election of 16 persons to Fellow grade was announced and fellowship certificates were presented. New fellows are: Rachel K. Clifton, Kerry W. Commander, Brian H. Houston, Darlene R. Ketten, Asbjorn Krokstad, David E. Marsh, Andrzej Rakowski, Patrick M. Hurdle, Leon H. Sibul, Andrea M. Simmons, David C. Swanson, and Lynne A. Werner. (See Fig. 7.)

The President expressed the Society's thanks to the Local Committee for the excellent execution of the meeting, which clearly evidenced meticulous planning. He introduced the Chair of the Meeting, Courtney B. Burroughs (see Fig. 8), who acknowledged the contributions of the members of his committee including: Richard M. Stern, Technical Program Chair; Thomas Sullivan, Audio-Visual; Lori Holt, Accompanying Persons Program; Erin Dugan, Signs; Jeffrey Vipperman, Technical Tours; and Efrem Reeves, Socials and Receptions. He also extended thanks to the members of the Technical Program Organizing Committee: Richard M. Stern, Technical Program Chair; Kyle Becker and David Palmer, Acoustical Oceanography; David Bradley, Animal Bioacoustics; David E. Marsh, Architectural Acoustics; Mark Schafer, Biomedical Ultrasound/Bioresponse to Vibration; Victor W. Sparrow, Education in Acoustics; William Thompson, Engineering Acoustics; Peter Hoekje, Musical Acoustics; Richard D. Godfrey and John Seiler, Noise; James Sabatier and Bart Lipkens, Physical Acoustics; Lawrence Feth, Psychological and Physiological Acoustics; Deborah Grove, Signal Processing in Acoustics; Will Hula, Susan Shaiman, and Emily A. Tobey, Speech Communication; Joseph W. Dickey, Structural Acoustics and Vibration; and John Perkins, Underwater Acoustics.

The Plenary Session concluded with the presentation of the Vice President's gavel to outgoing Vice President Janet M. Weisenberger and the President's Tuning Fork to outgoing President William M. Hartmann (see Fig. 9).

WILLIAM M. HARTMANN
President 2001–2002

FIG. 9. Incoming Vice President William Yost (l) with retiring ASA Vice President Janet Weisenberger (c) and President William Hartmann (r).

Reports of Technical Committees

(See September 2002 issue of JASA for reports of other committees)

Signal Processing in Acoustics

Signal and image processing form the basic nucleus of many acoustical applications. Signal processing is a specialty area that many acousticians apply in their daily technical regimen with great success such as the simplicity in Fourier analysis of vibrational data or in the complexity of analyzing the time-frequency response of dolphin sounds. Acoustical applications abound with unique processing approaches to solve the underlying problem. For instance, the localization of a target in the harsh underwater ocean acoustic environment not only challenges the acoustician, but also taxes the core of signal processing basics thereby requiring more sophistication and a priori knowledge to be incorporated into the processor. This particular application has led to many advances both in underwater signal and image processing as well in the development of a wide variety of so called model-based or physics-based processors. A prime example of this technology is the advent of the matched-field processor that has led not only to a solution of the target localization problem, but also to many applications in other acoustical areas such as nondestructive evaluation and biomedical

imaging. Over this year the Technical Committee on Signal Processing (SP) in Acoustics has sponsored many technical sessions jointly with the TCs and individually on Processing Tutorials discussing critical technologies in signal processing that directly impact many of the TC areas of high interest. The Gallery of Acoustics sponsored and administered annually by SP has become a staple at the ASA meetings. Our Technical Liaisons assure that we are continuously interacting at all levels with the other twelve TCs. The Signal Processing Challenge Problem on the ASA website along with our own new SP website provides a venue for signal processing colleagues to interact with us throughout the ASA. The website (http://www.sao.nrc.ca/ims/asa_sp/StartHere.html) provides the interested member a cross-sectional view of the activities of the TC-SP, its goals and objectives, representatives and its membership. Finally our Best Young Presenter awards have motivated many of our members to present their work and be recognized.

Signal and image processing are the underlying technologies that encompass many of the efforts in acoustics through the necessity to model, acquire, analyze and extract the required information from noisy measurement data. It is for these reasons that the Technical Committee on Signal Processing (SP) Acoustics continues to foster a growing interaction with each of the Technical Committees through the sponsoring of joint sessions and tutorials. This effort was made by the various signal processing related sessions throughout the Ft. Lauderdale and Pittsburgh meetings.

At the 142nd ASA meeting in Ft. Lauderdale, Florida, the SP sponsored or co-sponsored 7 sessions: 1 Topical Meeting, 3 contributed session and 3 special sessions. These sessions were entitled: ''Topical Meeting: Time Reversal and Applications'' (SP) Overall Chair: David H. Chambers; ''Theory and Basic Experiments in Time Reversal'' (SP) Chair: David H. Chambers; ''Time Reversal in Signal Processing'' (SP) Chair: James V. Candy; ''Time Reversal in the Ocean Environment'' (SP) Chair: Darrell R. Jackson; ''Time Reversal in Random and Reverberating Media'' (SP) Chair: George C. Papanicolaou; ''Implementing the Classroom Acoustics Standard'' (NS/AA/SP) Chair: John Erdreich; ''Acoustic Image Reconstruction Using Tomographic Techniques'' (SP/AO/UW/BB) Chair: Sean K. Lehman; ''Theory and Applications of Acoustic Time Reversal'' (SP) Chair: David H. Chambers; ''General Topics in Signal Processing I'' (SP) Chair: Leon H. Sibul; ''General Topics in Signal Processing II'' (SP) Chair: Deborah M. Grove.

We had our ''Best Young Presenter Award'' in which a cash prize was awarded to Liliana Borcea for the presentation entitled, ''Imaging in Random Media.'' This presentation was part of the Topical Meeting: Time Reversal and Applications. We also offered a short course entitled, ''Applied Acoustical Digital Signal Processing.''

At the 143rd ASA meeting in Pittsburgh, Pennsylvania, the SP sponsored or co-sponsored 4 sessions: 1 Hot Topics, 1 History presentations and 3 contributed sessions and 1 special session. These sessions were entitled: ''Applications of Time Reversal Processing'' (SP) Chair: Leon H. Sibul; ''History of Signal Processing in Acoustics'' (SP) by David I. Havelock Chair: James V. Candy; ''Signal Processing Techniques'' (SP) Chair: David C. Swanson; ''Shallow Water Propagation and Signal Processing'' (UW/SP) Chair: David M. Deveau; ''Hot Topics: Signal Processing in Acoustics'' (SP) by James V. Candy Chair: Mardi C. Hastings; ''Advances in Sonar Imaging Techniques Including Synthetic Aperture and Computed Tomography'' (SP/UW) Chairs: Brian Ferguson and Kerry W. Commander.

We had our ''Best Young Presenter Award'' in which a cash prize was awarded to Brian R Rapids for the presentation entitled, ''Forward-Scattered Acoustic Intensity From Prolate Spheroids.'' We offered a short course entitled, ''Signal Processing for Machinery and Structural Fatigue Prognostics.''

In a concerted effort to enhance the communications between the TC-SP and the other Technical Committees, Technical Liaisons (TL) were created for each TC. A Technical Liaison is a member of the SP who represents the interests of the group to other Technical Committees (e.g. Underwater Acoustics). The TL would attend the SP meeting as well as his particular Technical Committee. He would primarily facilitate the CO-SPONSORING of joint sessions with SP (our charter) and the Committee assuring no technical overlap with other sessions. The following SP members are the current Technical Liaisons: Acoustical Oceanography-Jean-Pierre Hermand, Animal Bioacoustics-Brian Ferguson, Architectural Acoustics-Deborah Grove/Ning Xiang, Biomedical Ultrasound/Bioresponse to Vibration-Sean Lehman, Engineering Acoustics-Stan Ehrlich, Musical Acoustics-John Impagliazzo, Noise-Dave Evans/Joe Pope, Physical Acoustics-Dave Havelock/Dave Chambers, Psychological and Physiological Acoustics-Open, Speech Communication-Jose Diaz, Structural Acoustics and Vibration-Stuart Bolton/Dave Swanson; Underwater Acoustics-Ed Sullivan/Geoff Edelson.

We also would like to recognize Charles Gaumond and Jose Diaz for constructing our first Student Challenge Problem on acoustical signal processing which is now featured on both the ASA and TC-SP websites. This problem is aimed to motivate (and award a cash prize) signal processing students to participate in some of our activities.

We also would like to recognize our JASA Associate Editor for Acoustical Signal Processing, John C. Burgess. His efforts often go unnoticed, but the results are clearly visible in a higher quality publication.

We are participating in Acoustics Research Letters Online (ARLO) and James V. Candy is the Associate Editor for Acoustical Signal Processing. This is an on-line medium offering the exploitation of color, imaging, sound and various multi-media presentations with a rapid turn-around policy for short articles (6-page) or letters. It is strictly complimentary to the normal full-length JASA aeticles.

The efforts of David Evans on the Standards Committee are also important to the SP. Our representative on the Medals and Awards Committee and Membership Committee are Stanley Ehrlich and David Havelock (respectively). We would also like to recognize, Dave Havelock for re-creating, updating, and maintaining our website, another task that requires much effort but yield little return. Surf to our site and get all of the current tidbits of information and links to other processing websites. Our web address is: *http://www.sao.nrc.ca/ims/asa_sp/StartHere.html*. Our Gallery of Acoustics still thrives through the efforts of Randy Smith and Preston Wilson and now with Sean Lehman. Our Student Council member, Hassan Namarvar, continues to represent the TC-SP in a diligent manner.

Finally, but most important, we would like to congratulate our new Fellows: Leon Sibul and David Swanson of Penn State University.

James V. Candy
Chair

Speech Communication

The Speech Technical Committee (TC) has been very active this past year. The current members of the Committee are: Mariko Aoki, Shari R. Baum, Catherine T. Best, Suzanne E. Boyce, Christopher S. Campbell, Rene Carre, Randy L. Diehl, David Dorado, Carol Y. Espy-Wilson, Marios S. Fourakis, Robert D. Frisina, Bruce Gerratt, John H. L. Hansen, Jean-Paul Haton, Sarah Hawkins, John W. Hawks, Mark S. Hedrick, Megan M. Hodge, Sun-Ah Jun, William F. Katz, Patricia A. Keating, Klaus J. Kohler, Jody E. Kreiman, Charissa R. Lansing, Paul A. Luce, Nancy S. McGarr, Diane L. Meador, Christopher A. Moore, Shrikanth S. Narayanan, John J. Ohala, Dwayne Paschall, Deborah M. Rekart, Ian E. Rogers, Robert Ruiz, Juergen Schroeter, Astrid Schmidt-Nielsen, Samuel A. Seddoh, Anu Sharma, Caroline L. Smith, Janet W. Stack, Elaine T. Stathopoulos, Winifred Strange, Mario A. Svirsky, Emily A. Tobey, Greg S. Turner, Rosalie M. Uchanski, Nagalapura Viswanath, and Gary G. Weismer. The ex officio members of the Committee are: Melissa Epstein, Keith R. Kluender, Anders Lofqvist, Shrikanth S. Narayanan, Douglas D. O'Shaughnessy, Christopher W. Turner, Maureen L. Stone, and James M. Hillenbrand. Special thanks to our paper sorters for the Technical Program, Betty Tuller and Gautam Vallabha for Ft. Lauderdale, and Susan Shaiman and Emily Tobey for Pittsburgh. If you would like to join the Committee, please contact Diane Kewley-Port.

Research Grants in Speech

There are two research grants under the purview of the Speech TC, the Raymond H. Stetson Scholarship in Phonetics and Speech Production and the Research Grant in Speech Science. The annual Stetson Scholarship supports a student in graduate study in scientific areas related to the field of phonetics and motor speech production. The past year's winner was Jeffery Jones, Department of Psychology, Queen's University, Canada and the award was $3000. Patricia Kearing chaired a subcommittee composed of William Katz, Roger Chan, Gary Weismer and James Hillenbrand to review the selection criteria and mechanics of selection. The Research Grant in Speech Science is a biannual award of $5000 supported by the Dennis Klatt Memorial Fund. This fund resides in the American Speech-Language-

Hearing Foundation (ASLHF). Since the Fund's inception the intention is that ASLHF and ASA would jointly sponsor and support this research grant. Over the past year Katherine Harris and Wayne Wright helped write a Memo of Understanding that specifies their respective responsibilities and has been signed between the two organizations of particular interest is that the review panel for the grants will be selected by the Speech TC chair. The grant recipient will be announced at the fall meetings of both ASLHA and ASA. The competition, which closed June 14, was widely advertised in both societies this year. ASA members wishing to contribute donations to the Stetson Scholarship Fund can do so to the Acoustical Society Foundation, Inc. Members who are interested in contributing to the Dennis Klatt Memorial Fund should send their donations to the American Speech-Language-Hearing Foundation.

Student Activities

The Committee sponsors two activities, an evening reception with other technical committees, and competition with a cash award for best oral or poster presentation, geared especially for students in Speech Communication. Attendance at the Ft. Lauderdale and Pittsburgh meeting student receptions was excellent.

Over 20 students at each of the Ft. Lauderdale and Pittsburgh meetings submitted their posters for consideration as the Best Student Paper Award. Megha Sundara was selected for the Best Paper Award in Ft. Lauderdale. Coordinators for the judging of the Best Student papers were Bruce Garratt and Jody Krieman. Under the new guidelines, in Pittsburgh Miranda Cleary was selected for the Best Paper Award, and Monica Padilla for the second best paper. Coordinators for judging in Pittsburgh were John Hawks and Marios Fourakis.

Melissa Epstein, now ''Dr. Epstein,'' has served as student council representative for Speech three years. Recent initiatives include a job bulletin board on the ASA web site, and coordinating roommates for students at meetings. Our new student council representatives are Tessa Bent and Ching Xu.

Associate Editors

Chris Turner and Keith Kluender will be relinquishing their editorships in the Journal over the summer months. Both editors have served with excellence. Anders Lofqvist and Douglas O'Shaughnessy will continue to serve as associate editors. Joining them will be new editors Randy Diehl and Peter Assmann.

Special Sessions

At the Ft. Lauderdale meeting, the Hot Topics session included speech communication. An excellent presentation was made by Peter Assmann and Philipos Loizou of the University of Texas at Dallas. Peggy Nelson helped with our joint special session, ''Speech intelligibility and the metrics used for its evaluation.'' In Pittsburgh, Speech TC participated in several special sessions. Of particular interest was a session in memory of Peter Jusczyk on ''The future of infant speech perception research,'' chaired by Rochelle Newman and Ruth Tincoff. In addition, a session ''Models of phonetic category formation and structure'' was chaired by Andrew Lotto and Lori Holt. Hideki Kawahara and Ingo Titze represented speech in a session, ''Naturalness in synthesized speech and music.''

Medals, Awards, and Fellows

Gary Weismer is the representative for Speech Communication to the Society's Medals and Awards Committee and Maureen Stone is our representative to the Membership Committee which makes decisions regarding Fellows of the Society. Please contact them if you wish to nominate an individual for either honor.

Submitted by Diane Kewley-Port, Chair of Speech Communication Technical Committee

Diane Kewley-Port
Chair

USA Meetings Calendar

Listed below is a summary of meetings related to acoustics to be held in the U.S. in the near future. The month/year notation refers to the issue in which a complete meeting announcement appeared.

2002

2–6 Dec. First Pan-American/Iberian Meeting on Acoustics (Joint Meeting: 144th Meeting of the Acoustical Society of America, 3rd Iberoamerican Congress of Acoustics, and 9th Mexican Congress on Acoustics) Cancun, Mexico [Acoustical Society of America, Suite 1NO1, 2 Huntington Quadrangle, Melville, NY 11747-4502; Tel.: 516-576-2360; Fax: 516-576-2377; E-mail: asa@aip.org; WWW: asa.aip.org/cancun/cancun.html].

2003

28 April–2 May 145th Meeting of the Acoustical Society of America, Nashville, TN [Acoustical Society of America, Suite 1NO1, 2 Huntington Quadrangle, Melville, NY 11747-4502; Tel.: 516-576-2360; Fax: 516-576-2377; E-mail: asa@aip.org; WWW: asa.aip.org].

5–8 May SAE Noise & Vibration Conference & Exhibition, Traverse City, MI [P. Kreh, SAE International, 755 W. Big Beaver Rd., Suite 1600, Troy, MI 48084; Fax: 724-776-1830; WWW: http://www.sae.org].

10–14 Nov. 146th Meeting of the Acoustical Society of America, Austin, TX [Acoustical Society of America, Suite 1NO1, 2 Huntington Quadrangle, Melville, NY 11747-4502; Tel.: 516-576-2360; Fax: 516-576-2377; E-mail: asa@aip.org; WWW: asa.aip.org].

2004

24–28 May 75th Anniversary Meeting (147th Meeting) of the Acoustical Society of America, New York, NY [Acoustical Society of America, Suite 1NO1, 2 Huntington Quadrangle, Melville, NY 11747-4502; Tel.: 516-576-2360; Fax: 516-576-2377; E-mail: asa@aip.org; WWW: asa.aip.org].

22–26 Nov. 148th Meeting of the Acoustical Society of America, San Diego, CA [Acoustical Society of America, Suite 1NO1, 2 Huntington Quadrangle, Melville, NY 11747-4502; Tel.: 516-576-2360; Fax: 516-576-2377; E-mail: asa@aip.org; WWW: asa.aip.org].

Cumulative Indexes to the *Journal of the Acoustical Society of America*

Ordering information: Orders must be paid by check or money order in U.S. funds drawn on a U.S. bank or by Mastercard, Visa, or American Express credit cards. Send orders to Circulation and Fulfillment Division, American Institute of Physics, Suite 1NO1, 2 Huntington Quadrangle, Melville, NY 11747-4502; Tel.:516-576-2270. Non-U.S. orders add $11 per index.

Some indexes are out of print as noted below.

Volumes 1–10, 1929–1938: JASA and Contemporary Literature, 1937–1939. Classified by subject and indexed by author. Pp. 131. Price: ASA members $5; Nonmembers $10.

Volumes 11–20, 1939–1948: JASA, Contemporary Literature, and Patents. Classified by subject and indexed by author and inventor. Pp. 395. Out of Print.

Volumes 21–30, 1949–1958: JASA, Contemporary Literature, and Patents. Classified by subject and indexed by author and inventor. Pp. 952. Price: ASA members $20; Nonmembers $75.

Volumes 31–35, 1959–1963: JASA, Contemporary Literature, and Patents.

Classified by subject and indexed by author and inventor. Pp. 1140. Price: ASA members $20; Nonmembers $90.

Volumes 36–44, 1964–1968: JASA and Patents. Classified by subject and indexed by author and inventor. Pp. 485. Out of Print.

Volumes 36–44, 1964–1968: Contemporary Literature. Classified by subject and indexed by author. Pp. 1060. Out of Print.

Volumes 45–54, 1969–1973: JASA and Patents. Classified by subject and indexed by author and inventor. Pp. 540. Price: $20 (paperbound); ASA members $25 (clothbound); Nonmembers $60 (clothbound).

Volumes 55–64, 1974–1978: JASA and Patents. Classified by subject and indexed by author and inventor. Pp. 816. Price: $20 (paperbound); ASA members $25 (clothbound); Nonmembers $60 (clothbound).

Volumes 65–74, 1979–1983: JASA and Patents. Classified by subject and indexed by author and inventor. Pp. 624. Price: ASA members $25 (paperbound); Nonmembers $75 (clothbound).

Volumes 75–84, 1984–1988: JASA and Patents. Classified by subject and indexed by author and inventor. Pp. 625. Price: ASA members $30 (paperbound); Nonmembers $80 (clothbound).

Volumes 85–94, 1989–1993: JASA and Patents. Classified by subject and indexed by author and inventor. Pp. 736. Price: ASA members $30 (paperbound); Nonmembers $80 (clothbound).

Volumes 95–104, 1994–1998: JASA and Patents. Classified by subject and indexed by author and inventor. Pp. 632. Price: ASA members $40 (paperbound); Nonmembers $90 (clothbound).

BOOK REVIEWS

P. L. Marston
Physics Department, Washington State University, Pullman, Washington 99164

These reviews of books and other forms of information express the opinions of the individual reviewers and are not necessarily endorsed by the Editorial Board of this Journal.

Editorial Policy: *If there is a negative review, the author of the book will be given a chance to respond to the review in this section of the Journal and the reviewer will be allowed to respond to the author's comments. [See "Book Reviews Editor's Note," J. Acoust. Soc. Am.* ***81****, 1651 (May 1987).]*

Foundations of Stuttering

Marcel E. Wingate

Academic Press, San Diego, 2002.
xxii+425 pp. Price: $75.00 (hardcover) ISBN: 0-12-759451-5.

Marcel Wingate has had a long and distinguished career during which his main research focus has been on stuttering. In that time he has authored four books (including the current one). Each of the earlier volumes is characterized by a clear writing style that gets immediately to the heart of the issue at hand. He is a man of steadfast opinions and happily presents his views and their support in a forthright manner. The current offering is no exception as illustrated when he lays out his intention in the preface: ''[The book's] objective is to establish a rational and scientifically defensible foundation for the study and management of the disorder, based on the fact that stuttering is manifestly a disorder of speech'' (Wingate, 2002, p. xvii). As with his earlier books, this represents a substantial contribution that, in the space allowed for review, is hard to do full justice.

The structure of the volume is as follows: There are four chapters in Part I. Chapters 1 and 2 criticize what he sees as a general, and unwarranted, preoccupation of the cause of stuttering. The two following chapters give his view about the objective specification of stuttering and what he considers to be well-supported facts about the disorder. The five chapters in Part II look at several forces that he considers obstruct a scientific study of the disorder. Part III includes four chapters in which he looks at linguistic factors that are associated with stuttering. Wingate holds the view that work on fluency and speech production have received insufficient (in fact he says ''minimal'') attention in the stuttering literature. The final chapter describes a strategy for ''management'' of the disorder based on the material in the previous chapters.

There is a stylistic matter that will not suit all readers: The book does not give detailed references in support of many of the points he makes (number of references is approximately equal to the number of pages). I often found myself going in vain to a footnote in the hope that I might find further details about some matter raised. Consequently, a reader relying on this text alone has to accept Wingate's distillation of the literature or, as he puts it, the information that he considers ''substantial, well-established, and stable, and that can be defended as contributing positively to understanding the basic substance of the disorder.'' (p. 3) As well as the problem associated with lack of full references in the book, it also appears at times that he is more familiar with the older literature. It is also apparent that the principal focus throughout his career has been on adult, rather than childhood, stuttering.

Choice of the word ''Foundations'' in the title suggests that he sees this contribution as providing aspects of the groundwork in the area with some notion of permanence of the ideas. The facts that he presents to the reader have a deductive theme to them (at least, one surmises, in Wingate's mind) that lead him to present conclusions as inescapable. As a consequence, the text has a certain logical coherence. On the other hand, however, the thrust of the volume depends to some extent on whether the reader accepts the elements in his argument. Though I found myself agreeing with a lot of what was said, many others were contentious to me and I am sure that a different reviewer would find a different mix of acceptable and contentious points. He also thinks the field is in a stage where theory about the disorder will not advance our understanding. Theory, in contrast to modeling, fulfills the role of unifying collected facts and drawing unforeseen predictions that can then be tested. The thread of the argument wending from stuttering as a speech disorder involving word onset, through onset and rhyme effects to the association of stuttering with stress nuclei, represents such a unifying view that predicts which techniques will be successful at ameliorating the disorder and which will not. At the very least, what is presented is more than a collection of dispassionate facts. I will identify the major topics in each chapter that Wingate considers.

The first chapter raises the view that theory is a ''distracting topic.'' Theories, he says, ''typically are simply pragmatic techniques retrofitted to a contended position'' (p. 4). He also objects that they are preoccupied with explaining the cause of the disorder. Instead of formulating theory, he establishes what he calls the three significant facts (all negative) about stuttering ''(1) its cause is unknown, (2) its essential nature is not understood, and (3) there is no known cure'' (p. 11). Chapter 2 critiques certain assumptions researchers have made in the field and the knock-on effects these have for explanations. The issues that I would single out here to alert readers about are his view that stuttering can be assessed reliably, and the unsatisfactory nature of current definitions. The former, in particular, is a hotly debated and on-going topic (for instance, between protagonists of time interval analysis and their critics). The chapter culminates in his own ''standard definition'' of stuttering that involves a hierarchy of features (speech predominant, motor acts secondary, and emotional factors possibly associated). The contrast between this definition and Johnson's view of stuttering as a psychological disorder is highlighted.

Chapter 3 looks at the factors behind stuttering in detail. He characterizes stuttering by the occurrence of two types of phenomena: (1) iteration (repetition) and (2) inaction. He then goes on to talk about iteration and protraction markers of stuttering events. There are four major points I noted about this chapter. (1) Iteration is used in preference to repetition as repetition can involve complete segments (as, for instance, in Johnson's typology of stuttering events that is discussed later in the book). Wingate considers that repetitions involving one or more whole words are not stuttering. (2) The iteration and protraction occurs at the onset of a word (or syllable). (3) The problem of stuttering involves making the transition between consonants at onset and a subsequent vowel. (4) (Referring back to the reliability issues first raised in Chap. 2) the stuttering events as Wingate defines them can be identified reliably (that might be brought about by concentration on iterated and protracted events, though this point is never defended).

Chapter 4 presents a selection of research findings that Wingate considers are reliable (p. 11). His selection starts with singing, rhythmic speaking, masking, and delayed auditory feedback (DAF), all of which ameliorate the disorder. Though this selection is sold to the reader by the reliability criterion, it is, to some extent subjective. In particular, the selection lends itself to Wingate's interpretation, in Chap. 2, that the problem of stuttering involves making a transition from the consonant onset to the following vowel. Both the interpretation and the selection can be criticized. In singing, for example, he presents data from Vennard and Irwin (1966) on consonant and vowel (C-V) time in speech and song and states that ''An obvious difference is that, in singing, there is a clear emphasis on voicing, as expressed through the vowel forms of the lyrics'' (p. 66). What the data actually show is that vowels take up the majority of time and that all phones are lengthened in singing proportional to the time they take in speech. This is an important point as, rather than showing that fluency-enhancing procedures affect the vowel (the C-V juncture in particular), the finding may just show that slowing speech ameliorates the problem that is an explanation that

 0001-4966/2002/112(4)/1229/3/$19.00

would apply to other procedures as well as those selected. Concerning his selection of studies, those on auditory influences are somewhat dated. Masking and DAF have undesirable side effects on speech. More recent techniques like frequency-shifted feedback (FSF) avoid these side effects (Howell *et al.*, 1987) and have been the subject of extensive research investigation. FSF is also available as a portable aid for the treatment of stuttering. FSF receives no mention in the volume either as a fluency-enhancing technique or in his consideration of devices (p. 377), possibly because they do not fit with his view that effective amelioration needs to operate specifically on the vowel portion.

Next he considers three related topics—that stuttering is a disorder of childhood, it remits in many individuals, and has a prevalence of about 1%. As he says, the interrelationship between these ''is captured by pointing out that prevalence of stuttering is some function of age because many stuttering youngsters no longer stutter as childhood passes'' (p. 70). One might ask, given Wingate's position that stuttering is a speech disorder, what aspect of speech has changed that leads some children to cease stuttering? I will offer some observations on this that also touch on point (1) I picked up on in Chap. 3, later in this review. Wingate's own focus on these matters is to caution about the supposed development of stuttering insofar as it leads to a preoccupation with ''learned behaviors'' (harping back to the issue about Johnson's work raised in the first chapter) whereas, for him, it is a disorder of speech production. Other topics covered are genetics, the gender ratio, mental retardation, personality, and universality.

Chapter 5 contains a coherent argument about whether understanding about the disorder is informed by the testimonies of people who stutter. Self-help groups will obviously have something to say about this, but it is not a topic I would wish to comment on. Chapter 6 discusses ''deceptive concepts'' where he debunks different extant ''theories.'' The consideration includes the distraction hypothesis of Bloodstein (1993) where stuttering is regarded as being ameliorated by distracting events (such as those considered in Chap. 4); whether consonants are more difficult than vowels; whether people who stutter avoid difficult sounds or feared words; why stuttering decreases when speaking the same material on subsequent occasions (the adaptation effect); and whether people who stutter anticipate their stuttering and attempt to avoid difficult sounds. These can pass with no comment other than alerting readers who would not want these dismissed as ''deceptive.'' A section on the two most important variants of learning theory (learning theory and conflict theory) that relate to the avoidance topic in the preceding list, follows. Both these variants, Wingate concludes, ''lack scientific merit'' (p. 129). Once again there are specialists around who will want to pick up on this and other details of this argument. For instance, though there was an initial connection between Johnson's original ideas about stuttering as a psychological problem and learning, it is not clear whether current practitioners using learning theory would necessarily want to link their ideas to Johnson's as Wingate implies.

Chapter 7 offers some directives on tightening up terms used in the field. Some (like whether the word ''stutterer'' is acceptable rather than the term ''person who stutters'') are not issues that I would want to defend or criticize. His point about this example is that the ''er'' at the end of ''stutterer'' is an agentive suffix and, as such, does not include anything disparaging about individuals who are referred to by this term. Other issues he raises (like the use of disfluency/dysfluency) are matters that professional associations rule on. However, there are more substantive issues raised in this chapter. (1) Repetition includes repetition at a variety of levels (an issue first raised in chapter three). (2) Hesitation events need subdividing and related to findings on fluent speech. (3) From the iteration-inaction perspective, stuttering only occurs on the first part of words. Therefore, whole word repetitions are not stuttering events [as in Conture's (1990) within word-between word scheme for classifying stutters]. (4) Similarly, Yairi and Ambrose's (1992) ''stuttering like disfluencies'' are not stuttering events. A propos the latter, Wingate's categorical definition implies that they either are, or they are not, stuttering, there is no half way about it (as use of the word ''like'' implies).

Both Conture and Yairi and Ambrose are concerned with stuttering in childhood that is not Wingate's specialization. Whole word repetition is common in children diagnosed by clinicians as stuttering and such repetitions occur mainly on function words (Howell *et al.*, 1999). Older speakers who stutter have problems on the first part of content words, which are the true signs of stuttering for Wingate (Howell *et al.*, 1999). The EXPLAN theory developed by my research group maintains that both these are indications of an underlying problem in the vicinity of function and content words that are grouped together phonologically. In an utterance like ''I split it,'' for example, the problem is considered to be the time taken to generate the spl-cluster. More time is needed to generate the rest of the plan (''-it'' in this case), and stuttering does not arise out of some error-prone planning process. According to EXPLAN, children who repeat function words are dealing with the unavailability of the last part of the plan by repetition and hesitation that stalls the time of onset of the following word, allowing more time for the generation of the last part. Adults who stutter advance from the function word to the first part of ''split'' trusting that the remaining part will be generated in the time taken for execution of the first part. If this fails, stuttering involving onsets on content words ensues. Howell *et al.* (1999) have shown that the two ways of dealing with this problem are reciprocally related over age groups. Thus, young children who stutter show a high proportion of word repetition on function words but a low rate on content words whereas adults who stutter show the opposite. This exchange between stuttering event types would not be captured if Wingate's way of identifying stutterings was adopted. It should be noted in passing that it also gives a different interpretation of the role of pauses (Howell and Au-Yeung, 2002). It suggests that the notions behind Conture's ideas about between and within stutterings (associated with function and content words, respectively) and Yairi and Ambrose's (1992) notion of stuttering-like disfluencies that emphasize the importance of context may provide important information about the way stuttering develops. Wingate denies such demonstrated development of the disorder over ages (as put emphatically on p. 372 ''Stuttering does not 'develop' ''). The theory also has treatment implications that are not ''retrofitted'' that have been tested (Howell *et al.*, 2001).

Chapter 8 makes the point that stuttering is not a form of speech that is related to normal nonfluencies (i.e., fluency breakdowns that fluent individuals suffer). (This topic is also aired in Chap. 10.) Chapter 9 stresses the importance of assessing speech and emphasizes that familiarity with written forms of language can be misleading to investigators and to sufferers of the disorder.

It is pointed out in Chap. 10 that there is a wealth of literature on fluent speakers that has ramifications about stuttering [particularly Goldman-Eisler's (1968) work on pause phenomena, the frequency with which they occur and that they are inherent to speech processes, not a disturbance to those processes]. On p. 200 he argues that people who stutter lie outside the range of what is normal in these respects (offering further support for his view that stuttering is an identifiable disorder, not nonfluent speech at the limits of the normal range). Picking up on the point about dated references made in paragraph 3, that bear on the issues raised in Chap. 7, Wingate does not seem to be familiar with a lot of important recent work on the role of pausing and repetition (Chap. 7) in fluent speech and in stuttering, for instance, Gee and Grosjean's work that shows pause location is not syntactically determined, and Levelt's (1983) perspective about hesitation phenomena (point of interruption) and repetition of words (retraces, which are a form of word repetition in repairs). Levelt's (1989) later work does get passing mention at other points in the book, but not the perspective he has given of fluency breakdown as a contextual effect that led to the covert repair hypothesis (Postma and Kolk, 1993). The latter is paid lip service at other points in the volume. Chapter 10 finishes with a critique of Johnson's categories for scoring stuttering that Wingate regards as obscuring the clearcut differences between the fluency groups considered.

Chapter 11 presents some details the author considers necessary to understand ''normal speech processes.'' The second half of this chapter contains a review of some important old studies on usage of different word types (function and content). The high usage of content words in early life is documented. The introduction of function words into speech with onset of syntax and changes in frequency of use may afford the basis of an explanation of developmental changes, but this topic is not developed. Increased speech rate over age groups appears to be brought about by ceasing using filled pauses (p. 277) and it is possible that children who stutter have difficulties making this transition (an issue, again, that is not discussed). The reader's attention is, however, drawn to aspects of lexical retrieval that change over development that may also address developmental changes in forms of fluency breakdown in fluent speakers. On p. 317, he notes that children's speech is simpler, has a limited vocabulary, slower, has clearer pauses and has a degree of redundancy. These are aspects how speech, not stuttering (as in Chap. 10), develops that might impact on the disorder. No indication is given, however, whether these could lead to, for example,

remission of the disorder in younger children (that is acknowledged on p. 70 in Chap. 3). Wingate's view that stuttering is a disorder of speech involving word onsets is extended. Content words carry stress in English and are the words that attract Wingate's form of stuttering (Howell *et al.*, 1999). The stress on content words may prevent speakers who stutter from blending the onset with the later part of the word (developed further in Chap. 12).

Chapter 12 builds on Wingate's (1988) review on linguistic determinants. He now sees grammatical class (content/function) as the principal underlying factor. Though the word-type distinction is important (Howell *et al.*, 1999), its essence is that it unifies several disparate influences (as Wingate recognizes, p. 313). However, the unification offered is to some extent language-specific (for instance, two differences between Spanish and English are that in the former there is less of a difference between function and content words in terms of phonological difficulty and that function words can carry stress in Spanish) that affect how the function-content distinction captures these attributes. Thus, different ways of specifying some of the variables controlling stuttering are needed for languages with different structural properties.

Chapter 13 includes details of the neural background that is largely restricted to an examination of the cerebral cortex and the thalamus. Little is said about brain imaging that has implicated other structures such as the cerebellum (see for instance, Ingham *et al.*, 1997).

Overall the volume presents a strong, clearly articulated position by one researcher. Such a strong statement is good for the field. Whether it is right in its entirely or in some of its foundation elements will be an issue debated for some years to come.

Bloodstein, O. (**1993**). *Stuttering: The Search for a Cause and a Cure* (Allyn & Bacon, Boston).

Conture, E. G. (**1990**). *Stuttering*, 2nd ed. (Prentice–Hall, Englewood Cliffs, NJ).

Goldman-Eisler, F. (**1968**). *Psycholinguistics: Experiments in Spontaneous Speech* (Academic, New York).

Howell, P., and Au-Yeung, J. (**2002**). ''The EXPLAN theory of fluency control and the diagnosis of stuttering.'' Pathology and therapy of speech disorders, in *Current Issues in Linguistic Theory* series, Volume Editor E. Fava (Benjamin, Amsterdam), pp. 75-94.

Howell, P., Au-Yeung, J., and Sackin, S. (**1999**). ''Exchange of Stuttering from Function Words to Content Words with Age,'' J. Speech Lang. Hear. Res. **42**, 345–354.

Howell, P., El-Yaniv, N., and Powell. D. J. (**1987**). ''Factors affecting fluency in stutterers when speaking under altered auditory feedback,'' in *Speech Motor Dynamics in Stuttering*, edited by H. Peters and W. Hulstijn (Springer, New York), pp. 361–369.

Howell, P., Au-Yeung, J., Charles, N., Davis, S., Thomas, C. Reed, P., Sackin, S., and Williams, R. (**2001**). ''Operant procedures that increase function word repetition used with children whose speech had not improved during previous treatment,'' in *Fluency Disorders: Theory, Research, Treatment and Self-Help, Proceedings of the Third World Congress of Fluency Disorders*, Nyborg, Denmark, edited by H-G. Bosshardt, J. S. Yaruss, and H. F. M. Peters (International Fluency Association, Nijmegen University Press, Nijmegen), pp. 133–137.

Ingham, R. J., Fox, P. T., and Ingham, J. C. (**1997**). ''An $H_2{}^{15}O$ position emission tomography (PET) study on adults who stutter,'' in *Speech Production: Motor Control, Brain Research and Fluency Disorders*, edited by W. Hulstijn, H. F. M. Peters, and P. H. H. M. van Lieshout (Elsevier, Amsterdam), pp. 293–305.

Levelt, W. (**1983**). ''Monitoring and self-repair in speech,'' Cognition **14**, 41–104.

Levelt, W. J. M. (**1989**). *Speaking: From Intention to Articulation* (Bradford, Cambridge, MA).

Postma, A., and Kolk, H. (**1993**). ''The covert repair hypothesis: Prearticulatory repair processes in normal and stuttered disfluencies,'' J. Speech Hear. Res. **36**, 472–487.

Vennard, W., and Irwin, J. W. (**1966**). ''Speech and song compared in sonograms,'' Natl. Assoc. Teach. Sing Bull. **23**, 18–23.

Wingate, M. E. (**1988**). *The Structure of Stuttering* (Springer-Verlag, New York).

Yairi, E., and Ambrose, N. (**1992**). ''A longitudinal study of stuttering in children: A preliminary report,'' J. Speech Hear. Res. **35**, 755–760.

PETER HOWELL
Psychology Department
University College London
London WC1H 0AP, United Kingdom

REVIEWS OF ACOUSTICAL PATENTS

Lloyd Rice
11222 Flatiron Drive, Lafayette, Colorado 80026

The purpose of these acoustical patent reviews is to provide enough information for a Journal reader to decide whether to seek more information from the patent itself. Any opinions expressed here are those of reviewers as individuals and are not legal opinions. Printed copies of United States Patents may be ordered at $3.00 each from the Commissioner of Patents and Trademarks, Washington, DC 20231. Patents are available via the Internet at http://www.uspto.gov.

Reviewers for this issue:

GEORGE L. AUGSPURGER, *Perception, Incorporated, Box 39536, Los Angeles, California 90039*
MARK KAHRS, *Department of Electrical Engineering, University of Pittsburgh, Pittsburgh, Pennsylvania 15261*
DAVID PREVES, *Micro-Tech Hearing Instruments, 3500 Holly Lane No., Suite 10, Plymouth, Minnesota 55447*
DANIEL R. RAICHEL, *2727 Moore Lane, Fort Collins, Colorado 80526*
CARL J. ROSENBERG, *Acentech, Incorporated, 33 Moulton Street, Cambridge, Massachusetts 02138*
ROBERT C. WAAG, *Univ. of Rochester, Department of Electrical and Computer Engineering, Rochester, New York 14627*

6,368,292

43.25.Vt METHOD FOR USING ACOUSTIC SHOCK WAVES IN THE TREATMENT OF MEDICAL CONDITIONS

John A. Ogden and John F. Warlick, assignors to Healthtronics, Incorporated
9 April 2002 (Class 601/2); filed 22 December 1999

The patent relates to methods for medical treatment of pathological conditions through the use of acoustic shock waves. Such pathological conditions include possibly planar warts, deep bone bruises, prostate cancer, benign prostatic hypertrophy, urinary incontinence, and spinal cord injuries, including the reduction or removal of scar tissue to aid in spinal cord regrowth.—DRR

6,359,991

43.38.Bs GREETINGS OR THE LIKE CARD

Henry Azima *et al.*, assignors to New Transducers Limited
19 March 2002 (Class 381/152); filed in the United Kingdom 2 September 1919

In the continuing stream of patents from NXT, this one is for using a thin honeycomb panel for a greeting card so that the panel itself can be used as the vibrating membrane.—MK

6,349,141

43.38.Fx DUAL BI-LAMINATE POLYMER AUDIO TRANSDUCER

Robert D. Corsaro, assignor to the United States of America as represented by the Secretary of the Navy
19 February 2002 (Class 381/190); filed 10 October 2000

The basic device is a kind of active leaf spring. A flexible, laminated assembly includes PVDF film strips **22** and **32**. Applied voltage expands or contracts the strips lengthwise, changing the height of the assembly along

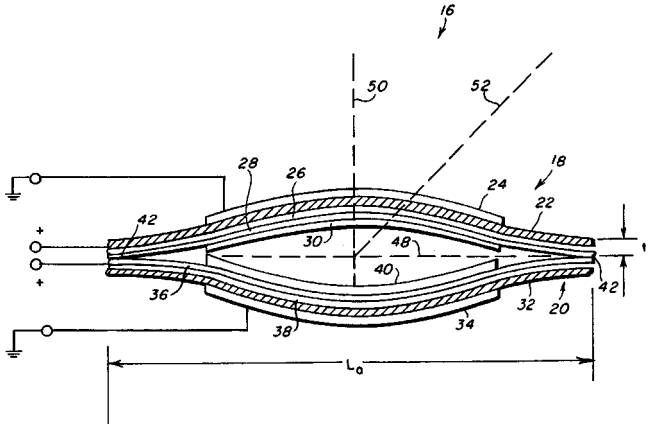

axis **50**. An array of these flextensional motors can be covered by a flat panel to form a thin, very light, loudspeaker. As with all such devices, the stiffness of the air trapped under the panel severely restricts low-frequency efficiency unless the air is vented to a relatively large rear cavity.—GLA

6,359,990

43.38.Hz PARAMETRIC RING EMITTER

Elwood G. Norris, assignor to American Technology Corporation
19 March 2002 (Class 381/77); filed 18 August 1998

By modulating a beam of ultrasonic energy, audible sound can be made to emanate from empty air. Considerable work has been devoted to this concept in recent years, but practical utilization seems to involve as many shortcomings as benefits. The patent suggests that a ring-shaped emitter of proper dimensions can be substantially more efficient than a continuous emitting surface of the same diameter.—GLA

6,351,542

43.38.Ja LOUDSPEAKERS WITH PANEL-FORM ACOUSTIC RADIATING ELEMENTS

Henry Azima *et al.*, assignors to New Transducers Limited
26 February 2002 (Class 381/345); filed in the United Kingdom 2 September 1995

Transducer **9** and sound-radiating panel **2** form a distributed mode loudspeaker, as described in several earlier patents. At low frequencies the panel is pneumatically driven by fluctuating air pressure from woofer **42**

 0001-4966/2002/112(4)/1233/16/$19.00

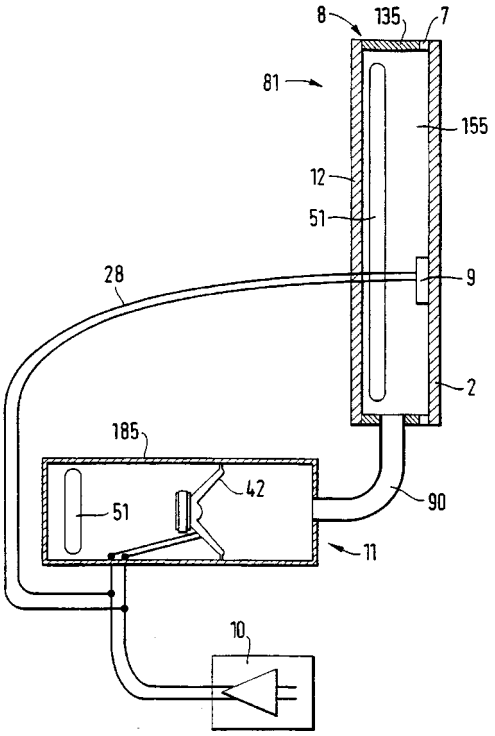

conducted through pipe **90**. Since air is compressible, the system as drawn is actually some kind of multi-resonant bandpass arrangement, which may or may not be what the inventors had in mind.—GLA

6,353,670

43.38.Ja ACTIVELY CONTROL SOUND TRANSDUCER

Donald R. Gasner, Torrance, California
5 March 2002 (Class 381/96); filed 27 August 1997

Loudspeaker experimenters are fascinated by "isobaric" designs in which the air cavity behind a loudspeaker **73** is effectively enlarged by the action of a second loudspeaker **79**. The inventor rightly points out that, with a suitable signal to the rear speaker, such a system can produce a variety of

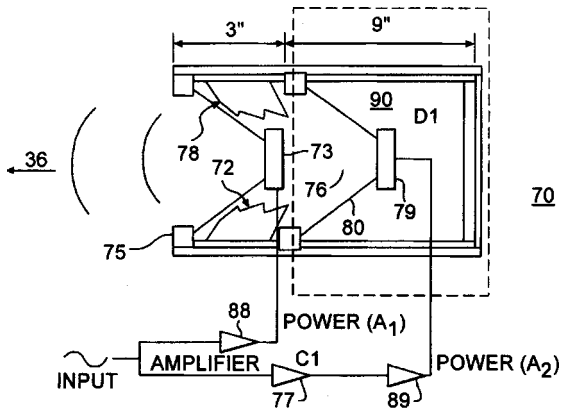

effects not possible with a passive air chamber. Yes, but couldn't those same effects be produced by feeding a suitable signal to the front speaker and dispensing with all the other paraphernalia?—GLA

6,359,996

43.38.Ja SPEAKER DEVICE

Yoshio Ohashi, assignor to Sony Corporation
19 March 2002 (Class 381/401); filed in Japan 19 November 1998

In this induction speaker, primary coil **17A** is fitted with a positioning

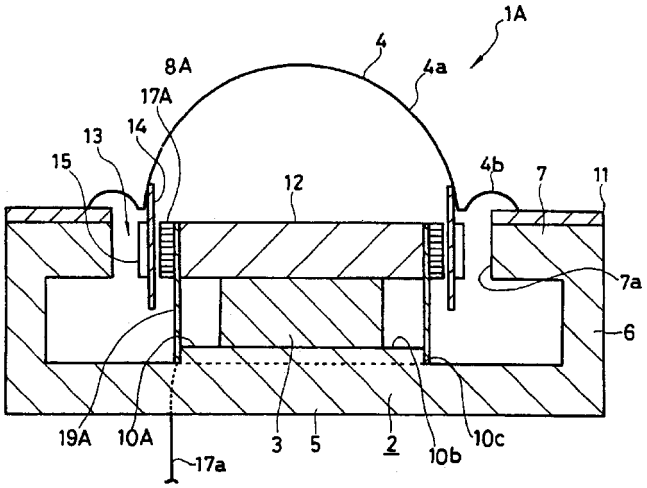

collar **19A** to simplify assembly and allow closer tolerances, thus improving efficiency.—GLA

6,356,643

43.38.Ja ELECTRO-ACOUSTIC TRANSDUCER

Makoto Yamagishi and Masao Fujihira, assignors to Sony Corporation
12 March 2002 (Class 381/349); filed in Japan 30 January 1998

The inventors have discovered that a loudspeaker enclosure in the shape of a doughnut miraculously eliminates standing waves, lowers distortion, and smooths frequency response. To support these assertions, comparative test results are shown: a conventional vented box versus a vented

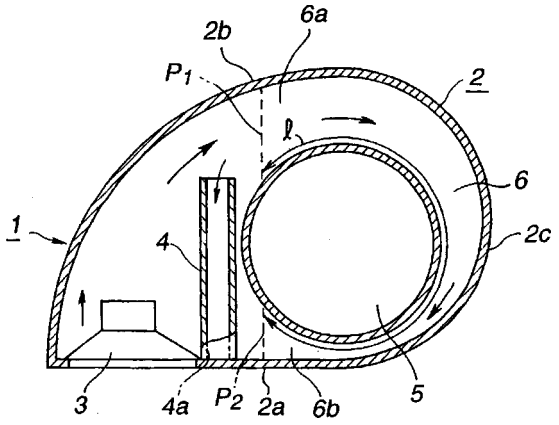

doughnut, and a conventional sealed box versus a sealed doughnut. To this reviewer, the conventional enclosures fare somewhat better, although performance is generally comparable. Apparently, distortion is in the eye of the beholder.—GLA

6,356,642

43.38.Ja MULTI-SPEAKER SYSTEM

Takeshi Nakamura *et al.*, assignors to Murata Manufacturing Company, Limited
12 March 2002 (Class 381/342); filed in Japan 27 December 1997

The upper ''saltshaker'' speaker assembly includes dome diaphragm **12** and rear labyrinth **30** exiting through openings **54**. This is described in two earlier patents (United States Patents 5,802,196 and 5,896,460) whose

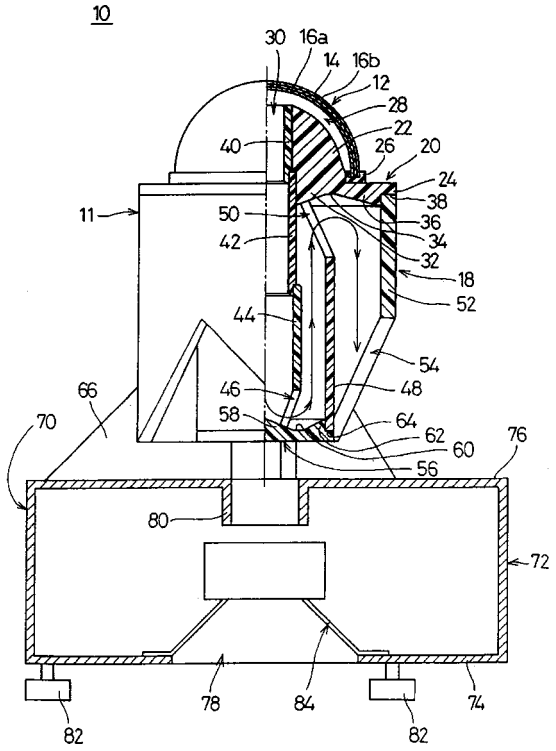

filings go back to 1996. The latest variant includes woofer **84** mounted in vented base cabinet **72**.—GLA

6,359,997

43.38.Ja LOUDSPEAKER HAVING RADIALLY MAGNETIZED MAGNETIC RING

Stefan Geisenberger and Gerhard Krump, assignors to Harman Audio Electronic Systems GmbH
19 March 2002 (Class 381/412); filed in Germany 26 April 1996

A gapless moving coil loudspeaker relies on stray flux from a radially magnetized permanent magnet to energize its voice coil. ''As can easily be seen, the induction from radially magnetized permanent magnets **12** is constant along the jacket surfaces **19**, **20** so that the voice coil **16** moves in a homogeneous magnetic field along its entire deflection path, which in the final analysis leads to a very linear operation of the loudspeaker **10**.''—GLA

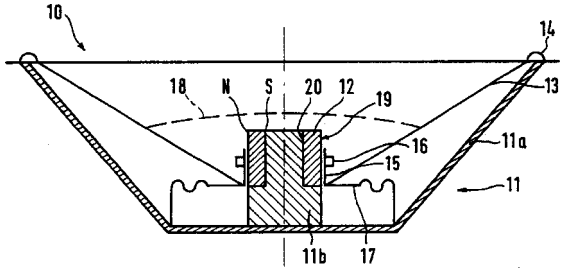

6,351,543

43.38.Kb MICRO-MICROPHONE

Hugo Lenhard-Backhaus and Richard Pribyl, assignors to AKG Acoustics GmbH
26 February 2002 (Class 381/360); filed in Austria 23 March 1999

Tiny ''grain of wheat'' microphones worn by performers are often in direct contact with the skin. Air pressure equalization for the chamber behind the diaphragm is normally provided by a small opening which can allow moisture to contaminate the interior of the microphone. The invention solves this problem by interposing a watertight flaccid membrane which effectively seals the interior of the microphone, yet can deform sufficiently to provide pressure compensation.—GLA

6,353,584

43.38.Md REPRODUCING AND RECORDING APPARATUS, DECODING APPARATUS, RECORDING APPARATUS, REPRODUCING AND RECORDING METHOD, DECODING METHOD AND RECORDING METHOD

Tomohiro Koyata, assignor to Sony Corporation
5 March 2002 (Class 369/47.13); filed in Japan 14 May 1998

Sony's ATRAC coder was used in the Minidisk™. This patent notices that you can change the ''acoustic characteristics'' of the final output by scaling the coded parameters. Besides fade in and out, limiting and compression are also possible.—MK

6,366,545

43.38.Md REPRODUCING AND RECORDING APPARATUS, DECODING APPARATUS, RECORDING APPARATUS, REPRODUCING AND RECORDING METHOD, DECODING METHOD AND RECORDING METHOD

Tomohiro Koyata, assignor to Sony Corporation
2 April 2002 (Class 369/59.16); filed in Japan 14 May 1998

This is another ATRAC™ patent from Sony, basically identical, word for word, with United States Patent 6,353,584, reviewed above.—MK

6,366,971

43.38.Md AUDIO SYSTEM FOR PLAYBACK OF WAVEFORM SAMPLE DATA

Tokiharu Ando and Takashi Suzuki, assignors to Yamaha Corporation
2 April 2002 (Class 710/53); filed in Japan 9 January 1998

This patent describes the mechanisms behind a PCI audio card with multiple input channels and using burst transfers across the bus to an onboard memory. The patent is neither grammatically written nor intended to be understood.—MK

6,372,974

43.38.Md METHOD AND APPARATUS FOR SHARING MUSIC CONTENT BETWEEN DEVICES

Mark T. Gross and Robert A. Jacobs, assignors to Intel Corporation
16 April 2002 (Class 84/609); filed 16 January 2001

This clearly patents the obvious. Infrared transfer of data between calculators or computers has been used for many years. Change the device to an MP3 player and that's it.—MK

6,356,644

43.38.Si EARPHONE (SURROUND SOUND) SPEAKER

Alex Pollak, assignor to Sony Corporation; Sony Electronics, Incorporated
12 March 2002 (Class 381/371); filed 20 February 1998

To reproduce surround sound through headphones one might argue that each ear should be surrounded by transducers. A number of such designs have already been patented. In this Sony variant, one speaker **23**

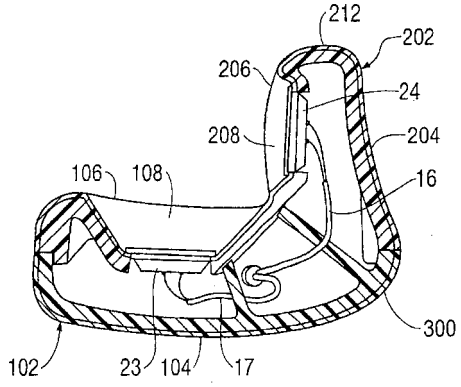

projects sound directly into the auricle. At least one additional speaker **24** is located farther away. Signals to the two speakers may be delayed, filtered, fed from separate channels, or any combination thereof.—GLA

6,349,285

43.38.Vk AUDIO BASS MANAGEMENT METHODS AND CIRCUITS AND SYSTEMS USING THE SAME

Pu Liu *et al.*, assignors to Cirrus Logic, Incorporated
19 February 2002 (Class 704/500); filed 28 June 1999

Owners of home theater systems are familiar with setup menus that allow each loudspeaker to be categorized as small, medium, or large. The system uses this information to set high-pass filters for each speaker. At the same time, two or more channels may be summed and the combined signal fed through a low-pass filter to a subwoofer. This process is essentially what the patent sets forth except that everything, including the filters, is implemented in software.—GLA

6,364,509

43.38.Zp SOUND RESPONSIVE ILLUMINATION DEVICE

Clifford Johnson III, assignor to J & J Creative Ideas
2 April 2002 (Class 362/252); filed 30 June 2000

As if we are not besieged enough by "boom cars," along comes this device for converting audio signals into a light show through conversion of

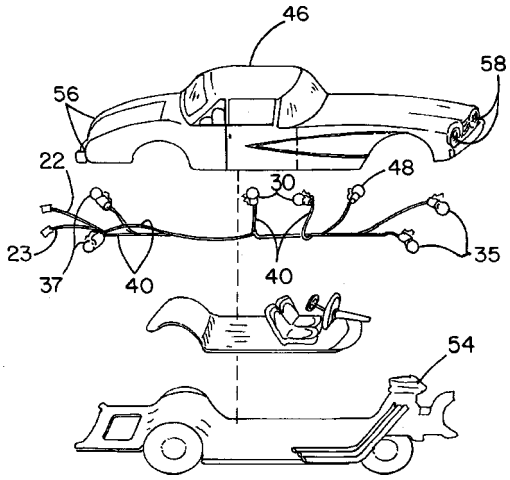

audio sound signals into electrical signals to control "musical" lights.—DRR

6,368,293

43.40.Ng RELAXATION DEVICE

Eric P. Orgeron, River Ridge and Philip J. Delatte, Metairie, both of Louisiana
9 April 2002 (Class 601/15); filed 23 December 1999

The device is a vibrating helmet intended to reduce tension and help a person to relax. It is made of a relatively soft, pliable material, with a relatively hard material such as PVC, ABS, PET, or some other plastic recessed therein in a network to transmit vibration from a central vibrator

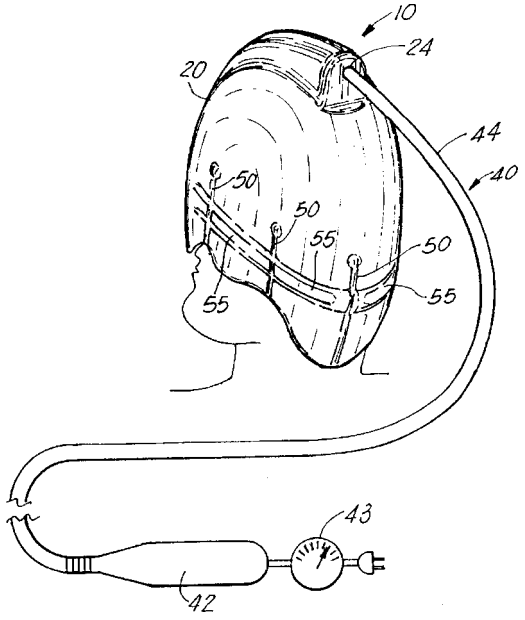

through the helmet. A small motor could generate the vibration and would have a speed control to vary the vibration intensity. The electric source of the vibration would be remote from the helmet to avoid any EMF problems.—DRR

6,362,746

43.40.Yq METHOD AND SYSTEM FOR MONITORING VIBRATION OF ROBOTS IN AN AUTOMATED STORAGE LIBRARY

Timothy C. Ostwald, assignor to Storage Technology Corporation
26 March 2002 (Class 340/683); filed 27 March 2001

This is a method and system for using a robot to store and retrieve digital media in an automated library of media storage cells, each housing a single media (e.g., a cartridge, CD, or DVD). The robot mechanism operates by moving through the storage library to access the media in the storage

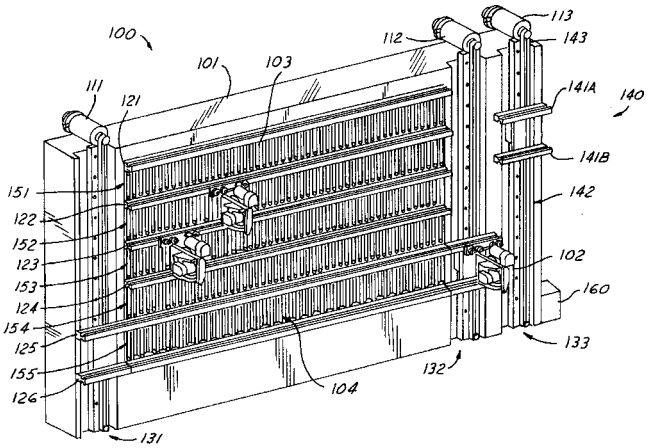

cells. The robotic mechanism includes a vibration sensor which triggers the controller to indicate abnormal vibration of the robotic mechanism. If such is the case, the controller generates a warning signal to alert the operator of a possible problem prior to the actual failure of the robotic mechanism.—DRR

6,370,957

43.40.Yq VIBRATION ANALYSIS FOR PREDICTIVE MAINTENANCE OF ROTATING MACHINES

Alexander Filippenko *et al.*, assignors to Square D Company
16 April 2002 (Class 73/660); filed 31 December 1999

A method is disclosed for determining the operational condition of a rotary machine. The method includes monitoring the machine under a baseline operating condition and baseline vibrational data. To facilitate detection of mechanical defects, the machine's mechanical vibration is converted to its electrical analog by a piezoceramic sensor, preconditioned, digitized, and recorded into a memory. The collected vibration data is used to calculate a set of statistical parameters of vibration such as root mean square (rms), kurtosis, crest factor, and high-frequency enveloping (HFE), as well as trending the mean values of selected areas of the averaged spectra.—DRR

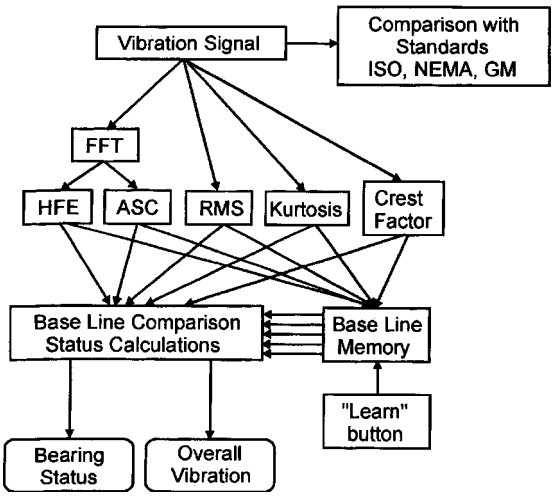

6,371,240

43.55.Pe ANECHOIC CHAMBER

Robert W. Hayes and John Phillips, assignors to Austin Acoustic Systems, Incorporated
16 April 2002 (Class 181/30); filed 23 May 2000

This modular anechoic panel system incorporates a structural support, a wedge base, and a separate removable wedge tip. The base has a metal and gypsum backing for improved transmission loss performance, and an air-

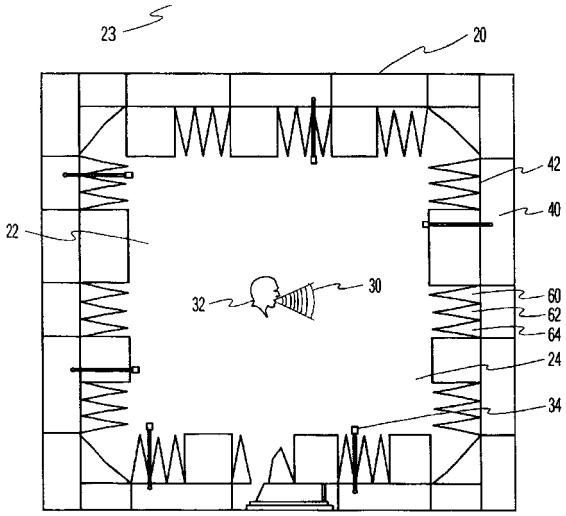

space for added low-frequency absorption. The wedge tip is protected by perforated metal and is attached to the base with a compression clip so it is easily removable.—CJR

6,368,438

43.55.Ti SOUND DEADENING AND STRUCTURAL REINFORCEMENT COMPOSITIONS AND METHODS OF USING THE SAME

Chin-Jui Chang and Gerald Fitzgerald, assignors to Sika Corporation
9 April 2002 (Class 156/79); filed 7 February 2000

The patent describes an expandable sealant and baffle composition for sealing hollow structural members of vehicles. The composition comprises a mixture of thermoplastic resin and epoxy resin that are injection moldable and lightweight. This foam can create a freestanding, self-sustaining support when injected onto a lattice-type nylon framework.—CJR

6,353,391

43.58.Wc BABY BOTTLE LOCATING SYSTEM

Kenneth N. Shearer, Medford, Oregon
5 March 2002 (Class 340/573.1); filed 15 September 2000

Lost baby bottles cause pain and suffering for both child and parent. It's obvious that just like a lost car in the mall parking lot, all you need is a radio transmitter and a sound emitter.—MK

6,360,476

43.58.Wc AUDIBLE FISHING LURE

Nelson Anastacio, Toronto, Ontario, Canada
26 March 2002 (Class 43/42.31); filed 18 April 2000

It is claimed that fish are attracted to sounds and hence a propeller **78**, **80** can be a sound generation mechanism. When the lure is pulled, the

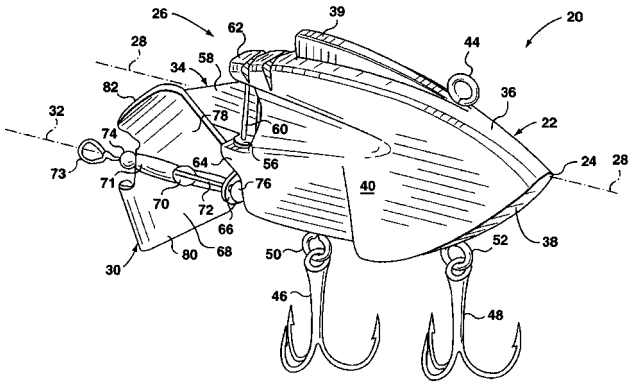

propeller rotates, hitting edge **34**, producing a clicking sound. Experimental results are not presented.—MK

6,371,053

43.58.Wc SIMULATED MOUSE TOY HAVING A PRERECORDED SOUND CHIP THEREIN

Steven Tsengas, Mentor, Ohio
16 April 2002 (Class 119/707); filed 7 January 2000

The inventor claims that cats particularly enjoy squeaking mice. So, by

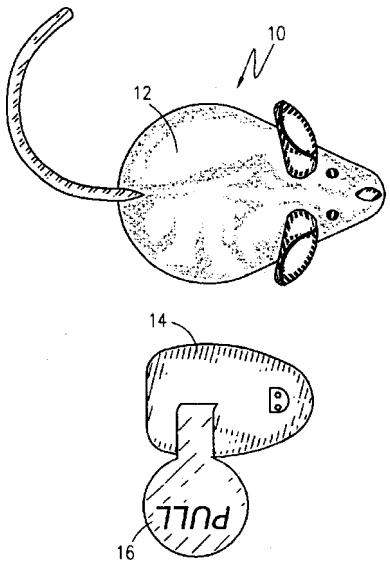

inserting a sound chip **14** into the body of a mechanical mouse, then your cat will be exercised and derive greater joy—worthy of 19 claims.—MK

6,363,514

43.60.Bf SOUND REPRODUCING SYSTEM AND METHOD CAPABLE OF DECODING AUDIO DATA EVEN IN CASE OF FAILURE OF DETECTING SYNCWORD

Takahiro Kawai and Chuya Hayashi, assignors to Mitsubishi Denki Kabushiki Kaisha
26 March 2002 (Class 714/798); filed in Japan 14 July 1998

This is a sound reproduction system that decodes audio data from frames, each provided with a syncword. Normally, a frame in which syncword detection fails would not be decoded. According to the patent, however, the frame would be decoded if a syncword is detected in a subsequent frame, if the bit stream information in the subsequent frame is proved correct, and if no cyclic redundancy check (CRC) error is detected (when CRC is included).—DRR

6,363,155

43.60.Lq PROCESS AND DEVICE FOR MIXING SOUND SIGNALS

Ulrich Horbach, assignor to Studer Professional Audio AG
26 March 2002 (Class 381/17); filed in Switzerland 24 September 1997

The patent describes a process and device for mixing sound signals. The process includes separating the signals and selectively delaying each separated signal. The process also includes selectively weighting each separated and delayed signal and adding the weighted signals into an intermediary signal. The intermediary signals may then be filtered and added to form an output signal. Each of multiple input channels may be composed of partial input channels, a decoder providing coupling between partials, intermediaries, and outputs.—DRR

6,370,255

43.66.Ts LOUDNESS-CONTROLLED PROCESSING OF ACOUSTIC SIGNALS

Artur Schaub and Remo Leber, assignors to Bernafon AG
9 April 2002 (Class 381/107); filed in Switzerland 19 July 1996

Loudness-controlled signal processing of acoustic signals within a hearing aid takes place completely in the time domain, avoiding conversion to the frequency domain with processing-intensive fast Fourier transforms. The traditional division of the audio frequency range into subbands, and the similar processing required in each subband, is also avoided. This technique is said to result in processing for loudness compensation with shorter delay times, less computational requirements, and lower power consumption. The goal of the processing is to ensure that the loudness of sounds perceived by hearing aid wearers is similar to that heard by normal-hearing persons.—DAP

6,366,678

43.66.Ts MICROPHONE ASSEMBLY FOR HEARING AID WITH JFET FLIP-CHIP BUFFER

Peter Madaffari *et al.*, assignors to Sarnoff Corporation; Tibbetts Industries, Incorporated
2 April 2002 (Class 381/324); filed 6 January 2000

A hearing aid electret microphone assembly includes a canister, a backplate **12**, and a substrate **16**, the latter two defining a cylindrical back chamber. A JFET buffer **10**, mounted on the substrate, has its gate attached directly to the backplate via conductive epoxy, thus keeping stray capacitance low and allowing use of FR4 printed circuit board material instead of a higher cost ceramic substrate. Components for the hearing aid amplifier are mounted on a second printed circuit substrate **50** also contained inside the microphone, thus eliminating several external wire connections.—DAP

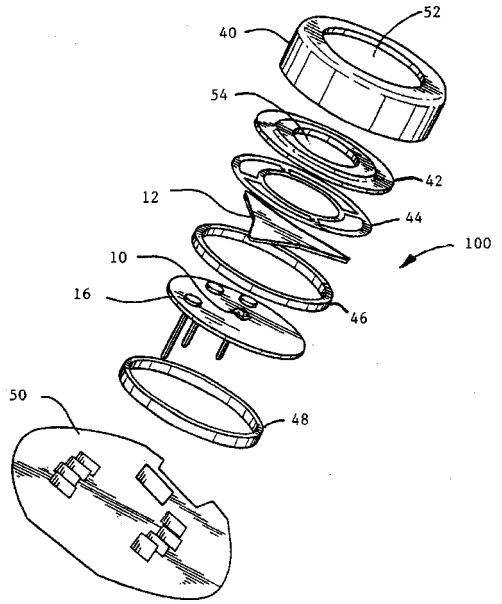

6,366,863

43.66.Yw PORTABLE HEARING-RELATED ANALYSIS SYSTEM

Gordon J. Bye *et al.*, assignors to Micro Ear Technology Incorporated
2 April 2002 (Class 702/57); filed 9 January 1998

To facilitate portability, small size, low cost, and convenience, the electronics for a hearing aid programmer, an audiometer, and a real ear hearing aid output measurement system are each packaged on PCMCIA cards. If a lap top, notebook, or hand-held host computer contains more than one PCMCIA slot, one or more of these instruments may be used. The PCMCIA cards have physical and electrical interfaces for attaching programming cords, headphones, insert earphones, patient response means, loudspeakers, and probe microphones for use in the three applications.—DAP

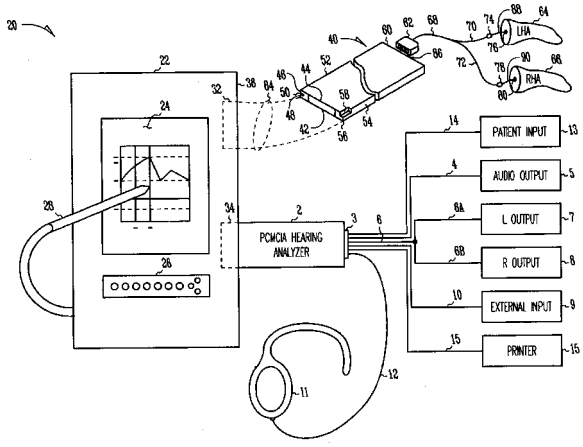

6,358,111

43.72.−p INTERACTIVE TALKING DOLLS

Peter Sui Lun Fong, Monterey Park, California and Chi Fai Mak, Kowloon, Hong Kong Special Admin. of the People's Republic of China
19 March 2002 (Class 446/297); filed 10 October 2000

The basic premise is simple enough: put a microprocessor and an infrared sensor in a doll and then it can communicate and converse with other similarly equipped dolls or TV remotes. The patent includes many hardware design details.—MK

6,366,886

43.72.Ne SYSTEM AND METHOD FOR PROVIDING REMOTE AUTOMATIC SPEECH RECOGNITION SERVICES VIA A PACKET NETWORK

Pamela Leigh Dragosh *et al.*, assignors to AT&T Corporation
2 April 2002 (Class 704/270.1); filed 24 March 2000

Automatic speech recognition (ASR) is made accessible at a remote location utilizing client-server communication over a packet network. Using ASR to order pizza over the Internet is an example provided in the patent. A grammar for the phrase to be recognized includes responses for size (i.e., large, medium, small) and a choice of topping. ASR is performed on streaming digitized speech from the client. The ASR server returns streaming text as it is recognized, even as ASR continues processing additional speech from the client. Returning recognized text quickly allows the client to provide corrections to text returned earlier for previously recognized speech.—DAP

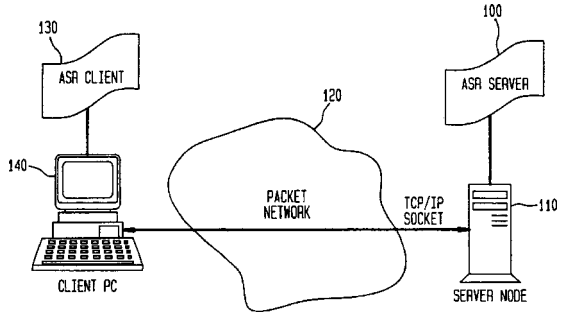

6,348,646

43.75.Gh MUSICAL INSTRUMENT STRINGS AND METHOD FOR MAKING THE SAME

Anthony Parker, Newton, Pennsylvania and Peter J. Rohrbacher, Bordentown, New Jersey
19 February 2002 (Class 84/297 R); filed 28 August 2000

The inventors propose the use of a cathodic core **15** (such as Ni or Ti) covered by a polymeric sheathing **19**. It is claimed to exhibit ''superior

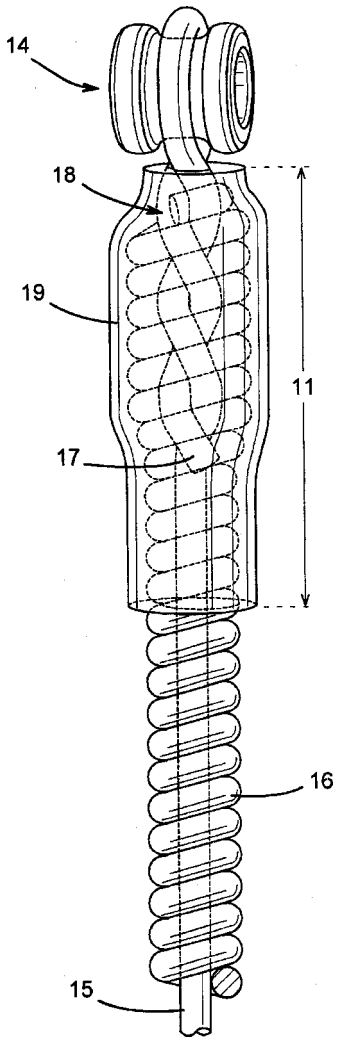

corrosion resistance and quality'' and ''low tension at pitch for reduced stress on musical instruments.'' The patent is written clearly and with a historical bent.—MK

6,372,971

43.75.Gh MODIFIED STRINGED MUSICAL INSTRUMENT

Jack Rogers, Hillsboro, Ohio
16 April 2002 (Class 84/298); filed 24 May 2000

The inventor has added a variable damper to the guitar bridge. The patent states that this ''reduces the stress on the musical instrument, improves the sound of the instrument and increases the operative life span of the instrument.''—MK

6,362,407

43.75.Hi DRUM PRACTICE PADS AND DRUM PAD MUSICAL INSTRUMENTS

Denny R. Dennis, Garden Grove and Marcel R. Daignault, Anaheim, both of California
26 March 2002 (Class 84/411 P); filed 27 April 2000

Drum pads need to be quiet. This patent proposes a maple substrate with a rubber covering. Surely this belongs to the obvious category?—MK

6,369,304

43.75.Hi SELECTED PERCUSSION ADDITIONS FOR STRINGED MUSICAL INSTRUMENTS

Nancy Tucker, Beacon Falls, Connecticut
9 April 2002 (Class 84/291); filed 20 March 2001

Drumming the top plate of a guitar is a well-known technique for adding percussive effects. The inventor proposes the addition of insertable percussion ''additions'' to the offset sound holes in commercial guitars. Additional miking may be required.—MK

6,362,406

43.75.Kk SHAKEN IDIOPHONE

Raymond Enhoffer *et al.*, assignors to Latin Percussion, Incorporated
26 March 2002 (Class 84/402); filed 17 January 2001

Take two halves **22** and **24**, attach them together with a screw and a

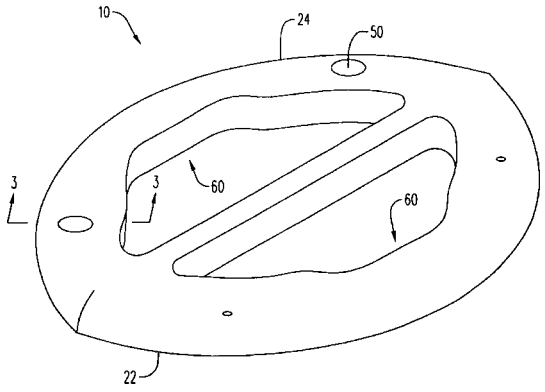

spring **50**, and you have an instrument worthy of shaking. The spring provides for a volume that will vary depending on hand pressure.—MK

6,359,207

43.75.Mn POSITION TRANSDUCER SYSTEM WITH BUILT-IN CALIBRATOR FOR MOVING OBJECT, METHOD FOR ACCURATELY DETERMINING POSITION OF MOVING OBJECT AND KEYBOARD MUSICAL INSTRUMENT EQUIPPED WITH THE POSITION TRANSDUCER SYSTEM

Yasuhiko Oba *et al.*, assignors to Yamaha Corporation
19 March 2002 (Class 84/658); filed in Japan 23 October 1998

To accurately reproduce a piano tone on a player piano, the key velocity must be measured, stored, and then mechanically reproduced. Another Yamaha Disklavier™ patent, it includes details of the sensor and suitable modifications to the hammer mechanism with actuators.—MK

6,362,405

43.75.Mn HYBRID MUSICAL INSTRUMENT EQUIPPED WITH STATUS REGISTER FOR QUICKLY CHANGING SOUND SOURCE AND PARAMETERS FOR ELECTRONIC TONES

Shinya Koseki and Haruki Uehara, assignors to Yahama Corporation
26 March 2002 (Class 84/2); filed in Japan 12 January 2000

The Diskclavier™ is a well-known Yamaha product that is not only capable of recording an artist's work but also playing it back. This particular patent describes the internal construction of the key mechanism that can

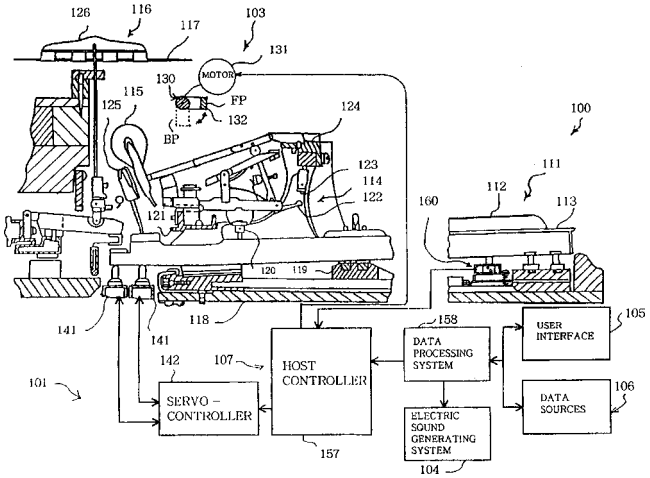

either act as a sensor **160** for an electronic synthesizer or generate acoustic piano sounds. The strings can also be hit by a solenoid key actuator **141**.—MK

6,362,412

43.75.Mn ANALYZER USED FOR PLURAL PHYSICAL QUANTITIED, METHOD USED THEREIN AND MUSICAL INSTRUMENT EQUIPPED WITH THE ANALYZER

Tomoyuki Ura, assignor to Yamaha Corporation
26 March 2002 (Class 84/658); filed in Japan 29 January 1999

An acoustic piano player develops an appreciation for the ''action.'' Electronic piano keys have lacked the tactile feedback that performers pre-

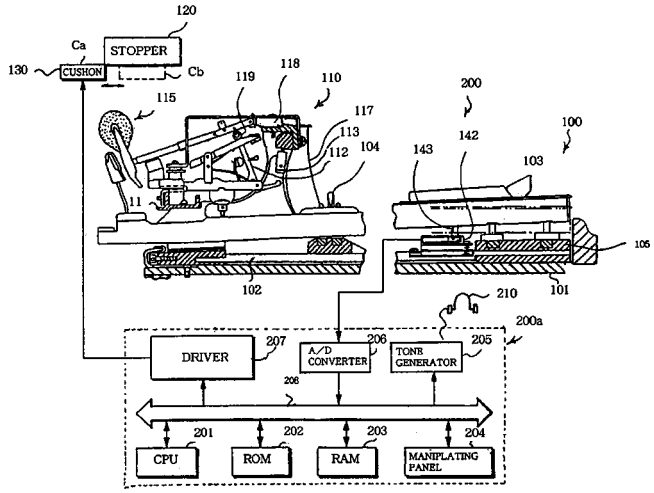

fer. This patent proposes the insertion of a photo sensor **142** under the key. The output of the sensor is digitized and used for the control of the sound.—MK

6,372,973

43.75.St MUSICAL INSTRUMENTS THAT GENERATE NOTES ACCORDING TO SOUNDS AND MANUALLY SELECTED SCALES

M. Bret Schneider, assignor to Schneidor Medical Technologies, Incorporated
16 April 2002 (Class 84/609); filed 18 May 1999

This conceptual patent proposes accompaniment to a vocal input but it lacks any reference to prior work on automatic accompaniment, much less DSP algorithms for pitch tracking and beat analysis.—MK

6,366,758

43.75.St MUSICAL CUBE

Steven Bryan Dunn and Norman Weinberger, assignors to Munchkin, Incorporated
2 April 2002 (Class 434/319); filed 20 October 1999

In keeping with the increased emphasis on early childhood musical education, this musical cube presents a set of progressively more complex

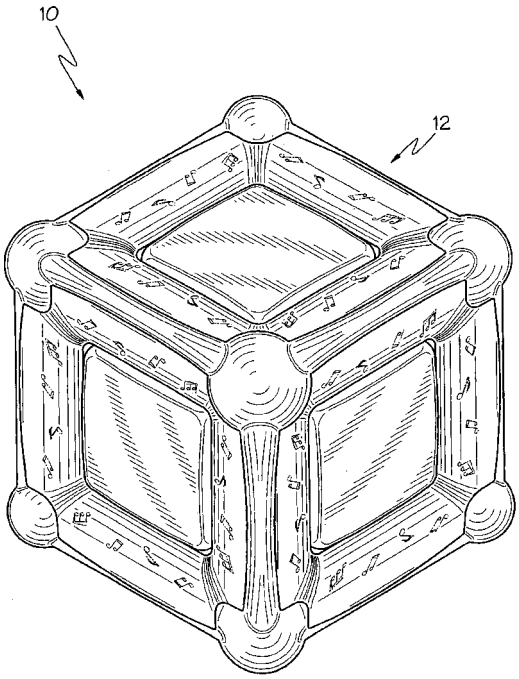

musical material that is (1) Western (or tonal), (2) Melodic, and (3) not too fast.—MK

6,369,313

43.75.St METHOD AND APPARATUS FOR SIMULATING A JAM SESSION AND INSTRUCTING A USER IN HOW TO PLAY THE DRUMS

John R. Devecka, Clifton, New Jersey
9 April 2002 (Class 84/743); filed 21 February 2001

A coin operating drum set features a screen **107** and a set of drum sensors. A willing user is calibrated by the system to determine skill level and then a drumming game begins. Alternatively, the user can receive a

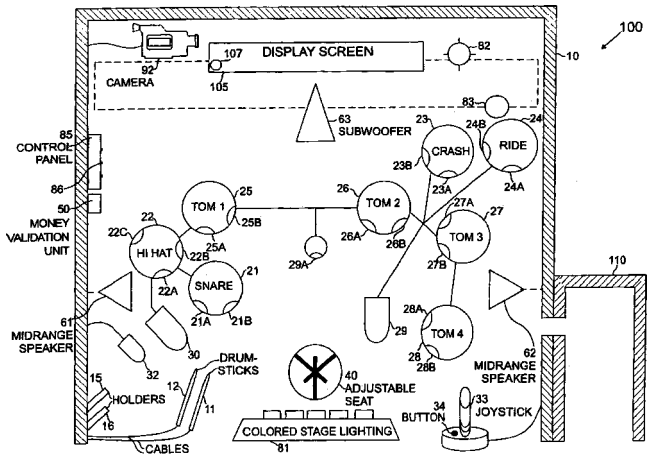

drum lesson by repeating patterns the machine generates. Unfortunately, no algorithms are presented so performance measurement is anyone's guess. —MK

6,349,851

43.75.Tv VOCAL DISPENSING DEVICE

Pao-Shu Lu, assignor to Allure Home Creation Company, Incorporated
26 February 2002 (Class 222/39); filed in Taiwan, Province of China, 4 October 2000

Already we've seen talking alcohol beverages (United States Patent 6,335,691) and food boxes (United States Patent 6,298,990). So why

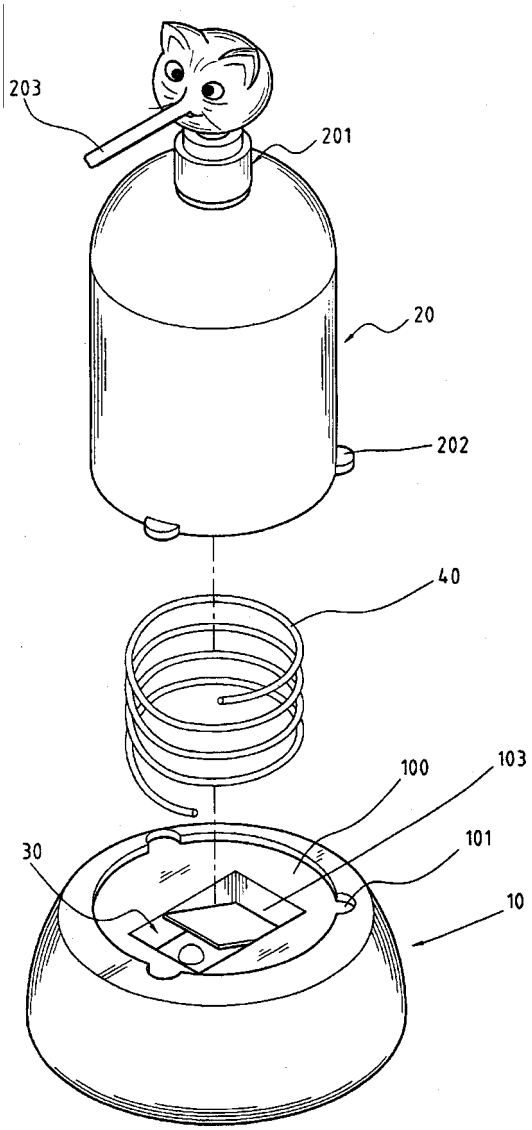

not soap dispensers? The patent describes different activation mechanisms. —MK

6,369,312

43.75.Tv METHOD FOR EXPRESSING VIBRATORY MUSIC AND APPARATUS THEREFOR

Akira Komatsu, assignor to Acouve Laboratory, Incorporated
9 April 2002 (Class 84/723); filed in Japan 14 September 1999

Imagine a chair with infrasound—in this case down to 16 Hz. The inventor claims that it is unsuitable for certain types of music (such as string quartets) but for heavy thumping rock and roll, this might be useful if the vibro-transducers can shake the user enough.—MK

6,351,225

43.75.Wx MULTIMEDIA PC KEYBOARD EXTENDED WITH MUSIC CONTROL KEYS

Enrique I. Moreno, assignor to Enrique I. Moreno
26 February 2002 (Class 341/22); filed 5 August 1999

Recipe for a combination keyboard: Take one PC keyboard. Mix together with a 3 octave subset of a piano. Add bad mechanical action.—MK

6,351,540

43.75.Wx DIGITAL ECHO CIRCUIT

Satoshi Suzuki and Takayasu Kondo, assignors to Yamaha Corporation
26 February 2002 (Class 381/63); filed in Japan 22 September 1998

Most reverb algorithms are considered proprietary, so this Yamaha patent is unusual. The object is to imitate the wow and flutter of earlier tape

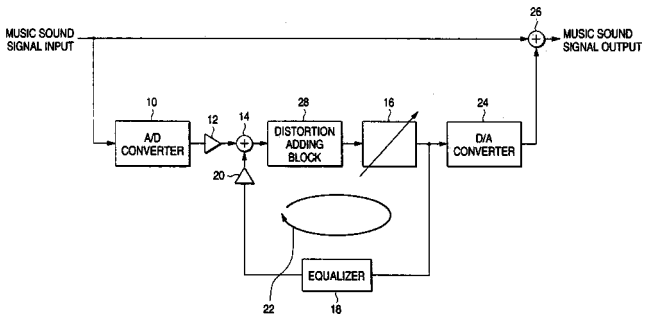

delays (''analog echo''). The addition of a distortion block **28** helps increase the garage band factor. A variable delay **16** combined with a feedback loop do the rest.—MK

6,362,409

43.75.Wx CUSTOMIZABLE SOFTWARE-BASED DIGITAL WAVETABLE SYNTHESIZER

Sharadchandra H. Gadre, assignor to IMMS, Incorporated
26 March 2002 (Class 84/603); filed 24 November 1999

Perhaps the only interesting aspect of this software synthesis patent is the explication of Indian music performance rules in section 1.4; the rest is well known to those ''versed in the art.''—MK

6,362,411

43.75.Wx APPARATUS FOR AND METHOD OF INPUTTING MUSIC-PERFORMANCE CONTROL DATA

Hideo Suzuki and Masao Sakama, assignors to Yamaha Corporation
26 March 2002 (Class 84/626); filed in Japan 29 January 1999

Understanding Yamaha's synthesis user interfaces is often difficult due to the complex and hidden user model. This patent attempts to explain the hidden meaning behind a sampling synthesizer with many time varying parameters. Caveat Lector.—MK

6,365,816

43.75.Wx DIGITAL SAMPLING INSTRUMENT EMPLOYING CACHE MEMORY

David P. Rossum, assignor to Creative Technology Limited
2 April 2002 (Class 84/603); filed 19 July 2000

This patent was originally filed in 1990 and can be found in three other United States Patents (5,698,803, 5,925,841, and 6,137,043)—only the number has been changed to protect the innocent. The basic idea is to use a cache as an intermediary between the address unit of an interpolating sampling synthesizer and the sample memory.—MK

6,371,120

43.80.Nd SNORE ELIMINATION DEVICE

Kuo-Chung Chiu and Wing-Yig Stephen Chan, both of A-Lein Hsiang, Kaohsiung Hsien, Taiwan, Province of China
16 April 2002 (Class 128/848); filed 15 June 2001

This amusing device consists of a wrist belt to be worn on one's wrist. The band contains a circuit board and a power source. The circuit amplifies the wearer's snores and relays the signal to a control circuit that activates a vibration motor. The user is supposed to sense the vibration, causing him/her to change sleep positions.—DRR

6,361,496

43.80.Qf PRESSURE TOURNIQUET WITH ULTRASOUND WINDOW AND METHOD OF USE

Arthur W. Zikorus *et al.*, assignors to VNUS Medical Technologies, Incorporated
26 March 2002 (Class 600/437); filed 28 May 1999

A pressure tourniquet to be wrapped around a leg or another anatomical structure containing veins incorporates a window transparent to ultrasound. An ultrasound transducer is positioned in contact with the window. The transducer probes a dilated vein with an ultrasonic signal and can measure the size of the vein and detect reflux. A pneumatic bladder on the

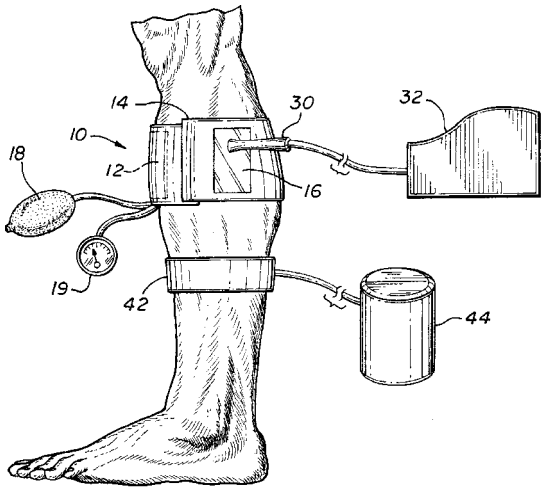

tourniquet inflates to apply pressure to the anatomical structure so that the vein will be compressed by the surrounding tissue. Since the pressure effectively reduces the diameter of the vein, competency of the vein valve can be temporarily restored to indicate the proper reduced diameter required to restore venous function. An electrode catheter is introduced into the vein to apply energy for durably molding the vein to the reduced diameter.—DRR

6,361,500

43.80.Qf THREE TRANSDUCER CATHETER

Donald Masters, assignor to Scimed Life Systems, Incorporated
26 March 2002 (Class 600/466); filed 7 February 2000

This diagnostic/therapeutic catheter for a medical ultrasonic system incorporates multiple ultrasound transducers. All of the transducers are located at the distal end of a catheter driver shaft. One embodiment provides for an ultrasound-generating transducer and two other transducers for receiving signals generated by the emitting transducer. The receiving transducers may have center frequencies substantially equal to the fundamental and the second harmonic of the emitting transducer. The transducers are mounted in such a manner as to form a preselected plane.—DRR

6,364,836

43.80.Qf ULTRASOUND DIAGNOSTIC APPARATUS

Hiroshi Fukukita *et al.*, assignors to Matsushita Electric Industrial Company, Limited
2 April 2002 (Class 600/443); filed in Japan 19 January 2000

This is an ultrasonic diagnostic apparatus that can operate in several different modes including a Doppler-based mode using steerable continuous wave. The device includes a probe that outputs rf signals. Phase detectors convert the rf signals to baseband. A reception beam former processes the baseband signals into a time-division-multiplexed signal by multiplying by phase shift data, then delaying and combining the baseband signals to generate multiplication-resultant signals.—DRR

6,364,837

43.80.Qf CONTACT DIGITAL ULTRASONIC DENSITOMETER

Richard B. Mazess *et al.*, assignors to Lunar Corporation
2 April 2002 (Class 600/449); filed 28 April 2000

This ultrasonic instrument employs a digital architecture in the attempt to provide improved stability in measuring the speed of sound in human bone *in vivo*. A digitization of the received ultrasonic signal allows numerical analyses to be applied to determine precise arrival time of the waveform. The microprocessor may initiate the ultrasonic signal transmission, detect its arrival, and control the strength of the transmitted signal and the amplification of the received signal in order to optimize the signal path.—DRR

6,364,838

43.80.Qf PULSED WAVE DOPPLER PROCESSING USING ALIASED SPECTRAL DATA

Paul D. Freiburger and Barry H. Friemel, assignors to Siemens Medical Solutions, USA, Incorporated
2 April 2002 (Class 600/455); filed 11 January 2000

This method for producing Doppler ultrasound data at a user-requested pulse repetition frequency (PRF) utilizes undersampled echo signals. Echos are generated from Doppler pulses transmitted into the patient at a rate less than the desired PRF. The echo signals are analyzed in the time domain to determine a representative velocity of scatterers in an area of tissue. From the velocity, the Doppler shift of the scatterers is determined. An interpolation produces the number of samples which would have been produced had the Doppler pulses been transmitted at the user-requested PRF. The interpolated echo signals are then analyzed in the frequency domain to yield spectra giving the velocity and direction of the moving scatterers. A spectrum is then chosen for display from the determined Doppler shift. The device can also be used to increase the amplitude of the pulses transmitted into a patient by lowering the transmit pulse frequency so that the total amount of ultrasonic energy delivered to the patient remains constant. The larger amplitude transmit pulses produce echo signals that presumably have a higher signal-to-noise ratio.—DRR

6,364,849

43.80.Qf SOFT TISSUE DIAGNOSTIC APPARATUS AND METHOD

Ariel Wilcox, assignor to Access Wellness and Physical Therapy
2 April 2002 (Class 600/587); filed 3 May 2000

This soft tissue diagnostic apparatus diagnoses stress and injury in anatomical soft tissue by detecting the response of the soft tissue to acoustic energy. The patent also covers a method of detecting soft tissue damage or stress and treating the tissue. An acoustic transmitter sends excitation acoustic energy toward a target area of soft tissue. An acoustic receiver receives acoustic energy generated by the soft tissue in response to the excitation and generates an output signal representative of the soft tissue response. An analyzer provides an indication of the stress and injury in the soft tissue on the basis of the output signal.—DRR

6,364,839

43.80.Qf ULTRASOUND DIAGNOSTIC INSTRUMENT HAVING SOFTWARE IN DETACHABLE SCANHEAD

Blake W. Little *et al.*, assignors to SonoSite, Incorporated
2 April 2002 (Class 600/459); filed 3 May 2000

This ultrasonic diagnostic instrument processes electrical signals for display. A transducer scanhead generates ultrasound waves, receives reflected waves, and is connected to a digital processor. An additional memory external to the console stores software and data requisite for the use of the

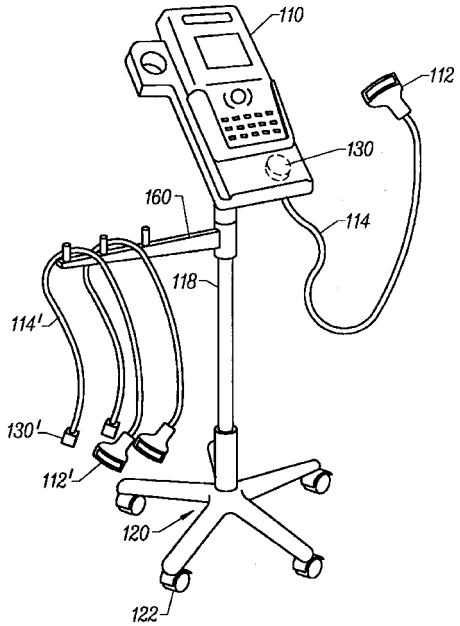

transducer scanhead in the ultrasonic diagnostic instrument. This second memory, housed either in the scanhead or in a connector, can include operational data unique to the transducer scanhead, operational software for executing special operations with the scanhead, and updates and upgrades of system executable code that resides in the console memory.—DRR

6,364,840

43.80.Qf ACOUSTIC IMAGING CATHETER AND THE LIKE

Robert J. Crowley, assignor to Boston Scientific Corporation
2 April 2002 (Class 600/463); filed 27 September 2000

An acoustic imaging balloon catheter is formed by a disposable liquid-confining sheath supporting a ''high-fidelity,'' flexible drive shaft that carries on its end an ultrasonic transducer and includes an inflatable dilation balloon. The shaft and transducer rotate with sufficient speed and fidelity to

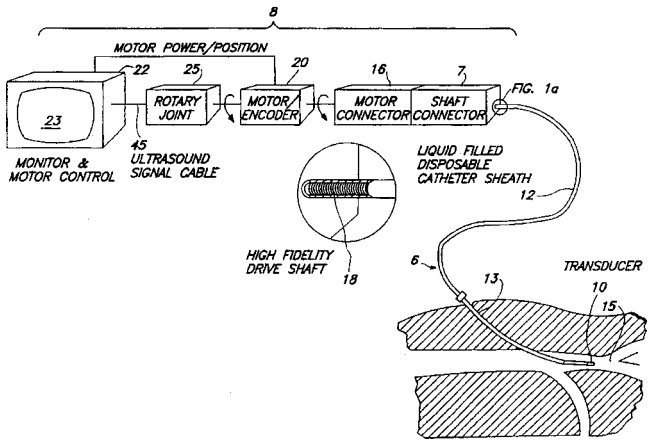

produce real time images on a TV screen. A number of selectable catheter sheaths are described, including one with an integral acoustically transparent window, another with end extension that aids in navigation of the catheter, another carrying a dilation or positioning balloon over the transducer, etc.—DRR

6,368,277

43.80.Qf DYNAMIC MEASUREMENT OF PARAMETERS WITHIN A SEQUENCE OF IMAGES

Zuhua Mao *et al.*, assignors to Siemens Medical Solutions USA, Incorporated
9 April 2002 (Class 600/441); filed 5 April 2000

A method is disclosed for dynamically measuring parameters within a series of images using image processing. A sequence of ultrasound images is produced by an ultrasound system. The user determines at least one region of interest within one of the images. Then a parameter for each region of interest is evaluated. For example, the number of pixels exceeding a predefined intensity might be counted. A new region is searched within an area around the predefined region of interest which best matches the region of interest. This is done for all images of the sequence whereby the best matching new region of the previous image becomes the region of interest for the following image.—DRR

6,368,286

43.80.Qf PNEUMOTHORAX DETECTOR

Eric D. Whitman, St. Louis, Missouri and Steven R. Frank, Jefferson, Colorado
9 April 2002 (Class 600/529); filed 28 May 1999

A method and device is described here for detecting life-threatening pneumothorax caused by air in the thoracic or chest cavity. This is done by passive auditory detection through the use of an array of transducers placed

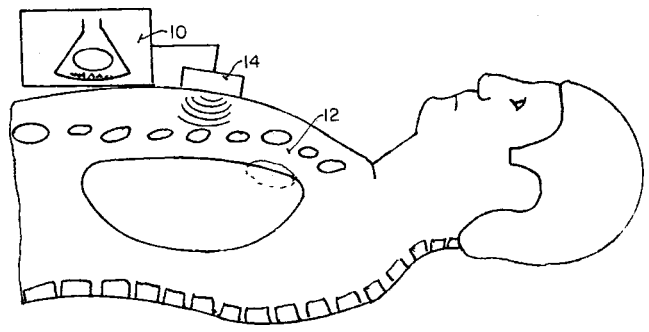

on the patient's chest and connected to a data processing unit. The unit is programmed to filter out sounds not in the harmonic of the bubbling air associated with a pneumothorax. In addition to passive auditory detection, ultrasound and radioactive gas detection may also be used.—DRR

6,370,433

43.80.Qf INTERROGATION OF AN IMPLANTABLE MEDICAL DEVICE USING BROADCAST AUDIBLE SOUND COMMUNICATION

Jerome T. Hartlaub *et al.*, assignors to Medtronic, Incorporated
9 April 2002 (Class 607/32); filed 25 January 2000

Methods and apparatus are disclosed to collect information from an implantable medical device (IMD) by rf transmission of audible sounds generated by the IMD. Such information may include interrogation of programmed parametric values, operating modes and conditions of operation, confirmation of program changes, interrogation of data stored in the IMD,

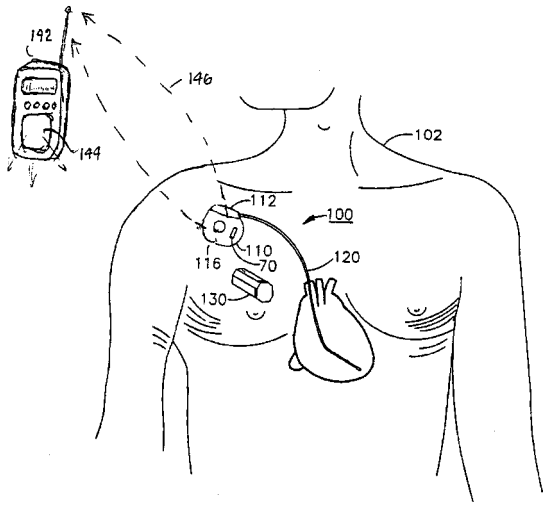

and patient warnings or other messages. The IMD contains a rf transmitter that broadcasts or transmits audible sounds including voice statements or musical tones stored in analog memory or responses to an event warning trigger. The broadcast radio signal is received and the audible sounds are demodulated and reproduced by a radio receiver as voiced statements or musical tones.—DRR

6,368,281

43.80.Qf TWO-DIMENSIONAL PHASED ARRAY ULTRASOUND TRANSDUCER WITH A CONVEX ENVIRONMENTAL BARRIER

Rodney J. Solomon, Andover and Benjamin M. Herrick, Boxborough, both of Massachusetts
9 April 2002 (Class 600/459); filed 30 July 1999

A two-dimensional phased array ultrasound transducer consists of a sensor and its housing and a convex environmental barrier for placement against, and maximizing contact with, a patient's body. The environmental

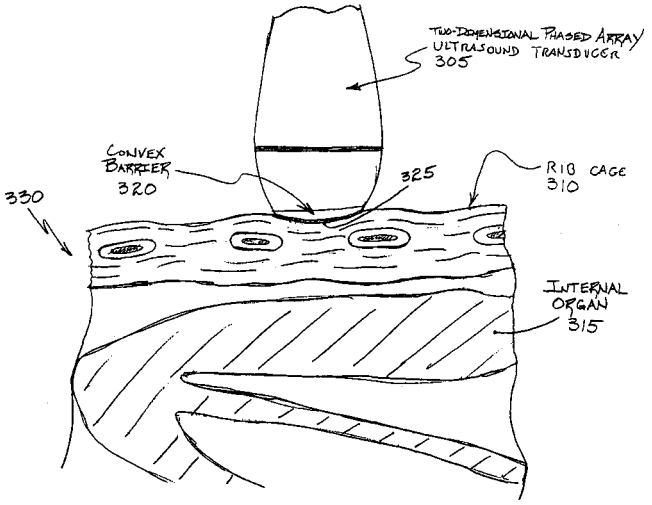

barrier does not necessarily provide focusing capability and hence the propagation speed of sound through the environmental barrier is approximately equal to the propagation speed of sound through tissue of the patient's body.—DRR

6,361,509

43.80.Sh THERAPY APPARATUS WITH A SOURCE OF ACOUSTIC WAVES

Thomas Reuner, assignor to Siemens Aktiengesellschaft
26 March 2002 (Class 601/2); filed in Germany 22 December 1998

The aim of this device is to simplify the alignment of a sound source with the treatment area inside the body of a patient. The source has a light

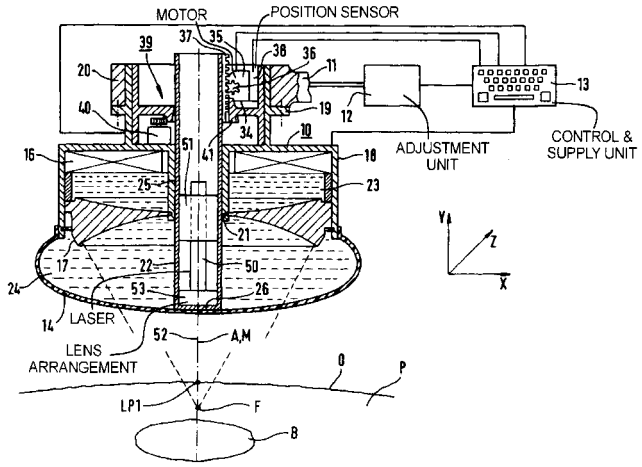

generator that emits a focused visible light beam with a substantially parallel beam path that generally coincides with the acoustic axis of the source and renders it visible.—DRR

6,361,531

43.80.Sh FOCUSED ULTRASOUND ABLATION DEVICES HAVING MALLEABLE HANDLE SHAFTS AND METHODS OF USING THE SAME

James B. Hissong, assignor to Medtronic Xomed, Incorporated
26 March 2002 (Class 606/27); filed 21 January 2000

The device is intended to provide treatment of anatomical tissue with high-intensity focused ultrasound energy. More particularly, it is a hand-held ultrasound ablation device with a handle shaft used to position an ultrasound emitter adjacent to tissue undergoing treatment. The handle shaft is malleable to permit selective, manual shaping to better access a selected anatomical site from a remote location and/or to orient the ultrasound emitter for contact with anatomical tissue at the site.—DRR

6,361,554

43.80.Sh METHODS AND APPARATUS FOR THE SUBCUTANEOUS DELIVERY OF ACOUSTIC VIBRATIONS

Axel F. Brisken, assignor to Pharmasonics, Incorporated
26 March 2002 (Class 623/1.1); filed 30 June 1999

Methods of delivering vibrational energy to subcutaneous tissue sites include generating acoustic energy externally and directing the energy to an implanted structure that is capable of resonating at a preselected frequency.

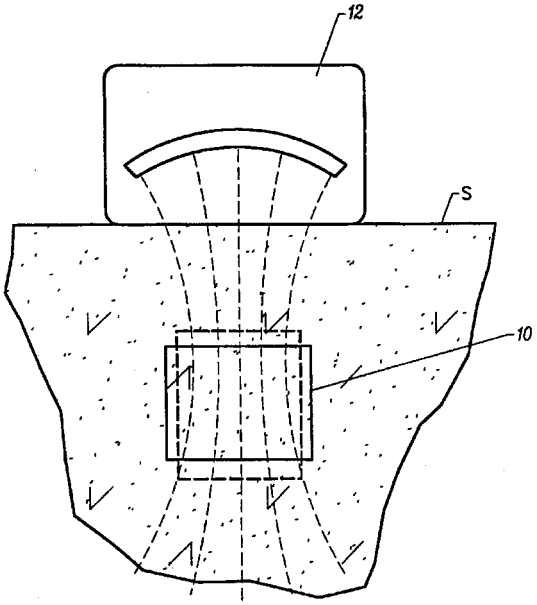

The vibration of the implanted structure, in turn, will radiate heat and mechanical energy into tissue surrounding the structure. In one example, the implanted structure is a stent and the vibrational energy is intended to inhibit hyperplasia in a blood vessel in which the stent is implanted.—DRR

6,361,510

43.80.Sh USE OF ULTRASOUNDS FOR THE TREATMENT OF DECOMPRESSION SICKNESS

Giovanni Zanini, Valdmadrera Lecco, Italy
26 March 2002 (Class 601/2); filed in Italy 5 January 1999

Decompression sickness in human patients is treated by applying ultrasound energy in the frequency range of 1 to 15 MHz in an amount and time sufficient to alleviate the symptoms. The device is supposed to work by destructing bubbles of inert gas in the blood and tissues that occur from too rapid pressure reduction in the environment.—DRR

6,368,299

43.80.Sh ULTRASONIC PROBE AND METHOD FOR IMPROVED FRAGMENTATION

William W. Cimino, Louisville, Colorado
9 April 2002 (Class 604/22); filed 9 October 1998

In the attempt to improve ultrasonic fragmentation or emulsification of soft tissue, this ultrasonic probe consists of a thin, longitudinal shank. A source of ultrasonic vibrational energy is connected to the proximal end. The distal end may have a blunt or a bullet-nosed tip. The shaft has one or more grooves **13** near the tip, which circumscribe the shaft of the longitudinal shank. The groove walls provide surface area on the distal end of the probe

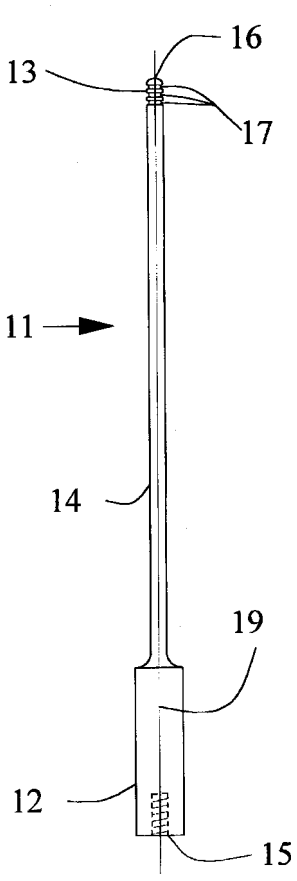

in planes generally perpendicular to the axis of the probe. This additional area is claimed to increase the tissue fragmenting surface area without increasing the diameter of the distal end of the probe. Because tissue does not contact the bottom of the grooves, the tissue contact surface area along and about the distal end of the probe is reduced, thus reducing the potential for tissue burns.—DRR

6,368,343

43.80.Sh METHOD OF USING ULTRASONIC VIBRATION TO SECURE BODY TISSUE

Peter M. Bonutti *et al.*, assignors to Peter M. Bonutti
9 April 2002 (Class 606/232); filed 13 March 2000

A suture and a suture retainer are strategically positioned in body tissue. Ultrasonic vibratory energy is applied to heat the suture retainer and bond portions of the retainer to each other and/or to the suture. Portions of the body tissue may be pressed into linear apposition with each other and held in place by cooperation between the suture and the retainer. If desired, the retainer may be omitted and sections of the suture may be bonded directly to each other.—DRR

6,361,498

43.80.Vj CONTRAST AGENT IMAGING WITH SUPPRESSION OF NONLINEAR TISSUE RESPONSE

George A. Brock-Fisher, Andover, Massachusetts
26 March 2002 (Class 600/458); filed 11 February 2000

Tissue echoes that conform to a polynomial model are suppressed relative to contrast agent echoes that do not conform to the model. In the method, ultrasound signals are transmitted and echoes are received. Transmit and receive gain factors are chosen so that combination of echoes in reception eliminates echo components conforming to the polynomial model and leaves nonconforming echo components.—RCW

6,361,499

43.80.Vj MULTIPLE ANGLE NEEDLE GUIDE

John D. Bates *et al.*, assignors to CIVCO Medical Instruments Incorporated
26 March 2002 (Class 600/461); filed 16 September 1998

This needle guide can be mounted on the head of a transducer in an ultrasonic imaging instrument. A slot in a guide with an adjustable angle is used to secure the needle. The guide is removable.—RCW

6,364,835

43.80.Vj MEDICAL DIAGNOSTIC ULTRASOUND IMAGING METHODS FOR EXTENDED FIELD OF VIEW

John A. Hossack *et al.*, assignors to Acuson Corporation
2 April 2002 (Class 600/443); filed 27 March 2000

These methods align essentially coplaner two-dimensional images to obtain an extended field of view by using compounding. A finite impulse response is used in the compounding and the compounding can depend on correlation between images, location within the image, and estimated motion.—RCW

6,368,279

43.80.Vj TIME-DELAY COMPENSATION SYSTEM AND METHOD FOR ADAPTIVE ULTRASOUND IMAGING

D-L. Donald Liu, assignor to Siemens Medical Solutions, USA, Incorporated
9 April 2002 (Class 600/443); filed 15 September 2000

Time-delay compensation in this system is achieved by partitioning echo waveforms from an array into groups, determining a control waveform for each group, shifting the control waveform by a trial time delay, and determining trial time delays for other waveforms in the group by interpolation. A waveform similarity factor is evaluated in each group repeatedly for different trial time shifts and the trial delay that yields the greatest waveform similarity factor is chosen as optimum. A global time compensation profile for the entire array is then determined by interpolation and applied in a beamformer to provide compensation in receive focusing and in subsequent transmit focusing.—RCW

6,370,413

43.80.Vj ULTRASOUND IMAGING SYSTEM AND METHOD TO ARCHIVE AND REVIEW 3-D ULTRASOUND DATA

Raul Alvarez *et al.*, assignors to Siemens Medical Solutions USA, Incorporated
9 April 2002 (Class 600/407); filed 2 November 1999

Settings of viewing parameters for two-dimensional images and for corresponding three-dimensional volumetric data are saved. Stored volumetric data is retrieved in the viewing configuration that was set when the two-dimensional images were saved. This allows return to work that was previously suspended or terminated.—RCW

6,370,480

43.80.Vj QUANTITATIVE ANALYSIS SYSTEM AND METHOD FOR CERTIFYING ULTRASOUND MEDICAL IMAGING EQUIPMENT

Rajiv Gupta *et al.*, assignors to General Electric Company
9 April 2002 (Class 702/39); filed 21 May 1999

An ultrasonic image of a standard phantom is acquired by the imager under test, parameters are derived from the image, and image quality indices are computed. The results are compared to prestored values of the parameters, quality indices, and a single composite index that together indicate the accuracy of the test image relative to a standard that has been established for the imager. The quality indices include image homogeniety, contrast, signal attenuation, and penetration.—RCW

6,371,913

43.80.Vj MEDICAL DIAGNOSTIC ULTRASOUND IMAGING METHODS FOR ESTIMATING MOTION BETWEEN COMPOSITE ULTRASONIC IMAGES AND RECOVERING COLOR DOPPLER VALUES FROM COMPOSITE IMAGES

Linyong Pang *et al.*, assignors to Acuson Corporation
16 April 2002 (Class 600/441); filed 8 December 2000

Means for estimating motion between composite ultrasonic images that include both b-mode and color Doppler information are comprised of three main steps. First, b-mode images are extracted from each of two composite images. Second, relative motion vectors are determined from the b-mode images. Third, selected components of the original composite images are registered using the determined motion vectors and combined to form an extended field of view or three-dimensional image.—RCW

6,371,914

43.80.Vj SINGLE-SHOT PHASE CANCELLATION ULTRASOUND CONTRAST IMAGING

Marcel Arditi, assignor to Bracco Research S.A.
16 April 2002 (Class 600/443); filed 13 April 2000

Cancellation is achieved by coding the transmitted waveform in an ultrasonic imaging system so that resulting echo waveforms give essentially zero contributions from linear scattering or tissues that do not contain nonlinearly responding contrast agent microbubbles and give significant contributions from nonlinear scattering that originates from contrast agent microbubbles. In the method, two pulses having spectra with known relative frequency dependencies and having known but differing amplitude and phase are used to produce an ultrasonic beam. From echo signals produced by the beam, two rf waveforms are deconvolved, aligned, normalized, and summed to cancel echo components caused by linear scattering.—RCW

Influence of velocity profile nonuniformity on minor losses for flow exiting thermoacoustic heat exchangers (L)

Ray Scott Wakeland[a] and Robert M. Keolian
The Pennsylvania State University, Graduate Program in Acoustics, P.O. Box 30, State College, Pennsylvania 16804-0030

(Received 4 March 2002; revised 11 June 2002; accepted 9 July 2002)

Nonuniform, time-dependent velocity profiles for laminar oscillating flow are employed in calculating effective minor loss exit coefficients. The results could represent an improvement over the Borda–Carnot formula for calculating flow losses at the exit from heat exchangers in thermoacoustic devices, since the Borda–Carnot formula assumes uniform velocity across a flow cross section. Results are presented for parallel plate and circular tube geometries. © *2002 Acoustical Society of America.* [DOI: 10.1121/1.1502896]

PACS numbers: 43.35.Ud, 43.25.Ed [MFH]

I. INTRODUCTION

Further progress in the development of thermoacoustic devices will require an increased understanding of various nonlinear effects. One of these effects is the dissipation of mechanical (acoustic) energy as oscillating gas flows across geometrical irregularities such as tees, bends, and changes in cross-sectional area. Referred to as ''minor losses'' by the engineers who design piping and duct systems, these losses can seriously degrade the performance of thermoacoustic devices. Little is known, however, about minor losses in oscillating flow. The present state-of-the-art is to append minor loss terms (and terms for other nonlinear losses) onto otherwise linear calculations. The form for the loss of acoustic power $\Delta\dot{E}$ derived by Swift and Ward is[1]

$$\Delta\dot{E} = -\frac{4}{3\pi}\frac{\rho_m A}{2}K|u_A|^3, \tag{1}$$

where ρ_m is the mean gas density, A is the cross-sectional area, u_A is the (peak) amplitude of the oscillating velocity averaged over the cross-sectional area, and K is the ''minor loss coefficient'' associated with the particular irregularity in flow geometry. Almost all minor loss coefficients are determined empirically, and for steady flow. For lack of comparable measurements on oscillating flows, it has been common practice to use the minor loss coefficients from steady flow experiments in models of thermoacoustic devices. The method (discussed in Sec. IV) is to assume that the steady flow result holds at each instant in time, and to average over an acoustic cycle.

One of the few minor loss coefficients that can be calculated is for an abrupt increase in flow cross-sectional area. In this letter, we calculate this ''expansion coefficient'' using velocity profiles derived from linear thermoacoustic theory. We hope that this will be an improvement on the use of the ''Borda–Carnot formula,'' $K_e=(1-\sigma)^2$, a steady flow result that is derived with the assumption of a *uniform* cross-sectional velocity profile both before and after the area change. In this expression, $\sigma=A_1/A_2$ is the ratio of the smaller area A_1 before the expansion to the larger area A_2 after the expansion. The assumption of uniform flow is justified by the observation that turbulent flow, found in most piping systems, has a nearly uniform velocity profile. For uniform flow from a small duct or pipe into a large reservoir, $\sigma=0$ and $K_e=1$. For fully developed laminar flow between parallel plates (Poiseuille flow), however, K_e approaches 1.54, not 1, for $\sigma=0$. Flows in thermoacoustic devices can fall anywhere between these two extremes.

The increase in cross-sectional area is usually referred to as an ''expansion,'' but it should be kept in mind that the fluid is assumed to be incompressible in this calculation, i.e., the cross-sectional area ''expands,'' but the gas density is assumed constant.

In what follows, the velocity $V(\mathbf{r})$ varies over the cross-sectional coordinates $\mathbf{r}$. The notation $\langle V\rangle$ indicates the spatial average over the cross section. Subscripts 1 and 2 indicate variables that correspond to locations before and after the area change, where the velocities are V_1 and V_2, respectively.

II. EXPANSION MINOR LOSS COEFFICIENTS FOR NONUNIFORM VELOCITY PROFILES

In steady flow, a sudden change in flow cross-sectional area results in a pressure change. Part of the pressure difference is inertial, and would exist even in a potential flow. For an expansion, a pressure increase is expected, since the fluid must decelerate. For actual flows, the pressure rise is smaller than the ''ideal'' increase,

$$\Delta P_{\text{ideal}} = (\rho_m/2)(\alpha_1\langle V_1\rangle^2 - \alpha_2\langle V_2\rangle^2), \tag{2}$$

obtained from the spatial average of the energy equation,[2] where α is defined below in Eq. (6). The difference between this ideal pressure increase and the actually observed increase is the ''minor loss'' pressure drop,

$$\Delta P_{\text{loss}} = \Delta P_{\text{ideal}} - \Delta P_{\text{actual}}. \tag{3}$$

The minor loss coefficient K_e is then defined so that

$$\Delta P_{\text{loss}} = K_e\frac{\rho_m\langle V_1\rangle^2}{2}. \tag{4}$$

[a]Electronic mail: wakeland@psu.edu

The coefficient for sudden expansion is one of the few that can be calculated. The result depends on the cross-sectional velocity profiles before and after the expansion. Because it is rarely needed, the complete expression for the expansion minor loss coefficient allowing for arbitrary velocity profiles is not commonly encountered, but it can be found in the *Handbook of Fluid Dynamics* edited by Streeter,[3]

$$K_e = \alpha_1 - 2\beta_1\sigma + (2\beta_2 - \alpha_2)\sigma^2, \tag{5}$$

where α and β are the ''kinetic energy coefficient'' and the ''momentum coefficient'' obtained from integrating the energy and momentum equations over the flow cross-section,

$$\alpha = \frac{\langle V^3 \rangle}{\langle V \rangle^3} \quad \text{and} \quad \beta = \frac{\langle V^2 \rangle}{\langle V \rangle^2}. \tag{6}$$

For fully developed laminar flow in a circular tube, $\alpha = 2$ and $\beta = \frac{4}{3}$. For parallel plates of infinite aspect ratio, $\alpha = \frac{54}{35} \simeq 1.54$ and $\beta = \frac{6}{5}$.

A form of Eq. (5) for the special case $\alpha_2 = \beta_2 = 1$ is given by Idelchik.[4] The choice of $\alpha_2 = \beta_2 = 1$ indicates that the pressure after the expansion is measured at a location where the flow profile is uniform. For steady flow exit from a heat exchanger, the exit duct is likely large enough that the flow is turbulent, and therefore approximately uniform in profile even after it once again becomes fully developed.

In apparent conflict with Eq. (5), the expression $K_e = 1 - 2\beta_1\sigma + (2\beta_2 - 1)\sigma^2$ is used by Kays,[5] and reproduced in graphical form by Kays and London in their reference *Compact Heat Exchangers*.[6] The discrepancy arises because Kays uses the energy equation for *uniform* velocities V_1 and V_2 to define his reference pressure change, $(\Delta P_{\text{ideal}})_{\text{conventional}} = (\rho_m/2)(V_1^2 - V_2^2)$, instead of Eq. (2). The resulting ''conventional'' minor loss coefficient[2] does give the correct pressure difference across an expansion when used in conjunction with this ''conventional'' definition of ΔP_{ideal}. However, this conventional K_e, plotted in Figs. 5-3 through 5-5 of Kays and London[6] *cannot* be inserted directly into Eq. (1) (or its steady flow equivalent) to calculate dissipation of mechanical energy, except for uniform flow profiles. This is demonstrated by the appearance of *negative* K_e in their plots 5-3 through 5-5 for all nonuniform flows. We therefore follow the convention of Fredrickson and Bird[3] and Idelchick.[4]

In Fig. 1, K_e for parallel plates is plotted as a function of σ for uniform flow (the dashed line, with $\alpha_1 = 1$ and $\beta_1 = 1$) and for fully developed laminar flow (the solid line, with $\alpha_1 = 1.54$ and $\beta_1 = 1.2$). Equivalent results for circular tubes are shown in Fig. 2. In all cases, $\alpha_2 = 1$ and $\beta_2 = 1$; that is, the flow profile is uniform a short distance after the expansion.[7]

As noted by Fredrickson and Bird in *Handbook of Fluid Dynamics*, at the exit from a heat exchanger it is possible to go from a fully developed flow in many small channels to a nearly uniform flow in a single large channel, even with very little change in total cross-sectional area. For parallel plates in this situation, K_e is 0.14, not zero, even for the limiting case of $\sigma = 1$, when there is *no* change in total cross-sectional area.

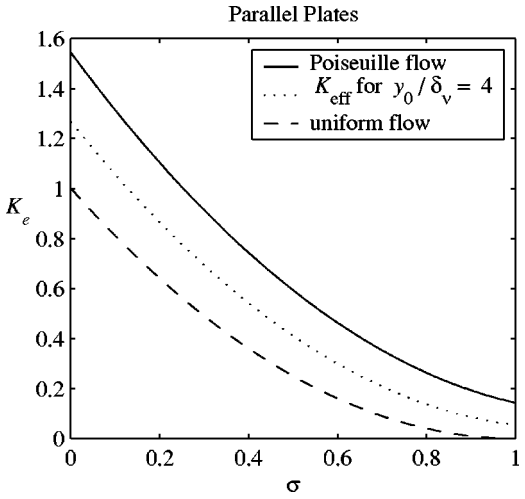

FIG. 1. The minor loss exit coefficient K_e is plotted as a function of the area ratio σ for parallel plates for three cases. The dashed and solid curves are steady flow results, with $\alpha_1 = 1$ and $\beta_1 = 1$ (dashed curve, uniform flow) and $\alpha_1 = 1.54$ and $\beta_1 = 1.2$ (solid curve, Poiseuille flow). The dotted curve is K_{eff}, the average, effective K_e for oscillating flow with $y_0/\delta_\nu = 4$ calculated from Eq. (12). In all cases, $\alpha_2 = 1$ and $\beta_2 = 1$; that is, the flow profile is uniform just after the expansion.

III. VELOCITY PROFILES IN OSCILLATING FLOW

To determine the increase in the exit minor loss for a heat exchanger in a thermoacoustic device, we need to know the velocity profile. While the exact nature of the acoustic flow near a sudden area change is not known to the authors, the velocity profile in the interior or the pore is probably a good indicator of the degree of nonuniformity in the velocity near the opening *during the exit portion of the cycle*. This velocity profile for a viscous fluid in laminar oscillating flow can be written as

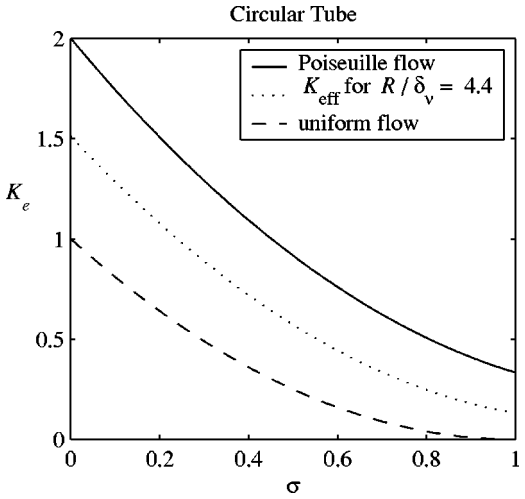

FIG. 2. The minor loss exit coefficient K_e is plotted as a function of the area ratio σ for a circular tube of radius R for three cases. The dashed and solid curves are steady flow results, with $\alpha_1 = 1$ and $\beta_1 = 1$ (dashed curve, uniform flow) and $\alpha_1 = 2$ and $\beta_1 = 1.33$ (solid curve, Poiseuille flow). The dotted curve is K_{eff}, the average, effective K_e for oscillating flow with $R/\delta_\nu = 4.4$ calculated from Eq. (12). In all cases, $\alpha_2 = 1$ and $\beta_2 = 1$; that is, the flow profile is uniform just after the expansion.

$$u(\mathbf{r},t)=u_A\frac{\mathrm{Re}[(1-h_\nu)e^{i\omega t}]}{\max\{\langle \mathrm{Re}[(1-h_\nu)e^{i\omega t}]\rangle\}}, \tag{7}$$

where the notation "Re" indicates "the real part of," "max" denotes the maximum value during the cycle, and h_ν is a function that depends on frequency, geometry, and gas parameters. This formalism is summarized in Ref. 8, including a tabulation of the functions h_ν for several important geometries. For parallel plates separated by a gap of $2y_0$,

$$h_\nu(y)=\frac{\cosh[(1+i)y/\delta_\nu]}{\cosh[(1+i)y_0/\delta_\nu]}, \tag{8}$$

where y is the distance from centerline ($-y_0\leqslant y\leqslant y_0$), and $\delta_\nu=\sqrt{(2\mu/\omega\rho_m)}$ is the viscous penetration depth at angular frequency ω in a fluid with dynamic viscosity μ. For a circular tube of radius R,

$$h_\nu(r)=\frac{J_0[(i-1)r/\delta_\nu]}{J_0[(i-i)R/\delta_\nu]}, \tag{9}$$

where r is the distance from centerline ($0\leqslant r\leqslant R$).

IV. EFFECTIVE K_e FOR OSCILLATING FLOW

Swift and Ward calculate Eq. (1) from

$$\Delta\dot{E}=\overline{\Delta p(t)\langle u(t)A\rangle}=-\frac{A\rho_m}{2}\,\overline{K|\langle u(t)\rangle|^3}, \tag{10}$$

using $\Delta p=-(\rho/2)\,K\,|\langle u(t)\rangle|\,\langle u(t)\rangle$, an oscillating flow adaptation of Eq. (4), with Δp negative for a pressure drop, and where the overbar indicates a time average. Using a constant K from a steady flow correlation, the time average is of the cube of $\langle u(t)\rangle=u_A\sin\omega t$, giving the factor of $4/3\pi$ in Eq. (1). In thermoacoustic devices, externally imposed pressure swings (from a standing wave, for example) may cause oscillations in the density at the site of the minor loss, which should be included in the time average in Eq. (10). However, we assume that oscillations in the density $\rho(t)=\rho_m+\rho_1(t)$ are small, so that the resulting additional term in $\Delta\dot{E}$, which goes as $\rho_1(t)/\rho_m$, can be neglected.

The velocity profile of Eq. (7) changes during the course of the cycle. That is, the profile is a function of time. Since K depends on the velocity profile, it, too, is a function of time. To calculate $\Delta\dot{E}$ using Eq. (10) requires the inclusion of $K_e(t)$ *within* the time average. We are assuming that the velocity profile is well approximated by Eqs. (7) and (8) or (9) during the half of the cycle when fluid is flowing from the smaller area into the larger area. To obtain the exit coefficient, the time average should be taken over the exit half of the cycle only, which would require identifying the beginning phase of the exit portion of the flow. Because of the time symmetry of the function $\langle u(t)\rangle$, however, it is mathematically equivalent to take the average of the absolute value $|K_e(t)\,\langle u(t)\rangle^3|$ over an entire period of oscillation, which is much more convenient. We can express the result as an effective, average minor loss coefficient K_{eff} that we may use in Eq. (1) by defining

$$K_{\mathrm{eff}}\,\overline{|\langle u(t)\rangle|^3}\equiv\overline{|K_e(t)\,\langle u(t)\rangle^3|}. \tag{11}$$

Applying Eqs. (5) and (6) to Eq. (11), with $\alpha_2=\beta_2=1$, gives

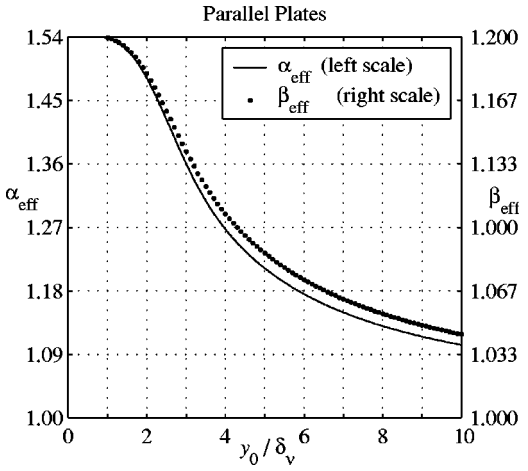

FIG. 3. The effective, average kinetic energy coefficient α_{eff} and momentum coefficient β_{eff} for laminar oscillating flow between parallel plates as a function of plate spacing. The distance between the plates is $2y_0$.

$$K_{\mathrm{eff}}\equiv\frac{\overline{|\langle u^3\rangle|}}{\overline{|\langle u\rangle|^3}}-2\frac{\overline{|\langle u^2\rangle\langle u\rangle|}}{\overline{|\langle u\rangle|^3}}\sigma+\sigma^2\equiv\alpha_{\mathrm{eff}}-2\beta_{\mathrm{eff}}\,\sigma+\sigma^2. \tag{12}$$

Once again, $\alpha_2=\beta_2=1$ indicates that the flow is assumed uniform in profile after the expansion. This is appropriate for oscillating flow, since the profile is presumably "plug flow" in the larger area region, where we expect $y_0/\delta_\nu\gg 1$. For clarification, the notation $\overline{|\langle u\rangle|^3}$ means to find $u(\mathbf{r},t)$ using Eq. (7), average over $\mathbf{r}$ to get the time-dependent $\langle u(t)\rangle$, take the absolute value, cube the result, and then average in time over a cycle. In all cases, the time average is the last operation performed.

V. RESULTS

The values of α_{eff} and β_{eff} depend on pore size (y_0/δ_ν or R/δ_ν). The effective coefficients α_{eff} and β_{eff} range between their values for Poiseuille and uniform flow, and are plotted up to $y_0/\delta_\nu=10$ for parallel plates in Fig. 3, and up to $R/\delta_\nu=10$ for circular tube in Fig. 4. The values fall about

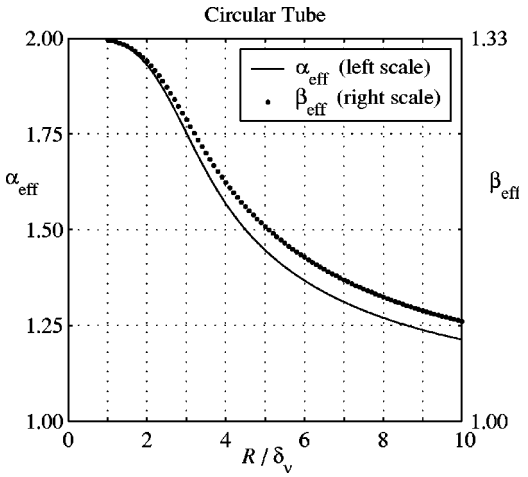

FIG. 4. The effective, average kinetic energy coefficient α_{eff} and momentum coefficient β_{eff} for laminar oscillating flow in a circular tube as a function of radius R.

half way between the Poiseuille and uniform limits when $y_0/\delta_\nu = 4$ for parallel plates and when $R/\delta_\nu = 4.4$ for circular tube. The resulting $K_{\text{eff}}(\sigma)$ are plotted as the dotted curves in Figs. 1 and 2. The curves for other plate spacings look similar, falling closer to one or the other of the steady flow curves.

Despite the fact that the nonuniform profile of the velocity varies in time in a complicated manner, the time- and space-averaged K_{eff} turns out to be a simple, smooth curve that is almost a weighted average of the curves for uniform or Poiseuille steady flow. The weighting factor can be estimated from the curves such as those in Fig. 3. For example, for $y_0/\delta_\nu = 3$, the value of α_{eff} is $\frac{2}{3}$ of the way from 1 to 1.54; K_{eff} can be estimated quite well by using a value $\frac{2}{3}$ of the way between K_{eff}(uniform) and K_{eff}(Poiseuille) for any σ.

The difference between K_{eff}(uniform) and K_{eff}(Poiseuille) can be quite large. For example, at $\sigma = 0.7$, a reasonable value for a parallel-plate heat exchanger, K_{eff}(Poiseuille)$=0.35$, which is 3.9 times greater than K_{eff}(uniform)$=0.09$ at that same plate spacing.

VI. CONCLUSIONS

Heat exchanger minor losses in thermoacoustics are sometimes estimated using Eq. (1) with coefficients K taken from steady flow results. For situations where the oscillating flow velocity profile $u(\mathbf{r},t)$ is known [such as those given by Eqs. (7) and (8)], we propose using Eq. (12) to calculate effective exit loss K-factors for use in Eq. (1). The results of the calculation are presented graphically for parallel plates and circular tubes in Figs. 3 and 4.

Real oscillating flow at an abrupt expansion is certainly more complicated than that given by Eq. (7), which applies only in the interior of a long, uniform tube. Nonetheless, Eq. (7) is probably a much *better* approximation than is uniform flow. Our results suggest that the appropriate minor loss coefficients are likely *greater* than $K_e = (1-\sigma)^2$ any time the hydraulic radius of the small pores is less than a few viscous penetration depths, as is the case in many of the heat exchangers used in thermoacoustic devices.

ACKNOWLEDGMENTS

This work was supported by the Office of Naval Research. Thanks to Andi Petculescu, Gabriela Petculescu, Larry Wilen, Bart Smith, Greg Swift, Bob Smith, Matt Poese, and Kevin Bastyr for helpful conversations and correspondence.

[1] G. W. Swift and W. C. Ward, "Simple harmonic analysis of regenerators," J. Thermophys. Heat Transfer **10**, 652–662 (1996). This derivation is in Sec. II.A., culminating in Eq. (12). Special cases appear as Eqs. (7.15) and (7.16) of J. H. M. Disselhorst and L. Van Wijngaarden, "Flow in the exit of open pipes during acoustic resonance," J. Fluid Mech. **99**, 293–319 (1980). This result also appears in the form of an additional term in the acoustic resistance in Eq. (18) of G. B. Thurson, L. E. Hargrove, Jr., and B. D. Cook, "Nonlinear properties of circular orifices," J. Acoust. Soc. Am. **29**, 992–1001 (1957).

[2] J. K. Vennard, "Basic equations of fluid flow," in *Handbook of Fluid Dynamics*, edited by Victor L. Streeter (McGraw–Hill, New York, 1961), pp. 3-5 to 3-7.

[3] A. G. Fredrickson and R. B. Bird, "Transport phenomena in multicomponent systems," in *Handbook of Fluid Dynamics*, edited by V. L. Streeter (McGraw–Hill, New York, 1961), Eq. (6.222).

[4] I. E. Idelchik, *Handbook of Hydraulic Resistance*, 3rd ed. (Begell House, New York, 1996), Eq. (4-3).

[5] W. M. Kays, "Loss coefficients for abrupt changes in flow cross section with low Reynolds number flow in single and multiple tube systems," Trans. ASME **72**, 1067–1074 (1950), Eq. (6).

[6] W. M. Kays and A. L. London, *Compact Heat Exchangers*, 3rd ed. (Krieger, Malibar, FL, 1998). Third edition copyright 1984. Originally published in 1955.

[7] See Ref. 4, p. 190. After the expansion, "vortices develop and gradually disappear" for a short distance, after which the flow begins to develop again in the larger duct.

[8] G. W. Swift, "Thermoacoustic engines and refrigerators," in *Encyclopedia of Applied Physics* (Wiley–VCH, New York, 1997), Vol. 21, pp. 245–264.

Intraglottal pressure distributions for a symmetric and oblique glottis with a uniform duct (L)

Ronald C. Scherer[a] and Daoud Shinwari
Department of Communication Disorders, Bowling Green State University, 200 Health Center, Bowling Green, Ohio 43402

Kenneth J. De Witt
Department of Communication Disorders, Bowling Green State University, 200 Health Center, Bowling Green, Ohio 43402 and Chemical Engineering, University of Toledo, 3060 Nitschke Hall, Toledo, Ohio 43606-3390

Chao Zhang, Bogdan R. Kucinschi, and Abdollah A. Afjeh
Mechanical, Industrial, and Manufacturing Engineering, University of Toledo, 4006D Nitschke Hall, Toledo, Ohio 43606-3390

(Received 29 June 2001; revised 8 June 2002; accepted 2 July 2002)

A Plexiglas model of the larynx, having a uniform duct shape and minimal diameter of 0.04 cm, was used to obtain wall pressure distributions resulting from internal airflow. Both a symmetric glottis (obliquity of 0 degrees) and a slanted glottis (obliquity of 20 degrees) were used. The oblique glottis (i.e., a glottis that slants relative to the axial tracheal flow) is present in both normal and abnormal phonation. Obliquity has been shown to create unequal cross-channel pressures on the vocal fold surfaces [Scherer *et al.*, J. Acoust. Soc. Am. **109**, 1616 (2001)], and the study here continues this line of research. For the oblique glottis, one side was divergent and the other convergent. Transglottal pressures from 3 to 15 cm H_2O using constant airflows were used. Results indicated that the pressure distributions on the two sides of the glottis were essentially equal for the symmetric uniform case (pressures differed slightly near the exit due to asymmetric flow downstream of the glottis). For the oblique glottis, the pressures on the vocal fold surfaces at glottal entry differed by 21.4% of the transglottal pressure, suggesting that this oblique glottis creates upstream glottal pressures that may influence out-of-phase motion of the two vocal folds. [DOI: 10.1121/1.1504849]

PACS numbers: 43.70.Aj, 43.70.Bk [AL]

I. INTRODUCTION

It is not uncommon in both abnormal and normal phonation to create oblique glottis conditions due to phasing differences between the two vocal folds (von Leden *et al.*, 1960; Svec and Schutte, 1996; Svec *et al.*, 1999). The intraglottal pressure forces pushing or pulling on the vocal folds for a slanted or oblique glottis may differ from those for the symmetric glottis having the same included angle. This report is the second in a series of studies of the intraglottal pressures of an oblique glottis. The first paper (Scherer *et al.*, 2001) demonstrated that the pressures on the glottal walls (that is, on the medial sides of the vocal folds) were different when the glottis was set obliquely at an angle of 15 degrees for a divergent glottis having an included angle of 10 degrees and a minimal diameter of 0.04 cm. Near the glottal entry and exit for the oblique condition, the pressures were lower on the divergent side, with pressures differing by 27% of the transglottal pressure at the glottal entrance.

This study considered a uniform glottis of diameter 0.04 cm using the same enlarged Plexiglas model and CFD approach as in the previous study. The glottal duct had parallel sides (an included angle of 0 degrees). As before, both the symmetric and an oblique glottal condition were considered. The symmetric condition placed the uniform glottis ''straight'' in the airway (an obliquity of 0 degrees), whereas the oblique condition tilted the uniform glottis at an angle of 20 degrees.

II. METHODS

A. Experimental methods

The methodological details are identical to those for the earlier study, and will only be summarized here. The Plexiglas model M5 is 7.5 times larger than a normal male larynx, had no false vocal folds, and was situated in a rectangular duct. The vocal folds were inserts into the model and had well-defined entrance and exit radii. Glottal length was 1.2 cm human size (9.0 cm in M5), and the glottal duct length was 0.3 cm human size (2.25 cm in M5).

Figure 1 shows the two glottal configurations for this experiment. Three pairs of vocal fold pieces were used. One pair [Fig. 1(a)] corresponded to the symmetric glottis. There were two sets of vocal fold pairs for the 20 degrees oblique glottis [Fig. 1(b)]. For each pair, one side had a divergent angle of 20 degrees, and the other side had a convergent angle of 20 degrees. Two pairs were needed because the pressure taps were only on one side of the glottis. By reversing the oblique orientation with a second pair of vocal folds, the pressures on ''both'' sides of the oblique glottis were

[a]Electronic mail: ronalds@bgnet.bgsu.edu

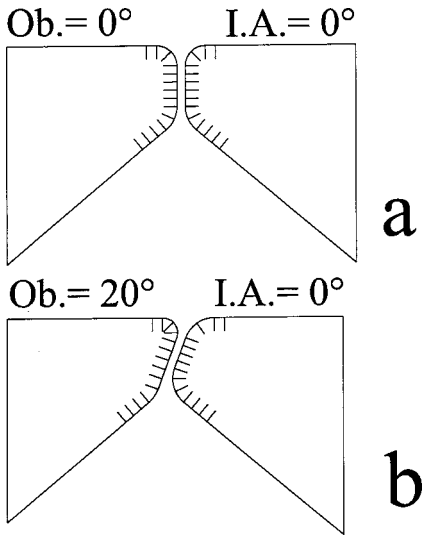

FIG. 1. The two glottal configurations of this study. (a) Outline of the symmetric uniform glottis. (b) Outline of the oblique uniform glottis with an obliquity of 20 degrees. The pressure taps are shown. During the experimental runs, pressure taps existed on one side only (see text).

obtained. There were 14 pressure taps along the vocal fold surface (Fig. 1). The pressure taps were placed near the center in the inferior to superior direction. The pressure taps had an inner diameter of 0.033 cm (actual size in the model vocal folds). There was also a pressure tap upstream in the side of the rectangular wind tunnel (the subglottal reference pressure), and two downstream in the side of the rectangular wind tunnel. Other methods of pressure scanning, flow measurement, and measurement accuracies were the same as in the earlier study.

During an experimental run for the symmetric condition, the air tended to move to one side of the duct downstream of the glottis. This supraglottal flow asymmetry was determined by noting the motion of a small group of human hairs on the end of a thin dowel rod when the rod was placed through the glottis and observed through the clear Plexiglas surface of the model. This observation is consistent with other studies of flow through a centrally located slit into a larger rectangular duct (Cherdron *et al.*, 1978; Tsui and Wang, 1995), attributed to disturbances generated at the exit of the expansion and amplified by shear layers. After the pressures were obtained, the flow direction was switched to the other side by momentarily placing a paper guide in the glottis. This method allowed the measurement of the effective pressures on ''both sides'' of the symmetric glottis using the same flow.

III. RESULTS

A. Pressure distributions for the symmetric uniform glottis

The pressure distributions for the symmetric uniform glottis are shown in Fig. 2 as the circular data points. There were two sets of empirical data for each transglottal pressure drop.[1] The ''flow wall'' refers to the side of the glottis that was the same side of the model toward which the air flowed downstream of the glottis. The ''non-flow wall'' refers to the opposite side. The pressures for the symmetric glottis were

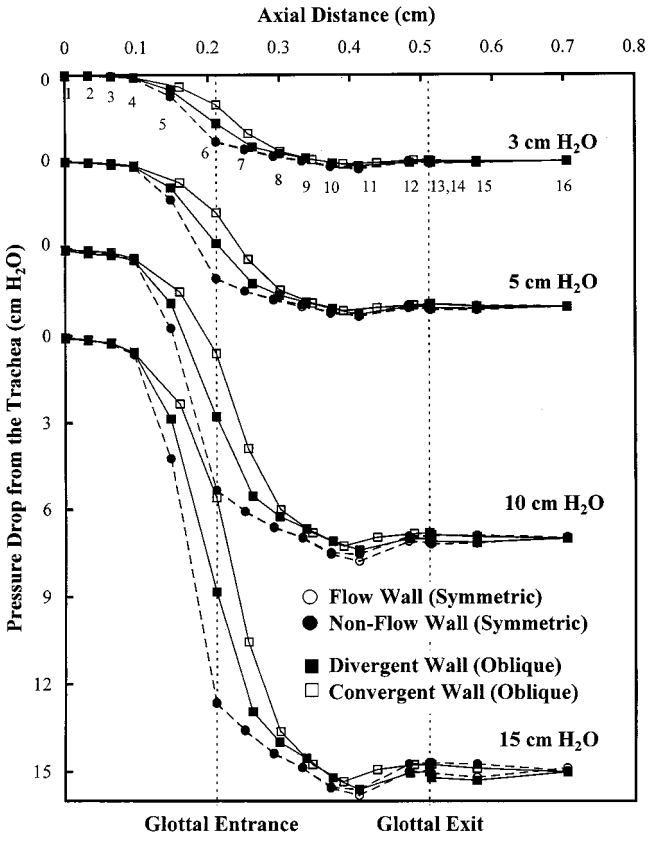

FIG. 2. Combined empirical pressure distributions for the symmetric and oblique uniform glottal configurations for 3, 5, 10, and 15 cm H_2O transglottal pressures. The corresponding flow values were 80.8, 106.4, 161.7, and 205.0 cm^3/s for the four transglottal pressures, respectively, for all conditions (±2%).

sensibly the same on both sides of the glottis for the 3 and 5 cm H_2O (low Reynolds number) cases. The pressures at tap 11 (where the glottal exit expansion began) and beyond had different values on opposite sides of the duct for the 10 and 15 cm H_2O (higher Reynolds number) cases due to downstream disturbances resulting from the skewing of the flow in the reservoir. The differences, however, were small. For example, the difference at tap 11 for the 15 cm H_2O case was only 0.20 cm H_2O, 1.35% of the transglottal pressure, and at tap 15, 0.46 cm H_2O, or 3.1% of the transglottal pressure.

If the downstream pressure at tap 16 were taken to be zero (atmospheric), then the first half of the glottis (up to tap 9) would have positive pressures that would apply forces to separate the vocal folds, and negative pressures from tap 9 to the glottal exit expansion to pull the vocal folds toward each other. This push and pull would tend to support a phase difference between the upper and lower pairs of the glottis.

B. Pressure distributions for the oblique uniform glottis

As Fig. 2 shows, unlike the symmetric glottal condition, the pressures on the two sides of the oblique uniform glottis at taps 5–7 were different. For the four transglottal pressures, the pressure was higher on the convergent side at tap 6 by 21.4% (sd=0.45%) of the transglottal pressure, and by 16.1% (sd=0.37%) at tap 7, as the flow had a higher imping-

ing force on the convergent side. The pressures on the two glottal sides in the oblique condition were about the same in the mid-section of the glottis (from tap 8 to tap 10) where the entrance effects were minimized. The pressures at tap 11, where the glottal exit expansion began, and at tap 12, in the middle of the exit expansion, demonstrated a return to higher pressures due to the increasing cross-sectional area. For tap 12, the cross-channel pressures differed by only 1.7% (sd $=0.8\%$) of the transglottal pressure.

In general, then, for the 20 degrees oblique condition for this uniform glottis, the convergent side had higher pressures applied to it in the glottis entrance region, with pressures that were relatively similar to each other elsewhere in the glottis. These differences would give rise to different forces on the two vocal folds in the entrance region, pushing outward more on the convergent side.

The cross-channel pressures on the vocal fold superior surface (taps 13 and 14) and at the pressure tap 15 just downstream of the vocal folds were slightly higher on the convergent side for the oblique condition, and on the non-flow wall for the symmetric condition (Fig. 2). These are the sides opposite the side toward which the air flowed downstream of the glottis. The differences were relatively small, however, ranging from 1.4% to 3.3% of the transglottal pressure for taps 13–15 (mean of 2.0%, sd=0.7%) for the oblique condition, and 1.9% to 4.4% (mean of 2.8%, sd=0.7%) for the symmetric condition.

C. Computational results for the oblique uniform glottis

FLUENT (Fluent, Inc., Lebanon, NH), a computational fluid dynamics package, was used as in the earlier study to obtain a deeper understanding of the physics of the oblique condition. The computer program solved the Navier–Stokes equations using a control-volume technique with structured and unstructured meshes, second-order solutions for momentum and pressure, and residuals of less than 10^{-4}.

Figure 3 shows streamlines, velocity profiles, and pressure contours for the oblique geometry for the 5 cm H_2O condition (the other conditions were similar).[2] For the same axial location, the velocities were greater and the pressures less on the divergent wall compared to the convergent wall up to the glottal exit region. The pressure contours of Fig. 3(c) show that glottal uniformity further downstream caused the pressures to be nearly constant across the duct (perpendicular to the glottal walls) indicating almost fully developed flow there for a short section of the mid-glottis. Figure 3(b) illustrates flow separation (S_1 and S_2) on both surfaces near the glottal exit due to the adverse pressure gradients on both surfaces. This separation occurred first on the converging wall (S_2) due to the higher rate of pressure increase as a result of higher wall curvature. The divergent wall separation (S_1) occurred further downstream.

D. Pressure comparisons between the symmetric and oblique uniform glottis conditions

The oblique glottal condition created a slightly larger glottal diameter at tap 6 than in the symmetric glottal condition. Instead of being 0.04 cm (human size) at the tap 6 (glottal entrance) location, the diameter was 18% greater (see Fig. 1). This larger diameter would create larger pressures at the tap 6 location (on both sides of the glottis) than would have existed for the symmetric condition. The larger pressures are indeed seen as smaller pressure drops between taps 1 and 6 in Fig. 2. The 18% increase in diameter predicts (by the Bernoulli equation) a reduction in pressure drop of 28.2%, a difference that was satisfied well by the pressures on the *divergent* side of the oblique glottis [on average within 2.7% (sd=0.74%) of the value 28.2% across the four transglottal pressures]. However, the *convergent* side showed a greater reduction in pressure drop (higher pressures) due to the higher impinging force.

The comparison of the symmetric with the oblique glottis results also indicates that the pressures within the glottis were consistently greater in the oblique case up to pressure tap 10, more than half-way through the glottis, due to the oblique geometry changing the direction of the flow. The

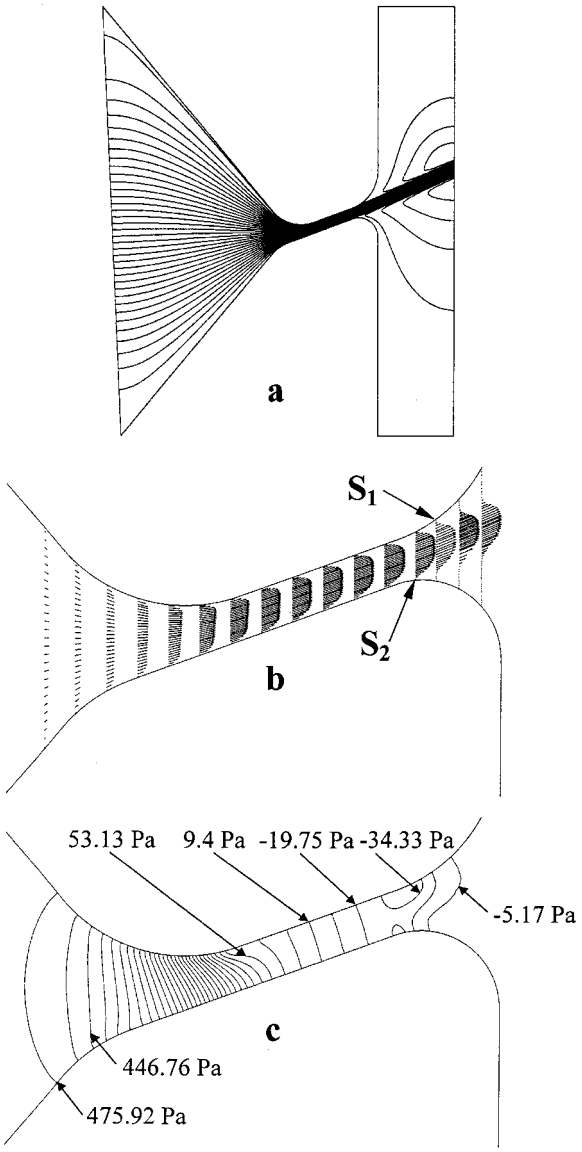

FIG. 3. Simulation using FLUENT for the oblique uniform glottis and a transglottal pressure of 5 cm H_2O: (a) streamlines, (b) velocity profiles, and (c) pressure contours. 1 Pa$=1.02\times10^{-2}$ cm H_2O.

differences for taps 8–10, however, were small due to the flow establishment resulting from the now uniform geometry. For example, the difference in pressure near tap 10 was only about 2.6% (relative to the transglottal pressure) between the symmetric and the oblique pressures.

IV. DISCUSSION

The results of this study are consistent with those of the prior study of an oblique divergent glottis (Scherer *et al.*, 2001); the obliquity created greater pressures on the convergent glottal wall compared to the divergent glottal wall in the entrance region of the glottis. The earlier study used the same minimal glottal diameter (0.04 cm) but with a divergent glottis of 10 degrees and an obliquity of 15 degrees. The cross-channel difference at the entrance to the oblique glottis was approximately 27%, which was similar to the 21.4% found in the present study. These pressure differences may change with different diameters and oblique glottal angles, and should be studied further. If these steady flow studies are strongly related to the physics of phonation, as the quasi-steady assumption suggests (Flanagan, 1972; Mongeau *et al.*, 1997), then an oblique glottis creates different driving forces on the vocal folds, strongest at glottal entrance for uniform and divergent glottal shapes. These different forces may influence the phasing differences between the two vocal folds because the convergent side receives higher pressures. The specific influence would depend upon the relative motion of the two vocal folds.

The current studies on glottal obliquity suggest that a more complete aerodynamic formulation regarding glottal pressure, flow, and geometry may require expressions specific to the medial surfaces of both vocal folds.

V. CONCLUSIONS

The results of this steady-flow study suggest that an oblique (20 degrees) uniform glottis will create significant cross-channel pressure differences near the entrance to the glottis. The cross-channel difference was 21.4% of the transglottal pressures from 3 to 15 cm H_2O. These results are consistent with a previous study of glottal obliquity for a divergent glottis (Scherer *et al.*, 2001). Yet to be determined is how glottal obliquity and the resulting differences in cross-channel pressures are related to phasing differences between the two vocal folds, as well as perturbations in glottal flow.

ACKNOWLEDGMENTS

The research was supported by NIH Grant No. 1 RO1 DC03577 from the National Institute on Deafness and Other Communication Disorders. The authors thank Anders Löfqvist and two anonymous reviewers for their comments.

[1]There is a difference between ''pressure'' and ''pressure drop.'' Figure 2 shows the pressure drop from the trachea to the pressure taps throughout the model. A pressure *drop* of 10 cm H_2O, for example, means that the pressure was 10 cm H_2O lower at a pressure tap downstream of the tracheal reference pressure tap. The greatest pressure is always at the tracheal pressure tap (the subglottal pressure).

[2]The average difference between the computational pressures and the empirical (M5) pressures was typically less than approximately 0.2 cm H_2O, with larger differences for higher transglottal pressures at tap 7.

Cherdron, W., Durst, F., and Whitelaw, J. H. (**1978**). ''Asymmetric flows and instabilities in symmetric ducts with sudden expansions,'' J. Fluid Mech. **84**(1), 13–31.

Flanagan, J. L. (**1972**). *Speech Analysis Synthesis and Perception, 2nd ed.* (Springer-Verlag, New York).

Mongeau, L., Franchek, N., Coker, C. H., and Kubli, R. A. (**1997**). ''Characteristics of a pulsating jet through a small modulated orifice, with application to voice production,'' J. Acoust. Soc. Am. **102**, 1121–1134.

Scherer, R. C., Shinwari, D., De Witt, K. J., Chang, C., Kucinschi, B. R., and Afjeh, A. A. (**2001**). ''Intraglottal pressure profiles for a symmetric and oblique glottis with a divergence angle of 10 degrees,'' J. Acoust. Soc. Am. **109**, 1616–1630.

Svec, J. G., and Schutte, H. K. (**1996**). ''Videokymography: High-speed line scanning of vocal fold vibration,'' J. Voice **10**(2), 201–205.

Svec, J. G., Schutte, H. K., and Sram, F. (**1999**). ''Variability of vibration of normal vocal folds as seen in videokymography,'' in *Communication and Its Disorders: A Science in Progress, Proceedings 24th Congress International Association of Logopedics and Phoniatrics,* edited by P. H. Dejonckere and H. F. M. Peters (International Association of Logopedics and Phoniatrics), Amsterdam, The Netherlands, 23–27 August 1998, Vol. 1, pp. 122–125.

Tsui, Y.-Y., and Wang, C.-K. (**1995**). ''Calculation of laminar separated flow in symmetric two-dimensional diffusers,'' J. Fluids Eng. **117**, 612–616.

von Leden, H., Moore, P., and Timcke, R. (**1960**). ''Laryngeal vibrations: Measurements of the glottic wave. Part III: The pathologic larynx,'' Arch. Otolaryngol. **71**, 16–35.

Innate phonetic boundaries revisited (L)

Richard N. Aslin[a)]
Department of Brain and Cognitive Sciences, University of Rochester, Rochester, New York 14627

Janet F. Werker
Department of Psychology, University of British Columbia, Vancouver, British Columbia V6T 1Z4, Canada

James L. Morgan
Department of Cognitive and Linguistic Sciences, Brown University, Providence, Rhode Island 02912

(Received 22 May 2002; accepted for publication 20 June 2002)

Nittrouer [J. Acoust. Soc. Am. **110**, 1598–1605 (2001)] raised several serious concerns with the so-called Universal Theory of phonetic category development that she characterized as the accepted wisdom in the field of infant speech perception. She then presented data from infants and children that were claimed to be inconsistent with Universal Theory and led her to question the entire notion of phonetic categories. Here we argue that Nittrouer not only misrepresented Universal Theory, but also provided no data to refute either this theory or the existence of phonetic categories. © *2002 Acoustical Society of America.* [DOI: 10.1121/1.1501904]

PACS numbers: 43.71.An, 43.71.Ft, 43.71.Hw [KRK]

The study of infant speech perception was initiated in 1971 by the publication of Eimas *et al.*'s seminal paper on young infants' discrimination of voicing differences in synthetic consonant-vowel syllables varying in voice-onset-time (VOT). Since 1971, dozens of experiments have confirmed the initial observation that discrimination of the acoustic correlates of consonant contrasts is discontinuous. That is, not all physically equal steps along synthetic speech continua are equally easy or difficult for infants to discriminate. Rather, depending on the regions in which they fall, some steps are difficult to discriminate, much like the chance levels of performance obtained from adults for within-category differences, whereas other steps are relatively easy to discriminate, much like between-category performance obtained from adults.

The initial account of these findings suggested that infants process speech with mechanisms that are both innate and specifically linguistic. However, since 1971 there has been considerable debate in the literature about the proper level of analysis to invoke to account for infants' discrimination of speech signals. A *phonemic* account, initially attractive because infants' putative category boundaries closely matched those of their native language environment, was swiftly shown to be untenable by experiments revealing that (a) many non-native speech contrasts were discriminable by infants, (b) adults were often unable to discriminate (or had reduced sensitivity to) these non-native contrasts, and (c) infants' category boundaries did not always correspond to adult values in the native language. Moreover, many of the same discontinuities in speech discrimination observed in infants were also present in nonhuman animals (Kuhl and Miller, 1975, 1978; Kuhl and Padden, 1982, 1983), casting doubt on a *phonetic* account of speech sound discrimination.

One result of this initial wave of follow-ups to the Eimas *et al.* (1971) study was a perspective summarized by Aslin and Pisoni (1980) in which speech discrimination by infants was accounted for largely by a general auditory rather than a phonetic mechanism. Consistent with the results of animal experiments, this perspective proposed that young infants were able to discriminate speech contrasts without recourse to a phonetic level of analysis by using general auditory mechanisms that were categorical in nature and independent of experience with any native language.[1] The role that experience with a native language played in speech perception was characterized by one of four mechanisms: (a) maturation—a gradual unfolding that was uninfluenced by experience, (b) induction—an unfolding that required specific experiences, (c) attunement—discriminative abilities that were partially present prior to the onset of experience and then shaped by that experience, or (d) maintenance—discriminative abilities that were fully mature at the onset of experience and were maintained or lost depending on the presence or absence of that experience. It is this last mechanism that Aslin and Pisoni described as a Universal Theory of the development of speech perception.

Nittrouer (2001) provides several challenges to what she claims are the major tenets of Universal Theory. First, she states, ''Those early studies of infant speech perception led to the widely accepted view that infants are born with sensitivities to phonetic boundaries for all languages (i.e., the universal set)'' (p. 1598). She then cites apparently contradictory findings from several studies of infants. One study (Holmberg *et al.*, 1977) found that infants have difficulty discriminating a fricative contrast, while another study (Lasky *et al.*, 1975) found that infants from a Spanish-speaking environment failed to discriminate a VOT contrast that is used in Spanish but succeeded in discriminating non-native VOT contrasts that are relevant in English and Thai. Nittrouer concludes, ''In spite of these seemingly contradictory findings, however, the notion of innate phonetic boundaries has persisted'' (p. 1599).

Ironically, Nittrouer (2001) cites the very results that Aslin and Pisoni (1980) used in support of Universal Theory.

[a)]Electronic mail: aslin@cvs.rochester.edu

The fact that infants in the Lasky *et al.* (1975) study discriminated the English and Thai boundaries but not the Spanish boundary, as well as evidence from Streeter (1976) that infants from a Kikuyu environment discriminated the English boundary that is not used by Kikuyu adults, led Aslin and Pisoni to posit that these discriminations were *not* the result of a phonetic level of analysis. Rather, these data, along with the results from animal experiments that showed similar VOT boundaries, were taken as evidence for a general auditory-based form of categorical perception in young infants. While Nittrouer summarizes this account of speech categories, she states, ''These variations, however, fail to contradict the basic tenets of the universal theory'' (p. 1599).

Missing from Nittrouer's (2001) summary of Universal Theory was how Aslin and Pisoni (1980) placed this theory in context: ''It is important to note here that we are *not* claiming that only one of these classes of theories [Universal, Attunement, Perceptual Learning] will uniquely account for the development of *all* speech contrasts. Rather, it may be the case that some hybrid of the theories provides the best description of the development of specific classes of speech-sound discrimination. In fact, this view of parallel developmental processes appears to be supported by current empirical findings'' (pp. 79–80). Aslin and Pisoni go on to state, ''The evidence on the development of voicing perception therefore appears to provide good support for the *attunement* theory'' (p. 84) [emphasis added], not the Universal Theory. Finally, Aslin and Pisoni make their position clear: ''From this brief summary of the perception of voicing contrasts in stop consonants, fricatives, vowels, and liquids, it should be apparent that the major roles of early experience that we outlined earlier cannot be uniformly invoked to account for the development of the abilities needed to discriminate *all* speech contrasts found in spoken language'' (p. 88).

Nittrouer's (2001) incomplete and misleading summary of Aslin and Pisoni's (1980) model of infant speech perception is mirrored in her treatment of more recent models, most notably that of Best (1994), which outlines several different ways in which classes of speech sounds are affected (or not) by early experience via a process of perceptual assimilation. Although Best did not adopt the term Universal Theory in her model, a mechanism analogous to maintenance is embedded, in part, in her conceptualization. Similarly, Werker and Tees (1984), who provided the first time-course data for the change in discriminative performance between 6 and 12 months of age for two non-native consonant contrasts, made it clear that this mechanism of age-related change was not ''loss'' *per se* (Werker, 1995), likely occurred through the application of more general learning mechanisms (Lalonde and Werker, 1995), and was not applicable to all phonetic contrasts (see also Best *et al.*, 1988; Polka and Bohn, 1996). Moreover, other more recent treatments of the effects of early experience on speech perception by infants (Aslin *et al.*, 1998; Jusczyk, 1997; Werker and Tees, 1999) provide a much more nuanced view than the one ascribed by Nittrouer (2001) under the guise of Universal Theory. Indeed, there is likely no one today who would describe the sensitivities shown by the newborn infant as straightforwardly ''innate.'' Werker and Tees (1992, 1999) characterize the mechanism accounting for newborn sensitivities as one of ''probabilistic epigenesis,'' whereas Jusczyk and Bertoncini (1988) describe it as one of ''innately guided learning.'' Much of the current research is focused on identifying precisely what the early biases and experiential mechanisms are that bring about both initial discrimination performance and subsequent change, from Jusczyk's WRAPSA model (1993) to Kuhl's (1991) Perceptual Magnet Model to Maye *et al.*'s (2002) and Anderson and Morgan's (2002) demonstrations of infants' abilities to use statistical information to alter category structure and to acquire auditory equivalence classes (Kuhl, 1983). In short, Nittrouer's straw man has no clothes.

The second challenge offered by Nittrouer (2001) is that infants are much worse at speech sound discrimination than one would expect from a reading of the previous literature. The irony here is that she claims on several occasions (including in the abstract) that her ''results did not differ from those reported by others.''[2] Nevertheless, she states that ''Overall these results fail to provide support for claims that universal phonetic boundaries are in place at birth. It is emphasized that the findings of this study do not really differ from those of others: success rates are similar across studies. What differs is the willingness of authors to use the results to support claims of innate phonetic boundaries'' (p. 1603). What leads Nittrouer to a different conclusion?

Her primary evidence for rejecting the notion of innate phonetic boundaries, setting aside the aforementioned arguments by some of us that these categories are not initially phonetic *per se*, is that not all infants succeed in discriminating them. That is, Nittrouer apparently believes that universal means ''in all cases'' and ''for all infants.'' Both of these criteria are misguided. First, we have already made the argument that Nittrouer incorrectly ascribed Universal Theory to all speech contrasts, which was never the claim of this theory since it was proposed in 1980. Thus, the fact that some speech contrasts are easier to discriminate than others simply cannot be used as an argument against Universal Theory, particularly since there are obvious differences in the acoustic salience of different speech contrasts. Nittrouer argues that ''success rates differed across contrasts'' (p. 1603) and that ''If procedures accounted for a large proportion of variance in success rates, we would have expected those rates to be similar across contrasts'' (p. 1603). But that statement flies in the face of compelling evidence that performance varies with simple acoustic parameters (e.g., changes in tone frequency) in the conditioned headturning paradigm (e.g., Olsho, 1984; Sinnott and Aslin, 1985). This finding that some distinctions are more difficult than others holds across a variety of methodologies in addition to conditioned headturning. These include visual habituation, heart rate deceleration, and mismatch negativity (MMN) in the event related potential (ERP) recorded from scalp electrodes. Yet, importantly, in all of these tasks infants consistently perform better on between- than on within-category differences (Miller and Morse, 1976; Best, 1994; Dehaene-Lambertz and Baillet, 1998). In addition to differences in discrimination, infants are better able to categorize some stimuli than others. At 6–8 months of age they treat multiple instances from within a dental category as equivalent, and as different from multiple

instances from a retroflex category, whereas they fail to categorize instances that span the dental/retroflex category boundary (Werker and Lalonde, 1988). It is this relative pattern of performance, rather than absolute levels of discriminability, which is important.

Second, no technique used to assess any aspect of infant performance succeeds in obtaining precisely the same data from the same infants upon repeated testing. Infants are notoriously difficult to test. We cannot directly instruct infants on the nature of experimental tasks, and their short attention spans preclude gradual shaping of desired behaviors. Rather, at best, procedures can be set up to maximize the likelihood that most infants will be sufficiently engaged in the task at hand to form approximately correct inductions about its nature most of the time. Thus, one has to work very hard to establish optimal conditions to obtain even adequate performance. Nittrouer's placement of infants in a car seat or high-chair alters the typical context in which testing is conducted in the conditioned headturning procedure and could easily result in suboptimal performance. Similarly, use of a very few test trials sets a strict standard that only a few infants, even under optimal conditions, will meet. For example, Nittrouer used a fixed criterion of 8 out of 10 correct responses to change trials as a threshold for concluding that infants discriminated a specific speech contrast. She notes that Werker's lab has used this same criterion in the past. However, with the exception of Werker and Tees (1984), where the criterion was 8 out of 10 responses to change trials only, Werker's lab has more typically used a floating criterion of correct responses to both change and control trials within a total of 25 trials. Thus, Nittrouer's criterion for successful discrimination is considerably more stringent than that of Werker and other researchers in the field who use the conditioned headturning technique.

As a result of her experiments with infants, Nittrouer (2001) expresses surprise that only 65% of her subjects discriminated the vowel contrasts and only 35% discriminated the consonant contrasts. But why should we expect all infants to ''pass'' a test of discrimination, particularly with her testing setup and performance criterion? Surely an inattentive adult would show less than perfect performance on any task, and infants are not immune from such lapses of attention and motivation. Nittrouer argues that these task variables should be independent of the difficulty of the speech contrast. But that argument is simply not compelling: surely one would expect performance to vary with task difficulty even if there are general task variables (e.g., criterion effects) operating to reduce optimal performance. These issues are moot, however, because Nittrouer claims that her data are not that different from what others have reported in the literature. Why then does she come to such a different conclusion about innate phonetic categories?

A key difference between Nittrouer's interpretation of her data and that of others in the field is that she holds an idealized view of categorical perception. This view posits that labeling functions have sharp category boundaries and that within-category discrimination is at chance while between-category discrimination is at ceiling. The problem is that no data from infants have ever supported such a ''strictly categorical'' view of speech perception. In fact, there are no labeling data at all from infants to complement their discontinuous discrimination data. Thus, at best, the infant literature supports a weak view of categorical perception. Interestingly, the adult literature supports a similar view, with reaction time (Pisoni and Tash, 1974), goodness ratings (Miller, 1994), and same-different judgments (Carney *et al.*, 1977) supporting a less definitive view of categorical perception than originally attributed to Liberman *et al*. (1967). But of course this does not imply, as suggested by Nittrouer, that ''Perhaps we should not even be asking if infants have well-formed phonetic categories, separated by boundaries, but rather if any language users do. In other words, the very concept of categories, and even more so of boundaries, needs to be reconsidered'' (p. 1604). Clearly, there is an interpretive agenda here that goes well beyond the infant data that Nittrouer reports and compares to the existing infant data in the literature: ''we have no evidence that boundaries exist in the natural world, or any account of how or why they might have evolved by natural selection. To extend to them any degree of psychological reality is unsupportable, and deleterious to efforts to understand how phonetic structure is indeed instantiated and retrieved from the speech signal'' (p. 1604). One can only imagine what Nittrouer believes is a sufficient replacement for the notion of speech categories (and their logically necessary boundaries) since she offers no such account.

In summary, Nittrouer (2001) has provided a naive and incomplete view of Universal Theory and of categorical perception. She used methods commonly employed in the infant speech perception literature, though in a strikingly suboptimal manner. As a result, her findings on speech discrimination are at the low end of those reported previously. This combination of factors—weak data and an idealized view of Universal Theory and categorical perception—led her to conclude that infants have no phonetic categories or boundaries between them. We believe these conclusions are misleading and do not fairly represent the current thinking in the field of infant speech perception. While we may disagree about some of the subtle aspects of infant speech perception, Nittrouer's article throws the entire ''baby'' out with a very muddied perspective on the ''bath water.'' As such, Nittrouer's challenge to the field of infant speech perception fails to measure up.

[1]Other past accounts, such as that of Werker and Pegg (1992), proposed three separate patterns: one corresponding to general auditory sensitivities, one to language-general phonetic differences, and one to language-specific meaning-based phonemic differences.

[2]In fact, the studies that Nittrouer cites as comparisons tested 2-month-olds in habituation procedures, rather than 6- to 14-month-olds with conditioned headturning. As discussed below, Nittrouer adopts an excessively stringent criterion; as might be expected, the proportion of subjects failing to reach criterion in Nittrouer's study was much higher than that of other studies testing infants of the same age with the same technique (e.g., Morgan, 1994; Werker and Tees, 1984).

Anderson, J. L., and Morgan, J. L. (**2002**). ''A statistical basis for speech sound discrimination,'' poster presentation at the International Conference on Infant Studies, Toronto, Canada.

Aslin, R. N., and Pisoni, D. B. (**1980**). ''Some developmental processes in speech perception,'' in *Child Phonology, Vol. 2, Perception*, edited by

G. H. Yeni-Komshian, J. F. Kavanagh, and C. A. Ferguson (Academic, New York), pp. 67–96.
Aslin, R. N., Jusczyk, P. W., and Pisoni, D. B. (**1998**). ''Speech and auditory processing during infancy: Constraints on and precursors to language,'' in *Handbook of Child Psychology, Vol. 2: Cognition, Perception & Language*, 5th ed., edited by D. Kuhn and R. Siegler (Wiley, New York), pp. 147–198.
Best, C. T. (**1994**). ''The emergence of native-language phonological influences in infants: A perceptual assimilation model,'' in *The Development of Speech Perception*, edited by J. C. Goodman and H. C. Nusbaum (MIT, Cambridge, MA), pp. 167–224.
Best, C. T., McRoberts, G. W., and Sithole, N. M. (**1988**). ''Examination of perceptual reorganization for nonnative speech contrasts: Zulu click discrimination by English–speaking adults and infants,'' J. Exp. Psychol. Hum. Percept. Perform. **4**, 45–60.
Carney, A. E., Widin, G. P., and Viemeister, N. F. (**1977**). ''Noncategorical perception of stop consonants differing in VOT,'' J. Acoust. Soc. Am. **62**, 961–970.
Dehaene-Lambertz, G. L., and Baillet, S. (**1998**). ''A phonological representation in the infant brain,'' NeuroReport **9**, 1885–1888.
Eimas, P. D., Siqueland, E. R., Jusczyk, P. W., and Vigorito, J. (**1971**). ''Speech perception in early infancy,'' Science **171**, 304–306.
Holmberg, T. L., Morgan, K. A., and Kuhl, P. K. (**1977**). ''Speech perception in early infancy: Discrimination of fricative consonants,'' J. Acoust. Soc. Am. Suppl. 1 **62**, S99.
Jusczyk, P. W. (**1993**). ''From general to language specific capacities: The WRAPSA model of how speech perception develops,'' J. Phonetics **21**, 3–28.
Jusczyk, P. W. (**1997**). *The Discovery of Spoken Language* (MIT, Cambridge, MA).
Jusczyk, P. W., and Bertoncini, J. (**1988**). ''Viewing the development of speech perception as an innately guided learning process,'' Lang Speech **31**, 217–235.
Kuhl, P. K. (**1983**). ''Perception of auditory equivalence classes for speech in early infancy,'' Infant Behav. Dev. **6**, 263–285.
Kuhl, P. K. (**1991**). ''Human adults and human infants show a 'perceptual magnet effect' for the prototypes of speech categories, monkeys do not,'' Percept. Psychophys. **50**, 93–107.
Kuhl, P. K., and Miller, J. D. (**1975**). ''Speech perception by the chinchilla: Voiced-voiceless distinction in the alveolar-plosive consonants,'' Science **190**, 69–72.
Kuhl, P. K., and Miller, J. D. (**1978**). ''Speech perception by the chinchilla: Identification functions for synthetic VOT stimuli,'' J. Acoust. Soc. Am. **63**, 905–917.
Kuhl, P. K., and Padden, D. M. (**1982**). ''Enhanced discriminability at the phonetic boundaries for the voicing feature in macaques,'' Percept. Psychophys. **32**, 542–550.
Kuhl, P. K., and Padden, C. (**1983**). ''Enhanced discriminability at the phonetic boundaries for the place feature in macaques,'' J. Acoust. Soc. Am. **73**, 1003–1010.
Lalonde, C., and Werker, J. F. (**1995**). ''Cognitive influences on cross-language speech perception in infancy,'' Infant Behav. Dev. **18**, 459–476.
Lasky, R. E., Syrdal-Lasky, A., and Klein, R. E. (**1975**). ''VOT discrimination by four to six and a half month old infants from Spanish environments,'' J. Exp. Child Psychol. **20**, 215–225.
Liberman, A. M., Cooper, F. S., Shankweiler, D. P., and Studdert-Kennedy, M. G. (**1967**). ''Perception of the speech code,'' Psychol. Rev. **74**, 431–461.
Maye, J., Werker, J. F., and Gerken, L. A. (**2002**). ''Infant sensitivity to distributional information can affect phonetic discrimination,'' Cognition **82**, B101–B111.
Miller, C. L., and Morse, P. A. (**1976**). ''The 'heart' of categorical speech discrimination in young infants,'' J. Speech Hear. Res. **19**, 578–589.
Miller, J. L. (**1994**). ''On the internal structure of phonetic categories: A progress report,'' Cognition **50**, 271–285.
Morgan, J. L. (**1994**). ''Converging measures of speech segmentation in preverbal infants,'' Infant Behav. Dev. **17**, 389–403.
Nittrouer, S. (**2001**). ''Challenging the notion of innate phonetic boundaries,'' J. Acoust. Soc. Am. **110**, 1598–1605.
Olsho, L. W. (**1984**). ''Infant frequency discrimination,'' Infant Behav. Dev. **7**, 27–35.
Pisoni, D. B., and Tash, J. (**1974**). ''Reaction times to comparisons within and across phonetic categories,'' Percept. Psychophys. **15**, 285–290.
Polka, L., and Bohn, O-S. (**1996**). ''A cross-language comparison of vowel perception in English-learning and German-learning infants,'' J. Acoust. Soc. Am. **100**, 577–592.
Sinnott, J. M., and Aslin, R. N. (**1985**). ''Frequency and intensity discrimination in human infants and adults,'' J. Acoust. Soc. Am. **78**, 1986–1992.
Streeter, L. A. (**1976**). ''Language perception of 2-month-old infants shows effects of both innate mechanisms and experience,'' Nature (London) **259**, 39–41.
Werker, J. F. (**1995**). ''Exploring developmental changes in cross-language speech perception,'' in *An Invitation to Cognitive Science. Part I: Language*, edited by L. Gleitman and M. Liberman (MIT, Cambridge, MA), pp. 87–106.
Werker, J. F., and Lalonde, C. E. (**1988**). ''Cross-language speech perception: Initial capabilities and developmental change,'' Dev. Psychol. **24**, 672–683.
Werker, J. F., and Pegg, J. E. (**1992**). ''Infant speech perception and phonological acquisition,'' in *Phonological Development: Models, Research, and Implications*, edited by C. Ferguson, L. Menn, and C. Stoel-Gammon (York, Parkton, MD), pp. 285–311.
Werker, J. F., and Tees, R. C. (**1984**). ''Cross-language speech perception: evidence for perceptual reorganization during the first year of life,'' Infant Behav. Dev. **7**, 49–63.
Werker, J. F., and Tees, R. C. (**1992**). ''The organization and reorganization of human speech perception,'' Annu. Rev. Neurosci. **15**, 377–402.
Werker, J. F., and Tees, R. C. (**1999**). ''Influences on infant speech processing: Toward a new synthesis,'' Annu. Rev. Psychol. **50**, 509–535.

A reply to "Innate phonetic boundaries revisited" [J. Acoust. Soc. Am. 112, 1257–1260 (2002)] (L)

Susan Nittrouer[a)]
Center for Persons with Disabilities, Utah State University, Logan, Utah 84322

(Received 17 June 2002; accepted 20 June 2002)
[DOI: 10.1121/1.1501906]
PACS numbers: 43.71.An, 43.71.Ft, 43.71.Hw [KRK]

Before launching into a response to the letter by Aslin, Werker, and Morgan (2002), I would like to make clear my belief that the work on infant speech perception has been well executed, and has been critical to the development of general theoretical perspectives on speech perception. I respect and appreciate the contributions of these authors, and consider my own work with children to be a natural extension of their and others' work on infant speech perception.

At the same time, the questions starting to be asked by speech researchers who are not focused solely on infant perception reflect a dramatic change in theoretical perspective, one that is not matched in magnitude by changes in perspective in the infant speech perception work. Many investigators in other areas of speech perception are no longer concerned with trying to identify the acoustic correlates of phonetic categories, or with asking at what age human listeners are able to classify those correlates, or with asking if nonhuman animals can classify those correlates. Nor are other investigators much concerned with distinctions between ''auditory'' and ''phonetic'' perception, a recurring theme in the letter of Aslin *et al.* A general paradigm shift is underway in studies of speech perception toward a focus on how listeners perceptually organize the many properties of the speech signal. For example, Robert Remez and his colleagues (e.g., Remez *et al.*, 1994) and Robert Shannon and his colleagues (e.g., Shannon *et al.*, 1995) have convincingly demonstrated that mature listeners can organize signals that are void of the detailed properties that we usually consider acoustic correlates (or ''cues'') of phonetic categories in such a way that they still manage to arrive at a phonetically structured message. Investigators studying cross-linguistic speech perception are grappling with fundamental notions of what the objects of speech perception are, and what that means for our understanding of how the perceptual organization of the speech signal is shaped by experiences with a native language (Strange, 1995). What we consider to be the initial state of the human capacity for speech perception affects the further development of theories related to these topics, as well as many others.

The purpose of the brief article serving as the target of Aslin *et al.*'s letter was to state explicitly that the evidence is weak to support the position that infants are born able to discriminate all the phonemes of the world's languages. The authors say it best themselves on page 1259 of their letter, ''Thus, at best, the infant literature supports a weak view of categorical perception.'' I believe it is imperative that we (i.e., those of us studying speech perception by immature listeners) make this point loudly and clearly to our colleagues studying related questions regarding speech perception. I think it is a fair representation of the field of infant speech perception to say that the collective message for several decades has been that infants are endowed with the ''universal set'' of phonetic categories (i.e., those that could occur in all the languages of the world), and that the ambient language functions to maintain those that will be used. According to this view, those that will not be used are lost, somehow. The Introduction of the target paper provides several examples of statements supporting this position, and they will not be repeated here. Many others exist, both in the writing of investigators doing the research and in the writing of others citing those investigators. For example, a popular text by Rhea Paul (2001) for students of speech-language pathology states ''Speech perception, for example, is biologically programmed. We know this because infants as young as 4 weeks can distinguish between phonemes, even when they have no comprehension of language'' (p. 399). In fact, that message has even made it into the popular media, with several PBS documentaries during the past decade or so featuring one or another infant speech perception researcher reporting that newborns are citizens of the world, able to discriminate all phonetic contrasts that can occur (i.e., the ''universal set''). Those of us who have been around for a while recognize this position as the perceptual counterpart of an older view of infants' productions, which was that infants babble all the sounds of the world's languages; those not supported by the ambient language are lost. [Locke (1983) reviews this position, and the evidence against it.]

Assumptions about initial states profoundly impact research with children. In 1974, Isabelle Liberman and her colleagues (Liberman *et al.*, 1974) found that kindergartners were not as skilled as second graders at counting phonetic segments in words. Since the kindergartners were much better at counting syllabic segments (than they were at counting phonetic segments), I. Liberman *et al.* concluded that the poor results for phonetic segments did not have to do with task demands, but instead accurately reflected the level of structure the children could access. Of course, explicitly accessing phonetic structure in a counting task is different from discriminating pairs of syllables that differ by one phonetic segment. Nonetheless, both tasks inform us about linguistic organization in very young listeners. Thus, we are faced with a paradox. If infants readily discriminate syllables that differ

[a)]Electronic mail: nittrouer@cpd2.usu.edu

by one phonetic segment, why aren't they able to access that phonetic structure at five years of age?

Assumptions about initial states impact research and intervention with children having trouble learning language. We know that children experiencing conditions such as poverty or chronic middle-ear effusion have greater difficulty than age-matched peers with speech perception and phonological awareness tasks (e.g., Eimas and Clarkson, 1986; Godfrey *et al.*, 1981; Mody *et al.*, 1999; Nittrouer, 1996). Those of us interested in these (and other) clinical populations would like to understand why such conditions produce speech perception problems, and what we can do about it. The way in which we conceptualize the speech perception capacities of the infant affects how we understand the constellation of findings across studies with infants, children, and children with risk factors for language problems. Consequently, I felt it was imperative to report my finding that not all infants demonstrate capacities for phonetic discrimination, and to emphasize that some other studies have supported the same conclusion. I could have kept my results to myself, and so avoided controversy, but I think such findings must be acknowledged in future theoretical development. In the remainder of this letter, I would like to address the major criticism made by Aslin *et al.* of the target paper.

But what *is* Aslin *et al.*'s major criticism? It is never clear. At some points in the letter the criticism seems to be that I was inaccurate in my assertion that infant speech perception investigators have said that infants are born able to discriminate every phonetic contrast that could occur in the world's languages, with maintenance or loss of those discriminative capacities determined by which contrasts are found in the ambient language (i.e., Universal Theory). The authors assert that I built a ''straw man with no clothes.'' At other points they suggest that I failed to dispel this very notion with the evidence I presented because my assumptions and data collection techniques were flawed. Because there is no focus, I will deal with each theme in the letter separately.

Aslin *et al.* fret that the target paper credited Aslin and Pisoni (1980) with offering Universal Theory as a good description of infant speech perception capacity. Perhaps the first author of the letter wants to distance himself from this position. If that is the case, let me assure him that I never attributed such a position either to him or to David Pisoni. The target paper was clear in stating that the conclusion reached by most investigators doing early infant speech perception research has been that newborns can discriminate all phonetic contrasts that could occur in the world's languages, and that over the first few months of life those not supported by the ambient language are ''lost.'' What the target paper states is that this view matches what Aslin and Pisoni termed Universal Theory. Specifically, the statement made was:

> Those early studies of infant speech perception led to the widely accepted view that infants are born with sensitivities to phonetic boundaries for all languages (i.e., the universal set). Experience listening to a native language during the first year of life, the theory holds, maintains those boundaries supported by the ambient language, and causes those boundaries not supported by the ambient language to dissolve. This view of perceptual development is what Aslin and Pisoni (1980) call a ''universal'' theory. (Nittrouer, 2001, p. 1598)

Aslin *et al.* are also concerned that I misrepresented Universal Theory, as defined by Aslin and Pisoni (1980). The text above shows how it was described in the target paper. Aslin and Pisoni wrote:

> Universal theory assumes that, at birth, infants are capable of discriminating all the possible phonetic contrasts that may be used phonologically in any natural language. According to this view, early experience functions to maintain the ability to discriminate phonologically relevant distinctions, those actually presented to the infant in the environment. However, the absence of phonologically irrelevant contrasts, which are obviously not presented to the infant, results in a selective loss of the abilities to discriminate those specific contrasts. (p. 79)

In fact, in discussing Aslin and Pisoni's chapter, Aslin *et al.* write:

> Maintenance—discriminative abilities that were fully mature at the onset of experience and were maintained or lost depending on the presence or absence of that experience. It is this last mechanism that Aslin and Pisoni described as a Universal Theory of the development of speech perception. (p. 1257)

I fail to see the alleged discrepancy between either the Aslin and Pisoni definition or that offered in the letter of Aslin *et al.* and my description of Universal Theory.

Similarly, Aslin *et al.* suggest that the target paper misrepresented other papers, but then present exactly the same interpretation of those papers as that provided in the target paper. For example, they write:

> Nittrouer's (2001) incomplete and misleading summary of Aslin and Pisoni's (1980) model of infant speech perception is mirrored in her treatment of more recent models, most notably that of Best (1994) which outlines several different ways in which classes of speech sounds are affected (or not) by early experience via a process of perceptual assimilation. Although Best did not adopt the term Universal Theory in her model, a mechanism analogous to maintenance is embedded, in part, in her conceptualization. (p. 1258)

I believe that is exactly what the target paper said: Best (1994) is offered as an example of a paper espousing a (slightly modified) version of Universal Theory.

As this example shows, there are places in the letter of Aslin *et al.* where the rhetoric is strong, yet no clear blow is struck. There are also places in the letter where the target paper is criticized for failing to appreciate aspects of current thinking regarding infant speech perception that no one could ever be expected to appreciate. For example, Aslin

et al. write ''Indeed, there is likely no one today who would describe the sensitivities shown by the newborn infant as straightforwardly 'innate.' '' (p. 1258) In this context, ''no one'' presumably means ''no one doing infant speech perception research'' since no one in any other area of investigation would describe the capacities of newborns as anything other than innate. ''Present in newborns or at birth'' is, in fact, the definition of the word ''innate.''

Aslin *et al.* offer many reasons why a demonstration of innate abilities to discriminate phonetic contrasts in all the world's languages should not be held to strict criteria. For example, they state that some speech contrasts are simply easier to discriminate than others, due to variation in acoustic salience. Given such a suggestion, it would have been nice if they had offered a hint as to how acoustic salience should be measured, but it doesn't really matter because appeals to such notions have never helped in our understanding of human speech perception. For any given phonetic contrast, regardless of its acoustic salience (however defined), listeners vary in their abilities to discriminate it, depending on their native language experience. That is, the acoustic salience of a given contrast presumably remains constant across listeners of different languages, yet abilities to discriminate it vary across listeners. If indeed discriminative capacities are fully mature at the onset of experience, then we should expect infants' discriminative capacities for phonetic contrasts to be as unaffected by variation in acoustic salience as those of adults. Besides, if the suggestion being made is that I failed to find evidence of discrimination for some contrasts because they were not acoustically salient, it should be recalled that the three contrasts used were ones that others have reported infants discriminate successfully (i.e., vowels, VOT, and sibilants).

Aslin *et al.* claim that the target paper was idiosyncratic in its view of categorical perception. They suggest that infant speech perception investigators have historically tested a version of categorical perception different from (i.e., weaker than) the one against which I was judging that work. However, all descriptions of paradigms being tested in the infant speech perception work are consistent with the classic notion of categorical speech perception, and there was nothing in the target paper to suggest that the view being discussed was different from (i.e., stronger than) the classic notion of categorical speech perception. In fact, Aslin *et al.* describe the collective finding of the infant speech perception work at the start of their letter by writing:

> Since 1971, dozens of experiments have confirmed the initial observation that discrimination of the acoustic correlates of consonant contrasts is discontinuous. That is, not all physically equal steps along synthetic continua are equally easy or difficult for infants to discriminate. Rather, depending on the regions in which they fall, some steps are difficult to discriminate, much like the chance levels of performance obtained from adults for within-category differences, whereas other steps are relatively easy to discriminate, much like between-category performance obtained from adults. (p. 1257)

That account certainly sounds like a description of classic categorical speech perception, and it sounds like the claim is being made that the performance of infants demonstrates classic categorical speech perception. The purpose of the target paper was explicitly to state that collective results from infants do not support such a strong claim. And in fact, Aslin *et al.* contradict their own statement (just above) toward the end of their letter when they write ''Thus, at best, the infant literature supports a weak view of categorical perception.''

Toward the end of the target paper, I raise the point that perhaps we should be asking questions about the concept of phonetic categories as objects of perception for all language users, not just for infants. And again, Aslin *et al.* seem to make a similar suggestion toward the end of their letter, citing evidence from other investigators showing that phonetic categories are not as solid as standard views of categorical speech perception suggest they would be. So, at this point in their letter (p. 1259), I am not sure where we disagree, and so am not sure what the source of their consternation is. In any event, worrying about the precise definition of categorical perception used is irrelevant, at least regarding the target paper. Notions of categorization differ in their views of boundary effects and of the basis of equivalence for members of a given category. The work reported in the target paper involved discrimination of natural tokens of phonetic categories. Any version of categorical perception would expect these tokens to be discriminated by listeners with representations of these categories.

Given that there actually seems to be agreement between the points made by the target paper and points made toward the end of Aslin *et al.*'s letter, it is unclear why my methods were so severely attacked. However, concerning that attack, let me say that such an approach to disagreement is disappointing among colleagues, and simply inappropriate. Although I spent several years tweaking the methods reported in the target paper, at no point did procedures differ drastically from those of others. And at no time did slight variations in methods alter outcomes: In addition to the 121 infants and children whose data were reported in the target paper, we tested roughly another 150 using slight variations of the methods reported there, and we never found strong evidence of discrimination. At all times methods were sound, reflecting my own background working with children and infants, and even doing some hearing testing with visual reinforcement methods. I had many well-respected colleagues at Boys Town National Research Hospital who were able to offer input concerning the use of visually reinforced head-turning procedures and psychophysical method, and I contacted several infant speech perception researchers across the country to obtain further guidance. Nonetheless, let us for a moment extend credence to the concerns of Aslin *et al.*, and address them.

The first criticism is that the use of an infant seat or highchair could negatively impact children's responding, as most other investigators have had infants sit on parents' laps. Although I really don't think we want to consider too seriously the possibility that infant speech perception might be affected by where the child sits, it should be said that my work did not represent the first use of an infant seat for

testing. I refer readers to the figure on p. 245 of Kuhl (1985). Here we see an infant being tested while in an infant seat.

The next criticism is that my criteria of requiring 8 out of 10 correct responses to change trials, with no more than one false alarm to a no-change trial, was overly strict. By the standards of most psychophysical testing, that simply is not a stringent criterion. On the contrary, using the criterion of 8 out of 10 correct responses, regardless of whether they are change or no-change trials, as the authors suggest, is really a very lax criterion. Assuming that the ratio of change to no-change trials is 0.5, this means that the infant need only turn to 3 out of 5 change trials (i.e., 60%) to be judged as making the discrimination. The other 5 trials judged as correct can all be no-change trials, and it is not difficult to maintain an infant's attention well enough that the probability of a spontaneous headturn is quite low. Thus we are left with Aslin *et al*. suggesting that if one adopts a conceptualization of ''weak'' phonetic categories, and uses a lax criterion to judge that infants recognize contrasts among these categories, we may expect an infant to successfully discriminate exemplars of phonetic categories, as long as she is not in an infant seat and the contrast is acoustically salient. In sum, if we must accept all the caveats and concessions to infant speech perception research that Aslin *et al.* propose, there are as yet no strong conclusions to be reached concerning infants' capacities for speech perception, which was the message of Nittrouer (2001).

I end this letter as I began it, by stating that the work of investigators studying infant speech perception is laudable, and has been instrumental in the development of our general theories of speech perception. However, it is time to abandon our old notions of phonetic categories as objects of perception for either infants or adults. We need both new conceptual frameworks and new methods. I do not have a solid suggestion (yet) for what we should set in place of phonetic categories as the objects of speech perception. But that does not mean we should cling to our old notions of categories and boundaries distributed along theoretical continua never observed in natural speech—particularly when these notions no longer advance our understanding of basic human speech perception, of what goes wrong when children fail to acquire speech normally, or of the best methods for intervention with such children. Most models of speech perception used for research and clinical practice involve (either explicitly or implicitly) some version of the phonetic segment as the basic unit of speech organization, the ''building block'' of language, as it is described in textbooks. Accordingly, the common view of speech perception is of listeners extracting cues (or features) and compiling them into phonemes from which they then create higher levels of linguistic structure. An alternative view suggested by a diverse range of studies (e.g., Browman and Goldstein, 1990; Nittrouer and Crowther, 2001; Remez *et al.*, 1994; Shannon *et al.*, 1995; Surprenant and Goldstein, 1998) is of listeners organizing the various properties of an acoustic signal into a precisely timed, language-specific perceptual structure from which linguistic (including phonetic) forms somehow emerge. Although not yet fully framed, this new view would fundamentally change our research paradigms and our clinical practice.

ACKNOWLEDGMENTS

This work was supported by research Grant No. R01 DC00633 from the National Institute on Deafness and Other Communication Disorders, the National Institutes of Health.

Aslin, R. N., and Pisoni, D. B. (**1980**). ''Some developmental processes in speech perception,'' in *Child Phonology*, edited by G. H. Yeni-Komshian, J. F. Kavanagh, and C. A. Ferguson (Academic, New York), Vol. 2, pp. 67–96.

Aslin, R. N., Werker, J. F., and Morgan, J. L. (**2002**). ''Innate phonetic boundaries revisited,'' J. Acoust. Soc. Am. **112**, 1257–1260.

Best, C. T. (**1994**). ''The emergence of native-language phonological influences in infants: A perceptual assimilation model,'' in *The Development of Speech Perception*, edited by J. C. Goodman and H. C. Nusbaum (MIT, Cambridge, MA), pp. 167–224.

Browman, C. P., and Goldstein, L. (**1990**). ''Representation and reality: Physical systems and phonological structure,'' J. Phonetics **18**, 411–424.

Eimas, P. D., and Clarkson, R. L. (**1986**). ''Speech perception in children: Are there effects of otitis media?'' in *Otitis Media and Child Development*, edited by J. F. Kavanagh (York, Parkton, MD), pp. 139–159.

Godfrey, J. J., Syrdal-Lasky, A. K., Millay, K. K., and Knox, C. M. (**1981**). ''Performance of dyslexic children on speech perception tests,'' J. Exp. Child Psychol. **32**, 401–424.

Kuhl, P. K. (**1985**). ''Methods in the study of infant speech perception,'' in *Measurement of Audition and Vision in the First Year of Postnatal Life*, edited by G. Gottlieb and N. A. Krasnegor (Ablex, Norwood, NJ), pp. 223–251.

Liberman, I. Y., Shankweiler, D. P., Fischer, F. W., and Carter, B. (**1974**). ''Explicit syllable and phoneme segmentation in the young child,'' J. Exp. Child Psychol. **18**, 201–212.

Locke, J. L. (**1983**). *Phonological Acquisition and Change* (Academic, New York).

Mody, M., Schwartz, R. G., Gravel, J. S., and Ruben, R. J. (**1999**). ''Speech perception and verbal memory in children with and without histories of otitis media,'' J. Speech Lang. Hear. Res. **42**, 1069–1079.

Nittrouer, S. (**1996**). ''The relation between speech perception and phonemic awareness: Evidence from low-SES children and children with chronic OM,'' J. Speech Hear. Res. **39**, 1059–1070.

Nitrouer, S. (**2001**). ''Challenging the notion of innate phonetic boundaries,'' J. Acoust. Soc. Am. **110**, 1598–1605.

Nittrouer, S., and Crowther, C. S., (**2001**). ''Coherence in children's speech perception,'' J. Acoust. Soc. Am. **110**, 2129–2140.

Paul, R. (**2001**). *Language Disorders: From Infancy through Adolescence* (Mosby, St. Louis).

Remez, R. E., Rubin, P. E., Berns, S. M., Pardo, J. S., and Lang, J. M. (**1994**). ''On the perceptual organization of speech,'' Psychol. Rev. **101**, 129–156.

Shannon, R. V., Zeng, F. G., Wygonski, J., Kamath, V., and Ekelid, M. (**1995**). ''Speech recognition with primarily temporal cues,'' Science **270**, 303–304.

Strange, W. (**1995**). *Speech Perception and Linguistic Experience: Issues in Cross-language Research* (York, Baltimore).

Surprenant, A. M., and Goldstein, L. (**1998**). ''The perception of speech gestures,'' J. Acoust. Soc. Am. **104**, 518–529.

BegoStone—a new stone phantom for shock wave lithotripsy research (L)

Yunbo Liu and Pei Zhong[a)]
Department of Mechanical Engineering and Materials Science, Duke University, Durham, North Carolina 27708

(Received 6 April 2002; revised 21 June 2002; accepted 28 June 2002)

BegoStone, a commercially available super-hard plaster originally developed for dental applications, was examined as a potential stone phantom material for shock wave lithotripsy (SWL) research. The physical properties of BegoStone were characterized by using an ultrasound pulse transmission method and a microhardness tester with a Vickers indenter. In addition, spherical BegoStone phantoms ($D=10$ mm) were fabricated and exposed to 25–500 shocks at the beam focus of an HM-3 lithotripter operated at 20 kV and 1-Hz pulse repetition rate. It was found that the physical properties of BegoStone are comparable to that of hard kidney stones such as calcium oxalate monohydrate stones. In comparison to the widely use stone phantoms made of plaster-of-Paris, BegoStone is much denser and harder, and more difficult to fragment in SWL. Yet, both types of stone phantoms comminute progressively in SWL. In addition, BegoStone is abrasion resistant and does not soften in urine. Therefore, BegoStone may provide a reliable and consistent phantom material for both *in vitro* and *in vivo* studies of stone comminution in SWL. © *2002 Acoustical Society of America.* [DOI: 10.1121/1.1501905]

PACS numbers: 43.80.Gx [FD]

I. INTRODUCTION

Since its introduction in the early 1980s, shock wave lithotripsy (SWL) has become a well-established treatment modality for kidney and upper ureteral stones worldwide (Chaussy *et al.*, 1982). In the past decade, significant efforts have been made to better understand the mechanisms of stone comminution (Coleman *et al.*, 1987; Sass *et al.*, 1991; Gracewski *et al.*, 1993; Zhong *et al.*, 1993b; Lokhandwalla and Sturtevant, 2000; Xi and Zhong, 2001; Eisenmenger, 2001) and tissue injury (Howard and Sturtevant, 1997; Zhong *et al.*, 2001) so that strategies can be developed to improve the treatment efficiency while reducing the adverse effects of SWL (Xi and Zhong, 2000; Zhong and Zhou, 2001). For mechanistic investigations, stone phantoms that can mimic the physical properties and fragmentation characteristics of renal calculi in SWL are highly desirable. Further, representative and reliable stone phantoms are important for comparison of different types of lithotripsy devices (Chuong *et al.*, 1992) and for routine quality assurance of clinical lithotripters.

Several different types of stone phantoms have been described previously, which are either readily available or easy to fabricate. The most popular one is made of plaster-of-Paris which can be mold conveniently into different sizes and geometries. The acoustic properties of plaster-of-Paris phantoms have been measured, which were found to be similar to those of struvite stones but much lower than the corresponding values of calcium oxalate monohydrate (COM) stones (Chuong *et al.*, 1992; Zhong *et al.*, 1993a). Other stone phantoms that have been evaluated include Z-brick, breeze blocks, glass marbles, and Iceland spar, although in many cases their physical properties were not completely characterized (Whelan and Finlayson, 1988; Delius *et al.*, 1994; Blitz *et al.*, 1995). More recently, artificial stones made of chemical substances found in kidney stones and with physical properties comparable to their natural counterparts have been developed (Heimbach *et al.*, 2000). Despite their advantage over other stone phantoms, the primary drawback of the artificial stones is that skillful work is required in fabrication and they are not commercially available.

BegoStone is a commercially available material originally developed for dental applications. In this study, we characterized the physical properties of BegoStone, which were found to be comparable to that of COM stones. In addition, consistent and reproducible fragmentation in SWL can be produced using stone phantoms made of BegoStone. A further advantageous property of BegoStone is that it is abrasion resistant and does not soften in urine. All together, it appears that BegoStone can provide a reliable and consistent phantom material for SWL research.

II. MATERIALS AND METHODS

A. BegoStone and sample preparation

BegoStone is a super-hard plaster of class 4 with extremely low expansion ($<0.1\%$), which was originally developed for dental applications. In this study, BegoStone (BEGO USA, Smithfield, RI) was used to fabricate spherical stone phantoms 10 mm in diameter, using a specially designed mold. Following the protocol provided by the manufacturer, a mixture of BegoStone was first prepared at room temperature (20 °C) using a powder/water mixing ratio of 5:1 by weight. After stirring rigorously for about 4 min, the mixture was then poured into the phantom mold before it

a)Author to whom correspondence should be addressed. Electronic mail: pzhong@duke.edu

TABLE I. Physical properties of stone phantoms and kidney stones. MAPH: magnesium ammonium phosphate hydrogen. COM: calcium oxalate monohydrate.

	Materials	C_L (m/s)	C_T (m/s)	ρ (Kg/m^3)	$\rho C_L \times 10^6$ (Kg/m^2*s)	$\rho C_T \times 10^6$ (Kg/m^2*s)	ν	E (GPa)	K (GPa)	G (GPa)	HV (MPa)
Phantom stones	Plaster of Paris	2478	1471	1670	4.138	2.456	0.228	8.875	6.641	3.614	~200
	BegoStone	4400±65	2271±18	2174±29	9.568	4.939	0.318	29.584	30.890	11.221	549±25
Kidney stones	MAPH	2798±82	1634±25	1587±68	4.444	2.539	0.241	10.519	6.778	4.237	257±80
	COM	4476±41	2247±14	1823±69	8.160	4.096	0.332	24.512	24.259	9.204	1046±88

became hardened. Subsequently, the stone phantoms were left to cure in the mold overnight before use.

In order to determine the physical properties of BegoStone, a large block of samples was also prepared following the same protocol. After curing, thin slices ($\sim 7.5\times 10\times 10$ mm, T×L×W) of BegoStone were cut from the block using a low-speed diamond saw. Each slice was then ground in sequence through a series of silicon papers (180–600 grit) and finally polished with 1 μm alumina. After air dry for overnight, portions of the samples to be prepared for microhardness measurements were sputter coated in order to enhance the surface reflection and to ensure an accurate reading of the size of the indentation impression.

B. Characterization of physical properties

An ultrasound pulse transmission method (Zhong *et al.*, 1993b) was employed to determine the longitudinal (C_L) and transverse (C_T) wave speeds in BegoStone by measuring the propagation time of an ultrasound pulse in a sample of known thickness. Before the measurement, each specimen was immersed in water for 30 min to fully saturate it with water. The longitudinal and transverse wave speeds were measured using a pair of 10-MHz longitudinal wave transducers and a pair of 5-MHz shear wave transducers, respectively. To ensure good coupling between the transducers and stone specimen, an ultrasound transmission gel (Parker Lab, Inc.) and a viscous coupler (Panametrics) were used for longitudinal and transverse wave speed measurements, respectively. In addition, the volume of the sample was calculated based on its dimension and the weight of the sample in wet state was measured using a precision balance, from which the density (ρ) of BegoStone was determined.

Based on the theory of elastic wave propagation in homogeneous and isotropic solids, we can further calculate the bulk (K), shear (G), Young's (E) modules, and Poisson's ratio (ν) of BegoStone using the following equations:

$$K=\rho c_L^2\left[1-\frac{4}{3}\left(\frac{c_T}{c_L}\right)^2\right], \tag{1}$$

$$E=\rho c_T^2\frac{3-4(c_T/c_L)^2}{1-(c_T/c_L)^2}, \quad G=\rho c_T^2, \tag{2}$$

$$\upsilon=\frac{1-2(c_T/c_L)^2}{2[1-(c_T/c_L)^2]}. \tag{3}$$

Moreover, acoustic impedance ($Z=\rho*c$) of BegoStone was determined by the product of density and wave speed. Finally, a microhardness tester (Micromet 2100, BUEHLER) equipped with a Vickers indenter was used to measure the Vickers hardness of BegoStone with a load of 100 g and a dwell time of 10 s. From the indentation impression, Vickers hardness (HV) was calculated using the following formula:

$$HV=18\,169\times 10^9 * P/d^2, \tag{4}$$

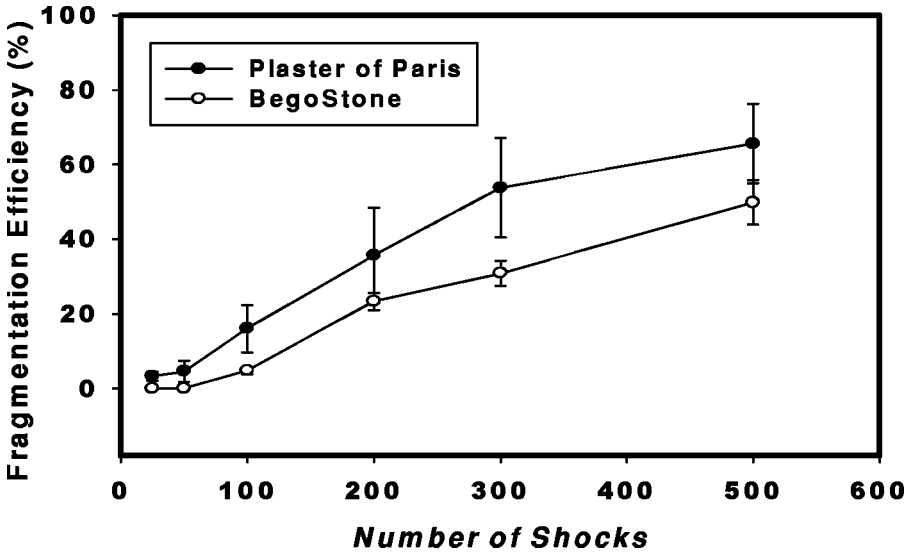

FIG. 1. Dose-dependent comminution of BegoStone and plaster-of-Paris phantoms produced by an HM-3 lithotripter at 20 kV and 1-Hz pulse repetition rate. The fragmentation efficiency is determined by the percentage of fragments less than 2 mm.

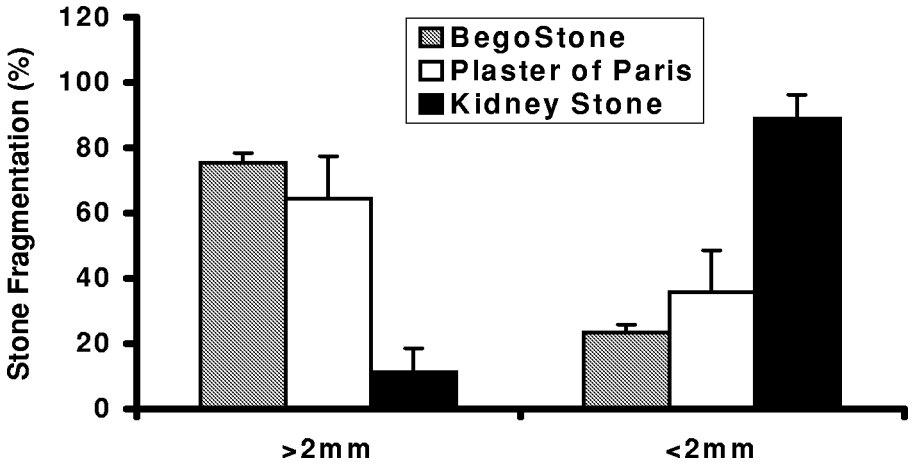

FIG. 2. Comparison of fragmentation of BegoStone, plaster-of-Paris, and kidney stones with a primary composition of calcium oxalate monohydrate after 200 shocks produced by an HM-3 lithotripter operated at 20 kV and 1-Hz pulse repetition rate.

where P is the indenter load and d is the averaged diagonal length of the indentation impression.

C. Stone comminution in SWL

To evaluate the fragmentation characteristics of BegoStone, the spherical phantoms were treated in an HM-3 lithotripter operated at 20 kV and 1-Hz pulse repetition rate. Under these conditions, the pressure waveform generated at the focus of the HM-3 lithotripter has a typical peak positive/negative pressure of 45/−8 MPa (Zhu *et al.*, 2002). To mimic stone comminution in the renal pelvis, each stone sample was placed in a plastic holder (filled with degassed water) with a bottom made of rubber finger cot. The sample holder was placed in an acrylic testing chamber (254*254*152–216 mm, L*W*H) filled with caster oil and with a 25-mm-thick tissue-mimicking phantom placed at the bottom to simulate tissue attenuation on the incident lithotripter shock waves (Zhong and Zhou, 2001).

To determine the dose dependency in stone comminution, BegoStone phantoms were randomly divided into six groups ($n=5$ in each group) with the samples in each group exposed to 25, 50, 100, 200, 300, and 500 shocks, respectively. Prior to the experiment, the weight of each sample was measured in dry state. Following shock wave treatment, all the fragments in the holder were carefully removed and let dry in air for 48 h. Subsequently, the size distribution of the fragments was determined by sequential sieving.

III. RESULTS

A. Physical properties

The physical properties of BegoStone were summarized in Table I, together with the corresponding values for plaster-of-Paris and kidney stones with a primary composition of either magnesium ammonium phosphate hydrogen (MAPH) or COM (Chuong *et al.*, 1992; Zhong *et al.*, 1993a). In comparison, BegoStone was found to have much higher values in longitudinal and transverse wave speeds, density, acoustic impedance, elastic moduli, and Vickers hardness than those of a plaster-of-Paris stone phantom. Except for Vickers hardness, the physical properties of BegoStone were also found to be similar to that of COM stones, which is one of the most difficult stones to fragment in SWL (Zhong *et al.*, 1993a). Although not as hard as COM stones, BegoStone is much harder than plaster-of-Paris phantoms and struvite stones; the physical properties of the later two were previously shown to be quite similar.

B. Fragmentation in SWL

Figure 1 shows the does-dependent comminution of BegoStone phantoms in the acoustic field of an HM-3 lithotripter. The efficiency of stone comminution was determined by the percentage of fragments less than 2 mm, which can pass spontaneously in urine following clinical SWL (Chaussy *et al.*, 1982). It was found that the comminution of BegoStone phantom in SWL increased progressively as the number of shocks increased from 25 to 500. A similar progressive fragmentation of plaster-of-Paris stone phantoms and kidney stones in SWL has been reported previously (Zhu *et al.*, 2002) and some of the data were reproduced here for comparison. Overall, BegoStone was found to be more difficult to fragment than plaster-of-Paris phantoms although the trends in stone comminution were similar for both phantoms. This finding is presumably related to the high elastic moduli and hardness of BegoStone.

Figure 2 compares the fragmentation efficiency of BegoStone, plaster-of-Paris, and kidney stones with a primary composition of COM. All of the samples were exposed to 200 shocks at 20 kV in an HM-3 lithotripter. The results indicate that kidney stones are easier to fragment than plaster-of-Paris and BegoStone phantoms. Two factors may contribute to this observation. First, the kidney stones used in this work were generally smaller than the 10-mm spherical phantoms (~68% by volume). Second, the kidney stones have heterogeneous layer structure, which makes them fragile to the impact of lithotripter shock waves due to internal wave reflection and fracture along interface of crystalline and matrix materials (Khan *et al.*, 1986; Cleveland *et al.*, 2001). Clinically, it has been reported that kidney stones with heterogeneous layer structure are much more fragile in SWL than stones with homogenous structure (Bhatta *et al.*, 1989).

Nevertheless, the results from this and previous studies (Zhu *et al.*, 2002) demonstrate that both BegoStone and plaster-of-Paris phantoms can mimic the basic fragmentation characteristics of kidney stones in SWL (Chaussy *et al.*, 1982; Khan *et al.*, 1986).

IV. DISCUSSION AND CONCLUSIONS

In this study, we evaluated the physical properties and fragmentation characteristics of BegoStone phantoms in SWL. It was found that BegoStone has acoustical and mechanical properties similar to that of COM stones. In addition, consistent and reproducible fragmentation in SWL can be produced using stone phantoms made of BegoStone. In comparison to the plaster-of-Paris stone phantoms widely used in SWL research, BegoStone can mimic more closely the physical properties of hard and dense kidney stones, such as COM stones. Moreover, a significant disadvantage of plaster-of-Paris and other artificial stone phantoms is that they will usually soften in urine, making it difficult to use these phantoms in animal studies. In contrast, BegoStone is abrasion resistant and does not soften in urine. Therefore, it may provide a better phantom material for *in vivo* stone comminution experiments. Overall, BegoStone appears to provide a reliable and consistent phantom material for SWL research.

ACKNOWLEDGMENTS

The authors would like to acknowledge the suggestion made by Wolfgang Merkle of EMS, Inc. for investigating the use of BegoStone as a phantom material for lithotripsy research. This work was supported in part by NIH thorough Grants Nos. RO1-DK52985 and RO1-DK58266.

Bhatta, K. M., Prien, E. L., and Dretler, S. P. (**1989**). ''Cystine calculi—rough and smooth: a new clinical distinction,'' J. Urol. **142**, 937–940.

Blitz, B. F., Lyon, E. S., and Gerber, G. S. (**1995**). ''Applicability of Iceland spar as a stone model standard for lithotripsy devices,'' J. Endourol **9**(6), 449–452.

Chaussy, C., Schmiedt, E., Jocham, D., Walther, V., Brendel, W., Forssmann, B., and Hepp, W. (**1982**). *Extracorporeal Shock Wave Lithotripsy: New Aspects in the Treatment of Kidney Stone Disease* (Karger, Basel).

Chuong, C. J., Zhong, P., and Preminger, G. M. (**1992**). ''A comparison of stone damage caused by different modes of shock wave generation,'' J. Urol. **148**, 200–205.

Cleveland, R. O., McAteer, J. A., and Müller, R. (**2001**). ''Time-lapse non-destructive assessment of shock wave damage to kidney stones *in vitro* using micro-computed tomography,'' J. Acoust. Soc. Am. **110**, 1733–1736.

Coleman, A. J., Saunders, J. E., Crum, L. A., and Dyson, M. (**1987**). ''Acoustic cavitation generated by an extracorporeal shockwave lithotripter,'' Ultrasound Med. Biol. **13**, 69–76.

Delius, M., Ueberle, F., and Gambihler, S. (**1994**). ''Destruction of gallstones and model stones by extracorporeal shock waves,'' Ultrasound Med. Biol. **20**(3), 251–258.

Eisenmenger, W. (**2001**). ''The mechanisms of stone fragmentation in ESWL,'' Ultrasound Med. Biol. **27**, 683–693.

Gracewski, S. M., Dahake, G., Ding, Z., Burns, S. J., and Everbach, E. C. (**1993**). ''Internal stress wave measurements in solids subjected to lithotripter pulses,'' J. Acoust. Soc. Am. **94**, 652–661.

Heimbach, D., Munver, R., Zhong, P., Jacobs, J., Hesse, A., Muller, S. C., and Preminger, G. M. (**2000**). ''Acoustic and mechanical properties of artificial stones in comparison to natural kidney stones,'' J. Urol. **164**(2), 537–544.

Howard, D., and Sturtevant, B. (**1997**). ''*In vitro* study of the mechanical effects of shock-wave lithotripsy,'' Ultrasound Med. Biol. **23**, 1107–1122.

Khan, S. R., Hackett, R. L., and Finlayson, B. (**1986**). ''Morphology of urinary stone particles resulting from ESWL treatment,'' J. Urol. **136**, 1367–1372.

Lokhandwalla, M., and Sturtevant, B. (**2000**). ''Fracture mechanics model of stone comminution in ESWL and implications for tissue damage,'' Phys. Med. Biol. **45**, 1923–1940.

Sass, W., Braunlich, W. M., Dreyer, H. P., Matura, E., Folberth, W., Priemeyer, H. G., and Seifert, J. (**1991**). ''The mechanisms of stone disintegration by shock eaves,'' Ultrasound Med. Biol. **7**(3), 239–243.

Whelan, J. P., and Finlayson, B. (**1988**). ''An experimental model for the systematic investigation of stone fracture by extracorporeal shock wave lithotripsy,'' J. Urol. **140**, 395–400.

Xi, X. F., and Zhong, P. (**2000**). ''Improvement of stone fragmentation during shock wave lithotripsy using a combined EH/PEAA shock wave generator—*In vitro* experiments,'' Ultrasound Med. Biol. **6**, 457–467.

Xi, X. F., and Zhong, P. (**2001**). ''Dynamic photoelastic study of the transient stress field in solids during shock wave lithotripsy,'' J. Acoust. Soc. Am. **109**, 1226–1239.

Zhong, P., and Zhou, Y. F. (**2001**). ''Suppression of large intraluminal bubble expansion in shock wave lithotripsy without compromising stone comminution: Methodology and *in vitro* experiments,'' J. Acoust. Soc. Am. **110**, 3283–3292.

Zhong, P., Chuong, C. J., and Preminger, G. M. (**1993a**). ''Characterization of fracture toughness of renal calculi using a microindentation technique,'' J. Mater. Sci. Lett. **12**, 1460–1462.

Zhong, P., Chuong, C. J., and Preminger, G. M. (**1993b**). ''Propagation of shock waves in elastic solids caused by the impact of cavitation microjets: Part II. Application to extracorporeal shock wave lithotripsy,'' J. Acoust. Soc. Am. **94**, 29–36.

Zhong, P., Zhou, Y. F., and Zhu, S. L. (**2001**). ''Dynamic of bubble oscillation in constrained media and mechanisms of vessel rupture in SWL,'' Ultrasound Med. Biol. **27**, 119–134.

Zhu, S. L., Cocks, F. H., Preminger, G. M., and Zhong, P. (**2002**). ''The role of stress waves and cavitation in stone comminution in shock wave lithotripsy,'' Ultrasound Med. Biol. **28**, 661–671.

An effective quiescent medium for sound propagating through an inhomogeneous, moving fluid

Oleg A. Godin[a)]
CIRES, University of Colorado at Boulder and NOAA/Environmental Technology Laboratory, Boulder, Colorado 80305-3328

(Received 24 May 2001; accepted for publication 10 July 2002)

The idea of similarity between acoustic fields in a moving fluid and in a certain ''effective'' quiescent medium, first put forward by Lord Rayleigh, proved very helpful in understanding and modeling sound propagation in an atmosphere with winds and in an ocean with currents, as well as in other applications involving flows with small velocity compared to sound speed. Known as effective sound speed approximation, the idea is routinely utilized in the contexts of the ray theory, normal mode representation of the sound field, and the parabolic approximation. Despite the wide use of the concept of effective sound speed in acoustics of moving media, no theoretical justification of Rayleigh's idea was published that would be independent of the chosen representation of the sound field and uniformly apply to distinct propagation regimes. In this paper, we present such a justification by reducing boundary conditions and a wave equation governing sound fields in the inhomogeneous moving fluid with a slow flow to boundary conditions and a wave equation in a quiescent fluid with effective sound speed and density. The derivation provides insight into validity conditions of the concept of effective quiescent fluid. Introduction of effective density in conjunction with effective sound speed is essential to ensure accurate reproduction of acoustic pressure amplitude in the effective medium. Effective parameters depend on sound speed, flow velocity, and density of the moving fluid as well as on sound propagation direction. Conditions are discussed under which the dependence on the propagation direction can be avoided or relaxed.
 [DOI: 10.1121/1.1504853]

PACS numbers: 43.20.Bi, 43.28.Py, 43.30.Es [ANN]

I. INTRODUCTION

In modeling sound propagation in the atmosphere,[1–11] the effects of ocean currents on underwater sound,[12–21] and acoustic waves in tubes with flow,[22–24] many researchers substitute the moving fluid by a motionless fluid with some ''effective'' sound speed. The concept of the effective motionless fluid was introduced by Lord Rayleigh in connection with his study of the two-dimensional (2D) problem of ray refraction due to wind. Without providing validation, he wrote: ''...the course of a ray in a moving, but otherwise homogeneous, medium, is the same as it would be in a medium, of which all parts are at rest, if the velocity of propagation is increased at every point by the component of the wind-velocity in the direction of the ray.'' [25] Apparently, Rayleigh believed that the correspondence between acoustic rays in a moving and effective medium is exact. In fact, the correspondence proves to be only approximate,[26,27] and generally requires that flow velocity is small compared to sound speed and is roughly aligned along or against the direction of sound propagation. A detailed analytical and numerical study of the errors introduced by the concept of the effective medium can be found in Ref. 28.

An approach that consists of substituting the problem of calculating the acoustic field in a moving medium by calculating the field in a motionless fluid with an effective sound speed, as proposed by Rayleigh, is usually called the effective sound speed approximation (ESSA). A more accurate representation of the acoustic field can be achieved when a flow velocity-dependent effective density (Ref. 28 and Ref. 29, Sec. 4.1) is introduced in addition to the effective sound speed. We will refer to this more general approach as the effective motionless medium approximation (EMMA).[30] The appeal of ESSA and EMMA is rooted in the fact that both the theory and numerical simulations of sound propagation are by far simpler in motionless than in moving media. Furthermore, available numerical models for simulating sound propagation are more numerous and better developed in the motionless case. ESSA and EMMA offer a valuable intuitive picture of the effects of medium motion on the acoustic field. These approximations preserve the property of the true acoustic field of being invariant[32] with respect to a simultaneous interchange in the source and receiver positions and reversal of the flow direction. This is of particular importance in ocean current tomography[18,19] and other applications[23,24] that rely on reciprocal transmissions for measuring flow velocity fields.

In addition to the ray theory, ESSA and/or EMMA were applied to study acoustics fields in moving media within the normal mode approach,[16,20,21] the parabolic approximation,[9,14,15,17,33] and with other full-field techniques.[4,7,10,11,33,34] Within the confines of the parabolic approximation[14,35] or the ray[26–28] and the normal mode representations of the field,[16,36] the accuracy of ESSA and EMMA can be evaluated by comparing resulting parabolic

[a)]Also affiliated with Acoustic Wave Propagation Laboratory, P. P. Shirshov Oceanography Institute of the Russian Academy of Sciences, Moscow 117851, Russia. Electronic mail: oleg.godin@noaa.gov

wave equations, ray equations, boundary value problems for local normal modes, or mode coupling equations, to those resulting from a rigorous theory.

Despite the wide use of the concept of effective sound speed in acoustics of moving media, to our knowledge, no theoretical justification of Rayleigh's idea was published that would be independent of the chosen representation of the sound field and uniformly apply to distinct propagation regimes in a three-dimensional (3D) inhomogeneous moving fluid. The objective of the present paper is to fill this void. We deduce effective motionless medium approximation from first principles by reducing boundary conditions and a wave equation governing sound fields in an inhomogeneous moving fluid with a slow flow, to boundary conditions and a wave equation in a quiescent fluid with effective sound speed and density.

With this introduction, the remainder of the paper is organized as follows. In Sec. II, we introduce a formal definition of the effective motionless fluid and demonstrate that the acoustic boundary conditions and the wave equation for sound in a moving fluid are approximately equivalent to the boundary conditions and the wave equation in the effective medium. General applicability conditions of EMMA and estimates of its accuracy are analyzed in Sec. III for four special cases of particular practical importance. Assumptions underlying EMMA and the degree of freedom available in choosing the effective medium parameters, are further discussed in Sec. IV. In Sec. V we summarize the major findings of this work. Derivation of the acoustic wave equation for a fluid with slow flows from the fluid mechanics equations and properties of the wave equation are reviewed in the Appendix.

II. DERIVATION OF EMMA

The starting point of our analysis is the wave equation for sound in moving fluid with slow currents,[37] which is discussed in the Appendix. For continuous acoustic waves of frequency ω, the wave equation (A10) becomes

$$\nabla\cdot\frac{\nabla p}{\rho}-\frac{d}{dt}\left(\frac{1}{\rho c^2}\frac{dp}{dt}\right)-\frac{2i}{\omega}\frac{\partial u_k}{\partial x_j}\frac{\partial}{\partial x_k}\left(\frac{1}{\rho}\frac{\partial p}{\partial x_j}\right)=O\left(M^2\frac{k^2}{\rho}p\right), \tag{1}$$

where p stands for acoustic pressure and $d/dt=-i\omega+\mathbf{u}\cdot\nabla$. Time dependence $\exp(-i\omega t)$ of the acoustic field is assumed and suppressed. In a fluid with arbitrary smooth dependence of sound speed c, density ρ, and flow velocity $\mathbf{u}$ on coordinates x_k, $k=1,2,3$, Eq. (1) is valid up to the terms of second order in the Mach number $M=u/c$. We want to demonstrate that, under some conditions, wave equation (1) is equivalent to the reduced wave equation

$$\nabla\cdot\frac{\nabla p}{\rho_e}+\frac{\omega^2}{\rho_e c_e^2}p=0 \tag{2}$$

describing acoustic fields in the quiescent fluid with "effective" sound speed c_e and density ρ_e.

As discussed in the Introduction, effective parameters depend on the direction of sound propagation. To formalize the requirement that the direction of propagation can be attributed to the acoustic field at a given point, we assume that

$$\nabla p=ik\mathbf{n}p+O(\epsilon+M),\quad k=\omega/c, \tag{3}$$

where $0<\epsilon\ll 1$. Physically, Eq. (3) means that approximately, up to small terms of the order of ϵ and M, the acoustic field is a locally plane wave with wave vector $k\mathbf{n}$. The real valued vector $\mathbf{n}$ specifies direction of wave propagation.[38] It is a function of position and, possibly, wave frequency.

We define the effective motionless medium as a fluid with

$$c_e=c+\mathbf{u}\cdot\mathbf{n},\quad \rho_e=\rho c^2/c_e^2 \tag{4}$$

and no ambient flow. Obviously, in the limit of vanishing current velocity $\mathbf{u}$, effective sound speed and density reduce to the sound speed and density of the real fluid.

Consider the difference, D, between the left-hand sides of wave equations (1) and (2). With the definition (4), we have

$$D=\nabla\cdot\left[\left(\frac{1}{\rho_e}-\frac{1}{\rho}\right)\nabla p\right]+\frac{2i}{\omega}\left[\frac{\partial u_j}{\partial x_k}\frac{\partial}{\partial x_j}\left(\frac{1}{\rho}\frac{\partial p}{\partial x_k}\right)-\frac{k^2}{\rho}\mathbf{u}\cdot\nabla p\right]+O\left(M^2\frac{k^2}{\rho}p\right). \tag{5}$$

Using Eq. (3) to express terms with derivatives of acoustic pressure in Eq. (5) in terms of $\mathbf{n}$ and p, after some algebra one finds that

$$D=\frac{2ip}{\rho c}\left[ku_j\mathbf{n}\cdot\nabla n_j-\frac{(\mathbf{n}\cdot\nabla u_j)}{\rho c}\frac{\partial\rho c}{\partial x_j}+\frac{\partial}{\partial x_j}(\mathbf{n}\cdot\nabla u_j)-\frac{k}{c}(\mathbf{n}\cdot\mathbf{u})\mathbf{n}\cdot\nabla c\right]+O\left((M+\epsilon)\frac{Mk^2}{\rho}p\right). \tag{6}$$

If the following three conditions

$$\frac{(\mathbf{n}\cdot\nabla)\mathbf{n}}{k}=O(\epsilon),\quad \frac{(\mathbf{n}\cdot\nabla)\mathbf{u}}{\omega}=O(\epsilon M),\quad \frac{\mathbf{n}\cdot\nabla c}{\omega}=O(\epsilon) \tag{7}$$

are met, the square bracket on the right-hand side of Eq. (6) can be estimated as $k^2cO(\epsilon M)$ and $D=O((\epsilon+M)Mk^2p/\rho)$. Hence, the reduced wave equation (2) correctly reproduces leading order terms due to fluid motion. Current effects are modeled by Eq. (2) with accuracy up to the factor $1+O(\epsilon+M)$.

When medium parameters are discontinuous across some interfaces, the acoustic wave equation has to be supplemented by boundary conditions. At an interface within a moving fluid, the linearized kinematic and dynamic boundary conditions are, respectively,[32]

$$[\mathbf{w}\cdot\mathbf{N}]_S=0, \tag{8a}$$

$$[p+(\mathbf{w}\cdot\mathbf{N})(\mathbf{N}\cdot\nabla p_0)]_S=0, \tag{8b}$$

where surface S is the interface in the absence of the acoustic wave, $\mathbf{N}$ is a unit normal to S, $\mathbf{w}$ is oscillatory displacement of fluid particles due to the wave, and $[\cdot]_S$ stands for the jump of the bracketed quantity across S. The oscillatory displacement is related to the acoustic pressure by the equation[32]

$$\rho\, d^2\mathbf{w}/dt^2 + \boldsymbol{\nabla} p = O(p\boldsymbol{\nabla} p_0/\rho c^2). \tag{9}$$

In an effective quiescent medium acoustic boundary conditions are (Ref. 31, Sec. 1.1)

$$\left[\frac{\boldsymbol{\nabla} p}{\omega^2 \rho_e}\cdot\mathbf{N}\right]_S = 0, \tag{10a}$$

$$[p]_S = 0. \tag{10b}$$

Let us compare the boundary conditions in moving and effective media. It is shown in the Appendix that $\boldsymbol{\nabla} p_0 = \rho c^2\, O(M^2)$ in a fluid with slow ambient flow (as long as gravity and Earth's rotation are neglected). Hence, the dynamic boundary conditions (8b) and (10b) differ only by second-order terms in M. Further, by iteratively solving Eq. (9) for $\mathbf{w}$, one finds that

$$\mathbf{w} = \frac{\boldsymbol{\nabla} p}{\omega^2\rho} - \frac{2i}{\omega}(\mathbf{u}\cdot\nabla)\frac{\boldsymbol{\nabla} p}{\omega^2\rho} + O\left(M^2\frac{\boldsymbol{\nabla} p}{\omega^2\rho}\right). \tag{11}$$

For the difference $\mathbf{D}_1 \equiv \mathbf{w} - \boldsymbol{\nabla} p/\omega^2\rho_e$ we have from Eqs. (3), (4), and (11)

$$\mathbf{D}_1 = \frac{2p(\mathbf{u}\cdot\boldsymbol{\nabla})\mathbf{n}}{\omega^2\rho c} + O\left(M^2\frac{\boldsymbol{\nabla} p}{\omega^2\rho}\right). \tag{12}$$

Assuming that [cf. Eq. (7)]

$$\omega^{-1}(\mathbf{u}\cdot\boldsymbol{\nabla})\mathbf{n} = O(\epsilon M), \quad \mathbf{r}\in S, \tag{13}$$

we have $\mathbf{D} \equiv O(M(M+\epsilon)\boldsymbol{\nabla} p/\omega^2\rho)$ from (12). Hence, the boundary conditions at the interface within the fluid are reproduced within the EMMA with accuracy up to the factor $1 + O(M(M+\epsilon))$. Quite similarly, the boundary conditions[32] $\mathbf{w}\cdot\mathbf{N} = 0$ at the rigid surface and $p + (\mathbf{w}\cdot\mathbf{N})\,(\mathbf{N}\cdot\boldsymbol{\nabla} p_0) = 0$ at the pressure-release surface in the moving fluid are approximated by their counterparts $\mathbf{N}\cdot\boldsymbol{\nabla} p = 0$ and $p = 0$ in the effective medium with accuracy up to the factor $1 + O(M(M+\epsilon))$.

In determining the accuracy of boundary conditions approximation within EMMA, we used Eq. (3) and implied that both incident and reflected waves can be approximately characterized by the same propagation direction $\mathbf{n}$. When the wave vector of the incident wave is $k\mathbf{n}$, the variation of the wave vector at reflection is $2k(\mathbf{n}\cdot\mathbf{N})\mathbf{N}$. For the difference in the propagation directions to be $O(\epsilon)$, we have to require that

$$\mathbf{n}\cdot\mathbf{N} = O(\epsilon), \tag{14}$$

that is, grazing angles with respect to the reflecting surface should be small.

To summarize, under conditions (3), (7), (13), and (14) the wave equation and boundary conditions for the acoustic field in a moving fluid with slow currents are approximated by the wave equation and boundary conditions in an effective quiescent fluid with parameters (4) with accuracy to the terms $O(M(M+\epsilon))$, which are much smaller than the leading terms $O(M)$ due to the currents. The physical meaning of the conditions (7) is that the relative variations of the sound speed and current velocity as well as the variation of the wave propagation direction are small compared to unity over distances of the order of wavelength. To be more precise, Eq. (7) requires the variations to be small *in the wave propagation direction* only. The condition (13) additionally requires that, along reflecting boundaries, variations in propagation direction are small, over the wavelength, in the direction of current velocity.

III. EXAMPLES

In this section we establish validity of EMMA for four important propagation regimes.

A. A weakly inhomogeneous moving medium

Consider a plane sound wave incident on a volume Ω occupied by a fluid with weak inhomogeneities in sound speed ($\delta c/c \ll 1$) and density ($\delta\rho/\rho \ll 1$) and slow currents ($M \ll 1$). As long as the intensity of the scattered waves remains small compared to the intensity of the incident wave, Eq. (3) holds, where $\mathbf{n}$ can be chosen as the unit vector in the direction of the wave vector of the incident wave. Then, the first and third conditions in Eq. (7) as well as condition (13) are met, but the second condition in (7) is not necessarily fulfilled. Still, taking into account that $\boldsymbol{\nabla}\cdot\mathbf{u} = O(M^3)$ (see the Appendix), we have $D = O((\epsilon + M)Mk^2p/\rho)$ from Eq. (6). Moreover, it follows from (6) that Eq. (7) can be substituted by

$$\begin{aligned} &\omega^{-1}\boldsymbol{\nabla} c = O(\epsilon), \quad (k\rho)^{-1}\nabla\rho = O(\epsilon), \\ &k^{-1}\nabla n_j = O(\epsilon), \quad j = 1,2,3 \end{aligned} \tag{15}$$

as a sufficient condition for the above estimate of the discrepancy D between the wave equations in moving and effective media to be valid.

Hence, EMMA is applicable in a weakly inhomogeneous medium without reflecting boundaries. Reflection at boundaries can also be considered within EMMA as long as condition (14) is met. Obviously, the above reasoning and the conclusions remain intact when the incident wave, instead of being plane, has a narrow angular spectrum of width $O(\epsilon)$ around the direction $\mathbf{n}$.

B. A duct with an axial flow

Consider normal modes in a regular three-dimensional wave guide with fluid flow. We choose the Ox coordinate axis along the wave guide axis and assume that medium parameters do not depend on x, and flow velocity is along the waveguide axis: $c = c(y,z)$, $\rho = \rho(y,z)$, $\mathbf{u} = (u(y,z),0,0)$. The boundaries of the duct are supposed to be cylindrical surfaces invariant with respect to translations along the Ox axis.

Acoustic pressure in the normal mode $p_s = \exp(i\xi_s x)\phi_s(y,z)$, where $s = 1,2,3,...$ stands for the mode order. When propagation constants ξ_s of normal modes are clustered around $k_0 = \text{const}$, that is

$$|\xi_s - k_0| \leqslant k_0 \epsilon_1, \quad 0 < \epsilon_1 \ll 1, \tag{16}$$

and cross-axis components of ∇p are small compared to the axial component, that is

$$\|\nabla \phi_s\| \leqslant k_0 \epsilon_2 \|\phi_s\|, \quad 0 < \epsilon_2 \ll 1, \tag{17}$$

one can ensure validity of condition (3) by choosing $\mathbf{n} = (k_0/k, 0, 0)$ and $\epsilon = \max(\epsilon_1, \epsilon_2)$. Then conditions (7), (13), and (14) are also met. Hence, EMMA is applicable in this problem.

In fact, the domain of EMMA applicability is even wider. As shown in the Appendix, the wave equation (A10) is exact in the case of a duct with an axial flow. For normal modes, (A10) reduces to a two-dimensional wave equation with respect to the mode shape functions ϕ_s:

$$\nabla \cdot \frac{\nabla \phi}{\rho \beta^2} + \left(\frac{\omega^2}{\rho c^2} - \frac{\xi^2}{\rho \beta^2} \right) \phi = 0, \quad \beta(\xi) = 1 - \frac{\xi u}{\omega}. \tag{18}$$

Supplemented by respective boundary conditions and/or conditions at $y^2 + z^2 \to \infty$, Eq. (18) specifies a 2D boundary value problem, of which mode propagation constants ξ_s are eigenvalues. Within EMMA, using effective sound speed and density (4), we obtain from Eq. (2),

$$\nabla \cdot \frac{\nabla \phi}{\rho_e} + \left(\frac{\omega^2}{\rho c^2} - \frac{\xi^2}{\rho_e} \right) \phi = 0. \tag{19}$$

For any given mode, its mode shape function calculated within EMMA can be made *exactly* equal to the true shape function by defining $\mathbf{n}$ in Eq. (4) is such a way that $\rho_e = \rho \beta^2(\xi_s)$ and, hence, $c_e = c/\beta(\xi_s)$. Comparing coefficients in Eqs. (18) and (19) we see that for modes with propagation constants in the interval $k_0 - \epsilon_1 k_0 < \xi < k_0 + \epsilon_1 k_0$, their propagation constants can be calculated within EMMA up to the factor $1 + O(\epsilon_1 M)$ by defining effective sound speed and density as $c_e = c/\beta(k_0)$ and $\rho_e = \rho \beta^2(k_0)$. Hence, condition (17), which restricts cross-axial components of pressure gradient, can be dropped; Eq. (16) is a sufficient condition for EMMA applicability.

The same conclusion can be obtained by evaluating the right-hand side of Eq. (5) in this special case of axial flow.

C. An almost-layered moving medium

Consider sound propagation at small grazing angles in a moving fluid the parameters of which are slowly varying functions of horizontal coordinates x and y, but which can vary rapidly with the vertical coordinate z: $c = c(\kappa x, \kappa y, z)$, $\rho = \rho(\kappa x, \kappa y, z)$, and $\mathbf{u} = \mathbf{u}(\kappa x, \kappa y, z)$, where $0 \leqslant \kappa \ll 1$. The vertical component of current velocity in such an almost-layered medium is known to be small: $u_3 = O(\kappa u)$ (Ref. 39, Sec. 7.3). We assume that the slope of the boundaries, if there are any, is $O(\kappa)$; that is, the boundaries are almost horizontal. These assumptions are valid, in particular, in the problem of long-range sound propagation in the ocean.

Let us define ϵ as the larger between the characteristic grazing angle χ and the anisotropy parameter κ, $\epsilon = \max(\kappa, \chi)$. Taking into account that horizontal refraction angles are of the order of $O(\kappa + M)$ (Ref. 39, Sec. 7.3), we see that condition (3) is met in the almost layered medium when $\mathbf{n}$ is chosen as a unit horizontal vector in the direction from source to receiver. Further, an inspection shows that all the conditions (7), (13), and (14) are met, and, hence, EMMA is applicable in the almost layered medium. Note that the effective sound speed (4) in this case is the sum of the sound speed and the horizontal component of the projection of the flow velocity on the source-receiver vertical plane. Such a definition of the effective sound speed is consistent with the definition normally implied in the applications of the effective medium approximation to problems in underwater and atmospheric acoustics.

D. High-frequency waves

Let the spatial scale of the medium parameters' variation, L, be large compared to acoustic wavelength: $kL \gg 1$. We do not impose restrictions on the amplitude of the relative variations in the parameters: $\delta c/c \lesssim 1$, $\delta \rho/\rho \lesssim 1$, $|\delta \mathbf{u}|/u \lesssim 1$. In this high-frequency case, the acoustic field can be described using the ray theory or its caustic modifications. For a field component corresponding to a ray arrival (and also to a set of strongly interfering, indistinguishable rays[40] in the vicinity of a caustic) we satisfy condition (3) by choosing $\mathbf{n}$ as a unit vector $\boldsymbol{\tau}$ tangent to the ray and $\epsilon = 1/kL$. The vector $\boldsymbol{\tau}$ significantly varies at distances of the order L. It is easy to verify that condition (7) is met and, hence, EMMA is applicable. In the limit of $kL \to \infty$, EMMA is accurate up to the terms $O(M^2)$. The disadvantage of this version of EMMA is that effective media are different for different rays. Although rather accurate, this version of EMMA is impractical.

A much more useful approximation is obtained when consideration is limited to paraxial wave fields. Let rays make a small angle with a certain constant vector $\mathbf{n}_0$. We designate χ as the characteristic angle between the rays and the vector $\mathbf{n}_0$ and define $\epsilon = \max(1/kL, \chi)$. Then Eq. (3) holds with $\mathbf{n} = \mathbf{n}_0$, and the effective medium defined by Eq. (4) is common for all components of the acoustic field. Condition (7) is also met and, hence, EMMA is applicable. According to (13) and (14), sound reflection can also be described within this version of EMMA as long as slopes of the reflecting surfaces with respect to $\mathbf{n}_0$ do not exceed $O(\chi)$. In the limit of $kL \to \infty$, $\epsilon = \chi$ and from the results of Sec. II, it follows that the version of EMMA at hand is accurate up to the terms $O(M\chi + M^2)$.[41]

IV. DISCUSSION

In order for the concept of the effective medium to be introduced, it was necessary to require that, in addition to the Mach number M, there is an additional small dimensionless parameter, ϵ, in the problem. This is because generic acoustic fields in a generic inhomogeneous medium do not necessarily have a specific direction of propagation, both in moving and motionless fluids. The physical meaning of ϵ is different in different problems. As has been shown above, ϵ can be related to the amplitude of relative variations in sound speed and density, to anisotropy in variation of medium parameters in the horizontal and vertical directions, or to the ratio of acoustic wavelength to the representative spatial scale of medium inhomogeneity. It is an important feature of EMMA

based on Eq. (4) that the wave equation and the boundary conditions in the effective medium reduce to the exact wave equation and boundary conditions in the limit of vanishing flow velocity. In other words, only the second-order terms $O(\epsilon M)$ and $O(M^2)$ are neglected in EMMA, but not the first-order terms $O(M)$ or any terms $O(\epsilon^s)$, $s=1,2,...$ without M.

In this respect, EMMA differs from the more crude linearized approximations, where terms $O(\epsilon^2)$ (such as terms of the second order in relative sound speed variations,[3,8] assumed to be small) are neglected. Sometimes ESSA and its domain of validity are examined (Ref. 42 and Ref. 29, Sec. 3.6) by comparing the results of such a linearized approach to exact ray calculations in moving fluid. As demonstrated in Ref. 28, the resulting conditions[42] are unnecessarily restrictive, with the accuracies and the validity domains of EMMA and the linearized approach being dramatically different in an underwater acoustics setting where $\epsilon \gg M$.

The conditions (3), (7), (13), and (14) imposed in Sec. II on the medium parameters and the acoustic field should be viewed as sufficient conditions of EMMA applicability. The examples considered in Sec. III suggest that the basic condition (3) can be relaxed and replaced with a less restrictive condition $\mathbf{u}\cdot\boldsymbol{\nabla} p = ik\mathbf{n}\cdot\mathbf{u}p + O(\epsilon M + M^2)$, which, unlike (3), does not impose any limitations on acoustic pressure variation in directions normal to flow velocity. The possibility of using the latter condition instead of (3) has not been established in the general case.

Note that the definition of the effective medium is not unique. The derivation of EMMA presented in Sec. II is little changed, and the result stands when effective sound speed and density differ from c_e and ρ_e, as defined by Eq. (4), by the terms $O(\epsilon M + M^2)$. For instance, for effective density one can take $\rho(1-2\mathbf{u}\cdot\mathbf{n}/c)$ rather than $\rho c^2/c_e^2$. However, neither the wave equation (1) nor boundary conditions can be approximated to the required accuracy $O(\epsilon M + M^2)$ without introducing a flow velocity-dependent effective density in addition to an effective sound speed.

The phase of the high-frequency waves is independent of density and density gradients and, hence, is not affected by ρ_e. Examination of explicit expressions for a high-frequency acoustic field in moving media within the WKB (Ref. 31, Sec. 8.1) and the ray[28] approximations shows that, without introduction of the effective density ρ_e (4), the amplitude error of EMMA would be $O(M)$.

We are not aware of any definition of the effective motionless medium that would systematically improve on the approximation of equations of linear acoustics of moving media compared to the accuracy $O(\epsilon M + M^2)$ of EMMA based on the definition (4).

V. CONCLUSION

The concept of an effective motionless medium first introduced in acoustics by Lord Rayleigh within the confines of the ray theory, can be successfully used in wave theoretical modeling of sound fields. Applicability of the concept and accuracy of the resulting effective motionless medium approximation rely on (i) the flow velocity being small compared to sound speed; (ii) various components of the acoustic field having similar propagation directions; and (iii) variations in the environmental parameters and the propagation directions being either small or gradual in the predominant direction of wave propagation. These conditions are formalized by Eqs. (3), (7), (13), (14), and (15). Parameters of the effective motionless fluid are defined by Eq. (4). It has been demonstrated that, when the conditions (3) and either (7) or (15) are met, the acoustic wave equation in a moving fluid reduces to the wave equation in the effective medium, up to the terms of second order in the small parameters of the problem. When conditions (14) and (15) are also met, the boundary conditions in moving fluid reduce to the boundary conditions in the effective medium. Introduction of a flow velocity-dependent effective density in addition to an effective sound speed proves to be necessary to ensure that there is correspondence between the equations governing acoustic fields in moving and effective media.

These results can serve as a justification of the past and present wide use of the effective medium approximation in various applications, but also indicate the limits of the approximation applicability and the circumstances under which more rigorous approaches[29,31,39] to modeling sound propagation in moving media become indispensable.

ACKNOWLEDGMENTS

This work was motivated by thought-provoking questions posed by the late Frederick D. Tappert. Discussions with A. G. Voronovich (NOAA/ETL), E. C. Shang (Scripps Institution of Oceanography, (UCSD), and V. E. Ostashev (CIRES, University of Colorado at Boulder) are gratefully acknowledged. The research leading to this paper was supported in part by the U.S. Office of Naval Research and a National Research Council Research Associateship Award at NOAA/ETL.

APPENDIX: WAVE EQUATION FOR ACOUSTIC WAVES IN AN INHOMOGENEOUS, MOVING FLUID

In this Appendix, we obtain from the first principles an approximate acoustic wave equation for sound in an inhomogeneous, moving fluid, where flow velocity is small compared to sound speed. The derivation presented below is a slightly simplified version of the original derivation outlined in Godin.[37]

Consider a fluid flow where, in the absence of acoustic waves, sound speed c, density ρ, and flow velocity $\mathbf{u}$ are arbitrary smooth functions of position and do not depend on time. The Mach number of the ambient flow, $M \equiv u/c$, is small compared to unity. We assume that fluid motion is adiabatic in the thermodynamic sense, neglecting irreversible thermodynamic processes associated with heat conduction and, in the case of multicomponent fluids like sea water, admixture diffusion. Then the entropy density and the concentrations of the admixtures are constant in the fluid particle during its motion. Consequently, convective derivatives of pressure and density are proportional to each other. For the ambient flow, the full nonlinear equations (Ref. 39, Sec. 4.1) of fluid dynamics become

$$\boldsymbol{\nabla} p_0 = -\rho(\mathbf{u}\cdot\boldsymbol{\nabla})\mathbf{u}, \tag{A1}$$

$$\boldsymbol{\nabla}\cdot(\rho\mathbf{u}) = 0, \tag{A2}$$

$$(\mathbf{u}\cdot\boldsymbol{\nabla})p_0=c^2(\mathbf{u}\cdot\boldsymbol{\nabla})\rho, \tag{A3}$$

where p_0 is pressure in the ambient flow. We neglect the force of gravity and the Earth's rotation. Note that, unlike the motionless case, in the moving medium sound speed $c(\mathbf{r})$ and density $\rho(\mathbf{r})$ fields cannot be prescribed independently. The fields have to be consistent with each other and the current velocity field as required by the fluid mechanics equations (A1)–(A3).

Note that $\boldsymbol{\nabla}p_0=O(M^2)$. From Eqs. (A1)–(A3) it follows that

$$\begin{aligned}\boldsymbol{\nabla}\cdot\mathbf{u}&=-\frac{1}{\rho}(\mathbf{u}\cdot\boldsymbol{\nabla})\rho\\&=-\frac{1}{\rho c^2}(\mathbf{u}\cdot\boldsymbol{\nabla})p_0=\frac{1}{c^2}\mathbf{u}\cdot(\mathbf{u}\cdot\boldsymbol{\nabla})\mathbf{u}=O(M^3).\end{aligned} \tag{A4}$$

Hence, for slow fluid flows, divergency of the flow velocity and variations of the medium density, sound speed, and flow velocity along the trajectory of the particle in the ambient flow are all negligibly small.

Perturbations $\mathbf{v}$ and p to the velocity of fluid particles and pressure due to acoustic waves are related by equations of fluid mechanics linearized with respect to the wave amplitude. The linearized equations can be written as (Ref. 39, Sec. 4.1)

$$\frac{d\mathbf{v}}{dt}+(\mathbf{v}\cdot\boldsymbol{\nabla})\mathbf{u}=-\frac{\boldsymbol{\nabla}p}{\rho}+O\left(\frac{p\boldsymbol{\nabla}p_0}{\rho^2c^2}\right),\quad \frac{d}{dt}=\frac{\partial}{\partial t}+\mathbf{u}\cdot\boldsymbol{\nabla}, \tag{A5}$$

$$\frac{1}{\rho c^2}\frac{dp}{dt}+\boldsymbol{\nabla}\cdot\mathbf{v}=O\left(\frac{p\boldsymbol{\nabla}\cdot\mathbf{u}}{\rho c^2}+\frac{p|\boldsymbol{\nabla}p_0|}{\rho^2c^3}\right), \tag{A6}$$

where d/dt stands for convective time derivative following ambient flow.

Our goal is to reduce Eqs. (A5) and (A6) to a closed-form equation with only one dependent variable, p. By applying operators $\boldsymbol{\nabla}$ and d/dt to Eqs. (A5) and (A6), respectively, and substracting the results, we find that

$$\begin{aligned}&\frac{d}{dt}\left(\frac{1}{\rho c^2}\frac{dp}{dt}\right)-\boldsymbol{\nabla}\cdot\frac{\boldsymbol{\nabla}p}{\rho}\\&\quad=2\frac{\partial u_k}{\partial x_j}\frac{\partial v_j}{\partial x_k}+O\left(\frac{1}{\rho^2c^3}\frac{dp}{dt}(\rho c\boldsymbol{\nabla}\cdot\mathbf{u}+|\boldsymbol{\nabla}p_0|)\right).\end{aligned} \tag{A7}$$

Summation over repeated indices j, $k=1,2,3$ is implied. To exclude components v_j of the unknown oscillatory velocity $\mathbf{v}$ from Eq. (A7), it is helpful to note that convective derivatives of v_j are related to acoustic pressure gradient by Eq. (A5). We apply the operator d/dt to Eq. (A7) and use Eq. (A5) to obtain

$$\begin{aligned}&\frac{d}{dt}\left[\frac{d}{dt}\left(\frac{1}{\rho c^2}\frac{dp}{dt}\right)-\boldsymbol{\nabla}\cdot\frac{\boldsymbol{\nabla}p}{\rho}\right]+2\frac{\partial u_k}{\partial x_j}\frac{\partial}{\partial x_k}\left(\frac{1}{\rho}\frac{\partial p}{\partial x_j}\right)\\&\quad=2Q+O\left(\frac{1}{\rho^2c^3}\frac{d^2p}{dt^2}(\rho c\boldsymbol{\nabla}\cdot\mathbf{u}+|\boldsymbol{\nabla}p_0|)\right),\end{aligned} \tag{A8}$$

where

$$Q=u_j\frac{\partial^2u_k}{\partial x_j\partial x_m}\frac{\partial v_m}{\partial x_k}-v_j\frac{\partial^2u_m}{\partial x_j\partial x_k}\frac{\partial u_k}{\partial x_m}-2\frac{\partial u_k}{\partial x_m}\frac{\partial u_m}{\partial x_j}\frac{\partial v_j}{\partial x_k}. \tag{A9}$$

Obviously, Q is proportional to M^2. Taking into account that $\boldsymbol{\nabla}p_0=O(M^2)$ and $\boldsymbol{\nabla}\cdot\mathbf{u}=O(M^3)$ and neglecting terms $O(M^2)$ in Eq. (A8), we arrive at an approximate wave equation

$$\frac{d}{dt}\left[\frac{d}{dt}\left(\frac{1}{\rho c^2}\frac{dp}{dt}\right)-\boldsymbol{\nabla}\cdot\frac{\boldsymbol{\nabla}p}{\rho}\right]+2\frac{\partial u_k}{\partial x_j}\frac{\partial}{\partial x_k}\left(\frac{1}{\rho}\frac{\partial p}{\partial x_j}\right)=0. \tag{A10}$$

This equation was first obtained in Ref. 37. Solutions to the equation correctly describe terms of the first order in M in the acoustic field, i.e., leading-order effects of weak currents. The solutions generally differ from the true field in the second-order terms.

In fact, the above derivation shows that the approximate wave equation (A10) has somewhat wider domain of validity than the case of slow currents ($M\ll1$) considered in Ref. 37. It follows from (A1), (A4), and (A9), that $\boldsymbol{\nabla}p_0=0$, $\boldsymbol{\nabla}\cdot\mathbf{u}=0$, and $Q=0$ when

$$(\mathbf{u}\cdot\boldsymbol{\nabla})\mathbf{u}=0 \tag{A11}$$

and

$$(\mathbf{u}\cdot\boldsymbol{\nabla})\frac{\partial\mathbf{u}}{\partial x_k}=0 \tag{A12}$$

for all $k=1,2,3$. Hence, for ambient flows satisfying conditions (A11) and (A12), the wave equation (A10) is *exact* in a 3D inhomogeneous moving fluid regardless of the Mach number value. It should be emphasized that no additional assumptions [aside from the ambient flow parameters being consistent with the fluid mechanics equations (A1)–(A3)] about sound speed and density variations need to be made for the wave equation (A10) to be exact.

Equations (A11) and (A12) describe a moving fluid in which the sound speed, density, flow velocity, and gradients of its components are all constant along streamlines of the ambient flow. Among flows satisfying conditions (A11) and (A12) are vertically stratified horizontal flow $\mathbf{u}=(u_1(z),u_2(z),0)$, which can serve as a reasonable first approximation to ocean currents and atmospheric wind, and unidirectional flow with arbitrary dependence on cross-flow coordinates $\mathbf{u}=(u_1(y,z),0,0)$, which may be a good model of flows in tubes and jets. Previously, for 3D inhomogeneous moving media, exact acoustic wave equations were derived[43] assuming the vertically stratified horizontal flow or the unidirectional flow. An inspection shows that (A10) reduces to known exact wave equations in these special cases. Equation (A10) also reduces to the well-known exact wave equations for plane stratified (Ref. 29, Sec. 4.1 and Ref. 31, Sec. 1.1) and cylindrically stratified[44] moving media.

Equation (A10) is just one member of a large family of approximate wave equations for sound in an inhomogeneous moving fluid. More accurate (and more cumbersome) wave equations are known that account for second-order terms in M in the case of general dependence of medium parameters on all three spatial coordinates. Other approximate wave equations take into account time dependence of the param-

eters and effects of gravity. Still other approximate wave equations are valid for arbitrary M, but only in a fluid with spatial and temporal scales of its inhomogeneity that are large compared to acoustic wavelength and period. Notably, these high-frequency wave equations include two concise equations derived by Pierce.[45] The reader is referred to Ref. 39, Sec. 4.1 and Ref. 29, Sec. 2.3 for a review of acoustic wave equations for moving media.

[1] A. R. Kriebel, "Refraction and attenuation of sound by wind and thermal profiles over a ground plane," J. Acoust. Soc. Am. **51**, 19–23 (1971).

[2] B. Hallberg, C. Larsson, and S. Israelson, "Measurements of meteorological effects on long-range sound propagation using *m*-sequence correlation," J. Acoust. Soc. Am. **78**, 1038–1044 (1985).

[3] A. V. Razin, "Calculation of acoustic fields in the atmospheric refraction wave guide," Izv., Acad. Sci., USSR, Atmos. Oceanic Phys. **21**, 544–548 (1985).

[4] K. B. Rasmussen, "Outdoor sound propagation under the influence of wind and temperature gradients," J. Sound Vib. **104**, 321–335 (1986).

[5] G. A. Daigle, T. F. W. Embleton, and J. E. Piercy, "Propagation of sound in the presence of gradients and turbulence near the ground," J. Acoust. Soc. Am. **79**, 613–1627 (1986).

[6] A. I. Otrezov and I. P. Chunchuzov, "Propagation of low-frequency acoustic waves in the surface layer of the atmosphere," Izv., Acad. Sci., USSR, Atmos. Oceanic Phys. **22**, 268–271 (1986).

[7] A. I. Otrezov and I. P. Chunchuzov, "The amplitude distribution of a low-frequency sound field near the surface of the Earth," Izv., Acad. Sci., USSR, Atmos. Oceanic Phys. **23**, 76–78 (1987).

[8] R. Makarewicz, "The shadow zone in a stratified medium," J. Acoust. Soc. Am. **85**, 1092–1096 (1989).

[9] K. E. Gilbert, R. Raspet, and X. Di, "Calculation of turbulence effects in an upward-refracting atmosphere," J. Acoust. Soc. Am. **87**, 2428–2437 (1990).

[10] E. M. Salomons, "Diffraction by a screen in downwind sound propagation: A parabolic equation approach," J. Acoust. Soc. Am. **95**, 3109–3117 (1994).

[11] K. B. Rasmussen, "Sound propagation over screened ground under upwind conditions," J. Acoust. Soc. Am. **100**, 3581–3586 (1996).

[12] E. R. Franchi and M. J. Jacobson, "Ray propagation in a channel with depth-variable sound speed and current," J. Acoust. Soc. Am. **52**, 316–331 (1972).

[13] T. B. Sanford, "Observations of strong current shears in the deep ocean and some implications on sound rays," J. Acoust. Soc. Am. **56**, 1118–1121 (1974).

[14] J. S. Robertson, W. L. Siegmann, and M. J. Jacobson, "Current and current shear effects in the parabolic approximation for underwater sound channels," J. Acoust. Soc. Am. **77**, 1768–1780 (1985).

[15] L. Nghiem-Phu and F. Tappert, "Parabolic equation modeling of the effects of ocean currents on sound transmission and reciprocity in the time domain," J. Acoust. Soc. Am. **78**, 642–648 (1985).

[16] N. S. Grigor'eva and M. I. Yavor, "Influence on the sound field in the ocean of a large-scale ocean current that qualitatively alters the nature of guided-wave sound propagation," Sov. Phys. Acoust. **32**, 482–485 (1986).

[17] M. J. Beran and A. M. Whitman, "Effect of random velocity fluctuations on underwater scattering," J. Acoust. Soc. Am. **81**, 647–649 (1987).

[18] B. M. Howe, P. F. Worcester, and R. C. Spindel, "Ocean acoustic tomography: Mesoscale velocity," J. Geophys. Res. **92**, 3785–3805 (1987).

[19] J. A. Mercer, "Nonreciprocity of simulated long-range acoustic transmissions," J. Acoust. Soc. Am. **84**, 999–1006 (1988).

[20] E. C. Shang, A. G. Voronovich, Y. Y. Wang, K. A. Naugolnykh, and L. Ostrovsky, "New schemes of ocean acoustic tomography," J. Comput. Acoust. **8**, 459–471 (2000).

[21] K. A. Naugolnykh, Y. Y. Wang, and E. C. Shang, "Numerical simulation of transverse current monitoring in the Fram Strait," J. Comp. Acoust. **9**, 413–425 (2001). press).

[22] M. S. Sodha, A. Kumar, I. C. Goyal, and A. K. Ghatak, "Sound wave propagation in cylindrical inhomogeneous waveguides," Acustica **41**, 232–237 (1979).

[23] H. Lechner, "Ultrasonic flow metering based on transit time differentials which are insensitive to flow profile," J. Acoust. Soc. Am. **74**, 955–959 (1983).

[24] M. Willatzen, "Perturbation theory applied to sound propagation in flowing media confined by a cylindrical waveguide," J. Acoust. Soc. Am. **109**, 102–107 (2001).

[25] J. W. Strutt (Baron Rayleigh), *The Theory of Sound*, Vol. 2, 2nd ed., revised and enlarged (MacMillan, London, New York, 1896), p. 132.

[26] C. H. E. Warren, "A note on refraction of sound in moving gas," J. Sound Vib. **1**, 175–178 (1964).

[27] R. J. Thompson, "Ray theory for an inhomogeneous moving medium," J. Acoust. Soc. Am. **51**, 1675–1682 (1972).

[28] O. A. Godin, D. Yu. Mikhin, and S. Ya. Molchanov, "Effective sound speed approximation in the acoustics of moving media," Izv., Acad. Sci., USSR, Atmos. Oceanic Phys. **29**, 179–186 (1993).

[29] V. E. Ostashev, *Acoustics in Moving Inhomogeneous Media* (Spon, London, 1997).

[30] In a vertically stratified medium with horizontal currents, EMMA, unlike ESSA, is exact for CW waves with harmonic dependence $\exp(i\xi_1 x+i\xi_2 y-i\omega t)$ on the horizontal coordinates x and y and time. Effective density and sound speed depend on the horizontal slowness vector $\mathbf{s}=(\xi_1/\omega,\xi_2/\omega)$ (Ref. 29, Sec. 4.1 and Ref. 31, Sec. 1.2). EMMA ceases to be exact and is valid only approximately when the spectrum of the acoustic field includes waves with different $\mathbf{s}$ values.

[31] L. M. Brekhovskikh and O. A. Godin, *Acoustics of Layered Media. 1: Plane and Quasi-Plane Waves* (Springer-Verlag, Berlin, Heidelberg, 1990 and 1998).

[32] O. A. Godin, "Reciprocity and energy theorems for waves in a compressible inhomogeneous moving fluid," Wave Motion **25**, 143–167 (1997).

[33] M. Karweit, Ph. Blanc-Benon, D. Juvé, and G. Comte-Bellot, "Simulation of propagation of an acoustic wave through a turbulent velocity field: A study of phase variance," J. Acoust. Soc. Am. **89**, 52–62 (1991).

[34] P. Elisseeff and H. Schmidt, "Acoustic propagation through a low Mach number, stratified flow," J. Acoust. Soc. Am. **101**, 1936–1944 (1997).

[35] O. A. Godin, "A wide-angle, energy-conserving parabolic equation for sound in a moving medium," in *Theoretical and Computational Acoustics '97*, edited by Y. C. Teng *et al.* (World Scientific, Singapore, 1999), pp. 329–340.

[36] O. A. Godin, "Coupled-mode sound propagation in a range-dependent, moving fluid," J. Acoust. Soc. Am. **111**, 1984–1995 (2002)

[37] O. A. Godin, "Wave equation for sound in a medium with slow currents," Dokl. Akad. Nauk SSSR **293**, 63–67 (1987) [in Russian].

[38] From the expression $I=(2\omega\rho)^{-1}\,\mathrm{Im}(p\boldsymbol{\nabla}p^*)$ for time-averaged density of acoustic energy flux in a motionless fluid, it follows that, up to the terms $O(\epsilon+M)$, the energy flux is parallel to $\mathbf{n}$.

[39] L. M. Brekhovskikh and O. A. Godin, *Acoustics of Layered Media. 2: Point Sources and Bounded Beams*, 2nd ed. (Springer-Verlag, Berlin, Heidelberg, 1999).

[40] Yu. A. Kravtsov and Yu. I. Orlov, *Geometrical Optics of Inhomogeneous Media* (Springer-Verlag, Berlin, Heidelberg, 1990), p. 96.

[41] The estimate can be improved in the important special case when current velocity $u_\parallel$ along $\mathbf{n}_0$ is large compared to current component $u_\perp$ across $\mathbf{n}_0$. Inspection of Eq. (5) shows that in the limit of $kL\to\infty$, the discrepancy between the wave equations in moving and effective media, $D=O([c^{-1}|\mathbf{u}\cdot(\boldsymbol{\tau}-\mathbf{n}_0)|+M^2]k^2p/\rho)=O([c^{-1}(u_\perp\chi+u_\parallel\chi^2)+M^2]k^2p/\rho)$. Hence, EMMA reproduces an acoustic field with accuracy up to the factor $1+O(c^{-1}(u_\perp\chi+u_\parallel\chi^2)+M^2)$. This result is consistent with the estimate obtained in Ref. 28 from other considerations.

[42] V. E. Ostashev, "Ray acoustics in a moving medium: a survey," Izv., Acad. Sci., USSR, Atmos. Oceanic Phys. **25**, 661–673 (1989).

[43] O. A. Godin, "On a layered moving medium approximation in acoustics," Dokl. Akad. Nauk SSSR **316**, 1378–1382 (1991) [Sov. Phys. Dokl. **36**, 168–172 (1991)].

[44] M. E. Goldstein, *Aeroacoustics* (McGraw-Hill, New York, 1976), Sec. 1.2.

[45] A. D. Pierce, "Wave equation for sound in fluids with unsteady inhomogeneous flow," J. Acoust. Soc. Am. **87**, 2292–2299 (1990).

A functional equation for the specular reflection of rays

A. Le Bot[a)]
Laboratoire de Tribologie et Dynamique des Systèmes, École Centrale de Lyon, 36, Avenue Guy de Collongues 69134 BP163 Ecully, France

(Received 2 October 2000; revised 29 June 2002; accepted 10 July 2002)

This paper aims to generalize the ''radiosity method'' when applied to specular reflection. Within the field of thermics, the radiosity method is also called the ''standard procedure.'' The integral equation for incident energy, which is usually derived for diffuse reflection, is replaced by a more appropriate functional equation. The latter is used to solve some specific problems and it is shown that all the classical features of specular reflection, for example, the existence of image sources, are embodied within this equation. This equation can be solved with the ray-tracing technique, despite the implemented mathematics being quite different. Several interesting features of the energy field are presented. © *2002 Acoustical Society of America.* [DOI: 10.1121/1.1504854]

PACS numbers: 43.20.Dk, 43.20.EI [ANN]

LIST OF SYMBOLS

ν	position parameter at the boundary
θ	emission angle
φ	incidence angle
r	receiver point
s	source point
p	point at the boundary
W	energy density
I	intensity vector
G	direct field for energy density
H	direct field for intensity
ω	circular frequency
c	speed of sound
m	attenuation factor

I. INTRODUCTION

The fact that waves propagate like rays is undoubtedly the oldest idea in wave motion. Many ideas on this topic have already been developed in depth. Rays have lost their fundamental status and are now regarded as high-frequency approximation of waves. The concept of ray is only valid for short wavelengths. However, rays are still widely encountered in modern science for several reasons.

First, solving governing wave equations is practical only for low frequencies due to computational limits of the finite-element method. At higher frequencies, ray methods are used and are often the only feasible solution. For instance, for room acoustics, the finite-element method is rarely applied. The majority of the audio range may be investigated using the ray-tracing technique[1] or other simple formulas based on the statistical properties of rays.[2]

Second, ray theories enable the ray paths and magnitudes to be determined separately. In some fields, only the paths are of interest, for instance the image formation study used for optical instrument design. Geometrical optics is a direct means of gaining access to targeted information without solving sophisticated equations.

Finally, beyond a mere approximation, ray theories may be regarded as an original view of wave motion whose spirit is quite different from the classical one. Many vibrational phenomena can be translated into ray terms, resulting in a particularly clear and intuitive representation.

For several years, a method based on energy considerations has been investigated in room acoustics.[3–5] This method leads to an integral equation where the unknown is the incident energy at the boundary. The equation has been applied to the calculation of time reverberation for rooms with nondiffuse noise. This method, sometimes called the ''radiosity method,'' [6] seems to stem from the ''standard procedure'' in thermics.[7] The problem of radiative heat exchange between n diffusely reflecting surfaces is reduced to a set of n-linear algebraic equations, coefficients of which are usually called view factors or angle factors. In Refs. 8 and 9, this method has been extended to structural acoustics. The radiosity method is actually a true ray method,[10] although its numerical implementation is quite different from that of classical ray-tracing algorithms. However, the radiosity method assumes ideally diffuse reflection at walls, whereas the ray-tracing technique is not limited to a particular law of reflection. A generalization of the radiosity method for partially diffuse reflection has been proposed in Ref. 11, where both the integral equation and the image-source technique are jointly employed. The effect of specular reflection leads to additional sources distributed behind the boundary, whereas the sources created by the diffuse reflection are localized at the boundary. This paper aims to adapt the radiosity method to *perfectly specular reflection* with some *sources localized on the boundary*. The integral equation is replaced by a more appropriate functional equation. The modified equation remains a ray method, and a large part of the paper is devoted to verifying that solutions of this equation match the classical properties of rays.

The outline of the present paper is as follows. In Sec. III, the vibration field is separated into elementary waves. These

a)Electronic mail: alain.le-bot@ec-lyon.fr

waves are assumed to be totally uncorrelated and consequently their energies are added to obtain the complete field. Some basic properties are also reviewed. In Secs. IV and V, a systematic application of the energy balance gives a set of equations for these energy variables. Section VI shows how the classical image-source method may be applied to solve the energy equations. A second example is studied in Sec. VII. Section VIII proposes an interpretation of in terms of rays. Finally, this theory is applied to a circular domain in Sec. IX.

II. MOTIVATION FOR THE STUDY

When using the radiosity method, it is assumed that the rays are ideally diffusely reflected. The cosine Lambert's law can be applied to fictitious sources of magnitude σ, which are distributed over the boundary Γ. The reflected energy at any point $\mathbf{r}$ inside the domain Ω is written

$$\int_{\Gamma} \sigma(\nu)\cos\theta \frac{d\nu}{r} \tag{1}$$

(two-dimensional case), where ν is the curvilinear abscissa of the boundary Γ, θ the emission angle, and $r=|\mathbf{r}-\mathbf{p}|$ the distance between the receiver point $\mathbf{r}$ and the fictitious source located at $\mathbf{p}$ of abscissa ν. The reflected energy is proportional to $1/r$.

The purpose of this paper is to extend the radiosity method to the case of pure specular reflection. However, it is expected that the reflected energy may still result from some fictitious sources distributed over the boundary as in Eq. (1). It is well-known that a source in front of a plane surface gives rise to a single image source, say $\mathbf{s}$. The reflected energy is thus $1/R$, where $R=|\mathbf{s}-\mathbf{r}|$ is the source–receiver distance. The question now arising is whether the reflected field $1/R$ can result from equivalent sources distributed over the boundary

$$\int_{\Gamma} \sigma(\nu,\theta)\frac{d\nu}{r} \stackrel{?}{=} \frac{1}{R}, \tag{2}$$

for a well-chosen function σ which is no longer restricted to follow Lambert's law. The answer is yes. To check this assertion, consider

$$\sigma(\nu,\theta)=\delta(\theta-\varphi)\cos\theta/l, \tag{3}$$

where $l=|\mathbf{s}-\mathbf{p}|$ is the distance between the image-source $\mathbf{s}$ and the fictitious source $\mathbf{p}$ of abscissa ν, and φ is the incidence angle [Fig. 1(a)]. With a change of variable $\nu\rightarrow\psi=\varphi-\theta$

$$\int_{-\infty}^{\infty}\delta(\theta-\varphi)\frac{\cos\theta}{l}\frac{d\nu}{r}=\int\delta(\psi)\frac{\cos\theta}{l}\frac{1}{r}\frac{d\nu}{d\psi}d\psi = \frac{\cos\theta_0}{l_0\times r_0}\Big/\left.\frac{d\psi}{d\nu}\right|_{\nu=\nu_0}, \tag{4}$$

where ν_0 is the position where the emission angle θ_0 is equal to the incidence angle φ_0, i.e., $\psi=0$. l_0, r_0 are the corresponding source–boundary and boundary–receiver distances [Fig. 1(a)]. An infinitesimal displacement $d\nu$ can be expressed as $d\nu=-rd\theta/\cos\theta$ [Fig. 1(b)]. Likewise, variation in $d\varphi$ results in $d\nu=ld\varphi/\cos\varphi$, and thus

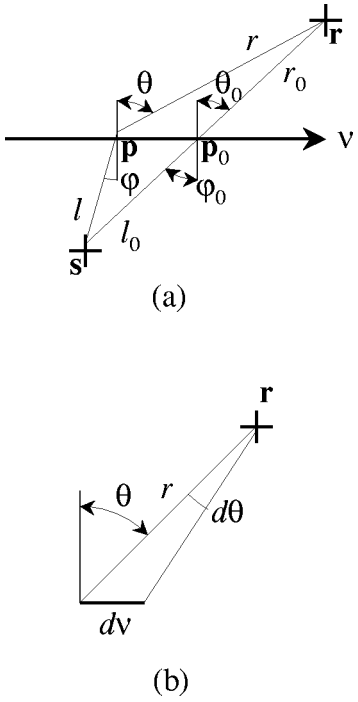

FIG. 1. Description of an image-source $\mathbf{s}$, which is behind the boundary, in terms of the fictitious sources located on the boundary.

$$\frac{d\psi}{d\nu}=\frac{d\varphi}{d\nu}-\frac{d\theta}{d\nu}=\frac{\cos\varphi}{l}+\frac{\cos\theta}{r}. \tag{5}$$

By substituting Eq. (5) into Eq. (4), the reflected energy is found to be

$$\frac{\cos\theta_0}{l_0\times r_0}\Big/\left(\frac{\cos\varphi_0}{l_0}+\frac{\cos\theta_0}{r_0}\right)=\frac{1}{l_0+r_0}=\frac{1}{R}, \tag{6}$$

since $\theta_0=\varphi_0$ and $R=l_0+r_0$. The expected result is thus obtained.

The plan is now to exploit this result and extend it for a general representation of reflected energy. Indeed, the question is how to determine the fictitious source distribution σ. It is shown in Sec. IV that the distribution σ is determined by a functional equation.

III. ENERGY REPRESENTATION OF WAVES

In the context of *linear acoustics with homogeneous and isotropic fluid*, two energy fields are referred to: the energy density $W=\rho|\mathbf{v}|^2/2+p^2/2\rho c^2$, where p is the acoustical pressure, $\mathbf{v}$ the velocity, ρ the volumic mass of fluid, and c the speed of sound, and the energy flow or intensity $\mathbf{I}=p\mathbf{v}$. The circular frequency is denoted as ω and the speed of the flow of energy is denoted as c. Various kinds of damping mechanisms are possible. The atmospheric absorption originates from several phenomena: dynamical viscosity of fluid, molecular absorption, etc. A local relationship is adopted between the power density which is dissipated p_{diss} and the energy density W, $p_{\text{diss}}=mcW$, where m is the attenuation factor. As the factor m is ω-dependent, this expression does not hold in the time domain. However, it remains an inter-

esting approximation for some transient problems which involve wave packets such as time reverberation in acoustics or structural acoustics, time arrival of rays in ultrasonic propagation, and so on. A simple proportional relationship holds between the energy flow and the energy density[12] of traveling waves, $I=cW$, where I is the magnitude of the energy flow vector $\mathbf{I}$. This relationship cannot be verified within the neighborhood of the excitation point, but it is applied under the assumption that *evanescent wave and the near field are neglected*.

Now, consider the direct field of a source $\mathbf{s}$ of unit power. In steady-state condition, $G(\mathbf{s},\mathbf{r})$ denotes the energy density at any point $\mathbf{r}$ and $\mathbf{H}(\mathbf{s},\mathbf{r})$ denotes the intensity. In the case of a transient source, the notation $G(\mathbf{s},\tau;\mathbf{r},t)$ and $\mathbf{H}(\mathbf{s},\tau;\mathbf{r},t)$ is used for the direct fields generated by an impulse excitation at $\mathbf{s}$ at time τ. The energy balance is then

$$\mathrm{div}_{\mathbf{r}}\cdot\mathbf{H}+mcG+\frac{\partial G}{\partial t}=\delta_{\mathbf{s},\tau}, \tag{7}$$

where the first term in the left-hand side is the net outgoing power per unit volume and the second term is the power density which is dissipated p_{diss}. The fields G and $\mathbf{H}$ depend only on the distance $s=|\mathbf{r}-\mathbf{s}|$. With the condition $H=cG$, the fields G and $\mathbf{H}$ can readily be found[8,9]

$$G(\mathbf{s},\mathbf{r})=\frac{1}{\gamma_0 c}\frac{e^{-ms}}{s^{n-1}}, \tag{8}$$

$$G(\mathbf{s},\tau;\mathbf{r},t)=G(\mathbf{s},\mathbf{r})\,\delta(t-\tau-s/c), \tag{9}$$

where $\gamma_0=2\pi$ or 4π depending on the dimension n. Furthermore, $\mathbf{H}=cG\mathbf{u_{sr}}$, where $\mathbf{u_{sr}}=(\mathbf{r}-\mathbf{s})/|\mathbf{r}-\mathbf{s}|$ is the unit vector from $\mathbf{s}$ to $\mathbf{r}$.

Actual sources rarely have a uniform output. For the nonuniform case, it is convenient to introduce the directional emissive power density $\rho(\mathbf{s},\mathbf{u},\tau)$, which gives the power injected along the direction $\mathbf{u}$ at time τ and at point $\mathbf{s}$. Directionality is not usually time dependent and thus $\rho(\mathbf{s},\mathbf{u},\tau)=f_{\mathbf{s}}(\mathbf{u})\rho(\tau)$, where $f_{\mathbf{s}}(\mathbf{u})$ is the directional function of the source $\mathbf{s}$. The injected power density p_{inj} is obtained by integrating the flux of $\rho\mathbf{H}$ over an infinitesimal sphere which surrounds the point $\mathbf{s}$

$$p_{\mathrm{inj}}(\mathbf{s},\tau)=\frac{1}{\gamma_0}\int_{S_{n-1}}\rho(\mathbf{s},\mathbf{u},\tau)\,dS_{\mathbf{u}}, \tag{10}$$

where dS is the surface measure on the unit sphere S_{n-1}. For an isotropic source, this relationship reduces to $p_{\mathrm{inj}}=\rho$.

Let us turn to the case where several sources simultaneously act in a bounded or unbounded smooth domain Ω with boundary Γ. To ensure a meaning for all subsequent integrals, it is assumed that an outward normal exists almost everywhere. It is also assumed that *all sources are uncorrelated* in order that linear superposition principle may be applied to energy fields. This approximation leads to the neglect of all interference effects and, as a consequence, modes cannot be predicted. The fields W and $\mathbf{I}$ result from the superposition of direct fields which emerge from primary sources ρ and diffracted fields which emerge from secondary sources σ distributed on the boundary Γ. For any $\mathbf{r}\in\Omega$

$$W(\mathbf{r},t)=\int_{\Omega}\rho(\mathbf{s},\mathbf{u_{sr}},t-s/c)G(\mathbf{s},\mathbf{r})\,d\Omega_{\mathbf{s}}+\int_{\Gamma}\sigma(\mathbf{p},\mathbf{u_{pr}},t-r/c)G(\mathbf{p},\mathbf{r})\,d\Gamma_{\mathbf{p}}, \tag{11}$$

$$\mathbf{I}(\mathbf{r},t)=\int_{\Omega}\rho(\mathbf{s},\mathbf{u_{sr}},t-s/c)\mathbf{H}(\mathbf{s},\mathbf{r})\,d\Omega_{\mathbf{s}}+\int_{\Gamma}\sigma(\mathbf{p},\mathbf{u_{pr}},t-r/c)\mathbf{H}(\mathbf{p},\mathbf{r})\,d\Gamma_{\mathbf{p}}, \tag{12}$$

where $s=|\mathbf{r}-\mathbf{s}|$ and $r=|\mathbf{r}-\mathbf{p}|$. $d\Omega$ is the Lebesgue measure in Ω, whereas $d\Gamma$ is the surface measure on Γ. The main difference between Eqs. (11), (12), and the corresponding equations for the radiosity method appears in the nature of the variable σ, which here depends on the direction $\mathbf{u_{pr}}$. The radiosity method is thus embodied in Eqs. (11) and (12) by adopting Lambert's law $\sigma(\mathbf{p},\mathbf{u},\tau)=\sigma(\mathbf{p},\tau)\cos\theta$, where θ is the emission angle between the outward normal of the boundary $\mathbf{n}$ and $\mathbf{u}$. The focus of this text is to show that by adopting well-chosen distributions σ, the diffracted field can become a plane wave or a cylindrical wave, which emanates from a unique image source. This result is surprising since the function G in Eq. (11) is a cylindrical wave.

The local power balance for the fields W and $\mathbf{I}$ is

$$\mathrm{div}.\mathbf{I}+mcW+\frac{\partial W}{\partial t}=p_{\mathrm{inj}}, \tag{13}$$

where p_{inj} has been given in Eq. (10). This can be checked by a direct substitution of Eqs. (11) and (12) on the left-hand side and by using Eq. (7) (Appendix A). The global power balance for the whole system Ω is obtained by integrating Eq. (13) over Ω. It yields

$$P_{\mathrm{out}}+mcW_{\Omega}+\frac{\partial W_{\Omega}}{\partial t}=P_{\mathrm{inj}}, \tag{14}$$

where $W_{\Omega}=\int_{\Omega}W\,d\Omega$ denotes the energy of the domain Ω. $P_{\mathrm{out}}=\int_{\Gamma}\mathbf{I}.\mathbf{n}\,d\Gamma$ is the outward energy flow. $P_{\mathrm{inj}}=\int_{\Omega}p_{\mathrm{inj}}\,d\Omega$ is the total power supplied by primary sources. This equality shows that for isolated systems ($P_{\mathrm{out}}=0$) in a steady-state condition with finite injected power ($P_{\mathrm{inj}}<\infty$), the total energy W_{Ω} is finite, i.e., the integral $\int_{\Omega}W\,d\Omega$ must converge. This result is not trivial for two reasons. First, the field W is singular in general. Isolated source points or focus points in certain situations may lead to singularities of W. Second, the domain Ω may be bounded or unbounded. In the latter case, the decrease of W in the far field must be sufficiently strong to ensure the convergence.

The relationships (11) and (12) give the fields W and $\mathbf{I}$ at any point within the domain Ω. But, similar relationships for the boundary Γ have not yet been sought although they are of interest from a theoretical point of view. The fields W and $\mathbf{I}$ for a regular point $\mathbf{p}\in\Gamma$ are

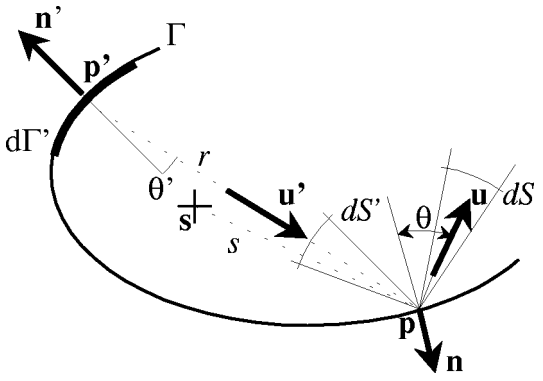

FIG. 2. Energy balance for **p** at the boundary; incident power stems from both actual sources **s**, which are located within the incident cone, and diffraction sources $\mathbf{p}'$, which are located on the part $d\Gamma'$ of the boundary.

$$W(\mathbf{p},t)=\int_{\Omega}\rho(\mathbf{s},\mathbf{u_{sp}},t-s/c)G(\mathbf{s},\mathbf{p})d\Omega_{\mathbf{s}}+\int_{\Gamma}^{*}\sigma(\mathbf{q},\mathbf{u_{qp}},t-r/c)G(\mathbf{q},\mathbf{p})d\Gamma_{\mathbf{q}}+\int_{HS}\frac{\sigma(\mathbf{p},\mathbf{u},t)}{\gamma_0 c\cos\theta}dS_{\mathbf{u}}, \tag{15}$$

$$\mathbf{I}(\mathbf{p},t)=\int_{\Omega}\rho(\mathbf{s},\mathbf{u_{sp}},t-s/c)\mathbf{H}(\mathbf{s},\mathbf{p})d\Omega_{\mathbf{s}}+\int_{\Gamma}^{*}\sigma(\mathbf{q},\mathbf{u_{qp}},t-r/c)\mathbf{H}(\mathbf{q},\mathbf{p})d\Gamma_{\mathbf{q}}+\int_{HS}\frac{\sigma(\mathbf{p},\mathbf{u},t)}{\gamma_0\cos\theta}\mathbf{u}\,dS_{\mathbf{u}}. \tag{16}$$

The asterisk designates the principal value of Cauchy. *HS* is the unit hemisphere of inward unit vectors, which is centered at **p**. Equations (15) and (16) are proved in Appendix A.

IV. SPECULAR REFLECTION AT BOUNDARY

This section is concerned with the derivation of an appropriate equation for the unknown σ on the basis of *specular reflection*. This equation is derived by applying the power balance at the boundary at any regular point $\mathbf{p}\in\Gamma$. Consider a solid angle dS along an emission direction **u**. The incident solid angle is dS' along $\mathbf{u}'$. Specularity implies that $\mathbf{u}'$, **u**, and **n** are coplanar, $\cos\theta=|\mathbf{u}\cdot\mathbf{n}|=|\mathbf{u}'\cdot\mathbf{n}|$ and $dS'=dS$. Let $\mathbf{p}'$ designate the point at the boundary from which the incident direction $\mathbf{u}'$ originates (Fig. 2). This point may or may not exist. It may or may not be unique. For simplicity, the ensuing calculation is performed for the case in which if $\mathbf{p}'$ exists, it is unique. Other cases are discussed below.

The incident power at **p** arising from primary sources **s** situated within the incident cone is denoted $\mathcal{P}_{\mathrm{dir}}$. The incident power due to secondary sources which are located within the region $d\Gamma'$ of the boundary which intersects the incident cone is denoted $\mathcal{P}_{\mathrm{dif}}$. The infinitesimal power emitted is denoted $\mathcal{P}_{\mathrm{emit}}$. Introducing an absorption coefficient α defined as the ratio of absorbed power over incident power, the power balance is

$$\mathcal{P}_{\mathrm{emit}}=[1-\alpha][\mathcal{P}_{\mathrm{dir}}+\mathcal{P}_{\mathrm{dif}}]. \tag{17}$$

The emitted power $\mathcal{P}_{\mathrm{emit}}$ is the flux of the energy flow vector from the source **p** of magnitude $\sigma(\mathbf{p},\mathbf{u},t)$ through the region of the sphere with a small radius ϵ which intersects the reflected cone dS. The area of this surface is $\epsilon^{n-1}\,dS$. Then

$$\mathcal{P}_{\mathrm{emit}}=\lim_{\epsilon\to 0}\left(\sigma(\mathbf{p},\mathbf{u},t-\epsilon/c)\frac{e^{-m\epsilon}}{\gamma_0\epsilon^{n-1}}\epsilon^{n-1}\,dS\right)=\sigma(\mathbf{p},\mathbf{u},t)\frac{dS}{\gamma_0}. \tag{18}$$

The incident power $\mathcal{P}_{\mathrm{dir}}$ stemming from the primary sources that are located inside the incident cone dS' is

$$\mathcal{P}_{\mathrm{dir}}=\int_{\mathbf{p}'\mathbf{p}}\rho(\mathbf{s},\mathbf{u}',t-s/c)\mathbf{H}(\mathbf{s},\mathbf{p})\cdot\mathbf{n}s^{n-1}\,ds\,dS'=\frac{1}{\gamma_0}\int_{\mathbf{p}'\mathbf{p}}\rho(\mathbf{s},\mathbf{u}',t-s/c)e^{-ms}\,ds\cos\theta\,dS', \tag{19}$$

where $s=|\mathbf{p}-\mathbf{s}|$. $s^{n-1}ds\,dS'$ is the infinitesimal volume in spherical coordinates. The integral is performed over the segment $\mathbf{p}'\mathbf{p}$. The incident power $\mathcal{P}_{\mathrm{dif}}$ stemming from secondary sources located on $d\Gamma'$ is

$$\mathcal{P}_{\mathrm{dif}}=\sigma(\mathbf{p}',\mathbf{u}',t')\mathbf{H}(\mathbf{p}',\mathbf{p})\cdot\mathbf{n}\,d\Gamma', \tag{20}$$

where $t'=t-r/c$ and $r=|\mathbf{p}-\mathbf{p}'|$. The infinitesimal surface $d\Gamma'$ is related to the solid angle dS' by $d\Gamma'=r^{n-1}dS'/\cos\theta'$, where θ' is the emission angle at $\mathbf{p}'$

$$\mathcal{P}_{\mathrm{dif}}=\frac{1}{\gamma_0}\sigma(\mathbf{p}',\mathbf{u}',t')e^{-mr}\frac{\cos\theta}{\cos\theta'}dS'. \tag{21}$$

By substituting Eqs. (18), (19), (21) into the power balance (17), the equation for σ is obtained for any regular point $\mathbf{p}\in\Gamma$

$$\frac{\sigma(\mathbf{p},\mathbf{u},t)}{\cos\theta}=(1-\alpha)\left[\frac{\sigma(\mathbf{p}',\mathbf{u}',t')}{\cos\theta'}e^{-mr}+\int_{\mathbf{p}'\mathbf{p}}\rho(\mathbf{s},\mathbf{u}',t-s/c)e^{-ms}\,ds\right]. \tag{22}$$

Equation (22) relates the value of σ at $(\mathbf{p},\mathbf{u},t)$ to the value of σ at $(\mathbf{p}',\mathbf{u}',t')$. It is thus a functional equation of the unknown σ.

If the point $\mathbf{p}'$ does not exist, the corresponding incident power $\mathcal{P}_{\mathrm{dif}}$ must be removed from the previous calculation. The first term of the right-hand side of Eq. (22) vanishes and Eq. (22) yields the direct solution of σ. In the case where $\mathbf{p}'$ is not unique, the contributions of all these points must be accounted for the calculation of $\mathcal{P}_{\mathrm{dif}}$. The complexity of the resulting expression depends upon whether there are a finite, countable infinite or uncountable infinite number of points. This case is not considered.

V. REFRACTION AT INTERFACE

The subscript $i=1,2$ is now introduced to denote both domains separated by an interface. Consider a point $\mathbf{p}\in\Gamma_1\cap\Gamma_2$ located on the interface. $\mathbf{n}_i$ $i=1,2$ denotes the outward unit normal at **p** ($\mathbf{n}_1=-\mathbf{n}_2$). Two diffraction sources

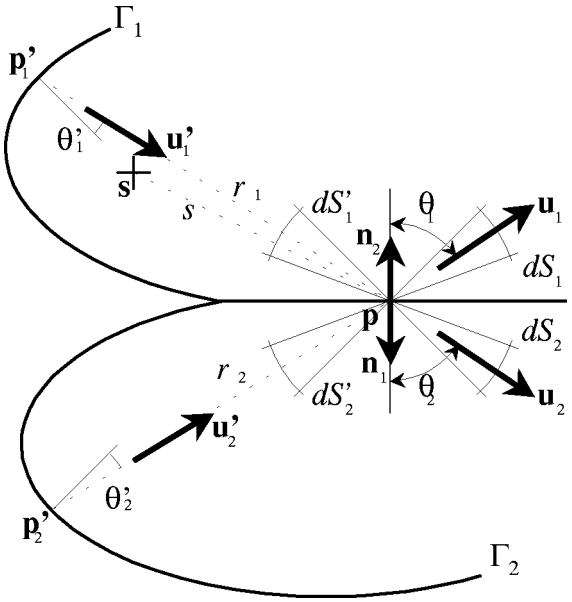

FIG. 3. Energy balance for $\mathbf{p}$ at the interface; power emitted toward $\mathbf{u}_1$ stems from the actual and the diffraction sources within Ω_1 and Ω_2.

σ_1 and σ_2 are present, one on each side of the interface. The incident power at $\mathbf{p}$ arising from the domain Ω_1 for instance, is partially reflected back towards Ω_1 and is also partially transmitted into Ω_2. If $\mathbf{u}_1'$ is the incident unit vector, $\mathbf{u}_1$ the reflected direction with emission angle θ_1, and $\mathbf{u}_2$ the refracted direction with emission angle θ_2, then the vectors $\mathbf{n}_1$, $\mathbf{n}_2$, $\mathbf{u}_1'$, $\mathbf{u}_1$, and $\mathbf{u}_2$ are coplanar and Snell's law states that $\sin\theta_1/c_1'=\sin\theta_2/c_2'$ where c_i' is the phase velocity in the medium i. The notations are summarized in Fig. 3.

The efficiency τ_{ij} is defined as the ratio of incident power coming from Ω_i to the power re-emitted towards Ω_j. This efficiency depends on the position $\mathbf{p}$ and the incident direction. When using a ray model, reflection and refraction phenomena follow the *principle of locality*. This allows the calculation of closed-form relationships. Deriving these efficiencies is a classical problem which is solved for many wave configuration in the literature.[13,14] It should be added that when the ''plane wave–plane surface'' approximation is applied to a general wave which impinges upon a curvilinear surface, the order of approximation is zero.[15] The efficiencies τ_{ij} must verify several constraints. The efficiencies are nonnegative factors less than unity

$$0\leqslant\tau_{ij}\leqslant 1. \tag{23}$$

If the interface is nondissipative, conservation of energy ensures that $\Sigma_j\tau_{ij}=1$. When absorption occurs, this sum is less than 1, $\Sigma_j\tau_{ij}<1$. By introducing the absorption coefficient α of the interface[16]

$$\sum_j \tau_{ij}+\alpha=1. \tag{24}$$

According to the *reciprocity principle*[17]

$$\tau_{ij}=\tau_{ji}. \tag{25}$$

This equality is only true along directions which are related to each other through Snell's law. However, the reciprocity principle does not hold for all systems. Counter examples do exist.[18]

Let us turn to the derivation of the functional equations for the secondary sources σ_1 and σ_2. The power emitted towards Ω_1, for instance, is the reflected part of the incident power stemming from the sources in Ω_1 plus the refracted part of the incident power stemming from the sources in Ω_2 (Fig. 3)

$$P_{1,\mathrm{emit}}=\tau_{11}[\mathcal{P}_{1,\mathrm{dir}}+\mathcal{P}_{1,\mathrm{dif}}]+\tau_{21}[\mathcal{P}_{2,\mathrm{dir}}+\mathcal{P}_{2,\mathrm{dif}}], \tag{26}$$

$$P_{2,\mathrm{emit}}=\tau_{12}[\mathcal{P}_{1,\mathrm{dir}}+\mathcal{P}_{1,\mathrm{dif}}]+\tau_{22}[\mathcal{P}_{2,\mathrm{dir}}+\mathcal{P}_{2,\mathrm{dif}}]. \tag{27}$$

The emitted powers were calculated in Eq. (18)

$$\mathcal{P}_{i,\mathrm{emit}}=\sigma_i(\mathbf{p},\mathbf{u}_i,t)\frac{dS_i}{\gamma_0}. \tag{28}$$

Similarly, Eqs. (19) and (21) are still valid

$$\mathcal{P}_{i,\mathrm{dir}}=\frac{1}{\gamma_0}\int_{\mathbf{p}_i'\mathbf{p}}\rho_i(\mathbf{s},\mathbf{u}_i',t-s/c_i)e^{-m_i s}ds\cos\theta_i\,dS_i', \tag{29}$$

for the incident power from the direct field and

$$\mathcal{P}_{i,\mathrm{dif}}=\frac{1}{\gamma_0}\sigma_i(\mathbf{p}_i',\mathbf{u}_i',t_i')e^{-m_i r_i}\frac{\cos\theta_i}{\cos\theta_i'}dS_i', \tag{30}$$

for the incident power from the diffracted field where $t_i'=t-r_i/c_i$, $r_i=|\mathbf{p}_i'-\mathbf{p}|$, and $s=|\mathbf{p}-\mathbf{s}|$.

The specular reflection law implies that $dS_i'=dS_i$ for $i=1,2$. By differentiating Snell's law, it follows that $\cos\theta_1\,d\theta_1/c_1'=\cos\theta_2\,d\theta_2/c_2'$. For two-dimensional systems, the solid angles dS_i match with the emission angles $d\theta_i$ and so $\cos\theta_1\,dS_1/c_1'=\cos\theta_2\,dS_2/c_2'$. For three-dimensional systems, a direction in space is fully determined by two angles: θ the polar angle and β the angle lying in the interface plane. The infinitesimal solid angle is $dS=\sin\theta\,d\theta\,d\beta$. Multiplying the Snell's law and its derivative gives $\cos\theta_1\,dS_1/c_1'^2=\cos\theta_2\,dS_2/c_2'^2$. In any dimension $n=1$, 2, or 3, the relationship between the solid angles is $\cos\theta_1\,dS_1/c_1'^{n-1}=\cos\theta_2\,dS_2/c_2'^{n-1}$. Introducing the above Eqs. (28), (29), (30) into (26), (27)

$$\begin{aligned}\frac{\sigma_1(\mathbf{p},\mathbf{u}_1,t)}{\cos\theta_1}=\tau_{11}\Bigg[&\frac{\sigma_1(\mathbf{p}_1',\mathbf{u}_1',t_1')}{\cos\theta_1'}e^{-m_1 r_1}\\&+\int_{\mathbf{p}_1'\mathbf{p}}\rho_1(\mathbf{s},\mathbf{u}_1',t-s/c_1)e^{-m_1 s}\,ds\Bigg]\\&+\left(\frac{c_2'}{c_1'}\right)^{n-1}\tau_{21}\Bigg[\frac{\sigma_2(\mathbf{p}_2',\mathbf{u}_2',t_2')}{\cos\theta_2'}e^{-m_2 r_2}\\&+\int_{\mathbf{p}_2'\mathbf{p}}\rho_2(\mathbf{s},\mathbf{u}_2',t-s/c_2)e^{-m_2 s}\,ds\Bigg],\end{aligned} \tag{31}$$

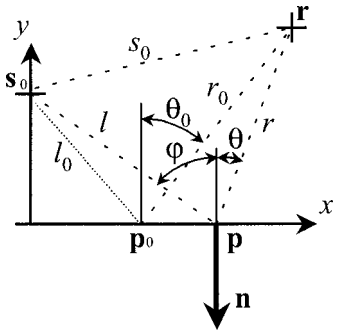

FIG. 4. A point source in a semi-infinite plane with a uniform reflectivity.

$$\frac{\sigma_2(\mathbf{p},\mathbf{u}_2,t)}{\cos\theta_2}=\left(\frac{c_1'}{c_2'}\right)^{n-1}\tau_{12}\left[\frac{\sigma_1(\mathbf{p}_1',\mathbf{u}_1',t_1')}{\cos\theta_1'}e^{-m_1r_1}+\int_{\mathbf{p}_1'\mathbf{p}}\rho_1(\mathbf{s},\mathbf{u}_1',t-s/c_1)e^{-m_1s}\,ds\right]+\tau_{22}\left[\frac{\sigma_2(\mathbf{p}_2',\mathbf{u}_2',t_2')}{\cos\theta_2'}e^{-m_2r_2}+\int_{\mathbf{p}_2'\mathbf{p}}\rho_2(\mathbf{s},\mathbf{u}_2',t-s/c_2)e^{-m_2s}\,ds\right]. \quad (32)$$

Thus, two functional equations are obtained for the unknown variables σ_1 and σ_2.

VI. IMAGE-SOURCE SOLUTION

The solution of Eq. (22) via the image-source technique is now presented. The calculations are based on the expression of the delta Dirac function in a polar coordinate system. Consider a half-plane where a single source $\mathbf{s}_0(0,h)$ acts as shown in Fig. 4. The source generates a time-varying injected power $P_{\text{inj}}(t)$. The boundary Γ, defined by $y=0$, has a uniform reflectivity $\tau=1-\alpha$. Let $\mathbf{p}(\nu,0)$ be any point on the boundary and θ any emission angle. Accounting for the nonexistence of the point $\mathbf{p}'$, Eq. (22) gives

$$\frac{\sigma(\nu,\theta,t)}{\cos\theta}=\tau\int_{\infty\mathbf{p}}\delta_{\mathbf{s}_0}(\mathbf{s})P_{\text{inj}}(t-s/c)e^{-ms}\,ds, \quad (33)$$

where $\infty\mathbf{p}$ is the semi-infinite incident line of direction $-\theta$, with an end point $\mathbf{p}$. As usual, $s=|\mathbf{p}-\mathbf{s}|$. For the polar coordinate system centered at $\mathbf{p}$, the delta Dirac function can be written as

$$\delta_{\mathbf{s}_0}(s,\theta)=\frac{\delta(s-l)}{s}\,\delta(\theta-\varphi), \quad (34)$$

where $l=|\mathbf{p}-\mathbf{s}_0|=(\nu^2+h^2)^{1/2}$ and φ is the incidence angle at $\mathbf{p}$ from $\mathbf{s}_0$. Then,

$$\sigma(\nu,\theta,t)=\tau P_{\text{inj}}(t-l/c)\cos\theta\frac{e^{-ml}}{l}\,\delta(\theta-\varphi). \quad (35)$$

The above equality fully determines the variable σ.

Let $\mathbf{r}(x,y)$ be any point within the domain Ω $(y>0)$ as shown in Fig. 4. Substituting into Eq. (35), Eq. (11) yields

$$W(\mathbf{r},t)=P_{\text{inj}}\left(t-\frac{s_0}{c}\right)\frac{e^{-ms_0}}{\gamma_0cs_0}+\tau\int_{-\infty}^{\infty}P_{\text{inj}}\left(t-\frac{l+r}{c}\right)\times\cos\theta\frac{e^{-ml}}{l}\,\delta(\theta-\varphi)\frac{e^{-mr}}{2\pi cr}\,d\nu,$$

where $s_0=|\mathbf{r}-\mathbf{s}_0|$, $r=|\mathbf{r}-\mathbf{p}|$.

It should be noted that

$$\int_a^b g(x)\,\delta[f(x)]dx=\int_{f(a)}^{f(b)}g\frac{\delta[f]}{df/dx}df=\sum_i\frac{g[x_i]}{|df/dx[x_i]|}, \quad (36)$$

where the sum is running over all zeros x_i of f for the interval $[a,b]$. The absolute value stems from $f(b)\leqslant 0\leqslant f(a)$ when $df/dx\leqslant 0$.

Let $\psi(\nu)=\theta-\varphi$. The equation $\psi(\nu)=0$ has a unique solution ν_0 as shown in Fig. 4, $\theta_0=\varphi_0$. Let $r_0=|\mathbf{p}_0-\mathbf{r}|$ and $l_0=|\mathbf{p}_0-\mathbf{s}_0|$. From Fig. 4, an explicit value of ψ can be found

$$\psi=\arctan\frac{\nu-x}{y}+\arctan\frac{\nu}{h}. \quad (37)$$

Hence,

$$\frac{d\psi}{d\nu}=\frac{1/y}{1+\left(\frac{\nu-x}{y}\right)^2}+\frac{1/h}{1+\left(\frac{\nu}{h}\right)^2}=\frac{\cos\theta}{r}+\frac{\cos\varphi}{l} \quad (38)$$

and

$$W(\mathbf{r},t)=P_{\text{inj}}\left(t-\frac{s_0}{c}\right)\frac{e^{-ms_0}}{\gamma_0cs_0}+\tau P_{\text{inj}}\left(t-\frac{l_0+r_0}{c}\right)\times\frac{e^{-ml_0}}{l_0}\frac{e^{-mr_0}}{2\pi cr_0}\frac{\cos\theta_0}{\frac{\cos\theta_0}{r_0}+\frac{\cos\varphi_0}{l_0}}. \quad (39)$$

After simplification

$$W(\mathbf{r},t)=P_{\text{inj}}\left(t-\frac{s_0}{c}\right)\frac{e^{-ms_0}}{2\pi cs_0}+\tau P_{\text{inj}}\left(t-\frac{s_1}{c}\right)\frac{e^{-ms_1}}{2\pi cs_1}, \quad (40)$$

where $s_1=l_0+r_0$. In a similar way, it can be found that

$$\mathbf{I}(\mathbf{r},t)=P_{\text{inj}}\left(t-\frac{s_0}{c}\right)\frac{e^{-ms_0}}{2\pi s_0}\mathbf{u}_{\mathbf{s}_0\mathbf{r}}+\tau P_{\text{inj}}\left(t-\frac{s_1}{c}\right)\frac{e^{-ms_1}}{2\pi s_1}\mathbf{u}_{\mathbf{p}_0\mathbf{r}}. \quad (41)$$

The fields W and $\mathbf{I}$ are the sum of a direct field emerging from the source $\mathbf{s}_0(0,h)$ and a diffracted field emerging from a virtual source $\mathbf{s}_1(0,-h)$. This result is also valid for one-dimensional and three-dimensional systems. The total contribution of the diffraction sources, the second integral in Eqs. (11) and (12), collapses to a single spherical wave, i.e., the second term in the right-hand side of Eqs. (40) and (41).

This example suggests that Eqs. (11), (12), and (22) can be solved with the image-source technique. This technique is

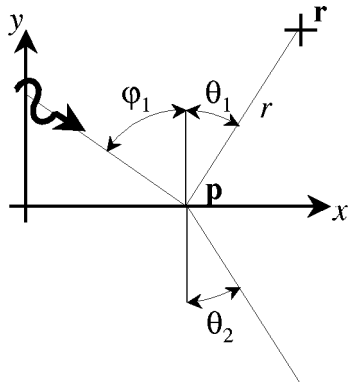

FIG. 5. Plane wave hitting an interface with uniform reflectivity.

efficient when the domain Ω has a simple form such as parallelepipeds or arbitrary polyhedra.[19] For convex domains, the image-sources $\mathbf{s}_i$ $i=1,2,\ldots$, are constructed by applying successive symmetries to the other sources with respect to the faces of the boundary. The number of symmetries k_i is referred to as the order of the image source. The fields within the domain Ω are constructed via the linear superposition of the fields created by actual and image sources

$$W(\mathbf{r},t)=\sum_{i=0}^{\infty} P_{\mathrm{inj}}(t-s_i/c)\,\tau^{k_i} G(\mathbf{s}_i,\mathbf{r}), \tag{42}$$

$$\mathbf{I}(\mathbf{r},t)=\sum_{i=0}^{\infty} P_{\mathrm{inj}}(t-s_i/c)\,\tau^{k_i} \mathbf{H}(\mathbf{s}_i,\mathbf{r}), \tag{43}$$

where $s_i=|\mathbf{r}-\mathbf{s}_i|$. The number of image sources may be finite or infinite. The solution of Eq. (22) is

$$\sigma(\mathbf{p},\theta,t)=-\gamma_0\sum_{i=1}^{\infty} P_{\mathrm{inj}}(t-s_i/c)\,\tau^{k_i}\mathbf{H}(\mathbf{s}_i,\mathbf{p})\cdot\mathbf{n}\,\delta(\theta-\theta_i), \tag{44}$$

with $s_i=|\mathbf{p}-\mathbf{s}_i|$, $\cos\theta_i=|\mathbf{n}\cdot\mathbf{u}_{\mathbf{s}_i\mathbf{p}}|$. Only image sources located behind point $\mathbf{p}$ contribute to an inward direction for σ. This solution provides an interpretation for the potential σ. The potential σ intercepts the power from all the image sources $\mathbf{s}_i$, re-emiting it regardless of the boundary.

VII. IRREVERSIBILITY AT THE INTERFACE

Consider an incident steady-state plane wave of magnitude A and direction $\mathbf{u}_1'$ hitting the interface between two semi-infinite undamped media with an angle of incidence φ_1, as shown in Fig. 5. The refracted angle is φ_2. For such a system, the diffraction source distributions σ_1, σ_2 do not depend upon the position and Eqs. (31), (32) take the form

$$\sigma_1(\theta_1)=A\tau_{11}\cos\theta_1\,\delta(\theta_1-\varphi_1), \tag{45}$$

$$\sigma_2(\theta_2)=A\frac{c_1'}{c_2'}\tau_{12}\cos\theta_2\,\delta(\theta_1-\varphi_1), \tag{46}$$

where θ_1 and θ_2 are related. Equation (11) leads to

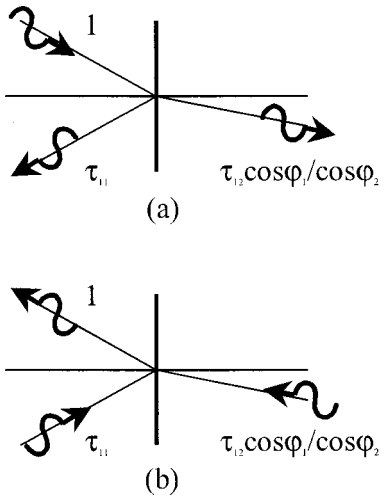

FIG. 6. Plane wave hitting an interface: (a) t-positive evolution, (b) t-negative evolution.

$$W_1(\mathbf{r})=\int_{-\pi/2}^{\pi/2}\frac{A}{2\pi c_1}\delta(\theta_1-\varphi_1)\,d\theta_1 + \int_{-\infty}^{\infty}\tau_{11}\frac{A}{2\pi c_1 r}\cos\theta_1\,\delta(\theta_1-\varphi_1)\,d\nu, \tag{47}$$

$$W_2(\mathbf{r})=\int_{-\infty}^{\infty}\tau_{12}\frac{A}{2\pi c_2 r}\frac{c_1'}{c_2'}\cos\theta_2\,\delta(\theta_1-\varphi_1)\,d\nu, \tag{48}$$

where $r=|\mathbf{r}-\mathbf{p}|$. With the changes of variable $d\nu=r\,d\theta_1/\cos\theta_1$ for the first equality and $d\nu=r\,d\theta_2/\cos\theta_2$ and $d\theta_2=c_2'\cos\theta_1\,d\theta_1/c_1'\cos\theta_2$ for the second equality

$$\begin{aligned} W_1(\mathbf{r}) &= \frac{A}{2\pi c_1}+\frac{A}{2\pi c_1}\int_{-\pi/2}^{\pi/2}\tau_{11}\frac{\cos\theta_1}{r} \times\delta(\theta_1-\varphi_1)\frac{r}{\cos\theta_1}d\theta_1 \\ &= \frac{A}{2\pi c_1}[1+\tau_{11}], \end{aligned} \tag{49}$$

$$\begin{aligned} W_2(\mathbf{r}) &= \frac{A}{2\pi c_2}\int_{-\pi/2}^{\pi/2}\tau_{12}\frac{c_1'}{c_2'}\delta(\theta_1-\varphi_1)\,d\theta_2 \\ &= \frac{A}{2\pi c_2}\int\tau_{12}\frac{\cos\theta_1}{\cos\theta_2}\delta(\theta_1-\varphi_1)\,d\theta_1 \\ &= \frac{A}{2\pi c_2}\tau_{12}\frac{\cos\varphi_1}{\cos\varphi_2}. \end{aligned} \tag{50}$$

Corresponding results for energy flow vectors are

$$\mathbf{I}_1(\mathbf{r})=\frac{A}{2\pi}[\mathbf{u}_1'+\tau_{11}\mathbf{u}_1], \tag{51}$$

$$\mathbf{I}_2(\mathbf{r})=\frac{A}{2\pi}\tau_{12}\frac{\cos\varphi_1}{\cos\varphi_2}\mathbf{u}_2. \tag{52}$$

The fields in domain Ω_1 are the sum of an incident plane wave of magnitude A and a reflected plane wave of magnitude $A\tau_{11}$. The fields in domain Ω_2 are a transmitted plane wave of magnitude $A\tau_{12}\cos\varphi_1/\cos\varphi_2$. Figure 6(a) provides

a summary for the case $A=1$.

Now, suppose that time evolution is inverted, leading to the situation shown in Fig. 6(b). Consider two plane waves simultaneously hit the interface with magnitudes τ_{11} and $\tau_{12}\cos\varphi_1/\cos\varphi_2$. They both contribute to the reflective wave of unit magnitude and also to the nonexistent reflective wave which enters the domain Ω_2. The former is the sum of the reflective part τ_{11}^2 of the incident wave τ_{11} plus the transmitted part $\tau_{21}\cos\varphi_2/\cos\varphi_1\times\tau_{12}\cos\varphi_1/\cos\varphi_2$. Hence

$$\tau_{11}^2+\tau_{12}\tau_{21}=1. \tag{53}$$

Similarly

$$(\tau_{11}+\tau_{22})\tau_{12}=0. \tag{54}$$

As efficiencies are non-negative factors less than unity, the two conditions (53), (54) are only true for two trivial cases

$$\tau_{12}=0 \quad \text{and} \quad \tau_{11}=\tau_{22}=1, \tag{55}$$

$$\tau_{11}=\tau_{22}=0 \quad \text{and} \quad \tau_{12}=\tau_{21}=1. \tag{56}$$

The first case defines an impermeable interface. The second case implies that the interface is nonexistent. For all other cases, Eqs. (53) and (54) cannot be verified. Hence, the situation obtained by time reversing leads to self-contradiction. This lack of invariance under time reversal shows that the present theory is fundamentally irreversible. This irreversibility cannot be attributed to dissipative phenomena as the previous argument was applied to nondissipative media separated by a conservative interface. Hence, this irreversibility is distinguishable from the thermodynamic irreversibility which stems from the conversion of mechanical energy into heat. Appendix C shows, via an example, that the irreversibility under discussion originates from the uncorrelation assumption, which is not symmetric under time reversal. Neglecting the interference of ingoing waves is not equivalent to neglecting the interference of outgoing waves.

VIII. RAY-TRACING SOLUTION

Equation (22) may be solved in a general fashion, leading to an interpretation by means of a ray path. Let $\mathbf{p}_0$ be any regular point on the boundary. Equation (22) introduces a point $\mathbf{p}'$, also noted as $\mathbf{p}_1$ in this section, from which the incident energy originates. Writing Eq. (22) for point $\mathbf{p}_1$ leads to the definition of point $\mathbf{p}_2$. Noting $\mathbf{p}_1$, $\mathbf{p}_2$, $\mathbf{p}_3$, and so on, the successive points from which the energy is reflected, and $t_1,t_2,\ldots$, the successive times for the reflection where $t_k=t_{k-1}-r_k/c$ and $r_k=|\mathbf{p}_k-\mathbf{p}_{k-1}|$, Eq. (22) gives the following recursive relationship:

$$\frac{\sigma_k}{\cos\theta_k}=\tau_k\left[\frac{\sigma_{k+1}}{\cos\theta_{k+1}}e^{-mr_{k+1}}+\int_{\mathbf{p}_{k+1}\mathbf{p}_k}\rho(\mathbf{s},\mathbf{u}_{k+1},t_k-s/c)e^{-ms}\,ds\right], \tag{57}$$

where $s=|\mathbf{s}-\mathbf{p}_k|$. The subscript $k=0,1,\ldots$, defines the locations of point $\mathbf{p}_k$ and $\sigma_k=\sigma(\mathbf{p}_k,\mathbf{u}_k,t_k)$. Successive substitution of each equation into the previous leads to

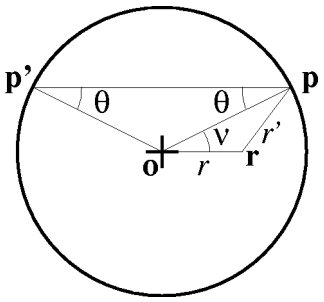

FIG. 7. Circular domain loaded at its center.

$$\frac{\sigma_0}{\cos\theta_0}=\sum_{k=0}^{n-1}\left(\prod_{i=0}^{k}\tau_i\right)\int_{\mathbf{p}_{k+1}\mathbf{p}_k}\rho(\mathbf{s},\mathbf{u}_{k+1},t-L(\mathbf{s})/c)\times e^{-mL(\mathbf{s})}\,dS+\mathcal{R}_n, \tag{58}$$

where $L(\mathbf{s})=s+r_k+\cdots+r_1$ is the total length from $\mathbf{s}$ to $\mathbf{p}_0$ and $\mathcal{R}_n=(\Pi_{i=0}^{n-1}\tau_i)\sigma_n e^{-mL(\mathbf{p}_n)}/\cos\theta_n$ and $L(\mathbf{p}_n)$ is the distance from $\mathbf{p}_n$ to $\mathbf{p}_0$ along the ray path. Assuming that the remaining term $\mathcal{R}_n$ tends to zero as n tends to infinite

$$\frac{\sigma(\mathbf{p}_0,\mathbf{u}_0,t)}{\cos\theta_0}=\sum_{k=0}^{\infty}\left(\prod_{i=0}^{k}\tau_i\right)\int_{\mathbf{p}_{k+1}\mathbf{p}_k}\rho(\mathbf{s},\mathbf{u}_{k+1},t-L(\mathbf{s})/c)e^{-mL(\mathbf{s})}\,ds. \tag{59}$$

Equation (59) may be considered the solution of Eq. (22) since it gives the diffraction sources σ solely in terms of the actual sources ρ.

The diffraction source σ at a point $\mathbf{p}_0$ in a direction $\mathbf{u}_0$ stems from the actual sources ρ located along the path $\mathbf{p}_0,\mathbf{p}_1,\ldots,\mathbf{p}_k\ldots$. Consider a source $\mathbf{s}$ located in the segment $\mathbf{p}_{k+1}\mathbf{p}_k$. This source contributes to the point $\mathbf{p}$ via the term $(\Pi_{i=0}^{k}\tau_i)\rho(\mathbf{s},\mathbf{u}_{k+1},t-L(\mathbf{s})/c)e^{-mL(\mathbf{s})}$. The reduction of the magnitude stems from the successive absorption phenomena due to the ray hitting the boundary $(\Pi_{i=0}^{k}\tau_i)$, and also the attenuation due to the propagation $(e^{-mL(\mathbf{s})})$.

This section highlights the analogy between the functional equations and the ray-tracing technique. More precisely, the exact solution of the functional equation may be found by determining the ray paths. In Appendix B, a simple example illustrates the difference between the ray-tracing technique and the functional equation method. Despite drastically different implementation, both methods produce similar results.

IX. CIRCULAR DOMAIN

The third example for which Eq. (22) is solved is a circular system of radius R. It is assumed that energy is supplied from a point load at the center $\mathbf{o}$. The reflectivity τ of the boundary is uniform.

Consider a point $\mathbf{p}$ located at the boundary with an emission angle θ. As a result of polar symmetry around $\mathbf{o}$, a field depends solely on the distance r from the center and not on the angular position. Hence, the potential $\sigma(\mathbf{p},\theta)$ reduces to $\sigma(\theta)$. Figure 7 shows the configuration of points $\mathbf{p}$, $\mathbf{p}'$, and $\mathbf{o}$. The triangle $\mathbf{pop}'$ is isosceles and hence angle θ' equals angle θ. In addition, $|\mathbf{p}-\mathbf{p}'|=2R\cos\theta$. Equation (22) yields

$$\frac{\sigma(\theta)}{\cos\theta}=\tau\frac{\sigma(\theta)}{\cos\theta}e^{-2mR\cos\theta}+\tau\int_{\mathbf{pp}'}A\,\delta_{\mathbf{o}}(\mathbf{s})e^{-ms}\,ds, \quad (60)$$

with $s=|\mathbf{s}-\mathbf{p}|$. Developing the delta Dirac function in the polar coordinates centered at $\mathbf{p}$, leads to

$$\sigma(\theta)=\frac{\tau\cos\theta}{1-\tau e^{-2mR\cos\theta}} \times\int_0^{2R\cos\theta}A\,\delta(\theta)\frac{\delta(s-R)}{s}e^{-ms}\,ds. \quad (61)$$

And

$$\sigma(\theta)=A\frac{e^{-mR}}{R}\frac{\tau}{1-\tau e^{-2mR}}\,\delta(\theta). \quad (62)$$

Consider a point $\mathbf{r}$ within domain Ω at a distance r from the center $\mathbf{o}$. The energy density is

$$W(r)=A\frac{e^{-mr}}{2\pi cr} +\int_0^{2\pi}A\frac{\tau e^{-mR}}{R(1-\tau e^{-2mR})}\,\delta(\theta)\frac{e^{-mr'}}{2\pi cr'}R\,d\nu, \quad (63)$$

where $r'=|\mathbf{p}-\mathbf{r}|$.

The first term on the right-hand side of Eq. (63) is the direct field, while the integral represents the diffracted field. As in Sec. VI, $\theta(\nu)=0$ must be solved. From Fig. 7, it is clear that $\theta(\nu)$ vanishes when $\nu=0$ and $\nu=\pi$. In addition, the triangle **rop** shows that $r\sin\nu=r'\sin\theta$. By differentiating with respect to ν

$$r\cos\nu=\frac{dr'}{d\nu}\sin\theta+r'\cos\theta\frac{d\theta}{d\nu}. \quad (64)$$

For $\nu=0$ and $\nu=\pi$

$$\nu=0\quad |\mathbf{p}_0-\mathbf{r}|=R-r\quad \frac{d\theta}{d\nu_{/\nu=0}}=\frac{r}{R-r}, \quad (65)$$

$$\nu=\pi\quad |\mathbf{p}_0-\mathbf{r}|=R+r\quad \frac{d\theta}{d\nu_{/\nu=\pi}}=\frac{-r}{R+r}. \quad (66)$$

Applying the equality (36)

$$W(r)=\frac{A}{2\pi c}\frac{e^{-mr}}{r}+\frac{A}{2\pi c}\frac{\tau e^{-mR}}{1-\tau e^{-2mR}} \times\left[\frac{e^{-m(R-r)}}{(R-r)\dfrac{r}{R-r}}+\frac{e^{-m(R+r)}}{(R+r)\dfrac{r}{R+r}}\right]. \quad (67)$$

And finally

$$W(r)=\frac{A}{2\pi c}\frac{1}{1-\tau e^{-2mR}}\frac{e^{-mr}}{r}+\frac{A}{2\pi c}\frac{\tau e^{-2mR}}{1-\tau e^{-2mR}}\frac{e^{mr}}{r}. \quad (68)$$

Similarly

$$I(r)=\frac{A}{2\pi}\frac{1}{1-\tau e^{-2mR}}\frac{e^{-mr}}{r}-\frac{A}{2\pi}\frac{\tau e^{-2mR}}{1-\tau e^{-2mR}}\frac{e^{mr}}{r}, \quad (69)$$

for the radial component of the energy flow. The orthoradial component vanishes.

The energy field is found to be the sum of a field emerging from the center together with a field directed towards the center. This result agrees with those obtained in Ref. 20, where a more direct approach was employed. The first field is a *propagating wave*, whereas the second is a *retropropagating wave*.

X. CONCLUSION

A mathematical formalism which extends the ''standard procedure'' or ''radiosity method'' when applied to specular reflection is proposed in this paper. Energy fields are constructed by a superposition of uncorrelated elementary waves.

The study of this formalism identifies several important features. First, the underlying equations may be solved via the image-source method and may be interpreted in terms of rays. The resulting solutions are similar to those of geometrical optics or acoustics when the phase of the ray is not considered. Second, this formalism is well-suited to the study of two media separated by an interface. Incident waves reflect according to the standard laws of reflection and refraction and the energy ratios are determined by the efficiencies. The situation is irreversible. The irreversibility is not due to dissipative phenomena, but is caused by the neglection of the interference between inward waves, which are asymmetric under time reversal. This is a typical example of where an approximation of a fundamentally reversible phenomenon leads to an apparent irreversibility.

The next stage of this study is the development of software, which is capable of solving of Eq. (22) for more complicated situations. This would provide an alternative to the standard ray-tracing softwares.

APPENDIX A

This Appendix determines whether the local power balance equation (13) holds for complete fields (11) and (12) and also gives the proof of Eqs. (15) and (16).

The left-hand side of Eq. (13) must be evaluated. Reversing the order of the derivative and integral

$$\begin{aligned}\mathrm{div}\cdot\mathbf{I}+mcW+\frac{\partial W}{\partial t}&=\int_\Omega \mathrm{grad}_{\mathbf{r}}\rho.\mathbf{H}+\frac{\partial\rho}{\partial t}G\,d\Omega_{\mathbf{s}}\\ &\quad+\int_\Omega\rho[\mathrm{div}_{\mathbf{r}}\cdot\mathbf{H}+mcG]\,d\Omega_{\mathbf{s}}\\ &\quad+\int_\Gamma \mathrm{grad}_{\mathbf{r}}\sigma\cdot\mathbf{H}+\frac{\partial\sigma}{\partial t}G\,d\Gamma_{\mathbf{p}}\\ &\quad+\int_\Gamma\sigma[\mathrm{div}_{\mathbf{r}}\cdot\mathbf{H}+mcG]\,d\Gamma_{\mathbf{p}}.\end{aligned} \quad (A1)$$

The similarity of the first and third integrals on the right-hand side of Eq. (A1) should be noted. The expression

$$\mathrm{grad}_{\mathbf{r}}\rho(\mathbf{s},\mathbf{u}_{\mathbf{sr}},t-s/c)\cdot\mathbf{H}(\mathbf{s},\mathbf{r})+\frac{\partial}{\partial t}\rho(\mathbf{s},\mathbf{u}_{\mathbf{sr}},t$$

$$-s/c)G(\mathbf{s},\mathbf{r}), \tag{A2}$$

with $s=|\mathbf{s}-\mathbf{r}|$, must be evaluated. Consider polar coordinates centered at **s**. The first term of Eq. (A2) is the radial component of the gradient. The above expression therefore becomes

$$\frac{\partial}{\partial s}\rho(\mathbf{s},\mathbf{u}_{\mathbf{sr}},t-s/c)cG+\frac{\partial}{\partial t}\rho(\mathbf{s},\mathbf{u}_{\mathbf{sr}},t-s/c)G=0. \tag{A3}$$

The first and third integrals in Eq. (A1) vanish. Using the local power balance for steady-state elementary waves[8]

$$\mathrm{div}_{\mathbf{r}}\cdot\mathbf{H}+mcG=\delta_{\mathbf{s}}, \tag{A4}$$

it yields

$$\mathrm{div}\cdot\mathbf{I}+mcW+\frac{\partial W}{\partial t}=\int_{\Omega}\rho\,\delta_{\mathbf{s}}(\mathbf{r})d\Omega_{\mathbf{s}}+\int_{\Gamma}\sigma\delta_{\mathbf{p}}(\mathbf{r})d\Gamma_{\mathbf{p}}. \tag{A5}$$

The second integral vanishes as the point **r** is inside Ω. In order to evaluate the first integral, the Dirac function is used with polar coordinates centered at **r**

$$\delta_{\mathbf{r}}(\mathbf{s})=\frac{1}{\gamma_0}\frac{\delta(s)}{s}. \tag{A6}$$

Expanding the integral

$$\int_{\Omega}\rho\,\delta_{\mathbf{r}}(\mathbf{s})d\Omega_{\mathbf{s}}=\int_0^{\infty}\int_{S_{n-1}}\rho\frac{\delta(s)}{\gamma_0 s}s\,dS\,ds. \tag{A7}$$

Thus

$$\mathrm{div}\cdot\mathbf{I}+mcW+\frac{\partial W}{\partial t}=p_{\mathrm{inj}}, \tag{A8}$$

with

$$p_{\mathrm{inj}}=\int_{S_{n-1}}\rho(\mathbf{r},\mathbf{u},t)dS_{\mathbf{u}}, \tag{A9}$$

which is the expected result.

For the proof of Eqs. (15) and (16) for the fields at the boundary Γ, consider a regular point $\mathbf{p}\in\Gamma$ and the hemisphere HS_ϵ, which is centered at **p**, with radius ϵ and is outside Ω (Fig. 8). Γ_ϵ denotes the segment of Γ which is outside the hemisphere HS_ϵ. Ω_ϵ denotes Ω plus the hemisphere HS_ϵ. When $\epsilon\to 0$ the boundary layer σ of the warped boundary must tend to a regular boundary. Consider the radiative intensity $I(\mathbf{p},\mathbf{u},t)$ of the surface $d\Gamma$ in the direction **u**, which is defined as the power per unit solid angle divided by the surface normal to the ray $d\Gamma_n=d\Gamma\cos\theta$ [Fig. 8(a)]. According to this definition, the source $\sigma\,d\Gamma$ radiates the intensity $I=\sigma(\mathbf{p},\mathbf{u},t)/\gamma_0\cos\theta$ in the direction **u**. On the other hand, the source $\sigma\,d\Gamma_{\mathbf{q}}$, located at a distance ϵ, emanates the intensity $I_\epsilon=\sigma(\mathbf{q},\mathbf{u},t-\epsilon/c)e^{-m\epsilon}/\gamma_0$ [Fig. 8(b)]. Both boundaries are equivalent, i.e., radiate the same intensity, under the condition that $\lim_{\epsilon\to 0}\sigma(\mathbf{q},\mathbf{u},t-\epsilon/c)e^{-m\epsilon}=\sigma(\mathbf{p},\mathbf{u},t)/\cos\theta$.

Evaluating the expressions (11) and (12) for the fields W and **I**, at point **p** in the domain $\Gamma_\epsilon\cup HS_\epsilon$

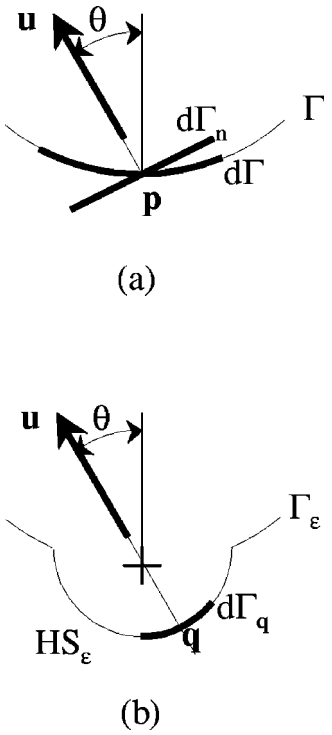

FIG. 8. Determination of the fields at the boundary: radiative intensity of the (a) regular boundary, (b) warped boundary.

$$W(\mathbf{p},t)=\int_{\Omega_\epsilon}\rho(\mathbf{s},\mathbf{u}_{\mathbf{sp}},t-s/c)G(\mathbf{s},\mathbf{p})d\Omega_{\mathbf{s}}$$

$$+\int_{\Gamma_\epsilon\cup HS_\epsilon}\sigma(\mathbf{q},\mathbf{u}_{\mathbf{qp}},t-\epsilon/c)G(\mathbf{q},\mathbf{p})d\Gamma_{\mathbf{q}}, \tag{A10}$$

$$\mathbf{I}(\mathbf{p},t)=\int_{\Omega_\epsilon}\rho(\mathbf{s},\mathbf{u}_{\mathbf{sp}},t-s/c)\mathbf{H}(\mathbf{s},\mathbf{p})d\Omega_{\mathbf{s}}$$

$$+\int_{\Gamma_\epsilon\cup HS_\epsilon}\sigma(\mathbf{q},\mathbf{u}_{\mathbf{qp}},t-\epsilon/c)\mathbf{H}(\mathbf{q},\mathbf{p})d\Gamma_{\mathbf{q}}, \tag{A11}$$

where $s=|\mathbf{s}-\mathbf{r}|$. When $\epsilon\to 0$, the first integral is regular and becomes $\lim_{\epsilon\to 0}\int_{\Omega_\epsilon}\rho G\,d\Omega=\int_\Omega\rho G\,d\Omega$. Separate the second integral in two terms gives $\int_{\Gamma_\epsilon}\sigma G\,d\Gamma+\int_{HS_\epsilon}\sigma G\,d\Gamma$. The first term tends to the principal value of Cauchy $\lim_{\epsilon\to 0}\int_{\Gamma_\epsilon}\sigma G\,d\Gamma=\int_\Gamma^{*}\sigma G\,d\Gamma$. For the second term, a change of variable is employed $d\Gamma_{\mathbf{q}}=\epsilon^{n-1}\,dS$

$$\int_{HS_\epsilon}\sigma G\,d\Gamma=\int_{HS}\sigma(\mathbf{q},\mathbf{u},t-\epsilon/c)\frac{e^{-m\epsilon}}{\gamma_0 c\,\epsilon^{n-1}}\epsilon^{n-1}\,dS_{\mathbf{u}}. \tag{A12}$$

Therefore, by virtue of the previous equivalence condition

$$\lim_{\epsilon\to 0}\int_{HS_\epsilon}\sigma G d\Gamma=\int_{HS}\frac{\sigma(\mathbf{p},\mathbf{u},t)}{\gamma_0 c\cos\theta}dS_{\mathbf{u}}. \tag{A13}$$

Equations (15), (16) for the fields on the boundary are hence proved.

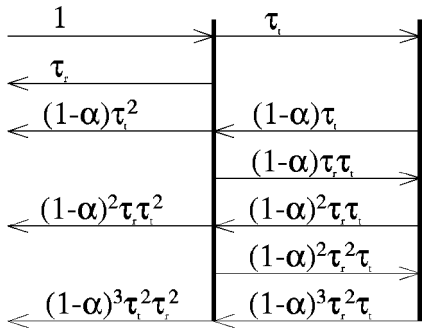

(a)

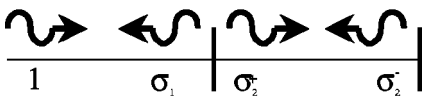

(b)

FIG. 9. Ray of unit magnitude hitting an interface: (a) ray-tracing solution; (b) solution via the use of Eqs. (22), (31), (32).

APPENDIX B

This Appendix is concerned with an example of a one-dimensional system, which illustrates the difference between the ray-tracing technique and the solving of the functional equations studied in this text.

Consider the one-dimensional system comprising two nondissipative media, one semi-infinite (on left), and the other finite (on right). For simplicity the interface is assumed to be reciprocal and the efficiencies are denoted τ_r and τ_t. α is the absorption factor of the right end. A right-traveling ray impinges on the interface.

The classical solution to this problem uses the ray-tracing technique.[13] When an incident ray of unit magnitude impinges upon the interface, it is separated into a reflected left-traveling ray in medium 1 of magnitude τ_r and a transmitted right-traveling ray in medium 2 of magnitude τ_t. The transmitted ray is partially reflected at the right end of the medium. The resulting reflected ray has the magnitude $(1-\alpha)\tau_t$. A new interface separation process occurs, giving two rays of magnitudes $(1-\alpha)\tau_t^2$ and $(1-\alpha)\tau_r\tau_t$. The latter is again reflected at the right end to produce a ray of magnitude $(1-\alpha)^2\tau_r\tau_t$, and so on. The ray paths and magnitudes are summarized in Fig. 9(a). The energies are obtained by summing the magnitudes of rays. The intensities are calculated by summing the algebraic magnitudes, taking into account the direction of propagation. Thus, the energies are

$$W_1 = 1+\tau_r+(1-\alpha)\tau_t^2\sum_{n=0}^{\infty}[(1-\alpha)\tau_r]^n = 1+\tau_r+\frac{(1-\alpha)\tau_t^2}{1-(1-\alpha)\tau_r}, \tag{B1}$$

$$W_2 = \tau_t[1+(1-\alpha)]\sum_{n=0}^{\infty}[(1-\alpha)\tau_r]^n = \frac{\tau_t(2-\alpha)}{1-(1-\alpha)\tau_r}. \tag{B2}$$

And the intensities

$$I_1 = c_1\left[1-\tau_r-(1-\alpha)\tau_t^2\sum_{n=0}^{\infty}[(1-\alpha)\tau_r]^n\right] = c_1\left[1-\tau_r-\frac{(1-\alpha)\tau_t^2}{1-(1-\alpha)\tau_r}\right], \tag{B3}$$

$$I_2 = c_2\left[\alpha\tau_t\sum_{n=0}^{\infty}[(1-\alpha)\tau_r]^n\right] = c_2\left[\frac{\tau_t\alpha}{1-(1-\alpha)\tau_r}\right]. \tag{B4}$$

An alternative means solving this problem is based on the formalism developed in this paper. The three boundary unknowns σ_1, σ_2^+, and σ_2^- [see Fig. 9(b)] are determined respectively by applying Eqs. (31), (32), and Eq. (22)

$$\begin{cases} \sigma_1 = \tau_r+\tau_t\sigma_2^- \\ \sigma_2^+ = \tau_t+\tau_r\sigma_2^- \\ \sigma_2^- = (1-\alpha)\sigma_2^+ \end{cases} \quad \text{then,} \quad \begin{cases} \sigma_1 = \tau_r+\dfrac{(1-\alpha)\tau_t^2}{1-(1-\alpha)\tau_r} \\ \sigma_2^+ = \dfrac{\tau_t}{1-(1-\alpha)\tau_r} \\ \sigma_2^- = \dfrac{\tau_t(1-\alpha)}{1-(1-\alpha)\tau_r}. \end{cases} \tag{B5}$$

The fields within the domains are given by Eqs. (11) and (12)

$$W_1 = 1+\sigma_1 = 1+\tau_r+\frac{(1-\alpha)\tau_t^2}{1-(1-\alpha)\tau_r}, \tag{B6}$$

$$W_2 = \sigma_2^+ + \sigma_2^- = \frac{\tau_t(2-\alpha)}{1-(1-\alpha)\tau_r}, \tag{B7}$$

$$I_1 = c_1[1-\sigma_1] = c_1\left[1-\tau_r-\frac{(1-\alpha)\tau_t^2}{1-(1-\alpha)\tau_r}\right], \tag{B8}$$

$$I_2 = c_2[\sigma_2^+ - \sigma_2^-] = c_2\left[\frac{\tau_t\alpha}{1-(1-\alpha)\tau_r}\right]. \tag{B9}$$

These results agree with those previously obtained.

Hence, the ray-tracing technique and the equations proposed in this paper may be considered as two alternative points of view for the same theory. The former is of a geometrical nature, whereas the latter is functional. The mathematical implementations are also quite different. The first method requires the calculation of a series, whereas the second method leads to a set of linear equations.

APPENDIX C

The noninvariance under time reversal means that neglecting the interference between waves entering to an interface is not equivalent to neglecting the interference between exiting waves. To check this assertion, consider two one-dimensional acoustical media with different velocities c_i and impedances Z_i $(i=1,2)$ jointed at $x=0$ as shown in Fig. 10.

In each medium the sound pressure may be viewed as the sum of a right-traveling wave $p_i^+(x)=a_i^+e^{j\omega(-x/c_i+t)}$

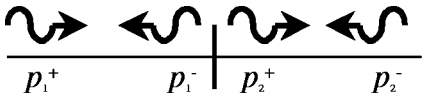

FIG. 10. Ingoing and outgoing waves hitting an interface between two acoustical one-dimensional media.

and a left-traveling wave $p_i^-(x)=a_i^- e^{j\omega(x/c_i+t)}$. At the interface, the conditions which ensure continuity of pressure and velocity are

$$\begin{aligned} &a_1^+ + a_1^- = a_2^+ + a_2^- \\ &(a_1^+ - a_1^-)/Z_1 = (a_2^+ - a_2^-)/Z_2. \end{aligned} \tag{C1}$$

Rearranging, to obtain the outgoing magnitudes in terms of entering magnitudes and conversely

$$\begin{cases} a_1^- = -\dfrac{Z_1 - Z_2}{Z_1 + Z_2} a_1^+ + \dfrac{2Z_1}{Z_1 + Z_2} a_2^- \\ a_2^+ = \dfrac{2Z_2}{Z_1 + Z_2} a_1^+ + \dfrac{Z_1 - Z_2}{Z_1 + Z_2} a_2^- \end{cases}$$

or (C2)

$$\begin{cases} a_1^+ = -\dfrac{Z_1 - Z_2}{Z_1 + Z_2} a_1^- + \dfrac{2Z_1}{Z_1 + Z_2} a_2^+ \\ a_2^- = \dfrac{2Z_2}{Z_1 + Z_2} a_1^- + \dfrac{Z_1 - Z_2}{Z_1 + Z_2} a_2^+. \end{cases}$$

The time-averaged energy flow supported by a plane wave is $P_i^{\pm} = |a_i^{\pm}|^2/2Z_i$. When the above systems are squared, the four powers $P_i^{\pm}$ appear with cross-product terms $|a_i a_j|$ which do not reduce to powers $P_i^{\pm}$. These terms are due to interference. As the waves are uncorrelated, these terms can be removed. Thus

$$\begin{pmatrix} P_1^- \\ P_2^+ \end{pmatrix}_i = \begin{pmatrix} \tau_r & \tau_t \\ \tau_t & \tau_r \end{pmatrix} \begin{pmatrix} P_1^+ \\ P_2^- \end{pmatrix}_i$$

or (C3)

$$\begin{pmatrix} P_1^+ \\ P_2^- \end{pmatrix}_o = \begin{pmatrix} \tau_r & \tau_t \\ \tau_t & \tau_r \end{pmatrix} \begin{pmatrix} P_1^- \\ P_2^+ \end{pmatrix}_o,$$

with $\tau_r = (Z_1 - Z_2)^2/(Z_1 + Z_2)^2$, $\tau_t = 4Z_1 Z_2/(Z_1 + Z_2)^2$, where the subscripts i and o denote, respectively, that ingoing and outgoing interferences have been neglected. Thus, the systems are shown not to be equivalent as the efficiency matrix is not unitary. As ingoing waves become outgoing waves, and vice versa when time evolution is reversed, the uncorrelation assumption is not invariant under time reversal.

[1] J. Barbry, "Techniques des images et des rayons (locaux vides)," Note Scientifique 51 INRS, France (1984).
[2] W. Joyce, "Sabine's reverberation time and ergodic auditoriums," J. Acoust. Soc. Am. **58**, 643–655 (1975).
[3] H. Kuttruff, "Simulierte nachhallkurven in rechteckräumen mit diffusem schallfeld," Acustica **25**, 333–342 (1971).
[4] R. Miles, "Sound field in a rectangular enclosure with diffusely reflecting boundaries," J. Sound Vib. **92**, 203–226 (1984).
[5] M. Carroll and C. Chien, "Decay of reverberent sound in a spherical enclosure," J. Acoust. Soc. Am. **62**, 1442–1446 (1977).
[6] H. Kuttruff, "Energetic sound propagation in rooms," Acta Acustica united with Acustica **83**, 622–628 (1997).
[7] M. F. Modest, *Radiative Heat Transfer* (McGraw-Hill, New York, 1993).
[8] A. Le Bot, "A vibroacoustic model for high frequency analysis," J. Sound Vib. **211**, 537–554 (1998).
[9] A. Le Bot, "Energy transfer for high frequencies in built-up structures," J. Sound Vib. **250**, 247–275 (2002).
[10] A. Le Bot and A. Bocquillet, "Comparison of an integral equation on energy and the ray-tracing technique for room acoustics," J. Acoust. Soc. Am. **108**, 1732–1740 (2000).
[11] H. Kuttruff, "Stationary propagation of sound energy in flat enclosures with partially diffuse surface reflection," Acta Acustica united with Acustica **86**, 1028–1033 (2000).
[12] H. Kuttruff, *Room Acoustics*, 3rd ed. (Elsevier Applied Science, London, 1991), see Eq. (1-15).
[13] J. Horner, and R. White, "Prediction of vibrational power transmission through jointed beams," Int. J. Mech. Sci. **32**, 215–223 (1990).
[14] W. Wöhle, T. Beckmann, and H. Schreckenbach, "Coupling loss factors for statistical energy analysis of sound transmission at rectangular slab joints. I," J. Sound Vib. **77**, 323–334 (1981).
[15] Y. Kravtsov and Y. Orlov, *Geometrical Optics of Inhomogeneous Media* (Springer, Berlin, 1990), see Sec. 2.5.
[16] R. Leung and R. Pinnington, "Wave propagation through right-angled joints with compliance-flexural incident wave," J. Sound Vib. **142**, 31–46 (1990), see Eq. (32).
[17] R. Langley, "A wave intensity technique for the analysis of high frequency vibrations," J. Sound Vib. **159**, 483–502 (1992), see Eq. (37).
[18] P. Morse and K. Ingard, *Theoritical Acoustics* (McGraw-Hill, New York, 1968), see Sec. 11.1.
[19] J. Borish, "Extension of the image model to arbitrary polyhedra," J. Acoust. Soc. Am. **75**, 1827–1836 (1984).
[20] A. Le Bot, "Geometric diffusion of vibrational energy and comparison with the vibrational conductivity approach," J. Sound Vib. **212**, 637–647 (1998).

Acoustic diffraction by a half-plane in a viscous fluid medium

Anthony M. J. Davis
Mathematics Department, University of Alabama, Tuscaloosa, Alabama 35487-0350

Raymond J. Nagem
Aerospace and Mechanical Engineering Department, Boston University, Boston, Massachusetts 02115

(Received 11 December 2001; revised 10 April 2002; accepted 22 June 2002)

We consider the diffraction of a time-harmonic acoustic plane wave by a rigid half-plane in a viscous fluid medium. The linearized equations of viscous fluid flow and the no-slip condition on the half-plane are used to derive a pair of disjoint Wiener–Hopf equations for the fluid stresses and velocities. The Wiener–Hopf equations are solved in conjunction with a requirement that the stresses are integrable near the edge of the half-plane. Specific wave components of the scattered velocity field are given analytically. A Padé approximation to the Wiener–Hopf kernel function is used to derive numerical results that show the effect of viscosity on the velocity field in the immediate vicinity of the edge of the half-plane. © *2002 Acoustical Society of America.*
[DOI: 10.1121/1.1502894]

PACS numbers: 43.20.El, 43.20.Fn [JGH]

I. INTRODUCTION

The diffraction of a two-dimensional sound wave by a semi-infinite planar screen is a fundamental problem in the theory of acoustic scattering. This diffraction problem is typically analyzed in terms of a potential function ϕ that is related to the irrotational acoustic velocity $\mathbf{v}$ by

$$\mathbf{v}=\nabla\phi. \tag{1}$$

For a time-harmonic acoustic field with radian frequency ω in an inviscid fluid medium, the potential ϕ satisfies the Helmholtz equation

$$\nabla^2\phi+k_0^2\phi=0, \quad k_0=\omega/c_0, \tag{2}$$

where c_0 is the speed of sound in the acoustic medium.

Since the Helmholtz equation (2) is a scalar equation of second order, it is not possible to impose both a far-field radiation condition and the ''no-slip'' boundary condition that the acoustic velocity vector $\mathbf{v}$ given by Eq. (1) vanishes on the screen. As in most acoustic scattering problems, only the velocity component normal to the screen is required to vanish on the screen. This ''no-penetration'' condition corresponds to the boundary condition

$$\frac{\partial\phi}{\partial n}=0, \tag{3}$$

where $\mathbf{n}$ is directed normal to the screen.

The exact solution of Eq. (2) that satisfies condition (3) on a semi-infinite screen and far-field conditions corresponding to an incident plane wave was first derived by Sommerfeld[1] in the context of an analogous electromagnetic scattering problem. It was soon realized[2] that the acoustic velocity field (1) derived from the Sommerfeld solution implies that the nonzero ''slip'' velocity on the screen is singular at the edge of the screen. Although the acoustic field derived from the Sommerfield solution agrees well with experimental measurements far from the screen, it is clear that this solution cannot be accurate in the vicinity of the edge.

A two-dimensional acoustic scattering formulation that incorporates the complete no-slip condition on a semi-infinite planar screen was first given by Alblas.[3] Alblas begins with the linearized equations of viscous fluid flow, and writes the acoustic velocity components in terms of a potential function ϕ and a stream function ψ. The relation between the acoustic pressure and the acoustic density is assumed to be linear and independent of temperature. In assuming the functions ϕ and ψ to be governed by uncoupled Helmholtz equations of the form (2), the ability to add conjugate harmonic functions to ϕ and ψ without changing the velocity field is overlooked. An incident plane wave at normal incidence to the screen is assumed, and the imposition of the no-slip condition on the screen leads to a Wiener–Hopf problem. Alblas later generalized his formulation to include the temperature dependent pressure–density relation and the temperature equation of linearized ideal gas dynamics.[4] Alblas' analyses are mainly formal, and few explicit results are given.

In this paper, we reconsider the problem of two-dimensional acoustic diffraction by a semi-infinite planar screen in a viscous fluid medium. The governing equations are essentially the same as in Ref. 3, but we do not introduce potential and stream functions into our solution procedure, though their role is mentioned for completeness of the presentation. This clarifies the nature of the solution in the interesting region near the edge of the screen, where ϕ, ψ are shown in the Appendix to become biharmonic. An incident plane wave with a general angle of incidence is assumed. Two disjoint Weiner–Hopf equations are derived for the Fourier transforms of the fluid stresses and velocities. A local analysis of the acoustic field near the edge of the screen provides an edge condition that is used in the solution of the Wiener–Hopf equations. Explicit analytic expressions are given for specific wave components of the scattered velocity field. A simple Padé approximation to the Weiner–Hopf kernel function is used to derive numerical results that show the

effects of viscosity on the velocity field in the immediate vicinity of the edge of the screen.

II. THEORY

The standard acoustic equations for linearized flow in a homogeneous viscous fluid medium are the continuity equation

$$\frac{\partial \rho}{\partial t}+\rho_0 \nabla\cdot\mathbf{v}=0, \tag{4}$$

the momentum equation

$$\frac{\partial \mathbf{v}}{\partial t}=-\frac{1}{\rho_0}\nabla p+\nu\nabla^2\mathbf{v}+\frac{\nu}{3}\nabla(\nabla\cdot\mathbf{v}), \tag{5}$$

and the equation of state

$$\frac{dp}{d\rho}=c_0^2, \tag{6}$$

in which $\mathbf{v}$ is the fluid velocity vector, ρ_0 is the ambient fluid density, ρ is the density perturbation, p is the fluid pressure and ν is the kinematic viscosity. It may be deduced from Eqs. (4)–(6) that the vorticity $\mathbf{\Omega}$ satisfies

$$\frac{\partial \mathbf{\Omega}}{\partial t}=\nu\nabla^2\mathbf{\Omega}, \tag{7}$$

as in unsteady creeping flow, while ρ and $\nabla\cdot\mathbf{v}$ satisfy an acoustic wave equation with viscous damping, namely

$$\frac{\partial^2}{\partial t^2}[\rho,\nabla\cdot\mathbf{v}]=\left(c_0^2+\frac{4\nu}{3}\frac{\partial}{\partial t}\right)\nabla^2[\rho,\nabla\cdot\mathbf{v}]. \tag{8}$$

In particular, an irrotational plane wave has velocity field of the form

$$\mathbf{v}=\frac{c_0^2}{\omega}\nabla\{\exp[i(k_a\mathbf{e}\cdot\mathbf{r}-\omega t)]\},\quad k_a^{-2}=\frac{c_0^2}{\omega^2}-i\frac{4\nu}{3\omega}, \tag{9}$$

where $\mathbf{e}$ denotes a unit vector. This is a convenient approximation to the field generated by a faraway point source. A full treatment of a point source disturbance would involve the superposition of plane waves.

A semi-infinite rigid plate, at which the no-slip condition $\mathbf{v}=\mathbf{0}$ is imposed, is at $y=0$, $x>0$ and a two-dimensional disturbance is generated by a plane wave of period $2\pi/\omega$, as illustrated by Fig. 1, in which α is acute. Obtuse values of α would require the incident disturbance to include reflection from a complete plane wall. Although Eqs. (7), (8) suggest the introduction of a stream function $\psi(x,y)$ and a potential $\phi(x,y)$ that define the flow field,[3] this is inappropriate here because the field is static, i.e., ψ and ϕ are biharmonic, in the vicinity of the sharp edge at the origin. A full explanation is given in the Appendix. Since the viscous decay length $(\nu/\omega)^{1/2}$ is assumed here to be much smaller than the acoustic length c_0/ω, the viscous effects are essentially confined to a thin region containing the barrier, as in air or water at normal acoustic frequencies.

Define

$$k_0=\frac{\omega}{c_0},\quad \epsilon^2=\frac{\omega\nu}{c_0^2}\ll 1, \tag{10}$$

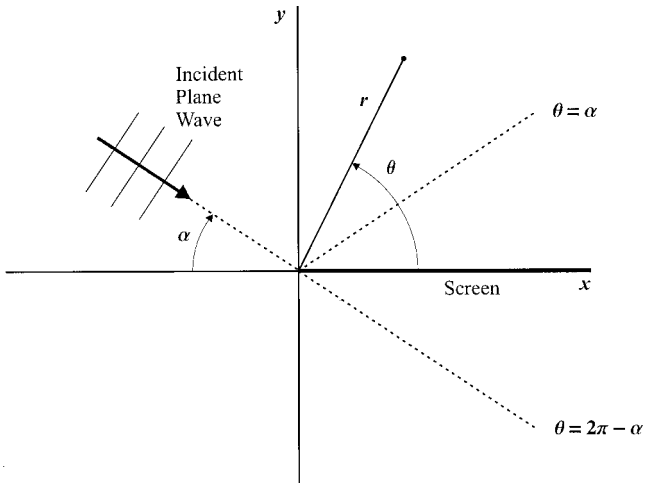

FIG. 1. Geometry of half-plane diffraction problem.

and suppress the time factor $e^{-i\omega t}$. Then Eq. (9) yields

$$k_a=\frac{k_0}{\left(1-\frac{4i}{3}\epsilon^2\right)^{1/2}}, \tag{11}$$

which lies just above the positive real axis, and an incident wave

$$\mathbf{v}_{\text{inc}}=(\mathbf{i}\cos\alpha-\mathbf{j}\sin\alpha)c_0\exp[ik_a(x\cos\alpha-y\sin\alpha)]$$
$$(0<\alpha<\pi/2). \tag{12}$$

Application of the no-slip condition on the barrier then shows that the scattered field $\mathbf{v}_{sc}$ must satisfy

$$\mathbf{v}_{sc}(x,0)=(-\mathbf{i}\cos\alpha+\mathbf{j}\sin\alpha)c_0\exp[ik_a x\cos\alpha]\quad (x>0), \tag{13}$$

and, from Eqs. (4)–(6), be governed by

$$\frac{i\omega}{\rho_0 c_0^2}p_{sc}=\nabla\cdot\mathbf{v}_{sc}, \tag{14}$$

$$\left(\nabla^2+\frac{i\omega}{\nu}\right)\mathbf{v}_{sc}=\frac{1-\frac{i}{3}\epsilon^2}{\rho_0\nu}\nabla p_{sc}. \tag{15}$$

It is assumed that, at infinity, $\mathbf{v}_{sc}$ has only plane and diffracted waves. Define the dimensionless Fourier transforms

$$[\mathbf{V},P]=\int_{-\infty}^{\infty}k_0\left[\frac{\mathbf{v}_{sc}}{c_0},\frac{p_{sc}}{\rho_0 c_0^2}\right]e^{-ikx}\,dx, \tag{16}$$

which, according to Eqs. (14), (15), are such that

$$ikV_x+\frac{dV_y}{dy}=\frac{i\omega}{c_0}P,$$

$$\left(\frac{d^2}{dy^2}-k^2+\frac{i\omega}{\nu}\right)\begin{bmatrix}V_x\\V_y\end{bmatrix}=\frac{c_0}{\nu}\left(1-\frac{i}{3}\epsilon^2\right)\begin{bmatrix}ikP\\\dfrac{dP}{dy}\end{bmatrix}. \tag{17}$$

Hence, with k_a defined by Eq. (9),

$$\frac{d^2P}{dy^2}=(k^2-k_a^2)P, \tag{18}$$

whose solution that vanishes as $|y|\to\infty$ is

$$P=[A(k)+B(k)\mathrm{sgn}(y)]\exp[-(k^2-k_a^2)^{1/2}|y|]. \tag{19}$$

Then the appropriate solution of Eq. (17) is

$$\begin{aligned}\mathbf{V}=&\begin{bmatrix} C(k)+D(k)\mathrm{sgn}(y) \\ \dfrac{ik}{\left(k^2-\dfrac{i\omega}{\nu}\right)^{1/2}}[C(k)\mathrm{sgn}(y)+D(k)]\end{bmatrix}\\ &\times\exp\left[-\left(k^2-\frac{i\omega}{\nu}\right)^{1/2}|y|\right]\\ &+\frac{k_0}{k_a^2}\begin{bmatrix} k[A(k)+B(k)\mathrm{sgn}(y)] \\ i(k^2-k_a^2)^{1/2}[A(k)\mathrm{sgn}(y)+B(k)]\end{bmatrix}\\ &\times\exp[-(k^2-k_a^2)^{1/2}|y|],\end{aligned} \tag{20}$$

after using the definition of k_a in Eq. (9). In Eqs. (19) and (20) the square roots must have positive real part for all real k.

The four functions $A(k)$, $B(k)$, $C(k)$, and $D(k)$ are determined by conditions at $y=0$. Continuity of $\mathbf{V}$ requires

$$D+\frac{k_0kB}{k_a^2}=0,\quad \frac{kC}{\left(k^2-\dfrac{i\omega}{\nu}\right)^{1/2}}+\frac{k_0(k^2-k_a^2)^{1/2}A}{k_a^2}=0. \tag{21}$$

Condition (13), when used in the Fourier transform (16), yields, for $\Im(k-k_a\cos\alpha)<0$,

$$\begin{aligned}(\mathbf{V})_{y=0}=&\frac{k_0}{c_0}\int_{-\infty}^{0}\mathbf{v}_{sc}(x,0)e^{-ikx}\,dx\\ &+\begin{bmatrix}-\cos\alpha\\ \sin\alpha\end{bmatrix}\frac{k_0}{i(k-k_a\cos\alpha)},\end{aligned}$$

in which the integral is analytic in an upper-half of the complex k-plane and is thus denoted by $\mathbf{V}^+(k)$. When the left-hand side is evaluated from Eq. (20), it follows, after substitution of Eq. (21), that

$$\begin{aligned}&K(k)\begin{bmatrix}C(k)/(k^2-k_a^2)^{1/2}\\ D(k)/ik\end{bmatrix}\\ &=\mathbf{V}^+(k)+\begin{bmatrix}-\cos\alpha\\ \sin\alpha\end{bmatrix}\frac{k_0}{i(k-k_a\cos\alpha)},\end{aligned} \tag{22}$$

where $K(k)$ is the Wiener–Hopf kernel defined by

$$K(k)=(k^2-k_a^2)^{1/2}-\frac{k^2}{\left(k^2-\dfrac{i\omega}{\nu}\right)^{1/2}}. \tag{23}$$

It will later be convenient to substitute k_0^2/ϵ^2 for ω/ν in $K(k)$, according to Eq. (10). The Fourier transforms of the tangential and normal stresses are, according to Eqs. (14), (16), $\rho_0c_0^2$ times

$$\frac{\nu}{\omega}\left(\frac{dV_x}{dy}+ikV_y\right)\quad\text{and}\quad -\frac{P}{k_0}\left(1+\frac{2i}{3}\epsilon^2\right)+\frac{2\nu}{\omega}\frac{dV_y}{dy},$$

respectively. Their discontinuities at $y=0$ are analytic in a lower half-plane because the stress discontinuities are confined to the barrier. Hence, by substitution of Eqs. (19)–(21),

$$\begin{bmatrix}S^-(k)\\ T^-(k)\end{bmatrix}=\begin{bmatrix} iC(k)\Big/\left(k^2-\dfrac{i\omega}{\nu}\right)^{1/2}\\ D(k)/k\end{bmatrix}. \tag{24}$$

Equations (22) now enable C, D to be eliminated, leaving a pair of disjoint Wiener–Hopf equations:

$$\begin{aligned}&K(k)\begin{bmatrix} S^-(k)\left(\dfrac{k^2-\dfrac{i\omega}{\nu}}{k^2-k_a^2}\right)^{1/2}\\ T^-(k)\end{bmatrix}\\ &=i\mathbf{V}^+(k)+\begin{bmatrix}-\cos\alpha\\ \sin\alpha\end{bmatrix}\frac{k_0}{(k-k_a\cos\alpha)}.\end{aligned} \tag{25}$$

Note that $K(k)$, the kernel of the second equation, has been defined with the inviscid limit in mind. Thus the kernel of the first equation, necessitated by viscosity, is obtained from Eq. (23) by interchanging the square roots.

Both kernels are analytic except for branch cuts from k_a to $k_0e^{i\pi/4}/\epsilon$ to $\infty e^{i\pi/4}$ and from $-k_a$ to $-k_0e^{i\pi/4}/\epsilon$ to $-\infty e^{i\pi/4}$. The product $K(k)[2(k^2-k_a^2)^{1/2}-K(k)]$ has zeros at $\pm k_K$, where, by use of Eq. (11), $k_K=k_0[1-(7i/3)\epsilon^2]^{-1/2}$. But the chosen branch cuts and the need for $[k^2-(i\omega/\nu)]^{1/2}$ and $(k^2-k_a^2)^{1/2}$ to have positive real part on the real k-axis imply that, at $k=\pm k_K$, $[k_K^2-(i\omega/\nu)]^{1/2}(k_K^2-k_a^2)^{1/2}=-k_K^2$, i.e., $K(\pm k_K)=2(k_K^2-k_a^2)^{1/2}$. Hence $K(k)$ has no zeros and its decomposition, namely

$$K(k)=(k^2-k_a^2)^{1/2}-\frac{k^2}{\left(k^2-\dfrac{ik_0^2}{\epsilon^2}\right)^{1/2}}=K^+(k)K^-(k), \tag{26}$$

allows Eqs. (25) to be rearranged as

$$\begin{aligned}&\frac{iV_x^+(k)}{K^+(k)}\left(\frac{k+k_a}{k+\dfrac{k_0}{\epsilon}e^{i\pi/4}}\right)^{1/2}\\ &\quad-\frac{k_0\cos\alpha}{k-k_a\cos\alpha}\left[\frac{1}{K^+(k)}\left(\frac{k+k_a}{k+\dfrac{k_0}{\epsilon}e^{i\pi/4}}\right)^{1/2}\right.\\ &\quad\left.-\frac{1}{K^+(k_a\cos\alpha)}\left(\frac{k_a[\cos\alpha+1]}{k_a\cos\alpha+\dfrac{k_0}{\epsilon}e^{i\pi/4}}\right)^{1/2}\right]\\ &=K^-(k)S^-(k)\left(\frac{k-\dfrac{k_0}{\epsilon}e^{i\pi/4}}{k-k_a}\right)^{1/2}\\ &\quad+\frac{k_0\cos\alpha}{k-k_a\cos\alpha}\frac{1}{K^+(k_a\cos\alpha)}\left(\frac{k_a[\cos\alpha+1]}{k_a\cos\alpha+\dfrac{k_0}{\epsilon}e^{i\pi/4}}\right)^{1/2},\end{aligned} \tag{27}$$

$$\frac{iV_y^+(k)}{K^+(k)}+\frac{k_0\sin\alpha}{k-k_a\cos\alpha}\left(\frac{1}{K^+(k)}-\frac{1}{K^+(k_a\cos\alpha)}\right)$$
$$=K^-(k)T^-(k)-\frac{k_0\sin\alpha}{k-k_a\cos\alpha}\frac{1}{K^+(k_a\cos\alpha)}. \quad (28)$$

In each of Eqs. (27), (28), the left hand side is analytic in $\Im(k+k_a)>0$ and the right hand side is analytic in $\Im(k-k_a\cos\alpha)<0$. Since these are overlapping half-planes, the equations define two entire functions whose structure is determined by their behavior at infinity. First, the symmetry of definition (23) shows that $K^+(-k)=K^-(k)$ and hence, due to the choice of branch cuts, K^+, K^- are $O(|k|^{-1/2})$ as $|k|\to\infty$. Next, the Appendix shows that the velocities and stresses are $O(r^{1/2})$, $O(r^{-1/2})$, respectively, as $r\to 0$ and hence V_x^+, V_y^+ are $O(k^{-3/2})$ and S^-, T^- are $O(k^{-1/2})$ as $|k|\to\infty$. When these properties are substituted into Eqs. (27), (28), the entire functions are seen to vanish at infinity and so, by Liouville's theorem, are identically zero. The resulting identities

$$iV_x^+(k)-\frac{k_0\cos\alpha}{k-k_a\cos\alpha}$$
$$=-\frac{k_0\cos\alpha}{k-k_a\cos\alpha}\frac{K^+(k)}{K^+(k_a\cos\alpha)}$$
$$\times\left(\frac{k+\frac{k_0}{\epsilon}e^{i\pi/4}}{k_a\cos\alpha+\frac{k_0}{\epsilon}e^{i\pi/4}}\right)^{1/2}\left(\frac{k_a[\cos\alpha+1]}{k+k_a}\right)^{1/2}, \quad (29)$$

$$iV_y^+(k)+\frac{k_0\sin\alpha}{k-k_a\cos\alpha}=\frac{k_0\sin\alpha}{k-k_a\cos\alpha}\frac{K^+(k)}{K^+(k_a\cos\alpha)} \quad (30)$$

determine $C(k)$, $D(k)$ from Eq. (22), and then the transforms of the velocity components, given from Eqs. (20), (21) by

$$V_x=[C(k)+D(k)\mathrm{sgn}(y)][e^{-(k^2-i\omega/\nu)^{1/2}|y|}$$
$$-e^{-(k^2-k_a^2)^{1/2}|y|}]+\frac{K(k)C(k)}{(k^2-k_a^2)^{1/2}}e^{-(k^2-k_a^2)^{1/2}|y|}, \quad (31)$$

$$V_y=[C(k)\mathrm{sgn}(y)+D(k)]\frac{ik}{\left(k^2-\frac{i\omega}{\nu}\right)^{1/2}}[e^{-(k^2-i\omega/\nu)^{1/2}|y|}$$
$$-e^{-(k^2-k_a^2)^{1/2}|y|}]-iK(k)\frac{D(k)}{k}e^{-(k^2-k_a^2)^{1/2}|y|}. \quad (32)$$

III. THE SCATTERED FIELD; INVERSION OF THE TRANSFORMS

Inversion of the transforms defined by Eq. (16) yields

$$\mathbf{v}_{sc}=\frac{c_0}{2\pi k_0}\int_{-\infty}^{\infty}\mathbf{V}e^{ikx}\,dk, \quad p_{sc}=\frac{\rho_0c_0^2}{2\pi k_0}\int_{-\infty}^{\infty}Pe^{ikx}\,dk, \quad (33)$$

in which it suffices to consider $\mathbf{v}_{sc}$. Note that, according to Eqs. (31), (32),

$$\mathbf{V}e^{ikx}=\left(\frac{\partial}{\partial y},-\frac{\partial}{\partial x}\right)\left[\frac{C(k)\mathrm{sgn}(y)}{\left(k^2-\frac{i\omega}{\nu}\right)^{1/2}}(e^{-|k||y|}-e^{-(k^2-i\omega/\nu)^{1/2}|y|})\right.$$
$$\left.\times e^{ikx}+D(k)\left(\frac{e^{-|k||y|}}{|k|}-\frac{e^{-(k^2-i\omega/\nu)^{1/2}|y|}}{(k^2-(i\omega/\nu)^{1/2}}\right)e^{ikx}\right]$$
$$+\left(\frac{\partial}{\partial x},\frac{\partial}{\partial y}\right)\left[\frac{C(k)}{ik}\left(\frac{|k|e^{-|k||y|}}{\left(k^2-\frac{i\omega}{\nu}\right)^{1/2}}\right.\right.$$
$$\left.+\left[\frac{K(k)}{(k^2-k_a^2)^{1/2}}-1\right]e^{-(k^2-k_a^2)^{1/2}|y|}\right)e^{ikx}$$
$$\left.+\frac{D(k)}{ik}\mathrm{sgn}(y)(e^{-|k||y|}-e^{-(k^2-k_a^2)^{1/2}|y|})e^{ikx}\right],$$

which demonstrates that $\mathbf{v}_{sc}$ can be derived from an acoustically modified stream function $\psi(x,y)$ for viscous flow and an acoustic potential $\phi(x,y)$ modified by viscosity. In these expressions, conjugate harmonic functions have been added to ensure continuity of ψ, ϕ without changing $\mathbf{V}$. Their estimates for small r are consistent with those given in the Appendix. Analyticity in k can be recovered by replacing $|k|$ by $(k^2+\delta^2)^{1/2}$ and subsequently letting $\delta\to 0$ but this is not needed below.

According to Noble,[5] integrals involving $e^{-(k^2-k_0^2)^{1/2}|y|}e^{ikx}$ can be efficiently estimated by deforming the contour from the real axis to a branch of the hyperbola $k=k_a\cos(\theta+it)$, $-\infty<t<\infty$ if $0<\theta<\pi$. Here the range $0<\theta<2\pi$ can be accommodated by setting $k=k_a\cos(\pi-|\pi-\theta|+it)$ and then, since $|\sin\theta|=\sin|\pi-\theta|$ and the square root has positive real part, the factor $e^{-(k^2-k_a^2)^{1/2}|y|}e^{ikx}$ reduces to $e^{ik_ar\cosh t}$ on the left or right branch of the hyperbola according as $|\pi-\theta|$ is acute or obtuse.

Consider first the terms

$$K(k)\left[\frac{C(k)}{(k^2-k_a^2)^{1/2}},-i\frac{D(k)}{k}\right]e^{-(k^2-k_a^2)^{1/2}|y|}$$
$$=\frac{k_0e^{-(k^2-k_a^2)^{1/2}|y|}}{i(k-k_a\cos\alpha)}\frac{K^+(k)}{K^+(k_a\cos\alpha)}$$
$$\times\left[-\cos\alpha\left(\frac{k+(k_0/\epsilon)\,e^{i\pi/4}}{k_a\cos\alpha+(k_0/\epsilon)\,e^{i\pi/4}}\right)^{1/2}\right.$$
$$\left.\times\left(\frac{k_a[\cos\alpha+1]}{k+k_a}\right)^{1/2},\sin\alpha\right]$$

in $[V_x,V_y]$. The integrals along the deformed contour can be estimated, for large enough r, by stationary phase methods and, if $\cos\theta>\cos\alpha$, i.e., in the reflection zone $0<\theta<\alpha$ or the shadow zone $2\pi-\alpha<\theta<2\pi$, the pole at $k=k_a\cos\alpha$ yields the expected terms

$$c_0[-\cos\alpha,\sin\alpha]e^{ik_a(x\cos\alpha+|y|\sin\alpha)}$$

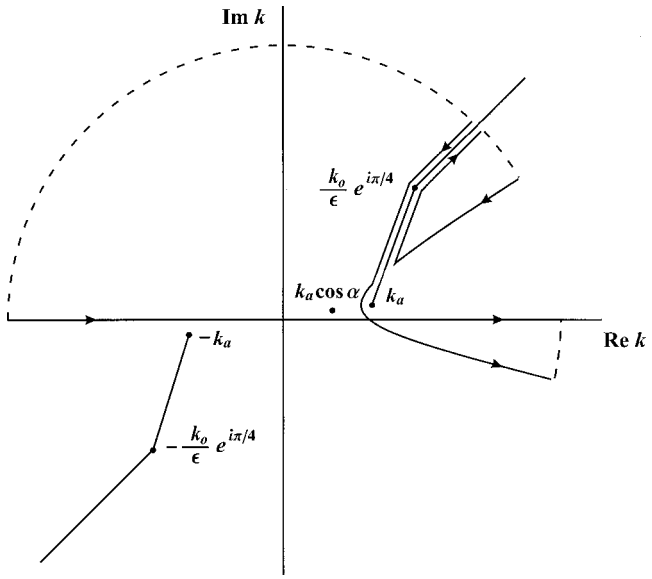

FIG. 2. Integration contours for evaluation of scattered velocity field.

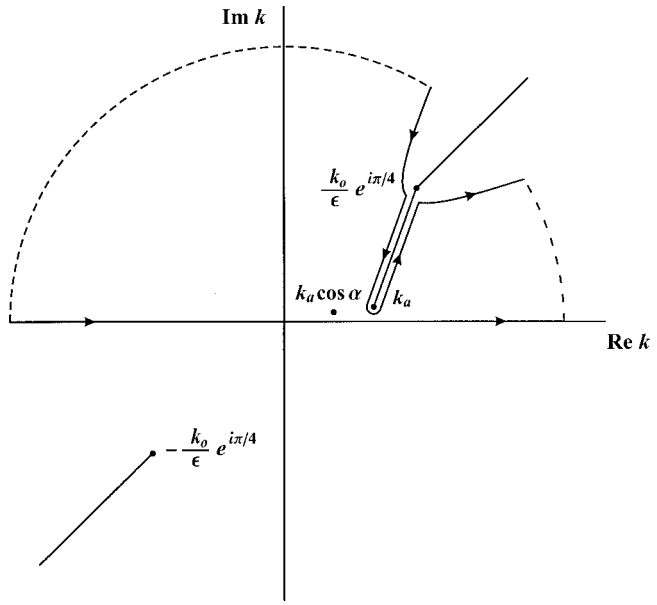

FIG. 3. Integration contours for evaluation of scattered velocity field.

in $[V_x, V_y]$. These account for the inhomogeneous terms in Eq. (13) but do not form a gradient field, i.e., they cannot be identified with any part of ϕ. In these integrals, $K^+(k)$ is replaced by $K(k)/K^-(k)$ in the lower half-plane. If $|\pi-\theta|$ differs from π or 0 by less than about $\pi/4$, the contour, displayed schematically in Fig. 2, has to be deformed around the right or left branch cut, respectively. The additional contributions that thereby may arise pertain to edge diffracted waves with rapid exponential decay.

Consider next the terms

$$[C(k)+D(k)\mathrm{sgn}(y)]\left[-1, \frac{-ik\,\mathrm{sgn}(y)}{\left(k^2-\frac{i\omega}{\nu}\right)^{1/2}}\right] e^{-(k^2-k_a^2)^{1/2}|y|}$$

$$=\left\{\cos\alpha\left(\frac{k+(k_0/\epsilon)\,e^{i\pi/4}}{k_a\cos\alpha+(k_0/\epsilon)\,e^{i\pi/4}}\right)^{1/2} \times(k-k_a)^{1/2}(k_a[\cos\alpha+1])^{1/2}-ik\,\mathrm{sgn}(y)\sin\alpha\right\} \times\frac{k_0}{i(k-k_a\cos\alpha)}\left[1, \frac{ik\,\mathrm{sgn}(y)}{\left(k^2-\frac{i\omega}{\nu}\right)^{1/2}}\right] \times\frac{e^{-(k^2-k_a^2)^{1/2}|y|}}{K^-(k)K^+(k_a\cos\alpha)}$$

in $[V_x, V_y]$. The integrals along the deformed contour (see Fig. 2) can be estimated, for large enough r, by stationary phase methods and, if $\cos\theta > \cos\alpha$, the pole at $k=k_a\cos\alpha$ yields

$$\frac{2c_0\,k_a\cos\alpha\sin\alpha}{K(k_a\cos\alpha)}\left[-i, \frac{k_a\cos\alpha}{\left(k_a^2\cos^2\alpha-\frac{i\omega}{\nu}\right)^{1/2}}\right] \times e^{ik_a(x\cos\alpha+y\sin\alpha)}$$

in the reflection zone but zero in the shadow zone. This wave has the phase velocity of a reflected wave but its contribution to $\mathbf{v}_{sc}$ is, since $\omega \gg \nu k_0^2$, almost parallel to the barrier. However, the total reflected wave is, by use of Eq. (23),

$$c_0(\cos\alpha,\sin\alpha)\left[\frac{\left(k_a^2\cos^2\alpha-\frac{i\omega}{\nu}\right)^{1/2}\sin\alpha+ik_a\cos^2\alpha}{\left(k_a^2\cos^2\alpha-\frac{i\omega}{\nu}\right)^{1/2}\sin\alpha-ik_a\cos^2\alpha}\right] \times e^{ik_a(x\cos\alpha+y\sin\alpha)},$$

in which the amplitude is less than unity and the phase is small and positive, due to viscous damping. The inviscid reflection is recovered in the limit $\nu\to 0$.

Consider last the terms

$$[C(k)+D(k)\mathrm{sgn}(y)]\left[1, \frac{ik\,\mathrm{sgn}(y)}{\left(k^2-\frac{i\omega}{\nu}\right)^{1/2}}\right] e^{-(k^2-i\omega/\nu)^{1/2}|y|}$$

$$=\left\{-\cos\alpha\left(\frac{k+(k_0/\epsilon)\,e^{i\pi/4}}{k_a\cos\alpha+(k_0/\epsilon)\,e^{i\pi/4}}\right)^{1/2} \times(k-k_a)^{1/2}(k_a[\cos\alpha+1])^{1/2}+ik\,\mathrm{sgn}(y)\sin\alpha\right\} \times\frac{k_0}{i(k-k_a\cos\alpha)}\left[1, \frac{ik\,\mathrm{sgn}(y)}{\left(k^2-\frac{i\omega}{\nu}\right)^{1/2}}\right] \times\frac{e^{-(k^2-i\omega/\nu)^{1/2}|y|}}{K^-(k)K^+(k_a\cos\alpha)}$$

in $[V_x, V_y]$, for which the contour deformation is given by $k=(k_0/\epsilon)e^{i\pi/4}\cos(\pi-|\pi-\theta|+it)$. The lack of a branch point at $-k_a$ renders the cut from $-k_a$ to $-(k_0/\epsilon)e^{i\pi/4}$ unnecessary for this term. The cut from k_a to $(k_0/\epsilon)e^{i\pi/4}$ requires the contour, shown schematically in Fig. 3, to be further deformed for field points such that

$$\frac{\pi}{2}-\theta \quad \text{or} \quad \theta-\frac{3\pi}{2}>\frac{1}{2}\arccos\left[\frac{(1+\frac{1}{9}\epsilon^4)^{1/2}-\epsilon^2}{(1+\frac{16}{9}\epsilon^4)^{1/2}}\right],$$

yielding diffracted waves with exponential dependence $e^{-(k_a^2-i\omega/\nu)^{1/2}|y|}e^{ik_ax}$. If the pole at $k=k_a\cos\alpha$ lies to the left of the hyperbola, it contributes

$$\frac{2c_0k_a\cos\alpha\sin\alpha}{K(k_a\cos\alpha)}\left[i,\frac{-k_a\cos\alpha}{\left(k_a^2\cos^2\nu-\dfrac{i\omega}{\nu}\right)^{1/2}}\right]$$
$$\times e^{-(k_a^2\cos^2\alpha-i\omega/\nu)^{1/2}y}e^{ik_ax\cos\alpha}$$

to $\mathbf{v}_{sc}$ in the sector

$$\frac{\epsilon^2\cos^2\alpha-(1+\epsilon^4[\frac{1}{3}+\sin^2\alpha]^2)^{1/2}}{(1+\frac{16}{9}\epsilon^4)^{1/2}}<\cos 2\theta<1$$

of the first quadrant but, as above, nothing in the fourth quadrant. This disturbance, confined to the ensonified side of the barrier, is a slight acoustic modification of the damped transverse wave generated in viscous fluid by a rigid boundary moving in its own plane.[6] It accounts for the viscous damping observed in the reflected wave in the sense that these two waves would form the entire scattered field if the barrier were of infinite extent.

IV. TANGENTIAL AND NORMAL INCIDENCE

In these two limiting cases, the simpler solutions allow further features of the scattered field to be identified. First, $C(k)$ and $D(k)$ are proportional to $\cos\alpha$ and $\sin\alpha$, respectively, and hence only one function appears in either case.

When $\alpha=0$ (tangential incidence), Eqs. (31), (32) yield

$$\mathbf{V}=C(k)[e^{-(k^2-i\omega/\nu)^{1/2}|y|}-e^{-(k^2-k_a^2)^{1/2}|y|}]$$
$$\times\left[1,\frac{ik\,\mathrm{sgn}(y)}{\left(k^2-\dfrac{i\omega}{\nu}\right)^{1/2}}\right]+\frac{C(k)K(k)}{(k^2-k_a^2)^{1/2}}e^{-(k^2-k_a^2)^{1/2}|y|}[1,0], \tag{34}$$

where

$$C(k)=\frac{ik_0}{K^-(k)K^+(k_a)}\left(\frac{k+\dfrac{k_0}{\epsilon}e^{i\pi/4}}{k_a\cos\alpha+\dfrac{k_0}{\epsilon}e^{i\pi/4}}\right)^{1/2}\left(\frac{2k_a}{k+k_a}\right)^{1/2}. \tag{35}$$

So, in the second term of Eq. (34),

$$\frac{C(k)K(k)}{(k^2-k_a^2)^{1/2}}=\frac{ik_0}{(k^2-k_a^2)^{1/2}}\left(\frac{2k_a}{k-k_a}\right)^{1/2}$$
$$+\text{a function regular at } k=k_a$$

and hence $\mathbf{v}_{sc}$, given by Eq. (33), has a contribution

$$\frac{c_0i}{2\pi}\int_{-\infty}^{\infty}\frac{e^{ikx}}{(k^2-k_a^2)^{1/2}}\left(\frac{2k_a}{k-k_a}\right)^{1/2}e^{-(k^2-k_a^2)^{1/2}|y|}\,dk[1,0].$$

This integral is of a type evaluated by Noble[5] in terms of the Fresnel integral $F(v)=\int_v^\infty e^{iu^2}du$ and the resulting vector is

$$-\frac{2c_0}{\sqrt{\pi}}e^{-i[k_ar\cos(\pi-\theta)+\pi/4]}F\left[(2k_ar)^{1/2}\cos\frac{1}{2}(\pi-\theta)\right][1,0]$$
$$=-\frac{2c_0}{\sqrt{\pi}}e^{i(k_ax-\pi/4)}F[\sqrt{k_a(r-x)}][1,0],$$

which represents edge diffracted waves, except on the barrier where its value is $-c_0e^{ik_ax}[1,0]$ as required by Eq. (13) to cancel the incident field. The remaining contributions to $\mathbf{v}_{sc}$ are edge diffracted waves. Evidently, an ''acoustic'' term in the **i** direction is required to cancel the incident wave at the barrier, even though this need is dictated by viscosity. The first vector in Eq. (34), which is a combination of ''viscous'' and ''acoustic'' velocities that vanishes on the line of the barrier, is needed to make possible the construction of an ''acoustic'' velocity that is a gradient field.

When $\alpha=\pi/2$ (normal incidence), Eqs. (31), (32) yield, after substituting for $D(k)$,

$$\mathbf{V}=\frac{k_0}{K^-(k)K^+(0)}[e^{-(k^2-i\omega/\nu)^{1/2}|y|}-e^{-(k^2-k_a^2)^{1/2}|y|}]$$
$$\times\left[1,\frac{ik\,\mathrm{sgn}(y)}{\left(k^2-\dfrac{i\omega}{\nu}\right)^{1/2}}\right]-\frac{ik_0}{k}\frac{K^+(k)}{K^+(0)}e^{-(k^2-k_a^2)^{1/2}|y|}[0,1]. \tag{36}$$

This case, the focus of Alblas' study,[3] is the one that separates acute values of α considered above from obtuse values of α, for which the incident field would be defined to include reflection from a complete rigid wall. The path of integration in Eq. (33) must be deformed below the pole at $k=0$ so that the corresponding residue yields $c_0e^{ik_a|y|}$ in $x>0$, as expected in the reflection and shadow regions, respectively. However, the ''acoustic'' reflection excites a ''viscous'' disturbance as described for the tangential case.

The total ''acoustic'' term in V_y is

$$\frac{c_0}{2\pi i}\int_{-\infty}^{\infty}\frac{e^{ikx}(k^2-k_a^2)^{1/2}}{kK^-(k)K^+(0)}e^{-(k^2-k_a^2)^{1/2}|y|}\,dk,$$

which, for points not close (0,0), can be approximated by

$$\frac{1}{ik_a}\frac{\partial}{\partial|y|}\left[\frac{c_0}{2\pi i}\int_{-\infty}^{\infty}\frac{e^{ikx}}{k}\left(\frac{k_a}{k_a-k}\right)^{1/2}e^{-(k^2-k_a^2)^{1/2}|y|}\,dk\right].$$

For this integral, the branch cuts can be drawn from $\pm k_a$ to $\pm k_a\infty$, respectively, allowing the contour to be deformed to a branch of the hyperbola $k=k_a\cos(\pi-|\pi-\theta|+it)$. Thus the ''acoustic'' potential ϕ is

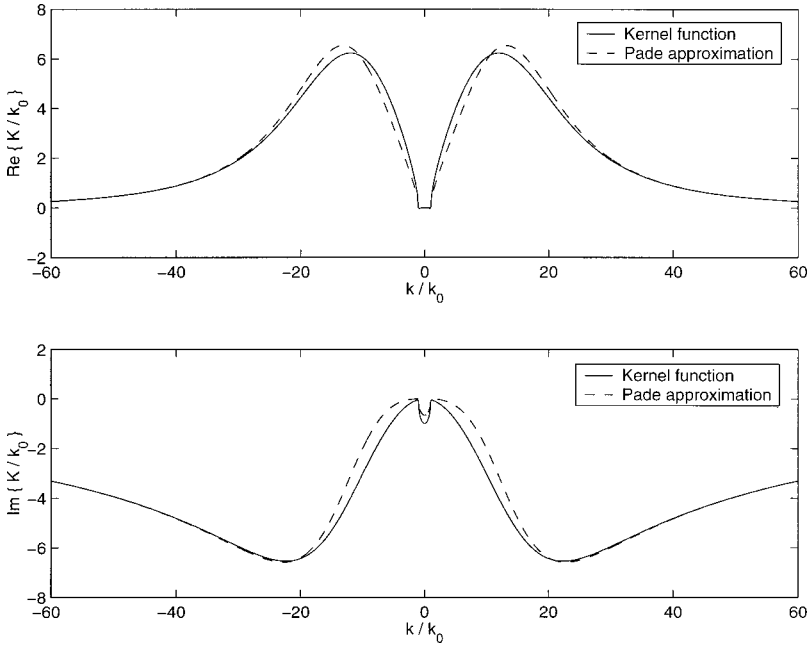

FIG. 4. Kernel function $K(k)$ and Padé approximation for $\epsilon=0.05$.

$$\frac{c_0\,\mathrm{sgn}(y)}{ik_a}\left\{e^{ik_a|y|}(|\pi-\theta|\ \ \text{obtuse})+\frac{1}{2\pi}\int_{-\infty}^{\infty}\frac{e^{ik_ar\cosh t}\sin[\frac{1}{2}(|\pi-\theta|-it)]}{\cos(|\pi-\theta|-it)}dt\right\}$$

$$=-\frac{c_0\,\mathrm{sgn}(y)}{2\pi k_a}I(k_a,|\pi-\theta|,\pi/2)$$

$$=-\frac{c_0\,\mathrm{sgn}(y)}{\pi^{1/2}k_a}e^{i\pi/4}\left\{-e^{-ik_ar\sin|\pi-\theta|}F\left[(2k_ar)^{1/2}\cos\frac{1}{2}\left(|\pi-\theta|-\frac{\pi}{2}\right)\right]+e^{ik_ar\sin|\pi-\theta|}F\left[(2k_ar)^{1/2}\cos\frac{1}{2}\left(|\pi-\theta|+\frac{\pi}{2}\right)\right]\right\}$$

$$=-\frac{c_0\,\mathrm{sgn}(y)}{\pi^{1/2}k_a}e^{i\pi/4}\left\{-e^{-ik_a|y|}F[k_a^{1/2}(r+|y|)^{1/2}]+e^{ik_a|y|}F\left[-x\left(\frac{k_a}{r+|y|}\right)^{1/2}\right]\right\},$$

where I is the integral defined and evaluated by[5] Eqs. (1.63), (1.65). In this way it is seen that the transitions into the reflection and shadow regions are modeled by a Fresnel integral.

V. NUMERICAL RESULTS

In order to obtain numerical results for the velocity field, it is necessary to evaluate the factored kernel functions $K^+(k)$ and $K^-(k)$. Although general integral representations of these functions are available,[5] it is simpler and still highly accurate to derive the functions $K^+(k)$ and $K^-(k)$ from a Padé approximation to the kernel function $K(k)$, as fully discussed by Abrahams.[7]

The function $K(k)$ in Eq. (26) can be written as

$$K(k)=(k^2-k_a^2)^{1/2}\left[1-\frac{k^2}{\left(k^2-\frac{ik_0^2}{\epsilon^2}\right)^{1/2}(k^2-k_a^2)^{1/2}}\right]. \quad (37)$$

The first factor on the right-hand side of Eq. (37) is needed to maintain the strip of regularity and can be factored by inspection. Since the velocity field near the edge of the diffracting screen is of particular interest here, the second factor on the right-hand side of Eq. (37) may be usefully replaced by the Padé approximation

$$K(k)\approx(k^2-k_a^2)^{1/2}\left[\frac{c_1k_0^2}{c_2k_0^2-k^2\epsilon^2}\right], \quad (38)$$

where the coefficients $c_1(\epsilon)$ and $c_2(\epsilon)$ are, after substituting Eq. (11), given by

$$c_1=\frac{1}{2}\left(i+\frac{\epsilon^2}{1-\frac{4i}{3}\epsilon^2}\right),\quad c_2=\frac{3}{2}c_1-\frac{\epsilon^2}{1-\frac{7i}{3}\epsilon^2}. \quad (39)$$

The kernel function $K(k)$ and the Padé approximation defined by Eq. (38) are shown in Fig. 4 for the case $\epsilon=0.05$. Although Eq. (38) is based on a simple Padé approximation with respect to the point at infinity, excellent agreement with the kernel function is obtained over the entire range $-\infty<k<\infty$, because the poles thus introduced are sufficiently far from the real k-axis. Approximations to the factored kernel functions $K^+(k)$ and $K^-(k)$ can be obtained directly from the immediate factorization of Eq. (38), and the Fourier integrals for the velocity components $v_x(x,y)$ and $v_y(x,y)$ can then be evaluated by standard numerical integration techniques.

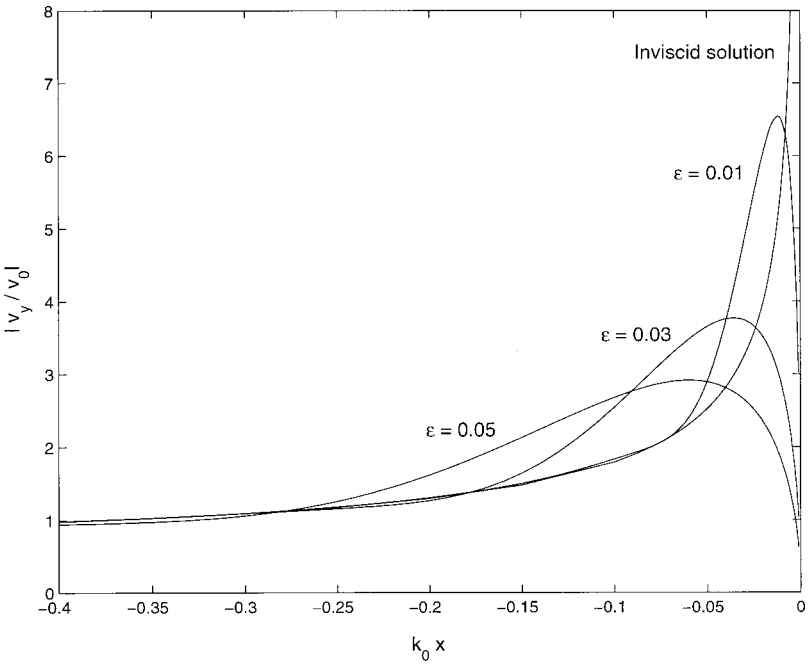

FIG. 5. Magnitude of velocity component v_y as function of k_0x for $y=0$.

Figure 5 shows the numerically evaluated magnitude of the velocity component $v_y(x,0)$ along the x-axis in the region to the left of the diffracting screen for the case of a normally incident ($\alpha=\pi/2$) plane wave. The scaling factor v_0 is the magnitude of the incident plane wave at $x=0$. According to the inviscid diffraction model discussed in the Introduction, the velocity v_y becomes infinite at the edge of the screen. For the small values of the dimensionless viscosity parameter ϵ shown in Fig. 5, v_y is zero the edge of the screen, attains a maximum as x decreases, and then rapidly becomes identical with the inviscid solution. Figure 5 clearly shows how viscosity eliminates the physically unrealistic inviscid velocity singularity, and also indicates the extent of the spatial domain near the screen in which viscous effects have an important influence on the flow field.

VI. SUMMARY

The influence of viscosity on the two-dimensional scattering of an acoustic plane wave by a rigid half-plane is completely described, with emphasis on the usual case of the viscous length being much less than the acoustic length. As expected, the significant effects are located close to the barrier where a damped transverse wave is generated and the field at the edge is of biharmonic type.

APPENDIX: EDGE SINGULARITY

When the similarity forms, referred to polar coordinates,

$$(v_r,v_\theta)\sim r^\lambda[f(\theta),g(\theta)],\quad p\sim\rho_0\nu r^{\lambda-1}h(\theta), \tag{A1}$$

are substituted into Eqs. (14), (15), the dominant terms, as $r\to 0$, yield

$$(\lambda+1)f+g'=i\epsilon^2 h, \tag{A2}$$

$$\begin{aligned}(\lambda^2-1)f+f''-2g'&=(\lambda-1)\left(1-\frac{i}{3}\epsilon^2\right)h,\\ (\lambda^2-1)g+g''+2f'&=\left(1-\frac{i}{3}\epsilon^2\right)h'.\end{aligned} \tag{A3}$$

Equations (A3) can be rearranged as Cauchy–Riemann equations to show that

$$r^{\lambda-1}\left[(\lambda+1)f+g'-\left(1-\frac{i}{3}\epsilon^2\right)h\right]+ir^{\lambda-1}[(\lambda+1)g-f']$$

is analytic, which, after use of (A2), shows that $r^{\lambda-1}h(\theta)$ is harmonic and that $\Omega+(i+\frac{4}{3}\epsilon^2)p/\rho_0\nu$ becomes an analytic function as $r\to 0$. On writing

$$\left(1-\frac{i}{3}\epsilon^2\right)h=2\,\mathrm{A}e^{i(\lambda-1)\theta}+2\,\mathrm{B}e^{-i(\lambda-1)\theta}, \tag{A4}$$

Eqs. (A3) can be rearranged as a pair of disjoint second order equations for $f\pm ig$ which yield

$$\begin{aligned}f+ig&=C_+e^{i(\lambda-1)\theta}+D_+e^{-i(\lambda+1)\theta}+\mathrm{B}e^{-i(\lambda-1)\theta},\\ f-ig&=C_-e^{-i(\lambda-1)\theta}+D_-e^{i(\lambda+1)\theta}+\mathrm{A}e^{i(\lambda-1)\theta}.\end{aligned} \tag{A5}$$

Substitution of Eqs. (A4), (A5) into Eq. (A2) then shows that

$$\lambda C_+ +\left(\frac{1-\frac{7i}{3}\epsilon^2}{1-\frac{i}{3}\epsilon^2}\right)A=0=\lambda C_-+\left(\frac{1-\frac{7i}{3}\epsilon^2}{1-\frac{i}{3}\epsilon^2}\right)B,$$

while application of the no-slip conditions $f=0=g$ at $\theta=0,\,2\pi$ yields

$$\begin{aligned}&C_++D_++B=0=C_-+D_-+A,\\ &C_+e^{2\pi i\lambda}+(D_++B)e^{-2\pi i\lambda}=0\\ &\qquad\qquad=C_-e^{-2\pi i\lambda}+(D_-+A)e^{2\pi i\lambda}.\end{aligned}$$

These six equations have a nontrivial solution if and only if $\sin 2\pi\lambda=0$ and the lowest admissible value of λ, for integrable stresses, is 1/2.

If the velocity field is derived from a potential and a stream function,[3] i.e.,

$$v_r=\frac{\partial\phi}{\partial r}+\frac{1}{r}\frac{\partial\psi}{\partial\theta},\quad v_\theta=\frac{1}{r}\frac{\partial\phi}{\partial\theta}-\frac{\partial\psi}{\partial r},$$

then, from Eqs. (A1), (A5),

$$\nabla^2\phi\sim 2i\epsilon^2 r^{\lambda-1}[\mathrm{A}e^{i(\lambda-1)\theta}+\mathrm{B}e^{-i(\lambda-1)\theta}],$$

$$\nabla^2\psi\sim -2i(1-i\epsilon^2)r^{\lambda-1}[\mathrm{A}e^{i(\lambda-1)\theta}-\mathrm{B}e^{-i(\lambda-1)\theta}],$$

which yields

$$\phi\sim\frac{i\epsilon^2}{2\lambda\left(1-\frac{i}{3}\epsilon^2\right)}r^{\lambda+1}[\mathrm{A}e^{i(\lambda-1)\theta}+\mathrm{B}e^{-i(\lambda-1)\theta}]$$

$$+\text{harmonic function},$$

$$\psi\sim-\frac{i}{2\lambda}\left(\frac{1-\frac{4i}{3}\epsilon^2}{1-\frac{i}{3}\epsilon^2}\right)r^{\lambda+1}[\mathrm{A}e^{i(\lambda-1)\theta}-\mathrm{B}e^{-i(\lambda-1)\theta}]$$

$$+\text{harmonic function}.$$

Thus these functions become biharmonic, as $r\to 0$, in agreement with the asymptotic forms of the equations

$$\nabla^2\left(\nabla^2-\frac{1}{\nu}\frac{\partial}{\partial t}\right)\psi=0,\quad \nabla^2\left[\left(1+\frac{\nu}{c_0^2}\frac{\partial}{\partial t}\right)\nabla^2-\frac{1}{c_0^2}\frac{\partial^2}{\partial t^2}\right]\phi=0,$$

derived from Eqs. (7), (8).

[1] A. Sommerfeld, "Mathematische theorie der diffraction," Math. Ann. **47**, 317–374 (1896).

[2] H. S. Carslaw, "Some multiform solutions of the partial differential equations of physics and their applications," Proc. London Math. Soc. **30**, 121–163 (1899).

[3] J. B. Alblas, "On the diffraction of sound waves in a viscous medium," Appl. Sci. Res., Sect. A **6**, 237–262 (1957).

[4] J. B. Alblas, "On the diffraction of sound waves in a heat-conducting viscous medium," Koninkl. Ned. Akad. Wetenschap. Proc. B **64**, 351–367 (1961).

[5] B. Noble, *Methods Based on the Wiener–Hopf Technique*, 2nd ed. (Chelsea Press, New York, 1988).

[6] G. K. Batchelor, *An Introduction to Fluid Dynamics* (Cambridge University Press, Cambridge, 1967).

[7] I. D. Abrahams, "The application of Padé approximants to Wiener–Hopf factorization," IMA J. Appl. Math. **65**, 257–281 (2000).

Field induced in inhomogeneous spheres by external sources. I. The scalar case

Gerassimos C. Kokkorakis, John G. Fikioris, and George Fikioris
Institute of Communication and Computer Systems, National Technical University of Athens, GR-157 73 Zografou, Greece

(Received 19 June 2001; revised 10 June 2002; accepted 10 June 2002)

The evaluation of acoustic or electromagnetic fields induced in the interior of inhomogeneous penetrable bodies by external sources is based on well-known volume integral equations; this is particularly true for bodies of arbitrary shape and/or composition, for which separation of variables fails. In this paper the investigation focuses on acoustic (scalar fields) in inhomogeneous spheres of arbitrary composition, i.e., with r-, θ- or even φ-dependent medium parameters. The volume integral equation is solved by a hybrid (analytical–numerical) method, which takes advantage of the orthogonal properties of spherical harmonics, and, in particular, of the so-called Dini's expansions of the radial functions, whose convergence is optimized. The numerical part comes at the end; it involves the evaluation of certain definite integrals and the matrix inversion for the expansion coefficients of the solution. The scalar case treated here serves as a steppingstone for the solution of the more difficult electromagnetic problem. © *2002 Acoustical Society of America.*
[DOI: 10.1121/1.1498274]

PACS numbers: 43.20.Fn [ANN]

I. INTRODUCTION

The evaluation of acoustic or electromagnetic fields induced inside penetrable media by given sources, as well as scattering from such bodies, is a basic problem of field theory with many practical applications.[1–9] The solution to the first (interior) problem provides answers to questions related to radiation hazards, to the setting of reliable safety field strength limits, in particular, in media like living tissue, human heads exposed to nearby electromagnetic sources, etc.

The main difficulties in the mathematical formulation and solution of such problems arise from the shape and/or the inhomogeneity of the penetrable bodies. Arbitrary shapes preclude, in general, the application of classical methods like separation of variables, and so does inhomogeneity of the medium. As a starting point for the mathematical formulation of such boundary value problems serve volume integral equations in which the unknown interior field, multiplied by a difference term, appears inside the volume integral as an equivalent source density. The difference term is the excess value of the basic medium parameter (dielectric constant for electromagnetic fields, compressibility and/or density for scalar, acoustic ones) over its constant ambient value in the surrounding medium (free space in general). For instance, in electromagnetics the corresponding volume integral equations are known as the EFIE or MFIE, i.e., electric or magnetic field integral equation.[1–3] In acoustics, on which we focus here, the corresponding volume integral equation is[4–6]

$$\Phi(\mathbf{r})=\Phi^{\mathrm{inc}}(\mathbf{r})+\int_V k_0^2\left[\frac{b(\mathbf{r}')}{b_0}-1\right]\Phi(\mathbf{r}')g(\mathbf{r},\mathbf{r}')dV' + \int_V \nabla'\cdot\left\{\left[\frac{\rho_0}{\rho(\mathbf{r}')}-1\right]\nabla'\Phi(\mathbf{r}')\right\}g(\mathbf{r},\mathbf{r}')dV', \tag{1}$$

for an inhomogeneous medium of density $\rho(\mathbf{r})$ and compressibility $b(\mathbf{r})$ occupying the volume V in a surrounding medium of constant ρ_0, b_0 values. An incident field $\Phi^{\mathrm{inc}}(\mathbf{r})$ impinges on V and induces the total (unknown) scalar field $\Phi(\mathbf{r})$. The harmonic time dependence is $\exp(i\omega t)$ and

$$g(\mathbf{r},\mathbf{r}')=e^{-ik_0R}/4\pi R,\quad R=|\mathbf{r}-\mathbf{r}'|,\quad k_0=\omega(b_0\rho_0)^{1/2}, \tag{2}$$

is the scalar Green's function of free space. Equation (1) simplifies considerably for a medium of constant density $\rho(\mathbf{r})=\rho_0$, equal to that of the surrounding medium

$$\Phi(\mathbf{r})=\Phi^{\mathrm{inc}}(\mathbf{r})+\int_V k_0^2\left[\frac{b(\mathbf{r}')}{b_0}-1\right]\Phi(\mathbf{r}')g(\mathbf{r},\mathbf{r}')dV'. \tag{3}$$

It can be shown that, as far as our hybrid method of solution for spherical V is concerned, the more complex nature of Eq. (1) in comparison with (3), although not affecting the basic analytic nature of the steps followed here, requires a more subtle and lengthy algebraic manipulation; it will be the subject of another paper. Furthermore, it may be noted that the accuracy of purely numerical approaches is substantially affected by the second integral in (1), which contains the derivatives of the unknown function. This point is also discussed in a recent paper,[6] which includes, further, a quite comprehensive list of references on scalar (acoustic) integral equations like (1) and (3). Another extended list of references is also included in Ref. 8.

It is worth noting also that Eq. (3) is similar to the corresponding one obtained from the Schrödinger equation in quantum mechanics. In this case the integral equation describes the scattering of a wave function $\Phi^{\mathrm{inc}}(\mathbf{r})$ from a potential proportional to $b(\mathbf{r})-b_0$.[10] Here, the notion of scattering may be extended to include cases such as field emission due to a certain potential.

We therefore limit ourselves here to the treatment of (3) for spherical volumes V for which, up to a certain point, analytical procedures are possible; such methods take advantage of the orthogonal properties of spherical harmonics and, in particular, of spherical Bessel functions associated with Dini's expansions. The importance of such steps will become apparent in what follows. Finally, it is worth observing that when $\mathbf{r}$ is taken outside V both (1) and (3) provide a relation for the exterior (scattered) field; when $\mathbf{r}$ is restricted inside V the equations stand as the aforementioned integral equations for the evaluation of the total internal field $\Phi(\mathbf{r})$ in V.

II. HYBRID METHOD OF SOLVING EQ. (3) BASED ON SPHERICAL HARMONIC- AND DINI'S-EXPANSIONS

We start by expanding $g(\mathbf{r},\mathbf{r}')$ and $\Phi(\mathbf{r})$

$$g(\mathbf{r},\mathbf{r}')=\frac{e^{-ik_0R}}{4\pi R}$$

$$=\frac{-ik_0}{4\pi}\sum_{n'=0}^{\infty}(2n'+1)j_{n'}(k_0r_<)h_{n'}(k_0r_>)$$

$$\times\sum_{m'=-n'}^{n'}\frac{(n'-m')!}{(n'+m')!}P_{n'}^{m'}(\cos\theta)$$

$$\times P_{n'}^{m'}(\cos\theta')e^{im'(\varphi-\varphi')}, \tag{4}$$

$$\Phi(\mathbf{r})=\sum_{n=0}^{\infty}\sum_{m=-n}^{n}f_{nm}(r)P_n^m(\cos\theta)e^{im\varphi}. \tag{5}$$

Equation (4) is the well-known expansion of the Green function in spherical coordinates;[11] $h_n\equiv h_n^{(2)}=j_n-in_n$ and $r_>(r_<)$ stands for the larger (smaller) of r,r'. In (5) $f_{nm}(r)$ are the unknown functions in $0\leqslant r\leqslant a$, a being the radius of V.

A. Inhomogeneity independent of θ, φ

Consider first the simpler case: $b(\mathbf{r})=b(r)$, independent of θ, φ. With a plane incident field $\Phi^{\text{inc}}(\mathbf{r})$ propagating along the z axis of the spherical coordinate system ($\mathbf{k}_0=k_0\hat{z}$), we have

$$\Phi^{\text{inc}}(\mathbf{r})=e^{-i\mathbf{k}_0\cdot\mathbf{r}}$$

$$=e^{-ikz}$$

$$=\sum_{n=0}^{\infty}(-i)^n(2n+1)j_n(k_0r)P_n(\cos\theta), \tag{6}$$

$$\Phi(\overline{r})=\sum_{n=0}^{\infty}f_n(r)P_n(\cos\theta). \tag{7}$$

Substituting in (3), carrying out the integrations with respect to θ', φ' [$dV'=r'^2\sin\theta'\,dr'\,d\theta'\,d\varphi'$], using the orthogonality relations for $e^{im\varphi'}$ and

$$\int_0^{\pi}P_n(\cos\theta')P_{n'}(\cos\theta')\sin\theta'\,d\theta'=\frac{2}{2n+1}\delta_{nn'} \tag{8}$$

for $P_n(\cos\theta')$, we end up with the relation

$$f_n(r)=(-i)^n(2n+1)j_n(k_0r)-ik_0^3\int_0^a\left[\frac{b(r')}{b_0}-1\right]$$

$$\times f_n(r')j_n(k_0r_<)h_n(k_0r_>)r'^2\,dr'. \tag{9}$$

Here, it is obvious that, in the case under consideration (independent of θ, φ), there is no interrelation between the integral equations (9) for different n. For each n ($n=0,1,2,...$) and $0\leqslant r\leqslant a$ the radial functions are now expanded in Dini's series as follows:

$$j_n(k_0r)=\sum_{l=1}^{\infty}J_{nl}j_n\left(\frac{\gamma_{nl}}{a}r\right), \tag{10}$$

$$f_n(r)=\sum_{l=1}^{\infty}B_{nl}j_n\left(\frac{\gamma_{nl}}{a}r\right), \tag{11}$$

$$f_n(r)\left[\frac{b(r)}{b_0}-1\right]=\sum_{l=1}^{\infty}A_{nl}j_n\left(\frac{\gamma_{nl}}{a}r\right). \tag{12}$$

The spherical Bessel functions $j_n([\gamma_{nl}/a]r)$ ($l=1,2,...$) form a complete and orthogonal set of eigenfunctions in the interval $0\leqslant r\leqslant a$[11–13] as long as the constants γ_{nl} are chosen as the roots of the eigenvalue equation

$$\gamma_{nl}j_n'(\gamma_{nl})/j_n(\gamma_{nl})=-t_n\quad(l=1,2,...). \tag{13}$$

Here, t_n is any chosen constant. Later, it will be chosen so as to improve the convergence of the Dini's expansion (11) for the unknown radial function $f_n(r)$; an all-important choice, particularly for the nonhomogeneous density and the electromagnetic case, which involve the first and the second derivatives of the unknown field function and require faster convergence of the Dini expansion. In the case of constant density, such an improvement of the convergence is not required for the solution of (9); however, it is necessary if one wants to find the derivative of $f_n(r)$, as will be shown later. The use of Dini's expansions in technical literature is somewhat limited; their completeness and convergence properties are characterized by certain features and special cases that should not be ignored for their correct application. These properties are summarized below, following their extensive treatment in Refs. 12 and 13.

Substituting now (12) in (9), separating the integral into two similar ones, from $r'=0$ to $r'=r$ and from $r'=r$ to $r'=a$, applying the standard integral formulas for the product of any two spherical Bessel functions[11,14] of the same order

$$\int d_n(\alpha x)g_n(\beta x)x^2dx$$

$$=\frac{x^2}{\alpha^2-\beta^2}\{\beta d_n(\alpha x)g_{n-1}(\beta x)-\alpha d_{n-1}(\alpha x)g_n(\beta x)\}$$

$$=\frac{x^2}{\alpha^2-\beta^2}\{\alpha d_{n+1}(\alpha x)g_n(\beta x)-\beta d_n(\alpha x)g_{n+1}(\beta x)\},$$

$$\alpha\neq\beta, \tag{14}$$

$$\int g_n^2(\beta x)x^2dx=\frac{x^3}{2}\{g_n^2(\beta x)-g_{n-1}(\beta x)g_{n+1}(\beta x)\}, \tag{15}$$

where α, β are two constants, we end up with the following equation:

$$f_n(r)=(-i)^n(2n+1)j_n(k_0r)-i(k_0a)^2\sum_{l=1}^{\infty}\frac{A_{nl}}{\gamma_{nl}^2-(k_0a)^2}\times\left[ij_n\left(\frac{\gamma_{nl}}{a}r\right)+(k_0a)^2j_n(k_0r)C_{nl}\right],\quad n=0,1,..., \tag{16}$$

where

$$C_{nl}=\frac{\gamma_{nl}}{k_0a}h_n(k_0a)j_{n+1}(\gamma_{nl})-h_{n+1}(k_0a)j_n(\gamma_{nl})=j_n(\gamma_{nl})\left[h_n'(k_0a)+t_n\frac{h_n(k_0a)}{k_0a}\right],\quad n=0,1,...,\quad l=1,2,.... \tag{17}$$

Here, it is obvious why in expansion (12) we used $j_n([\gamma_{nl}/a]r)$ as the expansion functions, instead of $j_p([\gamma_{pl}/a]r)$, $p\neq n$, $l=1,2,...$ as a more general possibility: there is no integral formula like (14) for the product $d_n(\alpha x)g_p(\beta x)x^2$ when $n\neq p$. Substituting now the expansions (10), (11) in (16) and using the orthogonality of the set $j_n([\gamma_{nl}/a]r)$, $l=1,2,...$, we get for each n

$$B_{nl}=(-i)^n(2n+1)J_{nl}(1-S_n)+\frac{(k_0a)^2}{\gamma_{nl}^2-(k_0a)^2}A_{nl},\quad l=1,2,..., \tag{18}$$

where

$$S_n=\frac{i(k_0a)^4}{(-i)^n(2n+1)}\sum_{q=1}^{\infty}\frac{C_{nq}A_{nq}}{\gamma_{nq}^2-(k_0a)^2}. \tag{19}$$

In (18), S_n is a constant with respect to l and related to the chosen value t_n (and the corresponding γ_{nl}); J_{nl} are given later in (26).

The last step is to eliminate A_{nl} from (18) and obtain a set of linear equations for the B_{nl}. This is accomplished by combining (11) and (12) in the form

$$f_n(r)\left(\frac{b(r)}{b_0}-1\right)=\sum_{p=1}^{\infty}A_{np}j_n\left(\frac{\gamma_{np}}{a}r\right)=\sum_{p=1}^{\infty}B_{np}\left(\frac{b(r)}{b_0}-1\right)j_n\left(\frac{\gamma_{np}}{a}r\right). \tag{20}$$

Multiplying the latter by $j_n([\gamma_{nl}/a]r)$ and using orthogonality, we get

$$A_{nl}=\frac{1}{N_{nl}}\sum_{p=1}^{\infty}D_{nlp}B_{np}, \tag{21}$$

in which

$$D_{nlp}=\int_0^a\left(\frac{b(r)}{b_0}-1\right)j_n\left(\frac{\gamma_{nl}}{a}r\right)j_n\left(\frac{\gamma_{np}}{a}r\right)r^2\,dr, \tag{22}$$

and

$$N_{nl}=\int_0^a j_n^2\left(\frac{\gamma_{nl}}{a}r\right)r^2\,dr=\frac{a^3}{2}[j_n^2(\gamma_{nl})-j_{n-1}(\gamma_{nl})j_{n+1}(\gamma_{nl})]=\frac{a^3}{2}j_n^2(\gamma_{nl})\left[1-\frac{(n+1-t_n)(n+t_n)}{\gamma_{nl}^2}\right]. \tag{23}$$

The D_{nlp} can be considered as the expansion coefficients of $([b(r)/b_0]-1)j_n([\gamma_{nl}/a]r)$ in the set $j_n([\gamma_{np}/a]r)$ and are the only ones that require numerical evaluation. With (21) substituted in (19), we obtain

$$S_n=\sum_{l=1}^{\infty}B_{nl}Z_{nl};\qquad Z_{nl}=\frac{i(k_0a)^4}{(-i)^n(2n+1)}\sum_{p=1}^{\infty}\frac{C_{np}D_{nlp}}{N_{np}[\gamma_{np}^2-(k_0a)^2]}. \tag{24}$$

So, we finally get the system of linear equations

$$B_{nl}=(-i)^n(2n+1)J_{nl}\left(1-\sum_{p=1}^{\infty}B_{np}Z_{np}\right)+\frac{1}{N_{nl}}\frac{(k_0a)^2}{\gamma_{nl}^2-(k_0a)^2}\sum_{p=1}^{\infty}B_{np}D_{nlp},\quad l=1,2,.... \tag{25}$$

This system is solved by truncation, and we obtain the desired unknown coefficients B_{nl} to calculate $f_n(r)$, $n=0,1,...$. In the Appendix, the system is solved analytically for $b(r)=b_1=$constant, recovering the well-known result from separation of variables.

B. Convergence and optimum form of Dini's expansions

We give first an explicit result for J_{nl}, the Dini's coefficients of $j_n(k_0r)$ in (10). Based on (13)–(15) one gets[12,13]

$$J_{nl}=2\frac{\gamma_{nl}^2j_n(k_0a)\left[t_n+\dfrac{(k_0a)j_n'(k_0a)}{j_n(k_0a)}\right]}{[\gamma_{nl}^2-(k_0a)^2]j_n(\gamma_{nl})[\gamma_{nl}^2-(n-t_n+1)(n+t_n)]}. \tag{26}$$

Concerning the convergence of Dini's expansion

$$g(r)=\sum_{l=1}^{\infty}A_{nl}j_n\left(\frac{\gamma_{nl}}{a}r\right),\quad 0\leqslant r\leqslant a, \tag{27}$$

of a continuous function $g(r)$ in the interval, the following facts should be taken into account.[12,13] γ_{nl} are the roots of the eigenvalue equation (13), while n and t_n can be any numbers; this implies an infinite variety of expansions (27) for the same $g(r)$. As long as $t_n>-n$ all roots $\pm\gamma_{nl}$ ($\gamma_{nl}\geqslant 0$) are real. For $t_n<-n$ the first root is imaginary $\pm i|\gamma_{n1}|$, and the first eigenfunction $i_n([|\gamma_{n1}|/a]r)$, the modified spherical Bessel function. The rest remain real and beyond that nothing changes in the previous formulas. For $t_n=-n$, one root (the first) is zero, the corresponding eigen-

function is $(r/a)^n$ in place of $j_n([\gamma_{n1}/a]r)$, and in (26) $J_{n1}=(2n+3)j_n(k_0a)/(k_0a)$. Also, expansions (10) and (16) now become

$$j_n(k_0r)=\left(\frac{r}{a}\right)^n\frac{2n+3}{k_0a}j_{n+1}(k_0a)+\sum_{l=2}^{\infty}J_{nl}j_n\left(\frac{\gamma_{nl}}{a}r\right), \tag{28}$$

$$\begin{aligned}f_n(r)=&(-i)^n(2n+1)j_n(k_0r)\\&+i\cdot[ir^n-(k_0a)^2a^nh_{n+1}(k_0a)j_n(k_0r)]A_{n1}\\&+i(k_0a)^2\sum_{l=2}^{\infty}\frac{A_{nl}}{(k_0a)^2-\gamma_{nl}^2}\left[i\cdot j_n\left(\frac{\gamma_{nl}}{a}r\right)\right.\\&\left.+(k_0a)^2j_n(k_0r)C_{nl}\right],\quad n=0,1,\ldots.\end{aligned} \tag{29}$$

These facts are important for the completeness of the set for $l=1,2,3,\ldots$ in these particular cases.

From the theory of Dini's series, developed in Ref. 12, it follows also that for continuous functions $g(r)$ the coefficients A_{nl} in (27) diminish, at least as $1/l$ as $l\to\infty$. This has been tested for all $g(r)$ used in our problem. In particular, this is true for the coefficients J_{nl} in (26). Taking into account that as $l\to\infty$ the roots γ_{nl} of (13) behave like $\gamma_{nl}\to l\pi+\delta$ (Ref. 12) (where δ is a small positive value that depends on n and t_n) and that $j_n(x)\to\sin(x-[n\pi/2])/x$ as $x\to\infty$, we conclude that the full series (27) converges at least as $1/l^2$ for continuous $g(r)$; this holds, in particular, for the expansion (10) of $j_n(k_0r)$. This rate can be further improved if the particular choice

$$t_n=-\frac{ag'(a)}{g(a)}, \tag{30}$$

is made. The details of this assertion can be found in Ref. 12. With this particular choice, the sequence of A_{nl} converges at least as fast as $1/l^2$, and Dini's expansion (27) at least as fast as $1/l^3$. In Fig. 6 a typical plot of $|B_{n,l+1}/B_{nl}|$ for various t_n [including the choice of (30)] and of $([l+1]/l)^j$, $j=1-3$, for large values of l (say, $l>25$) verifies the above assertion for $g(r)=5+5r/a$ (see below). It was verified for other $g(r)$ as well. This important fact, although not necessary in the acoustic case under consideration, with $\rho(r)=\rho_0=$constant, becomes a necessary condition when derivatives of such expansions are involved, as in the case of Eq. (1) or the electromagnetic one, where a rate of convergence of at least $1/l^3$ is required.

The problem we come up against when trying to apply these ideas here is that $f_n(r)$, the function that is being expanded, is unknown and t_n cannot be chosen according to (30) as yet. Choosing an arbitrary t_n and solving the problem may result in a good approximation of $f_n(a)$; on the other hand, there is no way whatsoever of obtaining $f_n'(a)$ by differentiation of the expansion, since the latter, in general, does not converge absolutely and does not represent $f_n'(r)$.[12] However, as shown in the following, the required values can be found from the exterior field with the aid of the boundary conditions at $r=a$.

In general, these conditions are[15]

$$\begin{aligned}&\Phi(\mathbf{r})|_{r=a-}=\Phi(\mathbf{r})|_{r=a+},\\&\frac{1}{\rho}\frac{\partial\Phi(\mathbf{r})}{\partial r}\bigg|_{r=a-}=\frac{1}{\rho}\frac{\partial\Phi(\mathbf{r})}{\partial r}\bigg|_{r=a+}.\end{aligned} \tag{31}$$

In the present case $\rho^+=\rho^-=\rho_0$, and taking into account the expansion (5) as well as the orthogonality of spherical harmonics we get

$$\begin{aligned}&f_{nm}(r=a_+)=f_{nm}(r=a_-),\\&f_{nm}'(r=a_+)=f_{nm}'(r=a_-),\end{aligned} \tag{32}$$

$n=0,1,\ldots,m=-n,\ldots,n$. For an inhomogeneity independent of θ, φ the index m disappears and we end up with

$$f_n(r=a_+)=f_n(r=a_-),\quad f_n'(r=a_+)=f_n'(r=a_-), \tag{33}$$

$n=0,1,\ldots$. Now it is a simple matter to obtain the values of f_n just outside the inhomogeneity. For $r\geqslant a$ we obtain from (3) an equation similar to (9)

$$f_n(r)=(-i)^n(2n+1)j_n(k_0r)-ik_0^3h_n(k_0r)\cdot I_n, \tag{34}$$

with

$$\begin{aligned}I_n=&\int_0^a\left[\frac{b(r')}{b_0}-1\right]f_n(r')j_n(k_0r')r'^2\,dr'\\=&\sum_{l=1}^{\infty}J_{nl}A_{nl}N_{nl},\end{aligned} \tag{35}$$

where Eqs. (10), (12), and (23) as well as the orthogonality of the set $j_n(\gamma_{nl}[r/a])$ in the interval $[0,a]$ have been used.

According to preceding remarks I_n is calculated easily and accurately regardless of the choice of t_n; the rate of convergence of (35) is at least $1/l^4$. Furthermore, we can differentiate Eq. (34) to obtain the required derivative, since I_n is a numerical constant.

So, the procedure is as follows: we start with an arbitrary t_n; we solve the system (25) for the B_{nl}, and getting the A_{nl} from (21) we calculate I_n from (35); from this the values $f_n(a)$ and $f_n'(a)$ follow from (34) and are substituted in (30) to derive the optimum value of t_n. Now the system (25) is solved once again with this choice of t_n to obtain the optimum values of B_{nl}, that converge faster with l and allow differentiation of (11) to obtain $f_n'(r)$, or even $f_n''(r)$, for $r\leqslant a$.

In the discussion of convergence a remark is necessary in connection with (26): The choice $t_n=-k_0aj_n'(k_0a)/j_n(k_0a)$ makes one eigenvalue, say $\gamma_{nl'}$, coincide with k_0a; then, all $J_{nl}=0$ except $J_{nl'}$ and this may suggest substantial simplification of the procedure and improvement of the convergence. However, owing to the term $\gamma_{nl}-k_0a$ in the denominator of (26), all expansion formulas for the coefficients require revision; this is laborious but can be carried out; it leads, however, to more complicated formulas with no improvement of convergence for the B_{nl}, A_{nl} over the values that correspond to an arbitrary choice of t_n.

Before closing this section, it is appropriate to compare the Dini's expansions for continuous functions, like (10)–(12) and (27), with other possible ones in the interval $0\leqslant r\leqslant a$. For instance, the complete and orthogonal set of trigo-

nometric functions $\sin(l\pi[r/a])$, $l=1,2,3,...$ or $\cos(l\pi[r/a])$, $l=0,1,2,...$. Their convergence, however, is in general inferior to the $1/l^2$ convergence of the Dini's series, which may be further improved by properly choosing t_n. Owing to the behavior of the function under expansion, $g(r)$, at the ends $r=0$ and/or $r=a$ the trigonometric series cannot converge faster than $1/l$ in general. Unless $g(0)=g(a)=0$ the sine series corresponds to a finite discontinuity at the ends and its convergence is restricted to $1/l$. Similar remarks apply to the cosine series as well as to other possible expansions. Finally, we may observe that while $j_n(0)=0$ $(n=1,2,...)$ we cannot expect $j_n(k_0a)$ to vanish, too. Therefore, the Dini series is superior to a sine series expansion for $j_n(k_0r)$ in $0\leqslant r\leqslant a$.

C. Inhomogeneity dependent on *r*, *θ*, *φ*

In the more general case $b(\mathbf{r})=b(r,\theta)$ it is no longer possible to solve the equations for $f_n(r)$ separately for each $n=0,1,...$. To avoid the additional complications introduced by dependence of certain quantities on φ, like $\Phi^{\text{inc}}(\mathbf{r})$ in (6) for arbitrary direction of incidence, we restrict ourselves here to incidence along the z axis, namely, we again set $\mathbf{k}_0=k_0\hat{z}$. Then, expansions (6) for $\Phi^{\text{inc}}(\mathbf{r})$ and (7) for $\Phi(\mathbf{r})=\Phi(r,\theta)$ remain the same, while (12) is now changed to

$$\left[\frac{b(r,\theta)}{b_0}-1\right]\Phi(r,\theta)=\sum_{n=0}^{\infty}P_n(\cos\theta)F_n(r)=\sum_{n=0}^{\infty}P_n(\cos\theta)\sum_{l=1}^{\infty}A_{nl}j_n\left(\frac{\gamma_{nl}}{a}r\right), \tag{36}$$

where the radial functions $F_n(r)$ are expanded in the same set of orthogonal functions $j_n([\gamma_{nl}/a]r)$ used in (7) for $\Phi(r,\theta)$. With these definitions the method proceeds through identical steps followed previously for $b(\mathbf{r})=b(r)$, and while Eqs. (18)–(19) do not change, Eq. (20) relating B_{nl} [the expansions coefficients of $f_n(r)$] to A_{nl} [those of $F_n(r)$] is now generalized to

$$\left[\frac{b(r,\theta)}{b_0}-1\right]\Phi(r,\theta)=\sum_{n'=0}^{\infty}P_{n'}(\cos\theta)\times\sum_{l'=1}^{\infty}A_{n'l'}j_{n'}\left(\frac{\gamma_{n'l'}}{a}r\right)=\sum_{q=0}^{\infty}P_q(\cos\theta)\sum_{p=1}^{\infty}B_{qp}j_q\left(\frac{\gamma_{qp}}{a}r\right)\times\left[\frac{b(r,\theta)}{b_0}-1\right]. \tag{37}$$

Multiplying this by $P_n(\cos\theta)j_n([\gamma_{nl}/a]r)\sin\theta r^2\,dr\,d\theta$, integrating, and taking advantage of orthogonality we get

$$A_{nl}=\frac{2n+1}{2N_{nl}}\sum_{q=0}^{\infty}\sum_{p=1}^{\infty}D(n,l,q,p)B_{qp}, \tag{38}$$

with the equivalent to (22) for D_{nlp}, relation

$$D(n,l,q,p)=\int_0^{\pi}\int_0^{a}\left(\frac{b(r,\theta)}{b_0}-1\right)P_n(\cos\theta)P_q(\cos\theta)j_n\times\left(\frac{\gamma_{nl}}{a}r\right)j_q\left(\frac{\gamma_{qp}}{a}r\right)r^2\sin\theta\,dr\,d\theta. \tag{39}$$

These latter coefficients are, in general, calculated by numerical integration. Combining (38) with (18), we obtain the linear system for the coefficients B_{nl}. It should be obvious also that even with φ-dependence of $\Phi(\mathbf{r})$ and/or $\Phi^{\text{inc}}(\mathbf{r})$, no fundamental complications are introduced in the procedure; simply the number of unknowns increases: for each $f_n(r)$ and B_{nl} we have $2n+1$ unknowns $f_{nm}(r)$ or B_{nlm} $(m=-n$ to $n)$; also, D in (38) and (39) requires two additional indices m and s. In the more restricted case $[b(r,\theta)/b_0]-1=F(r)G(\theta)$, the double integral in (39) is simplified into the product of two single integrals over r and θ, reducing the numerical burden, and, in certain special cases, allowing analytical evaluation of some integrals.

Again, the procedure starts with an arbitrary choice of t_n in (13). The optimum t_n follows again from the boundary conditions (32) at $r=a$ and an expression for the external field $(r\geqslant a)$ dependent on the constant I_n, similar to (34) and obtained from (3) when $r\geqslant a$. The significant difference in this case is that, owing to the coupling of relations for $f_n(r)$ for various n, I_n, the optimum value of t_n, and the corresponding eigenvalues γ_{nl} of (13), turn out to be complex. However, the convergence properties of B_{nl}, $l=1,2,...$ are improved as in the simpler case $b(\mathbf{r})=b(r)$.

The complex γ_{nl} roots of (13) are found starting with a real value of t_n equal to the real part of the optimum t_n. We then increase gradually the imaginary part of t_n until its final value, equal to the imaginary part of optimum t_n, is reached. In this gradual process for the estimation of the new complex roots γ_{nl} we use as starting values the ones found in the preceding step, implementing a Newton–Raphson approximation formula.

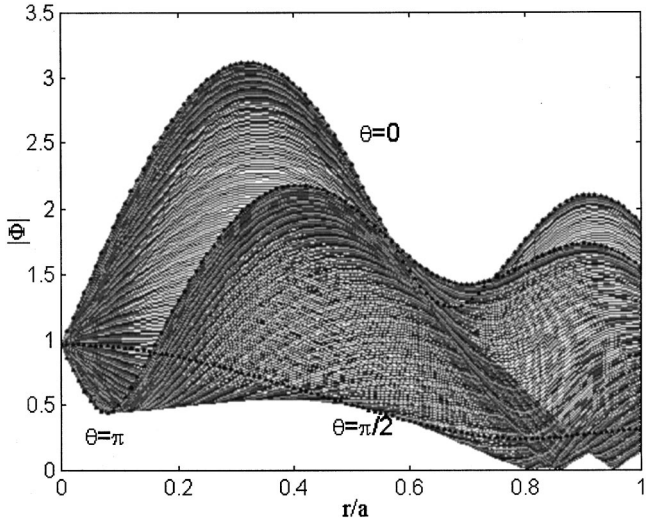

FIG. 1. Total field $|\Phi|$ inside a spherical inhomogeneity described by $b(r)/b_0=5+5r/a$ with $k_0a=2.0958$.

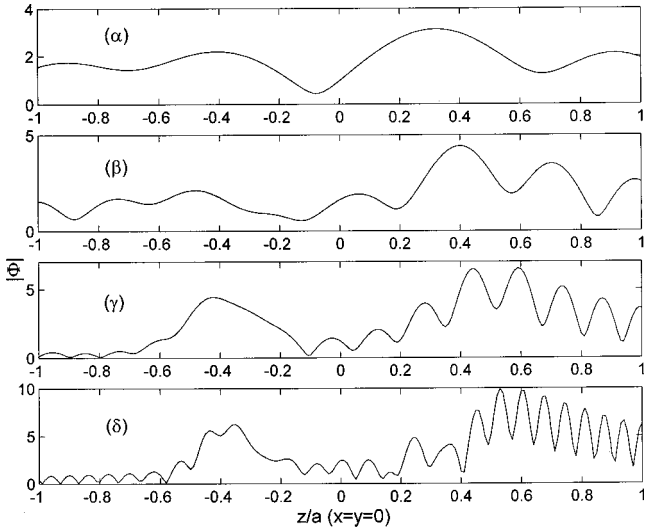

FIG. 2. Total field $|\Phi(0,0,z)|$ inside a spherical inhomogeneity described by $b(r)/b_0=5+5r/a$ with $k_0a=(\alpha)$ 2.0958; (β) 4.19169; (γ) 8.3834; (δ) 16.7668.

III. NUMERICAL RESULTS AND DISCUSSION

Numerical and plotted results were obtained mostly for θ,φ-independent compressibility $b(r)$. Five cases were examined

$$\text{(a)} \quad \frac{b(r)}{b_0}=5+5\frac{r}{a}$$

$$\text{(b)} \quad =7.5$$

$$\text{(c)} \quad =7.5-2.5\cos\left(\pi\frac{r}{a}\right)$$

$$\text{(d)} \quad =7.5-2.5\cos\left(3\pi\frac{r}{a}\right)$$

$$\text{(e)} \quad =\begin{cases} 7.5-10\left(\dfrac{r}{a}-0.5\right)^2, & 0\leqslant\dfrac{r}{a}\leqslant 0.5 \\ 7.5+10\left(\dfrac{r}{a}-0.5\right)^2, & 0.5\leqslant\dfrac{r}{a}\leqslant 1 \end{cases}. \qquad (40)$$

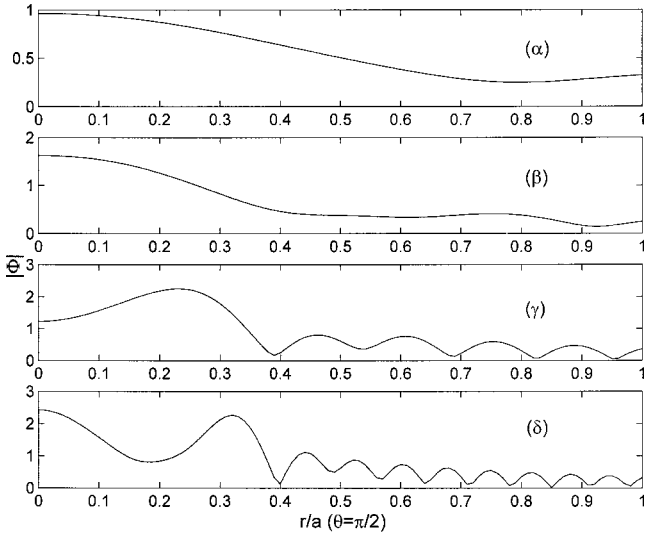

FIG. 3. Total field $|\Phi(x,y,0)|$ inside a spherical inhomogeneity described by $b(r)/b_0=5+5r/a$ with $k_0a=(\alpha)$ 2.0958; (β) 4.19169; (γ) 8.3834; (δ) 16.7668.

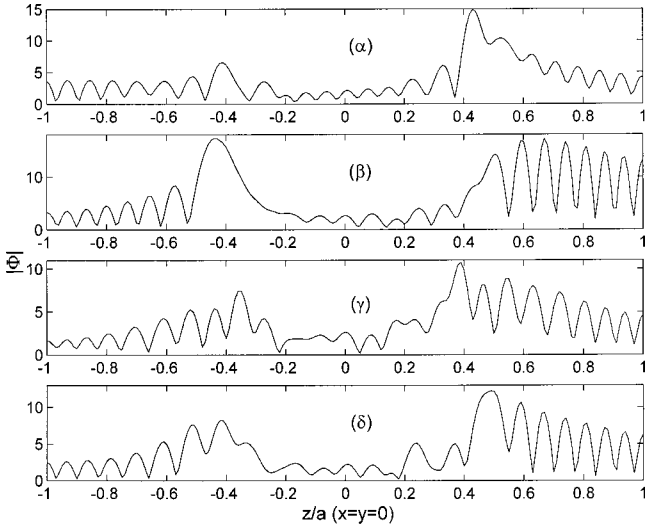

FIG. 4. Total field $|\Phi(0,0,z)|$ inside a spherical inhomogeneity with $k_0a=16.7668$ described by $b(r)/b_0=(\alpha)$ Eq. (40b); (β) Eq. (40c); (γ) Eq. (40d); (δ) Eq. (40e).

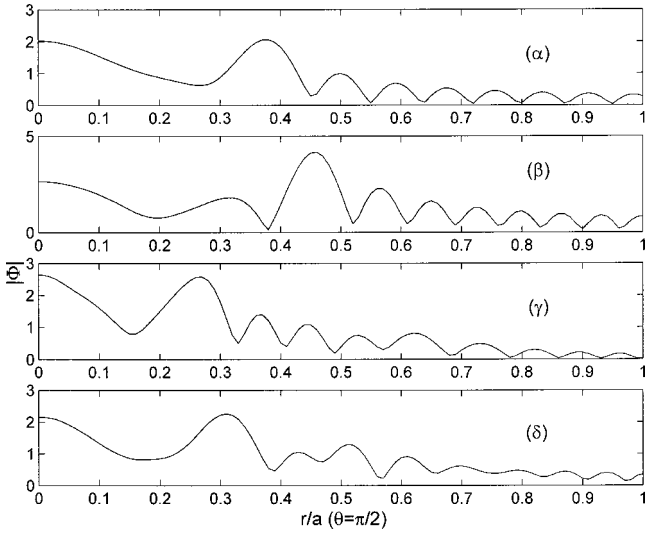

FIG. 5. Total field $|\Phi(x,y,0)|$ inside a spherical inhomogeneity with $k_0a=16.7668$ described by $b(r)/b_0=(\alpha)$ Eq. (40b); (β) Eq. (40c); (γ) Eq. (40d); (δ) Eq. (40e).

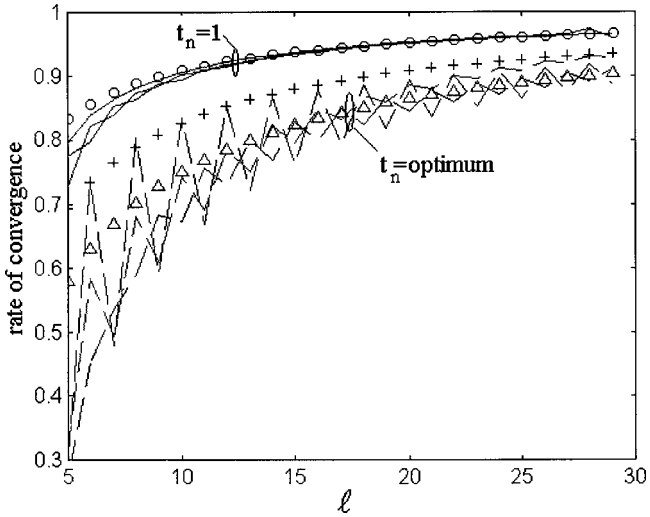

FIG. 6. Rate of convergence of $|B_{nl}|$ $(n=0-2)$, for $t_n=1$ (solid lines) and t_n=optimum (dashed lines) compared with the convergence of $1/l$ (circles), $1/l^2$ (crosses), and $1/l^3$ (triangles).

TABLE I. Maximum value of n and l required for $b(r)/b_0=5+5r/a$.

k_0a	$n_{\max}$	$l_{\max}$
2.095 84	6	6
4.191 69	11	12
6.287 53	15	18
8.383 38	16	18
10.479 2	18	21
12.575 1	21	25
14.670 9	23	28
16.766 8	27	31
18.862 6	29	33

In all cases we plot the magnitude of the total field inside the inhomogeneity, $|\Phi|$, vs r/a for three values of θ ($=0$, $\pi/2$, and π). As indicated in Fig. 1, where the curves of $|\Phi|$ are depicted for all values of θ, the above selected values of θ—the dotted curves of Fig. 1, which are also given in Figs. 2(a) and 3(a)—give a good idea of how $|\Phi|$ varies with θ, especially for small values of k_0a and relatively smooth inhomogeneous profiles. When k_0a increases or when $b(r)$ oscillates more rapidly, the variations with θ becomes more pronounced and increase in number. However, the above curves remain useful, especially the ones along the z axis ($\theta=0,\pi$), because they indicate, in general, the extremum of $|\Phi|$ and provide a fairly good idea of field penetration in the sphere.

So, in Figs. 2 and 3 we plot $|\Phi(0,0,z)|$ ($\theta=0,\pi$) and $|\Phi(x,y,0)|$ ($\theta=\pi/2$), respectively, for various k_0a in the case of (40a), i.e., linear $b(r)$. From the plots it is evident that the variations of $|\Phi|$ increase with k_0a. In Figs. 4 and 5 we show the same quantities, but, for the cases (40b)–(40e), all for $k_0a=16.7668$. In all figures we plot the internal field (inside the sphere); the exterior one can be easily calculated from (33).

To illustrate and verify the remarks on convergence in Sec. II B, we sketch in Fig. 6 the rate of convergence, i.e., values of $|B_{n,l+1}/B_{nl}|$, for the set B_{nl}, $l=5-30$. All these are shown in case (a)—linear $b(r)$—for $n=0,1,2$ and, for reasons of comparison, for an arbitrary choice of t_n ($=1$ here), shown by the solid lines, and the optimum t_n shown in dashed lines.

To check their rate of convergence against standard sequences of natural numbers like $1/l$, $1/l^2$, $1/l^3$ etc., we have also drawn the values of $l/(l+1)$ (circles), $[l/(l+1)]^2$ (crosses), and $[l/(l+1)]^3$ (triangles). In the case of $n=0$ the terms B_{0l} are divided into two subsequences ($l=$odd and even); in order to illustrate the convergence of the whole sequence in this case, we depict the mentioned ratios for the geometric mean of two consecutive terms. It is obvious that for the optimum t_n the convergence of B_{nl} is similar to $1/l^3$.

As far as the highest numbers of n ($n_{\max}$) and l ($l_{\max}$) required for the convergence of the corresponding expansions are concerned, we give their values in Table I, for various k_0a for the case (40a) of linear $b(r)$ and for optimum t_n; with these values of $n_{\max}$ and $l_{\max}$ the error of $|\Phi|$ in the sphere is less than 0.1%. Actually, the given value of $l_{\max}$ may be safely decreased for larger values of n, since the effect of $f_n(r)$ in the n series diminishes for higher n. Therefore, the corresponding matrix size is even smaller than these values indicate. Even for $k_0a\cong 19$ (last case of Table I) the matrix size, at most 33×33, shows how good the conver-

TABLE III. (a) Values of optimum t_n for $b(\mathbf{r})/b_0-1=(6.5-2.5\cos(\pi r/a))(2-\sin\theta)$. (b) Roots γ_{nl} for the optimum t_n.

(a)

n	t_n
0	$79.9235-37.2732i$
1	$7.6935-0.0239i$
2	$-3.0987+0.0918i$
3	$-17.7704+0.5472i$
4	$6.2941-0.1106i$
5	$4.3094+0.0069i$
6	$6.1331+0.0325i$
7	$7.9513+0.0279i$
8	$8.7696-0.0063i$
9	$9.7030-0.0085i$
10	$10.7610+0.0005i$

(b)

l	$n=0$	$n=1$	$n=2$
1	$3.1093-0.0150i$	$3.9540-0.0014i$	$0.1372+2.9461i$
2	$6.2186-0.0300i$	$6.9174-0.0017i$	$6.8386+0.0117i$
3	$9.3280-0.0448i$	$9.9218-0.0016i$	$10.3141+0.0084i$
4	$12.4375-0.0593i$	$12.9680-0.0014i$	$13.6189+0.0065i$
5	$15.5470-0.0735i$	$16.0422-0.0012i$	$16.8593+0.0053i$
6	$18.6567-0.0873i$	$19.1346-0.0011i$	$20.0675+0.0045i$
7	$21.7666-0.1006i$	$22.2390-0.0010i$	$23.2573+0.0039i$
8	$24.8767-0.1134i$	$25.3518-0.0009i$	$26.4354+0.0034i$
9	$27.9870-0.1256i$	$28.4704-0.0008i$	$29.6056+0.0031i$
10	$31.0975-0.1371i$	$31.5932-0.0007i$	$32.7703+0.0028i$
11	$34.2084-0.1479i$	$34.7193-0.0007i$	$35.9309+0.0025i$
12	$37.3197-0.1580i$	$37.8478-0.0006i$	$39.0884+0.0023i$
13	$40.4314-0.1674i$	$40.9783-0.0006i$	$42.2436+0.0022i$
14	$43.5436-0.1761i$	$44.1103-0.0005i$	$45.3968+0.0020i$
15	$46.6562-0.1839i$	$47.2435-0.0005i$	$48.5485+0.0019i$
16	$49.7694-0.1910i$	$50.3778-0.0005i$	$51.6990+0.0018i$
17	$52.8832-0.1974i$	$53.5129-0.0004i$	$54.8485+0.0017i$
18	$55.9976-0.2031i$	$56.6487-0.0004i$	$57.9971+0.0016i$
19	$59.1126-0.2080i$	$59.7851-0.0004i$	$61.1450+0.0015i$
20	$62.2283-0.2123i$	$62.9220-0.0004i$	$64.2923+0.0014i$

TABLE II. (a) Values of $f_n(r)$ at the boundary ($t_n=$optimum). (b) Values of $f_n(r)$ at the boundary ($t_n=1$).

(a)	$n=0$	$n=1$	$n=2$
$f_n(a-)$	$5.9886E-002-6.8665E-002i$	$2.1011E-001-1.0965E+000i$	$-1.2011E-001-3.3427E-002i$
$f_n(a+)$	$5.9886E-002-6.8665E-002i$	$2.1011E-001-1.0965E+000i$	$-1.2011E-001-3.3427E-002i$
(b)	$n=0$	$n=1$	$n=2$
$f_n(a-)$	$6.4258E-002-7.3676E-002i$	$2.0797E-001-1.0853E+000i$	$-9.9173E-002-2.7602E-002i$
$f_n(a+)$	$5.9893E-002-6.8671E-002i$	$2.1012E-001-1.0965E+000i$	$-1.2009E-001-3.3423E-002i$

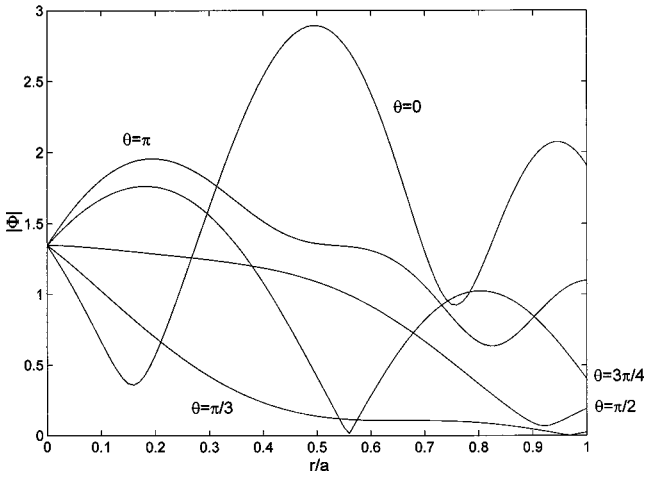

FIG. 7. Total field $|\Phi|$ inside a spherical inhomogeneity described by $b(\mathbf{r})/b_0=1+(6.5-2.5\cos(\pi r/a))(2-\sin\theta)$ with $k_0a=2.0958$.

gence of our method is, if one takes into account matrix size versus k_0a of other methods for spherical scatterers. Of course, with θ- (or φ-) variations present, these numbers are multiplied by the necessary number of terms to account properly for such variations of the inhomogeneity. Finally, in order to point out that the optimum choice of t_n ensures the accurate satisfaction of the boundary condition for $f_n(r)$ at $r=a$, as opposed to an arbitrary value of t_n, we show corresponding values of $f_n(a-)$ and $f_n(a+)$ in Table II, again for case (a). It is worth noting that, while $f_n(a+)$ is the same for either value of t_n, owing to the strong convergence of (35) (of order $1/l^4$), $f_n(a-)$ from (11) is accurate only for the optimum t_n.

In Table III(a) the optimum values of t_n are given for $[b(r,\theta)/b_0]-1=(6.5-2.5\cos(\pi r/a))(2-\sin\theta)$. In Table III(b) we give the corresponding values of γ_{nl}, $n=0-2$. In Fig. 7 we plot $|\Phi|$ for various values of θ in this case.

IV. CONCLUSIONS

Acoustic fields induced by external sources with inhomogeneous compressibility $b(\mathbf{r})$ have been treated by a direct hybrid (analytical–numerical) method; direct in the sense of an analytical treatment of the corresponding volume integral equation in the general case of arbitrary inhomogeneity, where simpler methods, like separation of variables, are no longer applicable. The restriction to spheres provides the advantage of using the orthogonal properties of spherical harmonics, and, in particular, of Dini's expansions (i.e., general type of Fourier–Bessel expansions) for the radial functions, whose convergence is shown to be superior to other possible sets of orthogonal expansions. Another important feature is the possibility of improving their rate of convergence by choosing the proper value of a crucial parameter in their eigenvalue equation. Plots of fields induced inside the sphere are shown in four typical cases of radial inhomogeneity $b=b(r)$ and in a more general one in which $b=b(r,\theta)$. As far as sphere size is concerned, there is no problem extending the method to sizes larger than $k_0a=20$. For instance, for $k_0a=18.86$ the maximum number of terms required in the n expansion is $n_{\max}=29$, while for the Dini's series, in this case, the number of needed terms, in the case of optimum convergence, is $l_{\max}=33$; this latter can be safely decreased for higher n values. These numbers provide a clear indication of the matrix sizes required for an approximate three-decimal accuracy for the induced field.

The scalar case of inhomogeneous density $\rho(\mathbf{r})$, as well as the electromagnetic problem, owing mainly to the difficulties introduced by the derivatives of $\rho(\mathbf{r})$ in the integral equations, are treated in a follow-up paper; the complications of such problems over the present simpler ones are by no means trivial.

ACKNOWLEDGMENTS

The present work has been supported by the program of basic research ''Archimides'' of the Institute of Communication and Computer Systems, National Technical University of Athens, Athens 15773, Greece. The work of G.F. was also supported in part by the General Secretariat of Research and Technology and by the State Scholarship Foundation of Greece.

APPENDIX

The solution of (3) or (9) in the special case $b(r)=b_1=\text{constant}$ $[\omega(b_1\rho_0)^{1/2}=k_1=\text{constant}]$ is obtainable by separation of variables. With boundary conditions $\Phi(\mathbf{r})$ and $\partial\Phi/\partial r$ [or $f_n(r)$ and $f_n'(r)$] continuous at $r=a$, this classical method proceeds by expanding the interior field in (7) by means of the spherical eigenfunctions of $\nabla^2\Phi(\mathbf{r})+k_1^2\Phi(\mathbf{r})=0$. Namely, by assuming in (7) and (11) that $f_n(r)=F_nj_n(k_1r)=\Sigma_{l=1}^{\infty}B_{nl}j_n([\gamma_{nl}/a]r)$ in $0\leqslant r\leqslant a$, while $\Phi(\mathbf{r})=\Sigma_{n=0}^{\infty}H_nh_n(k_0r)P_n(\cos\theta)$ for $r\geqslant a$; the final result is

$$F_n=\frac{(-i)^{n+1}(2n+1)}{(k_0a)^2\left[j_n(k_1a)h_n'(k_0a)-\dfrac{k_1}{k_0}j_n'(k_1a)h_n(k_0a)\right]}. \tag{A1}$$

We will show here that the same result is obtained by a direct solution of the integral equation (9), following the steps that were applied in the more general case $b(\mathbf{r})=b(r)$ and for arbitrary t_n in (13).

In this case $[b(r)/b_0]-1=k_1^2/k_0^2-1$, and from (21) and (22) one obtains

$$D_{nlp}=\left(\frac{k_1^2}{k_0^2}-1\right)N_{nl}\delta_{lp}. \tag{A2}$$

With this result (21), (23)–(25) are much simplified as follows:

$$A_{nl}=\left(\frac{k_1^2}{k_0^2}-1\right)B_{nl},$$
$$Z_{np}=\left(\frac{k_1^2}{k_0^2}-1\right)\frac{C_{np}}{\gamma_{np}^2-(k_0a)^2}\cdot\frac{i(k_0a)^4}{(-i)^n(2n+1)}, \tag{A3}$$

and

$$B_{nl}=(-i)^n(2n+1)J_{nl}-\left(\frac{k_1^2}{k_0^2}-1\right)\times\left[i(k_0a)^4J_{nl}\sum_{p=1}^{\infty}B_{np}\frac{C_{np}}{\gamma_{np}^2-(k_0a)^2}-B_{nl}\frac{(k_0a)^2}{\gamma_{nl}^2-(k_0a)^2}\right]. \tag{A4}$$

By combining terms and substituting C_{np} from (17) and J_{nl} from (26), Eq. (A4) can be put in the form

$$B_{nl}=T_na^3[t_nj_n(k_0a)+(k_0a)j_n'(k_0a)]\times\frac{j_n(\gamma_{nl})}{N_{nl}[\gamma_{nl}^2-(k_1a)^2]}, \tag{A5}$$

$$T_n=(-i)^n(2n+1)-\left(\frac{k_1^2}{k_0^2}-1\right)i(k_0a)^4\sum_{p=1}^{\infty}B_{np}\times\frac{C_{np}}{\gamma_{np}^2-(k_0a)^2}. \tag{A6}$$

For $r=a$ we get from (10) and (26)

$$j_n(k_0a)=\sum_{l=1}^{\infty}J_{nl}j_n(\gamma_{nl})=a^3[t_nj_n(k_0a)+(k_0a)j_n'(k_0a)]\times\sum_{l=1}^{\infty}\frac{j_n^2(\gamma_{nl})}{N_{nl}[\gamma_{nl}^2-(k_0a)^2]}, \tag{A7}$$

and by analogy with the latter

$$j_n(k_1a)=a^3[t_nj_n(k_1a)+(k_1a)j_n'(k_1a)]\times\sum_{l=1}^{\infty}\frac{j_n^2(\gamma_{nl})}{N_{nl}[\gamma_{nl}^2-(k_1a)^2]}. \tag{A8}$$

We can now evaluate the constant, with respect to l, T_n as follows: Substituting (A5) in (A6) and C_{np} from (17), we get

$$T_n=(-i)^n(2n+1)-i(k_0a)^2[(k_1a)^2-(k_0a)^2]T_na^3\cdot[t_nj_n(k_0a)+(k_0a)j_n'(k_0a)]\times\left[t_n\frac{h_n(k_0a)}{k_0a}+h_n'(k_0a)\right]M_n, \tag{A9}$$

with

$$M_n=\sum_{p=1}^{\infty}\frac{j_n^2(\gamma_{np})}{N_{np}[\gamma_{np}^2-(k_1a)^2][\gamma_{np}^2-(k_0a)^2]}.$$

Analyzing M_n into two terms

$$M_n=\frac{1}{(k_1a)^2-(k_0a)^2}\sum_{p=1}^{\infty}\frac{j_n^2(\gamma_{np})}{N_{np}}\times\left(\frac{1}{\gamma_{np}^2-(k_1a)^2}-\frac{1}{\gamma_{np}^2-(k_0a)^2}\right), \tag{A10}$$

we can evaluate the resulting sums using (A7) and (A8). Thus,

$$T_n=(-i)^n(2n+1)-i(k_0a)^2T_n[t_nj_n(k_0a)+(k_0a)j_n'(k_0a)]\left[t_n\frac{h_n(k_0a)}{k_0a}+h_n'(k_0a)\right]\times\left\{\frac{j_n(k_1a)}{t_nj_n(k_1a)+(k_1a)j_n'(k_1a)}\times-\frac{j_n(k_0a)}{t_nj_n(k_0a)+(k_0a)j_n'(k_0a)}\right\}. \tag{A11}$$

From this last relation one may evaluate the constant T_n explicitly. After some term cancellations and lengthy algebraic steps involving repeated use of the Wronskian relation

$$1-i(k_0a)^2h_n'(k_0a)j_n(k_0a)=-i(k_0a)^2h_n(k_0a)j_n'(k_0a), \tag{A12}$$

one ends up with

$$T_n=\frac{(-i)^{n+1}(2n+1)[t_nj_n(k_1a)+(k_1a)j_n'(k_1a)]}{(k_0a)^2[t_nj_n(k_0a)+(k_0a)j_n'(k_0a)]\left[j_n(k_1a)h_n'(k_0a)-\frac{k_1}{k_0}j_n'(k_1a)h_n(k_0a)\right]}. \tag{A13}$$

The final step in this particular case is to realize that

$$f_n(a)=F_nj_n(k_1a)=\sum_{l=1}^{\infty}B_{nl}j_n(\gamma_{nl})=T_na^3[t_nj_n(k_0a)+(k_0a)j_n'(k_0a)]\times\sum_{l=1}^{\infty}\frac{j_n^2(\gamma_{nl})}{N_{nl}[\gamma_{nl}^2-(k_1a)^2]}, \tag{A14}$$

where B_{nl} was substituted from (A5). The sum can be obtained from (A8), in terms of $j_n(k_1a)$, and one obtains

$$F_n=T_n\frac{t_nj_n(k_0a)+(k_0a)j_n'(k_0a)}{t_nj_n(k_1a)+(k_1a)j_n'(k_1a)}. \tag{A15}$$

Substituting T_n from (A13) we obtain for F_n the exact value given by separation of variables in (A1).

[1] D. S. Jones, *The Theory of Electromagnetism* (Pergamon, Oxford, 1964).
[2] J. G. Fikioris, "Electromagnetic field in the source region of continuously varying current density," Q. Appl. Math. **LIV**(No. 2), 201–209 (1996).
[3] J. G. Fikioris, "The EM field of constant current density distributions in

parallelepiped regions,'' IEEE Trans. Antennas Propag. **46**(No. 9), 1358–1364 (1998).
[4] W. C. Chew, *Waves and Fields in Inhomogeneous Media* (Van Nostrand Reinhold, New York, 1990).
[5] M. A. Jensen, ''A recursive Green's function technique for acoustic scattering from heterogeneous objects,'' J. Acoust. Soc. Am. **103**, 713–720 (1998).
[6] A. N. Ivakin, ''A unified approach to volume and roughness scattering,'' J. Acoust. Soc. Am. **103**, 827–837 (1998).
[7] B. H. Tracey and H. Schmidt, ''A self-consistent theory for seabed volume scattering,'' J. Acoust. Soc. Am. **106**, 2524–2534 (1999).
[8] P. A. Martin, ''Acoustic scattering by inhomogeneous spheres,'' J. Acoust. Soc. Am. **111**, 2013–2018 (2002).
[9] S. A. Stotts, ''Coupled-mode solutions in generalized ocean environments,'' J. Acoust. Soc. Am. **111**, 1623–1643 (2002).
[10] A. Messiah, *Quantum Mechanics* (Wiley, New York, 1958).
[11] P. M. Morse and H. Feshbach, *Methods of Theoretical Physics* (McGraw-Hill, New York, 1953).
[12] G. N. Watson, *A Treatise on the Theory of Bessel Functions*, 2nd ed. (Cambridge University Press, Cambridge, England, 1958).
[13] A. Erdelyi *et al.*, *Higher Transcendental Functions* (McGraw-Hill, New York, 1953).
[14] M. Abramowitz and I. A. Stegun, *Handbook of Mathematical Functions* (Dover, New York, 1972).
[15] A. Ishimaru, *Electromagnetic Wave Propagation, Radiation and Scattering* (Prentice-Hall, Englewood Cliffs, NJ, 1991).

A boundary integral equation method using auxiliary interior surface approach for acoustic radiation and scattering in two dimensions

S. A. Yang
Department of Naval Architecture and Marine Engineering, National Cheng Kung University, Tainan, Taiwan, Republic of China

(Received 5 February 2002; revised 5 July 2002; accepted 7 July 2002)

This paper presents an effective solution method for predicting acoustic radiation and scattering fields in two dimensions. The difficulty of the fictitious characteristic frequency is overcome by incorporating an auxiliary interior surface that satisfies certain boundary condition into the body surface. This process gives rise to a set of uniquely solvable boundary integral equations. Distributing monopoles with unknown strengths over the body and interior surfaces yields the simple source formulation. The modified boundary integral equations are further transformed to ordinary ones that contain nonsingular kernels only. This implementation allows direct application of standard quadrature formulas over the entire integration domain; that is, the collocation points are exactly the positions at which the integration points are located. Selecting the interior surface is an easy task. Moreover, only a few corresponding interior nodal points are sufficient for the computation. Numerical calculations consist of the acoustic radiation and scattering by acoustically hard elliptic and rectangular cylinders. Comparisons with analytical solutions are made. Numerical results demonstrate the efficiency and accuracy of the current solution method. © *2002 Acoustical Society of America.* [DOI: 10.1121/1.1504852]

PACS numbers: 43.20.Fn, 43.20.Tb [MO]

I. INTRODUCTION

The approach of boundary integral equation methods (BIEMs) is well recognized in various exterior wave propagation problems including acoustics, electromagnetism, and the surface-wave–body interactions. The related mathematical function can be traced back to the eighteenth century. The French mathematician Pierre-Simon de Laplace presented the singular solution $1/R$ for 3D Laplace equation in 1782, where R is the distance of the source and field points. The first numerical implementations of BIEMs date back to the 1960's decade; pioneering works include those of Refs. 1–5. The so-called boundary element methods (BEMs) are based on the discretization of boundary integral equation formulations; the notation BEM first appeared in the literature in 1978.[6] The main characteristic of the methods lies in that it is sufficient to discretize only the boundary surfaces where the unknowns are localized. Through the intensive investigation of several decades, the BIEMs/BEMs have nowadays become an efficient alternative to domain-based methods such as the finite-element and finite-difference methods.

The two main types of BIEMs are the indirect and direct methods. The indirect methods distribute sources/sinks (or high-order singularities such as dipoles, etc.) of adjustable strengths over the entire boundary surfaces. This approach results in a solution that is usually not of immediate physical interest. The direct methods make use of the related primary field variables, e.g., the surface acoustic pressure and the surface normal velocity, for deriving the integral formulation. Therefore, the direct integral representation results in a solution that is more physically meaningful. Both approaches, however, introduce their own particular complications; for the detailed discussion see, for example, Refs. 7 and 8. Selecting the method to adopt encompasses issues of problem dependence and, perhaps, personal-preference dependence. For certain characteristic frequencies, it is known that no solution of the simple source formulation exists in general and that there is no unique solution of the surface Helmholtz integral formulation. Nonexistence or nonuniqueness is a purely mathematical problem arising from the breakdown of boundary integral representation rather than from the nature of the physical problem. Nonexistence notably arises from the fact that the related compatibility condition is not satisfied; the fulfillment of the compatibility condition, however, leads to the nonuniqueness problem. The reasoning is ascribed to the fact that the source function does not have physical significance. Therefore, the compatibility condition is not satisfied in general.[9] Research in handling these nonexistence and nonuniqueness difficulties occurring in external wave propagation problems has been an active topic for many years.

The two commonly used formulations of the direct methods are due to Schenck[9] and Burton and Miller.[10] Schenck[9] proposed a combined Helmholtz integral equation formulation (CHIEF) that added some additional Helmholtz integral relations evaluated in the interior region. The resulting overdetermined system of equations could then be solved by a least-squares technique. To insure uniqueness of the solution at the characteristic frequencies, one needs at least one good interior point that does not fall on any nodal surface of the related interior problem. The selection of interior points may become an issue as the wave frequency increases. Thus, numerous modified versions of CHIEF have been put forth for the purpose of effectively treating interior points.

Seybert and Rengarajan[11] provided an ''interior point pressure checking'' procedure to detect the accuracy of the CHIEF solution. The concept of adding more constraints for each interior point was applied in Segalman and Lobitz's ''superCHIEF'' method,[12] Seybert and Wu's ''enhanced'' CHIEF method,[13] and Wu and Seybert's ''CHIEF-block'' method.[14] This implementation makes the proper selection of interior points less critical, but increases the complexity of computation.

Burton and Miller[10] linearly combined the Helmholtz integral equation with its normal derivative. Although Burton and Miller's method possesses a more rigorous mathematical background than the CHIEF method, the hypersingularity difficulty is known to largely hinder the numerical implementation of the composite equation. This fact accounts for why the CHIEF method has been extensively used in engineering applications nowadays. Burton and Miller[10] presented a method of double-surface integrals that reduced the order of the singularity. Such a formulation is inefficient in computation due to the presence of double integrals. Meyer *et al.*[15] applied tangent operators and approximated the surface variables as constant over flat triangular elements. On the basis of the Hadamard[16] finite-part interpretation, Krishnasamy *et al.*[17] applied the Taylor series expansion and Stokes' integral theorem for the regularization. Liu and Rizzo[18] presented a weakly singular form of the hypersingular integral equations by employing a two-term Taylor series subtraction from the density function. Certain integral identities for the static Green's function were used to evaluate the added-back terms. Chien *et al.*[7] applied some identities arising in the integral equation related to an interior Laplace problem so as to reduce the order of the kernel singularity. Yang[19] refined the process and attained integral equations containing bounded kernels only. Both the acoustically hard and soft scatterers were considered. The formulations are advantageous in that they can be computed by directly using standard quadrature formulas; that is, other specific techniques, e.g., the polar coordinate transformation or the logarithmic Gaussian quadrature, are not required. Yang[20] expressed the unknown functions as a truncated Fourier–Legendre series. Some weakly singular integrals and the hypersingular integral could then be evaluated analytically. This approach therefore greatly enhances the efficiency of the numerical implementation.

Another direct method is the off-boundary formulation.[21–23] The approach takes the entire collocation points interior to the boundary surface so as to avoid the singularities in the Green's function. Further applying Burton and Miller's method gets rid of the nonuniqueness difficulty. Thus, this approach can also be referred to as the off-boundary Burton and Miller's method. The off-boundary formulation is usually more costly to implement than, say, the CHIEF owing to its complicated integrands.

An early indirect method due to Kupradze[24] represented the pressure in the external region in terms of a distribution of monopoles on the radiating surface. Chen and Schweikert[25] numerically carried out the simple source method for various radiation and scattering problems. Later, the wave superposition methods,[26–28] an off-boundary approach, were developed by placing monopoles interior to the boundary surface. Further linearly combining monopoles and dipoles circumvented the nonexistence difficulty associated with the monopole distribution alone. Most of the implementations of this approach have employed a one-point integration scheme. The main deficiency of the wave superposition methods (also the off-boundary methods) lies in the selection of the inner surface, particularly when the boundary surface has discontinuities. Miller *et al.*[29] proposed some rules for selecting the inner surface; however, the optimum inner surface was determined by a process of trial and error. Krutitskii[30] developed a modified formulation that combined Kupradze's simple source method[24] and the principle of wave superposition without numerical implementation; that is, monopoles were distributed on the radiation/scattering body and inner surfaces.

In light of the above discussion, this paper aims to develop an efficient and robust solution method for treating 2D acoustic radiation and scattering problems. The various shortcomings appearing in the prior literature, such as the selection of the interior points of Schenck's method, the hypersingularity of Burton and Miller's method, and the selection of the interior surface of the wave superposition methods, should therefore be reduced to be a minimum. This paper presents a modified boundary integral formulation based on Krutitskii's simple source approach. Section II introduces the mathematical foundation of acoustic wave problems and Krutitskii's integral formulation. Section III describes a regularization technique that transforms the singular boundary integral equations to a form containing bounded kernels only. Section IV examines the availability and accuracy of the modified formulation. Numerical examples include the acoustic radiation and scattering by elliptic and rectangular cylinders. Comparisons with analytical solutions are made. Section V concludes this paper.

II. INTEGRAL EQUATION FORMULATION

Consider a radiation body with Kellogg regular surface[31] ∂B immersed in an unbounded ideal homogeneous fluid. The propagation of acoustic waves is described by the wave equation

$$\nabla^2 \phi(r,t) = \frac{1}{c^2} \frac{\partial^2 \phi(r,t)}{\partial t^2}, \tag{1}$$

where ∇^2 is the Laplacian operator in two dimensions, ϕ is the velocity potential that is twice continuously differentiable at point r and time t, and c is the speed of sound in the medium at the equilibrium state. For a steady-state excitation with a time factor $\exp(-i\omega t)$, Eq. (1) reduces to the Helmholtz wave equation

$$(\nabla^2 + k^2)\phi = 0, \tag{2}$$

where $i = \sqrt{-1}$ is the imaginary unit, ω is the angular frequency, and $k = \omega/c$ is the wave number. The excess acoustic pressure can be written as

$$p = -\rho_0 \frac{\partial \phi}{\partial t} = i\omega\rho_0 \phi, \tag{3}$$

where ρ_0 denotes the density of the fluid at the equilibrium state. On the body surface ∂B, the velocity potential ϕ satisfies the Neumann boundary condition

$$\frac{\partial \phi}{\partial n_r} = f(r), \tag{4}$$

where $\partial/\partial n_r$ denotes differentiation along the outward normal direction at $r \in \partial B$ and $f(r)$ is a given function. The velocity potential ϕ should also meet the Sommerfeld radiation conditions at infinity

$$\phi = O(r^{-1/2}), \quad \frac{\partial \phi}{\partial r} - ik\phi = O(r^{-1/2}), \tag{5}$$

as $r \to \infty$. The solution to the above boundary-value problem exists and is unique; see, for example, Colton and Kress[32] for the details. The related integral equations, however, suffer from either the nonuniqueness or the nonexistence problems, as was mentioned in Sec. I. To remove this difficulty, we introduce an additional surface ∂b interior to ∂B with the boundary condition

$$\frac{\partial \phi(r)}{\partial n_r} - i\phi(r) = 0, \quad r \in \partial b. \tag{6}$$

The surface ∂b is chosen in such a way that for any k from the set $S[0,\infty)$ the following interior Dirichlet problem (bounded by ∂b):

$$(\nabla^2 + k^2)\phi = 0, \tag{2'}$$

$$\phi(r) = 0, \quad r \in \partial b, \tag{7}$$

has only the trivial solution. Colton and Kress[32] took ∂b as a simple closed curve with diameter d that satisfies the estimation

$$d < \ln\left(1 + \frac{1}{2k_0^2}\right), \tag{8}$$

where k_0 is an arbitrary fixed positive number and $k \in [0,k_0]$. A convenient selection for facilitating the numerical implementation is taking ∂b as a circle with radius r^* that satisfies the estimation

$$r^* < 2.4048/k_0, \tag{9}$$

where the value $2.4048\ldots$ denotes the smallest positive zero of the Bessel function $J_0(k_0 r^*)$. Any solution to the modified problem, i.e., Eqs. (2), (4), (5), (6), and (8) [or (9)], is also a solution to the original problem.[30] Equation (6) is notably an additional constant for the unknown function ϕ so as to overcome the difficulty of the characteristic frequency. The motivation of this approach is similar to that of the CHIEF method that uses a related interior integral equation as the constraint.

According to potential theory, the velocity potential ϕ can be written in the form of the single layer potential on $\partial B \cup \partial b$ as

$$\phi(p) = \int_{\partial B \cup \partial b} \sigma(q) G_k(p,q) dS(q), \tag{10}$$

where the simple source function σ is assumed to be Hölder continuous at $p \in \partial B \cup \partial b$, $p(x,y)$ is the field point, and $q(x',y')$ is the source point. The free-space Green's function G_k for the Helmholtz equation in 2D can be expressed as

$$G_k(p,q) = \frac{i}{4} H_0^{(1)}(kR), \tag{11}$$

where $H_0^{(1)}(kR)$ denotes the Hankel function of the first kind and order zero, and R denotes the distance between the field point p and the source point q. By substituting Eq. (10) into boundary condition (4) and constraint (6), we obtain, from potential theory

$$-\frac{1}{2}\sigma(p) + \int_{\partial B \cup \partial b} \sigma(q) \frac{\partial G_k}{\partial n_p} dS(q) = f(p), \quad p \in \partial B, \tag{12}$$

$$-\frac{1}{2}\sigma(p) + \int_{\partial B \cup \partial b} \sigma(q) \left(\frac{\partial}{\partial n_p} - i \right) G_k dS(q) = 0, \quad p \in \partial b. \tag{13}$$

These are boundary integral equations of the second kind involving unknown source strength σ. Combining Eqs. (12) and (13) gives rise to unique solutions for all wave frequencies; see Krutitskii[30] for the detailed mathematical description.

According to the previous presentation, the velocity potential ϕ for the scattering problems can be written as

$$\phi(p) = \int_{\partial B \cup \partial b} \sigma(q) G_k(p,q) dS(q) + \phi^{\text{inc}}(p), \tag{14}$$

where ϕ^{inc} denotes the incident velocity potential. The two related boundary integral equations are

$$-\frac{1}{2}\sigma(p) + \int_{\partial B \cup \partial b} \sigma(q) \frac{\partial G_k}{\partial n_p} dS(q) + \frac{\partial \phi^{\text{inc}}(p)}{\partial n_p} = 0, \quad p \in \partial B, \tag{15}$$

$$-\frac{1}{2}\sigma(p) + \int_{\partial B \cup \partial b} \sigma(q) \left(\frac{\partial}{\partial n_p} - i \right) G_k dS(q) + \frac{\partial \phi^{\text{inc}}(p)}{\partial n_p} - i\phi^{\text{inc}}(p) = 0, \quad p \in \partial b, \tag{16}$$

where we have assumed $f(p) = 0$, i.e., an acoustically hard case. Equations (10) and (12)–(16) notably contain singular kernels. Section III presents a method for removing these singularities so as to enhance the efficiency of the numerical implementation.

III. ORDINARY INTEGRAL EQUATION FORMULATION

Equation (12) can be rewritten by applying the subtraction–addition technique as follows:

$$-\frac{1}{2}\sigma_1(p)+\int_{\partial B}\sigma_1(q)\left(\frac{\partial G_k}{\partial n_p}-\frac{\partial G}{\partial n_q}\right)dS(q)$$
$$+\int_{\partial B}(\sigma_1(q)-\sigma_1(p))\frac{\partial G}{\partial n_q}dS(q)+\sigma_1(p)\int_{\partial B}\frac{\partial G}{\partial n_q}dS(q)$$
$$+\int_{\partial b}\sigma_2(q)\frac{\partial G_k}{\partial n_p}dS(q)=f(p),\quad p\in\partial B, \tag{17}$$

where σ_1 is the source function on the body surface ∂B and σ_2 is the source function on the auxiliary inner surface ∂b. The free-space Green's function $G(p,q)$ for the 2D Laplace equation can be expressed as

$$G(p,q)=-\frac{1}{2\pi}\ln R. \tag{18}$$

Further substituting the Gauss flux theorem[31]

$$\int_{\partial B}\frac{\partial G(p,q)}{\partial n_q}dS(q)=-\frac{1}{2},\quad p\in\partial B, \tag{19}$$

into Eq. (17) yields

$$-\sigma_1(p)+\int_{\partial B}\sigma_1(q)\left(\frac{\partial G_k}{\partial n_p}-\frac{\partial G}{\partial n_q}\right)dS(q)+\int_{\partial B}(\sigma_1(q)$$
$$-\sigma_1(p))\frac{\partial G}{\partial n_q}dS(q)+\int_{\partial b}\sigma_2(q)\frac{\partial G_k}{\partial n_p}dS(q)$$
$$=f(p),\quad p\in\partial B. \tag{20}$$

The preceding integral equation notably contains bounded integration functions only. We observe that the first integrand can be set equal to zero as $p\to q$; in the second integral, we have

$$\lim_{p\to q}\frac{\partial G}{\partial n_q}=-\frac{\kappa(q)}{4\pi}, \tag{21}$$

where $\kappa(q)$ denotes the boundary curvature at point $p=q$;[33] the integration function in the third integral is obviously bounded since $p\neq q$.

Equation (13) can be rewritten as

$$-\frac{\sigma_2(p)}{2}+\int_{\partial B}\sigma_1(q)\left(\frac{\partial}{\partial n_p}-i\right)G_k dS(q)+\int_{\partial b}\sigma_2(q)$$
$$\times\left(\frac{\partial G_k}{\partial n_p}-\frac{\partial G}{\partial n_q}\right)dS(q)+\int_{\partial b}(\sigma_2(q)-\sigma_2(p))$$
$$\times\frac{\partial G}{\partial n_q}dS(q)+\sigma_2(p)\int_{\partial b}\frac{\partial G}{\partial n_q}dS(q)-i\int_{\partial b}\sigma_2(q)$$
$$\times(G_k-G)dS(q)-i\int_{\partial b}(\sigma_2(q)-\sigma_2(p))GdS(q)$$
$$-i\sigma_2(p)\int_{\partial b}GdS(q)=0,\quad p\in\partial b. \tag{22}$$

For convenience, as was discussed in Sec. II, choosing the interior surface ∂b as a circle with radius r^* results in

$$\int_{\partial b}G\ dS(q)=-r^*\ln r^*. \tag{23}$$

Substituting Eq. (23) and the Gauss flux theorem (19) into Eq. (22) leads to

$$-\sigma_2(p)+\int_{\partial B}\sigma_1(q)\left(\frac{\partial}{\partial n_p}-i\right)G_k\ dS(q)+\int_{\partial b}\sigma_2(q)$$
$$\times\left(\frac{\partial G_k}{\partial n_p}-\frac{\partial G}{\partial n_q}\right)dS(q)+\int_{\partial b}(\sigma_2(q)-\sigma_2(p))$$
$$\times\frac{\partial G}{\partial n_q}dS(q)-i\int_{\partial b}\sigma_2(q)(G_k-G)dS(q)-i\int_{\partial b}(\sigma_2(q)$$
$$-\sigma_2(p))GdS(q)+i\sigma_2(p)r^*\ln r^*=0,\quad p\in\partial b. \tag{24}$$

The first integral in the preceding equation is regular since $p\neq q$; the second, third, and fifth integrands can be set equal to zero as $p\to q$; in the fourth integral, Yang[19] obtained

$$\lim_{p\to q}(G_k-G)=-\frac{1}{2\pi}\left(\gamma+\ln\frac{k}{2}\right)+\frac{i}{4}, \tag{25}$$

where γ is the Euler's constant that is given by

$$\gamma=\lim_{n\to\infty}\left(\sum_{m=1}^{n}\frac{1}{m}-\ln n\right)=0.577\ 215\ldots\ .[34]$$

Equation (24) is therefore an ordinary integral equation. Equations (20) and (24) are conducive to numerical implementation for the unknown source functions σ_1 on ∂B and σ_2 on ∂b because they contain completely singularity-free integrals; that is, the standard quadrature rules can be directly applied for the computation without other specific techniques.

The velocity potential ϕ in the acoustic field can now be calculated from Eq. (10) once the density functions σ_1 and σ_2 are given. For ϕ on the body surface ∂B, the nonsingular form of Eq. (10) can be written as

$$\phi(p)=\int_{\partial B}\sigma_1(q)(G_k-G)dS(q)+\int_{\partial B}\left[\sigma_1(q)\right.$$
$$\left.-\sigma_1(p)\frac{\sigma^*(q)}{\sigma^*(p)}\right]G\ dS(q)-\frac{\sigma_1(p)}{\sigma^*(p)}\Phi_e$$
$$+\int_{\partial b}\sigma_2(q)G_k\ dS(q),\quad p\in\partial B, \tag{26}$$

where σ^* denotes a source distribution on ∂B and makes the surface an equipotential of potential Φ_e that is defined by

$$\Phi_e=-\int_{\partial B}\sigma^*(q)G\ dS(q). \tag{27}$$

The first integrand in Eq. (26) is bounded by observing the relationship (25); the second integrand is bounded since its value can be set equal to zero as $p\to q$; the last integral is regular since $p\neq q$. Equation (27) notably contains a loga-

rithmic type of singularity as $p(x,y)\to q(x',y')$. Observe that Φ_e remains constant in the interior domain of an equipotential surface; its value can then be computed by locating the field point p inside the boundary surface ∂B. For convenience, locating the field point p at the origin (inside the boundary surface), we then have $R^2=(x-x')^2+(y-y')^2=x'^2+y'^2$. This process leads to a regular integral

$$\Phi_e=\frac{1}{2\pi}\int_{\partial B}\sigma'(q)\ln(x'^2+y'^2)^{1/2}dS(q). \tag{28}$$

The preceding equation produces a unique solution σ^* for any given constant Φ_e, with one exception that the boundary ∂B is a Γ-contour.[31] For instance, for a circle of radius a, Eq. (28) gives

$$\Phi_e=a\sigma^*\ \ln\ a. \tag{29}$$

The function σ^* has no finite value according to Eq. (29) if $a=1$; Petrovsky[35] first observed this feature of the unit circle. This difficulty, however, can be averted by scaling. An alternative means of finding σ^* is using the fact that the velocity inside an equipotential body vanishes; this yields the following integral equation:

$$\sigma^*(p)=-2\int_{\partial B}\sigma^*(q)\frac{\partial G}{\partial n_p}dS(q),\quad p\in\partial B. \tag{30}$$

The singular kernel can be removed by rewriting this equation as follows:

$$\sigma^*(p)=-2\int_{\partial B}\left[\sigma^*(q)\frac{\partial G}{\partial n_p}-\sigma^*(p)\frac{\partial G}{\partial n_q}\right]dS(q)$$
$$-2\sigma^*(p)\int_{\partial B}\frac{\partial G}{\partial n_q}dS(q),\quad p\in\partial B. \tag{31}$$

Further applying the Gauss flux theorem (19) leads to

$$0=\int_{\partial B}\left[\sigma^*(q)\frac{\partial G}{\partial n_p}-\sigma^*(p)\frac{\partial G}{\partial n_q}\right]dS(q),\quad p\in\partial B. \tag{32}$$

The solution to Eq. (32) is not unique and requires specifying a given value of σ^* at any fixed point on the surface so as to make the solution unique. Note that it does not matter which solution to Eq. (32) is selected. For instance, by applying the iteration method, we have

$$\sigma^*_{m+1}(p)=\sigma^*_m(p)+\int_{\partial B}\left(\sigma^*_m(q)\frac{\partial G}{\partial n_p}\right.$$
$$\left.-\sigma^*_m(p)\frac{\partial G}{\partial n_q}\right)dS(q),\quad p\in\partial B, \tag{33}$$

where the subscript m refers to the mth iteration. The equipotential Φ_e can be obtained via Eq. (28) after solving σ^* from Eq. (33). Substituting σ^* and Φ_e into Eq. (26) solves the surface function ϕ by directly evaluating regular integrals.

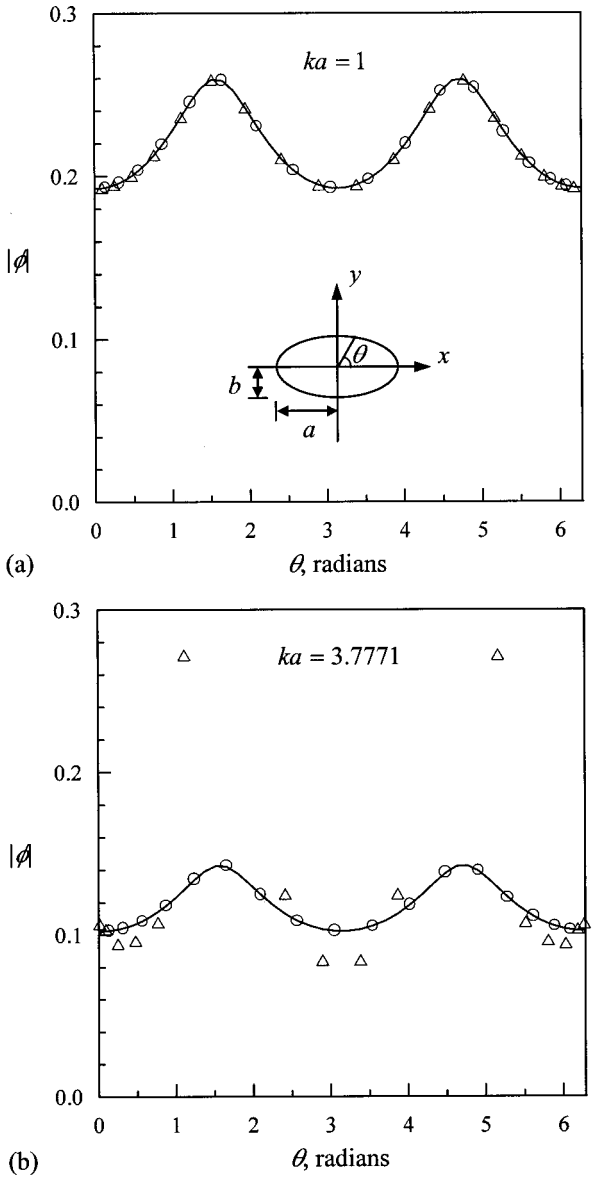

FIG. 1. Amplitude of surface function for a radiating elliptic cylinder of $a/b=2/1$ with normalized wave number (a) $ka=1$ and (b) $ka=3.7771$ [—: exact solution; ○: the present method, and $r^*/a=0.1$ where r^* is the radius of the auxiliary interior circle; △: the classical simple source method].

The corresponding singularity-free integral equations for the scattering problems can be obtained straightforwardly according to the previous presentation; further outlining them is therefore not necessary.

IV. NUMERICAL EXAMPLES

A. Application to radiation

Consider a radiating elliptic cylinder with the ratio of semimajor to semiminor axis $a:b=1:0.5$ (Fig. 1). The Cartesian coordinates x and y are related to the elliptic-cylinder coordinates η and θ by

$$x=f\ \cosh\ \eta\ \cos\ \theta,\quad y=f\ \sinh\ \eta\ \sin\ \theta, \tag{34}$$

where $f=(a^2-b^2)^{1/2}$, $a=f\ \cosh\ \eta_0$, $b=f\ \sinh\ \eta_0$, $0\leqslant\eta<\infty$, and $0\leqslant\theta<2\pi$. For convenience, a point source of unit strength was placed at the center of the elliptic cylinder so as

to simulate this radiation problem. The acoustic pressure and the velocity at the body surface were then explicitly determined; this velocity was used as the known boundary condition. We further placed a circle of radius $r^*=0.1a$, i.e., the auxiliary interior surface, at the center of the elliptic cylinder. The 60- and 5-point Gauss–Legendre quadrature formulas were applied along the body surface and the inner circle, respectively, for evaluating integrals in Eqs. (20) and (24). The source functions σ_1 and σ_2 were then calculated from the resulting system of linear algebraic equations that was solved in terms of the LU decomposition method. Equation (26) finally evaluated the surface function ϕ after solving σ^* from Eq. (33). Note in passing that the source function σ^* and the related equipotential Φ_e were derived in terms of certain properties of potential theory and therefore depend on the body shape only; that is, σ^* and Φ_e are independent of the wave frequencies and the boundary conditions of a given acoustical problem. For comparison, both the classical simple source method, i.e., distributing point sources over the body surface, and the current approach were tested. Figure 1 plots the computed amplitudes of the surface function ϕ for the cases of the normalized wave number $ka=1$ and 3.7771 where the value 3.7771 . . . is a characteristic number of the problem and corresponds to a root of the modified Mathieu function of the first kind and order zero. Figure 1 indicates that the numerical result of the current approach correlates well with the exact solution. Using the classical simple source formulation fails to predict the surface function for $ka=3.7771$, as Fig. 1(b) shows. Figure 2 plots the corresponding relative error ε, defined by |(computed result—exact solution)/maximum of exact solution on the surface|, of Fig. 1 so as to clearly examine the numerical accuracy. The case of $r^*/a=0.2$ with five collocation points is also included in this figure. Figure 2 indicates that the relative error of the current approach is less than 2×10^{-4} for $ka=1$ and 4×10^{-3} for $ka=3.7771$. The accuracy of the current approach is notably comparable to that of the classical simple source method, as Fig. 2(a) shows.

Consider next a radiating rectangular cylinder with $a:b=1:2$ (Fig. 3). Placing a point source of unit strength at the center again simulated this radiation problem. The 40- and 20-point Gauss–Legendre quadrature formulas were applied along the long and short sides, respectively. The 5-point quadrature formula was applied along a circle of radius $r^*/a=0.1$, i.e., the auxiliary interior surface, which was located at the center of the rectangular cylinder. The numerical procedures resembled that of the previous case. In particular, for a straight segment ∂B of length l, we have

$$\int_0^l \sigma_1(q)\frac{\partial G_k(p,q)}{\partial n_p}dS(q)=0, \quad p,q\in\partial B, \tag{35}$$

that is useful for evaluating Eq. (12); also, for a point x at the location h, we have[31]

$$\int_0^l \ln|x-\xi|\,d\xi = h(\ln h-1)+k(\ln k-1),$$
$$h+k=l, \quad x,\xi\in\partial B, \tag{36}$$

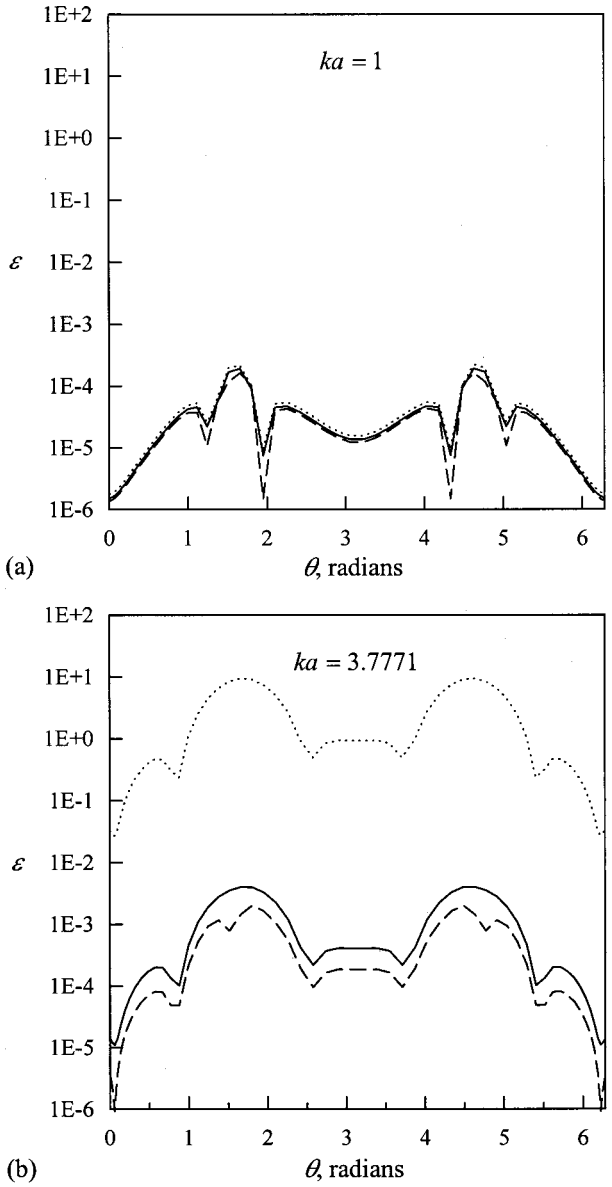

FIG. 2. Relative error ε of computed amplitude of surface function in Fig. 1 [—: the present method and $r^*/a=0.1$; ---: the present method and $r^*/a=0.2$; ⋯ : the classical simple source method].

that is useful for evaluating ϕ by expressing Eq. (10) in the form

$$\phi(p)=\int_{\partial B}\sigma_1(q)(G_k-G)dS(q)+\int_{\partial B}(\sigma_1(q)-\sigma_1(p))\times G\,dS(q)+\sigma_1(p)\int_{\partial B}G\,dS(q)+\int_{\partial b}\sigma_2(q)G_k\,dS(q). \tag{37}$$

Note that evaluating the equipotential Φ_e and the related source strength σ^* is not necessary for this case. Figure 3 plots the computed amplitudes of the surface function ϕ for the cases of $ka=1$ and 1.7562 where the value 1.7562 . . . is one of the characteristic numbers given by[36]

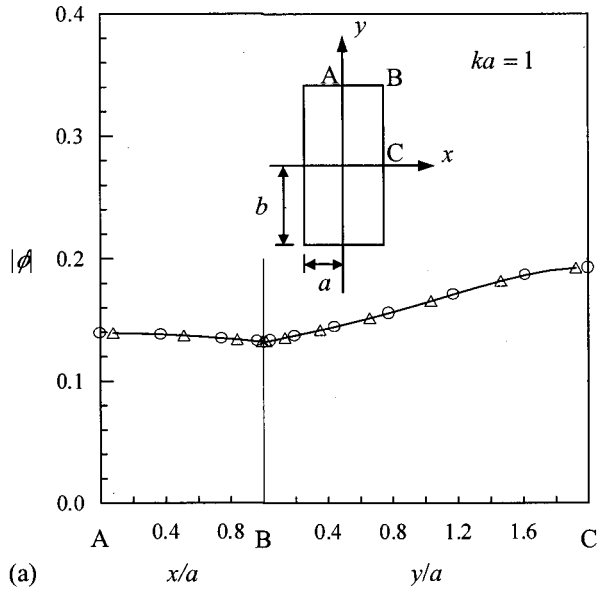

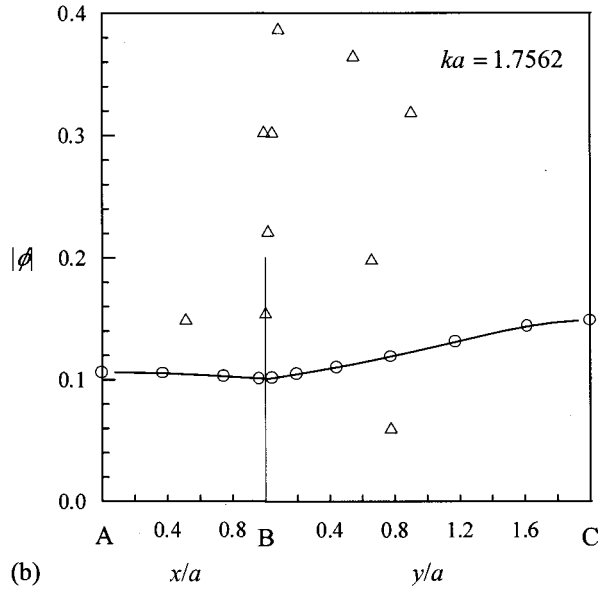

FIG. 3. Amplitude of surface function for a radiating rectangular cylinder of $a/b=1/2$ with normalized wave number (a) $ka=1$ and (b) $ka=1.7562$ [—: exact solution; ○: the present method, and $r^*/a=0.1$; △: the classical simple source method].

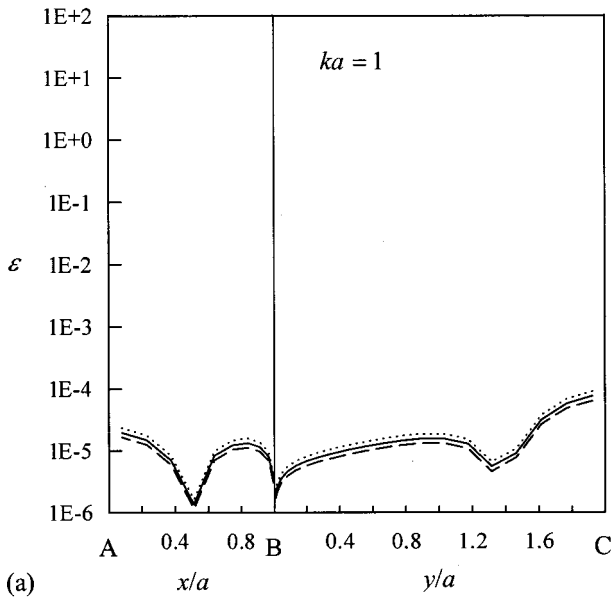

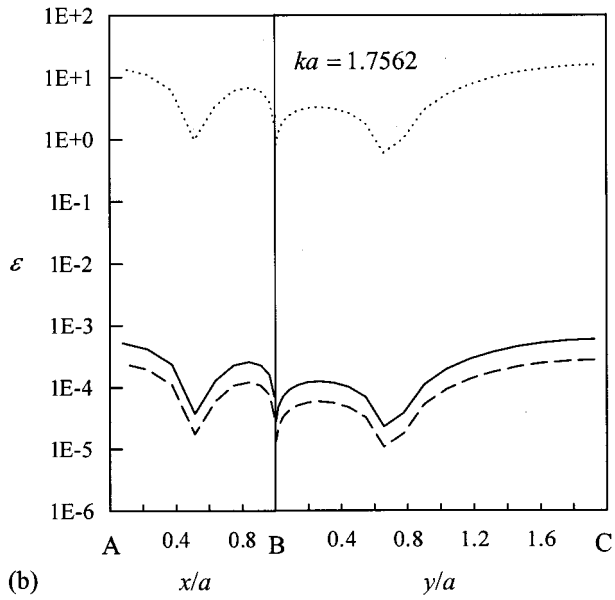

FIG. 4. Relative error ε of computed amplitude of surface function in Fig. 3 [—: the present method and $r^*/a=0.1$; ---: the present method and $r^*/a=0.2$; ⋯ : the classical simple source method].

$$k_{nm}^2=\left(\frac{n\pi}{2a}\right)^2+\left(\frac{m\pi}{2b}\right)^2, \quad n,m=0,1,2,\ldots . \tag{38}$$

Figure 3 indicates that the numerical result agrees well with the exact solution. A remarkable discrepancy occurs when applying the classical simple source method at $ka=1.7562$, as Fig. 3(b) shows. The surface function ϕ notably remains finite at the corners. Figure 4 examines the corresponding relative error ε of Fig. 3. Both numerical methods have the same degree of accuracy at $ka=1$, as Fig. 4(a) shows. The relative error of the current approach is less than 10^{-4} for $ka=1$ and 6×10^{-4} for $ka=1.7562$. The case of $r^*/a=0.2$ with five collocation points is also included in Fig. 4. The great accuracy implies that the selection of the inner surface is not critical for bodies with corners, when compared with the off-boundary approach including the off-boundary methods and the wave superposition methods.

B. Application to scattering

Consider a 1:0.5 acoustically hard elliptic cylinder exposed to a plane wave of unit amplitude at broadside incidence (Fig. 5). The discretization system and the numerical procedures resembled that of the previous radiation case. Figure 5 plots the computed amplitudes of the surface function ϕ for $ka=1$ and 3.7771. The corresponding exact solution of the surface function is also plotted, and can be written as[37]

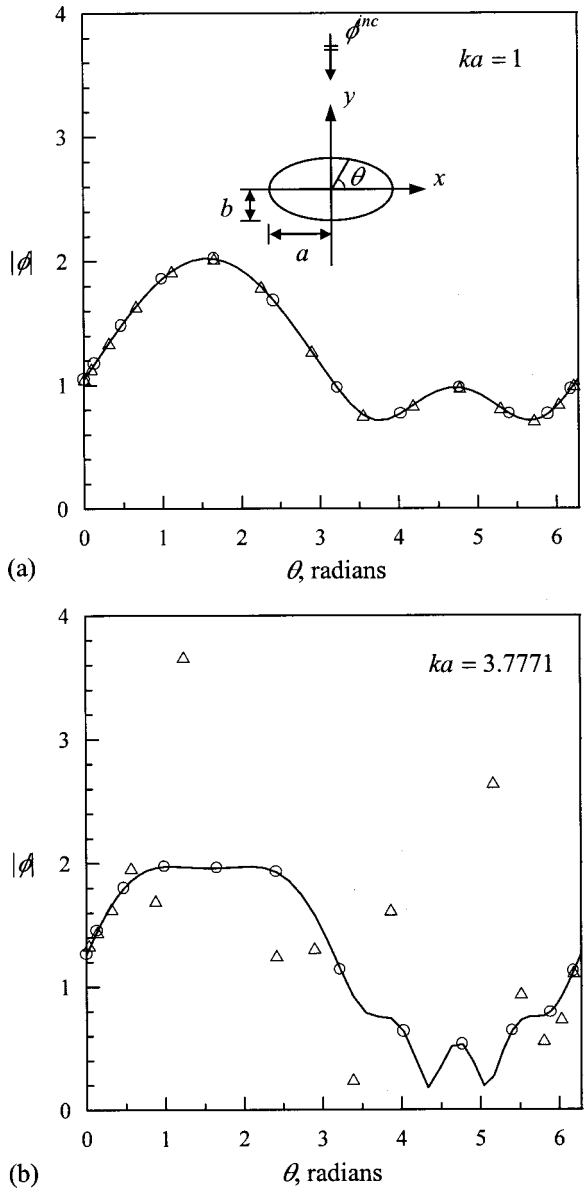

FIG. 5. Amplitude of surface function for a hard elliptic cylinder of $a/b=2/1$ exposed to a plane wave with normalized wave number (a) $ka=1$ and (b) $ka=3.7771$ [—: exact solution; ○: the present method, and $r^*/a=0.1$; △: the classical simple source method].

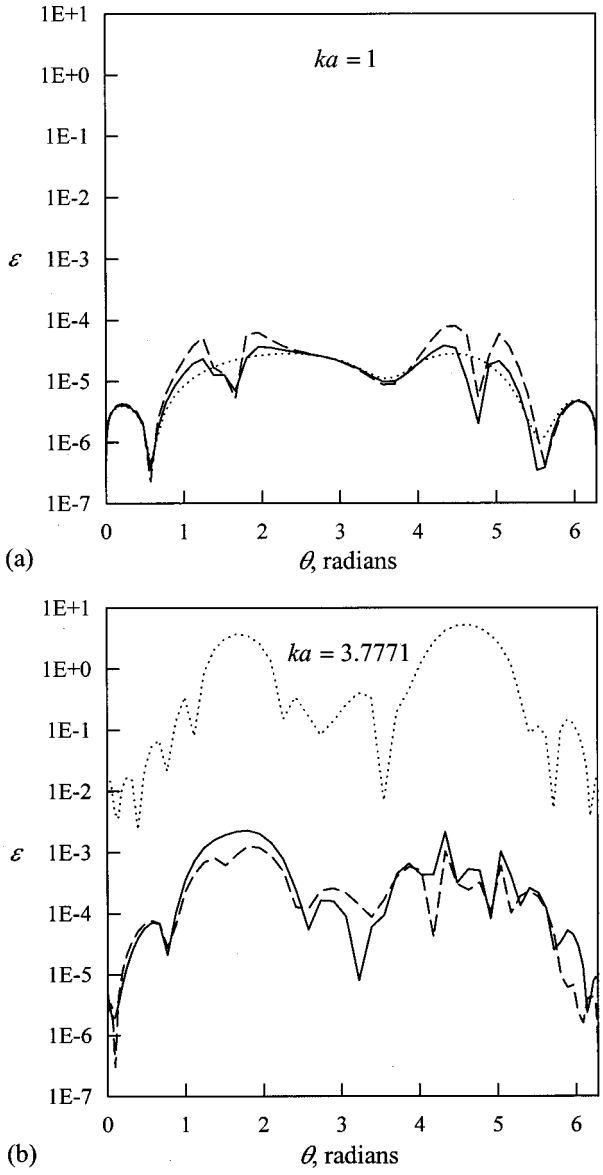

FIG. 6. Relative error ε of computed amplitude of surface function in Fig. 5 [—: the present method and $r^*/a=0.1$; ---: the present method and $r^*/a=0.2$; ⋯ : the classical simple source method].

$$\phi=\sqrt{\frac{8\pi}{\xi_0^2-1}}\sum_{m=0}^{\infty}(-1)^m \times\left[\frac{iSe_{2m}(\upsilon,0)}{N_{2m}^{(e)}}\frac{1}{(\partial/\partial\xi_0)Re_{2m}^{(3)}(\upsilon,\xi_0)}Se_{2m}(\upsilon,\tau) + \frac{So_{2m+1}(\upsilon,0)}{N_{2m+1}^{(o)}}\frac{1}{(\partial/\partial\xi_0)Ro_{2m+1}^{(3)}(\upsilon,\xi_0)}So_{2m+1}(\upsilon,\tau)\right], \tag{39}$$

where $\xi_0=\cosh\eta_0$, $\upsilon=kf$, $\tau=\cos\theta$, Se and So are the Mathieu even and odd angular functions, respectively, $Re^{(3)}$ and $Ro^{(3)}$ are the Mathieu even and odd radial functions of the third kind, respectively, and $N_i^{(e)}$ and $N_i^{(o)}$ are defined by the following orthogonal relations:

$$\int_0^{2\pi}Se_i(\upsilon,\cos\theta)Se_j(\upsilon,\cos\theta)d\theta=\begin{cases}0, & \text{for } i\neq j,\\ N_i^{(e)}, & \text{for } i=j,\end{cases} \tag{40}$$

$$\int_0^{2\pi}So_i(\upsilon,\cos\theta)So_j(\upsilon,\cos\theta)d\theta=\begin{cases}0, & \text{for } i\neq j,\\ N_i^{(o)}, & \text{for } i=j,\end{cases} \tag{41}$$

and

$$\int_0^{2\pi}Se_i(\upsilon,\cos\theta)So_j(\upsilon,\cos\theta)d\theta=0, \tag{42}$$

the last for $i=j$ as well as $i\neq j$; see Stratton[38] for definitions and further information of Mathieu functions. Figure 5 indicates that the current approach successfully predicts the acoustic scattering field and the classical simple source method breaks down at the characteristic number $ka=3.7771$. Figure 6 plots the relative error of Fig. 5. Both numerical methods have the same degree of accuracy for

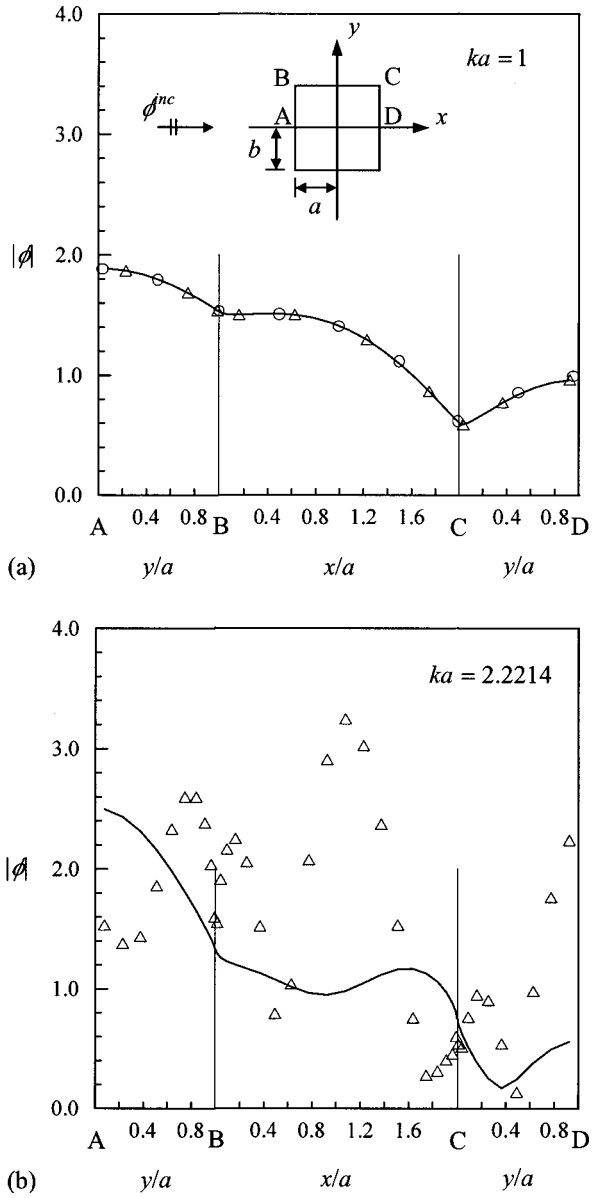

FIG. 7. Amplitude of surface function for a hard square cylinder, i.e., $a/b=1$, exposed to a plane wave with normalized wave number (a) $ka=1$ and (b) $ka=2.2214$ [—: the present method and $r^*/a=0.1$; ○: Mei and Van Bladel's numerical result; △: the classical simple source method].

$ka=1$, as Fig. 6(a) shows. The case of $r^*/a=0.2$ with five collocation points was also calculated. The relative error of the current approach is less than 10^{-4} for $ka=1$ and 2×10^{-3} for $ka=3.7771$. Figure 6 indicates that both cases of $r^*/a=0.1$ and 0.2 in general have the same degree of accuracy.

Consider finally an acoustically hard square cylinder exposed to a plane wave with unit amplitude directed along the positive x axis (Fig. 7). We applied the 20-point Gauss–Legendre quadrature formula along each side of the square cylinder, the 5-point quadrature along the interior circle of radius $r^*/a=0.1$, and the same numerical procedures as that in the previous radiation case. Figure 7 depicts the variation of the surface function $|\phi|$ for $ka=1$ and 2.2214 where the value 2.2214 . . . corresponds to a characteristic number of this problem. Figure 7(a) also plots Mei and Van Bladel's[2] numerical result for scattering by a perfectly conducting square cylinder. For analytical treatments of the perfectly and nonperfectly conducting rectangular cylinders we refer the reader to Refs. 39 and 40; however, numerically evaluating these solutions requires special techniques. Figure 7(a) indicates that the numerical result of the current approach correlates well with that of Mei and Van Bladel.[2] The simple source method fails at the characteristic number $ka=2.2214$, as to be expected. Observe again the continuity of the surface function ϕ at the corners. The satisfactory prediction for the scattering problems implies that the selection of the inner surface is also not critical for bodies with corners.

V. CONCLUSIONS

This paper has derived the singularity-free boundary integral formulation based on the auxiliary inner surface technique for investigating the acoustic scattering and radiation in two dimensions. The modified formulation is expressed in a form of distributing monopole functions on the whole boundary. Test examples include the cases of the elliptic and rectangular cylinders. Numerical calculations, with a careful examination of the accuracy, confirm the availability and efficiency of the modified formulation. We summarize other specific features of the current approach below.

(a) The singularity-free formulation allows the direct application of the standard quadrature rule over the entire integration domain; that is, the collocation points are exactly the positions at which the integration points are located. In the standard boundary element methods (BEMs), the integration points are usually much more than the collocation points at which the unknown function is evaluated, except using one-point quadrature for each element. This fact implies that the current approach is highly efficient since the establishment of the matrix is more economic in terms of the computer time. See Yang[41] for the detailed comparison on the efficiency of the two methods when treating potential flow problems. In this case, the CPU time of the current approach is about one half of that of the flat-element constant-source boundary element method when using 50 collocation points.

(b) The singularity-free formulation allows the element-free discretization of the boundary surfaces; that is, giving only boundary nodal data is sufficient for the computation, as was done in Sec. IV. For the arbitrarily shaped bodies, we can transform the integral equation formulation into a parametric form that provides necessary information of the nodal points; see Yang[19] for the detailed description and the related numerical implementation. In the BEMs, the boundary surfaces should be divided into small elements (planar or curved, etc.) with certain approximations on the density functions (constant or linearly varying strength, etc.). Such approximations are known to be the main source of numerical error in the BEMs; see, for example, Katz and Plotkin[42] for the history of the development from

low- to high-order versions for dealing with the related approximations. This observation implies that the current approach is highly accurate.

(c) The current approach avoids the evaluation of the hypersingular integrals arising in Burton and Miller's method. Treating the hypersingular integrals requires special techniques that involve different degrees of complexity in computation. Burton and Miller's method overcomes the fictitious characteristic frequency problem, but usually reduces the degree of accuracy of the solution as well; see, for example, Yang[20] for the details. This is a result arising from evaluating the double-normal derivative of the Green's function. Controlling the accuracy of high-order derivatives of a function is known to be more difficult than that of low-order derivatives. Section IV demonstrates that the current approach and the standard simple source method have in general the same degree of accuracy. This implies that the current approach can uniformly control the accuracy of the solution over a frequency range including the characteristic frequencies. This feature is of practical usefulness in engineering applications. Another drawback of Burton and Miller's method lies in imposing a more stringent smoothness requirement on the density function. This requirement may give rise to a serious problem in computation; see, for example, Liu and Rizzo[18] for the detailed description. The proposed formulation avoids such a difficulty. The current approach therefore provides a significant improvement over Burton and Miller's method.

(d) The auxiliary inner surface can be taken to be as small as possible such that placing only a few nodal points on it is sufficient for the computation. These nodal points are used to modify the singular matrices arising from the nonexistence problem. Previous experience in determining the ''good'' inner points is not required. Thus, selecting the effective inner points of the current approach is much easier than that of the CHIEF method. Note also that Benthien and Schenck[8] compared numerous commonly used methods and concluded that the CHIEF method, using one-point quadrature, is still a viable and highly efficient approach. The proposed formulation can also achieve the same level of the numerical efficiency by observing that both methods involve at most the first derivative of the Green's function.

(e) The numerical accuracy of the wave superposition methods is known to be sensitive to the location of the inner surface, particularly when the body surface has discontinuities. The selection of the inner surface of the current approach is easier than that of the wave superposition methods. We observe that the modified formulation evaluates the unknown function exactly on the body surface and the unknown on the inner surface is only used to modify the singular matrices. Thus, the solution to the modified formulation does not depend on the location of the inner surface. In the wave superposition methods, the collocation points are taken to lie on the inner surface so as to avoid the singular kernels. The satisfaction of the boundary conditions on the body surface then yields the associated integral equation. The surface solution is therefore evaluated indirectly from the calculated data on the inner surface. Such a procedure gives rise to the difficulty of effectively selecting the optimum inner surface. Moreover, the Burton–Miller-type of the wave superposition methods contains the double-normal derivative of the Green's function. Evaluating such a complicated integrand is time consuming and may reduce the degree of accuracy, as was discussed in (c).

According to the above discussion, the current approach provides a promising alternative for the related acoustic wave problems. Extension to 3D problems is conceptually straightforward by applying Yang's regularization technique.[43] In many circumstances, especially in industrial applications, the BEMs are known to be almost inevitable. Incorporating parts of the current approach into the BEMs is technically possible and thus merits attention.

ACKNOWLEDGMENTS

The author would like to thank the National Science Council, R.O.C., for partially supporting this research under Contract No. NSC 89-2611-E-006-051.

[1] M. B. Friedman and R. Shaw, ''Diffraction of pulses by cylindrical obstacles of arbitrary cross section,'' ASME J. Appl. Mech. **29**, 40–46 (1962).
[2] K. K. Mei and J. G. Van Bladel, ''Scattering by perfectly-conducting rectangular cylinders,'' IEEE Trans. Antennas Propag. **11**, 185–192 (1963).
[3] R. P. Banaugh and W. Goldsmith, ''Diffraction of steady elastic waves by surfaces of arbitrary shape,'' J. Acoust. Soc. Am. **35**, 1590–1601 (1963).
[4] F. J. Rizzo, ''An integral equation approach to boundary-value problems of classical elastostatics,'' Q. Appl. Math. **25**, 83–95 (1967).
[5] T. A. Cruse, ''Numerical solutions in three-dimensional elastostatics,'' Int. J. Solids Struct. **5**, 1259–1274 (1969).
[6] *Recent Advances in Boundary Element Methods*, edited by C. A. Brebbia (Pentech, London, 1978).
[7] C. C. Chien, H. Rajiyah, and S. N. Atluri, ''An effective method for solving the hypersingular integral equations in 3D acoustics,'' J. Acoust. Soc. Am. **88**, 918–937 (1990).
[8] W. Benthien and H. A. Schenck, ''Nonexistence and nonuniqueness problems associated with integral equation methods in acoustics,'' Comput. Struct. **65**, 295–305 (1997).
[9] H. A. Schenck, ''Improved integral formulation for acoustic radiation problems,'' J. Acoust. Soc. Am. **44**, 41–58 (1968).
[10] A. J. Burton and G. F. Miller, ''The application of integral equation methods to the numerical solution of some exterior boundary value problems,'' Proc. R. Soc. London, Ser. A **323**, 201–210 (1971).
[11] A. F. Seybert and T. K. Rengarajan, ''The use of CHIEF to obtain solutions for acoustic radiation using boundary integral equations,'' J. Acoust. Soc. Am. **81**, 1299–1306 (1987).
[12] D. J. Segalman and D. W. Lobitz, ''SuperCHIEF: A modified CHIEF method,'' SANDIA Labs Report SAND-90-1266 (1990).
[13] A. F. Seybert and T. W. Wu, BEMAP *User's Manual* (Spectronics, New York, 1989), Version 2.4.
[14] T. W. Wu and A. F. Seybert, ''A weighted residual formulation for the CHIEF method in acoustics,'' J. Acoust. Soc. Am. **90**, 1608–1614 (1991).
[15] W. L. Meyer, W. A. Bell, B. T. Zinn, and M. P. Stallybrass, ''Boundary integral solutions of three-dimensional acoustic radiation problems,'' J. Sound Vib. **59**, 245–262 (1978).
[16] J. Hadamard, *Lectures on Cauchy's Problem in Linear Partial Differential Equations* (Yale University Press, New Haven, CT, 1923).
[17] G. Krishnasamy, L. W. Schmerr, T. J. Rudolphi, and F. J. Rizzo, ''Hypersingular boundary integral equations: Some applications in acoustic and

elastic wave scattering,'' ASME J. Appl. Mech. **57**, 404–414 (1990).
[18] Y. Liu and F. J. Rizzo, ''A weakly singular form of the hypersingular boundary integral equation applied to 3-D acoustic wave problems,'' Comput. Methods Appl. Mech. Eng. **96**, 271–287 (1992).
[19] S. A. Yang, ''A boundary integral equation method for two-dimensional acoustic scattering problems,'' J. Acoust. Soc. Am. **105**, 93–105 (1999).
[20] S. A. Yang, ''Evaluation of 2D Green's boundary formula and its normal derivative using Legendre polynomials, with an application to acoustic scattering problems,'' Int. J. Numer. Methods Eng. **53**, 905–927 (2002).
[21] L. G. Copley, ''Integral equation method for radiation from vibrating bodies,'' J. Acoust. Soc. Am. **41**, 807–810 (1967).
[22] J. D. Achenbach, J. D. Kechter, and Y.-L. Xu, ''Off boundary approach to the boundary element method,'' Comput. Methods Appl. Mech. Eng. **70**, 191–201 (1988).
[23] K. A. Cunefare, G. Koopmann, and K. Brod, ''A boundary element method for acoustic radiation valid for all wave numbers,'' J. Acoust. Soc. Am. **85**, 39–48 (1989).
[24] V. D. Kupradze, ''Fundamental Problems in the Mathematical Theory of Diffractions,'' translated by C. D. Benster, NSB Rep. No. 2008 (1952).
[25] L. H. Chen and D. G. Schweikert, ''Sound radiation from an arbitrary body,'' J. Acoust. Soc. Am. **35**, 1626–1632 (1963).
[26] G. H. Koopmann, L. Song, and J. B. Fahnline, ''A method for computing acoustic fields based on the principle of wave superposition,'' J. Acoust. Soc. Am. **86**, 2433–2438 (1989).
[27] R. Jeans and I. C. Mathews, ''The wave superposition method as a robust technique for computing acoustic fields,'' J. Acoust. Soc. Am. **92**, 1156–1166 (1992).
[28] D. T. Wilton, I. C. Mathews, and R. A. Jeans, ''A clarification of nonexistence problems with superposition method,'' J. Acoust. Soc. Am. **94**, 1676–1680 (1993).
[29] R. D. Miller, E. T. Moyer, Jr., H. Huang, and H. Überall, ''A comparison between the boundary element method and the wave superposition approach for the analysis of the scattered fields from rigid bodies and elastic shells,'' J. Acoust. Soc. Am. **89**, 2185–2196 (1991).
[30] P. A. Krutitskii, ''A new approach to reduction of the Neumann problem in acoustic scattering to a nonhypersingular integral equation,'' IMA J. Appl. Math. **64**, 259–269 (2000).
[31] M. A. Jaswon and G. T. Symm, *Integrated Equation Methods in Potential Theory and Elastostatics* (Academic, London, 1977).
[32] D. Colton and R. Kress, *Integral Equation Methods in Scattering Theory* (Wiley, New York, 1983).
[33] V. I. Smirnov, *A Course of Higher Mathematics* (Pergamon, Oxford, 1964), Vol. IV.
[34] *Handbook of Mathematical Functions with Formulas, Graphs, and Mathematical Tables*, edited by M. Abramowitz and I. A. Stegun (Dover, New York, 1972).
[35] I. G. Petrovsky, *Lectures on Partial Differential Equations* (Interscience, New York, 1954).
[36] J. Van Bladel, *Electromagnetic Fields* (McGraw-Hill, New York, 1964).
[37] *Electromagnetic and Acoustic Scattering by Simple Shapes*, edited by J. J. Bowman, T. B. A. Senior, and P. L. E. Uslenghi (Hemisphere, New York, 1987).
[38] J. A. Stratton, *Electromagnetic Theory* (McGraw-Hill, New York, 1941).
[39] K. Kobayashi, ''Diffraction of a plane electromagnetic wave by a rectangular conducting rod (I)—rigorous solution by the Wiener-Hopf technique,'' Bull. Facul. Sci. & Eng., Chuo University **25**, 229–261 (1982).
[40] E. Topsakal, A. Büyükaksoy, and M. İdemen, ''Scattering of electromagnetic waves by a rectangular impedance cylinder,'' Wave Motion **31**, 273–296 (2000).
[41] S. A. Yang, ''A solution method for two-dimensional potential flow about bodies with smooth surfaces by direct use of the boundary integral equation,'' Commun. Num. Meth. Eng. **15**, 469–478 (1999).
[42] J. Katz and A. Plotkin, *Low-Speed Aerodynamics—From Wing Theory to Panel Methods* (McGraw-Hill, New York, 1991).
[43] S. A. Yang, ''Acoustic scattering by a hard or soft body across a wide frequency range by the Helmholtz integral equation method,'' J. Acoust. Soc. Am. **102**, 2511–2520 (1997).

Meridional ray backscattering enhancements for empty truncated tilted cylindrical shells: Measurements, ray model, and effects of a mode threshold

Scot F. Morse[a] and Philip L. Marston
Department of Physics, Washington State University, Pullman, Washington 99164-2814

(Received 26 February 2002; revised 3 July 2002; accepted 6 July 2002)

Narrow-band backscattering experiments are used to characterize a meridional ray enhancement on a tilted, finite empty cylindrical shell having a blunt truncation. The meridional ray of the lowest order flexural leaky Lamb wave is examined, which has previously been shown to lead to large backscattering enhancements for excitation frequencies near and above the shell's coincidence frequency. The measurements are used to validate a convolution formulation ray theory describing the far-field backscattered amplitudes. Comparisons are also made with an approximate partial wave series solution for the finite cylindrical shell. The amplitude of the meridional ray enhancement is dependent on the nature of the reflection of the leaky wave from the shell truncation. While the peak measured amplitude agrees with predictions at low frequencies, experiments indicate the enhancement is degraded at high frequencies and exhibits an abrupt drop near the frequency of the mode threshold (cutoff) for the next-highest flexural mode. The nature of the leaky wave end reflection is examined using an approximate calculation of the energy reflection coefficient for leaky waves on a semi-infinite free plate. Results suggest the observed degradation is the result of mode conversion effects. © *2002 Acoustical Society of America.* [DOI: 10.1121/1.1504470]

PACS numbers: 43.20.Fn, 43.40.Fz, 43.35.Pt [LLT]

I. INTRODUCTION

Previous experiments have shown that an enhancement in the backscattering by submerged, finite thick-walled cylindrical shells occurs at large tilt angles over a broad range of frequencies.[1–4] This enhancement has been attributed to the excitation of the lowest-order flexural type Lamb wave, called the a_0 mode, along the meridian of the cylinder. Figure 1 describes the general ray path which contributes most significantly to the far-field backscattering.

Due to the high frequencies examined and the thick-walled nature of the shell considered here (fractional thickness of 7.6%), existing thin-shell theories for membrane wave propagation[5,6] or scattering responses[7–9] are not directly applicable. In an earlier paper[1] an approximate partial wave series (PWS) solution that included three-dimensional linear elasticity was presented to calculate the far-field backscattering amplitude. The theory compared well with experiments for frequencies below $ka \approx 32$. Extending the PWS theory to higher frequencies is complicated since its implementation involves a relatively inefficient algorithm (more so than other PWS solutions) and is prone to difficulties in computing special functions at high frequencies. A more significant limitation of the PWS solution was demonstrated in higher-frequency measurements where the experimental results differed greatly from the PWS solution in a region where the meridional ray enhancement associated with the a_0 leaky lamb wave is affected by the proximity of the threshold for the propagation of the a_1 Lamb wave.[3] An understanding of the high-frequency response of tilted bluntly truncated cylinders is important for interpreting high-resolution sonar signatures.[10,11]

A ray formulation not inherently susceptible to these problems was developed by Marston for generalized surface waves on weakly curved elastic surfaces.[12] This ray theory has been successfully applied to the meridional ray enhancement in cases where exact solutions are known: infinite cylinders[12] and infinite cylindrical shells.[2] Recently, it was shown to agree well with the Rayleigh wave meridional enhancement on finite solid cylinders.[13]

In this paper the meridional ray enhancement for flexural waves on a finite cylindrical shell is examined in narrow-band backscattering experiments. The backscattering is examined in detail in Secs. II and III as the tilt angle of the shell is changed and as a function of frequency. The results are compared with the approximate PWS solution and with Marston's ray theory. An overview of the ray theory and limitations of the PWS solution are addressed in Sec. IV. It is found that an understanding of the nature of the reflection of the leaky wave from the shell truncation is important in understanding the observed meridional ray response. To address this, the behavior of leaky wave reflection from a truncation is discussed in Sec. V. An approximate calculation of the reflection coefficient for a leaky wave traveling on a flat plate is employed to qualitatively explain the observed scattering response.

II. NARROW-BAND BACKSCATTERING EXPERIMENT

Narrow-band backscattering experiments were performed in a cylindrical redwood water tank using a monostatic scattering setup. The finite cylindrical shell was suspended from a computer-controlled rotation stage by fine

[a]Now with Division of Computer Science, Western Oregon University, Monmouth, OR 97361.

 0001-4966/2002/112(4)/1318/9/$19.00

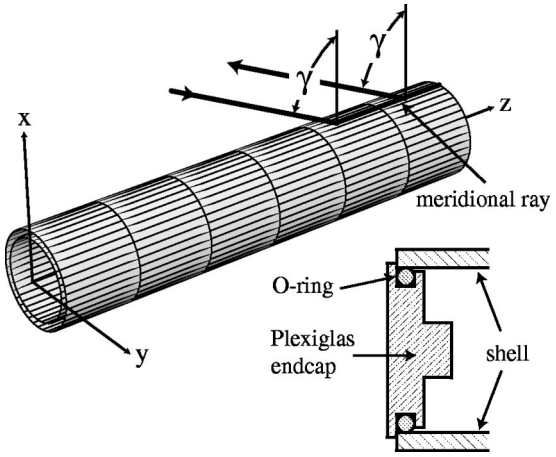

FIG. 1. Ray diagram for a meridional leaky ray backscattering enhancement on a truncated cylindrical shell, and sectional view of the endcaps used in the experiment. The meridional leaky ray which contributes to the far-field backscattering experiment is launched very near the far truncation along the cylinder's meridian. The ray also detaches from the shell close to the end.

polyethylene line attached to Plexiglas endcaps. A diagram of the endcaps is shown in Fig. 1. A single rubber O-ring at each end was used to form a water-tight seal and to form an end boundary condition compliant compared to a fixed or welded endcap. The bulk and shear moduli of the O-rings are very much less than the corresponding moduli of steel. Care was taken to minimize the contact area between the Plexiglass and the end of the shell. The majority of contact area was maintained by the rubber O-rings. The shell used was constructed from type 304 stainless steel and had an outer radius of $a=19.05$ mm, thickness to radius ratio of $h/a=0.076$, and a length of $L=22.86$ cm ($L/a=12$). This is the same shell examined in Refs. 1, 2, and 4. The shell was suspended approximately 2.3 m from the source—a 1-in. diam immersion type transducer having a resonance near 750 kHz. This source was operated in transmit/receive sequence using a Ritec™ Clamped Diplexer (model RCDS-2A) with a simple square envelope tone burst having 20 to 40 cycles of a selected frequency.

The meridional ray enhancement of the a_0 mode has been shown to be well isolated from other scattering features in the time domain.[4] It is found near the timing of the scattering by the closest rear corner of the cylinder (i.e., the timing of a signal propagating through the water to the closest portion of the far truncation of the cylinder and back to the receiver). Near the leaky wave coupling angle for a given frequency, the backscattered signal displays a simple enhancement feature which builds to steady state and decays quickly after the tone burst. An example is shown in Fig. 2(a). A measurement of the amplitude of the enhancement can be made over the apparent steady-state region. During the experiments the entire meridional ray enhancement was located and the signal averaged on a digital oscilloscope before being downloaded to the computer. The envelope of this signal was then found using the Hilbert transform. The steady-state region was identified manually and windowed; the overall enhancement level was then found by averaging the envelope inside this window. In some cases it was necessary to increase the number of cycles in the incident tone

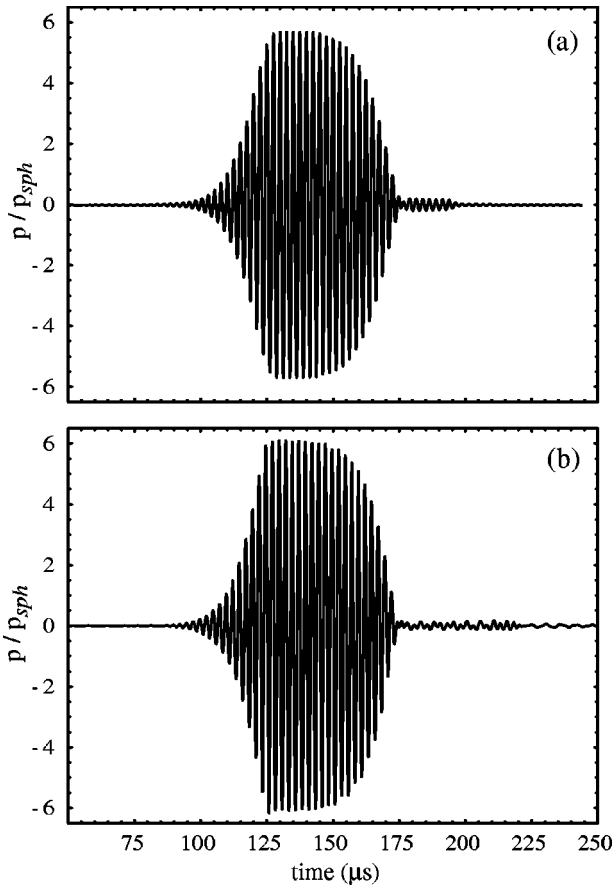

FIG. 2. (a) Measured backscattering pressure response after calibration from the finite cylindrical shell at the peak a_0 meridional ray amplitude for a 20-cycle tone burst with center frequency of 400 kHz ($ka=32.3$, $\gamma=48.0$ deg). (b) Synthesized time series for the same shell and tone burst derived from an approximate partial wave series solution. In the numerical solution the meridional ray peak occurs at 49.08 deg. The pressure amplitude is relative to the far-field scattered pressure amplitude of the specular reflection from a rigid sphere having the same radius as the cylindrical shell. No free parameters were used in the normalization. The time scale is zero referenced to the specular reflection from the cylinder at broadside incidence.

burst in order to obtain a satisfactory steady-state region.

The overall amplitude of the scattering response was calibrated relative to the specular reflection from a reference sphere. To obtain the normalization a solid stainless-steel sphere (type 440, radius=34.93 mm) was placed at approximately the same location as the center of the cylinder and a measurement made at the same frequency, driving voltage and water temperature as the cylinder measurements. The steady-state portion of the specular reflection was isolated and measured as discussed above. With knowledge of this amplitude and the amplitude found for scattering by the cylinder, as well as the distances from the source to the cylinder and the sphere and their radii, the backscattering form function may be found in a straightforward manner.[13] The procedure outlined in Ref. 13 was followed also to take into account, in an approximate way, the elastic properties of the reference sphere. After calibration, a form function of unity corresponds to the geometrically calculated amplitude of the specular reflection from a perfectly rigid, immovable sphere having the same radius as the cylinder. The time record in

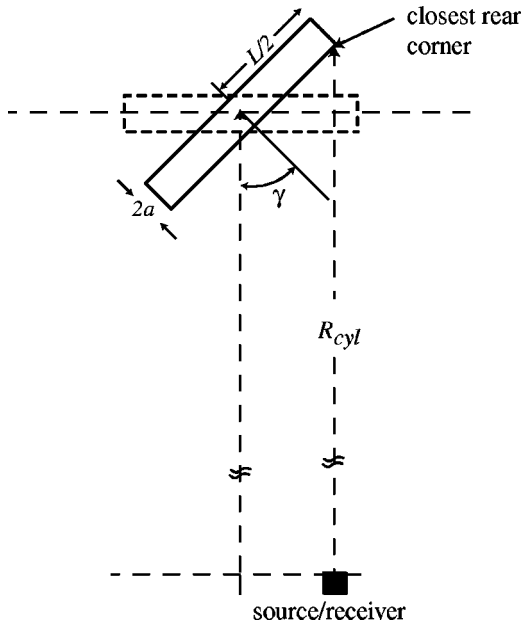

FIG. 3. Geometry of the experimental scattering setup. Notice the source/receiver has been translated horizontally to be in line with the closest rear corner of the cylinder. This is in attempt to eliminate the need for an angular correction which necessarily results from the finite source-to-target distance.

Fig. 2(a) shows the experimental scattered pressure after calibration.

There is one other detail of the experiment important to note. In a similar experiment examining the meridional enhancement for Rayleigh waves on a truncated solid cylinder, Gipson[13] noted an angular shift in the measured meridional peak relative to that expected from ray theory. This was attributed to the finite source-to-target distance and the associated changes in leaky wave coupling conditions. For a finite separation distance the tilt angle of the cylinder does not exactly equal the angle of incidence of a ray intersecting the surface of the cylinder near its truncation. A correction between tilt angle and launching angle was needed. The present experiment was arranged in such a way as to eliminate the need for an angular correction. Figure 3 notes this change. The source/receiver was translated laterally to such a point that it approximately lined up with the closest rear center of the truncation. For this setup, as long as the meridional ray is launched very near the truncation the leaky wave coupling angle will be nearly equal to the cylinder tilt angle regardless of the finite separation distance. The separation distance R_{cyl} was used in the calibration.

III. CHARACTERIZATION OF THE MERIDIONAL RAY ENHANCEMENT: VARIABLE INCIDENCE ANGLES AND FREQUENCY DEPENDENCE

Previous broadband backscattering experiments[1,2,4] covering frequencies up to 500 kHz ($ka=40$) have shown that this meridional ray enhancement of the a_0 mode is a relatively simple peak in the backscattering, originating at near end-on incidence at the coincidence frequency (here, $f \approx 190$ kHz, $ka \sim 16$) and curving smoothly toward lower tilt angles as the frequency is increased. The broadband measurements lacked calibration and were not carried out with sufficient resolution, in either frequency or tilt angle domains, to characterize the fine details of the enhancement or compare with ray theory or numerical calculations.

The narrow-band measurements detailed in Sec. II are well suited for this purpose. For selected frequencies the scattering response was measured and normalized over a narrow range of angles centered about the enhancement peak. Figure 4 shows these measurements for six frequencies. The experimental values are the empty circles. Also shown are the results of the ray theory (solid line) and an approximate partial wave series (PWS) solution, which are discussed in Sec. IV. Both the ray theory and the PWS solution predict the location and general shape of the enhancement. There remains an angular offset which is most noticeable at low frequencies, however. The cause of this offset was not determined, although it should be noted from an examination of Fig. 5(b) that the offset is small in comparison with the angular range over which the peak evolves. The ray and PWS solutions agree well, similar to the agreement of the same ray theory and the exact PWS solution for an infinite cylindrical

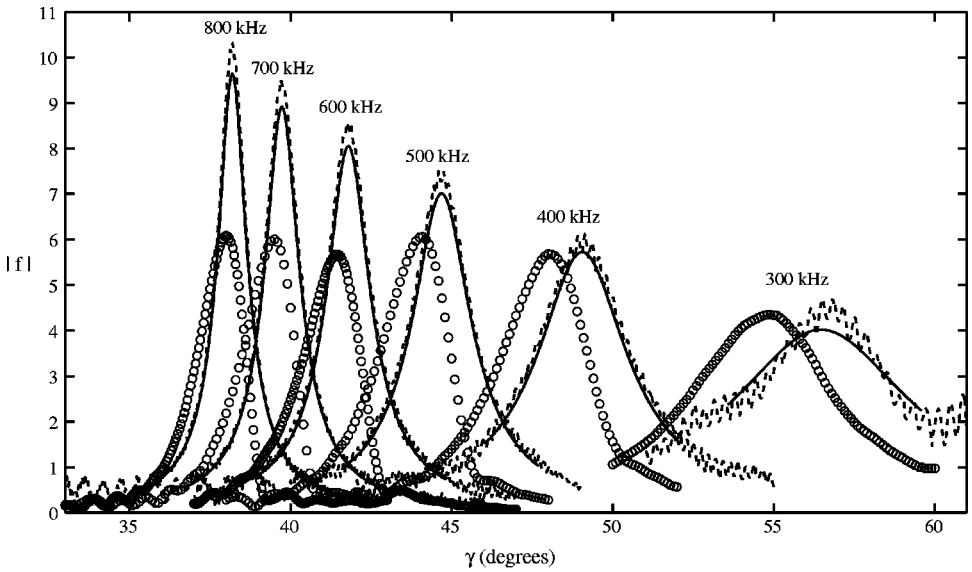

FIG. 4. Backscattering form function magnitude for the meridional ray enhancement of the a_0 mode as a function of cylinder tilt angle for a number of frequencies. Open circles are experimental values obtained with tone-burst measurements; the continuous lines are the result of the ray formulation (Ref. 14); and the dashed lines are calculated using the approximate partial wave series solution. Both the ray theory and PWS calculations are shown for a leaky wave end-reflection coefficient $|B|=1$. On this amplitude scale the backscattering form function for a rigid sphere having the same radius as the cylinder has $|f|=1$.

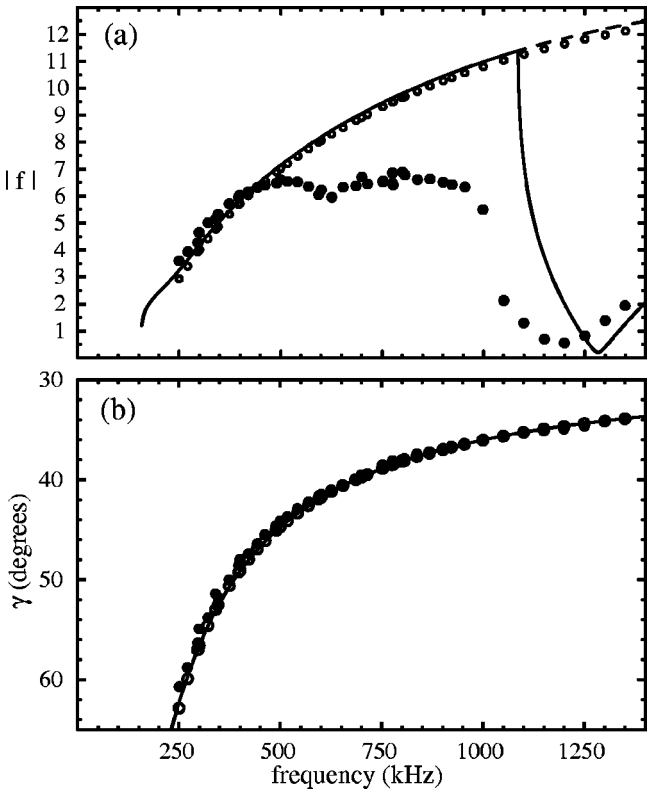

FIG. 5. (a) Form function magnitude at the peak meridional ray enhancement angle [shown in (b)] as a function of frequency. The solid points are experimental data, open circles are the results of the ray approximation using wave number values from an infinite fluid-loaded cylindrical shell and a unimodular end-reflection coefficient. The dashed curve is the same ray approximation but with wave number values for a flat plate fluid loaded on both sides; the solid curve is the same as the dashed curve except the approximate end-reflection coefficient from Sec. V is used (see Fig. 8). In (b) the solid curve corresponds to the leaky wave coupling angle for the a_0 mode for an infinite plate fluid loaded on both sides and the open circles are for the infinite cylindrical shell case.

shell.[2] The amplitude of the enhancement is comparable with the ray and PWS solutions below 400 kHz; however, as the frequency increases the amplitude predicted by theory increases steadily while the measured enhancement appears to remain near a value of $|f| \approx 6$.

To address this behavior additional measurements of just the peak enhancement amplitude were made at higher frequencies. The solid circles in Fig. 5(a) show the peak enhancement amplitude as a function of frequency up to 1.350 MHz. These values are taken from either the maximum value found in an automated angle scan (as in Fig. 4) or from a single scattering measurement found by manually optimizing the scattering response. In the latter case either the frequency was manually scanned (at low frequencies) or the tilt angle was manually scanned (at high frequencies) or both to localize the maximum in the scattering response. The tilt angle for the maximum response is shown as the solid circles in Fig. 5(b). Also shown in each of these figures are the amplitudes and locations predicted by the ray theory under several approximations as noted in Sec. IV.

The limit of increasing enhancement amplitude as seen in Fig. 4 can now be seen as part of a more general roll-off which continues to near 1 MHz. Near this frequency the amplitude decreases rapidly and then recovers slightly at the highest frequency shown. It should be noted that, for the three lowest amplitude data points (1.150, 1.200, and 1.250 MHz), there was difficulty obtaining an appropriate steady-state region over which to evaluate the scattering amplitude. These three points should therefore be considered upper bounds of the scattering response.

Before discussing the likely cause of these features and the comparisons with theory, some details of the ray theory and the approximate PWS solution should be presented. Although presented elsewhere[12,13] (with applications to solid rods), the following section provides an overview relevant to the present application to shells.

IV. MERIDIONAL RAY AMPLITUDES FROM RAY AND APPROXIMATE PARTIAL WAVE SERIES ANALYSES

The ray theory used in Figs. 4 and 5 is an extension of a convolution formulation ray theory valid for evaluating the amplitude of leaky waves traveling on weakly curved surfaces. In three cases the ray theory has been applied to cases where exact solutions are known: evaluating the far-field scattering form function near the meridional ray enhancement for scattering by infinite cylinders,[12] infinite cylindrical shells,[2] and including the associated helical wave contributions for infinite cylindrical shells.[15] An extension was made to apply it to the case of backscattering by a finite cylinder and for tilt angles adjacent to the enhancement peak.[13] As discussed in Ref. 13 the magnitude of the form function for backscattering by a finite cylinder, normalized by the far-field backscattering from an ideal rigid sphere, can be written as

$$|f_l(\gamma)| \approx 2|B| \sqrt{\frac{k_l}{\alpha_l}} F_\rho(\mu) \frac{e^{\mu\Delta_C}}{|\sqrt{\Delta_C \Delta_S}|} \left| \int_{\mu\Delta_C}^{\infty} \mathrm{erfc}(\sqrt{w\Delta_S}) dw \right|, \tag{1}$$

where $\mu = (\alpha_l a)\tan\theta_l$, $\Delta_C = \cos\theta_l / \cos\gamma$, $\Delta_S = 1 + i(k_l/\alpha_l)(\sin\gamma/\sin\theta_l - 1)$, $F_\rho(\mu) = [(\mu/F(\mu)) - \mu + (1/2)]^{-1/2}$ and $F(\mu) = e^\mu \sqrt{\pi\mu}\,\mathrm{erfc}(\sqrt{\mu})$. The angle θ_l is the leaky wave coupling angle given by the trace velocity matching condition $\theta_l = \sin^{-1}(c/c_l) = \sin^{-1}(k_l/k)$, where $k_l = \omega/c_l$ is the real part of the leaky wave number and $k = \omega/c$ is the incident wave number in the surrounding fluid. The leaky wave coupling angle also defines the peak enhancement angle. The imaginary part of the leaky wave number is given by α_l. The term erfc( ) is the complementary error function. The backscattering form function magnitude depends linearly on the magnitude of the end reflection coefficient B. This is the coefficient of reflection at the truncation of the cylinder for the leaky wave that is launched on the cylinder, as shown by the ray diagram in Fig. 1. The theory assumes the end is blunt, i.e., the cylinder is truncated in a plane perpendicular to the axis of the cylinder.

In order to evaluate Eq. (1) the real, k_l, and imaginary, α_l parts of the leaky wave number must be known. These were approximated by wave numbers calculated for an empty infinite cylindrical shell of the same configuration with exterior fluid loading. For meridional propagation the dispersion curves of the axisymmetric mode, having no cir-

cumferential propagating components, for the appropriate lowest-order flexural wave mode were calculated.[2] These dispersion curves were used in evaluating Eq. (1) for the ray theory curves in Fig. 4 and open circle points in Fig. 5. In both these cases the leaky wave end-reflection coefficient $|B|$ was taken to be unity. Because of the high frequencies examined in the present case (considerably above the ring frequency and the coincidence frequency) the propagation of leaky waves on the shell is nearly isotropic. (The weak anisotropy at these frequencies has been shown to be important, however, in extending the present ray theory to include helical flexural waves for tilt angles less than θ_l.[15]) In addition to the leaky wave numbers calculated for an infinite shell, the dispersion curves for a flat plate were evaluated. The dashed curve in Fig. 5 corresponds to the leaky wave numbers for a flat plate fluid loaded on both sides. To account for the radiation of energy into the fluid on only one side of the plate, as is the case for the hollow cylindrical shell, when using the flat plate results the imaginary part of the leaky wave number was reduced by a factor of one-half as an approximation.

In both cases when an end-reflection coefficient of unity is applied, the agreement with measurements at low frequencies is good but deviates slowly above 500 kHz and then abruptly near 1 MHz. As can be seen from Fig. 4 the approximate PWS solution follows the ray theory rather than the measurements. The PWS solution[1] takes into account the three-dimensional elasticity of the shell, in the same manner as the exact solution for an infinite thick-walled shell. However, it treats the finite end conditions as approximately simply supported. This condition requires that the radial u_ρ and the azimuthal u_ψ component of the displacement vector, as well as the axial stress resultant T_{zz}, vanish at all points on the cylinder truncation. Consider the intensity vector for simple isotropic elastic fields[16]

$$\boldsymbol{I} = -\left(\frac{\partial \boldsymbol{u}}{\partial t}\right) \cdot \underset{\sim}{\boldsymbol{T}}. \tag{2}$$

Here, $\boldsymbol{u}$ is the displacement vector and $\underset{\sim}{\boldsymbol{T}}$ is the stress dyadic. The intensity vector, or structural intensity, represents the density of energy flow in the elastic field and has units of power per unit area. The time-averaged power flow through the end of the cylindrical shell (surface S with area element dA) is then given by

$$\overline{P_z|_{z=\pm L/2}} = \overline{\int_S \pm(\hat{z}\cdot \boldsymbol{I})\, dA}$$

$$= \overline{\int_S -\left(\frac{\partial u_\rho}{\partial t} T_{\rho z} + \frac{\partial u_\psi}{\partial t} T_{\psi z} + \frac{\partial u_z}{\partial t} T_{zz}\right) dA}, \tag{3}$$

where the bar indicates a time average of the underlying quantity and cylindrical coordinates (ρ, ψ, z), having the origin at the center of the cylinder, are assumed. Because u_ρ, u_ψ, and T_{zz} must vanish on the end surfaces S, the total time-averaged power flow through each end vanishes identically. This then forces any leaky wave end-reflection coefficient to be unimodular; since in addition, coupling to other shell modes is not introduced in this end condition. This explains the similarity between the ray and approximate PWS theories.

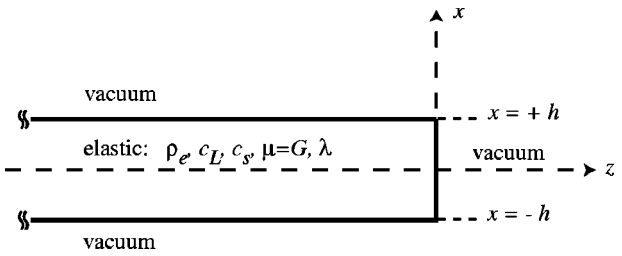

FIG. 6. Cross section of the end of a semi-infinite flat plate and the associated coordinate system used in the approximate calculation of the leaky wave end-reflection coefficient. A single Lamb mode is incident from the $-z$ direction which reflects off the truncation. The amplitude of the reflected wave depends on whether other modes of the same symmetry are propagating or evanescent at the selected frequency.

V. APPROXIMATE CALCULATION OF THE LAMB WAVE END-REFLECTION COEFFICIENT FOR A SEMI-INFINITE PLATE: MODE CONVERSION EFFECTS

The abrupt drop in the meridional ray enhancement near 1 MHz can be understood if one allows for mode conversion from the incident a_0 leaky wave into other propagating and nonpropagating modes when the wave reflects from the blunt end. It is known that when a Lamb wave on a free or submerged plate reflects from an abrupt truncation, it may be partially converted to a different mode of the same symmetry.[17–22] When all the other modes of the plate are nonpropagating, it is mostly the same mode which is reflected from the end. However, if other modes are propagating at that frequency then some portion of the incident energy can be reflected into the other modes.

A simple example illustrates this behavior and enables an approximation of the end-reflection coefficient for a semi-infinite flat plate *without fluid loading*. The modeling of a fluid-loaded semi-infinite plate or cylindrical shell would be considerably more difficult to illustrate, since no quantitative models are currently available that do not require extensive numerical modeling (such as finite-element or finite-difference calculations). Fluid-loading effects are not negligible for the frequencies examined here; however, the present approximation illustrates the abrupt drop in amplitude at the mode threshold and demonstrates the need for modeling the effects of fluid loading for frequencies even below cutoff.

Shen *et al.*[23] have derived a simple least-squares approach to calculating the behavior of Lamb wave reflection at the end of a semi-infinite free plate. The method involves satisfying the free end boundary condition at discrete points along the edge using the contribution of many modes, both propagating and evanescent, and then solving the resulting overdetermined set of linear equations in the least-squares sense. The reflected plate mode amplitudes are output directly and an estimate of the error (i.e., not satisfying the boundary condition) can be made. Consider the end region of a semi-infinite isotropic elastic plate. Figure 6 shows a schematic of the plate and a definition of the coordinate system used. A single propagating Lamb mode of the plate is excited

at some point at $z=-\infty$ and travels undisturbed toward the end at $z=0$. Since the plate is not fluid loaded (and assumed to be composed of a lossless elastic material) the term propagating strictly implies that the associated wave number is purely real. It is easy to see then that the Lamb wave experiences no damping as it propagates towards the end. We assume that the incident Lamb wave disturbance may be represented by the exact solution for a Lamb wave propagating in a semi-infinite thick plate right up to the plate end. At distances far from the end, relative to the plate thickness, this is a valid assumption. Severe limitations on this assumption exist, however, even at large distances when the frequency is near or above the first mode cutoff.[17] Near the edge the stress distribution of the incident wave may vary considerably from its infinite plate counterpart. However, since no rigorous solution for the semi-infinite or finite plate have been derived, even for stress-free boundaries, we proceed with the above assumption. Considering the incident Lamb wave, with a known stress and displacement distribution, one simply wishes to satisfy the required boundary conditions at the end (zero stress) with an as yet unknown set of reflected Lamb waves.

Following Shen, the boundary conditions at the end of the plate must be satisfied using the one incident mode and a large number of reflected modes. At the end, the total in-plane and tangential stress must vanish

$$\Sigma_{zz}(x)=T_{zz}^{\mathrm{inc}}(x)+\sum_{j=1}^{2N+2} A_j T_{zz}^{j}(x)=0,$$

$$z=0,\quad x\in[-h,h],$$

$$\Sigma_{xz}(x)=T_{xz}^{\mathrm{inc}}(x)+\sum_{j=1}^{2N+2} A_j T_{xz}^{j}(x)=0. \tag{4}$$

The A_j's are the unknown amplitudes of the reflected modes and T_{zz}^{inc} and T_{xz}^{inc} are the stress components of the incident mode. Since the stresses may be derived by means of a scalar and vector potential (having only one component), which have only one amplitude constant between them, it may be easily shown that the amplitude coefficients in Eqs. (4) are the same. It should be understood that the sums are carried out over the lowest two modes (labeled $-a_0$ and $-a_1$ in Fig. 7); thus the $+2$, plus N pairs (i.e., $2N$) of complex modes, where N is to be determined by the level of acceptable error in the calculation. The dispersion relation for either antisymmetric or symmetric modes of a plate has solutions in the general case consisting of two purely real roots, a finite number of purely imaginary roots and an infinite number of roots described by a complex wave number.

Equations (4) are then evaluated at $M+1$ evenly spaced discrete points

$$x_m=(2h/M)m-h,\quad m=0,1,\ldots,M, \tag{5}$$

along the end. This results in $2(M+1)$ equations having $2(N+1)$ unknowns (i.e., the A_j's). It is possible to solve this set of overdetermined equations (which have complex values) approximately in a least-squares sense. The mean-squared error to be minimized is

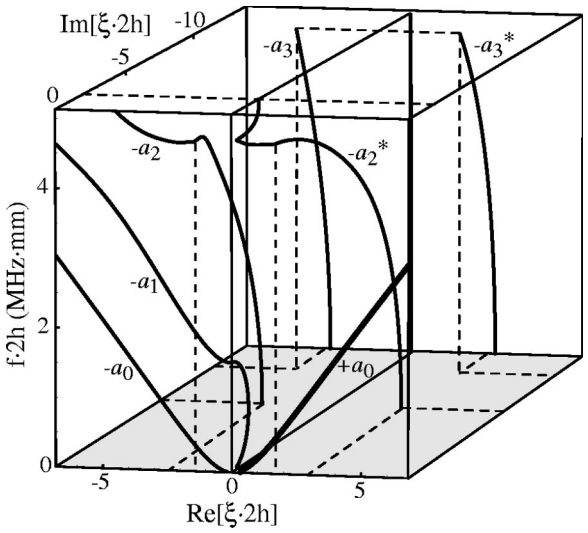

FIG. 7. Complex dispersion curves for the first several antisymmetric modes of an infinite free plate with thickness $2h$, where ξ is the in-plane (z axis) wave number. Modes labeled with a minus sign either propagate towards $z=-\infty$ (where the wave number is purely real) or decay as $z\to-\infty$ (when complex). The asterisk indicates the "conjugate" mode. The thicker black curve indicates the incident mode.

$$E=\sum_{m=0}^{M}\left[|\Sigma_{zz}(x_m)|^2+|\Sigma_{xz}(x_m)|^2\right]. \tag{6}$$

The amplitude coefficients in Eqs. (4) are not proportional to the energy in the wave in a simple way. To be of use, each mode must be normalized with respect to the time-averaged power flow of the incident wave. From Eq. (3), the time-averaged power flow is

$$\overline{\mathbf{P}_z|_{z=0}}=\overline{\int_{-h}^{h}(\nu_z T_{zz}+\nu_x T_{xz})dx}, \tag{7}$$

where ν_x and ν_z are the components of velocity and the bar indicates a time average. Since all quantities are time harmonic, ($e^{-i\omega t}$), the real part of this expression, representing real power flow, may be written

$$\mathrm{Re}[\mathbf{P}_z]|_{z=0}=\int_{-h}^{h}\left\{\frac{i\omega}{4}[u_z^* T_{zz}+u_x^* T_{xz})-(u_z T_{zz}^*+u_x T_{xz}^*)\right\}dx, \tag{8}$$

where the asterisk denotes complex conjugation. The relative power flow for the jth mode with respect to the incident mode is

$$\mathbf{P}_r^j=\frac{\mathrm{Re}[\mathbf{P}_z^j]}{\mathrm{Re}[\mathbf{P}_z^{\mathrm{inc}}]}. \tag{9}$$

Noting that the relative reflection amplitude coefficients, A_j, are simply multiplicative in Eq. (4), the reflection coefficient representative of power is found to be

$$R_j=(A_j^* A_j)\mathbf{P}_r^j, \tag{10}$$

which is real. A statement of conservation of energy then follows

$$\left| \sum_{j=1}^{2N+2} R_j \right| = 1. \tag{11}$$

Nonpropagating modes may have positive or negative R_j.

To minimize Eq. (6) and evaluate the reflection coefficient in Eq. (10), expressions for the stresses and displacements in the plate as well as the complete dispersion curves for all relevant modes must be known. The dispersion relations and associated displacements and stresses are well known for a free plate. For the antisymmetric modes the relevant expressions are listed in the Appendix. A search for roots of Eq. (A1) was carried out over the frequency range of interest.

An example of the lowest roots is shown in Fig. 7 in a manner similar to the dispersion of symmetric modes given by Mindlin.[24] The results are plotted in the familiar form of dispersion curves, which locate the root in the complex ξ plane for a given frequency. The vertical scale is in the units of frequency plate-thickness product (the wall thickness of the cylindrical shell is 1.45 mm). Only those complex modes having a negative imaginary part are shown; these are the only ones which are physical for the reflected waves. The complementary modes having a positive imaginary part grows exponentially as $z \to -\infty$ and are excluded. All the complex modes appear in what have been called ''conjugate'' pairs, pairs of evanescent modes, or pairs of waves having complex conjugate wave numbers.[17,19,23] This refers to the fact that the complex solutions of Eq. (A1) appear in pairs such that ξ^2 and $(\xi^2)^*$ are solutions. Only two of the complex pairs are shown in Fig. 7; however, another eight pairs were located and used in the subsequent calculation. These all have increasingly large negative imaginary parts of the wave number ξ and are less important in satisfying the boundary conditions. It is these pairs of complex modes which have been used to explain the phenomena of ''edge resonances'' in plates, disks, and rods.

The reflection coefficient in Eq. (10) was evaluated for an incident a_0 mode for the sample plate. Figure 8 shows the power reflection coefficients for the reflected a_0, a_1, a_2, and a_2^* modes. At the mode threshold of the a_1 (where the dispersion curve for the a_1 transitions from purely imaginary to purely real in Fig. 7), the amplitude of the reflected a_0 mode drops sharply as the amplitude of the a_1 mode converted wave increases. The amplitude of the a_0 mode increases again shortly after approaching zero, and increases to near-unity before exhibiting more complex behavior near the a_2 mode threshold. This behavior for the lowest antisymmetric mode is analogous to that of the lowest symmetric mode[23,25,26] and consistent with analytical[20,23,27] and numerical[28] results for antisymmetric modes. The only wave not labeled in Fig. 8 is the a_2^* mode, which is given by the barely visible dotted line. Below the a_2 mode threshold at 4.706 MHz mm the signs of the amplitude reflection coefficients for the a_2 and a_2^* modes are such that the total power carried by the conjugate pair vanishes.[29] Therefore, the small peaks shown for these subthreshold modes near 4.1 MHz mm cancel each other in Eq. (11). The reflection coefficient in Fig. 8 for the a_0 mode is applied, after the appropriate frequency plate-thickness scaling, to the effective plate corresponding to the finite cylindrical shell. The solid curve in Fig. 5(a) shows the ray theory result using $B = |R_{j=a_0}|$.

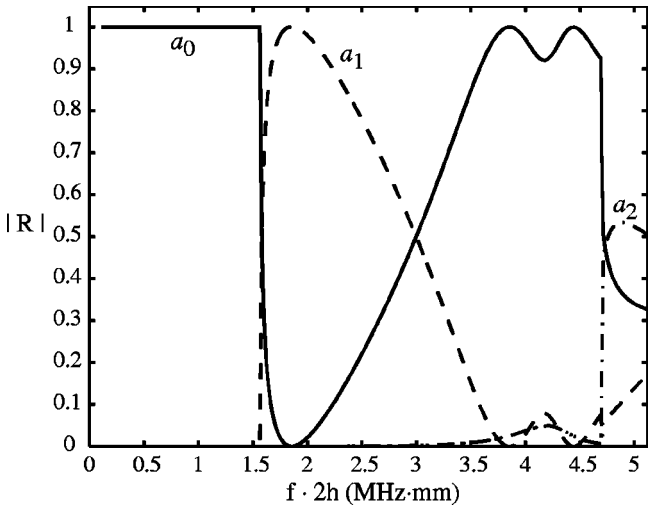

FIG. 8. Normalized power reflection coefficients for Lamb modes on a semi-infinite free plate with thickness $2h$ for an incident a_0 mode calculated using Shen's approximate least-squares method. The mode threshold of the a_1 occurs at 1.57 MHz mm. The a_2^* mode is the barely visible dotted curve (not labeled).

VI. DISCUSSION

The backscattering experiments reported here confirm that the meridional ray enhancement for antisymmetric leaky waves on finite cylindrical shells can significantly exceed backscattering levels for a rigid sphere having the same radius as the cylinder. These values greatly exceed those expected for a tilted bluntly truncated rigid cylinder of the same size.[12,30] When applied to this scattering problem, the convolution formulation ray theory accurately describes the angular response and amplitude of the far-field backscattering for the meridional enhancement of the a_0 mode. The ray theory includes a leaky wave end-reflection coefficient as an independent parameter. Approximating this with a reflection coefficient of unity provides for good agreement with experiments at low frequencies, where mode conversion and fluid-loading effects are small. It also agrees well for all frequencies with an approximate partial wave series solution for the finite cylindrical shell, which has an effective unimodular end-reflection coefficient. As the frequency increases the measured enhancement levels fail to increase as quickly as the ray theory suggests when fluid loading and end effects are neglected. Including the effects of mode conversion, while neglecting the fluid loading, explains the abrupt drop in the enhancement near 1 MHz, where the next antisymmetric mode becomes propagating. An approximate calculation of the reflection coefficient for a Lamb wave incident on the edge of a free semi-infinite flat plate is shown to provide a first approximation to the cylinder end-reflection coefficient.

One aspect of the calculations presented in Sec. V which may have implications for the experimental results in Figs. 4 and 5 was not discussed. From zero frequency to just below the mode threshold of the a_1 near 1.085 MHz, the mode amplitude (A_j) of the mode-converted (evanescent) a_1 mode increases smoothly with frequency, as opposed to increasing

abruptly from a small value to a large value at the mode threshold. As a consequence there are significant vibrations of the plate close to its end due to the reflected a_1 evanescent waves when the a_1 is nonpropagating. This would not be expected to influence the reflection coefficient for the incident a_0 wave when the plate is in a vacuum, however, for a plate with fluid loading at its end one may expect to find some radiation of sound into the fluid at the end of the plate because of the displacements introduced by the reflected a_1 wave. This loss would be manifest as a reduction in magnitude of the reflected a_0 wave. In the limit of negligible fluid loading considered here, the subthreshold a_1 motion radiates as if the a_1 wave is highly supersonic with respect to the surrounding liquid. This may help to explain the general roll-off of the a_0 meridional enhancement in Fig. 5 below the mode threshold of the a_1.

ACKNOWLEDGMENTS

This research was supported by the Office of Naval Research.

APPENDIX: EXPRESSIONS FOR ANTISYMMETRIC MODES OF A FREE PLATE

The dispersion relation for antisymmetric solutions of an infinite plate can be written as

$$(\nu^2-\xi^2)^2\sin(\eta h)\cos(\nu h)+4\eta\nu\xi^2\cos(\eta h)\sin(\nu h)=0, \tag{A1}$$

where $\nu=\sqrt{(\omega/c_S)^2-\xi^2}$, $\eta=\sqrt{(\omega/c_L)^2-\xi^2}$, ω is the angular frequency, ξ is the in-plane wave number, and c_L and c_S are the longitudinal and shear wave speeds in the elastic material, respectively. The relevant stresses and displacements within the plate are

$$\begin{aligned}
T_{zz}&=A\frac{G}{\sin(\nu h)}[-(\xi^2+\nu^2-2\eta^2)\sin(\nu h)\sin(\eta x)\\
&\quad-(\nu^2-\xi^2)\sin(\nu x)\sin(\eta h)],\\
T_{xz}&=A2i\frac{G\eta\xi}{\cos(\nu h)}[\cos(\nu h)\cos(\eta x)\\
&\quad-\cos(\nu x)\cos(\eta h)],\\
u_z&=A\frac{i}{2\xi\sin(\nu h)}[2\xi^2\sin(\nu h)\sin(\eta x)\\
&\quad+(\nu^2-\xi^2)\sin(\nu x)\sin(\eta h)],\\
u_x&=A\frac{\eta}{(\nu^2-\xi^2)\cos(\nu h)}[(\nu^2-\xi^2)\cos(\nu h)\cos(\eta x)\\
&\quad+2\xi^2\cos(\nu x)\cos(\eta h)],
\end{aligned} \tag{A2}$$

where G is the shear modulus and A is an arbitrary amplitude coefficient which is set equal to unity to simplify the notation. In each case the factor $\exp[i(\xi z-\omega t)]$ is assumed.

[1] S. F. Morse, P. I. Marston, and G. Kaduchak, "High frequency backscattering enhancements by thick finite cylindrical shells in water at oblique incidence: Experiments, interpretation, and calculations," J. Acoust. Soc. Am. **103**, 785–794 (1998).

[2] S. F. Morse and P. L. Marston, "Meridional ray contributions to scattering by tilted cylindrical shells above the coincidence frequency: Ray theory and computations," J. Acoust. Soc. Am. **106**, 2595–2600 (1999).

[3] S. F. Morse and P. L. Marston, "Degradation of meridional ray backscattering enhancements for tilted cylinders by mode conversion: Wideband observations using a chirped PVDF sheet source," IEEE J. Ocean. Eng. **26**, 152–155 (2001).

[4] S. F. Morse and P. L. Marston, "Backscattering of transients by tilted truncated cylindrical shells: Time-frequency identification of ray contributions from measurements," J. Acoust. Soc. Am. **111**, 1289–1294 (2002).

[5] A. N. Norris and D. A. Rebinsky, "Acoustic coupling to membrane waves on elastic shells," J. Acoust. Soc. Am. **95**, 1809–1829 (1994).

[6] L. B. Felsen, J. M. Ho, and I. T. Lu, "Three-dimensional Green's function for fluid-loaded thin elastic cylindrical shell: Formulation and solution," J. Acoust. Soc. Am. **87**, 543–553 (1990).

[7] M. Tran-Van-Nhieu, "Scattering from a finite cylindrical shell," J. Acoust. Soc. Am. **91**, 670–679 (1991).

[8] M. L. Rumerman, "Contribution of membrane wave reradiation to scattering from finite cylindrical steel shells in water," J. Acoust. Soc. Am. **93**, 55–65 (1993).

[9] E. A. Skelton, "Acoustic scattering by a closed semi-infinite fluid loaded elastic cylindrical shell," Proc. R. Soc. London, Ser. A **455**, 1637–1681 (1999).

[10] G. Kaduchak, C. M. Wassmuth, and C. M. Loeffler, "Elastic wave contributions in high resolution acoustic images of fluid filled, finite cylindrical shells in water," J. Acoust. Soc. Am. **100**, 64–71 (1996).

[11] A. Tesei, W. L. J. Fox, A. Maguer, and A. Lovik, "Target parameter estimation using resonance scattering analysis applied to air-filled, cylindrical shells in water," J. Acoust. Soc. Am. **108**, 2891–2900 (2000).

[12] P. L. Marston, "Approximate meridional leaky ray amplitudes for tilted cylinders: End-backscattering enhancements and comparisons with exact theory for infinite solid cylinders," J. Acoust. Soc. Am. **102**, 358–369 (1997); **103**, 2236(E) (1998).

[13] K. Gipson and P. L. Marston, "Backscattering enhancements due to reflection of meridional leaky Rayleigh waves at the blunt truncation of a tilted solid cylinder in water: Observations and theory," J. Acoust. Soc. Am. **106**, 1673–1680 (1999).

[14] Actual parameters used in the evaluation of the ray model are: 300 kHz ($ka=24.2542$), $k_la=20.2455$, $\alpha a=0.7185$; 400 kHz ($ka=32.3390$), $k_la=24.4347$, $\alpha a=0.5576$; 500 kHz ($ka=40.4237$), $k_l28.4322$, $\alpha a=0.4890$; 600 kHz ($ka=48.5085$), $k_la=32.3315$, $\alpha a=0.4528$; 700 kHz ($ka=56.5932$), $k_la=36.1759$, $\alpha a=0.4323$; 800 kHz ($ka=64.6780$), $k_la=39.9902$, $\alpha a=0.4206$. These wave numbers are calculated for an infinite empty cylindrical shell with exterior fluid loading as discussed in the text.

[15] F. J. Blonigen and P. L. Marston, "Leaky helical flexural wave scattering contributions from tilted cylindrical shells: Ray theory and wave-vector anisotropy," J. Acoust. Soc. Am. **110**, 1764–1769 (2001).

[16] P. M. Morse and H. Feshbach, *Methods of Theoretical Physics* (McGraw-Hill, New York, 1953).

[17] P. J. Torvik, "Reflection of wave trains in semi-infinite plates," J. Acoust. Soc. Am. **41**, 346–353 (1967).

[18] I. A. Viktorov, *Rayleigh and Lamb Waves* (Plenum, New York, 1967).

[19] B. A. Auld and E. M. Tsao, "A variational analysis of edge resonances in a semi-infinite plate," IEEE Trans. Sonics Ultrason. **SU-24**, 317–326 (1977).

[20] S. Y. Zhang, J. Z. Shen, and C. F. Ying, "The reflection of the Lamb wave by a free plate edge: Visualization and theory," Mater. Eval. **46**, 638–641 (1988).

[21] M. Ech-Cherif El-Kettani, P. Pareige, F. Luppe, and J. Ripoche, "Experimental study of the conversion of Lamb waves at the end of an immersed plate," Acustica **82**, 251–259 (1996).

[22] R. Briers, O. Leroy, and G. N. Shkerdin, "Conversion of a Stoneley wave at the extremity of a fluid-loaded plate," J. Acoust. Soc. Am. **101**, 1347–1357 (1997).

[23] J. Shen, S. Zhang, and C. Ying, "The reflection of the Lamb wave in a semi-infinite plate," Chin. J. Acoustics **9**, 27–35 (1990).

[24] R. D. Mindlin, "Waves and vibrations in isotropic, elastic plates," in *Structural Mechanics, Proceedings of the First Symposium on Naval Structural Mechanics* (Pergamon, Oxford, 1960).

[25] T. R. Kane, "Reflection of dilational waves at the edge of a plate," J. Appl. Mech. **24**, 219–227 (1957).

[26] R. D. Gregory and I. Gladwell, ''The reflection of a symmetric Rayleigh–Lamb wave at the fixed or free edge of a plate,'' J. Elast. **13**, 185–206 (1983).
[27] T. R. Kane, ''Reflection of flexural waves at the edge of a plate,'' J. Appl. Mech. **21**, 213–220 (1954).
[28] Y. Cho and J. L. Rose, ''A boundary element solution for a mode conversion study on the edge reflection of Lamb waves,'' J. Acoust. Soc. Am. **99**, 2097–2109 (1996).
[29] S. F. Morse, ''High Frequency Acoustic Backscattering Enhancements for Finite Cylindrical Shells in Water at Oblique Incidence,'' Ph.D. dissertation, Washington State University, Department of Physics, 1998.
[30] P. Y. Ufimtsev, ''Theory of acoustical edge waves,'' J. Acoust. Soc. Am. **86**, 463–474 (1989).

Free field measurements of the absorption coefficient for nonlocally reacting sound absorbing porous layers

G. Jansens, W. Lauriks, and G. Vermeir
Laboratorium voor Akoestiek en Thermische Fysica, Katholieke Universiteit Leuven, Celestijnenlaan 200D B-3001 Heverlee, Belgium

J. F. Allard
Institut d'Acoustique et de Mechanique, Universite du Maine, Avenue Olivier Messiaen, 72085 Le Mans, France

(Received 11 December 2000; revised 7 May 2002; accepted 26 June 2002)

A simple asymptotic approximation with two parameters (the plane wave reflection coefficient and a correction factor) has been derived by Brekhovskikh and Godin [*Acoustics of Layered Media II. Point Sources and Bounded Beams* (Springer, New York, 1992)], for the spherical field reflected by nonlocally reacting surfaces. In the present work, an expression for the correction factor is obtained for the case of a homogeneous and isotropic porous layer. A free field method for evaluating reflection and absorption coefficients with this approximation is presented. The evaluation of the absorption coefficient at normal incidence is performed on a porous layer on a rigid backing, and compared to measurements performed using a two microphone technique and an impedance tube. [DOI: 10.1121/1.1504851]

PACS numbers: 43.20.Jr, 43.50.Cb [DEC]

I. INTRODUCTION

Numerous methods of measuring the surface impedance and the absorption coefficient in a free field with a point source have been worked out in different domains of acoustics. The methods are related to different approximations of the reflected field, except the Tamura method,[1] where a holographic analysis of the actual acoustic field is performed. Different versions[2–4] of Tamura's method have been used to measure the surface impedance and the reflection or absorption coefficient of porous layers at oblique incidence and for inhomogeneous waves. A drawback of the method is the relative complexity of the mechanical equipment which makes the measurements difficult out of a laboratory. For the source-receiver geometry of Fig. 1, a simple approximation for the reflected field pressure at M related to a source of amplitude p_0 can be given by

$$p_r(M)=p_0\frac{\exp(ikR_1)}{R_1}v(\sin\theta_0), \tag{1}$$

where k is the wave number in air, θ_0 is the angle of specular reflection, R_1 is the distance between the image source S' and M, and $v(\sin\theta_0)$ the plane wave reflection coefficient at an angle of incidence $\theta=\theta_0$, related to the impedance $Z_s(\sin\theta_0)$ of the reflecting surface by (Z is the characteristic impedance of air)

$$v(\sin\theta_0)=\frac{Z_s(\sin\theta_0)-Z/\cos\theta_0}{Z_s(\sin(\theta_0)+Z/\cos\theta_0}, \tag{2}$$

and to the absorption coefficient α by

$$\alpha(\sin\theta_0)=1-|v(\sin(\theta_0)|^2. \tag{3}$$

Equation (1) can be a good approximation for very large kR_1, but for large distances from the source and the receivers to the reflecting surface, a precise measurement of p_r is difficult *in situ* in presence of other reflecting surfaces and a diffuse field. Moreover, the effect of the finite dimension of the reflecting surface increases with the distance between the source and the surface. An exact integral expression for p_r obtained from the Sommerfeld integral[5] is

$$p_r=\frac{ik}{2}p_0\int_{-\infty}^{+\infty}\frac{q\,dq}{\mu}v(q)H_0^1(kqr)\exp(i\mu k(z+z_0)), \tag{4}$$

where $\mu=\sqrt{1-q^2}$, $\mathrm{Im}(\mu)>0$, r is the horizontal distance between the source and the receiver, z and z_0 the height of the source S and the receiver at M, respectively, and H_0^1 is the zero order Hankel function.

For locally reacting materials, Z_s in Eq. (2) does not depend on θ_0 and the evaluation of α and v from pressure measurements can be simplified.[6] For courant porous absorbing materials, sound propagates in the air saturating the porous frame, not in the porous frame that remains motionless in the presence of an aerial source. Let n be the refraction index ($n=k_1/k$, where k is the wave number in free air and k_1 is the wave number in the air saturating the porous material. Materials having a flow resistivity larger than 10^5 Ns/m^4 mainly behave as locally reacting media in the audible frequency range, $|n|$ being sufficiently large for the complex angle of refraction θ_1 (defined by Snell's law $\sin\theta_1=\sin\theta/n$) to be close to zero for real angles of incidence. As a result, Z_s defined by Eq. (A5) does not depend noticeably on θ. It is not possible to define a frequency range where a porous layer of medium flow resistivity is locally reacting if the other macroscopic parameters, tortuosity and characteristic dimensions, are not known. In the present work, a material with a low flow resistivity (see Table I) and a thickness ℓ set on a rigid impervious backing is considered. The calculated refraction index is close to 1, which means that the material is nonlocally reacting in the whole audible fre-

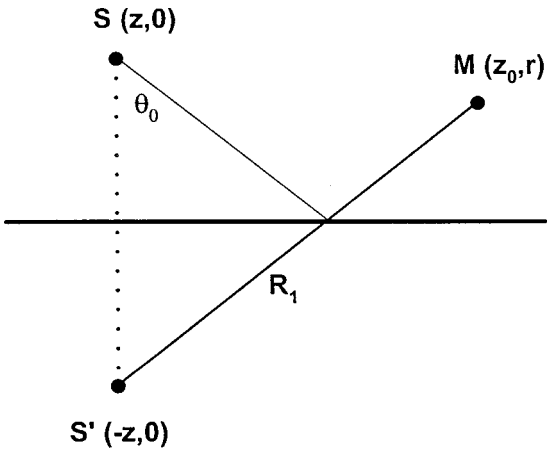

FIG. 1. The source S, its image S' and the receiver at M in air above a reflecting surface. The specular angle of reflection is θ_0.

quency range. The predicted surface impedance Z_s, obtained with the model described in Appendix A from the parameters of Table I, is represented in Fig. 2 as a function of the angle of incidence at 2500 Hz. Large variations of Z_s occur, related to the fact that the refraction index n is close to 1 (the calculations give $n=1.22+i0.2$). The measurement of surface impedances *in situ* at normal incidence with two microphones has been performed by using Eq. (1) to obtain a first approximation for Z_s followed by an iterative process using the expression by Nobile and Hayek[6] for the pressure reflected by a locally reacting surface. This method can lead to systematic errors for many porous sound absorbing materials which are nonlocally reacting in the medium and high frequency range.

If kR_1 is sufficiently large, a simple approximation for p_r is obtained with the steepest descent method, the integration being performed in the $\sin\theta$ plane on the steepest descent path defined by $\cos(\theta-\theta_0)=1-is^2$, $-\infty<s<\infty$, including the stationary point $q_0=\sin\theta_0$. The reflected field can be written:[1]

$$p_r=p_0\frac{\exp(ikR_1)}{R_1}\left[v(\sin\theta_0)-\frac{iN}{kR_1}\right], \tag{5}$$

where N does not depend on R_1 and is given by

$$N=\left[\frac{1-q^2}{2}\frac{\partial^2 v}{\partial q^2}+\frac{1-2q^2}{2q}\frac{\partial v}{\partial q}\right]_{q=\sin\theta_0}. \tag{6}$$

Equation (5) can be rewritten

$$p_r=p_0\frac{\exp(ikR_1)}{R_1}v(\sin\theta_0)+p_0\frac{\exp(ikR_1)}{R_1^2}A(\sin\theta_0), \tag{7}$$

where v and $A=-iN/k$ only depend on θ_0. An evaluation of v and α should in principle be obtained from three pressure measurements at $\theta_0=$constant and three different positions R_1. It has been pointed out by Brekhovskikh and Godin[5] that Eqs. (5) and (6) obtained from the steepest descent path method are valid under the condition of arbitrary dependence of v on q. It is also shown in Ref. 5 that the steepest descent method [and hence Eq. (5)] must be modified if a pole of the reflection coefficient $q_p=\sin\theta_p$ is close to the stationary point $q_0=\sin\theta_0$. The noncloseness condition in Ref. 5 is $|u|\gg 1$, u being the numerical distance defined by

$$u=\exp\left(i\frac{3\pi}{4}\right)(2kR_1)^{1/2}\sin\left(\frac{\theta_p-\theta_0}{2}\right). \tag{8}$$

From Eq. (8), $kR_1\gg 1$ does not lead to $|u|\gg 1$ if θ_p and θ_0 are sufficiently close.[7] This can arise, as shown in the next section, around grazing incidence for porous layers such that $|k_1\ell|<1$ because for these layers, a pole exists[8] at θ_p close to 90°. A pole close to grazing incidence also exists for thick layers of high flow resistivity.[9] For locally reacting materials,

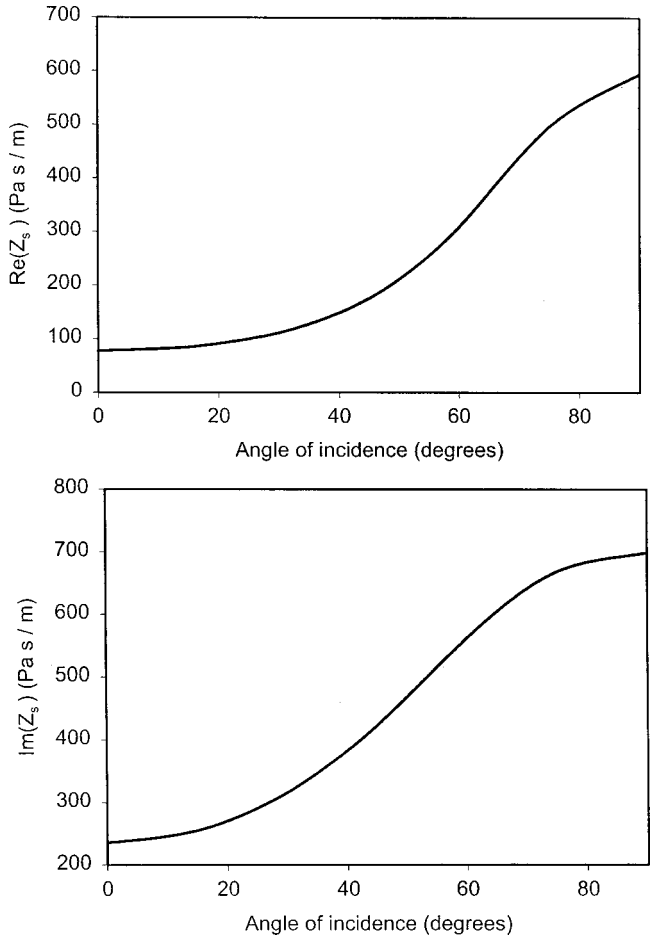

FIG. 2. Surface impedance Z_s of the porous layer of Table I at 2500 Hz as a function of the angle of incidence.

TABLE I. Parameters for the studied porous layer.

Thickness ℓ (m)	Tortuosity α_∞	Porosity ϕ	Flow resistivity σ [Ns/m^4]	Viscous dimension Λ [μm]	Thermal dimension Λ' [μm]
0.02	1.1	0.99	3700	150	300

Brekhovskikh and Godin have given an expression for p_r valid for small and large $|u|$ (Eq. 1-4-10 of Ref. 5). This expression for large $|u|$ is equivalent to Eqs. (5) and (6) plus the possible contribution of a pole. This expression, around grazing incidence and for large $|Z_s/Z|$, is equivalent to the simple result previously obtained by Chien and Soroka,[10] after the works by Rudnick,[11] Lawhead and Rudnick,[12] and Banos,[13] which can be written

$$p_r = p_0 \frac{\exp(ikR_1)}{R_1}[v(\sin\theta_0) + (1 - v(\sin\theta_0)W(u))], \qquad (9)$$

where $W(u) = 1 + \sqrt{\pi} u \exp(u^2)\mathrm{erf}(-u)$, and u given by Eq. (8) can be rewritten

$$u = \exp(i3\pi/4))(\tfrac{1}{2}kR_1)^{1/2}(Z/Z_s + \cos\theta_0). \qquad (10)$$

Equation (9) has been used extensively to evaluate Z_s in the context of outdoor sound propagation. A description of the state of the art can be found in a work by Attenborough.[14] Equation (9) has also been used for porous layers considered as locally reacting surfaces.[15–17] Equation (5) must also be modified at large $|u|$, if the real $\sin\theta$ axis cuts a pole when it is deformed into the steepest descend path: the contribution of the pole must be added at the right-hand side of Eq (5). For the nonlocally reacting material of Table I, precise predictions of the surface impedance Z_s can be obtained with the model described in Appendix A. In Sec. II the possible occurrence of a crossed pole contribution is considered. In Sec. III the validity of Eq. (5) is studied by using a new exact expression for N (given in Appendix B) for homogeneous and isotropic porous layers on a rigid backing. A method of measuring the absorption coefficient based on Eq. (5) is presented in Sec. IV.

II. POLE TRAJECTORY AND STEEPEST DESCENT PATH

There are an infinite number of poles for the reflection coefficient of a nonlocally reacting porous layer, related to the complex angles θ_p such that

$$Z/\cos\theta_p + Z_s(\sin\theta_p) = 0. \qquad (11)$$

At low frequencies or for thin porous layers, for $|k_1\ell| \ll 1$, one of these poles, which will be called the main pole in the following, is localized in the complex $\sin\theta$ plane at $q_p = \sin\theta_p$, given at the second order approximation in $k\ell$ by[8]

$$q_p = 1 + \frac{1}{2}k^2\ell^2(n^2-1)^2\phi^2\frac{Z^2}{Z_1^2}, \qquad (12)$$

where ϕ is the porosity and Z_1 the characteristic impedance of the porous material (see Appendix A). Equation (12) is valid for all porous media, for instance for sands[9] having a large flow resistivity and a small porosity. Thin layers present a pole close to $q_p = \sin\theta_p = 1$, and θ_p is close to 90°. This pole can be detected with Tamura's method.[9] When $|k_1\ell|$ increases, q_p can be predicted numerically by continuity. For large thicknesses $[\mathrm{Im}(k_1\ell) \gg 1]$, layers behave acoustically as semi-infinite media and the main pole is located at q_p given by

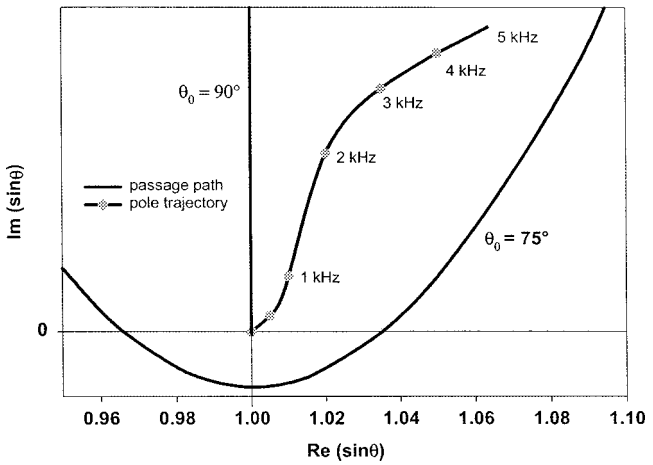

FIG. 3. The trajectory of the main pole for the porous layer of Table I and the passage path at $\theta_0 = 75$ degrees.

$$q_p = \left(\left(\frac{m^2}{\phi^2} - n^2\right) \Big/ \left(\frac{m^2}{\phi^2} - 1\right)\right)^{1/2}, \qquad (13)$$

where $m = \rho_1/\rho$ is the ratio of the effective density ρ_1 (see Appendix A) to the air density ρ. For materials having a large flow resistivity,[9] q_p given by Eq. (13) is very close to 1 and θ_p very close to 90°. For lower flow resistivities, θ_p remains close to 90°. This pole is related to the Zenneck wave[9,10,13] which exist only for small $|u|$. For the layer of Table I, the trajectory of the main pole in the $\sin\theta$ plane is represented in Fig. 3 up to 5 kHz. The trajectory remains close to $\sin\theta = 1$. The trajectory for materials of large flow resistivities present the same feature. The steepest descent path, defined by $\cos(\theta - \theta_0) = 1 + is^2$, $-\infty < s < +\infty$, is represented for $\theta_0 = 75$ degrees in the same figure. Up to 5 kHz, the main pole is not cut by the real $\sin\theta$ axis when it is deformed into the steepest descent path for $\theta_0 = 75$ degrees and smaller angles of specular reflection. Other poles can be cut far from the real $\sin\theta$ axis, their contribution to the reflected field being negligible in all simulations we have performed. For the layer of Table I, and also for layers of larger thickness or larger flow resistivity, a contribution of the main pole only exists close to grazing incidence, and Eq. (5) can be used in a large range of angles of incidence, provided $|u|$ and kR_1 are sufficiently large. The trajectories for the main pole lie around $\sin\theta = 1$, and the maximum for $|u|$ is reached for a given R_1 around normal incidence. At normal incidence, where the steepest descent path is the real $\sin\theta$ axis and the initial path of integration is not modified, there is no possible occurrence of a pole cut, but it is not possible to predict a general range of validity of Eq. (5) around normal incidence for complex sound absorbing layers.

III. VALIDITY OF THE PASSAGE PATH APPROXIMATION

In a first step, the validity of the asymptotic Eq. (5) and of Eq. (B5) for N has been verified at a large angle of specu-

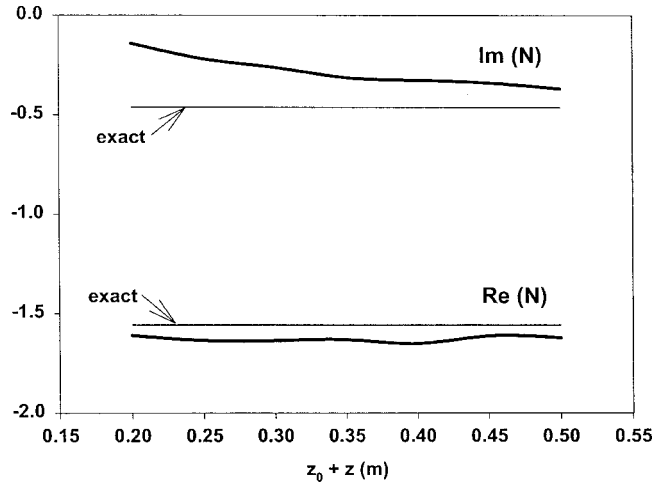

FIG. 4. N as a function of z_0+z at $\theta_0=60$ degrees and 2.5 kHz. Exact evaluation from Eq. (B5) (horizontal line) and evaluation from Eq. (9).

lar reflection: $\theta_0=60°$. The coefficient N given by Eq. (B5) is compared to the evaluation of N obtained from Eq. (5) rewritten

$$N=[p_r R_1 \exp(-ikR_1)-v(\sin\theta_0)]ikR_1, \tag{14}$$

p_r being calculated without approximation with Eq. (4). The comparison presented in Fig. 4 is performed at 2.5 kHz, $\theta_0=60$ degrees and $z+z_0$ varying from 0.2 m to 0.5 m. For $z+z_0=0.2$ m, $kR_1=18.5$, and $|u|=2.06$, and these quantities are too small for a precise evaluation of N by Eq. (14) to be obtained. The difference between the exact value of N and the estimation with Eq. (14) increases when $z+z_0$ decreases and also when the frequency decreases. Nevertheless, Eq. (5) remains valid if N is replaced by a slowly varying parameter, approximated as a constant in the interval of R_1 where measurements are performed.

Direct comparison of p_r evaluated from Eqs. (5) and (6) and Eq. (4) are shown in Fig. 5 at 2500 Hz for $z+z_0$ varying from 0.2 m to 0.5 m. For the first use of Eq. (5) to evaluate absorption coefficients in a free field, experiments are performed at normal incidence in the next section to allow comparison with impedance tube measurements. The direct comparison for both evaluations of p_r is also performed at normal incidence. The reflected pressure p_r is divided by the direct pressure $p_d=p_0\exp(ikR_2)/R_2$ to remove the fast variations in phase and amplitude. The small difference between both evaluations considerably decreases from $z+z_0=0.2$ m to $z+z_0=0.5$ m.

IV. EVALUATION OF THE ABSORPTION COEFFICIENT

A straightforward evaluation of v and α with Eq. (5) can be performed with the experimental setup represented in Fig. 6. The three locations M_1, M_2, M_3 of the receiver are related to the same angle of specular reflection θ_0. The pressure field at M_i, using Eq. (7), is given by

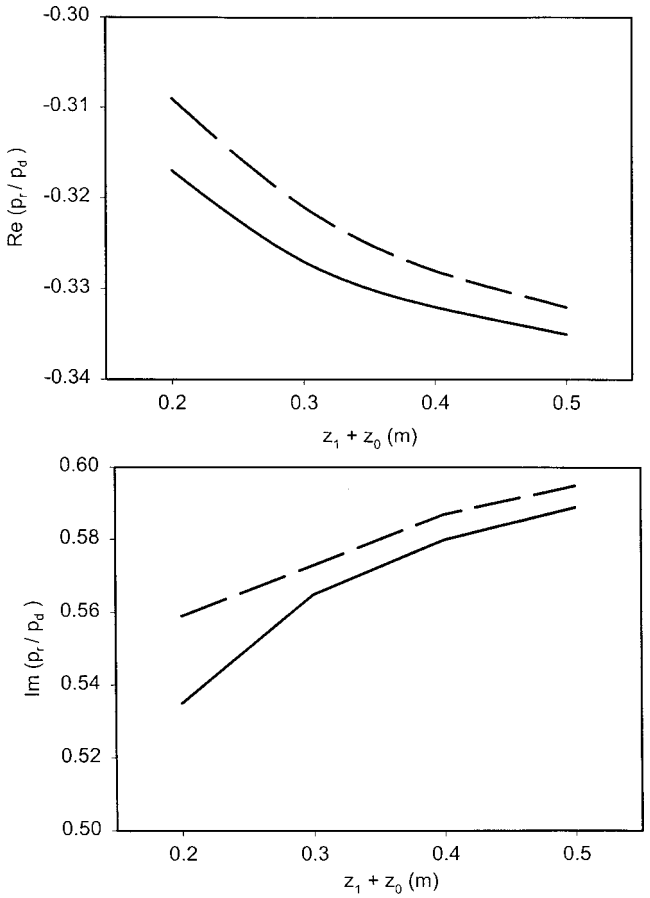

FIG. 5. p_r/p_d as a function of $z+z_0$ for the layer of Table I at 2500 Hz, $p_d=p_0\exp(ikR_2)/R_2$ is the direct field. —, p_r evaluated with the passage path method, Eqs. (5) and (6). — — —, exact p_r evaluated with Eq. (4).

$$p(M_i)=p_0\left(\frac{\exp(ikR_{2i})}{R_{2i}}+\frac{\exp(ikR_{1i})}{R_{1i}}\left(v(\sin\theta_0)+\frac{A(\sin\theta_0)}{R_{1i}}\right)\right), \tag{15}$$

where R_{1i} is the distance from the image of the source S' to the receiver at M_i, and R_{2i} is the distance from the source S to the receiver, p_0, $v(\sin\theta_0)$ and A_0 are three unknown quantities. The absorption coefficient can be obtained from Eq. (3), where $v(\sin\theta_0)$ is given by

$$v(\sin\theta_0)=-\frac{D_1}{D_2}, \tag{16}$$

$$D_1=\begin{vmatrix} p(M_1) & \exp(ikR_{11})/R_{11}^2 & \exp(ikR_{21})/R_{21} \\ p(M_2) & \exp(ikR_{12})/R_{12}^2 & \exp(ikR_{22})/R_{22} \\ p(M_3) & \exp(ikR_{13})/R_{13}^2 & \exp(ikR_{23})/R_{23} \end{vmatrix}, \tag{17}$$

$$D_2=\begin{vmatrix} p(M_1) & \exp(ikR_{11})/R_{11}^2 & \exp(ikR_{11})/R_{11} \\ p(M_2) & \exp(ikR_{12})/R_{12}^2 & \exp(ikR_{12})/R_{12} \\ p(M_3) & \exp(ikR_{13})/R_{13}^2 & \exp(ikR_{13})/R_{13} \end{vmatrix}, \tag{18}$$

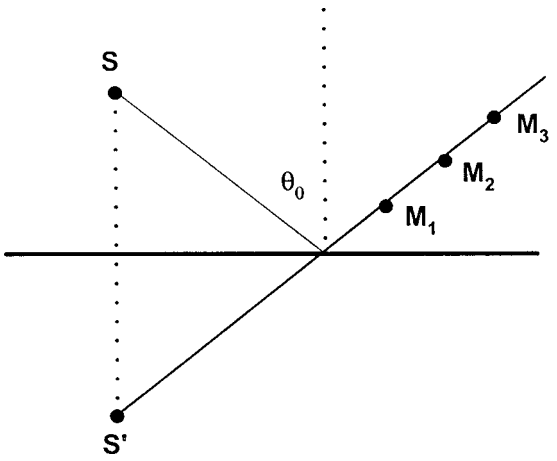

FIG. 6. Experimental setup for the evaluation of $v(\sin\theta)$.

with the two microphone technique, Eq. (15) is replaced by Eq. (1) and $v(\sin\theta_0)$, obtained from two measurements at M_1 and M_2, is given by

$$v(\sin\theta_0) = -\frac{D_1'}{D_2'}, \tag{19}$$

$$D_1' = \begin{vmatrix} p(M_1) & \exp(ikR_{21})/R_{21} \\ p(M_2) & \exp(ikR_{22})/R_{22} \end{vmatrix}, \tag{20}$$

$$D_2' = \begin{vmatrix} p(M_1) & \exp(ikR_{11})/R_{11} \\ p(M_2) & \exp(ikR_{12})/R_{12} \end{vmatrix}. \tag{21}$$

The experimental setup for the two-microphone method consists of a source (a pipe excited with a compression driver) located at a distance z from the reflecting surface, and two microphones at z_1 and z_2 connected to an FFT analyzer. In an anechoic room, the order of magnitude for z is normally 1 meter or more. The two microphones are set at a few centimeters from the surface. For *in situ* measurements, the diffraction effects due to the finite lateral dimensions of the sample and reflections from the walls can be minimized by positioning the source and the microphones as close as possible to the reflecting surface. As an example, for *in situ* measurements previously performed in a cafeteria on a carpet,[7] the following distances were used: $z=0.2$ m, 0.35 m, and 0.65 m, $z_1=1.5$ cm, and $z_2=7.1$ cm. Comparison with measurements performed in an anechoic room show that the effect of wall reflection can be neglected at distances smaller than $z=0.2$ m. In the preceding section, it is shown that at normal incidence, a small difference exists between the exact and the asymptotic evaluation of p_r at 2500 Hz for $z+z_0$ varying from 0.2 m to 0.5 m. Simulations are performed to evaluate how the difference between the exact pressure and the asymptotic evaluation limit the use of the three microphone method. Simulations and measurements are performed at $\theta_0=0°$ for the first approach of the method, allowing comparison with impedance tube measurements. (See Fig. 6.)

Simulated measurements with the three-microphone method obtained from Eqs. (3), (16) and with the two-microphone method from Eqs. (3), (19), $p_r(M_i)$ being calculated with Eq. (4), are compared in Fig. 7(a) to the exact

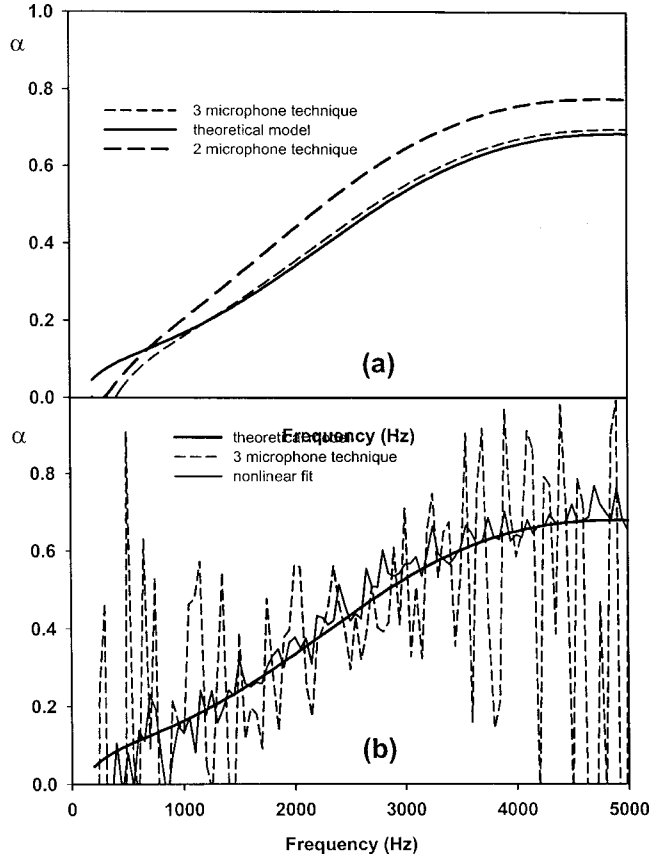

FIG. 7. Numerical simulation of the experiment. The surface impedance has been calculated with the model of Appendix A and the data of Table I. The sound pressure above the layer has been calculated using Eq. (4). All results obtained with a source height of 0.21 m and at normal incidence. (a) Results of simulation, thick black line, Eq. (A5); thick dashed line, the two-microphone technique $z_1=0.07$ m, $z_2=0.27$ m; thin dashed line, the three-microphone technique [Eq. (16)] $z_1=0.07$ m, $z_2=0.27$ m, $z_3=0.47$ m. (b) Results of simulation with 2% of broadband noise added to the calculation of the sound pressure. Thick black line, Eq. (A5); dashed line, the three-microphone technique [Eq. (16)] $z_1=0.07$ m, $z_2=0.27$ m, $z_3=0.47$ m; thin black line, results of least square fit of 50 equally spaced datapoints (between $z=0.03$ m and $z=0.152$ m) to Eq. (15). The results of the two-microphone technique (not shown) are only slightly influenced by the noise.

absorption coefficient calculated from Eqs. (2) and (3). The one geometrical parameter for the prediction of $p_r(M_i)$ is $z+z_i=R_{1i}$ which varies from 0.28 m for the first microphone to 0.698 m. In the simulation, the main source of error is the use of Eq. (15) at M_1. At 1 kHz, $kR_{11}=5.17$, this quantity is too small for the asymptotic evaluation of p_r to be reliable. Nevertheless, the simulation indicates a correct evaluation of α with three microphones at frequencies larger than 750 Hz. The simulation also shows that the systematic error which appears when A is not taken into account in Eq. (15) (as with the two-microphone technique) considerably decreases when the full Eq. (15) is used. However, when digitally generated broadband noise is added to the values of $p(M_i)$ calculated from Eq. (4), the situation changes dramatically. Figure 7(b) shows the results from Eq. (16) with noise added to the values of $p(M_i)$ (the amplitude of the broadband noise was 2% of the amplitude of p). The three-microphone technique appears to be extremely sensitive to the presence of noise. During one experiment, the perturbation introduced by a slight

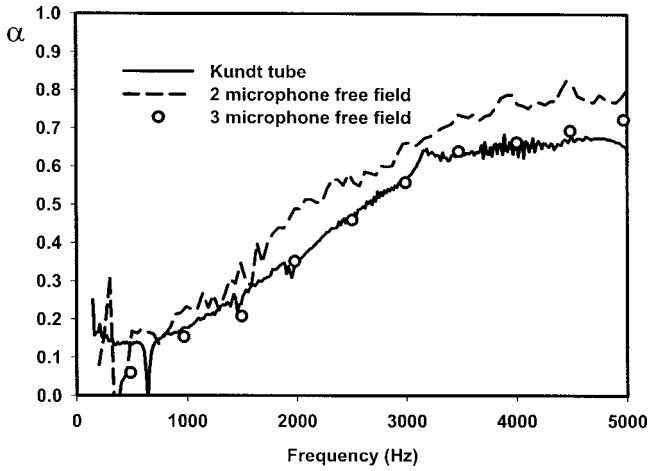

FIG. 8. Experimental results obtained in the anechoic room on a foam with material parameters as in Table I (see Refs. 18 and 19). Position of source and receivers are the same as in Fig. 7.

increase in temperature due to lighting in the anechoic room was enough to render the data useless. The classical two-microphone technique on the other hand appears to be very robust for noise (a numerical simulation, results not shown in the figure, gives results that are almost identical to the simulation without noise). One way to get rid of the noise is to measure the pressure in a lot of points as a function of height above the sample and to perform a nonlinear fit on these data using Eq. (15), with p_0, v, and A as fit parameters. Figure 7(b) shows the result of a nonlinear fit using Eq. (15), 50 datapoints (equally spaced between 0.03 m and 0.152 m) 2% of added broadband noise.

Measurements performed in an anechoic room at normal incidence with the same source height ($z=21$ cm) as for Fig. 7 and in an impedance tube are presented in Fig. 8. The porous material is a foam described by the parameters of Table I (see Refs. 18 and 19), the sample in the anechoic room is square shaped with lateral dimensions of 2 meter by 2 meter. Evaluation of the absorption coefficient from Eqs. (3)–(7) with a least square estimation are compared with measurements performed with the two-microphone method and in an impedance tube. At frequencies lower than 600 Hz, both free field methods completely fail. At higher frequencies, the precision of the result from Eq. (7) is much better than the one from Eq. (1) with the two-microphone technique. It can be noticed that the domain where the method can be used is significantly larger than the one where Eqs. (5) and (6) provide a precise estimation of p_r. Different limitations of the three-microphone method have been indicated for the case of a porous medium of low flow resistivity. For porous materials (like ground) having a very large flow resistivity, whatever the thickness of the layer, the surface impedance Z_s does not noticeably depend on the angle of incidence. Around normal incidence, measurements are difficult to perform due to the weak sound absorption which makes the field very reactive.[20,21] The use of Eq. (9) with measurements performed at grazing incidence is more suited to the case of materials with a very large flow resistivity.

V. CONCLUSION

The passage path method provides a simple expression of the spherical acoustic field reflected by a nonlocally reacting medium. The plane wave reflection coefficient related to a given angle of specular reflection can be evaluated from three measurements at the same angle of specular reflection. The systematic errors which appear when the sphericity of the incident field and the nonlocally reacting nature of the reflecting surface are not taken into account are avoided with this estimation. A major drawback of the method is that the evaluation of v is not robust in the presence of noise and fast temperature variations. A least square adjustment of the predicted and measured pressure field at a large number of points reduces the impact of noise sufficiently to obtain a robust estimation of the absorption factor. Large angles of specular reflection must be avoided, due to a possible extra contribution of the main pole to the reflected field. The domain of frequencies and of distances between the reflecting surface and the source and the receiver, where the method can be used, is larger than the one where the passage path method provides a precise estimation of the reflected pressure.

APPENDIX A: FREE FIELD EQUIVALENT TO AIR SATURATING A POROUS MEDIUM

Following Johnson *et al.*[22] and Champoux and Allard,[23] the equivalent fluid is characterized by an effective density ρ_1 and an incompressibility χ_1, which are given by [the time dependence is $\exp(-i\omega t)$]

$$\rho_1=\alpha_\infty\rho\left(1+\frac{i\sigma\phi}{\omega\rho\alpha_\infty}\left(1-\frac{4i\alpha_\infty^2\eta\rho\omega}{\sigma^2\Lambda^2\phi^2}\right)^{1/2}\right), \tag{A1}$$

$$\chi_1=\frac{\gamma P_0}{\gamma-(\gamma-1)\left[1+\frac{i8\eta}{\Lambda'^2\,\mathrm{Pr}\,\omega\rho}\left(1-i\frac{\rho\omega\,\mathrm{Pr}\,\Lambda'^2}{16\eta}\right)^{1/2}\right]^{-1}}, \tag{A2}$$

where ϕ is the porosity, Λ and Λ' are the viscous and thermal characteristic length, σ is the flow resistivity, and α_∞ is the tortuosity. The parameters related to air are the Prandtl number Pr, the viscosity η, the density ρ, the ratio of the specific heats γ, and P_0 is the static atmospheric pressure. Using the same notations as Brekhovkikh and Godin, the density ratio m is defined by $m=\rho_1/\rho$, and the characteristic impedance Z_1 and the wave number k_1 are given by, respectively,

$$Z_1=(\rho_1\chi_1)^{1/2}, \tag{A3}$$

$$k_1=\omega(\rho_1/\chi_1)^{1/2}. \tag{A4}$$

The surface impedance Z_s of a porous layer of thickness ℓ, backed by a rigid wall, can be written

$$Z_s=\frac{iZ_1}{\phi\cos\theta_1}\cot k_1\ell\cos\theta_1. \tag{A5}$$

In this equation, θ_1 is the refraction angle, and $\cos\theta_1$ is given by

$$\cos\theta_1 = 1 - \frac{\sin^2\theta}{n^2}, \tag{A6}$$

where n is the refraction index, $n = k_1/k$.

APPENDIX B: EVALUATION OF N FOR A POROUS LAYER OF FINITE THICKNESS

The reflection coefficient $v(q)$ can be rewritten

$$v(q) = \frac{-\sqrt{n^2-q^2} + in\dfrac{Z_1}{\phi Z}\sqrt{1-q^2}\cot(k\ell\sqrt{n^2-q^2})}{+\sqrt{n^2-q^2} + in\dfrac{Z_1}{\phi Z}\sqrt{1-q^2}\cot(k\ell\sqrt{n^2-q^2})}, \tag{B1}$$

and N is given by

$$N = \left[\frac{1-q^2}{2}\frac{\partial^2 v}{\partial q^2} + \frac{1-2q^2}{2q}\frac{\partial v}{\partial q}\right]_{q=q_0}. \tag{B2}$$

The derivatives $\partial v/\partial q$, $\partial^2 v/\partial q^2$, and N are given by, respectively,

$$\frac{\partial v}{\partial q} = \frac{2m'q(1-n^2)}{\sqrt{n^2-q^2}\sqrt{1-q^2}(m'\sqrt{1-q^2}+\sqrt{n^2-q^2})^2} \times\left[1 + \frac{2\sqrt{n^2-q^2}(1-q^2)k\ell}{\sin(2\ell\sqrt{n^2-q^2})(1-n^2)}\right], \tag{B3}$$

$$\frac{\partial^2 v}{\partial q^2} = \frac{4(1-n^2)m'qk\ell n}{\sqrt{n^2-q^2}\cos\theta(m'\sqrt{1-q^2}+\sqrt{n^2-q^2})^2(1-n^2)}\left[\frac{2k_1\ell(1-q^2)k\ell(1-q^2)q\cos(2k\ell\sqrt{n^2-q^2})}{n^2\sin^2(2k\ell\sqrt{n^2-q^2})} - \frac{q\left(\dfrac{1-q^2}{\sqrt{n^2-q^2}} + 2\sqrt{n^2-q^2}\right)}{n\sin 2k\ell\sqrt{n^2-q^2}}\right] + \left[1 + \frac{2(1-q^2)k\ell\sqrt{n^2-q^2}}{(1-n^2)\sin^2 2k\ell\sqrt{n^2-q^2}}\right]\frac{2m'k\ell q}{\sqrt{n^2-q^2}\sin 2k\ell\sqrt{n^2-q^2}} \times\left[\frac{2(1-n^2)q}{\sqrt{n^2-q^2}\sqrt{1-q^2}(m'\sqrt{1-q^2}+\sqrt{n^2-q^2})^2} - \frac{4(1-n^2)m'^2q}{\sqrt{n^2-q^2}\sqrt{1-q^2}(m'\sqrt{1-q^2}+\sqrt{n^2-q^2})^3}\right], \tag{B4}$$

$$N = \left[1 + \frac{2k\ell(1-q_0^2)\sqrt{n^2-q_0^2}}{(1-n^2)\sin 2k\ell\sqrt{n^2-q_0^2}}\right]\left[M(m') + \frac{2(1-q_0^2)(1-n^2)q_0^2(-m'\sqrt{1-q_0^2}+\sqrt{n^2-q_0^2})m'k\ell}{(n^2-q_0^2)\sqrt{1-q_0^2}(m'\sqrt{1-q_0^2}+\sqrt{n^2-q_0^2})^3\sin 2k\ell\sqrt{n^2-q_0^2}}\right] + \frac{(1-q_0^2)2m'q_0(1-n^2)k\ell n}{\sqrt{n^2-q_0^2}\sqrt{1-q_0^2}(m'\sqrt{1-q_0^2}+\sqrt{n^2-q_0^2})(1-n^2)}\left[\frac{2k_1\ell q_0(1-q_0^2)\cos 2k\ell\sqrt{n^2-q_0^2}}{n^2\sin^2 2k\ell\sqrt{n^2-q_0^2}} - \frac{q_0(1-q_0^2+2(n^2-q_0^2))}{n^2\sin 2k\ell\sqrt{n^2-q_0^2}\sqrt{n^2-q_0^2}}\right], \tag{B5}$$

where m' and $M(m')$ are given by

$$m' = i\frac{m}{\phi}\cot k\ell\sqrt{n^2-q^2}, \tag{B6}$$

$$M(m') = \frac{m'(1-n^2)[2m'(n^2-1)+3m'(1-q_0^2)-m'(1-q_0^2)^2+\sqrt{n^2-q_0^2}\sqrt{1-q_0^2}(2n^2+q_0^2)]}{(m'\sqrt{1-q_0^2}+\sqrt{n^2-q_0^2})^3(n^2-q_0^2)^{3/2}}. \tag{B7}$$

[1] M. Tamura, "Spatial Fourier transform method of measuring reflection coefficient at oblique incidence," J. Acoust. Soc. Am. **88**, 2259–2264 (1990).

[2] Z. Hu and J. S. Bolton, "The measurement of plane-wave reflection coefficients by using two-dimensional spatial transforms," J. Acoust. Soc. Am. **88**, Suppl. 1, S173 (1990).

[3] Z. Hu, "Measurement and prediction of sound propagation over an absorbing plane," Ph.D. thesis, Purdue University, 1992.

[4] B. Brouard, D. Lafarge, J. F. Allard, and M. Tamura, "Measurement and prediction of the reflection coefficient of porous layers at oblique incidence and for inhomogeneous waves," J. Acoust. Soc. Am. **99**, 100–107 (1998).

[5] L. M. Brekhovskikh and O. A. Godin, *Acoustics of Layered Media II. Point Sources and Bounded Beams*, Springer Series on Wave Phenomena (Springer, New York, 1992).

[6] M. A. Nobile and S. I. Hayek, "Acoustic propagation over an impedance plane," J. Acoust. Soc. Am. **78**, 1325–1336 (1986).

[7] J. F. Allard and Y. Champoux, "In situ free field measurements of the surface acoustic impedance of materials," Noise Control Eng. J. **32**, 15–23 (1989).

[8] W. Lauriks, L. Kelders, and J. F. Allard, "Poles and zeros of the reflection coefficient of a porous layer having a motionless frame in contact with air," Wave Motion **28**, 59–67 (1998).

[9] J. F. Allard, M. Henry, J. Tizianel, J. Nicolas, and Y. Miki, "Pole contri-

bution to the field reflected by sand layers,'' J. Acoust. Soc. Am. **111**, 685–689 (2002).
[10] C. F. Chien and W. W. Soroka, ''Sound propagation along an impedance plane,'' J. Sound Vib. **43**, 9–20 (1975).
[11] L. Rudnick, ''Propagation of an acoustic wave along a boundary,'' J. Acoust. Soc. Am. **19**, 348–356 (1947).
[12] R. B. Lawhead and I. Rudnick, ''Acoustic wave propagation along a constant normal impedance boundary,'' J. Acoust. Soc. Am. **23**, 546–549 (1951).
[13] A. Banos, *Dipole Radiation in the Presence of a Conducting Half-Space* (Pergamon, Oxford, 1966).
[14] K. Attenborough, ''Review of ground effects on outdoor sound propagation from continuous broadband sources,'' Appl. Acoust. **24**, 289–319 (1988).
[15] C. Nocke, V. Mellert, T. Waters-Fuller, K. Attenborough, and K. M. Li, ''Impedance deduction from broad-band, point source measurements at grazing incidence,'' Acust. Acta Acust. **83**, 1085–1090 (1997).
[16] C. Nocke, H. V. Fuchs, and V. Mellert, ''Acoustic impedance determination of large absorbing linings,'' Euro Noise **98**, 853–858 (1998).
[17] C. Nocke, ''Improved impedance deduction from measurements near grazing incidence,'' Acust. Acta Acust. **85**, 586–590 (1999).
[18] J. F. Allard, B. Castagnede, M. Henry, and W. Lauriks, ''Evaluation of tortuosity in acoustic porous materials saturated by air,'' Rev. Sci. Instrum. **65**, 754–755 (1994).
[19] Ph. Leclaire, L. Kelders, W. Lauriks, M. Melon, N. Brown, and B. Castagnede, ''Determination of the viscous and the thermal characteristic lengths of plastic foams by ultrasonic measurements in helium and air,'' J. Appl. Phys. **80**, 2009–2012 (1996).
[20] T. Legouis and J. Nicolas, ''Phase gradient method of measuring the acoustic impedance of materials,'' J. Acoust. Soc. Am. **81**, 44–50 (1987).
[21] G. A. Daigle and M. R. Stinson, ''Impedance of grass covered ground at low frequencies measured using a phase difference technique,'' J. Acoust. Soc. Am. **81**, 62–68 (1987).
[22] D. L. Johnson, J. Koplik, and R. Dashen, ''Theory of dynamic permeability and tortuosity in fluid saturated porous media,'' J. Fluid Mech. **176**, 379–402 (1987).
[23] Y. Champoux and J. F. Allard, ''Dynamic tortuosity and bulk modulus in air saturated porous media,'' J. Appl. Phys. **70**, 1975–1979 (1991).

The complex phase gradient method applied to leaky Lamb waves

O. Lenoir, J. M. Conoir, and J. L. Izbicki
Laboratoire d'Acoustique Ultrasonore et d'Electronique (LAUE), UMR CNRS 6068, Université du Havre, Place Robert Schuman, 76610 Le Havre, France

(Received 10 October 2001; revised 22 May 2002; accepted 24 May 2002)

The classical phase gradient method applied to the characterization of the angular resonances of an immersed elastic plate, i.e., the angular poles of its reflection coefficient $\underline{R}$, was proved to be efficient when their real parts are close to the real zeros of $\underline{R}$ and their imaginary parts are not too large compared to their real parts. This method consists of plotting the partial reflection coefficient phase derivative with respect to the sine of the incidence angle, considered as real, versus incidence angle. In the vicinity of a resonance, this curve exhibits a Breit–Wigner shape, whose minimum is located at the pole real part and whose amplitude is the inverse of its imaginary part. However, when the imaginary part is large, this method is not sufficiently accurate compared to the exact calculation of the complex angular root. An improvement of this method consists of plotting, in 3D, in the complex angle plane and at a given frequency, the angular phase derivative with respect to the real part of the sine of the incidence angle, considered as complex. When the angular pole is reached, the 3D curve shows a clear-cut transition whose position is easily obtained. [DOI: 10.1121/1.1497370]

PACS numbers: 43.20.Ks, 43.20.Tb, 43.20.Gp [DEC]

I. INTRODUCTION

In this paper, the complex angular poles as well as the zeros of the reflection coefficient $\underline{R}$ of an elastic plate immersed in a fluid are investigated. We are particularly interested in finding an accurate method of obtaining its complex angular poles (whose real parts may be quite different from its real zeros[1]) without having to make exact calculations in the complex angle plane.

Among the roots of the characteristic equation of an unloaded elastic plate, the real roots are assigned to the well-known Lamb modes,[2] which are harmonic, nonattenuated propagating waves. In the case of a plate immersed in a fluid, there are two extreme ways to determine the so-called generalized Lamb modes, looking for the complex roots of the characteristic equation. In the first way, we consider that the reemission angle of the guided wave is real and the frequency complex. We then talk about generalized transient Lamb modes[3,4] (more simply, transient Lamb modes). In the second way, we consider that the frequency is real and the reemission angle complex, and we obtain the classically so-called generalized leaky Lamb modes (more simply, the leaky Lamb modes).[5,6] Because the characteristic equation corresponds to the nullity of the denominator of the reflection coefficient $\underline{R}$, the transient Lamb modes are assigned to its frequency poles and the leaky Lamb modes to its angular poles. It can be shown numerically that the dispersion curves of the transient Lamb modes are superimposed on those of the Lamb modes, except for the A_0 and S_0 modes.[3,4] We can also verify that the real parts of these modes nearly correspond to the reflection coefficient real-frequency zeros at a fixed real-incidence angle. These coincidences led Fiorito *et al.*[7] to apply the resonance scattering theory (RST) approximate formalism to elastic plates and to emphasize the frequency resonant behavior of the reflection and transmission coefficients. In these conditions, the frequency poles are associated with the frequency resonances of the immersed plate. Such coincidences are much less obvious when we compare the leaky Lamb root real parts, the unloaded plate real roots, and the reflection coefficient real-angular zeros[1,6,8] at a fixed real frequency. When the leaky Lamb root imaginary parts are large compared to their real parts, one may observe noticeable differences between the pole real parts and the real-angular zeros. Moreover, the dispersion curves of particular leaky Lamb modes can sometimes be fundamentally different from those of the corresponding Lamb modes, as is the case for the S_1 mode.[9] In fact, their dispersion curves can be found to be relatively close to those of unloaded plate modes corresponding to complex roots, denoted as complex Lamb modes.[10,11] In particular, we can follow leaky Lamb modes with negative imaginary parts whose dispersion curves are close to those of complex Lamb modes with negative imaginary parts; these modes are shown to have negative group velocities.[12–14] In these cases, the reflection coefficient has complex zeros close to complex poles. Because their effects nearly balance, the plot of the modulus of the reflection coefficient, at a fixed real-frequency, versus real-incident angle, can exhibit neither those poles nor those zeros. Therefore, RST formalism is no longer valid to show the angular resonant behavior of the plate, the angular resonances being associated with the angular poles of the reflection coefficient.

The classical phase gradient method was introduced as an alternative method to laborious calculations in the complex frequency and angle planes in order to obtain the frequency and angular resonances of a target, whatever its geometry.[15–18] For simplicity's sake, the general principle is recalled for the case of plane geometry, even though it was first explained for cylindrical shapes.[15] In this paper, it is

shown that the study of the reflection coefficient phase derivative with respect to the sine of the incident angle permits angular poles to be determined with greater accuracy than when using RST. However, when the imaginary parts of the angular poles are of the same order, or larger than their real parts, we cannot obtain them with sufficient accuracy. In order to improve the precision, still using the phase properties, but considering now a complex incidence angle, we study the phase derivative with respect to the real part of the sine of the incidence angle in the complex angle plane at a fixed real frequency. It is shown in this paper that a 3D plot of this derivative allows us to locate the angular poles as well as the complex angular zeros of $\underline{R}$ in the complex angle plane accurately.

In Sec. II, we present dispersion curves obtained from exact calculations of the complex angular roots (leaky Lamb modes) of the characteristic equation for an aluminum plate immersed in water. They are compared to the dispersion curves derived from exact calculations of the complex angular roots (complex Lamb modes) using the characteristic equation for the unloaded aluminum plate. In Sec. III, the phase gradient method as it is applied to obtain the angular resonances of a water-loaded aluminum plate is briefly restated. In Sec. IV, the complex phase gradient method is presented. Examples dealing with the leaky Lamb modes LS_1, LS_2' (with a negative imaginary part) and LA_3 of an aluminum plate are given.

II. EXACT CALCULATIONS IN THE COMPLEX ANGLE PLANE

In this section, we compare the dispersion curves of the leaky Lamb modes (L modes) propagating in the water-loaded aluminum plate to both Lamb modes and complex Lamb modes (C modes) propagating in the unloaded plate. The differences occurring between particular leaky Lamb modes and Lamb modes are outlined, as in Refs. 9 and 17. It is numerically shown that the L modes are close to C modes in these cases. The results exhibited here are used as a reference in the following sections.

Considering a plate immersed in a fluid in which guided waves can propagate along an x axis, the characteristic equation derived from the writing of the boundary conditions is classically written in the following factorized form:

$$\underline{D}(f,\underline{y})=\underline{A}(f,\underline{y})\underline{S}(f,\underline{y})=0.$$

The underlined letters indicate complex functions or variables. In the following, the frequency f is always supposed to have a real value; $\underline{y}$ is the normalized x component of the complex wave vector $\underline{\mathbf{K}}$ of each wave involved in the problem. The normalization is achieved with respect to the wave number K_F in the fluid. $\underline{y}$ also corresponds to the complex sine of a complex reemission angle in the fluid.[19] The function $\underline{A}$ (respectively $\underline{S}$) has complex angular roots assigned to antisymmetric A (respectively, symmetric S) modes. These functions may be written as

$$\underline{A}(f,\underline{y})=C_A(f,\underline{y})+j\tau(\underline{y})$$

$$\underline{S}(f,\underline{y})=C_S(f,\underline{y})-j\tau(\underline{y}).$$

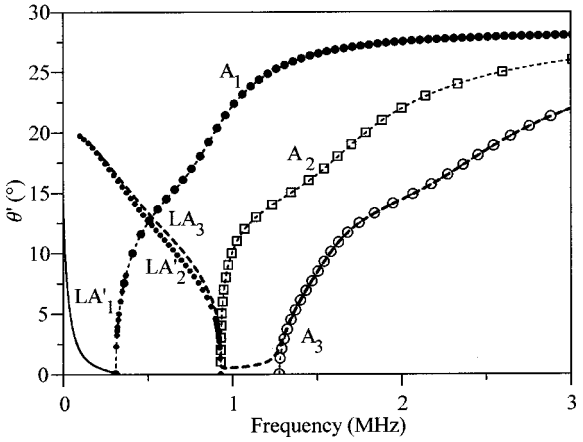

FIG. 1. Plots of the dispersion curves of Lamb modes A_1, A_2, A_3 and of leaky Lamb modes LA_1', LA_2', LA_3 (filled circles: A1 mode, boxes: A2 mode, circles: A3 mode; solid line: LA_1' mode, dot line: LA_2' mode, dotted line: LA_3 mode).

$C_{A,S}$ are, respectively, the characteristic functions whose zeros correspond to the antisymmetric and symmetric modes of the unloaded plate, and τ is the ratio of the acoustic impedance in the fluid compared to that of the plate. Their expressions are given in the Appendix.

The real roots of $C_{A,S}$, corresponding to nonattenuated propagating waves, are assigned to the so-called Lamb modes A or S. There are, of course, other types of roots for those functions: pure imaginary roots and complex roots, generally with large imaginary parts, which are both said to be related to nonpropagating waves[8] (Rokhlin showed that these waves do not transfer energy along the plate). In order to distinguish clearly the different modes obtained in each case, we choose to denote the modes associated with complex angular roots of $C_{A,S}$ as complex Lamb modes CA_i or CS_i. As well, we denote as leaky Lamb modes LA_i or LS_i, the modes associated with complex angular roots of $\underline{A}$ or $\underline{S}$ and as transient Lamb modes TA_i or TS_i, the modes associated to complex frequency roots of $\underline{A}$ or $\underline{S}$.

The dispersion curves which are exhibited in the following are obtained for a 5-mm-thick water-loaded aluminum plate. The aluminum density is $\rho_S=2800$ kg/m^3. The phase velocities of the longitudinal and transverse waves propagating in aluminum are $c_L=6380$ m/s and $c_T=3100$ m/s. When the plate is water loaded, the water parameters used are $\rho_F=1000$ kg/m^3 and $c_F=1470$ m/s.

We are interested in the lowest nonzero order A- and S-leaky Lamb modes. For a given mode, we represent the real part of the complex reemission angle as a function of real frequency as a dispersion curve. In the case when the dispersion curves of the transient Lamb modes differ a lot from those of the leaky Lamb modes, the two types of dispersion curves are shown. A transient Lamb mode dispersion curve corresponds to the plot of a real reemission angle as a function of the real part of a complex frequency root of the characteristic equation. For clarity, the dispersion curves of the antisymmetric and symmetric modes have been separated.

In Fig. 1, we present on one hand the dispersion curves of Lamb modes A_1, A_2, and A_3, which correspond to the plots of the real angular roots of C_A, versus frequency, and

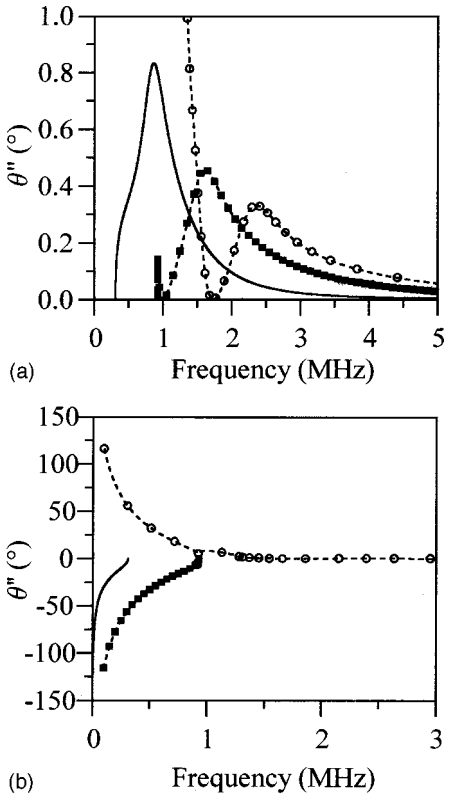

FIG. 2. (a) Frequency evolution of the imaginary parts of the angular roots assigned to leaky Lamb modes LA_1, LA_2, and LA_3 (solid line: LA_1 mode, filled boxes: LA_2 mode, circles: LA_3 mode). (b) Frequency evolution of the imaginary parts of the angular roots assigned to leaky Lamb modes LA_1', LA_2', and LA_3 (solid line: LA_1' mode, filled boxes: LA_2' mode, circles: LA_3 mode).

on the other hand the dispersion curves of leaky Lamb modes, LA_1', LA_2', and LA_3, which correspond to the plots of the real parts of complex angular roots of $\underline{A}$ versus frequency. The superscript $'$ indicates that the imaginary parts are negative.[18] The labeling of these leaky modes is quite difficult; we have chosen to label the two first modes LA_1' and LA_2' because their dispersion curves tend to the cutoff of modes A_1 and A_2; the third one is labeled LA_3 because at high frequencies, its dispersion curve tends to that of Lamb mode A_3. The dispersion curves of transient Lamb modes, TA_1, TA_2, and TA_3, and those of leaky Lamb modes, LA_1 and LA_2 are not shown in Fig. 1, because it is impossible to distinguish them from corresponding Lamb modes A_1, A_2, and A_3. We classically observe on the dispersion curves of the Lamb modes that the angle increases for increasing frequencies. On the contrary, on the dispersion curves of leaky Lamb modes LA_1' and LA_2', the real part of the remission angle decreases for increasing frequencies, up to the cutoff frequencies of Lamb modes A_1 and A_2. The dispersion curve of mode LA_3 is more complicated. It exhibits three parts. At low frequency, up to the cutoff frequency of mode A_2, it shows a similar evolution as that of mode LA_2'. Between the cutoff frequencies of modes A_2 (0.93 MHz) and A_3 (1.276 MHz), mode LA_3 is nearly nondispersive, and, then from the cutoff frequency of mode A_3, its dispersion curve tends to that of mode A_3.

In Fig. 2(a) the evolutions of the imaginary parts of the complex angles versus frequency for modes LA_1, LA_2, and LA_3 are presented. For the first two modes the imaginary parts have small values ranging from 0.01° to at most 0.9°, in their whole observation frequency range. These modes are little attenuated, so we may suppose that they propagate over a large distance and that they should be easily detected experimentally. This is also the case for mode LA_3, but only when its dispersion curve is nearly superimposed with that of mode TA_3. In Fig. 2(b), the frequency evolutions of the imaginary parts of the complex angles assigned to modes LA_1', LA_2', and LA_3 are exhibited. We observe that these modes are very strongly attenuated. So, except in the vicinity of their cutoff frequencies where their imaginary parts are not too large, they should not be detected experimentally.

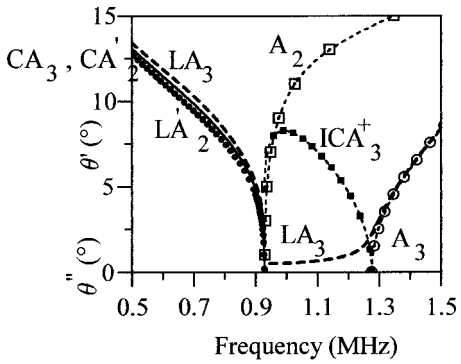

FIG. 3. Plots of the dispersion curves of Lamb modes A_2 and A_3, of complex Lamb modes CA_2' and CA_3 (identical), of leaky Lamb modes LA_2' and LA_3, and of the frequency evolution of the imaginary parts of ICA_3^+ roots (boxes: A_2 mode, circles: A_3 mode, solid line: CA_2' and CA_3 modes, dots: LA_2' mode, dotted line: LA_3 mode, filled boxes: ICA_3^+ mode).

In Fig. 3, we compare the dispersion curves of modes LA_2' and LA_3 to those of complex modes CA_2' and CA_3, which correspond to the complex roots of the unloaded plate dispersion equation. The calculations show that these complex Lamb modes are assigned to complex conjugate roots. Thus, they have a common dispersion curve and the frequency evolutions of their imaginary parts are opposite, nearly identical to those of modes LA_2' and LA_3, as shown in Fig. 2(b). We observe that the dispersion curve of mode LA_3 is slightly shifted towards the high-angle real parts and that the one of mode LA_2' is slightly shifted towards the low-angle real parts, when compared to the common dispersion curve of modes CA_3 and CA_2'. If we look for the complex roots assigned to mode CA_3, in the region where mode LA_3 is nearly nondispersive, we obtain conjugate pure imaginary roots. They are assigned to modes denoted as ICA_3^+ and ICA_3^-. The frequency evolution of the positive imaginary roots (ICA_3^+ mode) is plotted in dotted lines in Fig. 3, ranging from about the cutoff of mode A_2 to the cutoff of mode A_3.

As pointed out earlier, nearly every transient Lamb mode is associated with a Lamb mode. The previous curves show that each leaky Lamb mode can be associated with either a Lamb mode or a complex Lamb mode.

Similar results are obtained for symmetric modes. In Fig. 4, the dispersion curves of modes TS_1 and TS_2 (which are almost identical to those of modes S_1 and S_2), the dis-

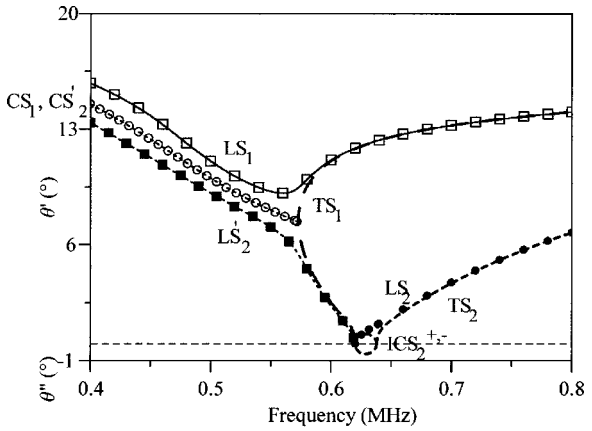

FIG. 4. Plots of the dispersion curves of transient Lamb modes TS_1 and TS_2, of complex Lamb modes CS_1 and CS_2', of leaky Lamb modes LS_1, LS_2, and LS_2', and of the frequency evolutions of the imaginary parts of $ICS_3^{+,-}$ roots (dashed line: TS_1 mode; dotted line: TS_2 mode; circles: CS_1 and CS_2' modes; boxes: LS_1 mode; filled boxes: LS_2' mode; filled circles: LS_2 mode; bold dotted line: $ICS_2^{+,-}$ modes).

persion curves of modes LS_1 and LS_2', as well as the dispersion curves of modes CS_1 and CS_2' are plotted. The peculiar shape of the TS_1 mode dispersion curve is well-known: after its cutoff frequency, the angle increases for decreasing frequencies down to a minimum frequency value, but then the angle continues to increase for increasing frequencies. We can observe that the common dispersion curve of modes CS_1 and CS_2', on which the real-part angle is constantly decreasing for increasing frequencies, nearly reaches the dispersion curve of mode S_1 at its minimum frequency. At low frequencies, the dispersion curve of mode LS_1 is higher than the one of mode CS_1 and the dispersion curve of mode LS_2' is lower. At high frequencies, the dispersion curve of mode LS_1 is superimposed on the one of mode TS_1. We can also observe that modes LS_2 and TS_2 have different cutoff frequencies. The cutoff frequency of mode TS_2 is almost the same as that of the S_2 mode, whereas the one of mode LS_2 tends to that of mode TS_1, which is also the same as that of mode LS_2'. Between the cutoff frequencies of modes TS_1 and TS_2, we can also find conjugate imaginary roots for the unloaded plate dispersion equation. They are assigned to modes denoted as ICS_2^+ and ICS_2^-, according to the sign of their imaginary parts. The frequency evolutions of their imaginary parts are also plotted in Fig. 4. We may observe that these curves link the cutoff frequencies of modes LS_2 and TS_2.

In the case of symmetric modes, we still notice that the search for the real roots of the unloaded plate dispersion equation is insufficient to predict all the generalized leaky Lamb modes and their realistic dispersion curves.

In this section, we have presented results obtained from rather tedious but exact calculations in the complex angle plane. In a previous paper, the classical phase gradient method (PGM) was introduced in order to avoid such bother.[17] However, their calculations were necessary because the results presented in this section will be used as a reference in the following ones, thus allowing those provided by alternative methods to be compared to them in order to evaluate their accuracy. In the following section, the bases of the PGM are recalled, following which we will present an improvement of that method, which can be used to obtain the angular poles with great accuracy, whatever the values of their imaginary part.

III. THEORETICAL BASIS OF THE PHASE GRADIENT METHOD

In this section, we briefly recall the interest of the study of the partial reflection coefficient phase derivative with respect to the sine of the incident angle to obtain the angular resonances of an immersed plate. These angular resonances correspond to the complex angular poles of the reflection coefficient. We use, in the following, the notation introduced by Fiorito *et al.*[7] to express the angular pole:

$$\underline{y}_P = y_P + j\frac{\gamma}{2},$$

where $\gamma/2$ is the half-width of the associated angular resonance.

When a water-loaded elastic plate is insonified by a homogeneous harmonic plane wave at a real incidence angle θ, its reflection coefficient $\underline{R}$ can be written as

$$\underline{R}(y) = \frac{C_A(y)C_S(y) - \tau^2(y)}{\underline{A}(y)\underline{S}(y)}, \tag{1}$$

where $y = \sin\theta$.

In the case of an aluminum plate immersed in water, the impedance ratio τ is very small compared to unity; thus, the zeros of $\underline{R}(y)$ correspond to the real zeros of $C_{A,S}(y)$, and consequently to the Lamb modes. For a real variation of the incidence angle, the numerator of $\underline{R}(y)$ is always real, positive or negative, and the change of sign occurs at its zeros. In the vicinity of a zero, denoted as y_Z, the phase change of the numerator is of the type $\pm\pi H(y - y_Z)$, where $H(y)$ is the Heaviside function. Therefore, the phase derivative of the numerator with respect to y is numerically negligible. We only take into account the phase changes of the reflection coefficient due to its poles. According to these assumptions, the reflection coefficient phase is written as

$$\phi_R = \phi_S + \phi_A, \tag{2a}$$

where

$$\phi_S(y) = a\tan\left(\frac{\tau(y)}{C_S(y)}\right), \tag{2b}$$

and

$$\phi_A(y) = -a\tan\left(\frac{\tau(y)}{C_A(y)}\right). \tag{2c}$$

$\phi_{A,S}(y)$ are, respectively, the phase changes due to the antisymmetric and symmetric poles.

The exact partial derivatives of the phases $\phi_{A,S}(y)$, with respect to y, have the following expressions:

$$\frac{\partial\phi_{A,S}}{\partial y} = \mp\frac{C_{A,S}\dfrac{\partial\tau}{\partial y} - \tau\dfrac{\partial C_{A,S}}{\partial y}}{C_{A,S}^2 + \tau^2}. \tag{3}$$

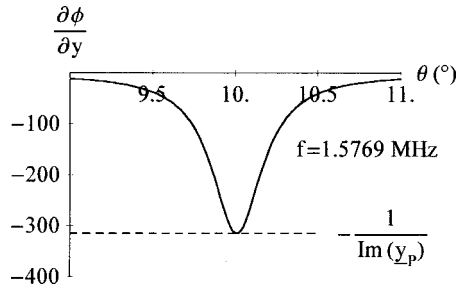

FIG. 5. Plot of the exact angle phase derivative $\partial\phi/\partial y$, versus incidence angle, at the vicinity of mode LA_3, at $f=1.5769$ MHz.

The angular partial derivatives of $C_{A,S}(y)$ and $\tau(y)$ are given in Ref. 17.

In Fig. 5, we have plotted the angular evolution of the exact angular phase derivative, at frequency $f=1.5769$ MHz for which $C_A(y)$ is null, at $\theta=10°$. In these conditions, the exact calculation in the complex angle plane gives the following root of $\underline{A}(\underline{y})$:

$$\underline{y}_P = 0.173\,81 + j\ \ 0.0031\,180\,9$$

or

$$\underline{\theta}_P = a\ \sin(\underline{y}_P) = (10.0095 + j\ \ 0.185\,07)°.$$

We observe that the curve shows a Breit–Wigner shape, whose minimum is located at 10° and minimum amplitude $(-0.003\,181)$ corresponds to the opposite of the inverse of the imaginary part of $\underline{y}_P$ (indicated by a horizontal dashed line) with a precision of 0.03%.

In this case, the real part of the complex root of $\underline{A}(\underline{y})$, which corresponds to mode LA_3, is nearly the same as the real root of $C_A(y)$ which corresponds to mode A_3. The RST approximation is thus valid and we can write an approximate expression of the reflection coefficient, in the vicinity of mode LA_3 as

$$\underline{R}_{\text{app}}(y) = \frac{y - y_P}{y - y_P - j\,\dfrac{\gamma}{2}}. \tag{4}$$

The approximate phase derived from Eq. (4) is

$$\phi_{\text{app}}(y) = a\,\tan\left(\frac{\gamma/2}{y - y_P}\right). \tag{5}$$

The angular derivative of this approximate phase is expressed as

$$\frac{\partial\phi_{\text{app}}}{\partial y}(y) = \frac{-\gamma/2}{(y - y_P)^2 + (\gamma/2)^2}. \tag{6}$$

We obtain, from Eq. (6)

$$\frac{\partial\phi_{\text{app}}}{\partial y}(y_P) = -\frac{2}{\gamma}. \tag{7}$$

The numerical results presented above and in Fig. 5 confirm the validity of the latter equation. Therefore, the phase gradient method appears to be a simple method to obtain the angular poles of the reflection coefficient accurately, when their imaginary parts are small (generally lower than 1°) compared to their real parts.

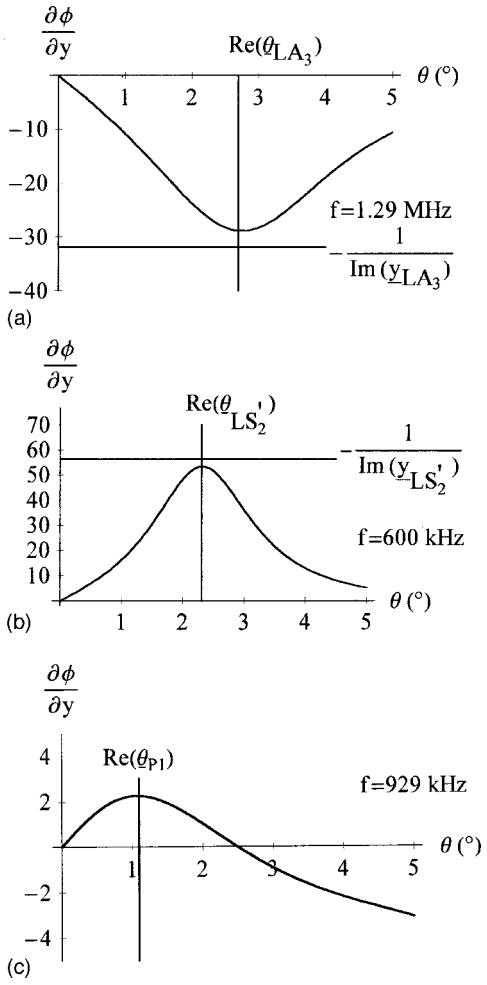

FIG. 6. (a) Plot of the exact angle phase derivative $\partial\phi/\partial y$, versus incidence angle, in the vicinity of mode LA_3, at $f=1.29$ MHz. (b) Plot of the exact angle phase derivative $\partial\phi/\partial y$, versus incidence angle, in the vicinity of mode LS_2', at $f=600$ kHz. (c) Plot of the exact angle phase derivative $\partial\phi/\partial y$, versus incidence angle, in the vicinity of modes LA_2' and LA_3, at $f=929$ kHz.

Now, let us consider the case when the real part of a complex angular root of the water-loaded plate dispersion equation differs significantly from the closest real root of the unloaded plate dispersion equation. At $f=1.29$ MHz, $C_{\underline{A}}(y)$ is null for $\theta=2°$ $(y=0.034\,899)$, and $\underline{A}(\underline{y})$ is null for $\underline{\theta}_P = (2.6913 + j\ 1.7982)°$ or $\underline{y}_P = 0.046\,98 + j\ 0.031\,355$. These results are referred to as case 1, in the following. These roots correspond, respectively, to modes A_3 and LA_3.

Figure 6(a) shows the plot of the exact angular phase derivative, versus real angle, in the vicinity of mode LA_3. The solid vertical line indicates the real part of the complex root and the horizontal one the opposite of the inverse of its imaginary part. We notice that the curve minimum is still located at the real part of the complex root [significantly different from the real root of $C_A(y)$], but the modulus of the minimum amplitude is quite different from the inverse of the imaginary part. Numerically, the minimum amplitude allows us to obtain the value of this imaginary part with an error of about 10%. This is due to the fact that the pole imaginary part (greater than 1°) is of the same order as its real part. Although not dramatically incorrect in this case, the phase

gradient method is insufficiently accurate to completely characterize the complex angular pole or the angular resonance.

The PGM also allows us to detect complex roots whose imaginary part is negative. For example, at $f=600$ kHz, $\underline{S}(\underline{y})$ is null for $\underline{\theta}_P=(2.307-j\ 1.0176)°$ or $\underline{y}_P=0.040\,26-\underline{j}\ 0.017\,75$. This root is assigned to mode LS_2'. For this frequency and in the vicinity of the pole, $C_S(y)$ is null for $\theta_{S1}=2.18°$. This root is assigned to the S_1 Lamb mode. These results are referred to as case 2, in the following. In Fig. 6(b), the plot of the exact angular derivative versus real angle, which exhibits a resonant Breit–Wigner shape, reaches its maximum at the real part of $\underline{\theta}_P$ and not at θ_{S1}. Equation (6) clearly indicates that the imaginary part of $\underline{y}_P$, i.e., the half-width of the associated angular resonance $\gamma/2$, is negative. Unfortunately, the maximum amplitude only allows us to obtain the value of the imaginary part $\underline{y}_P$ with a precision of about 10%. It is still due to the fact that the pole imaginary part is large compared to the real part.

A final example is given to demonstrate the possible lack of accuracy of the classical PGM. At $f=929$ kHz, $\underline{A}(\underline{y})$ has two roots: $\underline{\theta}_{P1}=(1.0925+j\ 5.0145)°$, assigned to mode LA_3 and $\underline{\theta}_{P2}=(0.3932-j\ 2.507)°$, assigned to mode LA_2'. In Fig. 6(c) the plot of the exact angular derivative shows a maximum, located at the real part of $\underline{\theta}_{P1}$. Because the imaginary part of this root is positive, we expected to observe a minimum and not a maximum. Moreover, the maximum amplitude corresponds neither to the imaginary part of $\underline{y}_{P1}$ nor to the one of $\underline{y}_{P2}$ ($\underline{y}_{P1,2}$ are the complex sine values associated with the complex angles $\underline{\theta}_{P1,2}$). It should be noticed that this case corresponds to a very limited case (the imaginary parts are too large), for which it is unrealistic to expect accurate results.

As a partial conclusion, we can say that the classical PGM is very efficient, but only when the dispersion curves of the leaky Lamb modes and the ones of the Lamb modes are superimposed. As soon as this condition ceases to be fulfilled even in a minor way, this method loses its efficiency and may even become totally inaccurate. For this reason, an improvement of this classical method is developed in the following section.

IV. THE COMPLEX PHASE GRADIENT METHOD

The lack of accuracy of the classical PGM mainly occurs when a complex root assigned to a generalized leaky Lamb mode differs from the real root assigned to the corresponding Lamb mode. Thus, we now consider the reflection from the immersed plate, when it is insonified by an evanescent plane wave whose wave vector is complex (its imaginary part being perpendicular to the real part). In other words, we consider an incident wave impinging on the plate at a complex incidence angle.[19]

A. Basis of the method

We consider now a complex incidence angle at a fixed frequency, denoted as $\underline{\theta}=\theta'+j\,\theta''$, whose sine is denoted as $\underline{y}=y'+jy''$. Formally, to take into account a complex angle does not change the expression of the reflection coefficient given in Eq. (1), but the functions $C_{A,S}(\underline{y})$ and $\tau(\underline{y})$ become complex, as well as the numerator of $\underline{R}(\underline{y})$. We write the reflection coefficient as

$$\underline{R}(\underline{y})=\frac{\underline{N}(\underline{y})}{\underline{A}(\underline{y})\cdot\underline{S}(\underline{y})}. \tag{8}$$

In this way, the whole phase of the reflection coefficient, taking into account the antisymmetric and symmetric complex poles and the complex zeros, can be written as

$$\phi(\underline{y})=\phi_{\underline{N}}(\underline{y})-\phi_{\underline{A}}(\underline{y})-\phi_{\underline{S}}(\underline{y}), \tag{9}$$

where

$$\phi_{\underline{X}}(\underline{y})=a\tan\left(\frac{X_{\mathrm{I}}(\underline{y})}{X_{\mathrm{R}}(\underline{y})}\right),\quad \underline{X}(\underline{y})=\underline{N}(\underline{y}),\underline{A}(\underline{y}),\underline{S}(\underline{y}). \tag{10}$$

The subscripts R and I indicate, respectively, the real and imaginary parts of the complex function $\underline{X}(\underline{y})$.

The complex PGM consists of studying the partial derivative of $\phi(\underline{y})$ with respect to the real part of $\underline{y}$, namely y'. This derivative can be written as the sum of three terms

$$\frac{\partial\phi}{\partial y'}=\frac{\partial\phi_{\underline{N}}}{\partial y'}-\frac{\partial\phi_{\underline{A}}}{\partial y'}-\frac{\partial\phi_{\underline{S}}}{\partial y'}, \tag{11}$$

where

$$\frac{\partial\phi_{\underline{X}}}{\partial y'}=\frac{X_{\mathrm{R}}\dfrac{\partial X_{\mathrm{I}}}{\partial y'}-X_{\mathrm{I}}\dfrac{\partial X_{\mathrm{R}}}{\partial y'}}{X_{\mathrm{R}}^2+X_{\mathrm{I}}^2}. \tag{12}$$

Their analytical expressions are too long to be reproduced in this paper.

In the vicinity of a complex zero or a complex pole of $\underline{R}(\underline{y})$, the corresponding complex function $\underline{X}(\underline{y})$ is null and the phase derivative $\partial\phi/\partial y'$ is about to exhibit a sharp transition between $+\infty$ and $-\infty$. So, a 3D representation of $\partial\phi/\partial y'$ or of its modulus in the complex angle plane makes it possible to localize the zeros and the poles of $\underline{R}(\underline{y})$ easily. Theoretically, according to Eq. (11) we can separate in the whole phase derivative the term corresponding to either complex zeros, antisymmetric poles or symmetric poles, and achieve the 3D plot of each phase derivative component separately.

It can be shown that the pole $-\underline{y}_P$ is associated with each pole $\underline{y}_P$ and both the zero $-\underline{y}_Z$ and the conjugate zero $\underline{y}_Z^*$ are associated with each angular zero $\underline{y}_Z$ (the asterisk denotes the complex conjugate). If the 3D representation in the complex angle plane is limited to the complex angles whose real part is positive, we can distinguish a pole from a zero, thanks to the second property of the complex zero. On the contrary, nothing can differentiate an antisymmetric pole from a symmetric one.

In the following, we use this new method to study different cases for which the PGM lacks efficiency.

B. Pole real parts different from real zeros of $\underline{R}$

In this subsection, we study case 1 of Sec. III by means of the complex PGM. In Fig. 7(a) for a fixed frequency f

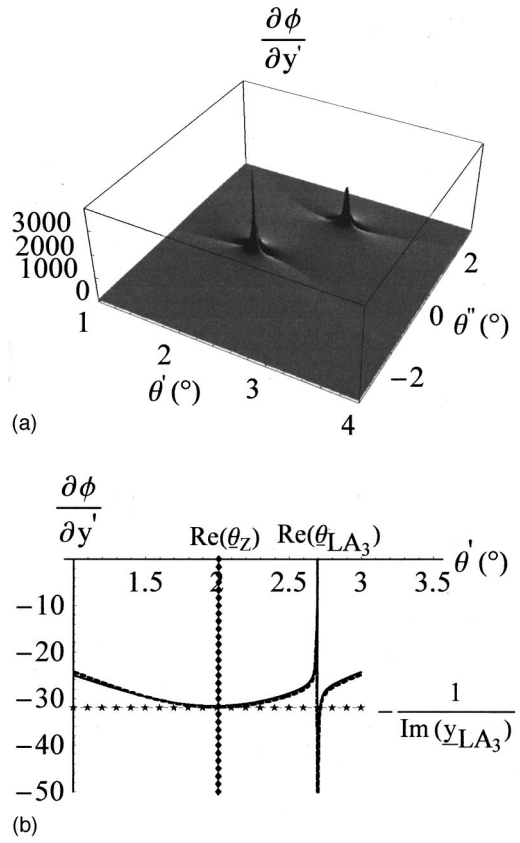

FIG. 7. (a) 3D plot of the exact phase derivative $\partial\phi/\partial y'$, in the complex angle plane, in the vicinity of modes A_3 and LA_3, at $f=1.29$ MHz. (b) Plots of the exact phase derivative $\partial\phi/\partial y'$ (solid line) and of the approximate phase derivative $\partial\phi_{app}/\partial y'$ (dashed line), versus real part of the complex incidence angle θ', $\theta''=\mathrm{Im}(\theta_{LA_3})$, at $f=1.29$ MHz.

$=1.29$ MHz, we present the 3D plot of the modulus of $[\partial\phi/\partial y'](\underline{\theta})$, for complex angle real parts θ' ranging from 1° to 4°, and imaginary parts θ'' from $-3°$ to 3°, in order to detect a complex pole assigned to the LA_3 mode. In this figure, we can observe two peaks of very large amplitude with respect to the background level (this amplitude has no real meaning: theoretically, it tends to infinity, but numerically, its depends on the calculation step). A cursor allows us to determine the exact loci of the peaks. The peak located on the real axis at $\theta'=2°$ is associated with a real zero of $\underline{R}(\underline{\theta})$ [corresponding to a real zero of $C_A(\underline{\theta})$]; it can be assigned to mode A_3. The second peak located at $(\theta',\theta'')=(2.69°,1.8°)$ corresponds to a pole assigned to mode LA_3. Therefore, contrary to the PGM, the complex PGM allows us to determine both pole real and imaginary parts precisely. In Fig. 7(b), we present a cross section of Fig. 7(a) [in fact, a 2D plot of $[\partial\phi/\partial y'](\theta')$, not of its modulus], for which θ'' corresponds exactly to the imaginary part of the complex pole detected. This plot of $[\partial\phi/\partial y'](\theta')$ (the solid line) versus θ' exhibits two phenomena. First, we obviously observe a clear-cut transition related to the pole, when $\theta'=2.69°$, and second, we observe a minimum located at the real zero $\theta'=2°$, indicated by a dotted vertical line whose amplitude is nearly the opposite of the inverse of the imaginary part of the pole (indicated by the horizontal line). This result is surprising because the value of the pole imaginary part is not obtained in the close vicinity of the pole itself, but at the zero location. Even though they are not very close, this result show that the zeros and poles are connected.

We can explain this latter observation by expanding the RST approximation as it is valid on the real-angle axis in the complex angle plane. Indeed, in the vicinity of an isolated complex pole $\underline{y}_P=\sin\underline{\theta}_P$, but which contains a complex zero $\underline{y}_Z=\sin\underline{\theta}_Z$, the reflection coefficient can be modelized by

$$\underline{R}_{\mathrm{app}}(\underline{y})=\frac{\underline{y}-\underline{y}_Z}{\underline{y}-\underline{y}_P}. \tag{13}$$

The phase derivative of this approximate reflection coefficient can be written as

$$\frac{\partial\phi_{\mathrm{app}}}{\partial y'}(\underline{y})=-\frac{\mathrm{Im}(\underline{y}-\underline{y}_Z)}{\mathrm{Re}^2(\underline{y}-\underline{y}_Z)+\mathrm{Im}^2(\underline{y}-\underline{y}_Z)}+\frac{\mathrm{Im}(\underline{y}-\underline{y}_P)}{\mathrm{Re}^2(\underline{y}-\underline{y}_P)+\mathrm{Im}^2(\underline{y}-\underline{y}_P)}. \tag{14}$$

In Fig. 7(b), we have fixed the imaginary part of $\underline{\theta}$ at the value of the pole imaginary part $\mathrm{Im}(\underline{\theta}_P)$. Hence, we have to write

$$\underline{y}=\sin\theta'\cosh(\mathrm{Im}(\underline{\theta}_P))+j\cos\theta'\sinh(\mathrm{Im}(\underline{\theta}_P)).$$

Consequently, when $\mathrm{Re}(\underline{\theta})=\mathrm{Re}(\underline{\theta}_Z)$, we obtain

$$\frac{\partial\phi_{\mathrm{app}}}{\partial y'}(\sin(\mathrm{Re}(\underline{\theta}_Z))\cosh(\mathrm{Im}(\underline{\theta}_P))+j\cos(\mathrm{Re}(\underline{\theta}_Z))\sinh(\mathrm{Im}(\underline{\theta}_P)))$$

$$=-\cos(\mathrm{Re}(\underline{\theta}_Z))(\sinh(\mathrm{Im}(\underline{\theta}_P))-\sinh(\mathrm{Im}(\underline{\theta}_Z)))\Big/\left(\begin{array}{c}\sin^2(\mathrm{Re}(\underline{\theta}_Z))\left(\begin{array}{c}\cosh(\mathrm{Im}(\underline{\theta}_P))\\-\cosh(\mathrm{Im}(\underline{\theta}_Z))\end{array}\right)^2\\+\cos^2(\mathrm{Re}(\underline{\theta}_Z))\left(\begin{array}{c}\sinh(\mathrm{Im}(\underline{\theta}_P))\\-\sinh(\mathrm{Im}(\underline{\theta}_Z))\end{array}\right)^2\end{array}\right)$$

$$+\sinh(\mathrm{Im}(\underline{\theta}_P))(\cos(\mathrm{Re}(\underline{\theta}_Z))-\cos(\mathrm{Re}(\underline{\theta}_P)))\Big/\left(\begin{array}{c}\cosh^2(\mathrm{Im}(\underline{\theta}_P))\left(\begin{array}{c}\sin(\mathrm{Re}(\underline{\theta}_Z))\\-\sin(\mathrm{Re}(\underline{\theta}_P))\end{array}\right)^2\\+\sinh^2(\mathrm{Im}(\underline{\theta}_P))\left(\begin{array}{c}\cos(\mathrm{Re}(\underline{\theta}_Z))\\-\cos(\mathrm{Re}(\underline{\theta}_P))\end{array}\right)^2\end{array}\right). \tag{15}$$

Assuming that the complex pole and zero are very close, it can be shown numerically that, on one hand, the first term of the preceding equation is predominant, and, on the other hand, the first term of its denominator can be neglected. So, we can write

$$\frac{\partial \phi_{\text{app}}}{\partial y'}(\sin(\text{Re}(\underline{\theta}_Z))\cosh(\text{Im}(\underline{\theta}_P)) + j\cos(\text{Re}(\underline{\theta}_Z))\sinh(\text{Im}(\underline{\theta}_P))) \simeq -\frac{1}{\cos(\text{Re}(\underline{\theta}_Z))\cdot(\sinh(\text{Im}(\underline{\theta}_P))-\sinh(\text{Im}(\underline{\theta}_Z)))}. \tag{16}$$

If, in addition $\underline{\theta}_Z$ is real, we obtain

$$\frac{\partial \phi_{\text{app}}}{\partial y'}(\sin(\text{Re}(\underline{\theta}_Z))\cosh(\text{Im}(\underline{\theta}_P)) + j\cos(\text{Re}(\underline{\theta}_Z))\sinh(\text{Im}(\underline{\theta}_P))) \simeq -\frac{1}{\cos(\text{Re}(\underline{\theta}_Z))\sinh(\text{Im}(\underline{\theta}_P))}. \tag{17}$$

If $\text{Re}(\underline{\theta}_Z)$ is very close to $\text{Re}(\underline{\theta}_P)$, we find finally

$$\frac{\partial \phi_{\text{app}}}{\partial y'}(\sin(\text{Re}(\underline{\theta}_Z))\cosh(\text{Im}(\underline{\theta}_P)) + j\cos(\text{Re}(\underline{\theta}_Z))\sinh(\text{Im}(\underline{\theta}_P))) \simeq -\frac{1}{\cos(\text{Re}(\underline{\theta}_P))\sinh(\text{Im}(\underline{\theta}_P))} = -\frac{1}{\text{Im}(\underline{y}_P)}. \tag{18}$$

In Fig. 7(b), we have added the plot of the approximate phase derivative derived from Eq. (14); one may observe the close agreement between the two curves.

C. Poles with large negative imaginary parts

In this subsection, we study case 2 of Sec. III by means of the complex PGM. In Fig. 8(a), at a fixed frequency of f $=600$ kHz, we present the 3D plot of the modulus of $[\partial\phi/\partial y'](\underline{\theta})$, for real parts θ', ranging from 0° to 13°, and imaginary parts θ'', from $-2°$ to 2°, in order to detect the complex poles assigned to modes LS_1 and LS_2'. The exact calculations give $\underline{\theta}_{\text{LS}_1}=(11.12+j\ 0.307)°$, $\underline{\theta}_{\text{LS}_2'}=(2.307 - j\ 1.018)°$, and real zeros can be observed at $\theta'=11.113°$ and $\theta'=2.186°$. The 3D plot of Fig. 8(a) does indeed show two peaks on the real-angle axis and two other peaks corresponding to the poles at the positions predicted by the exact calculations. A cross section of Fig. 8(a) when θ'' is fixed at $\text{Im}(\underline{\theta}_{\text{LS}_2'})$ is presented in Fig. 8(b). We obtain a sharp transition when $\theta'=\text{Re}(\underline{\theta}_{\text{LS}_2'})$ and a maximum located at $\theta' =2.186°$, which is the locus of the closest real zero. The horizontal line indicates the opposite of the inverse of the imaginary part. We note that the maximum amplitude does not reach the horizontal line. The approximate phase derivative $[\partial\phi_{\text{app}}/\partial y'](\theta')$ of Eq. (14), plotted in a dashed line, shows a maximum whose amplitude corresponds to the opposite of the inverse of the imaginary part. The model of the reflection coefficient, chosen in Eq. (13), dealing with only one pole and one zero, is in that case too poor and the approximate phase derivative $[\partial\phi_{\text{app}}/\partial y'](\theta')$ does not accurately coincide with the exact one. If the pole is not isolated, this model may be enriched by taking into account the closest pole and zero. When the pole $\underline{y}_P$ and the zero $\underline{y}_Z$ are relatively close to the imaginary angle axis, as is the case here, an improvement of the model consists of taking into account the pole $-\underline{y}_P$ and the zero $-\underline{y}_Z$. In this model with two zeros and two poles, the approximate factorized expression of the reflection coefficient can then be written as

$$\underline{R}_{2\text{app}}(\underline{y}) = \frac{(\underline{y}-\underline{y}_Z)(\underline{y}+\underline{y}_Z)}{(\underline{y}-\underline{y}_P)(\underline{y}+\underline{y}_P)}. \tag{19}$$

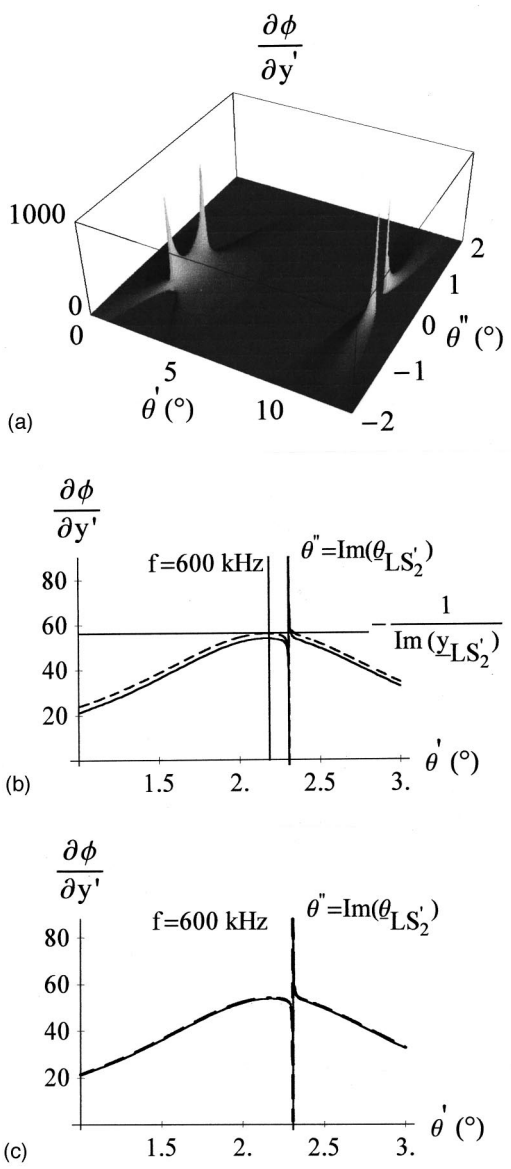

FIG. 8. (a) 3D plot of the exact phase derivative $\partial\phi/\partial y'$, in the complex angle plane, in the vicinity of modes S_1, S_2, LS_1, and LS_2', at $f=600$ kHz. (b) Comparison of the plots of the exact phase derivative $\partial\phi/\partial y'$ (solid line) and of the approximate phase derivative $\partial\phi_{\text{app}}/\partial y'$ (dashed line), versus real part of the complex incidence angle θ', $\theta''=\text{Im}(\underline{\theta}_{\text{LS}_2'})$, at $f=600$ kHz. (c) Comparison of the plots of the exact phase derivative $\partial\phi/\partial y'$ (solid line) and of the approximate phase derivative $\partial\phi_{\text{app2}}/\partial y'$ (dashed line), versus real part of the complex incidence angle θ', $\theta''=\text{Im}(\underline{\theta}_{\text{LS}_2'})$, at $f=600$ kHz.

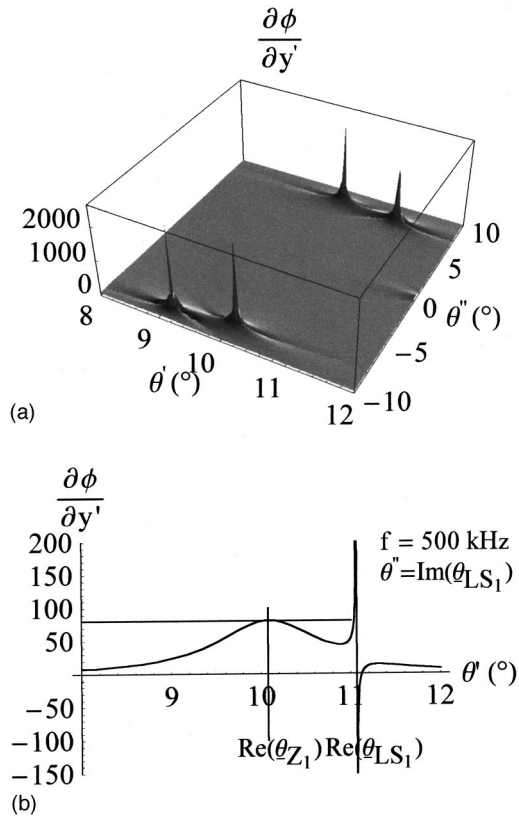

FIG. 9. (a) 3D plot of the exact phase derivative $\partial\phi/\partial y'$, in the complex angle plane, in the vicinity of modes S_1, S_2, LS_1, and LS_2', at $f=500$ kHz. (b) Plot of the exact phase derivative $\partial\phi/\partial y'$, versus real part of the complex incidence angle θ', $\theta''=\mathrm{Im}(\underline{\theta}_{LS_1})$, at $f=500$ kHz.

The phase derivative of this approximate reflection coefficient, denoted as $[\partial\phi_{2\mathrm{app}}/\partial y'](\underline{y})$, is quite complicated, and anyway cannot give the imaginary part of the angular pole analytically in a simple way. However, we have tested the validity of this model by comparing the plots of the exact phase derivative $[\partial\phi/\partial y'](\theta')$ and of $[\partial\phi_{2\mathrm{app}}/\partial y'](\theta')$, in Fig. 8(c). One may observe the quite close agreement of the two plots.

D. Poles close to complex zeros of *R*

We can consider the case when $\underline{R}(\underline{y})$ actually shows a complex pole and a close complex zero. At $f=500$ kHz, according to the dispersion curves of Fig. 4, we can detect the leaky Lamb modes LS_1 and LS_2', and the complex Lamb modes CS_1 and CS_2' (close to complex zeros of $\underline{R}(\underline{y})$). The exact calculations give $\underline{\theta}_{LS_1}=(11.0611+j\ 7.655)°$, $\underline{\theta}_{LS_2'}=(9.133-j\ 9.0985)°$, $\underline{\theta}_{CS_1}=(10.0275+j\ 8.3985)°=\underline{\theta}^*_{CS_2'}$ for the different modes, and $\underline{\theta}_{Z1}=(10.073+j\ 8.3689)°=\underline{\theta}^*_{Z2}$ for the zeros of $\underline{R}$. We may notice that the complex zeros of $\underline{R}$ do not correspond exactly with the complex zeros of C_S. Figure 9(a) shows the 3D plot of $[\partial\phi/\partial y'](\underline{\theta})$, in a region where θ' ranges from 9° to 12°, and θ'' from −10° to 10°. We observe two peaks located at complex conjugate angles which are assigned to the complex zeros of the reflection coefficient, and two other peaks located at the complex angles associated with modes LS_1 and LS_2'.

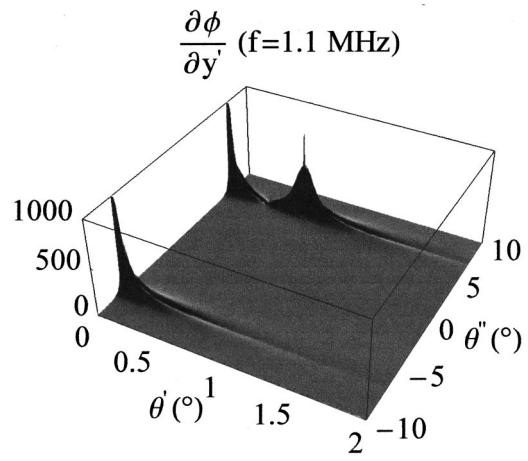

FIG. 10. 3D plot of the exact phase derivative $\partial\phi/\partial y'$, in the complex angle plane, in the vicinity of modes CA_3 and LA_3, at $f=1.1$ MHz.

In Fig. 9(b), θ'' being fixed to $\mathrm{Im}(\underline{\theta}_{LS1})$, the exact derivative $[\partial\phi/\partial y'](\theta')$ and the approximate one $[\partial\phi_{\mathrm{app}}/\partial y'](\theta')$ are plotted versus θ'. The agreement between the two plots is good. We observe a transition indicating the real part of the pole $\underline{\theta}_{LS_1}$ and a maximum located at the real part of the zero $\underline{\theta}_{Z1}$ (indicated by a vertical line). Once again, we verify that when an isolated pole and the closest complex zero of $\underline{R}(\underline{y})$ are far from the axis of the imaginary angles, a model with one pole and one zero is sufficient to simulate the exact phase derivative efficiently. Even if the angular pole and the angular zero are not very close, we have checked the validity of the approximate relation [Eq. (16)]. In Fig. 9(b), the horizontal line indicates the value of $-1/[\cos(\mathrm{Re}(\underline{\theta}_{Z1}))(\sinh(\mathrm{Im}(\underline{\theta}_{LS_1}))-\sinh(\mathrm{Im}(\underline{\theta}_{Z1})))]$; we can remark that it nearly corresponds to the maximum of $[\partial\phi/\partial y'](\theta')$, which is located at the real part of the zero $\underline{\theta}_{Z1}$.

E. Poles close to imaginary poles of *R*

As a last example, we consider the case when $\underline{R}$ exhibits an imaginary zero and a close complex pole. At $f=1.1$ MHz, we can detect two conjugate imaginary roots of C_A, at $\underline{\theta}=\pm j\ 7.055\,799°$ (the positive one being assigned to mode CA_3^+), two conjugate zeros of $\underline{R}$ at $\underline{\theta}=\pm j\ 7.052\,416°$, and a complex root of $\underline{A}$, at $\underline{\theta}=(0.666\,05+j\ 7.085\,95)°$ (which is assigned to the mode LA_3). No leaky Lamb root with a negative imaginary part can be found. Figure 10 shows the 3D plot of the exact phase derivative, $[\partial\phi/\partial y'](\underline{\theta})$, in a region where θ' ranges from 0° to 2°, and θ'', from −10° to 10°. We can, in fact, observe two peaks located on the imaginary axis at conjugate loci which can be assigned to the imaginary zeros of $\underline{R}$, and another peak located at $\underline{\theta}=(0.67+j\ 7.1)°$, corresponding to mode LA_3. No other peak is observed.

In this section, we have chosen cases for which the PGM loses accuracy, especially in the exact evaluation of pole imaginary parts. All the examples shown, using the complex PGM, prove that this new method is well adapted to the accurate evaluation of the poles as well as the zeros of the reflection coefficient.

V. CONCLUSIONS

In this paper, we have been interested in obtaining the angular poles of the reflection coefficient of an elastic plate immersed in a fluid. These poles are associated with the leaky Lamb modes. Thanks to several examples, it has been recalled that the dispersion curves of the Lamb modes resulting from the search for the real roots of the unloaded plate dispersion equation are insufficient to predict the dispersion curves of all the leaky Lamb modes. The search for the complex angular roots of the water-loaded plate dispersion equation assigned to the leaky Lamb modes may be quite tedious, and the choice of a good guess is often crucial.

This is why an alternative method was presented in a previous paper: the ''classical'' phase gradient method. The efficiency of this method has been recalled in the present paper. This method is even more accurate when the pole is close to a real zero of the reflection coefficient. When the pole imaginary part is large or when the closest zero to the pole is also complex, the value obtained for the imaginary part is less reliable. Therefore, an improvement of this ''classical'' method has been presented in this paper.

The complex phase gradient method consists in plotting the exact phase derivative of the reflection coefficient at a real frequency, in the complex angle plane, with respect to the real part of the sine of an incidence angle, considered as complex. This method allows us to determine the loci of the complex angular poles accurately, as well as the complex angular zeros of the reflection coefficient. Thanks to this method, we can eliminate the problem of the choice of a good guess, provided that the region of the complex angle plane in which we are looking for the poles and zeros is wide enough.

The complex phase gradient method can be viewed as a simple, accurate, alternative method of finding the generalized leaky Lamb modes which are assigned to the angular poles of the reflection coefficient of a plate.

Provided that the phase and its partial derivatives may be obtained analytically, this method is not limited to plane geometries, and work is currently in progress in order to apply it to cylindrical and spherical geometries.

ACKNOWLEDGMENTS

The authors wish to thank P. Rembert and F. Luppé, from LAUE, for the fruitful discussions we have had, and particularly F. Luppé and D. Hallidy for the rereading of this paper. Moreover, we would like to indicate that the dispersion curves of the leaky Lamb modes and those of the complex Lamb modes were already compared several years ago, by J. Duclos, from LAUE, and by M. Talmant, from LIP (Laboratoire d'Imagerie Paramétrique, UMR CNRS 7623, Université Pierre et Marie Curie (Paris VI), France), but their work was not published in international journals.

APPENDIX:

$$C_A(f,y)=\left(1-2\left(\frac{c_T}{c_F}y\right)^2\right)^2\tan\left(\frac{\pi fd}{c_L}\sqrt{1-\left(\frac{c_L}{c_F}y\right)^2}\right)+4\frac{c_T^3y^2}{c_Lc_F^2}\sqrt{1-\left(\frac{c_L}{c_F}y\right)^2}\sqrt{1-\left(\frac{c_T}{c_F}y\right)^2}\times\tan\left(\frac{\pi fd}{c_T}\sqrt{1-\left(\frac{c_T}{c_F}y\right)^2}\right),\tag{A1}$$

$$C_S(f,y)=\left(1-2\left(\frac{c_T}{c_F}y\right)^2\right)^2\operatorname{cotan}\left(\frac{\pi fd}{c_L}\sqrt{1-\left(\frac{c_L}{c_F}y\right)^2}\right)+4\frac{c_T^3y^2}{c_Lc_F^2}\sqrt{1-\left(\frac{c_L}{c_F}y\right)^2}\sqrt{1-\left(\frac{c_T}{c_F}y\right)^2}\times\operatorname{cotan}\left(\frac{\pi fd}{c_T}\sqrt{1-\left(\frac{c_T}{c_F}y\right)^2}\right),\tag{A2}$$

$$\tau(y)=\frac{\rho_Fc_F}{\rho_Sc_L}\frac{\sqrt{1-\left(\frac{c_L}{c_F}y\right)^2}}{\sqrt{1-y^2}},\tag{A3}$$

where c_L is the bulk longitudinal phase velocity in the plate, c_T is the bulk transverse phase velocity in the plate, c_F is the bulk phase velocity in the fluid, ρ_S and ρ_F are the densities of the plate and the fluid.

[1] D. E. Chimenti and S. I. Rokhlin, ''Relationship between leaky Lamb modes and reflection coefficient zeroes for a fluid-coupled elastic layer,'' J. Acoust. Soc. Am. **88**, 1603–1611 (1990).

[2] H. Lamb, ''On waves in an elastic plate,'' Proc. R. Soc. London, Ser. A **93**, 11–128 (1917).

[3] O. Poncelet and M. Deschamps, ''Lamb waves generated by complex harmonic inhomogeneous plane waves,'' J. Acoust. Soc. Am. **102**, 292–300 (1997).

[4] M. Deschamps and O. Poncelet, ''Transient Lamb waves: Comparison between theory and experiment,'' J. Acoust. Soc. Am. **107**, 3120–3129 (2000).

[5] M. F. M. Osborne and S. D. Hart, ''Transmission, reflection and guiding of an exponential pulse by a steel plate in water. I. Theory,'' J. Acoust. Soc. Am. **17**, 1–18 (1945).

[6] L. E. Pitts, T. J. Plona, and W. G. Mayer, ''Theoretical similarities of Rayleigh and Lamb modes of vibration,'' J. Acoust. Soc. Am. **60**, 374–377 (1976).

[7] R. Fiorito, W. Madigosky, and H. Überall, ''Resonance theory of acoustic waves interacting with an elastic plate,'' J. Acoust. Soc. Am. **66**, 1857–1866 (1979).

[8] S. I. Rokhlin, D. E. Chimenti, and A. H. Nayfeh, ''On the topology of the complex wave spectrum in a fluid-coupled elastic plate,'' J. Acoust. Soc. Am. **85**, 1074–1080 (1989).

[9] G. Durinck, W. Thys, P. Rembert, and J. L. Izbicki, ''Experimental observation on a frequency spectrum of a plate mode of a predominantly leaky nature,'' Ultrasonics **37**, 373–376 (1999).

[10] R. D. Mindlin, ''Waves and vibrations in isotropic elastic plates,'' in *Structural Mechanics* (Pergamon, New York, 1960), pp. 199–232.

[11] A. H. Meitzler, ''Backward-wave transmission of stress pulses in elastic cylinders and plates,'' J. Acoust. Soc. Am. **38**, 835–842 (1965).

[12] K. Negishi, ''Existence of negative group velocities in Lamb waves,'' Jpn. J. Appl. Phys., Part 1 **26**, 171–173 (1987).

[13] J. Wolf, T. D. K. Ngoc, R. Kille, and W. G. Mayer, ''Investigation of Lamb waves having a negative group velocity,'' J. Acoust. Soc. Am. **83**, 122–126 (1988).

[14] Y. Eudeline, H. Duflo, and J. Duclos, ''Mesures d'ondes de Lamb à vitesse d'énergie négative'' (''Measurements of Lamb wave negative energy velocities''), 4^e Congrès Français d'Acoustique, Marseille 14–18 Avril 1997, TEKNEA, 2, 837–840 (1997).

[15] J. M. Conoir, ''Etude des résonances d'un tube élastique basées sur les propriétés de la dérivée de la phase de la matrice de diffusion'' (''Study of the resonances of an elastic tube based upon the properties of the derivatives of the phase of the scattering matrix''), J. Acoust. **4**, 1–24 (1991).
[16] J. M. Conoir, J. L. Izbicki, and O. Lenoir, ''Phase gradient method applied to scattering by an elastic shell,'' Ultrasonics **35**, 157–169 (1996).
[17] O. Lenoir, J. Duclos, J. M. Conoir, and J. L. Izbicki, ''Study of Lamb waves based upon the frequential and angular derivatives of the phase of the reflection coefficient,'' J. Acoust. Soc. Am. **94**, 330–343 (1993).
[18] J. Duclos, J. L. Izbicki, O. Lenoir, and J. M. Conoir, ''Resonant formalism for the liquid–solid interface Rayleigh mode,'' Acta Acust. (Beijing) **2**, 375–378 (1994).
[19] B. Poirée, ''Complex harmonic plane waves,'' in *Proceedings of the Symposium on Physical Acoustics: Fundamentals and Applications, Kortrijk, Belgium*, edited by O. Leroy and M. Breazeale (Plenum, New York and London, 1990), pp. 99–117.

Coupled dynamics of translation and collapse of acoustically driven microbubbles

Anil J. Reddy and Andrew J. Szeri[a)]
Department of Mechanical Engineering, University of California at Berkeley, Berkeley, California 94720-1740

(Received 12 April 2000; accepted for publication 9 July 2002)

Pressure gradients drive the motion of microbubbles relative to liquids in which they are suspended. Examples include the hydrostatic pressure due to a gravitational field, and the pressure gradients in a sound field, useful for acoustic levitation. In this paper, the equations describing the coupled dynamics of radial oscillation and translation of a microbubble are given. The formulation is based on a recently derived expression for the hydrodynamic force on a bubble of changing size in an incompressible liquid [J. Magnaudet and D. Legendre, Phys. Fluids **10**, 550–556 (1998)]. The complex interaction between radial and translation dynamics is best understood by examination of the added momentum associated with the liquid motion caused by the moving bubble. Translation is maximized when the bubble collapses violently. The new theory for coupled collapse and translation dynamics is compared to past experiments and to previous theories for decoupled translation dynamics. Special attention is paid to bubbles of relevance in biomedical applications.
 [DOI: 10.1121/1.1502899]

PACS numbers: 43.25.Ts, 43.25.Yw [MFH]

I. INTRODUCTION

In this paper, we consider the nonlinear dynamics of microbubble translation in an acoustic field. Such a study will find application in several areas, which we now briefly mention.

In medicine, microbubbles injected into the blood stream are commonly used in both diagnostic and therapeutic applications of ultrasound. In a diagnostic mode, bubbles are used as image contrast agents, their acoustic echoes being substantially different from that of human tissue.[1] Bubbles can be used to determine the volume flow rate of blood through an artery. One possible concern in application of this technique was recently identified by Dayton *et al.*,[2] who described the drift of bubbles excited using acoustic waves. They discovered that this drift toward the wall of the vessel was followed by bubble aggregation. These bubble clusters have different echo characteristics than their constituent parts, as well as having echoes different from that of a larger single bubble.

In a second medical application, bubbles are used to carry reagents to the site of tumor tissue, for example, or to the known location of a blood clot.[3] Once they reach their target, the bubbles are acoustically excited to a violent collapse, releasing reagents transported within the bubble that can combat the tumor[4] or clot. The targeting of microbubbles could be further improved by intelligent use of the acoustic force.

Much has been learned about the translational dynamics of microbubbles from acoustic levitation. In this technique, an acoustic standing wave is used to trap a bubble at a particular location despite the influence of buoyancy.[5,6] Bubbles of sufficiently small radius are drawn toward the antinodes of the standing pressure wave, whereas bubbles of larger radius are attracted to the nodes. The stability of positional equilibria is determined in part by the direction of the primary Bjerknes force acting on a bubble displaced from an equilibrium. The Bjerknes force is the resultant force due to the pressure gradient acting over the surface of an object submerged in a liquid. In the case of a spherical object, the primary Bjerknes force is easily derived:[7]

$$F_B = -V(t)\nabla P_\infty(X,t), \tag{1}$$

where $V(t)$ is the volume of the sphere, and $P_\infty(X,t)$ is the pressure in the liquid. In a standing wave, the pressure is a separable function of position and time.

A bubble driven at less than its resonant frequency (*subresonant forcing*) will oscillate in phase with the forcing. A bubble driven at greater than its resonant frequency (*superresonant forcing*) will oscillate out of phase: its radius increases when the pressure is increasing. Hence the time-averaged Bjerknes force will have opposite sign for sub- and super-resonant forcing.

If a bubble translates within the liquid to the nodes (or antinodes) of a standing pressure wave, it is necessary to consider drag forces along with the Bjerknes force to determine the precise motion of the bubble. The recent paper by Parlitz *et al.*[8] is the most complete study to date of the translation dynamics of bubbles submerged in a fluid; the primary focus of that paper is to understand how the spatial structure of a multi-bubble cloud forms in a standing wave. In addition to viscous drag and the primary Bjerknes force on a test bubble, the authors take into account the secondary Bjerknes force, associated with the acoustic radiation emitted from a nearby bubble. In developing their equations of motion, Parlitz *et al.* time average the full equations of motion, utilizing the assumption that translation occurs at a much slower time

a)Author to whom correspondence should be addressed. Electronic mail: aszeri@me.berkeley.edu

scale than the radial dynamics. The consequence of such an assumption is that only average radial quantities are used to compute the translation dynamics. Time averaging was necessary because Parlitz *et al.* used an expression for the drag force that is a function of the average speed and radius of the bubble. This expression was found by Crum[5] to match well the experimental data for weakly forced bubbles.

In the present paper, we make use of a new expression for the hydrodynamic force on a bubble developed by Magnaudet and Legendre[9] to formulate the equations of motion for the coupled dynamics of radial and translational motions of a microbubble driven by a pressure field. At sufficiently small driving pressure amplitudes, the predictions of the present theory are in accord with the prior work mentioned above. However, we show that averaging must be done with care, particularly at elevated forcing. It is not in general appropriate when the bubbles suffer violent radial collapses to decouple the radial and translational motions of the bubble. In fact, we find that such bubbles lurch forward during radial collapse but are otherwise virtually motionless. These observations lead to a better understanding of the mechanisms leading to bubble translation.

II. EQUATIONS OF MOTION

The equations governing the bubble dynamics are introduced in this section. First, the well-known Raleigh–Plesset equation (RPE) determines the bubble radial response $R(t)$ to a general forcing $P_\infty(X,t)$. The equation governing bubble translation $X(t)$ is then derived using the balance of linear momentum. The translation equation includes acoustic and drag forces, and takes into account changes in bubble volume. The radial and translational equations of motion are coupled.

A. Radial equation of motion

We shall make use of the RPE of Moss *et al.*[10] in this paper:

$$\dot{R}(t)\ddot{R}(t)+\frac{3}{2}\dot{R}^2(t)=\frac{1}{\rho}\left[P_l(t)-P_\infty(t)+\frac{R(t)}{c_l}\frac{\mathrm{d}}{\mathrm{d}t}(P_l-P_\infty)\right]. \tag{2}$$

This form of the RPE is suitable for strongly collapsing microbubbles, as the derivation takes into account both liquid and gas compressibility. Here the pressure $P_l(t)$ in the liquid at the bubble wall is given as

$$P_l(t)=P_g(t)+\frac{R(t)}{3c_g(t)}\frac{\mathrm{d}}{\mathrm{d}t}P_g-\frac{4\mu\dot{R}(t)}{R(t)}-\frac{2\sigma}{R(t)}, \tag{3}$$

where the gas pressure inside the bubble is $P_g(t)=P_{g0}(R_0/R(t))^{3\kappa}$, and the sound speed in the gas is $c_g(t)=c_{g0}(R_0/R(t))^{3(\kappa-1)/2}$. R_0 is the equilibrium bubble radius. The polytropic exponent is taken to be $\kappa=1$ when $R(t)>R_0$ and $\kappa=\gamma$ the ratio of specific heats when $R(t)<R_0$.

The far-field driving pressure (in the present case, from an acoustic traveling wave) is

TABLE I. Material properties used in water and blood calculations.

Property	Symbol	Water	Blood
Density	ρ (g/cm^3)	0.998	1.005
Surface tension	σ (g/s^2)	72.8	69.56
Viscosity	μ (g/cm·s)	0.001	0.004
Sound speed	c_l (cm/s)	148 470	146 070
Temperature	(C)	20	39.6

$$P_\infty(X,t)=P_0[1+P_a\sin(2\pi X(t)/\lambda-2\pi f_d t)]. \tag{4}$$

For air bubbles in water or blood, the material properties are shown in Table I. The ambient pressure is $P_0=1\,013\,250$ g/(cm s^2). The initial internal gas pressure, P_{g0}, is given by $P_{g0}=P_0-P_v+2\sigma/R_0$ where P_v is the vapor pressure at the ambient temperature. For the forcing conditions and bubble sizes considered in the present work, stability to nonspherical shape disturbances may be assumed.[11]

B. Equation of motion governing translation

Magnaudet and Legendre[9] develop in detail an expression for the hydrodynamic force acting on a bubble of changing radius translating with respect to the surrounding incompressible liquid. The authors introduce two dimensionless parameters of relevance here: the translation Reynolds number $\mathrm{Re}=\rho R(t)|U(t)|/\mu$ and the ratio of the radial velocity to the translation velocity $\mathcal{U}=|\dot{R}(t)/U(t)|$. We note that $U(t)$ is the liquid velocity in the far field relative to the bubble. The absolute velocity of the liquid (relative to an inertial frame) is $U_a(t)=\dot{X}(t)+U(t)$, where $X(t)$ is the position of the bubble in the inertial frame. Only one dimension of translational motion is considered in the present work.

Magnaudet and Legendre develop two different expressions for the force on a bubble translating relative to the surrounding liquid and changing in size. When $\mathcal{U}\mathrm{Re}\ll 1$ *and* $\mathrm{Re}\ll 1$, i.e., when the bubble is slowly translating with slow radial dynamics, the expression for the hydrodynamic force on the bubble is

$$F_H(t)=4\pi\mu R(t)U(t)+\frac{2\pi}{3}\rho\frac{\mathrm{d}}{\mathrm{d}t}(R(t)^3U(t))+\frac{4\pi}{3}\rho R(t)^3\dot{U}_a(t)+F_{BB}. \tag{5}$$

The first term in (5) is the Stokes-like drag term in the limit of small Reynolds number. Because neither the bubble radius nor the translation velocity is constant, the associated flow in the fluid is also variable in time; this leads to the second (added mass) term. The third term in (5) is an inertial force due to the fact that the expression for the drag was derived in the noninertial frame translating with the bubble (see Refs. 9 and 12). The fourth term F_{BB} is the history force, analogous to the Basset–Boussinesq force on a sphere, which arises owing to the wake behind the bubble:

$$F_{BB}=8\pi\mu\int_0^t w(s,t)\frac{\mathrm{d}}{\mathrm{d}s}[R(s)\dot{X}(s)]\,\mathrm{d}s, \tag{6}$$

where the weight function, $w(s,t)$ is given by

$$w(s,t)=\exp\left[9\nu\int_s^t\frac{1}{R(\hat{s})^2}\,\mathrm{d}\hat{s}\right]\mathrm{erfc}\left[\sqrt{9\nu\int_s^t\frac{1}{R(\hat{s})^2}\,\mathrm{d}\hat{s}}\right]. \tag{7}$$

When $\mathcal{U}\mathrm{Re}\gg 1$ *or* $\mathrm{Re}\gg 1$ the hydrodynamic force on the bubble is

$$F_H(t)=12\pi\mu R(t)U(t)+\frac{2\pi}{3}\rho\frac{\mathrm{d}}{\mathrm{d}t}(R(t)^3U(t)) + \frac{4\pi}{3}\rho R(t)^3\dot{U}_a(t). \tag{8}$$

We emphasize that this latter form is valid when either $\mathcal{U}\mathrm{Re}\gg 1$ *or* $\mathrm{Re}\gg 1$; Magnaudet and Legendre make the point that when $\mathcal{U}\mathrm{Re}\gg 1$, the ratio of inertial to viscous effects is properly $\mathcal{U}\mathrm{Re}$ and not simply Re. Note that there is no history force in the limit $\mathcal{U}\mathrm{Re}\gg 1$ or $\mathrm{Re}\gg 1$, but that the first term in (8) is three times greater than in the limit $\mathcal{U}\mathrm{Re}\ll 1$ and $\mathrm{Re}\ll 1$. Magnaudet and Legendre verify these expressions for drag by comparing to numerical integrations of the full unsteady Navier–Stokes equations in several situations.[9,13] As we show below, they are also verified by comparison to data from acoustic levitation experiments.

A balance of fluid momentum in the far field (in the acoustic limit) gives

$$\rho\dot{U}_a\approx-\nabla P_\infty. \tag{9}$$

This enables one to write the final term in (8) as the Bjerknes force, $-V\nabla P_\infty$. In assembling the balance of linear momentum for the bubble, which is simply $F_H=0$, two assumptions are made: (*i*) the mass of the gas within the bubble is negligible, and (*ii*) when the bubble is strongly forced, the appropriate limit is $\mathcal{U}\mathrm{Re}\gg 1$. The second assumption will be justified shortly. The equation governing bubble translation is readily determined to be

$$\frac{2\pi}{3}\rho\frac{\mathrm{d}}{\mathrm{d}t}(R(t)^3(U_a(t)-\dot{X}(t))) = \frac{4\pi}{3}R(t)^3\nabla P_\infty(X(t),t)-12\pi\mu R(t)(U_a(t)-\dot{X}(t)). \tag{10}$$

This equation is related to Eq. (34) of Ref. 13, except for the application to the case of acoustic forcing.

III. RESULTS AND DISCUSSION

A. Illustrative simulations

The motion of the bubble is characterized by two coupled second-order ordinary differential equations (ODEs), whose solution may be determined numerically. Several natural scales can be used to define dimensionless variables (ξ,r,τ):

$$X\equiv R_0\xi,\quad R\equiv R_0 r,\quad t\equiv\frac{1}{f_n}\tau, \tag{11}$$

where f_n is the natural frequency. Integration of the (dimensionless forms of the) coupled differential equations (2) and (10) is performed numerically. The integrations start from a quiescent state.

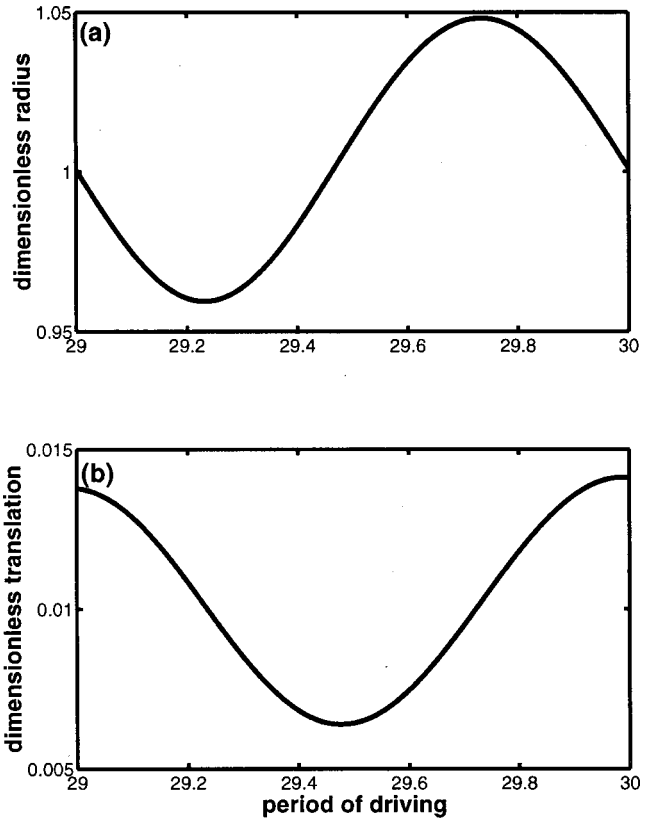

FIG. 1. Steady-state radial and translation response of a bubble ($R_0=2.0\ \mu$m) to a single period of mild, super-resonant traveling wave excitation ($f_r=2.5, P_a=1$), after 29 periods of forcing.

The first observation is that for acoustic traveling wave driving of microbubbles in water or blood at MHz frequencies, the bubble translation velocity and radial dynamics quickly become periodic with the forcing. Following a short transient time, usually less than ten cycles of forcing, the bubble moves a fixed distance over each ensuing cycle of forcing with a small oscillation about a uniform translation velocity. This was also observed in the (standing wave) experiments of Crum and Eller.[14] We note that because the acoustic wave moves much faster through the fluid than the bubble, the acoustic pressure terms in the equations of motion can be evaluated at the averaged bubble position, introducing only a minor error.

B. The appropriate limit of $\mathcal{U}\mathrm{Re}$

In order to assess which form one should use for the force (5) or (8), we consider two typical cases: a mild collapse and a more violent collapse. These correspond to moderate super-resonant forcing and subresonant forcing, respectively. A $R_0=2\ \mu$m bubble has a natural frequency of about 1.69 MHz. In the super-resonant case with mild radial dynamics, the bubble is excited at frequency ratio $f_r=f_d/f_n=2.5$ and $P_a=1$ (Figs. 1 and 2). In the subresonant case with a more violent collapse, the excitation is $f_r=0.5$ and $P_a=1$ (Figs. 3 and 4). In both cases the calculations we report were made with (8).

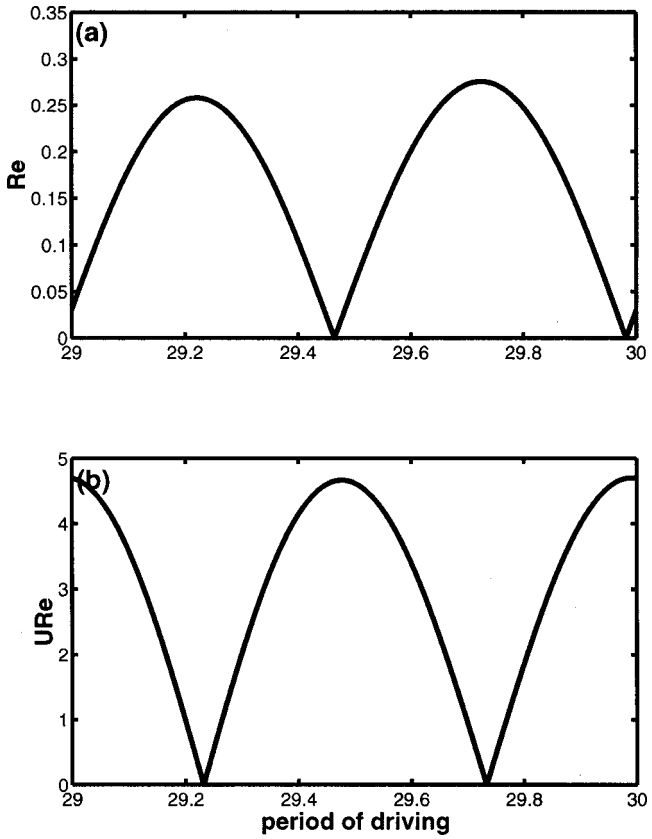

FIG. 2. Evolution of Re and the product $\mathcal{U}\mathrm{Re}$, versus time for the bubble in Fig. 1.

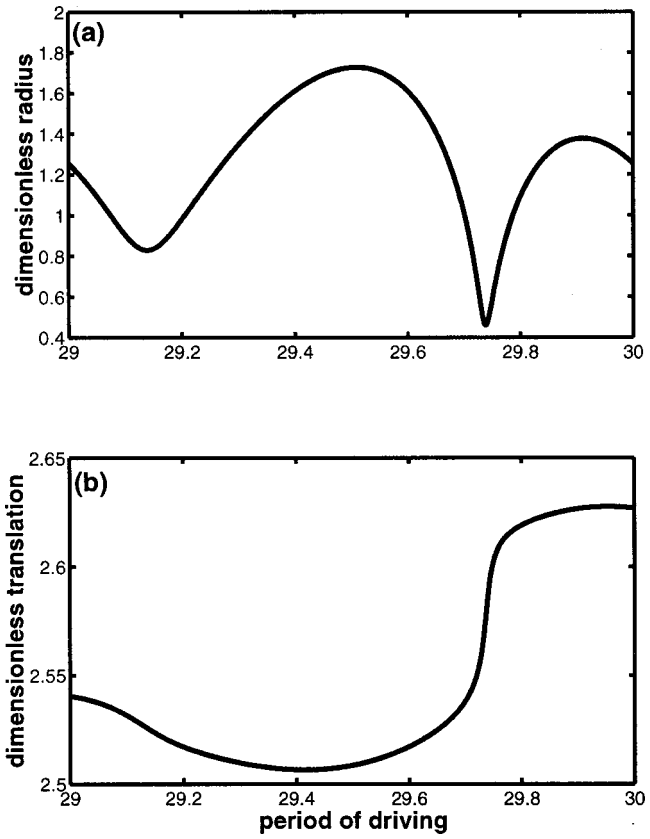

FIG. 3. Same as Fig. 1, but for a single period of subresonant traveling wave excitation ($f_r=0.5, P_a=1$). Bubble displacement is greatest during the violent radial collapse.

In the mild, super-resonant case, the radial oscillation is nearly sinusoidal in time. The translation velocity varies gradually, with $\mathrm{Re}<1$ throughout the cycle and $\mathcal{U}\mathrm{Re}$ peaking at about 5 (Fig. 2). According to the verification calculations by Magnaudet and Legendre, this case is within the range where (5) is accurate. We note, however, that the use of (8) gives very similar answers.

In the more violent subresonant case, the picture is rather different. The bubble translation velocity is observed to be greatest during the strong radial collapse; see Fig. 3. We found in general that the more violent the radial collapse, the greater the peak translation velocity. In general, subresonant excitation causes much more violent collapses than super-resonant excitation of a similar magnitude. In this case, $\mathcal{U}\mathrm{Re}$ is about 40 when the bubble is rapidly translating during the collapse. According to the verification calculations by Magnaudet and Legendre, this case is within the range where (8) is accurate.

It is worth considering, briefly, what happens when the bubble suddenly lurches forward during radial collapse. We shall refer to the terms in (10) as follows: $R^3(t)(U_a(t)-\dot{X}(t))$ is the added momentum, $12\pi\mu R(t)(U_a(t)-\dot{X}(t))$ is the viscous drag, and the last term $-V(t)\nabla P_\infty$ is the Bjerknes force. First, we remark that it is the Bjerknes force that prevents the bubble from simply moving with the fluid in the acoustic wave. As the bubble grows, the magnitude of the Bjerknes force increases, due in part to the greater surface area upon which the pressure gradient acts. However, because a large bubble pushes more fluid when it moves, the bubble translates only slowly at large radii. During bubble growth, the added momentum of the displaced fluid increases considerably. Upon collapse, the Bjerknes force is small enough to be negligible. Because the radius decreases rapidly and the added momentum decreases only slowly due to viscous dissipation, the translation speed increases dramatically in the collapse. The process described here is analogous to the changes in angular momentum and angular velocity of an ice skater as she draws in her arms in order to spin faster. Although the angular momentum is slowly decreasing due to dissipation, the moment of inertia decreases more rapidly as she draws in her arms; consequently the angular velocity increases briefly. However, the dissipation eventually dominates, and the skater slows to a stop.

Based on these representative simulations, we conclude that it is better to use the second expression for the force on the bubble (8) in all cases for two reasons: (*i*) it is reasonably accurate for microbubbles at MHz frequencies, even when $\mathcal{U}\mathrm{Re}\ll 1$ and $\mathrm{Re}\ll 1$, and (*ii*) if there are violent collapses, then almost all of the translation occurs when $\mathrm{Re}\gg 1$ and $\mathcal{U}\mathrm{Re}\gg 1$; outside of the collapse, both (5) and (8) predict virtually zero translational velocity. Thus, for the remainder of this paper, only (8) is used; Eq. (10), then, is the equation of motion.

C. Comparison with existing experimental data in the case of mild collapses

A further verification of the present work can be obtained by comparison with the pioneering experiments of

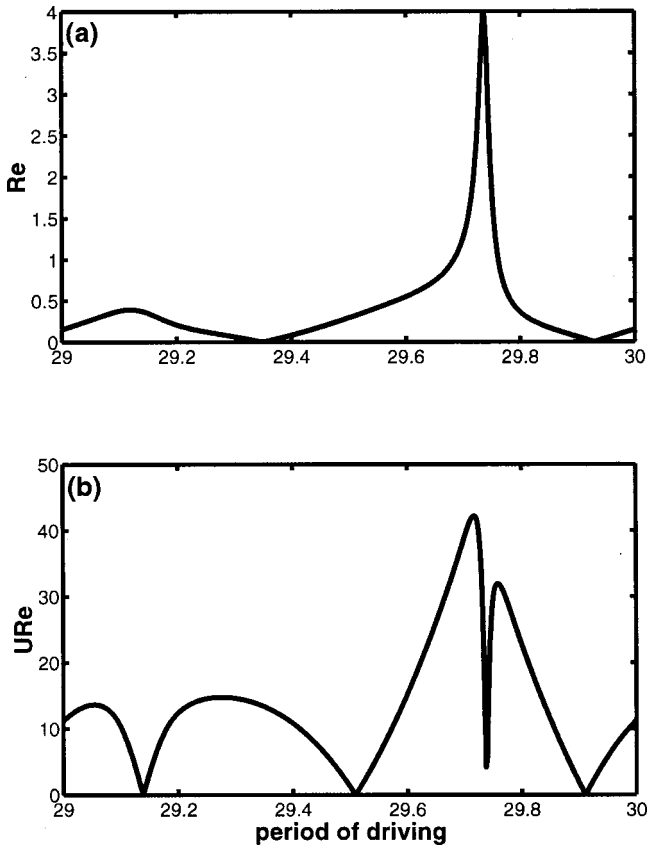

FIG. 4. Evolution of Re and the product $\mathcal{U}\,\mathrm{Re}$, versus time for the bubble in Fig. 3.

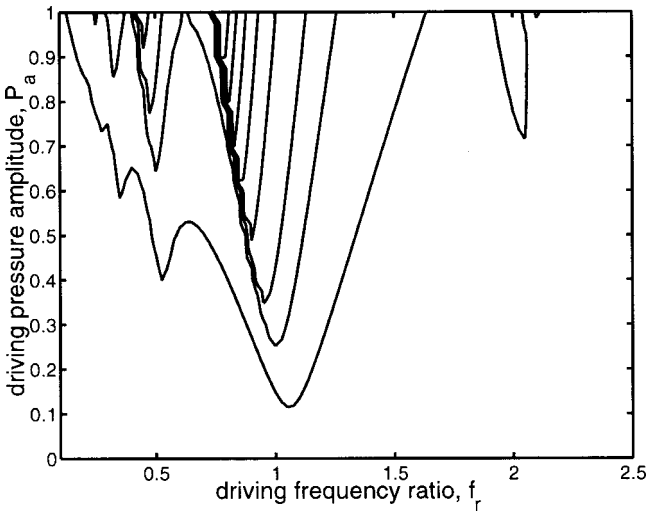

FIG. 5. Contour plot of the average linear speed of a 2-μm-radius bubble versus the ratio of driving to natural frequencies f_r and the driving pressure amplitude P_a. The contours show speeds of 1, 5, 10, 20, 30, 40, 50, and 60 cm/s, with the lowest speeds at the lowest P_a.

Crum and Eller,[14] which concern mild subresonant acoustic forcing. We find good agreement between the average velocity calculated using the present equations and the results obtained by Crum and Eller (presented in their Fig. 3). As one expects in this weakly forced case, the average velocity computed using (8) overpredicts the drag, and therefore underpredicts the average velocity. The average velocity computed using (5) with $F_{BB}=0$ underpredicts the drag, and therefore overpredicts the average velocity. In other words, the Basset term F_{BB} does play a role in these weakly forced bubbles. These findings constitute an experimental verification of the expression for the hydrodynamic force due to Magnaudet and Legendre, and of the equation of motion of the bubble for the case when $\mathcal{U}\,\mathrm{Re}\ll 1$ and $\mathrm{Re}\ll 1$. For completeness, it is worth mentioning that in their analysis, Crum and Eller linearize the radial dynamics, neglect the added mass term, and use a drag force based on the average bubble radius.

To aid in further discussion, we now consider a bubble driven in a steady way by a traveling wave, which achieves a uniform translation velocity plus a small periodic oscillation at steady state:

$$X(t)=\overline{V}t+\tilde{X}(t), \tag{12}$$

where $\tilde{X}(t)\equiv\tilde{X}(t+T)$ serves to define $\tilde{X}(t)$. If we assume that the radial dynamics is periodic, and the absolute fluid velocity $U_a(t)$ is periodic at every spatial location, then the hydrodynamic force on the bubble not attributed to the Bjerknes force (i.e., the drag force) may be written in terms of a drag coefficient [see Ref. 14 as $C_D=(\langle F_H\rangle+\langle V\nabla P_\infty\rangle)/(-\rho\overline{V^2}\pi\langle R\rangle^2/2)$] to give

$$C_D=\frac{48}{\mathrm{Re}_C}\left[1+\frac{\langle R\tilde{X}_{,t}\rangle}{\langle R\rangle\overline{V}}-\frac{\langle RU_a\rangle}{\langle R\rangle\overline{V}}\right], \tag{13}$$

where Crum's Reynolds number was defined as $\mathrm{Re}_C=2\rho\langle R\rangle\overline{V}/\mu$.

Crum states that his experimental data for the drag on a bubble agrees with the empirical formula of Haberman and Morton:[15]

$$C_D=27.0\,\mathrm{Re}_C^{-0.78}. \tag{14}$$

In their recent paper, Parlitz *et al.*[8] use a more convenient (but equivalent) fit of Haberman and Morton's expression for the drag force. When the bubble does *not* undergo rapid radial collapses, the average of products of radial and translational factors in (13) is approximately equal to the product of the averages. By virtue of the periodicity of $\tilde{X}$ and of U_a, this yields $C_D\approx 48/\mathrm{Re}_C$, which is in agreement with (14) for Reynolds numbers up to approximately 40. Hence in the case of weak forcing with mild collapses, where we can decouple the averages $\langle R\tilde{X}_{,t}\rangle\approx\langle R\rangle\langle\tilde{X}_{,t}\rangle=0$ and $\langle RU_a\rangle\approx\langle R\rangle\langle U_a\rangle=0$, the force on the bubble agrees with the empirical formula of Haberman and Morton used by Crum, and, in a different form by Parlitz *et al.*

D. The case of strong collapses

Unfortunately there is no similar experimental data to which we can compare the theory in the case of stronger collapses. In order to obtain an idea of the magnitude of the translation speeds one would expect, we show in Figs. 5 and 6 contour plots of the speed of $R_0=2$ μm bubbles driven at frequency ratio f_r and driving pressure amplitude P_a in water and in blood. One can see traces of the primary resonance and $\frac{2}{1}$ ultra-harmonic resonance in both figures, as well as the $\frac{1}{2}$ subharmonic in the water (Fig. 5); we refer the reader to the

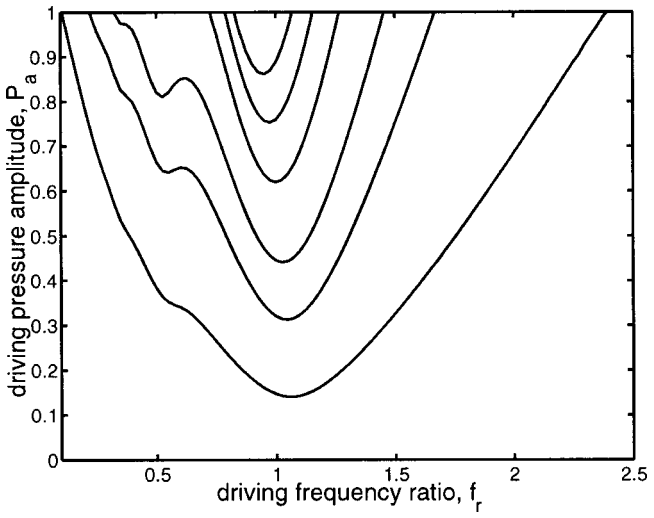

FIG. 6. Same as Fig. 5 but for a 2-μm-radius bubble in blood. The contours show speeds of 0.1, 0.5, 1, 2, 3, 4, and 5 cm/s, with the lowest speeds at the lowest P_a.

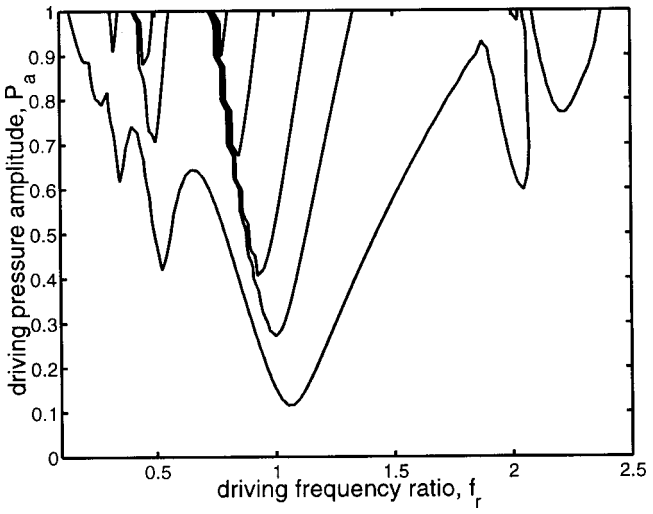

FIG. 7. A repeat of Fig. 5, but with only the first term of (15), i.e., assuming the radial collapses and oscillations about uniform translation speed are totally uncorrelated. This assumption leads to an underestimate of the average translation speed for strongly collapsing bubbles, and to errors of either sign in cases of milder collapses.

classic paper by Lauterborn[16] for a complete exposition of these resonances. The fastest translation speeds are at the main resonance, roughly 50 cm/s in water and 5 cm/s in blood at $P_a=1$. These average speeds can be readily interpreted with the aid of the averaged translation dynamics equation,

$$\overline{V}=-\frac{\langle V\nabla P_\infty\rangle}{12\pi\mu\langle R\rangle}+\frac{\langle \dot{R}\tilde{X}\rangle}{\langle R\rangle}+\frac{\langle RU_a\rangle}{\langle R\rangle}. \tag{15}$$

Note that the second term has been integrated by parts, and that we have neglected a small term of order $\overline{V}T/\lambda$. We did not compute translation speeds at higher P_a in order to avoid the parameter regime of shape instabilities[11] and to keep within the range where the Mach numbers of the collapses are small. This was necessary because the theory for the hydrodynamic force[9] is developed for an incompressible liquid. In all the calculations we report, the maximum (liquid) Mach number of the collapses is about 0.05.

If one takes the decoupling approximation $\langle R\tilde{X}_{,t}\rangle\approx\langle R\rangle\times\langle\tilde{X}_{,t}\rangle=0$ and $\langle RU_a\rangle\approx\langle R\rangle\langle U_a\rangle=0$, then the omission of the second and third terms in (15) is an error. These terms can be dominant in the expression for $\overline{V}$. For example, for the parameters used in Figs. 3 and 4 ($R_0=2\ \mu\text{m}, f_r=0.5, P_a=1$), (15) predicts a (large) average velocity approximately 35% in error if the second and third terms are neglected. For the parameters used in Figs. 1 and 2 ($R_0=2\ \mu\text{m}, f_r=2.5, P_a=1$), (15) predicts a (small) average velocity approximately 120% in error if the second and third terms are neglected.

Finally, in Fig. 7 we repeat the calculation of Fig. 5, but with only the first term of (15). For relatively mild forcing conditions, $-\langle V(t)\nabla P_\infty\rangle/(12\pi\mu\langle R\rangle)$ suffices as an estimate for $\overline{V}$ and the traditional (decoupling) averaging scheme may be used. At elevated forcing, the second and third terms becomes increasingly important.

IV. CONCLUSIONS

The purpose of this paper has been to introduce the equations coupling translational motion to the radial response of a bubble subject to acoustic forcing. The behavior of a strongly collapsing, translating bubble is as follows: at large radius, the Bjerknes force increases the momentum of the bubble and fluid. During a violent collapse, the momentum decreases gradually due to the work done by the viscous drag. However, the radius decreases much more rapidly, causing the bubble to lurch forward. The more violent the bubble collapse, the greater the peak translation velocity. Hence, the assumption that the average translation dynamics depends only on averaged radial dynamics should be made with care. It is not generally valid.

ACKNOWLEDGMENTS

This work was supported by a grant from the National Science Foundation.

[1] B. B. Goldberg, J.-B. Liu, and F. Forsberg, "Ultrasound contrast agents—a review," Ultrasound Med. Biol. **20**, 319–333 (1994).
[2] P. A. Dayton, K. E. Morgan, A. L. Klibanov, G. Brandenburger, K. R. Nightingale, and K. W. Ferrara, "A preliminary evaluation of the effects of primary and secondary radiation forces on acoustic contrast agents," IEEE Trans. Ultrason. Ferroelectr. Freq. Control **44**, 1264–1277 (1997).
[3] Y. Wu, E. C. Unger, T. P. McCreery, R. H. Sweitzer, D. Shen, G. Wu, and M. D. Vielhauer, "Binding and lysing of blood clots using MRX-408," Invest. Radiol. **33**, 880–885 (1998).
[4] K. Kawabata and S. Umemura, "Effect of second-harmonic superimposition on efficient induction of sonochemical effect," Ultrason. Sonochem. **3**, 1–5 (1996).
[5] L. A. Crum, "Bjerknes forces on bubbles in a stationary sound field," J. Acoust. Soc. Am. **57**, 1363–1370 (1975).
[6] E. H. Trinh and C.-J. Hsu, "Equilibrium shapes of acoustically levitated drops," J. Acoust. Soc. Am. **79**, 1335–1338 (1986).
[7] T. G. Leighton, *The Acoustic Bubble* (Academic, San Diego, 1994).
[8] U. Parlitz, R. Mettin, S. Luther, I. Akhatov, M. Voss, and W. Lauterborn, "Spatio-temporal dynamics of acoustic cavitation bubble clouds," Philos. Trans. R. Soc. London, Ser. A **357**, 313–334 (1999).

[9] J. Magnaudet and D. Legendre, ''The viscous drag force on a spherical bubble with a time-dependent radius,'' Phys. Fluids **10**, 550–554 (1998).
[10] W. C. Moss, J. L. Levatin, and A. J. Szeri, ''A new damping mechanism in strongly collapsing bubbles,'' Proc. R. Soc. London, Ser. A **456**, 2983–2994 (2000).
[11] S. Grossmann, S. Hilgenfeldt, and D. Lohse, ''Sound radiation of 3-MHz driven gas bubbles,'' J. Acoust. Soc. Am. **102**, 1223–1230 (1997).
[12] G. K. Batchelor, *An Introduction to Fluid Dynamics* (Cambridge U. P., Cambridge, 1967).
[13] D. Legendre, J. Borée, and J. Magnaudet, ''Thermal and dynamic evolution of a spherical bubble moving steadily in a superheated or subcooled liquid,'' Phys. Fluids **10**, 1256–1272 (1998).
[14] L. A. Crum and A. I. Eller, ''Motion of bubbles in a stationary sound field,'' J. Acoust. Soc. Am. **48**, 181–189 (1970).
[15] W. L. Haberman and R. H. Morton, ''An experimental investigation of the drag an shape of air bubbles rising in various liquids,'' David Taylor Model Basin Report. No. 802 (1953).
[16] W. Lauterborn, ''Numerical investigation of nonlinear oscillations of gas bubbles in liquids,'' J. Acoust. Soc. Am. **59**, 283–293 (1976).

Band gaps and defect modes in periodically structured waveguides

J. N. Munday, C. Brad Bennett, and W. M. Robertson[a)]
Department of Physics and Astronomy, Middle Tennessee State University, Murfreesboro, Tennessee 37132

(Received 7 August 2001; revised 28 May 2002; accepted 1 June 2002)

This work examines a simple one-dimensional acoustic band gap system made from a diameter-modulated waveguide. Experimental and theoretical results are presented on perfectly periodic waveguide arrays showing the presence of band gaps—frequency intervals in which the transmission of sound is forbidden. The introduction of defects in the perfect periodicity leads to narrow frequency transmission bands—defect states—within the forbidden band gaps. The circular cross-section waveguide system is straightforward to simulate theoretically and experimental results demonstrate good agreement with theory. The experimental transmission of the periodic waveguide arrays is measured using an impulse response technique. © *2002 Acoustical Society of America.*
[DOI: 10.1121/1.1497625]

PACS numbers: 43.28.Bj, 43.28.Dm, 43.25.Ts [LLT]

I. INTRODUCTION

In this paper the properties of acoustic band gaps and defect modes in periodically structured waveguides are examined theoretically and experimentally. There has been considerable recent interest in the propagation of classical waves—electromagnetic and acoustic—in periodically structured environments. The goal of much of this research is to design and create composite materials—so-called photonic or acoustic band gap arrays—that can manipulate the properties of the radiation field. In the electromagnetic case the ability to engineer light has led to the suggestion and/or development of a number of important applications.[1–4] Similar practical applications for acoustic waves have been suggested[5–7] although research in this area is far less extensive.

Many of the projected applications of acoustic and photonic band gap materials require composite systems with forbidden transmission in all three spatial dimensions—so-called complete band gap materials. In practice such materials are difficult to realize because they require a three-dimensional periodic composite between two materials with considerably different impedances. As a consequence much work has focused on band gap phenomena in systems with periodicity, and hence band gaps, in two[8,9] or one dimensions.[10,11] Studies of lower dimensional systems are conducted as analogs of three-dimensional systems and for applications in their own right. In the work described here we reexamine a one-dimensional periodic waveguide system that has received considerable theoretical and experimental attention.[12–16] The specific emphasis in this work is the examination of defect modes created when the perfect periodicity is broken. Defect modes are an essential ingredient in many of the proposed applications of photonic or acoustic band gap systems. Although the properties of periodic acoustic waveguides have been long studied, little attention has been given to the properties of defect modes.

The basis of acoustic band gap effects rests on the fact that in a perfectly periodic composite system consisting of two materials with significantly different acoustic impedances, the coherent effects of scattering and interference lead to frequency intervals in which propagation of sound is forbidden—so-called acoustic or sonic band gaps. Because of the close analogy of this process to the scattering and interference of electron wave functions by the periodic potential of a crystalline lattice, much of the terminology and theoretical methods of solid state physics have been adopted in the treatment of acoustic (and electromagnetic) band gap phenomena. A key success of solid state physics was the unfolding of the role of the electron state band gap in explaining and understanding the properties of semiconductors. However, an essential step in going from an understanding of the properties of perfectly crystalline semiconductors to practical devices involved the addition of defects. Small quantities of donor or acceptor defect atoms were found to perturb the perfect lattice and create isolated electron states within the forbidden band gap. A similar sequence is adopted in the work described here. We first examine a perfectly periodically structured acoustic waveguide system and show the existence of forbidden transmission bands. The periodic system consists of a series of equal length segments of circular cross-section waveguides with diameters varying between two different values. Next, we introduce a single defect in the perfect periodicity, and we show that this defect produces a narrow band of transmission within the previously forbidden band gap. The defect is produced by altering the length of the central segment of the series of waveguides. Depending on the precise nature of the defect we observe either donor-like or acceptor-like behavior.

There are many methods to calculate the acoustic response of a one-dimensional waveguide.[13,15] In the work described here, an iterative theoretical formalism is adapted from Fresnel's equations to calculate the reflection and transmission of the periodic waveguide system. The theoretical calculations show that it should be possible to produce extremely narrow band filters using defects in this simple

a)Electronic mail: wmr@physics.mstu.edu

waveguide configuration. We demonstrate that although it is possible to produce narrow band filters, the extremely narrow theoretical predictions are not realized in practice. We discuss the experimental limitations that do not allow us to realize the narrowest filters and explain the steps that could be taken to circumvent these limitations.

II. THEORY

The experimental system that we chose to investigate in this work consisted of a waveguide of circular cross section with a diameter that was modulated periodically between a small and large diameter as a function of length. The waveguide dimensions and the frequency interval explored were selected so that our measurements were all conducted in the lowest transverse mode of the waveguide. This criterion was assured by using frequencies below the cutoff frequency, f_c, of the next higher transverse mode given by[17,18]

$$f_c = 0.92\frac{c}{\pi a},$$

where c is the speed of sound and a the larger tube diameter. Furthermore, the lengths of the waveguide sections were chosen to be much larger than the diameter of the largest tube so that the stop band phenomena observed in our experiments were due to interference in the longitudinal direction and not due to radial resonances in the waveguide segments themselves. The cavity resonance effect will occur at frequencies well above those used in our experiments here.

A detailed description of the exact waveguide parameters used in the measurements and in the associated theoretical calculations is given in the following experimental description. The reflection and transmission of the periodically diameter-modulated waveguide system can be easily modeled theoretically. The different diameter waveguides have different acoustic impedance values, Z. In the long wavelength approximation, Z is given by the simple expression[19]

$$Z = \frac{\rho c}{S},$$

where ρ is the density of air, and S is the cross-sectional area of the waveguide. Provided that the long wavelength condition is met, the impedance is independent of frequency. The amplitude reflection coefficient, r_{ij}, at the junction between two waveguide sections with different impedances is given by[19]

$$r_{ij} = \frac{Z_i - Z_j}{Z_i + Z_j}.$$

To extend the theoretical reflection expression to include a second boundary at a distance, d, from the first, the effects of multiple reflection and interference must be taken into account. The corresponding expression for the three media (two boundary) system is

$$r_{123} = \frac{r_{12} + r_{23}e^{2ikd}}{1 + r_{12}r_{23}e^{2ikd}},$$

where $k = 2\pi/\lambda$ is the wave vector at the frequency of interest, and r_{12} and r_{23} are the amplitude reflection coefficients at the first and second boundaries, respectively. Finally, this process can be applied recursively to determine the reflectivity from any number of boundaries with arbitrary spacings. To illustrate the process, consider a four medium system in which the distances between the three boundaries are d_1 and d_2. The total amplitude reflectivity, r_{1234}, is given by

$$r_{1234} = \frac{r_{12} + r_{234}e^{2ikd_1}}{1 + r_{12}r_{234}e^{2ikd_1}},$$

where r_{234} is given by

$$r_{234} = \frac{r_{23} + r_{34}e^{2ikd_2}}{1 + r_{23}r_{34}e^{2ikd_2}}.$$

This recursive procedure can be easily programmed to calculate the amplitude reflectivity for any number of boundaries. The absolute squared magnitude of the amplitude reflectivity, r, is the intensity reflectivity, R. Because there is no loss in this simple model, the intensity transmission, T, is simply $1-R$. As we demonstrate in Sec. IV, the theoretical calculations of the gap and defect frequencies made with this model are generally in excellent agreement with the experimentally measured transmission data. It should be noted that there are many methods to calculate the response of a periodic system (Refs. 13 and 15, and references therein). The iterative method described here offers two particular advantages: (i) the method does not invoke Bloch wave propagation so that it can be equally well applied to random or aperiodic systems and (ii) the calculation of effective reflectivities at the interfaces bounding each waveguide segment means that it is possible to determine the longitudinal mode profile within each segment.

III. EXPERIMENTAL CONFIGURATION AND PROCEDURE

The experimental configuration is shown schematically in Fig. 1. The basic experiment consisted of sending an acoustic impulse through a one-dimensional periodic waveguide array and recording the transmitted signal. A numerical Fourier transform of the recorded time-domain signal was used to determine the frequency-dependent transfer function of the sample. The pulse was numerically generated in MATLAB and saved as a standard computer sound file (.wav format). The functional shape of the pulse was chosen to be the second derivative of a Gaussian with a time duration of about 20 ms such that the Fourier transform contained significant frequency components up to 2200 Hz. The form of the pulse was selected because it contained the appropriate spread of frequencies in the range we wished to consider, and it was readily reproducible by the speaker. It should be noted that in addition to the impulse response method we also repeated many of the experiments using a spectrum analyzer and a white noise source. The results with the spectrum analyzer were essentially identical to those obtained with the impulse method.

The time-domain signal used in the data analysis was not due to a single pulse, but rather was the result of a sequence of (typically) 50 pulses that were recorded and averaged. The purpose of this add-and-average procedure was to

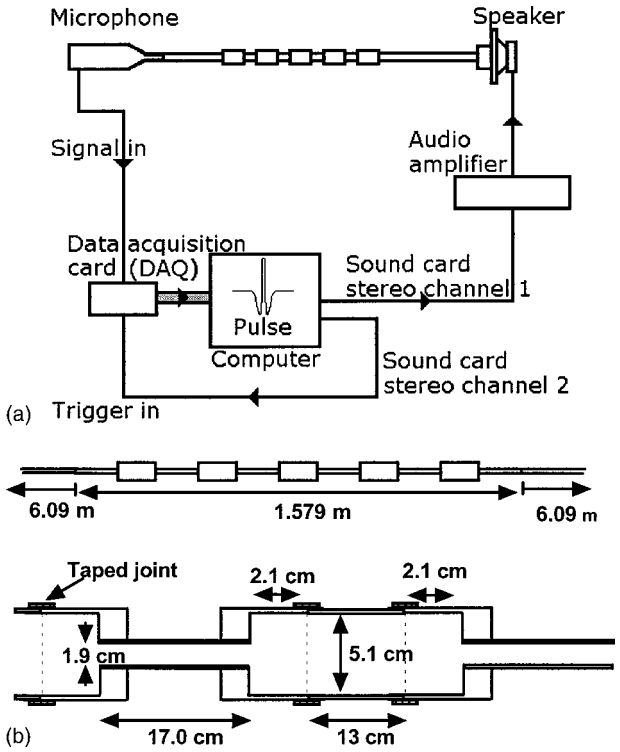

FIG. 1. (a) Schematic representation of the experimental configuration. (b) Schematic representation of the nine-element, diameter-modulated array showing the dimensions.

acquire time-domain data with a high signal-to-noise ratio. The method works because signals reaching the microphone from the speaker added coherently whereas random background noise was quickly averaged out. Because of multiple scattering within the periodic array and from the ends of the sample, some sound persists in the waveguide array for a long time after the initial impulse. To eliminate this long-lived signal we found that, for our particular waveguide parameters, a 7 s delay between successive pulses was required to eliminate interference due to coherent reflections. The validity of this add-and-average method at reducing signal noise can be observed from the initial flat response of the time domain data before the impulse showing that any background sound from previous pulses has been greatly attenuated.

The waveguide structure consisted of three sections of polyvinyl chloride (PVC) pipe being connected, with the speaker at one end and the microphone at the opposite end as shown in Fig. 1(a). The two outer sections of the structure were 6.096 m in length with a diameter of 1.9 cm. The interchangeable middle section contained the diameter-modulated array, which will be described in detail shortly. Each section of pipe was then attached to the adjacent one with masking tape to secure the connection. We found that the use of interlocking PVC pipe connectors to join the sections resulted in backreflections due to the small gap between adjacent pipes within the connectors. The acoustic impedance change due to these gaps led to reflection of the acoustic waves. Although weak, these backreflections were noticeable in the time-domain data. The use of masking tape to join the sections greatly reduced this effect.

At the speaker end, an adapter was constructed to efficiently couple the sound from the speaker to the waveguide. The adapter consisted of a 6-mm-thick piece of Plexiglas™ bolted to the speaker with a 2.0 cm hole centered directly in front of the speaker cone. A 5.1–1.9 cm PVC connector was then attached to the Plexiglas surface. This allowed the unobstructed acoustic impulse from the speaker to be transmitted to the structure. With the adapter in place, there was a distance of 3.8 cm between the cone of the speaker and the waveguide. A pliable foam insulator was then wrapped around the speaker and adapter to reduce the amount of sound emitted into the room.

The microphone was then inserted into the opposite end of the waveguide to a depth of 5.7 cm and was similarly wrapped with a pliable foam insulator. This isolated it from any room reflections that may have been caused by the speaker's initial impulse.

The sequence of events in a typical experiment was as follows. The numerically generated impulse sound file was played through the computer's audio card. The mono wav file was split into the two stereo channels such that each contained an identical version of the pulse. The first channel was sent through the amplifier (Technics model SU-V66) to the speaker (Optimus model number 40-1030, max power 80 W, 8 Ω nominal impedance). The speaker then transmitted the acoustic impulse, which traversed the structure and was received by the microphone (Brüel & Kjaer type 2215 precision sound level meter/octave analyzer). The microphone's signal was then digitized and stored by the data acquisition card (National Instruments PCI 6034E) as shown in Fig. 1(a). The second channel was sent directly to the data acquisition card to act as a trigger to initiate the recording of data. Accurate registration between the trigger and the audio pulse was crucial to the success of the add-and-average process. The sound file of the impulse signal was played by an audio program that looped the sound file so that it repeated at 7 s intervals.

Two acoustic filter structures with different physical parameters were tested. Each structure consisted of a sequence of alternating sections of different diameter PVC pipes. The first experiments used 1.9- and 5.1-cm-diam pipes for the nine-element array as shown in Fig. 1(b). The pipes were cut such that the periodicity of the system was 17.5 cm (distance between changes in cross-sectional area). To couple the two pipes with differing diameters, it was necessary to use 5.1–1.9 cm interlocking PVC pipe adapters. The adapters consisted of essentially two parts, a 5.1-cm-diam part and a 1.9-cm-diam part. The 5.1-cm-diam part of the adapter added a length of 2.1 cm, whereas the 1.9-cm-diam part of the adapter added a length of 0.2 cm. The 5.1-cm-diam pipes were cut to a length of 13.5 cm, and the 1.9-cm-diam pipes were cut to a length of 17.0 cm. Thus, the actual lengths of the sections of pipe were 17.7 cm for the 5.1-cm-diam section and 17.4 cm for the 1.9-cm-diam section. The total length of the periodic array was measured to be 157.9 cm. There was a discrepancy of 0.2 cm throughout the entire length of the array due to minor fabrication and cutting errors in the individual pipe sections. A 1.9 cm straight pipe of identical length was also cut and studied for comparison. The

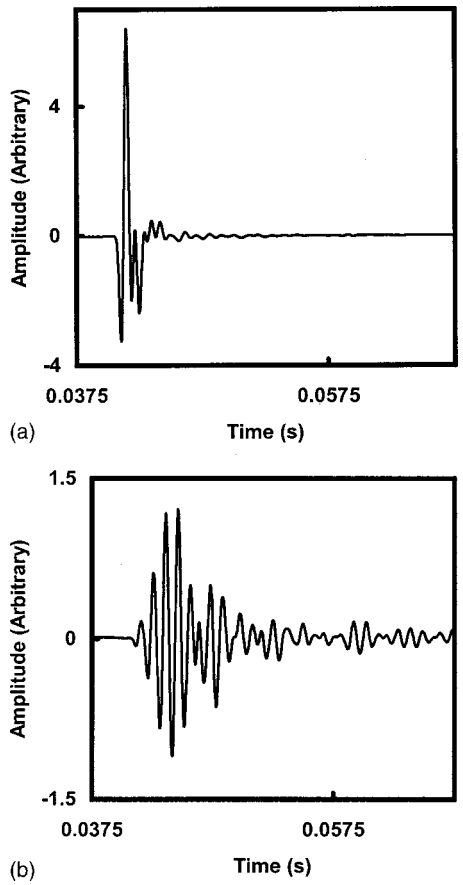

FIG. 2. The transmitted time-domain data obtained for a pulse sent through (a) the straight pipe structure and (b) the nine-element, 1.9- to 5.1-cm-diam modulated waveguide.

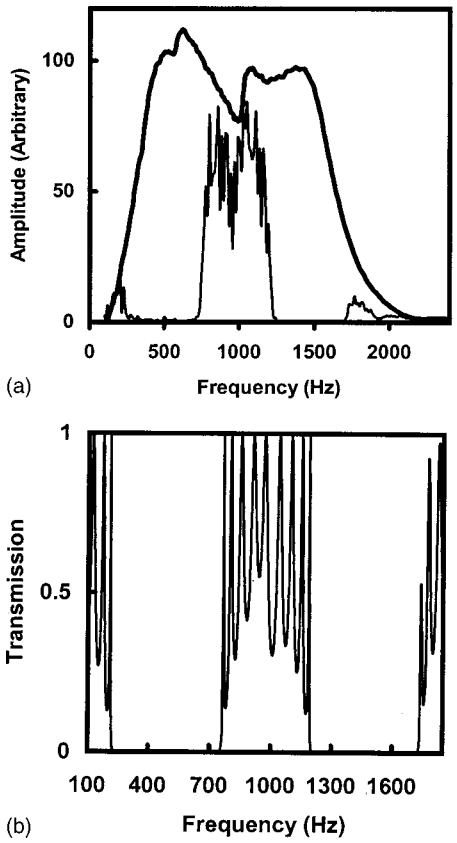

FIG. 3. (a) Composite of the Fourier spectra obtained from the pulses corresponding to Fig. 2(a) (upper dark line) and Fig. 2(b) (lower dark line). (b) Theoretical calculations showing the transmission of the perfectly periodic system.

second acoustic filter structure was similar in construction but with 3.2-cm-diam rather than 5.1-cm-diam segments.

IV. RESULTS AND DISCUSSION

Figures 2(a) and (b) show the transmitted time-domain data obtained from the straight pipe structure and the 1.9- to 5.1-cm-diam modulated waveguide, respectively. The oscillations after the initial pulse in Fig. 2(a) are primarily due to ringing in the speaker and adapter. In Fig. 2(b), the strong extended oscillations after the initial pulse are the result of multiple reflections within the periodic array.

Figure 3(a) is a composite figure of the frequency-domain data obtained from a numerical Fourier transform of the time-domain data for the unobstructed pulse without the array (upper dark line) and the pulse that traversed the diameter-modulated array (lower dark line). By comparing the curves, it can be seen that there are band gaps from 230 to 720 and 1200 to 1700 Hz. This matches closely with the predicted band gaps of 230–720 and 1200–1730 Hz from theoretical calculations as shown in Fig. 3(b).

Next, we altered the array to induce a defect state that would allow an extremely narrow band of frequencies to exist within a band gap. To do this, we modified the length of the middle pipe (5.1 cm diameter) within the nine-element array [see Fig. 1(b)]. We then repeated the above-outlined experimental procedure with middle pipes of various lengths. The frequency-domain data were then obtained from the Fourier transform of these time-domain data. Defect states deep within the band gap region are shown in Fig. 4 for four such structures. Theoretical calculations predict the existence of these modes; however, they predict very narrow (<1 Hz) transmission bands with peaks that ride to a transmission value of 1. One drawback to the narrowness of these defect states is that any minor flaw within the diameter-modulated waveguide will cause the defect states to be greatly attenuated. Inconsistencies within the segment lengths or cross sections of the diameter-modulated waveguide perturb the interference condition and cause slightly different frequencies to pass through the different parts of the waveguide. By the time the pulse gets through the array, very little of the amplitude of the defect frequencies will have added coherently throughout the entire waveguide. For this reason, the second acoustic filter structure with a lower impedance contrast was built. In a sample with a lower impedance contrast, theory predicts defect modes that are less narrow.

With a smaller change in acoustic impedance between adjacent segments, the band gaps become less pronounced and the defect modes become slightly wider. This allows for the coherent addition of a larger group of frequencies within the band gap and thus, greater transmission. Figure 5(a) shows experimental data for two such defect modes within the 1.9- to 3.2-cm-diam modulated waveguide. Figure 5(b) shows a theoretical calculation for the same system indicating that the theory replicates the defect frequencies with high accuracy.

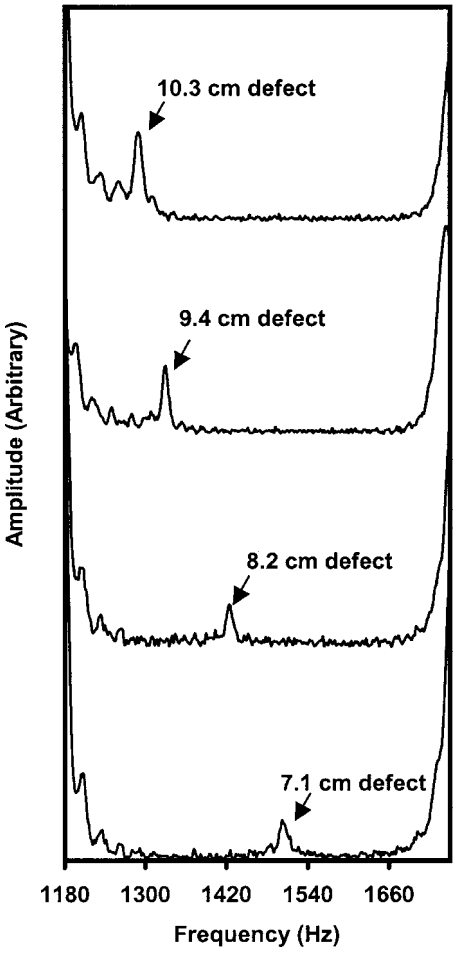

FIG. 4. Composite figure showing the Fourier spectra obtained from four different defects. Data were obtained from the nine-element, 1.9- to 5.1-cm-diam modulated waveguide with middle defects of length 7.1, 8.2, 9.4, and 10.3 cm.

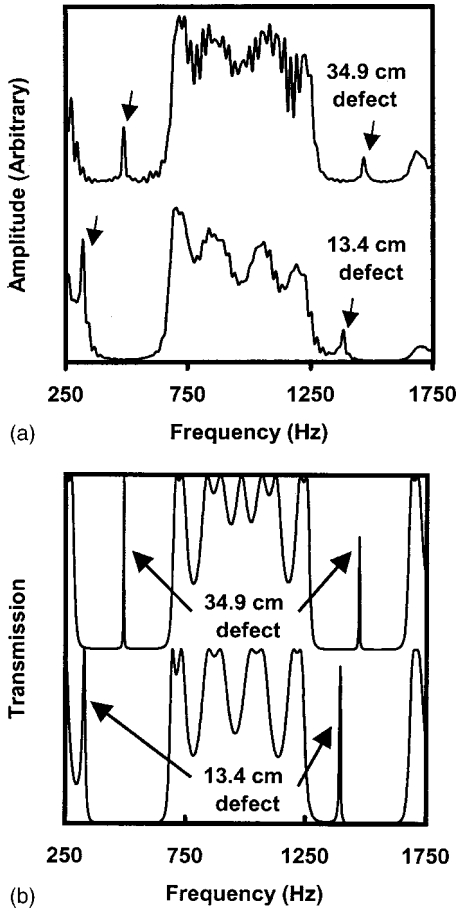

FIG. 5. (a) Composite figure of the Fourier spectra data obtained from the nine-element, 1.9- to 3.2-cm-diam modulated waveguide with middle defects of length 13.4 and 34.9 cm. Defect mode frequencies 489, 1465 Hz (top trace) and 322, 1385 Hz (bottom trace). (b) Theoretical calculations corresponding to the two defect modes in (a). Defect mode frequencies 491, 1474 Hz (top trace) and 326, 1395 Hz (bottom trace).

There are several interesting observations to make concerning the behavior of the defect modes within the band gap. When the induced defect in the middle pipe is shorter than its counterpart in the diameter-modulated array, the defect state in the frequency-domain data enters from the low-frequency side of the band gap (acceptor-like in solid state terms). As shorter defect pipes are used, the defect state moves from low to higher frequency within the band gap. For a defect pipe that is exactly one-half the length of the original pipe within the array, the defect mode appears directly in the middle of the band gap. When larger defect pipes are used, the defect mode enters from the high frequency side of the band gap (donor-like) and moves to lower frequency with increasing length. When the length is exactly double the length of the original pipe within the array, the defect mode again appears directly in the middle of the band gap.

These results can be qualitatively understood by analyzing the physical mechanism that leads to filtering action in these structures. For an array with no defect there is a maximum in reflection (and a corresponding minimum in transmission) at a frequency for which the length of individual array segments equal a quarter wavelength. The enhanced reflection results from constructive interference of the waves partially reflected from each successive junction between array elements of different diameters. For wavelengths that exactly match the quarter-wavelength condition, the successive partial reflections are always precisely in phase because of the combined effects of the half-wavelength round trip between junctions and the inversion upon reflection from a low-to-high impedance junction. The attenuation is a maximum for the design wavelength; however, there is significant filtering action over a broader band of surrounding frequencies leading to the band gap. Now if a defect is introduced by making the center element of the array twice as long, the interference dynamic is altered. The partial reflections from successive interfaces up to the defect are adding coherently to give rise to a strong backreflection. However, the addition of an extra half-wavelength round trip introduced by the defect means that the partial reflections from subsequent half of the array are out of phase resulting in destructive interference in the reflected signal. The net effect is that a narrow transmission band—the defect state—opens up precisely at the design wavelength. Altering the length of the defect will change the wavelength that experiences the half wavelength phase shift and hence will shift the position of the narrow transmission band within the band gap.

It is also interesting to note how the amplitude of the

defect mode varies with position within the band gap. As the defect mode moves deeper into the gap, the amplitude of the defect mode becomes increasingly attenuated. This effect is independent of which side of the band gap the defect mode enters. This phenomenon is similar to that seen in optical filters, and it can be understood because the attenuation is greatest at the center of the band gap where the quarter-wavelength interference condition is best satisfied. The defect in the center of the band is thus strongly confined spatially and therefore very narrow in frequency. Again, any imperfections in the segment lengths or cross-sectional uniformity lead to changes in coupling frequency, which dramatically alter the coupling to the very narrow defect mode. Thus the amplitude of the experimentally measured defect modes is smallest near the band center where the mode confinement is the greatest and progressively larger with proximity to the band edges.

V. CONCLUSION

The results presented here show that the diameter-modulated waveguide array is a simple yet elegant model for investigating acoustic band gap properties. Other similar one-dimensional systems based on dangling side branch arrays have been investigated recently.[11,20] Although the dangling side branch systems are simple experimentally they are less easy to treat theoretically because, unlike the circular cross section waveguide case, there is no simple expression for the acoustic impedance, which in this case depends on frequency.[19] Much of the interesting applications of acoustic band gap systems are associated with the production of defect states in an otherwise perfectly periodic array. The results here demonstrate the experimental limits that prevent the realization of some of the more extreme predictions of theory. Better results could be realized by a more accurate fabrication of the diameter modulated waveguide.

Finally, this simple system should prove useful for the experimental exploration of many of the fundamental effects such as tunneling and localization that are being investigated in acoustic band gap systems.

ACKNOWLEDGMENTS

This work was funded in part by NSF Grant No. ECS-9988797. C.B.B. was supported by a summer research grant from the McNair program.

[1] R. F. Cregan, B. J. Mangan, J. C. Knight, T. A. Birks, P. S. Russell, P. J. Roberts, and D. C. Allan, ''Single-mode photonic band gap guidance of light in air,'' Science **285**, 1537–1539 (1999).
[2] J. C. Chen, H. A. Haus, S. Fan, P. R. Villeneuve, and J. D. Joannopoulos, ''Optical filters from photonic band gap air bridges,'' J. Lightwave Technol. **14**, 2575–2580 (1996).
[3] S. Y. Lin, E. Chow, V. Hietala, P. R. Villeneuve, and J. D. Joannopoulos, ''Experimental demonstration of guiding and bending of electromagnetic waves in a photonic crystal,'' Science **282**, 274–276 (1998).
[4] E. Yablonovitch, ''Inhibited spontaneous emission in solid state physics and electronics,'' Phys. Rev. Lett. **58**, 2059–2062 (1987).
[5] M. S. Kushwaha, P. Halevi, L. Dobrzynski, and B. Djafari-Rouhani, ''Acoustic band structure of periodic elastic composites,'' Phys. Rev. Lett. **71**, 2022–2025 (1993).
[6] Z. Ye and E. Hoskinson, ''Band gaps and localization in acoustic propagation in water with air cylinders,'' Appl. Phys. Lett. **77**, 4428–4430 (2000).
[7] A. Diez, G. Kakarantzas, T. A. Birks, and P. St. J. Russell, ''Photonic stop bands in optical fibre periodic microstructures,'' Appl. Phys. Lett. **76**, 3481–3483 (2000).
[8] W. M. Robertson and J. F. Rudy, ''Measurement of acoustic stop bands in two-dimensional periodic scattering arrays,'' J. Acoust. Soc. Am. **104**, 694–699 (1998).
[9] J. V. Sanchez, D. Caballero, R. Martinez-Sala, J. Sancho, C. Rubio, J. Sanchez-Dehesa, F. Meseguer, J. Llinares, and F. Galvez, ''Sound attenuation by two dimensional array of rigid cylinders,'' Phys. Rev. Lett. **80**, 5325–5328 (1998).
[10] B. Djafari-Rouhani, J. O. Vasseur, A. Akjouj, L. Dobryznski, M. S. Kushwaha, P. A. Deymer, and J. Zemmouri, ''Giant stop bands and defect modes in one-dimensional waveguide with dangling side branches,'' Prog. Surf. Sci. **59**, 255–264 (1998).
[11] M. S. Kushwaha, A. Akjouj, B. Djafari-Rouhani, L. Dobrzynski, and J. O. Vasseur, ''Acoustic spectral gaps and discrete transmission in slender tubes,'' Solid State Commun. **106**, 659–663 (1998).
[12] W. P. Mason, *Electromechanical Transducers and Wave Filters* (Van Nostrand, Princeton, 1948), pp. 28–31.
[13] C. E. Bradley, ''Time harmonic acoustic Bloch wave propagation in periodic waveguides. I. Theory,'' J. Acoust. Soc. Am. **96**, 1844–1853 (1994).
[14] C. E. Bradley, ''Time harmonic acoustic Bloch wave propagation in periodic waveguides. II. Experiment,'' J. Acoust. Soc. Am. **96**, 1854–1862 (1994).
[15] R. S. Langley, ''The frequency band-averaged wave transmission coefficient of a periodic structure,'' J. Acoust. Soc. Am. **100**, 304–311 (1996).
[16] R. S. Langley, ''Wave transmission through one-dimensional near periodic structures: Optimum and random disorder,'' J. Sound Vib. **188**, 717–743 (1995).
[17] T. D. Rossing, ''Experiments with an impedance tube in the acoustics laboratory,'' Am. J. Phys. **50**, 1137–1141 (1982).
[18] P. M. Morse, *Vibration and Sound* (McGraw–Hill, New York, 1936), Chap 7.
[19] L. E. Kinsler, A. R. Frey, A. J. Coppens, and J. V. Sanders, *Fundamentals of Acoustics* (Wiley, New York, 1982).
[20] J. Ash and W. M. Robertson, ''Breaking the sound barrier: Tunneling of acoustic pulses through the forbidden transmission region of a one-dimensional acoustic band gap array,'' Am. J. Phys. **70**, 689–693 (2002).

Internal-wave time evolution effect on ocean acoustic rays

Stanley M. Flatté[a] and Michael D. Vera
Physics Department, University of California at Santa Cruz, Santa Cruz, California 95064

(Received 2 January 2001; revised 19 April 2002; accepted 26 June 2002)

A range-dependent field of sound speed in the ocean, $c(x,z)$, caused by internal waves, can give rise to instabilities in acoustic ray paths. Past work has shown the importance of the background, range-independent, sound-speed profile; the ray initial conditions; the source-receiver geometry (depths and range); and the strength of the internal waves. However, in the past the time evolution of the internal waves has been ignored on the grounds that the speed of internal waves is much slower than the speed of the acoustic wave. It is shown here by numerical simulation that two rays with identical initial conditions, traveling through an ocean with the same background profile and the same random realization of internal waves, but with the internal waves frozen in one case and evolving in the other, travel significantly different trajectories. The dependence of this ''frozen–unfrozen'' difference on the initial ray launch angle, the background profile, and the strength of the internal-wave spectrum, is investigated. The launch-angle difference that generates similar arrival-depth differences to those induced by internal-wave time evolution is on the order of 100 μrad. The pattern of differences is measured here by the arrival depth at the final range of 1000 km. The observed pattern as a function of launch angle, change in the background profile, and change in internal-wave strength is found to be nearly the same for ''frozen–unfrozen'' change as for a slight change in launch angle. © *2002 Acoustical Society of America.* [DOI: 10.1121/1.1501897]

PACS numbers: 43.30.Cq, 43.30.Ft, 43.25.Rq, 92.10.Ns, 05.45.Pq [DLB]

I. INTRODUCTION

Previous numerical simulations of ocean-acoustic ray propagation through internal waves have investigated arrival-depth differences induced by launch-angle differences at ranges of order 1 Mm.[1] Such investigations have excluded the time evolution of internal waves on the grounds that the speed of the acoustic wave is much larger than the speed of the internal waves. This assumption is termed the ''frozen-field'' hypothesis. Under this hypothesis it has been observed that the pattern of arrival-depth difference between two rays that have slight differences in launch angle (chosen to be 0.1 μrad) is quite variable with launch angle, background sound-speed profile, and internal-wave spectral strength.[1–4]

This paper is an investigation into the effects of internal-wave time evolution on numerically simulated ray travel. The differences between the frozen and unfrozen situations are examined and described. Important simplifications, in addition to the geometrical-optics approximation which allows for an analysis based on rays, include the restriction that the rays and internal waves travel in the two-dimensional plane which joins source and receiver, and the use of a subset of possible internal waves; hence our specific numbers are qualitative; our conclusions are not.

Aside from the initial condition (launch angle), two other general parameters have been varied to observe their effects on the character of the instabilities caused by the ''frozen–unfrozen'' difference. First, two different profiles are used in an attempt to understand the effect of the range-averaged, or background profile. Second, the effects of variation in the internal-wave energy are investigated.

It should be noted that past studies have chosen to vary only one of several possible initial conditions. The choice of launch-angle difference rather than source-depth difference is rather arbitrary. When choosing a slight variation in the internal-wave structure one can imagine a host of different choices. However, only one represents a common approximation used in wave propagation: the ''frozen-field'' hypothesis. By observing the ''frozen–unfrozen'' difference we not only study a slight change in the medium; we also observe the effect of a common approximation.

The paper is organized as follows. Section II addresses the model of the ocean environment used in the simulations. The properties of the range-averaged profiles and of the internal-wave models are presented. The methods used for the simulation of ray propagation are given in Sec. III. Section IV presents the ray arrival-depth differences between the frozen and unfrozen simulations as a function of launch angle. The results are presented for two different profiles. In Sec. V, the structure and magnitude of these differences are compared to those generated by small shifts of the launch angle. Section VI examines the effect on the ''frozen–unfrozen'' differences of overall reductions in the strength of the internal waves. Section VII contains a summary.

II. OCEAN ENVIRONMENT

The environmental model used in the simulations consists of one of two background profiles, $\overline{c}(z)$, and range-dependent variability induced by a model of internal waves (Fig. 1). The Munk Canonical profile[5] is an analytic model and takes the following form:

$$\overline{c}(z) = C_{\text{axis}}[1 + \epsilon(e^{\eta} - \eta - 1)], \tag{1}$$

[a]Electronic mail: flatte@physics.ucsc.edu

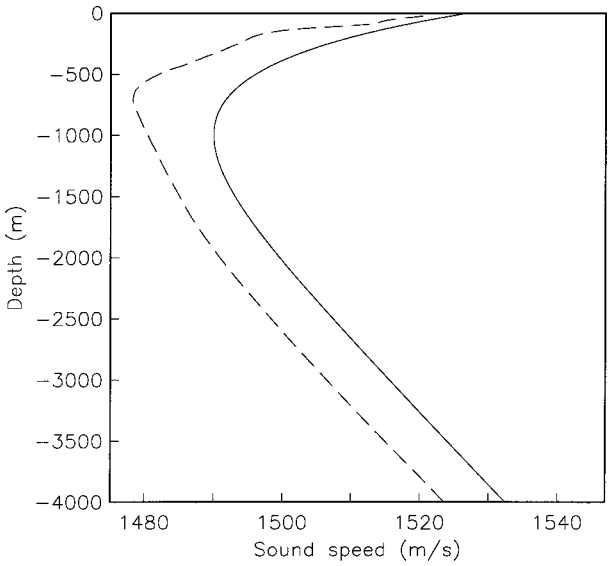

FIG. 1. Sound-speed profiles used in these simulations. The Canonical profile is a solid line; the Slice89 profile is a dashed line.

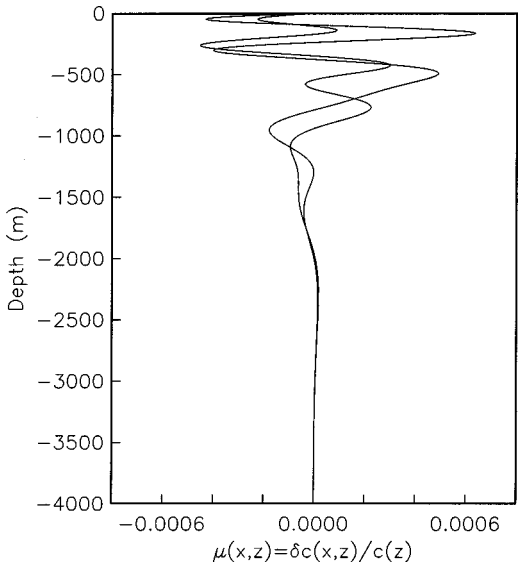

FIG. 2. Fractional sound-speed variability induced by internal waves at two different ranges.

$$\eta = 2(z - z_{\text{axis}})/B. \tag{2}$$

The parameters used here are $\epsilon = 5.7 \times 10^{-3}$, $C_{\text{axis}} = 1490$ m/s, $z_{\text{axis}} = -1000$ m, and $B = 1000$ m.

The other profile contained in Fig. 1 has been taken from the data collected for the Slice89 experiment in the North Pacific.[6] It has greater curvature at the axis as well as additional structure absent in the smooth, analytic Canonical profile.

Internal waves cause the vertical displacement of water from the equilibrium position established by the density gradient of the water column. The usual fluid equations, in linear form, give the following equation for the eigenmodes of such displacements:[1,7]

$$\partial_{zz} W_j + \left(\frac{n^2(z) - \omega^2}{\omega^2 - \omega_i^2} \right) k_j^2 W_j = 0, \tag{3}$$

$$W_j = 0 \qquad \text{at } z = 0, \tag{4}$$

$$W_j = 0 \qquad \text{at } z = -D = -4000 \text{ m}. \tag{5}$$

The depth D is chosen as 4000 m. The inertial frequency, ω_i, is set at 1 cycle per day—its value at 30° latitude. The buoyancy frequency, $n(z)$ is exponential:

$$n(z) = n_0 e^{(z/B)}, \tag{6}$$

where $n_0 = 3$ cph and, as already mentioned, $B = 1000$ m. A single internal-wave frequency is chosen. The most appropriate single frequency is the M2 tidal frequency; this frequency often has a substantial energy in experiment, and it is also a reasonable average frequency with which to represent the continuum that runs from the inertial frequency to the buoyancy frequency. The M2 tidal frequency is taken as $\omega = 1/12.5$ cph. One of the reasons that we do not use a continuum of frequencies is to avoid any aspect of time evolution that changes within a short time. Thus the total travel time ($\sim$ 700 s) of the acoustic pulse in our case is less than 2% of the internal-wave period. With these choices, a series of internal-wave modes, $W_j(z)$, can be found along with their associated horizontal wave vectors, k_j. The first ten of these modes are used in this paper; the sound-speed variability that they induce is illustrated in Fig. 2. This internal-wave model is more than qualitative with respect to variance and vertical structure. It has the correct variance of sound speed with depth, and the slopes of the spectra in wave number are close to the empirical Garrett-Munk (GM) result.[8] Its frequency spectrum, however, is significantly different, such that the results we find for ray propagation behavior must be regarded as qualitative.

The total vertical displacement is generated by a sum over mode number:

$$\zeta(x,z,t) = \text{Re}\left[\sum_{j=1}^{10} A_j W_j(z) \exp i(k_j x - \omega t + \phi_j) \right]. \tag{7}$$

The $-\omega t$ term in the argument of the exponential is central to this paper. It accounts for internal-wave evolution during the finite time necessary for acoustic energy to propagate from source to receiver. It is excluded, as an approximation, in frozen simulations and remains in unfrozen simulations. A_j and ϕ_j are random variables corresponding to the amplitude and phase of the mode under consideration. A_j is weighted by mode number in the following way:

$$\langle A_j^2 \rangle = \frac{a}{(j^2 + j_*^2)}, \tag{8}$$

where $j_* = 3$, as it does for some parts of the ocean.

The above is intended to reproduce approximately the mode-number dependence of the full Garrett–Munk spectrum.[8] Others have shown that the use of the first ten modes is sufficient for an accurate calculation of travel-time variances and accounts for nearly all the energy involved in internal-wave modes.[1,9] In order to achieve realistic values for the total internal-wave displacement, ζ_{rms}, when extrapolated to the surface, is set to 7.3 m. This, in conjunction with the normalization chosen for $W_j(z)$, determines the value of a.

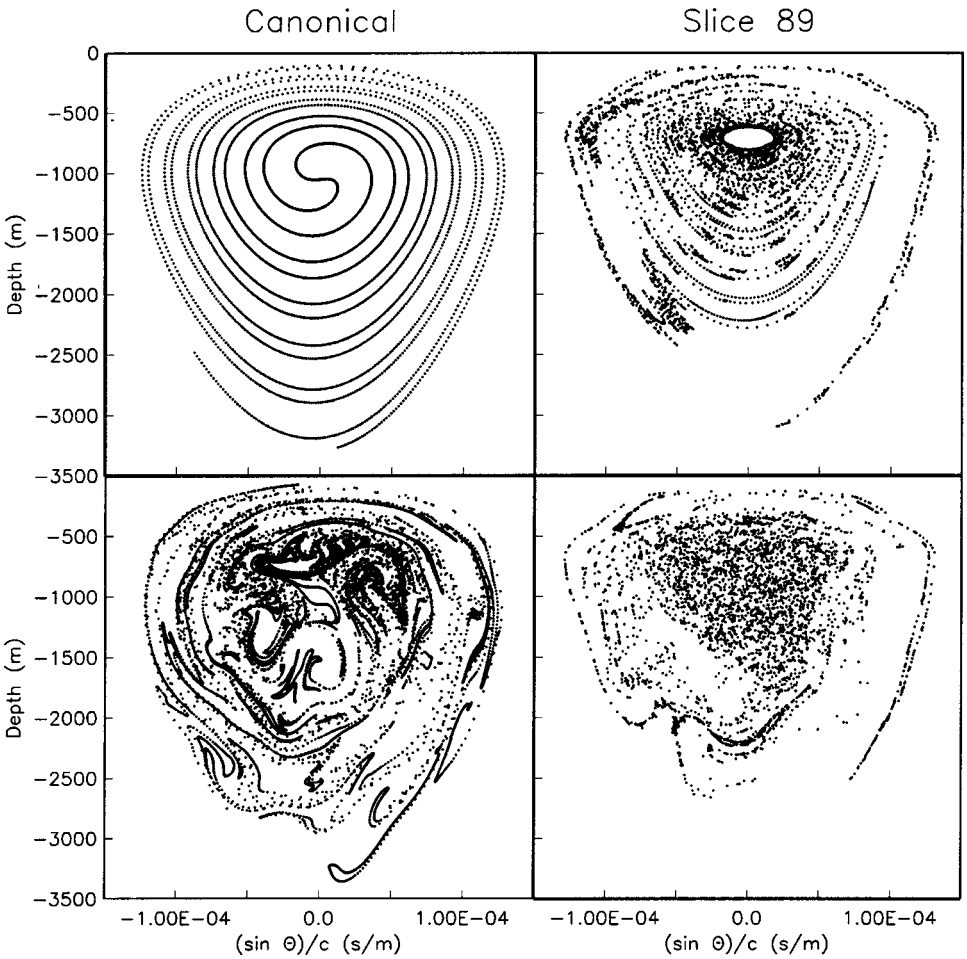

FIG. 3. Phase-space diagrams for both profiles, both with and without internal waves. The plots on the left-hand side use the Canonical profile; those on the right-hand side use the Slice89 profile. The upper panels are constructed in the absence of internal waves: the lower panels show the effect of range-dependent internal waves.

Finally, the internal waves induce sound-speed variability according to

$$\mu(x,z,t)\equiv\frac{\delta c(x,z,t)}{\overline{c}(z)}=F\frac{n^2(z)}{g}\zeta(x,z,t), \tag{9}$$

where F is a dimensionless constant[10] set to 30, $n(z)$ is given previously, and $\delta c(x,z,t)=c(x,z,t)-\overline{c}(z)$.[1,7,10]

III. RAY METHODS

The version of the ray equations used in these simulations is based on the full Helmholtz wave equation. These equations can be written as a Hamiltonian system in the variables z and $p=\sin\theta/c$, where θ is the ray angle relative to the horizontal. An additional equation is also required in order to track the ray travel time.[1] The variables z and p together form the coordinates of phase space,

$$\frac{dz}{dr}=\frac{\partial H}{\partial p}, \tag{10}$$

$$\frac{dp}{dr}=-\frac{\partial H}{\partial z}, \tag{11}$$

$$H=-(c^{-2}-p^2)^{1/2}, \tag{12}$$

$$\frac{dt}{dr}=c^{-1}(1-(pc)^2)^{-1/2}. \tag{13}$$

The simulations described in this paper follow a fan of rays starting at a single depth z_0 (-1050 m for Canonical, -800 m for Slice89), and with launch angles in regular increments between $\pm\theta_0$, where $\theta_0=0.2$ rad. Thus on the phase-space plot the initial rays form a horizontal straight line; they all start at the same depth z_0, and their p coordinate runs from $-p_0$ to $+p_0$, where

$$p_0=\frac{\sin\theta_0}{c(z_0)}.$$

The rays propagate forward in range according to Eqs. (10)–(13). This propagation is performed in double precision, using a modified fourth-order Runge-Kutta technique with an adaptive step size.[1,11]

The range dependence of the sound speed has significant consequences for the ray system. It implies that the Hamiltonian is not conserved as the ray propagates. It is well to remember here that the ray picture is an approximation to a wave propagation. Propagation of an acoustic wave in a deterministic waveguide filled with internal waves has a direct analogy with a one-dimensional quantum mechanical problem in which the potential is time dependent.[12,13] In the ray approximation, range dependence renders the system nonintegrable—it cannot be solved by the separation of variables. Figure 3 shows phase-space plots of the simulated ray arrivals for each profile, both with and without the intervening internal waves, for a range of 1000 km. In the absence of

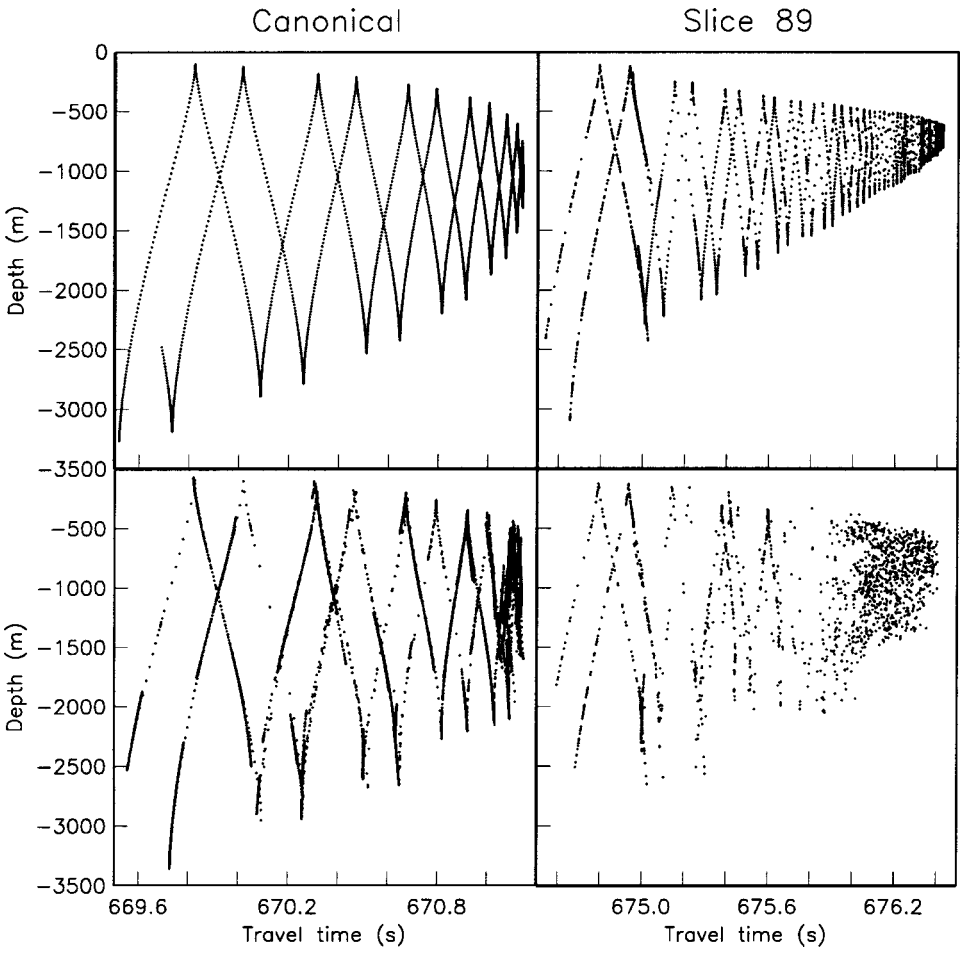

FIG. 4. Time fronts constructed from the arrival times and depths of each ray. The panels on the left-hand side (right-hand side) are for the Canonical (Slice89) case. The upper plots do not include internal waves. The lower plots illustrate the effect of internal waves on front structure.

range dependence, the ray arrivals are regular and the total number of concentric spirals directly corresponds to the total range traversed. This regularity does not hold in the presence of the internal waves. Though the Canonical version contains visible segments in which stability persists and adjacent rays arrive with nearby coordinates, there are also regions in which rays with similar initial launch angles are nearly uncorrelated. These regions of strong instability appear as scattered points, lacking any apparent continuity. A large central region of instability is the dominant feature of the Slice89 phase plot in the presence of internal waves.

The effect of the internal waves can also be examined using time fronts—a plot of the arrival depth and travel time of each ray at the arrival range. The panels of Fig. 4 show the ray arrivals that correspond to the phase-space plots in Fig. 3, for a range of 1000 km. Much like the corresponding phase plots, the arrivals in the absence of internal waves show a pronounced regularity—the well-known ''accordion'' shape induced by the presence of a temperature profile.[1,14] Again, nearby rays fall onto a clearly discernible, continuous pattern. The arrivals from simulations that include the internal waves display many of the expected effects of range dependence on the time front.[1,15] The late-arriving part of the time front no longer displays the nearly linear segments that characterize both the range-independent arrivals and the early arriving portions of the range-dependent front. The transmission finalé has been both shifted in time and broadened in depth—though the details of the depth effect may depend on the higher modes neglected in this paper.[9,15] Additionally, the smearing of the points throughout the front suggests variability in intensity since, to a reasonable approximation, the distance between ray arrivals with a given launch-angle increment is inversely proportional to the acoustic intensity.[1]

IV. DIFFERENCES INDUCED BY TIME EVOLUTION

Range dependence in the sound speed due to internal waves can cause the ray paths to exhibit instabilities. Small changes in the ray launch angle or the properties of the sound-speed field can dramatically change any of the ray coordinates (depth, travel time, or p). The use of a time-evolution model of internal waves represents just such a slight alteration. A simulation range of 1000 km leads to ray travel times, for either profile, of about 700 s. Because all internal-wave modes in the simulation have a single frequency ($\omega = 1/12.5$ cph), none of the internal waves have undergone a significant fraction of their total period while the rays have propagated from source to receiver. Nevertheless, two rays with the same launch angle, but traversing frozen and unfrozen fields, respectively, can arrive at the receiver range with significantly different depths. Figure 5 plots this depth difference against initial launch angle for the Canonical and Slice89 profiles.

The difference, or ''bubble,'' plots generated for each profile are qualitatively quite different.[1] The Canonical dif-

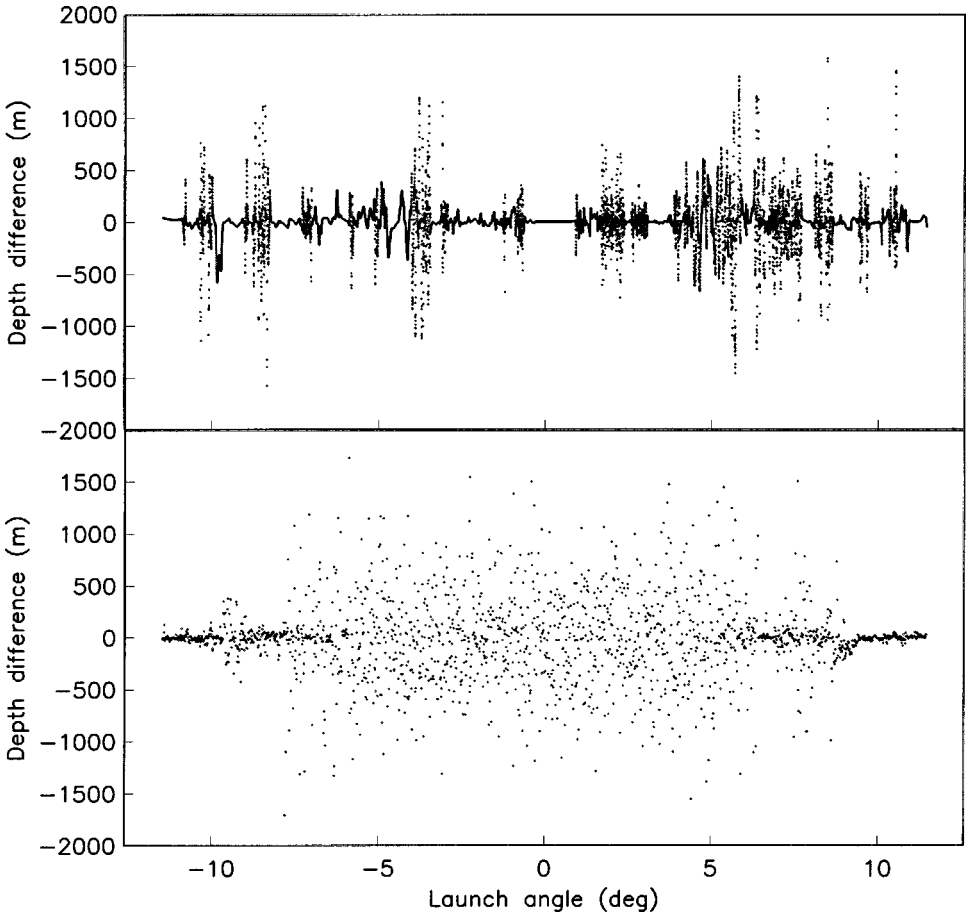

FIG. 5. The differences induced in ray arrival depths by internal-wave time evolution (i.e., ''frozen-unfrozen'' differences). The top panel contains Canonical results; the bottom panel contains Slice89 results.

ference plot as a function of launch angle reveals alternating regions of relative stability and instability. The Slice89 simulations, by contrast, generate a central region of shallow launch angle with significant instability, while steep angles, both positive and negative, are relatively stable. While the largest differences present in either plot are comparable, $O(2000\ \mathrm{m})$, the Slice89 case generates a higher overall variance (see Fig. 6 and Table I) since a larger fraction of the launch angles are within unstable regions. (The variances in Fig. 6 and Table I are calculated from results like those in Figs. 5 and 7: that is, from launch-angle regions within one realization.) The greater overall instability exhibited by the Slice89 results is related to the greater curvature at the sound axis; previous authors have suggested a normalized curvature parameter related to the small-scale time front folding that is characteristic of ray instability.[2]

V. COMPARISON OF DIFFERENCES WITH THOSE INDUCED BY A LAUNCH-ANGLE SHIFT

In order to establish a basis of comparison for the time-evolution effect, the depth-of-reception differences generated by simulations that differ by small amounts in initial launch angle are examined. This is the method used by Simmen *et al.*[1] to map the stability of rays at various launch angles. Using an angle shift of 0.1 μrad, those authors found that the Slice89 and Canonical profiles generate overall difference magnitudes which are very much smaller than those induced by time evolution in this paper. In order to find angle shifts that generate differences comparable to those resulting from time evolution, a series of simulations to a range of 1000 km were performed with each profile, using angle shifts ranging from 10^{-3} to 1000 μrad.

Figure 6 is a plot of the depth-difference variances versus the angle shifts. The dependence on the angle shift is quite different for each of the two profiles. The Slice89 variance is only weakly dependent on the angle shift, when com-

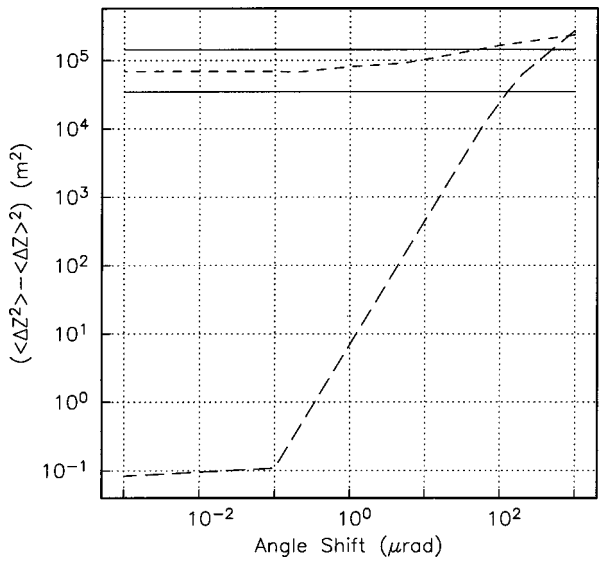

FIG. 6. The variance in depth differences versus the inducing launch angle shift. The curve with the longer dashes is the Canonical version; the shorter dashed is the Slice89 counterpart. The solid lines are the variances caused by internal-wave time evolution—Canonical generates the lower solid line.

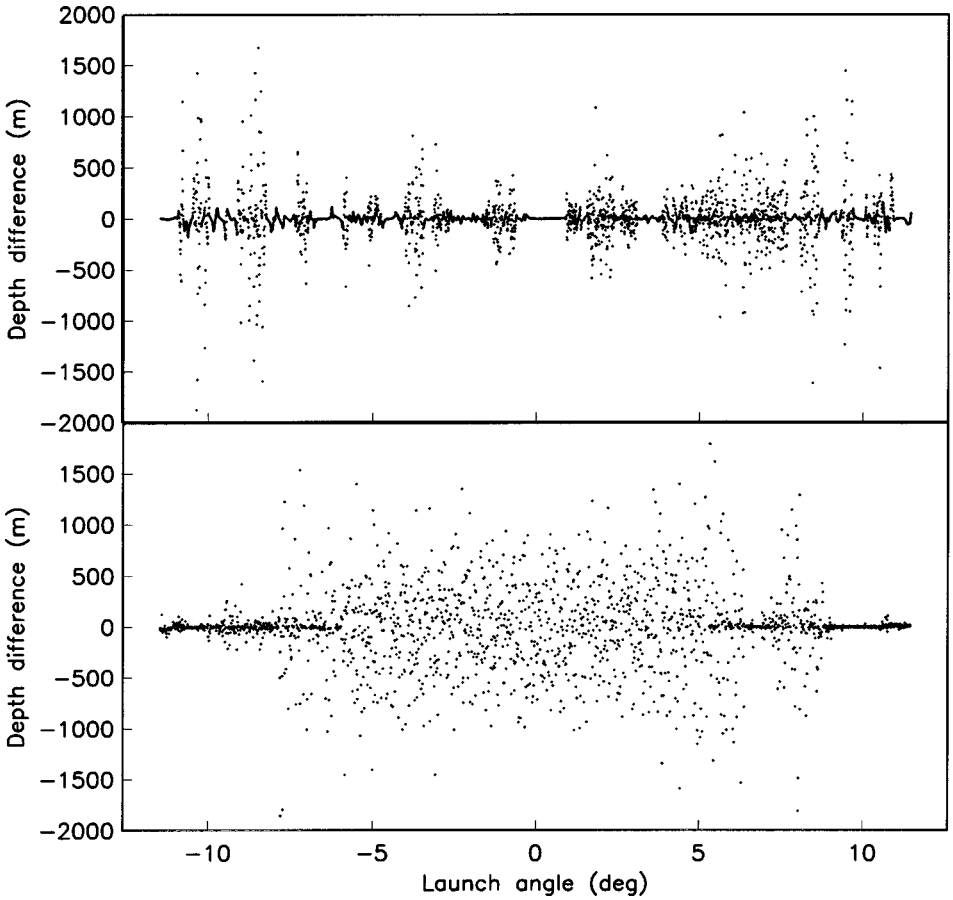

FIG. 7. The differences induced in ray arrival depths by launch-angle shifts of 125 (70) μrad for the Canonical (Slice89) profiles. The angle shift values were chosen to reproduce the difference magnitude caused by the ''frozen–unfrozen'' difference, shown in Fig. 5. The top (bottom) panel refers to the Canonical (Slice 89) profile. The resulting difference patterns are very similar to those seen in Fig. 5.

pared to the corresponding Canonical results. Over most of the angle-shift domain examined, the Canonical variance dependence is greater than linear, while the Slice89 dependence is less than linear. An interesting feature of the Canonical variance curve is the apparent transition near 0.1 μrad where the dependence on angle shift, rather suddenly, becomes much stronger. For each profile, a launch-angle shift value was found that induced a variance nearly equal to that of time evolution. In the Canonical case, it was 125 μrad, and in the Slice89 case it was 70 μrad. The resulting depth differences as a function of launch angle are illustrated in Fig. 7.

The differences induced by launch-angle shifts, as a function of launch angle, are strikingly similar to the frozen–unfrozen differences shown in Fig. 5. As before, regions of stability and instability alternate in the Canonical case. The central region of stability is a recurring feature of Canonical ray chaos simulations; Smith *et al.* find the same feature using disturbances that are periodic in range, without the multiple k_j of internal waves.[4] The Slice89 case also shows a central region of instability corresponding to shallow launch angles and relative stability at steep launch angles, as in Fig. 5.

The overall magnitudes of the differences in these angle-shift difference plots are equal, by construction, to those of the corresponding frozen–unfrozen counterparts. That the resulting difference structures are so similar strongly suggests that the structures can be regarded as signatures of the range-averaged profiles. Also, the profiles present clearly distinct dependencies of the difference magnitude on launch-angle shift over the six orders of magnitude examined. This is independent evidence that the range-averaged profile is of central importance to the nature of the arrival-depth differences at 1000 km.

VI. SCALING WITH INTERNAL-WAVE ENERGY

Table I collects the variance results of simulations performed using one half and one quarter of the previous internal-wave energy. All simulations had a receiver range of 1000 km. In addition to the variance result that includes all

TABLE I. The calculated depth-difference variance, $[\langle \Delta Z^2 \rangle - \langle \Delta Z \rangle^2]$, due to time evolution, with one, one-half, and one-quarter GM internal-wave energy levels. The first row for each profile includes all launch angles between -0.2 and $+0.2$ radians. The second row includes only a specified region of launch angle determined to be unstable in even the one-quarter GM case. The third and final row uses a region of launch angle found to be stable with the full 1-GM internal-wave energy. The Canonical differences show a much stronger dependence on the internal-wave energy.

	Internal-wave energy		
	Full	Half	Quarter
Canonical profile: Depth-difference variances (m^2)			
All launch angles	3.48×10^{4}	7.38×10^{3}	1.50×10^{3}
$5°<\theta<6°$	1.86×10^{5}	4.54×10^{4}	6.10×10^{3}
$-0.6°<\theta<0.6°$	2.99×10^{1}	1.02×10^{-1}	7.29×10^{-3}
Slice89 profile: Depth-difference variances (m^2)			
All launch angles	1.44×10^{5}	7.26×10^{4}	3.93×10^{4}
$-5°<\theta<5°$	2.10×10^{5}	1.16×10^{5}	7.71×10^{4}
$\theta<-10°$, $\theta>9°$	1.68×10^{3}	5.03×10^{2}	1.60×10^{2}

the rays in the simulation, the same quantity is also reported for regions determined to be stable and unstable in all cases. The unstable region is chosen as a range in launch angle with significant arrival-depth differences, even in the quarter-energy case. Likewise, the stable region is chosen by examining the full-strength results.

The variances from Slice89 simulations are greater than the Canonical counterparts in every case. One might look for a straight-line behavior on a log–log plot, but no such simple behavior is seen. Roughly, the Canonical depth-difference variances increase faster as a function of internal-wave strength. This holds for each case, though it is clearest in the case of the launch-angle intervals that are labeled as ''stable.'' The ''unstable'' intervals have larger depth-difference variances and the response to energy reductions is less, as a fraction of the initial values.

VII. CONCLUSION

The effect of internal-wave time evolution on acoustic propagation in the ocean has been examined using numerical simulations of ray travel over a 1000 km range. A model internal-wave field was used to introduce range dependence into each environment. The model field consists of the first ten modes, specified by a chosen frequency (the M2 tide) and a simple exponential buoyancy profile, traveling along the direction between the source and the receiver. Such a model has a quantitatively correct vertical structure, but a qualitative horizontal and time structure. The entire travel time to the final range is less than 2% of the chosen internal-wave period. The resulting time fronts showed the expected ''accordion'' shape for early arrivals caused by the profile's refraction of ray trajectories, as well as the blurring and reshaping of the transmission finalé characteristic of a range-dependent sound-speed field.

Arrival-depth differences were evaluated between simulations that include the internal-wave time evolution and those that suppress it. This ''frozen–unfrozen'' difference was studied as a function of launch angle, background sound-speed profile, and internal-wave spectral energy. These ''frozen–unfrozen'' differences were also compared with the differences generated by shifts in the initial launch angle. From this analysis, the following conclusions can be drawn

(1) The ''frozen–unfrozen'' differences were comparable to differences caused by launch-angle differences of about 100 μrad.

(2) The pattern of differences as a function of launch angle was indistinguishable between ''frozen–unfrozen'' differences and ''launch-angle'' differences.

(3) It has been established by previous work that the pattern of ''launch-angle'' differences as a function of launch angle changes dramatically for different profiles.[1] We have established that the pattern of ''frozen–unfrozen'' differences does the same, in fact following the pattern of ''launch-angle'' differences quite closely.

(4) The variance of the ''frozen–unfrozen'' difference for each group of launch angles were determined for three different values of internal-wave spectral energy. No consistent scaling behavior was found for any launch-angle region. In all cases the Canonical variance increased more quickly with internal-wave energy than did the Slice89 result [but the Slice89 variances were much larger, see conclusion (3)].

The overall conclusion of our study is that very slight changes in the internal-wave medium causes substantial changes in the arrival depth of a ray that has traveled 1000 km. Movements in the internal-wave field that represent only 2% of the internal-wave period can cause arrival-depth differences of order 1000 m. This observation also has implications for the common ''frozen-field'' approximation, which ignores such movements. Whether such changes are important to any particular experiment or simulation calculation must be evaluated in each particular case. For example, Simmen *et al.*[1] evaluated the pattern of chaotic versus stable rays as a function of launch angle using the frozen approximation and launch-angle differences of 0.1 μrad. If they had included internal-wave time evolution for both rays, presumably they would have gotten similar results, without realizing that the paths they were following in the two cases would have been drastically different by far more than the differences they were looking at.

ACKNOWLEDGMENTS

This research was supported in part by the U.S. Office of Naval Research Ocean Acoustics Program, Code No. 321OA. This is Contribution No. 433 of the Institute of Tectonics.

[1] J. Simmen, S. M. Flatté, and G.-Y. Wang, ''Wave front folding, chaos, and diffraction for sound propagation through ocean internal waves,'' J. Acoust. Soc. Am. **102**, 239–255 (1997).
[2] T. F. Duda and J. B. Bowlin, ''Ray-acoustic caustic formation and timing effects from ocean sound-speed relative curvature,'' J. Acoust. Soc. Am. **96**, 1033–1046 (1994).
[3] K. Smith, M. Brown, and F. Tappert, ''Acoustic ray chaos induced by mesoscale ocean structure,'' J. Acoust. Soc. Am. **91**, 1950–1959 (1992).
[4] K. Smith, M. Brown, and F. Tappert, ''Ray chaos in underwater acoustics,'' J. Acoust. Soc. Am. **91**, 1939–1949 (1992).
[5] W. H. Munk, ''Sound channel in an exponentially stratified ocean, with application to SOFAR,'' J. Acoust. Soc. Am. **55**, 220–226 (1974).
[6] T. Duda, S. M. Flatté, J. Colosi, B. Cornuelle, J. Hildebrand, W. Hodgkiss, Jr., P. Worcester, B. Howe, J. Mercer, and R. Spindel, ''Measured wave front fluctuations in 1000-km pulse propagation in the Pacific Ocean,'' J. Acoust. Soc. Am. **92**, 939–955 (1992).
[7] S. Flatté, R. Dashen, W. Munk, K. Watson, and F. Zachariasen, *Sound Transmission Through a Fluctuating Ocean*, Cambridge Monographs on Mechanics and Applied Mathematics (Cambridge University Press, Cambridge, 1979), 299 pp.
[8] W. Munk and C. Garrett, ''Internal waves in the ocean,'' Annu. Rev. Fluid Mech. **11**, 339–369 (1979).
[9] J. Colosi, S. M. Flatté, and C. Bracher, ''Internal-wave effects on 1000-km oceanic acoustic pulse propagation: Simulation and comparison with experiment,'' J. Acoust. Soc. Am. **96**, 452–468 (1994).
[10] K. Noble and S. Flatté, ''Predicting acoustic effects of internal waves from the basic climatology of the world ocean,'' J. Acoust. Soc. Am. **107**, 747–757 (2000).
[11] W. Press, S. Teukolsky, W. Vetterling, and B. Flannery, *Numerical Recipes in FORTRAN* (Cambridge University Press, Cambridge, 1992).
[12] M. C. Gutzwiller, *Chaos in Classical and Quantum Mechanics*, Interdisciplinary Applied Mathematics, Vol. 1 (Springer, Berlin, 1990).
[13] S. Flatté, ''The Schrödinger equation in classical physics,'' Am. J. Phys. **54**, 1088–1092 (1986).
[14] W. Munk, P. Worcester, and C. Wunsch, *Ocean Acoustic Tomography* (Cambridge University Press, Cambridge, 1995).
[15] J. Colosi, Ph.D. thesis, University of California at Santa Cruz, 1993.

The effect of reverberation on the damping of bubbles

T. G. Leighton,[a] P. R. White, C. L. Morfey, and J. W. L. Clarke
Institute of Sound and Vibration Research, University of Southampton, Highfield, Southampton SO17 1BJ, United Kingdom

G. J. Heald
QinetiQ, Sound Concepts Department, Winfrith Technology Centre, Building A22, Winfrith Newburgh, Dorchester, Dorset DT2 8XJ, United Kingdom

H. A. Dumbrell
QinetiQ, Offshore and Acoustics Department, Newton Road, Bincleaves, Weymouth, Dorset DT4 8UR, United Kingdom

K. R. Holland
Institute of Sound and Vibration Research, University of Southampton, Highfield, Southampton SO17 1BJ, United Kingdom

(Received 27 July 1998; revised 23 January 2002; accepted 26 June 2002)

The measurement of an acoustic emission, or scatter, from a bubble is not difficult. However, an accurate interpretation of that signal in terms of the bubble dynamics may require careful consideration. The study presented here is at first sight relatively simple: comparison of the predicted and measured quality factors of injected bubbles. While the measurement is normally done by monitoring the decay of passive emissions from a bubble, this technique becomes difficult with smaller bubbles. Therefore an active technique is introduced, which removes all the frequency-dependent effects on the measurement (such as transducer response) bar one. That, critically, is the effect of the change in the bubble resonance (frequency and damping) which results from the loading on the bubble due to the reverberant field. The vast majority of theoretical treatments of bubble acoustics assume free field conditions, yet the environmental conditions rarely if ever match these. Therefore measurements of bubble damping are compared both with the established free field theory, and with a new theory relevant to the prevailing reverberant conditions (whether caused by tank surfaces, monochromatic neighboring bubbles, or both). [DOI: 10.1121/1.1501895]

PACS numbers: 43.30.Jx, 43.30.Ft [DLB]

I. INTRODUCTION

It is usually supposed that one of the simplest experiments in bubble acoustics is the estimation of the equilibrium radius of the bubble (R) and its quality factor (Q) from the exponentially decaying sinusoidal pressure trace obtained when an air bubble is injected into water. The use of formulations resembling those of Minnaert[1] or Devin[2] is almost taken for granted in many tests. For example, to the authors' knowledge, all sparging studies on the use of passive acoustic emissions to characterize the bubble population cite Minnaert's equation at the outset[3–8] (with the exception of those which eschew equations[9,10]). Sparging experiments (and indeed almost all such tank tests involving the low kilohertz regime) include reverberation, yet like the vast majority of papers on bubble acoustics the assumption of free-field conditions, implicit in the underlying formulations, is not questioned. This is true throughout the topic, extending to the application of nonlinear equations of motion describing high amplitude bubble oscillation.

For the particular and common task of inferring bubble size from its resonance or natural frequency, the authors[11] previously showed that the presence of a reverberant field could lead to significant errors if free-field formulations, such as that of Minnaert, were used. In the present paper, the rather more difficult problem of calculating the effect of reverberation on bubble damping is attempted. The importance of this work can be judged by considering the following: There are few end-point equations in bubble acoustics that do not incorporate the resonance frequency and damping; and there are few measurements taken in the strictly free-field conditions upon which the common methods of calculating the resonance characteristics are based. Reverberation can arise from the free surface, or from neighboring bubbles, and even from ''anechoically lined'' container walls since these have limitations with respect to absorption and frequency range.

The simplest way of describing bubble damping is through use of a dimensionless damping coefficient,[2,12–15] δ_{tot} (otherwise known as a loss factor). This parameter equals the sum of three dimensionless damping coefficients, corresponding to viscous losses (δ_{vis}), thermal losses (δ_{th}), and the acoustic radiation from the bubble itself (δ_{rad}). For linear systems at resonance, δ_{tot} represents the reciprocal of the quality factor, Q. Despite the fact that the damping coefficient is very widely used, it is not always appreciated that the standard formulations[2,14,15] are valid for monochromatic

[a]Electronic mail: tgl@soton.ac.uk

 0001-4966/2002/112(4)/1366/11/$19.00

bubble pulsations only (which means the steady state linear response to a single-frequency excitation) in the free field. Even the more sophisticated studies[16–21] available, which would for example allow the calculation of damping during the interval prior to steady state, still maintain an assumption of free-field conditions.

Section II describes the general theory. This is followed by an image interpretation. The technique for measuring in isolation the effect of reverberation on bubble damping is then described.

II. METHOD

Section II A gives the general theory for the effect of reverberation on the fluid loading impedance on a small bubble in a test tank of rectangular cross section. Section II B describes the implications of this theory with respect to the effect of reverberation on the bubble resonance frequency and radiation damping. Section II C describes an image technique for calculating the effect which the tank surfaces and any neighboring bubbles have on the resonance of each bubble in a population in monochromatic conditions. Section II D describes a new experimental method for taking measurements in a reverberant tank, which eliminates all the effects of reverberation except for the loading on the bubble wall, making it possible to study this effect in isolation.

A. Theory for the radiation loading on a small bubble in a tank

The impedance presented to a spherically pulsating bubble, radius R, is estimated from the average pressure on a sphere of radius R that surrounds a point monopole having the same volume velocity as the bubble. Consider a liquid-filled rectangular tank that has rigid walls except for the upper surface, which is assumed to be pressure-release. The complex eigenvalues of the tank are denoted by K_N^2. These are the forced-mode eigenvalues, and depend in principle on the forcing frequency. However since this paper is concerned only with modes which exhibit low damping and resonant behavior, the exact frequency dependence of K_N^2 is not critical provided its value can be modeled close to resonance. Let $k_0=\omega/c$ be the acoustic wave number corresponding to acoustic phase speed c and angular frequency ω, and η_N be the loss factor for mode N (defined as the ratio of the imaginary and real parts of K_N^2, at resonance). Then (assuming an implicit time factor of $e^{j\omega t}$)

$$K_N^2=k_N^2+jk_0k_N\eta_N \quad (k_N \text{ real};\ N=1,2,3,\ldots). \tag{1}$$

The analysis that follows allows ck_N to be interpreted as the mode resonance frequency, provided $\eta_N \ll 1$. The first stage of the analysis requires derivation of the acoustic impedance presented to a pulsating spherical surface in this environment [Eq. (6)]. This equation is derived in greater detail by Morse and Ingard[22] [their Eq. (9.4.6)], but an outline derivation is given here to assist understanding of the terms in Eq. (6).

The pressure at point $\boldsymbol{x}$ in the tank, due to a point volume velocity source at point $\boldsymbol{x}_0$, is given[22] by

$$p(\mathbf{x})=\frac{j\omega\rho U}{V}\sum_{N=1}^{\infty}\frac{\psi_N(\mathbf{x})\psi_N(\mathbf{x}_0)}{\Lambda_N(K_N^2-k_0^2)}. \tag{2}$$

Here U is the source volume velocity; the mode shape functions, $\psi_N(\mathbf{x})$, are evaluated at the positions of the receiver $(\mathbf{x})$ and the source $(\mathbf{x}_0)$; and Λ_N is a normalization constant defined by

$$\int \psi_N^2(\mathbf{x})dV=\Lambda_N V, \tag{3}$$

where V is the volume of the tank. The average pressure on a small spherical surface of radius R, centered on the source, can be evaluated explicitly in the low-frequency limit ($k_0R\to 0$) using the expression for $p(\mathbf{x})$ in Eq. (2). The result is[22]

$$\langle p(R)\rangle \approx \frac{j\omega\rho}{4\pi R}U \quad \left(k_0R\to 0;\quad R\ll\frac{k_0^2V}{4\pi}\right); \tag{4}$$

provided that the mode with $k_N=0$ (for a hard-walled cavity) is not included.[23]

Equation (4) is the free-field result, as expected. It follows that if $k_0R\ll 1$ (but has a finite value), and if the tank is sufficiently large for Eq. (4) to be valid (i.e., $k_0^2V\gg 4\pi R$), then an improved approximation is

$$\begin{aligned}\langle p(R)\rangle &\approx \frac{j\omega\rho}{4\pi R}U+\langle p(R)\rangle|_{k_0R}-\langle p(R)\rangle|_0\\ &=j\omega\rho U\left(\frac{1}{4\pi R}+\frac{1}{V}\sum_{N=1}^{\infty}\frac{1}{\Lambda_N}\psi_N^2(\mathbf{x}_0)\right.\\ &\quad\left.\times\left(\frac{1}{K_N^2-k_0^2}-\frac{1}{K_N^2}\right)\right),\end{aligned} \tag{5}$$

where vector $\mathbf{x}_0$ is the position of the center of the sphere, and the difference between ψ_N at the center and ψ_N on the surface has been neglected.[24] The fluid loading impedance on a small bubble in a tank can now be estimated by dividing both sides of Eq. (5) by U and simplifying:

$$Z_s=\frac{\langle p(R)\rangle}{U}\approx j\omega\rho\left(\frac{1}{4\pi R}+\frac{k_0^2}{V}\sum_{N=1}^{\infty}\frac{\psi_N^2(\mathbf{x}_0)}{\Lambda_N K_N^2(K_N^2-k_0^2)}\right)$$
$$(k_0R\ll 1). \tag{6}$$

This expression is the Morse and Ingard result [Eq. (9.4.6)] for the acoustic impedance presented to a pulsating spherical surface of radius R, which represents a single bubble in the tank.

The first term in the brackets on the right-hand side of Eq. (6) is purely reactive; it dominates in the limit $k_0R\to 0$. However, it simply represents the free-field inertial fluid loading on the bubble. What is more interesting is the deviation from the free-field impedance, as given by the modal summation terms. In particular, the bubble radiation damping comes entirely from the modal summation terms (note that no local viscous or thermal damping has been included at this stage). At low frequencies, the resistance $Z_s^R=\mathrm{Re}(Z_s)$ consists of a sequence of resonant modal peaks. At suffi-

ciently high frequencies the overlap of many modal peaks will produce a smooth curve, corresponding to

$$Z_s^R \approx \frac{\rho c k_0^2}{4\pi}, \tag{7}$$

which is equivalent to the free-field radiation resistance. This last result is derived in the analysis that follows [see Eq. (30)].

The modal loss factors and resonance frequencies can be found experimentally from transmission measurements in the tank. Note from Eq. (2) that, in the neighborhood of a resonance, the pressure at $\mathbf{x}$ due to a point source at $\mathbf{x}_0$ will vary as

$$p(\mathbf{x}) \propto \frac{1}{K_N^2 - k_0^2} = \frac{1}{(k_N^2 - k_0^2) + j\,\eta_N k_N k_0} = \frac{1}{D}, \tag{8}$$

where the denominator D describes the resonance.

At the modal peak, $k_N = k_0$. Therefore at the half-power points on the resonance curve,

$$|k_N^2 - k_0^2| = \eta_N k_N k_0, \tag{9}$$

i.e.,

$$|k_N - k_0| \approx \tfrac{1}{2}\eta_N k_N \quad (\eta_N \ll 1). \tag{10}$$

It follows that the quality factor for the Nth mode of the tank is equal to η_N^{-1}. Once this is known, the real and imaginary parts of Z_s can be found explicitly from Eq. (6). Provided the loss factors η_N are small, and omitting terms in η_N^2 (except where they occur in $|D|^2$, in the following) the resistance can be approximated by

$$Z_s^R \approx \frac{\rho c}{k_0 V} \sum_{N=1}^{\infty} S_N, \tag{11}$$

where

$$S_N = \frac{\psi_N^2(\mathbf{x}_0)}{\Lambda_N} \frac{(2-\nu_N^2)\,\eta_N \nu_N^5}{|D|^2}. \tag{12}$$

Here $|D|^2 = (1-\nu_N^2)^2 + (\eta_N \nu_N)^2$ and $\nu_N = k_0/k_N$ is the ratio of the driving frequency to the resonance frequency of mode N. In a similar way the reactance can be approximated by

$$Z_s^I = \mathrm{Im}(Z_s) \approx \frac{\omega \rho}{4\pi R} + \frac{\rho c}{k_0 V} \sum_{N=1}^{\infty} T_N, \tag{13}$$

where

$$T_N = \frac{\psi_N^2(\mathbf{x}_0)}{\Lambda_N} \frac{(1-\nu_N^2)\,\nu_N^4}{|D|^2}. \tag{14}$$

Note that the modal summation terms S_N in the resistance, Eq. (12), exhibit resonance, while the T_N terms in the reactance vanish at resonance [i.e., when $\nu_N = 1$; Eq. (14)].

For modes of very high order, i.e., $k_N \to \infty$ or $\nu_N \to 0$, the summation terms S_N of Eq. (11) behave like

$$S_N \sim \nu_N^5 \tag{15}$$

and the summation terms T_N of Eq. (13) behave like

$$T_N \sim \nu_N^4. \tag{16}$$

There should therefore be no problem over convergence. We can check this by using the asymptotic relations

$$N \sim k_N^3 - \nu_N^{-3}, \quad \frac{dN}{d\nu_N} = n(\nu_N) \sim \nu_N^{-4}. \tag{17}$$

The product of the modal density $n(\nu_N)$ with S_N or T_N remains finite, in the limit $\nu_N \to 0$.

Note that the sums in Eqs. (11) and (13) extend from $N=1$ to $N=\infty$ over integer N. They may be estimated beyond some lower limit N_0 by replacing the sum over N with an integral over ν that involves the modal density $n(\nu)$:

$$\sum_{N=N_0}^{\infty} S_N \simeq \int_{\nu_0}^{0} S(\nu) n(\nu)\, d\nu, \tag{18}$$

and similarly for $\Sigma_{N=N_0}^{\infty} T_N$. The lower limit ν_0 is given by

$$\nu_0 = k_0 L_0, \tag{19}$$

where L_0 is the length that characterizes the tank dimensions. Thus ν_0 is a dimensionless frequency above which the modes of the tank are sufficiently close-spaced to be regarded as a continuum for the purposes of Eqs. (11) and (13). The upper limits of the integrals are zero, corresponding to $k_N \to \infty$.

Note that the modal density $n(\nu)$ follows from the asymptotic mode count $N(k)$:

$$N(k) \simeq \frac{k^3 V}{6\pi^2}, \tag{20}$$

where V is the tank volume. Thus

$$N(k_N) = \frac{k_N^3 V}{6\pi^2} = \left(\frac{k_0}{\nu_N}\right)^3 \frac{V}{6\pi^2}, \tag{21}$$

and

$$\frac{dN}{d\nu} = -\frac{k_0^3 V}{2\pi^2} \nu^{-4} = n(\nu), \tag{22}$$

by definition. In Eq. (22) ν is regarded as a continuous variable. Replacement of the summation step ($\Delta N = 1$) in Eqs. (11) and (13) by an integration increment, $dN = n(\nu)\,d\nu$, leads to Eq. (18).

The final expression for Z_s, based on summation of Eqs. (11) and (13) up to mode N_0, followed by the integral approximation of Eq. (14) for $N > N_0$, is as follows. The real component of Z_s is

$$Z_s^R = \frac{\rho c}{k_0 V}\left(\sum_{N=1}^{N_0} S_N + \frac{k_0^3 V}{2\pi^2} \int_0^{\nu_0} \frac{(2-\nu^2)\,\eta\nu}{(1-\nu^2)^2 + \eta^2\nu^2}\, d\nu \right), \tag{23}$$

and the imaginary component is

$$Z_s^I = \frac{\omega\rho}{4\pi R} + \frac{\rho c}{k_0 V}\left(\sum_{N=1}^{N_0} T_N + \frac{k_0^3 V}{2\pi^2}\int_0^{\nu_0} \frac{(1-\nu^2)}{(1-\nu^2)^2+\eta^2\nu^2}\, d\nu \right). \quad (24)$$

To obtain Eqs. (23) and (24), Eq. (22) for $n(\nu)$ has been substituted into Eq. (18). The expressions for $S(\nu)$ and $T(\nu)$, Eqs. (12) and (14), have been approximated by replacing $\psi_N^2(\mathbf{x}_0)/\Lambda_N$ with its average value of unity.

Equations (23) and (24) are the main results of the theoretical analysis of this section. Two limiting cases can usefully be distinguished, corresponding to low and high frequencies. In the low frequency limit, defined by

$$k_0 L_0 = \nu_0 \ll 1, \quad (25)$$

the contribution of the integral terms is small compared with that of the summation terms. Note that the integrals in this case do not pass through any resonances.

In the high frequency limit, defined by

$$k_0 L_0 = \nu_0 \gg 1, \quad (26)$$

the contribution of the integral terms is dominant. Provided the overlap of individual-mode responses is sufficient to justify the continuous-distribution model, particularly in the region close to resonance ($\nu \approx 1$) where the integrands are largest, we can estimate the resistance and reactance as follows:

$$Z_s^R \simeq \frac{\rho c k_0^2}{2\pi^2} I_{\text{res}} \frac{\pi}{2}\, \eta_{\text{res}}, \quad (27)$$

$$Z_s^I \simeq \frac{\omega\rho}{4\pi R}. \quad (28)$$

Note that the integral contribution in Eq. (24) tends to cancel either side of $\nu \approx 1$, which is why Eq. (28) gives just the free field value. In Eq. (27), I_{res} represents the value of the integrand in Eq. (23) at the resonant peak, i.e.,

$$I_{\text{res}} = \frac{1}{\eta_{\text{res}}} \quad (\nu = 1). \quad (29)$$

Thus

$$Z_s^R(\text{high frequency}) \simeq \frac{\rho c k_0^2}{4\pi}, \quad (30)$$

which is the free field value (as expected).

B. Practical implications

The practical implications of the radiation loading result of Eqs. (11) and (13) are interesting, in terms of estimating the bubble radius and damping from the measured acoustic emissions of a single bubble. We define Z_b as the acoustic impedance of the bubble,[25] that is, the ratio of the pressure change Δp to the inwards volume velocity at the bubble wall. If Z_a is the external acoustic impedance due to fluid loading on the bubble, then resonance occurs when

$$Z_a + Z_b = 0. \quad (31)$$

Equation (31) can be used to determine the relationship between the pulsation resonance frequency and the equilibrium bubble radius. For example, since the apparent bulk modulus of the gas within the bubble (of volume V_b) when subject to a pressure change Δp is $B = -V_b \Delta p/\Delta V_b$, then assuming single-frequency simple harmonic motion at circular frequency ω, the acoustic impedance of the bubble at low frequencies ($k_0 R \ll 1$) is

$$Z_b \approx \frac{\Delta p}{-U} = \frac{\Delta p}{-j\omega \Delta V_b} = \frac{B}{j\omega V_b}. \quad (32)$$

If the gas within the spherical bubble is assumed to behave polytropically (i.e., $pV^\kappa = \text{constant}$), then $B = \kappa p_0$, where p_0 is the ambient static pressure on the bubble and κ is the polytropic index. The bubble at resonance ($\omega = \omega_0$) is described by Eq. (31) (where in the reverberant conditions of the tank, Z_a is described by Z_s from Sec. II A). If damping is small and hence the resistive terms are neglected, then Z_a and Z_b are almost entirely reactive, ω_0 is real, and Eq. (13) gives

$$\frac{j\kappa p_0}{\omega_0 V_b} \approx j\omega_0 \rho \left(\frac{1}{4\pi R} + \frac{1}{k_0^2 V} \sum_{N=1}^{\infty} T_N \right) \quad (k_0 R \ll 1), \quad (33)$$

where T_N is defined in Eq. (14). The summation term in Eq. (33) represents a reverberant-field correction to the free-field radiation reactance. Neglecting the correction leads to the free-field expression for the resonance frequency of the bubble:[1]

$$\omega_0 \simeq \sqrt{\frac{4\pi R \kappa p_0}{\rho V_b}} = \frac{1}{R}\sqrt{\frac{3\kappa p_0}{\rho}} = \omega_{0f}. \quad (34)$$

An improved approximation is found by evaluating the reverberant correction term at the Minnaert frequency ω_{0f}. The corrected resonance frequency for bubble pulsation in a tank follows from Eq. (34), with the substitution

$$\frac{1}{R} \to \frac{1}{R} + \frac{4\pi c^2}{\omega_{0f}^2 V} \sum_{N=1}^{\infty} T_{Nf} = \frac{1}{R} + \frac{4\pi\rho c^2}{3\kappa p_0 V} R^2 \sum_{N=1}^{\infty} T_{Nf}. \quad (35)$$

Here T_{Nf} denotes T_N of Eq. (14) evaluated at $\omega_0 = \omega_{0f}$. The presence of the summation in Eq. (35) can be seen as a correction which modifies the "free-field" resonance frequency for bubble pulsation. A similar correction factor was used by Leighton *et al.*[11] to modify free-field theory, and thus to estimate the bubble size from the resonance frequency measured in reverberant conditions in a pipe.

However there is a critical difference when calculating how the presence of reverberation changes the bubble damping. As can be seen from Eq. (11) there is no equivalent free-field term: the radiation damping result is entirely made up of the summation terms, and hence the modal structure of the field has to be very well characterized to evaluate this. This can be attempted by measuring the character of the sound field (removing, of course, transducer response, etc., see Sec. II C) and identifying the component modes through

use of Eq. (5). The data can then be converted into effective measurements of the radiation resistance. An alternative but equivalent approach to estimating the reverberation effect is described in Sec. II C. Here an image model is used to calculate the effect of tank surfaces on the radiation impedance of a single oscillating bubble. The technique can also be used to characterize the resonance of each bubble in a *population* driven to steady state by some external source: the effect on each bubble of both the tank's surfaces and of the neighboring bubbles can be incorporated.

C. Method of images

The effect of neighboring reflective boundaries on the radiation impedance of a bubble can be modeled using the method of images. For the specific case of the tank of rectangular cross-section discussed in Sec. II A, the location of the images is calculated from the position of the bubble relative to each wall, the result being an infinite number of images arranged in a grid-like pattern. If the complex pressure reflection coefficient of the various tank walls were of unit magnitude for the frequencies emitted by the bubble, then a continuously emitting bubble would of course generate reverberant acoustic intensities at the bubble surface which would grow with time. This produces a coherent radiation version of Olbers' paradox,[26] by which Halley, Cheseaux, and Olbers realized that, if the number density of stars were constant and the absorption of light in interstellar space were negligible, then unless the universe were finite, the night sky would generate at the observer an intensity equal to the average surface intensity of the stars.

The pressure field radiated by the bubble p consists of a direct field p_d and a reverberant one p_ν:

$$p = p_d + p_\nu, \tag{36}$$

where in the condition $k_0 R \ll 1$ the reverberant field is virtually constant over the bubble surface and very similar to that produced at the bubble center location by a point source having the same volume velocity as the bubble. The total acoustic impedance presented to the bubble, Z_a, is

$$Z_a = \frac{p}{U} = \frac{p_d}{U} + \frac{p_\nu}{U}, \tag{37}$$

where p_d is the direct field on the bubble surface:

$$p_d = \frac{j\rho\omega}{4\pi R} + \frac{\rho\omega^2}{4\pi c} \quad (k_0 R \ll 1) \tag{38}$$

(suppressing the harmonic time dependence throughout). Consider two bubbles emitting monochromatic monopole ($kR \ll 1$) radiation, the first having volume velocity U and the second having source strength FU. The pressure at bubble 1 as a result of the radiation from bubble 2 is

$$p_{12} = j\omega\rho F U\left(\frac{e^{-jkr}}{4\pi r}\right), \tag{39}$$

where the bubble separation r introduces both a phase factor and an attenuation. The impedance of Eq. (38) resulting from a population of monochromatic bubbles is therefore

$$\begin{aligned} Z_a &= \frac{j\rho\omega}{4\pi R} + \frac{\rho\omega^2}{4\pi c} + \frac{j\rho\omega}{4\pi}\sum_{m=2}^{m_{\max}} \frac{F_m}{r_m} e^{-jkr_m} \\ &= \frac{j\rho\omega}{4\pi R} + \frac{\rho\omega^2}{4\pi c} + \frac{\rho\omega}{4\pi}\sum_{m=2}^{m_{\max}} \frac{|F_m|}{r_m}(\sin(kr_m - \vartheta_m) \\ &\quad + j\,\cos(kr_m - \vartheta_m)), \end{aligned} \tag{40}$$

where the subscript $m = 2,3,\ldots,m_{\max}$ indicates all bubbles other than bubble 1. These entities may be real bubbles driven linearly at steady state by an external monochromatic source. Equation (40) might also describe the impedance of a single bubble in a tank (where the bubbles $m = 2,3,\ldots,\infty$ are images); or indeed be used to calculate the resonance characteristics of each bubble in a monochromatic population within a tank (in which case the population comprises both real and image bubbles). To compare with the calculation of Sec. II A and II B, a single bubble in a rectangular tank would have images characterized by a range term r_m (equal to twice the shortest distance between the real bubble and the wall); and a complex amplitude term $F_m = |F_m| e^{-j(k_m r_m - \vartheta_m)}$ which would depend on the complex reflection coefficient of the boundary in question. Then if the small-damping polytropic conditions of Sec. II B apply, the resonance condition occurs when

$$\begin{aligned} \frac{j\kappa p_0}{\omega_0 V} &\approx \frac{j\rho\omega}{4\pi R} + \frac{\rho\omega^2}{4\pi c} + \frac{\rho\omega}{4\pi}\sum_{m=2}^{\infty} \frac{|F_m|}{r_m}(\sin(kr_m - \vartheta_m) \\ &\quad + j\,\cos(kr_m - \vartheta_m)). \end{aligned} \tag{41}$$

Equating the imaginary parts gives the resonance frequency

$$\omega_0 \approx \frac{(1/R)\sqrt{3\kappa p_0/\rho}}{\sqrt{1 + \Sigma_{m=2}^{\infty}(R/r_m)|F_m|\cos(kr_m - \vartheta_m)}}, \tag{42}$$

which reduces to the Minnaert equation [Eq. (34)] when, in the free field, the summation term is zero.

The effect of neighboring bubbles and boundaries on radiation damping can also be calculated by this method. Assume that the radiation damping in free space is to be characterized by the dimensionless damping coefficient, $\delta_{\text{rad,free}}$, which is proportional to the real part of the total acoustic impedance presented to the bubble in free space, $\rho\omega^2/4\pi c = \rho\omega k/4\pi$. The ratio of the damping in reverberant conditions, $\delta_{\text{rad,reverb}}$, to that in free space, equals the ratio of the real parts of the respective total acoustic impedances presented to the bubble. Taking again the case of Sec. II A (a single bubble emitting into a rectangular tank) the ratio of the real component of Eq. (41) to the free-space value is

$$\frac{\delta_{\text{rad,reverb}}}{\delta_{\text{rad,free}}} = 1 + \sum_{m=2}^{\infty} \frac{|F_m|\sin(kr_m - \vartheta_m)}{kr_m}. \tag{43}$$

For solution of the tank case described in Sec. II A and Eqs. (42) and (43), the spatial distribution of the images is calculated geometrically, and the frequency-dependent complex reflection coefficient associated with each image is simply calculated from the number of reflections from the tank boundaries. The predicted quality factor for a bubble in reverberant conditions is then

$$Q = 1/\delta_{\text{tot}} = 1/(\delta_{\text{rad,reverb}} + \delta_{\text{th}} + \delta_{\text{vis}}), \tag{44}$$

where δ_{th} and δ_{vis} are found from the usual monochromatic formulations,[2] and where $\delta_{\text{rad,reverb}}$ is calculated by substituting into Eq. (43) the monochromatic value of $\delta_{\text{rad,free}}$, again calculated from literature.[2]

With reference to the comments at the start of this section, it should be noted that Eqs. (42) and (43) assume that the emission from the images is steady. If for example the source bubble emits an exponentially decaying sinusoid typical of injection, then the nonsteady nature of the returns introduces an error of order δ_{tot}^2.

D. Experimental measurements

The method used in this paper for measuring the bubble resonance and damping relies upon estimation of the impulse response of bubbles injected one at a time into a tank measuring 0.6 m×0.2 m×0.23 m deep internally, and having glass walls of 6 mm thickness. For the ''passive'' technique, this consisted of simply measuring the hydrophone signal detected following injection of the bubble through a needle. For the ''active'' technique, the hydrophone signal of interest is not that emitted by the bubble on injection. Rather, it is the signal scattered by the bubble some time later, when it is driven by band filtered white noise (1–25 kHz, generated using a Bruel and Kjaer Type 2032 dual channel signal analyzer). The bubbles examined in this paper have natural frequencies in the range 4–11 kHz. The bubble rises after injection, and is driven into oscillation by the pseudorandom driving field. Its buoyant passage through a 1 MHz beam triggers the data acquisition from the hydrophone. It is important to know the location of the bubble and hydrophone for comparison with theory. The active technique is particularly useful in measuring the resonance characteristics of the smaller bubbles, whose natural emissions after injection are of insufficient amplitude above the noise to obtain sufficient cycles for a precise measurement of their decay. The following describes how the scattered signal is estimated when the active technique is used.

The received signal at the measurement hydrophone, $y(t)$, in the active configuration, can be considered as the superposition of two components, i.e.,

$$y(t) = y_d(t) + y_s(t), \tag{45}$$

where $y_d(t)$ is the signal due to the direct field (i.e., the signal that is observed in the absence of a bubble), and $y_s(t)$ is the signal arising from the acoustic field generated by scattering from the bubble. In practice the magnitude of the direct field component is sufficient to corrupt measurements of quantities, such as quality factors, based on the raw data $y(t)$. If no bubble is present, then evidently the measured signal is solely due to the direct field component, $y_d(t)$.

Figure 1(a) illustrates a typical example of the spectrum of a signal received at a hydrophone when an active configuration is employed with a bubble being present. The spectrum of the electronic signal used to drive the projector (band limited Gaussian noise) is also shown. The resulting hydrophone signal contains contributions from the direct field and the scattered signal. The ''N''-shaped feature at approximately 3 kHz is a result of bubble scattering.[27] The problems of exploiting this data are evident. The comparatively low level of the scattered signal relative to the direct field render the feature difficult to discern even in this relatively small frequency range (its peak is of a similar magnitude to the nonbubble feature at around 6 kHz); and estimation of the bubble quality factor from such a feature is prone to error (see the following). Our methodology aims to reduce the direct field contribution and allow accurate measurements to be made.

To estimate the scattered field we first make measurements in the *absence* of a bubble. A known band limited white noise signal, $x(t)$, is used as an input to the projector and the resulting hydrophone signal is measured. Using standard linear systems theory[28] we can construct an estimate of the system impulse response, $h_d(t)$, from these two measurements. Assuming that the modeling is successful then

$$y_d(t) = h(t) * x(t), \tag{46}$$

where an asterisk is used to denote linear convolution. The accuracy of the model can be assessed as a function of frequency by computing and examining the coherence function.[28]

A bubble is then introduced to the system. Once again a band limited white noise signal, $x(t)$, is used to drive the projector. From the driving signal an estimate of the direct field component of the hydrophone signal is constructed by convolving it with the estimated impulse response, $h(t)$, leading to an estimate of the scattered signal:

$$\hat{y}_s(t) = y(t) - h(t) * x(t). \tag{47}$$

Here $\hat{y}_s(t)$ is an estimate of the contribution of the bubble to the acoustic field. The results of applying this procedure to the data in Fig. 1(a) are shown in Fig. 1(b). The spectrum of the signal after the effect of the direct field has been subtracted shows a distinct peak close to 3 kHz, for which the ratio of center frequency to the bandwidth gives the bubble quality factor. Figure 1(b) illustrates the error that would have been introduced if one had erroneously assumed that Q could be obtained from the equivalent parameters associated with the 3 kHz peak in Fig. 1(a).

This model takes account of any shaping of the excitation spectrum that may occur as a result of a modal field within the tank. This having been removed, what remains is the effect of reverberant loading on the bubble resonance and damping.

III. RESULTS

Figure 2 shows the quality factor of the bubble as a function of its natural (for the ''passive'' measurements: ■,●) or resonance (for the ''active'' measurements: □,○,×) frequency. Results from tap, distilled, and newly acquired seawater are shown. The solid curve indicates the quality factor predicted by Devin's theory, which relates to free field conditions. The dashed line indicates the result predicted by Eq. (43), with the dotted lines on either side indicating the maximum and minimum values found by recalculating the prediction repeatedly, allowing the bubble position and the wall reflection coefficient to vary within the limits of uncer-

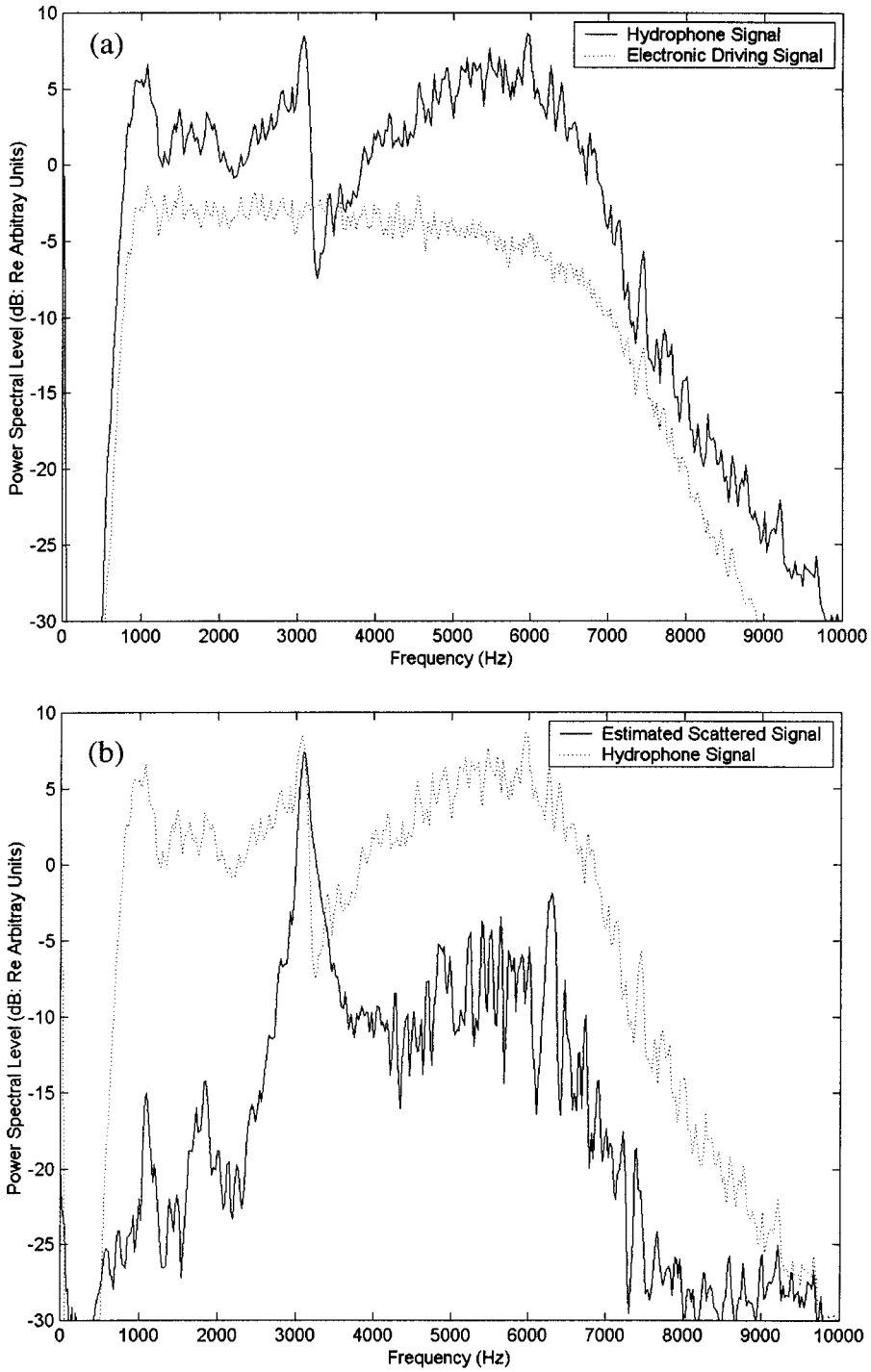

FIG. 1. (a) Spectra of driving signal and hydrophone signal. The driving signal in this example case consists of Gaussian noise, band limited to a frequency range of approximately 1–7 kHz (though 1–25 kHz was required for the data of Fig. 2). (b) Spectra of the hydrophone signal before and after the effect of the direct field has been removed.

tainty of each (the latter having a much smaller contribution that the former, the prediction being fairly robust within the allowed variation of reflection coefficient). For clarity, error bars are not shown (± 75 Hz; ± 1 in Q for $f<6$ kHz; ± 2 in Q for $6<f<9$ kHz; ± 4 in Q for $f>9$ kHz). The lack of passive data above 6 kHz reflects the signal-to-noise problem, described in Sec. II C, which makes the technique difficult for the smaller bubbles. The active technique is not limited in this way.

The discrepancy between observation and the prediction of Devin is less than the error associated with the observation for 26 of the 96 data points. There being negligible uncertainty on this scale in the uncertainty associated with the Devin curve, the conclusion is that Devin's theory is inappropriate for the reverberant conditions found in this typical test tank, in the frequency range most often studied in bubble acoustics. In contrast 76 of the 96 bubbles lie within one error of the theory presented in this paper. This comparison needs interpreting with some caution, as discussed in the following.

IV. DISCUSSION

Although the disagreement between measurement and Devin's theory indicates the need for a theory applicable to reverberant conditions, and while the authors have faith in

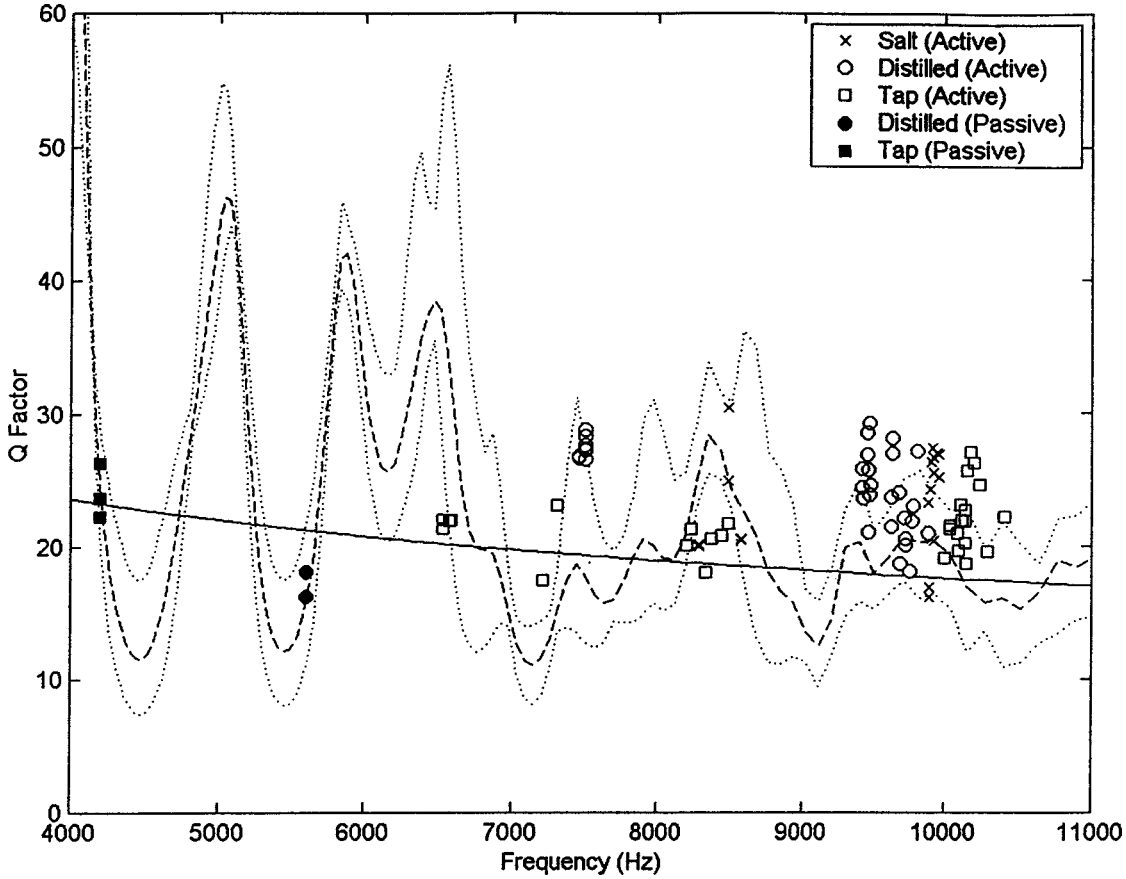

FIG. 2. Graph of the quality factor of the bubble as a function of its natural (for the "passive" measurements, ■, ●) or resonance (for the "active" measurements, □ ○ ×) frequency. Results from tap (■, □), distilled (●, ○) and newly-acquired seawater (×) are shown. For clarity, error bars are not shown (±75 Hz; ±1 in Q for $f<6$ kHz; ±2 in Q for $6<f<9$ kHz; ±4 in Q for $f>9$ kHz). The curves indicate predictions of the theory of Devin (—) and of this paper (---), either side of which is a dotted line indicating the limits of uncertainty in the latter.

the theories of Sec. II, implementation of that theory to calculate the modification to bubble resonance imparted by reverberant loading is not easy. Whereas calculation of the effect on resonance frequency[11] is possible by using Eq. (37), the effect on the damping is very sensitive to details of the reverberation. The resulting uncertainty allows a range of predicted values for Q at each frequency in Fig. 2, while the standard free-field theory predicts a single value. The sensitivity of the prediction to the reverberation parameters is of course greatest at the peaks and troughs in the plots, and hence the extreme predictions of $Q>40$ should be interpreted with caution. For the most part the reverberant theory suggests for this tank there will be deviations from free-field predictions of usually up to $Q\sim 60\%$, and these are observed. In addition the predicted sign of the deviation (which can be positive or negative depending on the frequency) is borne out in the data.

While the magnitude of the discrepancy is difficult to calculate precisely, the form for the quality factor of bubbles in this reverberant environment that is predicted by the method of images technique described in Sec. II C, agrees with the trends expected from the general theory of Sec. II A. Equation (7) predicts that at sufficiently high frequencies, the damping will tend to a smooth function following the "free-field" solution. This is a result of modal overlap. The prediction in Fig. 2 bears this out, although in the range considered the influence of distinct modes is evident. At the lower frequencies the calculation becomes difficult because of convergence problems [note that $|D|^2=(1-\nu_N^2)^2+(\eta_N\nu_N)^2$ in Eqs. (11) and (12) becomes very large when $k_0\rightarrow k_N$, then $\nu_N\rightarrow 1$]. Paradoxically this means that the effect of reverberation can be easier to calculate in small tanks than in larger ones. This is because the bubbles most often considered in test tanks have natural frequencies of the low kilohertz order (see the following). Therefore unless the tank is sufficiently vast and sufficiently damped that this range is higher than the Schroeder frequency, then to ignore reverberation the bubble natural frequency must be significantly less than that of the first tank mode[11] (depending on the losses, which are generally lowest for these low frequencies). In tanks of several meters on a side this in practice would likely occur only for bubbles resonant at O (10 Hz). Such bubbles would generally be much larger than those typically studied in a test tank. It is well-known that if the intention is to inject single bubbles into a tank for controlled tests, there is a range of bubble size outside of which this process becomes difficult. Bubbles of centimeter-size break up, and bubbles of less than around 200 μm tend to coalesce into larger bubbles at the nozzle.[29] Even exotic methods (e.g., manipulation of the surface tension or pressure head, vibration of the needle, etc.) can only expand this range to a

limited degree. Of course smaller bubbles can be produced by sparging, wave breaking,[30] etc., but these bubbles almost always comprise a subset of a population which includes larger bubbles giving significant natural emissions at roughly 1–10 kHz.

As this paper has shown, this may well be a problematic range: the frequencies may be insufficiently high to generate, via model overlap, the effectively ''free-field'' solution of Eq. (7); yet they may be so low that anechoic linings are insufficient to remove reverberation. For example, even with the free surface replaced by lining, the ''anechoically'' lined tank of Bjørnø and Kjeldgaard had a pressure amplitude reflection coefficient of ~0.3 at 10 kHz, the lowest frequency they measured. The actual performance of linings at the frequencies of interest is not always reported in bubble tests.

As an illustration of the problem, a preliminary attempt was made to use the results of Fig. 2 to confirm or counter the suggestion[31,32] that bubble damping may depend on salinity. That suggestion followed from a study of the injection of single bubbles into a tank having ''acoustically transparent'' walls. This smaller tank was suspended in a larger $2.5 \times 3.6 \times 3.6$ m^3 water tank, where ''the bottom and walls of the [larger] tank were lined with 82-cm high redwood wedges with 30 cm×30 cm bases; these wedges have a large acoustic absorption.''[33] Being cognizant that such statements depend on the frequency of interest, an investigation[33] was made to determine which modes could be excited in the largest tank at frequencies of less than 1 kHz, and identified ones at around 540 and 950 Hz.

It is well known that dissolved salt can affect *populations* of bubbles, those formed in salt water tend to be more numerous, particularly regarding the smallest bubbles, and less prone to coalesce than bubbles in fresh water.[34–39] When comparing wave breaking in fresh water with that in salt, it is one thing to attribute acoustic differences to changes in populations of bubbles which, as individuals, have unchanged acoustic properties. That is to say that, even though the collective effect may be affected by differences between the fresh and salt water bubble populations, the single-bubble acoustics is the same (although modifications may be necessary to surface tension and thermal damping terms, etc., as a result of the ''dirty'' nature of sea water[40]). It is quite another to suggest that the single-bubble dynamics might be different, which is one possible interpretation of the findings of the study[31] mentioned previously. In that, measurements were made of the logarithmic decrement of relatively large single bubbles (1.1–2.4 mm radius) injected into water having a salinity range of $0^\circ/_{\circ\circ}$–$35^\circ/_{\circ\circ}$ (obtained using commercial salt[41]). Both the sound pressure level and the quality factor were observed to change with salinity, but no mechanism for such a single-bubble effect has been proposed. If such a single-bubble effect was robust (and not, as speculated in the following, a by-product of the reverberation), it would have major implications throughout ocean bubble acoustics, for example in measurements of the bubble population[42–46] and the response of bubbles to short acoustic pulses.[47–50]

Prior to the current paper, no account has been taken in test tanks of the effect of the reverberant field on the bubble damping. That two distinct modes at 540 and 950 Hz could be identified in the tank used in the earlier study[33] suggests that the data were taken in the frequency range (roughly 1–3 kHz) at which the effect of reverberation is most problematic, as discussed previously. Taking reverberation into account, the results of Fig. 2 are unable to confirm or deny the earlier proposition that salinity affects the damping of single bubbles: the seawater data (×) show a similar measure of agreement with the prediction of reverberant theory that is exhibited by tap and distilled water. Hence the disagreement which is seen in this paper between the seawater data and the prediction of Devin can be attributed to reverberation. That is not to prove that reverberation was responsible for the earlier finding.[31,32] However the potential for reverberation to complicate the observation is clear. As an example, even small changes in frequency/sound speed can tune in or out of the effect of a given mode, leading to significant changes in Q (Fig. 2). While varying the salinity will change the sound speed in a predictable manner[51] in single-bubble tests, when *populations* are entrained there is a second, and often greater effect. If changes in salinity affect the population of bubbles entrained, for example by a breaking wave, then varying the salinity will indirectly affect both the amount of reverberation and (through the effect of the bubble population on the sound speed) change the modal frequencies of the tank. Figure 2 suggests that mode frequency changes of O (1%) can cause changes in Q of O (10%). Therefore it is strongly recommended that reverberation be considered in tank tests, and other reverberant environments.[52]

The importance of reverberation on bubble resonances should not be underestimated, and its effect cannot be easily dismissed. It is not confined only to frequencies of tank modes: apart from the frequency region well below the first mode,[11] or well above the Schroeder frequency, the effect is potentially very problematic for three reasons.

(1) Calculation of its influence on radiation damping in particular (and, to a lesser extent, on the relationship between the bubble radius and natural frequency) requires detailed knowledge of the reverberation.
(2) Small changes in damping can have major effects close to bubble resonance, and discrepancies from the free field predictions of up to ~60% are here observed.
(3) True free-field conditions are rarely found in bubble acoustics, with even the ''open'' ocean containing a free-surface, and scatterers which include other bubbles; and ''anechoic'' fittings can give significant reflections at the resonant frequencies of the larger bubbles.

Finally it should be recalled that the ubiquitous assumption of free-field conditions extends beyond bubble entrainment emissions and linear scattering, to the nonlinear models of bubble motion (such as the Rayleigh–Plesset, Herring–Keller, and Gilmore-Akulichev formulations). Certain scenarios exploit modal fields, such as in measurement of the bubble size distribution.[53–55] Of particular note is the common practice of levitating bubbles in a modal sound field for measurements of, for example, sonoluminescence,[56] rectified diffusion,[57] or (with the comment of this paper particularly in mind) resonance and damping.[58,59] In such circumstances the

effect and validity of the free-field assumption must be assessed.

ACKNOWLEDGMENTS

The authors would like to acknowledge the support of QINETIQ, Bincleaves, UK. T.G.L. is grateful to the Royal Society Leverhulme Trust, and the EPSRC (GR/M38094) for support.

[1] M. Minnaert, "On musical air-bubbles and sounds of running water," Philos. Mag. **16**, 235–248 (1933).
[2] C. Devin, Jr., "Survey of thermal, radiation, and viscous damping of pulsating air bubbles in water," J. Acoust. Soc. Am. **31**, 1654 (1959).
[3] R. His, M. Tay, D. Bukur, and G. Tatterson, "Sound spectra of gas dispersion in an agitated tank," Chem. Eng. J. **31**, 153–161 (1985).
[4] L. S. De More, W. F. Pafford, and G. B. Tatterson, "Cavity sound resonance and mass transfer in aerated agitated tank," AIChE J. **34**, 1922–1926 (1988).
[5] J. W. R. Boyd and J. Varley, "Sound measurement as a means of gas-bubble sizing in aerated agitated tank," AIChE J. **44**, 1731–1739 (1998).
[6] A. B. Pandit, J. Varley, R. B. Thorpe, and J. F. Davidson, "Measurement of bubble size distribution: An acoustic technique," Chem. Eng. Sci. **47**, 1079–1089 (1992).
[7] R. Manasseh, R. F. LaFontaine, J. Davy, I. Shepherd, and Y-G Zhu, "Passive acoustic bubble sizing in sparged systems," Exp. Fluids (in press).
[8] R. Manasseh, A. Bui, J. Sandercock, and A. Ooi, "Sound emission processes on bubble detachment," Proceedings of the 14th Australasian Fluid Mechanics Conference (in press).
[9] T. A. Sutter, G. L. Morrison, and G. B. Tatterson, "Sound spectra in an aerated agitated tank," AIChE J. **33**, 668–671 (1987).
[10] W. R. Usry, G. L. Morrison, and G. B. Tatterson, "On the interrelationship between mass transfer and sound spectra in an aerated agitated tank," Chem. Eng. Sci. **42**, 1856–1859 (1987).
[11] T. G. Leighton, D. G. Ramble, A. D. Phelps, C. L. Morfey, and P. P. Harris, "Acoustic detection of gas bubbles in a pipe," Acta Acust. **84**, 801–814 (1998).
[12] H. Pfriem, "Zur thermischen dämpfung in kugelsymmetrisch schwingenden gasblasen," Akust. Zh. **5**, 202–207 (1940).
[13] Z. Saneyoshi, Electro-technical Journal (Japan) **5**, 49 (1941).
[14] A. I. Eller, "Damping constants of pulsating bubbles," J. Acoust. Soc. Am. **47**, 1469–1470 (1970).
[15] A. Prosperetti, "Thermal effects and damping mechanisms in the forced radial oscillations of gas bubbles in liquids," J. Acoust. Soc. Am. **61**, 17–27 (1977).
[16] R. I. Nigmatulin and N. S. Khabeev, "Heat exchange between a gas bubble and a liquid," Fluid Dyn. **9**, 759–764 (1974).
[17] R. I. Nigmatulin and N. S. Khabeev, "Dynamics of vapour-gas bubbles," Fluid Dyn. **12**, 867–871 (1977).
[18] F. B. Nagiev and N. S. Khabeev, "Heat-transfer and phase transition effects associated with oscillations of vapour-gas bubbles," Sov. Phys. Acoust. **25**, 148–152 (1979).
[19] R. I. Nigmatulin, N. S. Khabeev, and F. B. Nagiev, "Dynamics, heat and mass transfer of vapour-gas bubbles in a liquid," Int. J. Heat Mass Transf. **24**, 1033–1044 (1981).
[20] A. Prosperetti, L. A. Crum, and K. W. Commander, "Nonlinear bubble dynamics," J. Acoust. Soc. Am. **83**, 502–514 (1988).
[21] A. Prosperetti, "The thermal behaviour of oscillating gas bubbles," J. Fluid Mech. **222**, 587–616 (1991).
[22] P. M. Morse and K. U. Ingard, *Theoretical Acoustics* (Princeton University Press, Princeton, 1986), 555 pp.
[23] This mode, if it exists, is labeled $N=0$. It corresponds to a uniform pressure $p_0(\mathbf{x})=\rho c^2 U/j\omega V$. Its contribution in the limit $k_0\to 0$ (i.e., $\omega\to 0$) would be infinite. Since we are dealing with a tank containing a free surface, there is no $N=0$ mode.
[24] This approximation requires $K_N R \ll 1$, and so sets an upper limit to K_N, or equivalently an upper limit to N in the summation. However the limitation becomes important for Z, only if $k_0 R$ is not much less than unity, and therefore will not apply to this paper because the condition $k_0 R \ll 1$ was stated at the outset.
[25] T. G. Leighton, *The Acoustic Bubble* (Academic Press, New York, 1994), Sec. 3.2.1c(iii), 3.3.1(b), 3.5.2, 3.7.3.
[26] M. Rowan-Robinson, *Cosmology*, 2nd ed. (Oxford University Press, Oxford, 1981), p. 56.
[27] T. G. Leighton, A. D. Phelps, D. G. Ramble, and D. A. Sharpe, "Comparison of the abilities of eight acoustic techniques to detect and size a single bubble," Ultrasonics **34**, 661–667 (1996).
[28] J. K. Hammond, "Fundamentals of signal processing," in *Fundamentals of Noise and Vibration*, edited by F. J. Fahy and J. Walker (E&FN Spon, London, 1998), Chap. 6, pp. 311–370.
[29] T. G. Leighton, K. J. Fagan, and J. E. Field, "Acoustic and photographic studies of injected bubbles," Eur. J. Phys. **12**, 77–85 (1991).
[30] A. R. Kolaini, L. A. Crum, and R. A. Roy, "Bubble production by capillary-gravity waves," J. Acoust. Soc. Am. **95**, 1913–1921 (1994).
[31] A. R. Kolaini, "Effects of salt on bubble radiation," in *Natural Physical Processes Associated with Sea Surface Sound*, edited by T. G. Leighton (University of Southampton, Southampton, 1997), pp. 240–249.
[32] A. R. Kolaini, "Sound radiation by various types of laboratory breaking waves in fresh and salt water," J. Acoust. Soc. Am. **103**, 300–308 (1998).
[33] A. R. Kolaini and L. A. Crum, "Observations of underwater sound from laboratory breaking waves and the implications concerning ambient noise in the ocean," J. Acoust. Soc. Am. **96**, 1755–1765 (1994).
[34] J. A. Kitchener, "Foams and free liquid film," *Recent Progress in Surface Science* (Academic, New York, 1964), Vol. I, pp. 51–93.
[35] E. C. Monahan and C. R. Zeitlow, "Laboratory comparisons of fresh-water and salt-water whitecap," J. Geophys. Res. **74**, 6961–6966 (1969).
[36] J. C. Scott, "The role of salt in whitecap persistence," Deep-Sea Res. Oceanogr. Abstr. **22**, 653–657 (1975).
[37] S. A. Thorpe, "The role of bubbles produced by breaking waves in supersaturating the near-surface ocean mixing layer with oxygen," Ann. Geophys. (Gauthier-Villars, 1983–1985) **2**, 53–56 (1984).
[38] L. Memery and L. Merlivat, "Modeling of gas flux through bubbles at the air-water interface," Tellus, Ser. B **37B**, 272–285 (1985).
[39] C. Pounder, "Sodium chloride and water temperature effects on bubbles," in *Oceanic Whitecap and Their Role in Air-Sea Exchange Processes*, edited by E. C. Monahan and G. Mac Niocaill (Reidel, Dordrecht, 1986).
[40] W. M. Carey, J. W. Fitzgerald, E. C. Monohan, and Q. Wang, "Measurement of the sound produced by a tipping trough with fresh and salt water," J. Acoust. Soc. Am. **93**, 3178–3192 (1993).
[41] A. R. Kolaini (personal communication).
[42] N. Breitz and H. Medwin, "Instrumentation for *in situ* acoustical measurements of bubble spectra under breaking waves," J. Acoust. Soc. Am. **86**, 739–743 (1989).
[43] D. M. Farmer and S. Vagle, "Waveguide propagation of ambient sound in the ocean-surface bubble layer," J. Acoust. Soc. Am. **86**, 1897–1908 (1989).
[44] A. D. Phelps, D. G. Ramble, and T. G. Leighton, "The use of a combination frequency technique to measure the surf zone bubble population," J. Acoust. Soc. Am. **101**, 1981–1989 (1997).
[45] W. K. Melville, E. Terrill, and F. Veron, "Bubbles and turbulence under breaking waves," in *Natural Physical Processes Associated with Sea Surface Sound*, edited by T. G. Leighton (University of Southampton, Southampton, 1997), pp. 135–146.
[46] I. N. Didenkulov, S. I. Muyakshin, and D. A. Selivanovsky, "Bubble counting in the subsurface ocean layer," in *Acoustical Oceanography*, Proceedings of the Institute of Acoustics, Vol. 23 Part 2, 2001, edited by T. G. Leighton, G. J. Heald, H. Griffiths, and G. Griffiths (Institute of Acoustics, 2001), pp. 220–226.
[47] V. A. Akulichev, V. A. Bulanov, and S. A. Klenin, "Acoustic sensing of gas bubbles in the ocean medium," Sov. Phys. Acoust. **32**, 177–180 (1986).
[48] J. L. Leander, "A note on transient underwater bubble sound," J. Acoust. Soc. Am. **103**, 1205–1208 (1998).
[49] J. W. L. Clarke and T. G. Leighton, "A method for estimating time-dependent acoustic cross-sections of bubbles and bubble clouds prior to the steady state," J. Acoust. Soc. Am. **107**, 1922–1929 (2000).
[50] S. D. Meers, T. G. Leighton, J. W. L. Clarke, G. J. Heald, H. A. Dumbrell, and P. R. White, "The importance of bubble ring-up and pulse length in estimating the bubble distribution from propagation measurements," in Ref. 46, pp. 235–241.
[51] J. L. Spiesberger and K. Metzger, "New estimates of sound speed in water," J. Acoust. Soc. Am. **89**, 1697–1700 (1991).
[52] Equation (43) was used to correct for reverberation in the surf zone by T. G. Leighton, "Surf zone bubble spectrometry: The role of the acoustic cross section," J. Acoust. Soc. Am. **110**, 2694 (2001).
[53] N. Breitz and H. Medwin, "Instrumentation for *in situ* acoustical measure-

ments of bubble spectra under breaking waves,'' J. Acoust. Soc. Am. **86**, 739–743 (1989).
[54] M. Y. Su, D. Todoroff, and J. Cartmill, ''Laboratory comparisons of acoustical and optical sensors for microbubble measurement,'' J. Atmos. Ocean. Technol. **11**, 170–181 (1998).
[55] D. M. Farmer, S. Vagle, and A. D. Booth, ''A free-flooding acoustical resonator for measurement of bubble size distributions,'' J. Atmos. Ocean. Technol. **15**, 1132–1146 (1998).
[56] D. F. Gaitan and L. A. Crum, ''Observation of sonoluminescence from a single cavitation bubble in a water/glycerine mixture,'' in *Frontiers of Nonlinear Acoustics, 12th ISNA*, edited by M. F. Hamilton and D. T. Blackstock (Elsevier, New York, 1990), p. 459.
[57] A. I. Eller, ''Growth of bubbles by rectified diffusion,'' J. Acoust. Soc. Am. **52**, 1447–1449 (1972).
[58] L. A. Crum, ''The polytropic exponent of gas contained within air bubbles pulsating in a liquid,'' J. Acoust. Soc. Am. **73**, 116–120 (1983).
[59] L. A. Crum and A. Prosperetti, ''Nonlinear oscillations of gas bubbles in liquids: An interpretation of some experimental results,'' J. Acoust. Soc. Am. **73**, 121–127 (1983).

Geoacoustic inversion of ambient noise: A simple method

C. H. Harrison[a)]
SACLANT Undersea Research Centre, Viale S. Bartolomeo 400, 19138 La Spezia, Italy

D. G. Simons[b)]
TNO Physics and Electronics Laboratory, Oude Waalsdorperweg 63, 2509 JG The Hague, The Netherlands

(Received 19 November 2001; revised 7 June 2002; accepted 26 June 2002)

The vertical directionality of ambient noise is strongly influenced by seabed reflections. Therefore, potentially, geoacoustic parameters can be inferred by inversion of the noise. In this approach, using vertical array measurements, the reflection loss is found directly by comparing the upward- with the downward-going noise. Theory suggests that this simple ratio is, in fact, the power reflection coefficient—potentially a function of angle and frequency. Modeling and parameter searching are minimized, and the method does not require a detailed knowledge of the noise source distribution. The approach can handle stratified environments and is believed to tolerate range dependence. Experimental data from five sites, four in the Mediterranean, one on the New Jersey Shelf, are described. Most of the Mediterranean sites had temporally varying noise directionality, yet yielded the same reflection properties, as one would hope. One site was visited in conditions of very low surface noise. This paper concentrates on an experimental demonstration of the feasibility of the method and data quality issues rather than automatic search techniques for geoacoustic parameters.
 [DOI: 10.1121/1.1506365]

PACS numbers: 43.30.Nb, 43.30.Ma [DLB]

I. INTRODUCTION

It is well known that in shallow water the coherence and directionality of ambient noise depend on the noise source distribution and environmental parameters such as bathymetry, sound-speed profile, and bottom reflection properties. In general, knowing the environment, one could use a detailed propagation model to predict noise. Potentially, one could therefore deduce bottom properties from the noise without a specialized sound source or even a ship. Pioneering work on inverting the noise to deduce geoacoustic parameters has been successfully accomplished [Buckingham and Jones (1987); Carbone *et al.* (1998); Aredov and Furduev (1994)] in environments that are range- and azimuth independent, and where one can rely on the sources being uniformly distributed. Carbone used a vertically separated pair of hydrophones to measure the broadband noise coherence, which was then compared with model calculations searching over geoacoustic parameter space.

In the Mediterranean, where shipping densities are high, the uniform source distribution assumption is frequently violated. Furthermore, the source distribution may change over a period of hours, and there may be more dramatic changes associated with individual ships at short ranges. For this reason an alternative method [an extension of Aredov and Furduev (1994)] is investigated in this paper. A preliminary account of this work was given by Harrison and Simons (2001). It is shown below that it is indeed possible to make deductions about the seabed properties *without* knowing the detailed source distribution. In fact, the reflection loss versus angle can be found directly by comparing the noise intensity arriving from equal up and down elevation angles. In some applications, particularly at high frequencies, a solution in the form of a reflection loss may be more appropriate or useful than the conventional geoacoustic parameters. An additional benefit is that we do not need a detailed noise model, but on the other hand we do need a vertical array to resolve angles. Here, we demonstrate the potential of the method with experimental data from five sites in the Mediterranean and one on the New Jersey Shelf. A future paper will discuss techniques for automatic geoacoustic parameter searching.

Ground truth is conveniently provided by independent conventional geoacoustic inversion carried out either during the same experiments or on different occasions. There are also a number of cores and geoacoustic models in most of the areas. Specific references will be made later.

II. THEORY

A. Noise theory

It is fairly obvious that the noise field depends on the reflection properties of the seabed, but not so obvious that the plane wave reflection coefficient is so simply related to the noise directionality. The array response to a directional noise field can be represented as an integral over ray arrivals [Chapman (1988), Harrison (1996)] or as a wave integral of a Green's function [Eq. (9.14) of Jensen *et al.* (1994)]. The ray approach for a range-dependent environment is spelled out in the Appendix. Here, we avoid these cumbersome derivations by choosing a simple energy flux argument to explain the effect in a more concise and convincing way.

Consider a block of sea water, Fig. 1, bounded by the sea surface, the seabed, and two vertical imaginary lines (planes) in an otherwise infinite horizontally uniform, vertically stratified environment. Insert an infinite source layer at

[a)]Electronic mail: harrison@saclantc.nato.int
[b)]Electronic mail: simons@fel.tno.nl

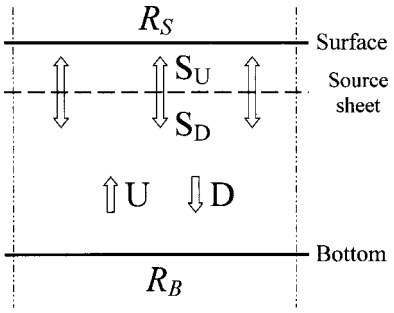

FIG. 1. Diagram showing a finite block from an infinitely wide range-independent sea. Although sound may propagate obliquely the horizontal flux balances out, so here we only show the vertical components. Up- and down-going components of (plane wave) flux S_U, S_D emanate from a horizontal sheet source just below the sea surface. The vertical balance leaves components U and D in the body of the water, which are simply related to the bottom reflection loss R_B.

some small (finite) depth below the surface. Now, consider the balance of the upward and downward component of flux in the box (both above and below this source sheet). Note that because of the horizontal uniformity there is no net horizontal flux, so we can ignore the horizontal component. We regard the infinite source as emitting an incoherent plane wave (as a distant light bulb would!) at a given angle which subsequently obeys Snell's law at the various depths. Let the sheet source emit flux S_U upwards and S_D downwards (at the given angle). Beneath the source we define upward and downward fluxes (at the corresponding Snell angle) as U and D, respectively. Just below the source the total downward flux includes the surface reflected upward-going flux

$$D = S_D + R_s(S_U + U), \tag{1}$$

where R_s is the surface power reflection coefficient.

By the definition of the bottom power reflection coefficient R_b, we have

$$U = DR_b. \tag{2}$$

If we define an ''effective'' source strength S (since R_s may not be unity) as

$$S = S_D + R_s S_U, \tag{3}$$

then we find

$$D = S/(1 - R_s R_b), \tag{4}$$

$$U = R_b S/(1 - R_s R_b). \tag{5}$$

These are exactly the formulas obtained by Chapman (1988) and Harrison (1996) [also seen in Eqs. (A6) and (A3) of the Appendix and Harrison (1997a)] but with volume absorption set to zero. Including absorption in the flux argument is straightforward. Dividing Eq. (5) by Eq. (4), we obtain the up-to-down noise ratio which is evidently the same as Eq. (2). This is no surprise since it is the definition of reflection coefficient! If we now put a receiver in this field we can measure U and D, and hence deduce R_b, but clearly the original field consisted of plane waves so we will deduce a *plane wave reflection coefficient*. Also, the ratio depends on local bottom properties, i.e., within about one ray cycle for the angle in question.

Note that no matter where the sources are, as long as they are far enough away or large enough to be considered plane wave sources, Eq. (2) is always true. Therefore, the underlying tenet of this paper still holds. The plane wave condition reduces to being able to ensure that U, D at the receiver are substantially the same as at the bottom. Clearly, local point sources (that cannot, in some way, be spatially or temporally averaged out) violate these assumptions.

This is a powerful derivation for the following reasons:

(i) We have made no assumption about rays, modes, or waves.
(ii) We have made no assumption about the dipole or monopole nature of the source.
(iii) We have made no assumption about the spectrum of the source.
(iv) Refraction makes no difference to the argument as long as energy gets from the surface to the receiver via the bottom (see the Appendix for more details).
(v) A small net horizontal component of flux does not alter the vertical component. Therefore, neither non-uniform distant sources nor range-dependent environments spoil the argument (see the Appendix for more details).

Thus, this approach can tolerate arbitrary arrangements of distant ships and simultaneous local or distant wind noise. However, nearby point sources (with slight asymmetry in eigenray angles) that do not average out over time lead to problems that can nevertheless be anticipated and isolated by inspection of the array's beam response.

A dramatic demonstration of the correctness of the theory (at least for range-independent environments) is given by Harrison and Baldacci (2002). Within the confines of one wave model, one can construct both the ''ground truth'' reflection loss and the result of the proposed VLA processing technique. First, OASR [Schmidt (1999)] was used to calculate the bottom reflection loss for a given environment (similar to the Sand site, Sec. IV A later); a preview is shown in Fig. 2(a). Then, the array response to a sheet noise source was found from the correlation matrix option of OASN [Schmidt (1999)], and the up-to-down noise ratio was obtained from it [Fig. 2(b)]. In this example the array spans the full water column and these two plots are very nearly identical. Naturally, as the array size is reduced the deduced reflection loss gradually degrades.

B. Possible analysis procedures

There are several ways we can process this type of VLA data. First, it is possible to leave the output as reflection loss versus frequency and angle since this is exactly what is required for some propagation models, e.g., ray traces. Furthermore, it is possible to make comparisons with other reflection measurement techniques such as the ''move-out'' method where pulse travel times and known geometry allow direct measurement [Holland and Osler (2000)]. Second, it is possible to try to convert the data to frequency-independent geoacoustic parameters by using a search algorithm and a plane wave reflection formula or model (as opposed to a

noise model, i.e., one which needs to assume a complete environment and noise source distribution—precisely what we hope to avoid with this method). In the present paper we will venture no further than hand searches, the main point being to demonstrate merely that a solution is possible. The precise meaning of ''hand search'' will be explained during discussion of the examples in Sec. IV—the point is that there is a logical sequence in which one searches for one parameter at a time. A third possibility is to use amplitudes and fringe patterns to calculate layer thicknesses and velocities directly by methods more akin to those used in geophysical prospecting. By Fourier transforming from frequency to time it is, in principle, possible to convert the fringes (being a power spectrum) to the layers' autocorrelation function (a series of delta functions at delays corresponding to all layer separations). This time-domain information is then available as a function of angle.

In all three methods we first need to map the up-to-down ratio from the angle measured (by beamforming) at the receiver θ_r to the angle at the seabed θ_b. Thus, knowing the sound-speed profile, by Snell's law we have

$$\theta_b = \mathrm{acos}((c_b/c_r)\cos(\theta_r)), \tag{6}$$

and with upward refraction, zero bottom grazing angle maps to a finite nonzero angle at the array. Conversely, with downward refraction, zero angle at the array maps to a nonzero angle at the bottom, and there will be a small range of angles at the bottom that is not detectable. It is also necessary that the path connect with the sea surface—otherwise, there could not be any measured surface noise at the given angle. If there is a sound speed higher than that at the receiver depth anywhere above the receiver c_m, there is a possibility of a ''noise notch,'' a range of angles that is surface-noise-free. The edge of this range obviously corresponds to a nonzero angle at the receiver

$$\theta_m = \mathrm{acos}(c_r/c_m). \tag{7}$$

Beyond this, the bottom angle may be greater or smaller than the angle at the receiver according to Eq. (6).

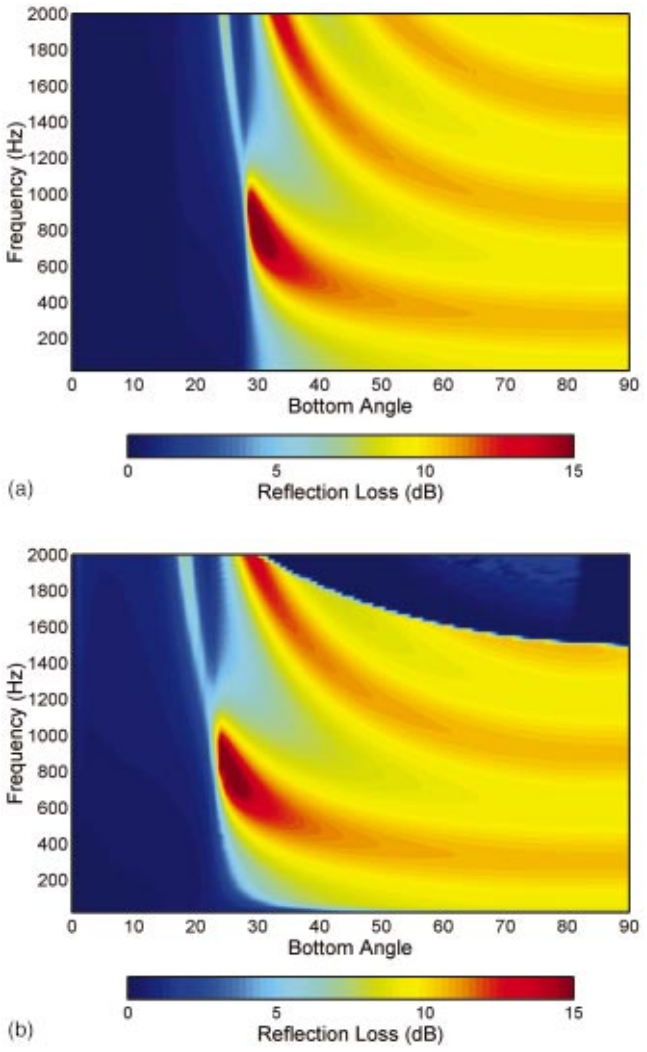

FIG. 2. (a) Plane wave reflection loss for a hypothetical three-layer environment similar to the Sicily sand case modeled with OASR, and (b) the ratio of upward-to-downward noise for a 0.5-m-spaced vertical array spanning the water column calculated by OASN assuming a sheet source and the same environment.

C. Simulated bottom reflection and beamforming

In the subsequent sections we make comparisons between measurements and predictions. Unless otherwise stated, the predictions are based on a three-layer (two-boundary) model with the bottom layer supporting shear waves. In some cases an extra intermediate fluid layer has been added. Theory is based on the analytical solutions from Jensen *et al.* (1994), Eqs. (1.49) (for shear), (1.57) (for three-layer), and (1.65) (for extension to *m* layer). The effect of the finite beamwidth could be estimated by using a full-noise model such as OASN [Schmidt (1999)] or CANARY [Harrison (1997b)]. This is taken up by Harrison and Baldacci (2002). Instead, for demonstration purposes we note here that, in the case where the noise sources are uniformly distributed dipoles and the environment is independent of range, the directional noise can easily be calculated (see the Appendix). We can therefore estimate the array response knowing the beam pattern. Dividing downward by upward array response we obtain the ratio of beam responses $\Re$, which is an approximation to R_b

$$\frac{A(-\theta_o)}{A(+\theta_o)} = \Re(\theta_b(\theta_o)). \tag{8}$$

Thus, for each experimental plot we can provide an unmodified layer model plot and also a beam-smudged version.

III. EXPERIMENTS

Experiments have been carried out at five sites in the Mediterranean Sea. Three sites are south of Sicily, near the Ragusa Ridge [Fig. 3(a)], one near the Adventure Bank during ADVENT99 in May 1999, and the other two on the Malta Plateau during MAPEX2000bis in November 2000. The other two are north and east of Elba [Fig. 3(b)] also during MAPEX2000bis. Bottom types include sand, silt, mud, and rock, and one of the sites was visited twice first

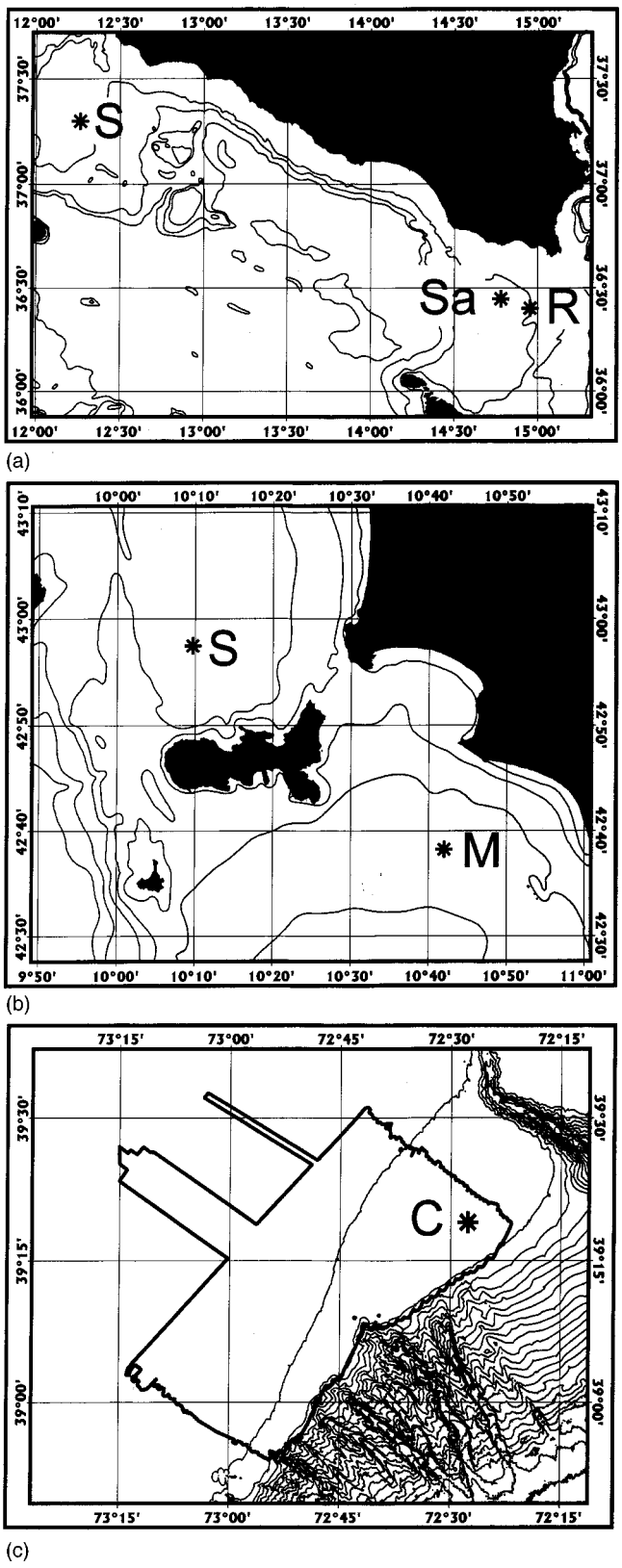

FIG. 3. (a) Three experimental sites south of Sicily [Adventure Bank (labeled "S"), ADVENT99 and Ragusa Ridge (labeled "Sa" and "R"), MAPEX2000bis]; (b) two sites to the north ("S") and east ("M") of the Island of Elba (MAPEX2000bis); (c) one site on the New Jersey Shelf ("C"), BOUNDARY2001 showing the area extensively surveyed by Goff *et al.* (1999).

with, then without, significant wind noise. Another site was visited on the New Jersey Shelf during BOUNDARY2001 [Fig. 3(c)].

In all cases SACLANTCEN's moored 64-element vertical array (VLA) was used for the noise measurements (Troiano *et al.*, 1995). The same array was used in conjunction with sound sources both fixed and towed by SACLANTCEN's ship, RV ALLIANCE, for conventional geoacoustic inversion experiments (Siderius *et al.*, 2001). The 62-m array was roughly centered in the water column, and although all 64 hydrophones were available only the middle 32 regularly spaced ones (i.e., total length 16 m at half-meter separation) were used for these noise calculations.

Noise was sampled at 6 kHz on an automatically repeated sequence. During ADVENT99 the sequence consisted of two roughly 15-s windows every 4 min interlaced with active transmissions. This arrangement led to less than ideal gain settings for the noise measurements and a tendency to introduce quantization effects. In all the other cases noise measurements were taken for 10 s every 10 s while the RV ALLIANCE was quiet. The electronics provided a flat band between about 100 Hz and 2 kHz. Processing consisted of manually selecting portions without obvious contamination, and then beamforming them in the frequency domain.

IV. ANALYSIS OF RESULTS

The experimental beamformed array response can be determined conveniently by calculating the cross-spectral density between all pairs of channels, $C_{ij}(f)$, using a proprietary routine including FFT averaging, then multiplying by the steer vectors $w_i^*(\theta_o, f)$, $w_j(\theta_o, f)$ for frequency f, and summing

$$A(\theta_o, f) = \mathbf{w}^{\mathrm{T}}\mathbf{C}\mathbf{w} = \sum_i \sum_j w_i^*(\theta_o) C_{ij}(f) w_j(\theta_o). \quad (9)$$

Each array response was calculated for 181 steer angles from the cross-spectral density matrix for the middle 32 elements (17–48) of the 64-element array. The bottom hydrophone (number 1) was moored at 11 m above the seabed in the Mediterranean cases and 14 m in the New Jersey case. The cross-spectral density used nonoverlapping 128-point FFTs, sampling at 6000 Hz, averaging over the 10 s of the file. Further power averaging was carried out over 10 to 30 files. In most cases a total of about 5 min of data (though carefully selected) proved adequate.

The Mediterranean sites have fairly heavy shipping, particularly those on the Malta Plateau and Adventure Bank. In a separate experiment in the vicinity (MAPEX2000), noise measurements made with a 256-element horizontal array easily detected about 14 nearby ships passing in 4 h (Harrison, 2001). It is thought that there were no ships close enough to spoil the "distant ship" approximation, although clearly a nonuniform and evolving distribution is to be expected. At the sites near Elba there tend to be occasional ferries and small fishing boats rather than container ships. In contrast,

TABLE I. Important sound speeds for angle mapping.

Date dd-mm-yyyy	Site	Depths (m) Water	Depths (m) Array center	Sound speeds (m/s) Array c_r	Sound speeds (m/s) Bottom c_b	Sound speeds (m/s) Max. $c_{\max}$	Min. bottom angle (°)	Wind (kt)
06-05-1999	Adv. Bank	80	39	1509.4	1511.2	1513.5	···	5–8
22-11-2000	S. Sicily	139	96	1512.0	1512.0	1524.2	0.00	20–22
23-11-2000	S. Sicily	99	56	1512.8	1511.4	1522.5	2.47	5–6
29-11-2000	N. Elba	121	78	1520.5	1512.1	1520.8	6.03	3–5
30-11-2000	E. Elba	125	82	1520.4	1508.8	1520.6	7.08	12–16
01-12-2000	N. Elba	121	78	1519.9	1513.9	1519.9	5.09	3–4
17-05-2001	N.J. Shelf	140	92	1499.3	1499.3	1500.5	0.00	10–14

there was hardly any nearby shipping at the New Jersey Shelf site. Wind speeds are shown in Table I. Sound-speed profiles at the various sites are shown in Fig. 4.

A. "Sand" site: S. Sicily (near Ragusa Ridge), 22 November 2000

The array response versus angle and frequency is shown in Fig. 5(a). There are various features common to all the following cases. On the right the intensity falls off rapidly because of a 2-kHz antialiasing filter. The general broadening towards the left is a manifestation of the poorer angle resolution at lower frequency. The double spikes near the horizontal span a noise notch caused, as explained earlier, by the sound-speed profile (see Fig. 4). Straight away we can see a considerable difference between up- and down-going intensity. The "up-to-down" ratio is shown in Fig. 5(b). Angles have been corrected from that at the receiver to that at the seabed according to the sound speeds shown in Table I. (Note that Table I also shows the minimum bottom angle for rays that connect with the sea surface; below this, data should be ignored.) Interpreting this picture now as a bottom reflection loss, the main features are low loss up to a critical angle and two interference lobes beyond this. This is classic behavior for a high sound-speed bottom (see, e.g., Jensen *et al.*, 1994 and Nagl *et al.*, 1982); once the critical angle is exceeded there is the possibility of simultaneous reflections from deeper layer boundaries which arrive later and therefore interfere. Indeed, this interference pattern is evidence that there is at least one other layer boundary present. Furthermore, in this case the regularity of the fringes with frequency suggests exactly two boundaries. The drop to low loss at the top of the picture is an artifact caused by the grating lobe that arcs from 90° at 1500 Hz (the design frequency) to 40° at 2 kHz in Fig. 5(a). Similarly, the low losses at low frequencies are caused by the inevitable poor angle resolution which degrades the up-to-down ratio. In fact, with this array the beamwidths to 3-dB points at 1500, 1000, 500, 200 Hz are, respectively, 6.7, 10, 20, 50 degs. In retrospect, all these features, particularly the two fringes, can be discerned by eye quite clearly in the original array response plot.

We can model these effects by applying the three-layer (two-boundary) model of Sec. II C with some appropriate geoacoustic parameters. Geoacoustic models for the vicinity are given by Max *et al.* (2000), core analysis by Tonarelli *et al.* (1993), and independent inversion results from MAPEX2000bis by Siderius *et al.* (to be published, 2002). As shown in Table II, we take parameters from the first reference as a starting point and then make minor adjustments by hand; in particular, we adjust the layer thickness for agreement of fringe separation. The reflection loss is shown in Fig. 5(c). If we then simulate the effect of beamforming (see the Appendix), the result is remarkably similar to the experimental plot [Fig. 5(d)].

B. "Silt" site: N. Elba, 1 December 2000

Experimental array response (AR) and reflection loss (RL) curves for a silt bottom are shown in Figs. 6(a) and (b). There is now no noise notch because the array has no maximum sound speed above it. The most noticeable feature of the reflection plot is the irregularity of the interference fringes and the features at low grazing angles. In fact, we see superimposed fine and coarse fringes demonstrating that there must be more than two layer boundaries. Furthermore, since low frequencies tend not to be affected by thin layers, we can see that the lower part of Fig. 6(b) is dominated by fine fringes (200-Hz separation) caused by a thick layer with critical angle ~20°. In contrast, the coarser fringes seen starting at 1200 Hz, 90° must be caused by a thinner layer (a

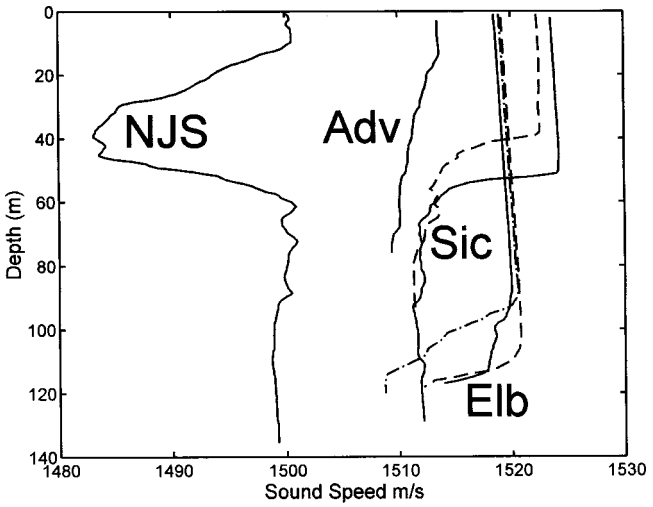

FIG. 4. Sound-speed profiles for all sites derived from near simultaneous CTDs for all sites except New Jersey, which was XBT. Labels indicate New Jersey Shelf (NJS), Adventure Bank (Adv), S. Sicily (Sic), "sand" site (solid), "rock" site (dashed), and Elba (Elb), "silt" site (solid), "silt" site without wind (dashed), "mud" site (dot-dash).

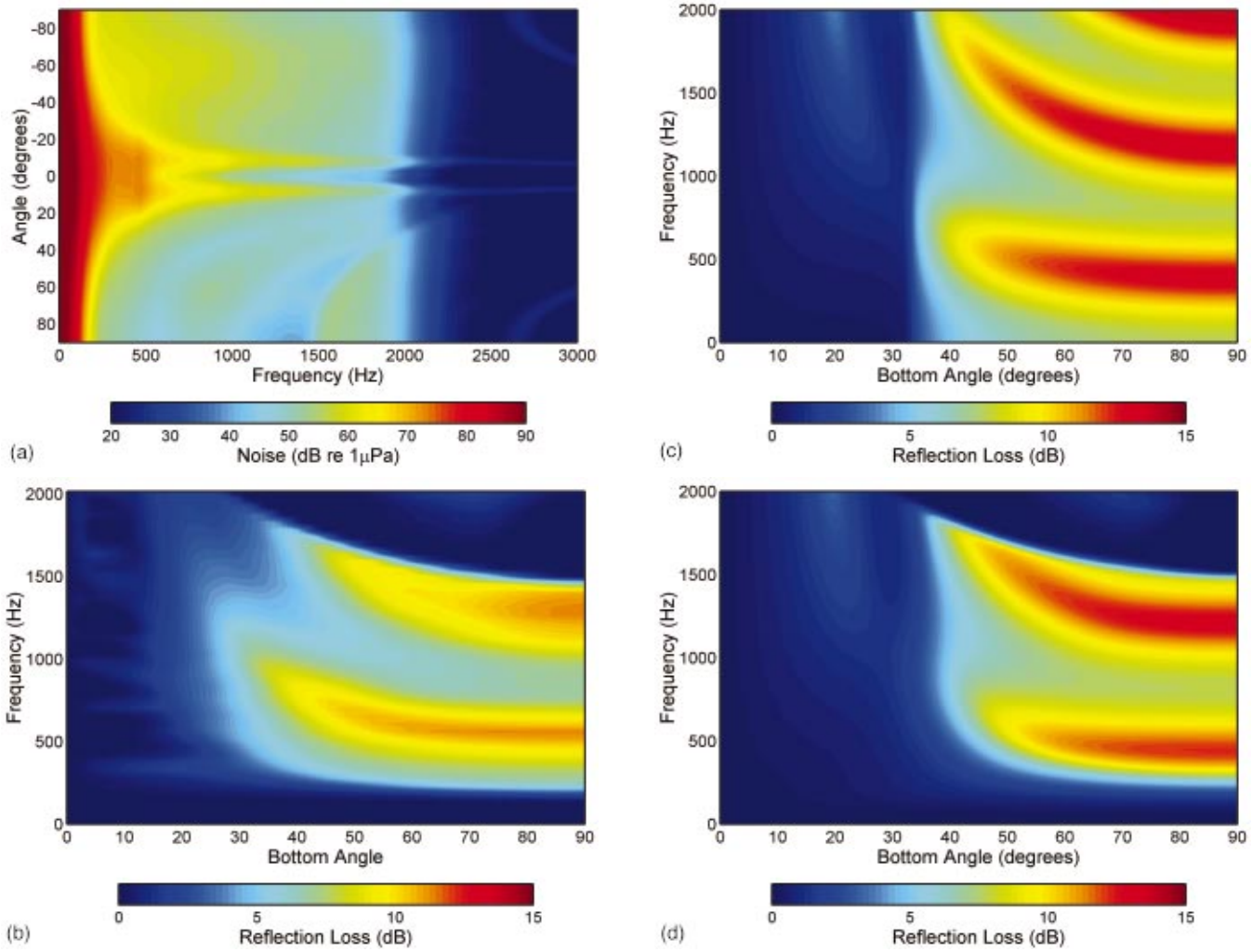

FIG. 5. (a) Experimental VLA beam response with 32 elements @ 0.5-m separation at the Ragusa Ridge, S. Sicily, ''sand'' site. (b) Reflection loss deduced from the up-to-down ratio of the beams from the VLA (min. bottom angle 0°). (c) Reflection loss from a simple layer model with parameters adjusted by hand as in Table II. (d) Beamformed noise resulting from the modeled reflection loss in a simple sheet noise model [Eqs. (A1), (A2), (A6)].

factor of 3 or 4 thinner, judging by the fringes) with a somewhat larger critical angle. This already provides strong clues to the bottom structure. Notice that the evidence for multiple layers is only manifest above about 900 Hz.

In earlier experiments at nearby sites, Jensen (1974) found a good two-boundary fit at low frequencies using normal-mode propagation modeling, and this was used as a starting point for subsequent inversion work by Gingras and

TABLE II. Geoacoustic parameters for all sites (initial from reference and final).

	Speed (m/s)[a]				Thickness (m)[a]		Density (gm/cc)[a]			Attenuation (dB/λ)[a]			
Site	c1	c2	c3	c4	h2	h3	ρ2	ρ3	ρ4	α2	α3	α4	Ref.[b]
''silt''	···	1690	···	1750	4.3	···	1.9	···	2.0	0.4	···	0.4	TTMA
Adv. B.	**1511**	**1630**	···	**1650**	**2.5**	···	**1.9**	···	**1.9**	**0.4**	···	**0.4**	**Fig 9**
''sand''	···	1554	···	1950	5	···	1.3	···	2.0	0.18	···	0.3	MFHTB
Ragusa	**1512**	**1554**	···	**1800**	**1.0**	···	**1.2**	···	**2.0**	**0.18**	···	**0.2**	**Fig 5**
''silt''	···	1600	1530	1600	0.2	2.5	?	1.75	1.8	?	0.13	0.15	MWJ
N. Elba	**1514**	**1600**	**1530**	**1600**	**0.7**	**2.1**	**1.8**	**1.75**	**1.8**	**0.13**	**0.14**	**0.15**	**Fig 6**
''mud''	···	1645	1471	1600	0.3	6	?	1.5	1.8	?	0.06	0.15	MWJ
E. Elba	**1509**	**1530**	**1471**	**1530**	**0.8**	**3.5**	**1.4**	**1.2**	**1.8**	**0.14**	**0.06**	**0.15**	**Fig 7**
''clay''	···	1530	···	?	···	···	1.4	···	?	0.1	···	?	H
N.J. Sh.	**1499**	**1695**	···	1700	**3.0**	···	**1.85**	···	**1.95**	**0.15**	···	**0.15**	**Fig 10**

[a]Layers are numbered 1–4 from the top. Layer 1 is always water, but only the sound speed is shown. Layer 4 is always a half-space. Sometimes layer 3 is missing, i.e., zero thickness. A ''?'' indicates that no information was available from the reference cited.
[b]Bold characters indicate values actually used in the calculations for the figure indicated. Normal characters indicate values suggested by the references cited. TTMA=Tonarelli *et al.* (1993); MFHTB=Max *et al.* (2000); MWJ=Murphy *et al.* (1976); H=Hamilton (1980).

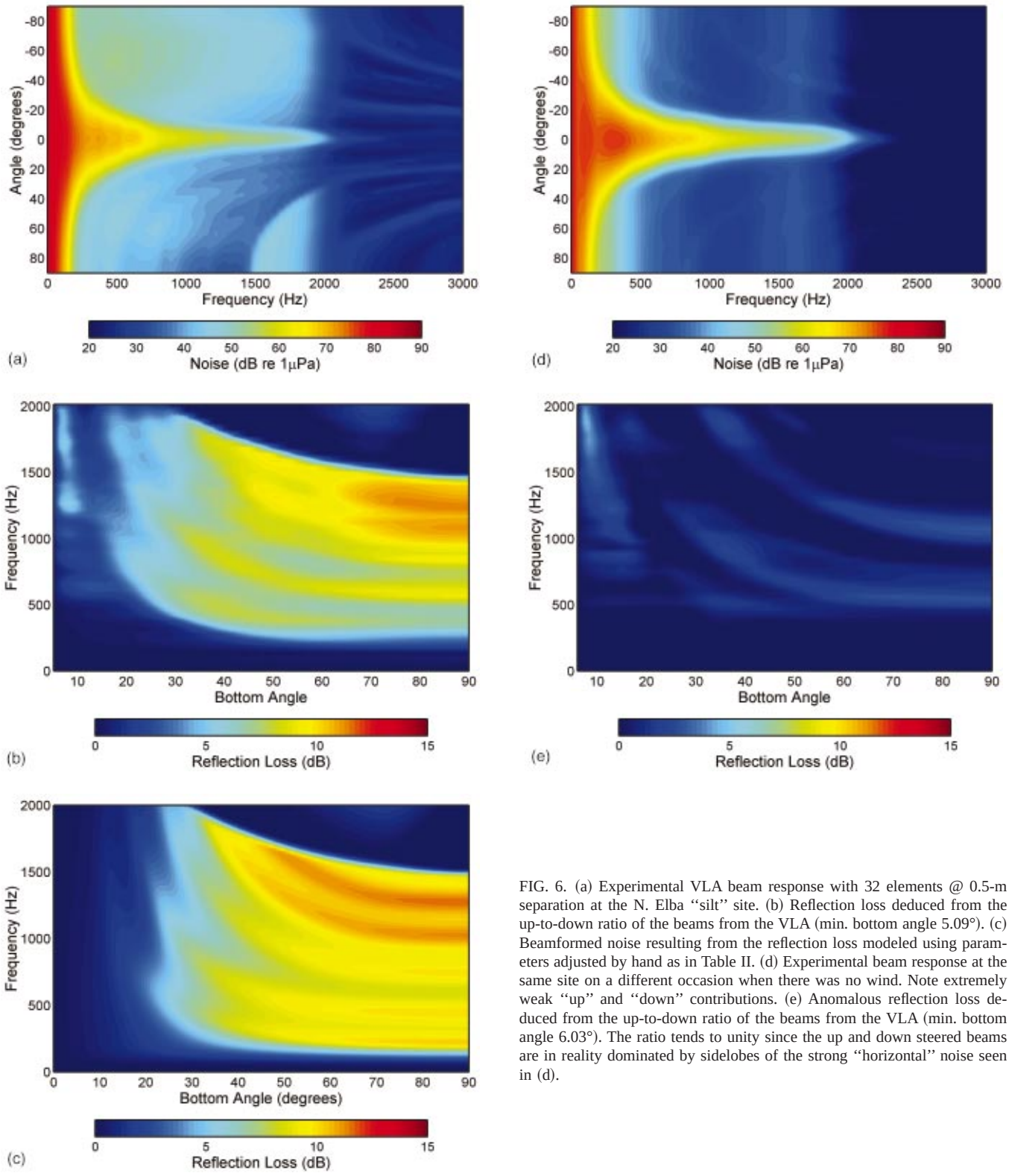

FIG. 6. (a) Experimental VLA beam response with 32 elements @ 0.5-m separation at the N. Elba ''silt'' site. (b) Reflection loss deduced from the up-to-down ratio of the beams from the VLA (min. bottom angle 5.09°). (c) Beamformed noise resulting from the reflection loss modeled using parameters adjusted by hand as in Table II. (d) Experimental beam response at the same site on a different occasion when there was no wind. Note extremely weak ''up'' and ''down'' contributions. (e) Anomalous reflection loss deduced from the up-to-down ratio of the beams from the VLA (min. bottom angle 6.03°). The ratio tends to unity since the up and down steered beams are in reality dominated by sidelobes of the strong ''horizontal'' noise seen in (d).

Gerstoft (1995). Parameters are given in Table II. These parameters, when inserted in the noise model, give good agreement with Fig. 6(b) at low frequencies, but to improve agreement at high frequencies we need to insert a thin layer with high sound speed (Table II). In fact, there is a lot of evidence from core analysis for such a thin, high-velocity layer sitting on top of the sediment near this site [Akal *et al.* (1972); Murphy and Olesen (1974); Jensen (1974); Murphy, Wasiljeff, and Jensen (1976); Holland and Osler (2000)]. In Fig. 6(c) we show a very good fit with a four-layer model.

C. ''Silt'' site, no wind: N. Elba, 29 November 2000

The silt site was also visited on an occasion when the sea was flat, calm, and there was hardly any wind ($\leqslant$3 kt). There is a dramatic difference, visible immediately from the

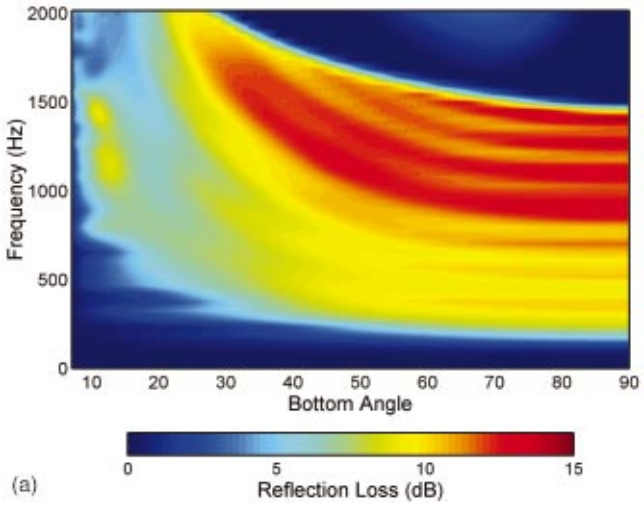

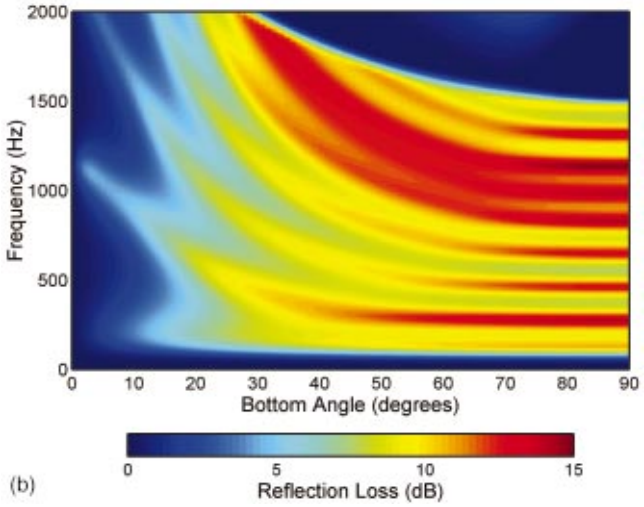

FIG. 7. (a) Reflection loss deduced from the up-to-down ratio of the beams from the VLA at the E. Elba ''mud'' site (min. bottom angle 7.08°). (b) Beamformed noise resulting from the reflection loss modeled using parameters adjusted by hand as in Table II.

AR plot. The ''up'' and ''down'' levels are understandably both much weaker, but there are still sources near horizontal, probably distant shipping. On the assumption that there is no vertical noise at all, the beamformed responses are really responses of sidelobes to this horizontal noise. The response is therefore virtually the same up as down, and the ratio tends to unity (zero dB). This is essentially what we see in Figs. 6(d) and (e). Although there is structure it is mainly anomalous. However, it is very obvious from both the symmetry in AR plot and the differences in level between vertical and horizontal in the AR plot that this has happened, so the technique is reasonably robust from this point of view. It is stressed that it is the beamforming that is breaking down rather than the theory of this method; the up-to-down ratio is just difficult to measure in the presence of the loud horizontal sources.

D. ''Mud'' site: E. Elba, 30 November 2000

The mud site was expected to be lossy with sound speeds lower than that in water [Murphy, Wasiljeff, and Jensen (1976)]. In Fig. 7(a) there is evidence of higher losses at low angles, i.e., an absence of a clear critical angle. Again, there are two superimposed fringe patterns, one fine—with seven or eight loss maxima visible at, say 90°, and one coarse—with only one maximum and one minimum visible. This suggests three boundaries, two of which are wide apart and two of which are close together. Murphy, Wasiljeff, and Jensen (1976) demonstrate that there is again a thin, high-velocity layer at this site but now in the middle of the sediment layer. The result of a hand search with a three-boundary model, assuming a thin layer above the slow sediment layer, including beamforming, is shown in Fig. 7(b) (parameters are in Table II). By setting first sound speeds, then layer thicknesses, then density and absorption, it is possible independently to control the two sets of fringes, their relative amplitudes, and the low angle dependence. The search can be extended to a fourth boundary, simulating the position of the thin, fast layer within the main sediment layer, but this does not appear to improve the agreement.

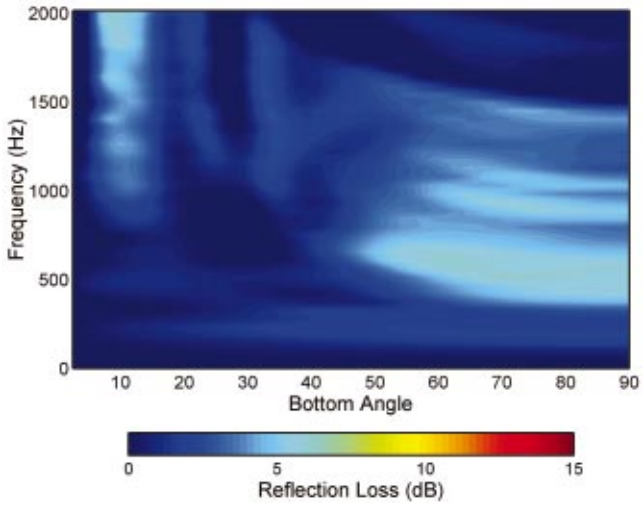

FIG. 8. Reflection loss deduced from the up-to-down ratio of the beams from the VLA at the Ragusa Ridge, S. Sicily, ''rock'' site (min. bottom angle 2.47°).

E. ''Rock'' site: S. Sicily (Ragusa Ridge), 23 November 2000

This site is included here for completeness, but we suspect that, as in Figs. 6(d) and (e), the wind was not strong enough to avoid artifacts, being 5–6 kts. Nevertheless, in Fig. 8 one can still see weak structure resembling that seen in earlier pictures and evidence of interference through layering, for instance an interrupted thin layer of silt above rock. Although one would expect rock to be a strong reflector, a half-space with impedance twice that of water would still have a reflection loss of 9 dB or so at high angles.

F. ''Silt'' site: SW Sicily (Adventure Bank), 6 May 1999

The peak values of reflection loss at this site [Fig. 9(a)] appear to be weaker than at the earlier ones. Suitable environmental data are provided by Tonarelli *et al.* (1993); Caiti *et al.* (1996); Caiti (1996); Snellen *et al.* (2001); Siderius *et al.* (2001) (see Table II). There is quite a spread of param-

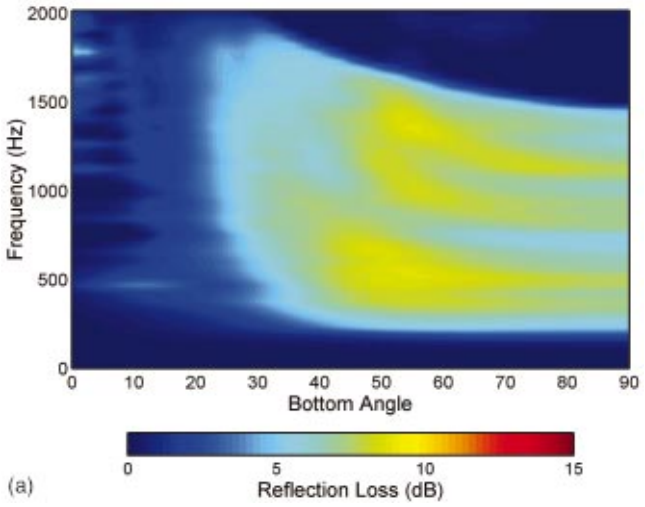

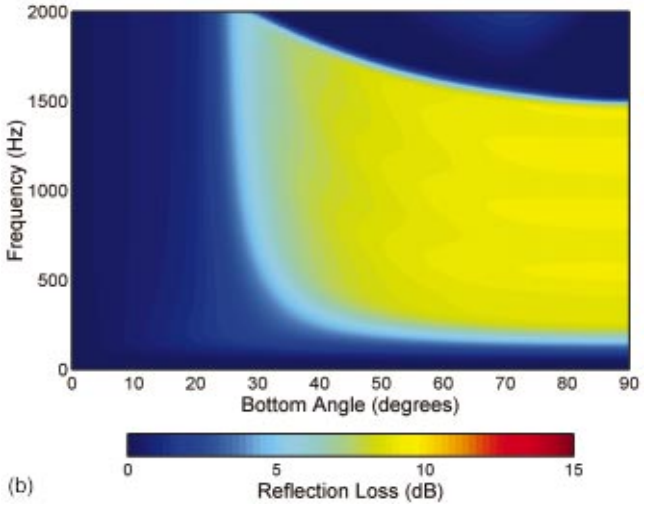

FIG. 9. (a) Reflection loss deduced from the up-to-down ratio of the beams from the VLA at the Adventure Bank, S. W. Sicily, ''silt'' site (zero bottom angle corresponds to 2.80° at the array). (b) Beamformed noise resulting from the reflection loss modeled using parameters adjusted by hand as in Table II.

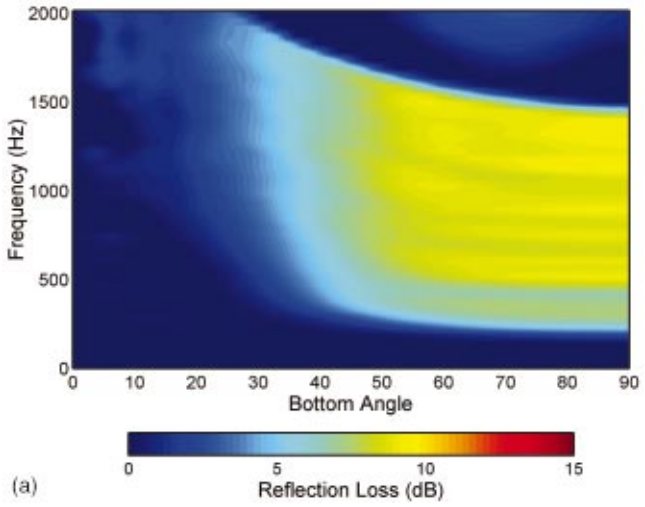

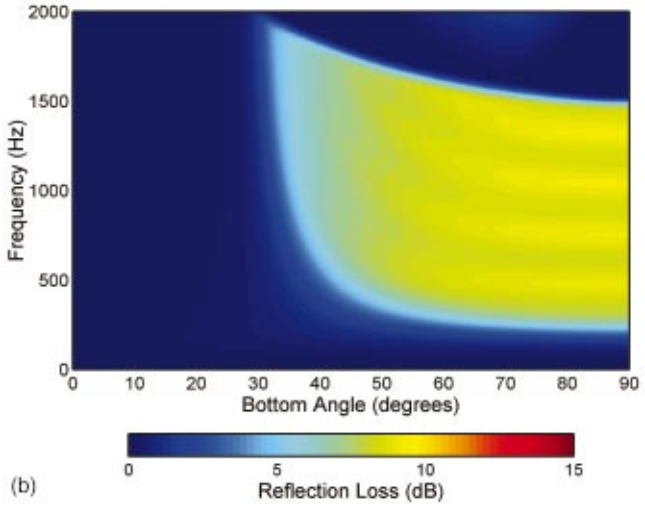

FIG. 10. (a) Reflection loss deduced from the up-to-down ratio of the beams from the VLA at the New Jersey Shelf ''stiff clay'' site (min. bottom angle 0°). (b) Beamformed noise resulting from the reflection loss modeled using parameters adjusted by hand as in Table II.

eters between these references, partly because of real spatial variability, with sediment densities from 1.6 and 1.9 and sound speeds from 1670 and 1750 in the first few meters. The model fits shown in Fig. 9(b) are good but not quite as good as in the other cases. It is possible that deeper high-speed layers could account for the ''lamb chop'' shape of the experimental fringes (by providing loss peaks at the higher critical angle), but in retrospect these shapes look rather suspiciously unlike theoretical curves. The prime suspect is the addition of nonacoustic noise which artificially reduces the up-to-down ratio. It is known that these data were affected by a form of uncorrelated (pink) noise, namely, quantization noise when the gains had been set for experimental purposes other than gathering noise.

An interesting separate point, taken up in Harrison and Simons (2001), is that, although there are changes over several hours in noise directionality that are obvious in the beam response, the derived reflection loss is more or less immune to them.

G. "Stiff clay" site: New Jersey Shelf, 17 May 2001

There appears to be little quantitative geoacoustic data available for this site, although it is thought to be a stiff clay (Goff *et al.*, 1999). Hamilton (1980, 1987) provides some average properties for ''continental terrace (shelf and slope) environment.'' Between clayey silt and silty clay, sound speeds are 1546–1517 m/s and densities are 1.489–1.480 g/cc. Silt clays have a low loss of about 0.1 dB/wavelength. Initial parameters are shown in Table II.

The experimental reflection loss curve in Fig. 10(a) shows some layer structure, but the main feature is a simple step at around 35° up to about 10-dB loss. This can be modeled either as a half-space or as a multiple boundary. The sound speed in the basement is determined by the obvious critical angle, and the layer thickness is determined by the fringe separation. To get a good fit to the depth of modulation, while treating the layer as clay, it was necessary to choose a density close to that of water (1.05), but this conflicts with the assumption of a clay sediment. Equally convincing fits can be obtained by assuming either a half-space

of fine sand with sound speed 1700 m/s and density 1.8 g/cc (Hamilton, 1987), or a 3-m layer and basement of slightly differing properties close to that of fine sand. The effect of beamforming with the parameters of Table II is shown in Fig. 10(b). Note that this example happens to reveal an ambiguity or nonuniqueness in the inversion process which is common to many inversion methods. The experimental noise technique deduces a reflection loss which may indeed have measurement errors, but the reflection properties are not ambiguous in the same sense as the geoacoustic properties. A sensitivity analysis, particularly in this case, would be interesting but it is felt to be outside the scope of this paper. Some of these issues are discussed in Sec. V.

H. Data quality

The dynamic range of the reflection loss (i.e., depth of modulation of fringes) sometimes appears to be slightly smaller in the measurement than in the calculation. An obvious possible cause is the addition of (frequency-dependent) uncorrelated noise which potentially spoils the up-to-down ratio. It has the effect of disproportionately boosting the weak, upward-going signal, thus making the bottom appear to be a stronger reflector. In terms of the cross-spectral density matrix for the array, uncorrelated noise adds to the diagonal only. Adding the equivalent of 10% of the downward power to both up and down would result in a 10-dB ceiling in measured RL.

A form of uncorrelated noise (in the ADVENT99 data case only) was quantization noise. Another contender is rattling or knocking of hydrophones in their oil-filled pipe. The latter was found on several occasions and it has been possible to find, at one site (New Jersey Shelf), a morning with intermittent knocking [multichannel time series in Fig. 11(a)] and an afternoon without [Fig. 11(b)]. The surprising finding is that, although the noise directionality has changed between morning and afternoon, this degree of interference makes no visible difference to the corresponding derived reflection loss; Fig. 12 shows the equivalent of Fig. 10(a) but with knocking. Evidently, although the raw noise time series looks severely contaminated in the morning, the added absolute power is insignificant.

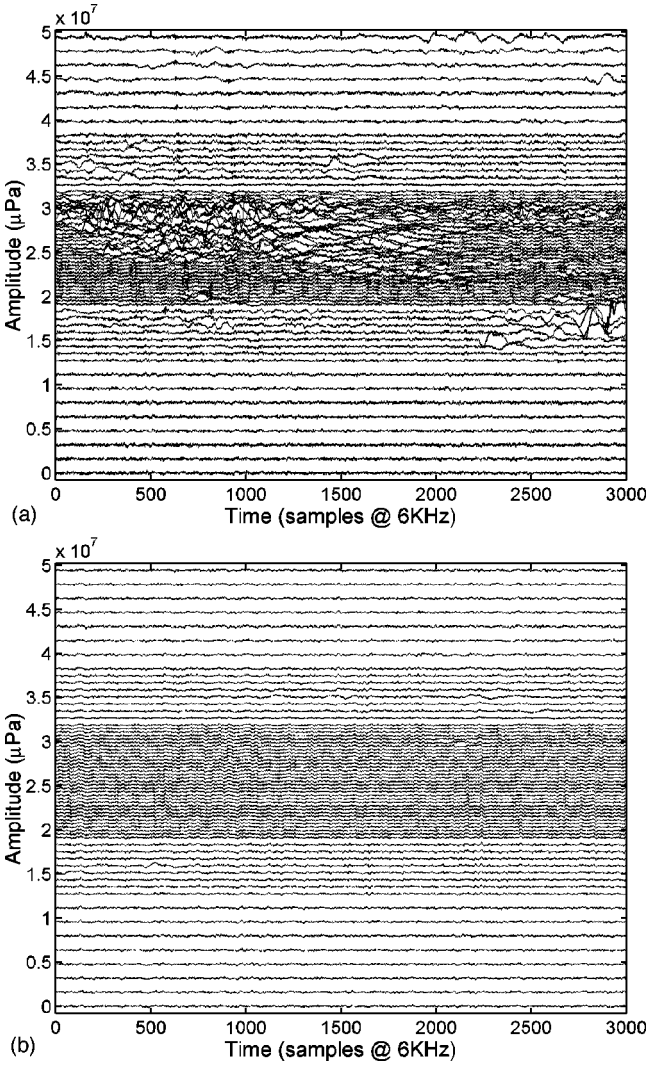

FIG. 11. (a) Complete 64 channels of time series (AM, 17-05-01) showing poor quality data with sound emanating from points on the array. Vertical channel separation is proportional to hydrophone separation. (b) Complete 64 channels of time series (PM, 17-05-01) showing good quality data.

V. DISCUSSION OF PERFORMANCE

A. Strengths

The experimental data demonstrate a number of strengths of the noise inversion method.

(i) No sound source is required.
(ii) No propagation or noise model is required.
(iii) The method tolerates unknown source distributions and noise directionality. It is self-compensating.
(iv) The method tolerates distant point sources and ships.
(v) The method tolerates refracting environments.
(vi) The method tolerates range-dependent environments.
(vii) In contrast with most other inversion methods, high-frequency performance is good.
(viii) The method explicitly shows the critical angle and an indication of the number of layers; one can distinguish by eye between one, two, and more than two bottom layers. Therefore, it is possible to isolate by hand the sound speed and thickness in the top few layers. The depth of modulation is controlled by the relative strengths of the boundary reflections, i.e., their impedance mismatches, so, having fixed the sound speeds one can determine the densities.
(ix) The method is tolerant to poor data quality.

An interesting question is, if the bottom loss varies with position, does this method measure a spatial average bottom loss or is it spatially biased? Ray theory (see the Appendix) suggests that the crucial bottom area is quite near to the receiver. In fact, it should be in the vicinity of the first bottom bounce which, of course, is a function of angle. This hypothesis has been confirmed by conducting a numerical experiment with a range-dependent wave model in which a variable size area beneath the array has distinguishable reflection properties from more distant points (Harrison and Baldacci, 2002). The corollary is that a drifting array could use this method to survey spatial bottom variations. Indeed,

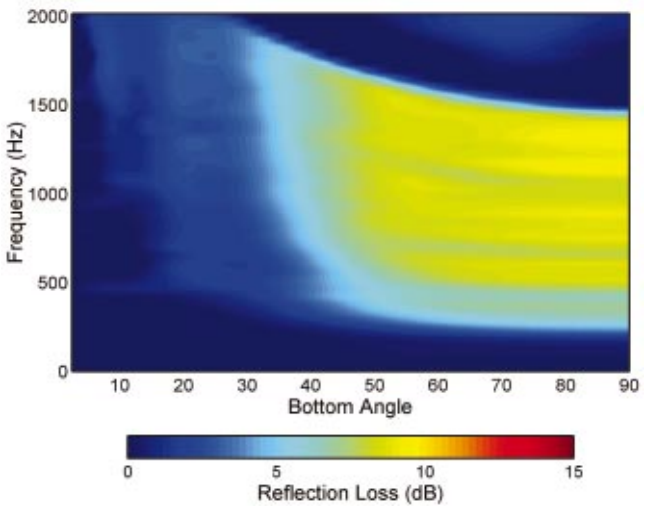

FIG. 12. Reflection loss deduced from the up-to-down ratio of the beams from the VLA at the New Jersey Shelf ''stiff clay'' site but using *poor quality data* as shown in Fig. 11(a). Note that differences between this and the good quality data result [Fig. 10(a)] are barely perceptible.

this drift technique has been tried in a recent experiment (BOUNDARY2002, April 2002, unpublished), again using the 16-m central part of the VLA. Convincing bottom changes were seen during a several mile drift.

B. Analysis issues

1. Random errors

Assessing the impact of errors quantitatively is a difficult problem, and the purpose of Harrison and Baldacci (2002) was to investigate some of these problems by numerical simulation. Among the problems discussed elsewhere in this paper are: addition of uncorrelated noise to the hydrophones; deviation of the array from the vertical; sidelobe leakage in the presence of powerful directional sources; errors in up–down ratio for small angles where low losses are expected; resolvable eigenrays from nearby shipping.

2. Systematic errors

Two effects are obvious in all the comparisons between experimental and modeled reflection loss (including the OASR, OASN pair in Fig. 2). One is that, inevitably, at angles as small as the beam resolution the up-to-down ratio tends to unity. Thus, there is a predictable region near horizontal where the result is anomalous. The region gets wider as frequency lowers, but improvements are possible either by using techniques such as adaptive beamforming or by increasing the aperture. Another effect that depends on hydrophone separation rather than array size is the onset of a grating lobe at the design frequency. This typically results in anomalously low reflection loss.

3. Inversion problems

Even given an error-free measurement of (power) reflection loss, the geoacoustic properties that result from inversion are not necessarily unique. This is common and well known with many inversion techniques, and the usual solution is to introduce constraints on the magnitudes and behavior of the physical parameters. An additional weakness in the noise case is that we have lost all *absolute* phase information, although we have retained some *relative* phase information in the form of the interference fringes. If we were to Fourier transform a complex (frequency-dependent) reflection coefficient we would, in principle, obtain an impulse response of the layers akin to standard geophysical displays [see the ''move-out'' technique in Holland and Osler (2000)]. The inversion ambiguity would therefore be the same as for those techniques. If, on the other hand, we Fourier transform the modulus square of the reflection coefficient we would obtain the autocorrelation function of the impulse response. Thus, layer spacing information is still there but it is mixed up to the extent that one cannot distinguish the order of, say, a thick layer and a thin layer. Nevertheless, even with a power reflection coefficient, the evident critical angle, intensity contrast, and fringe separation mean that sound speed, impedance mismatch, and layer thicknesses are fairly well determined as long as we assume a reasonably small number of layers.

C. Experimental issues

In general, there are a number of experimental issues.

1. Requirement for a VLA

It is true that the existing experimental arrangement using a 62-meter VLA is cumbersome and expensive. However, the aperture used in all the cases shown here is only 15.5 meters (32 elements @ 0.5-m separation), and one could contemplate two alternatives. One is an expendable VLA that is left to drift in much the same way as a sonobuoy. The other is a drifting or moored synthetic aperture, where one hydrophone is fixed in depth and the other moves up and down. In this way one could obtain vertical coherence, or rather, cross-spectral density for all necessary separations as required by Eq. (9).

2. Up–down beamforming contrast

Although the interference patterns seen in the experimental curves resemble those seen in theory, the theoretical reflection loss curves often contain taller spikes. This effect is, of course, highlighted by displaying in dBs, but there are various possible causes that could, in principle, be serious. Possibilities include addition of nonacoustic noise (electrical, quantization) or uncorrelated noise (strumming, knocking) or poor beamforming (incorrect assumptions on hydrophone gain, hydrophone separation or location, poor angle discrimination, poor knowledge of sound-speed profile). Most can be checked by inspection of ω-K plots, intensity histograms of individual channels, or the cross-spectral density matrix near the diagonal.

3. Array tilt

Even if the tilt is known, it is difficult to compensate mathematically without knowing the horizontal noise source distribution—but to know this defeats the object of this method, i.e., simplicity. Therefore, we need to make sure that the tilt stays inside some bounds set by the array's angle

resolution. However, fortuitously, when the resolution is poor (for low frequencies and steep angles) the reflection loss varies slowly with angle. This is no coincidence; the former depends on the *vertical* scale of the array, whereas the latter depends on the *vertical* scale of the layers. In fact, a glance at any of the reflection loss plots shows relatively gradual changes with angle, so that a tilt-induced spread of a few degrees cannot produce significant effects (Harrison and Baldacci, 2002).

4. Low-angle (near-horizontal) data

In this approach the reflection loss for very small angles depends on small differences between large quantities. It is therefore intrinsically unreliable. The true reflection loss must tend to zero at 0° so one could, perhaps, make use of this fact and loss values just inside the critical angle to deduce the absorption of the top sediment layer.

VI. CONCLUSIONS

A simple technique for extracting geoacoustic parameters from ambient noise measurements has been proposed and demonstrated with experimental data. Unlike coherence-based methods that use a hydrophone pair, this technique does not require a noise model. It can therefore still work when the noise directionality and bathymetry are unknown. The workable frequency range is determined by the array design frequency at high frequency, where grating lobes spoil the up-to-down beam ratio, and by its angle resolution at low frequency. In practical systems this complements conventional active inversion techniques where sound-speed fluctuations impede model matching at high frequencies (Siderius *et al.*, 2001).

A theoretical justification was given in terms of acoustic flux and also ray theory. This was supported by the results of a separate numerical study, using the wave models OASN and OASR, in which there was close agreement between the up-to-down beam ratio and the hypothesised ''true'' plane wave bottom loss.

A major point of the paper is that there are very clear variations from site to site that are unaffected by temporal changes in noise directionalities at those sites. In addition, the reflection loss interference patterns can be simply modeled with parameters close to those already found in other studies for the same sites. So far, the hand-searching technique has relied on inspecting the experimental plot for critical angle, fringe spacing, and depth of modulation to find a solution. It is felt that the method is now ripe for an automated search.

The method appears to be robust against most common forms of experimental data contamination except, of course, for absence of wind.

ACKNOWLEDGMENTS

The authors would like to thank the Captain and crew of RV ALLIANCE and the chief scientists on the three cruises: Jorgen Sellschopp (ADVENT99), Martin Siderius (MAPEX2000bis), and Charles Holland (BOUNDARY2000) for making time available for these experiments. Particular thanks are due to Martin Siderius and Charles Holland for help in choosing sites. The first author acknowledges a conversation with David Chapman, Defense Research Establishment Atlantic (DREA), on this technique long before having the opportunity to do experiments.

APPENDIX: REFLECTION LOSS RELATION TO NOISE DIRECTIONALITY IN A RANGE-DEPENDENT ENVIRONMENT

Here, we choose a ray approach in order to allow for spatially varying environments and source distributions as already been developed by Harrison (1997a). Given a noise directionality $N(\phi,\theta)$ (a function of elevation angle θ and azimuth ϕ) and the vertical array's beam pattern $B(\theta,\theta_o)$ for each steer angle θ_o, the array response $A(\theta_o)$ is given by

$$A(\theta_o)=\int\int N(\phi,\theta)B(\theta,\theta_o)\cos\theta\, d\theta\, d\phi. \tag{A1}$$

In a range-dependent environment the directionality $N(\phi,\theta)$ can be expressed as two multiplicative terms [Harrison (1997a)]; in the equivalent formula for coherence the beam pattern is simply replaced by a phase term

$$N(\phi,\theta)=Q(\theta)F(\phi,\theta). \tag{A2}$$

The function F is generally a complicated function of bathymetry, sound speed, and noise source distribution including multiple arrivals for each angle, although under certain conditions it can still be expressed in closed form [Harrison (1997a)]. For instance, it is a geometric series in a range-independent environment. The function Q is simply

$$\begin{aligned} Q(\theta)&=\exp(-as_p), \quad \theta\geqslant 0\\ &=R_b(\theta_b)\exp(-a(s_c-s_p)), \quad \theta<0, \end{aligned} \tag{A3}$$

where $R_b(\theta_b)$ is the local (within one ray cycle of the receiver) bottom (power) reflection coefficient, and θ_b is related by Snell's law to θ at the receiver. The exponential terms represent, respectively, the attenuations along the residual parts of the ray directly from the surface (s_p) and directly from the bottom (s_c-s_p). If we could access the directionality itself, dividing the downward N by the upward N, we would eliminate the function F, leaving

$$\frac{N(\phi,-\theta)}{N(\phi,+\theta)}=\frac{Q(-\theta)}{Q(+\theta)}=R_b(\theta_b)\exp(-a(s_c-2s_p)). \tag{A4}$$

Since this is true for all azimuths ϕ, it is also true for the azimuth integral $\int N(\phi,\theta)d\phi$. Assuming that the effects of absorption over one ray cycle are small, we obtain

$$\frac{\int N(\phi,-\theta)d\phi}{\int N(\phi,+\theta)d\phi}=R_b(\theta_b). \tag{A5}$$

Given appropriate angular resolution in Eq. (A1), we can actually measure R_b as a function of θ and hence θ_b, since the beam response tends to the noise directionality N.

From the ray point of view the reason for this simplicity, despite inclusion of spatial variation of the environment and noise source distribution, can be seen as follows. Imagine a distant point noise source from which a single ray extends,

after multiple surface and bottom reflections, to the receiver. For every such ray arriving directly (i.e., most recently) from the surface, there is a corresponding ray arriving from the seabed with exactly one extra bottom reflection, the same number of surface reflections, and almost the same horizontal wave number. Provided the environment changes only slowly over one ray cycle, the slight shifts in position of reflection points have no effect. So, all distant point sources, regardless of their strength, will appear weaker by $R_b(\theta_b)$ for downward θ than for upward θ. In addition, we can relax the ''distant source'' condition provided the source distribution is close to uniform as in the subsequent part of Harrison (1997a). The reasoning here is that with a sheet source there is no geometric spreading (it cancels out), so the only difference between an upgoing and a downgoing ray at exactly the same angle is the nearby bottom reflection. The same argument applies even if there have been several ray cycles between the surface source and the receiver.

In order to simulate the effects of beamforming on the directionality [see Eq. (A1)] we note that, in the case where the noise sources are uniformly distributed dipoles and the environment is independent of range, the function F in Eq. (A2) reduces to

$$F(\phi,\theta)=\sin\theta_s/[1-R_s(\theta_s)R_b(\theta_b)\exp(-as_c)], \quad \text{(A6)}$$

with R_s and θ_s being surface loss and surface angle, respectively. We can therefore estimate the array response using Eqs. (A1) and (A2) knowing the beam pattern (from the array dimensions). Dividing downward by upward array response, we obtain the ratio of beam responses $\Re$, which is an approximation to R_b

$$\frac{A(-\theta_o)}{A(+\theta_o)}=\Re(\theta_b(\theta_o)). \quad \text{(A7)}$$

We note that, although F does not truly cancel out, its influence on the ratio $\Re(\theta_b(\theta_o))$ is weak. Therefore, we assume that an estimate of F under the ideal conditions of a uniform noise source distribution, as in Eq. (A6), will suffice.

Akal, T., Gehin, C., Matteucci, B., and Tonarelli, B. (**1972**). ''Measured and computed physical properties of sediment cores: Island of Elba zone,'' SACLANT ASW Research Centre, La Spezia, Italy, Special Report No. M-82.

Aredov, A. A., and Furduev, A. V. (**1994**). ''Angular and frequency dependencies of the bottom reflection coefficient from the anisotropic characteristics of a noise field,'' Acoust. Phys. **40**, 176–180.

Buckingham, M. J., and Jones, S. A. S. (**1987**). ''A new shallow-ocean technique for determining the critical angle of the seabed from the vertical directionality of the ambient noise in the water column,'' J. Acoust. Soc. Am. **81**, 938–946.

Caiti, A., Ingenito, F., Kristensen, A., and Max, M. D. (**1996**). ''Geoacoustic models for selected shallow water areas,'' SACLANT ASW Research Centre, La Spezia, Italy, Report No. SM-305.

Caiti, A. (**1996**). ''Geoacoustic seafloor exploration with a towed array in a shallow water area in the Strait of Sicily,'' IEEE J. Ocean. Eng. **21**, 355–366.

Carbone, N. M., Deane, G. B., and Buckingham, M. J. (**1998**). ''Estimating the compressional and shear wave speeds of a shallow-water seabed from the vertical coherence of ambient noise in the water column,'' J. Acoust. Soc. Am. **103**, 801–813.

Chapman, D. (**1988**). ''Surface-generated noise in shallow water: A model,'' Proceedings of (UK) I.O.A. Conference **9**, 1–11.

Gingras, D. F., and Gerstoft, P. (**1995**). ''Inversion for geometric and geoacoustic parameters in shallow water: Experimental results,'' J. Acoust. Soc. Am. **97**, 3589–3598.

Goff, J. A., Swift, D. J. P., Duncan, C. S., Mayer, L. A., and Hughes-Clarke, J. (**1999**). ''High-resolution swath sonar investigation of sand ridge, dune, and ribbon morphology in the offshore environment of the New Jersey margin,'' Mar. Geol. **161**, 307–337.

Hamilton, E. L. (**1980**). ''Geoacoustic modeling of the sea floor,'' J. Acoust. Soc. Am. **68**, 1313–1340.

Hamilton, E. L. (**1987**). ''Acoustic properties of sediments,'' in *Acoustics and Ocean Bottom*, edited by A. Lara-Saenz, C. Ranz-Guerra, and C. Carbo-Fite (F.A.S.E. Conference, Madrid).

Harrison, C. H. (**1996**). ''Formulas for ambient noise level and coherence,'' J. Acoust. Soc. Am. **99**, 2055–2066.

Harrison, C. H. (**1997a**). ''Noise directionality for surface sources in range-dependent environments,'' J. Acoust. Soc. Am. **102**, 2655–2662.

Harrison, C. H. (**1997b**). ''CANARY: A simple model of ambient noise and coherence,'' Appl. Acoust. **51**, 289–315.

Harrison, C. H., and Simons, D. G. (**2001**). ''Geoacoustic inversion of ambient noise: A simple method,'' Conference on ''Acoustical Oceanography,'' Southampton, UK, 9–12 April 2001, edited by T. G. Leighton, Proc. Inst. of Acoust. **23**, 91–98.

Harrison, C. H., Brind, R., and Cowley, A. (**2001**). ''Computation of noise directionality, coherence, and array response in range-dependent media with CANARY,'' J. Computational Acoust. **9**, 327–345.

Harrison, C. H. (**2001**). ''Noise measurements during MAPEX2000,'' SACLANT ASW Research Centre, La Spezia, Italy, Report No. SM-391.

Harrison, C. H., and Baldacci, A. (**2002**). ''Bottom reflection properties deduced from ambient noise: Simulation of a processing technique,'' SACLANT ASW Research Centre, La Spezia, Italy, Report No. SM-392.

Holland, C. W., and Osler, J. (**2000**). ''High-resolution geoacoustic inversion in shallow water: A joint time- and frequency-domain technique,'' J. Acoust. Soc. Am. **107**, 1263–1279.

Jensen, F. B. (**1974**). ''Comparison of transmission loss data for different shallow water areas with theoretical results provided by a three-fluid normal-mode propagation model,'' in *Sound Propagation in Shallow Water*, edited by O. F. Hastrup and O. V. Olesen, Conference Proceedings CP-14 (SACLANT ASW Research Centre, La Spezia, Italy), pp. 79–92.

Jensen, F. B., Kuperman, W. A., Porter, M. B., and Schmidt, H. (**1994**). *Computational Ocean Acoustics* (AIP, New York), pp. 46, 50, 52, 54, 521.

Max, M. D., Fawcett, J., Hollett, R., Thomason, R., and Berkson, J. M. (**2000**). ''Acoustic propagation and geoacoustic models for the Ragusa and West Malta Plateau geoacoustic terranes off SE Sicily,'' SACLANT ASW Research Centre, La Spezia, Italy, Report No. SM-337.

Murphy, E. L., and Olesen, O. V. (**1974**). ''Broadband sound-propagation trials in shallow water near the island of Elba,'' SACLANT ASW Research Centre, La Spezia, Italy, Report No. SM-39.

Murphy, E. L., Wasiljeff, A., and Jensen, F. B. (**1976**). ''Frequency-dependent influence of the sea bottom on the near-surface sound field in shallow water,'' J. Acoust. Soc. Am. **59**, 839–845.

Nagl, A., Uberall, H., and Hoover, W. R. (**1982**). ''Resonances in acoustic bottom reflection and their relation to the ocean bottom properties,'' IEEE Trans. Geosci. Remote Sens. **GE-20**, 332–337.

Schmidt, H. (**1999**). ''OASES: Version 2.2. User's Guide and Reference Manual,'' Dept. of Ocean Engineering, Massachusetts Inst. of Technology. Obtained via http://acoustics.mit.edu/arctic0/henrik/www/oases.html

Siderius, M., Nielsen, P. L., Sellschopp, J., Snellen, M., and Simons, D. (**2001**). ''Experimental study of geo-acoustic inversion uncertainty due to ocean sound-speed fluctuations,'' J. Acoust. Soc. Am. **110**, 769–781.

Siderius, M., Nielsen, P., and Gerstoft, P. ''Range-dependent seabed characterization by inversion of acoustic data from a towed array,'' J. Acoust. Soc. Am. (to be published).

Snellen, M., Simons, D., Siderius, M., Sellschopp, J., and Nielsen, P. L. (**2001**). ''An evaluation of the accuracy of shallow water matched field inversion results,'' J. Acoust. Soc. Am. **109**, 514–527.

Tonarelli, B., Turgutcan, F., Max, M. D., and Akal, T. (**1993**). ''A comparison of shallow sediment properties in four locations on the Sicilian–Tunisian platform,'' SACLANT ASW Research Centre, La Spezia, Italy, Report No. SM-267.

Troiano, L., Guerrini, P., and Barbagelata, A. (**1995**). ''SACLANTCEN towed and vertical array system characteristics,'' SACLANT ASW Research Centre, La Spezia, Italy, Special Report No. M-117.

Effects of incoherent and coherent source spectral information in geoacoustic inversion

Stan E. Dosso[a] and Michael J. Wilmut
School of Earth and Ocean Sciences, University of Victoria, Victoria, British Columbia V8W 3P6, Canada

(Received 25 January 2002; revised 17 June 2002; accepted 9 July 2002)

This paper examines the effect on matched-field geoacoustic inversion of including source spectral information, as can be available in controlled-source acoustic surveys. Source information can consist of relative or absolute knowledge of the source amplitude and/or phase spectra, and can allow frequency-coherent processing of spatial acoustic-field data. A number of multi-frequency acoustic processors, appropriate for specific types of source information, are defined based on the likelihood function for complex acoustic-field data with Gaussian noise. The information content of the various processors is quantified in terms of marginal probability distributions and highest-probability density intervals for the unknown geoacoustic and geometric parameters, which define the accuracy expected in inversion. Marginal distributions are estimated using a fast Gibbs sampler approach to Bayesian inversion, which provides an efficient, unbiased sampling of the multi-dimensional posterior probability density. The analysis is illustrated for incoherent and coherent processors corresponding to several types of source knowledge ranging from complete information to no information, and the results are considered as a function of the spatial and frequency sampling of the acoustic fields. © *2002 Acoustical Society of America.*
[DOI: 10.1121/1.1502897]

PACS numbers: 43.30.Pc, 43.60.Pt [WLS]

I. INTRODUCTION

Determining seabed geoacoustic properties from measured ocean acoustic fields represents a challenging nonlinear inverse problem which has received a great deal of attention in recent years, e.g., Refs. 1–21. Most commonly, an optimization approach known as matched-field inversion (MFI) has been applied. MFI assumes a bounded search space for a discrete model $\mathbf{m}$ of unknown geoacoustic and geometric parameters, and minimizes an error function (processor) $E(\mathbf{m})$ that quantifies the mismatch between measured and modeled acoustic fields. A wide range of algorithms have been applied to this minimization, including iteratively refined grid search methods,[1–3] global search methods such as simulated annealing[4–7] and genetic algorithms,[8–11] and hybrid inversions.[12–16] However, considerably less effort has been applied to the problem of evaluating the information content of the processor that is minimized.

Most applications of MFI to date have been based on the information contained in the spatial coherence of the complex acoustic field across an array of sensors at a single frequency, or on spatial information summed incoherently across a number of frequencies. This approach requires no knowledge of the source spectrum, similar to incoherent matched-field processing (MFP) approaches to passive source localization,[22,23] where the properties of the unknown acoustic source are often unavailable. However, geoacoustic surveys often make use of a controlled acoustic source, and hence it is reasonable to examine MFI approaches that exploit source knowledge (e.g., from a calibrated source or *in situ* recordings of source transmissions at an adjacent sensor) to quantify the possible improvement in constraining geoacoustic parameters.

Source information can consist of absolute or relative knowledge of the transmitted amplitude and/or phase spectrum, with knowledge of both allowing frequency-coherent processing of spatial acoustic-field data. The most common approach to coherent processing consists of applying the Bartlett or linear processor (defined in Sec. II) to augmented data and replica vectors formed by concatenating the spatial field measurements at the constituent frequencies, as first suggested for MFP localization by Tolstoy.[24] This approach implicitly requires knowledge of the relative amplitude and phase spectra (i.e., the amplitude and phase are known to within a frequency-independent scaling and phase shift, respectively). Several approaches have been developed to overcome this requirement for coherent MFP localization. Michalopoulou and Porter[25] and Michalopoulou[26] normalized the fields and removed the phase differences by rotating the fields at each frequency to a common phase at the first sensor. Orris *et al.*[27] treated the relative phases between frequencies as additional unknowns in the localization problem, which was solved using simulated annealing optimization. Approaches such as these allow coherent localization of an unknown source, albeit with reduced information content compared to coherent processing with explicit source knowledge.

Coherent geoacoustic inversion has been considered by several authors. Taroudakis and Markaki[10] compared incoherent and coherent Bartlett processors (assuming relative spectral knowledge) for several noise-free synthetic test cases, with results that did not clearly favor either processor. Michalopoulou[3] carried out geoacoustic inversion using time-domain matching of the ocean waveguide impulse re-

[a]Electronic mail: sdosso@uvic.ca

sponse. Hermand[17] used a similar approach, inverting broadband data at both a vertical array and at single sensors with excellent results. Time-domain matching typically applies knowledge of source phase, at least to within a linear shift (to account for an unknown source instant), which can be searched for independently as the lag-time of a cross-correlation function.

This paper seeks to quantify the effects of including explicit source spectral information of various types in geoacoustic inversion. To this end, a variety of acoustic processors, appropriate for specific types of spectral information, are defined using a maximum-likelihood approach, as suggested by Mecklenbräuker and Gerstoft.[18] A total of nine likelihood-based processors are derived here, with their applicability depending on the following two factors: (i) whether the source amplitude spectrum is known absolutely, is known to within a frequency-independent scaling, or is unknown at each frequency, and (ii) whether the source phase spectrum is known absolutely, is known to within a frequency-independent phase shift, or is unknown at each frequency. The two cases in which the amplitude and phase spectra are both unknown or are both known in a relative sense lead to the incoherent or coherent Bartlett processors, respectively.

The various spectral processors are compared here using a Bayesian approach to quantifying their geoacoustic information content. In Bayesian inversion,[28–31] the solution is characterized in terms of the posterior probability density (PPD) for the unknown parameters, which combines data information with available prior information. Data information is expressed in terms of a likelihood function, with different likelihood functions resulting for different types of spectral knowledge. The information for individual geoacoustic parameters is examined here in terms of marginal probability distributions and highest-probability density intervals, which define the accuracy expected in inversion. This analysis provides a quantitative measure of the effect of including source information of various types on geoacoustic parameter uncertainties.

Gerstoft[8] and Gerstoft and Mecklenbräuker[11] first applied a Bayesian formalism to geoacoustic inversion, using a genetic-algorithms-based approach to sample the PPD during MFI. Dosso[20] developed a fast Gibbs sampler (FGS) approach, which was validated by comparison with exhaustive methods for several benchmark test cases. When sampled to convergence, the marginal distributions were found to generally have simple, smooth forms that facilitate straightforward comparisons for different cases. Moreover, marginal distributions for measured data were found to agree well with those for synthetic test cases,[21] illustrating that simulations can provide a meaningful evaluation of practical cases. The FGS approach is applied here to examine various spectral processors; a similar approach was used to investigate the effects of experimental and propagation modeling factors in Refs. 32 and 33, respectively.

The goal of this paper is to develop a Bayesian approach to quantify the geoacoustic information that results from incorporating different types of source information. The approach is illustrated using a benchmark-standard test case[19] and considered as a function of the spatial and frequency sampling of the acoustic fields (i.e., the number of sensors and frequencies employed). The remainder of this paper is organized as follows. Section II derives the likelihood-based processors, and briefly describes the theory and computational approach to estimating the corresponding marginal distributions for geoacoustic parameters. Section III presents a number of examples of the analysis considering several processors, including those containing no source information (incoherent processing), relative source information (coherent processing), and absolute source information. Finally, Sec. IV summarizes and discusses this work.

II. THEORY

A. Likelihood-based acoustic processors

This section derives a set of likelihood-based acoustic processors[18] corresponding to different possible states of source knowledge. Consider complex acoustic pressure-field data $\mathbf{d}=\{\mathbf{d}_f, f=1,F\}$ as measured at an array of N spatially-distributed sensors and F frequencies (i.e., $\mathbf{d}_f$ represents a column vector with N elements). Assuming complex, zero-mean, Gaussian-distributed random errors, incoherent across frequency, the data likelihood function is given by

$$L(\mathbf{d}|\mathbf{m})=\frac{1}{\pi^F}\prod_{f=1}^{F}\frac{1}{|\mathbf{C}_f|}\exp\{-[\mathbf{d}_f-\mathbf{d}_f(\mathbf{m})]^\dagger\mathbf{C}_f^{-1}\times[\mathbf{d}_f-\mathbf{d}_f(\mathbf{m})]\}, \tag{1}$$

where $\mathbf{d}_f(\mathbf{m})$ is the replica field for model $\mathbf{m}$ and $\mathbf{C}_f$ is the data covariance matrix at the fth frequency († denotes conjugate transpose). This likelihood function can be written in the form

$$L(\mathbf{d}|\mathbf{m})\propto\exp[-E(\mathbf{m})], \tag{2}$$

where the error function (processor) $E(\mathbf{m})$ is defined

$$E(\mathbf{m})=\sum_{f=1}^{F}[\mathbf{d}_f-\mathbf{d}_f(\mathbf{m})]^\dagger\mathbf{C}_f^{-1}[\mathbf{d}_f-\mathbf{d}_f(\mathbf{m})]. \tag{3}$$

It is convenient to apply the Cholesky decomposition $\mathbf{C}_f^{-1}=\mathbf{L}_f\mathbf{L}_f^\dagger$, and define transformed data $\tilde{\mathbf{d}}_f=\mathbf{L}_f^\dagger\mathbf{d}_f$ and replicas $\tilde{\mathbf{d}}_f(\mathbf{m})=\mathbf{L}_f^\dagger\mathbf{d}_f(\mathbf{m})$. In the transformed space, the errors are uncorrelated spatially, and are complex Gaussian distributed at each sensor with unit standard deviation. Applying the Cholesky decomposition essentially absorbs the data covariance matrix into scaled and rotated data vectors, simplifying the following development (this step is not required, but if omitted the covariance term must be carried through all equations). Note that under the common assumption of spatially independent errors it follows that $\tilde{\mathbf{d}}_f=\mathbf{d}_f/\sigma_f$ and $\tilde{\mathbf{d}}_f(\mathbf{m})=\mathbf{d}_f(\mathbf{m})/\sigma_f$, where σ_f is the standard deviation at the fth frequency. Under the general transformation, Eq. (3) can be written

TABLE I. Maximum-likelihood processors for various states of knowledge of the source amplitude and phase spectra: a—absolute knowledge, r—relative knowledge, u—unknown. S_f refers to the complex source representation used in derivation of processor E.

Amplitude	Phase	S_f	Processor, E
a	a	$\cdots$	$\Sigma_{f=1}^{F}[\lvert\tilde{\mathbf{d}}_f\rvert^2+\lvert\tilde{\mathbf{D}}_f\rvert^2-2\mathcal{R}\{\tilde{\mathbf{d}}_f^\dagger\tilde{\mathbf{D}}_f\}]$ (Absolute processor)
u	u	$A_f e^{i\theta_f}$	$\Sigma_{f=1}^{F}[\lvert\tilde{\mathbf{d}}_f\rvert^2-\lvert\tilde{\mathbf{d}}_f^\dagger\tilde{\mathbf{D}}_f\rvert^2/\lvert\tilde{\mathbf{D}}_f\rvert^2]$ (Incoherent Bartlett)
r	r	$Ae^{i\theta}$	$\Sigma_{f=1}^{F}\lvert\tilde{\mathbf{d}}_f\rvert^2-\lvert\Sigma_f\tilde{\mathbf{D}}_f^\dagger\tilde{\mathbf{d}}_f\rvert^2/\Sigma_f\lvert\tilde{\mathbf{D}}_f\rvert^2$ (Coherent Bartlett)
r	a	A	$\Sigma_{f=1}^{F}\lvert\tilde{\mathbf{d}}_f\rvert^2-\mathcal{R}\{\Sigma_f\tilde{\mathbf{d}}_f^\dagger\tilde{\mathbf{D}}_f\}^2/\Sigma_f\lvert\tilde{\mathbf{D}}_f\rvert^2$
u	a	A_f	$\Sigma_{f=1}^{F}[\lvert\tilde{\mathbf{d}}_f\rvert^2-\mathcal{R}\{\tilde{\mathbf{d}}_f^\dagger\tilde{\mathbf{D}}_f\}^2/\lvert\tilde{\mathbf{D}}_f\rvert^2]$
u	r	$A_f e^{i\theta}$	$\Sigma_{f=1}^{F}\left[\lvert\tilde{\mathbf{d}}_f\rvert^2-\frac{\mathcal{R}\{(\tilde{\mathbf{d}}_f^\dagger\tilde{\mathbf{D}}_f)^2\sqrt{\Sigma_j(\tilde{\mathbf{D}}_j^\dagger\tilde{\mathbf{d}}_j)^2/\Sigma_j(\tilde{\mathbf{d}}_j^\dagger\tilde{\mathbf{D}}_j)^2}\}+\lvert\tilde{\mathbf{d}}_f^\dagger\tilde{\mathbf{D}}_f\rvert^2}{2\lvert\tilde{\mathbf{D}}_f\rvert^2}\right]$
r	u	$Ae^{i\theta_f}$	$\Sigma_{f=1}^{F}\lvert\tilde{\mathbf{d}}_f\rvert^2-(\Sigma_f\lvert\tilde{\mathbf{d}}_f^\dagger\tilde{\mathbf{D}}_f\rvert)^2/\Sigma_f\lvert\tilde{\mathbf{D}}_f\rvert^2$
a	u	$e^{i\theta_f}$	$\Sigma_{f=1}^{F}[\lvert\tilde{\mathbf{d}}_f\rvert^2+\lvert\tilde{\mathbf{D}}_f\rvert^2-2\lvert\tilde{\mathbf{d}}_f^\dagger\tilde{\mathbf{D}}_f\rvert]$
a	r	$e^{i\theta}$	$\Sigma_{f=1}^{F}[\lvert\tilde{\mathbf{d}}_f\rvert^2+\lvert\tilde{\mathbf{D}}_f\rvert^2]-2\lvert\Sigma_{f=1}^{F}\tilde{\mathbf{d}}_f^\dagger\tilde{\mathbf{D}}_f\rvert$

$$E(\mathbf{m})=\sum_{f=1}^{F}\lvert\tilde{\mathbf{d}}_f-\tilde{\mathbf{d}}_f(\mathbf{m})\rvert^2$$
$$=\sum_{f=1}^{F}[\lvert\tilde{\mathbf{d}}_f\rvert^2+\lvert\tilde{\mathbf{D}}_f\rvert^2-2\mathcal{R}\{\tilde{\mathbf{d}}_f^\dagger\tilde{\mathbf{D}}_f\}], \tag{4}$$

where $\mathcal{R}\{\cdot\}$ represents the real part. Equation (4) provides the appropriate error function for the case where the source amplitude and phase spectra are known in an absolute sense at each frequency, and is referred to here as the absolute processor.

In some MFI applications, absolute knowledge of the source spectrum may not be available (e.g., inversion based on sources of opportunity, ambient noise, or explosive charges). In such cases, appropriate acoustic processors can be derived by considering the replica fields as $\tilde{\mathbf{d}}_f(\mathbf{m})=S_f\tilde{\mathbf{D}}_f(\mathbf{m})$ and maximizing the likelihood over S_f, where S_f represents the state of available knowledge (absolute, relative, or unknown) of the complex source strength (amplitude and phase) at frequency f and $\tilde{\mathbf{D}}_f(\mathbf{m})$ is the replica field computed via a numerical propagation model without source information.

Consider first the case where source amplitude and phase are both unknown at each frequency, i.e., $S_f=A_f e^{i\theta_f}$ with A_f and θ_f unknown for $f=1, F$. The appropriate error function is obtained by minimizing E (hence maximizing L) over S_f at each frequency. This procedure is presented in detail in Refs. 11, 18, and 21, and is only summarized here. Substituting $\tilde{\mathbf{d}}_f(\mathbf{m})=A_f e^{i\theta_f}\tilde{\mathbf{D}}_f(\mathbf{m})$ into Eq. (4), setting $\partial E/\partial A_f=0$ and $\partial E/\partial\theta_f=0$, and substituting the resulting solutions for A_f and θ_f back into Eq. (4) leads to

$$E=\sum_{f=1}^{F}\left[\lvert\tilde{\mathbf{d}}_f\rvert^2-\frac{\lvert\tilde{\mathbf{d}}_f^\dagger\tilde{\mathbf{D}}_f\rvert^2}{\lvert\tilde{\mathbf{D}}_f\rvert^2}\right], \tag{5}$$

where the explicit dependence of E and $\tilde{\mathbf{D}}_f$ on $\mathbf{m}$ is suppressed. The term in square brackets in Eq. (5) consists of the standard Bartlett mismatch between measured and replica fields at the fth frequency. The error function consists of an incoherent summation of Bartlett mismatches over frequency, and is referred to here as the incoherent processor.

Next consider the case where the source strength is known from frequency to frequency in a relative sense, but the absolute amplitude and phase are unknown. In this case $S_f=Ae^{i\theta}$, i.e., the unknown amplitude scaling and phase shift are independent of frequency. Minimizing E over A and θ as before leads to

$$E=\sum_{f=1}^{F}\lvert\tilde{\mathbf{d}}_f\rvert^2-\frac{\lvert\Sigma_f\tilde{\mathbf{D}}_f^\dagger\tilde{\mathbf{d}}_f\rvert^2}{\Sigma_f\lvert\tilde{\mathbf{D}}_f\rvert^2}. \tag{6}$$

Equation (6) represents an error function based on a coherent summation over frequency of Bartlett correlations, and is referred to here as the coherent processor. Note that the coherent processor is equivalent to applying the standard Bartlett mismatch to augmented vectors for the data and replica constructed by concatenating the spatial fields at the constituent frequencies.

The geoacoustic information content of the absolute, incoherent, and coherent processors is examined via Bayesian analysis in Sec. III. The absolute processor involves complete knowledge of the source, while the incoherent processor involves no source information. These represent the two extremes of the acoustic processors considered here, with the coherent processor representing an intermediate level of source information. Other processors involving intermediate source information of various types may be appropriate in particular cases. These are derived in a manner similar to that above, and are summarized in Table I, but, for brevity, are not examined in detail in this paper. Several straightforward observations can be made about the processors in Table I. In terms of knowledge of the source amplitude spectrum, when absolute information is available, no scaling of the replica fields $\tilde{\mathbf{D}}_f$ is applied. For relative amplitude information, the replicas are scaled by the frequency-independent factor $\Sigma_f\lvert\tilde{\mathbf{D}}_f\rvert^2$. For unknown amplitudes, the replica at each frequency is normalized by its amplitude (e.g., $\mathbf{D}_f/\lvert\mathbf{D}_f\rvert$). In terms of knowledge of the source phase spectrum, when no information is available, the processors involve summation over the magnitude of complex inner products at each fre-

quency. For relative or absolute phase information, the processors include summation over complex inner products or their real parts (both of which retain phase information). Finally, cases in which both amplitude and phase are known in either an absolute or relative sense lead to frequency-coherent processors (i.e., summation over frequencies can be replaced by augmented data and replica vectors).

B. Bayesian uncertainty analysis via fast Gibbs sampling

This section briefly describes the theory and implementation of the fast Gibbs sampler (FGS) approach to Bayesian geoacoustic inversion used to quantify the information content of likelihood-based acoustic processors. More complete treatments of FGS are available in Refs. 20 and 21, and of Bayesian theory in Refs. 29–31. Let $\mathbf{m}$ and $\mathbf{d}$ represent model and data vectors, respectively, with elements m_i and d_i considered to be random variables. Bayes' rule for conditional probabilities leads to

$$P(\mathbf{m}|\mathbf{d}) \propto L(\mathbf{d}|\mathbf{m}) P(\mathbf{m}), \tag{7}$$

where $P(\mathbf{m}|\mathbf{d})$ represents the PPD, $L(\mathbf{d}|\mathbf{m})$ is the likelihood function, and $P(\mathbf{m})$ is the prior probability distribution. The likelihood function is determined by the form of the data and noise; appropriate likelihood functions for MFI are of the general form $L(\mathbf{d}|\mathbf{m}) \propto \exp[-E(\mathbf{m})]$, as discussed in Sec. II A. Hence, the normalized PPD can be written

$$P(\mathbf{m}|\mathbf{d}) = \frac{\exp[-E(\mathbf{m})] P(\mathbf{m})}{\int_{\mathcal{M}} \exp[-E(\mathbf{m}')] P(\mathbf{m}')\, d\mathbf{m}'}, \tag{8}$$

where the integral is over the multi-dimensional model space $\mathcal{M}$.

To interpret the multi-dimensional PPD requires computation of its integral properties. The properties considered in this paper to characterize parameter uncertainties are marginal probability distributions and highest posterior density (HPD) intervals.[31] The marginal distribution for parameter m_i is defined

$$P(m_i|\mathbf{d}) = \int_{\mathcal{M}} \delta(m_i' - m_i) P(\mathbf{m}'|\mathbf{d})\, d\mathbf{m}', \tag{9}$$

where δ is the Dirac delta function. The α% HPD interval represents the interval of minimum width containing α% of the area of the marginal distribution.

The multi-dimensional integral for the marginal distributions, Eq. (9), can be written in the standard form

$$I = \int_{\mathcal{M}} f(\mathbf{m}') P(\mathbf{m}'|\mathbf{d})\, d\mathbf{m}'. \tag{10}$$

Monte Carlo methods provide a standard approach to such integrals based on a sample of models drawn at random from a uniform distribution over the parameter space. However, if the integrand is concentrated in localized regions of the space, many of these models will not contribute significantly to the integral. The method of importance sampling draws samples from regions that contribute most to the integral, resulting in more efficient sampling. Let $g(\mathbf{m})$ denote the (normalized) sample generating function from which Q samples are drawn; the integral of Eq. (10) can then be written

$$I = \int_{\mathcal{M}} \left[\frac{f(\mathbf{m}') P(\mathbf{m}'|\mathbf{d})}{g(\mathbf{m}')} \right] g(\mathbf{m}')\, d\mathbf{m}' \approx \frac{1}{Q} \sum_{i=1}^{Q} \frac{f(\mathbf{m}_i) P(\mathbf{m}_i|\mathbf{d})}{g(\mathbf{m}_i)}. \tag{11}$$

An effective approach to importance sampling in Bayesian inversion is given by Gibbs sampling (GS) in which the model is perturbed repeatedly, with perturbations accepted if a uniform random number ξ drawn from the interval [0, 1] satisfies the condition

$$\xi \leqslant \exp[-\Delta E/T], \tag{12}$$

where T is a control parameter referred to as temperature. Markov-chain analysis[29,30] indicates that the equilibrium distribution of the GS is given by the Gibbs' distribution

$$P_G(\mathbf{m}) = \frac{\exp[-E(\mathbf{m})/T]}{\Sigma_{\mathcal{M}} \exp[-E(\mathbf{m})/T]}, \tag{13}$$

where the summation over $\mathcal{M}$ represents all possible models. Comparison of $P_G(\mathbf{m})$ of Eq. (13) with $P(\mathbf{m}|\mathbf{d})$ of Eq. (8) indicates that the two are identical at temperature $T=1$ for the case of uniform prior distributions (the standard case in MFI). Therefore, in the limit of a large number of perturbations, GS provides an unbiased sampling of the PPD. Employing GS in importance sampling, the sampling function is $g(\mathbf{m}) = P(\mathbf{m}|\mathbf{d})$, and Eq. (11) becomes

$$I \approx \frac{1}{Q} \sum_{i=1}^{Q} f(\mathbf{m}_i). \tag{14}$$

Accordingly, marginal probability distributions are represented by histograms computed from the sample of models collected by the GS algorithm.

The fast Gibbs sampler (FGS) employed here is based on accelerating standard GS in the following ways.[20] (i) FGS is initiated at high T and cooled rapidly to $T=1$ prior to accumulating the sample to ensure the sampling begins in high-probability regions of the model space. (ii) Standard GS perturbs parameters along the coordinate axes, and can be inefficient for problems involving correlated parameters. FGS overcomes this by applying the perturbations in a rotated model space[6] obtained by an orthogonal transformation that diagonalizes the parameter covariance matrix as estimated from a small initial sampling. (iii) In GS, each parameter perturbation is drawn over the entire parameter bounds, which can result in many large perturbations that are inevitably rejected. In FGS, the maximum perturbation size for each parameter is determined adaptively to apply perturbations of the maximum size accepted with noninfinitesimal probability. The convergence test for FGS involves simultaneously collecting two independent samples of models and intercomparing their cumulative marginal distributions. Convergence is achieved when the maximum difference is suitably small (<0.1), and the final sample is taken to be the union of the two independent samples. The FGS algorithm has been compared to standard GS and Monte Carlo integra-

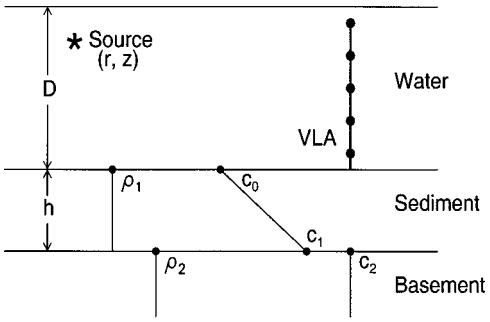

FIG. 1. Unknown geoacoustic and geometric parameters for the benchmark test cases (VLA denotes a vertical line array of sensors).

tion for several benchmark test cases for geoacoustic inversion and found to produce identical results (within the convergence criterion) in orders of magnitude less computation time.[20]

III. PROCESSOR INFORMATION CONTENT

This section applies Bayesian analysis to examine the geoacoustic information content of acoustic processors incorporating varying degrees of source knowledge. The example used here is adopted from the 1997 Geoacoustic Inversion Workshop[19] (Workshop97), which provided synthetic test cases designed to serve as benchmark standards for geoacoustic inversion. The test case, referred to as WA at Workshop97, involves acoustic propagation in a shallow-water environment with a two-layer seabed consisting of a sediment layer over a semi-infinite basement (illustrated in Fig. 1). The case includes a total of nine unknown parameters consisting of three geometric parameters: source range and depth, r and z, and water depth, D, and six seabed parameters: sediment thickness, h, sound speeds at the top and bottom of the sediment layer, c_0 and c_1, sound speed of the basement, c_2, and densities of the sediment and basement, ρ_1 and ρ_2, respectively. The seabed attenuation is fixed at 0.23 dB/wavelength in the WA benchmark case (i.e., not treated as an unknown parameter). The data consist of complex acoustic pressure measurements at a vertical line array of sensors. Although the original benchmark test cases involved accurate data, to simulate meaningful inversions, errors were added to the data for the cases considered here. The data errors were modeled as complex, Gaussian-distributed random variables, incoherent both spatially and across frequencies. A flat spectrum from 20 to 200 Hz was used, and the signal-to-noise-ratio was taken to be SNR$=$10 dB at each frequency, since previous analysis of geoacoustic survey data indicated that this was a reasonable level to represent noise and mismatch error.[21] In addition, the parameter search bounds were taken to be wider than those of the original benchmark case, so that the data information and not the bounds constrain the solution. In the examples presented here, the FGS algorithm typically sampled 20 000–40 000 accepted models for convergence, and required about 8 h of CPU time on a 400-MHz Pentium PC. Replica acoustic fields were computed using the normal-mode model ORCA.[34]

The first case considered involves acoustic data that are well sampled both spatially and with respect to frequency, with measurements at 20 sensors evenly spaced over the water column at 10-Hz intervals from 20 to 200 Hz (i.e., 19 frequencies). The marginal probability distributions for this case are shown in Fig. 2 for the incoherent Bartlett processor

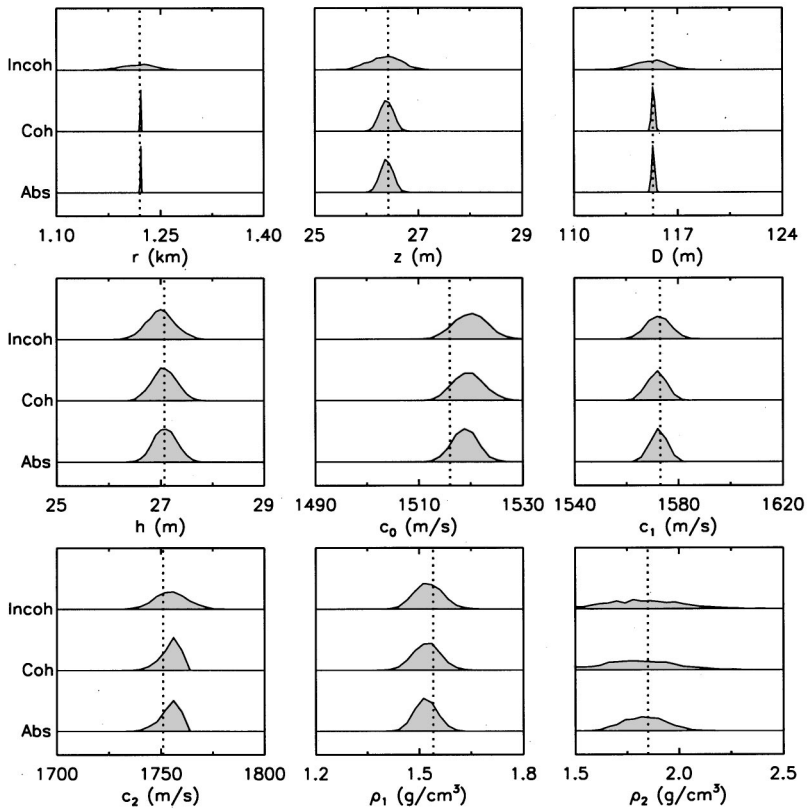

FIG. 2. Marginal probability distributions for acoustic-field measurements at 20 sensors evenly spaced over the water column and 19 frequencies in the band 20–200 Hz for the incoherent, coherent, and absolute processors. Dotted lines indicate true parameter values.

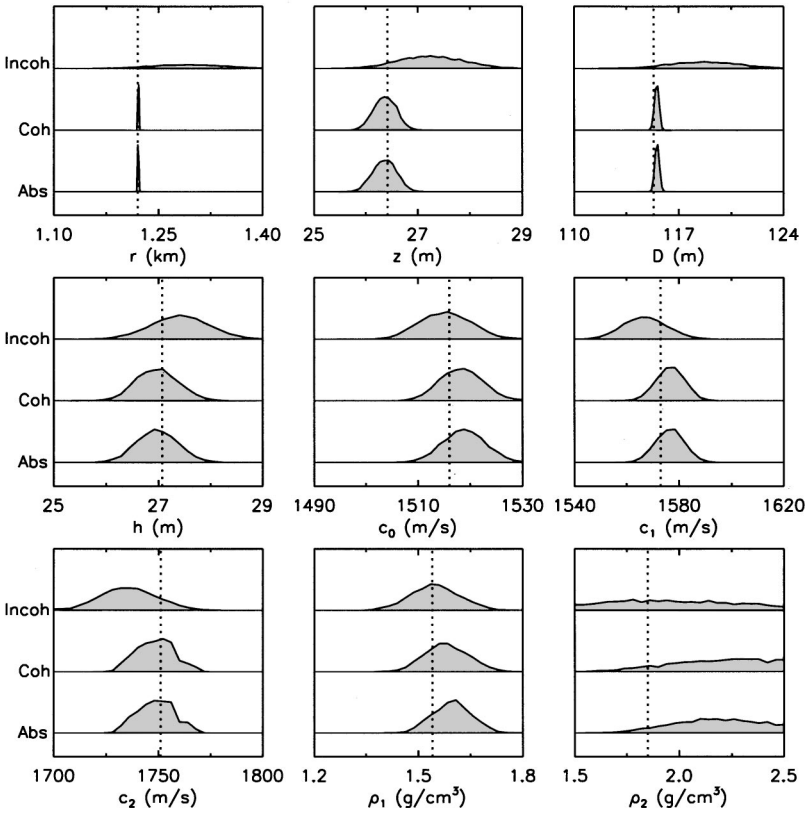

FIG. 3. Marginal probability distributions for acoustic-field measurements at 5 sensors evenly spaced over the water column and 19 frequencies in the band 20–200 Hz for the incoherent, coherent, and absolute processors. Dotted lines indicate true parameter values.

(no source spectral information), coherent Bartlett processor (relative spectral information), and absolute processor (absolute spectral information). In this and subsequent figures, the normalization applied to the distributions for each parameter (i.e., each panel) was chosen for graphical purposes, and is not necessarily the same from parameter to parameter or from figure to figure. However, since the interpretation of parameter uncertainties is based on the relative widths (rather than amplitudes) of the marginal distributions, differing normalizations do not preclude comparisons between parameters or figures (quantitative comparisons are made in terms of HPD intervals, and are not affected by plotting normalizations). The marginal distributions in Fig. 2 are generally unimodal with reasonably smooth and simple forms in each case. Note that since noisy data were inverted, the maxima of the marginal distributions are not necessarily expected to correspond to the true parameter values. Figure 2 shows that including source spectral information has a strong effect for the geometric parameters r, z, and D, with substantially narrower uncertainty distributions obtained for the coherent and absolute processors than for the incoherent processor. The effect of source information on the uncertainties of the six seabed parameters is not as strong, but is still significant for several parameters. Marginal probability distributions computed for similar cases but with reduced spatial sampling (five sensors over the water column) and frequency sampling (five frequencies in the band 20–200 Hz) are shown in Figs. 3 and 4, respectively. The parameter uncertainty distributions obtained in these cases are significantly wider than those in Fig. 2, and in each case the effects of source knowledge are strongest on the geometric parameters.

A more precise comparison of the results for the various processors and for different spatial and frequency samplings can be made in terms of HPD intervals derived from the marginal distributions. In particular, parameter uncertainties are quantified here by the width of the minimum interval containing 95% of the area of the marginal distribution. To examine the relative effects of source spectral information, Fig. 5 compares the width of the 95% HPD intervals for the incoherent, coherent, and absolute processors. This figure shows that smaller uncertainties are obtained for the coherent processor than for the incoherent processor for all parameters and samplings. The uncertainties for the absolute processor are almost always smaller than for the coherent processor, although this difference is typically less pronounced and in several cases an (insignificant) increase is observed. The uncertainty in range r is affected profoundly by source information, with the normalized HPD width for the coherent and absolute processors reduced by a factor of $\sim$400 compared to that for the incoherent processor for all spatial and frequency samplings. The uncertainties in source depth z and water depth D are also strongly affected by source knowledge, with HPD intervals reduced by factors greater than 2 and 10, respectively. As noted previously, the improvements in resolving the seabed parameters that result from source information are typically more modest, with reductions in uncertainty by factors of approximately 1.2–2.4 between the incoherent and coherent processors, and typically smaller improvements between the coherent and absolute processors.

Figure 5 also shows that the finer spatial and frequency sampling (20 sensors, 19 frequencies) leads to significantly smaller uncertainties for all parameters and all processors. In fact, better results for the seabed parameters are usually obtained for incoherent processing of well-sampled fields than

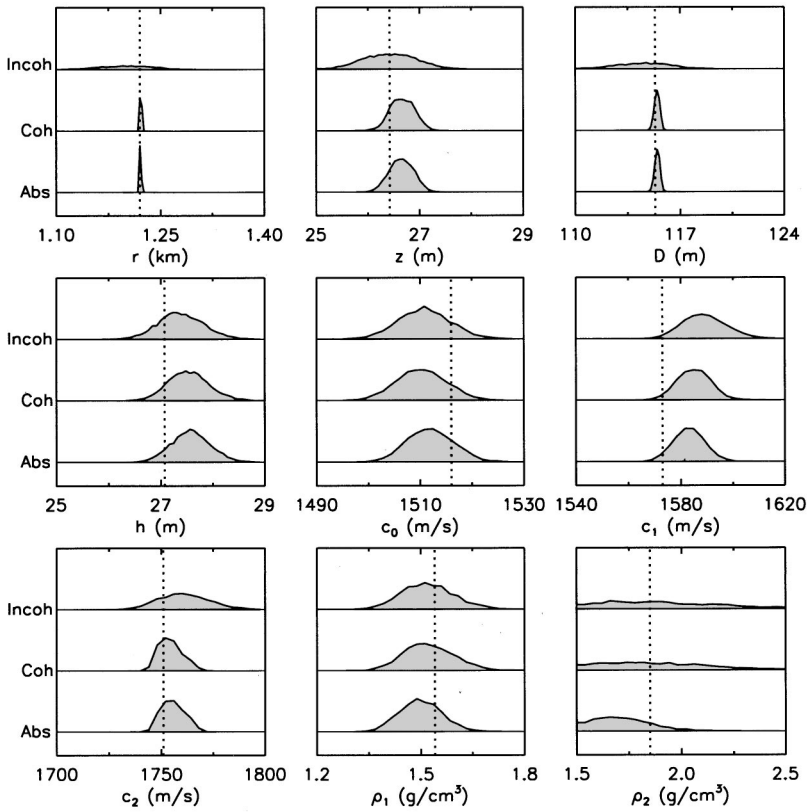

FIG. 4. Marginal probability distributions for acoustic-field measurements at 20 sensors evenly spaced over the water column and 5 frequencies in the band 20–200 Hz for the incoherent, coherent, and absolute processors. Dotted lines indicate true parameter values.

for coherent or absolute processing with poorer sampling in space or frequency. However, for the geometric parameters, coherent and absolute processing yield substantially better results than incoherent processing regardless of the sampling. Figure 5 also shows that, for this test case, whether the largest uncertainties result from reduced sampling in space or frequency varies from parameter to parameter. Improvements in geoacoustic uncertainties by increasing the number of frequencies included in the inversion have been observed previously for measured data by Hermand and Gerstoft[35] and Dosso and Nielsen.[21]

To further consider the effects of spatial and frequency

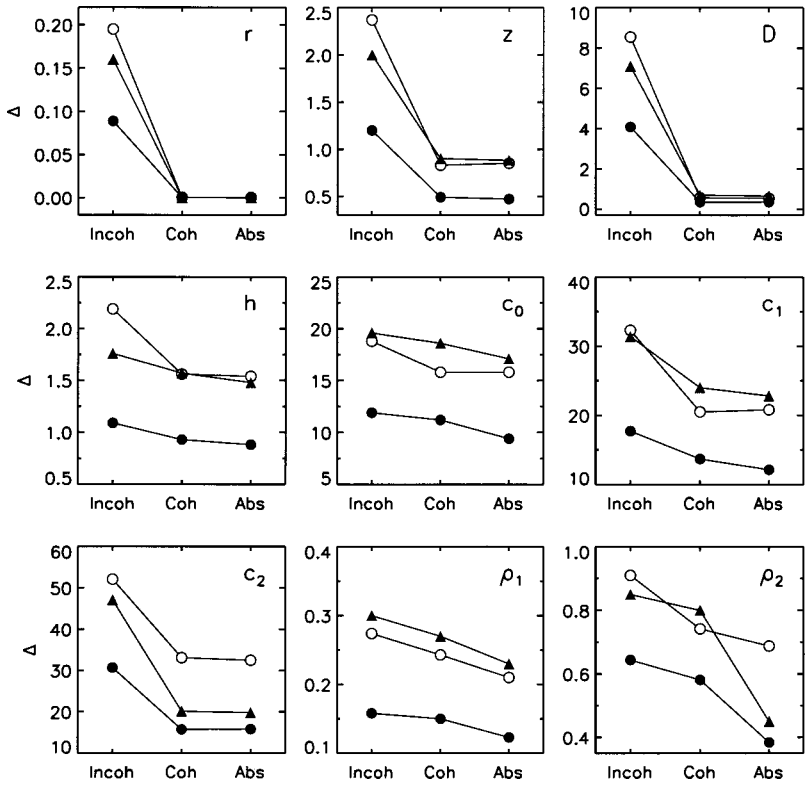

FIG. 5. 95% HPD interval widths Δ for the incoherent, coherent, and absolute processors (parameters have same units as in Figs. 2–4). Solid circles—20 sensors, 19 frequencies; open circles—5 sensors, 19 frequencies; triangles—20 sensors, 5 frequencies.

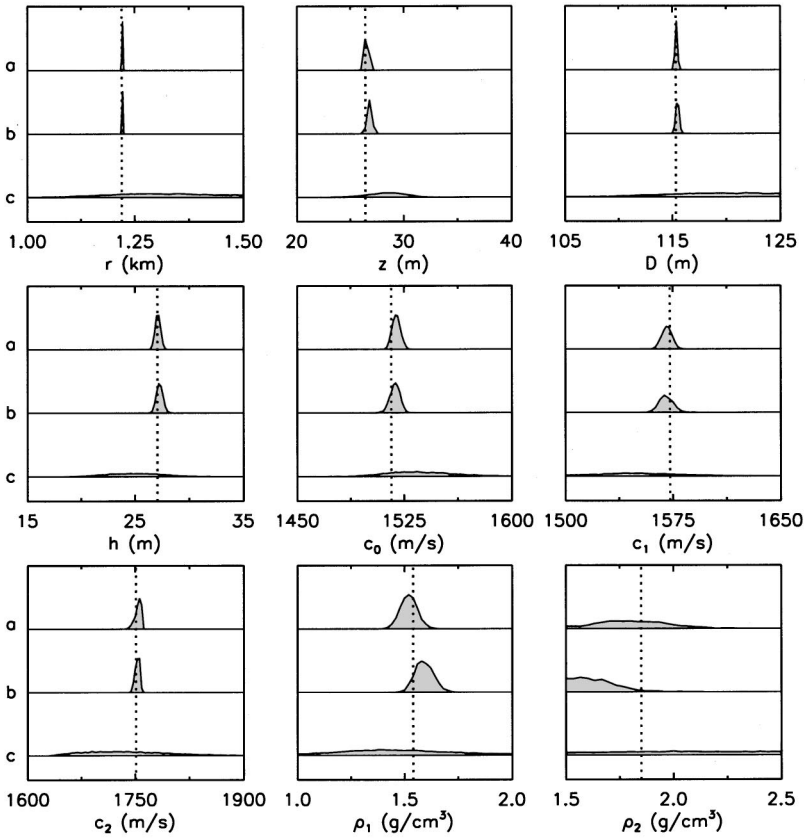

FIG. 6. Marginal probability distributions for the coherent processor with (a) 20 sensors, 19 frequencies; (b) 1 sensor, 101 frequencies, and (c) 20 sensors, 1 frequency. Dotted lines indicate true parameter values.

sampling, Fig. 6 compares the marginal probability distributions computed for the coherent processor for acoustic fields sampled at 20 sensors and 19 frequencies from 20 to 200 Hz (same as in Fig. 2) to those computed for a single sensor and 101 frequencies, and for 20 sensors and a single frequency (100 Hz). Note that the horizontal scales of this figure differ from those of Figs. 2–4 to accommodate wider marginal distributions. The marginal distributions shown in Fig. 6(b) for a single sensor were computed with an interfrequency spacing of 1.8 Hz over 20–200 Hz to approximate the results of broadband or time-domain pulse processing. Marginal distributions for single sensors at a number of different depths were computed and varied slightly; the results shown in Fig. 6(b) were for a sensor located at mid-depth in the water column which provided some of the better results. The marginal distributions in Fig. 6(b) are comparable to those computed for the multi-sensor, multi-frequency case in Fig. 6(a), indicating that geoacoustic and geometric parameters can be well determined using a single sensor, given adequate frequency sampling (i.e., the acoustic-field variation over frequency provides sufficient information content). This conclusion agrees with the analysis of broadband single-sensor MFI for measured data carried out by Hermand.[17] It should be noted, however, that the assumption of independent errors across frequencies will be probably not be satisfied for experimentally measured data with small frequency spacings; hence, the results presented here may be somewhat optimistic. Finally, the marginal distributions shown in Fig. 6(c) for an array of sensors and a single frequency represent a substantial degradation in information content, precluding meaningful estimates for a number of parameters.

IV. SUMMARY AND DISCUSSION

Geoacoustic surveys typically employ controlled acoustic sources; hence, source spectral information can be available to provide additional information in geoacoustic inversion, although this has not commonly been done to date. This paper considered the problem of evaluating the effects of incorporating source spectral information in matched-field geoacoustic inversion. Various types of source information were treated by defining appropriate acoustic processors based on the corresponding likelihood functions for complex acoustic-field data. Nine processors were defined depending on whether the source amplitude and phase spectra are known in an absolute or relative sense or are unknown at each frequency, with both amplitude and phase knowledge leading to frequency-coherent processors. Three processors corresponding to different levels of source knowledge were studied quantitatively. These included the absolute processor which includes complete (absolute) source spectral information, the coherent Bartlett processor which includes relative spectral information, and the incoherent Bartlett processor which involves no source information.

The effect of source knowledge was examined by quantifying the information content of the various processors in terms of marginal probability distributions and highest probability density intervals for the unknown geoacoustic parameters computed using a fast Gibbs sampler approach to Bayesian inversion. The analysis was applied to a benchmark test case involving six unknown seabed parameters and three geometric parameters, with a SNR of 10 dB. Estimation of the geometric parameters was substantially improved by in-

corporating source information (relative or absolute), with HPD-interval widths for the water depth and source range reduced by one and more than two orders of magnitude, respectively. Improvements for the seabed parameters were significant but more modest, with HPD intervals reduced by factors of 1.2–2.4 between the incoherent and coherent processors, and typically smaller improvements between the coherent and absolute processors. Significantly smaller parameter uncertainties were obtained for well-sampled acoustic fields than for fields with reduced sampling in space or frequency. In fact, better results for the seabed parameters were typically obtained for well-sampled fields and incoherent processing than for reduced sampling and coherent or absolute processing; however, the opposite was true for the geometric parameters. Relatively poor results were obtained for acoustic fields sampled at an array of sensors at a single frequency. However, single-sensor coherent processing of fields at a large number of frequencies (approximating broadband analysis) produced good results.

The analysis described in this paper was also applied to the same test case at different SNRs as well as to two other benchmark test cases (denoted SO and AT at Workshop97), with similar results to those presented here. In particular, the AT test case involved sediment and basement attenuation as unknown parameters. The acoustic data were found to be relatively insensitive to the attenuations, which were poorly constrained and showed only modest improvement for coherent or absolute processing.

Finally, it should be noted that the results of studies such as this can be case dependent and could vary somewhat for different geoacoustic models, frequency ranges, noise levels, etc. However, it is believed that the conclusions of this study, summarized above, are generally applicable. In particular, including source spectral knowledge in the form of frequency-coherent processing can significantly reduce the uncertainties of seabed geoacoustic parameters, and substantially improve geometric parameter estimates. Quantitative studies such as this should help guide in designing efficient and effective geoacoustic surveying methods.

[1] A. Tolstoy, ''Using matched-field processing to estimate shallow water bottom properties from shot data taken in the Mediterranean Sea,'' IEEE J. Ocean. Eng. **21**, 471–479 (1996).

[2] A. Tolstoy, ''MFP benchmark inversions via the Rigs method,'' J. Comput. Acoust. **6**, 185–203 (1998).

[3] Z.-H. Michalopoulou, ''Matched-impulse-response processing for shallow-water localization and geoacoustic inversion,'' J. Acoust. Soc. Am. **108**, 2082–2090 (2000).

[4] M. D. Collins, W. A. Kuperman, and H. Schmidt, ''Nonlinear inversion for ocean-bottom properties,'' J. Acoust. Soc. Am. **92**, 2770–2783 (1992).

[5] S. E. Dosso, M. L. Yeremey, J. M. Ozard, and N. R. Chapman, ''Estimation of ocean-bottom properties by matched-field inversion of acoustic field data,'' IEEE J. Ocean. Eng. **18**, 232–239 (1993).

[6] M. D. Collins and L. Fishman, ''Efficient navigation of parameter landscapes,'' J. Acoust. Soc. Am. **98**, 1637–1644 (1995).

[7] M. R. Fallat and S. E. Dosso, ''Geoacoustic inversion for the Workshop97 benchmark test cases using simulated annealing,'' J. Comput. Acoust. **6**, 29–43 (1998).

[8] P. Gerstoft, ''Inversion of seismoacoustic data using genetic algorithms and *a posteriori* probability distributions,'' J. Acoust. Soc. Am. **95**, 770–782 (1994).

[9] M. Siderius, P. Gerstoft, and P. Nielsen, ''Broadband geoacoustic inversion from sparse data using genetic algorithms,'' J. Comput. Acoust. **6**, 117–134 (1998).

[10] M. I. Taroudakis and M. G. Markaki, ''Bottom geoacoustic inversion by 'broadband' matched-field processing,'' J. Comput. Acoust. **6**, 167–184 (1998).

[11] P. Gerstoft and C. F. Mecklenbräuker, ''Ocean acoustic inversion with estimation of *a posteriori* probability distributions,'' J. Acoust. Soc. Am. **104**, 808–819 (1998).

[12] P. Gerstoft, ''Inversion of acoustic data using a combination of genetic algorithms and the Gauss-Newton approach,'' J. Acoust. Soc. Am. **97**, 2181–2190 (1995).

[13] M. R. Fallat and S. E. Dosso, ''Geoacoustic inversion via local, global and hybrid algorithms,'' J. Acoust. Soc. Am. **105**, 3219–3230 (1999).

[14] M. Musil, M. J. Wilmut, and N. R. Chapman, ''A hybrid simplex genetic algorithm for estimating geoacoustic parameters using matched-field inversion,'' IEEE J. Ocean. Eng. **24**, 358–369 (1999).

[15] M. R. Fallat, P. L. Nielsen, and S. E. Dosso, ''Hybrid geoacoustic inversion of broadband Mediterranean Sea data,'' J. Acoust. Soc. Am. **107**, 1967–1977 (2000).

[16] S. E. Dosso, M. J. Wilmut, and A. S. Lapinski, ''An adaptive hybrid algorithm for geoacoustic inversion,'' IEEE J. Ocean. Eng. **26**, 324–336 (2001).

[17] J.-P. Hermand, ''Broad-band geoacoustic inversion in shallow water from waveguide impulse response measurements on a single hydrophone: Theory and experimental results,'' IEEE J. Ocean. Eng. **24**, 41–66 (1999).

[18] C. F. Mecklenbräuker and P. Gerstoft, ''Objective functions for ocean acoustic inversion derived by likelihood methods,'' J. Comput. Acoust. **8**, 259–270 (2000).

[19] A. Tolstoy, N. R. Chapman, and G. H. Brooke, ''Workshop97: Benchmarking for geoacoustic inversion in shallow water,'' J. Comput. Acoust. **6**, 1–28 (1998).

[20] S. E. Dosso, ''Quantifying uncertainty in geoacoustic inversion I: A fast Gibbs sampler approach,'' J. Acoust. Soc. Am. **111**, 129–142 (2002).

[21] S. E. Dosso and P. L. Nielsen, ''Quantifying uncertainty in geoacoustic inversion II: Application to broadband, shallow-water data,'' J. Acoust. Soc. Am. **111**, 143–159 (2002).

[22] A. Tolstoy, *Matched Field Processing for Underwater Acoustics* (World Scientific, Singapore, 1993).

[23] A. B. Baggeroer, W. A. Kuperman, and P. N. Mikhalevsky, ''An overview of matched field methods in ocean acoustics,'' IEEE J. Ocean. Eng. **18**, 401–424 (1993).

[24] A. Tolstoy, ''Computational aspects of matched field processing in underwater acoustics,'' in *Computational Acoustics*, edited by D. Lee, A. Cakmak, and R. Vichnevetsky (North-Holland, Amsterdam, 1990), Vol. 3, pp. 303–310.

[25] Z.-H. Michalopoulou and M. B. Porter, ''Matched field processing for broad-band source localization,'' IEEE J. Ocean. Eng. **21**, 384–392 (1996).

[26] Z.-H. Michalopoulou, ''Robust multi-tonal matched-field inversion: A coherent approach,'' J. Acoust. Soc. Am. **104**, 163–170 (1998).

[27] G. J. Orris, M. Nicholas, and J. S. Perkins, ''The matched-phase coherent multi-frequency matched-field processor,'' J. Acoust. Soc. Am. **107**, 2563–2575 (2000).

[28] A. Tarantola, *Inverse Problem Theory: Methods for Data Fitting and Model Parameter Estimation* (Elsevier, Amsterdam, 1987).

[29] M. K. Sen and P. L. Stoffa, *Global Optimization Methods in Geophysical Inversion* (Elsevier, Amsterdam, 1995).

[30] W. R. Gilks, S. Richardson, and G. J. Spiegelhalter, *Markov Chain Monte Carlo in Practice* (Chapman and Hall, London, 1996).

[31] D. Gamerman, *Markov Chain Monte Carlo: Stochastic Simulation for Bayesian Inference* (Chapman and Hall, London, 1997).

[32] S. E. Dosso and M. J. Wilmut, ''Quantifying data information content in geoacoustic inversion,'' IEEE J. Ocean. Eng. **27**, 296–304 (2002).

[33] S. E. Dosso, ''Benchmarking range-dependent propagation modeling in matched-field inversion,'' J. Comput. Acoust. **10**, 231–242 (2002).

[34] E. K. Westwood, C. T. Tindle, and N. R. Chapman, ''A normal mode model for acousto-elastic ocean environments,'' J. Acoust. Soc. Am. **100**, 3631–3645 (1996).

[35] J.-P. Hermand and P. Gerstoft, ''Inversion of broadband multitone acoustic data from the Yellowshark summer experiments,'' IEEE J. Ocean. Eng. **21**, 324–345 (1996).

A new 1-D integral representation for dynamic response of anisotropic elastic solids due to a point force

Kuang-Chong Wu
Institute of Applied Mechanics, National Taiwan University, Taipei 106, Taiwan

(Received 27 August 2001; revised 24 May 2002; accepted 8 July 2002)

A new 1-D integral is presented for calculating the transient response due to a suddenly applied point force in a general anisotropic solid. The integral is based on a 2-D solution for a line force. It is shown that the integral reduces to a simple expression for the static Green's function immediately after the passage of the last bulk wave. The computational efficiency and accuracy of the proposed formulation are demonstrated by numerical examples for zinc and copper. © *2002 Acoustical Society of America.* [DOI: 10.1121/1.1502900]

PACS numbers: 43.35.Cg [LLT]

I. INTRODUCTION

The displacement response due to a point impulsive force in an unbounded solid, or elastodynamic Green's function, is important in many applications. It is the fundamental solution on which the boundary element method for analyzing the transient response of a finite elastic body is based. It is also useful in such areas as crystal acoustic, nondestructive testing, and seismology.

The Green's function for an isotropic elastic solid is well known and can be found in many books.[1,2] For anisotropic elastic solids, the Green's function has been expressed in various forms. Burridge[3] obtained the Green's function as an integral over the unit sphere with the use of the plane wave expansion of Dirac's delta function. An integral representation over the slowness surface was also derived by Burridge. Similar result was derived by Yeatts[4] and Wang and Achenbach[5] using Radon transforms and Every and Kim[6] by Fourier integral methods. Norris[7] extended Burridge's formulation to piezoelectric, thermoelastic, and poroelastic solids. van der Hijden[8] used a modified Cagniard–de Hoop method to obtain the Green's function in the form of a 1-D integral over a unit circle. Tewary[9] gave a 1-D integral representation in terms of Dirac's delta function. An extensive discussion on the types of wave arrival singularities has been provided by Every and Kim.[6] Payton[10] found closed-form expressions for the dynamic response functions along the symmetry axis of transversely isotropic media.

In this paper the dynamic response of a general anisotropic solid due to a point force of Heaviside unit step function time dependence is considered. This time dependence is assumed as the calculations may be performed more directly. A time derivative of the dynamic response function would give the Green's function. Another reason for the choice is that the static Green's function may be anticipated for a sufficiently long time. The 2-D Radon transform is employed to reduce the 3-D problem to the 2-D problem corresponding to a line force,[11,12] for which an explicit solution is available.[13] A 1-D integral representation for the 3-D dynamic response function is obtained from its 2-D counterpart using the inverse Radon transform. The 1-D integral is also integrated over a unit circle as that of van der Hijden.[8] However, the present integral depends explicitly on the eigenvalue and eigenvector of a 6-D matrix in general and no iterations are needed. Indeed the closed-form solutions for isotropic media or transversely isotropic media can be easily obtained with the new integral. It is shown that upon the arrival of the last bulk wave, the integral can be evaluated without solving the eigenvalue problem. In fact, under the circumstances the integral is the same as that of Synge[14] for the static Green's function. For illustration and comparison purposes, numerical examples are provided for zinc, which is a transversely isotropic material, and copper, which is a cubic material.

II. DYNAMIC RESPONSE TENSOR

Consider an infinite anisotropic elastic solid subjected to a suddenly applied point force at the origin $\mathbf{x}=0$ at $t=0$. The dynamic response function tensor $\mathbf{g}(\mathbf{x},t)$ is governed by

$$C_{ijks}\frac{\partial^2 g_{kn}}{\partial x_j \partial x_s}+\delta_{in}\delta(\mathbf{x})H(t)=\rho\frac{\partial^2 g_{in}}{\partial t^2}, \tag{1}$$

where C_{ijks} is the elastic constant, ρ is the density, δ_{in} is Kronecker's delta, δ is Dirac's delta function, and H the Heaviside step function. In Eq. (1), repeated indices are summed from 1 to 3. The Green's function $\mathbf{G}(\mathbf{x},t)$ due to an impulse force of $\delta(t)$ time dependence is related to $\mathbf{g}(\mathbf{x},t)$ by

$$\mathbf{G}(\mathbf{x},t)=\frac{\partial \mathbf{g}(\mathbf{x},t)}{\partial t}.$$

Let $\hat{\mathbf{g}}$ be the 2-D Radon transform of $\mathbf{g}$ defined as[15]

$$\hat{\mathbf{g}}(\xi_1,x_2,\phi,t)=\mathcal{R}(\mathbf{g}(\mathbf{x},t))$$
$$=\int_{-\infty}^{\infty}\int_{-\infty}^{\infty}\mathbf{g}(\mathbf{x},t)\,\delta(\xi_1-\mathbf{n}\cdot\mathbf{x})\,dx_1\,dx_3, \tag{2}$$

where $\mathbf{n}=[\cos\phi,0,-\sin\phi]^T$. Application of the Radon transform to Eq. (1) leads to

$$\mathbf{Q}(\phi)\frac{\partial^2\hat{\mathbf{g}}}{\partial\xi_1^2}+(\mathbf{R}(\phi)+\mathbf{R}(\phi)^T)\frac{\partial^2\hat{\mathbf{g}}}{\partial\xi_1\partial x_2}+\mathbf{T}\frac{\partial^2\hat{\mathbf{g}}}{\partial x_2^2}$$
$$+\delta(\xi_1)\delta(x_2)H(t)\mathbf{I}=\rho\frac{\partial^2\hat{\mathbf{g}}}{\partial t^2}, \tag{3}$$

where $\mathbf{I}$ is the identity matrix and the elements of the 3×3 matrices $\mathbf{Q}(\phi)$, $\mathbf{R}(\phi)$, and $\mathbf{T}(\phi)$ are given by

$$Q_{ik}(\phi)=C_{ijks}n_jn_s,\quad R_{ik}(\phi)=C_{ijks}n_jm_s,$$
$$T_{ik}=C_{ijks}m_jm_s=C_{i2k2}, \tag{4}$$

where $\mathbf{m}=[0,1,0]^T$. In deriving Eq. (3), the following property of the Radon transform was used

$$\mathcal{R}\left(\frac{\partial \mathbf{g}}{\partial x_i}\right)=n_i\frac{\partial \hat{\mathbf{g}}}{\partial \xi_1},\quad i=1,3. \tag{5}$$

The matrices $\mathbf{Q}(\phi)$, $\mathbf{R}(\phi)$, and $\mathbf{T}$ can also be expressed as[12]

$$\mathbf{Q}(\phi)=\mathbf{\Omega}^T\mathbf{Q}^*(\phi)\mathbf{\Omega},\quad \mathbf{R}(\phi)=\mathbf{\Omega}^T\mathbf{R}^*(\phi)\mathbf{\Omega},$$
$$\mathbf{T}=\mathbf{\Omega}^T\mathbf{T}^*(\phi)\mathbf{\Omega}, \tag{6}$$

where $Q^*_{ik}=C^*_{i1k1}$, $R^*_{ik}=C^*_{i1k2}$, and $T^*_{ik}=C^*_{21k2}$, superscript T denotes matrix transpose, and

$$\mathbf{\Omega}=\begin{bmatrix}\cos\phi & 0 & -\sin\phi\\ 0 & 1 & 0\\ \sin\phi & 0 & \cos\phi\end{bmatrix}.$$

Here C^*_{ijks} is the elastic constant with respect to the coordinate system obtained by rotating an angle ϕ about the x_2 axis. Substitution of Eq. (6) into Eq. (3) yields

$$\mathbf{Q}^*\frac{\partial^2\hat{\mathbf{g}}^*}{\partial\xi_1^2}+(\mathbf{R}^*+\mathbf{R}^{*T})\frac{\partial^2\hat{\mathbf{g}}^*}{\partial\xi_1\partial x_2}+\mathbf{T}^*\frac{\partial^2\hat{\mathbf{g}}^*}{\partial x_2^2}$$
$$+\delta(\xi_1)\delta(x_2)H(t)\mathbf{I}=\rho\frac{\partial^2\hat{\mathbf{g}}^*}{\partial t^2}, \tag{7}$$

where

$$\hat{\mathbf{g}}^*=\mathbf{\Omega}\hat{\mathbf{g}}\mathbf{\Omega}^T. \tag{8}$$

Equations (7) and (8) show that $\hat{\mathbf{g}}$ and $\hat{\mathbf{g}}^*$ are the 2-D dynamic response functions corresponding to a line force on the line $\xi_1=x_2=0$ with respect to the original and the rotated coordinate systems, respectively. Thus $\mathbf{g}$ due to a point force can be obtained from $\hat{\mathbf{g}}$ due to a line force by the inverse Radon transform as[15]

$$\mathbf{g}(\mathbf{x},t)=2\int_0^{\pi}\hat{\mathbf{g}}(\mathbf{n}\cdot\mathbf{x},x_2,\phi,t)\,d\phi, \tag{9}$$

where $\hat{\mathbf{g}}$ is given by

$$\hat{\mathbf{g}}(\mathbf{n}\cdot\mathbf{x},x_2,\phi,t)$$
$$=-\frac{1}{4\pi^2}\int_{-\infty}^{\infty}\frac{1}{\xi_1-\mathbf{n}\cdot\mathbf{x}-i0}\frac{\partial\hat{\mathbf{g}}(\xi_1,x_2,\phi,t)}{\partial\xi_1}\,d\xi_1. \tag{10}$$

With Eq. (8), the derivative $\partial\hat{\mathbf{g}}/\partial\xi_1$ in Eq. (10) is given by

$$\frac{\partial\hat{\mathbf{g}}(\xi_1,x_2,\phi,t)}{\partial\xi_1}=\mathbf{\Omega}^T\frac{\partial\hat{\mathbf{g}}^*(\xi_1,x_2,\phi,t)}{\partial\xi_1}\mathbf{\Omega}, \tag{11}$$

where $\partial\hat{\mathbf{g}}^*/\partial\xi_1$ may be expressed as[13]

$$\frac{\partial\hat{\mathbf{g}}^*(\xi_1,x_2,\phi,t)}{\partial\xi_1}=\frac{1}{2\pi}\sum_{k=1}^{n_+}\mathrm{Im}\left[\frac{\mathbf{a}_k^*\mathbf{a}_k^{*T}}{(\xi_1+p_kx_2)\mathbf{a}_k^{*T}\hat{\mathbf{b}}_k^*}\right]. \tag{12}$$

In the preceding equation the 3×1 vectors $\mathbf{a}_k^*(\xi_1/t,x_2/t,\phi)$, $\hat{\mathbf{b}}_k^*(\xi_1/t,x_2/t,\phi)$ and the scalar $p_k(\xi_1/t,x_2/t,\phi)$ are determined by the following sextic eigenvalue problem:

$$\begin{pmatrix}\hat{\mathbf{N}}_1^* & \hat{\mathbf{N}}_2^*\\ \hat{\mathbf{N}}_3^* & \hat{\mathbf{N}}_1^{*T}\end{pmatrix}\begin{pmatrix}\mathbf{a}^*\\ \hat{\mathbf{b}}^*\end{pmatrix}=p\begin{pmatrix}\mathbf{a}^*\\ \hat{\mathbf{b}}^*\end{pmatrix}, \tag{13}$$

where

$$\hat{\mathbf{N}}_1^*=-\hat{\mathbf{T}}^{*-1}\hat{\mathbf{R}}^{*T},\quad \hat{\mathbf{N}}_2^*=\hat{\mathbf{T}}^{*-1},$$
$$\hat{\mathbf{N}}_3^*=\hat{\mathbf{R}}^*\hat{\mathbf{T}}^{*-1}\hat{\mathbf{R}}^{*T}-\hat{\mathbf{Q}}^*,$$
$$\hat{\mathbf{Q}}^*=\mathbf{Q}^*-\rho\left(\frac{\xi_1}{t}\right)^2\mathbf{I},\quad \hat{\mathbf{R}}^*=\mathbf{R}^*-\rho\frac{\xi_1x_2}{t^2}\mathbf{I},$$
$$\hat{\mathbf{T}}^*=\mathbf{T}^*-\rho\left(\frac{x_2}{t}\right)^2\mathbf{I},$$

and n_+ is the number of p_k with positive imaginary part. Substitution of Eq. (6) into Eq. (13) leads to

$$\begin{pmatrix}\hat{\mathbf{N}}_1 & \hat{\mathbf{N}}_2\\ \hat{\mathbf{N}}_3 & \hat{\mathbf{N}}_1^T\end{pmatrix}\begin{pmatrix}\mathbf{a}\\ \hat{\mathbf{b}}\end{pmatrix}=p\begin{pmatrix}\mathbf{a}\\ \hat{\mathbf{b}}\end{pmatrix}, \tag{14}$$

where

$$\hat{\mathbf{N}}_1=-\hat{\mathbf{T}}^{-1}\hat{\mathbf{R}}^T,\quad \hat{\mathbf{N}}_2=\hat{\mathbf{T}}^{-1},\quad \hat{\mathbf{N}}_3=\hat{\mathbf{R}}\hat{\mathbf{T}}^{-1}\hat{\mathbf{R}}^T-\hat{\mathbf{Q}},$$
$$\hat{\mathbf{Q}}=\mathbf{Q}-\rho\left(\frac{\xi_1}{t}\right)^2\mathbf{I},\quad \hat{\mathbf{R}}=\mathbf{R}-\frac{\xi_1x_2}{t^2}\mathbf{I},\quad \hat{\mathbf{T}}=\mathbf{T}-\rho\left(\frac{x_2}{t}\right)^2\mathbf{I},$$

and

$$\mathbf{a}=\mathbf{\Omega}^T\mathbf{a}^*,\quad \hat{\mathbf{b}}=\mathbf{\Omega}^T\hat{\mathbf{b}}^*. \tag{15}$$

From Eqs. (12) and (15), Eq. (11) becomes

$$\frac{\partial\hat{\mathbf{g}}}{\partial\xi_1}=\frac{1}{2\pi}\sum_{k=1}^{n_+}\mathrm{lm}\left[\frac{\mathbf{a}_k\mathbf{a}_k^T}{(\xi_1+p_kx_2)\mathbf{a}_k^T\hat{\mathbf{b}}_k}\right]. \tag{16}$$

With Eq. (16) and Cauchy integral theorem, Eq. (10) gives

$$\hat{\mathbf{g}}(\mathbf{n}\cdot\mathbf{x},x_2,\phi,t)=-\frac{1}{8\pi^2}\sum_{k=1}^{n_+}\mathrm{Re}\left[\frac{\mathbf{a}_k\mathbf{a}_k^T}{(\mathbf{n}\cdot\mathbf{x}+p_kx_2)\mathbf{a}_k^T\hat{\mathbf{b}}_k}\right], \tag{17}$$

where $\mathbf{a}_k$, $\hat{\mathbf{b}}_k$, and p_k are determined by Eq. (14) with $\xi_1=\mathbf{n}\cdot\mathbf{x}+i0$. Substitution of Eq. (17) into Eq. (9) finally yields

$$\mathbf{g}(\mathbf{x},t)=-\frac{1}{4\pi^2}\sum_{k=1}^{n_+}\mathrm{Re}\left[\int_0^{\pi}\frac{\mathbf{a}_k\mathbf{a}_k^T}{(\mathbf{n}\cdot\mathbf{x}+p_kx_2)\mathbf{a}_k^T\hat{\mathbf{b}}_k}\,d\phi\right]. \tag{18}$$

Since no particular elastic symmetries are assumed in deriving Eq. (18), without loss of generality we may orient the x_2 axis to pass through the observation point so that $x_1=x_3=0$ and $x_2=r>0$. Equation (18) may then be simplified as

$$\mathbf{g}(r,t) = -\frac{1}{4\pi^2 r}\sum_{k=1}^{n_+}\int_0^{\pi}\mathrm{Re}\left[\frac{\mathbf{a}_k\mathbf{a}_k^T}{p_k\mathbf{a}_k^T\hat{\mathbf{b}}_k}\right]d\phi. \tag{19}$$

Equation (19) may be further simplified for $t>r/c_{\min}$, $c_{\min}$ being the minimum bulk wave speed in the x_2 direction. In this case the eigenvalues p_k appear as three complex conjugate pairs and $n_+=3$. It can be shown that[16]

$$\sum_{k=1}^{3}\mathrm{Re}\left[\frac{\mathbf{a}_k\mathbf{a}_k^T}{\mathbf{a}_k^T\hat{\mathbf{b}}_k}\right]=\mathbf{0}, \quad \sum_{k=1}^{3}\mathrm{Re}\left[\frac{\hat{\mathbf{b}}_k\mathbf{a}_k^T}{\mathbf{a}_k^T\hat{\mathbf{b}}_k}\right]=\mathbf{1}. \tag{20}$$

On the other hand, Eq. (14) with $\xi_1=0$ yields

$$\frac{\mathbf{a}_k}{p_k} = -[\mathbf{Q}^{-1}(\phi)\mathbf{R}(\phi)\mathbf{a}_k+\mathbf{Q}^{-1}(\phi)\hat{\mathbf{b}}_k]. \tag{21}$$

Equations (20) and (21) give

$$\sum_{k=1}^{3}\mathrm{Re}\left[\frac{\mathbf{a}_k\mathbf{a}_k^T}{p_k\mathbf{a}_k^T\hat{\mathbf{b}}_k}\right]=-\mathbf{Q}^{-1}(\phi),$$

and Eq. (19) becomes

$$\mathbf{g}(r,t)=\frac{1}{4\pi^2 r}\int_0^{\pi}\mathbf{Q}^{-1}(\phi)\,d\phi. \tag{22}$$

Equation (22) is free of the eigenvalues and eigenvectors and is thus applicable to degenerate materials as well. In fact this is the static Green's function developed by Synge.[14] Since Eq. (22) is independent of t, $\mathbf{g},(\mathbf{x},t)$ takes on the corresponding static value immediately after the arrival of the last bulk wave.

In general Eq. (19) must be evaluated numerically. However, if the material is isotropic or the x_2 axis is the symmetry axis of a transversely isotropic material, closed form expression can be obtained. For these materials

$$\begin{aligned}\mathbf{a}\left(i0,\frac{r}{t},\phi\right)&=\mathbf{\Omega}^T(\phi)\mathbf{a}^*\left(i0,\frac{r}{t}\right),\\ \hat{\mathbf{b}}\left(i0,\frac{r}{t},\phi\right)&=\mathbf{\Omega}^T(\phi)\hat{\mathbf{b}}^*\left(i0,\frac{r}{t}\right),\end{aligned} \tag{23}$$

p_k is independent of θ, and Eq. (19) may be easily integrated. The resulting nonzero components of $\mathbf{g}(r,t)$ are

$$g_{11}=g_{33}=-\frac{1}{8\pi r}(k_{11}^*+k_{33}^*), \quad G_{22}=-\frac{k_{22}^*}{4\pi r}, \tag{24}$$

where

$$\mathbf{k}^*=\sum_{k=1}^{n_+}\mathrm{Re}\left[\frac{\mathbf{a}_k^*\mathbf{a}_k^{*T}}{p_k\mathbf{a}_k^*\hat{\mathbf{b}}_k^*}\right]. \tag{25}$$

Similar closed form solutions have been derived by Payton.[10] As an illustration consider isotropic materials in the range $r/c_1<t<r/c_2$, c_1 and c_2 being the longitudinal wave and the transverse wave speed, respectively. In this case $n_+=1$ and

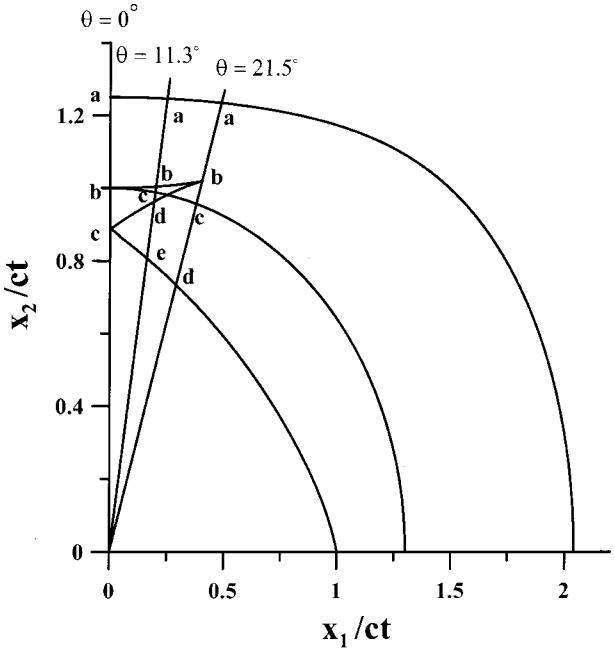

FIG. 1. A section of the wave surface for zinc.

$$\mathbf{a}_1^*=\begin{pmatrix}1\\ p_1\\ 0\end{pmatrix}, \quad \hat{\mathbf{b}}_1^*=\begin{pmatrix}\left(2c_2^2-\left(\frac{r}{t}\right)^2\right)\rho p_1\\ -2\rho c_2^2\\ 0\end{pmatrix},$$
$$p_1=\frac{ic_1}{\sqrt{c_1^2-r^2/t^2}}. \tag{26}$$

Substituting Eq. (26) into Eq. (25), we have

$$k_{11}^*=\frac{1}{\rho}\left(\left(\frac{t}{r}\right)^2-\frac{1}{c_1^2}\right), \quad k_{22}^*=-\frac{1}{\rho}\left(\frac{t}{r}\right)^2, \quad k_{33}^*=0,$$

and the classical result is recovered.

III. NUMERICAL EXAMPLES

Consider first the case of zinc, which is a transversely isotropic material. Let the x_2 axis coincide with the symmetry axis. Since all planes containing the x_2 axis are equivalent symmetry planes, we may restrict our attention to the (x_1,x_2) plane. The independent material constants were taken as $C_{11}=165$, $C_{22}=62$, $C_{12}=50$, $C_{13}=31$, and $C_{44}=39.6$ (in GPa). The section of the wave surface in the (x_1,x_2) plane is shown in Fig. 1, where x_1 and x_2 are scaled by c_0t, $c_0=\sqrt{C_{44}/\rho}$.

To calculate the response at a point $x_1=r\sin\theta$, $x_2=r\cos\theta$, the coordinate system is first rotated such that the point of interest lies on the new x_2 axis. After Eq. (19) is evaluated, the result is then rotated back to the original coordinate system so that

$$\mathbf{g}(r,\theta,t)=\mathbf{M}(\theta)^T\mathbf{g}_\theta(r,t)\mathbf{M}(\theta),$$

where $\mathbf{M}(\theta)$ is given by

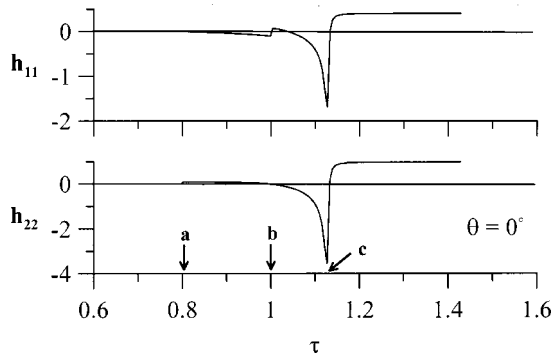

FIG. 2. h_{11} and h_{22} for zinc in the direction $\theta=0$ degrees.

$$\mathbf{M}(\theta)=\begin{pmatrix} \cos\theta & -\sin\theta & 0 \\ \sin\theta & \cos\theta & 0 \\ 0 & 0 & 1 \end{pmatrix}$$

and $\mathbf{g}_\theta$ is the response function with respect to the rotated coordinate system. The numerical integration of Eq. (19) is carried out with Gaussian quadrature. To expedite the numerical computation of Eq. (19), a small but finite positive imaginary number has been assigned to ξ_1 in Eq. (14). This is done at the cost of smoothing the discontinuities at the wave arrivals. Since $\mathbf{g}^T=\mathbf{g}$ and $g_{31}=g_{32}=0$ due to the material symmetry, it is only necessary to consider the "in-plane" components $g_{\alpha,\beta}$, $\alpha,\beta=1,2$, and the "out-of-plane" component g_{33}. The result is expressed in terms of the dimensionless $\mathbf{h}(\tau,\theta)$ defined as

$$\mathbf{h}(\tau,\theta)=4\pi r c_{44}\mathbf{g}(r,\theta,t),$$

where $\tau=c_0 t/r$. The values of θ considered are shown in Fig. 1. Also shown in Fig. 1 are the wave arrivals denoted by $a,b,\ldots,$ for each selected value of θ. For a time step of 0.004 the computational time for *all* the components of **h** at a given value of θ is of the order of 40 and 80 s on a personal computer with an AMD Athlon 700 MHz CPU.

Figure 2 shows h_{11} and h_{22} along the symmetry axis $\theta=0$ degrees. In this direction, $h_{33}=h_{11}$ and $h_{12}=0$. The components h_{11} and h_{22} exhibit discontinuities at b and a, respectively. Both components have a singularity followed by a discontinuity at c. Our result is in excellent agreement with that reported by Payton.[10] Figure 3 shows the nonzero components for $\theta=11.3$ degrees. In this direction h_{11} displays a kink at a, another kink at b, a discontinuity at c, a singularity at d, and another discontinuity at e. For h_{12} and h_{22}, there appear a discontinuity at a, a change in slope at b, a singularity at d, and another discontinuity at e. The features of h_{33} are similar to those of h_{11} except for the absence of singularity at d. The h_{11} component agrees very well with that calculated by Daro and Antes[17] and h_{22} and h_{33} with those of Every and Kim.[6] Figure 4 shows the components for $\theta=21.5$ degrees. The component h_{11} has a kink at a, a singularity at b, and a discontinuity at d. The components h_{12} and h_{22} have discontinuities at a and d in addition to a singularity at the cusp point b. The component h_{33} has a vertical slope at c and kinks at a, b, and d. The diagonal components h_{kk}, $k=1,2,3$, are essentially the same as those calculated by Every and Kim.[6]

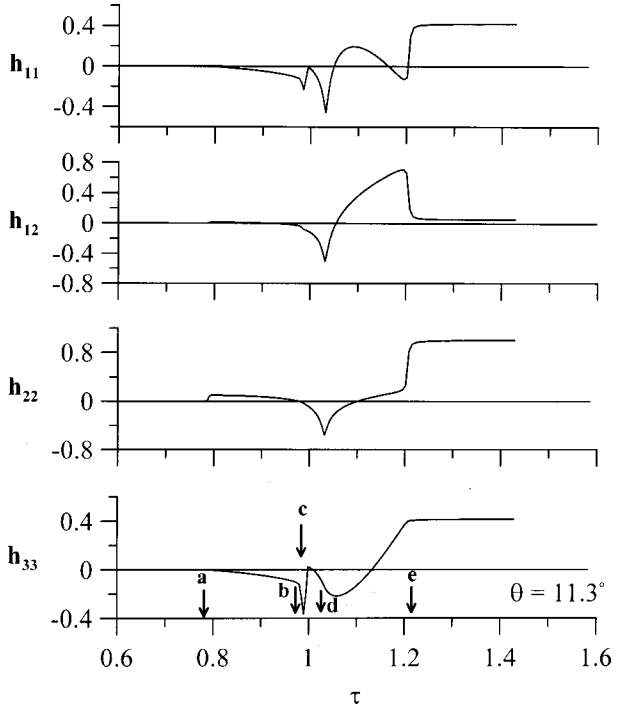

FIG. 3. h_{11}, h_{12}, h_{22}, and h_{33} for zinc in the direction $\theta=11.3$ degrees.

Consider next the case of copper, which is a cubic material. The coordinate axes are assumed to coincide with the symmetry axes. The independent material constants were taken to be $C_{11}=160$, $C_{12}=121$, and $C_{44}=75.3$ (in GPa). The section of the wave surface in the (x_1,x_2) plane is depicted in Fig. 5, where the angles of observation and the associated wave arrivals are also indicated. Due to the material symmetry, the only possible nonzero components are $h_{\alpha,\beta}$, $\alpha,\beta=1,2$, and h_{33}.

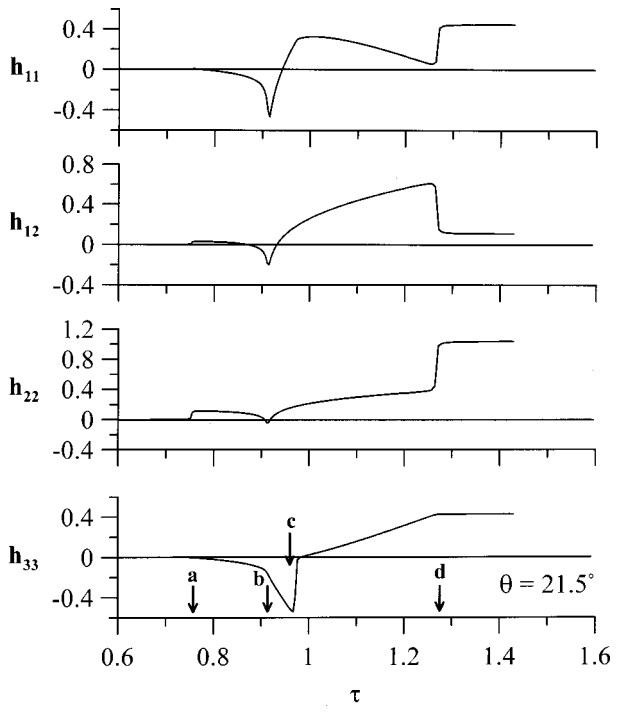

FIG. 4. h_{11}, h_{12}, h_{22}, and h_{33} for zinc in the direction $\theta=21.5$ degrees.

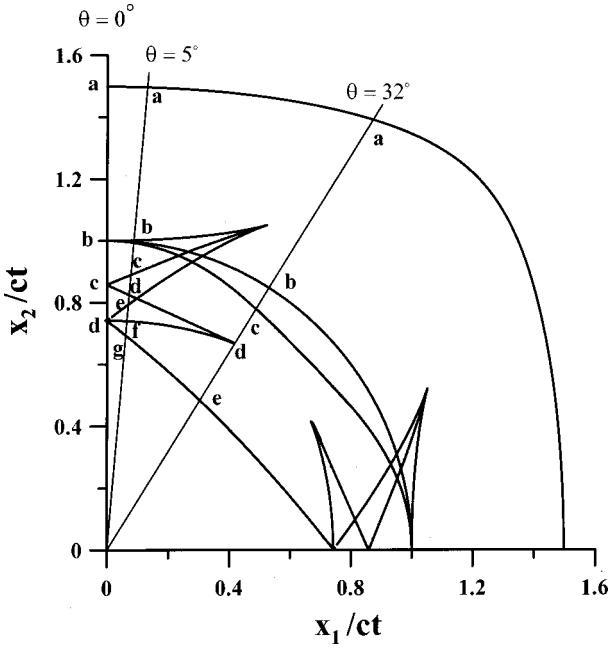

FIG. 5. A section of the wave surface for copper.

Figure 6 gives $h_{11}=h_{33}$ and h_{22} along the symmetry axis $\theta=0$ degrees. The component h_{11} exhibits a kink at *a*, discontinuity at *b*, a singularity at *c*, and another discontinuity at *d*. For h_{22}, there is a discontinuity at *a*, a change in slope at *b*, a singularity at *c*, and another discontinuity at *d*. The components for $\theta=5$ degrees are shown in Fig. 7. There are as many as eight wave arrivals in this direction. The component h_{11} and h_{33} have a change in slope at *a*, a discontinuity at *b*, and singularities at *c* and *d*. The h_{11} component is discontinuous at *e* and *g* and h_{33} at *f*. The components h_{12} and h_{22} display a discontinuity at *a*, a kink at *b*, singularities at *c* and *d*, and discontinuities at *e* and *g*. Figure 8 shows the components for $\theta=32$ degrees. The components $h_{\alpha\beta}$, $\alpha,\beta=1,2$, have a discontinuity at *a*, *c*, *e*, and a singularity at *d*, while h_{33} has a change of slope at *a*, a singularity at *b*, and discontinuities at *c* and *d*.

IV. CONCLUSION

A new method is presented for calculating the transient response due to a suddenly applied point force in a general anisotropic solid. In contrast to the standard Fourier transform approach, which requires integration over an infinite four-dimensional space, the proposed integral is a finite 1-D integral, constructed on the basis of an explicit 2-D solution for a line force using an extended Stroh's formalism.[13] The extended Stroh's formulation resembles that for elastostatics[16] in that general solutions are expressed explicitly in terms of eigenvalues and eigenvectors of a six-dimensional matrix. In fact, the six-dimensional matrix for

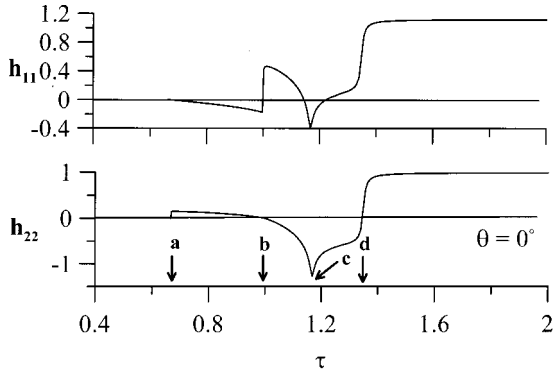

FIG. 6. h_{11} and h_{22} for copper in the direction $\theta=0$ degrees.

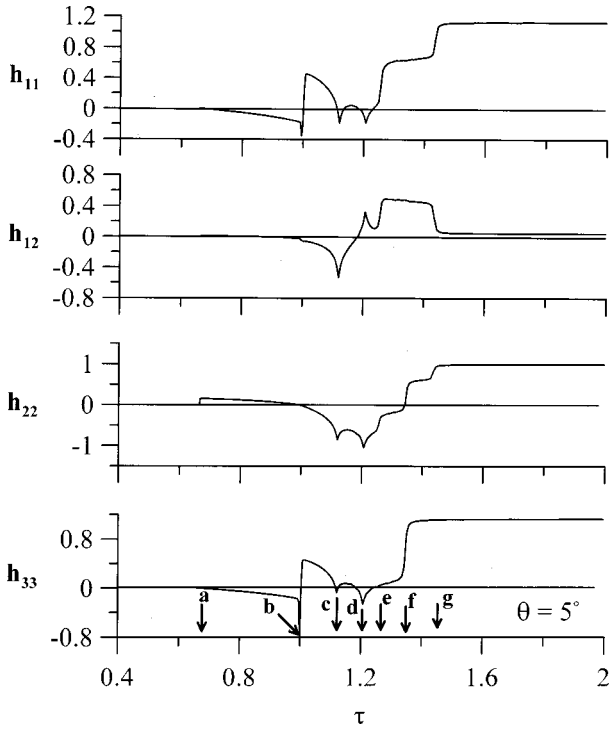

FIG. 7. h_{11}, h_{22}, and h_{33} for copper in the direction $\theta=5$ degrees.

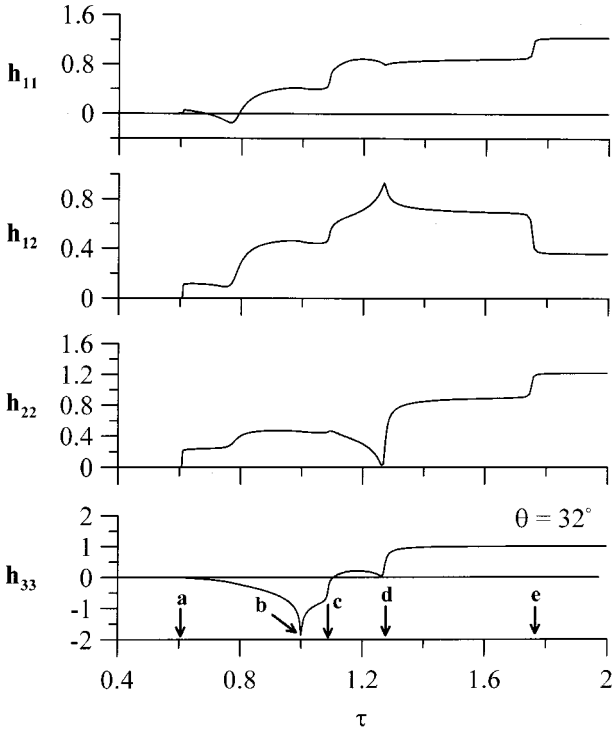

FIG. 8. h_{11}, h_{22}, and h_{33} for copper in the direction $\theta=32$ degrees.

the dynamic case [Eq. (13)] can be obtained from that for the static case simply by replacing the elastic constants with the dynamic elastic constants.[18] Thus the calculation of the 1-D integral is a purely algebraic work. Moreover, because of the common structure, many characteristics of the static formalism also exist in the dynamic counterpart. For example, the same orthogonality relations for eigenvectors are valid in either the static or the dynamic formalism. Such relations have been used to show that the static limit is achieved at a space point soon after the last of the bulk waves has passed through. It should be mentioned that the extended Stroh's formulation is limited to self-similar problems such as the one considered here.

It is also shown that existing closed-form solutions for transversely isotropic and isotropic media may be obtained easily with the new integral. The computational efficiency and accuracy have been demonstrated by numerical examples for zinc and copper. The present method can be extended to piezoelectric materials and the related work is in progress.

[1] J. D. Achenbech, *Wave Propagation in Elastic Solids* (North-Holland, New York, 1973).
[2] J. Miklowwitz, *The Theory of Elastic Waves and Wave Guides* (North-Holland, Amsterdam, 1978).
[3] R. Buridge, ''The singularity on the plane lids of the wave surface of elastic media with cubic symmetry,'' Q. J. Mech. Appl. Math. **20**, 41–56 (1967).
[4] F. R. Yeatts, ''Elastic radiation from a point force in an anisotropic medium,'' Phys. Rev. B **29**, 1674–1684 (1984).
[5] C.-Y. Wang and J. D. Achenbach, ''A new method to obtain 3-D Green's function for anisotropic solids,'' Wave Motion **18**, 273–289 (1993).
[6] A. G. Every and K. Y. Kim, ''Time domain dynamic response functions of elastically anisotropic solids,'' J. Acoust. Soc. Am. **95**, 2505–2516 (1994).
[7] A. N. Norris, ''Dynamic Green's functions in anisotropic piezoelectric, thermoelastic and poroelastic solids,'' Proc. R. Soc. London, Ser. A **447**, 175–188 (1994).
[8] J. H. M. T. van der Hijden, *Propagation of Transient Elastic Waves in Stratified Anisotropic Media* (North-Holland, Amsterdam, 1987).
[9] V. K. Tewary, ''Computationally efficient representation for elastostatic and elastodynamic Green's functions for anisotropic solids,'' Phys. Rev. B **51**, 15695–15702 (1995).
[10] R. G. Payton, ''Symmetry-axis elastic waves for transversely isotropic media,'' Q. Appl. Math. **35**, 63–73 (1977).
[11] C.-Y. Wang and J. D. Achenbach, ''Lamb's problem for solids of general anisotropy,'' Wave Motion **24**, 227–242 (1996).
[12] K.-C. Wu, ''Generalization of the Stroh Formalism to Three-Dimensional Anisotropic Elasticity,'' J. Elast. **51**, 213–225 (1998).
[13] K.-C. Wu, ''Extension of Stroh's formalism to self-similar problems in two-dimensional elastodynamics,'' Proc. R. Soc. London, Ser. A **456**, 869–890 (2000).
[14] J. L. Synge, *The Hyper Circle in Mathematical Physics* (Cambridge U. P., Cambridge, 1957).
[15] S. R. Deans, *The Radon Transform and Some of its Applications* (Krieger, Malabar, FL, 1983).
[16] T. C. T. Ting, *Anisotropic Elasticity—Theory and Application* (Oxford U. P., New York, 1996).
[17] C. J. Daros and H. Antes, ''Dynamic fundamental solutions for transversely isotropic piezoelectric materials of crystal class 6 mm,'' Int. J. Solids Struct. **37**, 1639–1658 (2000).
[18] D. M. Barnett and J. Lothe, ''Synthesis of the sextic and the integral formalism for dislocations, Greens functions and surface waves in anisotropic elastic solids,'' Phys. Norv. **7**, 13–19 (1973).

Influence of ultrasonic frequency on multibubble sonoluminescence

Kyuichi Yasui
National Institute of Advanced Industrial Science and Technology (AIST), 2266-98 Anagahora, Shimoshidami, Moriyama-ku, Nagoya 463-8560, Japan

(Received 22 March 2002; revised 30 May 2002; accepted 5 July 2002)

Computer simulations of bubble oscillations are performed under conditions of multibubble sonoluminescence (MBSL) in water for various ultrasonic frequencies. The range of the ambient bubble radius for sonoluminescing bubbles narrows as the ultrasonic frequency increases; at 20 kHz it is 0.1–100 μm while at 1 MHz it is 0.1–3 μm. At 1 MHz, any sonoluminescing bubble disintegrates into a mass of smaller bubbles in a few or a few tens of acoustic cycles, while at 20 kHz and 140 kHz some sonoluminescing bubbles are shape stable. The mechanism of the light emission also depends on the ultrasonic frequency. As the ultrasonic frequency increases, the amount of water vapor trapped inside bubbles at the collapse decreases. As a result, MBSL originates mainly in plasma emissions at 1 MHz while it originates in chemiluminescence of OH radicals and plasma emissions at 20 kHz. © *2002 Acoustical Society of America.*
[DOI: 10.1121/1.1502898]

PACS numbers: 43.35.Ei, 43.35.Hl, 43.25.Yw [AS]

I. INTRODUCTION

When a liquid is irradiated by a strong ultrasound, many tiny bubbles are created, which is called acoustic cavitation.[1,2] According to the pressure oscillation of ultrasound, the bubbles repeat expansion and contraction. When the ultrasound is strong enough, the bubbles emit light at the collapse, which is called multibubble sonoluminescence (MBSL).[1–3] The mechanism of the light emission is chemiluminescence and plasma emissions from gases and vapor inside bubbles heated by quasiadiabatic compression where ''quasi'' means appreciable thermal conduction takes place between a bubble and the surrounding liquid.[4,5] It should be noted that single-bubble sonoluminescence (SBSL),[6,7] which is the light emission phenomenon from a stably oscillating bubble trapped at the pressure antinode of a standing ultrasoinc wave, originates in plasma emissions from weakly ionized gases inside a bubble heated by quasiadiabatic compression.[7–10] The main difference between MBSL and SBSL is the amplitude of an ultrasonic wave; 5–10 bar for MBSL, while about 1.5 bar for SBSL.[4,11] Because a SBSL bubble should be trapped at the pressure antinode of a standing ultrasonic wave while there is no restriction for MBSL bubbles.[4]

Inside collapsing bubbles in liquid water, water vapor is dissociated because the bubble temperature increases dramatically.[12] As a result, OH radicals and H_2O_2 molecules are created inside bubbles and dispersed in the liquid.[13] As OH radicals and H_2O_2 molecules are strong oxidants, solutes are easily oxidized. On the other hand, volatile solutes enter bubbles and many kinds of chemical reactions take place inside collapsing bubbles.[14] The chemistry using acoustic cavitation is called sonochemistry.[13] For the industrial application of sonochemistry, a detailed understanding of cavitation bubbles is required. In the present study, computer simulations of bubble oscillations are performed in order to study the influence of ultrasonic frequency on the cavitation bubbles and multibubble sonoluminescence.

In the present paper, a classification of cavitation bubbles is described based on the results of computer simulations of bubble oscillations. Leighton[1] described in his book a classification of cavitation bubbles similar to the present one. The comparison between the two classifications is given in Sec. III. In Leighton's book,[1] however, the range of the ambient bubble radius for each category of bubbles and its dependence on the ultrasonic frequency are not described.

II. MODEL

In the present model of bubble dynamics, the following effects are taken into account; nonequilibrium evaporation and condensation of water vapor at the bubble wall, thermal conduction both inside and outside a bubble, chemical reactions of gases and vapor inside a bubble, ionization of gases and vapor inside a bubble, radiation process inside a bubble, diffusion of gases in the liquid, dissolution of the chemical products into the surrounding liquid, and liquid compressibility.

The present model is essentially the same as that described in Refs. 5 and 12. There is one modification made in the present study. It is the inclusion of the gas diffusion in the liquid (the rectified diffusion). According to the Eller–Flynn theory,[15] the rate of the gas diffusion into the bubble is given by Eq. (1),

$$\frac{dN_{\mathrm{diff}}}{dt} = -4\pi R^2 D \frac{A}{B} \frac{c_i - c_\infty}{(R_0/R)^2 R_0}, \tag{1}$$

where dN_{diff}/dt is the number of gas molecules flowing into the bubble per unit time, R is the bubble radius, D is the diffusion coefficient of the gas in the liquid, $A=\langle (R/R_0) \rangle$, $B=\langle (R/R_0)^4 \rangle$, $\langle\ \rangle$ denotes the time averaged value, R_0 is

the ambient bubble radius, c_i is the concentration of the gas near the bubble surface, and c_∞ is that at infinity. At the bubble expansion, the pressure inside a bubble decreases and c_i decreases according to the Henry law. Accordingly, the gas diffuses into the bubble. On the other hand, at the bubble collapse, the pressure inside a bubble increases and the gas diffuses out of the bubble.

In deriving Eq. (1), it is assumed that the gas concentration in the liquid changes only in the thin boundary layer near the bubble wall.[15] The assumption is valid universally in time only when the net flux of the gas into or out of the bubble is nearly zero.[15] When the net flux of the gas is far from zero, Eq. (1) is valid only near the beginning of the diffusion; $t \leqslant R^2/D$, where t is the time from the beginning of the diffusion, R is the bubble radius, and D is the diffusion coefficient of the gas in the liquid.[15] For the more sophisticated theory of the rectified diffusion, see Ref. 16.

In the present study, the criterion for the fragmentation of a bubble is that the amplitude of a distortion of the spherical bubble surface exceeds the mean radius of a bubble.[17] A small distortion of the spherical surface is described by $R(t)+a_n(t)Y_n$, where $R(t)$ is the mean radius of a bubble at time t, $a_n(t)$ is the distortion amplitude, and Y_n is a spherical harmonic of degree n.[17] The dynamics for the distortion amplitude $a_n(t)$ is given by

$$\ddot{a}_n + B_n(t)\dot{a}_n - A_n(t)a_n = 0, \tag{2}$$

where the overdot denotes the time derivative (d/dt),

$$A_n(t) = (n-1)\frac{\ddot{R}}{R} - \frac{\beta_n \sigma}{\rho_L R^3} - \left[(n-1)(n+2) + 2n(n+2)(n-1)\frac{\delta}{R}\right]\frac{2\mu\dot{R}}{R^3} \tag{3}$$

and

$$B_n(t) = \frac{3\dot{R}}{R} + \left[(n+2)(2n+1) - 2n(n+2)^2\frac{\delta}{R}\right]\frac{2\mu}{R^2}, \tag{4}$$

where $\beta_n = (n-1)(n+1)(n+2)$, σ is the surface tension, ρ_L is the liquid density, μ is the liquid viscosity, and δ is the thickness of the thin layer where fluid flows

$$\delta = \min\left(\sqrt{\frac{\mu}{\omega}}, \frac{R}{2n}\right),$$

where ω is the angular frequency of ultrasound.[17,18] Under the conditions considered in the present study, the distortion amplitude of the mode $n=2$ is the largest and the criterion for the fragmentation of a bubble is $a_2 > R$.

Two kinds of forces act on a bubble.[1] One is the buoyant force (f_b),

$$f_b = \rho_L g \left\langle \tfrac{4}{3}\pi R^3 \right\rangle, \tag{5}$$

where ρ_L is the liquid density, g is the gravitational acceleration, R is the bubble radius, and $\langle\ \rangle$ denotes the time averaged value. The other is the force originated from the pressure difference across a bubble (radiation force) (f_r),

TABLE I. The five categories of bubbles.

	Dissolving bubbles	Stable SL bubbles	Unstable SL bubbles	Unstable bubbles	"degas" bubbles
Shape stability	Stable	Stable	Unstable	Unstable	Stable
Light emission	No	Yes	Yes	No	No
Gas diffusion	Dissolution	Growth	Growth	Growth	Growth

$$f_r = -\left\langle \frac{4}{3}\pi R^3 \frac{dp}{dx} \right\rangle, \tag{6}$$

where dp/dx is the pressure gradient. When the pressure field consists only of the progressive ultrasonic wave $[p = p_a \sin(\omega t - kx)]$,

$$f_r = k p_a \left\langle \tfrac{4}{3}\pi R^3 \cos(\omega t - kx) \right\rangle, \tag{7}$$

where k is the wave number, p_a is the acoustic amplitude, and ω is the angular frequency. When the pressure field consists only of the standing ultrasonic wave $[p = p_a \cos(kx)\sin(\omega t)]$,

$$f_r = k p_a \sin(kx) \left\langle \tfrac{4}{3}\pi R^3 \sin(\omega t) \right\rangle, \tag{8}$$

where f_r is called the Bjerknes force in this case.[1]

III. RESULTS

Computer simulations of bubble oscillations are performed for three frequencies of ultrasound; 20 kHz, 140 kHz, and 1 MHz (=1000 kHz), which are frequently used ones in the experiments of multibubble sonoluminescence and sonochemistry.[11,13,19–25] The condition is that of a spherical bubble in liquid water irradiated by ultrasound whose wavelength is over an order of magnitude longer than the bubble radius. Computer simulations are performed for various ambient radii of a bubble (R_0) and various amplitudes of ultrasound (p_a) for each frequency of ultrasound. The simulations have revealed that bubbles are classified into five categories by their ambient radii. They are summarized in Table I.

"Dissolving bubbles" gradually dissolve into the liquid by the gas diffusion. Bubbles which grow gradually by the rectified diffusion[1] are classified into four categories. Two of them are light emitting bubbles (sonoluminescing bubbles). The other two of them are nonlight emitting bubbles. The light emitting bubbles are classified into two categories; stable sonoluminescing (SL) bubbles and unstable sonoluminescing (SL) bubbles. The difference between the two categories is the shape stability of a bubble. A "stable SL bubble" is shape stable, while an "unstable SL bubble" disintegrates into a mass of smaller bubbles after a few acoustic cycles or a few tens of acoustic cycles. The two categories of nonlight emitting bubbles are unstable bubbles and "degas" bubbles. The difference between the two categories is the shape stability of a bubble. An "unstable bubble" disintegrates into a mass of smaller bubbles after a few acoustic cycles or a few tens of acoustic cycles, while a "degas" bubble is shape stable indefinitely long.

Now we compare the present classification (Table I) and the Leighton's classification.[1] Unstable SL bubbles, stable SL

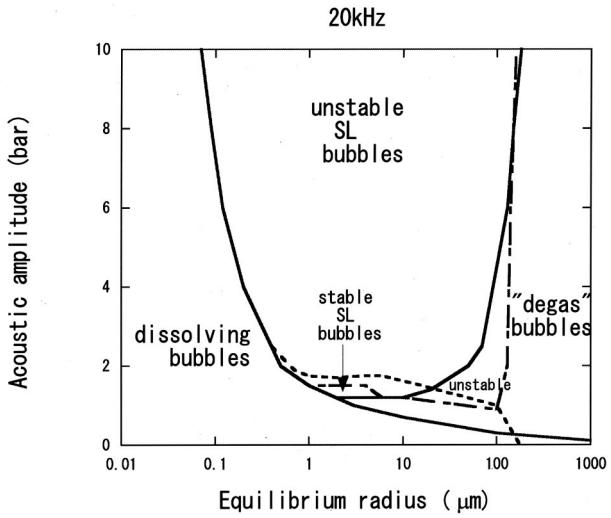

FIG. 1. The region for each category of bubbles in the space of the ambient bubble radius (R_0) and the acoustic amplitude (p_a) when the frequency of ultrasound is 20 kHz.

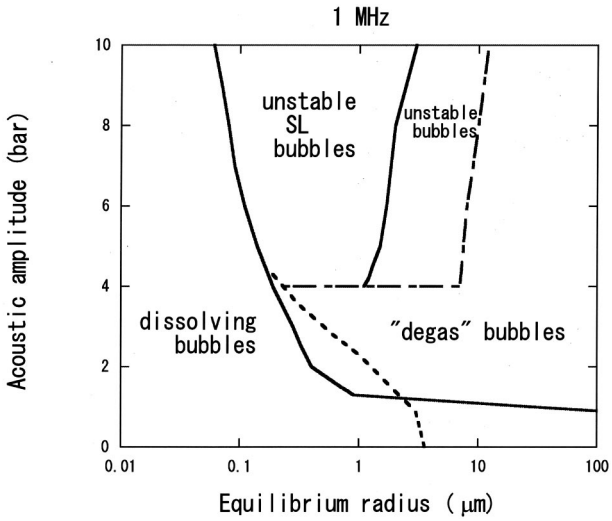

FIG. 3. The region for each category of bubbles in R_0-p_a space when the frequency of ultrasound is 1 MHz. Note the shorter range of the horizontal axis (R_0) compared to that of Figs. 1 and 2.

bubbles, and ''degas'' bubbles in the present classification correspond to ''fragmentary transient cavitation bubbles,'' ''repetitive transient cavitation bubbles'' (or ''high-energy stable cavitation bubbles''), and ''stable cavitation bubbles,'' respectively, in the classification of Leighton.[1] Unstable bubbles in the present classification may be included in ''fragmentary transient cavitation bubbles'' in Leighton's classification.[1]

The range of the ambient bubble radius (R_0) and that of the acoustic amplitude (p_a) for each category of bubbles are shown in Figs. 1–3 for ultrasonic frequencies of 20 kHz, 140 kHz, and 1 MHz, respectively. For all the figures, a bubble is shape stable below the dashed–dotted line. Above the dashed–dotted line, a bubble disintegrates into a mass of smaller bubbles in a few acoustic cycles or a few tens of acoustic cycles. Below the dotted line, a bubble is attracted to the pressure antinode when the ultrasonic wave forms a standing wave. Above the dotted line, a bubble is repelled from the pressure antinode. Thus, SBSL is produced only below the dotted line because a SBSL bubble should be trapped at the pressure antinode of a standing ultrasonic wave. From Figs. 1–3, it is seen that it is difficult to produce SBSL at 1 MHz because the region for SBSL in R_0-p_a space, which is the region of SL bubbles below the dotted line, is very narrow (only at $R_0\sim 0.19\ \mu$m, $p_a\sim 4.3$ bar), while at 20 kHz it is much easier to produce SBSL because the region for SBSL in R_0-p_a space is much larger than that at 1 MHz. It should be noted here that at 1 MHz only unstable SBSL is producible, which is SBSL from a bubble pinching off daughter bubbles and dancing around the pressure antinode. Unstable SBSL has been observed at ultrasonic frequency of 20–30 kHz.[26,27]

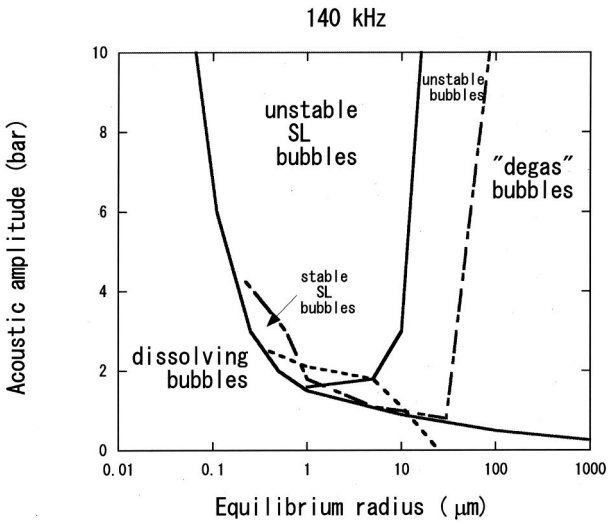

FIG. 2. The region for each category of bubbles in R_0-p_a space when the frequency of ultrasound is 140 kHz.

From the figures, it is seen that the region for each category of bubbles in R_0-p_a space strongly depends on the ultrasonic frequency. As the ultrasonic frequency increases, the range of the ambient bubble radius for SL bubbles narrows; at 20 kHz it is 0.1–100 μm while at 1 MHz it is 0.1–3 μm. Because as the ultrasonic frequency increases a bubble expands less due to the shorter period of ultrasound and the bubble collapse becomes milder. From Fig. 3, it is seen that the region for stable SL bubbles in R_0-p_a space disappears at 1 MHz. In other words, at 1 MHz any sonoluminescing bubble disintegrates into a mass of smaller bubbles in a few or a few tens of acoustic cycles, while at 20 kHz and 140 kHz some sonoluminescing bubbles are shape stable.

In Fig. 4, an example of the radius-time curve of a ''dissolving bubble'' is shown when the frequency and amplitude of ultrasound are 140 kHz and 5 bar, respectively, and the initial ambient radius of a bubble is 0.1 μm. From Fig. 4, it is seen that the mean radius of a bubble decreases by the gas diffusion while the instantaneous bubble radius oscillates according to the pressure oscillation of ultrasound. The amplitude of the radial oscillation of a ''dissolving bubble'' is quite small because the excess pressure due to surface tension for a small bubble is quite large as the excess pressure is inversely proportional to the bubble radius.[1] Due to the small amplitude of the radial oscillation, the internal pressure of a

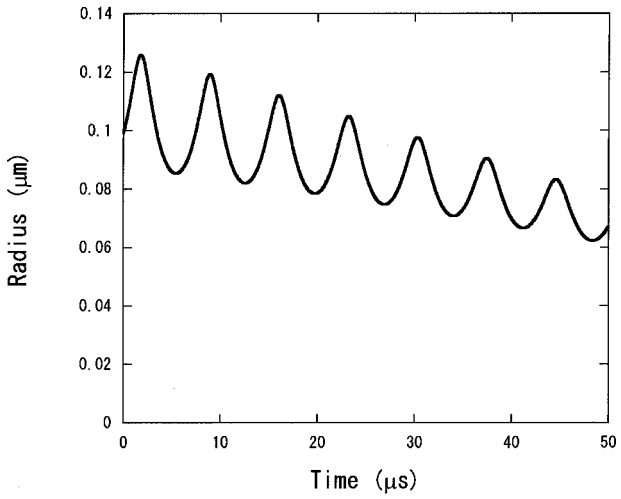

FIG. 4. A radius-time curve of a dissolving bubble when the initial ambient bubble radius is 0.1 μm and the frequency and amplitude of ultrasound are 140 kHz and 5 bar, respectively.

bubble is always larger than the liquid pressure far from the bubble and gas diffuses from the bubble to the surrounding liquid [see Eq. (1)]. In other words, such a small bubble gradually dissolves into the liquid. As the amplitude of the radial oscillation is small, the collapse is mild and no light is emitted. The distortion amplitude of a ''dissolving bubble'' is always quite small compared to its radius and a ''dissolving bubble'' is shape stable.

It should be noted here that Eq. (1) is strictly valid only near the beginning of the diffusion. Thus, Eq. (1) is less valid near the right-hand side of Fig. 4.

The threshold amplitude of ultrasound for dissolution is shown in Figs. 1–3 by the curve showing the region of ''dissolving bubbles'' in the R_0–p_a space. Below the curve, a bubble gradually dissolves into the liquid (dissolving bubbles). Above the curve, a bubble gradually grows by the gas diffusion. When the radial oscillation is large enough, the amount of gas diffusing into a bubble at the bubble expansion is larger than that of gas diffusing out of a bubble at the bubble collapse because the rate of the gas diffusion increases as the bubble radius increases according to Eq. (1). The gas diffusion into an oscillating bubble from the surrounding liquid is called rectified diffusion.[1] For each frequency of ultrasound (Figs. 1–3), the threshold amplitude of ultrasound for dissolution decreases as the ambient bubble radius increases because the excess pressure due to surface tension decreases and a bubble expands enough for rectified diffusion at lower acoustic amplitude. From Figs. 1–3, it is seen that the threshold amplitude of ultrasound for dissolution is almost independent of the ultrasonic frequency for bubbles smaller than 1 μm in ambient radius. For such small bubbles ($R_0<1$ μm), the threshold amplitude of ultrasound for dissolution nearly coincides with the *transient cavitation threshold* calculated by Flynn and Church in 1984.[28]

An example of a ''stable SL bubble'' is shown in Fig. 5 when the frequency and amplitude of ultrasound are 140 kHz and 2.5 bar, respectively, and the initial ambient bubble radius is 0.5 μm. From Fig. 5(a), it is seen that a bubble ex-

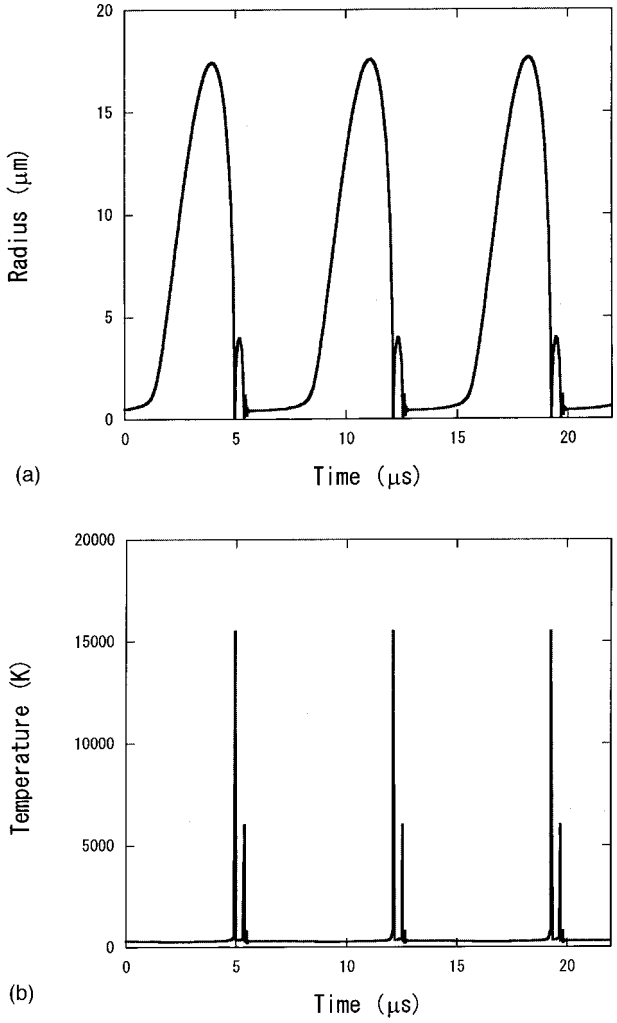

FIG. 5. The calculated results of a stable SL bubble when the initial ambient bubble radius is 0.5 μm and the frequency and amplitude of ultrasound are 140 kHz ands 2.5 bar, respectively. (a) The bubble radius. (b) The temperature inside a bubble.

pands to a size over 30 times of its ambient radius, while in the case of a ''dissolving bubble'' it expands to a size less than 1.3 times of its ambient radius (Fig. 4). Due to the large radial expansion, the subsequent collapse is strong enough for the light emission. The temperature inside a bubble is shown in Fig. 5(b) as a function of time with the same time axis as that of Fig. 5(a). It is seen that the bubble temperature increases up to 15 500 K at the collapse which is sufficiently high for the light emission. The mechanism of the light emission in this case is plasma emissions; electron–atom bremsstrahlung, radiative recombination of electrons and ions, and radiative attachment of electrons to neutral atoms.[5,9] The criterion for the light emission from a bubble is crudely that the bubble temperature exceeds 6000 K. Thus faint light is emitted also at the weaker collapse followed by the strongest collapse as seen in Fig. 5(b).

The accommodation coefficient of water vapor condensation used in the present calculations[12] is derived from the molecular dynamics simulations by Matsumoto,[29] which is reliable. Furthermore, the present model of bubble dynamics including evaporation and condensation of water vapor at the bubble wall has been validated from the studies of single-

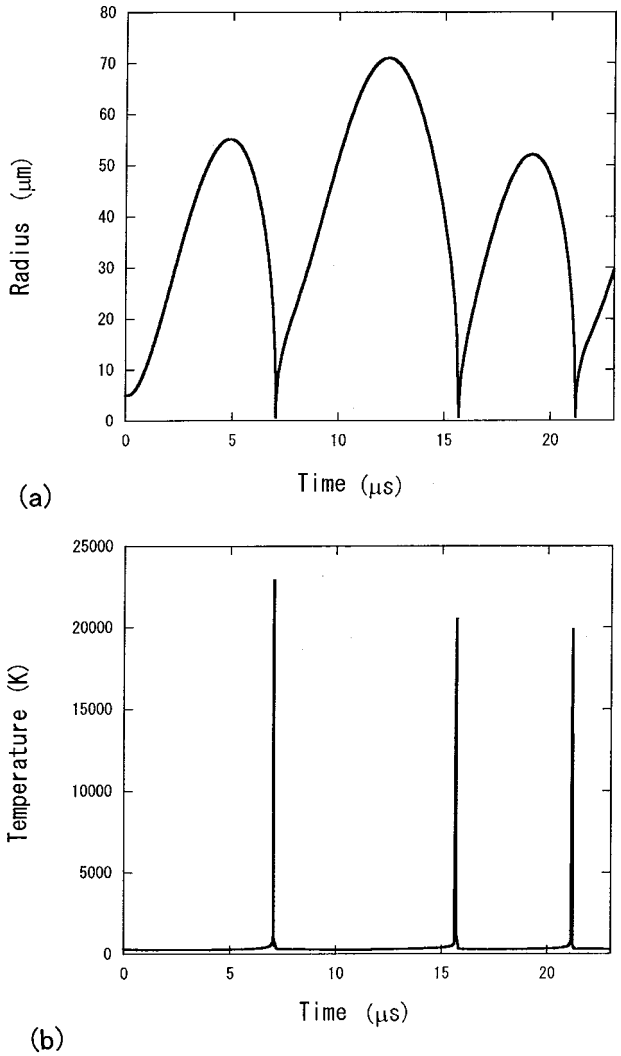

FIG. 6. The calculated results of an unstable SL bubble when the initial ambient bubble radius is 5 μm and the frequency and amplitude of ultrasound are 140 kHz and 5 bar, respectively. The bubble disintegrates into a mass of smaller bubbles just after the third collapse ($t \sim 22\ \mu$s). (a) The bubble radius. (b) The temperature inside a bubble.

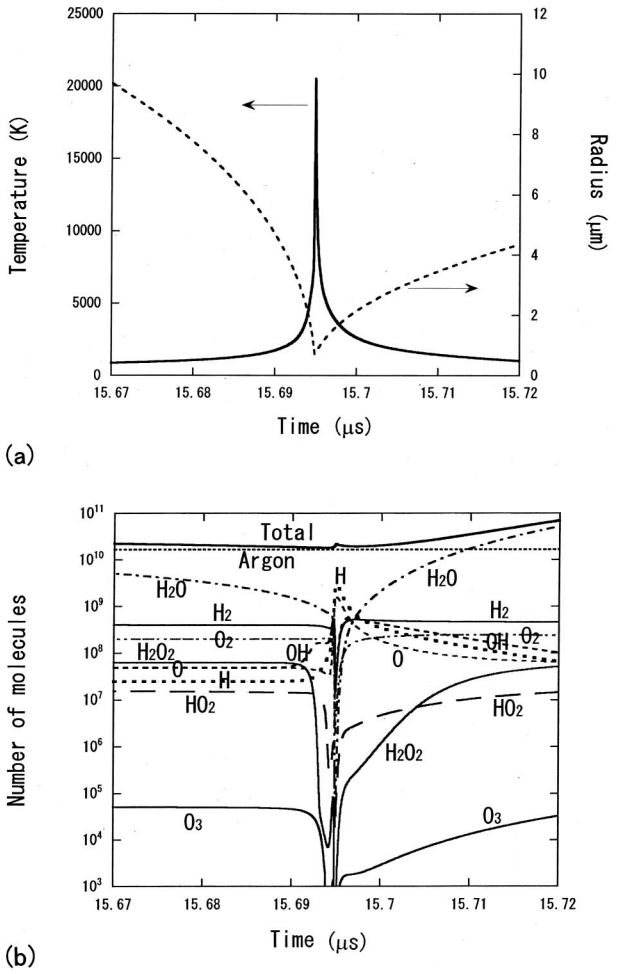

FIG. 7. The enlarged view at around the second collapse of an unstable SL bubble shown in Fig. 6 for 0.05 μs. (a) The bubble radius and the temperature inside a bubble. (b) The numbers of molecules inside a bubble with logarithmic vertical axis.

bubble sonoluminescence.[30] Nevertheless, it should be noted here that the maximum bubble temperature depends on the value of the accommodation coefficient. For example, when the value reported by Li *et al.*[31] is used, the maximum bubble temperature at the strongest collapse under the condition of Fig. 5 is below 10 000 K.

The ambient bubble radius (R_0) increases gradually by the rectified diffusion in this case to 0.55 μm in 110 μs (15.4 acoustic cycles) and to 0.6 μm in 233 μs (32.6 acoustic cycles). It should be noted here that Eq. (1) is valid in the time range considered here in this case.

In Fig. 6, an example of the calculated results of an ''unstable SL bubble'' is shown when the frequency and amplitude of ultrasound are 140 kHz and 5 bar, respectively, and the initial ambient bubble radius is 5 μm. In Fig. 6(a), the radius–time curve is shown. The bubble disintegrates into a mass of smaller bubbles just after the third collapse ($t \sim 22\ \mu$s). In Fig. 6(a), no small bounce of the bubble radius is seen, while in the case of a stable SL bubble [Fig. 5(a)] small bounces are seen after the strongest collapse. It should be noted that an ''unstable SL bubble'' also sometimes bounces a few times after the strongest collapse. In Fig. 6(b), the temperature inside a bubble is shown as a function of time with the same time axis as that of Fig. 6(a). The temperature increases up to 20 000–23 000 K at the collapse in this case. The mechanism of the light emission is plasma emissions; electron–atom bremsstrahlung, radiative recombination of electrons and ions, and electron–ion bremsstrahlung.[5,9]

The light intensity in this case is much larger than that in the case of a stable SL bubble (Fig. 5) due both to the larger size of a bubble and the higher bubble temperature. The energy of the emitted light per collapse in this case is 7.2 pJ, while it is 7.9×10^{-4} pJ in the case of Fig. 5.

The enlarged view at around the end of the second collapse ($t \sim 15.695\ \mu$s) is shown in Fig. 7 for 0.05 μs. In Fig. 7(a), the bubble radius and the temperature inside a bubble are shown as functions of time. The temperature increases up to 20 500 K at the collapse. In Fig. 7(b), the numbers of molecules inside a bubble are shown as functions of time with logarithmic vertical axis. It is seen that the appreciable amount of chemical products such as H_2, O_2, H_2O_2, O, H, HO_2, O_3 created at the previous collapse survive inside a

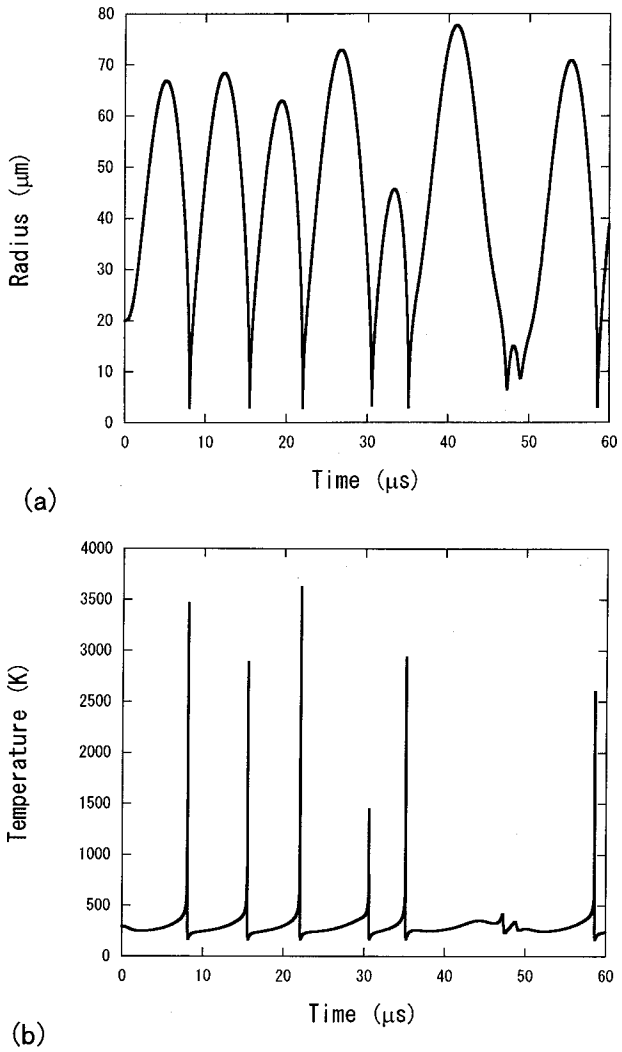

FIG. 8. The calculated results of an unstable bubble when the initial ambient bubble radius is 20 μm and the frequency and amplitude of ultrasound are 140 kHz and 5 bar, respectively. The bubble disintegrates into a mass of smaller bubbles just after the eight collapse ($t \sim 60\ \mu$s). (a) The bubble radius. (b) The temperature inside a bubble.

bubble until the next collapse. It should be noted here that in the present simulations the dissolution of chemical products into the surrounding liquid is taken into account.[5] About 80% of chemical products created at the previous collapse survive until the next collapse. Although most of them are once dissociated at the collapse, the amount of each species created at the collapse is larger than that created at the previous collapse.

An example of the calculated results of an ''unstable bubble'' is shown in Fig. 8 when the frequency and amplitude of ultrasound are 140 kHz and 5 bar, respectively and the initial ambient bubble radius is 20 μm. In Fig. 8(a), the radius–time curve is shown. The bubble disintegrates into a mass of smaller bubbles just after the eight collapse ($t \sim 60\ \mu$s). In Fig. 8(b), the temperature inside a bubble is shown as a function of time with the same time axis as that of Fig. 8(a). It is seen that the bubble temperature increases only up to 3500 K at the collapse, which is insufficient for the light emission.

In Fig. 9, the radius–time curve of a ''degas'' bubble is

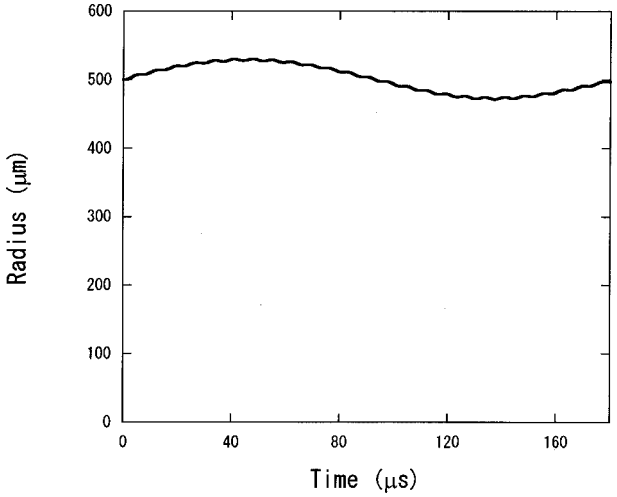

FIG. 9. A radius–time curve of a ''degas'' bubble when the initial ambient bubble radius is 500 μm and the frequency and amplitude of ultrasound are 140 kHz and 5 bar, respectively.

shown when the frequency and amplitude of ultrasound are 140 kHz and 5 bar, respectively, and the initial ambient bubble radius is 500 μm. As the natural frequency of such a large bubble is quite small (5.5 kHz in this case) compared to the ultrasonic frequency (140 kHz), the amplitude of radial oscillation is quite small compared to its ambient radius. The bubble oscillates slowly with its natural frequency (5.5 kHz, which corresponds to the period of 181 μs), while it also oscillates a little with ultrasonic frequency (140 kHz, which corresponds to the period of 7 μs). It should be noted here that the natural frequency (f_n) of a bubble which oscillates isothermally is given by Eq. (9),[32]

$$f_n = \frac{1}{2\pi}\sqrt{\frac{3p_\infty}{\rho R_0^2}}, \tag{9}$$

where p_∞ is the ambient liquid pressure, ρ is the liquid density, and R_0 is the ambient bubble radius. In many experiments of multibubble sonoluminescence and sonochemistry,[11,13,19–24] a liquid is irradiated by ultrasound from the bottom of the liquid container and ''degas'' bubbles move towards the liquid surface by the radiation force. In the case of Fig. 9, the radiation force is 2.5×10^{-4} N, while the buoyant force is 5.3×10^{-6} N when the ultrasonic wave is a pure progressive wave [Eq. (7)]. When a liquid is irradiated by strong ultrasound, a liquid is gradually degassed,[1] which is mainly caused by ''degas'' bubbles because they move to the liquid surface by the radiation force and carry the gas into the air. Thus we call such large stable bubbles ''degas'' bubbles.

Now we discuss the mechanism of nucleation of bubbles. There are three mechanisms in nucleation of bubbles.[1] One is the pre-existing bubbles in the liquid, which are stabilized against dissolution because the bubble surface is covered by the contaminants (surfactants). Another is the nucleation at crevices in motes in the liquid. At a crevice, the pressure inside the gas pocket is *lower* than that of the liquid outside the gas pocket because the surface of the gas pocket is concave and the surface tension reduces the internal gas pressure. Additionally, the pressure inside the gas

pocket decreases considerably when the pressure of ultrasound is negative. When the pressure inside the gas pocket is lower than the liquid pressure far from the bubble, gas diffuses into the gas pocket from the surrounding liquid and the gas pocket grows. Finally, a bubble is created because the gas pocket departs from the crevice by the radiation force. The other is the creation of new bubbles by the fragmentation of a large bubble, which is the most important process once acoustic cavitation begins.

Now we discuss a life of bubbles. When a new bubble is created, it is characterized by its ambient radius (R_0) and the acoustic amplitude (p_a) at the place where the bubble is created. It should be noted here that the acoustic amplitude (p_a) varies in a liquid because an ultrasonic wave is gradually attenuated as it progresses and it consists mainly of a spherical wave whose pressure amplitude is inversely proportional to the distance when a liquid is irradiated by an ultrasonic wave using a horn.[13] Thus a newly created bubble is described by a point in the R_0-p_a space (Figs. 1–3). If the point is in the region of dissolving bubbles, a newly created bubble gradually dissolves into the liquid. If the point is in the region of unstable SL bubbles, a newly created bubble starts sonoluminescing immediately. But in a few acoustic cycles or a few tens of acoustic cycles, it disintegrates into a mass of smaller bubbles. If the point is in the region of stable SL bubbles, a newly created bubble starts sonoluminescing immediately. The bubble emits light at each violent collapse repeatedly until the ambient radius increases by the rectified diffusion to the threshold one for unstable SL bubbles. Finally, the bubble disintegrates into a mass of smaller bubbles. If the point is in the region of unstable bubbles, a newly created bubble never emit light and disintegrates into a mass of smaller bubbles in a few acoustic cycles or a few tens of acoustic cycles. If the point is in the region of ''degas'' bubbles, a newly created bubble is shape stable indefinitely long. A bubble moves towards the liquid surface by the radiation force and is annihilated at the liquid surface.

Bubbles pulsating in phase are attracted to each other by the radiation force called the secondary Bjerknes force.[1] Such bubbles finally coalesce and form a bigger bubble. It is a very important process for the growth of bubbles. Dissolving bubbles coalesce each other and become a stable SL bubble or an unstable SL bubble; otherwise they gradually dissolve into the liquid. Unstable SL bubbles or unstable bubbles coalesce each other and become a ''degas'' bubble; otherwise they disintegrate into a mass of smaller bubbles in a few or a few tens of acoustic cycles. Thus, the main mechanism of the bubble growth to a ''degas'' bubble is not the rectified diffusion but coalescence. Actually, Leighton[1] and Hatanaka *et al.*[21] observed frequent coalescence of bubbles.

A life of bubbles is summarized in Table II. It should be noted here that the dissolution of daughter bubbles created by the fragmentation of unstable SL bubbles is a very important process in sonochemistry because OH radicals and H_2O_2 molecules created inside bubbles are dispersed into the liquid effectively by this process.[33–35]

Now we discuss the relationship between the ultrasonic frequency and the mechanism of the light emission. According to the present computer simulations, the mechanism of the light emission is mainly plasma emissions at 140 kHz and 1 MHz at least at the acoustic amplitude below 10 bar, while at 20 kHz the light originates in both chemiluminescence of OH radicals and plasma emissions. When the acoustic amplitude is above 2 bar at 20 kHz, the bubble content at the end of the bubble collapse is mostly water vapor because the bubble expansion is so large that a large amount of water evaporates into a bubble at the bubble expansion.[4,5] At the bubble collapse, water vapor inside the bubble are dissociated by the high bubble temperature and strong chemiluminescence of OH radicals takes place.[4,5] On the other hand, at 140 kHz and 1 MHz, the amount of water vapor trapped inside a bubble at the end of the collapse is much smaller than that at 20 kHz because the bubble expansion is smaller due to the shorter period of ultrasound and a lesser amount of water evaporates into a bubble at the bubble expansion. Thus, at 140 kHz and 1 MHz, chemiluminescence of OH radicals is much weaker than that at 20 kHz and the light originates mainly in plasma emissions. Indeed, Weninger *et al.*[11] and Didenko *et al.*[25] reported that the MBSL spectra at 1 MHz have a much weaker OH line (chemiluminescence) than that at 20 kHz.

TABLE II. The diagram of a life of bubbles.

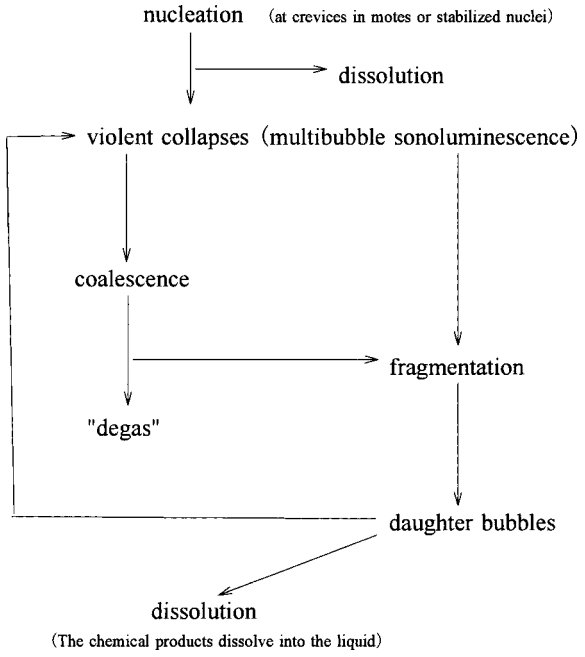

Now we discuss the widely used theory[36,37] of a life of bubbles under conditions of multibubble sonoluminescence. It has been believed that a small bubble repeats weak expansion and collapse, and grows gradually by the rectified diffusion. Finally, a bubble reaches a critical size and expands dramatically absorbing the energy of ultrasound, which is followed by a violent collapse which results in the light emission (sonoluminescence). The critical size is considered to be the linear resonance size.[32]

$$R_r = \sqrt{\frac{3\gamma p_\infty}{\rho \omega^2}}, \tag{10}$$

where R_r is the linear resonance radius, γ is the specific heat ratio of the gas inside a bubble, p_∞ is the ambient liquid

pressure, ρ is the liquid density, and ω is the angular frequency of ultrasound. The linear resonance radii of an argon bubble are 178 μm at 20 kHz, 25.4 μm at 140 kHz, and 3.56 μm at 1 MHz.

As seen in the Leighton's book[1] and the present paper, however, the widely used theory[36,37] is wrong. A bubble expands very much and collapses violently immediately after its appearance if the ambient bubble radius and the acoustic amplitude at the place where a bubble is created satisfy the condition for sonoluminescence (the region of unstable SL bubbles and stable SL bubbles in R_0-p_a space in Figs. 1–3). The range of the ambient bubble radius for sonoluminescence is over an order of magnitude and does not coincide with the linear resonance radius.

Now we discuss the widely used classification of bubbles;[38] transient cavitation bubbles and stable cavitation bubbles. As is understood from the terminology, a ''transient cavitation bubble'' exists only a few acoustic cycles or less. It expands to many times of its ambient size and collapses violently, often disintegrating into a mass of smaller bubbles. They are filled mainly with vapor.[38] A ''stable cavitation bubble'' exists for a long period of time. It repeats expansion and collapses many times. They contain mainly a permanent gas.[38] According to the present study, the widely used classification of bubbles[38] covers only a fraction of bubbles. ''Transient cavitation bubbles'' correspond to the unstable SL bubbles at high acoustic amplitude at low ultrasonic frequency in the present classification. ''Stable cavitation bubbles'' correspond to the stable SL bubbles.

IV. CONCLUSION

Computer simulations of bubble oscillations have revealed that the range of the ambient bubble radius for sonoluminescing bubbles narrows as the ultrasonic frequency increases because the bubble collapse becomes milder due to the shorter period of the bubble expansion. Any sonoluminescing bubble disintegrates into a mass of smaller bubbles in a few or a few tens of acoustic cycles at 1 MHz, while at 20 kHz and 140 kHz some sonoluminescing bubbles are shape stable, which are widely known as stable SBSL bubbles. The mechanism of the light emission depends on the ultrasonic frequency; at 1 MHz the light mainly originates in plasma emissions while at 20 kHz it originates both in chemiluminescence of OH radicals and plasma emissions. Because as the ultrasonic frequency increases a bubble expands less and the amount of vapor trapped inside a bubble decreases.

ACKNOWLEDGMENTS

The author thanks T. Tuziuti, H. Mitome, and Y. Iida for useful discussions and encouragements. This study was supported by Special Coordination Funds for Promoting Science and Technology from the Ministry of Education, Culture, Sports, Science, and Technology of Japan.

[1] T. G. Leighton, *The Acoustic Bubble* (Academic, London, 1994).
[2] W. Lauterborn, T. Kurz, R. Mettin, and C. D. Ohl, ''Experimental and theoretical bubble dynamics,'' Adv. Chem. Phys. **110**, 295–380 (1999).
[3] A. J. Walton and G. T. Reynolds, ''Sonoluminescence,'' Adv. Phys. **33**, 595–660 (1984).
[4] K. Yasui, ''Temperature in multibubble sonoluminescence,'' J. Chem. Phys. **115**, 2893–2896 (2001).
[5] K. Yasui, ''Effect of liquid temperature on sonoluminescence,'' Phys. Rev. E **64**, 016310 (2001).
[6] B. P. Barber, R. A. Hiller, R. Löfstedt, S. J. Putterman, and K. R. Weninger, ''Defining the unknowns of sonoluminescence,'' Phys. Rep. **281**, 66–143 (1997).
[7] M. P. Brenner, S. Hilgenfeldt, and D. Lohse, ''Single-bubble sonoluminescence,'' Rev. Mod. Phys. **74**, 425–484 (2002).
[8] S. Hilgenfeldt, S. Grossmann, and D. Lohse, ''A simple explanation of light emission in sonoluminescence,'' Nature (London) **398**, 402–405 (1999).
[9] K. Yasui, ''Mechanism of single-bubble sonoluminescence,'' Phys. Rev. E **60**, 1754–1758 (1999).
[10] D. Hammer and L. Frommhold, ''Spectra of sonoluminescent rare-gas bubbles,'' Phys. Rev. Lett. **85**, 1326–1329 (2000).
[11] K. R. Weninger, C. G. Camara, and S. J. Putterman, ''Observation of bubble dynamics within luminescent cavitation clouds: sonoluminescence at the nano-scale,'' Phys. Rev. E **63**, 016310 (2001).
[12] K. Yasui, ''Alternative model of single-bubble sonoluminescence,'' Phys. Rev. E **56**, 6750–6760 (1997).
[13] *Advances in Sonochemistry*, edited by T. J. Mason (JAI, London, 1990–2001), Vols. 1–6.
[14] K. Yasui, ''Effect of volatile solutes on sonoluminescence,'' J. Chem. Phys. **116**, 2945–2954 (2002).
[15] A. Eller and H. G. Flynn, ''Rectified diffusion during nonlinear pulsations of cavitation bubbles,'' J. Am. Chem. Soc. **37**, 493–503 (1965).
[16] M. M. Fyrillas and A. J. Szeri, ''Dissolution or growth of soluble spherical oscillating bubbles,'' J. Fluid Mech. **277**, 381–407 (1994).
[17] S. Hilgenfeldt, D. Lohse, and M. P. Brenner, ''Phase diagrams for sonoluminescing bubbles,'' Phys. Fluids **8**, 2808–2826 (1996).
[18] K. Yasui, ''Single-bubble dynamics in liquid nitrogen,'' Phys. Rev. E **58**, 471–479 (1998).
[19] S. Hatanaka, H. Mitome, T. Tuziuti, T. Kozuka, M. Kuwabara, and S. Asai, ''Relationship between a standing-wave field and a sonoluminescing field,'' Jpn. J. Appl. Phys., Part 1 **38**, 3053–3057 (1999).
[20] S. Hatanaka, K. Yasui, T. Tuziuti, and H. Mitome, ''Difference in threshold between sono- and sonochemical luminescence,'' Jpn. J. Appl. Phys., Part 1 **39**, 2962–2966 (2000).
[21] S. Hatanaka, K. Yasui, T. Tuziuti, T. Kozuka, and H. Mitome, ''Quenching mechanism of multibubble sonoluminescence at excessive sound pressure,'' Jpn. J. Appl. Phys., Part 1 **40**, 3856–3860 (2001).
[22] S. Hatanaka, K. Yasui, T. Kozuka, T. Tuziuti, and H. Mitome, ''Influence of bubble clustering on multibubble sonoluminescence,'' Ultrasonics **40**, 655–660 (2002).
[23] T. Tuziuti, S. Hatanaka, K. Yasui, T. Kozuka, and H. Mitome, ''Effect of ambient-pressure reduction on multibubble sonochemiluminescence,'' J. Chem. Phys. **116**, 6221–6227 (2002).
[24] N. Miyoshi, S. Hatanaka, K. Yasui, H. Mitome, and M. Fukuda, ''Effects of pH and surfactants on the ultrasound-induced chemiluminescence of luminol,'' Jpn. J. Appl. Phys., Part 1 **40**, 4097–4100 (2001).
[25] Y. T. Didenko, D. N. Nastich, S. P. Pugach, Y. A. Polovinka, and V. I. Kvochka, ''The effect of bulk solution temperature on the intensity and spectra of water sonoluminescence,'' Ultrasonics **32**, 71–76 (1994).
[26] B. P. Barber, K. Weninger, R. Löfstedt, and S. J. Putterman, ''Observation of a new phase of sonoluminescence at low partial pressures,'' Phys. Rev. Lett. **74**, 5276–5279 (1995).
[27] T. Kozuka (private communication); T. Kozuka, S. Hatanaka, T. Tuziuti, K. Yasui, and H. Mitome, ''Observation of a sonoluminescing bubble using a stroboscope,'' Jpn. J. Appl. Phys. Part 1 **39**, 2967–2968 (2000).
[28] H. G. Flynn and C. C. Church, ''A mechanism for the generation of cavitation maxima by pulsed ultrasound,'' J. Acoust. Soc. Am. **76**, 505–512 (1984).
[29] M. Matsumoto, ''Molecular dynamics simulation of interphase transport at liquid surfaces,'' Fluid Phase Equilib. **125**, 195–203 (1996).
[30] K. Yasui, ''Single-bubble sonoluminescence from noble gases,'' Phys. Rev. E **63**, 035301 (2001).
[31] Y. Q. Li, P. Davidovits, Q. Shi, J. T. Jayne, C. E. Kolb, and D. R. Worsnop, ''Mass and thermal accommodation coefficient of $H_2O(g)$ on liquid water as a function of temperature,'' J. Phys. Chem. A **105**, 10627–10634 (2001).

[32] F. R. Young, *Cavitation* (McGraw-Hill, London, 1989).
[33] A. J. Colussi, L. K. Weavers, and M. R. Hoffmann, ''Chemical bubble dynamics and quantitative sonochemistry,'' J. Phys. Chem. A **102**, 6927–6934 (1998).
[34] B. D. Storey and A. J. Szeri, ''Water vapour, sonoluminescence and sonochemistry,'' Proc. R. Soc. London, Ser. A **456**, 1685–1709 (2000).
[35] S. Hatanaka, H. Mitome, K. Yasui, and S. Hayashi (unpublished).
[36] K. S. Suslick, ''The chemical effects of ultrasound,'' Sci. Am. **260**, 62–68 (1989).
[37] M. A. Beckett and I. Hua, ''Impact of ultrasonic frequency on aqueous sonoluminescence and sonochemistry,'' J. Phys. Chem. A **105**, 3796–3802 (2001).
[38] A. Henglein, ''Sonochemistry: historical developments and modern aspects,'' Ultrasonics **25**, 6–16 (1987).

Theory of inert gas-condensing vapor thermoacoustics: Propagation equation[a)]

Richard Raspet,[b)] William V. Slaton,[c)] Craig J. Hickey, and Robert A. Hiller
Department of Physics and Astronomy and National Center for Physical Acoustics, University of Mississippi, University, Mississippi 38677

(Received 20 November 2001; revised 3 July 2002; accepted 11 July 2002)

The theory of acoustic propagation in an inert gas-condensing vapor mixture contained in a cylindrical pore with wet walls and an imposed temperature gradient is developed. It is shown that the vapor diffusion effects in the mixture are analogous to the heat diffusion effects in the thermoacoustics of inert gases, and that these effects occur in parallel with the heat diffusion effects in the wet system. The vapor diffusion effects can be expressed in terms of the thermoviscous function $F(\lambda)$ used in the theory of sound propagation of constant cross-section tubes. As such, these results can be extended to any shape parallel-walled tube. The propagation equations predict that the temperature gradient required for onset of sound amplification in a wet-walled prime mover is much lower than the corresponding temperature gradient for an inert gas prime mover. The results of a measurement of the onset temperature of a simple demonstration prime mover in air with a dry stack and with a stack wetted with water provide a qualitative verification of the theory. [DOI: 10.1121/1.1508113]

PACS numbers: 43.35.Ud [MRS]

LIST OF SYMBOLS

ρ, ρ_1, ρ_2	density of the mixture, gas, and vapor
P, P_1, P_2	pressure of the mixture, gas, and vapor
T	temperature of the mixture
$\mathbf{v}, \mathbf{v}_1, \mathbf{v}_2$	hydrodynamic velocity of the mixture, gas, and vapor
$\mathbf{i}$	density-weighted species difference velocity
s	entropy per unit mass of mixture
C_1	gas concentration
m_1, m_2	molecular mass of the gas, and vapor
n, n_1, n_2	total number density, number density of the gas, and vapor
μ	dynamic viscosity of the mixture
β	bulk viscosity of mixture
κ	thermal conductivity of the mixture
D_{12}	mass diffusion coefficient
k_T, k_p	thermal diffusion ratio and pressure diffusion ratio
c_p	specific heat per unit mass at constant pressure of the mixture
μ_c	chemical potential of mixture per unit mass
$\gamma, \gamma_1, \gamma_2$	ratio of specific heats of the mixture, gas, and vapor
l	latent heat of vaporization (J/mole)
c_s	speed of sound in the mixture
R_0	universal gas constant (8.3143 J/mole-K)
k	Boltzmann's constant
R	tube radius
$N_{\mathrm{Pr}}, N_{\mathrm{Sc}}$	Prandtl number, Schmitt number
ω	angular frequency
$\xi = \omega z/c_s$	nondimensional axial variable
$\eta = r/R$	nondimensional radial variable
$\Omega = \omega R/c_s$	reduced frequency
$\lambda_\mu = R\sqrt{\rho\omega/\mu}$	shear wave number
$\lambda_T = R\sqrt{\rho\omega c_p/\kappa}$	thermal wave number
$\lambda_D = R\sqrt{\omega/D_{12}}$	diffusion wave number
φ	latent heat parameter

I. INTRODUCTION

Recent work has developed the theory of sound propagation in inert gas-condensing vapor mixtures in narrow pores with wet walls.[1–3] The assumptions made about the gas, vapor, and pore wall are straightforward, namely: the wavelength and characteristic pore dimension must be much larger than the mean free path of the gas and vapor molecules, steady flow of the gas or vapor is second order in acoustic quantities and may be ignored in the first-order analysis, the amplitude of the acoustic pressure fluctuations is small, and end effects may be ignored. It is assumed that a thin layer of condensed vapor coats the solid surface of the

[a)]Portions of this work have been presented in: W. V. Slaton and R. Raspet, "Thermoacoustics of moist air with wet stacks," J. Acoust. Soc. Am. **106**, 2265 (1999); "Wet-walled thermoacoustics," *ibid.* **108**, 2569 (2000); R. Raspet, "Thermoacoustics Research at the University of Mississippi," First International Workshop on Thermoacoustics, 's-Hertogenbosch, The Netherlands, 22–25 April (2001); R. Raspet, "Thermoacoustic Refrigeration as an Application of Porous Media Theory," 4th Workshop on Applications of the Physics of Porous Media, Puerto Vallarta, Mexico, 31 Oct.–4 Nov. (2001); W. V. Slaton, J. W. Rayburn, R. A. Hiller, and R. Raspet, "Reduced onset temperature in wet thermoacoustic engines," J. Acoust. Soc. Am. **110**, 2677 (2001).

[b)]Author to whom correspondence should be addressed. Electronic mail: raspet@olemiss.edu

[c)]Current address: Physics Department, Eindhoven University of Technology, Eindhoven, The Netherlands.

pore wall. The layer is assumed thin enough to neglect its heat capacity. This layer is the site for evaporation and condensation of vapor. The pores are assumed to be on the order of a few mass diffusion lengths in radius so that condensation will occur preferentially on the walls rather than at any condensation centers in the bulk of the mixture. Considering an evaporation and condensation process implies that the vapor can enter the thin layer but the inert gas cannot. It is also assumed that there are no other sources or sinks of vapor or inert gas within the pore, that the heat capacity and thermal conductivity of the pore walls are high enough to ignore temperature fluctuations in the solid, and finally that the walls can be considered rigid.

The theory demonstrates that the terms describing the diffusion of the vapor are analogous in form to the terms describing thermal diffusion in the mixture, so that heat and mass transfer terms in an inert gas-condensing vapor mixture in a thermoacoustic engine have similar forms. If mixtures could be found with heat and mass transfer terms acting together, then the heat pumping capacity or coefficient of performance of a thermoacoustic refrigerator could be increased.

The thermodynamic cycle an inert gas–vapor mixture undergoes within a standing-wave thermoacoustic refrigerator is similar to that of a pure inert gas, with the addition that during the compressive part of the acoustic cycle the partial pressure of the vapor is raised above the saturation pressure at the temperature of the nearby stack wall so the vapor condenses. Conversely, during the rarefaction part of the acoustic cycle liquid on the stack evaporates. In this way, an inert gas–vapor working fluid will transport both heat and vapor from one end of the stack to the other, towards the pressure antinode. If a temperature gradient is imposed such that the temperature of the wall increases toward the antinode, thermal energy will be transported toward the antinode unless the temperature of the wall is raised to the point that it matches or exceeds the temperature of the mixture. This condition establishes a maximum temperature gradient for heat transfer in that direction. In the system with wet walls, increasing the wall temperature gradient also increases the saturation vapor pressure gradient at the wall. As the vapor pressure gradient at the wall is increased, acoustic vapor transport will occur until the vapor pressure at the wall is equal to the partial pressure of the vapor in the transported parcel. This establishes a different critical temperature gradient for the acoustic vapor transport. The transport of heat from the mixture to the wall depends solely on the transverse temperature gradients in the pore. The transport of vapor to the wall depends solely on the transverse gradient of the partial pressure or concentration in the mixture. The vapor transport also carries heat, since evaporating and condensing vapor transports entropy.

In this paper we develop the acoustic propagation equation in a wet-walled pore with an imposed temperature gradient. This is an extension of the dry inert gas thermoacoustic propagation formulation known as Rott's equation. This equation will be analyzed to display the potential of inert gas-condensing vapor to improve thermoacoustic prime movers and refrigerators. We employ the notation of Arnott *et al.*[4] for the thermoviscous functions. In Sec. II the hydrodynamic equations describing the system are introduced and Tijdeman's[5] ''low reduced frequency'' approximation is applied to this system of equations. The gradient in ambient quantities associated with the ambient temperature gradient is evaluated. The acoustic boundary conditions are described and the system of equations is then solved for the acoustic wave equation. In Sec. III the derived form of the wave equation is compared to the form found in Raspet *et al.*[1] for wet-walled tubes without an ambient temperature gradient and to the form for dry thermoacoustics.[4,6] Section IV contains a discussion of our formulation with respect to a thermoacoustic prime mover. Section V contains a summary of results underlying our model of ''wet'' thermoacoustics and the conclusions.

II. THEORY OF SOUND PROPAGATION

A. Basic equations

The model presented here employs the assumptions used by Raspet *et al.*[1] in the calculation of sound propagation in wet cylinders. A pore consists of a rigid cylindrical tube filled with an inert gas and saturated vapor. A thin layer of liquid coats the interior of the tube. It is assumed that the heat capacity of the tube wall is high enough that the temperature of the tube wall and the layer of liquid do not fluctuate.[3] The gas component cannot penetrate the tube wall or the liquid layer, and the gas–vapor mixture does not slip with respect to the liquid layer. The gas and vapor are treated as ideal gases, and properties of the mixture are computed according to the theory of gas mixtures.[7] It is also assumed that terms containing k_T, the thermal diffusion ratio, and k_p, the pressure diffusion ratio, can be neglected. The effect of k_T on sound propagation in wet pores has been shown to be small for this system.[2] The effects of streaming on the acoustic propagation are assumed to be negligible.

Equations governing sound propagation in an ideal gas–vapor mixture are presented. The Navier–Stokes equation for the mixture is

$$\rho \frac{D\mathbf{v}}{Dt} = -\boldsymbol{\nabla} P + \mu \nabla^2 \mathbf{v} + \left(\beta + \frac{\mu}{3}\right) \boldsymbol{\nabla}(\boldsymbol{\nabla} \cdot \mathbf{v}). \tag{1}$$

The continuity equation for the gas can be written in terms of the gas concentration as

$$\rho \frac{DC_1}{Dt} + \boldsymbol{\nabla} \cdot \mathbf{i} = 0, \tag{2}$$

where the gas concentration is $C_1 = \rho_1 / \rho$ and the density-weighted species difference velocity is given by $\mathbf{i} = (\rho_1 \rho_2 / \rho)(\mathbf{v}_1 - \mathbf{v}_2)$. The continuity equation for the vapor is

$$\frac{\partial \rho_2}{\partial t} + \boldsymbol{\nabla} \cdot (\rho_2 \mathbf{v}_2) = 0, \tag{3}$$

and the continuity equation for the mixture is

$$\frac{\partial \rho}{\partial t} + \boldsymbol{\nabla} \cdot (\rho \mathbf{v}) = 0, \tag{4}$$

where the mixture density is given by $\rho = \rho_1 + \rho_2$ and the

hydrodynamic velocity for the mixture is defined as $\mathbf{v}=(\rho_1\mathbf{v}_1+\rho_2\mathbf{v}_2)/\rho$. Only two independent continuity equations are required to complete the system of equations. The entropy equation for the mixture is

$$\rho T\frac{Ds}{Dt}=\sigma'_{ik}\frac{\partial v_i}{\partial x_k}-\nabla\cdot(\mathbf{q}-\mu_c\mathbf{i})-\mathbf{i}\cdot\nabla\mu_c, \tag{5a}$$

where the heat flux is given by

$$\mathbf{q}=\left[k_T\left(\frac{\partial\mu_c}{\partial C_1}\right)_{P,T}-T\left(\frac{\partial\mu_c}{\partial T}\right)_{P,C_1}+\mu_c\right]\mathbf{i}-\kappa\nabla T, \tag{5b}$$

the chemical potential for the mixture is

$$\mu_c=\frac{\mu'_1}{m_1}-\frac{\mu'_2}{m_2}, \tag{5c}$$

where μ'_1 and μ'_2 are the chemical potential per molecule of the gas and vapor respectively and σ'_{ik} is the viscous stress tensor.[8] The ideal gas equation of state is used for both the gas and vapor components, and for the mixture

$$P=nkT, \tag{6a}$$

where the temperature of the components are equal, $T=T_1=T_2$, the total mixture pressure is the sum of the partial pressures, $P=P_1+P_2$, and the total number density is given as $n=n_1+n_2$. In terms of concentration the equation of state is

$$P=nkT=\rho kT\left(\frac{n}{\rho}\right)=\rho kT\left[\left(\frac{m_2-m_1}{m_1m_2}\right)C_1+\frac{1}{m_2}\right]. \tag{6b}$$

The diffusion equation for the mixture is

$$\mathbf{i}=-\rho_0 D_{12}\left[\nabla C_1+\frac{k_T}{T_0}\nabla T+\frac{k_P}{P_0}\nabla P\right]. \tag{7}$$

For the wet-wall boundary conditions the concentration term dominates the diffusion process and k_T and k_P may be neglected. This differs from the acoustically driven mass diffusion studies,[9,10] which have dry pore walls and the principal contribution to diffusion is the k_T term.

The ratio of specific heats, γ, for the mixture can be related to the ratios of the two component gases by

$$\frac{n\gamma}{\gamma-1}=\frac{n_1\gamma_1}{\gamma_1-1}+\frac{n_2\gamma_2}{\gamma_2-1}. \tag{8}$$

Please see the list of symbols for a complete guide to variables and symbols used in the equations.

To reduce these equations to a useful form, we follow the analysis of Raspet *et al.*[1,2] For the sake of brevity we list the required steps and the resulting equations.

(1) Linearize equations assuming that steady flows are negligible and retaining terms in dT_0/dz and $d\rho_0/dz$.
(2) Neglect temperature-driven diffusion (Soret effect) and pressure-driven diffusion (Dufour effect); $k_T=0$, $k_P=0$.
(3) Assume that the tubes are small enough that we may use cylindrical coordinates with no azimuthal dependence.
(4) Introduce normalized variables with $e^{-i\omega t}$ time dependence

$$P=(\rho_0c_s^2/\gamma)(1+P^*e^{-i\omega t}), \tag{9}$$

$$\rho=\rho_0(1+\rho^*e^{-i\omega t}), \tag{10}$$

$$C_1=C_1^0+C_1^*e^{-i\omega t}, \tag{11}$$

$$T=T_0(1+T^*e^{-i\omega t}), \tag{12}$$

$$\mathbf{v}=c_s\mathbf{v}^*e^{-i\omega t}, \tag{13}$$

$$\mathbf{\Delta}=\mathbf{v}_1-\mathbf{v}_2=c_s\mathbf{\Delta}^*e^{-i\omega t}, \tag{14}$$

where c_s denotes the ambient speed of sound in the mixture. Symbols with a superscripted "*" denote small dimensionless quantities, while a subscripted "0" denotes ambient quantities. For convenience, we define

$$\mathbf{v}^*=u^*\hat{e}_z+v^*\hat{e}_r, \tag{15}$$

and

$$\mathbf{\Delta}^*=U^*\hat{e}_z+V^*\hat{e}_r. \tag{16}$$

(5) Define the normalized axial coordinate as

$$\xi=\frac{\omega z}{c_s}, \tag{17}$$

and the normalized radial coordinate as

$$\eta=\frac{r}{R}, \tag{18}$$

where R is the tube radius.
(6) Another normalized axial variable is given by

$$Z=\frac{z}{L}, \tag{19}$$

where L is the stack length and will be used to describe ambient gradients.

The components of the Navier–Stokes equation are unchanged from the analysis of Raspet *et al.*[1]

$$iu^*=\frac{1}{\gamma}\frac{\partial P^*}{\partial\xi}-\frac{\mu}{\rho_0\omega R^2}\left\{\frac{\partial^2u^*}{\partial\eta^2}+\frac{1}{\eta}\frac{\partial u^*}{\partial\eta}+\left(\frac{\omega R}{c_s}\right)^2\frac{\partial^2u^*}{\partial\xi^2}\right\}-\frac{\mu}{\rho_0\omega R^2}\left(\frac{\beta}{\mu}+\frac{1}{3}\right)\frac{\partial}{\partial\xi}\left\{\left(\frac{\omega R}{c_s}\right)\frac{\partial u^*}{\partial\xi}+\frac{\partial v^*}{\partial\eta}+\frac{v^*}{\eta}\right\}, \tag{20}$$

and

$$iv^*=\frac{1}{\gamma}\left(\frac{c_s}{\omega R}\right)\frac{\partial P^*}{\partial\xi}-\frac{\mu}{\rho_0\omega R^2}\times\left\{\frac{\partial^2v^*}{\partial\eta^2}+\frac{1}{\eta}\frac{\partial v^*}{\partial\eta}-\frac{v^*}{\eta^2}+\left(\frac{\omega R}{c_s}\right)^2\frac{\partial^2v^*}{\partial\xi^2}\right\}-\frac{\mu}{\rho_0\omega R^2}\left(\frac{\beta}{\mu}+\frac{1}{3}\right)\frac{\partial}{\partial\eta}\left\{\left(\frac{\omega R}{c_s}\right)\frac{\partial u^*}{\partial\xi}+\frac{\partial v^*}{\partial\eta}+\frac{v^*}{\eta}\right\}. \tag{21}$$

The continuity equation for the mixture is

$$i\left(\frac{\omega R}{c_s}\right)\rho^*=\left(\frac{\omega R}{c_s}\right)\frac{\partial u^*}{\partial\xi}+\frac{1}{\eta}\frac{\partial}{\partial\eta}(\eta v^*)+\frac{u^*}{\rho_0}\left[\frac{R}{L}\right]\frac{d\rho_0}{dZ}, \tag{22}$$

and the continuity of gas in terms of concentration is

$$i\left(\frac{\omega R}{c_s}\right)C_1^*=\frac{\rho_1^0\rho_2^0}{\rho_0^2}\left[\frac{1}{\eta}\frac{\partial}{\partial\eta}(\eta V^*)+\left(\frac{\omega R}{c_s}\right)\frac{\partial U^*}{\partial\xi}\right]+\frac{U^*}{\rho_0}\left[\frac{R}{L}\right]\frac{d}{dZ}\left[\frac{\rho_1^0\rho_2^0}{\rho_0}\right]+u^*\left[\frac{R}{L}\right]\frac{d}{dZ}\left[\frac{\rho_1^0}{\rho_0}\right]. \tag{23}$$

Following the development of Landau and Lifshitz,[8] Chap. VI, and using the ideal gas relation for the thermal expansion coefficient, the entropy equation is

$$i\left(\frac{\omega R}{c_s}\right)\left\{T^*+\frac{\gamma-1}{\gamma}P^*\right\}=-\frac{\kappa}{\rho_0 c_p\omega R^2}\left(\frac{\omega R}{c_s}\right)\left\{\frac{\partial^2 T^*}{\partial\eta^2}+\frac{1}{\eta}\frac{\partial T^*}{\partial\eta}+\left(\frac{\omega R}{c_s}\right)^2\frac{\partial^2 T^*}{\partial\xi^2}\right\}+\frac{u^*}{T_0}\left[\frac{R}{L}\right]\frac{dT_0}{dZ}+\frac{\rho_1^0\rho_2^0}{\rho_0^2}\frac{U^*}{c_p T_0}\left[\frac{R}{L}\right]\frac{d}{dZ}\times\left(\frac{\mu_c}{T_0}-T_0\left(\frac{\partial}{\partial T}\left(\frac{\mu_c}{T_0}\right)\right)_{P,C_1}\right). \tag{24}$$

Use of the continuity equations and the diffusion equation in the equation of state yields

$$\left(\frac{\omega R}{c_s}\right)\{P^*-T^*-\rho^*\}=i\frac{n_1^0 n_2^0}{n_0\rho_0}(m_1-m_2)\left\{\left(\frac{\omega R}{c_s}\right)\frac{\partial U^*}{\partial\xi}+\frac{1}{\eta}\frac{\partial}{\partial\eta}(\eta V^*)\right\}+i\frac{\rho_0}{n_0}\left(\frac{m_1-m_2}{m_1 m_2}\right)\left[\frac{R}{L}\right]\left\{u^*\frac{d}{dZ}\left[\frac{\rho_1^0}{\rho_0}\right]+\frac{U^*}{\rho_0}\frac{d}{dZ}\left[\frac{\rho_1^0\rho_2^0}{\rho_0}\right]\right\}. \tag{25}$$

The axial component of diffusion is

$$i\frac{\rho_1^0\rho_2^0}{\rho_0}U^*=-\frac{\rho_0 D_{12}}{\omega R^2}\left(\frac{\rho_1^0\rho_2^0}{\rho_0^2}\left(\frac{\omega R}{c_s}\right)\frac{\partial}{\partial\xi}\left[\frac{1}{\eta}\frac{\partial}{\partial\eta}(\eta V^*)+\left(\frac{\omega R}{c_s}\right)\frac{\partial U^*}{\partial\xi}\right]\right)-\frac{\rho_0 D_{12}}{\omega R^2}\left(\left[\frac{1}{\eta}\frac{\partial}{\partial\eta}(\eta V^*)+\left(\frac{\omega R}{c_s}\right)\frac{\partial U^*}{\partial\xi}\right]\times\left[\frac{R}{L}\right]\frac{d}{dZ}\left[\frac{\rho_1^0\rho_2^0}{\rho_0^2}\right]\right)-\frac{\rho_0 D_{12}}{\omega R^2}\left(\frac{U^*}{\rho_0}\left[\frac{R}{L}\right]^2\frac{d^2}{dZ^2}\left[\frac{\rho_1^0\rho_2^0}{\rho_0}\right]+\frac{R^2}{\rho_0}\left(\frac{\omega R}{c_s}\right)\frac{\partial U^*}{\partial\xi}\left[\frac{R}{L}\right]\frac{d}{dZ}\left[\frac{\rho_1^0\rho_2^0}{\rho_0}\right]\right)-\frac{\rho_0 D_{12}}{\omega R^2}\left(u^*\left[\frac{R}{L}\right]^2\frac{d^2}{dZ^2}\left[\frac{\rho_1^0}{\rho_0}\right]+R^2\left(\frac{\omega R}{c_s}\right)\frac{\partial u^*}{\partial\xi}\left[\frac{R}{L}\right]\frac{d}{dZ}\left[\frac{\rho_1^0}{\rho_0}\right]\right), \tag{26}$$

and the radial component of diffusion is

$$i\frac{\rho_1^0\rho_2^0}{\rho_0^2}V^*=-\frac{D_{12}}{\omega R^2}\left(\frac{\rho_1^0\rho_2^0}{\rho_0^2}\frac{\partial}{\partial\eta}\left[\frac{1}{\eta}\frac{\partial}{\partial\eta}(\eta V^*)+\left(\frac{\omega R}{c_s}\right)\frac{\partial U^*}{\partial\xi}\right]\right)-\frac{D_{12}}{\omega R^2}\left(\frac{1}{\rho_0}\frac{\partial U^*}{\partial\eta}\left[\frac{R}{L}\right]\frac{d}{dZ}\left[\frac{\rho_1^0\rho_2^0}{\rho_0}\right]\right)-\frac{D_{12}}{\omega R^2}\left(\frac{\partial u^*}{\partial\eta}\left[\frac{R}{L}\right]\frac{d}{dZ}\left[\frac{\rho_1^0}{\rho_0}\right]\right). \tag{27}$$

The eight equations above form a complete set for the variables, u^*, v^*, P^*, ρ^*, U^*, V^*, T^*, C_1^*. We note that the system of equations can be solved for u^*, v^*, P^*, ρ^*, U^*, V^*, T^* without using Eq. (23). This equation is retained here for convenience in future calculations.

B. Evaluation of ambient gradients

Derivatives with respect to the ambient density, ρ_0, and ambient concentration, ρ_1^0/ρ_0, must be evaluated. In dry thermoacoustics the ambient density is inversely proportional to the ambient temperature. In a wet-walled stack with a temperature gradient, the temperature dependence of the vapor pressure of the liquid coating the stack must be taken into account. This will affect the ambient ratio of gas to vapor in the mixture. Since the total pressure in the resonator is a constant, then at high ambient temperature there is a higher ratio of vapor to gas in the mixture; likewise, at lower ambient temperature there is a lower ratio of vapor to gas in the mixture.

We assume that the pore is small enough so that the ambient partial pressure is a function only of the axial position. This is equivalent to the assumption that the ambient gas temperature is a function only of the axial position assumed in inert gas thermoacoustics.

Using the expressions $\rho_0=\rho_1+\rho_2$, $\rho_1=n_1 m_1$, and $\rho_2=n_2 m_2$, derivatives with respect to the ambient density can be written as

$$\frac{d\rho_0}{dZ}=m_1\frac{dn_1^0}{dZ}+m_2\frac{dn_2^0}{dZ}=m_1\frac{dn_0}{dZ}+(m_2-m_1)\frac{dn_2^0}{dZ}=m_1\frac{dn_0}{dT_0}\frac{dT_0}{dZ}+(m_2-m_1)\frac{dn_2^0}{dT_0}\frac{dT_0}{dZ}. \tag{28}$$

The term, dn_0/dT_0, can be calculated using the ideal gas law, yielding $dn_0/dT_0=-n_0/T_0$ after simplification. The Clausius–Clapeyron[11] equation for the vapor pressure is

$$P_2 = P_{\text{ref}} \exp\left[-\frac{l}{R_0}\left(\frac{1}{T_0} - \frac{1}{T_{\text{ref}}}\right)\right] = n_2 k T_0, \tag{29}$$

where T_{ref} is the boiling point at pressure P_{ref}. Evaluating for dn_2^0/dT_0 yields

$$\frac{dn_2^0}{dT_0} = \frac{n_2^0}{T_0}\left(\frac{l}{R_0 T_0} - 1\right). \tag{30}$$

We now introduce the "latent heat parameter," $\varphi = [(\gamma - 1)/\gamma](l/R_0 T_0)$, as defined by Marble.[12] Substituting into Eq. (28), the derivative of the ambient density, after some manipulation, can be expressed as

$$\frac{d\rho_0}{dZ} = -\frac{\rho_0}{T_0}\frac{dT_0}{dZ}\left[1 - \varphi\frac{\gamma}{\gamma - 1}\left(1 - \frac{m_1}{m_2}\right)\frac{\rho_2^0}{\rho_0}\right]. \tag{31}$$

Derivatives of the ambient gas concentration, ρ_1^0/ρ_0, can be evaluated in a similar fashion

$$\begin{aligned}\frac{d}{dZ}\left[\frac{\rho_1^0}{\rho_0}\right] &= \frac{1}{\rho_0}\frac{d\rho_1^0}{dZ} + \rho_1^0 \frac{d}{dZ}\left[\frac{1}{\rho_0}\right] \\ &= \frac{1}{\rho_0^2}\left\{(\rho_1^0 + \rho_2^0)\frac{d\rho_1^0}{dZ} - \rho_1^0\frac{d\rho_1^0}{dZ} - \rho_1^0\frac{d\rho_2^0}{dZ}\right\} \\ &= \frac{m_1 m_2}{\rho_0^2}\left\{n_2^0\frac{dn_0}{dT_0}\frac{dT_0}{dZ} - n_0\frac{dn_2^0}{dT_0}\frac{dT_0}{dZ}\right\}. \end{aligned} \tag{32}$$

Making use of the derivatives found earlier for dn_0/dT_0 and dn_2^0/dT_0, our expression simplifies to

$$\frac{dC_1^0}{dZ} = \frac{d}{dZ}\left[\frac{\rho_1^0}{\rho_0}\right] = -\varphi\frac{\gamma}{\gamma - 1}\frac{\rho_1^0\rho_2^0}{\rho_0^2}\frac{n_0}{n_1^0}\frac{1}{T_0}\frac{dT_0}{dZ}. \tag{33}$$

If there is no vapor present, then there is no ambient gradient in the gas concentration. Note also that this term, like the one above for the derivative of the ambient density, is scaled by the latent heat parameter.

C. Boundary conditions

The boundary conditions at the wall of the tube, $\eta = 1$, and at the center, $\eta = 0$, are the same as used by Raspet *et al.*[1] These boundary conditions must be cast into the present variables. The boundary conditions at the tube wall, $\eta = 1$, are as follows.

(1) It is assumed that the heat capacity of the tube wall is high enough that the temperature of the tube wall and the layer of condensate do not fluctuate
$$T^* = 0. \tag{34}$$
(2) No axial slip for the mixture hydrodynamic velocity
$$u^* = 0. \tag{35}$$
(3) The gas cannot penetrate the tube wall or condensate layer, $v_1^* = 0$, which can be written as
$$v^* + \frac{\rho_2^0}{\rho_0}V^* = 0. \tag{36}$$
(4) The vapor pressure is constant at the wall since the vapor pressure is only a function of temperature, and by the first boundary condition we have assumed that there are no temperature fluctuations at the wall. This implies that $p_2^* = 0$ at the wall. Use of the continuity conditions, the definition of Δ, and the equation of state gives
$$i\Omega P^* = \frac{n_1^0}{n_0}\frac{1}{\eta}\frac{\partial}{\partial\eta}(\eta V^*). \tag{37}$$

The boundary conditions on the axis of the tube, $\eta = 0$, are that P^*, T^*, u^*, U^*, ρ_1^*, and ρ_2^* be finite. The latter two conditions on ρ_1^* and ρ_2^* can be related to v^* and V^* by the continuity equations, which are singular unless v and V are zero at $\eta = 0$. Thus, our final boundary conditions are

(5) Axis of tube is not a source or sink of vapor
$$V^* = 0. \tag{38}$$
(6) Axis of tube is not a source or sink of mixture
$$v^* = 0. \tag{39}$$

D. Solution

A formal approach to the approximation and interpretation of the complicated equations of wet thermoacoustics is the "low reduced frequency" analysis of Tijdeman.[5] This technique has been applied to the mass transfer problem by Raspet *et al.*[1]

The principal approximation is to require that the reduced frequency, Ω, be small

$$\Omega = \frac{\omega R}{c_s} = \frac{2\pi R}{\lambda} \ll 1. \tag{40}$$

This spans a wide range of frequencies for small tubes and in fact includes regions where the Kirchhoff wide-tube approximation holds, as well as the Rayleigh narrow-tube/low-frequency region. The physical meaning of this approximation is to assume that the tube radius is much smaller than the wavelength. This assures that there will be no cross modes within the tube and that radial derivatives are much larger than axial derivatives. A second set of criteria is also used to retain some terms that would otherwise be neglected

$$u^* \gg v^*, \tag{41}$$

and

$$v^* \approx V^*. \tag{42}$$

We expect the first condition to be met since the radial velocity must be zero at the center and the displacement per cycle is at most on the order of one radius. The second condition arises since v^* and V^* are the same order of magnitude at the wall and both are zero at the center, since the tube axis is not a source or sink. The above criteria are the same as those of Raspet *et al.*[1] Generalization to include an ambient temperature gradient naturally implies a length scale, which has been chosen to be the stack length L. It is usually justifiable to assume that the characteristic pore dimension, i.e., pore radius, is much smaller than the stack length

$$\frac{R}{L} \ll 1. \tag{43}$$

The system is solvable without this assumption, but this added complexity is not justified in this study.

Certain nondimensional groupings of parameters may be identified:

the dimensionless shear wave number

$$\lambda_\mu = R\sqrt{\frac{\rho\omega}{\mu}} = \frac{\sqrt{2}R}{\delta_\mu}, \tag{44}$$

the dimensionless thermal wave number

$$\lambda_T = R\sqrt{\frac{nk\gamma}{\gamma-1}\frac{\omega}{\kappa}} = R\sqrt{\frac{\rho\omega c_p}{\kappa}} = \frac{\sqrt{2}R}{\delta_T}, \tag{45}$$

and the dimensionless diffusion wave number,

$$\lambda_D = R\sqrt{\frac{\omega}{D_{12}}} = \frac{\sqrt{2}R}{\delta_D}. \tag{46}$$

These wave numbers are inversely proportional to the associated penetration depths.

We rewrite Eqs. (20)–(27) using Eqs. (31) and (33) for ambient gradients and retain the lowest-order terms in Ω and R/L. We treat terms in v^* and V^* as first-order terms in Ω, which is consistent with Eq. (40) and Eq. (43). With the definitions above and the application of the low reduced frequency approximation, the axial component of Navier–Stokes is

$$iu^* = \frac{1}{\gamma}\frac{\partial P^*}{\partial \xi} - \frac{1}{\lambda_\mu^2}\left[\frac{\partial^2 u^*}{\partial \eta^2} + \frac{1}{\eta}\frac{\partial u^*}{\partial \eta}\right], \tag{47}$$

and the radial component of Navier–Stokes is

$$\frac{1}{\gamma}\frac{\partial P^*}{\partial \eta} = 0. \tag{48}$$

The axial diffusion equation simplifies to

$$iU^* = 0, \tag{49}$$

which will be used to eliminate U^* and $\partial U^*/\partial\xi$ in the following equations. The radial diffusion equation is

$$iV^* = -\frac{1}{\lambda_D^2}\left\{\frac{\partial}{\partial\eta}\left(\frac{1}{\eta}\frac{\partial}{\partial\eta}(\eta V^*)\right) - \varphi\frac{\gamma}{\gamma-1}\frac{n_0}{n_1^0}\left[\frac{R}{L}\right]\frac{1}{T_0}\frac{dT_0}{dZ}\frac{\partial u^*}{\partial\eta}\right\}. \tag{50}$$

The continuity of the gas in terms of concentration is

$$i\Omega C_1^* = \frac{\rho_1^0\rho_2^0}{\rho_0^2}\frac{1}{\eta}\frac{\partial}{\partial\eta}(\eta V^*) - u^*\varphi\frac{\gamma}{\gamma-1}\frac{\rho_1^0\rho_2^0}{\rho_0^2}\frac{n_0}{n_1^0}\left[\frac{R}{L}\right]\frac{1}{T_0}\frac{dT_0}{dZ}, \tag{51}$$

the continuity equation for the mixture is

$$i\Omega\rho^* = \Omega\frac{\partial u^*}{\partial\xi} + \frac{1}{\eta}\frac{\partial}{\partial\eta}(\eta v^*) - \left[\frac{R}{L}\right]\frac{u^*}{T_0}\frac{dT_0}{dZ}\left(1-\varphi\frac{\gamma}{\gamma-1}\left(1-\frac{m_1}{m_2}\right)\frac{\rho_2^0}{\rho_0}\right), \tag{52}$$

the entropy equation is

$$i\Omega T^* - i\Omega\frac{\gamma-1}{\gamma}P^* + \frac{\Omega}{\lambda_T^2}\left[\frac{\partial^2 T^*}{\partial\eta^2} + \frac{1}{\eta}\frac{\partial T^*}{\partial\eta}\right] = \left[\frac{R}{L}\right]\frac{u^*}{T_0}\frac{dT_0}{dZ}, \tag{53}$$

and the equation of state is

$$\Omega(P^* - T^* - \rho^*) = i\frac{n_1^0 n_2^0}{n_0\rho_0}(m_1-m_2)\left[\frac{1}{\eta}\frac{\partial}{\partial\eta}(\eta V^*) - u^*\varphi\frac{\gamma}{\gamma-1}\frac{n_0}{n_1^0}\left[\frac{R}{L}\right]\frac{1}{T_0}\frac{dT_0}{dZ}\right]. \tag{54}$$

The axial and radial components of the Navier–Stokes equation are unchanged and demonstrate that the pressure is not a function of radial position. The axial component (47) shows that acoustic velocity is generated by axial gradients in pressure, with some modifications to account for shearing due to the pore walls. The terms on the right-hand side of the continuity equation (52) represent mass entering or leaving a region due to acoustic density fluctuations or by acoustic convection of a density gradient. The entropy equation (53) describes how temperature fluctuations are generated by pressure oscillations and by fluid oscillating between regions with varying ambient temperature. The equation of state (54) describes how the density fluctuations are generated by pressure and temperature oscillations as well as diffusion of vapor into or out of a region. Density fluctuations are also generated by fluid oscillating back and forth between regions with different ambient temperatures. However, if the two components have the same mass, diffusion does not contribute to density fluctuations since the additional term describes density changes due to the species velocity differing from the hydrodynamic velocity. Last, the radial diffusion equation (50) describes how interspecies diffusion is driven by gradients in the radial diffusion velocity and by fluid oscillating between regions of different ambient temperatures.

Note that the Navier–Stokes, entropy, and diffusion equations are decoupled. The solutions will be in terms of separate diffusion, thermal, and viscous wave numbers. This is the principal result of the low reduced frequency approximation. This shows that these processes are independent, to first order, and only coupled in the equation of continuity and equation of state for the mixture.

The axial Navier–Stokes equation is solved by noting that the pressure is only a function of the axial coordinate and by applying the no-slip boundary condition at the wall to obtain the axial hydrodynamic velocity

$$u^* = -\frac{i}{\gamma}\frac{dP^*}{d\xi}\left[1-\frac{J_0(\sqrt{i}\lambda_\mu\eta)}{J_0(\sqrt{i}\lambda_\mu)}\right] = -\frac{i}{\gamma}\frac{dP^*}{d\xi}\mathbf{F}_\mu(\eta). \tag{55}$$

We have introduced here the definitions

$$\mathbf{F}_j(\eta) = 1 - \frac{J_0(\sqrt{i}\lambda_j\eta)}{J_0(\sqrt{i}\lambda_j)}, \tag{56a}$$

where

$$\int_0^1 \mathbf{F}_j(\eta)\,\eta\,d\eta = \frac{1}{2}\left(1-\frac{2J_1(\sqrt{i}\lambda_j)}{\sqrt{i}\lambda_j J_0(\sqrt{i}\lambda_j)}\right) = \frac{1}{2}F(\lambda_j). \tag{56b}$$

$F(\lambda_j)$ is the porous media dissipation function for cylindrical tubes and $j=T,D,\mu$. The recursion relation for the Bessel functions has been used to evaluate the integral. The evaluation in terms of generalized dissipation functions is given in Ref. 4.

Making use of this solution and the boundary condition on vapor pressure at the wall, the radial diffusion equation is solved using separation of variables to obtain the radial diffusion velocity

$$V^*=i\Omega\frac{n_0}{n_1^0}\left[\left\{P^*-\frac{1}{\Omega}\frac{1}{1-N_{\mathrm{Sc}}}\frac{\varphi}{\gamma-1}\frac{1}{T_0}\frac{dT_0}{dZ}\left[\frac{R}{L}\right]\frac{dP^*}{d\xi}\right\}\times\frac{J_1(\sqrt{i}\lambda_D\eta)}{\sqrt{i}\lambda_D J_0(\sqrt{i}\lambda_D)}+\frac{1}{\Omega}\frac{1}{1-N_{\mathrm{Sc}}}\frac{\varphi}{\gamma-1}\frac{1}{T_0}\frac{dT_0}{dZ}\times\left[\frac{R}{L}\right]\frac{dP^*}{d\xi}\frac{J_1(\sqrt{i}\lambda_\mu\eta)}{\sqrt{i}\lambda_\mu J_0(\sqrt{i}\lambda_\mu)}\right], \tag{57}$$

where the Schmidt number is $N_{\mathrm{Sc}}=\lambda_D^2/\lambda_\mu^2=\mu/\rho_0 D_{12}$.

In anticipation of later results it is convenient to calculate the fluctuating component of the gas concentration, C_1^* by making use of the solutions for u^* and V^* above to obtain

$$C_1^*=\frac{\rho_1^0\rho_2^0}{\rho_0^2}\frac{n_0}{n_1^0}\left[P^*(1-\mathbf{F}_D(\eta))+\frac{1}{\Omega}\frac{\varphi}{\gamma-1}\frac{1}{T_0}\frac{dT_0}{dZ}\left[\frac{R}{L}\right]\frac{dP^*}{d\xi}\mathbf{F}_\mu(\eta)+\frac{1}{\Omega}\frac{\varphi}{\gamma-1}\frac{1}{T_0}\frac{dT_0}{dZ}\left[\frac{R}{L}\right]\frac{dP^*}{d\xi}\frac{\mathbf{F}_D(\eta)-\mathbf{F}_\mu(\eta)}{1-N_{\mathrm{Sc}}}\right]. \tag{58}$$

Substituting the solution for u^* into the entropy equation and using the boundary condition, $T^*=0$ at $\eta=1$ yields the dimensionless temperature fluctuations

$$T^*=\frac{\gamma-1}{\gamma}P^*\mathbf{F}_T(\eta)-\frac{1}{\Omega}\frac{1}{\gamma}\frac{dP^*}{d\xi}\left[\frac{R}{L}\right]\frac{1}{T_0}\frac{dT_0}{dZ}\left[\frac{\mathbf{F}_T(\eta)-N_{\mathrm{Pr}}\mathbf{F}_u(\eta)}{1-N_{\mathrm{Pr}}}\right], \tag{59}$$

where the Prandtl number $N_{\mathrm{Pr}}=\lambda_T^2/\lambda_\mu^2=\mu c_p/\kappa$.

We eliminate ρ^* from the equation of state using Eq. (52) and substitute the solutions for T^*, V^*, and u^* to find

$$\frac{1}{\eta}\frac{\partial}{\partial\eta}(\eta v^*)=\frac{i\Omega}{\gamma}\frac{d^2P^*}{d\xi^2}\mathbf{F}_\mu(\eta)+i\Omega P^*\left(1-\frac{\gamma-1}{\gamma}\mathbf{F}_T(\eta)\right)+\frac{n_1^0n_2^0}{n_0\rho_0}(m_1-m_2)\frac{1}{\eta}\frac{\partial}{\partial\eta}(\eta V^*)+\frac{i}{\gamma}\left[\frac{R}{L}\right]\frac{1}{T_0}\frac{dT_0}{dZ}\frac{dP^*}{d\xi}\times\left\{\frac{\mathbf{F}_T(\eta)-N_{\mathrm{Pr}}\mathbf{F}_\mu(\eta)}{1-N_{\mathrm{Pr}}}-\mathbf{F}_\mu(\eta)\right\}. \tag{60}$$

Multiply through by $\eta\,d\eta$ and integrate from 0 to 1 using the boundary condition on v^* and V^* at $\eta=0$ to eliminate the constants of integration

$$v^*|_{\eta=1}=\frac{i\Omega}{\gamma}\frac{d^2P^*}{d\xi^2}\frac{F(\lambda_\mu)}{2}+\frac{i\Omega P^*}{2}\left(1-\frac{\gamma-1}{\gamma}F(\lambda_T)\right)+\frac{n_1^0n_2^0}{n_0\rho_0}(m_1-m_2)V^*|_{\eta=1}+\frac{i}{2\gamma}\left[\frac{R}{L}\right]\frac{1}{T_0}\frac{dT_0}{dZ}\frac{dP^*}{d\xi}\times\left\{\frac{F(\lambda_T)-N_{\mathrm{Pr}}F(\lambda_\mu)}{1-N_{\mathrm{Pr}}}-F(\lambda_\mu)\right\}. \tag{61}$$

Now, employ the final boundary condition, $v^*+(\rho_2^0/\rho_0)V^*=0$ at $\eta=1$, using the above expression for the dimensionless radial diffusion velocity evaluated at $\eta=1$, to obtain the following form:

$$\frac{d^2P^*}{d\xi^2}F(\lambda_\mu)+\gamma P^*\left(1-\frac{\gamma-1}{\gamma}F(\lambda_T)+\frac{n_2^0}{n_1^0}(1-F(\lambda_D))\right)+\frac{1}{\Omega}\left[\frac{R}{L}\right]\frac{1}{T_0}\frac{dT_0}{dZ}\frac{dP^*}{d\xi}\left\{\frac{F(\lambda_T)-F(\lambda_\mu)}{1-N_{\mathrm{Pr}}}+\varphi\frac{n_2^0}{n_1^0}\frac{\gamma}{\gamma-1}\left(\frac{F(\lambda_D)-F(\lambda_\mu)}{1-N_{\mathrm{Sc}}}\right)\right\}=0. \tag{62}$$

Converting to dimensional form in terms of the complex pressure amplitude, $P_{\mathrm{AC}}=P_0P^*$, we have

$$\frac{d^2P_{\mathrm{AC}}}{dz^2}+2\alpha\frac{dP_{\mathrm{AC}}}{dz}+k^2P_{\mathrm{AC}}=0, \tag{63}$$

where

$$\alpha=\frac{1}{2}\frac{1}{T_0}\frac{dT_0}{dz}\left\{\frac{F(\lambda_T)/F(\lambda_\mu)-1}{1-N_{\mathrm{Pr}}}+\varphi\frac{\gamma}{\gamma-1}\frac{n_2^0}{n_1^0}\frac{F(\lambda_D)/F(\lambda_\mu)-1}{1-N_{\mathrm{Sc}}}\right\}, \tag{64}$$

and

$$k^2=\frac{\omega^2}{c^2}\frac{\gamma}{F(\lambda_\mu)}\left\{1-\frac{\gamma-1}{\gamma}F(\lambda_T)+\frac{n_2^0}{n_1^0}(1-F(\lambda_D))\right\}. \tag{65}$$

Equation (63) describes the acoustic pressure fluctuations in a wet-walled tube with a temperature gradient. We note that although we have solved this for cylindrical pores, parallel walled pores of other shapes can be described by substitution of the appropriate thermoviscous dissipation function, $F(\lambda_j)$.[4]

For purposes of discussion and numerical integration, it is useful to rewrite Eq. (63) as two first-order differential equations in the acoustic pressure and volume velocity. Averaging Eq. (55), the axial hydrodynamic velocity, over the cross-sectional area of the pore in terms of the dimensionless radial coordinate $\eta=r/R$ and ignoring the thin condensate layer gives

$$u^*_{\mathrm{Ave}}=\frac{1}{A_{\mathrm{pore}}}\int_{A_{\mathrm{pore}}} u^*\,dA_{\mathrm{pore}}$$
$$=-\frac{2i}{\gamma}\frac{dP^*}{d\xi}\int_0^1\left(1-\frac{J_0(\sqrt{i}\lambda_\mu\eta)}{J_0(\sqrt{i}\lambda_\mu)}\right)\eta\,d\eta$$
$$=-\frac{2i}{\gamma}\frac{dP^*}{d\xi}\frac{F(\lambda_\mu)}{2}, \tag{66}$$

where recursion relations for the Bessel functions have been used to evaluate the integral. Rearranging to solve for the acoustic pressure gradient while making use of the following expressions, $P^*=P_{\mathrm{AC}}/P_0$, $P_0=\rho_0 c_s^2/\gamma$, and $\xi=\omega z/c_s$, and realizing that the acoustic volumetric velocity $U_{\mathrm{vol}}=A_{\mathrm{mix}}c_s u^*_{\mathrm{Ave}}$ yields

$$\frac{dP_{\mathrm{AC}}}{dz}=\frac{i\omega\rho_0}{A_{\mathrm{mix}}}\frac{U_{\mathrm{vol}}}{F(\lambda_\mu)}, \tag{67}$$

where A_{mix} is the total stack cross-sectional area available to the gas/vapor mixture. Using this expression in Eq. (63) and using the expressions above for P^*, P_0, and ξ gives, after rearrangement

$$\frac{dU_{\mathrm{vol}}}{dz}=-\frac{A_{\mathrm{mix}}}{i\omega\rho_0}F(\lambda_\mu)k^2P_{\mathrm{AC}}-2\alpha U_{\mathrm{vol}}, \tag{68}$$

where α and k^2 are defined in Eq. (64) and Eq. (65). Equations (67) and (68) are coupled first-order equations for acoustic pressure fluctuations and acoustic volumetric velocity fluctuations.

III. LIMITING CASES

A. Acoustics of wet porous media

To compare to recent work in porous media theory, we let the ambient temperature gradient, dT_0/dz, go to zero in Eqs. (63)–(65). This makes the term $\alpha=0$, and our acoustic wave equation becomes

$$\frac{d^2P_{\mathrm{AC}}}{dz^2}+k^2P_{\mathrm{AC}}=0, \tag{69}$$

with

$$k^2=\frac{\omega^2}{c^2}\frac{\gamma}{F(\lambda_\mu)}\left\{1-\frac{\gamma-1}{\gamma}F(\lambda_T)+\frac{n_2^0}{n_1^0}(1-F(\lambda_D))\right\}. \tag{70}$$

This agrees with Raspet *et al.*[1] subject to the assumption that the thermal diffusion ratio, k_T, is zero.

B. Dry thermoacoustics

To compare to dry thermoacoustics, we let the number density of the vapor, n_2^0, go to zero in Eqs. (63)–(65). The solution for the wave equation then becomes

$$\frac{d^2P_{\mathrm{AC}}}{dz^2}+2\alpha\frac{dP_{\mathrm{AC}}}{dz}+k^2P_{\mathrm{AC}}=0, \tag{71}$$

with

$$\alpha=\frac{1}{2}\frac{1}{T_0}\frac{dT_0}{dz}\left\{\frac{F(\lambda_T)/F(\lambda_\mu)-1}{1-N_{\mathrm{Pr}}}\right\}, \tag{72}$$

and

$$k^2=\frac{\omega^2}{c^2}\frac{\gamma}{F(\lambda_\mu)}\left\{1-\frac{\gamma-1}{\gamma}F(\lambda_T)\right\}. \tag{73}$$

Note that this compares with the solution obtained by Arnott *et al.*[4] To compare with the Rott formulation,[6] note that the relation between shear wave number, λ_μ, and viscous penetration depth, δ_μ, is given by $\lambda_\mu=\sqrt{2}R/\delta_\mu$, and the relation between thermal wave number, λ_T, and thermal penetration depth, δ_T, is given by $\lambda_T=\sqrt{2}R/\delta_T$, where R is the effective radius defined as twice the pore area divided by the pore perimeter. The relations between $F(\lambda_\mu)$ and $F(\lambda_T)$ and the Rott functions, $\mathbf{f}_\nu$ and $\mathbf{f}_\kappa$, are given by, $\tilde{F}(\lambda_\mu)=1-\mathbf{f}_\nu$ and $\tilde{F}(\lambda_T)=1-\mathbf{f}_\kappa$. The complex conjugate arises due to our use of $e^{-i\omega t}$ notation, rather than Rott's $e^{i\omega t}$ notation.

IV. DISCUSSION

Equations (63)–(68) clearly demonstrate that the thermal diffusion terms for inert gas thermoacoustics are augmented by additional analogous terms in mass diffusion in the inert gas-condensing vapor mixture in pores with wet walls. Swift[13] discusses the contribution of each term in the equations of inert gas thermoacoustics corresponding to Eqs. (67) and (68). The term corresponding to $-2\alpha U_{\mathrm{Vol}}$ is identified as the temperature-gradient-dependent complex acoustic gain/attenuation. For standing-wave devices, the imaginary part of this term is the dominant contribution to the gain; in a pure traveling wave device it is the real part that is the dominant contribution. Losses are primarily determined by the imaginary part of k, the complex square root of Eq. (65). For the inert gas–vapor mixtures we have examined, λ_D and λ_T are of the same order of magnitude, while φ can be quite large. The additional gain terms are larger than the additional loss terms so that lower onset temperatures and higher work can be expected from a wet prime mover.

In order to test these ideas, measurements were made of onset temperature in an extremely simple thermoacoustic prime mover, which operates in atmospheric air. The gas properties needed to compare the dry and wet gain and loss terms have been estimated using the methods of Ref. 1. The condensable fluid used is water, which was applied to the stack plates with an atomizer. The engine is a modification of a demonstration device developed by Reh-Lin Chen.[14] The resonator section is a 100-ml Pyrex graduated cylinder (diameter 26 mm, length 240 mm) which forms a closed–open resonator exposed to the atmosphere. The stack is a 1-in.-long cylindrical section of Celcor square-celled ceramic honeycomb with 200 cells per square inch. The lower end is woven with about 250 mm of 30-AWG nichrome wire which can be electrically heated. The upper, cold, end of the stack has no heat exchanger at all, and dissipates heat into the nearby glass wall, convection of the air above it, and its own heat capacity.

Beginning with the entire system at ambient temperature, electrical power is applied to the heating wire over

20–30 s to produce an increasing temperature gradient across the stack, measured with thermocouples cemented to the stack at each end. The temperatures are recorded when sound is detected radiating from the open end of the resonator. Measurements were made with the stack at various positions in the resonator, and with the stack either dry or with a film of water. The stack was located near its optimum location for low onset temperature. Since there is no cold heat exchanger, these experiments were performed with rapid heating. With only two thermocouples, we could not measure the actual temperature distribution in the stack. For this reason careful comparison of data and theory is not justified. These experiments showed a dramatic decrease in the temperature difference required for the onset of thermoacoustic oscillations when liquid water was present on the surface of the stack. With a wet stack, the onset temperature difference was about 80 K, with a dry stack about 280 K. At the average temperature of the wet stack (330 K), $n_2/n_1 = 0.22$, $\phi = 4.2$, $\gamma = 1.388$. This gives a coefficient of about 3.2 for the diffusion-related gain term in Eq. (64). The coefficient of the diffusion loss term is 0.22 in Eq. (65), while the coefficient of the thermal loss term is about 0.29. The viscous losses are usually larger than the thermal losses, and the viscosity of dry air at 430 K is larger than the viscosity of saturated air at 330 K (2.4×10^{-5} vs $1.8\,10^{-5}$ kg/m s). If the viscous, thermal, and diffusion lengths are approximated as equal, then the ratio of the critical temperature gradient with and without diffusion should be on the order of 4. This agrees reasonably well with the measured ratio of 3.5. The measurements provide qualitative confirmation that the gains predicted by the theory can be realized in a real system. Measurements with better instrumentation may provide quantitative confirmation in the future.

These results are promising for improving the heat flow and efficiency of thermoacoustic refrigeration, since the mass diffusion effects act in parallel with the heat diffusion effects and can augment the heat transport. To analyze such a system requires expressions for the enthalpy, heat, and work flows within the stack. The derivation of these expressions and the analysis of ''wet'' thermoacoustic refrigeration are presented in the following paper.

V. CONCLUSIONS

The basic propagation equations and equations for first-order acoustic variables have been derived for an inert gas-condensing vapor mixture in wet-walled tubes with imposed temperature gradients. These equations demonstrate that the addition of wet walls and condensing and evaporating vapor increases the acoustic gain produced for a given temperature difference across the stack. A simple measurement demonstrates that the predicted gains can be realized in physical systems. The derived equations also form the basis for the development of work and heat flow equations and therefore the analysis of ''wet'' thermoacoustic refrigeration.

ACKNOWLEDGMENTS

This research was supported by the Office of Naval Research. We wish to thank Henry E. Bass for valuable discussions and encouragement, and Dr. F. Eisinger for sharing his observations about thermoacoustic oscillations in burner/furnace systems.

[1] R. Raspet, C. Hickey, and J. Sabatier, ''The effect of evaporation–condensation on sound propagation in cylindrical tubes using the low reduced frequency approximation,'' J. Acoust. Soc. Am. **105**, 65–73 (1999).
[2] C. Hickey, R. Raspet, and W. Slaton, ''Effects of thermal diffusion on sound attenuation in evaporating and condensing gas–vapor mixtures in tubes,'' J. Acoust. Soc. Am. **107**, 1126–1130 (2000).
[3] W. Slaton, R. Raspet, and C. Hickey, ''The effect of the physical properties of the tube wall on the attenuation of sound in evaporating and condensing gas–vapor mixtures,'' J. Acoust. Soc. Am. **108**, 2120–2124 (2000).
[4] W. P. Arnott, H. E. Bass, and R. Raspet, ''General formulation of thermoacoustics for stacks having arbitrarily shaped pore cross sections,'' J. Acoust. Soc. Am. **90**, 3228–3237 (1991).
[5] H. Tijdeman, ''On the propagation of sound waves in cylindrical tubes,'' J. Sound Vib. **39**, 1–33 (1975).
[6] G. Swift, *Thermoacoustics: A Unifying Perspective for some Engines and Refrigerators*, LA-UR-99-895 (Los Alamos National Laboratory, Los Alamos, NM, 1999).
[7] J. V. Hirschfelder, C. Curtiss, and R. B. Bird, *Molecular Theory of Gases and Liquids* (Wiley, New York, 1954).
[8] L. D. Landau and E. M. Liftshitz, *Fluid Mechanics*, 2nd ed. (Butterworth-Heinemann, Oxford, 1997).
[9] G. W. Swift and P. S. Spoor, ''Thermal diffusion and mixture separation in the acoustic boundary layer,'' J. Acoust. Soc. Am. **106**, 1794–1800 (1999).
[10] D. A. Geller and G. W. Swift, ''Saturation of thermoacoustic mixture separation,'' J. Acoust. Soc. Am. **111**, 1675–1684 (2002).
[11] F. Reif, *Fundamentals of Statistical and Thermal Physics* (McGraw-Hill, New York, 1965).
[12] F. Marble, ''Some gas dynamic problems in the flow of condensing vapors,'' Astronaut. Acta. **14**, 585–614 (1969).
[13] G. Swift, *Thermoacoustics: A Unifying Perspective for some Engines and Refrigerators*, LA-UR-99-895 (Los Alamos National Laboratory, Los Alamos, NM, 1999), see pp. 59–62.
[14] S. L. Garrett and S. Backhaus, ''The power of sound,'' Am. Sci. **88**, 516–525 (2000).

Theory of inert gas-condensing vapor thermoacoustics: Transport equations[a)]

William V. Slaton,[b)] Richard Raspet,[c)] Craig J. Hickey, and Robert A. Hiller
Department of Physics and Astronomy and National Center for Physical Acoustics, University of Mississippi, University, Mississippi 38677

(Received 20 November 2001; revised 3 July 2002; accepted 11 July 2002)

The preceding paper [J. Acoust. Soc. Am. **112**, 1414–1422 (2002)] derives the propagation equation for sound in an inert gas-condensing vapor mixture in a wet-walled pore with an imposed temperature gradient. In this paper the mass, enthalpy, heat, and work transport equations necessary to describe the steady-state operation of a wet-walled thermoacoustic refrigerator are derived and presented in a form suitable for numerical evaluation. The requirement that the refrigerator operate in the steady state imposes zero mass flux for each species through a cross section. This in turn leads to the evaluation of the mass flux of vapor in the system. The vapor transport and heat transport are shown to work in parallel to produce additional cooling power in the wet refrigerator. An idealized calculation of the coefficient of performance (COP) of a wet-walled thermoacoustic refrigerator is derived and evaluated for a refrigeration system. The results of this calculation indicate that the wet-walled system can improve the performance of thermoacoustic refrigerators. Several experimental and practical questions and problems that must be addressed before a practical device can be designed and tested are described.
[DOI: 10.1121/1.1508114]

PACS numbers: 43.35.Ud [MRS]

I. INTRODUCTION

In a companion paper [J. Acoust, Soc. Am. **112**, 1414–1422 (2002)], hereafter referred to as Paper I, the acoustic propagation equation was derived for the pressure wave in an inert gas-condensing vapor mixture in a wet-walled pore with an applied temperature gradient.[1] The expressions for other first-order acoustic variables were also derived, such as the acoustic temperature fluctuations, acoustic velocity fluctuations, and acoustic concentration fluctuations. A complete analysis of the potential of the inert gas-condensing vapor system to thermoacoustic refrigeration requires expressions for the total axial enthalpy flux, heat, and work fluxes, as well as the total mass flux. With these expressions the coefficient of performance can be evaluated and compared to the analogous expressions for inert gas thermoacoustics. In addition, the system of equations for numerical integration of realistic stacks can be developed. In the derivations we use Swift's review article[2] as a guide, but employ the notation of Arnott *et al.*[3] Cylindrical geometry is chosen for the pores within the stack for simplicity. The resulting equations may be adapted to other pore shapes by substituting different functional forms of the porous media dissipation functions. The work of Arnott *et al.*[3] contains expressions for the porous media dissipation functions for various pore geometries. Also, Swift's thermoacoustics textbook contains these dissipation functions in Rott's notation.[4] The use of Arnott's notation is consistent with our earlier papers on sound propagation in wet pores.[5–7]

In a ''wet'' thermoacoustic refrigerator, energy is transported along the temperature gradient in the stack both in the form of heat and as energy carried by the condensable species. The vapor condenses and evaporates on a thin layer of liquid on the wall of the pore. Proper phasing between the evaporation/condensation of vapor from this film and the axial acoustic velocity will result in net pumping of vapor from one end of the stack to the other. In its simplest form, we suppose that the condensable fluid returns by flow in the thin liquid layer. This represents a loss mechanism analogous to heat conduction in the stack and its contribution must be evaluated.

DeltaE is a well-established numerical code for modeling the performance of thermoacoustic devices.[8] The transport equations will be evaluated in forms suitable for use in DeltaE. DeltaE uses the conservation of the total time-averaged, second-order steady-state enthalpy flow within the stack to calculate the temperature gradient and temperature profile through the stack. The enthalpy is conserved because the stack and refrigerator are assumed to be insulated and that heat exchange with the environment only occurs at the heat exchangers at each end of the stack. This assumption is also valid for the wet system.

In Sec. II, the first-order differential equations for the volumetric velocity and acoustic pressure are presented and their use in numerical calculations discussed. Section III develops the expression for the mass flux in the stack in steady-state operation. Section IV develops the equations for the time-averaged enthalpy flux, and the heat and work fluxes in the stack. From the expression for the total enthalpy flow, the

[a)]Portions of this work have been presented in William V. Slaton and Richard Raspet, ''Wet-walled Thermoacoustics,'' First International Workshop on Thermoacoustics, 's-Hertogenbosch, The Netherlands, 22–25 April (2001); William V. Slaton and Richard Raspet, ''Wet-walled thermoacoustics,'' J. Acoust. Soc. Am. **110**, 2677 (2001).

[b)]Current address: Physics Department, Eindhoven University of Technology, Eindhoven, The Netherlands.
[c)]Author to whom correspondence should be addressed. Electronic mail: raspet@olemiss.edu

heat and mass pumping by acoustic processes and loss mechanisms may be identified. Section V describes the process occurring in a wet thermoacoustic refrigerator stack and identifies a useful regime of operation. The coefficient of performance of an idealized inert gas–vapor thermoacoustic refrigerator is developed in Sec. VI. This expression for the coefficient of performance is then analyzed to determine the potential of wet-walled system to improve the practicality of thermoacoustic refrigeration. Section VII contains the conclusions of this research.

II. PROPAGATION EQUATIONS

DeltaE numerically integrates the two coupled first-order differential equations in acoustic pressure and volumetric velocity to determine the acoustic propagation through the stack. From Ref. 1 we have

$$\frac{dP_{\mathrm{AC}}}{dz}=\frac{i\omega\rho_0}{A_{\mathrm{mix}}}\frac{U_{\mathrm{vol}}}{F(\lambda_\mu)}, \tag{1}$$

where A_{mix} is the total stack cross-sectional area available to the gas–vapor mixture, U_{vol} is the volume velocity in the stack governed by

$$\frac{dU_{\mathrm{vol}}}{dz}=-\frac{A_{\mathrm{mix}}}{i\omega\rho_0}F(\lambda_\mu)k^2P_{\mathrm{AC}}-2\alpha U_{\mathrm{vol}}, \tag{2}$$

where α and k^2 are defined as

$$\alpha=\frac{1}{2}\frac{1}{T_0}\frac{dT_0}{dz}\left\{\frac{F(\lambda_T)/F(\lambda_\mu)-1}{1-N_{\mathrm{Pr}}}+\varphi\frac{\gamma}{\gamma-1}\frac{n_2^0}{n_1^0}\frac{F(\lambda_D)/F(\lambda_\mu)-1}{1-N_{\mathrm{Sc}}}\right\}, \tag{3}$$

and

$$k^2=\frac{\omega^2}{c^2}\frac{\gamma}{F(\lambda_\mu)}\left\{1-\frac{\gamma-1}{\gamma}F(\lambda_T)+\frac{n_2^0}{n_1^0}(1-F(\lambda_D))\right\}. \tag{4}$$

Equations (1) and (2) are coupled first-order equations for acoustic pressure fluctuations and acoustic volumetric velocity fluctuations. In steady state, knowledge of the value of the fluctuating variables and the total enthalpy within the stack at one location allows calculation of the fluctuating variables at another location within the stack. It can be seen that thermal and mass transfer processes have similar functional forms in Eqs. (3) and (4). The behavior of the ambient temperature gradient is evaluated from the enthalpy equation to be derived in Sec. IV.

III. MASS FLUX

Within a closed resonator in steady state, the second-order time-averaged mass flux of the inert gas must be zero. Acoustic pumping of inert gas in the axial direction must be balanced by an axial return mean flow of gas to equalize the mean pressure within the resonator. Thus, we may write

$$\int(\overline{\rho_1\mathbf{v}}+\rho_1^0\mathbf{v}_{s,1})_z dA_{\mathrm{mix}}=0, \tag{5}$$

where $\mathbf{v}_{s,1}$ is the steady-state flow velocity of inert gas. $\mathbf{v}$ is the first-order acoustic fluctuation velocity. In Ref. 1 it is shown that there is no axial acoustic difference velocity term in the low reduced frequency solution. Therefore, the acoustic velocity of each species is the same as the mixture acoustic velocity. We have proposed an acoustic propagation model in which there is a net mass flux of vapor due to acoustic processes. An analogous expression may be written for the vapor

$$\int(\overline{\rho_2\mathbf{v}}+\rho_2^0\mathbf{v}_{s,2})_z dA_{\mathrm{mix}}=\dot{m}_{\mathrm{vapor}}=-\dot{m}_{\mathrm{liquid}}, \tag{6}$$

where $\dot{m}_{\mathrm{liquid}}$ is the mass flow rate in the condensed liquid layer and $\mathbf{v}_{s,2}$ is the steady-state flow velocity of the vapor. For steady-state operation the vapor transported in one direction in the mixture must return as liquid flow in the other direction. The ambient steady flow of inert gas and vapor is also related to the ambient concentration of the inert gas within the stack. This is illustrated by recalling the expression for the ambient-density-weighted species difference velocity

$$\mathbf{i}_0=-\rho_0D_{12}\nabla C_1^0=\frac{\rho_1^0\rho_2^0}{\rho_0}(\mathbf{v}_{s,1}-\mathbf{v}_{s,2}), \tag{7}$$

and that the acoustic concentration fluctuation can be expressed by

$$C_1^*=\frac{\rho_1^0\rho_2^0(\rho_1^*-\rho_2^*)}{\rho_0^2}. \tag{8}$$

Equations (5)–(8) may be combined and rearranged to form two useful expressions. The first is

$$\int(\overline{\mathbf{v}C_1^*}-D_{12}\nabla C_1^0)_z dA_{\mathrm{mix}}=-\frac{\rho_1^0}{\rho_0^2}\dot{m}_{\mathrm{vapor}}=\frac{\rho_1^0}{\rho_0^2}\dot{m}_{\mathrm{liquid}}, \tag{9}$$

and the second is

$$\int(\overline{\rho\mathbf{v}}+\rho_0\mathbf{v}_s)_z dA_{\mathrm{mix}}=\dot{m}_{\mathrm{vapor}}=-\dot{m}_{\mathrm{liquid}}, \tag{10}$$

where $\mathbf{v}_s=(\rho_1^0\mathbf{v}_{s,1}+\rho_2^0\mathbf{v}_{s,2})/\rho_0$ is the ambient hydrodynamic steady flow of the mixture.

Using expressions for C_1^0, C_1^*, and u^* from Ref. 1 and expressing the time average of the product of the acoustic quantities as $\frac{1}{2}\mathrm{Re}[u^*\tilde{C}_1^*]$, we find

$$\dot{m}_{\mathrm{vapor}}=-\frac{1}{2}A_{\mathrm{mix}}\frac{\rho_0^2}{\rho_1^0}\left\{c_s\,\mathrm{Re}\left[\frac{1}{\pi}\int_0^1 u^*\tilde{C}_1^*2\pi\eta\,d\eta\right]\right\}-\varphi\frac{n_0}{n_1}\frac{\gamma}{\gamma-1}\frac{A_{\mathrm{mix}}D_{12}\rho_2^0}{T_0}\frac{dT_0}{dz}, \tag{11}$$

where $\varphi=[(\gamma-1)/\gamma](l/R_0T_0)$.

Substitution of u^* and $\tilde{C}_1^*$ yield integrals of $\mathbf{F}_i(\eta)$ or of products $\mathbf{F}_i(\eta)\tilde{\mathbf{F}}_j(\eta)$. Reference 4 shows that these integrals are given as

$$\int_0^1\tilde{\mathbf{F}}_i(\eta)\mathbf{F}_i(\eta)\eta\,d\eta=\tfrac{1}{2}\mathrm{Re}[F(\lambda_i)], \tag{12a}$$

$$\int_0^1 \tilde{\mathbf{F}}_i(\eta)\mathbf{F}_j(\eta)\,\eta\,d\eta = \frac{1}{2}\frac{F(\lambda_j)N_{ij}+\tilde{F}(\lambda_i)}{N_{ij}+1}, \tag{12b}$$

and

$$\int_0^1 \mathbf{F}_i(\eta)\,\eta\,d\eta = \tfrac{1}{2}F(\lambda_i), \tag{12c}$$

where $N_{ij}=\lambda_i^2/\lambda_j^2$.

Using these integrals, we find

$$\dot{m}_{\text{vapor}} = \frac{1}{2}\frac{\rho_2^0}{\rho_0}\frac{n_0}{n_1^0}\frac{\gamma}{\gamma-1}\frac{1}{T_0 c_p}\left[\text{Re}[\tilde{P}_{\text{AC}}U_{\text{vol}}\Xi_1(\lambda_D)] - \varphi\frac{c_p\rho_0}{\omega A_{\text{mix}}}\frac{dT_0}{dz}\left|\frac{U_{\text{vol}}}{F(\lambda_\mu)}\right|^2 \text{Im}[\Xi_2(\lambda_D)]\right] - \varphi\frac{n_0}{n_1^0}\frac{\gamma}{\gamma-1}\frac{A_{\text{mix}}D_{12}\rho_2^0}{T_0}\frac{dT_0}{dz}, \tag{13}$$

where we introduce the notation

$$\Xi_1(\lambda_j) = \frac{\tilde{F}(\lambda_j)/F(\lambda_\mu)-1}{1+N_j}, \tag{14}$$

and

$$\Xi_2(\lambda_j) = \frac{F(\lambda_\mu)N_j+\tilde{F}(\lambda_j)}{1-N_j^2}, \tag{15}$$

with j taken as T referring to thermal effects or D referring to mass diffusion effects and N_j referring either to the Prandtl number for thermal effects or the Schmidt number for mass diffusion effects.

The acoustically driven terms can be recognized as very similar in form to the heat transport equations for inert gas thermoacoustics: there is an acoustically driven term independent of temperature gradient and another acoustically driven term proportional to temperature gradient. Determination of the direction of these terms is most easily accomplished by comparison with the well-understood enthalpy flux terms of inert gas thermoacoustics, so we defer the discussion of the direction of mass flux until the enthalpy and heat flux terms have been derived and discussed.

IV. ENTHALPY BALANCE

The enthalpy flow expression is derived from the energy density equation given by Landau and Lifshitz[9]

$$\frac{\partial}{\partial t}\left(\frac{1}{2}\rho v^2+\rho\varepsilon\right) = -\boldsymbol{\nabla}\cdot\left[\rho\mathbf{v}\left(\frac{1}{2}v^2+w\right)-\mathbf{v}\cdot\boldsymbol{\sigma}'+\mathbf{q}_0\right]. \tag{16}$$

ε is the internal energy per unit mass, w is the enthalpy per unit mass, $\mathbf{v}\cdot\boldsymbol{\sigma}'$ is the energy flux due to internal friction, and $\mathbf{q}_0$ is the heat flux. Use of this basic expression insures that we have included all relevant terms in our derivation at the cost of initial complexity. The terms in the divergence represent the energy flux within the stack. The axial component of the enthalpy flux within the stack is of interest because it is a conserved quantity in steady-state operation. The time-averaged axial enthalpy flow is found by averaging Eq. (16) over the whole stack and taking the time average. The integral over the whole stack can be broken up into integrals over the solid, liquid, and open areas of the stack. We retain second-order terms in acoustically fluctuating variables and steady-state terms in the time average, and ignore acoustic terms in the solid and liquid layer and all viscous heating terms, $\mathbf{v}\cdot\boldsymbol{\sigma}'$. Streaming velocities are assumed to be at least first order in acoustic quantities. Thus, the axial component of the total enthalpy flux is

$$\overline{\dot{H}} = \int (w_{\text{mix}}^0(\overline{\mathbf{v}\rho}+\rho_0\mathbf{v}_s)+\rho_0\overline{\mathbf{v}w}+\mathbf{q}_0)_z dA_{\text{mix}} + \int\left(\rho_{\text{liquid}}^0 v_{\text{liquid}}^0 w_{\text{liquid}}^0 - \kappa_{\text{liquid}}\frac{dT_0}{dz}\right)dA_{\text{liquid}} - \int \kappa_{\text{solid}}\frac{dT_0}{dz}dA_{\text{solid}}, \tag{17}$$

where the overbars denote time averaging, and the ambient loss mechanisms within the gas mixture are contained within

$$\mathbf{q}_0 = \left[\mu_c - T_0\left(\frac{\partial\mu_c}{\partial T}\right)_{P,C_1}\right]\mathbf{i}_0 - \kappa\boldsymbol{\nabla}T_0. \tag{18}$$

The Soret effect coefficient, k_T, and the Dufour effect coefficient, k_P, have been ignored to conform with earlier derivations. μ_c is the chemical potential of the mixture and is defined as $\mu_c=(\mu_1'/m_1)-(\mu_2'/m_2)$, where μ_1' and μ_2' are the chemical potentials per molecule. Using Eq. (7) for the ambient-density-weighted species difference velocity, Eq. (18) may be rewritten as

$$\mathbf{q}_0 = -(w_1^0-w_2^0)\rho_0 D_{12}\boldsymbol{\nabla}C_1^0 - \kappa\boldsymbol{\nabla}T_0, \tag{19}$$

where w_j^0 is the ambient enthalpy per unit mass of species j.

Equation (10) can be used to express the enthalpy flux for the mixture in terms of $\dot{m}_{\text{liquid}}$ or $\dot{m}_{\text{vapor}}$

$$\overline{\dot{H}} = (w_{\text{mix}}^0-w_{\text{liquid}}^0)\dot{m}_{\text{vapor}} + \int\left(\rho_0\overline{uw_{\text{mix}}} - (w_1^0-w_2^0)\rho_0 D_{12}\frac{dC_1^0}{dz} - \kappa_{\text{mix}}\frac{dT_0}{dz}\right)dA_{\text{mix}} - \int\kappa_{\text{solid}}\frac{dT_0}{dz}dA_{\text{solid}} - \int\kappa_{\text{liquid}}\frac{dT_0}{dz}dA_{\text{liquid}}. \tag{20}$$

Terms in Eq. (20) may be identified: $\rho_0\overline{uw}$ represents the enthalpy flow down the stack due to acoustics. The term containing $w_1^0-w_2^0$ represents the enthalpy flow due to the ambient diffusion of the inert gas and vapor. The term $(w_{\text{mix}}^0-w_{\text{liquid}}^0)\dot{m}_{\text{vapor}}$ represents the enthalpy flow due to the net transport of the gas mixture and the return flow in the liquid layer. The diffusion loss and the ambient steady flow loss terms will be combined to form a simpler expression below. The loss mechanism of ambient thermal conduction through the gas mixture and solid stack material are given by $\kappa_{\text{mix}}(dT_0/dz)$ and $\kappa_{\text{solid}}(dT_0/dz)$, respectively, while $\kappa_{\text{liquid}}(dT_0/dz)$ represents an additional loss by thermal conduction through the liquid layer. Use of Eqs. (9) and (10) leads to considerable simplifications as various terms combine.

The acoustically fluctuating enthalpy for an ideal mixture is written in terms of temperature and concentration fluctuations, and is given by $w_{\mathrm{mix}}=c_pT_0T^*+\mu_cC_1^*$, where c_p is the mixture isobaric specific heat and μ_c is the mixture chemical potential. The integration over the solid, liquid, and gaseous parts of the stack is performed and the expressions for the normalized temperature, axial acoustic velocity, and concentration fluctuations are substituted and time averaged. With these modifications, Eq. (20) becomes

$$\begin{aligned}\overline{\dot{H}}=&\frac{1}{2}A_{\mathrm{mix}}\,\mathrm{Re}\left[\rho_0c_s\int_0^1u^*c_pT_0\tilde{T}^*2\,\eta\,d\,\eta\right]\\&+\frac{1}{2}A_{\mathrm{mix}}\,\mathrm{Re}\left[\rho_0c_s\left(\mu_c-\frac{\rho_0}{\rho_1^0}w_{\mathrm{mix}}^0+\frac{\rho_0}{\rho_1^0}w_{\mathrm{liquid}}^0\right)\right.\\&\left.\times\int_0^1u^*\tilde{C}_1^*2\,\eta\,d\,\eta\right]+A_{\mathrm{mix}}\left[\frac{\rho_0}{\rho_1^0}(w_{\mathrm{mix}}^0-w_{\mathrm{liquid}}^0)\right.\\&\left.-(w_1^0-w_2^0)\right]\rho_0D_{12}\frac{dC_1^0}{dz}-[\kappa_{\mathrm{mix}}A_{\mathrm{mix}}\\&+\kappa_{\mathrm{liquid}}A_{\mathrm{liquid}}+\kappa_{\mathrm{solid}}A_{\mathrm{solid}}]\frac{dT_0}{dz},\end{aligned}\tag{21}$$

where the integral over the mixture has been converted to an integral over a single pore in terms of the dimensionless radial coordinate η. Use of standard thermodynamic identities yields further simplifications

$$\mu_c-\frac{\rho_0}{\rho_1^0}w_{\mathrm{mix}}^0+\frac{\rho_0}{\rho_1^0}w_{\mathrm{liquid}}^0=-\frac{\rho_0}{\rho_1^0}T_0(s_{\mathrm{mix}}^0-s_{\mathrm{liquid}}^0),\tag{22a}$$

and

$$(w_{\mathrm{mix}}^0-w_{\mathrm{liquid}}^0)\frac{\rho_0}{\rho_1^0}-(w_1^0-w_2^0)=\frac{\rho_0}{\rho_1^0}T_0(s_2^0-s_{\mathrm{liquid}}^0),\tag{22b}$$

where s_{mix}^0, s_2^0, and s_{liquid}^0 are the ambient entropies per unit mass of the mixture, vapor, and liquid at the temperature T_0, respectively. With the identity for dC_1^0/dz from Ref. 1, Eq. (21) becomes

$$\begin{aligned}\overline{\dot{H}}=&\frac{1}{2}A_{\mathrm{mix}}\,\mathrm{Re}\left[\rho_0c_s\int_0^1u^*c_pT_0\tilde{T}^*2\,\eta\,d\,\eta\right]\\&-\frac{1}{2}A_{\mathrm{mix}}\,\mathrm{Re}\left[\frac{\rho_0^2}{\rho_1^0}c_sT_0(s_{\mathrm{mix}}^0-s_{\mathrm{liquid}}^0)\int_0^1u^*\tilde{C}_1^*2\,\eta\,d\,\eta\right]\\&-A_{\mathrm{mix}}\left[\varphi\frac{\gamma}{\gamma-1}\rho_2^0\frac{n_0}{n_1}(s_2^0-s_{\mathrm{liquid}}^0)D_{12}\right]\frac{dT_0}{dz}\\&-[\kappa_{\mathrm{mix}}A_{\mathrm{mix}}+\kappa_{\mathrm{liquid}}A_{\mathrm{liquid}}+\kappa_{\mathrm{solid}}A_{\mathrm{solid}}]\frac{dT_0}{dz}.\end{aligned}\tag{23}$$

The first two terms represent the acoustically transported enthalpy $\dot{Q}_{\mathrm{AC}}+\dot{W}_{\mathrm{AC}}$. The first term can be evaluated much like Eq. (11) or can be recognized as the acoustic heat flux term of inert gas thermoacoustics.[2,3] The second term is $T_0(s_{\mathrm{mix}}^0-s_{\mathrm{liquid}}^0)$ times the acoustic mass transport of vapor. The integrals for acoustic mass transport are evaluated in Eq. (12). The third term is the enthalpy loss term due to the steady flow of vapor and its subsequent return flow as a liquid.

Equation (23) is the most convenient form for evaluation from first-order acoustic quantities, but is not the best form for understanding the physical properties of the system. If the $\rho_0\overline{uw}$ term in Eq. (20) is expressed in terms of $\dot{m}_{\mathrm{vapor}}$, we find

$$\begin{aligned}\overline{\dot{H}}=&\frac{1}{2}A_{\mathrm{mix}}\,\mathrm{Re}\left[\rho_0c_s\int_0^1u^*c_pT_0\tilde{T}^*2\,\eta\,d\,\eta\right]\\&+T_0(s_{\mathrm{mix}}^0-s_{\mathrm{liquid}}^0)\dot{m}_{\mathrm{vapor}}-A_{\mathrm{mix}}T_0(s_1^0-s_2^0)\rho_0D_{12}\frac{dC_1^0}{dz}\\&-(\kappa_{\mathrm{mix}}A_{\mathrm{mix}}+\kappa_{\mathrm{liquid}}A_{\mathrm{liquid}}+\kappa_{\mathrm{solid}}A_{\mathrm{solid}})\frac{dT_0}{dz}.\end{aligned}\tag{24}$$

This form resolves the additional transport terms into entropy transport due to the mass transport of the mixture and the return flow of the liquid and entropy transport due to the ambient diffusion of the inert gas and vapor components.

Evaluation in terms of the volume velocity yields

$$\begin{aligned}\overline{\dot{H}}=&\tfrac{1}{2}\mathrm{Re}[\tilde{P}_{\mathrm{AC}}U_{\mathrm{vol}}]+\tfrac{1}{2}\mathrm{Re}[\tilde{P}_{\mathrm{AC}}U_{\mathrm{vol}}(\Xi_1(\lambda_T)\\&+\varepsilon_D\Xi_1(\lambda_D))]-\frac{c_p\rho_0}{2\omega A_{\mathrm{mix}}}\frac{dT_0}{dz}\left|\frac{U_{\mathrm{vol}}}{F(\lambda_\mu)}\right|^2\\&\times\mathrm{Im}[\Xi_2(\lambda_T)+\varepsilon_D\varphi\Xi_2(\lambda_D)]-\overline{\dot{Q}_{\mathrm{loss}}},\end{aligned}\tag{25}$$

where

$$\varepsilon_D=\frac{1}{c_p}\frac{\rho_2^0}{\rho_0}\frac{n_0}{n_1^0}\frac{\gamma}{\gamma-1}(s_{\mathrm{mix}}^0-s_{\mathrm{liquid}}^0),\tag{26}$$

$$\begin{aligned}\overline{\dot{Q}_{\mathrm{loss}}}=&(A_{\mathrm{mix}}\kappa_{\mathrm{mix}}+A_{\mathrm{solid}}\kappa_{\mathrm{solid}}+A_{\mathrm{liquid}}\kappa_{\mathrm{liquid}})\frac{dT_0}{dz}\\&+A_{\mathrm{mix}}\left[\varphi\frac{\gamma}{\gamma-1}\rho_2\frac{n_0}{n_1^0}(s_2^0-s_{\mathrm{liquid}}^0)D_{12}\right]\frac{dT_0}{dz},\end{aligned}\tag{27}$$

and the functions $\Xi_1(\lambda_j)$ and $\Xi_2(\lambda_j)$ are defined in Eq. (14) and Eq. (15).

We assume that the liquid layer coating all surface area of the stack represents a small fraction of the total cross-sectional area of the stack and that the heat conduction through the liquid film may be neglected. This assumption must be investigated experimentally. Since the axial acoustic density weighted species difference velocity is shown to be zero in Ref. 1, the time-averaged acoustic power is

$$\overline{\dot{W}_{\mathrm{AC}}}=\tfrac{1}{2}\mathrm{Re}[\tilde{P}_{\mathrm{AC}}U_{\mathrm{vol}}].\tag{28}$$

This is the first term in Eq. (25). The remainder of Eq. (25) is the total heat flux $\dot{Q}$.

Equations (25) and (28) provide a complete description of energy fluxes in a thermoacoustic stack with an inert gas-condensing vapor working fluid in a pore with wet walls under the approximations described above.

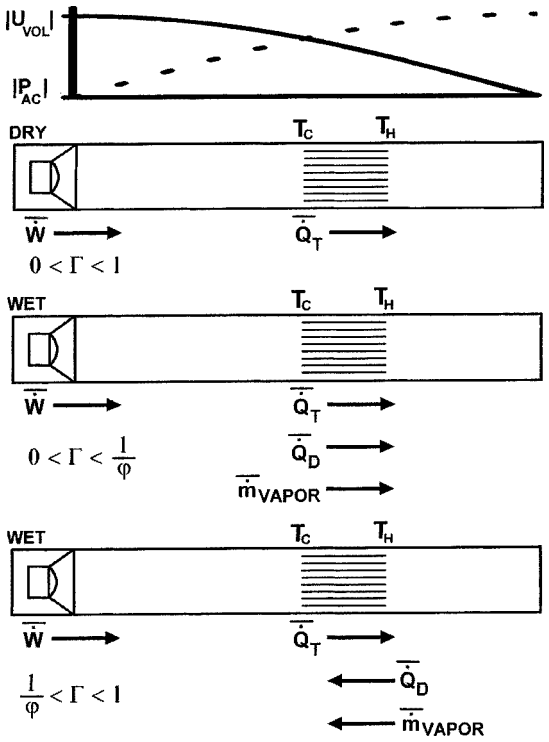

FIG. 1. Mass transport directions in an inert gas-condensing vapor refrigerator for different values of the temperature gradient compared to the heat transport in an inert gas refrigerator. $\dot{Q}_T$ is the thermal heat transport flux, $\dot{Q}_D$ is the heat transport by evaporation–condensation, and $\dot{m}_{\text{vapor}}$ is the mass flux of vapor.

V. DISCUSSION

Although Eq. (25) is quite complex, the behavior of the different terms can be explained in terms of the well-understood inert gas thermoacoustic refrigerator. The terms in Eq. (25) containing λ_T are identical to those in Ref. 3 for inert gas refrigeration, as are the gas and solid material heat conduction terms. The new terms, those containing λ_D and the additional term due to steady flow and diffusion, contain the same functions evaluated for slightly different variables. N_{Pr} and N_{Sc} are both on the order of 1, so the behavior of the heat diffusion and mass diffusion terms are similar.

Figure 1 shows that in an inert gas refrigerator with the stack properly positioned, the acoustic power difference across the stack is converted into heat flow toward the hot end of the stack (maintained near room temperature by a heat exchanger). This removes heat from the cold end of the stack leading to cooling below room temperature. The acoustic heat flow is opposed by heat conduction in the gas and stack material and by the second acoustically driven heat term. If losses are ignored, cooling is possible until the temperature gradient is large enough so that the second acoustic heat flux term is equal to and opposite in direction to the first term. This establishes a critical gradient for refrigeration and that the term $\frac{1}{2}\text{Re}[P_{\text{AC}}U_{\text{vol}}\Xi_1(\lambda_T)]$ produces a heat flux away from the cold end of the stack and the term containing $\text{Im}[\Xi_2(\lambda_T)]$ produces a heat flux toward the cold end.

Equation (13) for the mass flux contains the same functions as the heat flux but evaluated for mass diffusion rather than heat diffusion. The vapor flux terms are in the same direction as the heat flux terms. When the temperature gradient is small, the total vapor mass flux resulting from the two diffusion terms is in the same direction as the acoustic heat transfer. The ideal critical gradient for the vapor transfer to stop and reverse directions is equal to the critical gradient for heat diffusion multiplied by the factor $1/\varphi$. φ is usually greater than 1. Here, ''ideal'' means that the third term in Eq. (13) describing ambient diffusion can be neglected.

The vapor transport heat flux terms in Eq. (25) display the same behavior as the mass flux. We expect ε_D to be positive, since the entropy of the mixture should be greater than the liquid entropy, so that the vapor transport terms add to the acoustic heat transfer terms when the normalized temperature gradient is less than $1/\varphi$. When the temperature gradient exceeds the critical gradient for vapor transport, the flow of vapor reverses and the heat transport by acoustic heat diffusion and vapor diffusion oppose each other.

VI. IDEAL COEFFICIENT OF PERFORMANCE AND HEAT TRANSFER

A. Theoretical expressions

The coefficient of performance (COP) is a measure of the efficiency of a refrigerator and is equal to the amount of heat pumped from a cold reservoir divided by the net work input. Thus, the coefficient of performance is

$$\text{COP}=\frac{\overline{\dot{Q}_{\text{Net}}},_C}{\Delta\overline{\dot{W}}}. \tag{29}$$

The COP can be evaluated numerically by integrating through the stack using Eqs. (1) and (2) and the constancy of Eq. (25). Then, the net work can be evaluated from Eq. (28) evaluated at each end of the stack and by $\dot{Q}_{\text{Net},C}$ evaluated at the cold end of the stack using Eqs. (25) and (28). For this preliminary paper, the inert gas-condensing vapor COP is compared to the inert gas COP in an idealized form to provide an estimate of the potential improvements provided by the wet-walled system. We shall consider the coefficient of performance of an inert gas–vapor thermoacoustic refrigerator in the inviscid, boundary layer, and standing wave limit. The amount of acoustic work used to pump $\dot{Q}_C$ is the difference in acoustic intensity on the hot and cold sides of the stack. Thus,

$$\begin{aligned}\Delta\overline{\dot{W}} &= -A_{\text{mix}}[(\overline{P_{\text{AC}}u})_{\text{right}}-(\overline{P_{\text{AC}}u})_{\text{left}}]\\ &= -L\frac{d}{dz}(\overline{P_{\text{AC}}U_{\text{vol}}})\\ &= -\frac{L}{2}\frac{d}{dz}(\text{Re}[P_{\text{AC}}\tilde{U}_{\text{vol}}])\\ &= -\frac{L}{2}\text{Re}\left[P_{\text{AC}}\frac{d\tilde{U}_{\text{vol}}}{dz}+\frac{dP_{\text{AC}}}{dz}\tilde{U}_{\text{vol}}\right],\end{aligned} \tag{30}$$

where we have used the fact that $A_{\text{mix}}u=U_{\text{vol}}$ and L is the stack length. The coordinates are indicated in Fig. 1. This approximation puts an upper bound on COP since it assumes losses in other parts of the refrigerator are negligible.

In the standing wave limit, $U_{\mathrm{vol}}=U_{\mathrm{vol},S}$ and $P_{\mathrm{AC}}=iP_{\mathrm{AC},S}$. The boundary layer limit of the $F(\lambda_j)$ functions is

$$F(\lambda_j)=1-2\sqrt{i}/\lambda_j=1-(1-i)\,\delta_j/R, \tag{31}$$

with j taken as T referring to thermal effects or D referring to mass diffusion effects.

Applying these limits to the change in acoustic work yields

$$\overline{\Delta\dot{W}}=-\frac{L}{2}\left[P_{\mathrm{AC},S}^2\frac{\omega A_{\mathrm{mix}}}{\rho_0 c_p T_0}\left\{\frac{\delta_T}{R}+\frac{n_2^0}{n_1^0}\frac{\gamma}{\gamma-1}\frac{\delta_D}{R}\right\}-\frac{P_{\mathrm{AC},S}U_{\mathrm{vol},S}}{T_0}\frac{dT_0}{dz}\left\{\frac{\delta_T}{R}+\varphi\frac{n_2^0}{n_1^0}\frac{\gamma}{\gamma-1}\frac{\delta_D}{R}\right\}\right]. \tag{32}$$

The acoustic heat pumped from the cold reservoir can be written with these limits as

$$\overline{\dot{Q}_C}=\frac{-P_{\mathrm{AC},S}U_{\mathrm{vol},S}}{2}\left\{\frac{\delta_T}{R}+\varepsilon_D\frac{\delta_D}{R}\right\}+\frac{c_p\rho_0}{2\omega A_{\mathrm{mix}}}U_{\mathrm{vol},S}^2\frac{dT_0}{dz}\left\{\frac{\delta_T}{R}+\varepsilon_D\varphi\frac{\dot{\delta}_D}{R}\right\}. \tag{33}$$

Taking the ratio of Eq. (33) and Eq. (32) and factoring out $-P_{\mathrm{AC},S}U_{\mathrm{vol},S}/2$ from the numerator and $-L\omega A_{\mathrm{mix}}\times P_{\mathrm{AC},S}^2/\rho_0 c_p T_0$ from the denominator yields

$$\mathrm{COP}=\frac{\rho_0 c_p U_{\mathrm{vol}}}{\omega A_{\mathrm{mix}}P_{\mathrm{AC}}}\frac{T_0}{L}\left[\frac{\{\delta_T+\varepsilon_D\delta_D\}-\dfrac{c_p\rho_0U_{\mathrm{vol},S}}{\omega A_{\mathrm{mix}}P_{\mathrm{AC},S}}\dfrac{dT_0}{dz}\{\delta_T+\varepsilon_D\varphi\delta_D\}}{\left\{\delta_T+\dfrac{n_2^0}{n_1^0}\dfrac{\gamma}{\gamma-1}\delta_D\right\}-\dfrac{c_p\rho_0U_{\mathrm{vol},S}}{\omega A_{\mathrm{mix}}P_{\mathrm{AC},S}}\dfrac{dT_0}{dz}\left\{\delta_T+\varphi\dfrac{n_2^0}{n_1^0}\dfrac{\gamma}{\gamma-1}\delta_D\right\}}\right]. \tag{34}$$

Two factors used in the literature[2] of inert gas thermoacoustics can be identified:

the dry critical temperature gradient

$$\nabla T_{\mathrm{crit}}=\frac{\omega A_{\mathrm{mix}}P_{\mathrm{AC},S}}{c_p\rho_0U_{\mathrm{vol},S}}, \tag{35}$$

and the normalized temperature gradient

$$\Gamma=\frac{\nabla T_{\mathrm{mean}}}{\nabla T_{\mathrm{crit}}}=\frac{dT_0/dz}{\nabla T_{\mathrm{crit}}}. \tag{36}$$

The critical temperature gradient is the ambient temperature gradient at which the temperature oscillations in the mixture due to acoustic pressure changes are the same as the local stack temperature when the acoustic wave displaces the mixture along the stack. In other words, at the critical gradient a parcel of gas in the mixture will always be in thermal equilibrium with the local stack temperature and thus will not exchange thermal energy with the stack. However, in a wet system heat is transported by the vapor, as long as the changes in the partial pressure of vapor due to acoustic pressure changes are different from the vapor pressure at the stack wall. The partial pressure at the wall depends only on the temperature and the latent heat through the parameter φ.

We further identify and approximate the Carnot coefficient of performance as

$$\mathrm{COP}_{\mathrm{Carnot}}=\frac{T_C}{T_H-T_C}\cong\frac{T_0}{L}\frac{dz}{dT_0}. \tag{37}$$

This approximation assumes that the temperature gradient is linear and that the cold temperature and the stack average temperature are comparable. Equation (34) can then be expressed as

$$\mathrm{COP}=\Gamma\mathrm{COP}_{\mathrm{Carnot}}\frac{\delta_T(1-\Gamma)+\varepsilon_D\delta_D(1-\varphi\Gamma)}{\delta_T(1-\Gamma)+\dfrac{\gamma}{\gamma-1}\dfrac{n_2^0}{n_1^0}\delta_D(1-\varphi\Gamma)}. \tag{38}$$

If there is no vapor in the system, $n_2=\varepsilon_D=0$ and the coefficient of performance reduces to the expression $\mathrm{COP}=\Gamma\mathrm{COP}_{\mathrm{Carnot}}$, which agrees with Swift's expression for inert gas thermoacoustics.[2]

This idealized expression is a valuable aid to understanding the transport properties. The relationship of the change in sign of the mass diffusion acoustic transport as Γ exceeds $1/\varphi$ is clear. The ideal COP will be increased for systems in which the normalized temperature gradient is between zero and $1/\varphi$. If the normalized gradient exceeds $1/\varphi$, the mass diffusion effects oppose the heat diffusion effects. If $\varepsilon_D>(\gamma/\gamma-1)(n_2^0/n_1^0)$ and the normalized gradient is between 0 and $1/\varphi$, the COP of the wet system will be greater than the COP of the dry system with the same dry properties.

B. Example analysis for selected inert gas–vapor mixtures

As an indicator of the potential of inert gas-condensing vapor mixtures to improve thermoacoustic refrigeration, we have calculated the ideal COPs relative to Carnot from Eq. (38) for a thermoacoustic cooler operating between 280 and 310 K as a function of the normalized temperature gradient Γ. Physical properties of the pure gas and vapor at standard state and as functions of temperature may be found in numerous reference books.[10,11] Transport properties, such as viscosity, thermal conductivity, or diffusion coefficient, of pure gases and binary mixtures of gases are calculated based on gas dynamic theory.[12] Thermophysical properties such as the specific heat and the ratio of specific heats of the mixture

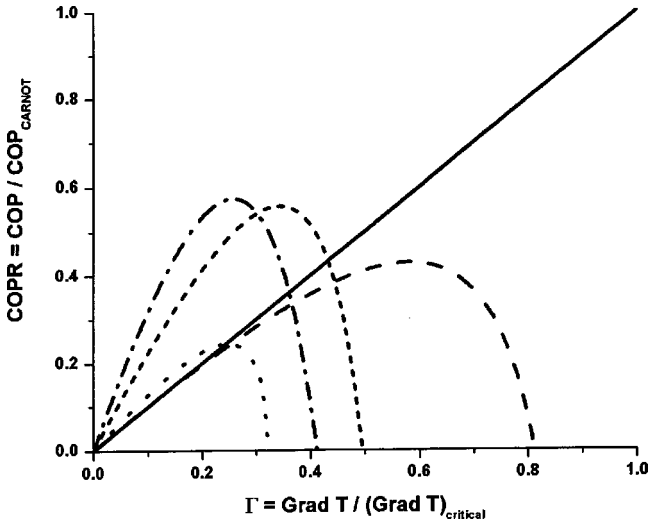

FIG. 2. Coefficient of performance relative to the Carnot coefficient of performance versus normalized temperature gradient for pure helium ———, helium and water vapor – – –, helium and ammonia · · · ·, helium and butane -·-, helium and R134a ---.

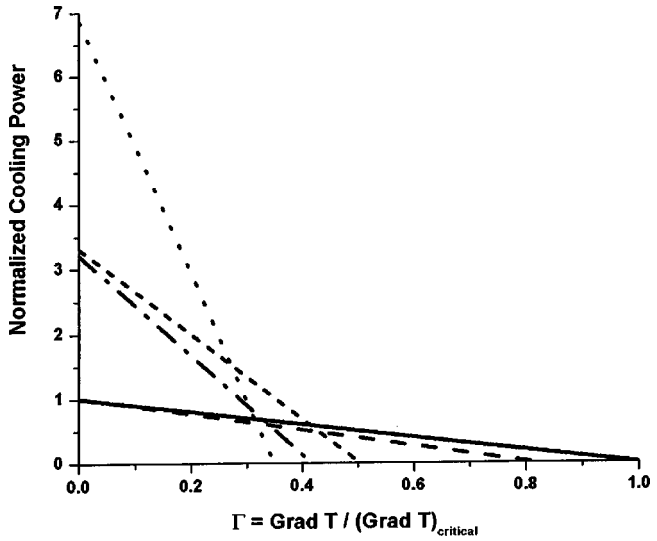

FIG. 3. Normalized cooling power versus normalized temperature gradient for pure helium ———, helium and water vapor – – –, helium and ammonia · · · ·, helium and butane -·-, helium and R134a ---.

are calculated with mole fraction weighting.[13] The mole fractions of gas and vapor in the mixture are calculated from the Clausius–Claperyon equation as a function of ambient local temperature.[14] When calculating the mole fractions it is assumed that the mean pressure in the model refrigerator is a constant; thus, an air and water vapor mixture would have equal mole fractions for a mean pressure of 2 atmospheres at 373 K. The numerator of the coefficient of performance relative to Carnot, Eq. (38), is the heat pumped from the cold side of the stack. Thus, the thermophysical quantities of the mixture in the numerator are calculated at an ambient temperature of 280 K. The denominator of Eq. (38) is the work required to pump the heat and is evaluated at the average temperature across the stack (295 K).

Figure 2 indicates that the coefficient of performance of the helium-condensing vapor mixture is higher than that of helium for low normalized temperature gradients. The pure helium system can achieve higher COPs relative to Carnot at higher critical gradients, but as will be demonstrated below, for much lower cooling powers than the helium–ammonia, helium–butane, or helium–R134a mixtures.

Swift[2] suggests that the potential for different gas mixtures to transport energy can be investigated by assuming $|P_{\mathrm{AC}}| \approx \rho c |u_{\mathrm{AC}}|$ and that the highest acoustic Mach number ($M = |u_{\mathrm{AC}}/c|$) achievable in an acoustic system is constant at approximately 0.1. Further, we set the ratio δ_T/R for each system equal. This corresponds to optimizing the stack spacing for each mixture. Under these assumptions Eq. (33) becomes

$$|\overline{\dot{Q}_c}| = \frac{\rho c^3 M^2}{2}\left(\frac{\delta_T}{R}\right)[(1-\Gamma)+\varepsilon_D(1-\phi\Gamma)]. \tag{39}$$

In Fig. 3 we plot the normalized cooling power

$$|\overline{\dot{Q}}|_{\mathrm{normalized}} = \frac{\rho c^3[(1-\Gamma)+\varepsilon_D(1-\phi\Gamma)]}{(\rho c^3)_{\mathrm{helium}}}. \tag{40}$$

The relative cooling power for the pure helium system is then given by $(1-\Gamma)$. The thermophysical properties for this calculation are evaluated at 10 atmospheres and 280 K. Large gains in heat flux from the cold heat exchanger are predicted at relatively high COPRs. These results are encouraging, but a more realistic calculation should include the additional stack length and attendant increased losses. Initial estimates of the new loss terms in Eq. (25) which have not been included in this analysis indicate that they are at most on the order of the heat conduction losses in inert gas thermoacoustics, but this must also be confirmed by numerical calculations.

VII. CONCLUSIONS

The transport equations for wet thermoacoustics have been developed. The heat energy transported and the coefficient of performance are both increased for wet stacks operated between a temperature gradient of zero and the critical temperature gradient for mass transport. The cooling by vapor transport is analogous to a conventional vapor cycle refrigerator. High entropy vapor is transported from the cold side of the stack to the ambient where it condenses. This system combines thermoacoustic refrigeration with vapor cycle refrigeration in a simple acoustically driven device.

Several experimental and calculational questions must be answered before it can be determined if inert gas-condensing vapor thermoacoustics can be exploited to improve thermoacoustic refrigerators.

(1) A full numerical calculation must be performed to see if the improvement in cooling power shown above can be achieved in a realistic refrigerator. In this paper we have derived the necessary relations for calculations in DeltaE.[8]
(2) The behavior of the condensed liquid layer in the stacks must be investigated experimentally for a variety of stack materials and vapor substances. We have performed our calculations with the simplest assumption:

that the liquid layer is thin everywhere and that natural flow occurs in the steady state to return the transported and condensed vapor.

(3) The behavior of the heat and mass transfer at the heat exchangers must be investigated. Our analysis of enthalpy flow is only valid within the stacks.

(4) The assumption that the temperature-driven diffusion effect (k_T terms) are negligible should be investigated in more detail. We have relied on the analysis of Ref. 6 in our neglect of k_T, but k_T may be larger in a given candidate system.

There are, of course, other questions and considerations besides those listed above. Nonetheless, this is a promising and interesting field of investigation.

ACKNOWLEDGMENTS

This work is supported by the Office of Naval Research. The authors thank H. E. Bass and Greg Swift for general discussions and the reviewers for their insightful comments and suggestions.

[1] R. Raspet, W. Slaton, C. Hickey, and R. Hiller, "Theory of inert gas—condensing vapor thermoacoustics: The propagation equation," J. Acoust. Soc. Am. **112**, 1414–1422 (2002).

[2] G. Swift, "Thermoacoustic engines," J. Acoust. Soc. Am. **84**, 1145–1180 (1988).

[3] W. Arnott, H. Bass, and R. Raspet, "General formulation of thermoacoustics for stacks having arbitrarily shaped pore cross sections," J. Acoust. Soc. Am. **90**, 3228–3237 (1991).

[4] G. Swift, "Thermoacoustics: A Unifying Perspective for some Engines and Refrigerators," LA-UR-99-895 (1999).

[5] R. Raspet, C. Hickey, and J. Sabatier, "The effect of evaporation–condensation on sound propagation in cylindrical tubes using the low reduced frequency approximation," J. Acoust. Soc. Am. **105**, 65–73 (1999).

[6] C. Hickey, R. Raspet, and W. Slaton, "Effects of thermal diffusion in evaporating and condensing gas–vapor mixtures in tubes," J. Acoust. Soc. Am. **107**, 1126–1130 (2000).

[7] W. Slaton, R. Raspet, and C. Hickey, "The effect of the physical properties of the tube wall on the attenuation of sound in evaporating and condensing gas–vapor mixtures," J. Acoust. Soc. Am. **108**, 2120–2124 (2000).

[8] B. Ward and G. Swift, *Design Environment for Low-amplitude Thermoacoustic Engines* (Los Alamos National Library, Los Alamos, NM, 1994).

[9] L. D. Landau and E. M. Lifshitz, *Fluid Mechanics*, 2nd ed. (Butterworth-Heinemann, Oxford, 1997).

[10] D. R. Lide, *Handbook of Chemistry and Physics* (CRC Press, New York, 1997).

[11] Carl L. Yaws, *Chemical Properties Handbook* (McGraw-Hill, New York, 1999).

[12] J. V. Hirschfelder, C. Curtiss, and R. B. Bird, *Molecular Theory of Gases and Liquids* (Wiley, New York, 1964).

[13] J. R. Belcher, W. V. Slaton, R. Raspet, H. E. Bass, and J. Lightfoot, "Working gases in thermoacoustic engines," J. Acoust. Soc. Am. **105**, 2677–2684 (1999).

[14] F. Reif, *Fundamentals of Statistical and Thermal Physics* (McGraw-Hill, New York, 1965).

A nonlinear model of thermoacoustic devices

Sergey Karpov and Andrea Prosperetti[a)]
Department of Mechanical Engineering, The Johns Hopkins University, Baltimore, Maryland 21218

(Received 22 October 2001; revised 21 June 2002; accepted 25 June 2002)

This paper presents a nonlinear, time-domain model of thermoacoustic devices based on cross-sectional averaged equations. Heat transfer perpendicular to the device axis—which lies at the core of thermoacoustic effects—is modeled in a novel and more realistic way. Heat conduction in the solid surfaces surrounding the fluid medium is included. Contrary to the previous versions of this model [Watanabe *et al.*, J. Acoust. Soc. Am. **102**, 3484–3496 (1997)], the present version does not require artificial damping and is numerically robust. The model performance is illustrated on several examples: a prime mover, an externally driven thermoacoustic refrigerator, and a combined prime mover/refrigerator system. © *2002 Acoustical Society of America.* [DOI: 10.1121/1.1501277]

PACS numbers: 43.35.Ud, 43.25.Gf, 84.60.Rb, 43.20.Ks [RR]

I. INTRODUCTION

The physical process at the heart of thermoacoustic prime movers and refrigerators is the exchange of energy between the working fluid and the solid structure in contact with it (see, e.g., Rott, 1980; Wheatley, 1986; Swift, 1988). While in a multidimensional description of these devices the modeling of this exchange process arises naturally through the solution of the balance equations for momentum and energy, in a quasi-one-dimensional description specific models are needed (see, e.g., Watanabe *et al.*, 1997; Mozurkewich, 1998a).

In our earlier work on one such quasi-one-dimensional description (Watanabe *et al.*, 1997; Yuan *et al.*, 1997), we have used relatively crude models inspired by a straightforward application of linear theory. We found that, while many features of the nonlinear behavior of thermoacoustic prime movers observed in experiment could be reproduced by the model, numerical difficulties remained that deprived the calculation of the degree of robustness necessary for a widespread acceptance of the formulation.

The primary purpose of the present paper is to present a better model for the description of the exchange of momentum and energy between the fluid and the solid. At a cost of a minimal increase in complexity, we achieve a greater physical realism, a much stronger degree of numerical stability, and we are able to dispense with the introduction of artificial numerical damping that was needed in our earlier model (Yuan *et al.*, 1997). A second purpose of the paper is to include heat transport by conduction in the stack and in the heat exchangers that was neglected in the earlier formulations.

As a result of these two extensions, we present a general time-domain, fully nonlinear model of thermoacoustic devices that is capable of predicting the response of such systems to cross-sectional area variations, stack position, fluid properties, and many other design variables. While the model is not exact due to the averaging over the cross section, in the frequency domain and for small amplitudes it reduces to the standard linear theory. In addition, it is able to describe nonlinear phenomena such as the finite-amplitude saturation of the thermoacoustic instability while, at the same time, remaining substantially simpler than a truly multidimensional model. We thus hope that our model can be useful in filling the current gap in the levels of description available for thermoacoustic systems.

In particular, only limited theoretical information exists on nonlinear phenomena in thermoacoustic devices. Examples of analytical studies include Bauwens (1996, 1998), who studied large-amplitude oscillations in the limit of a nearly uniform gas temperature over the cross section of a round tube, Gopinath *et al.* (1998), who investigated the steady-state temperature distribution in the stack by a second-order regular perturbation theory, and a recent one by the present authors where the time-dependent nonlinear saturation of the thermoacoustic instability was obtained by a method of multiple time scales carried to fourth order (Karpov and Prosperetti, 2000). Numerical work includes a paper by Cao *et al.* (1996), in which the heat exchange between the gas and zero-thickness stack plates in a thermoacoustic couple is calculated, and the papers by Worlikar and Knio (1996, 1999), Worlikar *et al.* (1998), and the thesis by Worlikar (1997), which focus on the two-dimensional modeling of flow and heat transfer in the stack region including the blockage effect of the stack; in these studies—unlike the present formulation—the rest of the system is modeled as a single-frequency acoustic wave. In a very recent paper Hamilton *et al.* (2002) present an interesting nonlinear model constructed on boundary-layer-like approximations.

Although understandable in view of the complexity of the problem, the paucity of papers devoted to nonlinear effects is unfortunate as ample experimental evidence exists as to their importance. The very fact that the thermoacoustic instability in a prime mover ultimately saturates at a finite pressure amplitude is an obvious consequence of nonlinearity.[1] More subtly, as pointed out by Worlikar *et al.* (1998), some of the differences between linear theory and experiment encountered by Atchley *et al.* (1990a) are to be attributed to nonlinearity already at drive ratios as low as

[a)]Also at Faculty of Applied Physics and Twente Institute of Mechanics, University of Twente, AE 7500 Enschede, The Netherlands, and Burgerscentrum, The Netherlands.

2%. Furthermore, it may be argued that the effective exploitation of thermoacoustic systems requires operation in the nonlinear regime. The strongly nonlinear resonators described by Ilinskii *et al.* (1998) are a particularly interesting possibility.

II. SIMPLIFIED MODELS OF THERMOACOUSTIC DEVICES

We begin by a summary of the simplified model of thermoacoustic devices used in our previous papers (Watanabe *et al.*, 1997; Yuan *et al.*, 1997).

The key simplification rests on the observation that, in most thermoacoustic devices, the dimensions of the system in the direction of the fluid particle displacement are much greater than those normal to it. This circumstance suggests the use of a quasi-one-dimensional model in which the conservation equations for mass, momentum, and energy are averaged over the cross section of the system. Details on the derivation can be found in Watanabe *et al.* (1997), and here we simply summarize the results.

The equation of continuity is

$$\frac{\partial \rho}{\partial t}+\frac{1}{S}\frac{\partial}{\partial x}(S\rho u)=0. \tag{1}$$

Here, x is the coordinate along the axis of the device (not necessarily rectilinear), $S(x)$ is the local cross-sectional area, and ρ and u are the gas density and axial velocity, respectively, averaged over the cross-sectional area. The momentum equation takes the form

$$\frac{\partial}{\partial t}(\rho u)+\frac{1}{S}\frac{\partial}{\partial x}(S\rho u^2)+\frac{\partial p}{\partial x}=-\ \rho\ \mathcal{D}(u), \tag{2}$$

where p is the cross-sectional average of the gas pressure and the term $\mathcal{D}(u)$ accounts for momentum exchange between the fluid and the surrounding solid surfaces and will be specified shortly. On the assumption of perfect-gas behavior, the energy equation is written in the form

$$\frac{\partial}{\partial t}\left(\frac{1}{\gamma-1}\ p+\frac{1}{2}\rho u^2\right)+\frac{1}{S}\frac{\partial}{\partial x}\left[uS\left(\frac{\gamma}{\gamma-1}\ p+\frac{1}{2}\rho u^2\right)\right]$$
$$=\rho c_p\left[\mathcal{H}(T_w-T)-\frac{dT_w}{dx}\mathcal{Q}\ u\right], \tag{3}$$

where γ is the ratio of the gas-specific heats, T the cross-sectional average of the gas temperature, and T_w the surface temperature of the solid surfaces in contact with the gas. The terms $\mathcal{H}$, $\mathcal{Q}$ are analogous to $\mathcal{D}$ and account for the exchange of energy between the fluid and the solid; these quantities are at the core of the present study and will be discussed in detail below [some comments on the form of the right-hand side of (3) are given in the Appendix]. It is further postulated that the perfect gas equation of state

$$p=\mathcal{R}\rho T, \tag{4}$$

where $\mathcal{R}$ is the universal gas constant divided by the gas molecular mass, is satisfied by the cross-sectional averages.

Closure of the model requires knowledge of the temperature distribution T_w along the axis of the device. In our earlier papers this quantity was taken as given and independent of time, but one can easily remove this restriction by once more using a cross-sectional average, this time over the solid material that constitutes the stack. Although it is not necessary to specify the geometrical structure of the stack, for ease of exposition we will think of it as constituted by a set of parallel plates. Area averaging is justified by the fact that the plates are usually thin; a similar remark would apply to pin stacks or other geometrical arrangements. In this way, one finds

$$\rho_s c_s\frac{\partial T_w}{\partial t}=\frac{1}{S_s}\frac{\partial}{\partial x}\left(k_s S_s\frac{\partial T_w}{\partial x}\right)$$
$$-\ \rho c_p\left[\mathcal{H}(T_w-T)-\frac{dT_w}{dx}\mathcal{Q}\ u\right], \tag{5}$$

where ρ_s, c_s, k_s, and S_s are the density, specific heat, thermal conductivity, and cross-sectional area of the plates, respectively. The heat exchangers are modeled in a similar way, except that their thermal conductivity is taken to be infinite so that their temperature is spatially uniform.[2] For the sake of simplicity, in the examples that follow we assume that the stack plates are in perfect thermal contact with the cold and hot heat exchangers.

Away from the stack region, one could use a similar formulation for the resonator tube walls, or one could couple the model equations with the conduction equations in the walls. In this study, for simplicity, we shall simply assume that the tube wall temperature is prescribed.

A variety of boundary conditions can be associated with the mathematical model described before depending on the situation that it is desired to model. For example, for the prime mover case with standing waves, it might be reasonable to assume that the end walls of the tube are rigid, so that the velocity vanishes

$$u=0 \quad \text{at } x=0, \quad x=L. \tag{6}$$

The momentum equation (2) then implies that

$$\frac{\partial p}{\partial x}=0 \quad \text{at } x=0, \quad x=L. \tag{7}$$

Equations (1) and (3) written at the endpoints ($x=0$, L) then give

$$\frac{\partial \rho}{\partial t}+\rho\frac{\partial u}{\partial x}=0, \tag{8}$$

$$\frac{\partial p}{\partial t}+\ \gamma p\frac{\partial u}{\partial x}=(\gamma-1)\ \rho c_p\ \mathcal{H}(T_w-T). \tag{9}$$

Upon eliminating $\partial u/\partial x$, one finds

$$\frac{\partial T}{\partial t}=\frac{\gamma-1}{\gamma}\frac{T}{p}\frac{\partial p}{\partial t}+\ \mathcal{H}(T_w-T). \tag{10}$$

This relation shows that a knowledge of p at the boundary completely specifies T. No additional boundary conditions are therefore necessary. Since the heat transfer term $\mathcal{H}$ is very small outside the stack region, this relation then essentially implies the adiabatic pressure-temperature relation of perfect gases.

In general, the relation (10) would result in a temperature jump from the T given by this relation to the end-wall temperature. This is a consequence of the neglect of axial conduction in the derivation of the energy equation (3). Axial conduction would introduce a term $\partial^2 T/\partial x^2$, important only near the end walls, the role of which would be to re-establish continuity of temperature by means of a thin boundary layer. The temperature in this layer would adjust itself so as to match the value given by (10). This is an essentially passive process with negligible effects on the temperature distribution elsewhere in the device and can therefore be disregarded. If desired, however, the expression for $\mathcal{H}$ can be adjusted to give a heat transfer coefficient at the tube ends.

For the case of standing waves forced by a piston, as in a refrigerator arrangement, one might consider two limit cases. The piston may be located at a velocity antinode, corresponding to a pressure node. In this case one may assume a vanishing pressure disturbance and an imposed fluid velocity at this location. Conversely, for a piston located at a pressure antinode, one may use an imposed pressure condition and a zero velocity condition.

These models can of course be refined. For example, more complicated end-wall impedances may be accounted for by prescribing, in place of (6), (7), a relation coupling pressure and velocity at $x=0, L$. The use of periodicity conditions at the tube ends would permit to model a toroidal traveling wave system, and so on.

III. THE EXCHANGE TERMS

It was shown in Watanabe *et al.* (1997) that, upon linearization, in the frequency domain the model (1) to (4) leads to the following eigenvalue equation for the pressure perturbation p':

$$\frac{1}{S}\frac{d}{dx}\left[\frac{Sc_A^2}{1+\hat{D}/(i\omega)}\frac{dp'}{dx}\right]+\omega^2 p' + \frac{\hat{H}}{i\omega}\left\{\frac{c_A^2}{S}\frac{d}{dx}\left[\frac{S}{1+\hat{D}/(i\omega)}\frac{dp'}{dx}\right]+\gamma\omega^2 p'\right\} + \frac{(\gamma-1)c_p}{1+\hat{D}/(i\omega)}\frac{dT_w}{dx}\hat{Q}\frac{dp'}{dx}=0, \tag{11}$$

where $c_A^2=\gamma\mathcal{R}T_w$ is the local adiabatic sound speed, and proportionality to $\exp(i\omega t)$ has been assumed. In deriving this equation we have set

$$\mathcal{D}(u)=\hat{D}(\omega)u, \quad \mathcal{H}(T_w-T)=\hat{H}(\omega)(T_w-T), \quad \mathcal{Q}u=\hat{Q}(\omega)u. \tag{12}$$

In the same paper it was also shown that the choices

$$\hat{D}(\omega)=i\omega\frac{f_V}{1-f_V}, \tag{13}$$

$$\hat{H}(\omega)=i\omega\frac{f_K}{1-f_K}, \quad \hat{Q}(\omega)=\frac{1}{1-\sigma}\left(\frac{f_V}{1-f_V}-\frac{\sigma f_K}{1-f_K}\right), \tag{14}$$

reduce (11) to the well-known linear formulation of Rott (1976, 1980; see also Swift, 1988). In (13) and (14) the quantities $f_{V,K}$ depend on the ratio of the diffusion lengths to the hydraulic diameter of the flow passage (Rott, 1980; Wheatley, 1986; Swift, 1988; Arnott *et al.*, 1991). The viscous and thermal diffusion lengths $\delta_{V,K}$ are given by

$$\delta_V=\sqrt{\frac{2\nu}{\omega}}, \quad \delta_K=\sqrt{\frac{2\alpha}{\omega}}=\frac{\delta_V}{\sqrt{\sigma}}, \tag{15}$$

respectively, with ν the kinematic viscosity, σ the Prandtl number, and $\alpha=\nu/\sigma$ the thermal diffusivity. We keep the Prandtl number constant, but we account for the dependence of ν and α on the local temperature and pressure.

For parallel plates with a spacing l, one has (Swift, 1988)

$$f=(1-i)\frac{\delta}{l}\tanh(1+i)\frac{l}{2\delta}, \tag{16}$$

with index V or K; graphs of $if/(1-f)$ for this case are given in Watanabe *et al.* (1997). For circular flow passages with radius r_0 (Rott, 1969)

$$f=\frac{2J_1((i-1)(r_0/\delta))}{(i-1)(r_0/\delta)\,J_0((i-1)(r_0/\delta))}, \tag{17}$$

where $J_{0,1}$ are Bessel functions.

Since a very well developed theory exists for the linear problem in the frequency domain, the value of the present simplified model consists of its ability to give information on nonlinear, time-domain processes for which no exact theory is available short of direct, multidimensional numerical simulations. In order to accomplish this goal, however, it is necessary to develop a suitable time-domain formulation for the transfer terms.

In our earlier work (Yuan *et al.*, 1997), our first attempt was to simply take[3]

$$\mathcal{D}(u)=D\left(1+\theta_D\frac{\partial}{\partial t}\right)u, \tag{18}$$

with D,θ_D constants determined in such a way that

$$D(1+i\omega_1\theta_D)=\hat{D}(\omega_1), \tag{19}$$

where ω_1 is the real part of the frequency of the fundamental mode of the system; similar forms were postulated for the other exchange terms. This choice was based on the fact that the fundamental mode at frequency ω_1 is usually the most important one, and it was therefore desirable to simulate it as precisely as possible. Unfortunately, as discussed in Yuan *et al.* (1997), this simple choice is inadequate as it causes many high-order modes of the system to become unphysically unstable, which causes difficulties in numerical work; an example was given in Fig. 1 of that paper.

In order to remedy the situation, an *ad hoc* damping contribution was artificially added to the term $\mathcal{H}$, which resulted in a spectrum with the desired stability features. While effective, this procedure is undesirable for two reasons, one practical and one of principle. On the practical side, the determination of the parameters of the new term requires the ability to calculate the eigenvalue spectrum of (a suitably

modified form of) Eq. (11), which is a nontrivial task. As a matter of principle, the new dissipative term appears suspicious due to its lack of a physical basis. These considerations led us to an attempt to improve the situation that we now describe.

IV. NEW FORM OF THE ENERGY AND MOMENTUM EXCHANGE TERMS

In attempting to tackle the problem mentioned in the previous section, we decided to follow the suggestion of Achard and Lespinard (1981), who were interested in finding a quasi-one-dimensional formulation for the time-dependent viscous flow of a fluid in a duct. While, with the assumption of fully developed flow, the problem is linear and can be solved by Laplace transform methods, they realized that no form for the drag term short of a time convolution can capture exactly the physics of the process. For this reason, they proposed an approximation in which the momentum transfer term was not given by a single constant, but was found by solving an ordinary differential equation in time.

The simplest form is

$$a_D \frac{d\mathcal{D}}{dt} + \mathcal{D} = b_D \left(1 + c_D \frac{d}{dt}\right) u, \tag{20}$$

with a_D, b_D, c_D three suitable real constants. If $a_D = 0$, this relation reduces to the earlier choice (18) but, in general, it contains one additional parameter that can be chosen so as to improve the representation of the fluid–solid momentum transfer. We proceed in a similar fashion for the other exchange terms as well

$$a_H \frac{d\mathcal{H}}{dt} + \mathcal{H} = b_H \left(1 + c_H \frac{d}{dt}\right) (T_w - T), \tag{21}$$

$$a_Q \frac{d\mathcal{Q}u}{dt} + \mathcal{Q}u = b_Q \left(1 + c_Q \frac{d}{dt}\right) u. \tag{22}$$

In the frequency domain, all these prescriptions reduce to (12) with $\hat{D}$, $\hat{H}$, $\hat{Q}$ replaced by

$$\tilde{D}(\omega) = b_D \frac{1 + i\omega c_D}{1 + i\omega a_D}, \tag{23}$$

etc. We are now at liberty to impose three conditions in order to determine the model parameters *a*, *b*, *c*. As in our earlier model, in view of the importance of the fundamental mode at frequency ω_1, we impose that

$$\tilde{D}(\omega_1) = b_D \frac{1 + i\omega_1 c_D}{1 + i\omega_1 a_D} = \hat{D}(\omega_1), \tag{24}$$

with $\hat{D}(\omega)$ given by (13); here, as before, ω_1 is the real part of the complex eigenfrequency $\hat{\omega}_1$ of the first mode. Satisfaction of this condition ensures that the eigenvalue of the first mode of Rott's theory is reproduced. Upon separating real and imaginary parts, we find two equations among the three real parameters a_D, b_D, c_D.

For the remaining condition there is considerable latitude. Physically, since the transverse dimensions of the flow passages in the stack are usually much smaller than the stack length, one can make the approximation of fully developed flow in the stack. If the physical properties of the fluid were constant, this approximation would have the effect of rendering the left-hand side of the exact conservation equations linear, which would permit one to consider each mode separately.[4] From this point of view, the best approach would be to choose the remaining constant so as to minimize the difference between the exact and approximate linear spectra. This objective can be achieved, but once more at the cost of solving the eigenvalue problem exactly.

Hence, we propose a simpler alternative. In a thermoacoustic prime mover, it is usually the first mode that is unstable. As its amplitude grows, it loses energy to the second and higher modes by nonlinear couplings. The second mode is excited the most and, since it is stable, it will represent the greatest energy sink for the system. The situation is similar in a thermoacoustic refrigerator, where the forcing typically energizes the fundamental mode the most with, again, the second mode providing the greatest energy loss (after the fundamental). These considerations suggest that an effective second condition for the determination of the last free constant in the exchange terms is to impose that the damping of the second mode be correctly described. We cannot use condition (24) for the second mode since the real and imaginary parts of the relation (24) give two equations, but only one free constant remains available. To choose the right condition we use as a guide an earlier result [Karpov and Prosperetti (1998), Eqs. (33), (34); Karpov and Prosperetti (2000), Eq. (5.4)] according to which the linear growth (or damping) rate of the generic *n*th mode can be approximated by

$$\begin{aligned} \mathrm{Im}\ \hat{\omega}_n = \frac{1}{2Vp_0^2\omega_n} \int_0^L dx\ S \Bigg[& \frac{c_A^2}{\omega_n} \mathrm{Re}\ \hat{D}(\omega_n) \left(\frac{dP_n}{dx}\right)^2 \\ & + \gamma\omega_n\ \mathrm{Re}\ \hat{H}(\omega_n) P_n (P_n - \mathcal{R}R_n T_w) \\ & + (\gamma - 1)\ \mathrm{Im}\ \hat{Q}(\omega_n) c_p \frac{dT_w}{dx} P_n \frac{dP_n}{dx} \Bigg]. \end{aligned} \tag{25}$$

This result shows that $\mathrm{Im}\ \hat{\omega}_n$ depends on $\mathrm{Re}\,\hat{D}(\omega_n)$, $\mathrm{Re}\,\hat{H}(\omega_n)$, and $\mathrm{Im}\ \hat{Q}(\omega_n)$, which suggests the following conditions:

$$\mathrm{Re}\ \hat{D}(\omega_2) = b_D\ \mathrm{Re} \frac{1 + i\omega_2 c_D}{1 + i\omega_2 a_D}, \tag{26}$$

$$\begin{aligned} \mathrm{Re}\ \hat{H}(\omega_2) &= b_H\ \mathrm{Re} \frac{1 + i\omega_2 c_H}{1 + i\omega_2 a_H}, \\ \mathrm{Im}\ \hat{Q}(\omega_2) &= b_Q\ \ \mathrm{Im} \frac{1 + i\omega_2 c_Q}{1 + i\omega_2 a_Q}. \end{aligned} \tag{27}$$

Here, ω_2 is the real part of the complex eigenfrequency of the second mode $\hat{\omega}_2$.[5]

In order to demonstrate the quality of the approximations thus obtained, in Figs. 1 and 2 we compare the ω-dependence of the functions $\tilde{D}$ and $\tilde{Q}$ given by (20), (22) with the expressions $\hat{D}$, $\hat{Q}$ given in (13), (14). The Prandtl number is $\sigma = 0.71$ and, at the frequency ω_1, $\delta_K/l = 0.34$. Since the expression for the operator $\mathcal{H}$ is similar to the expression for operator $\mathcal{D}$, we do not show it.

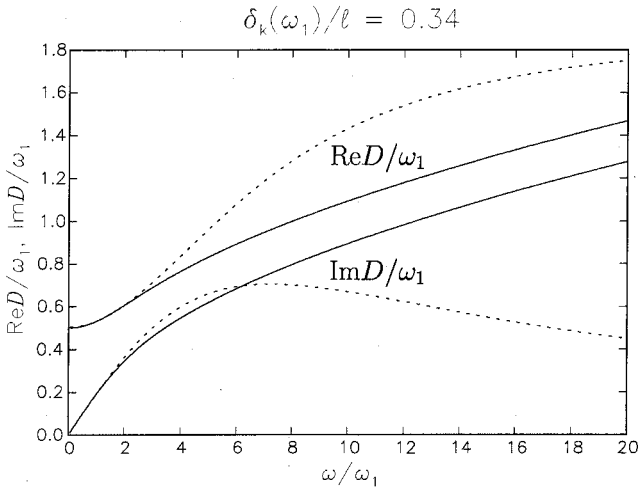

FIG. 1. Real and imaginary parts of the exact function $\hat{D}(\omega)$ defined in (13) (solid lines) compared with real and imaginary parts of the approximation for $\tilde{D}(\omega)$ given by (23) (dotted lines) for the ratio $\delta_K(\omega_1)/l=0.34$ and Prandtl number $\sigma=0.71$.

As formulated above, it would seem that the determination of the model requires the solution of the linear eigenvalue problem, at least for the determination of $\hat{\omega}_1$ and $\hat{\omega}_2$. Actually, this task can be considerably simplified as the real part of the eigenfrequencies is very well approximated by neglecting the exchange terms in the eigenvalue equation (11)

$$\frac{1}{S}\frac{d}{dx}\left(Sc_A^2\frac{dp'}{dx}\right)+\omega_1^2 p'=0. \tag{28}$$

A further simplification is obtained by using, for c_A, a value based on the average temperature of the resonator

$$T_e=\frac{1}{L}\int_0^L T_w\,\mathrm{d}x. \tag{29}$$

In particular, for a cylindrical tube closed at the two ends, one may take

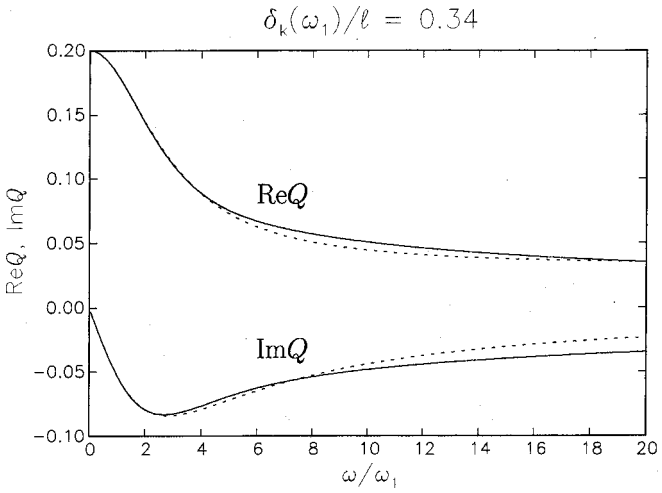

FIG. 2. Real and imaginary parts of the exact function $\hat{Q}(\omega)$ defined in (14) (solid lines) compared with real and imaginary parts of the approximation for $\tilde{Q}(\omega)$ given by the analog of (23) (dotted lines) for the ratio $\delta_K(\omega_1)/l=0.34$ and Prandtl number $\sigma=0.71$.

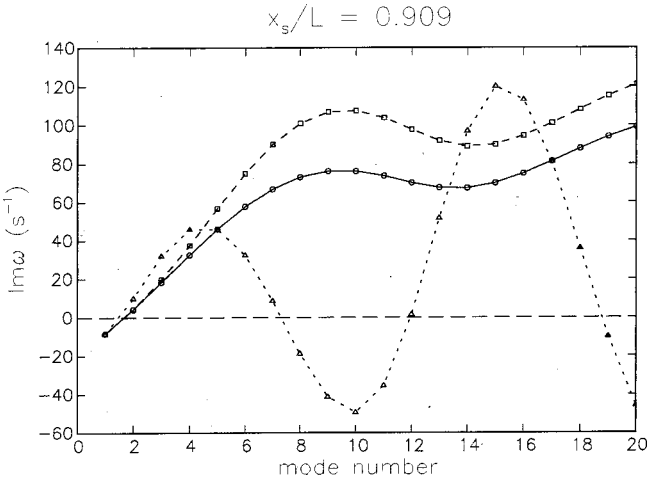

FIG. 3. Damping constant of the first 20 eigenmodes for the system and conditions described in Sec. IV; the stack is located at $x_s/L=0.909$. The circles are the results of Rott's linear theory. The squares and triangles correspond to the differential equation approximation (20)–(22) to the momentum and energy exchange terms and to the simple explicit form (19), respectively. The lines are only meant as guides to the eye.

$$\omega_1 \simeq \frac{\pi}{L}\sqrt{\gamma\mathcal{R}T_e},\quad \omega_2 \simeq 2\omega_1. \tag{30}$$

We found that usually this approximation for ω_1 is sufficient. Approximations are also available for tubes of nonuniform cross section (see, e.g., Rayleigh, 1896), although (30) may give an adequate approximation in many of these cases as well.

As examples of the effect of the previous approximations on the linear spectrum of the problem, Figs. 3, 4, and 5 show the damping constant of the first 20 eigenmodes as a function of the mode number for three different positions of the stack midpoint, $x_s/L=0.91,0.77,0.68$; instability corresponds to a negative value of the quantity shown. The circles connected by the solid line are the result of the standard linear theory (11). Note that in all the examples only the first

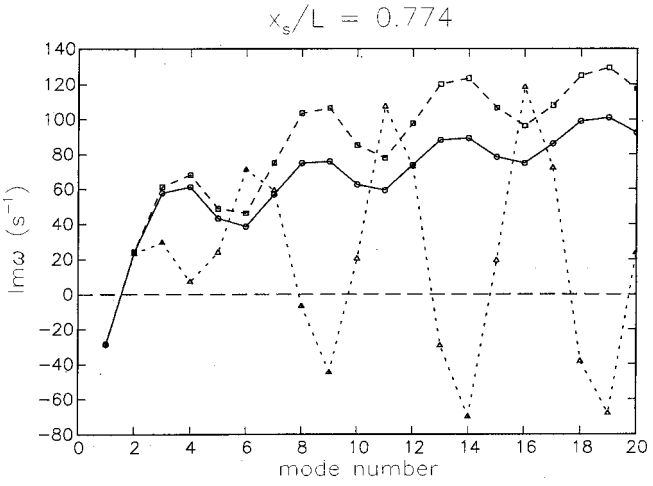

FIG. 4. Damping constant of the first 20 eigenmodes for the system and conditions described in Sec. IV; the stack is located at $x_s/L=0.774$. The circles are the results of Rott's linear theory. The squares and triangles correspond to the differential equation approximation (20)–(22) to the momentum and energy exchange terms and to the simple explicit form (19), respectively. The lines are only meant as guides to the eye.

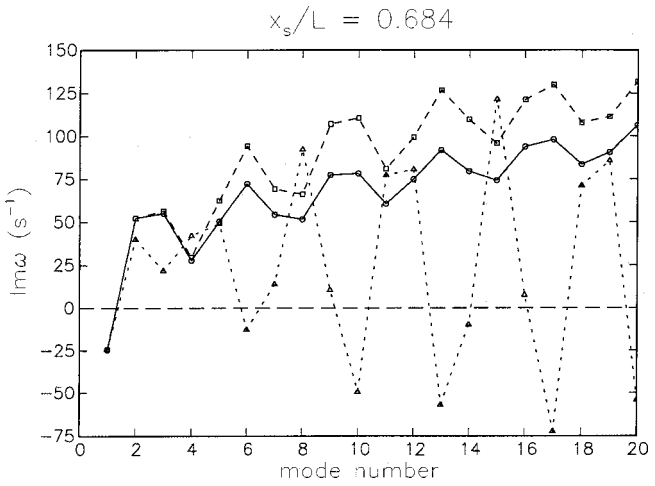

FIG. 5. Damping constant of the first 20 eigenmodes for the system and conditions described in Sec. IV; the stack is located at $x_s/L=0.684$. The circles are the results of Rott's linear theory. The squares and triangles correspond to the differential equation approximation (20)–(22) to the momentum and energy exchange terms and to the simple explicit form (19), respectively. The lines are only meant as guides to the eye.

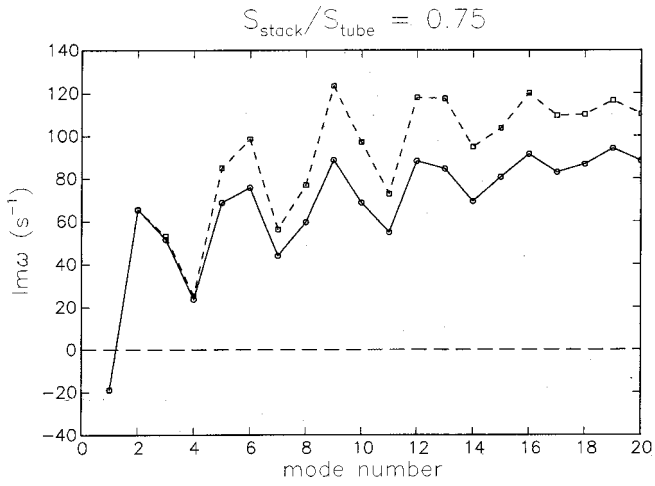

FIG. 6. Damping constant of the first 20 eigenmodes for the same case as in the previous figure, but including the 25% blockage (75% porosity) of finite-thickness plates.

mode is unstable. The results shown by the squares and the dashed line correspond to the differential equation formulation (20)–(22), while the triangles connected by the dotted line correspond to the simple formulation (13) and (14) for the exchange operators. Although both models give good results for the first few modes, the simple formulation (13)–(14) makes some higher modes negatively damped, i.e., unstable; this circumstance was at the root of the numerical difficulties encountered in our previous work (Yuan *et al.*, 1997). On the other hand, the differential equation approximation (20)–(22) gives a good agreement with the linear-theory results for the first few modes and reasonable estimates for the higher modes. Since the fraction of energy contained in these higher modes is usually very small, the associated error is likely to be acceptable.

These numerical results are for a system consisting of a 1-m-long cylindrical tube filled with helium ($\gamma=5/3$, $\sigma=0.71$, $c_p=5.2$ kJ/kg K). The stack has a length of 30 mm and consists of parallel plates of negligible thickness spaced by 0.77 mm. The radius of the tube is assumed to be large so that drag and heat transfer effects are small outside the stack region. The mean pressure is 307 kPa. The tube wall temperature at the left of the stack is $T_C=293$ K, and at the right $T_H=415$ K, so that $T_H-T_C=122$ K. In the stack region the wall temperature is independent of time and a linear function of position. Over the temperature range of interest the thermal conductivity data were fitted by a linear function of temperature as $k=0.151+3.228\times10^{-4}(T-300)$, with k in W/m K and T in K. We have included this effect in the calculations as the value of k determines the thermal penetration thickness, and therefore has a significant impact on the heat transfer parameters. The frequencies ω_1 and ω_2 were evaluated using the approximation (30).

The present model can accommodate tubes with a non-uniform cross section. To illustrate this effect, we show in Fig. 6 results similar to Figs. 3–5 but including the blockage caused by a finite stack-plate thickness. Here, $S_{\text{stack}}/S_{\text{tube}}=0.75$ and the stack is positioned at $x_s/L=0.684$. As another example, in Figs. 7 and 8 we consider a tube with a cross-sectional area given by

$$\frac{S(x)}{S(0)}=\begin{cases}1 & 0\leqslant\frac{2}{5}L\\ [1+Z\,\cos^2\{5\pi/2(2x/L-1)\}]^2 & \frac{2}{5}L\leqslant x\leqslant\frac{3}{5}L,\\ 1 & \frac{3}{5}L\leqslant x\leqslant L\end{cases} \tag{31}$$

for Z equal to 0.4 and -0.4, respectively; the stack position is $x_s/L=0.684$ and the thickness of the stack plates is neglected. In all these examples the frequencies ω_1 and ω_2 were evaluated using the simple approximation (30), which remains fairly accurate in spite of the cross section variation. For example, for the case of (31) with $Z=0.4$, the error for the fundamental mode is less than 3% and for the second mode about 10%.

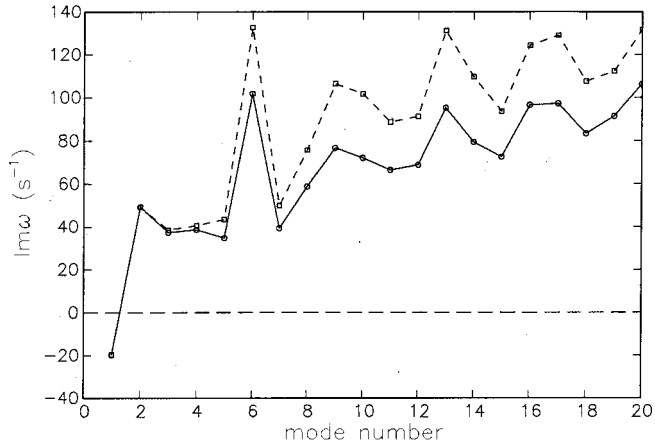

FIG. 7. Damping constant of the first 20 eigenmodes for a resonator with a wider midsection according to (31) with $Z=0.4$; see Sec. IV for a description of the system modeled. The stack is located at $x_s/L=0.684$ as in the previous two figures. The circles are the results of Rott's linear theory. The squares and triangles correspond to the differential equation approximation (20)–(22) to the momentum and energy exchange terms and to the simple explicit form (19), respectively. The lines are only meant as guides to the eye.

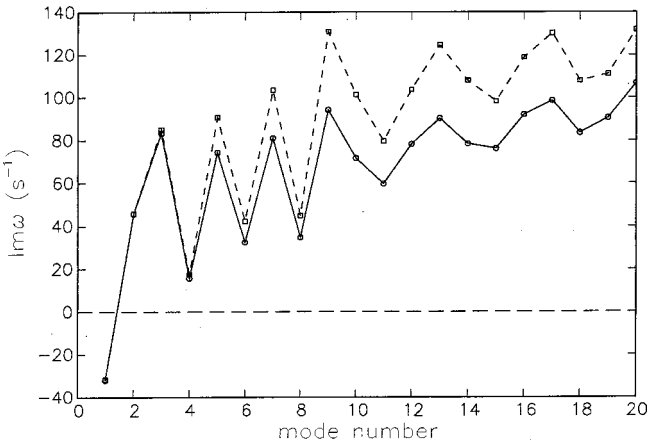

FIG. 8. As in the preceding figure, but with $Z=-0.4$.

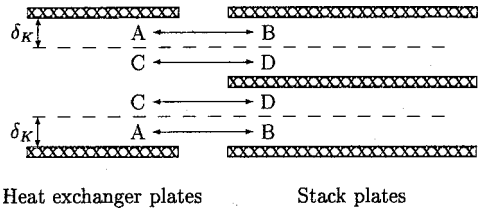

FIG. 9. Schematic representation of a case in which the gap between stack plates is half that between heat exchanger plates. The gas particles moving between points A and B exchange heat with the heat exchanger plates since the point A is within a thermal penetration depth δ_K. In contrast, the gas particles moving between points C and D do not exchange heat with the heat exchanger plates. Therefore, the middle stack plate does not participate in the heat transport along the stack.

V. NUMERICS

In order to solve the equations of the present model numerically, we use the total-variation-diminishing scheme of Harten (1983) described in Yuan *et al.* (1997), to which the reader is referred for details. This method has proven to be effective, robust, and accurate. It is second-order accurate in space, except near regions of very rapid variation of the solution, where it prevents the appearance of the spurious oscillations which contaminate the more traditional schemes.

Since, as is well known (see, e.g., Cao *et al.*, 1996), sharp temperature gradients exist near the ends of the stack while the fields are smooth away from the stack region, the use of a variable spatial node spacing improves efficiency. For the numerical examples that follow, in which the tube length is approximately 1 m, a node spacing Δx of 1 mm outside the stack region and 0.25 mm inside the stack gave converged results.

The time integration is explicit, with the time step Δt chosen on the basis of a CFL criterion $\max(c\Delta t/\Delta x \leqslant)$ 0.4, where Δx is the length of the spatial step and c the local speed of sound; the maximum is evaluated over the entire grid at each time step. With the estimate (30) of the time scale of the oscillations, this choice gives $\omega_1 \Delta t \simeq 0.2\ \Delta x/L$ and is therefore adequate to accurately track the time evolution of the system.

VI. ILLUSTRATIVE RESULTS

In order to illustrate the behavior of the model described before, we now consider several examples: a prime mover with a temperature gradient above onset, an externally driven thermoacoustic refrigerator, and a prime mover/refrigerator combination.

A. Prime mover

The first example is a model of the prime mover system studied by Atchley *et al.* (1990b) and Atchley (1992, 1994). It consists of a 38.2-mm-diameter tube with a length of 99.89 cm, a stack of 35 stainless-steel plates located 90.13 cm from the cold end, and two heat exchangers. The plates are 35 mm long, with a thickness of 0.28 mm and a spacing of 0.77 mm. We take handbook values for the physical properties: $\rho_s = 7900$ kg/m^3, $c_s = 480$ J/(kg K), $k_s = 14.9$ W/(m K). The cold heat exchanger at the left end of the stack consists of two identical structures separated by 1.5 mm, each with 25 nickel plates 0.45 mm thick, spaced by 1.04 mm and 10.2 mm. The hot heat exchanger is attached to the right of the stack and is built like the cold one except that it consists of only one 7.62-mm-long structure. The area blockage is about 30% (70% porosity) in the heat exchangers and 27% (73% porosity) in the stack.

In this system, a feature to be noted is the difference in the number of stack and heat exchanger plates. For the conditions of the experiment the thermal penetration length at the temperature of the cold heat exchanger is approximately 0.19 mm, which is about 25% of the stack plate spacing but only 18% of the heat exchanger plate spacing. At the hot heat exchanger temperature, $\delta_K \simeq 0.38$ mm and the corresponding ratios are 49% and 37%. Since a gas particle only exchanges heat if it is within 1–2 thermal penetration lengths from the plates, as sketched in Fig. 9, it may be expected that some of the stack plates are effectively not contributing as the gas particles that move along them make only an imperfect thermal contact with the heat exchangers, particularly at the cold end where δ_K is smaller.

To account in a rough way for this effect, one may say that only as many stack plates as there are heat exchanger plates take part in the heat transfer. Alternatively, the effect of each stack flow passage, as represented by the heat exchange terms $\mathcal{H}$ and $\mathcal{Q}$, should be reduced by a factor $K_h = 25/35 \simeq 0.71$.

In order to show that this is a reasonable estimate we first consider the linear case. With the correction factor K_h, upon linearization and in the frequency domain, in place of (11) the system (1) to (3) leads to the following eigenvalue equation for the pressure perturbation p':

$$\frac{1}{S}\frac{d}{dx}\left[\frac{Sc_A^2}{1+\hat{D}(\omega)/(i\omega)}\frac{dp'}{dx}\right]+K_h\frac{\hat{H}(\omega)}{i\omega}\frac{c_A^2}{S}\frac{d}{dx}$$
$$\times\left[\frac{S}{1+\hat{D}(\omega)/(i\omega)}\frac{dp'}{dx}\right]+\left(1+K_h\,\gamma\,\frac{\hat{H}(\omega)}{i\omega}\right)\omega^2 p'$$
$$+K_h\,\hat{Q}(\omega)\,\frac{(\gamma-1)c_p}{1+\hat{D}(\omega)/(i\omega)}\frac{dT_w}{dx}\frac{dp'}{dx}=0, \qquad (32)$$

where, as before, c_A is the local adiabatic sound speed and $\hat{D}(\omega)$, $\hat{H}(\omega)$, and $\hat{Q}(\omega)$ are defined in (13) and (14).

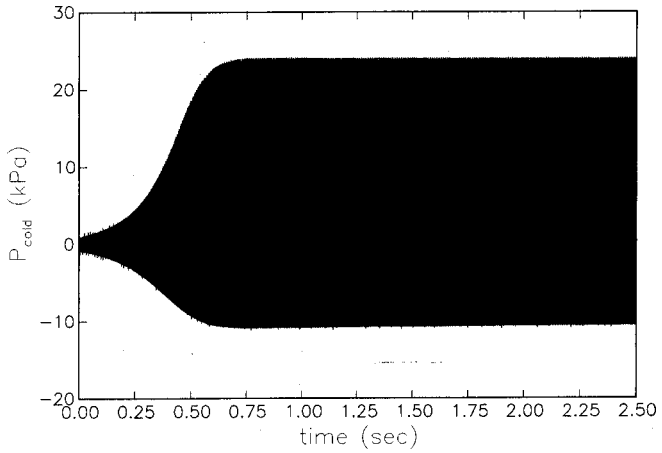

FIG. 10. Transient behavior of the pressure at the cold end of the tube for a prime mover with a temperature difference $T_H - T_C = 368$ K described by Atchley *et al.* (1990b).

In the experiments of Atchley *et al.* (1990b) the temperature difference of 325 K was slightly above onset. A solution of Eq. (32) gives an onset temperature difference of 279.6 K for $K_h = 1$ and 319.1 K for $K_h = 0.71$. From the data reported in Atchley (1994), for a mean pressure of 376 kPa and a temperature difference along the stack of 379 K, the linear temporal growth rate of the perturbation is 5.0 s^{-1}. The solution of Eq. (32) gives a linear growth rate of 11.87 s^{-1} for $K_h = 1$ and 5.64 for $K_h = 0.71$. Obviously, the correction embodied in K_h gives a much better agreement of the linear theory with the experimental results and, for this reason, we feel justified in using the same correction factor K_h for the nonlinear problem as well.

Figures 10 and 11 show the transient and steady-state temporal waveforms of the pressure at the cold end of the tube for the case with a temperature difference $T_H - T_C = 368$ K described by Atchley *et al.* (1990b). The calculation is started with a linear temperature distribution in the stack and a small amplitude of the first system normal mode. The helium mean pressure is 307 kPa. Figure 12 shows the temperature deviation from the initial value as a function of time

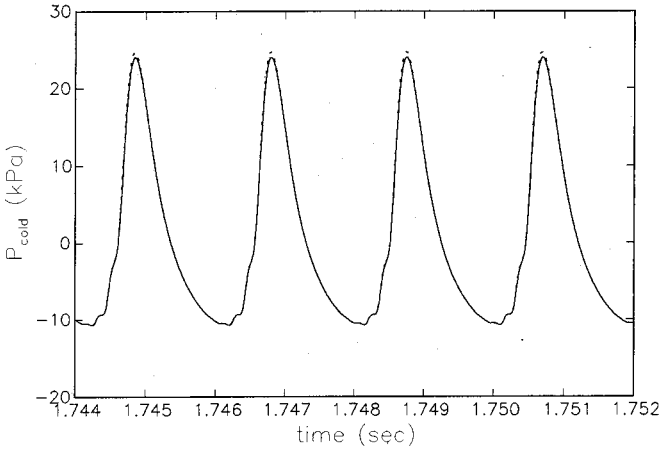

FIG. 11. Steady-state temporal waveform of the pressure at the cold end of the tube for the prime mover of the previous figure. The dotted line corresponds to a fixed linear temperature distribution in the stack; the solid line is calculated with the numerically determined steady-state temperature distribution at the end of the transient.

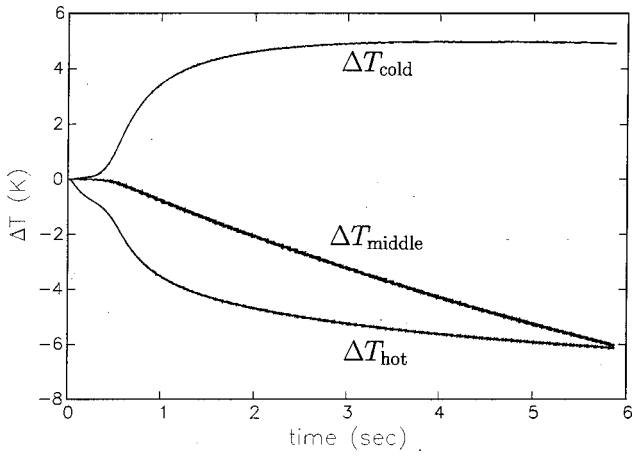

FIG. 12. Temperature deviation from the initial value as a function of time at the center of the stack and 1 mm away from the cold and hot ends for the prime mover of the previous two figures. Initially the temperature near the cold end increases and that near the hot end decreases very rapidly. The difference between the initial and steady-state temperature is approximately 5 and 6 K for the cold and hot ends of the stack, respectively. In contrast, the temperature in the middle of the stack decreases slowly to its steady-state value (not shown in this figure). The final stack temperature distribution is shown in the next figure.

at the center of the stack and 1 mm away from its cold and hot ends. The temperature near the cold end increases and that near the hot end decreases rapidly during the first second, after which they slowly reach the steady-state values. The difference between the initial and steady-state temperatures is approximately 5 and 6 K for the cold and hot ends of the stack, respectively. In contrast, the temperature in the middle of the stack decreases slowly to its steady-state value (not yet achieved in this figure). The final stack temperature distribution averaged over one cycle is shown in Fig. 13. The solid line is the mean wall temperature and the dotted line the mean gas temperature. One can see that there are near-jumps in the temperature of the solid structure at the ends of the stack. The correctness (at least qualitative) of this result is confirmed by the experiments and analysis of Brewster *et al.* (1997) and the calculations of Worlikar (1997) and Worlikar *et al.* (1998). These near-jumps effectively reduce

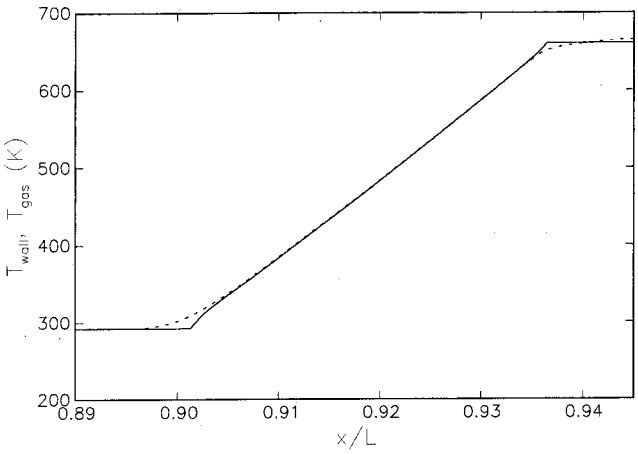

FIG. 13. The final mean temperature distribution in the stack (solid line) and in the gas (dotted line) for the prime mover of the previous three figures. Note the jumps in the solid structure temperature at the ends of the stack.

the available temperature difference in the stack, thus reducing the steady-state oscillation amplitude in comparison with what would be obtained by assuming a time-independent linear stack temperature distribution equal to $T_H - T_C$. This effect is shown in Fig. 11 by the dotted line, which represents the results with the assumption that the wall temperature in the stack region is a time-independent linear function of position. For this particular case the difference between the two results is however small. Figure 11 should be compared with Fig. 4 of Atchley *et al.* (1990b). Qualitatively, the numerical results are close to the experimental ones. The period, 1.95 ms, is identical within the precision with which it can be read from the figure. The waveform exhibits a strong asymmetry, with the negative amplitude much smaller than the positive one. The major difference between calculations and experiment is the amplitude, which is about 24.0 kPa in Fig. 11, but 13.5 kPa in the data. In order to match with measured wave amplitude, the temperature difference $T_H - T_C$ should be decreased by about 25 K. A possible explanation for this difference may be the following. First, the temperature values reported in Atchley *et al.* were measured at the surface of the tube, rather than in the middle of the heat exchanger plates. For the conditions of the experiment it is not unreasonable to expect a temperature difference of the order of 10–20 K between these two points.[6] In addition, the experimental setup most likely includes several loss mechanisms (e.g., form drag of the plates, natural convection) not included in our model.

B. Piston-driven refrigerator

Now, we consider a simple model of a thermoacoustic refrigerator in which a piston at the left end of the tube sets up a standing wave; the right end is modeled as rigid.

The driving frequency is equal to the natural frequency of the tube open at one end, namely $\omega = 2\pi\sqrt{\gamma \mathcal{R} T_i}/(4L)$, where $L = 0.5$ m is the tube length and $T_i = 293$ K the initial uniform temperature of the gas and solid structures. An oscillating velocity $u(t) = U_A \sin \omega t$ is prescribed at $x = 0$ and $p' = \rho' = T' = 0$ there as discussed at the end of Sec. II. The gas is helium at a mean pressure $P_0 = 307$ kPa. The stack consists of 0.28-mm-thick, 30-mm-long plates spaced by 0.77 mm with a thermal conductivity of $k_s = 0.48$ W/(K m) characteristic of fiberglass. It is well known from linear theory (see, e.g., Swift, 1988; Karpov and Prosperetti, 1998) that the thermoacoustic heat flux is strongest when the stack is positioned midway between a velocity node and antinode. Since in this case the tube length is one-quarter of the acoustic wavelength, we position the stack at $x_s/L = 0.5$.

The hot heat exchanger is modeled by assuming a spatially and temporally constant temperature. The cold heat exchanger is assumed to be unloaded and to only exchange heat with the gas and the stack. It is therefore modeled assuming a spatially uniform, time-dependent temperature, the mean value of which will decrease with time under the action of the sound waves. Since the thermal conductivity is assumed to be very large, this cold heat exchanger is simply characterized by the product $\rho_s c_s$. The duration of the transient of the system increases with the value of this quantity and therefore, in order to limit the computational time, we choose $\rho_s c_s = 480$ kW/(K m^3) which is about one order of magnitude smaller than the appropriate value for realistic materials. In spite of this limitation, the results that follow are useful to demonstrate the performance of the model. For simplicity, we disregard blockage effects and take both f_V and f_K to vanish outside the stack and heat exchanger region, thus neglecting momentum and energy exchange with the resonator tube walls.

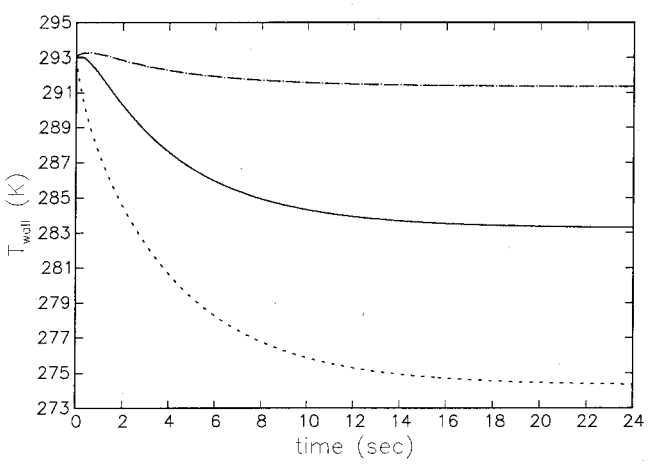

FIG. 14. Mean wall temperature as a function of time at the cold heat exchanger (dotted line), at the stack midpoint (solid line), and 1 mm away from the hot heat exchanger (dot-dash line) for a driven tube with a drive ratio of 4%. The final temperature difference between the heat exchangers is 18.5 K.

Figure 14 shows the temperature T_w as a function of time at the cold heat exchanger (lowest line), at the stack midpoint (middle line), and 1 mm away from the end of the hot heat exchanger. Here, the imposed velocity amplitude U_A is 24.2 m/s which, when converted to pressure according to the standard acoustic relation $U_A = P_A/\rho c_A$, corresponds to a drive ratio $P_A/P_0 = 0.04$. The temperature of the cold heat exchanger initially decreases with time and finally stabilizes at about 18.5 K less than the initial temperature. At steady state, on average, the heat extracted from the heat exchanger by the gas must balance the heat gained by conduction from the stack plates. Thus, the acoustic power supplied to the

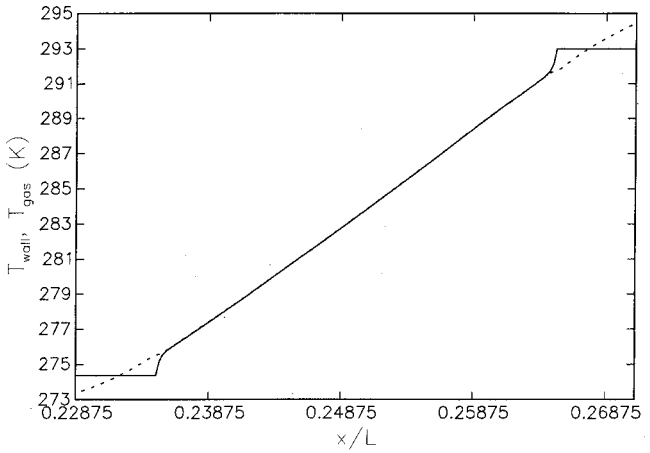

FIG. 15. Mean steady-state temperature distribution in the region of the stack and the heat exchangers for the solid surfaces (solid line) and the gas (dotted line) for the driven tube of the previous figure.

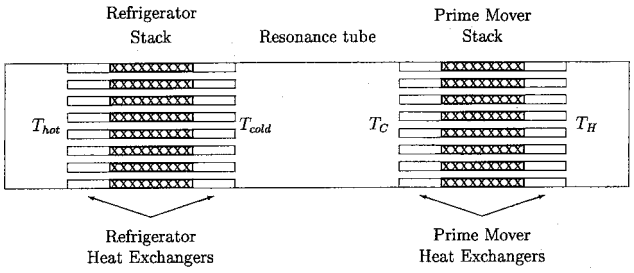

FIG. 16. Schematic representation of a thermoacoustic prime mover/thermoacoustic refrigerator combination. A temperature difference $T_H - T_C$ is maintained across the prime mover stack by its heat exchangers. The standing wave generated by the prime mover stack causes a temperature difference across the refrigerator stack.

system by the piston is spent only to maintain this steady state by removing during each cycle the same amount of heat from the cold heat exchanger that it receives from the stack by conduction. Figure 15 shows the final mean temperature distribution in the region of the stack and the heat exchangers. The mean temperature of the solids is shown by the solid line, and that of the gas by the dotted line. There are near-jumps in the temperature of the solid structure at the ends of the stack similar to those found in Fig. 13. Note that a significant difference between the gas and solid structure temperatures occurs only in the heat exchanger regions, whereas the temperature of the gas and the plates is almost the same over most of the stack. The mean temperature of the gas is higher than that of the solid structure over one part of the heat exchanger, and lower over the other part. The same result was found in the two-dimensional calculation of Worlikar (1997), Worlikar and Knio (1999), and Mozurkewich (1998b).

C. Thermoacoustic refrigerator coupled with prime mover

As a final example, we consider the combination of a thermoacoustic prime mover and a thermoacoustic refrigerator sketched in Fig. 16 housed in a 1-m-long rigidly terminated tube. The prime mover stack is located in the right part of the tube at $x_s/L = 0.26$ and the standing wave that it generates induces a temperature difference across the refrigerator stack positioned in the left part of the tube at $x_s/L = 0.73$.

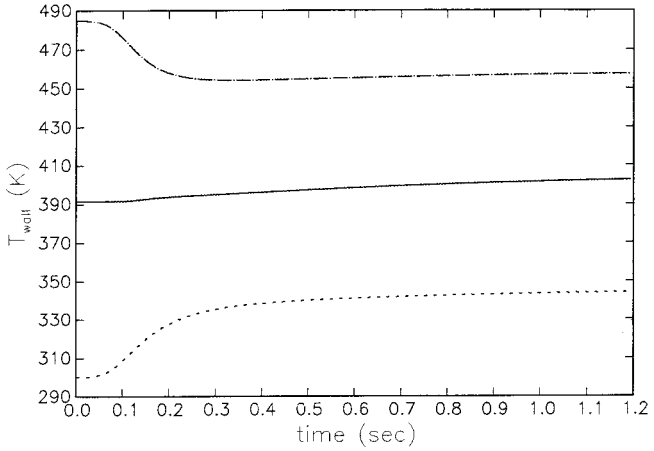

FIG. 18. Temperature vs time at three positions in the prime mover stack for the thermoacoustic prime mover/refrigerator combination of the previous two figures. The dot-dash and dotted lines are for points 1 mm away from the hot and cold heat exchangers, respectively; the solid line is for the stack midpoint. The initial temperature gradient of 6.67 K/mm is reduced to only 4 K/mm at steady state.

As before, we neglect blockage effects and gas–solid momentum and energy exchanges away from the stack/heat exchangers region. The gas is helium at a mean pressure of 307 kPa. The stacks and heat exchangers consist of 0.28-mm-thick parallel plates spaced by 0.77 mm with a length of 30 and 1.5 mm, respectively. For the same reasons mentioned above we set the product $\rho_s c_s$ to 480 kW/(K m^3). The thermal conductivity of the stack plates is $k_s = 0.48$ W/(K m) as before, whereas the plates of the refrigerator heat exchangers are assumed to have infinite thermal conductivity. The temperature of the prime-mover heat exchangers is prescribed to be $T_C = 293$ K, $T_H = 493$ K, and held fixed. The temperatures of the refrigerator heat exchangers are allowed to change in a manner similar to the cold heat exchanger of the previous example. Initially the temperature is a uniform

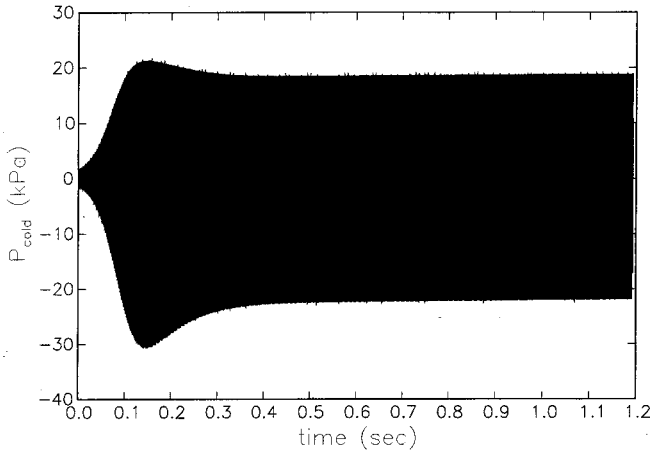

FIG. 17. Transient behavior of the pressure at the cold end of the tube for the thermoacoustic prime mover/refrigerator combination sketched in the previous figure. Note the nonmonotonic behavior of the pressure amplitude.

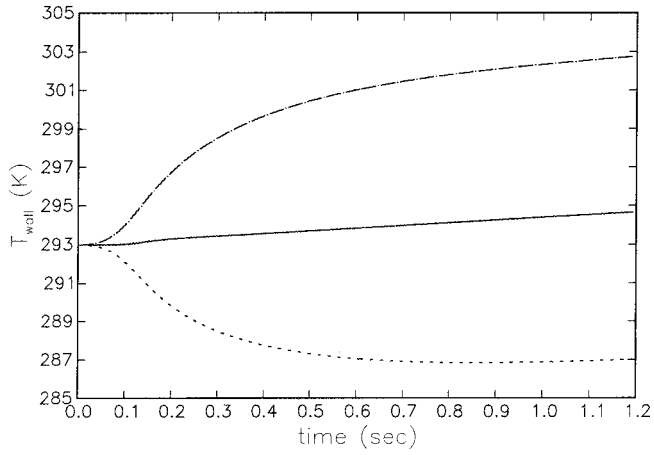

FIG. 19. Temperature vs time of the cold (dotted line) and hot (dot-dash line) heat exchangers and the stack midpoint (solid line) in the refrigerator unit of the thermoacoustic prime mover/refrigerator combination of the previous three figures.

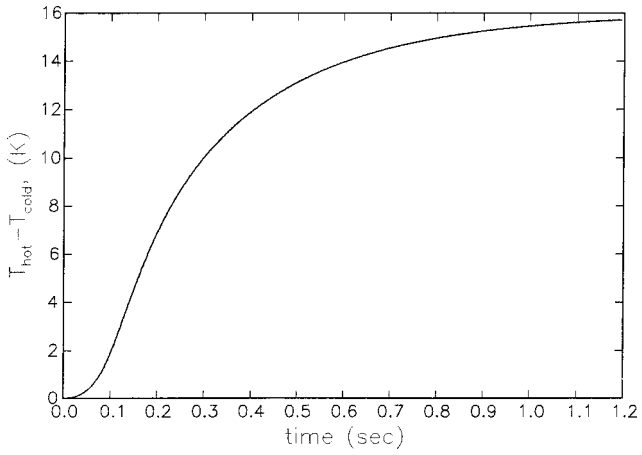

FIG. 20. Temperature difference between the two heat exchangers versus time in the refrigerator unit of the thermoacoustic prime mover/refrigerator combination of the previous figures.

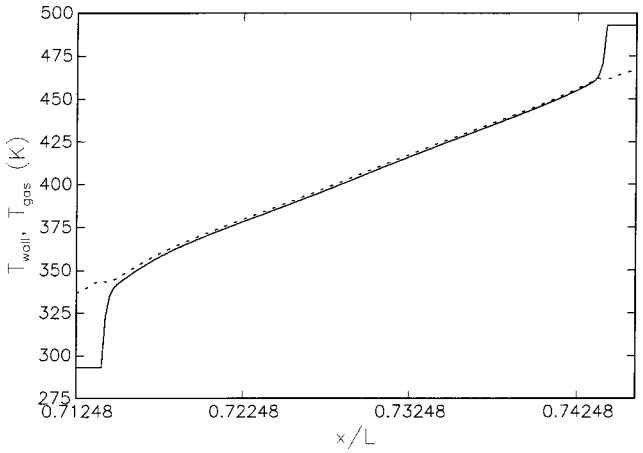

FIG. 22. Mean steady-state temperature distributions in the prime-mover stack and connected heat exchangers for the solid surfaces (solid line) and the gas (dotted line) for the thermoacoustic prime mover/refrigerator combination sketched in Fig. 16.

293 K along the refrigerator stack, while it is a linear function along the prime mover stack.

Figure 17 shows the pressure at the cold end of the tube as a function of time. There is an initial fairly rapid rise up to a maximum amplitude reached at about 0.15 s, followed by a decline to the steady-state regime which is essentially attained at 0.4 s. In order to understand this nonmonotonic behavior, we show in Fig. 18 the temperature at three positions in the prime-mover stack, the midpoint, and 1 mm away from each end. We see here that the temperatures near the two ends of the stack move in opposite directions, approaching each other so much so that the initial temperature gradient of 6.67 K/mm prevailing along most of the stack is reduced at steady state to only 4 K/mm (except for the 1-mm-long segments adjacent to the heat exchangers). The amplitude decrease of Fig. 17 clearly occurs as a consequence of this trend. While the pressure reaches steady state at about 0.4 s, the stack temperatures continue to slowly adjust after this time but without a significant change in the temperature gradient.

Turning now to the refrigerator section, we show in Fig. 19 the temperatures of the two heat exchangers and of the stack midpoint, all as functions of time. The temperatures of the cold and hot heat exchangers initially move in opposite directions, as expected. However, after about 1.0 s, the temperature of the cold heat exchanger starts increasing due to viscous and thermal heating of the refrigerator stack and its heat exchangers. For the refrigerator stack the temperature changes much more slowly than for the prime-mover stack, reaching its steady state only after 1.2 s. Figure 20 shows the temperature difference between the two refrigerator section heat exchangers as a function of time.

Figures 21 and 22 show the final mean temperature distributions for the refrigerator and prime-mover stacks and connected heat exchangers. Significant temperature differences between the plates (solid lines) and the gas occur only near the heat exchangers. For the refrigerator stack the gas temperature is higher than the solid temperature over one part of the heat exchanger and lower over another part, as found before.

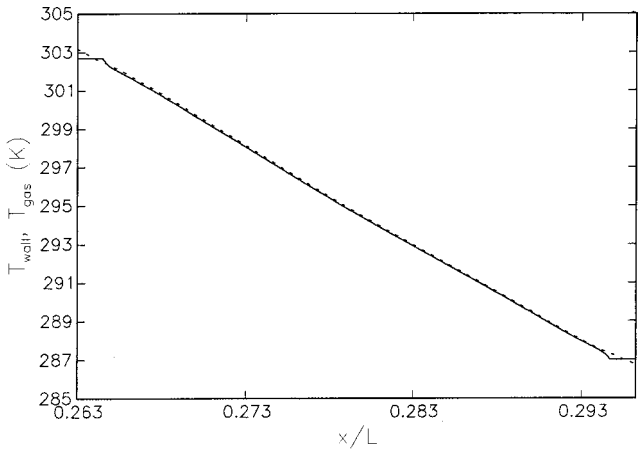

FIG. 21. Mean steady-state temperature distributions in the refrigerator stack and connected heat exchangers for the solid surfaces (solid line) and the gas (dotted line) for the thermoacoustic prime mover/refrigerator combination sketched in Fig. 16.

VII. CONCLUSIONS

The mathematical model of thermoacoustic prime movers and heat pumps presented in this paper derives from an earlier formulation by the authors (Watanabe *et al.*, 1997; Yuan *et al.*, 1997). With respect to that model the present one has been considerably improved in a key respect, namely the modeling of momentum and energy exchanges between the gas and the solid boundaries with which it is in contact. The present model is more realistic (as it well approximates the linear results of Rott's theory for a significant number of modes) and, as an added advantage, is more numerically robust. The previous formulation has been improved in another significant respect, in that the temperature of the solid surfaces of the device is now calculated rather than prescribed.

The model described in this paper is quite flexible as demonstrated by the examples that we have presented: a prime mover, a combined prime mover/refrigerator system, and a piston-driven refrigerator. We have been able to follow in the time domain the evolution of these systems and, for

the first two, we have presented results that trace the evolution of the initial linear instability to the nonlinear regime, and finally to steady state where the instability saturates to a finite amplitude. This is a specifically nonlinear effect that cannot possibly be captured by models based on a linear approximation. We have also tested the model successfully for the prime mover/refrigerator combination assuming periodicity boundary conditions; we have not shown these results as, for the conditions tested, the system turned out to be stable.

It is apparent from the formulation presented in Secs. I, III, and IV, that the model includes several nonlinear mechanisms. In the first place, it accounts for mode–mode coupling. Even though in actual thermoacoustic engines the resonator is built so as to detune the harmonics, at sufficiently large amplitudes a coupling still exists and represents a significant mechanism for energy loss. In a thermoacoustic engine, typically it is only the fundamental mode that is unstable, while all higher modes are damped. Hence, energy leaking out of the fundamental mode into higher ones is dissipated; a weakly nonlinear analysis of this phenomenon is presented in Karpov and Prosperetti (2000). Similarly, in a refrigerator the stack is badly positioned with respect to the spatial distribution of pressure and velocity for modes other than the fundamental, which leads to a loss of efficiency. Secondly, the model does not contain any limitation on the displacement s of the fluid particles and, therefore, it dispenses with the standard assumption of linear theory in which $s\, dT_w/dx \ll T_w$. Third, although the models for the cross-stream momentum and heat exchange are patterned after the linear form (justified by the fact that, typically, the stack is many hydraulic diameters long), we do retain the dependence on the local temperature and pressure thus recovering, at least in part, the mechanism of thermal harmonic wave generation described in Gusev *et al.* (2001).

Some streaming effects [and, in particular, the pressure buildup in the direction of the tube ends, see Waxler (2001)] are included due to the nonlinearities retained in the cross-sectional averaged model, but others (specifically the Rayleigh streaming due to boundary layer effects) are not. In any event, the role of streaming in thermoacoustic systems does not seem to have been completely elucidated (see, e.g., Olson and Swift, 1998; Gopinath *et al.*, 1998; Gusev *et al.*, 2000; Bailliet *et al.*, 2001; Waxler, 2001).

Absent from the model are transition/turbulence phenomena in the stack and vortex shedding from geometric discontinuities such as the ends of the stack and of the heat exchangers. While the impact of the latter on momentum transfer could possibly be accounted for by lumped resistances in a finite-difference implementation, inclusion of the former would require a modification of the exchange parameters $\mathcal{D}$, $\mathcal{H}$, and $\mathcal{Q}$. Two-dimensional nonlinear simulations suggest the presence of some transitional effects only at very high drive ratios, in excess of 6% (Besnoin, 2001). As for the impact of vortex shedding on heat transfer, their significance and role is still an open question.

While these and other mechanisms and other details of a real thermoacoustic system may not be easily incorporated in the present model, a great variety of design parameters can be accounted for such as geometry (and in particular a nonconstant cross section), physical properties, temperature conditions, standing and traveling waves, and others. Thus we believe that—at the very least—the present model can be used in a relative sense to compare the effect of proposed design modifications and to gain insight into the performance of new systems.

ACKNOWLEDGMENT

The authors express their gratitude to the Office of Naval Research for the support of this work.

APPENDIX: MODELING OF HEAT EXCHANGE

Heat transfer between the solid structure and the fluid in Eqs. (3) and (5) is modeled in a somewhat unconventional manner which warrants some clarification (see also Watanabe *et al.*, 1997).

Application of cross-sectional averaging to the exact energy balance equation for the fluid gives $(\mathcal{P}/S)\ \overline{\mathbf{q}\cdot\mathbf{n}}$, where $\mathcal{P}$ is the perimeter of the ''wetted'' area and $\overline{\mathbf{q}\cdot\mathbf{n}}$ is the area-averaged heat flux out of the gas. What we have done in Eq. (3) is to set

$$\frac{\mathcal{P}}{S}\,\overline{\mathbf{q}\cdot\mathbf{n}} = \rho c_p \left[\mathcal{H}(T_w - T) - \frac{dT_w}{dx}\mathcal{Q}\, u \right]. \tag{A1}$$

The parametrization that we use is motivated by the results of the linear theory for cross-stream energy exchange according to which, in the frequency domain (Watanabe *et al.*, 1997),

$$\frac{\mathcal{P}}{S}\,\overline{\mathbf{q}\cdot\mathbf{n}} = \rho c_p \frac{i\omega f_K}{1-f_K}(T_w - T) - \frac{1}{1-\sigma} \times \left(\frac{f_v}{1-f_v} - \frac{\sigma f_K}{1-f_K} \right) \rho c_p \frac{dT_w}{dx}\, u. \tag{A2}$$

Here, as before, T and u are the cross-section averaged fluid temperature and velocity. The coefficient of $T_w - T$ in the first term is just a generalization of the standard heat transfer coefficient. Indeed, if we consider the limit of steady flow, in which $\omega \to 0$, using the asymptotic approximation of f_K [Watanabe *et al.*, 1997, Eq. (60)]

$$f_K = 1 - \frac{i l^2}{2\delta_K^2} + O\left(\frac{l}{\eta}\right)^4, \tag{A3}$$

we find

$$\overline{\mathbf{q}\cdot\mathbf{n}} \simeq 8\frac{k}{l}(T_w - T), \tag{A4}$$

which coincides with the standard result for steady, fully developed flow in a channel (see, e.g., Incropera and DeWitt, 1996, p. 430). The complex, ω-dependent form that appears in (A2) accounts for the phase relation that is crucial in an oscillatory flow. The same parametrization of this term as for the momentum transfer coefficient is justified by the similar-

ity between the two transfer processes, which is also apparent by the similar functional form of the two terms [cf. Eqs. (13) and (14)].

Of greater interest is the second term in (A2) which does not arise in conventional heat transfer, in which wall temperature gradients are usually not accounted for explicitly. The physics behind this term may be better understood if it is noted that linearization of the energy equation (3), use of the equation of state (4), and of the continuity equation (1) permit us to write

$$\rho c_p\left[i\omega T' + (1+\mathcal{Q})\, u\frac{dT_w}{dx}\right] - i\omega p' = -\mathcal{H}T', \qquad \text{(A5)}$$

where $T' = T - T_w$, $p' = p - P_0$. This relation shows that $\mathcal{Q}$ represents a correction to the convective transport term, the origin of which lies in the nonuniformity of the velocity distribution over the channel. Consider the enthalpy convected by the fluid during a time dt across a cross section located at x: the particles very near the wall will carry an enthalpy close to $c_p T_w(x)$, because they will have moved very little due to the no-slip condition. However, particles further way from the wall will come from further upstream, where the temperature is significantly different from $T_w(x)$. Thus, the enthalpy convected by the average velocity u should not be $c_p T_w(x)$, but should be modified: the factor $1+\mathcal{Q}$ has precisely the role to effect this modification. This analysis is supported by the fact that, in the absence of viscosity ($\sigma = 0$) the velocity distribution is uniform and one finds indeed $\mathcal{Q} = 0$ because, then, all the fluid particles transport the same enthalpy.

[1]Heat flow limitations in the heat exchangers can also affect the saturation level quantitatively; the existence of the saturation phenomenon itself, however, is a nonlinear effect.

[2]It appears possible to modify this equation to account for possible heat flow limitations of the heat exchangers (e.g., by adding a term mimicking, by means of a heat transfer coefficient, the coupling with external thermal reservoirs), although we do not pursue this possibility here.

[3]In Yuan *et al.* (1997) this definition was extended to the nonlinear domain by replacing $\partial/\partial t$ by the convective, or material, derivative. In later work (Karpov and Prosperetti, 2000) it was shown, however, that the nonlinear terms thus introduced have a very minor effect. For this reason, and in view of the uncertainty in the proper nonlinear extension, they are neglected here.

[4]The reader is reminded that the temperature and pressure variation of the physical properties are included in the present model.

[5]It is seen from (14) that Q is a combination of D and H. However, the presence of the factor $i\omega$ in these two quantities shows that the physical effect accounted for by D and H is in phase with the particle displacement, rather than the velocity, as the effect of Q. For this reason, in the time domain, it is not desirable to derive the expression of $\mathcal{Q}$ from those of $\mathcal{D}$ and $\mathcal{H}$, but to proceed directly as in (14).

[6]Since Atchley *et al.* do not report measurements of heat fluxes, it is not possible to estimate the likely temperature drop between the central region of the heat exchanger plates and the tube surface.

Achard, J. L., and Lespinard, G. M. (**1981**). ''Structure of the transient wall-friction law in one-dimensional models of laminar pipe flows,'' J. Fluid Mech. **113**, 283–298.

Arnott, W. P., Bass, H. E., and Raspet, R. (**1991**). ''General formulation of thermoacoustics for stacks having arbitrarily shaped pore cross sections,'' J. Acoust. Soc. Am. **90**, 3228–3237.

Atchley, A. A. (**1992**). ''Standing wave analysis of a thermoacoustic prime mover below onset of self-oscillation,'' J. Acoust. Soc. Am. **92**, 2907–2914.

Atchley, A. A. (**1994**). ''Analysis of the initial build-up of oscillations in a thermoacoustic prime mover,'' J. Acoust. Soc. Am. **95**, 1661–1664.

Atchley, A. A., Hofler, T. J., Muzzerall, M. L., Kite, M. D., and Ao, C. (**1990a**). ''Acoustically generated temperature gradients in short plates,'' J. Acoust. Soc. Am. **88**, 251–263.

Atchley, A. A., Bass, H. E., and Hofler, T. J. (**1990b**). ''Development of nonlinear waves in a thermoacoustic prime mover,'' in *Frontiers in Nonlinear Acoustics*, edited by M. F. Hamilton and D. T. Blackstock (Elsevier, Amsterdam), pp. 603–608.

Bailliet, H., Gusev, V., Raspet, R., and Hiller, R. A. (**2001**). ''Acoustic streaming in closed thermoacoustic devices,'' J. Acoust. Soc. Am. **110**, 1808–1821.

Bauwens, L. (**1996**). ''Oscillating flow of a heat-conducting fluid in a narrow tube,'' J. Fluid Mech. **324**, 135–161.

Bauwens, L. (**1998**). ''Thermoacoustics: Transient regimes and singular temperature profiles,'' Phys. Fluids **10**, 807–818.

Besnoin, E. (**2001**). ''Numerical Study of Thermoacoustic Heat Exchangers,'' Doctoral dissertation, Department of Mechanical Engineering, The Johns Hopkins University.

Brewster, J. R., Raspet, R., and Bass, H. E. (**1997**). ''Temperature discontinuities between elements of thermoacoustic devices,'' J. Acoust. Soc. Am. **102**, 3355–3360.

Cao, N., Olson, J. R., Swift, G. W., and Chen, S. (**1996**). ''Energy flux density in a thermoacoustic couple,'' J. Acoust. Soc. Am. **99**, 3456–3464.

Gopinath, A., Tait, N. L., and Garrett, S. L. (**1998**). ''Thermoacoustic streaming in a resonant channel: The time-averaged temperature distribution,'' J. Acoust. Soc. Am. **103**, 1388–1405.

Gusev, V., Job, S., Bailliet, H., Lotton, P., and Bruneau, M. (**2000**). ''Acoustic streaming in annular thermo-acoustic prime movers,'' J. Acoust. Soc. Am. **108**, 934–945.

Gusev, V., Lotton, P., Bailliet, H., Job, S., and Bruneau, M. (**2001**). ''Thermal wave harmonics generation in the hydrodynamical heat transport in thermoacoustics,'' J. Acoust. Soc. Am. **109**, 84–90.

Hamilton, M. F., Ilinski, Y. A., and Zabolotskaya, F. A. (**2002**). ''Nonlinear two-dimensional model for thermoacoustic engines,'' J. Acoust. Soc. Am. **111**, 2076–2086.

Harten, A. (**1983**). ''High resolution schemes for hyperbolic conservation laws,'' J. Comput. Phys. **49**, 357–393.

Ilinskii, Y. A., Lipkens, B., Lucas, T. S., van Doren, T. W., and Zabolotskaya, E. A. (**1998**). ''Nonlinear standing waves in an acoustical resonator,'' J. Acoust. Soc. Am. **104**, 2664–2674.

Incropera, F. P., and DeWitt, D. P. (**1996**). *Fundamentals of Heat and Mass Transfer*, 4th ed. (Wiley, New York).

Karpov, S., and Prosperetti, A. (**1998**). ''Linear thermoacoustic instability in the time domain,'' J. Acoust. Soc. Am. **103**, 3309–3317.

Karpov, S., and Prosperetti, A. (**2000**). ''Nonlinear saturation of the thermoacoustic instability,'' J. Acoust. Soc. Am. **107**, 3130–3147.

Mozurkewich, G. (**1998a**). ''A model for transverse heat transfer in thermoacoustics,'' J. Acoust. Soc. Am. **103**, 3318–3326.

Mozurkewich, G. (**1998b**). ''Time-average temperature distribution in a thermoacoustic stack,'' J. Acoust. Soc. Am. **103**, 380–388; **105**, 567(E) (1999). Erratum: ''Time-average temperature distribution in a thermoacoustic stack [J. Acoust. Soc. Am. **103**, 380–388 (1998)].

Olson, J. R., and Swift, G. W. (**1998**). ''Acoustic streaming in pulse tube refrigerator: Tapered pulse tubes,'' Cryogenics **37**, 769–776.

Rott, N. (**1969**). ''Damped and thermally driven acoustic oscillations in wide and narrow tubes,'' Z. Angew. Math. Phys. **20**, 230–243.

Rott, N. (**1976**). ''Thermally driven acoustic oscillations, IV: Tubes with variable cross section,'' Z. Angew. Math. Phys. **27**, 197–224.

Rott, N. (**1980**). ''Thermoacoustics,'' Adv. Appl. Mech. **20**, 135–175.

Strutt, J. W. (Lord Rayleigh) (**1896**). *The Theory of Sound* (Macmillan, London; reprinted by Dover, New York, 1945), Chap. 12.

Swift, G. W. (**1988**). ''Thermoacoustic engines,'' J. Acoust. Soc. Am. **84**, 1145–1180.

Watanabe, M., Prosperetti, A., and Yuan, H. (**1997**). ''A simplified model for linear and nonlinear processes in thermoacoustic prime movers. I. Model and linear theory,'' J. Acoust. Soc. Am. **102**, 3484–3496.

Waxler, R. (**2001**). ''Stationary velocity and pressure gradients in a thermoacoustic stack,'' J. Acoust. Soc. Am. **109**, 2739–2750.

Wheatley, J. (**1986**). ''Intrinsically irreversible or natural heat engines,'' in *Frontiers in Physical Acoustics*, edited by D. Sette (North-Holland, Amsterdam), pp. 35–475.

Worlikar, A. S. (**1997**). ''Numerical Simulation of a Thermoacoustic Refrigerator,'' Ph.D. dissertation, Johns Hopkins University.

Worlikar, A. S., and Knio, O. M. (**1996**). ''Numerical simulation of a thermoacoustic refrigerator. I: Unsteady adiabatic flow around the stack,'' J. Comput. Phys. **127**, 424–451.
Worlikar, A. S., and Knio, O. M. (**1999**). ''Numerical study of oscillatory flow and heat transfer in a loaded thermoacoustic stack,'' Numer. Heat Transfer **35**, 49–65.
Worlikar, A. S., Knio, O. M., and Klein, R. (**1998**). ''Numerical simulation of a thermoacoustic refrigerator. II Stratified flow around the stack,'' J. Comput. Phys. **144**, 299–324.
Yuan, H., Karpov, S., and Prosperetti, A. (**1997**). ''A simplified model for linear and nonlinear processes in thermoacoustic prime movers. II. Nonlinear oscillations,'' J. Acoust. Soc. Am. **102**, 3497–3506.

Dynamics of two-dimensional composites of elastic and viscoelastic layers

Michael El-Raheb[a)]
1000 Oak Forest Lane, Pasadena, California 91107

(Received 4 November 2001; revised 2 May 2002; accepted 14 June 2002)

Models of frequency response, acoustic transmission, and transient wave propagation are presented for a two-dimensional composite of elastic and viscoelastic layers, simply supported at the two boundaries. The three models adopt transfer matrices to relate state variables over the two faces of a layer. In the frequency domain, a viscoelastic constitutive law is derived by nonlinear fitting a Padé series to measured data of complex shear modulus. For an elastic material, the eigenproblem admits positive real eigenvalues and their negatives. For a viscoelastic material, it admits positive complex eigenvalues and their negative conjugates. The imaginary part of the eigenvalue acts as a velocity-dependent viscous damper. Modal analysis solving transient response utilizes the complex eigenquantities and the static-dynamic superposition method. © *2002 Acoustical Society of America.* [DOI: 10.1121/1.1501907]

PACS numbers: 43.40.At, 43.20.Bi [ANN]

I. INTRODUCTION

The use of viscoelastic materials is common practice in many applications. In structural elements, vibration and noise reduction is achieved by coating metal panels with viscoelastic polymers or in a constrained layer configuration. Reducing acoustic radiation from an underwater structure is accomplished by coating it with a thick compliant polymer layer to reduce amplitude of transmitted vibrations. A recent application concerns trauma on human body from low velocity impact of light nonpenetrating projectiles. The human body consists of a light and stiff elastic bone structure surrounded by a heavier compliant viscoelastic tissue, sealed by skin, a stiffer viscoelastic lining. This layered composite reacts to sudden mechanical pressure triggering sensation by superficial nerves in the skin. A continuum model of this composite should include the viscoelastic properties of each layer and not a homogenized approximation of these properties. Another application in medicine concerns acoustic tomography replacing x rays in noninvasive pathological diagnosis.

The problem of linear stress wave propagation in layered elastic materials is well documented in the literature.[1–9] When the material is viscoelastic, material memory must be included in the model to reproduce delay in propagation and attenuation caused by irreversible energy conversion to heat. References 10–13 report experiments to measure properties of viscoelastic materials using transient response information. References 14–23 treat wave propagation in composites of elastic and viscoelastic layers adopting plate flexure, one-dimensional and two-dimensional (2D) theories. Reference 24 adopts Laplace transform in time and Fourier transform in space to solve for the wave propagation of a three-layer sandwich composite of infinite extent in the plane of the layers including the constitutive law of a linear viscoelastic solid. Reference 25 presents a complete historical expose of wave propagation in layered viscoelastic media adopting transfer matrices. It explains the source of the numerical instability from a large number of layers and high frequencies, and the difficulty arising from complex frequencies and wave numbers when viscoelasticity is considered.

One approximation to viscoelasticity is a frequency independent complex modulus valid in a narrow frequency range. Speed of sound in the material relates to the real part of the modulus while dissipation relates to its imaginary part. This approximation fails when applied to transient waves from impulse of short duration because complex modulus varies substantially over the frequency spectrum of the exciting pulse. Measuring phase velocity in a flier plate experiment produces an equation of state applicable to discretization methods like finite element and finite difference.

An alternative approach compatible to a modal analysis is a frequency-dependent complex modulus within the spectrum of the transient excitation. Data of complex modulus versus frequency are either measured directly in the frequency domain, or indirectly by fixing frequency and changing temperature based on the thermodynamic temperature-frequency equivalence in viscoelasticity.[26] Recently the Hamilton variational method was used for identification of the viscoelastic parameters by direct ultrasonic measurement.[27] The most general constitutive law of linear viscoelastic solids[28] relates the sum of all temporal derivatives of stress to those of strain. When applied to frequency response, the constitutive relation reduces to a Padé series, which is the ratio of two complex power series in frequency. A nonlinear fit of the complex data produces the unknown coefficients in the series.

A modal analysis including frequency-dependent complex moduli yields a complex eigen-problem. The imaginary part of each eigenvalue is equivalent to a viscous damping coefficient factoring velocity in the ordinary differential equation of the generalized coordinate associated with that eigenvalue.

Two hybrid analytical-numerical models are developed

a)Electronic mail: mertrident@earthlink.net

treating the dynamics of a viscoelastic composite panel:

(a) frequency response to external mechanical excitation,
(b) transient response and wave propagation from mechanical shock.

To allow for thick viscoelastic layers and large differences in properties among layers in the composite, a 2D linear elastodynamic analysis is utilized. The analysis includes x and z dependencies where x is along the surface of the panel and z is across its thickness while y extends from $-\infty$ to $+\infty$.

Frequency response of the composite is analyzed in Sec. II adopting the methods in Ref. 29. The x dependence is expressed as a sum of trigonometric functions satisfying simply supported boundary conditions at $x=0$ and l_x, where axial displacement and normal stress vanish. This reduces the independent variables to z only. Transfer matrices relating state vectors $\mathbf{S}_j(0)$ to $\mathbf{S}_j(h_j)$ at the two faces of the jth layer $z_j=0$, h_j and continuity of $\mathbf{S}_j(h_j)$ and $\mathbf{S}_{j+1}(0)$ at interfaces of layers produces a system of tridiagonal block matrices in $\mathbf{S}_j(0)$.[29] Transient response to an external pulse is treated in Sec. III by modal analysis adopting the complex eigenquantities determined in Sec. II. The static-dynamic superposition method is applied to ensure accuracy of all variables in the vicinity of the excitation footprint (see Ref. 29). Finally, typical results from the models are discussed in Sec. IV.

II. FREQUENCY RESPONSE

Consider a 2D composite panel of N_l linear elastic and viscoelastic layers allowing no slip at the interfaces. Let x be the coordinate along the layers with origin at one boundary and z_j a local coordinate across the thickness of the jth layer with origin at an interface. All layers extend from $-\infty$ to $+\infty$ along y. Let (E_j,ν_j,ρ_j,h_j) be Young's modulus, Poisson ratio, mass density, and thickness of the jth layer, and l_x the length of the panel along x. The linear dynamic equilibrium equations of a layer are

$$\sigma_{ij,j}=\rho\frac{\partial^2 u_i}{\partial t^2};\quad i,j\equiv x,z,$$
$$\sigma_{ij}\Rightarrow(\sigma_{xx},\tau_{xz},\sigma_{zz}),\qquad (1)$$
$$u_i=(u,w),$$

where σ_{ij} is stress tensor, u_i is displacement along the ith coordinate, t is time, and $(\ )_{,j}$ is derivative with respect to the jth coordinate. In 2D, the third equilibrium equation is excluded since v and $\partial/\partial y$ vanish.

For a linear elastic solid, the constitutive and strain-displacement relations are

$$\sigma_{ij}=\lambda\,\Delta\,\delta_{ij}+2\mu\,\varepsilon_{ij},$$
$$\Delta=\varepsilon_{ii}=\nabla\cdot u,\quad i,j\equiv x,z,\qquad (2)$$
$$\varepsilon_{ij}=\tfrac{1}{2}(u_{i,j}+u_{j,i}),$$

where u is displacement vector, Δ is volumetric strain, (λ,μ) are Lamé constants, and δ_{ij} is the Kronecker delta. Substituting Eq. (2) in Eq. (1) yields Navier's equations of elastodynamics:

$$\mu\boldsymbol{\nabla}^2\mathbf{u}+(\lambda+\mu)\boldsymbol{\nabla}(\boldsymbol{\nabla}\cdot\mathbf{u})=\rho\frac{\partial^2\mathbf{u}}{\partial t^2}.\qquad (3a)$$

For harmonic motions in time with radian frequency ω and simply supported boundaries as defined in the following

$$w(x,z;t)\equiv\sigma_{xx}(x,z;t)\equiv 0\quad \text{at}\ \ x=0,l_x.\qquad (3b)$$

Noting that Eq. (3) has constant coefficients allows separation of variables yielding the following expansion in (u,w):

$$u(x,z;t)=-\sum_{m=1}^{M}u_m(z)\,\cos(k_m x)\,e^{i\omega t},\quad i=\sqrt{-1},$$
$$w(x,z;t)=+\sum_{m=1}^{M}w_m(z)\,\sin(k_m x)\,e^{i\omega t},\quad k_m=m\pi/l_x,\qquad (4)$$
$$u_m(z)=B_m\,e^{\beta z},\quad w_m(z)=D_m\,e^{\beta z}.$$

Substituting Eq. (4) in Eq. (3) produces the homogeneous equations

$$\begin{bmatrix}-(-e_1k_m^2+e_2\beta^2+\rho\omega^2) & e_3k_m\beta\\ e_3k_m\beta & (-e_2k_m^2+e_1\beta^2+\rho\omega^2)\end{bmatrix}\times\begin{Bmatrix}B_m\\ D_m\end{Bmatrix}=0.\qquad (5)$$

A nontrivial solution to Eq. (5) yields the dispersion relation

$$-(-e_1k_m^2+e_2\beta^2+\rho\omega^2)(-e_2k_m^2+e_1\beta^2+\rho\omega^2)-(e_3k_m\beta)^2=0,\qquad (6)$$
$$e_1=\lambda+2\mu,\quad e_2=\mu,\quad e_3=\lambda+\mu,$$

which is quadratic in β^2 and depends on k_m,ω and material properties (λ,μ,ρ). Consequently,

$$u_m(z)=\sum_{j=1}^{4}B_{mj}\,e^{\beta_{mj}z},\quad w_m(z)=\sum_{j=1}^{4}D_{mj}e^{\beta_{mj}z}.\qquad (7)$$

Equation (5) also relates B_{mj} to D_{mj},

$$B_{mj}=\frac{e_3k_m\beta_{mj}}{-e_1^2k_m^2+e_2\beta_{mj}^2+\rho\omega^2}D_{mj}.\qquad (8)$$

Following Eq. (4), the expressions for stress are

$$\sigma_{xx}(x,z;t)=\sum_{m=1}^{M}\sigma_{xxm}(z)\,\sin(k_m x)e^{i\omega t},$$
$$\sigma_{zz}(x,z;t)=\sum_{m=1}^{M}\sigma_{zzm}(z)\,\sin(k_m x)e^{i\omega t},\qquad (9)$$
$$\tau_{xz}(x,z;t)=\sum_{m=1}^{M}\tau_{xzm}(z)\,\cos(k_m x)e^{i\omega t}.$$

Substituting Eqs. (4) and (9) in Eq. (2) yields

$$\sigma_{xxm}(z)=\sum_{j=1}^{4}\left[(\lambda+2\mu)B_{mj}k_m+\lambda D_{mj}\beta_{mj}\right]\,e^{\beta_{mj}z},$$

$$\sigma_{zzm}(z)=\sum_{j=1}^{4}\left[(\lambda+2\mu)D_{mj}\beta_{mj}+\lambda B_{mj}k_m\right]\,e^{\beta_{mj}z}, \quad (10)$$

$$\tau_{xzm}(z)=\sum_{j=1}^{4}\mu(-B_{mj}\beta_{mj}+D_{mj}k_m)\,e^{\beta_{mj}z}.$$

Define the state vector at an interface of two layers as

$$\mathbf{S}(x,z)=\{\mathbf{f},\mathbf{g}\}^T=\{\sigma_{xx},\tau_{xz};\,u,w\}=\sum_{m=1}^{M}\mathbf{X}_m(x)\cdot\mathbf{S}_m(z), \quad (11)$$

$$\mathbf{X}_m(x)=\mathrm{diag}[\sin(k_mx),\cos(k_mx),\cos(k_mx),\sin(k_mx)].$$

Substituting Eqs. (7) and (10) in Eq. (11) and eliminating B_{mj} using Eq. (8) gives

$$\mathbf{S}_m(z)=\overline{\mathbf{B}}_m(z)\mathbf{D}_m,\qquad \mathbf{D}_m=\{D_{m1},D_{m2},D_{m3},D_{m4}\}^T. \quad (12)$$

Evaluating Eq. (12) at $z=0$ and h for a layer then eliminating D_m produces the modal transfer matrix of a layer along z

$$\mathbf{S}_m(h)=\mathbf{T}_m\cdot\mathbf{S}_m(0),$$

$$\mathbf{T}_m=\overline{\mathbf{B}}_m(h)\cdot\overline{\mathbf{B}}_m^{-1}(0)\equiv\begin{bmatrix}\mathbf{t}_{11} & \mathbf{t}_{12}\\ \mathbf{t}_{21} & \mathbf{t}_{22}\end{bmatrix}_m, \quad (13)$$

$$\mathbf{D}_m=\overline{\mathbf{B}}_m^{-1}(0)\cdot\mathbf{S}_m(0).$$

Let $\mathbf{F}_o(x)$ be the vector of external traction on face 1 and face N_l+1 of the composite

$$\mathbf{F}_o(x)=\{\mathbf{F}_{o1}(x),\mathbf{F}_2(x),\ldots,\mathbf{F}_{oN+1}(x)\}^T,$$

$$\mathbf{F}_{oj}(x)=0,\quad 2\leqslant j\leqslant N,$$

$$\mathbf{F}_{o1}(x)=\mathbf{f}_{o1}q_1(x), \quad (14)$$

$$\mathbf{F}_{oN+1}(x)=\mathbf{f}_{oN+1}q_{N+1}(x),$$

$$\mathbf{f}_{oj}=\{\sigma_{zzo},0,0,0\}_j^T.$$

Enforcing the external tractions on the two end faces and continuity of $\mathbf{S}_m$ at interfaces of layers produces a global transfer matrix $\mathbf{T}_{\mathrm{Gm}}$ operating on $\mathbf{S}_{\mathrm{Gm}}$, the ensemble of $\mathbf{S}_{mj}$ at each interface and end faces

$$\sum_{m=1}^{M}\mathbf{X}_{\mathrm{Gm}}(x)\cdot\mathbf{T}_{\mathrm{Gm}}\cdot\mathbf{S}_{\mathrm{Gm}}=\mathbf{F}_o(x), \quad (15)$$

where

$$\mathbf{T}_{\mathrm{Gm}}=\begin{bmatrix}
-\mathbf{I} & \mathbf{0} & & & & & & \\
\mathbf{t}_{11}^1 & \mathbf{t}_{12}^1 & -\mathbf{I} & \mathbf{0} & & & & \\
\mathbf{t}_{21}^1 & \mathbf{t}_{22}^1 & \mathbf{0} & -\mathbf{I} & & & & \\
 & & \mathbf{t}_{11}^2 & \mathbf{t}_{12}^2 & -\mathbf{I} & \mathbf{0} & & \\
 & & \mathbf{t}_{21}^2 & \mathbf{t}_{22}^2 & \mathbf{0} & -\mathbf{I} & & \\
 & & & & . & . & & \\
 & & & & . & . & \mathbf{t}_{11}^N\ t_{12}^N & -\mathbf{I}\ \mathbf{0} \\
 & & & & & & \mathbf{t}_{21}^N\ \mathbf{t}_{22}^N & \mathbf{0}\ -\mathbf{I} \\
 & & & & & & & -\mathbf{I}\ \mathbf{0}
\end{bmatrix}.$$

$\mathbf{I}$ is a 2×2 unit matrix and $\mathbf{X}_{\mathrm{Gm}}$ is a $4(N_l+1)\times4(N_l+1)$ diagonal matrix made of N_l+1 identical $\mathbf{X}_m(x)$ submatrices in Eq. (11), and $\mathbf{t}_{ij}^k$. Enforcing the orthogonality of $\mathbf{X}_m(x)$ yields M uncoupled tridiagonal block matrices for each wave number m,

$$\mathbf{T}_{\mathrm{Gm}}\cdot\mathbf{S}_{\mathrm{Gm}}=\mathbf{P}_{om};\quad m=1,M,\qquad \mathbf{P}_{om}=\frac{2}{l_x}\int_0^{l_x}\mathbf{X}_{\mathrm{Gm}}(x)\cdot\mathbf{F}_o(x)\,dx. \quad (16)$$

The above-given derivation is valid when $\mathbf{f}_{oj}=\{\sigma_{zzo},0,0,0\}_j^T$ in Eq. (14). However if $\mathbf{f}_{oj}=\{\sigma_{zzo},\tau_{xzo},0,0\}_j^T$, the set in Eq. (4) is augmented by one term:

$$u_{M+1}(x,z)=-\overline{u}_{M+1}(z),\qquad w_{M+1}(x,z)=0 \quad (17)$$

to account for external forces along x on the boundaries. This situation arises when the exciting force is oblique rather than normal to the boundary. In this case, the pressure is decomposed into a normal and a shear component. The static and dynamic $\mathbf{T}_{M+1}$ are derived in Appendix A. The static solution is needed in the static-dynamic superposition method adopted in solving the transient response problem presented in Sec. III.

For a linear viscoelastic material, Ref. 14 derives a constitutive law in the form

$$\sum_{j=0}^{N_\sigma}a_j\frac{\partial^j\boldsymbol{\sigma}}{\partial t^j}=\sum_{k=0}^{N_\varepsilon}b_k\frac{\partial^k\boldsymbol{\varepsilon}}{\partial t^k}, \quad (18a)$$

where (σ,ε) are normal or deviatoric stress and strain and (a_j,b_k) are complex constant coefficients. For periodic motions in time with radian frequency ω, Eq. (18a) reduces to a *Padé* series:

$$\sigma=V_e(N_\sigma,N_\varepsilon;\omega)\varepsilon,\qquad V_e(N_\sigma,N_\varepsilon;\omega)=\frac{\Sigma_{k=0}^{N_\varepsilon}b_k(i\omega)^k}{\Sigma_{j=0}^{N_\sigma}a_j(i\omega)^j}. \quad (18b)$$

In Eq. (18b) (a_j,b_k) are determined by a nonlinear fit to experimental data of complex shear and bulk moduli (G_c,B_c) in a wide frequency range. In this work, Poisson

ratio is assumed independent of frequency thus relating G_c to B_c by a constant function of Poisson ratio ν. Formulation and an example of the nonlinear fit are given in Appendix B.

III. TRANSIENT RESPONSE

Transient response of the composite panel to an external pulse is determined by a modal expansion and the static-dynamic superposition method.[15] For each wave number m, complex eigenvalues and eigenfunctions of the stack $\{\omega,\varphi_m(z)\}_j$ are determined from the homogeneous set in Eq. (16),

$$\mathbf{S}_{\mathrm{Gm}}=\{\boldsymbol{\varphi}_{mj}(z)\}, \tag{19a}$$

$$\mathbf{T}_{\mathrm{Gm}}\cdot\boldsymbol{\varphi}_m=\mathbf{0}\Rightarrow \det[\mathbf{T}_{\mathrm{Gm}}]=0, \tag{19b}$$

$$\boldsymbol{\varphi}_m=\{\varphi_{m1},\varphi_{m2},\ldots\varphi_{nj},\ldots,\varphi_{mn_z}\}^T.$$

Express total displacement $u(x,z;t)$ as a superposition of two terms,

$$\mathbf{u}(x,z;t)=\mathbf{u}_s(x,z)f_p(t)+\mathbf{u}_d(x,z;t), \tag{20}$$

where $\mathbf{u}_s(x,z)$ is static displacement vector from a unit pressure acting over the footprint of the forcing pulse $f_p(t)$, and $\mathbf{u}_d(x,z;t)$ is dynamic displacement vector satisfying the homogeneous dynamic equation of motion (1). $\mathbf{u}_s(x,z)$ satisfies the equation of motion (1) when time derivative vanishes as derived in Appendix C. Express $\mathbf{u}_d(x,z;t)$ in the eigenfunctions $\boldsymbol{\Phi}_j(x,z)$,

$$\mathbf{u}_d(x,z;t)=\sum_j a_j(t)\boldsymbol{\Phi}_j(x,z),$$

$$\boldsymbol{\Phi}_j(x,z)=\sum_m \mathbf{X}_{\mathrm{Gm}}(x)\boldsymbol{\varphi}_{mj}(z), \tag{21}$$

where $a_j(t)$ is a generalized coordinate. Substituting Eq. (21) in the dynamic equations of motion and enforcing orthogonality of $\boldsymbol{\Phi}_j(x,z)$ yields uncoupled equations in $a_j(t)$.

For an undamped composite of elastic layers with constitutive law given by Eq. (2), eigenvalues and resonant frequencies are synonymous. In this case, if ω_j is an eigenvalue then $-\omega_j$ is also an eigenvalue. Consequently the equation governing $a_j(t)$ is

$$\left(\frac{d}{dt}-i\omega_j\right)\left(\frac{d}{dt}+i\omega_j\right)a_j(t)=\overline{f}_j(t),$$

$$\overline{f}_j(t)=N_{aj}f_p(t)/N_j,$$

$$N_{aj}=\int_0^{l_x}\sum_{n=1}^{N_l}\int_0^{h_n}\mathbf{u}_s(x,z_n)\cdot\boldsymbol{\Phi}_j(x,z_n)\,dz_n dx, \tag{22}$$

$$N_j=\int_0^{l_x}\sum_{n=1}^{N_l}\int_0^{h_n}\boldsymbol{\Phi}_j(x,z_n)\cdot\boldsymbol{\Phi}_j(x,z_n)\,dz_n dx.$$

Equation (22) admits a solution in the form

$$a_j(t)=-\frac{1}{\omega_j}\int_0^t \sin\,\omega_j(t-\tau)\,\overline{f}_j(\tau)\,d\tau. \tag{23}$$

For a damped composite panel that includes elastic and viscoelastic layers with complex constitutive law given by Eq. (18b), the eigenvalues ω_j and eigenfunctions $\boldsymbol{\Phi}_j(x,z)$ are both complex,

$$\omega_j=\omega_{Rj}+i\omega_{Ij},$$

$$N_j=\int_0^{l_x}\sum_{n=1}^{N_l}\int_0^{h_n}\boldsymbol{\Phi}_j(x,z_n)\cdot\boldsymbol{\Phi}_j^*(x,z_n)\,dz_n dx, \tag{24}$$

where $\Phi_j^*(x,z_n)$ is the complex conjugate of the eigenfunction. Unlike the purely elastic case where $\pm\omega_j$ are two admissible eigenvalues for each eigenfunction, in the viscoelastic case $+\omega_j$ and $-\omega_j^*$ (not $-\omega_j$) are the two admissible eigenvalues where $(\,)^*$ stands for complex conjugate. This means that $\omega_{1j}=\omega_{Rj}+i\omega_{Ij}$ and $\omega_{2j}=-\omega_{Rj}+i\omega_{Ij}$. The reason ω_I retains the same sign for both solutions is that ω_I is a measure of damping which reduces amplitude whether real frequency is $+\omega_{Rj}$ or $-\omega_{Rj}$. Consequently the equation governing $a_j(t)$ becomes

$$\left(\frac{d}{dt}-i\omega_j\right)\left(\frac{d}{dt}+i\omega_j^*\right)a_j(t)=\overline{f}_j(t)$$

$$\Rightarrow\left[\frac{d^2}{dt^2}+i(\omega_j^*-\omega_j)\frac{d}{dt}+\omega_j\omega_j^*\right]a_j(t)=\overline{f}_j(t). \tag{25a}$$

Noting that $i(\omega_j^*-\omega_j)=2\omega_{Ij}$ and $\omega_j\omega_j^*=\omega_R^2+\omega_I^2$, Eq. (28a) simplifies to

$$\left[\frac{d^2}{dt^2}+2\omega_{Ij}\frac{d}{dt}+\omega_{Rj}^2+\omega_{Ij}^2\right]a_j(t)=\overline{f_j(t)}. \tag{25b}$$

Clearly, ω_{Ij} acts as a velocity proportional viscous damper. Rewriting Eq. (25b) in standard form:

$$\left[\frac{d^2}{dt^2}+2\zeta_j\overline{\omega}_j\frac{d}{dt}+\overline{\omega}_j^2\right]a_j(t)=\overline{f}_j(t),$$

$$\zeta_j=\frac{\omega_{Ij}}{\overline{\omega}_j},\quad \overline{\omega}_j=\sqrt{\omega_{Rj}^2+\omega_{Ij}^2}, \tag{26}$$

yields a solution in terms of a *Duhamel* integral:

$$a_j(t)=-\frac{1}{\hat{\omega}_j}\int_0^t e^{-\zeta_j\overline{\omega}_j(t-\tau)}\sin\,\hat{\omega}_j(t-\tau)\,\overline{f}_j(\tau)\,d\tau, \tag{27}$$

where $\hat{\omega}_j=\overline{\omega}_j\sqrt{1-\zeta_j^2}$.

For frequency response, substituting $e^{i\omega t}$ in Eq. (29) with $f_p(t)=1$ yields a_j,

$$a_j=\frac{\overline{f}_j}{[\overline{\omega}_j^2-\omega^2+2i\zeta_j\overline{\omega}_j\omega]}. \tag{28}$$

The real part of the damped resonant frequency follows from Eq. (28),

$$\omega_{rj}=\overline{\omega}_j(1-\zeta_j^2)^{1/2}. \tag{29}$$

From the definitions in Eq. (26)

$$\omega_{rj}\simeq\omega_{Rj}(1+\zeta_j^2)^{1/2}(1-\zeta_j^2)^{1/2}$$

$$=\omega_{Rj}(1-\zeta_j^4)^{1/2}\simeq\omega_{Rj}(1-\zeta_j^4/2). \tag{30}$$

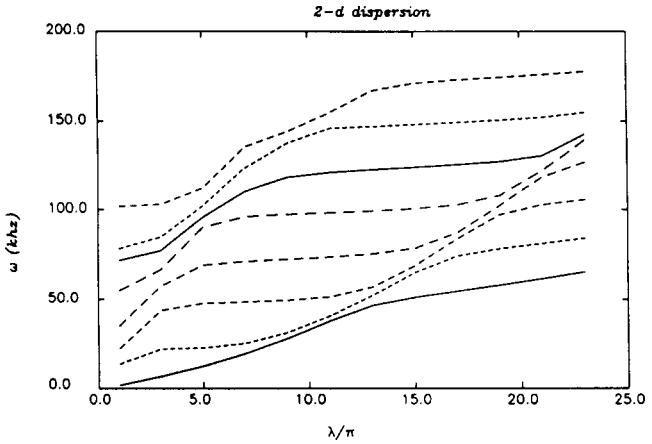

FIG. 1. Modal spectrum of composite.

Equation (30) reveals that the resonant frequency of a viscoelastic material below critical damping ($\eta_j<1$) is approximately that of an equivalent elastic material with the same G_R. In this case, resonant frequency differs from eigenvalue. The result in Eq. (30) also suggests that when iterating to determine complex eigenvalues a good initial guess for ω_j is

$$\omega_j \simeq \omega_{Rj}(1+i\zeta_j), \tag{31}$$

where ω_{Rj} is the resonant frequency of the elastic material with the same $G_R(\omega_{rj})$ but with $G_I=0$.

IV. RESULTS

Consider a three layer composite panel made of a 0.5-in.-thick viscoelastic core layer, confined symmetrically by two 0.1-in.-thick metal skin layers. For transient response prior to reflections from the boundaries, only a short 5-in. segment of panel is needed. Material properties of the skin layers and viscoelastic core are

$$E_s=6.895\times10^{11}\ \text{dyn/cm}^2,\quad \rho_s=2.67\ \text{g/cm}^3,\quad \nu_s=0.25,$$
$$E_{\text{cr}}=1.38\times10^{11}\ \text{dyn/cm}^2,\quad \rho_c=1.28\ \text{g/cm}^3,\quad \nu_c=0.48, \tag{32}$$

where E, ρ, ν are Young's modulus, mass density and Poisson ratio, and the subscript s and c stand for skin and core materials, respectively. The skin material is assumed linear elastic, while the core material is assumed linear viscoelastic following the linear viscoelastic solid constitutive law. In the frequency domain, it has the form

$$(1+i\omega\tau_\varepsilon)\sigma=E_{\text{cr}}(1+i\omega\tau_\sigma)\varepsilon \Rightarrow G_{\text{re}}=E_{\text{cr}}\left(\frac{1+\omega^2\tau_\sigma^2}{1+\omega^2\tau_\varepsilon^2}\right)^{1/2},$$
$$\eta=\frac{\omega(\tau_\sigma-\tau_\varepsilon)}{\sqrt{(1+\omega^2\tau_\sigma^2)(1+\omega^2\tau_\varepsilon^2)}}, \tag{33}$$

where (σ,ε) are stress and strain, ω is radian frequency, $(\tau_\varepsilon,\tau_\sigma)$ are creep and relaxation time constants, and E_{cr} is rubbery modulus. For the core material assume $\tau_\sigma=10^{-5}$ s and $\tau_\varepsilon=5\times10^{-7}$ s.

Figure 1 plots the panel's modal spectrum of circular eigenfrequency Ω versus wave number λ/π along x, and for the first eight axial wave numbers k_z as parameter. Note that the almost horizontal portions of the modal lines correspond to shear modes consistent with the geometry of the composite with a thick core. Figure 2 plots the core's viscoelastic properties $\log_{10}|G_{\text{re}}|$ and η vs $\log_{10}(\Omega)$. Transition occurs at $\Omega_T=1/(2\pi\sqrt{\tau_\sigma\tau_\varepsilon})=70$ kHz and the ratio of glassy to rubbery moduli is $E_{cg}/E_{\text{cr}}\equiv\tau_\sigma/\tau_\varepsilon=20$.

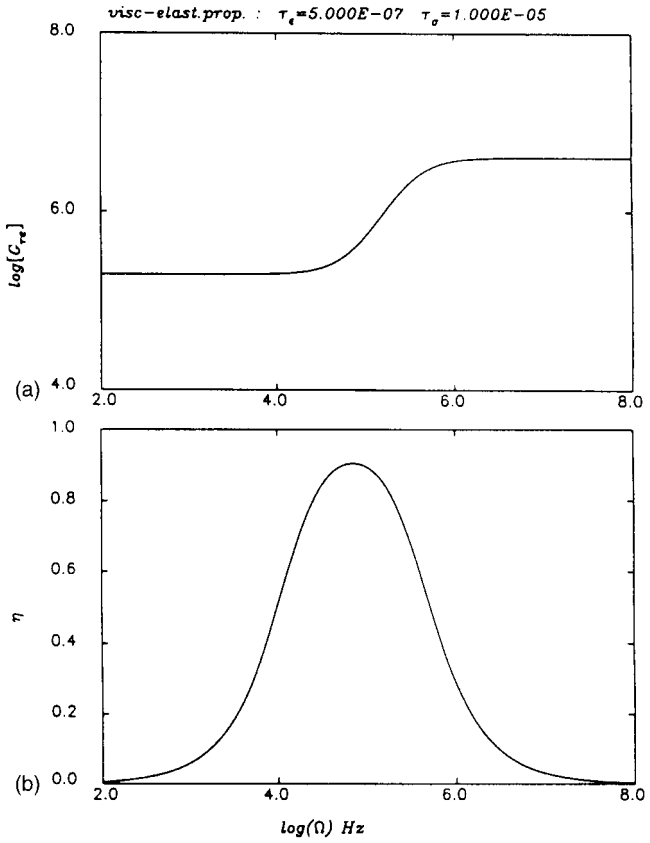

FIG. 2. Viscoelastic properties of core in the frequency domain (a) $\log_{10}|G_{\text{re}}|$, (b) $\eta=G_{\text{im}}/G_{\text{re}}$.

With the properties defined in Eqs. (32) and (33), frequency response of the panel was computed for a periodic excitation from a uniform pressure over a 1.27 cm footprint centrally located on the panel. Figure 3 plots $\log_{10}|w|$ vs Ω for the damped and undamped configurations. The undamped

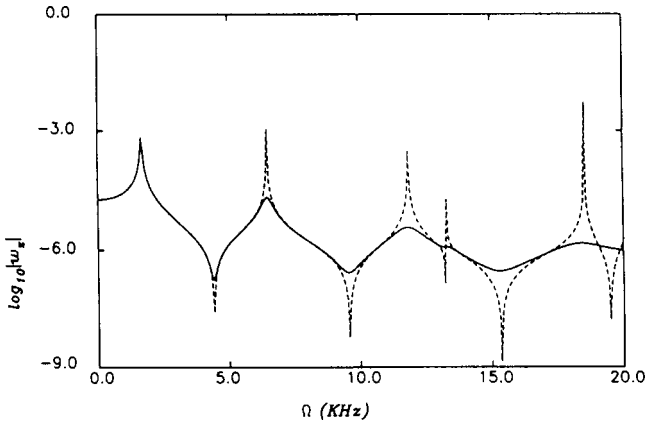

FIG. 3. Frequency response of damped and undamped composite: (—) damped; (---) undamped.

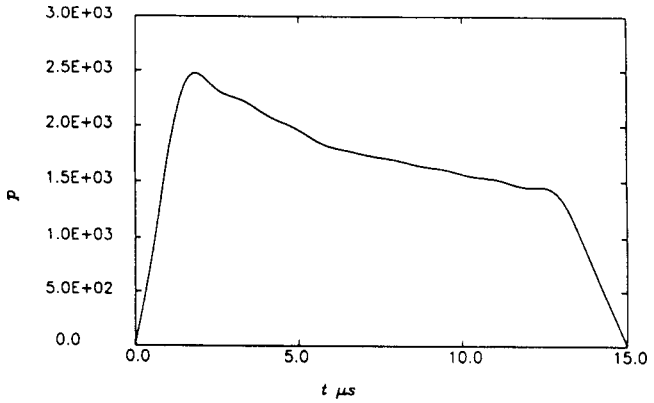

FIG. 4. Forcing pulse.

frequency response shown as a dashed line exhibits sharp peaks and valleys at the resonances and antiresonances of the panel. The damped frequency response line shown as a solid line follows closely the undamped line remote from resonances and antiresonances. At these states, the frequencies of the two cases coincide as predicted by Eq. (30), while peaks and valleys of the damped case are reduced substantially by viscoelasticity of the core. Although the peak at the fundamental is not affected by damping, subsequent peaks become shallower as frequency increases. Transient response to a pulse of short duration assumes a uniformly distributed pressure over a 1.27 cm footprint centrally located on the panel. The time dependence of the pressure pulse is shown in Fig. 4. This pulse is produced by a 20 m/s impact on the panel of a plastic cylindrical projectile 1.27 cm in diameter and 2.54 cm long. The modal expansion includes 22 modes along x $(1 \leqslant m \leqslant 22)$, and 8 modes along z for each m. Figure 5 plots axial displacement w of the undamped and damped cases on top of layers 1 and 3 at three sensors along x from center of impact: $x_{\mathrm{sns}}=0$, 0.635 cm, and 1.27 cm. Note that w of the damped case is only 15% lower than that of the undamped case. Also for the damped case, response lines at the three sensors are closer to each other than in the undamped case. This implies that the damped response mode has smaller curvature. Figure 6 plots flexural stress σ_{xx} on top of each layer. For the damped case, σ_{xx} is almost 1/3 that of the undamped case at all sensors consistent with the reduced curvature observed in Fig. 5. Since viscoelastic damping in the core increases with frequency (see Fig. 3), it reduces the contribution of high frequency modes with larger curvature. This can be demonstrated by snapshots of the deformed panel at fixed times during response. Figure 7 illustrates the deformed shapes for both undamped and damped cases at $t=8$, 16, and 25 μs. A comparison of snapshots for the two cases reveals once more a smoother w distribution in the damped case than in the undamped, and the disappearance of the hump at the wave front where curvature vanishes.

Dissipation from damping is sensitive to the relative position of modal frequency and transition frequency of the viscoelastic material where loss factor η reaches its maximum. A shift of $\log_{10}|G_{\mathrm{re}}|$ and η to lower or higher frequencies may reduce dissipation as properties approach the glassy or rubbery states where η is reduced. In fact assuming τ_σ

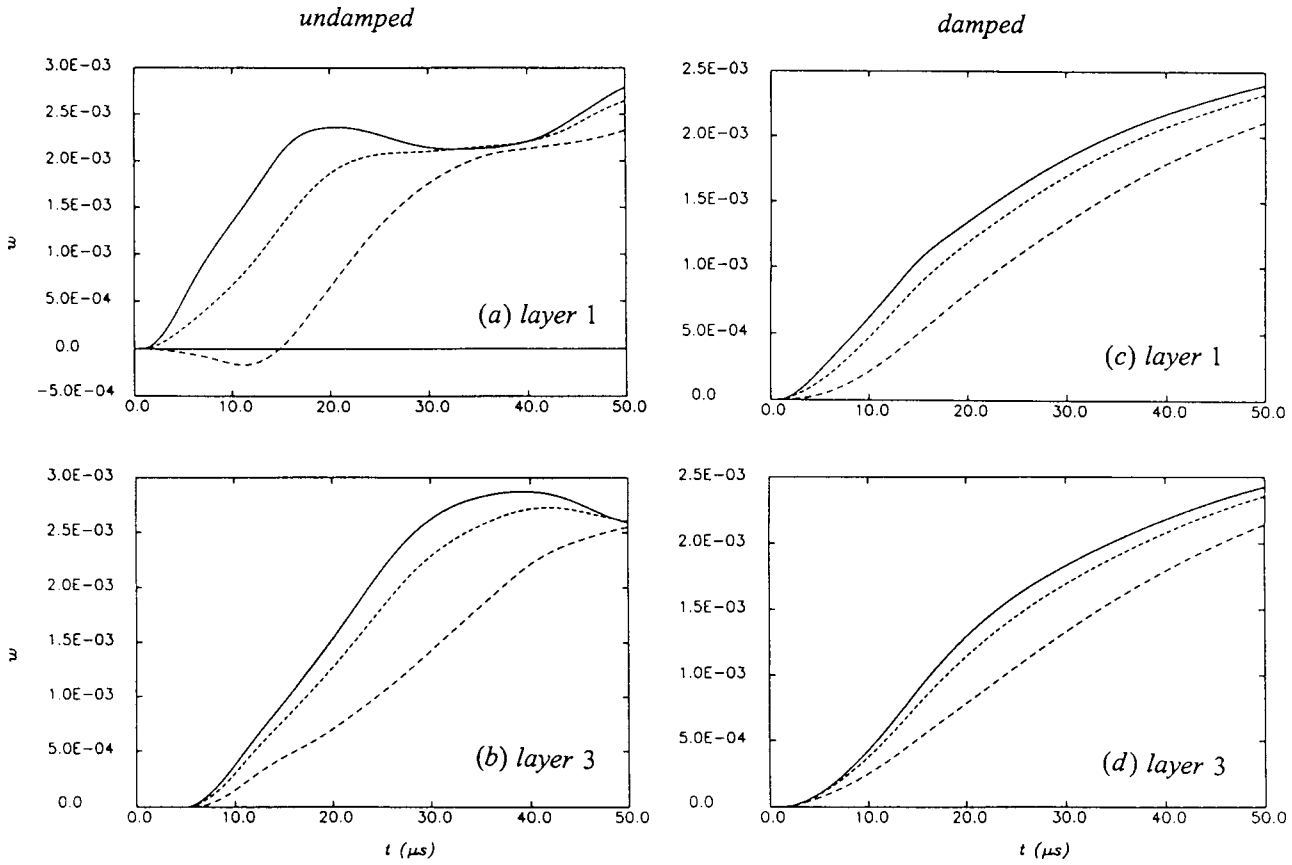

FIG. 5. Transient histories of w for undamped and damped composite: (a), (b) undamped; (c), (d) damped.

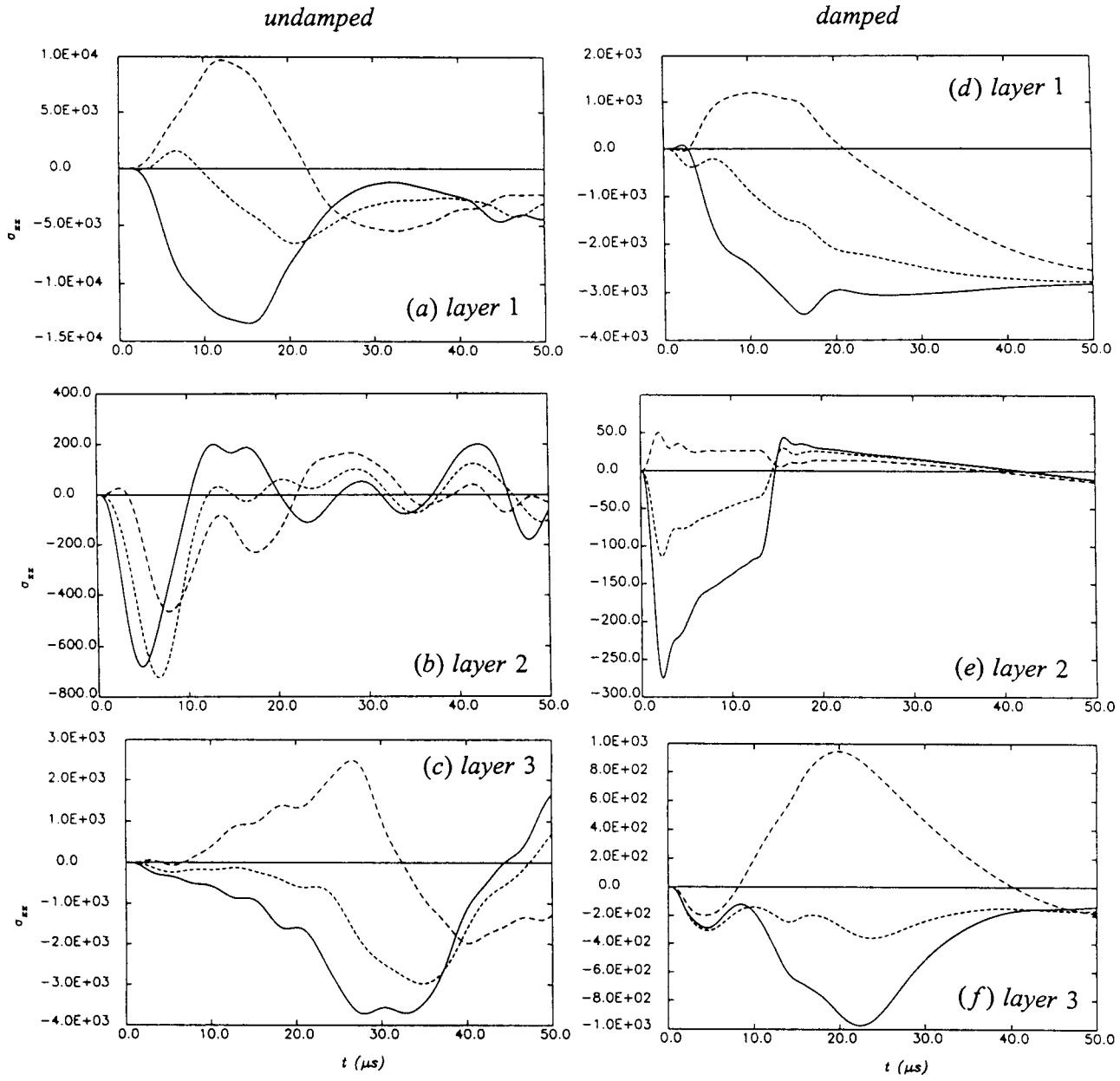

FIG. 6. Transient histories of σ_{xx} for undamped and damped composite: (a)–(c) undamped; (d)–(f) damped.

$=10^{-4}$ s and $\tau_\varepsilon = 5\times 10^{-6}$ s yields response histories commensurate to the undamped case.

V. CONCLUSION

The dynamics of 2D composites of elastic and viscoelastic layers was analyzed adopting transfer matrices relating displacement and traction at interfaces of layers. Viscoelasticity of the material was included as a frequency dependent complex modulus. Noteworthy results are the following.

(1) The Padé series is an accurate model of the constitutive law of typical linear viscoelastic materials in a wide frequency range.

(2) Viscoelasticity of the material does not shift resonant frequencies. It only reduces sharp peaks and valleys at high frequency resonances and antiresonances.

(3) When adopting modal analysis to model a viscoelastic continuum, damping yields complex eigenquantities following the complex nature of the material properties. The imaginary part of each eigenvalue acts as a viscous damping coefficient multiplying the rate-dependent term in the ordinary differential equation for generalized coordinate. In this way each modal equation is equivalent to a damped one degree of freedom oscillator. Contrary to its classical model where damped resonance is shifted from the undamped one, in viscoelasticity the inertia term also changes in a way that damped and undamped resonances coincide.

(4) Although damping has a small effect on displacement, its effect on flexural stress is large as viscoelasticity diminishes the contribution of constituent modes with large curvature.

(5) Damping produced by a viscoelastic core reduces

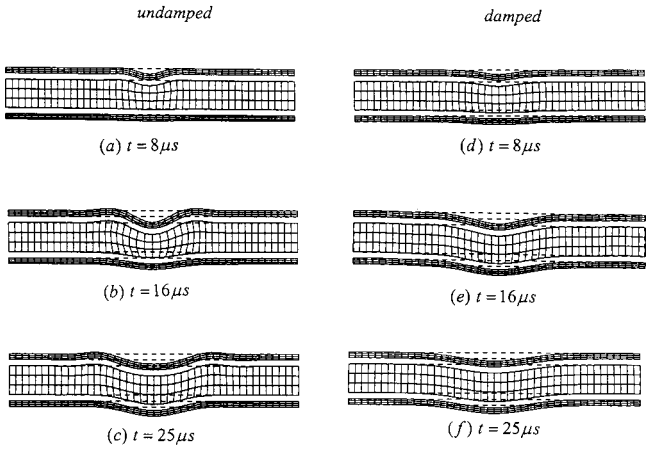

FIG. 7. Time snapshots of undamped and damped composite: (a)–(c) undamped, (d)–(f) damped.

flexural stress substantially, while displacement is not affected.

APPENDIX A: STATIC AND DYNAMIC RESPONSE OF SHEAR MODE

Consider a composite of N_l layers of linear elastic material bonded rigidly at the interface. Let (E,ν,ρ,h) be Young's modulus, Poisson ratio, mass density, and thickness of layer. Shear tractions (τ_{o1},τ_{o2}) are applied to faces 1 and N_l+1 (see Fig. 1). For static response, the equilibrium equation of the jth layer in the displacement $u_j(x,z_j)$ is

$$\frac{\partial^2 u_j}{\partial z_j^2}=0, \tag{A1}$$

where z_j is coordinate across the thickness of the jth layer. Equation (A1) admits a solution for $u_j(x,z_j)$,

$$u_j(z_j)=C_{1j}+C_{2j}z_j, \tag{A2}$$

and shear stress

$$\tau_{xzj}=G_j\frac{\partial u_j}{\partial z_j}\equiv G_jC_{2j}\equiv\text{const.} \tag{A3}$$

Enforcing the traction condition over face 1 on Eq. (A3) yields

$$G_jC_{2j}=\tau_{o1}\Rightarrow C_{2j}=\tau_{o1}/G_j. \tag{A4}$$

Substituting $z_j=0$ in Eq. (A2) and C_{2j} from Eq. (A4) determines $u_j(z_j)$,

$$u_j(z_j)=u_j(0)+\frac{\tau_{o1}}{G_j}z_j,\quad 0\leqslant z_j\leqslant h_j. \tag{A5}$$

Continuity of $u_j(z_j)$ at the $(j+1)$th interface requires

$$u_j(h_j)=u_{j+1}(0). \tag{A6a}$$

Substituting Eq. (A6a) in Eq. (A5) and evaluating at $z_j=h_j$,

$$u_{j+1}(0)=u_j(0)+\frac{\tau_{o1}}{G_j}h_j. \tag{A6b}$$

Expressing $u_j(0)$ in terms of $u_1(0)$ by applying the difference relation (A6b) for all j yields

$$u_{j+1}(0)=u_1(0)+\tau_{o1}\sum_{k=1}^{j}\frac{h_k}{G_k}, \tag{A7}$$

where $u_1(0)$ is still undetermined. To find $u_1(0)$, consider the frequency response of the composite forced by (τ_{o1},τ_{o2}) where $\tau_{o1}=-\tau_{o2}$ for global equilibrium. Since net external traction on the composite is zero, so is net momentum, i.e.,

$$\sum_{j=1}^{N_l}m_ju_{jcg}=0, \tag{A8a}$$

where (m_j,u_{jcg}) are mass and velocity of center of mass of the jth layer. In the limit when frequency approaches zero, Eq. (A8a) reduces to

$$\sum_{j=1}^{N_l}m_ju_{jcg}=0. \tag{A8b}$$

Since $u_j(z_j)$ varies linearly with z_j [see Eq. (A2)], u_{jcg} simplifies to

$$u_{jcg}=\tfrac{1}{2}(u_j(0)+u_j(h_j))=\tfrac{1}{2}(u_j(0)+u_{j+1}(0)). \tag{A9}$$

Substituting Eq. (A9) in Eq. (A8b) produces

$$\sum_{j=1}^{N_l-1}\frac{1}{2}\rho_jh_j(u_j(0)+u_{j+1}(0))+\frac{1}{2}\rho_{N_l}h_{N_l}(u_{N_l}(0)+u_{N_l+1}(0))=0. \tag{A10}$$

Applying Eq. (A7) for each $j>1$ then substituting in Eq. (A10) determines $u_1(0)$,

$$u_1(0)=-\frac{\tau_{o1}}{2M_o}\sum_{j=1}^{N_l}\rho_jh_j\left[\sum_{k=1}^{j}\frac{h_k}{G_k}\right],\quad M_o=\sum_{j=1}^{N_l}\rho_jh_j. \tag{A11}$$

All other $u_j(0)$, $j=2,N_l$ follow from Eq. (A7) and $u_j(z_j)$ from Eq. (A5).

For frequency response, the dynamic equilibrium equation of the jth layer in terms of $u_j(x,z_j)$ is

$$\frac{\partial^2 u_j}{\partial z_j^2}+\frac{\omega^2}{c_{sj}^2}u_j=0,\quad 0\leqslant z_j\leqslant h_j, \tag{A12}$$

where $c_{sj}=\sqrt{G_j/\rho_j}$ is speed of shear waves. Equation (A12) is independent of x and admits a solution

$$\begin{aligned}&u_j(z_j)=C_{1j}e^{\beta_jz_j}+C_{2j}e^{-\beta_jz_j},\\&\beta_j=ik_j=i\omega/c_{sj},\end{aligned} \tag{A13}$$

with shear stress

$$\tau_{xzj}(z_j)=G_j\beta_j(C_{1j}e^{\beta_jz_j}-C_{2j}e^{-\beta_jz_j}). \tag{A14}$$

Combining Eqs. (A13) and (A14) expresses the state vector $\mathbf{S}_j=\{\tau_{xzj},u_j\}^T$ in terms of constant coefficients $\mathbf{C}_j=\{C_{1j},C_{2j}\}^T$,

$$\begin{aligned}&\mathbf{S}_j(z_j)=\mathbf{B}_j(z_j)\cdot\mathbf{C}_j,\\&\mathbf{B}_j(z_j)=\begin{bmatrix}G\beta e^{\beta z} & -G\beta e^{-\beta z}\\ e^{\beta z} & e^{-\beta z}\end{bmatrix}_j.\end{aligned} \tag{A15}$$

Evaluating Eq. (A15) at $z_j=0$, h_j then eliminating $\mathbf{C}_j$ produces the transfer matrix

$$\begin{aligned}&\mathbf{S}_j(h_j)=\mathbf{T}_j\cdot\mathbf{S}_j(0),\\&\mathbf{T}_j=\mathbf{B}_j(h_j)\cdot\mathbf{B}_j^{-1}(0)\\&\quad=\begin{bmatrix}\cos kh & -kG\sin kh\\ \dfrac{\sin kh}{kG} & \cos kh\end{bmatrix}_j,\end{aligned}\tag{A16}$$

where k_j is defined in Eq. (A13). To solve for the global $\mathbf{S}_G=\{\mathbf{S}_1,\mathbf{S}_2,\ldots,\mathbf{S}_{N_l+1}\}^T$ follow the same steps adopted for other modes as derived in the text.

APPENDIX B: NONLINEAR FIT TO COMPLEX MODULUS DATA BY PADÉ SERIES

Consider the general constitutive law for a linear viscoelastic material given by Eq. (18a),

$$\sum_{j=0}^{N_\sigma} a_j\frac{\partial^j\sigma}{\partial t^j}=\sum_{k=0}^{N_\varepsilon} b_k\frac{\partial^k\varepsilon}{\partial t^k}.\tag{B1}$$

For a sinusoidal time dependence, Eq. (B1) assumes the form of a *Padé* series

$$\begin{aligned}&\sigma=V_e(N_\sigma,N_\varepsilon;\omega)\varepsilon,\\&V_e(N_\sigma,N_\varepsilon;\omega)=\frac{\Sigma_{k=0}^{N_\varepsilon}b_k(i\omega)^k}{\Sigma_{j=0}^{N_\sigma}a_j(i\omega)^j}=G_{\rm re}+iG_{\rm im},\end{aligned}\tag{B2}$$

where $(G_{\rm re},G_{\rm im})$ are two real functions of ω. Define the set $(x_n,y_n)|_{n=1}^{2M}$ as

$$\begin{aligned}&(x_n,y_n)|_{n=1}^{n=M}=(\omega_n,G_{{\rm re},n})|_{n=1}^{M},\\&(x_n,y_n)|_{n=M+1}^{n=2M}=(\omega_n,G_{{\rm im},n})|_{n=1}^{M},\end{aligned}\tag{B3}$$

where $(\omega_n,G_{{\rm re},n})|_{n=1}^{M}$ and $(\omega_n,G_{{\rm im},n})|_{n=1}^{M}$ are the two sets of M experimental data point diads defining $(G_{\rm re},G_{\rm im})$. Fitting the sets (B3) with the *Padé* series (B2) requires expressing $(G_{\rm re},G_{\rm im})$ in terms of $(\tau_\sigma,\chi_\sigma)$, $(\tau_\varepsilon,\chi_\varepsilon)$ the real and imaginary parts of the complex parameters b_k and a_j in Eq. (B2) where $b_k=(\tau_\sigma+i\chi_\sigma)_k$ and $a_j=(\tau_\varepsilon+i\chi_\varepsilon)_j$,

$$\begin{aligned}&G_{\rm re}=G_1/G_2,\quad G_{\rm im}=G_3/G_2,\\&G_1=(d_{es}+e_{os})(d_{ee}+e_{oe})+(d_{os}-e_{es})(d_{oe}-e_{ee}),\\&G_2=(d_{ee}+e_{oe})^2+(d_{oe}-e_{ee})^2,\\&G_3=(d_{es}+e_{os})(d_{oe}-e_{ee})-(d_{ee}+e_{oe})(d_{os}-e_{es}),\\&d_{os}=\sum_{k=1}^{N_\sigma/2}(-1)^k\omega^{2k-1}\tau_{\sigma,2k-1},\\&d_{es}=\tau_{\sigma,0}+\sum_{k=1}^{N_\sigma/2}(-1)^k\omega^{2k}\tau_{\sigma,2k},\\&d_{oe}=\sum_{k=1}^{N_\varepsilon/2}(-1)^k\omega^{2k-1}\tau_{\varepsilon,2k-1},\\&d_{ee}=\sum_{k=1}^{N_\varepsilon/2}(-1)^k\omega^{2k}\tau_{\varepsilon,2k}.\end{aligned}\tag{B14}$$

Expressions for $(e_{os},e_{es},e_{oe},e_{ee})$ are obtained by replacing $(\tau_\sigma,\tau_\varepsilon)$ by $(\chi_\sigma,\chi_\varepsilon)$ in $(d_{os},d_{es},d_{oe},d_{ee})$. The nonlinear fit also requires analytical expressions of partial derivatives of $(G_{\rm re},G_{\rm im})$ with respect to the parameters $(\tau_\sigma,\chi_\sigma)_k$ and $(\tau_\varepsilon,\chi_\varepsilon)_j$. For $G_{\rm re}$ these are

$$\begin{aligned}&\frac{\partial G_{\rm re}}{\partial\tau_{\sigma,2k-1}}=(-1)^k\omega^{2k-1}(d_{oe}-e_{ee})/G_2,\\&\frac{\partial G_{\rm re}}{\partial\chi_{\sigma,2k-1}}=(-1)^k\omega^{2k-1}(d_{ee}+e_{oe})/G_2,\\&\frac{\partial G_{\rm re}}{\partial\tau_{\sigma,2k}}=(-1)^k\omega^{2k}(d_{ee}+e_{oe})/G_2,\\&\frac{\partial G_{\rm re}}{\partial\chi_{\sigma,2k}}=-(-1)^k\omega^{2k}(d_{oe}-e_{ee})/G_2,\\&\frac{\partial G_{\rm re}}{\partial\tau_{\varepsilon,2j-1}}=(-1)^j\omega^{2j-1}(d_{os}-e_{es}-2(d_{oe}-e_{ee})G_1/G_2)/G_2,\\&\frac{\partial G_{\rm re}}{\partial\chi_{\varepsilon,2j-1}}=(-1)^j\omega^{2j-1}\\&\qquad\times(d_{es}+e_{os}-2(d_{ee}+e_{oe})G_1/G_2)/G_2,\\&\frac{\partial G_{\rm re}}{\partial\tau_{\varepsilon,2j}}=(-1)^j\omega^{2j}(d_{es}+e_{os}-2(d_{ee}+e_{oe})G_1/G_2)/G_2,\\&\frac{\partial G_{\rm re}}{\partial\chi_{\varepsilon,2j}}=-(-1)^j\omega^{2j}(d_{os}-e_{es}-2(d_{oe}-e_{ee})G_1/G_2)/G_2,\end{aligned}\tag{B5}$$

and similar expressions for the derivatives of $G_{\rm im}$.

The gradient method[30] minimizes the merit function

$$\mu^2(\mathbf{a})=\sum_{n=1}^{M}\left[\frac{y_n-y(x_n;\mathbf{a})}{\sigma_n}\right]^2,\tag{B6}$$

where $(x_n,y_n)|_{n=1}^{2M}$ are data points to be fitted by the nonlinear function $y(x;\mathbf{a})\equiv V_e(N_\sigma,N_\varepsilon;\omega)$, $\mathbf{a}=\{\tau_{\sigma,k},\tau_{\varepsilon,j},\chi_{\sigma,k},\chi_{\varepsilon,j}\}^T$ is the vector of unknown parameters and σ_m is standard deviation. Expand μ^2 in Taylor series near $\mathbf{a}=\mathbf{a}_o$,

$$\mu^2(\mathbf{a})\approx\mu^2(\mathbf{a}_o)+\sum_k\frac{\partial\mu^2}{\partial a_{ok}}a_{ok}+\frac{1}{2}\sum_{k,l}\frac{\partial^2\mu^2}{\partial a_{ok}\partial a_{ol}}a_{ok}a_{ol},\tag{B7}$$

where

$$\begin{aligned}&\frac{\partial\mu^2}{\partial a_{ok}}\equiv-2\beta_k=-2\sum_{n=1}^{2M}\frac{[y_n-y(x_n;\mathbf{a}_o)]}{\sigma_n^2}\frac{\partial y(x_n;\mathbf{a}_o)}{\partial a_{ok}},\\&\frac{\partial^2\mu^2}{\partial a_{ok}\partial a_{ol}}\equiv2\alpha_{kl}\approx2\sum_{n=1}^{2M}\frac{1}{\sigma_n^2}\frac{\partial y(x_n;\mathbf{a})}{\partial a_{ok}}\frac{\partial y(x_n;\mathbf{a}_o)}{\partial a_{ol}}.\end{aligned}\tag{B8}$$

In the second relation of Eq. (B8) $[\partial^2 y(x_n;\mathbf{a}_o]/\partial a_{ok}\partial a_{ol}$ is neglected. A minimum of μ^2 is reached when $\nabla\mu^2=0$ which when applied to Eq. (B7) produces the matrix equation for successive increments $\delta\mathbf{a}=\mathbf{a}-\mathbf{a}_o$,

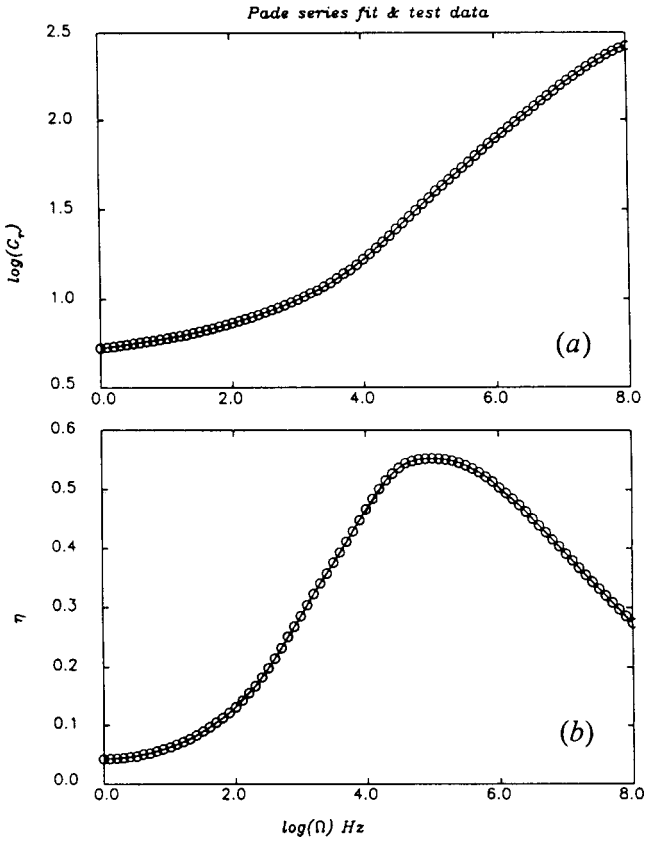

FIG. 8. Nonlinear fit to experimental data by Padé series (a) $\log_{10}|G_{\rm re}|$, (b) $\eta = G_{\rm im}/G_{\rm re}$, (—) nonlinear fit, (○) experimental data.

$$\sum_{l=1}^{L} \alpha_{kl}\delta a_l = \beta_k, \quad k=1,L, \quad L=2(N_\sigma+N_\varepsilon). \tag{B9}$$

Marquardt's method combines the above-described gradient method with the method of steepest descent to accelerate convergence of the iterative process. It replaces the diagonal terms α_{jj} in Eq. (B9) by $\alpha_{jj}(1+\lambda)$ where λ is positive definite. λ starts with a value less than order unity then throughout the iterations, increases or decreases by a factor of 10 say, depending on the relative magnitude of consecutive iterates of μ^2.

Figure 8 plots experimental data for a typical polymer shown as hollow circles and the *Padé* series fit shown as a solid line of $\log_{10}|G_{\rm re}|$ in MPa and $\eta = G_{\rm im}/G_{\rm re}$. The frequency range spanning eight decades was fitted by four different series each encompassing two decades. The fitted series included terms up ω^4. The data and fit are almost indistinguishable.

APPENDIX C: STATIC RESPONSE

Setting $\partial^2\mathbf{u}/\partial t^2 = \mathbf{0}$ in Eq. (3) of the text yields the elasto-static equations

$$\mu\nabla^2\mathbf{u} + (\lambda+\mu)\boldsymbol{\nabla}(\boldsymbol{\nabla}\cdot\mathbf{u}) = \mathbf{0} \tag{C1a}$$

with constitutive relations

$$\sigma_{ij} = \lambda\,\Delta\,\delta_{ij} + 2\mu\,\varepsilon_{ij}. \tag{C1b}$$

For plain strain, $\varepsilon_{yy}=0$ reducing Eq. (C1a) to the uncoupled biharmonic set

$$(\lambda+2\mu)\mu\,\nabla^4(u,w)=0, \quad \nabla^4 \equiv \left(\frac{\partial^2}{\partial x^2}+\frac{\partial^2}{\partial z^2}\right)^2. \tag{C2}$$

For plane stress,

$$\sigma_{yy}=0 \Rightarrow \varepsilon_{yy} = -\frac{\lambda}{(\lambda+2\mu)}(\varepsilon_{xx}+\varepsilon_{zz})$$

simplifying the constitutive relations (C1b) to

$$\begin{Bmatrix} \sigma_{xx} \\ \sigma_{zz} \\ \tau_{xz} \end{Bmatrix} = \frac{E}{(1-\nu^2)} \begin{bmatrix} \partial_x & \nu\partial_z \\ \nu\partial_x & \partial_z \\ \dfrac{1-\nu}{2}\partial_z & \dfrac{1-\nu}{2}\partial_x \end{bmatrix} \begin{Bmatrix} u \\ w \end{Bmatrix} \tag{C3a}$$

and the same uncoupled biharmonic set

$$\frac{(1-\nu)}{2}\nabla^4(u,w)=0. \tag{C3b}$$

For simply supported boundaries, the solution of Eq. (C2) or Eq. (C3b) assumes the form $(u,w)\propto e^{ik_m x}e^{\beta_m z}$ which when substituted into Eq. (C3b) yields the characteristic equation

$$(\beta_{jm}^2 - k_m^2)^2 = 0 \tag{C4a}$$

and corresponding solution

$$\begin{aligned} u = &-\sum_{m=1}^{M} \cos(k_m x)(B_{1m}e^{k_m z} + B_{2m}e^{-k_m z} \\ &+ B_{3m}k_m z\, e^{k_m z} + B_{4m}k_m z\, e^{k_m z}), \\ w = &\sum_{m=1}^{M} \sin(k_m x)(D_{1m}e^{k_m z} + D_{2m}e^{-k_m z} + D_{3m}k_m z\, e^{k_m z} \\ &+ D_{4m}k_m z\, e^{k_m z}). \end{aligned} \tag{C4b}$$

Substitute Eq. (C4b) in either Eq. (C1b) or Eq. (C3a) then in the first equation of Eq. (1) and equate coefficients of each function of z to yield

$$\begin{aligned} &D_{1m} = -B_{1m} + \hat{\nu}B_{3m}, \quad D_{3m} = -B_{3m}, \\ &D_{2m} = B_{2m} + \hat{\nu}B_{4m}, \quad D_{4m} = B_{4m}, \\ &\hat{\nu} = \frac{(3-\nu)}{(1+\nu)}\ (\text{plane stress}), \quad \hat{\nu} = 3-4\nu\ (\text{plane strain}). \end{aligned} \tag{C5c}$$

Expressions for stress follow by substituting the solution (C4b) in Eq. (C1b).

Define the state vector $\mathbf{S}_l$ of stress and displacement at the interface of the lth layer

$$S_l(x,z) \equiv [\boldsymbol{\Psi}_l, \boldsymbol{\Phi}_l]\mathbf{C} = \{\sigma_{zz}, \tau_{xz};\ u, w\}_l^T. \tag{C6}$$

$\boldsymbol{\Phi},\boldsymbol{\Psi}$ are matrices of the functions in displacement (C4a) or (C5b) and corresponding stress, and $\mathbf{C}=\{C_{jm}\}$. Continuity of $\mathbf{S}_l(x,z)$ at the interface of layers "l" and "$l+1$" requires

$$\mathbf{S}_l(x,h) - \mathbf{S}_{l+1}(x,0) = \mathbf{0}, \quad 1 \leqslant l \leqslant N_l - 1, \tag{C7}$$

where h is layer thickness. Traction conditions at the free faces take the form

$$\boldsymbol{\Psi}_1(x,0)\ \mathbf{C}_1=\{\sigma_{zzo},0\}^T,$$
$$\boldsymbol{\Psi}_{N_l}(x,0)\ \mathbf{C}_{N_l}=\{0,0\}^T. \tag{C8}$$

The x dependence in Eq. (C7) is eliminated by orthogonality of the trigonometric functions. This determines a set of tridiagonal block matrices in the form

$$\begin{bmatrix} \mathbf{A}_{10} & & & & & & \\ \mathbf{A}_{1h} & -\mathbf{A}_{20} & & & & & \\ \mathbf{B}_{1h} & -\mathbf{B}_{20} & & & & & \\ & \mathbf{A}_{2h} & -\mathbf{A}_{30} & & & & \\ & & \cdot & \cdot & \cdot & & \\ & & & & \mathbf{A}_{(N_l-1)h} & -\mathbf{A}_{N_l0} & \\ & & & & \mathbf{B}_{(N_l-1)h} & -\mathbf{B}_{N_l0} & \\ & & & & & \mathbf{A}_{N_lh} & \end{bmatrix} \begin{Bmatrix} \mathbf{C}_1 \\ \mathbf{C}_2 \\ \mathbf{C}_3 \\ \cdot \\ \cdot \\ \cdot \\ \mathbf{C}_{N_l-1} \\ \mathbf{C}_{N_l} \end{Bmatrix}$$
$$= \begin{Bmatrix} \mathbf{F}_o \\ \mathbf{0} \\ \mathbf{0} \\ \cdot \\ \cdot \\ \cdot \\ \mathbf{0} \\ \mathbf{0} \end{Bmatrix}, \tag{C9}$$

where

$$\mathbf{F}_o=\{f_{oj}\}, \quad f_{oj}=\begin{cases} -\sigma_{zzo}|\sin(k_m x)\rangle, & j=1,2M \\ 0, & j=2M+1,4M \end{cases}$$

and $\mathbf{A}_{lz}, \mathbf{B}_{lz}$ are $(2M\times 4M)$ matrices constructed by combining all $(\boldsymbol{\Psi}_l, \boldsymbol{\Phi}_l)$ matrices in Eqs. (C7) and (C8).

[1] W. Thomson, "Transmission of elastic waves through a stratified solid medium," J. Appl. Phys. **21**, 89–93 (1950).
[2] N. Haskell, "Dispersion of surface waves on multilayered media," Bull. Seismol. Soc. Am. **43**, 17–34 (1953).
[3] F. Schwab and L. Knopoff, "Surface waves on multilayered anelastic media," Bull. Seismol. Soc. Am. **61**, 893–912 (1971).
[4] J. Dunkin, "Computation of modal solutions in layered elastic media at high frequencies," Bull. Seismol. Soc. Am. **55**, 335–358 (1965).
[5] R. Scott, "Wave propagation in a layered elastic plate," Int. J. Solids Struct. **8**, 833–845 (1972).
[6] D. Viano and J Miklowitz, "Transient wave propagation in a symmetrically layered elastic plate," ASME J. Appl. Mech. **41**, 684–690 (1974).
[7] T. Ting, "Dynamic response of composites," Appl. Mech. Rev. **433**, 1629–1635 (1980).
[8] P. Xu and A. Mal, "Calculation of the inplane Green's function for a layered viscoelastic solid," Bull. Seismol. Soc. Am. **77**, 1821–1837 (1987).
[9] A. Mal, "Wave propagation in layered composite laminates under periodic surface loads," Wave Motion **10**, 257–266 (1988).
[10] I. Lin and J. Sackman, "Identification of the dynamic properties of nonlinear viscoelastic materials and the associated wave propagation problem," Int. J. Solids Struct. **11**, 1145–1159 (1975).
[11] P. Theocaris and N. Papadopoulos, "Propagation of stress waves in viscoelastic media," Polymer **19**, 215–219 (1978).
[12] J. Lallemand, "Exact method for the study of viscoelastic material propagation characteristics," Mech. Res. Commun. **8**, 213–222 (1981).
[13] Y. Sogabe and M. Tsuzuli, "Identification of the dynamic properties of linear viscoelastic materials by wave propagation testing," Bull. Jpn Soc. Mech. Eng. **29**, 2410–2417 (1986).
[14] C. Chen and R. Clifton, "Asymptotic solutions for wave propagation in elastic and viscoelastic bilaminates," Brown University, Div. of Eng. Technical Report No. MRLE-89, 1974.
[15] T. Ting and I. Mukonoki, "A theory of viscoelastic analogy for wave propagation normal to the layering of a layered medium," ASME J. Appl. Mech. **46**, 329–336 (1979).
[16] I. Mukuonoki and T. Ting, "Transient wave propagation normal to the layering of a finite layered medium," Int. J. Solids Struct. **16**, 239–251 (1980).
[17] M. Birlik and Y. Mengi, "Transient wave propagation in a viscoelastic layered composite—an approximate theory," J. Sound Vib. **113**, 141–153 (1975).
[18] M. Kim and Y. Hwang, "An analysis of wave dispersion in coarsely laminated symmetric composite plates," J. Acoust. Soc. Am. **100**, 1981–1991 (1996).
[19] K. Schuler, J. Nunziato, and E. Walsh, "Recent results in nonlinear viscoelastic wave propagation," Int. J. Solids Struct. **9**, 1237–1281 (1973).
[20] V. Karnaukhov, "An approximate method for solving problems of wave propagation in viscoelastic materials," Prikl. Mekh. **8**, 91–96 (1972).
[21] G. Warhola and A. Pipkin, "Shock structure in viscoelastic materials," IMA J. Appl. Math. **41**, 47–66 (1988).
[22] H. Hazanov, "On shock waves in materials with memory," Wave Motion **25**, 73–81 (1997).
[23] D. Levesque and L. Piche, "A robust matrix formulation for the ultrasonic response of multilayered absorbing media," J. Acoust. Soc. Am. **92**, 452–467 (1992).
[24] D. Nkemzi and W. Green, "Transient wave propagation in a viscoelastic sandwich plate," Acta Mech. **102**, 167–182 (1994).
[25] M. Lowe, "Matrix techniques for modeling ultrasonic waves in multilayered media," IEEE Trans. Ultrason. Ferroelectr. Freq. Control **42**, 525–542 (1995).
[26] J. C. Piquette, "Determination of the complex dynamic bulk modulus of elastomers by inverse scattering," J. Acoust. Soc. Am. **77**, 1665–1673 (1985).
[27] A. Di Meglio and L. Sheng Wang, "A variational method for identification of visco-elastic parameters," J. Acoust. Soc. Am. **108**, 2746–2753 (2000).
[28] Y. C. Fung, *Foundations of Solid Mechanics*, 1st ed. (Prentice–Hall, Englewood Cliffs, NJ, 1965), pp. 412–420.
[29] M. El-Raheb and P. Wagner, "Transient response of finite layered media: Two-dimensional axisymmetric analysis," J. Acoust. Soc. Am. **99**, 3513–3527 (1996).
[30] W. Press, B. Flannery, S. Teukolsky, and W. Vetterling, *Numerical Recipes* (Cambridge University Press, New York, 1986), 3rd ed., 1988, pp. 521–525.

Flexural vibration of perforated plates and porous elastic materials under acoustic loading[a)]

D. Takahashi
Department of Architectural Systems, Kyoto University, Yoshida Honmachi, Sakyo-ku, Kyoto 606-8501, Japan

M. Tanaka
Building Research Corporation, Fujisirodai 5-8-1, Suita 565-0873, Japan

(Received 22 June 2001; revised 27 February 2002; accepted 11 June 2002)

This paper presents a method of theoretical treatment of acoustic coupling due to flexural vibration of perforated plates and plates of porous elastic materials. The analytical model is developed by introducing flow continuity at the plate surface in a spatially mean sense and air–solid interaction within the plate material. To demonstrate the method of application, some fundamental acoustic problems based on a classical thin-plate theory are analyzed and discussed in relation to the interactive effect of flexural vibration and plate permeability. For acoustic radiation from a vibrating plate excited by a harmonic point-force, the attenuation effect of power radiation appears at frequencies below the critical frequency of coincidence. In the problem of sound absorption of a perforated plate or a plate of porous elastic material backed by an air layer, as permeability decreases, the effect of plate vibration increases. For perforated absorber systems including plate vibration effects, the trend of variation from ordinary theory depends on plate thickness. © *2002 Acoustical Society of America.* [DOI: 10.1121/1.1497624]

PACS numbers: 43.40.Dx, 43.40.Rj, 43.55.Ev [ANN]

I. INTRODUCTION

In elastic solids shaped into plate-like form, three types of waves occur: quasitransverse shear, quasilongitudinal, and flexural waves. Of these wave types, flexural waves are by far the most important in the field of noise and vibration control because of their direct contribution to sound radiation. In theoretical treatment of flexural vibration of plates, thin-plate theory is the most popular and widely used, while theory of thick plates including the effect of shear deformation in the plate cross section has been often used as a corrected plate theory. Both theories are based on general (classical) elastic theory for homogeneous and isotropic media. Therefore, application of these plate theories is limited to materials of this type.

In problems of structural–acoustic coupling due to plate vibration, the boundary surface of the plate is assumed to be homogeneous. There are also some materials, such as perforated plates or plates of porous materials having extensive range of application in machinery noise control and architectural acoustics, to which ordinary methods of setting the boundary condition cannot be applied. In the case of perforated plates with a smaller hole diameter, the phase of flexural vibration naturally appears as demonstrated by the experimental work of Lee.[1] However, the effect of plate vibration on sound absorption of microperforated plates[1–3] has been disregarded since the pioneering work of Rayleigh.[4]

A similar situation can be seen in the plate-like form of glass wool or rock wool used for ordinary purposes of sound absorption and/or heat insulation; i.e., flexural-mode vibration as well as properties of dilatational wave-propagation media exist. Furthermore, in the case of newly developed sound absorbing panels with pores of a solid frame,[5] as permeability decreases the effect of flexural vibration may become so serious that it cannot be disregarded.

The present paper focuses on development of a generalized approach to investigate problems surrounding structural–acoustic coupling for both perforated plates and plates of porous elastic materials. As a similar problem, Göransson[6] studied the problem of a flexible porous material assuming that the material is limp (the plate stiffness effect is neglected); in that study, solid frame motion is included only by the viscous drag force due to relative motion between the solid frame and the fluid. Owing to the latter assumption, however, this model does not allow for studies of effects of mechanical excitation applied to the material. More recently, Horoshenkov *et al.*,[7,8] analyzed acoustic response of porous elastic materials, including the effect of plate vibration, which is similar to the present problem. They introduced a simple boundary condition as a coupling condition between the plate and surrounding air at the plate surface, which is different from the model herein. In Horoshenkov's model, flow continuity at the plate surface is used by assuming that the particle velocity of surrounding air equals the sum of frame velocity and particle velocity of the wave-propagation medium modeled as a usual static porous material. In this model the effect of air–solid interaction within the material is neglected.

In the present analytical model, the plate is assumed to be a thin plate governed by classical thin-plate theory, with the same fluid (air) on both sides. Interaction between the plate and surrounding air is introduced in a spatially mean

[a)]Portions of this work were presented in "Effects of flow resistance on acoustic performance of permeable elastic-plate absorbers," Proceedings of the 16th International Congress on Acoustics, Seattle, WA, June 1998.

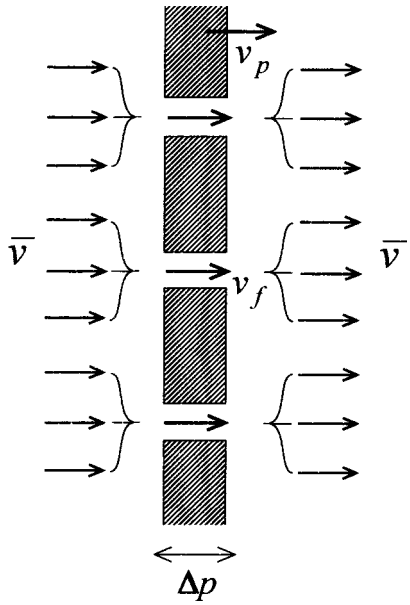

FIG. 1. Analytical model of a perforated plate.

sense by combining flow continuity at the plate surface with the force due to relative motion at the air-solid interface within the plate material. As a result, the effect of inhomogeneity of the boundary surface is smoothed out, i.e., it is assumed in this study that the length scales of structure components of the boundary surface are relatively small compared to the acoustic wavelength. A similar treatment can be seen in Leppington's work[9] for analysis of acoustic response of a perforated sandwich plate; there, he formulated the problem in terms of a hypothetical compound surface with homogeneous boundary conditions. Abrahamas[10] applied this method to the same sandwich plate system for calculations of sound radiation due to a line excitation. The analytical model employed by both researchers is eventually homogeneous impermeable elastic plate with homogeneous boundary conditions that is different on the two sides: one is acoustically hard and the other has properties of a Helmholtz resonator.

To demonstrate the method of application of the simplified model proposed here, some fundamental acoustic problems are analyzed and discussed in relation to the interactive effect of plate vibration and permeability.

II. THEORY

A. Acoustic coupling for perforated plates

Shown schematically in Fig. 1 is a cross-sectional view of a perforated plate that is vibrating in flexural mode with a velocity v_p under any acoustic loading with the pressure difference Δp. Consider the case, in which the plate itself is at rest ($v_p=0$), the mean particle velocity $\overline{v}$ of surrounding air can be written as $\overline{v}=\sigma v_f$, where v_f is the spatially averaged velocity in the hole and σ is the ratio of perforation. Let Z_0 be the acoustic impedance of the hole, and Z be the overall acoustic impedance of the plate surface, which are defined as

$$Z_0=\frac{\Delta p}{v_f}=\frac{\Delta p}{\overline{v}}\sigma=Z\sigma. \tag{1}$$

The resistance term Z_{resist} of the acoustic impedance Z_0 ($\equiv Z_{\text{resist}}+Z_{\text{react}}$) is related to air–solid interaction. Thus, when $v_p=0$, Eq. (1) can be rewritten as

$$Z_{\text{resist}}v_f+Z_{\text{react}}v_f=\Delta p. \tag{2}$$

Consider next the case in which the plate is vibrating under the same acoustic loading; the mean particle velocity $\overline{v}$ becomes

$$\overline{v}=v_p+(v_f-v_p)\sigma. \tag{3}$$

In this case, the viscous force at the air–solid interface in the hole depends on relative velocity v_f-v_p. Owing to this alteration, Eq. (2) is modified as $Z_{\text{resist}}(v_f-v_p)+Z_{\text{react}}v_f=\Delta p$, which yields

$$v_f-v_p=\frac{\Delta p}{Z_0}-\frac{Z_{\text{react}}}{Z_0}v_p. \tag{4}$$

Thus from Eqs. (1) and (4), Eq. (3) becomes

$$\overline{v}=\zeta_I v_p+\frac{\Delta p}{Z_0}\sigma=\zeta_I v_p+\frac{\Delta p}{Z}, \tag{5}$$

where $\zeta_I=1-(Z_{\text{react}}/Z_0)\sigma$. The simple and easy way of realizing this approach is to substitute the flow resistance for the impedance Z, which is measured using an ordinary flow-resistance apparatus with a steady flow. This simple approach was introduced into the theory for acoustic properties of permeable membranes;[11] it gives good quantitative predictions that show good agreement with experimental results. In the case of elastic plates, however, due to thickness of the plate, there exist other factors such as air mass inertia in the hole and the radiation effect at the hole entrance. These factors contribute mainly to the imaginary part of the impedance. Then, the flow resistance alone seems to be insufficient for analyzing the perforated plate. In the present case, therefore, an expression developed by Maa[2] is adopted, which is

$$\begin{aligned} Z_0&=Z_{\text{resist}}+Z_{\text{react}}\\ &=\frac{8\eta_0}{(d/2)^2}\left(\sqrt{1+\frac{X^2}{32}}+\frac{\sqrt{2}dX}{8h}\right)\\ &\quad -i\rho_0\omega h\left(1+\frac{1}{\sqrt{9+X^2/2}}+\frac{0.85d}{h}\right), \end{aligned} \tag{6}$$

where $X=(d/2)\sqrt{\rho_0\omega/\eta_0}$, with d, h as the diameter of the hole and plate thickness, respectively, η_0 as the air viscosity ($=1.8\times10^{-5}$ N·s/m^2 in the normal condition), and ρ_0 as the air density. Equation (6) is an approximation of the analytical solution for wave propagation in a tube having a circular cross section,[12,13] and is given end corrections.[14]

In any problems concerning structural–acoustic coupling due to flexural vibration, the continuity condition at the interface is used as the boundary condition. Let v be the particle velocity of air on the boundary surface of the vibrating plate. The boundary condition can be written as $v=v_p$ for the case that the plate surface is assumed homogeneous; the rigid boundary moves concomitant with the velocity v_p. In contrast, in the case of a perforated plate with the acoustic impedance Z_0 of the orifice, by using velocity $\overline{v}$ of Eq. (5)

with a spatially averaged sense over the plate surface as shown in Eq. (3), the boundary condition can be written as

$$v = \zeta_I v_p + \frac{\Delta p}{Z_0}\sigma. \tag{7}$$

B. Acoustic coupling for porous elastic plates

Porous elastic materials have a two-phase structure as the wave propagation media, air within the pores and the frame. Many theoretical models for wave propagation in porous media have been presented since the initial conceptual model was developed by Rayleigh.[12] These are classified roughly into the following three categories: the method for modeling acoustic behavior in the pores, the method for taking into account the effect of frame vibration,[6,15,16] and development of a mixed two-phase model based on the general elastic theory.[17] Furthermore, some empirical models[18–20] derived from the original conception of Delany and Bazley[21] have been presented. Works concerned with such materials are extensively reviewed by Attenborough[22,23] and Allard.[24]

In application of these theories to the practical acoustic problems such as absorption and reflection of sound, many parameters for detailed description of wave motion in the medium, e.g., porosity, shape factor, tortuosity, and so on, are integrated into an equivalent homogeneous wave-propagation medium. Thus, such porous materials replaced by the homogeneous medium can be characterized by two parameters: the propagation constant and the characteristic impedance, or equivalently the complex density and the complex bulk modulus. For practical applications in engineering, such materials are often shaped into plate-like form. In this case, it is expected that waves in the material approximate the flexural type; this tendency may become more remarkable with decreased permeability. As a related problem, Theodorakopoulos and Beskos[25] derived governing equations for flexural vibrations of thin, fluid-saturated, poroelastic plates, which are based on Biot's theory. The derivation process is similar to those in classical thin-plate theory based on homogeneous elastic theory. They argued about the dynamic response of the plate neglecting the effect of acoustic loading.

The approach used herein for such porous elastic plates in structural–acoustic problems can be considered in a similar manner as described in the preceding section; that is, the boundary condition at the air–structure interface at the plate surface can be described by combining continuity of flow in a spatially mean sense with air–solid interaction within the plate material. From the concept of this model, to adopt any values for both the propagation constant and the characteristic impedance, it is required to use any rigid-frame model of porous media.

Let p be the sound pressure in the equivalent medium characterized by the propagation constant γ and the characteristic impedance Z_c, of any porous elastic material composed of rigid frame and pores. The particle velocity of the medium can be written as $(-1/\gamma Z_c)\,\mathrm{grad}\,p$. In the case where the material is shaped into plate-like form lying in the $x-y$ plane, and vibrating in the z direction with the velocity v_p, a similar method used in the preceding section can be applied; that is, reasoning that the resistance term of γZ_c is related to air–solid interaction within the material gives an expression of the form

$$v_f - v_p = -\frac{1}{\gamma Z_c}\frac{\partial p}{\partial z} - \frac{[\gamma Z_c]_{\mathrm{react}}}{\gamma Z_c} v_p, \tag{8}$$

where v_f is the particle velocity in pores and $[\gamma Z_c]_{\mathrm{react}}$ represents the reactance term of γZ_c. The particle velocity in an averaged sense of the surrounding air on the plate surface vibrating in the flexural mode can be expressed by Eq. (3). Substituting Eq. (8) into Eq. (3) yields

$$\overline{v} = \xi_I v_p - \frac{1}{\gamma Z_c}\frac{\partial p}{\partial z}\sigma, \tag{9}$$

where $\xi_I = 1 - [\gamma Z_c]_{\mathrm{react}}\sigma/\gamma Z_c$ and σ is the porosity defined in the same manner as described by Biot.[17] For quantities γ and Z_c, any model is available for porous media, provided that its frame is assumed to be rigid. In the following section, we will use an empirical model developed by Allard,[26] which is

$$\gamma Z_c = -i\rho_0\omega\left[1 - \frac{(1 - i\pi\rho_0 f/R_F)^{1/2}}{i2\pi\rho_0 f/R_F}\right], \tag{10}$$

where R_F represents the flow resistivity [$\mathrm{N\cdot s/m^4}$] of the material and f is frequency. The reactance term of γZ_c is given as $[\gamma Z_c]_{\mathrm{react}} = i\,\mathrm{Im}\{\gamma Z_c\}$.

III. APPLICATION TO FUNDUMENTAL ACOUSTIC PROBLEMS

Fundamental acoustic problems related to flexural plate vibration are, for example, sound radiation due to mechanical excitation of a force, transmission of sound caused by an acoustic excitation, and sound absorption of a plate. In these problems, if the plate is permeable, response may seriously undergo effects of changed permeability. A method of acoustic coupling described in the preceding section can be used for such cases. Methods of application for several acoustic problems due to flexural motion of permeable plates are outlined in this section; also, some numerical examples are presented to illustrate general characteristics of response including permeability effects.

A. Sound radiation of a perforated single plate excited by a point force

1. Formulation of the problem

Consider a perforated thin elastic plate of infinite extent with the same fluid (air) on both sides, lying in the plane $z = 0$; the plate vibrates under a concentrated normal force acting at the origin of cylindrical coordinates (r, θ, z) as shown in Fig. 2(a). The equation of motion for the axisymmetric displacement $w(r)$ can be written as

$$D\nabla^4 w - \rho h\omega^2 w = p_1 + \frac{\delta(r)}{2\pi r} - p_2, \tag{11}$$

where $\nabla^4 = [(\partial^2/\partial r^2) + (1/r)(\partial/\partial r)]^2$, and where $\delta(r)$ is the Dirac delta function, D, ρ, and h represent the plate's flexural rigidity, density, and thickness, respectively. Let $\mathbf{r}$ be the vec-

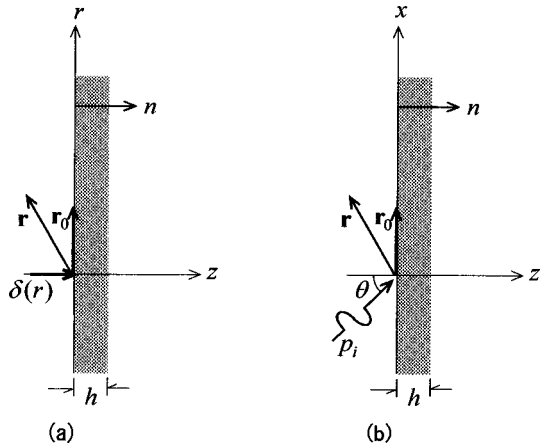

FIG. 2. Geometry of a plate (a) excited by a point force, and (b) with a plane wave incidence.

tor denoting a position in the region or on the boundary surface S, and $\mathbf{r}_0$ a position on S. With a Helmholtz integral formula, the radiated sound pressure p_1 on the surface S of the region $z \leqslant 0$ can be expressed as

$$p_1(\mathbf{r}) = 2\int\int_S G(\mathbf{r}|\mathbf{r}_0)\frac{\partial p_1(\mathbf{r}_0)}{\partial n}d\mathbf{r}_0, \tag{12}$$

where G is the free space Green's function given by

$$G(\mathbf{r}|\mathbf{r}_0) = \frac{e^{ik_0R}}{4\pi R}, \quad R = |\mathbf{r}-\mathbf{r}_0|, \tag{13}$$

with $k_0 = \omega/c_0$ as the acoustic wave number, c_0 as the speed of sound, and n as the outward normal to the surface. Applying the relation of Eq. (7) to the pressure gradient of Eq. (12) yields

$$\frac{\partial p_1}{\partial n} = \left.\frac{\partial p_1}{\partial z}\right|_{z=0} = i\rho_0\omega\left(-i\omega\zeta_I w + \frac{p_1 - p_2}{Z_0}\sigma\right). \tag{14}$$

Substitution of Eqs. (13) and (14) into Eq. (12) yields

$$p_1(\mathbf{r}) = \frac{1}{2\pi}\int\int_S [\rho_0\omega^2\zeta_I w + ik_0\beta(p_1 - p_2)]\frac{e^{ik_0R}}{R}d\mathbf{r}_0, \tag{15}$$

where $\beta = \rho_0 c_0 \sigma/Z_0$. Similarly, the radiated sound pressure p_2 on the surface of the region $z \geqslant 0$ is given by

$$p_2(\mathbf{r}) = -p_1(\mathbf{r}). \tag{16}$$

Equations (11), (15), and (16) form a set of simultaneous equations with unknown quantities w, p_1, and p_2. The solution can be obtained in the wave-number space by using the Hankel transform technique. The transform pair with respect to r and the wave-number space k is defined, for example, as

$$w(r) = \int_0^\infty W(k)J_0(kr)k\,dk, \tag{17}$$

$$W(k) = \int_0^\infty w(r)J_0(kr)r\,dr, \tag{18}$$

where $J_0(kr)$ denotes the Besell function of order zero. Solutions for the transformed expression w, p_1, and p_2 are

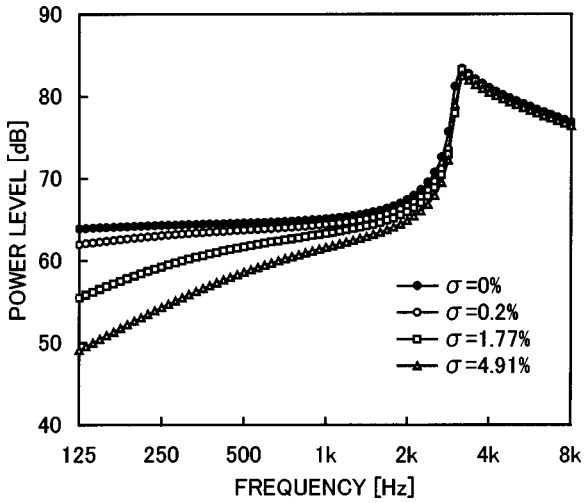

FIG. 3. Sound power level in dB *re* 10^{-12} W radiated from a perforated acrylic plate of thickness 9 mm, under a normal point excitation of $1N$ force. The parameter is the ratio of perforation σ.

$$W(k) = (\sqrt{k_0^2 - k^2} + 2k_0\beta)F_1(k), \tag{19}$$

$$P_2(k) = -P_1(k) = -i\rho_0\omega^2\zeta_I F_1(k), \tag{20}$$

where

$$F_1(k) = \frac{1/[2\pi D(k^4 - k_F^4)]}{\sqrt{k_0^2 - k^2} + 2k_0\beta - 2i\rho_0\omega^2\zeta_I/[D(k^4 - k_F^4)]} \tag{21}$$

and $k_F^4 = \rho h\omega^2/D$. Taking the inverse transform of these equations gives the solution for w, p_1, and p_2. The energy flow across the surface with the sound pressure p_2 and the particle velocity v_2 normal to the surface is given by $\mathrm{Re}\{p_2 v_2^*\}/2$, where a symbol $*$ represents the complex conjugate. From Eqs. (7) and (16) it can be shown that

$$v_2 = -i\omega\zeta_I w - \frac{2\beta}{\rho_0 c_0}p_2. \tag{22}$$

The acoustic power P_W radiated from this surface under a point excitation of $1N$ force can be obtained by integrating the energy flow over the whole area of the surface, which is given by

$$P_W = \pi\rho_0\omega^3|\zeta_I|^2\int_0^{k_0}|F_1(k)|^2\sqrt{k_0^2 - k^2}k\,dk. \tag{23}$$

2. Numerical results and discussion

An example of results calculated for the radiated power is shown in Fig. 3. The results are presented showing the power level (in dB re 10^{-12} W) radiated from a perforated acrylic panel of thickness 9 mm under a point excitation of $1N$ force, with a parameter of the ratio of perforation σ. Other factors related to flexural vibration of the plate are Young's modulus, E; density, ρ; loss factor, η; which are assumed here as follows: $E = 5.6\times10^9$ N/m^2, $\rho = 1150$ kg/m^3, $\eta = 0.02$. For density, the actual value $\rho(1-\sigma)$ was used instead of ρ, while all other parameters were assumed to be constant regardless of perforation change. The hole diameter was taken as $d = 1$, 3, and 5 mm with 20 mm

hole spacing, also, corresponding perforation was 0.2%, 1.77%, and 4.91%, respectively. The critical frequency of coincidence f_c was about 3 kHz, that is slightly shifted by perforation change. Clearly, the effect of change in σ is quite different above and below f_c. At frequencies above f_c the radiated power is little affected by change in σ; below f_c, however, the effect increases monotonically as frequency decreases. As expected, sound radiation from a vibrating permeable plate strongly depends on both sound absorption and sound transmission characteristics. Some explanations concerning this matter are given in Sec. III B 2.

B. Sound absorption and sound transmission of a perforated single plate

1. Formulation of the problem

Consider the case of Fig. 2(b), in which the same plate as in the preceding section is vibrating under an incident plane wave at angle θ. The analytical procedure is the same as that described in the previous work for permeable membranes,[11] except for the method of modeling the permeability. Then only the outline will be described below. With a Helmholtz integral formula for a two-dimensional problem, the sound pressure $p_1(x)$ at the surface of the source side can be expressed as

$$p_1(x)=2p_i(x)+\frac{i}{2}\int_{-\infty}^{\infty}\frac{\partial p_1(x_0)}{\partial n}H_0^{(1)}(k_0|x-x_0|)dx_0, \tag{24}$$

where $H_0^{(1)}(k_0|x-x_0|)$ denotes the Hankel function of the first kind of order zero. The sound pressure associated with the plane wave of unit amplitude is the form $p_i=e^{ik_0(\sin\theta\cdot x+\cos\theta\cdot z)}$. Applying Eq. (7) to this case and substituting Eq. (14) into Eq. (24) yields

$$p_1(x)=2p_i(x)+\frac{i}{2}\int_{-\infty}^{\infty}[\rho_0\omega^2\zeta_I w+ik_0\beta(p_1-p_2)]\times H_0^{(1)}(k_0|x-x_0|)dx_0. \tag{25}$$

Similarly, the sound pressure $p_2(x)$ on the surface of the transmitted side can be expressed as

$$p_2(x)=-\frac{i}{2}\int_{-\infty}^{\infty}[\rho_0\omega^2\zeta_I w+ik_0\beta(p_1-p_2)]\times H_0^{(1)}(k_0|x-x_0|)dx_0. \tag{26}$$

The pressure difference p_1-p_2 causes plate vibration, which is governed by

$$D\nabla^4 w-\rho h\omega^2 w=p_1-p_2, \tag{27}$$

where $\nabla^4=(\partial^2/\partial x^2+\partial^2/\partial z^2)^2$. A set of simultaneous equations, Eqs. (25)–(27), can be solved analytically by using the Fourier transform technique. Details of the procedure are presented in Ref. 6. Finally the closed form solutions for the reflected sound pressure p_r, and the transmitted sound pressure p_2 at an arbitrary point (x,z) are written as follows:

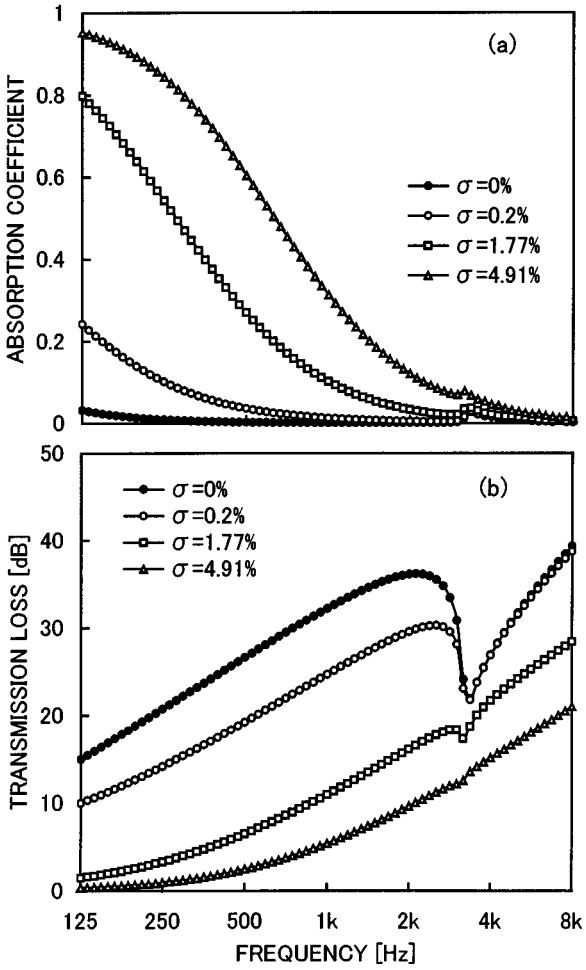

FIG. 4. Effect of the perforation ratio σ on (a) the sound absorption coefficient, and (b) the sound transmission loss.

$$p_r(x,z)=\frac{\cos\theta+i\rho_0\omega^2\zeta_I F_2(k_0\sin\theta)\cos\theta}{\cos\theta+2\beta}\times e^{ik_0(\sin\theta\cdot x-\cos\theta\cdot z)}, \tag{28}$$

$$p_2(x,z)=\frac{2\beta-i\rho_0\omega^2\zeta_I F_2(k_0\sin\theta)\cos\theta}{\cos\theta+2\beta}\times e^{ik_0(\sin\theta\cdot x+\cos\theta\cdot z)}, \tag{29}$$

where $F_2(k)=4\pi F_1(k)$. The absorption coefficient at an incident angle θ can be calculated as $1-|p_r/p_i|^2$; the sound transmission loss is given by $10\log_{10}(|p_i/p_2|^2)$. In the following sections, these are statistically averaged over the range of incident angles that corresponds to field incidence.

2. Numerical results and discussion

Sound absorption of microperforated plates was investigated by some authors[1–3] for the purpose of developing effective absorbers at low frequencies. For this purpose, the value of σ must be made smaller, to such an extent that the effect of plate vibration cannot be disregarded. In the case that a single perforated plate is used as a partition, we are interested in the effect of permeability on sound transmission as well as sound absorption. Figure 4 shows such numerical

examples calculated for the same plate material as in Sec. III A 2, in which lines and symbols are as indicated for Fig. 3.

Characteristics of transmission loss change with the perforation ratio, corresponding to sound absorption change. In the limit case of $\sigma=0$, as a matter of course, the theoretical expressions of Eqs. (28) and (29) agree well with existing theoretical results.[27,28] Results of further investigations (not shown here) indicate that the resistance term of the hole impedance Z_0 has an effect on response at high frequencies; also, the reactance term strongly affects response at low frequencies. In addition, overall, alteration of the reactance term produces greater variation in both sound absorption and sound transmission than that of the resistance term. For this reason, characteristics are somewhat different from those obtained in permeable membranes analysis,[11] in which only the resistance term is taken into account. The same tendency as in Fig. 4(a) can also be seen in radiation characteristics of Fig. 3. This similarity implies that sound radiation from the vibrating surface may depend strongly on surface absorption characteristics. Comparing sound absorption and sound transmission characteristics reveals that sound transmission at high frequencies above coincidence is almost entirely dependent on energy dissipation in the hole, which differs from the membrane case.

C. Sound absorption of a plate backed by an air layer

In any practical application for noise control engineering, perforated plates and porous materials are used extensively as a part of the sound absorbing structure as shown in Fig. 5. The case in which the facing is an ordinary (impermeable) plate was investigated in Ref. 27, while the case where perforated facings without the plate vibration effect has been studied extensively by many authors. In the case of porous materials, the method for predicting sound absorption is known as the theory using impedance matching for homogeneous layers of finite thickness.[29] In this section, the method for analyzing sound absorption of a facing backed by an air layer is outlined, including the interactive effects of plate vibration and permeability.

1. Perforated plates

When a plane wave, $p_i(=e^{ik_0(\sin\theta\cdot x+\cos\theta\cdot z)})$, impinges on a perforated plate at an angle of incidence θ. The sound pressure p_1 on the surface of the source side is given by Eq. (25), in which p_2 is, in this case, the sound pressure at the plate-cavity interface. The sound pressure and the particle velocity in the cavity can be written as

$$p_2(x,z)=(p_2^+e^{ik_0\cos\theta\cdot z}+p_2^-e^{-ik_0\cos\theta\cdot z})e^{ik_0\sin\theta\cdot x}, \tag{30}$$

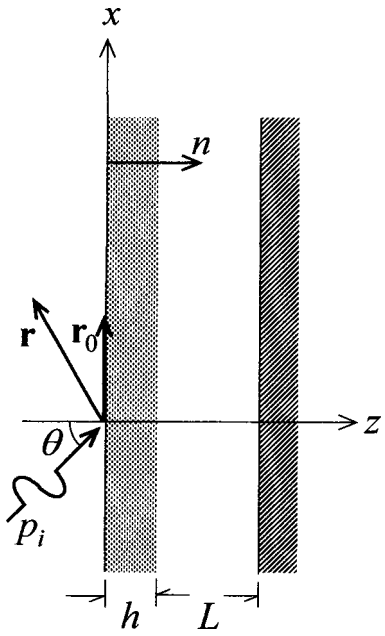

FIG. 5. Geometry of a permeable plate with a backed layer for a problem of sound absorption.

$$v_2(x,z)=\frac{\cos\theta}{\rho_0c_0}(p_2^+e^{ik_0\cos\theta\cdot z}-p_2^-e^{-ik_0\cos\theta\cdot z})e^{ik_0\sin\theta\cdot x}, \tag{31}$$

where unknown quantities $p_2^{\pm}$ denote the amplitude associated with propagating waves toward the $\pm z$ direction. The pressure difference p_1-p_2 is the distributed excitation force for flexural vibration of the plate, which is governed by Eq. (27). The boundary condition for the cavity at the plate interface can be written from Eq. (7) as

$$v_2(x,h)=-i\omega\zeta_I w+\frac{\beta}{\rho_0c_0}(p_1-p_2), \tag{32}$$

and at the back wall with the terminal impedance Z_B, the boundary condition is

$$v_2(x,h+L)=p_2(x,h+L)/Z_B. \tag{33}$$

Equations (25), (27), (32), and (33) form a set of simultaneous equations with unknown quantities p_1, p_2^+, p_2^-, and w. Mathematical details of the solution and derivation of the closed form expression for the reflected sound pressure p_r are presented in Refs. 11 and 27. The final result is

$$p_r(x,z)=\frac{\cos\theta-\beta_2+i\rho_0\omega^2\zeta_I\beta_1\cos\theta F_3}{\cos\theta+\beta_2}\times e^{ik_0(\sin\theta\cdot x-\cos\theta\cdot z)}, \tag{34}$$

where

$$F_3=\frac{2\beta_1/[D(k_0^4\sin^4\theta-k_F^4)]}{k_0(\cos\theta+\beta_2)-i\rho_0\omega^2\zeta_I[\zeta(\cos\theta+\beta_2)+\beta_1^2]/[D(k_0^4\sin^4\theta-k_F^4)]}, \tag{35}$$

and where $\beta_1=1-\beta\zeta$, $\beta_2=\beta(1-\beta\zeta)$ with

$$\zeta=\frac{(\cos\theta+\rho_0c_0/Z_B)\tan(k_0L\cos\theta)}{(\cos^2\theta+\rho_0c_0/Z_B)\tan(k_0L\cos\theta)+i\cos\theta(\beta+\rho_0c_0/Z_B)}. \tag{36}$$

2. Plates of porous elastic materials

In the case that a plate of a porous elastic material, which is assumed to be homogeneous and isotropic medium, is placed parallel to a back wall as shown in Fig. 5, the sound pressure p_a and the particle velocity v_a in the medium can be written as[30]

$$p_a(x,z)=(p_a^+e^{-qz}+p_a^-e^{qz})e^{ik_0\sin\theta\cdot x}, \tag{37}$$

$$v_a(x,z)=\frac{q}{\gamma Z_c}(p_a^+e^{-qz}-p_a^-e^{qz})e^{ik_0\sin\theta\cdot x}, \tag{38}$$

where $q=\gamma[1+(k_0\sin\theta/\gamma)^2]^{1/2}$ with $\mathrm{Re}\{q\}\geqslant 0$ and $\mathrm{Im}\{q\}\leqslant 0$. In these equations, γ and Z_c are the propagation constant and the characteristic impedance of the medium as appeared in Eq. (9). For the sound pressure on the plate surface of the source side, Eq. (9) can be applied to the pressure gradient $\partial p_1/\partial n$ in Eq. (24). Thus the sound pressure becomes

$$p_1(x)=2p_i(x)+\frac{\rho_0\omega}{2}\int_{-\infty}^{\infty}[i\omega\xi_I w-v_a(x_0,0)\sigma]\times H_0^{(1)}(k_0|x-x_0|)dx_0, \tag{39}$$

with the boundary condition

$$p_1(x)=p_a(x,0). \tag{40}$$

For the cavity, the same expression as denoted in the preceding section [Eqs. (30) and (31)] can be used. The boundary condition on the back wall is given by Eq. (33), and on the plate surface, which can be written as follows:

$$v_2(x,h)=-i\omega\xi_I w+v_a(x,h)\sigma, \tag{41}$$

$$p_2(x,h)=p_a(x,h). \tag{42}$$

Equations (27), (33), (39)–(42) form a set of simultaneous equations with unknown quantities p_1, $p_a^{\pm}$, $p_2^{\pm}$, and w, which can be solved analytically by using the Fourier transform technique as described in Refs. 11 and 27. Final results for the reflected sound pressure p_r are given as follows:

$$p_r(x,z)=\frac{\cos\theta-\beta_4+i\rho_0\omega^2\xi_I\beta_3\cos\theta F_4}{\cos\theta+\beta_4}\times e^{ik_0(\sin\theta\cdot x-\cos\theta\cdot z)}, \tag{43}$$

where

$$F_4=\frac{2\beta_3/[D(k_0^4\sin^4\theta-k_F^4)]}{k_0(\cos\theta+\beta_4)-i\rho_0\omega^2\xi_I[\xi(\cos\theta+\beta_4)+\beta_3^2]/[D(k_0^4\sin^4\theta-k_F^4)]}, \tag{44}$$

and where

$$\beta_3=\frac{\cosh qh+\alpha\sinh qh-1}{\cosh qh+\alpha\sinh qh}, \tag{45}$$

$$\beta_4=\frac{\rho_0c_0q\sigma}{\gamma Z_c}\frac{\alpha+\tanh qh}{1+\alpha\tanh qh}, \tag{46}$$

$$\xi=\frac{\gamma Z_c}{\rho_0c_0q\sigma}\frac{\tanh qh}{1+\alpha\tanh qh}, \tag{47}$$

$$\alpha=\frac{\gamma Z_c}{\rho_0c_0q\sigma}\frac{-i\cos\theta\tan(k_0L\cos\theta)+\rho_0c_0/Z_B}{\cos\theta-i\tan(k_0L\cos\theta)\rho_0c_0/Z_B}. \tag{48}$$

3. Numerical results and discussion

Figure 6 shows some numerical examples. The solid line shows results neglecting plate vibration, in which the material is a perforated plate of 6 mm thickness with 5 mm hole diameter, 20 mm hole spacing (ratio of perforation is 4.9%), and 0.1 m air layer of thickness. Values of the terminal impedance Z_B of the cavity are assumed as those obtained from experimental data for a wooden plate.[27] In the case including the effect of plate vibration calculated for an acrylic plate used in Sec. III A 2, the difference is too little to be distinguished in the graph. On the whole, characteristics of this case show good agreement with that obtained from existing theory for perforated absorber systems.[31] In calculated results for a plate of the same thickness, 6 mm, with 0.5 mm hole diameter, and 10 mm hole spacing, (perforation ratio of 0.2%) backed by the same cavity, plate vibration produces appreciably increased absorption. In results for a 0.5-mm-thick plate with the same perforation of 0.2%, plate vibration gives the reverse effect of reducing absorption. Thus, it should be noted that the effect of plate vibration on the perforated absorber system depends on plate thickness.

Figure 7 shows calculated results for the sound absorber system of Fig. 5 with the facing of porous elastic plate of 50 mm thickness, and a rigidly backed layer of 0.1 m thickness. Plate material is plastic foam, which is used by Allard[32] as an example for calculation using Biot's theory. Parameters are as follows: Young's modulus, 5×10^5 N/m^2; density, 30

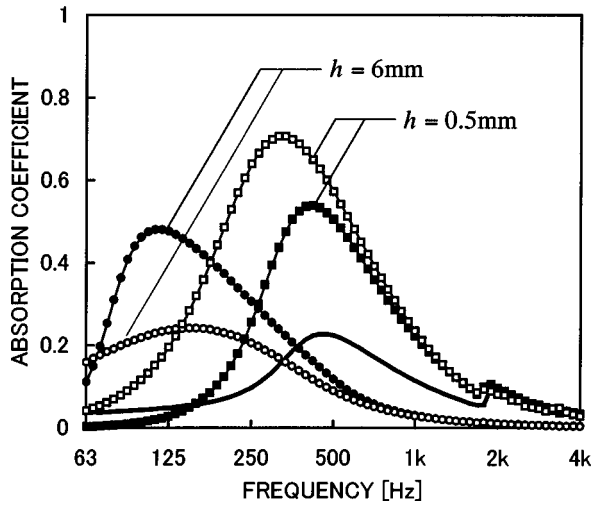

FIG. 6. Effect of flexural vibration on the sound absorption coefficient of a perforated plate with a backed layer of 0.1 m thickness. The results for a plate of 6 mm thickness and $\sigma=4.9\%$(—). With (–●–) and without (–○–) the vibration effect for a plate of 6 mm thickness and $\sigma=0.2\%$. With (–■–) and without (–□–) the vibration effect for a plate of 0.5 mm thickness and $\sigma=0.2\%$.

kg/m^3; Poisson's ratio, 0.4; loss factor, 0.1; and porosity, 0.93. The flow resistivity R_F, which seems to be the most effective for absorption of the system, is assumed as 5.5×10^4 and 1.1×10^4 N·s/m^4. The former case is the same used by Allard. Alteration of flow resistivity normally has an effect on other parameters, especially on porosity. In the present calculation, however, these are assumed to be independent. For reference, results for calculations supposing that porosity is 1.0 show the variation, which is too little to be detected in the graph. From these results, in the case of $R_F=1.1\times10^4$, absorption is little affected by plate vibration, while the case with a value five times this amount shows appreciable effects of plate vibration.

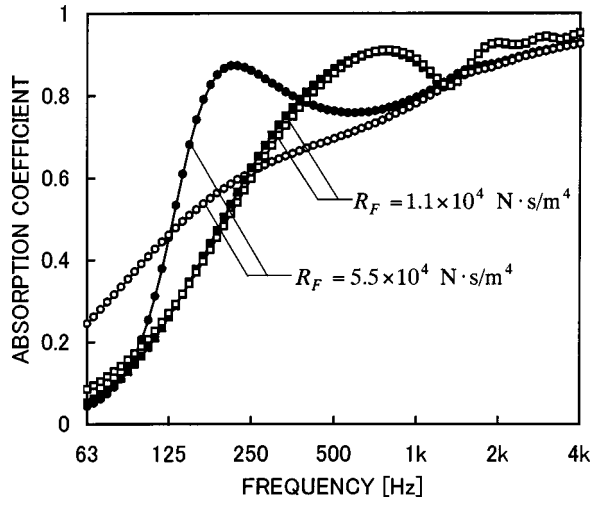

FIG. 7. Effect of flexural vibration on the sound absorption coefficient of a porous elastic plate with a backed layer of 0.1 m thickness. With (–●–) and without (–○–) the vibration effect for a plate of $R_F=5.5\times10^4$ N·s/m^4, and with (–■–) and without (–□–) the vibration effect for a plate of $R_F=1.1\times10^4$ N·s/m^4.

IV. CONCLUSIONS

A new method for analyzing acoustic problems concerning structural–acoustic coupling due to flexural vibration of plates was presented. It takes into account the effect of permeability (perforation) of plates and the effect of flexural mode of vibration of porous elastic materials. For perforated plates, this method enables treatment of plates with ratios of perforation between 0–1, i.e., from impermeability to acoustic transparency. The impermeable case corresponds to an ordinary theory for acoustic coupling due to flexural vibration of plates. As the ratio of perforation increases, this method gives results approaching those obtained by an ordinary method for immovable perforated plates. In the case of a sound absorber system composed of a plate backed by an air layer, the tendency of the perforation effect depends on plate thickness. For porous elastic materials shaped into a plate-like form, this method makes it possible to deal with various material states, from a flexural mode to a mode of dilatational wave-propagation media, depending on the synthetic effect of flow resistivity and porosity.

[1] J. Lee and G. W. Swenson, Jr., "Compact sound absorbers for low frequencies," Noise Control Eng. J. **38**, 109–117 (1992).
[2] D. Y. Maa, "Microperforated-panel wideband absorbers," Noise Control Eng. J. **29**, 77–84 (1987).
[3] H. V. Fucs and X. Zha, "The application of micro-perforated plates as sound absorbers with inherent damping," Acustica **81**, 107–116 (1995) (in German).
[4] Lord Rayleigh, *Theory of Sound* (Dover, New York, 1945), Vol. II, Sec. 351, pp. 328–333.
[5] S. Koga, "Desirable construction of porous sound absorber with rigid frame," J. Acoust. Soc. Jpn. **53**, 501–509 (1997) (in Japanese).
[6] P. Göransson, "Acoustic finite element formulation of a flexible porous material—A correction for inertia effects," J. Sound Vib. **185**, 559–580 (1995).
[7] K. V. Horoshenkov and K. Sakagami, "Acoustic response of a thin poroelastic plate," in *Proceedings of the 16th International Congress on Acoustics* (1998), pp. 1897–1898.
[8] K. V. Horoshenkov and K. Sakagami, "A method to calculate the acoustic response of a thin, baffled, simply supported poroelastic plate," J. Acoust. Soc. Am. **110**, 904–917 (2001).
[9] F. G. Leppington, "The effective boundary conditions for a perforated elastic sandwich panel in a compressible fluid," Proc. R. Soc. London, Ser. A **427**, 385–399 (1990).
[10] I. David Abrahams, "Sound radiation from a line forced perforated elastic sandwich panel," J. Acoust. Soc. Am. **105**, 3009–3020 (1999).
[11] D. Takahashi, K. Sakagami, and M. Morimoto, "Acoustic properties of permeable membranes," J. Acoust. Soc. Am. **99**, 3003–3009 (1996).
[12] Reference 4, Secs. 348–350, pp. 319–328.
[13] C. Zwikker and C. W. Kosten, *Sound Absorbing Materials* (Elsevier, New York, 1945), pp. 26–29.
[14] U. Ingard, "On the theory and design of acoustic resonators," J. Acoust. Soc. Am. **25**, 1037–1061 (1953).
[15] L. L. Beranek, "Acoustical properties of homogeneous, isotropic rigid tiles and blankets," J. Acoust. Soc. Am. **19**, 556–568 (1947).
[16] Y. Kawasima, "Sound propagation in a fiber block as a composite medium," Acustica **10**, 208–217 (1960).
[17] M. A. Biot, "Theory of elasticity and consolidation for a porous anisotropic solid," J. Appl. Phys. **26**, 182–185 (1955).
[18] I. P. Dunn and W. A. Davern, "Calculation of acoustic impedance of multi-layer absorbers," Appl. Acoust. **19**, 321–334 (1986).
[19] W. Qunli, "Empirical relations between acoustical properties and flow resistivity of porous plastic open-cell foam," Appl. Acoust. **25**, 141–148 (1988).
[20] Y. Miki, "Acoustical properties of porous materials, modification of Delany–Bazley models," J. Acoust. Soc. Jpn. **11**, 19–24(E) (1990).
[21] M. E. Delany and Bazley, "Acoustical properties of fibrous absorbent materials," Appl. Acoust. **3**, 105–116 (1970).

[22] K. Attenborough, ''The influence of microstructure on propagation in porous fibrous absorbents,'' J. Sound Vib. **16**, 419–442 (1971).
[23] K. Attenborough, ''Acoustical characteristics of porous materials,'' Phys. Rep. **82**, 179–227 (1982).
[24] J. F. Allard, *Propagation of Sound in Porous Media* (Elsevier, London, 1993), Chaps. 5 and 6, pp. 79–144.
[25] D. D. Theodorakopoulos and D. E. Beskos, ''Flexural vibrations of poroelastic plates,'' Acta Mech. **103**, 191–203 (1994).
[26] J. F. Allard and Y. Champoux, ''New empirical equations for sound propagation in rigid frame fibrous materials,'' J. Acoust. Soc. Am. **91**, 3346–3353 (1992).
[27] K. Sakagami, D. Takahashi, H. Gen, and M. Morimoto, ''Acoustic properties of an infinite elastic plate with a back cavity,'' Acustica **78**, 288–295 (1993).
[28] M. Heckl, ''The tenth Sir Richard Fairey memorial lecture,'' J. Sound Vib. **77**, 165–189 (1981).
[29] Reference 11, Chap. I, pp. 1–24.
[30] J. S. Pyett, ''The acoustic impedance of a porous layer at oblique incidence,'' Acustica **3**, 375–382 (1953).
[31] D. Takahashi, ''A new method for predicting the sound absorption of perforated absorber systems,'' Appl. Acoust. **51**, 71–84 (1997).
[32] Reference 22, Chap. 6, pp. 141–143.

Diffuse wavefields in cylindrical coordinates

R. S. Langley[a)]
Department of Engineering, University of Cambridge, Trumpington Street, Cambridge CB2 1PZ, United Kingdom

P. J. Shorter
Vibro-Acoustic Sciences, Inc., 12555 High Bluff Drive, Suite 310, San Diego, California 92130

(Received 12 September 2001; accepted for publication 9 July 2002)

A diffuse wavefield is normally defined in terms of plane waves—to quote one textbook definition ''plane waves are incident from all directions with equal probability and random phase.'' In some vibro-acoustic problems the response of a two-dimensional component such as a plate is more conveniently expressed in terms of cylindrical waves, and it is not immediately obvious what properties should be assigned to the cylindrical waves to constitute a diffuse field. It is shown here that a diffuse wavefield can be modeled as a summation of statistically independent cylindrical waves, apart from the fact that each outgoing wave of a particular order is fully correlated to an incoming wave of the same order. A simple relationship is derived between the energy flow P in each wave component and the energy density e of the wavefield: $P = ec_g/k$, where c_g is the group velocity and k is the wavenumber. This result is shown to hold true for both bending waves and in-plane waves (longitudinal and shear) in a plate. The work has application to the calculation of coupling loss factors in statistical energy analysis. © *2002 Acoustical Society of America.*
[DOI: 10.1121/1.1502895]

PACS numbers: 43.40.Qi, 43.20.Ks, 43.40.Dx [RLW]

I. INTRODUCTION

The concept of a diffuse field is used widely in vibro-acoustics to describe the high-frequency response of a structural component or acoustic volume. This concept can be expressed in terms of either wave motion or the distribution of resonant modal energy, as discussed, for example, by Lyon and DeJong (1995) and Weaver (1982, 1985). A wave viewpoint is adopted in the present work, and in this context a number of textbook definitions of a diffuse wavefield in an acoustic volume are as follows: ''plane waves are incident from all directions with equal probability and random phase'' (Fahy, 1985, p. 157); ''the average energy density is the same throughout the volume of the enclosure, and all directions of propagation are equally probable'' (Kinsler *et al.*, 1982, p. 313); ''the sound energy arriving at any point inside the enclosure is uniformly distributed over all possible directions of incidence'' (Kuttruff, 1997, p. 1110). A mathematical, rather than descriptive, statement of this concept has been given by Morse and Ingard (1968, p. 576) and Pierce (1989, p. 255); in the former case the response is represented as an integral over a continuum of plane wave headings, while in the latter case a sum over a large number of discrete wave headings is employed. Thus it is clear that plane wave motion is central to the concept of a diffuse field, and, moreover, the response of the system is considered to be a superposition of plane waves that propagate with equal intensity in all directions—a concept that is equally applicable to structural components. As described in what follows, the present work is concerned with the extension of the notion of a diffuse field to other types of wave motion, specifically cylindrical waves in two-dimensional components.

One application of the concept of a diffuse wavefield is the calculation of the flow of vibrational energy between various components of a dynamic system. If it is known how a single plane wave transmits energy from one component to an adjoining component, then an expression for the total energy flow can be obtained by assuming that the component carries a diffuse wavefield and summing over all the incident waves. This approach forms one method of computing the coupling loss factors that are employed in the statistical energy analysis (SEA) approach to high-frequency noise and vibration analysis (Lyon and DeJong, 1995). A large literature exists regarding the transmission of plane waves between various types of component (for example, Cremer and Heckl, 1988; Graff, 1975; Lyon and DeJong, 1995), and thus coupling loss factors can be computed for a wide range of problems. However, in certain cases the plane wave view of vibration transmission is not ideal: consider, for example, a plate with a cantilever beam that is attached normal to the plate surface. Vibrations of the beam will produce cylindrical waves rather than plane waves in the plate. Similarly, vibration transmission from the plate to the beam is more naturally phrased in terms of incoming cylindrical waves rather than incoming plane waves, since the scattered waves are cylindrical. The question then arises as to how a diffuse wavefield in the plate might be described in terms of cylindrical waves, in order that a coupling loss factor can be derived. One potential complication is that at any prescribed frequency the plate can carry an uncountably infinite number of plane wave headings while there are a countably infinite number of possible cylindrical waves—the implications of this regarding energy flow in the wave components is not immediately obvious. These issues are addressed in the present work.

[a)]Electronic mail: rsl21@eng.cam.ac.uk

In Sec. II it is shown how a diffuse scalar wavefield (such as that corresponding to bending waves in a plate) can be expressed in terms of cylindrical waves. This work is then extended to in-plane waves in Sec. III and it is shown that a simple and general relation exists between the energy flow in any cylindrical wave component and the energy density of the diffuse field.

II. DIFFUSE BENDING WAVES IN CYLINDRICAL COORDINATES

A. Diffuse plane waves

At any prescribed frequency ω a two-dimensional wavefield in an isotropic medium can be represented as a superposition of plane waves in the form

$$u(x,y)=\mathrm{Re}\int_0^{2\pi} A(\theta)\ \exp\ (i\omega t-ikx\ \cos\ \theta - iky\ \sin\ \theta)\ d\theta. \tag{1}$$

Here $u(x,y)$ is the displacement of the system at the location $\boldsymbol{x}=(x,y)$, k is the wavenumber associated with the frequency ω, and $A(\theta)$ represents a measure of the complex "amplitude" of the wave that has heading θ. Equation (1) relates to waves that produce a displacement in only one direction, such as bending waves in a plate, or out-of-plane waves in a tensioned membrane; more complicated types of wave are considered in Sec. III. The complex amplitude $A(\theta)$ is a random variable in the ensemble sense, and Eq. (1) will (by definition) represent a diffuse field only if $E[A(\theta_1)A^*(\theta_2)]=B\delta(\theta_1-\theta_2)$ where B is a constant, i.e., the wave components are statistically independent and of equal average intensity. It follows from Eq. (1) that the time average of the squared displacement is given by

$$|u(\boldsymbol{x})|^2=\frac{1}{2}\int_0^{2\pi}\int_0^{2\pi}\{A(\theta_1)A^*(\theta_2)\ \exp\ (-ikx\ \cos\ \theta_1 - iky\ \sin\ \theta_1+ikx\ \cos\ \theta_2 + iky\ \sin\ \theta_2)\}\ d\theta_1\ d\theta_2, \tag{2}$$

and the ensemble average of this result then yields

$$E[|u(\mathbf{x})|^2]=\pi B. \tag{3}$$

This implies that (*i*) the constant B can be related directly to the mean squared displacement, and (*ii*) as would be expected for a diffuse field (and, in fact, following directly from the assumed properties of the amplitude A), the description afforded by Eq. (1) is homogeneous, in the sense that the mean squared displacement is the same for all values of $\boldsymbol{x}$.

B. Transformation to cylindrical coordinates

Suppose now that the angular variation in the amplitude of the various plane waves is expressed using a Fourier series so that

$$A(\theta)=a_0+\sum_{n=1}^{\infty} a_n\ \cos\ n\theta+b_n\ \sin\ n\theta, \tag{4}$$

where the various coefficients of the Fourier series are given by

$$a_0=\frac{1}{2\pi}\int_0^{2\pi} A(\theta)\ d\theta, \tag{5a}$$

$$a_n=\frac{1}{\pi}\int_0^{2\pi} A(\theta)\ \cos\ n\theta\ d\theta, \tag{5b}$$

$$b_n=\frac{1}{\pi}\int_0^{2\pi} A(\theta)\ \sin\ n\theta\ d\theta. \tag{5c}$$

Since the amplitude distribution $A(\theta)$ is a random function, the Fourier coefficients will be random variables. From the properties of $A(\theta)$ and Eqs. (5a)–(5c), it follows that the Fourier coefficients have the following properties:

$$E[a_m b_n^*]=0, \tag{6a}$$

$$E[b_m b_n^*]=(B/\pi)\delta_{mn}, \tag{6b}$$

$$E[a_m a_n^*]=\begin{cases}(B/2\pi), & m=n=0\\ (B/\pi)\delta_{mn}, & m,n\neq 0.\end{cases} \tag{6c}$$

Substituting Eq. (4) into Eq. (1) and writing the displacement field u in terms of polar coordinates r and ϕ (so that $x=r\ \cos\ \phi$ and $y=r\ \sin\ \phi$) gives

$$u(r,\phi)=\mathrm{Re}\sum_n\ \int_0^{2\pi}(a_n\ \cos\ n\theta+b_n\ \sin\ n\theta) \times\exp\ [i\omega t-ikr\ \cos\ (\theta-\phi)]\ d\theta, \tag{7}$$

where for ease of notion the sum over n covers the range 0 to ∞, and b_0 is defined to be zero. Making the substitution $\psi=\theta-\phi$ gives

$$u(r,\phi)=\mathrm{Re}\sum_n\ \Big\{(a_n\ \cos\ n\phi+b_n\ \sin\ n\phi) \times\int_0^{2\pi}\cos\ n\psi\ \exp\ (i\omega t-ikr\ \cos\ \psi)\ d\psi + (-a_n\ \sin\ n\phi+b_n\ \cos\ n\phi) \times\int_0^{2\pi}\sin\ n\psi\ \exp\ (i\omega t-ikr\ \cos\ \psi)\ d\psi\Big\}, \tag{8}$$

which can be integrated to give

$$u(r,\phi)=\mathrm{Re}\sum_n\ (a_n\ \cos\ n\phi+b_n\ \sin\ n\phi) \times(-i)^n 2\pi J_n(kr)\ \exp\ (i\omega t), \tag{9}$$

where J_n is the nth-order Bessel function of the first kind. The previous expression can also be written in terms of Hankel functions to give

$$u(r,\phi)=\mathrm{Re}\Bigg\{\sum_{n=0}^{\infty} a_n \cos n\phi (-i)^n \pi [H_n^{(1)}(kr) + H_n^{(2)}(kr)] \exp(i\omega t) + \sum_{n=1}^{\infty} b_n \sin n\phi \times (-i)^n \pi [H_n^{(1)}(kr) + H_n^{(2)}(kr)] \exp(i\omega t)\Bigg\}. \quad (10)$$

For a time dependency of $\exp(i\omega t)$ the Hankel function of the second kind, $H_n^{(2)}(kr)=J_n(kr)-iY_n(kr)$, represents an outgoing cylindrical wave while the Hankel function of the first kind, $H_n^{(1)}(kr)=J_n(kr)+iY_n(kr)$, represents an incoming cylindrical wave (Cremer and Heckl, 1988). Equation (10) is therefore a general expression for a diffuse wavefield phrased in terms of cylindrical waves. Each Fourier coefficient is associated with two separate waves, an outgoing wave and an incoming wave. It is interesting to note that in the cylindrical description of a diffuse field the incoming and outgoing cylindrical waves associated with a given a_n or b_n are phase locked and of equal amplitude. This may perhaps be expected from physical considerations since it ensures that the net energy flow associated with the two waves is zero and that the displacement field is finite when r equals zero [the Bessel function $Y_n(kr)$ is singular at $r=0$]. It follows from Eq. (6) that each cylindrical wave component has the same mean squared amplitude, apart from those waves associated with a_0 where a factor of $\frac{1}{2}$ occurs. Furthermore, apart from the phase locking mentioned above, all the wave components are statistically independent. Examples of the superposition of the incoming and outgoing waves associated with different Fourier coefficients in Eq. (10) are shown in Fig. 1.

The time average magnitude squared of the displacement field is given by

$$|u(r,\phi)|^2=\frac{1}{2}(2\pi)^2\sum_{m,n}\{a_m a_n^* \cos m\phi \cos n\phi + a_n^* b_m \sin m\phi \cos n\phi + a_m b_n^* \cos m\phi \sin n\phi + b_m b_n^* \sin m\phi \sin n\phi\} \times (-1)^{m+n} i^{m-n} J_m(kr) J_n(kr). \quad (11)$$

It follows from Eq. (6) that the expected value of this result is

$$E[|u(r,\phi)|^2]=\pi B\left[J_0^2(kr)+2\sum_{n=1}^{\infty} J_n^2(kr)\right]=\pi B. \quad (12)$$

This result has employed identity 9.1.76 of (Abramowitz and Stegun, 1965) to evaluate the summation of the Bessel functions. A comparison of Eqs. (3) and (12) demonstrates the consistency between the plane wave and cylindrical wave descriptions.

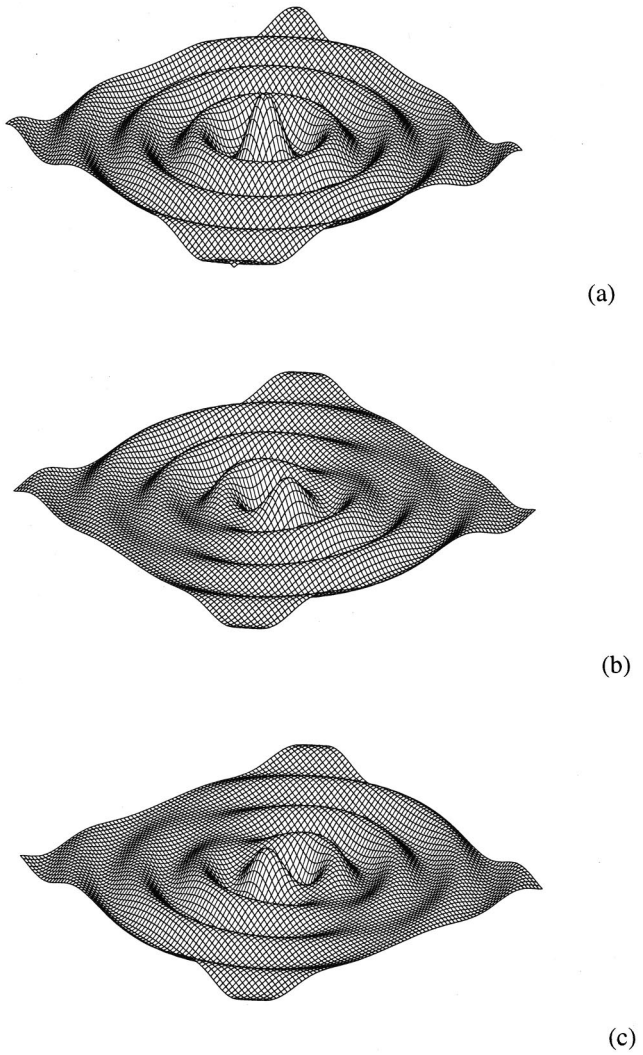

FIG. 1. Examples of the displacement field for the superposition of incoming and outgoing waves associated with different Fourier coefficients: (a) a_0, (b) a_1, and (c) b_1.

C. Energetics

The cylindrical waves constitute orthogonal stores of energy since, in the absence of any discontinuities, energy stored in a given cylindrical wave does not leak into other waves. It is useful to establish the relationship between the energy density, the intensity, and the amplitude of a given wave. The average total energy (kinetic plus potential) in a narrow annulus of width dr located at radius r associated with the propagation of an nth-order outgoing wave $H_n^{(2)}(kr)$ is given by

$$E=m'\omega^2\int_0^{2\pi} E[|u_n(r,\phi)|^2]r\, d\phi\, dr, \quad (13)$$

where m' is the mass per unit area of the system and it has been noted that the total energy is equal to twice the kinetic energy for wave propagation (see, for example, Langley, 1996). The term u_n in Eq. (13) represents the physical displacement associated with the wave, so that, from Eq. (10), $u_n=\mathrm{Re}\{a_n \cos n\phi (-i)^n \pi H_n^{(2)}(kr) \exp(i\omega t)\}$; alternatively, $a_n \cos n\phi$ could be replaced by $b_n \sin n\phi$ in this expression without changing any of the following analysis.

Note that time averaging is assumed implicitly in Eq. (13) and in all the following equations. Using Eq. (6) and integrating over ϕ now gives

$$E=\tfrac{1}{2}m'\omega^2\pi^2B|H_n^{(2)}(kr)|^2rdr. \tag{14}$$

For large values of kr the asymptotic behavior of the Hankel function is given by (Abramowitz and Stegun, 1965)

$$\lim_{kr\to\infty} H_n^{(2)}(kr)=\sqrt{\frac{2}{\pi kr}}\exp\left(-ikr+\frac{in\pi}{2}+\frac{i\pi}{4}\right), \tag{15}$$

and it then follows from Eq. (14) that the average total energy in an annulus in the far field is given by

$$E=\frac{m'\omega^2\pi B}{k}dr. \tag{16}$$

This result is independent of n and thus the energy in the annulus is the same for each outgoing cylindrical wave (including the $n=0$ wave). The rate at which this energy flows is given by the group velocity c_g so that the power P across the circumference of a circle of radius r is given by

$$P=\left(\frac{E}{dr}\right)c_g=m'\omega\pi Bcc_g, \tag{17}$$

where $c=\omega/k$ is the phase speed. This result is, as expected, independent of r, since power is conserved in the wave. Now from Eq. (3), the average total energy density e in the diffuse field is given by

$$e=m'\omega^2E[|u|^2]=m'\omega^2\pi B, \tag{18}$$

and thus the power associated with a given cylindrical wave is related to the total energy density by

$$P=\frac{ec_g}{k}. \tag{19}$$

This analysis can be repeated for an nth-order incoming wave $H_n^{(1)}(kr)$, and Eq. (19) is again obtained. This leads to the key result that a diffuse wavefield can be modeled as a superposition of incoming and outgoing cylindrical waves in accordance with Eq. (10), and the power in *every* wave component is given by Eq. (19), where e is the total energy density of the system.

As an aside, in wave transmission problems it is useful to know the power associated with *unit amplitude* waves ($a_n=1$ or $b_n=1$). This is given by

$$P=\begin{cases}2m'\omega\pi^2cc_g, & a_0=1, \qquad (20)\\ m'\omega\pi^2cc_g, & a_n=1,\ b_n=1,\ n\neq 0. \qquad (21)\end{cases}$$

III. DIFFUSE IN-PLANE WAVES IN CYLINDRICAL COORDINATES

A. Wave potentials

The previous section was concerned with a diffuse wavefield in which the waves produce a single displacement component $u(\mathbf{x})$, as in the case of bending waves in a plate, where the displacement is normal to the plane of the plate. In contrast, longitudinal and shear waves in a plate produce in-plane displacements, and a diffuse field of either type will produce displacements in both the x and y directions. It is not immediately obvious how such a diffuse field can be represented in cylindrical coordinates, and this issue is addressed in the present section.

The in-plane displacements produced by longitudinal and shear waves can be represented in terms of the longitudinal wave potential ψ and the shear wave potential ϕ (Morfey, 1994). Each of these potentials satisfies the wave equation so that

$$\nabla^2\psi+k_l^2\psi=0, \quad \nabla^2\phi+k_s^2\phi=0, \tag{22}$$

where the longitudinal wavenumber k_l and the shear wavenumber k_s are given by

$$k_l^2=\omega^2\rho(1-\nu^2)/E_{\mathrm{Y}}, \tag{23a}$$

$$k_s^2=\omega^2\rho/G. \tag{23b}$$

Here E_{Y} and G are the Young's modulus and shear modulus of the material, ν is the Poisson ratio, and ρ is the density. The in-plane displacements u and v in the x and y directions are related to the wave potentials by

$$u=\frac{\partial\psi}{\partial x}+\frac{\partial\phi}{\partial y}, \tag{24a}$$

$$\nu=\frac{\partial\psi}{\partial y}-\frac{\partial\phi}{\partial x}. \tag{24b}$$

Now, analogous to Eq. (1), the longitudinal and shear potentials can be expressed in terms of a set of diffuse plane waves by

$$\psi=\mathrm{Re}\left\{\frac{i}{k_l}\int_0^{2\pi}A_l(\theta)\exp\left(i\omega t-ik_lx\cos\theta-ik_ly\sin\theta\right)d\theta\right\}, \tag{25a}$$

$$\phi=\mathrm{Re}\left\{\frac{i}{k_s}\int_0^{2\pi}A_s(\theta)\exp\left(i\omega t-ik_sx\cos\theta-ik_sy\sin\theta\right)d\theta\right\}, \tag{25b}$$

where the subscripts l and s have been added to the amplitude $A(\theta)$ to indicate longitudinal and shear waves, respectively, and the factor of i/k has been introduced so that $A(\theta)d\theta$ is the displacement amplitude of the wave component with heading θ. If the wavefields are diffuse with $E[A_l(\theta_1)A_l^*(\theta_2)]=B_l\delta(\theta_1-\theta_2)$ and $E[A_s(\theta_1)A_s^*(\theta_2)]=B_s\delta(\theta_1-\theta_2)$, then it follows from Eqs. (24) and (25) that

$$E[|u_l|^2+|\nu_l|^2]=\pi B_l, \tag{26a}$$

$$E[|u_s|^2+|\nu_s|^2]=\pi B_s. \tag{26b}$$

Here $E[|u|^2+|\nu|^2]$ is the expected value of the time-averaged resultant mean squared displacement, and the subscripts l and s relate to the displacements caused by longitudinal and shear waves, respectively. Now by analogy with

Eqs. (4)–(10), Eq. (25) can be reexpressed in cylindrical coordinates (r,θ) to yield

$$\psi = \mathrm{Re}\left\{ \frac{i}{k_l} \sum_n \; (a_n^l \cos n\theta + b_n^l \sin n\theta)(-i)^n \right.$$
$$\left. \times \pi [H_n^{(1)}(k_l r) + H_n^{(2)}(k_l r)] \exp(i\omega t) \right\}, \qquad (27)$$

and

$$\phi = \mathrm{Re}\left\{ \frac{i}{k_s} \sum_n \; (a_n^s \cos n\theta + b_n^s \sin n\theta)(-i)^n \right.$$
$$\left. \times \pi [H_n^{(1)}(k_s r) + H_n^{(2)}(k_s r)] \exp(i\omega t) \right\}, \qquad (28)$$

where a_n^l and b_n^l are the coefficients in the Fourier expansion of $A_l(\theta)$, and likewise a_n^s and b_n^s relate to the Fourier expansion of $A_s(\theta)$. These coefficients have the properties detailed in Eq. (6). Equations (27) and (28) show that the diffuse longitudinal and shear wavefields can be represented as a combination of incoming and outgoing cylindrical waves. The energetics of these waves can be investigated by considering initially the radial and tangential components of the motion, as described in what follows.

B. Radial and tangential components of the displacement field

The radial and tangential components of the displacement field are related to the shear and longitudinal potentials as follows (Morfey, 1994):

$$u_r = \frac{\partial \psi}{\partial r} + \frac{1}{r}\frac{\partial \phi}{\partial \theta}, \qquad (29a)$$

$$u_\theta = \frac{1}{r}\frac{\partial \psi}{\partial \theta} - \frac{\partial \phi}{\partial r}. \qquad (29b)$$

The components of the in-plane displacement associated with a longitudinal wavefield ψ are therefore given by

$$u_{r,l} = \mathrm{Re}\left\{ i \sum_n \; (a_n^l \cos n\theta + b_n^l \sin n\theta)(-i)^n \right.$$
$$\left. \times \pi [H_n'^{(1)}(k_l r) + H_n'^{(2)}(k_l r)] \exp(i\omega t) \right\}, \qquad (30a)$$

$$u_{\theta,l} = \mathrm{Re}\left\{ i \sum_n \; (n/k_l r)(-a_n^l \sin n\theta + b_n^l \cos n\theta)(-i)^n \right.$$
$$\left. \times \pi [H_n^{(1)}(k_l r) + H_n^{(2)}(k_l r)] \exp(i\omega t) \right\}, \qquad (30b)$$

where the derivatives of the Hankel function are given by (Abramowitz and Stegun, 1965)

$$H_n' = \tfrac{1}{2}(H_{n-1} - H_{n+1}). \qquad (31)$$

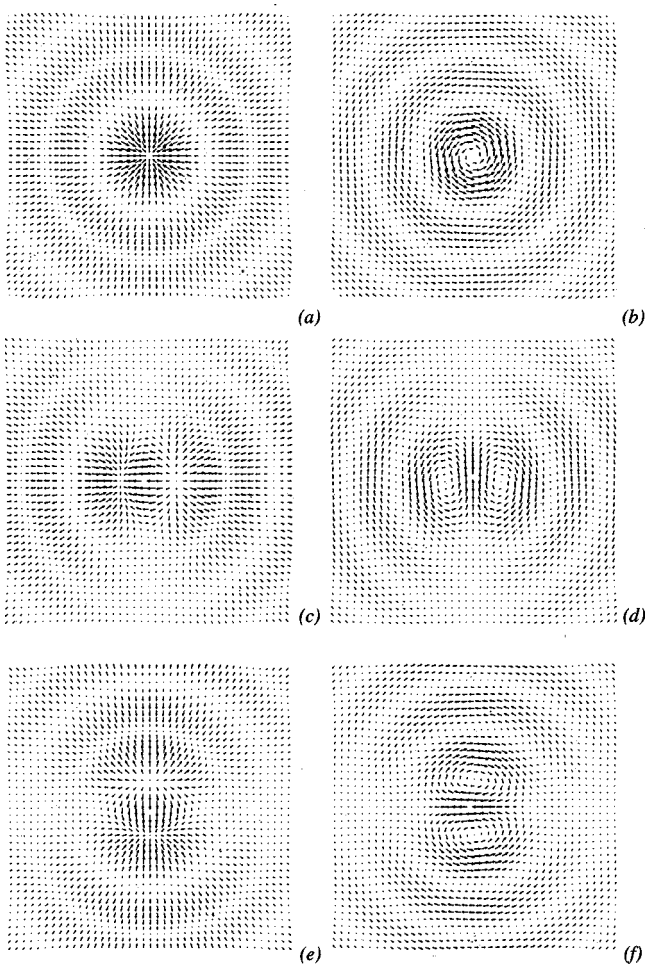

FIG. 2. In-plane displacement fields associated with incoming and outgoing longitudinal waves (left column) and shear waves (right column) for various Fourier coefficients: (a) longitudinal and (b) shear for a_0; (c) longitudinal and (d) shear for a_1; (e) longitudinal and (f) shear for b_1.

Similarly, the radial and tangential components of the in-plane displacement associated with a shear wavefield are given by

$$u_{r,s} = \mathrm{Re}\left\{ i \sum_n \; (n/k_s r)(-a_n^s \sin n\theta + b_n^s \cos n\theta)(-i)^n \right.$$
$$\left. \times \pi [H_n^{(1)}(k_s r) + H_n^{(2)}(k_s r)] \exp(i\omega t) \right\}, \qquad (32a)$$

$$u_{\theta,s} = -\mathrm{Re}\left\{ i \sum_n \; (a_n^s \cos n\theta + b_n^s \sin n\theta)(-i)^n \right.$$
$$\left. \times \pi [H_n'^{(1)}(k_s r) + H_n'^{(2)}(k_s r)] \exp(i\omega t) \right\}. \qquad (32b)$$

Examples of the in-plane displacement field associated with the superposition of outgoing and incoming longitudinal and shear waves are shown in Fig. 2 (note the plots are normalized so that the longitudinal and shear wavenumbers are equal).

C. Energetics

For longitudinal waves the time average energy stored in a narrow annulus of inner radius r and width dr can be written as

$$E = m' \omega^2 \int_0^{2\pi} E[|u_{r,l}|^2 + |u_{\theta,l}|^2] r \, d\theta \, dr. \tag{33}$$

Now considering the outgoing wave component $H_n^{(2)}(k_l)$ associated with the Fourier coefficient a_n^l. It follows from Eqs. (30) and (6) that

$$E[|u_{r,l}|^2] = \frac{\pi B_l}{2(1+\delta_{no})} \cos^2 n\theta |H_n'^{(2)}(k_l r)|^2, \tag{34a}$$

$$E[|u_{\theta,l}|^2] = \frac{\pi B_l n^2}{2k_l^2 r^2 (1+\delta_{no})} \sin^2 n\theta |H_n^{(2)}(k_l r)|^2, \tag{34b}$$

where δ_{no} is zero unless $n=0$, in which case $\delta_{no}=1$. Now for large $k_l r$ the Hankel functions have the following asymptotic behavior:

$$\lim_{k_l r \to \infty} |H_n^{(2)}(k_l r)|^2 = \lim_{k_l r \to \infty} |H_n'^{(2)}(k_l r)|^2 = \frac{2}{\pi k_l r}. \tag{35}$$

Thus for an annulus in the far field (large $k_l r$), only the radial component of displacement makes a significant contribution to Eq. (33), and the result is

$$E = \frac{m' \omega^2 \pi B_l}{k_l} dr, \tag{36}$$

where it can be noted that this result is independent of n. The same result can be derived for the outgoing wave associated with the Fourier coefficient b_n^l, and for each incoming wave $H_n^{(1)}(k_l r)$. The energy flow in the wave can be deduced by noting that power is transmitted at the group velocity $c_{g,l}$ and thus

$$P_l = \frac{m' \omega \pi B_l c_{g,l}}{k_l} = \frac{e_l c_{g,l}}{k_l}, \tag{37}$$

where e_l is the energy density of the diffuse field, which can be deduced from Eq. (26) to be $e_l = m' \omega^2 \pi B_l$. Hence the following result has been demonstrated: a diffuse longitudinal wavefield can be represented as a superposition of outgoing and incoming waves in accordance with Eq. (27), and the power in every wave component is given by Eq. (37), where e_l is the energy density of the diffuse field.

The foregoing analysis can be repeated for diffuse shear waves—as might be expected it is the tangential component $u_{\theta,s}$ that constitutes the far-field response in this case. The final result is

$$P_s = \frac{e_s c_{g,s}}{k_s}. \tag{38}$$

Clearly Eq. (37) or (38) is identical to Eq. (19) and it represents a general result that applies to all of the wave types considered here.

Finally, it can be noted that the power associated with an in-plane cylindrical wave of unit amplitude ($a_n=1$ or $b_n=1$) is again given by Eqs. (20) and (21), with the appropriate minor changes in notation.

IV. SUMMARY

The main result of this paper is that a diffuse wavefield can be represented in terms of cylindrical waves in the form of Eq. (10). The Fourier amplitudes that appear in this equation have the properties given by Eq. (6), where the constant B is related to the mean squared response via Eq. (3). Each cylindrical wave carries an identical amount of power, and this is given by Eq. (19). When the wavefield corresponds to longitudinal or shear waves in a plate, so that the wave motion produces a displacement in two spatial directions, Eq. (10) is replaced by either Eq. (30) or Eq. (32), but Eqs. (6) and (19) still apply.

The methodology employed in the present work can readily be extended to other coordinate systems, for example spherical waves in an acoustic cavity, thus allowing a more general view of the concept of a diffuse field. The applications of the work include the evaluation of coupling loss factors for systems where cylindrical waves, rather than plane waves, form a natural basis for studying wave transmission—for example, point couplings on plate structures. This aspect will be reported in a future publication.

ACKNOWLEDGMENTS

This work was funded by Vibro-Acoustic Sciences Inc. and performed while the first author was a Visiting Acoustic Scientist with the company.

Abramowitz, M., and Stegun, I. A. (eds.) (**1965**). *Handbook of Mathematical Functions* (Dover, New York).
Cremer, L., and Heckl, M. (**1988**). *Structure-borne Sound*, 2nd ed. (Springer-Verlag, Berlin).
Fahy, F. J. (**1985**). *Sound and Structural Vibration* (Academic, London).
Graff, K. F. (**1975**). *Wave Motion in Elastic Solids* (Dover, New York).
Kinsler, L. E., Frey, A. R., Coppens, A. B., and Sanders, J. V. (**1982**). *Fundamentals of Acoustics*, 3rd ed. (Wiley, New York).
Kuttruff, H. (**1997**). "Sound in enclosures," in *Encyclopedia of Acoustics*, edited by M. J. Crocker (Wiley, New York), pp. 1101–1114.
Langley, R. S. (**1996**). "A transfer matrix analysis of the energetics of structural wave motion and harmonic vibration," Proc. R. Soc. London, Ser. A **452**, 1631–1648.
Lyon, R. H., and DeJong, R. G. (**1995**). *Theory and Application of Statistical Energy Analysis*, 2nd ed. (Butterworth-Heinemann, Boston).
Morfey, C. L. (**1994**). "Cylindrical in-plane waves in an elastic plate," J. Sound Vib. **173**, 557–560.
Morse, P. M., and Ingard, K. U. (**1968**). *Theoretical Acoustics* (Princeton U. P., Princeton).
Pierce, A. D. (**1989**). *Acoustics: An Introduction to Its Physical Principles and Applications* (Acoustical Society of America, Woodbury).
Weaver, R. L. (**1982**). "On diffuse waves in solid media," J. Acoust. Soc. Am. **71**, 1608–1609.
Weaver, R. L. (**1985**). "Diffuse elastic waves at a free surface," J. Acoust. Soc. Am. **78**, 131–136.

Novel active noise-reducing headset using earshell vibration control

Boaz Rafaely,[a] Joao Carrilho, and Paolo Gardonio
Institute of Sound and Vibration Research, University of Southampton, Southampton SO17 1BJ, United Kingdom

(Received 24 September 2001; revised 3 July 2002; accepted 6 July 2002)

Active noise-reducing (ANR) headsets are available commercially in applications varying from aviation communication to consumer audio. Current ANR systems use passive attenuation at high frequencies and loudspeaker-based active noise control at low frequencies to achieve broadband noise reduction. This paper presents a novel ANR headset in which the external noise transmitted to the user's ear via earshell vibration is reduced by controlling the vibration of the earshell using force actuators acting against an inertial mass or the earshell headband. Model-based theoretical analysis using velocity feedback control showed that current piezoelectric actuators provide sufficient force but require lower stiffness for improved low-frequency performance. Control simulations based on experimental data from a laboratory headset showed that good performance can potentially be achieved in practice by a robust feedback controller, while a single-frequency real-time control experiment verified that noise reduction can be achieved using earshell vibration control. © *2002 Acoustical Society of America.* [DOI: 10.1121/1.1504469]

PACS numbers: 43.50.Ki, 43.50.Hg, 43.66.Vt [MRS]

I. INTRODUCTION

Active noise-reducing (ANR) headsets are used to protect the ear from overexposure to noise, in situations where the passive circumaural headset does not provide, by itself, sufficient reduction in the noise level. Active attenuation, usually dominant at low frequencies, is complemented by passive attenuation at high frequencies to produce improved overall noise reduction performance. ANR headsets are widely used in aviation and military communication and in noisy industrial environments, and are one of the most commercially successful applications of the active noise control technology.

ANR headsets which employ a loudspeaker and a microphone inside the earshell connected via an analog feedback controller were studied in the 50's by Meeker, Hawley, and Simshauser.[1–3] Wheeler[4] studied the design of ANR headset for aviation communication, while Bai and Lee[5] proposed the use of modern controller design techniques for the ANR system. Recent studies proposed the use of digital systems to improve performance.[6–8] The ANR headsets described above and those currently used in commercial applications employ active attenuation by using a loudspeaker to produce the antinoise at the low frequencies, therefore reducing the noise level at the user's ear. Current active headsets could benefit from further improvements, particularly when operating in severe environments, by increasing sound attenuation and by improving mechanical robustness.

This paper proposes a novel approach to ANR headsets,[9] which can be applied as an alternative or as a complement to conventional systems, and which has the potential for improving both performance and mechanical robustness through the use of vibration transducers. Instead of generating sound inside the headset earshell using a loudspeaker, the noise level at the ear is reduced by attenuating the vibration transmission through the shell, using vibration actuators. The vibration actuator is attached to the earshell and produces a force that opposes the force imposed by the external noise, therefore reducing earshell vibration. An accelerometer mounted on the earshell can be used as a control sensor. At relatively low frequencies where the coupled response of the earshell and acoustic cavity could be modeled to be equivalent to that of a lumped mass (the earshell) connected to two lumped springs (the headset cushion and the air in the cavity),[10] the proposed control approach can be regarded as a typical active vibration isolation problem as described by Fuller *et al.*[11] in Chap. 7.2. At higher frequencies, where the sound transmission is controlled by the coupling of the earshell modes with the cavity modes, the proposed control approach should be regarded as a special case of active structural acoustic control (ASAC) as presented by Fuller *et al.*[11] in Chap. 9.

This paper presents a theoretical analysis of the new ANR headset, supplemented by simulations and an experimental study using a laboratory ANR headset system.

II. HEADSET SYSTEM MODELING

This section presents a model-based theoretical analysis of the ANR headsets studied in this paper. The models are later used to study performance with velocity feedback control. Since the ANR headsets described in this paper are designed around a passive noise-reducing headset,[10] this section starts with a brief description of a passive headset, followed by modeling of an active headset which uses ideal secondary force, and more practical secondary forces generated by force actuators. The first actuator is connected between the earshell and an inertial mass, and is therefore re-

[a]Electronic mail: br@isvr.soton.ac.uk

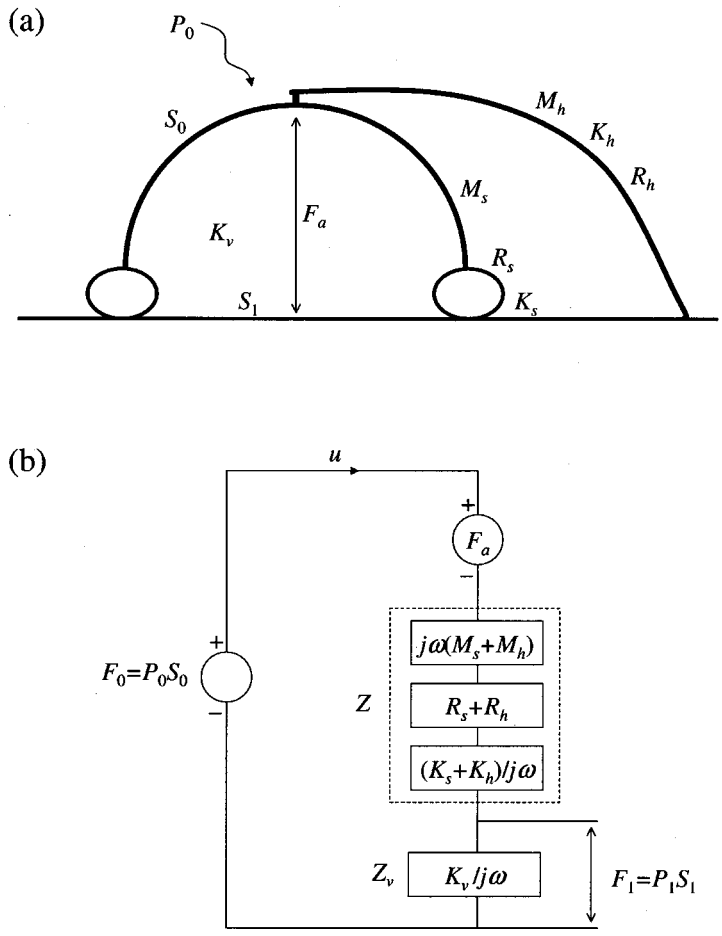

FIG. 1. (a) Schematic diagram of the headset system, and (b) an equivalent impedance block diagram.

ferred to as an inertial actuator, and the second actuator is mounted between the earshell and the headband, and is referred to as a headband force actuator.

Lumped-element models previously used by Shaw and Thiessen[10] provide a simple representation of the underlying systems' dynamics, and are used here to analyze the combined passive–active headset systems. The model provides good approximation of system performance at the low-frequency range, where the acoustic wavelength is larger than the earshell dimensions.

It should be noted that the simplified physical model is employed here to study potential performance and the suitability and limitations of the actuator, and provides an insight to the behavior of the system. It is not suggested as a model from which a practical controller could be designed. The measured headset response is used for the latter, as presented in Sec. IV.

A. Passive headset

The sound transmission in noise-reducing headsets has been found to be similar to the vibration transmission in a mass–spring–damper system.[10] Figure 1(a) shows an idealized headset earshell consisting of a rigid earshell of mass M_s, sealed by a cushion of stiffness K_s and damping R_s to a rigid surface representing the head. The earshell is allowed to move only in the plane perpendicular to the surface, and the external noise, represented by the sound pressure P_0, is transmitted into the earshell inner volume through the earshell movements, assuming no leaks exist in the sealing of the earshell to the head. The earshell is assumed to be held in place by a headband, which has a mass M_h, stiffness K_h, and damping R_h. The mechanical impedance diagram shown in Fig. 1(b) was developed to represent the headset system,[10] with F_0 denoting the external force applied by the external acoustic pressure P_0 over the external earshell area S_0, and F_1 denoting the force applied inside the earshell volume by the inner pressure P_1, with S_1 the area enclosed by the cushion. In the case of the passive headset described here, it is assumed that the secondary force F_a in Fig. 1 is zero. From the diagram in Fig. 1(b), an expression for the sound transmission P_1/P_0 can be calculated as

$$\frac{P_1}{P_0}=\frac{S_0}{S_1}\frac{Z_v}{Z_v+Z}=\frac{S_0}{S_1}\frac{K_v}{K_v+K_s+K_h+j\omega(R_s+R_h)-\omega^2(M_s+M_h)}, \tag{1}$$

where $K_v=\rho c^2 S_1^2/V$ is the stiffness of the air volume V enclosed by the earshell, which is interacting with the earshell mass over the area S_1, and ρ and c are the air density and speed of sound, respectively. Equation (1) describes the transmission of a second order system with a resonance frequency at

$$\omega_0 = \sqrt{\frac{K_S + K_v + K_h}{M_S + M_h}}. \tag{2}$$

At frequencies below the resonance, the transmission reduces to

$$\frac{P_1}{P_0} = \frac{S_0}{S_1} \frac{K_v}{K_v + K_s + K_h}, \tag{3}$$

and the transmission magnitude is controlled solely by the stiffness of the headband, cushion, and the volume of air inside the earshell. Larger internal volume and larger cushion and headband stiffness will increase the noise attenuation at the lower frequencies.

B. Active headset with ideal secondary force

The vibration of the headset earshell can be reduced by introducing a secondary force which opposes the force generated by the external sound field. This will then reduce the sound developed inside the earshell volume, and therefore the sound preceived by the user. In this section it is assumed that a secondary force can be applied to the earshell, in an ''ideal'', way, where the dynamics of potential actuators is not taken into account. The latter is introduced later in this section. The force F_a in Fig. 1(a) represents an ideal control force, acting between the earshell and the rigid surface. The sound pressure inside the earshell volume, P_1, can be expressed using Fig. 1(b) as the superposition of the contributions of the two sources

$$P_1 = AP_0 + BF_a, \tag{4}$$

where A and B are given by

$$A = \frac{S_0}{S_1} \frac{Z_v}{Z_v + Z}, \quad B = -\frac{1}{S_1} \frac{Z_v}{Z_v + Z}. \tag{5}$$

The optimal arrangement for completely canceling the sound transmission can be calculated from Eqs. (4) and (5) by setting P_1 to zero, which produces an optimal secondary force of $F_a = P_0 S_0$. This can be implemented in practice by feeding the signal from an external reference microphone measuring P_0, to the input of a control actuator generating F_a, in a feedforward control arrangement. The latter will provide good broadband performance if the delay of the controller is sufficiently small.[12] Although this approach could potentially provide a control solution, it is not studied in this work, but suggested for future study.

The control approach considered in this paper is feedback control, where velocity feedback is initially studied due to its simplicity and potential to provide both good performance and stability when used to actively increase damping.[11] Using the earshell velocity u to feed F_a, such that $F_a = -gu$, where g is a gain constant with units of Ns/m, and writing u as F_1/Z_v, the sound transmission with velocity feedback can be written using Eq. (4) as

$$\frac{P_1}{P_0} = \frac{A}{1 + \frac{gS_1}{Z_v} B}. \tag{6}$$

C. Active headset with inertial force actuator

An inertial actuator can be modeled at low frequencies by a lumped mass–spring system, composed of the inertial mass M_a and the stiffness K_a of the force actuator. The inertial actuator, when mounted on the earshell system, as shown in Fig. 2(a), becomes what is known as a tuned vibration neutralizer,[13] and is most effective in reducing the earshell vibration at the resonance frequency of the inertial actuator system, $\omega_a = \sqrt{K_a/M_a}$. It should be noted that M_a denotes the inertial mass, while the mass of the actuator itself, including casing and transduction elements, are not considered separately but can be lumped into the earshell mass. Figure 2(b) shows the impedance diagram developed for this system. Assuming velocity feedback control is applied here as described above, Eq. (6) also applies here, and A and B can be found by superposition of the primary and secondary sources as

$$\begin{aligned} A &= \frac{S_0}{S_1} \frac{Z_v}{Z + Z_v + Z_{Ka} \| Z_{Ma}}, \\ B &= -\frac{1}{S_1} \frac{Z_{Ma} \| (Z + Z_v)}{Z_{Ka} + Z_{Ma} \| (Z + Z_v)} \frac{Z_v}{Z + Z_v}, \end{aligned} \tag{7}$$

where the notation $Z_1 \| Z_2$ denotes a parallel connection of impedances, calculated as $Z_1 Z_2/(Z_1 + Z_2)$.

D. Active headset with force actuator attached to the headband

An alternative to the inertial actuator described above is to mount the force actuator between the earshell mass and the headband, allowing the force actuator to react against the headband rather than the inertial mass, M_a. The latter is assumed to be removed from the actuator before mounting and is not used in this configuration, while the mass of the actuator itself is lumped into the earshell mass as described above. The advantage of this configuration, which is illustrated in Fig. 3(a), is that it does not require the additional mass used by the inertial actuator, which increases the overall weight of the headset, therefore compromising comfort and imposing a phase shift,[14] therefore potentially compromising control performance. In this arrangement, the headband impedance, Z_h, composed of the headband stiffness K_h, mass M_h, and damping R_h, is separated from the earshell impedance Z_s due to the mounting of the actuator between the heaband and the earshell. Figure 3(b) shows the impedance diagram for this arrangement. Similar to the case of the inertial actuator presented above, the transmission of sound through the earshell can be calculated from Eq. (6), with A and B given by

$$\begin{aligned} A &= \frac{S_0}{S_1} \frac{Z_v}{Z_s + Z_v + Z_{Ka} \| Z_h}, \\ B &= -\frac{1}{S_1} \frac{Z_h \| (Z_s + Z_v)}{Z_{Ka} + Z_h \| (Z_s + Z_v)} \frac{Z_v}{Z_s + Z_v}. \end{aligned} \tag{8}$$

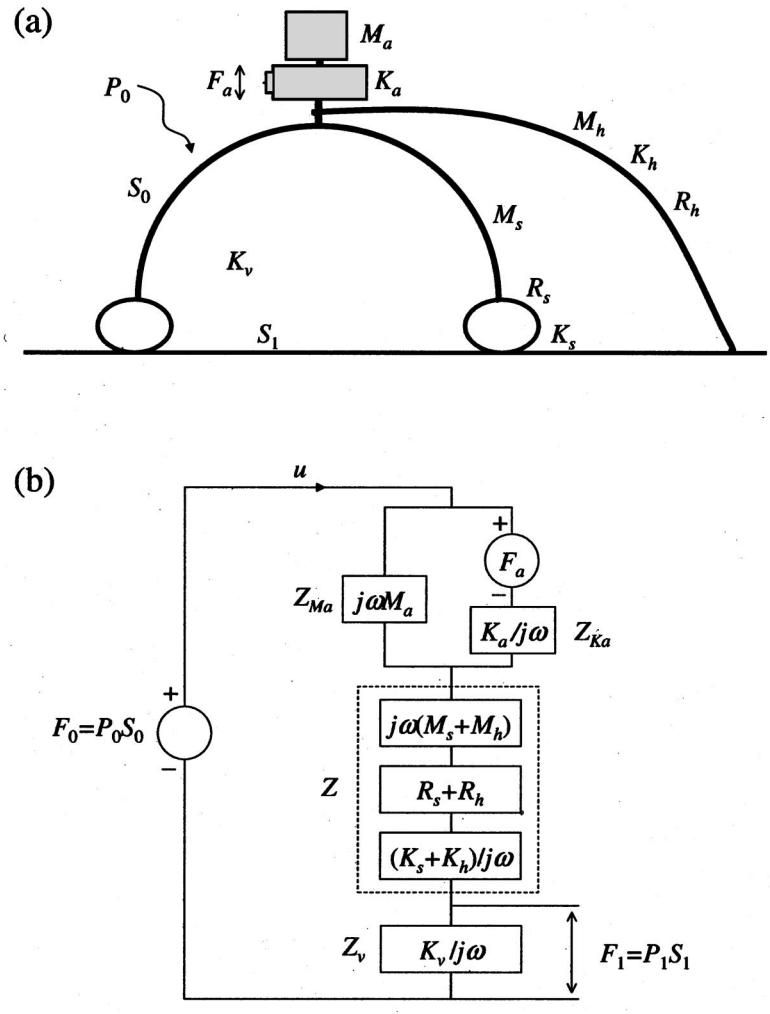

FIG. 2. (a) Schematic diagram of the active headset system with an inertial force actuator, and (b) an equivalent impedance block diagram.

III. VELOCITY FEEDBACK CONTROL SIMULATIONS USING HEADSET MODELS

The models developed above for the active headset are used in this section to simulate noise reduction performance and the force and displacement requirements from the actuator in the various configurations. Velocity feedback control is studied due to its simplicity and since it has shown to produce good performance with large stability margins in other applications by increasing the system damping.[11] This section starts by verifying the model of a commercial passive noise-reducing headset at the low frequencies, and then simulating control performance for the various active headset configurations.

A. The passive noise-reducing headset

The control simulations in this section use the headset model presented above, with the parameters taken from a commercial light-weight passive noise-reducing headset, manufactured by JSP, model KMO7236. Most of the headset parameters have been estimated from measurements, while some parameters, such as the damping of the earshell cushion, have been estimated by fitting the attenuation curve to manufacturer's data. The parameters and their values are listed in Table I. Figure 4 presents the passive transmission of sound through the headset, or passive attenuation, as calculated using Eq. (1) compared to manufacturer's data, showing good agreement at the lower frequencies. Since high-frequency acoustical and mechanical system dynamics were not included in the model, the attenuation is not predicted accurately at the high-frequency range. Nevertheless, the simplified model provides an insight into the behavior of the system and can be used to analyze performance at the low frequencies, which is normally the frequency range of interest for active control.

B. Control with ideal secondary force

Figure 5(a) shows a plot of the transmission P_1/P_0 for the passive system described in Fig. 1(a) and calculated using Eq. (1) and Table I, and for the active system with velocity feedback control and an ideal secondary force calculated using Eq. (6). The effect of velocity feedback is to increase the damping of the system, and indeed the active attenuation is increased mostly around the resonance frequency of the passive system. Figure 5(b) shows the Nyquist diagram for the open-loop system with velocity feedback control, with the gain parameter g set to -2900. The curve is completely in the positive-real quadrants, which gives this type of feedback control the advantage of large stability margins.[11] In practice, however, actuators must be used to produce the secondary force, and so control simulations with the two actuator configurations are presented next.

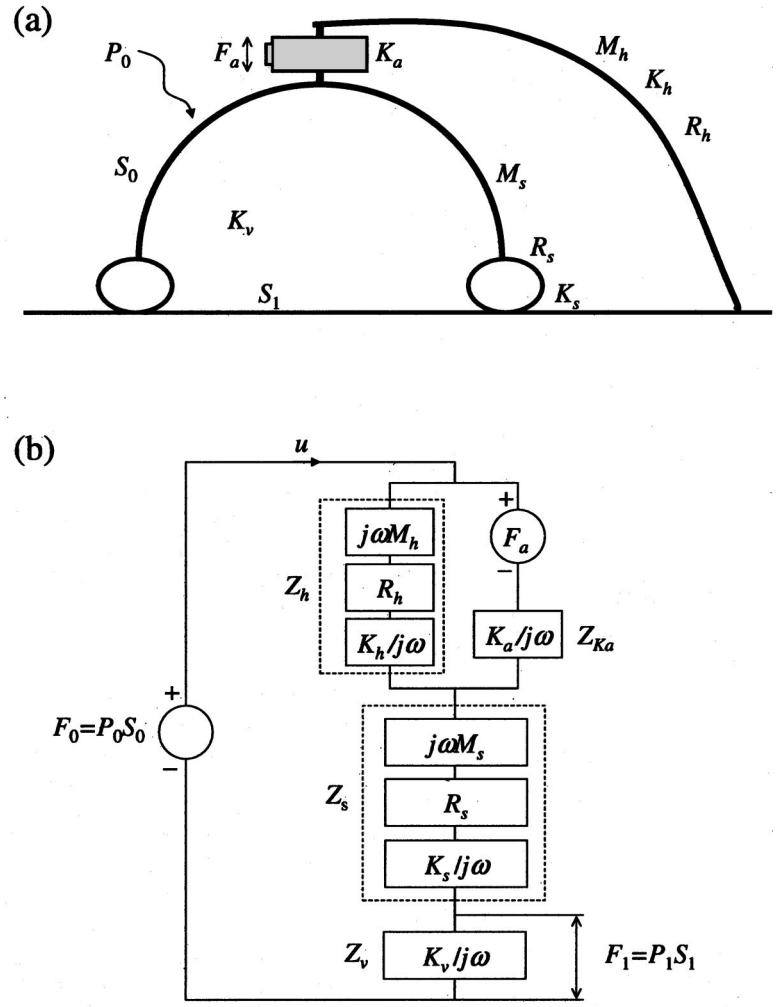

FIG. 3. (a) Schematic diagram of the active headset system with a force actuator fitted between the earshell and the headband, and (b) an equivalent impedance block diagram.

C. Control with inertial force actuator

Control simulations with an inertial force actuator attached to the earshell are presented in this section. Figure 6(a) shows simulations of the sound transmission for the original passive system calculated using Eq. (1); the active system with no control, calculated using Eqs. (6) and (7) and $g=0$; and the active system with control, calculated using Eqs. (6) and (7) and $g=-305$. The parameters for the inertial force actuator are presented in Table II, which represents a PCB 712A02 force actuator. This force actuator was chosen since it is mechanically robust, can produce relatively large forces, and is designed to work in the low-frequency range, i.e., 150 to 500 Hz according to its specifications.

TABLE I. JSP KMO7236 headset parameters.

Parameter	Value	Description
M_s	77 g	Earshell mass
K_s	$7\cdot10^4$ N/m	Cushion stiffness
R_s	90 Ns/m	Cushion damping
M_h	8 g	Headband effective mass
K_h	50 N/m	Headband stiffness
R_h	5 Ns/m	Headband damping
V	180 cc	Earshell cavity volume
S_0	79 cm^2	Outer earshell area
S_1	25 cm^2	Inner earshell area

The effect of mounting the inertial actuator is to provide additional attenuation around its resonance frequency, i.e., 250 Hz, with an increase in transmission above the resonance frequency. The resonance frequency of the earshell around 100 Hz is also decreased due to the added inertial mass of 150g.

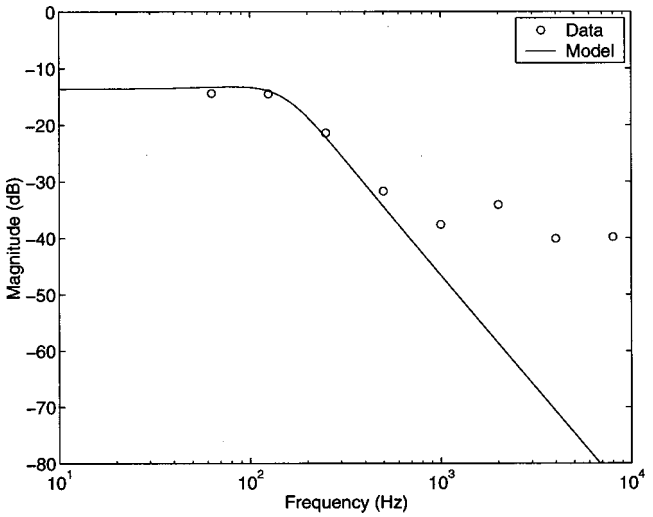

FIG. 4. Passive attenuation of the headset as simulated using Eq. (1) compared to manufacturer's data.

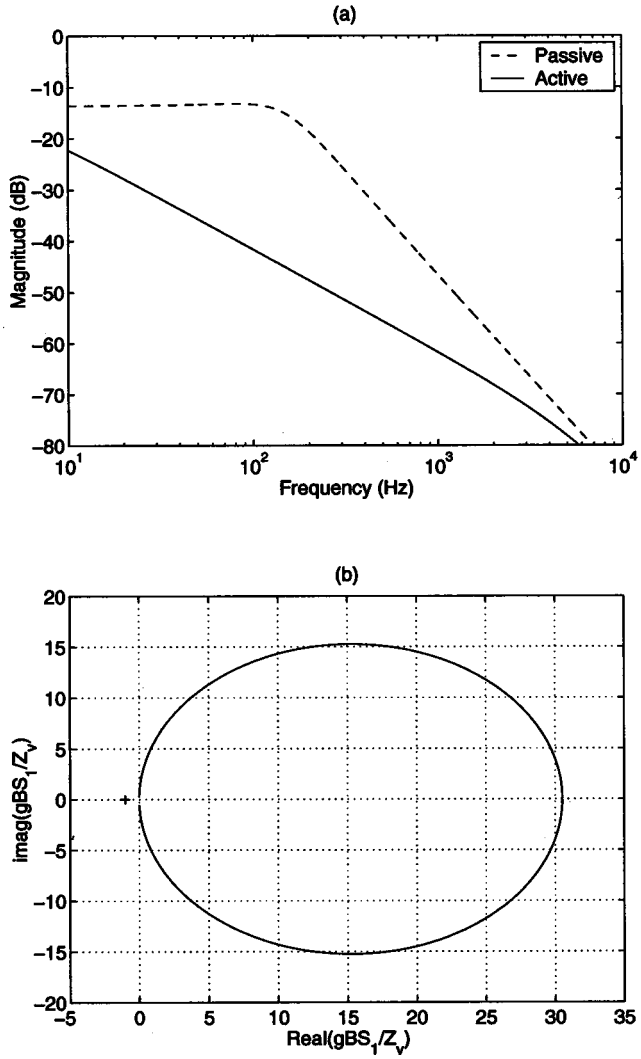

FIG. 5. (a) Theoretical comparison of sound transmission between the passive headset and an active system with an ideal secondary force, and (b) the corresponding Nyquist diagram of the open-loop response of the active system.

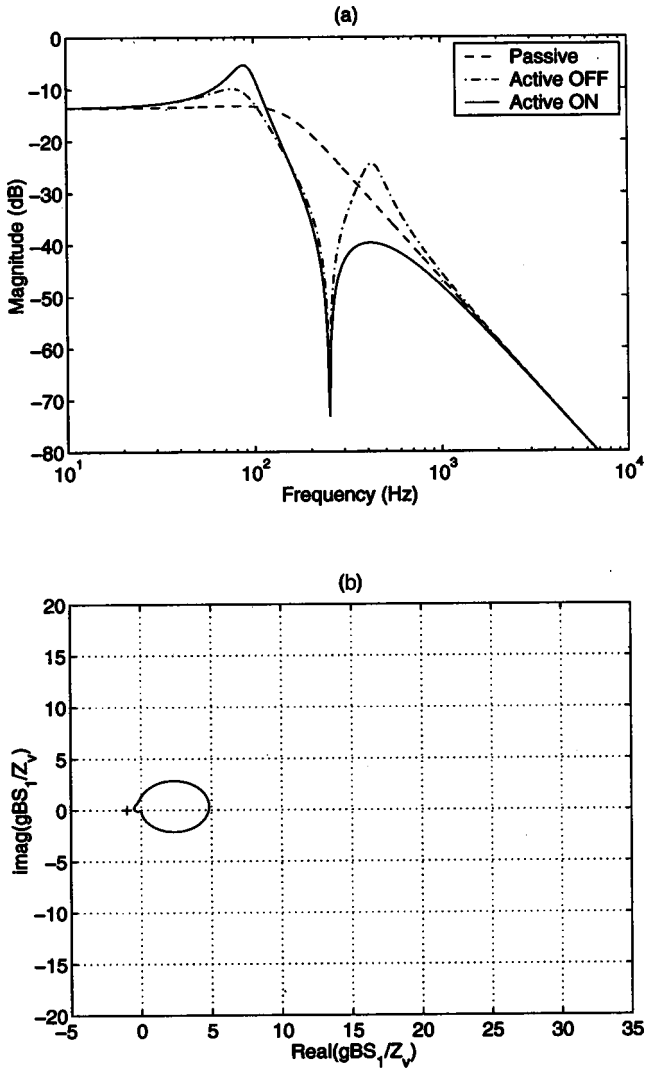

FIG. 6. (a) Theoretical comparison of sound transmission between the passive headset and an active system with an inertial actuator, and (b) the corresponding Nyquist diagram of the open-loop response of the active system.

Once control is applied, the transmission is attenuated above the actuator resonance frequency, and slightly enhanced at the earshell resonance frequency. The latter can be explained by Fig. 6(b), which shows the Nyquist plot for the inertial actuator system. Although the curve is mostly on the right-hand side and therefore provides good stability, it has a small negative real part corresponding to the low-frequency enhancement. An inertial actuator with a lower resonance frequency will produce attenuation at a lower frequency range, with amplification at an even lower frequency, which will be more useful in practice. Such an actuator, however, will require large inertial mass and low stiffness, making it less attractive in practice.

The analysis presented here showed that the dynamics of the actuator system could impose a limit on performance, if stability is to be maintained.

D. Control with a headband force actuator

The sound transmission of the active headset with a force actuator attached between the earshell and the headband is simulated in this section. Figure 7(a) shows the simulated sound transmission for the passive system; the active system with no control, calculated using Eqs. (6) and (8) and $g=0$; and the active system with control, calculated using Eqs. (6) and (8) and $g=-1600$. As above, the parameters for the headset and actuator are presented in Tables I and II. The mounting of the actuator has a small effect on the sound transmission, while the highest active attenuation is observed above the mounted resonance frequency, which is around 1 kHz. Figure 7(b) shows that stability margins in this case are larger compared to the inertial actuator configuration in Fig.

TABLE II. PCB 712A02 force actuator parameters.

Parameter	Value	Description
M_a	150 g	Actuator inertial mass
K_a	$3.7\cdot 10^5$ N/m	Actuator stiffness
f_{0_a}	250 Hz	Resonance frequency
F_{cl}	6.7 N	Clamped force (peak)
X_{fr}	6.5 μm	Free displacement (peak)

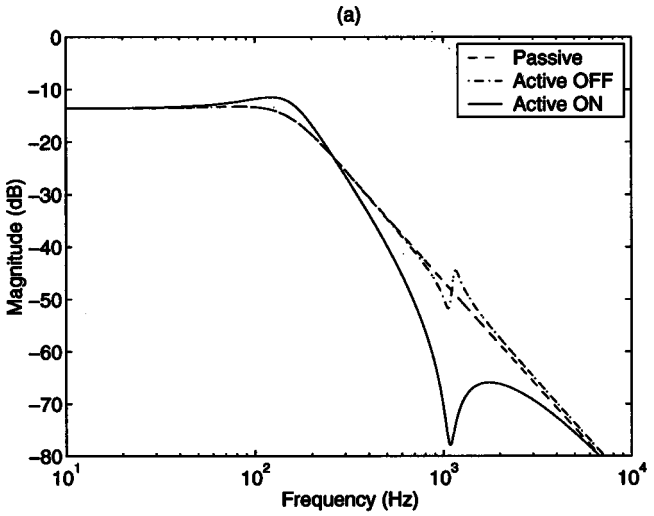

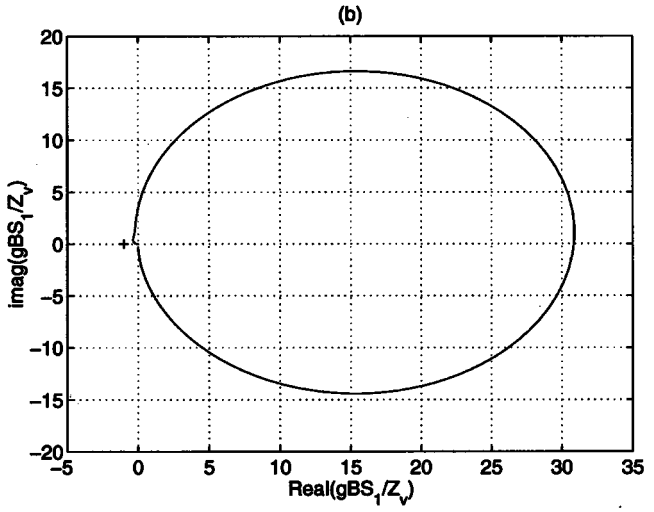

FIG. 7. (a) Theoretical comparison of sound transmission between the passive headset and the active system with the actuator fitted between the earshell and the headband, and (b) the corresponding Nyquist diagram of the open-loop response of the active system.

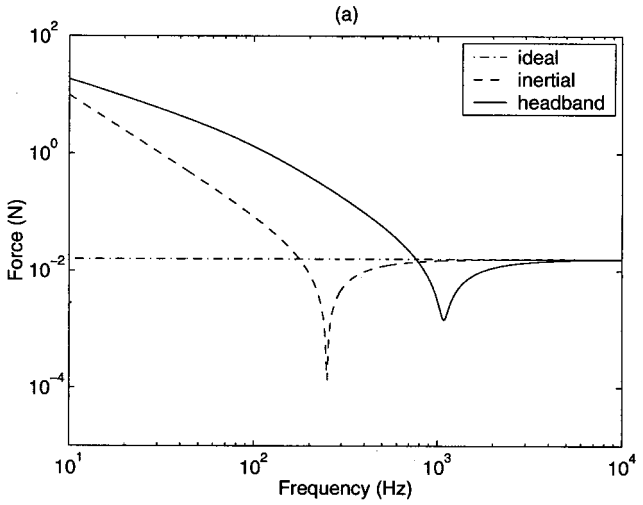

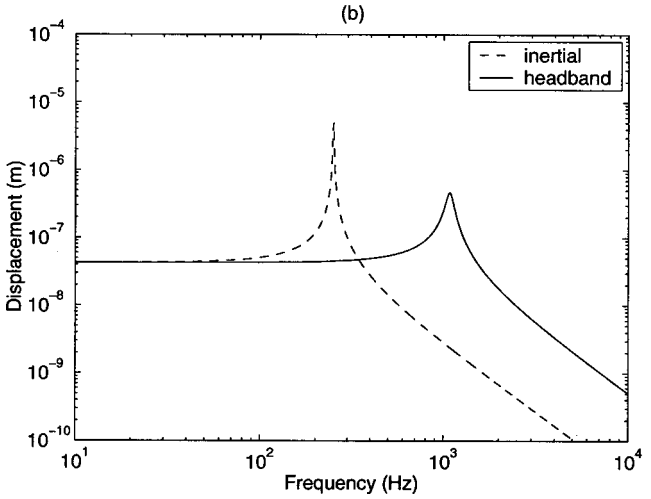

FIG. 8. (a) Force required to completely cancel 100-dB SPL noise, with three secondary source configurations: ideal, inertial actuator, and headband actuator, and (b) actuator displacement, or stroke, required to completely cancel 100-dB SPL noise, with two secondary source configuration: inertial actuator, and headband actuator. Note that displacement is zero for the ideal source case.

6(b). Nevertheless, an actuator with a smaller stiffness will be required to produce attenuation at a lower frequency range to better complement the passive attenuation.

E. Control forces and actuator displacement

The simulation presented above showed that an actuator with lower stiffness is required if active attenuation is to be achieved at the low-frequency range, i.e., below 1 kHz. Other important actuator parameters are the force and displacement required to cancel the primary disturbance. These are evaluated here using simulations with a primary noise of 100 dB SPL. Assuming the pressure inside the earshell in Eq. (4) is completely canceled, the corresponding optimal control force is given by

$$F_{a_{\text{opt}}} = -\frac{AP_0}{B}. \tag{9}$$

Figure 8(a) shows the optimal control force for the three control configurations of an ideal source, inertial actuator, and headband actuator. A constant force is required in the ideal source case, while a higher force is required from the actuators at low frequencies in the other two configurations due to the relatively low impedance of the supporting inertial mass and headband. Lower forces are required around the mounted actuator resonance frequencies.

The optimal force cancels the primary disturbance and therefore reduces the displacement of the earshell to zero. The ''actuator'' displacement, or stroke, in the ideal source case is therefore zero. The actuator stroke in the inertial actuator configuration can therefore be calculated by setting the velocity u to zero in Fig. 2(b), as

$$X_{a_{\text{opt}}} = -\frac{1}{j\omega}\frac{F_{a_{\text{opt}}}}{Z_{M_a}+Z_{K_a}}, \tag{10}$$

and for the headband actuator using Fig. 3(b) as

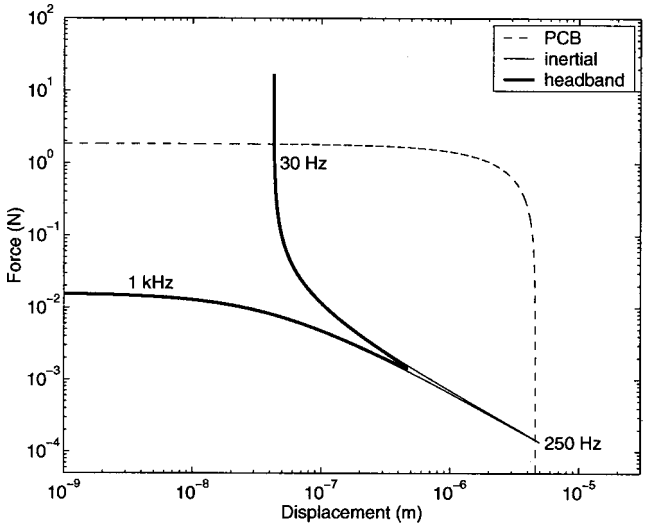

FIG. 9. The maximum force and actuator displacement, or stroke, provided by the actuator, compared to force and stroke required to cancel external noise of 100 dB SPL in the two actuator configurations.

$$X_{a_{\text{opt}}} = -\frac{1}{j\omega}\frac{F_{a_{\text{opt}}}}{Z_h + Z_{K_a}}. \tag{11}$$

Figure 8(b) shows that the stroke required from the actuators is highest around the mounted resonance frequencies.

The next simulation is used to investigate whether the force and stroke required to cancel 100-dB SPL noise, as calculated above, can be produced by the PCB actuator described in Table II. The relation between the maximum force produced by the actuator for a given displacement is assumed to behave linearly,[15] and is calculated from the clamped force and free displacement provided in Table II. This is then compared to the actual force and stroke required as calculated above. Figure 9 shows the maximum force vs actuator displacement, or stroke, provided by the PCB actuator compared to the required values. Some frequency values of the force and displacement pairs are also denoted. At most of the working frequency range the required force and displacement are within the actuator limits, except at very low frequencies, where the force required is slightly higher than the force available, for both actuator configurations. Also, at the resonance frequency of the inertial actuator system, the displacement required is slightly higher than the actuator limit. Overall, at most of the working range, the PCB actuator considered can provide the required force and stroke to cancel an external noise of 100 dB SPL.

If the level of the surrounding primary noise is higher than 100 dB SPL, e.g., near very noisy machines or engines, the limitation imposed by this actuator might compromise performance. In this case an improved actuator is required. The design of such an actuator is suggested for future work.

IV. ROBUST CONTROL SIMULATIONS USING MEASURED DATA

A simulation study using data measured on a laboratory active headset system was performed to investigate the potential performance of the active headset in practice. First, measurements were obtained from the laboratory active headset. Then, the measured data were used to design a controller and simulate its performance and robustness. The setup, and measurement and simulation results are presented in this section.

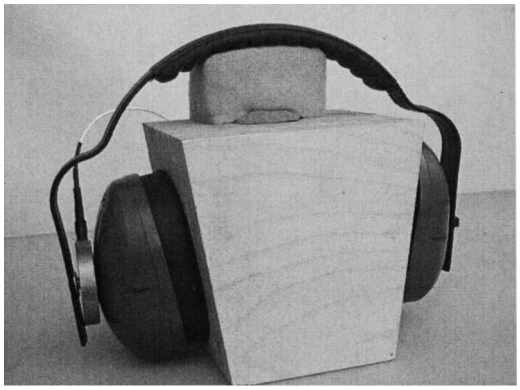

FIG. 10. A photo of the active headset with the PCB actuator mounted between the earshell and the headband.

A. Setup

A laboratory active headset has been constructed and control simulations have been performed using data measured from the laboratory headset. The experimental active headset included a passive JSP noise-reducing headset, mounted on a wooden block with dimensions of an average human head. One electret microphone was mounted inside the earshell, and one outside. A PCB type 712A02 piezoelectric force actuator was mounted on the earshell in the two configurations, i.e., as an inertial actuator with an inertial mass of 150 g, and between the headband and earshell, as illustrated in Figs. 2(a) and 3(a), and was driven by an AVL power amplifier model 790. A Bruel & Kjaer accelerometer type 4375 connected to a charge amplifier type 2635 was mounted on the earshell, colocated with the actuator, and measured earshell velocity. The measurements were recorded using an Advantest R9211C FFT analyzer, and used in the control simulations. A photo of the headset with the PCB actuator mounted between the earshell and the headband is shown in Fig. 10.

B. Control with inertial force actuator

The performance of the active headset system with the inertial actuator was investigated in this section using simulations with data measured on the laboratory system. The acoustic transmission between the external and internal microphones denoted by A was measured by introducing broadband noise through an external loudspeaker. The response between the voltage input to the force actuator's amplifier and the velocity output measured by the accelerometer's charge amplifier, denoted by H, was also measured. Then, a feedback controller with a frequency response C was designed to control the plant H, as described below. It is assumed that the reduction in the earshell vibration due to the control, denoted by $1/(1+CH)$, is proportional to the reduction in the sound transmission, and so the latter with active control can be calculated by

$$\frac{P_1}{P_0} = \frac{A}{1+CH}. \tag{12}$$

Initial control simulation employed a constant velocity-feedback control filter C. The performance of the active headset was very poor due to high-frequency dynamics of the active headset system, which generated negative-real values in the Nyquist open-loop response. The model-based simulations in Sec. III, which showed good performance using velocity feedback, didn't include the system's high-frequency acoustic and structural dynamics, and so when these were included in the measured headset response, the constant gain controller provided poor performance if it was to maintain stability. A feedback controller was therefore designed using an internal model control (IMC) configuration,[16] with a finite impulse response (FIR) control filter with 256 coefficients, and a sampling rate of 20 kHz. The controller was designed to minimize the mean-square vibration signal at the control frequency range, but was made robust for multiplicative uncertainties of 100%,[17,18] which guaranteed stability for any deviation smaller than 6 dB of the plant response from the measured response used in the design.

It should be noted that the aim of the study in this section is to show potential performance with a feedback control filter, and so other feedback controller design methods could have been used (e.g., H_∞ control[19]). Also, the plant uncertainty value of 100% was introduced to provide some robustness in the design. It is clear that a more comprehensive study of the system's response and its variability are required for the design of a controller that is to be implemented in practice. This is, however, suggested for future work.

Figure 11(a) shows the sound transmission through the earshell for the inertial actuator configuration as simulated from the measured data, before and after the control force is applied. The notch at around 250 Hz is due to the mounting of the actuator system acting as a tuned neutralizer. The control filter was designed to provide best attenuation at the frequency range of 250–600 Hz, therefore attenuating the resonance of the mounted system. An attenuation of up to 20 dB is achieved in the control frequency range, showing potential for good performance in practice. A slight increase in the sound transmission is observed at the low frequencies, which is in line with the results predicted in the model-based simulations presented in Fig. 6(a). It should be noted that the curve denoted "Active OFF" in Fig. 11(a), which represents passive transmission, is different from the curve denoted "Data" in Fig. 4, which also represents passive attenuation, in two aspects. First, the former includes the effect of the mounted actuator, and second, the latter was taken from manufacturer's data, while the former was measured on the laboratory headset system used in this work. These two factors contributed to the dissimilarity between the two passive transmission curves.

Figure 11(b) shows the Nyquist plot of the open-loop response CH for the measured plant H and the feedback controller C designed above. The controller maintains reasonable margins from the instability point $(-1,0)$, while achieving an open-loop gain of about 10 on the positive-real quadrant.

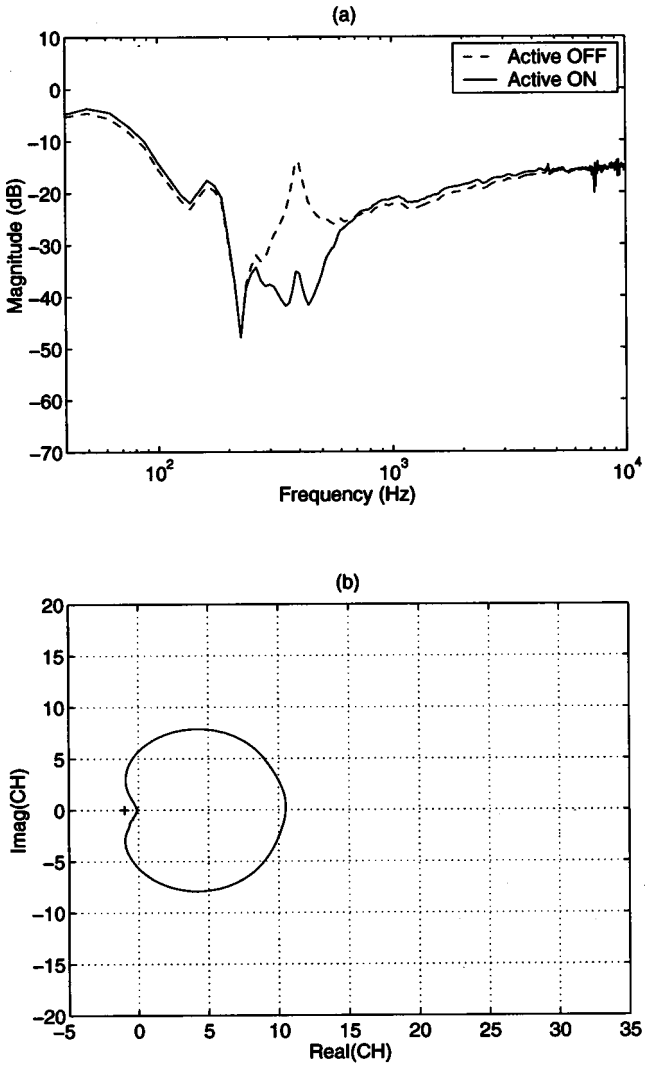

FIG. 11. (a) Sound transmission simulated from measured data for the inertial control actuator configuration, and (b) the corresponding Nyquist diagram of the open-loop response of the active system.

C. Control with headband force actuator

A laboratory headset system with the actuator placed between the headband and the earshell was constructed as described above, and performance was investigated through control simulations from measured data. As for the inertial actuator configuration, velocity feedback control produced poor performance due to high-frequency dynamics, and so a control filter C was designed as described above with a control bandwidth that includes the frequencies below 800 Hz. Figure 12(a) show the sound transmission simulated from measured data before and after control. Attenuation of up to 10 dB is achieved in this broadband control bandwidth. Note that the sound transmission at low frequencies is higher than expected, which can be explained by imperfect sealing of the headset in the experimental setup. Figure 12(b) presents the Nyquist plot of the open-loop response, showing that good

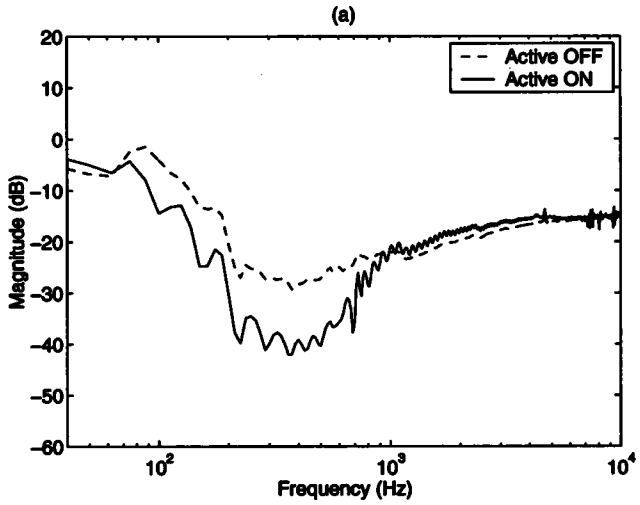

FIG. 12. (a) Sound transmission simulated from measured data for the headband control actuator configuration, and (b) the corresponding Nyquist diagram of the open-loop response of the active system.

stability margins are achieved with a maximum open-loop gain of about 5. The results presented here also show potential for useful performance in practice.

It should be noted that the potential delay of a digital controller originating from the sampling process and the low-pass filters was not considered in the performance analysis in this work. The predicted performance may therefore be achieved by a digital system with a high sampling rate and therefore small delay, or an analog system with a similar frequency response. Although the design of such broadband real-time controllers is suggested for future work, a single-frequency real-time control system was designed and implemented, and is presented below.

V. REAL-TIME CONTROL EXPERIMENT

A real-time control experiment was performed in which single-frequency tonal noise was attenuated by the laboratory headset system with the actuator attached to the headband. A digital controller was designed which implemented a finite impulse response (FIR) control filter having 128 coefficients, adapted using the LMS algorithm,[20] and an FIR plant model

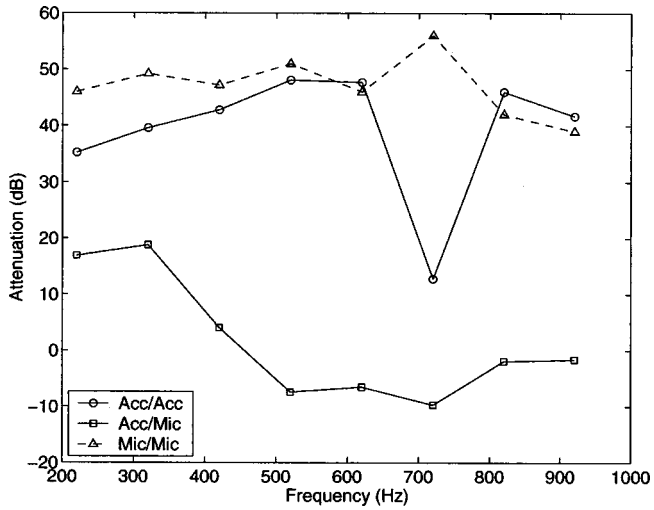

FIG. 13. Single frequency attenuation in the real-time control experiment, when the accelerometer was used for both control and attenuation measurement (Acc/Acc); when the accelerometer was used for control but the microphone used for the attenuation measurement (Acc/Mic); and when the microphone was used for both control and attenuation measurement (Mic/Mic).

of the same length. Both filters were part of an IMC controller[21] operating at a sampling frequency of 5 kHz. A system identification routine based on the LMS algorithm[20] was initiated first to calculate the value of the plant model filter, after which the primary source was turned on, and the control filter adapted to minimize the mean-squared sensor signal. Once the control filter converged, the level of the signal at the sensor was measured and compared to its level before control, giving the attenuation due to the active control system.

Due to the relatively large delay of the adaptive system, based on a Texas Instruments TMS320C54x DSP kit, the performance was limited to narrow-band or tonal disturbances. For this reason the broadband controllers designed in Sec. IV could not be successfully implemented in real time using the current DSP system, and so performance was studied using single-frequency tones, and an LMS-based adaptive control system, which is well suited to control such disturbance. Nevertheless, the real-time experiment presented below showed that indeed active control can be performed using force actuators mounted on the headset earshell as suggested in this paper. The experiment also provides an interesting comparison of performance when the sensing transducer is either an accelerometer or a microphone.

An experimental setup similar to that described in Sec. IV was used in the real-time control experiment. In addition, the output of the DSP controller was connected to the actuator amplifier, while the input of the DSP controller was connected to the output of the sensor, which was either the accelerometer or the microphone inside the earshell. A loudspeaker positioned near the headset setup was used to generate the primary excitation.

Figure 13 (the two solid curves) shows the attenuation at the tonal excitation frequencies as measured by the accelerometer, mounted opposite the force acuator, in a colocated manner, and the microphone. In this case the accelerometer

was used as the control sensor, such that the control filter attempted to minimize the mean-square error of the accelerometer signal. Although large attenuation is achieved at the control sensor, an attenuation of more than 10 dB at the microphone is only achieved at the low frequencies, and in fact at high frequencies the noise is actually amplified.

This behavior can be explained by the fact that although the vibration of the earshell is reduced at the accelerometer location, other parts of the earshell could still vibrate by exciting higher-order modes, specially at high frequencies, therefore radiating sound into the earshell inner volume. Another contributing factor for this behavior could be transmission paths other than via earshell vibration, such as acoustic leaks, which are not eliminated by reducing headset vibration.

A second experiment was performed, this time with the microphone as the control sensor. As can be seen from Fig. 13 (dashed curve), high attenuation is achieved at a wide frequency range. In this case the controller is attempting to minimize the microphone signal directly, and so rather then reducing the earshell vibration, the actuator forces the earshell to vibrate in such a way that minimizes the sound level inside the earshell, therefore overcoming the potential problems when minimizing the vibration signal as discussed above.

The results presented here suggest that a microphone can be more useful as a control sensor since it measures the sound inside the earshel directly. Measuring the sound indirectly, using an accelerometer mounted on the earshell, results in reduction in the earshell vibration, but due to high-frequency dynamics and leaks, this reduction might not produce as significant a reduction in the sound. The microphone control sensor could therefore provide a more attractive alternative for a practical active headset system.

VI. CONCLUSIONS

This paper presented a novel approach to ANR headsets, which employ earshell vibration control to attenuate the noise inside the earshell volume. The theory of the new approach, supported by simulations and an experimental study, suggested that good performance can potentially be achieved in practice.

Two actuator configurations were studied, i.e., an inertial force actuator and a force actuator placed between the earshell and the headband. Model-based simulations highlighted the requirement for a reduced stiffness from the actuator, and provided actuator's force and stroke requirements, while simulations from data measured on a laboratory headset system showed that good performance could potentially be achieved.

The configuration with a force actuator placed between the headband and the earshell is preferred since it doesn't require an inertial mass which will increase system weight and compromise comfort. Furthermore, the piezoelectric actuator considered here requires high-input voltage, which might be difficult to obtain in a commercial active headset.

Another important issue is the effect of leaks caused by an imperfect seal of the headset to the head and the effect of high-frequency system dynamics. The use of a microphone rather than an accelerometer which will detect noise generated by both vibration transmission and sound leak paths was shown to be preferable, through a single-frequency real-time control experiment.

The study and design of more suitable actuators and their implementation in an active noise-reducing headset are proposed for future research. The subjective effect of noise reduction through earshell vibration should also be investigated as sound might be perceived via bone conduction. Another important issue is the mechanical coupling between left and right headset systems via the headband, for example, which should be investigated and be taken into account if found significant.

ACKNOWLEDGMENTS

The authors would like to thank Lectret Precision Pte. Ltd. for supporting the research work.

[1] E. D. Simshauser and M. E. Hawley, ''The noise canceling headset—An active ear defender,'' J. Acoust. Soc. Am. **27**, 207 (1955).
[2] M. H. Hawley, ''Acoustic interference for noise control,'' Noise Control **2**, 61–63 (1956).
[3] W. F. Meeker, ''Components characteristics for an active ear defender,'' J. Acoust. Soc. Am. **29**, 1252 (1957).
[4] P. D. Weeler, ''Voice communication in the cockpit noise environment,'' Ph.D. thesis, University of Southampton, England, 1986.
[5] M. S. Bai and D. Lee, ''Implementation of an active headset by using H_∞ robust control theory,'' J. Acoust. Soc. Am. **102**, 2184–2190 (1997).
[6] A. J. Brammer, G. J. Pan, and R. B. Crabtree, ''Adaptive feedforward active noise reduction headset for low-frequency noise,'' Proceedings of ACTIVE 97 conference, Budapest, Hungary, August 1997, pp. 365–372.
[7] A. V. Oppenheim, E. Weinstien, K. C. Zangi, M. Feder, and D. Gauger, ''Single-sensor active noise cancellation,'' IEEE Trans. Audio Speech Proc. **2**(2), 285–290 (1994).
[8] B. Rafaely and M. Jones, ''Combined feedback-feedforward active noise-reducing headset—The effect of acoustics on broadband performance,'' J. Acoust. Soc. Am. (in press).
[9] B. Rafaely, P. Gardonio, and J. Carhillo, ''Novel active headset,'' Patent GB2361379.
[10] E. A. G. Shaw and G. J. Thiessen, ''Acoustics of circumaural earphones,'' J. Acoust. Soc. Am. **34**, 1233–1246 (1962).
[11] C. R. Fuller, S. J. Elliott, and P. A. Nelson, *Active Control of Vibration* (Academic, London, 1997).
[12] P. A. Nelson and S. J. Elliott, *Active Control of Sound* (Academic, London, 1992).
[13] C. M. Harris and C. E. Crede, *Shock and Vibration Handbook* (McGraw-Hill, New York, 1976).
[14] S. J. Elliott, M. Serrand, and P. Gardonio, ''Feedback stability for active isolation systems with reactive and inertial actuators,'' ASME J. Vibr. Acoust. **123**(2), 250–261 (2001).
[15] M. J. Brennan, J. Garcia-Bonito, S. J. Elliott, A. David, and R. J. Pinnington, ''Experimental investigation of different actuator technologies for active vibration control,'' Smart Mater. Struct. **8**, 145–153 (1999).
[16] M. Morari and E. Zafiriou, *Robust Process Control* (Prentice-Hall, Englewood Cliffs, NJ, 1989).
[17] B. Rafaely and S. J. Elliott, ''H_2/H_∞ active control of sound in a headrest: Design and implementation,'' IEEE Trans. Control Syst. Technol. **7**(1), 79–84 (1999).
[18] S. J. Elliott and T. J. Sutton, ''Performance of feedback and feedforward systems for active control,'' IEEE Trans. Speech Audio Proc. **4**(3), 214–223 (1996).
[19] M. S. Bai and D. Lee, ''Implementation of an active headset by using H-infinity robust control theory,'' J. Acoust. Soc. Am. **102**, 2184–2190 (1997).
[20] B. Widrow and S. D. Stearns, *Adaptive Signal Processing* (Prentice-Hall, Englewood Cliffs, NJ, 1985).
[21] B. Rafaely and S. J. Elliott, ''An adaptive and robust feedback controller for active control of sound and vibration,'' Proceedings of CONTROL'96 conference, University of Exeter, UK, 1996, pp. 1149–1153.

Theoretical and experimental investigations on coherence of traffic noise transmission through an open window into a rectangular room in high-rise buildings

Jiping Zhang[a)]
State Key Laboratory of Vibration, Shock & Noise, Shanghai Jiao Tong University, Shanghai 200030, China; Zhejiang Research and Design Institute of Environmental Protection, Hangzhou 310007, China; and State Key Laboratory of Modern Acoustics, Nanjing University, Nanjing 210093, China

Weikang Jiang
State Key Laboratory of Vibration, Shock & Noise, Shanghai Jiao Tong University, Shanghai 200030, China

Ningrong Li
State Key Laboratory of Modern Acoustics, Nanjing University, Nanjing 210093, China

(Received 27 February 2001; revised 10 April 2002; accepted 30 April 2002)

A method for theoretically calculating the coherence between sound pressure inside a rectangular room in a high-rise building and that outside the open window of the room is proposed. The traffic noise transmitted into a room is generally dominated by low-frequency components, to which active noise control (ANC) technology may find an application. However, good coherence between reference and error signals is essential for an effective noise reduction and should be checked first. Based on traffic noise prediction methods, wave theory, and mode coupling theory, the results of this paper enabled one to determine the potentials and limitations of ANC used to reduce such a transmission. Experimental coherence results are shown for two similar, empty rectangular rooms located on the 17th and 30th floors of a 34 floor high-rise building. The calculated results with the proposed method are generally in good agreement with the experimental results and demonstrate the usefulness of the method for predicting the coherence.
[DOI: 10.1121/1.1488653]

PACS numbers: 43.50.Ki, 43.50.Vt, 43.50.Lj [MRS]

LIST OF SYMBOLS

A_{mn}	mode coupling factor
A_{suj}	corresponds to the temporal change of source strength of the uth-type vehicles on the sth lane at a distance of r_{suj}
$A(\omega)$	source strength related to the surface vibration velocity of the vehicle and the characteristics of the air
a	height of the open window
b	width of the open window
c	velocity of sound in air
C	matrix of a constructed equation set
C_r	reflection coefficient determined by characteristics of the ground
C_r'	reflection coefficient determined by characteristics of the building facade
d	distance between the road and the high-rise building
f	frequency of sound
h	altitude of the room in the investigated high-rise building above the earth's surface
i	unit of imaginary number
j	denotes mutually independent random time or location point at which any one vehicle appears
KK'	coefficients of Fourier cosine series
k	wave number of sound
L_s	half-length of the sth lane of the road segment directly facing the high-rise building
l_x, l_y, l_z	height, length, and width of the room cavity
M	air absorption coefficient
$m(\omega, r)$	reduction factor of the air absorption or the influence of winds, temperatures, and obstacles
m,n	mode number
N	flow of vehicles, that is, the number of passed vehicles on the road per second
N_s	flow of vehicles on each lane
N_{su}	flow of the uth type of vehicles
n_s	number of vehicles in road segment considered
n_{su}	number of the uth type of vehicles appearing in the n_s
$p(r, \omega, t)$	sound pressure at distance r at frequency ω
$p(x, y, z, \omega, t)$	sound pressure
p,q	mode number
r, r_{suj}	distance between a vehicle and a receiver
S, S'	virtual surface of an open window
t	time
T	superscript indicating transpose of a matrix
v	average vehicle moving speed
v_x, v_y, v_z	air particle velocity at x, y, and z direction, respectively

[a)]Electronic mail: jpzhang@mail.hz.zj.cn

X,Y,Z	location in the transformed coordinates
X_0,Y_0,Z_0	location of the reference sensor
x,y,z	location of the receiver
∇	divergence
δ	delta impulse response function
ρ	denstiy of air
ω	frequency of sound ($=2\pi f$)
$\gamma^2(\omega)$	coherence coefficient at frequency ω
*	superscript indicating complex conjugate of a variable

I. INTRODUCTION

Traffic noise is one of the major environmental problems in urban societies. The numbers of high-rise buildings in modern cities are increasing. Sound barriers and window insulation are commonly used for traffic noise control but these techniques are mainly effective at the middle and high frequencies. Much of the high-frequency noise reaching a high-rise building will be absorbed by the air, leaving the lower-frequency components. Sometimes, due to resonance in a room, the low-frequency traffic noise transmitted into a room can become severe because the wavelength is of the order of the room dimensions.[1] Active noise control is now recognized as an important technology for reduction of the low-frequency noise. Therefore, it is worth studying the feasibility of active noise control technology for control of the low-frequency traffic noise transmitted into a room, especially in a high-rise building.

According to the comfortable-living criteria of rooms in architectural acoustics, two cases should be considered, a room with an open window and a room with a closed window. Therefore, active control of noise transmission into a room is also divided into two such situations.

In the case of a closed window, we have active control of noise transmission into a sealed or closed acoustic enclosure. Considerable research on this subject has been reported in the literature. Earlier research focused on the average performance of the sound transmission through a rectangular panel or window backed by a rectangular room, where the transient behavior was not considered (for instance, see Refs. 2 and 3). Current research interest on active control of interior noise is focused on enclosures with flexible boundaries, because there is a real need to control low-frequency noise in lightweight systems such as aircraft and vehicles.[4] The glass of a closed window can be approximated as a flexible boundary. An empty, rectangular room with a closed window is better modeled as a panel with a back cavity. Much previous work can be applied directly to analyze the problem (e.g., the work of Pan *et al.*,[5,6] Snyder,[7] Kim and Brennan,[8] and Sampath and Balachamdran[9]). However, only little attention has been paid to the active control of noise transmission into a building.

In the case of an open window, it is much more important and difficult to control traffic noise. Duhamel and Sergent have presented the concept of active traffic noise control in Ref. 10. However, their work was mainly concerned with active control of the outdoor noise created by an incoherent line source. Although their latest investigation was extended to the numerical calculation of the pressure crossing an aperture in a rigid plane (set in free space) to simulate the noise entering a room through an open window, the diffraction of the aperture is much different than that of a real window on the wall of a room with a closed door. Martin presented a strategy[11] to reduce traffic noise by active controlling the deterministic and slowly varying noise radiated by a moving source such as an airplane taking off, a train, or a car, but only in the open air. Kropp and Berillen proposed a theoretical model to investigate the acoustic performance of a building balcony in the low- and middle-frequency range just used for determining optimal balcony design,[12,13] where full opening front wall was used simply instead of a true opening balcony. There still exists a gap between the prediction of traffic noise transmitting into an open window room and its active control, since the complexity of the physical system may limit the reduction.

In controlling actively the noise transmitted through an open window into a room, global control should be considered as nearly impossible. Finding local zones of quiet is a more possible and applicable strategy, even though local control may cause an increase of noise level in areas away from the error sensors. Since the traffic noise reaching at the receiver is broadband (random) in the low-frequency range, just using a simple feedback algorithm will be not enough and the quiet zone could be small and unstable because of the time delay in the devices. Because a reference sensor can be easily located outside the room, e.g., below the window-sill, the sound transmission mechanisms suggest a feedforward strategy. The benefits of this placement might more effectively reduce the positive feedback from the reflections of the walls or surfaces and the secondary sources in the room toward the reference sensor. The coherence between signals measured by all the reference and error sensors will conversely influence or determine the control performance. A method to compensate for the weakness of the above algorithm is to use a combined or hybrid feedback and feedforward control,[14,15] but more information at a very limited number of sensors has to be obtained. Nevertheless, once the feedforward strategy is used in the transmission control, the coherence between signals passing through the open window and at the receiver will become an important issue to be studied.

The work in this paper intends to fill, in part, this gap. First, though, the coherence between the error signal inside the room and the reference signal outside the window should be investigated, if a feedforward control strategy is to be adopted. This function determines the feasibility of noise reduction. In this paper we extend the work of Duhamel and Sergent by developing a theoretical method for calculating the coherence for an empty rectangular room in a high-rise building, including the interaction of a fully open window. Experimental verification of the method is given and numerical examples are presented that demonstrate the coherence of the system.

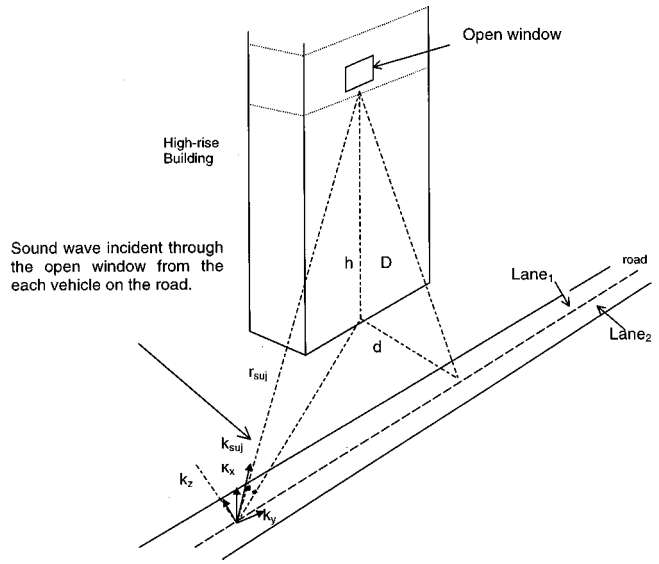

FIG. 1. Sketch of a high-rise building at a traffic road.

II. THEORY

A. Traffic sound pressure on the building facade

A high-rise building at a traffic road is shown in Fig. 1. The following assumptions are adopted: There are no other obstacles between the building and the road; the road in front of the building has two vehicle lanes, the traffic flow through each lane has identical averaged speed v, for three types of vehicles, including automobiles, heavy vehicles (including buses and trucks), and motorcycles, with the vehicles flow for the road being N per second, and the flow of each lane being $N_s=N/2$; the flow of the uth type of vehicles is designated N_{su}, such that $N_s=\Sigma_{u=1}^{3}N_{su}=N/2$. The vehicle flow within a particular segment $[-L_s,L_s]$ of the sth lane, directly facing the building, is n_s, and the flow of the uth type of vehicle is n_{su},

$$\left(n_s=\sum_{u=1}^{3} n_{su}\right).$$

A vehicle can be represented by a monopole sound source moving along the road close to the earth surface when the observation point is far away from it. Therefore the sound pressure due to a vehicle at a reception position can be expressed in the frequency domain as follows:

$$p(r,\omega,t)=(1+Cr)\cdot A(\omega)\cdot m(\omega,r)\exp[i(\omega t-kr)]/4\pi r, \tag{1}$$

where $A(\omega)$ is the source strength related to the surface vibrating velocity of the vehicle and the characteristics of the air; Cr is the reflection coefficient of ground; r is the distance between the vehicle and the reception point; ω is the sound frequency $(=2\pi f)$; t is time; k is the wave number $(=\omega/c)$; $m(\omega,r)$ is the reduction due to air absorption or the influence of wind, temperature, and obstacles, which can be expressed as $m(\omega,r)=\exp(-M\omega)$ in the simplest case (here, M denotes the air absorption coefficient).

The vehicles moving on the road are described by some statistical distribution (e.g., a Poisson distribution) so the sound pressure on the high-rise building facade from the road can be calculated as

$$p(\omega,t)=\sum_{s=1}^{2}\sum_{u=1}^{3}\sum_{j=1}^{N_{su}} A_{suj}\frac{\exp\lfloor i(\omega t-k_{suj}r_{suj})\rfloor}{4\pi r_{suj}}$$

$$\approx\sum_{s=1}^{2}\sum_{u=1}^{3}\sum_{j=1}^{n_{su}} A_{suj}\frac{\exp\lfloor i(\omega t-k_{suj}r_{suj})\rfloor}{4\pi r_{suj}}, \tag{2}$$

$$E(A_{suj}\cdot A^{*}_{s'u'j'})=E(|A_{suj}|^2)\,\delta(s-s')\,\delta(u-u')\,\delta(j-j'), \tag{3}$$

where

$$r_{suj}=\sqrt{D^2+v^2(t-t_{uj})^2},$$
$$D=\sqrt{d^2+h^2}. \tag{4}$$

In Eqs. (2)–(4), the sound pressure $p(r,\omega,t)$ is assumed to be affected only by the vehicles in the time interval $[t-L_s/v,t+L_s/v]$; j denotes an independent random time or vehicle location. Each complex independent random variable $A_{suj}=(1+Cr)\cdot A\cdot m(\omega,r)$ corresponds to the temporal change of the uth-type vehicles on the sth lane with an arbitrary density function at the distance of r_{suj}. A^{*}_{suj} is the complex conjugate of A_{suj}, and the t_{uj} are independent random time variables for when the vehicle and its sound pressure appears. The distances D, d, h are shown in Fig. 1.

B. Theoretical model of sound transmission into a high-rise building

A room with an open window on the facade of a high-rise building can be modeled as a partially open rectangular cavity in a rigid baffle, as shown in Fig. 2. The sound level inside the room depends on the size of the window, the acoustical absorptive characteristics of the walls surfaces, and the room dimensions. Above the Schröder frequency, the sound field will be diffuse. At low frequencies, the sound pressure has distinct resonance peaks. For frequencies of interest below 100 Hz, the wavelength will be greater than 3.4 m, comparable with the dimensions of the room, taken as about $3\times3\times4$ m^3.

As shown in Fig. 2, the room cavity has length l_y, width l_z, and height l_x; the open window has a height a and a width b. The sound pressure $p(x,y,z,\omega,t)$ inside the room is described by the wave equation:

$$\nabla^2 p=\frac{1}{c}\frac{\partial^2 p}{\partial t^2}, \tag{5}$$

with the boundary conditions, as follows:

$$v_x(x=0,x=l_z)=-\frac{1}{i\rho\omega}\frac{\partial p}{\partial x}\bigg|_{x=0,x=lx}=0,$$

$$v_y(y=0,y=l_y)=-\frac{1}{i\rho\omega}\frac{\partial p}{\partial y}\bigg|_{y=0,y=ly}=0, \tag{6}$$

$$v_z(z=l_z)=-\frac{1}{i\rho\omega}\frac{\partial p}{\partial z}\bigg|_{z=l_z}=0.$$

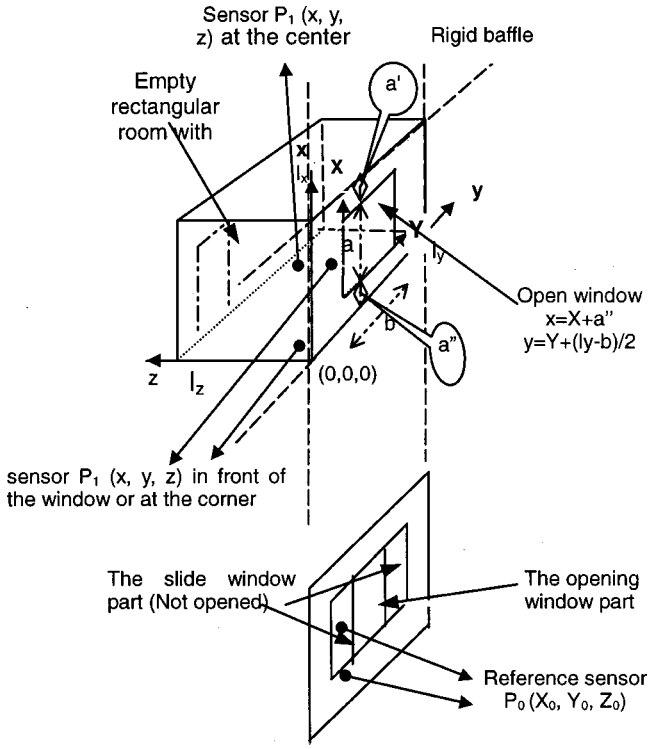

FIG. 2. Sketch of the open window room with coordinates, parameters, and sensor locations.

The solution for Eqs. (5) and (6) inside the room will be

$$P(x,y,z,\omega)=\sum_{m=0}^{\infty}\sum_{n=0}^{\infty}A_{mn}\exp(-ik_{mn}l_z)\cos\left(\frac{m\pi x}{l_x}\right)\times\cos\left(\frac{n\pi y}{l_y}\right)\cos[k_{mn}(l_z-z)]\exp(i\omega t),$$
$$k_{mn}=\sqrt{k^2-\left(\frac{m\pi}{l_x}\right)^2-\left(\frac{n\pi}{l_y}\right)^2}. \tag{7}$$

It should be noticed that in Eq. (7), when $k^2\geqslant(m\pi/l_x)^2+(n\pi/l_y)^2$, k_{mn} is positive; when $k^2<(m\pi/l_x)^2+(n\pi/l_y)^2$, $k_{mn}=-i\cdot\sqrt{(m\pi/l_x)^2+(n\pi/l_y)^2-k^2}$.

Next, the following assumptions are adopted: $p_{\rm in}$, $p_{\rm re}$, and $p_{\rm rad}$ represent the sound pressure of the incident and reflected traffic noise field and the radiated sound field at the open window, respectively, and $p_s=p_{\rm in}+p_{\rm re}$. Parameters $v_{\rm inz}$, $v_{\rm rez}$, and v_{rz} represent the velocities due to the incident and reflected traffic noise ($v_{sz}=v_{\rm inz}+v_{\rm rez}$) and the velocity of the radiated sound field ($v_{\rm re}=v_{rz}$) in the room where $z=0$. With the addition of the boundary condition of Eq. (6), the boundary conditions on the front open window shown in Fig. 2 are, for

$$\left(a''<x<a''+a,\frac{ly-b}{2}<y<\frac{ly+b}{2}\right)$$

and

$$(a+a'+a''=l_x),$$
$$\nu_z(z=0)=(\nu_{\rm inz}+\nu_{\rm rez}+\nu_{\rm re})|_{z=0}=\nu_{sz}+\nu_{rz},$$

or

$$\nu_z=-\frac{1}{i\rho\omega}\frac{\partial p}{\partial z}, \tag{8}$$
$$p_z(x,y,0,\omega)=(p_{\rm in}+p_{\rm re}+p_{\rm rad})|_{z=0}=p_s+p_{\rm rad},$$

and

$$\nu_z(z=0)=0, \tag{9}$$

for

$$\left(0<x<l_x,0<y<\frac{l_y-b}{2}\right),\ \left(0<x<l_x,\frac{l_y+b}{2}<y<l_y\right),$$
$$\left(0<x<a'',\frac{l_y-b}{2}<y<\frac{l_y+b}{2}\right),$$
$$\left(a+a''<x<l_x,\frac{l_y-b}{2}<y<\frac{l_y+b}{2}\right).$$

We make a coordinate transformation (see Fig. 2),

$$x=X+a'',\quad y=Y+\frac{l_y-b}{2}, \tag{10}$$

and separate the wave number k or k_{suj} from any one vehicle in Fig. 1 into k_x, k_y, and k_z as follows:

$$k_x=k_{suj}\frac{H}{r_{suj}},$$
$$k_y=k_{suj}\sqrt{1-\frac{D^2}{r_{suj}^2}},\quad k_z=k_{suj}\frac{d}{r_{suj}}. \tag{11}$$

Because the facade of the high-rise building is modeled as a baffle, the sound pressure propagates from each vehicle on the road to the cavity, as shown in Fig. 1. Applying a Taylor expansion to the farfield of Eq. (2) (see Appendix A), we obtain

$$\begin{aligned}p_s&=p_{\rm in}+p_{\rm re}\\&=\sum_{s=1}^{2}\sum_{u=1}^{3}\sum_{j=1}^{N_{su}}\frac{(1+C_r')A_{suj}}{4\pi r_{suj}}\\&\quad\times\exp[i(\omega t-k_{suj}r_{suj})]\exp[-i(k_xx+k_yy)]\cos(k_zz)\\&\approx\sum_{s=1}^{2}\sum_{u=1}^{3}\sum_{j=1}^{N_{su}}\frac{2A_{suj}}{4\pi r_{suj}}\exp[i(\omega t-k_{suj}r_{suj})]\\&\quad\times\exp[-i(k_xx+k_yy)]\cos(k_zz),\end{aligned} \tag{12}$$

where C_r' is the reflection coefficient corresponding to the characteristics of the building facade, and here, $C_r'\approx1$.

The sound radiation from the open window back into the free space can be calculated using the Rayleigh integral as if there was a virtual radiating surface on the rigid baffle. Therefore,

$$p_{\rm rad}=\frac{i\omega\rho}{2\pi}\int_S\nu_{r_z}\frac{\exp(-ikr_z)}{r_z}ds,$$
$$r_z=\sqrt{(X-X')^2+(Y-Y')^2}, \tag{13}$$

where v_{rz} is the velocity in the normal direction (i.e., in the z direction) at a point (X',Y') on the virtual interface (the opening window); r_z is the distance between the point

(X',Y') and the receiving point (X,Y), both on the interface.

The values of A_{mn} in Eq. (7) can be determined from the boundary conditions at $z=0$ or $Z=0$. The detailed calculations are shown in Appendix B.

From Eq. (7) and Eq. (B13), the complete sound field solution for the traffic noise transmission into a room in a high-rise building is obtained, but the noise strength of the transient traffic flowing must be known in advance.

C. Coherence between the sound pressure inside the room and that outside the window

The open window can be treated as a virtual surface sound reradiator. An assumed reference sensor is placed outside the window, where the impact of sound reflection toward the sensor is negligible if it is properly located or directed. The autocorrelation sequence of sound pressure at the sensor can be calculated by using Eqs. (12) and (3). Locating the reference sensor at (X_0,Y_0,Z_0), then

$$\int_{-\infty}^{+\infty} p_s \cdot p_s^* \, dt = \sum_{s=1}^{2}\sum_{u=1}^{3}\sum_{j=1}^{N_{su}} \frac{4|A_{suj}|^2}{16\pi^2}\int_{-\infty}^{+\infty}\frac{\cos^2(k_z Z_0)}{r_{suj}^2}dt. \tag{14}$$

The autocorrelation sequence of sound pressure at any point inside the rectangular room in the high-rise building can be calculated using Eqs. (7), (B13), and (3). Locating the error sensor at (x,y,z), where the noise from the road is considered to be cancelled in the near field or locally, and H_{mn} and $D_1(p,q)$ are defined as (see Appendices B and D)

$$\begin{aligned} H_{mn} &= \exp(-ik_{mn}l_z)\cos\left(\frac{m\pi x}{l_x}\right)\cos\left(\frac{n\pi y}{l_y}\right) \\ &\quad \times \cos[k_{mn}(l_z - z)], \\ \vec{H} = [H] &= (H_{00}, H_{01}, H_{02}, \ldots, H_{0N}, H_{10}, \ldots H_{1N}, \\ &\quad H_{2N}, \ldots H_{mn}, \ldots H_{N0}, H_{N1}, \ldots H_{NN})^T, \end{aligned} \tag{15}$$

$$\begin{aligned} D_{1(pq)} &= -\frac{k_x k_y}{r}\frac{[\exp(-ik_x a)\cos(p\pi)-1][\exp(-ik_y b)\cos(q\pi)-1]}{\left[k_x^2-\left(\frac{p\pi}{a}\right)^2\right]\left[k_y^2-\left(\frac{q\pi}{b}\right)^2\right]}, \\ \vec{D}_1 = [D_1] &= (D_{1(00)}, D_{1(01)}, D_{1(02)}, \ldots, D_{1(0N)}, D_{1(10)}, \ldots D_{1(1N)}, D_{1(2N)}, \ldots D_{1(pq)}, \ldots D_{1(N0)}, D_{1(N1)}, \ldots D_{1(NN)})^T \end{aligned} \tag{16}$$

then

$$\int_{-\infty}^{+\infty} p(x,y,z,\omega,t)\cdot p^*(x,y,z,\omega,t)dt = \sum_{s=1}^{2}\sum_{u=1}^{3}\sum_{j=1}^{N_{su}} \frac{4|A_{suj}|^2}{16\pi^2}\frac{1}{a^2b^2}\left[H^T C^{-T}\left(\int_{-\infty}^{+\infty} D_1\cdot(D_1^T)^* dt\right)(C^{-1})^* H^*\right]. \tag{17}$$

A definition is made for $D_{2(p,q)}$,

$$\begin{aligned} D_{2(p,q)} &= \int_{-\infty}^{+\infty}\frac{(-k_x k_y)}{r_{suj}^2}\frac{[\exp(-ik_x a)\cos(p\pi)-1][\exp(-ik_y b)\cos(q\pi)-1]}{[k_x^2-(p\pi/a)^2][k_y^2-(q\pi/b)^2]}\cdot\exp[i(k_x X_0 + k_y Y_0)]\cos(k_z Z_0)dt, \\ \vec{D}_2 = [D_2] &= (D_{2(00)}, D_{2(01)}, D_{2(02)}, \ldots, D_{2(0N)}, D_{2(10)}, \ldots D_{2(1N)}, D_{2(2N)}, \ldots D_{2(pq)}, \ldots D_{2(N0)}, D_{2(N1)}, \ldots D_{2(NN)})^T. \end{aligned} \tag{18}$$

Therefore, the cross-correlation sequence of the sound pressure between the error sensor and the reference sensor can be calculated by using Eq. (3),

$$\int_{-\infty}^{+\infty} p(x,y,z,\omega)\cdot p_s^* \, dt = \sum_{s=1}^{2}\sum_{u=1}^{3}\sum_{j=1}^{N_{su}} \frac{4|A_{suj}|^2}{16\pi^2}\frac{1}{ab}H^T C^{-T} D_2. \tag{19}$$

Using Eqs. (14), (17), and (19), the coherence $\gamma^2(\omega)$ can be expressed as follows:

$$\begin{aligned} \gamma^2(\omega) &= \frac{\left|\int_{-\infty}^{+\infty} p(x,y,z,\omega,t)\cdot p_s^* \, dt\right|^2}{\left[\int_{-\infty}^{+\infty} p_s \cdot p_s^* \, dt\right]\left[\int_{-\infty}^{+\infty} p(x,y,z,\omega,t)\cdot p^*(x,y,z,\omega,t)dt\right]} \\ &= \frac{|H^T C^{-T} D_2|^2}{\left[\int_{-\infty}^{+\infty}[\cos^2(k_z Z_0)/r^2]\,dt\right][H^T C^{-T}(\int_{-\infty}^{+\infty} D_1\cdot(D_1^T)^* dt)(C^{-1})^* H^*]}, \end{aligned} \tag{20}$$

where $r=\sqrt{d^2+h^2+(\nu t)^2}$. $[C]$ is the matrix of coefficients defined in Eqs. (B8)–(B11); H, D_1, and D_2 are the vectors defined in Eqs. (15), (16), and (18), respectively.

Using the independent relationship or the orthogonal conditions in Eq. (3) and the integrals for t or r from $-\infty$ to $+\infty$, the coherence calculation can be greatly simplified because of the removal of the impact items from the road traffic. Equation (20) also implies that the averaged coherence is mainly determined by the locations of the room, the window, and the road.

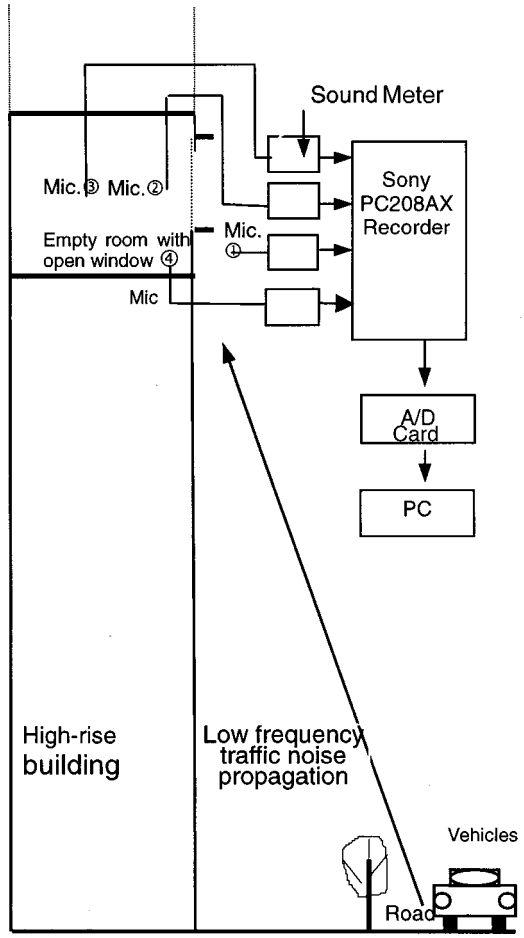

FIG. 3. The schematic of an experiment for investigating the coherence of traffic noise.

III. EXPERIMENTS

To verify experimentally the present theoretical method, we require the simultaneous measurement of sound pressures inside the test room in a high-rise building and outside the open window room. Two similar, empty rectangular rooms were chosen, located on the 17th floor (Room 1704) and the 30th floor (Room 3004) in a 34 floor high-rise building. The building is the central one of ten new, empty buildings named Yeuliang Wan Square, located on the north side of Coacheng Men Road in Nanjing City, China. Except for vehicle traffic noise from the road, there is no obvious noise transmitted into the rooms of the building.

Between the building and the road, there is grassland and no other obstacles, and the distance d between the building and the road is 168 m. The two rooms studied have a slide window centered on the south wall of the rooms facing the road, and a door on the north back wall of the rooms. During the measurements, the doors of the rooms were closed and the slide windows were fully opened, as shown in Fig. 2.

The measurements were carried out between 14:00 and 18:00, when the traffic flows on Coacheng Men Road were 1300–1950 vehicles/h. During each measurement period of five minutes, the traffic flow numbers were obtained.

A schematic of the measurement system is shown in Fig. 3. An eight-channel digital recorder (type Sony PC208AX)[16] was used for simultaneously recording the road sound pressure signals inside the room and those outside the open window room. The frequency bandwidth of the PC208AX is 5 kHz at normal speed and 10 kHz at double speed. One reference sensor was set at a position of outside the open window, locating at $P_0(X_0,Y_0,Z_0)$, and the other two to three sensors were arranged inside the room for measuring the sound pressure separately at the positions of $P_1(X_i,Y_i,Z_i)$ $(i=1,\ 2,\ \text{or}\ 3)$, typically representing the different receivers that outside the opening window, that at the center of the room, and that in front of the open window inside the room, or that at the corner of the room. A type 2610 Bruel & Kjaer measurement amplifier was connected between the reference sensor and the recorder. Type 2230, type 2235, and type 2215 B&K precision sound level meters were used to measure pressures at the center sensor, the front sensor, and the corner sensor inside the room.

After the one-site measurements, the instruments were moved back to the laboratory at Nanjing University. Using an A/D card attached to the recorder, the recorded signals (on a DAT cassette) were transmitted into a personal computer as digital time series data. They were then used to evaluate the expressions for the coherence in the frequency domain according to the coherence definition.[17]

All the sensor locations were listed in Table I. After the experiments, these parameters were used to compute the coherence between the reference sensor location $P_0(X_0,Y_0,Z_0)$ and the error sensor location $P_1(x_i,y_i,z_i)$ using the proposed theoretical coherence calculation method. In the calculation, the thickness of the window and the walls were assumed to be the same. The mode number m or p was truncated at (0,1,2,...,7) and n or q, as (0,1,2,...,9), in accordance with the room dimensions. That is, the total number, NN, is 80, chosen according to the cutoff frequency f_{mn} shown in the following equations, (21) and (22), for frequencies below 200 Hz. The room dimensions in the x and y directions[18] were approximated as a case between a short duct with one end sealed and a small rectangular room with the door and window closed, but not completely the same as the sound propagating in the duct or in the room because of the open window at the other end or the wall:

$$f_{mn}\approx\frac{c}{2}\sqrt{\left(\frac{m}{l_x}\right)^2+\left(\frac{n}{l_y}\right)^2}, \tag{21}$$

$$N\approx\frac{4\pi f^2V}{3c^3}+\frac{\pi f^2S}{4c^2}+\frac{fL}{8c}, \tag{22}$$

where N is the average wave number for different frequency f; V, S, and L are, respectively, the volume, the internal surface area, and the total edge length of the rectangular room.

For programming the coherence calculation, special consideration needs to be paid to Eq. (B11) since the integral has a singularity when $X=X'$ and $Y=Y'$. The detailed calculation is shown in Appendix E.

The calculated and experimental coherence results are shown in Figs. 4(a)–(g). The figure shows that the coherences calculated using the proposed method are generally in good agreement with the experimental results.

TABLE I. Parameters of the rooms and the locations of the sensors in the experimental building.

Room number	Room 1704	Room 3004	Notes[a]
Room dimensions	$l_x=2.62$ m	$l_x=2.62$ m	
$(l_x\times l_y\times l_z$ m$^3)$	$l_y=4.60$ m	$l_y=4.60$ m	
	$l_z=3.50$ m	$l_z=3.50$ m	
Window dimensions	$a=1.35$ m	$a=1.35$ m	$b=2.30$ m when no glass window; $b=1.15$ m when the slide window is moved and opened completely.
$(a\times b$ m$^2)$	$b=1.15$ m	$b=1.15$ m	
	$(a''=1.05$ m)	$(a''=1.05$ m)	
Reference sensor	$X_0=0.68$	$X_0=0.68$	The reference sensor points were above the movable slide window surface.
location	$Y_0=-0.29$	$Y_0=-0.29$	
$P_0(X_0,Y_0,X_0)$	$Z_0=-0.10$	$Z_0=-0.10$	
	$X_0=-0.20$		The reference sensor point in room 1704 was below the windowsill.
	$Y_0=-0.29$		
	$Z_0=-0.10$		
Center sensor location	$x=1.25$	$x=1.27$	
$P_1(x,y,z)$	$y=2.30$	$y=2.30$	
	$z=1.75$	$z=2.19$	
Front sensor location	$x=1.25$	$x=1.24$	
$P_1(x,y,z)$	$y=2.30$	$y=2.30$	
	$z=0.25$	$z=0.25$	
Corner sensor location		$x=0.35$	The corner point at the room 3004 was near the front wall.
$P_1(x,y,z)$		$y=0.20$	
		$z=0.30$	

[a]The detailed meanings of the parameters are shown in Fig. 2.

It can be seen in Fig. 4 that the calculated coherence values tend to be a little larger than the experimental values. This is likely due to the simplifications and approximations in the theoretical calculation method. For example, in the real measurement situation, vehicles on the road would move at a varying speed and the noise strength of any one vehicle would also vary—this is not included in the proposed method. Other background noise, such as stochastic horn sounds from the vehicles (mainly lower-frequency components) can cause the sound pressure values to give poor coherence between the reference sensor and the error sensor. In addition, the difference in thickness of the open window, the closed door, and the walls has not been considered and the open window boundary has been treated as a rigid baffle. Finally, sound absorption has not been included in this calculation. In general, it is believed that the errors are not serious and that acceptable values of coherence are predicted at lower frequencies.

As can be anticipated, the calculated values at low frequencies below 20–50 Hz approaching unity. The experimental coherence curves at these low frequencies are low because of the instrumental limitations of the sound level meters.

The above comparisons demonstrate the usefulness of the proposed method for predicting the coherence. It will be of assistance in determining the physical limitations for the implementation of active traffic noise control in high-rise buildings.

IV. NUMERICAL EXAMPLE CALCULATION, PREDICTION, AND THEIR DISCUSSIONS

In this section, the coherence functions are calculated for a hypothetical room. The room length l_z is 4.2 m, the width l_y is 3.3 m, and the height l_x is 2.6 m, the size of a typical living room. The dimensions, a and b, of the open window are 1.4×1.4 m^2, centered in the y direction, and the height a'' of the windowsill is 0.9 m. The room is on the 20th floor with a height h of 53 m. The distance d between the road and the building, is 200 m. The vehicle speed v, on the road is assumed to be 40 km/h. A reference point outside the window was chosen at $P_0(X=-0.2$ m, $Y=0.0$ m, $Z=-0.1$ m), and the two receiver (observation) points inside the room were selected at $P_1(x=0.7$ m, $y=3.0$ m, $z=2.0$ m), which could be a reasonable location for placing a bed, or $P_1(x=l_x/2$ m, $y=l_y/2$ m, $z=l_z/2$ m), which is at the center of the room. The coherence functions $\gamma^2(f)$ of P_1 to P_0 were calculated for frequencies below 200 Hz. The road segment impacting the sound pressure at the receivers was chosen with length of $2L$ or time of $2L/v$ as 300 s.

For the simulation, the mode number m or p was truncated at (0,1,2,...,7), and n or q, at (0,1,2,...,9), that is, the total number[18] NN is 80.

The numerical results are shown in Fig. 5. From this figure, we can see the tendency of the coherence curves. As expected, the coherence at very low frequencies approaches unity, although the results below 20 Hz have little relevance to human hearing. When the location of receiving point $P_1(x,y,z)$ is changed, the coherence result is also different because of the phenomena of stationary waves.

In Fig. 5, one coherence curve has been produced assuming that the vehicle speed v is identically zero. The result approaches 1.00 for all frequencies. It can be expected that the coherence for fixed (not moving) monopoles on the road is 1.00, so this calculation provides a check on the validity of the proposed theory.

When the dimensions, a and b, of the open window are chosen at 1.0×0.7, 1.0×1.4, or 1.4×0.7 m^2, with $P_1(x=0.7$ m, $y=3.0$ m, $z=2.0$ m), the coherence curves shown in Fig. 6 are obtained. The figure indicates that the dimensions

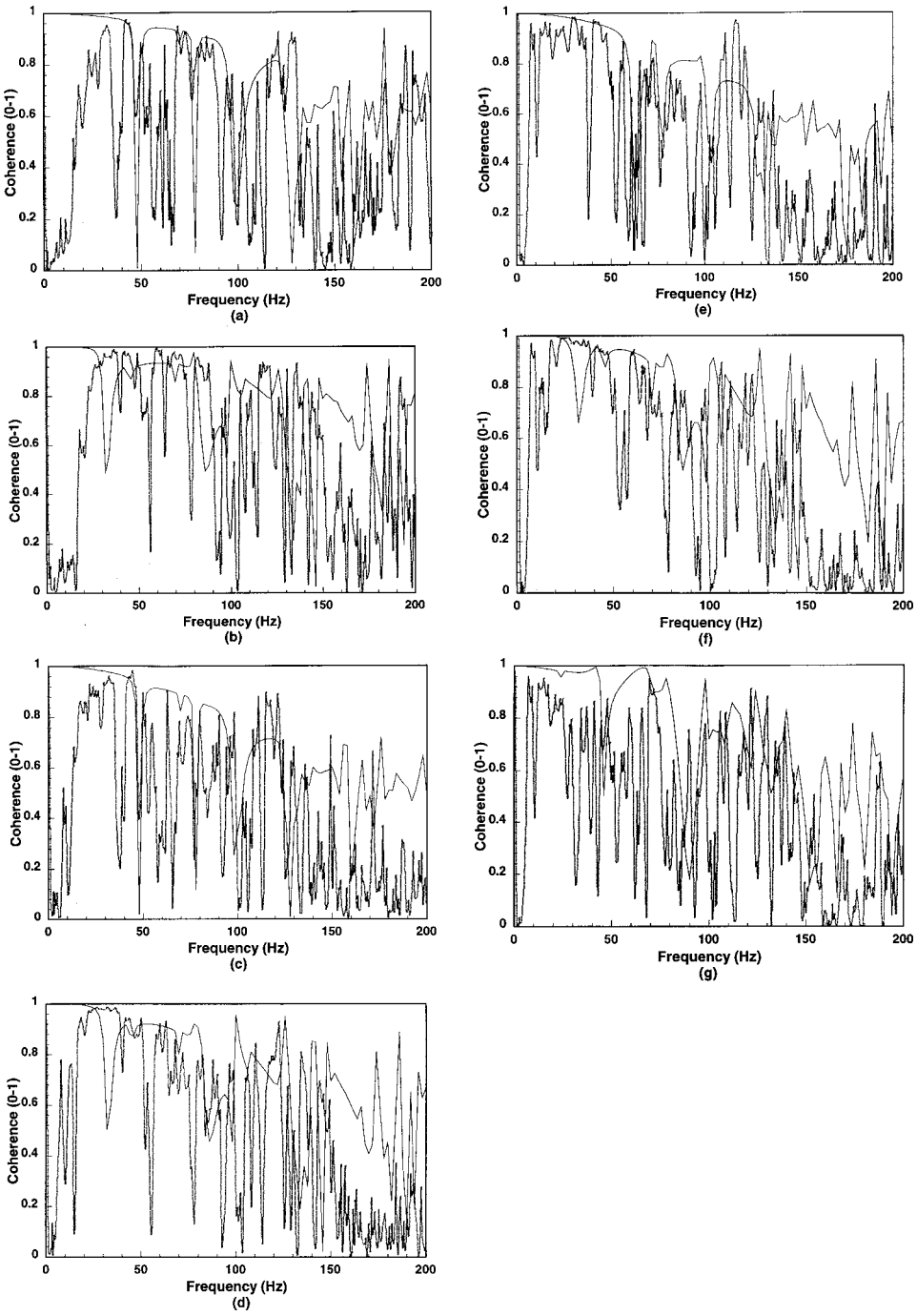

FIG. 4. (a)–(g); A comparison between the calculated coherence value curves and the experimental ones (—calculation; --- experiment). (a) On the 17th floor, P_1 at the center of the room, P_0 below the windowsill; traffic flow is 1848 vehicles/hour. (b) On the 17th floor, P_1 in the front of the room window, P_0 below the windowsill; traffic flow is 1848 vehicles/hour. (c) On the 17th floor, P_1 at the center of the room, P_0 above the slide not open window part; traffic flow is 1920 vehicles/hour. (d) On the 17th floor, P_1 in the front of the room window, P_0 above the slide not open window part; traffic flow is 1920 vehicles/hour. (e) On the 30th floor, P_1 at the center of the room, P_0 above the slide not open window part; traffic flow is 1365 vehicles/hour. (f) On the 30th floor, P_1 in the front of the room window, P_0 above the slide not open window part; traffic flow is 1365 vehicles/hour. (g) On the 30th floor, P_1 at the corner of the room, P_0 above the slide not open window part; traffic flow is 1365 vehicles/hour.

of the open window affects the shape of the coherence curves.

When the location of point $P_0(X,Y,Z)$ was changed, the coherence results also changed. Figure 7 shows the curves for $P_0(X=0.700,\ Y=-0.175,\ Z=-0.100)$, $P_0(X=0.700,\ Y=+0.175,\ Z=-0.100)$, and $P_0(X=-0.200,\ Y=0.000,\ Z=-0.100)$, all with $P_1(x=0.7$ m, $y=3.0$ m, $z=2.0$ m).

Similar calculations were performed to determine the effect of distant roads, high building floors, and different vehicle speeds. The coherence functions were nearly independent of the parameters h, d, and v. Although these parameters have little impact on the farfield coherence properties, they do have an important effect on the spectrum of moving vehicles in the frequency domain [see Eqs. (1) and (2)]. Therefore, with larger parameters h and d, and smaller v, i.e., a room in a very tall building with the road far away, the sound of the road traffic noise outside the open window and inside the room are dominated by very low frequencies, so such situations satisfy the conditions for a high coherence.

From Figs. 5–7, we find that the coherent curves may be the best candidates for a feedforward control strategy at very low frequencies, at least below 150 Hz. At higher frequencies, more than one reference sensor would need to be considered. It should be noted that the effect of A weighting for sound pressure has not been included in the calculations of the coherence functions.

V. CONCLUSIONS

The sound field in a rectangular room caused by road traffic noise was investigated in this paper, using wave

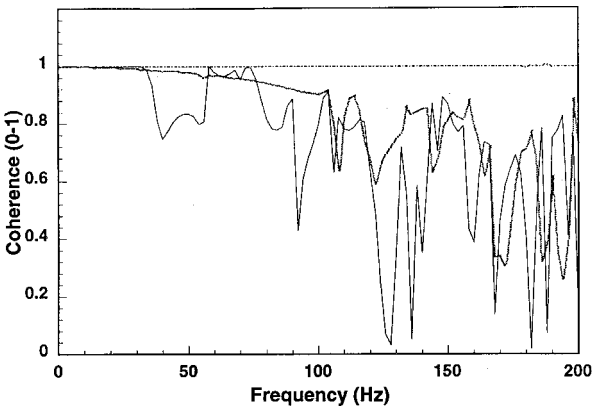

FIG. 5. Calculated coherence curves of the numerical examples. Legend: —, $v=40$ Km/h, P_1 ($x=0.7$ m, $y=3.0$ m, $z=2.0$ m)/P_0 ($X=-0.2$ m, $Y=0.0$ m, $Z=-0.1$ m); ---, $v=40$ Km/h, P_1 ($x=l_x/2$ m, $y=l_y/2$ m, $z=l_z/2$ m)/P_0 ($X=-0.2$ m, $Y=0.0$ m, $Z=-0.1$ m); --·--, $v=0$ Km/h, P_1 ($x=0.7$ m, $y=3.0$ m, $z=2.0$ m)/P_0 ($X=-0.2$ m, $Y=0.0$ m, $Z=-0.1$ m).

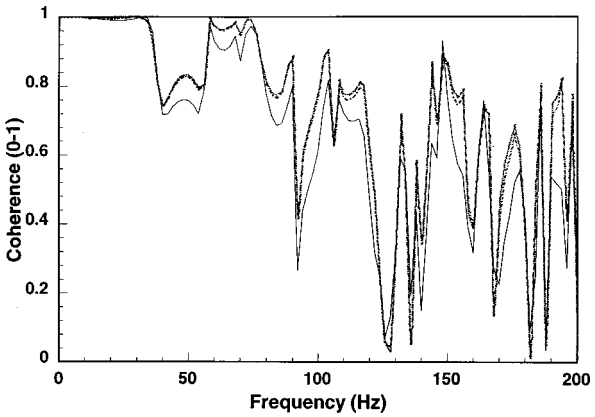

FIG. 7. Coherence curves of the numerical example with changes of P_0 locations when P_1 ($x=0.7$ m, $y=3.0$ m, $z=2.0$ m) and $a\times b=1.4\times1.4$ m^2. Legend: —, P_0 ($X=0.700$, $Y=-0.175$, $Z=-0.100$); ---, P_0 ($X=-0.200$, $Y=0.000$, $Z=-0.100$); --·--, P_0 ($X=0.700$, $Y=+0.175$, $Z=-0.100$).

theory, modal analysis, and a traffic noise model. A method for predicting the coherence between the sound pressure inside a rectangular room in a high-rise building and that outside the opening window of the room was derived theoretically. Finally, the coherence functions were calculated and verified by experiment. The experience shows that the calculated results with the proposed calculation method are generally in good agreement with the experimental results.

The new method has some distinct advantages over existing ones for such a noise transmission system. First, a room with an open window has been studied rather than using the front or end wall fully opened to approximate a real open window. Second, the calculated coherence results show that all of the items related to every one of vehicles do not appear with the orthogonality on a road, which has made the theoretical calculations for the coherence possible. And third, this work has focused on the low-frequency traffic noise far away from a road, so damping and absorption were not considered for simplicity. If the impact of damping and absorption is added, it is easy to expand the calculation to the middle- or higher-frequency range, which could lead to a meaningful extension to the method of prediction of traffic noise from outdoor to indoor.

Because of the complexity of wave theory, the proposed method or idea is mainly used for a rectangular or a regular room. Consequently, with this approach, we can make some preliminary qualitative predictions concerning the potential and limitations of applying active noise control technology to the open window room in high-rise buildings. For a room of arbitrary shape, other methods such as FEM, BEM, or experimental measurement should be considered, but it may then be difficult to get a physical insight.

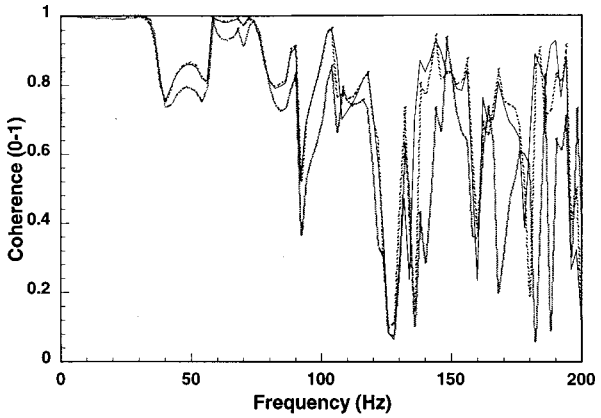

FIG. 6. Coherence curves of the numerical example with changes of a and b; P_1 ($x=0.7$ m, $y=0.3$ m, $z=2.0$ m)/P_0 ($X=-0.2$ m, $Y=-0.175$ m, $Z=-0.1$ m). Legend: —, $a=1.0$, $b=0.7$; ---, $a=1.0$, $b=1.5$; --·--, $a=1.4$, $b=0.7$.

ACKNOWLEDGMENTS

This work was supported by the Environmental Protection Agency in Zhejiang province as a science and technology project numbered 9809 and by the State Key Lab of Modem Acoustics at Nanjing University as an opening scientific research project numbered 9906 (listed in time turn).

APPENDIX A

We assume that a single vehicle on the road, located at the point $R(x,y,z)$ (shown in the diagram in this appendix) can be represented as a monopole with amplitude A_{suj}. The sound is incident at angles θ_i and Ψ_i on the surface (window boundary $z=0$). The equation for the incoming wave is given as

$$P_i(R,R_0)=A_{suj}\cdot\exp(-ik|R-R_0|)/(4\pi|R-R_0|), \tag{A1}$$

where

$$|R-R_0|=\sqrt{(x_0-x)^2+(y_0-y)^2+(z_0-z)^2}.$$

The wave reflected from the window surface with amplitude B_{suj} must have the form as follows:

$$P_s(R_1,R_0)=B_{suj}\cdot\exp(-ik|R_1-R_0|)/(4\pi|R_1-R_0|), \tag{A2}$$

where $|R_1-R_0|=\sqrt{(x_0-x)^2+(y_0-y)^2+(z_0+z)^2}$, i.e., it is an image of the monopole with amplitude B_{suj}; (x_0,y_0,z_0) is located near the boundary surface, with the assumption

that the surface of the open window has an average reflection coefficient Cr', and $Cr'=B_{suj}/A_{suj}$.

The farfield pressures at the boundary can be obtained by expanding the distances $|R-R_0|$ and $|R_1-R_0|$ for large r. Thus

$$|R-R_0|\approx r(1-x\cdot x_0/r^2-y\cdot y_0/r^2-z\cdot z_0/r^2), \qquad \text{(A3)}$$

where $r=\sqrt{x^2+y^2+z^2}$. A similar expression for $|R_1-R_0|$ can be obtained with z replaced by $-z$. The farfield pressures in the case of the open window boundary are then obtained by substituting these expansions into Eqs. (A1) and (A2). That is,

$$P_i(r,\theta_i,\Psi_i)=A_{suj}\cdot\exp(-ikr)\exp[-ik(x\sin\theta_i\cdot\cos\Psi_i + y\sin\theta_i\cdot\sin\Psi_i+z\cos\theta_i)]/4\pi r,$$

$$P_s(r,\theta_i,\Psi_i)=Cr'\cdot A_{suj}\cdot\exp(-ikr)\exp[-ik(x\sin\theta_i \cdot\cos\Psi_i+y\sin\theta_i\cdot\sin\Psi_i-z\cos\theta_i)]/4\pi r.$$

The total pressure in the farfield is

$$\begin{aligned}P(R,\theta_i,\Psi_i)&=P_i(R,\theta_i,\Psi_i)+P_s(R,\theta_i,\Psi_i)\\&=A_{suj}\cdot\exp(-ikr)\exp[-ik(x\cdot\sin\theta_i\cdot\cos\Psi_i\\&\quad+y\cdot\sin\theta_i\sin\Psi_i)][\exp(-ikz\cos\theta_i)\\&\quad+Cr'\exp(+ikz\cos\theta_i)]/4\pi r\\&=A_{suj}\cdot\exp(-ikr)\exp[-i(k_x\cdot x+k_y\cdot y)]\\&\quad\cdot\exp(-ik_z\cdot z)+Cr'\exp(+ik_z\cdot z)]/4\pi r.\end{aligned} \qquad \text{(A4)}$$

If $Cr=0$, the boundary is soft,

$$\begin{aligned}P(R,\theta_i,\Psi_i)&=A_{suj}\cdot\exp(-ikr)\exp[-ik(x\cdot\sin\theta_i\cdot\cos\Psi_i\\&\quad+y\cdot\sin\theta_i\sin\Psi_i+z\cos\theta_i)]/4\pi r\\&=P_i(R,\theta_i,\Psi_i),\end{aligned}$$

i.e., there exists only an incident wave. And if $Cr=1$, the boundary is hard,

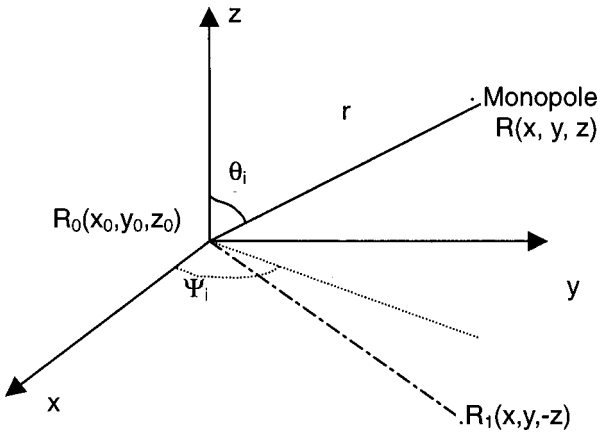

Diagram 1: sound reflecting by a window open surface.

$$\begin{aligned}P(R,\theta_i,\Psi_i)&=P_i(R,\theta_i,\Psi_i)+P_s(R,\theta_i,\Psi_i)\\&=A_{suj}\cdot\exp(-ikr)\exp[-ik(x\cdot\sin\theta_i\cdot\cos\Psi_i\\&\quad+y\cdot\sin\theta_i\sin\Psi_i)]\cos(k\cdot z\cdot\cos\theta_i)/2\pi r.\end{aligned}$$

In order to simplify the solution for the low-frequency noise, the open window boundary is assumed to act as a rigid baffle, where the velocity in the normal direction will be zero (such an approximation has been applied by Kropp and Berillon in Ref. 12), so that $Cr'\approx 1$.

Using Eq. (11) from earlier in the text, one can get Eq. (12) as

$$\begin{aligned}p_s&=p_{\text{in}}+p_{\text{re}}\\&=\sum_{s=1}^{2}\sum_{u=1}^{3}\sum_{j=0}^{N_{su}}\frac{2A_{suj}}{4\pi r_{suj}}\exp[i(\omega t-k_{suj}r_{suj})]\\&\quad\times\exp[-i(k_x x+k_y y)]\cos(k_z z).\end{aligned}$$

APPENDIX B

From Eq. (7),

$$p(x,y,0,\omega,t)=\sum_{m=0}^{\infty}\sum_{n=0}^{\infty}A_{mn}\exp(-ik_{mn}l_z)\times\cos\left(\frac{m\pi x}{l_x}\right)\cos\left(\frac{n\pi y}{l_y}\right)\cos(k_{mn}l_z)\exp(i\omega t). \qquad \text{(B1)}$$

For $p(x,y,0,\omega,t)$, a limited Fourier cosine transformation is made to simplify the calculation by using orthogonality:

$$\begin{aligned}P_{m'n'}&=\int_0^a\int_0^b p(x,y,0,\omega)\cos\left(\frac{m'\pi X}{a}\right)\times\cos\left(\frac{n'\pi Y}{b}\right)\exp(i\omega t)\,dX\,dY\\&\quad{}^{m=m',n=n'}\\&=\quad P_{mn}=abA_{mn}\exp(-ik_{mn}l_z)\times\cos(k_{mn}l_z)I_1(m)I_2(n)\exp(i\omega t),\end{aligned} \qquad \text{(B2)}$$

where the detailed expressions for $I_1(m)$ and $I_2(n)$ are represented in Appendix C. Then, making an inverse limited Fourier Cosine transformation to P_{mn}, we can get

$$p(X,Y,0,\omega,t)=\sum_{m=0}^{\infty}\sum_{n=0}^{\infty}KK'A_{mn}\exp(-ik_{mn}l_z)\times\cos(k_{mn}l_z)I_1(m)I_2(n)\times\cos\left(\frac{m\pi X}{a}\right)\cos\left(\frac{n\pi Y}{b}\right)\exp(i\omega t), \qquad \text{(B3)}$$

where

$$KK'=\begin{cases}1 & (when\ \ m=0\ \ and\ \ n=0),\\ 2 & (when\ \ m=0\ \ and\ \ n\neq 0,\ or\\ & \ \ m\neq 0\ \ and\ \ n=0),\\ 4 & (when\ \ m\neq 0\ \ and\ \ n\neq 0).\end{cases}$$

Similarly, $v_z=-(1/i\rho\omega)(\partial p/\partial z)$,

$$v_z(X,Y,0,\omega,t)=-\frac{1}{i\rho\omega}\sum_{m=0}^{\infty}\sum_{n=0}^{\infty}A_{mn}k_{mn}\exp(-ik_{mn}l_z)\times\cos\left[\frac{m\pi}{l_x}(X+a'')\right]\cos\left[\frac{n\pi}{l_y}\left(Y+\frac{l_y-b}{2}\right)\right]\times\sin(k_{mn}l_z)\exp(i\omega t). \tag{B4}$$

For $v_z(X,Y,0,\omega,t)$, a limited Fourier cosine transformation is made to simplify the calculation by self-orthogonality:

$$\begin{aligned}V_{z_{m''n''}}&=\int_0^a\int_0^b v_z(x,y,0,\omega)\cos\left(\frac{m''\pi X}{a}\right)\times\cos\left(\frac{n''\pi Y}{b}\right)\exp(i\omega t)dX\,dY\\&=\int_0^{l_x}\int_0^{l_y}v_z(x,y,0,\omega)\cos\left(\frac{m''\pi}{a}(x-a'')\right)\times\cos\left(\frac{n''\pi}{b}\left(y-\frac{l_y-b}{2}\right)\right)\exp(i\omega t)dx\,dy,\end{aligned} \tag{B5}$$

$$\begin{aligned}{}^{m=m'',n=n''}&=V_{z_{mn}}=-\frac{l_xl_y}{\rho\omega}A_{mn}k_{mn}\exp(-ik_{mn}l_z)\\&\times\sin(k_{mn}l_z)\mathrm{II}_1(m)\mathrm{II}_2(n)\exp(i\omega t),\end{aligned}$$

where $\mathrm{II}_1(m)$ and $\mathrm{II}_2(n)$ are presented in Appendix C. Then, an inverse-limited Fourier cosine transformation is made to $v_{z_{mn}}$, giving

$$v_z(X,Y,0,\omega,t)=-\frac{l_xl_y}{iab\rho\omega}\sum_{m=0}^{\infty}\sum_{n=0}^{\infty}KK'A_{mn}k_{mn}\times\exp(-ik_{mn}l_z)\sin(k_{mn}l_z)\mathrm{II}_1(m)\mathrm{II}_2(n)\times\cos\left(\frac{m\pi X}{a}\right)\cos\left(\frac{n\pi Y}{b}\right)\exp(i\omega t). \tag{B6}$$

Substituting Eqs. (11), (12), (13), (B1), (B3), (B6), and $v_{s_z}=-(1/i\rho\omega)(\partial p_s/\partial z)|_{z=0}=0$ into the successive conditions in Eqs. (8) and (9), one can get an infinite set of linear equations for A_{mn}:

$$\sum_{m=0}^{\infty}\sum_{n=0}^{\infty}C_{mn}(p,q)A_{mn}=D(p,q), \tag{B7}$$

$$C_{mn}(p,q)=[C_1(p,q)\delta(p-m)\delta(q-n)+C_2(m,n)C_3(m,n)], \tag{B8}$$

where

$$C_1(p,q)=\exp(-ik_{pq}l_z)\cos(k_{pq}l_z)I_1(p)I_2(q), \tag{B9}$$

$$C_2(m,n)=KK'\frac{l_xl_y}{2\pi a^2b^2}k_{mn}\exp(-ik_{mn}l_z)\sin(k_{mn}l_z)\times\mathrm{II}_1(m)\mathrm{II}_2(n), \tag{B10}$$

$$C_3(m,n)=\int_S\int_{S'}\frac{\cos\left(\frac{m\pi}{a}X\right)\cos\left(\frac{n\pi}{b}Y\right)\cos\left(\frac{m\pi}{a}X'\right)\cos\left(\frac{n\pi}{b}y'\right)}{r_z}\exp(-ikr_z)dS\,dS', \tag{B11}$$

$$D_{pq}=\frac{1}{ab}\sum_{s=1}^{2}\sum_{u=1}^{3}\sum_{j=1}^{N_{su}}\frac{2A_{suj}}{4\pi r_{suj}}\exp[-ik_{suj}r_{suj}]\cdot\exp\left[-i\left(k_xa''+k_y\frac{l_y-b}{2}\right)\right]\times\frac{(-1)k_xk_y[\exp(-ik_xa)\cos(p\pi)-1]\exp(-ik_yb)\cos(q\pi)-1]}{\left[k_x^2-\left(\frac{p\pi}{a}\right)^2\right]\left[k_y^2-\left(\frac{q\pi}{b}\right)^2\right]}, \tag{B12}$$

and $m,s,p,q=0,1,2,...,\infty$. For low-frequency traffic noise, m, n, p, and q can be truncated as $0,1,2,...,N$. Consequently, Eqs. (B7)–(B12) can be written in a more compact matrix form. Let us define

$$\vec{D}=[D]=(D_{00},D_{01},D_{02},\ldots,D_{0N},D_{10},\ldots D_{1N},D_{2N},\ldots D_{N0},D_{N1},\ldots D_{NN})^T,$$

$$\vec{A}=[A]=(A_{00},A_{01},A_{02},\ldots,A_{0N},A_{10},\ldots A_{1N},A_{2N},\ldots A_{mn},\ldots A_{N0},A_{N1},\ldots A_{NN})^T,$$

$$[C]=[C_{00}(p,q),C_{01}(p,q),\ldots,C_{0N}(p,q),C_{10},\ldots C_{1N},\ldots C_{mn}(p,q)\ldots C_{N0},\ldots C_{NN}]^T,$$

so

$$A=C^{-T}D. \tag{B13}$$

APPENDIX C:

Equation (B2) is simplified by the following derivations:

$$\int_0^a \cos\left[\frac{m\pi}{l_x}(X+a'')\right]\cos\left[\frac{m\pi X}{a}\right]dX = a \quad (m=0)$$

$$\overset{m\neq 0}{=} \frac{al_x}{m\pi(a-lx)}\sin\left(\frac{am\pi}{2lx}-\frac{m\pi}{2}\right)\cos\left[\frac{m\pi(a+2a'')}{2lx}-\frac{m\pi}{2}\right] + \frac{al_x}{m\pi(a+lx)}\sin\left(\frac{am\pi}{2lx}+\frac{m\pi}{2}\right)\cos\left[\frac{m\pi(a+2a'')}{2lx}+\frac{m\pi}{2}\right], \tag{C1}$$

$$\int_0^b \cos\left[\frac{n\pi}{l_y}\left(Y+\frac{ly-b}{2}\right)\right]\cos\left[\frac{n\pi Y}{b}\right]dY = b \quad (n=0)$$

$$\overset{n\neq 0}{=} \frac{bl_y}{n\pi(b-ly)}\sin\left(\frac{bn\pi}{2ly}-\frac{n\pi}{2}\right)+\frac{bl_y}{n\pi(b+ly)}\sin\left(\frac{bm\pi}{2ly}+\frac{n\pi}{2}\right)\cos[n\pi]. \tag{C2}$$

We define

$$I_1(m)=\begin{cases} 1 \quad (m=0), \\ \dfrac{l_x}{m\pi(a-lx)}\sin\left(\dfrac{am\pi}{2lx}-\dfrac{m\pi}{2}\right)\cos\left[\dfrac{m\pi(a+2a'')}{2lx}-\dfrac{m\pi}{2}\right] \\ \quad + \dfrac{l_x}{m\pi(a+lx)}\sin\left(\dfrac{am\pi}{2lx}+\dfrac{m\pi}{2}\right)\cos\left[\dfrac{m\pi(a+2a'')}{2lx}+\dfrac{m\pi}{2}\right] \quad (m\neq 0); \end{cases} \tag{C3}$$

$$I_2(n)=\begin{cases} 1 \quad (n=0), \\ \dfrac{l_y}{n\pi(b-ly)}\sin\left(\dfrac{bn\pi}{2ly}-\dfrac{n\pi}{2}\right)+\dfrac{l_y}{n\pi(b+ly)}\sin\left(\dfrac{bm\pi}{2ly}+\dfrac{n\pi}{2}\right)\cos[n\pi] \quad (n\neq 0). \end{cases} \tag{C4}$$

Equation (B5) is simplified by the following derivations:

$$\int_0^{lx} \cos\left[\frac{m\pi}{l_x}x\right]\cos\left[\frac{m\pi}{a}(x-a'')\right]dx = l_x \quad (m=0)$$

$$\overset{m\neq 0}{=} \frac{al_x}{m\pi(a+lx)}\sin\left(\frac{a+l_x}{2a}m\pi\right)\cos\left(\frac{a+l_x-2a''}{2a}m\pi\right) + \frac{al_x}{m\pi(a-lx)}\cos\left(\frac{a-l_x+2a''}{2a}m\pi\right)\sin\left(\frac{a-l_x}{2a}m\pi\right); \tag{C5}$$

$$\int_0^{ly} \cos\left[\frac{n\pi}{l_y}y\right]\cos\left[\frac{n\pi}{b}\left(y-\frac{ly-b}{2}\right)\right]dy = l_y \quad (n=0)$$

$$\overset{n\neq 0}{=} \frac{bl_y}{n\pi(b+ly)}\sin\left(\frac{b+l_y}{2b}n\pi\right)\cos(n\pi)+\frac{bl_y}{n\pi(b-ly)}\sin\left(\frac{b-l_y}{2ly}n\pi\right). \tag{C6}$$

We define

$$\mathrm{II}_1(m)=\begin{cases} 1 \quad (m=0), \\ \dfrac{a}{m\pi}\left[\dfrac{1}{(a+lx)}\sin\left(\dfrac{a+l_x}{2a}m\pi\right)\cos\left(\dfrac{a+l_x-2a''}{2a}m\pi\right)+\dfrac{1}{(a-lx)}\cos\left(\dfrac{a-l_x+2a''}{2a}m\pi\right)\sin\left(\dfrac{a-l_x}{2a}m\pi\right)\right] \quad (m\neq 0); \end{cases} \tag{C7}$$

$$\mathrm{II}_2(n)=\begin{cases} 1 \quad (n=0), \\ \dfrac{b}{n\pi}\left[\dfrac{1}{(b+ly)}\sin\left(\dfrac{b+l_y}{2b}n\pi\right)\cos(n\pi)+\dfrac{1}{(b-ly)}\sin\left(\dfrac{b-l_y}{2ly}n\pi\right)\right] \quad (n\neq 0). \end{cases} \tag{C8}$$

APPENDIX D:

In order to apply Eq. (3) to remove the term $|A_{suj}|^2$, the following deduction is made for Eq. (17):

$$\int_{-\infty}^{+\infty} p(x,y,z,\omega,t)\cdot p^*(x,y,z,\omega,t)dt = \int_{-\infty}^{+\infty} (H^T A)(H^T A)^*\, dt$$

$$= \int_{-\infty}^{+\infty} (H^T A)[(H^T A)^*]^T\, dt$$

$$= \int_{-\infty}^{+\infty} H^T (C^{-T} D_1)[(C^{-T} D_1)^T H]^*\, dt$$

$$= \int_{-\infty}^{+\infty} H^T (C^{-T} D_1)[D_1^T C^{-1} H]^*\, dt$$

$$= H^T C^{-T}\left[\int_{-\infty}^{+\infty} D_1 (D_1^T)^*\, dt\right](C^{-1})^* H^*. \tag{D1}$$

APPENDIX E:

For Eq. (B11),

$$C_3(m,n) = \int_S \int_{S'} \frac{\cos\left(\frac{m\pi}{a}X\right)\cos\left(\frac{n\pi}{b}Y\right)\cos\left(\frac{m\pi}{a}X'\right)\cos\left(\frac{n\pi}{b}Y'\right)}{r_z}\exp(-ikr_z)dS\,dS'. \tag{E1}$$

For the separated part where ($r_z \approx 0$) or ($X \approx X'$ and $Y \approx Y'$):

$$\approx \frac{a}{step_1}\frac{a}{step_2}\frac{b}{step_1}\frac{b}{step_2}\int_0^{step_1}\int_0^{step_2}\int_0^{step_1}\int_0^{step_2} \cos^2\left(\frac{m\pi X}{a}\right)\cos^2\left(\frac{n\pi Y}{b}\right)\frac{\exp(-ikr_z)}{r_z}dX\,dY\,dX'\,dY'$$

$$= \left(\frac{ab}{step_1\cdot step_2}\right)^2 \int_0^{step_1}\int_0^{step_2} \cos^2\left(\frac{m\pi X}{a}\right)\cos^2\left(\frac{n\pi Y}{b}\right)dX\,dY \int_0^{2\pi}\int_0^{R} \exp(-ikr_z)d\theta\,dr_z$$

$$= \frac{2\pi i}{k}\left(\frac{ab}{step_1\cdot step_2}\right)^2 [\exp(-ikR)-1]\left[\frac{step_1}{2} + \frac{a}{4m\pi}\sin\left(\frac{2m\pi\cdot step_1}{a}\right)\right]\left[\frac{step_2}{2} + \frac{b}{4n\pi}\sin\left(\frac{2n\pi\cdot step_2}{b}\right)\right], \tag{E2}$$

where $step_1$ and $step_2$ denote the smallest unit by which the parameters a and b are divided into small parts, respectively.

Because $dS = dS' = \pi R^2 \approx step_1\cdot step_2$,

$$R = \sqrt{\frac{step_1\cdot step_2}{\pi}}. \tag{E3}$$

[1] M. Nieemas, "Vibration and noise in dwellings generated by traffic," *Proceedings of Inter-Noise 97*, Budapest, Hungary, 25–27 August 1997, pp. 555–558.

[2] R. W. Guy, "The steady state transmission of sound at normal and oblique incidence through a thin panel backed by a rectangular room—a multimodal analysis," Acustica **43**, 295–304 (1979).

[3] T. Kihlman, "Sound radiation into a rectangular room—applications to airborne sound transmission in buildings," Acustica **18**, 11–20 (1967).

[4] C. H. Hansen and B. S. Cazzolato, "Recent advance in the active control of interior noise," presented at *The 6th International Congress on Sound and Vibration*, 1999, pp. 1–43.

[5] J. Pan and D. Bies, "The effect of fluid–structural coupling on sound waves in an enclosure-theoretical part, experimental part," J. Acoust. Soc. Am. **87**, 691–717 (1990).

[6] J. Pan, C. H. Hansen, and D. A. Bies, "Active control of noise transmission through a panel into a cavity: I. Analytical study, II. Experimental study, III. Effect of the actuator location," J. Acoust. Soc. Am. **87**, 2098–2108 (1990); **90**, 1488–1501 (1991).

[7] S. D. Snyder, "The design of systems to control actively periodic sound transmission into enclosed spaces. Part I: Analytical models; Part II: Mechanisms and trends," J. Sound Vib. **170**, 433–472 (1994).

[8] S. M. Kim and M. J. Brennan, "A comparative study of feedforward control of harmonic and random sound transmission into an acoustic enclosure," J. Sound Vib. **226**, 549–571 (1999).

[9] A. Sampath and B. Balachamdran, "Active control of multipole tones in an enclosure," J. Acoust. Soc. Am. **106**, 211–225 (1999).

[10] D. Duhamel and P. Sergent, "Active noise control of an incoherent line source," J. Sound Vib. **212**, 141–164 (1998).

[11] V. Martin, "Active control of moving sound source radiation-numerical modeling in the space-frequency and space-time domains," J. Sound Vib. **228**, 477–509 (1999).

[12] W. Kropp and J. Berillon, "A theoretical model to investigate the acoustic performance of building facades in the low and middle frequency range," Acustica **84**, 681–688 (1998).

[13] T. Kihlman and W. Wropp, "The influence of room resonance on the propagation of traffic noise into small rooms," *Proceedings of Inter-Noise '98*, Christchurch, NZ, 16–18 November, I-INCE Classification No. 31, 1998, pp. 391–394.

[14] S. M. Kuo and D. Vijayan, "Hybrid active noise control," in *Proceedings of the International Conference on Signal Processing Applications*

& Technology, 1994, pp. 1272–1277.
[15] W. K. Tseng, B. Rafaely, and S. J. Elliot, "Combined feedback-feedforward active control of sound in a room," J. Acoust. Soc. Am. **104**, 3417–3425 (1998).
[16] Sony Company, *PC208AX Instrumentation Cassette Recorder Digital Operation Manual*, 1st ed. (revised 3, 1996.10).
[17] J. S. Bendat and A. G. Piersol, *Engineering Applications of Correlation and Spectral Analysis* (Wiley-Interscience, New York, 1980).
[18] D. Gonghuan, Z. Zheming, and G. Xioufeng, *Basic Acoustics*, 2nd ed. (Nanjing University, Nanjing, 2001), Chap. 5 (in Chinese).

Fuzzy models for accumulation of reported community noise annoyance from combined sources

Dick Botteldooren[a] and Andy Verkeyn
Acoustics Group, Department of Information Technology, Ghent University, St. Pietersnieuwstraat 41, 9000 Gent, Belgium

(Received 14 January 2002; revised 12 July 2002; accepted 15 July 2002)

Many scientists have investigated noise annoyance caused by combined sources. However, general annoyance reported in a social survey still has many unknown features. In this work the cognitive process involved in coming to a general noise rating based on a known, in context, rating of annoyance by particular sources is studied. A comparison of classical and fuzzy models is used for this. The new fuzzy linguistic models give a meaning to the successful strongest component or dominant source model that was used in previous work. They also explain to some extent particular features not included in that previous model. The variance not predicted by the fuzzy linguistic model is contrasted with personal data of the test subjects (age, gender, and education level) and the context of the question in the questionnaire. Only age seems to play a significant role. © *2002 Acoustical Society of America.* [DOI: 10.1121/1.1506366]

PACS numbers: 43.50.Qp, 43.50.Rq [MRS]

I. INTRODUCTION

The assessment of human reaction to a combination of sound originating from different (types of) sources has been a topic of debate for many years. Both laboratory studies and field research have been used to address the problem.

Laboratory studies have used a variety of well-controlled stimuli and assess both loudness and annoyance experience by a group of test subjects.[1–3] Several interesting review articles have been published, comparing the models resulting from this research.[4–6] The classical models used as a reference in this paper are extracted from these studies.

Total noise annoyance reported in social surveys tends to be less accurately predicted using models such as those proposed in Refs. 1–3. This should not surprise the reader too much since several conditions differ significantly between laboratory research and social survey reports. Several authors have outlined complications that arise in field research on combined noise exposure. Ratings for combined annoyance that are lower than expected or even lower than the annoyance caused by one of the sources alone often occur. This is called the principle of compromise by some authors.[4] Others refer to the context in which the annoyance question is presented to the subject as its cause. The wording of annoyance questions and the interpretation of them by subjects may at least partly explain the combined noise sources paradox.[7] Exposure is less clear in field situations than in well-controlled laboratory setups. This may include different time windows for the contributing sources or different direction of incidence. Aircraft noise may be heard all around the house, for example, while road noise is present only in front of the façade. Finally, it has also been proposed that additional elements such as attitude, social environment, and lifestyle[8] or general and specific noise sensitivity[9] may influence the global noise annoyance judgement of combined sources.

Inspired by the difficulties encountered in interpreting and predicting the response to community noise in general as observed by social surveys, some authors have argued that such efforts should not be made all together. They argue that the fundamental annoyance experience is always related to a particular source (traffic, neighbors,$\cdots$) and that asking for a combined rating forces subjects into some kind of mathematical exercise they are not really able to perform. However, when analyzing the quality of the living environment or predicting the impact of a particular policy (e.g., pushing freight transport from road to rail) noise is only a tiny part of the picture. Hence, aggregation of the impact of all sources is required to allow comparing it to other environmental issues. It makes sense to use the opinion of the public as a guideline for this aggregation. Many surveys concerning the quality of life include only questions about the general appreciation of the noise environment. The development of better models for annoyance accumulation remains an important topic of research because it can help to understand how people aggregate and improve total noise impact prediction.

In this paper we introduce a fuzzy rule based model to predict the outcome of a general noise annoyance question in a social survey based on the knowledge of the level of annoyance caused by various individual sources. Rule-based systems are used in artificial intelligence to make predictions based on expert knowledge and classical logic reasoning. A fuzzy rule based model extends classical logic and reasoning to noncrisp variables. The level of noise annoyance indicated by a word (linguistic term), is a typical example of such a noncrisp or fuzzy quantity. This paper does not include an

[a]Electronic mail: dick.botteldooren@intec.rug.ac.be

investigation of the relation between exposure and annoyance nor the modifiers that may influence this relation. Recent work in this field may be found in Refs. 10, 11. The proposed model thus focuses on the cognitive processes involved in general noise annoyance judgement. A subset of the available classical models is reinvestigated for a comparison. Particular attention is paid to the observation that reported general annoyance could be weaker than the stronger partial annoyance. We will refer to this as context dependence since this is the term most often encountered in a fuzzy system. Related terms used in other publications are ''principle of compromise'' and ''dependence on frame of reference'' or ''combined noise sources paradox.'' The conclusion section elaborates further on the more precise choice of words that may best describe the accumulation effect in general.

II. THE SOCIAL SURVEY

A. Survey

A social survey was conducted with 3200 people in Flanders, Belgium. The general topic of the survey was the influence of odor, noise, and too much light on the living environment. The survey was presented as such to the subjects. The selection of subjects was done in two stages. In a first stage households were randomly selected. The member of each selected household aged above 16 that had its birthday coming up first was contacted by telephone, convincing him or her to participate in the study. This process was repeated, making sure that the sample was representative on the demographic factors age, gender, and province. The selected subjects were then sent the questionnaire by mail. They were reminded to participate in the survey after three weeks by telephone if they did not send the questionnaire back promptly. Finally, 64% of the questionnaires that were sent out, were received.

The survey was part of the Investigation of the Environmental Living Quality performed on behalf of the Flemish Environmental Administration (AMINAL) by Deloitte & Touche and M.A.S.

B. Noise annoyance questions

The questions of importance for this study are the general noise annoyance question and the questions concerning noise annoyance by particular sources.

The general noise annoyance question appears on the first page of the questionnaire and is preceded by two questions only.[12] The first one inquires about the general appreciation of the living environment. The second one asks whether the subject would stimulate a friend to live in this neighborhood and why (why not). There is no filter question. The general noise annoyance question then appears in a group of three questions concerning odor, noise, and light in that order. The formulation of the question is in overall agreement with the ICBEN recommendation put forward in Ref. 13: ''Als u denkt aan de voorbije 12 maanden, in welke mate bent u gehinderd of niet gehinderd door geluid in en om uw woning?'' (When thinking about the past 12 months, how annoyed or not annoyed are you by noise in and around your home) and the subjects are asked to answer this question using a five-point categorical scale.

The question concerning noise annoyance by particular sources follows on the third page, the second page being devoted to coping, change in situation, and description of the living environment. With this arrangement subjects do not see the detailed list while answering the total annoyance question unless they turn back to the first page after reading the third one. A small prestudy learned that the majority of subjects tend to fill in the written questionnaire from beginning to end without ever returning to previously answered questions. The wording of the detailed annoyance question is: ''In volgende tabel worden enkele mogelijke bronnen van geluidshinder aangegeven. Als u denkt aan de voorbije 12 maanden, hoe gehinderd of niet gehinderd bent u door het geluid van de volgende bronnen in en om uw woning'' (The following table contains a number of possible sources of noise annoyance. When thinking about the past 12 months, how annoyed or not annoyed are you by the sound of the following sources in and around your house) and it is followed by a list of sources: road traffic, air traffic, railway traffic, etc. For reasons out of our control, the list contains a few very specific sources that are not expected to cause much annoyance.

At the end of the list of named sources of noise annoyance the possibility was given to the subjects to add additional sources also rating them on a five-point annoyance scale.

The answers to these annoyance questions will be labeled A_t and A_s, where t refers to the overall annoyance and s runs over all sources.

C. Overview of the annoyance data

To report on the results of this survey, the most similar terms in English for the five Dutch modifiers used for labeling the answer categories (''helemaal niet'', ''een beetje'', ''tamelijk'', ''ernstig'', ''extreem'') will be used. Similarity is defined in a fuzzy set theoretical way.[14] The resulting labels are *not at all*, *slightly*, *fairly*, *strongly*, and *extremely*.

Table I shows the number of test subjects in each response category for all sources considered and for the general noise annoyance question. The data contain much more subjects who rated their noise annoyance rather low compared to the number of subjects who rated their noise annoyance in the higher categories. This will have to be taken into account when evaluating the performance of models. The fact that the data is representative for the population of a larger region (Flanders) rather than being focused on noisy areas, distinguishes this research from the bulk of studies carried out in this field. Our results could be influenced by it in the following way. Inevitably there will be more

TABLE I. Occurrence of all levels of annoyance for the individual sources and the general noise annoyance rating available in the database.

	Not at all	Slightly	Fairly	Strongly	Extremely	Incorrect
Noise in general	1071	1086	600	304	68	79
Road traffic	1239	953	546	322	71	77
Rail traffic	2585	304	78	24	5	212
Air traffic	2139	566	195	77	21	210
Water traffic	2929	32	3	1	1	242
Truck loading and unloading	2594	307	96	49	17	145
Small businesses	2762	182	56	15	8	185
Factories	2683	211	84	41	9	180
Commerce	2838	126	33	19	6	186
Building activities	2605	274	80	45	10	194
Dancing halls	2917	97	28	14	14	138
Restaurants and cafes	2850	148	35	21	8	146
Entertainment parks	3031	12	1	4	0	160
Fancy fairs and festivals	2699	267	54	20	10	158
Sports events	2869	146	28	9	3	153
Car and motor race tracks	2936	80	15	7	4	166
Agriculture equipment	2634	359	59	9	4	143
Farm animals	2873	129	32	10	4	160
Stable ventilators	2989	35	10	4	1	169
Playing children	2608	324	67	22	3	184
Pet animals	2134	623	182	75	28	166
DIY noises	2369	483	107	39	16	194

low-exposure situations in the dataset. In most cases low exposure means fewer events, leaving the time in between quiet for observing other noise sources. The simultaneous occurrence of the noise of each of the separate sources, the typical stimulus in laboratory research, will be rare at low exposure levels.

Out of the test subjects that participated in the survey, 52% were female. Their age was 16 and older with a distribution corresponding to the demography of the Flemish (northern part of Belgian) population (16–30: 11%, 30–50: 45%, 50–65: 28%, above 65: 16%).

III. QUALITY MEASURES FOR PREDICTION MODELS

Models for the accumulation of community noise annoyance can be compared on the basis of their success in predicting the outcome of surveys such as the one described above. In Ref. 15 the reader is warned about the use of a correlation between model results and data as a measure of quality for models. In Ref. 4 this observation leads the authors to the conclusion that model building blocks and principles must be evaluated on their theoretical soundness as well. In other words, the theory behind a model is as important as its success in predicting measurements.

In this work the concern on generalization and a strong theoretical foundation of the model led to the rejection of general purpose methods such as fuzzy clustering or (fuzzy) neural networks. These models are popular tools for extracting (nonlinear) knowledge from a dataset, but lack the constraint of an underlying theoretical model.

Although the criterion of solid and sound foundations will be important for comparing models, checking their performance in predicting experimental results remains necessary. Two measures of model performance are used in this work. The first is a quadratic prediction error weighted by the occurrence of each level of annoyance in the dataset,

$$\sqrt{\sum_{i=1}^{N} \frac{(A_{t,i}-A_{t,i}^{m})^2}{n(A_{t,i}^{m})}}, \tag{1}$$

where the superscript m refers to the measured value, N is the number of subjects, and the function $n(x)$ represents the number of subjects reporting annoyance in category x. The index i runs over all subjects. This error measure is less tolerant than correlation since it does not allow for a scaling factor.

The second performance measure is a weighted number of correctly predicted survey results. Here again the weighting takes into account the occurrence of each of the five levels in the dataset,

$$\sum_{\text{correctly predicted}} \frac{N/5}{n(A_{t,i}^{m})}. \tag{2}$$

Fuzzy models can only be analyzed in this way if their output is defuzzified first. In this process some of the information in the result is ignored. As will be explained in detail below, the result of a fuzzy model is a possibility P for each of the five categories to be given by the subject as their general noise annoyance rating. A useful prediction error is defined as the summation of two contributions:

$$e=\frac{\sum_i \frac{1}{n(A_{t,i}^m)}((\max_{L\neq A_{t,i}^m}[P(A_{t,i}\ \text{is}\ L)]-P(A_{t,i}\ \text{is}\ A_{t,i}^m))}{\sum_i \frac{1}{n(A_{t,i}^m)}|(\max_{L\neq A_{t,i}^m}[P(A_{t,i}\ \text{is}\ L)]-P(A_{t,i}\ \text{is}\ A_{t,i}^m))|}+\sum_{\text{wrong prediction}}\frac{N}{n(A_{t,i}^m)}\alpha, \tag{3}$$

where L is one of the five category labels and the maximum is taken over all labels not corresponding to the measured level of total annoyance. The first term is a summation (weighted as before) of the difference between the highest predicted possibility for a category that turns out not to be the one chosen by the subject and the predicted possibility for the measured annoyance category. The normalization measures the average range by summing absolute values. The second term is a weighted number of incorrect predictions (defuzzified) multiplied by a constant α.

IV. CLASSICAL MODELS

A. Strongest component

The strongest component or dominant source model can take two forms. The perceptual form that is of concern in this paper simply states that the level of general noise annoyance reported by a test subject is the strongest of the annoyance caused by any of the particular noise sources that the subject may be exposed to

$$A_t=\max_s(A_s). \tag{4}$$

Several authors have reported very successful prediction of annoyance accumulation[1,5] using the strongest component model both in field study and in lab research, especially when one of the sources dominates. The theoretical background of this model is nevertheless very weak and one can even argue that it is counterintuitive. Indeed, one expects several sources of comparable (but unequal) loudness to result in higher annoyance than the annoyance caused by the loudest source.

The quality of the strongest component model for predicting the survey results studied here, is also reasonably high (Table II). In Fig. 1 the reported general noise annoyance is compared to the predicted general noise annoyance by showing the number of observations for each combination. The occurrence is scaled to take into account the number of observations involving each annoyance level that is available in the database. From the figure it is obvious that the model overestimates general annoyance and that this overestimation is independent of the annoyance level. As mentioned in the Introduction, many authors observed this and gave different explanations for it. This will be a main focal point when deriving the fuzzy models.

TABLE II. Quality of classical models for predicting annoyance accumulation as reported in the social survey. The value between parentheses is the prediction error for the training set (2000 samples).

	Prediction error	Correctly predicted
Strongest component	2.17	55.5%
Vector summation	4.97	24.1%
Vector summation scaled	4.06	34.1%
Linear regression	2.40 (2.43)	42.2%

B. Vector summation model

The vector summation model has a more general background in perception research (noise, odor, binocular brightness,...).[1] For two sources causing annoyance levels A_i and A_j, the vector summation model predicts the general annoyance to be

$$A_t=(A_i^2+A_j^2+2A_iA_j\cos\alpha_{ij})^{1/2}, \tag{5}$$

where α_{ij} is a constant that depends on the combination of sources. This constant has to be determined from experimental data. Values for α_{ij} of about 90° have been found[16] for the summation of loudness and annoyance as occurring in field conditions; that is, in the presence of other sources that may partly mask the loudness. Increasing the constant above 90° can lead to a general annoyance that is lower than the strongest component or dominant source method, thus indirectly solving the overestimation problem mentioned in Sec. IV A. A generalization of this model to more than two sources is a rather cumbersome task. If $\alpha_{ij}=90$ for all i and j, it can reasonably be assumed that the n noise sources span an n-dimensional space thus leading to the extended model

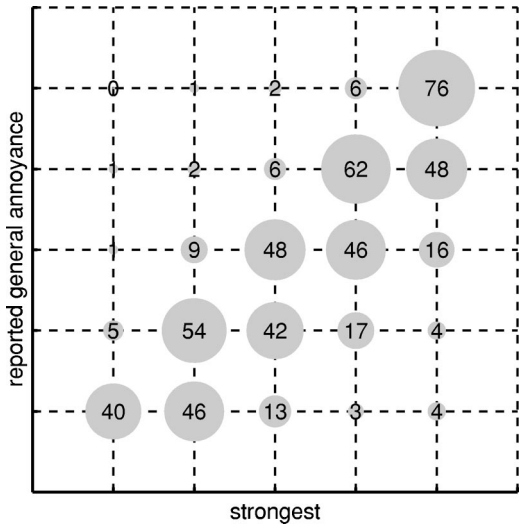

FIG. 1. Relative occurrence of various combinations of predicted (strongest component) and reported general annoyance; the area of the bubbles is proportional to the percentage shown.

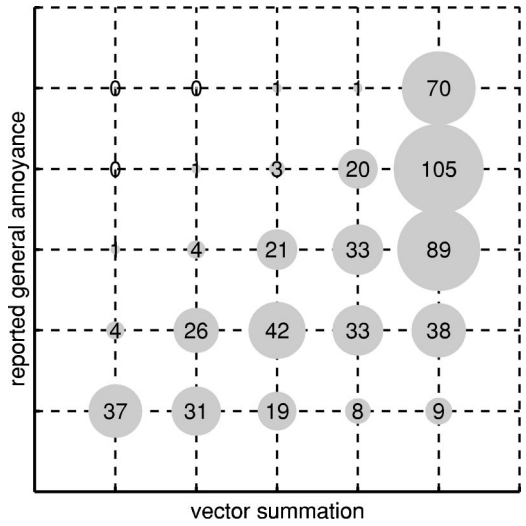

FIG. 2. Relative occurrence of various combinations of predicted (vector summation, 90°) and reported general annoyance; the area of the bubbles is proportional to the percentage shown.

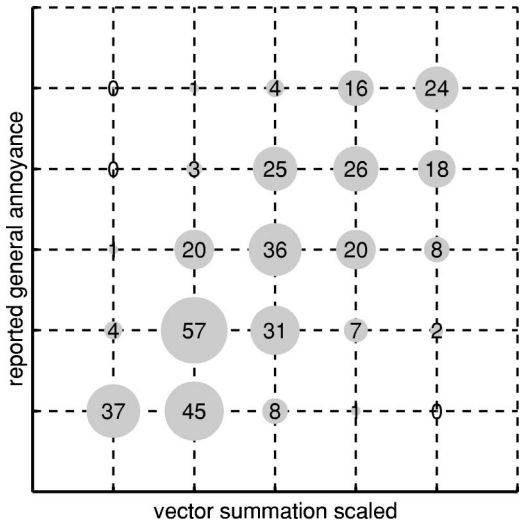

FIG. 3. Relative occurrence of various combinations of predicted (vector summation, 90°, linearly scaled) and reported general annoyance; the area of the bubbles is proportional to the percentage shown.

$$A_t = \left(\sum_s A_s^2 \right)^{1/2}, \tag{6}$$

where the summation runs over all sources. This extension is both associative and symmetric.

Table II also includes the performance of the vector summation model for predicting the general noise annoyance reported in the survey based on the known annoyance caused by a selection of community noises. Both the prediction error and the percentage correctly predicted general annoyance levels are significantly worse than for the strongest component model. From Fig. 2 which shows the relative occurrence of each combination of predicted and reported general annoyance level, it becomes clear that a general overestimation is the problem. Since the vector summation model is based on simultaneous exposure to all sources and does not include any form of compromise, an overestimation could indeed be expected. The difference between model and survey increases with the general noise annoyance level. Including a linear scaling (by a factor 0.59) as a first attempt to describe a compromise, the prediction error reduces to 3.97, which is still worse than the performance of the strongest component model. Figure 3 reveals that the scaled model still overestimates the lowest annoyance levels (in particular, ''not at all annoyed'').

Changing the α_{ij} for all combinations of sources would improve the performance of a vector summation model. However, it is not clear how this should be done in a multisource (more than two source) environment and therefore we do not elaborate further on this possibility.

C. Summation and inhibition model

The summation and inhibition model proposed by Powell[2] is a two-step model. In a first step, the annoyance by each source as heard within the total sound is calculated. This process involves partial masking. Then these annoyance levels are arithmetically summed to obtain general or total annoyance. In a field study, reported annoyance by a single source is already annoyance as heard within the total sound so the first step becomes obsolete. Moreover, due to temporal mismatch, partial masking will seldom occur. Hence the model reduces to a special case of the linear regression model discussed below.

D. Linear regression model

All previously described models have the disadvantage that they do not allow us to differentiate between sources. They implicitly assume that the reported level of annoyance has exactly the same meaning for all sources of noise. Moreover, they assume that this annoyance contributes equally to the general appreciation of the noise climate. A straightforward multiple linear regression model describes the global annoyance as a weighted sum (and thus allows to differentiate between sources),

$$A_t = \sum_s w_s A_s, \tag{7}$$

with w_s a set of well-chosen weights. There is no perceptual-cognitive theory underlying this model, which makes it less valuable in view of the quality measure introduced in Sec. III. In Ref. 17, the weights in a multiple linear regression are related to the ''on-time'' of the sources. The importance of ''on-time'' is confirmed by the analyses of the cognitive processes involved in global noise annoyance judgments by Hallman *et al.*[18] These authors find that permanence of the noise is among the four most important factors in the process of arriving at a global noise annoyance judgement.

The weights in the linear regression model are extracted from 2000 randomly selected records in the survey database. Performance is measured on the full database and is shown in Table II. The prediction error is slightly higher for the linear regression model than for the strongest component model. Prediction error on the 2000 sample training set is a little higher than prediction error on the remainder of the database, which indicates that the model generalizes quite well, or, in other words, does not overfit the data. The per-

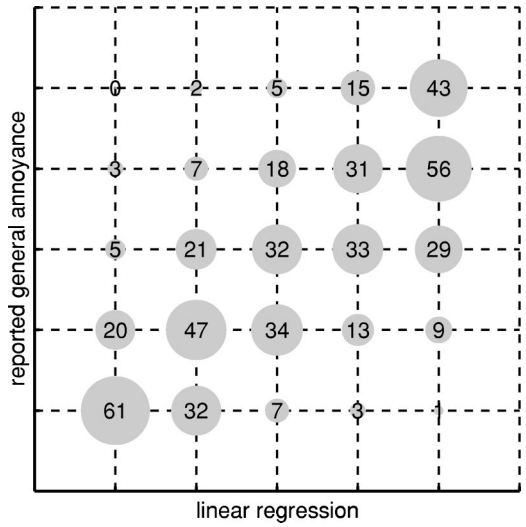

FIG. 4. Relative occurrence of various combinations of predicted (linear regression) and reported general annoyance; the area of bubbles is proportional to the percentage shown.

centage correctly predicted general annoyance response is significantly worse than for the strongest component model. In Fig. 4, the reported general noise annoyance is compared to the predicted general noise annoyance by showing the relative number of observations for each combination. At low annoyance levels the overestimation is reduced compared to the strongest component model. At high annoyance levels, however, the predicted noise annoyance is, on average, higher than the reported one. Moreover, the linear regression model tends to generate a number of far-off predictions.

The weights, w_s, that were extracted are shown in Fig. 5. The figure also contains the average annoyance level. The correlation between weight and average annoyance is very low ($r^2=0.16$), indicating that the weighted average does not favor highly annoying or very common sources. Extracting weights by optimizing the prediction error is rather tricky. Some of the factors may not influence the result strongly enough for the minimum to be very clear. This may occur for sources of sound that are rare (no exposure) or not annoying or have a different character in different situations (for different test subjects). The more elegant way to illustrate how accurately one can expect the weights to be determined is to include the interval that makes the prediction error deviate a fixed amount from its minimum. Here a 1% deviation is used to obtain the sensitivity interval shown as error bars in the figure.

Trying to explain the weights in terms of ''on-time'' seems to work to some extent. Indeed, road traffic noise gets a higher weight than air traffic noise, which, in turn, seems more important than rail traffic noise. When exposed to these sources, this is indeed proportional to the ''on-time'' that one can expect. For other sources ''on-time'' does not seem to be an adequate explanation. Industrial noise, for example, has a rather low weight while the ''on-time'' of the noise is long when the source is present. The noise from dancing halls gets a high weight, which indicates that ''on-time'' must be interpreted in a time window that spans minutes or hours rather

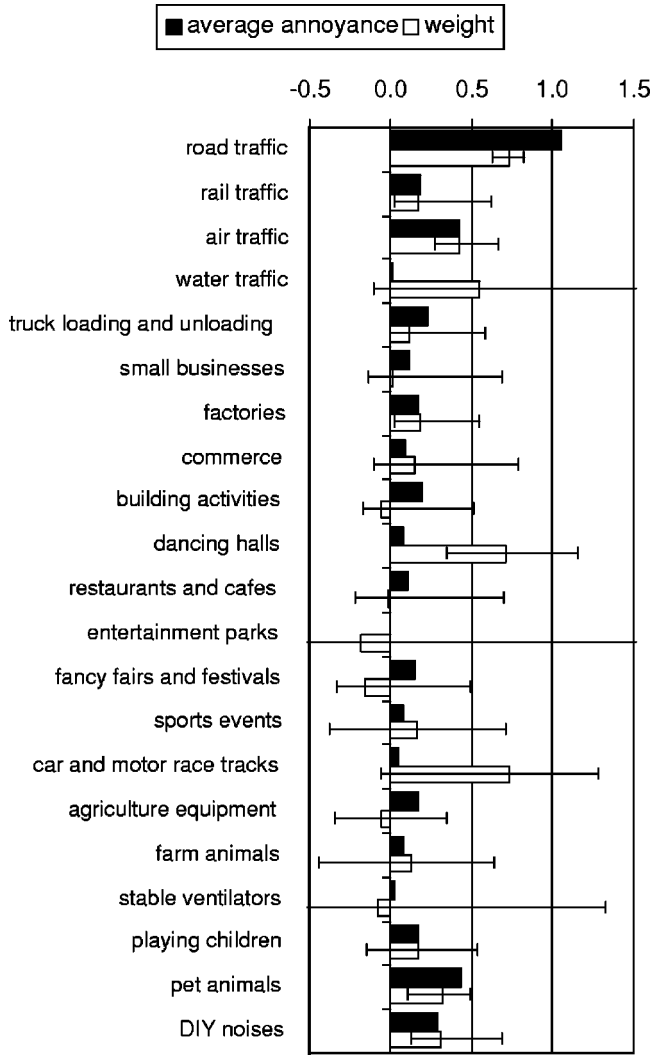

FIG. 5. Average annoyance and weights w_s in a linear regression; the error bar corresponds to a change in w_s that changes the prediction error by 1%.

than weeks. The in-between weight found for pet noises and do-it-yourself noise is also consistent with such an interpretation.

When introducing the fuzzy model in the next section a more general interpretation of the weights will be given.

V. FUZZY MODELS

A. Formulation of the strongest component model in classical logic

The simplicity and relative success of the strongest component model suggests using it as a starting point for deriving a fuzzy annoyance accumulation model in a formal way. The maximum-operator in (4) is a mathematical construct that has become very common in everyday tasks performed by many people. However, an explicit formulation using classical logic may be more closely related to the cognitive task that is performed when a subject tries to answer a general noise annoyance question. In language the strongest component model is equivalent to using the following set of logical rules:

IF annoyance by one of the sources is *extreme* THEN general annoyance is *extreme*
IF annoyance by one of the sources is *strongly* THEN general annoyance is *strongly*
UNLESS general annoyance is already *extreme*
IF annoyance by one of the sources is *fairly* THEN general annoyance is *fairly*
UNLESS general annoyance is already *strongly* or *extreme*
…

In mathematical form this reads, for $i=5,4,...,1$, as

$$\text{If } \left(\underset{s}{\vee}(A_s \text{ is } L_i)\right) \text{Then } A_t^n \text{ is } L_i \text{ Unless } A_t \text{ is } \left(\underset{j>i}{\vee} L_j\right), \tag{8}$$

where L_i is the ith element in the array of the possible degrees of annoyance {*not at all, slightly, fairly, strongly, extreme*}. In Eq. (8) the symbol $\vee$ is used for the logical *OR* operator. The antecedent is TRUE if any of the noise sources, s, is rated L_i annoying. A_t^n is the new estimate for the general noise annoyance. These logical equations can only be executed in the order indicated, that is, from *extreme* to *not at all*. Finally, all estimates for A_t must be aggregated to a single result. In classical logic, only one rule will fire so this operation is trivial.

In preparation of the fuzzification that will be introduced in the next section, the ''If...Then...Unless...'' rule described by Eq. (8) can be transformed to a conjunction of two ''If... Then...'' expression:

$$\text{If } \left\{\left[\underset{s}{\vee}(A_s \text{ is } L_i)\right] \wedge \left[A_t \text{ is } \neg \left(\underset{j>i}{\vee} L_j\right)\right]\right\} \text{ Then } A_t^n \text{ is } L_i, \tag{9}$$

$$\text{If } \left\{\left[\underset{s}{\vee}(A_s \text{ is } L_i)\right] \wedge \left[A_t \text{ is } \left(\underset{j>i}{\vee} L_j\right)\right]\right\} \text{ Then } A_t^n \text{ is } \neg L_i, \tag{10}$$

where the symbols $\vee$, $\wedge$, and $\neg$ are used to indicate logical *OR*, *AND*, and *NOT* operators. The necessity of rule (10) can be argued. Alternatively, the consequent of this second rule may read A_t is *unknown* or *unspecified*.

B. Fuzzifying the logic model

The classical logic model is now fuzzified. To illustrate the possible benefit of this action, consider the following situation. Assume that a person has primary knowledge on the meaning of words describing the degree of annoyance that a person can experience. But assume also that he or she only knows about a single relation: IF annoyance by road traffic noise is *extreme* THEN general annoyance is *extreme*. Given the fact that road traffic noise annoyance is *strong*, can this person give any information on the expected general annoyance? In classical logic the answer is clearly NO. Since the condition that is stated in the antecedent of the single known rule, is not met, the rule does not fire, and no information becomes available. A human reasoner may argue that *strong* is not that much weaker than *extreme* so it is possible to some extent that the consequent is true. He or she may also argue that since *strong* is weaker than *extreme*, the consequent of the rule is also weakened to read ''general annoyance is *strong*.'' Finally the human reasoner may conclude that since *not at all* or *slightly* are so different from *extreme* it is unlikely that general noise annoyance will take these values.

The above example illustrates why fuzzy logic is such an interesting approach for the problem addressed in this paper. Fuzzy logic provides the mathematical background to imitate human-like reasoning.[22] Because of this, a fuzzy rule based model is also very well suited to construct a model that wants to imitate human cognition.

A first step in the fuzzification process consists in fuzzifying the facts, e.g., A_s is L_i. This allows relating the words used as labels on the response scale, to each other. Remark that this was also done in classical models by associating numeric values {0,1,2,3,4} to the labels, but there the numerical values remained crisp. Fuzzification of the labels, L, is based on possibility distributions or membership functions, $\pi_L(u)$, defined on a suitable universe U. In the case of noise annoyance, the chosen universe is a continuous annoyance interval [0, 10]. Membership functions can be extracted in different ways. Here we use a technique that is based on the probability for test subjects to select a point on the continuous scale as representative for a given verbal label. Details on the construction of these membership functions can be found in Refs. 19 and 14. Figure 6 shows the membership functions for the (Dutch) labels used in the questionnaire.

Basic logic operators *AND* ($\wedge$), *OR* ($\vee$) and *NOT* ($\neg$)

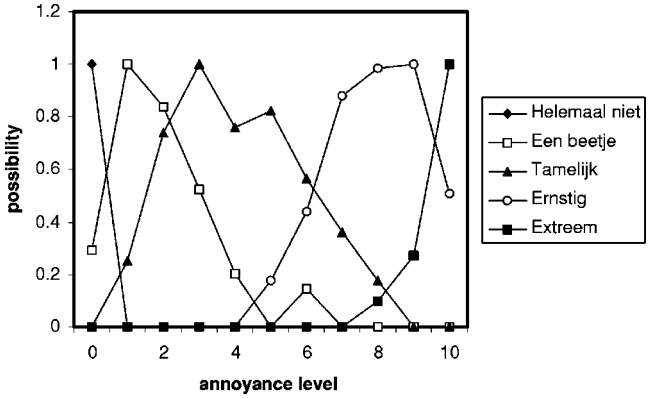

FIG. 6. Possibility distributions for the five labels that are used in the questionnaire.

have been fuzzified[20] by introducing triangular norms (*t*-norms) and *t*-conorms to represent the $\wedge$ and the $\vee$ operation. The $\neg$ operation is most often fuzzified by an inversion of the possibility distribution: $\pi_{\neg A}(u)=1-\pi_A(u)$. Several mathematical expressions fulfill the requirements imposed on a *t*-norm and *t*-conorm so many of these operators are available. In the Appendix A we give the definitions of the operators and a few implementations. In these analyses the Lukasiewicz *t*-norm and *t*-conorm are used. This *t*-norm is defined by, for x and y in $[0,1]$, $W(x,y)=\max(0,x+y-1)$. The associated conorm is $W^*(x,y)=\min(1,x+y)$. In these expressions, x and y are the membership degrees of the possibility distributions of the two fuzzy sets A and B, that are combined using the logic operator.

Given the rule IF X is A THEN Y is B, information concerning Y can be extracted from information on X. This inference by modus ponens is fuzzified to the so-called generalized modus ponens. B', the inferred possibility distribution of Y, is calculated with the compositional rule of inference:

$$(\forall \nu \in V)(B'(\nu)=\sup_{u\in U}\min(A'(u),R(u,\nu))), \tag{11}$$

where R is the representation of the rule and A' is the fuzzy input given to the rule.

A semantic analysis of fuzzy IF–THEN rules revealed three different rule interpretations, depending on the operator used to construct the rule representation R.[21,22] It was shown that the relation R is lower bounded when a triangular norm or *t*-norm is used (conjunction model), and upper bounded when a fuzzy extension of the classical implication operator is applied (implication model). The former case leads to possibility qualifying rules, to be interpreted as ''the more X is A, the more possible B is a range for Y.'' The latter can be seen as truth-qualifying (or gradual) rules, ''the more X is A, the more Y is B,'' in case of a residual implicator. For an S implicator, one gets certainty qualifying rules with an associated interpretation ''the more X is A, the more certain Y is B.'' The rules in the formulation of the strongest component model in binary logic are formulated with the possibility interpretation in mind: the antecedent is required to make the consequent (general annoyance) possible. Therefore, R is modeled using a t-norm.

In the fuzzy extension of the set of rules representing the strongest component model, each rule creates the possibility for general annoyance to take the value specified in its consequent. Each rule therefore includes complementary information that must be taken into account as separate estimates for the outcome of the model. With the possibility interpretation of rules in mind, aggregation is based on an *OR* operator.

The fuzzy model obtains a possibility distribution, $\pi_t(u)$, over U for the general annoyance, A_t, based on the annoyance, A_s, by particular sources, the latter being reported by choosing one of the labels from the universe $U_L=\{$*not at all, slightly, fairly, strongly, extremely*$\}$. To interpret or defuzzify this result, $\pi_t(u)$ is mapped to a possibility distribution, $P_t(L)$, over U_L using

$$P_t(L)=\mathrm{Sim}(\pi_t,\pi_L), \tag{12}$$

where Sim is any similarity measure. Mathematically speaking, a similarity measure on a universe U is a $[0,1]$-valued indicator suitable for the comparison of fuzzy sets on U, i.e., a binary fuzzy relation on $\mathcal{F}(U)$ the collection of all fuzzy sets related to linguistic terms. A wide variety of similarity measures was proposed in the literature.[23] Here a degree of compatibility,

$$S_2(A,B)=\frac{\Sigma_{u\in U}T(A(u),B(u))}{\Sigma_{u\in U}S(A(u),B(u))}, \tag{13}$$

is used.

The fuzzy logic equivalent of the strongest component model thus results in a fuzzy set over U_L. It opens the possibility that labels other than the one corresponding to the strongest component are reported as a general annoyance level. However, the highest possibility is still assigned to that label corresponding to the strongest component if a Zadeh norm and conorm are used. Therefore the final step in the defuzzifying process would select this level as the outcome of the model and the percentage correctly predicted reported general annoyance would be exactly the same as for the strongest component model. Small differences may occur because the fuzzy model handles missing data somewhat better, but this is just a small artifact of the procedure.

Other *t*-norms (e.g., Lukasiewicz or Product) combine information in their arguments more subtle than the Zadeh norm. Combined with the overlap between L's and the order in which the rules are fired (from stronger to lower annoyance), this can result in a rating for A_t that is higher than the strongest component if several sources cause a similar annoyance. A kind of inhibition process thus emerges naturally when a vague interpretation of the binary logic rules involved in the cognitive process of rating general noise annoyance is introduced. Performance on the dataset of this model is worse than that of the strongest component model or the fuzzy model using a Zadeh *t*-norm. The reason for this anomaly turns out to be the on average overestimation of general noise annoyance by the strongest component model. Increasing the predicted level therefore decreases performance.

There seems to be no benefit in making the logic model fuzzy unless additional features are added, as illustrated in the next paragraphs.

C. Adding sufficiency to the rules

It became clear from the discussion of the classical models that an improved annoyance accumulation model should differentiate between sources. In fuzzy rule based systems the importance of each rule can be modified by assigning a sufficiency degree $\lambda\in[0,1]$ to the rule. This degree expresses to what extent the consequent can be guaranteed possible when the antecedent is true. In the noise annoyance accumulation model, a linguistic rule including sufficiency could read, for example, as

It is 0.8 sufficient for annoyance by road traffic to be *strong* for general annoyance to be *strong*
UNLESS general annoyance is already *extreme*

For possibility-qualifying rules implemented using a conjunction model, the sufficiency of a rule can be translated to adapting the membership function of the consequent of this rule using

$$B^*(\nu) = \min(B(\nu), \lambda). \tag{14}$$

A sufficiency degree λ_{sL} has to be determined for each rule, that is, for each combination of a source, *s*, and a level of annoyance, *L*. To reduce complexity, we assume $\lambda_{sL} = \lambda_s \cdot \lambda_L$, where λ_s depends on the source and λ_L on the level of annoyance. Both sets of degrees of sufficiency are extracted from a 2000 sample training set extracted from the data by minimization of the prediction error defined in Eq. (3). The training set was the same as the one used for extracting the weights in the linear regression model The optimization is performed by a genetic algorithm.

The resulting model predicts general annoyance for 59.0% (weighted) of all subjects and for 60.4% of the subjects in the training set. This percentage is only slightly better than the strongest component model. By comparing the difference between predicted and reported general annoyance for both models, the average error (unweighted) is proven to be very significantly lower (using a *t*-test) for the fuzzy model. Figure 7 shows the relative occurrence of each combination of the predicted and reported general annoyance level. The fuzzy model overpredicts the general annoyance level less often than the strongest component model, especially at low annoyance levels. In Fig. 8 the weights extracted in a linear regression model are compared to the degrees of sufficiency extracted in the fuzzy model. The correlation between *w* and λ is small ($r^2 = 0.2$). This is partly due to the insensitivity of the prediction error for changes in these parameters for some of the sources. This can be seen from the error bars. For traffic noise, similar conclusions can be drawn from rule sufficiency as from the linear regression weights: Annoyance by rail traffic is much less sufficient for reporting general noise annoyance than other transportation noises. Annoyance by noise from industry, small business, and commerce are also sufficient for reporting general noise annoyance. A similar conclusion could not be drawn from the linear regression weights. Comparable observations can be made for noise from stable ventilators and DIY noise.

To evaluate the solidity and soundness of the building blocks of the proposed model, a reasonable background for adding sufficiency has to be given. We argue that the cognitive process resulting in the reported general annoyance level may also include such a variable. Subjects may or may not

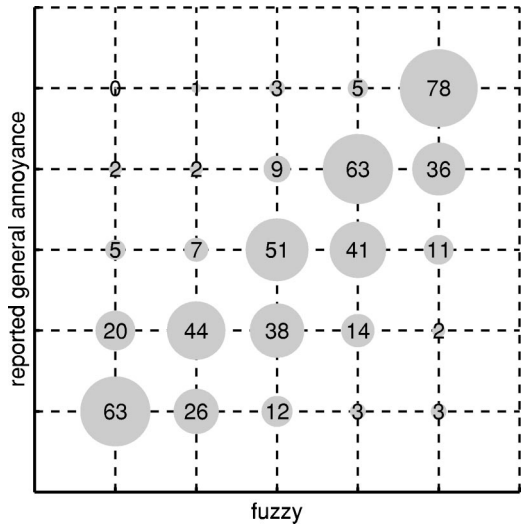

FIG. 7. Relative occurrence of various combinations of predicted (fuzzy model) and reported general annoyance; the area of bubbles is proportional to the percentage shown.

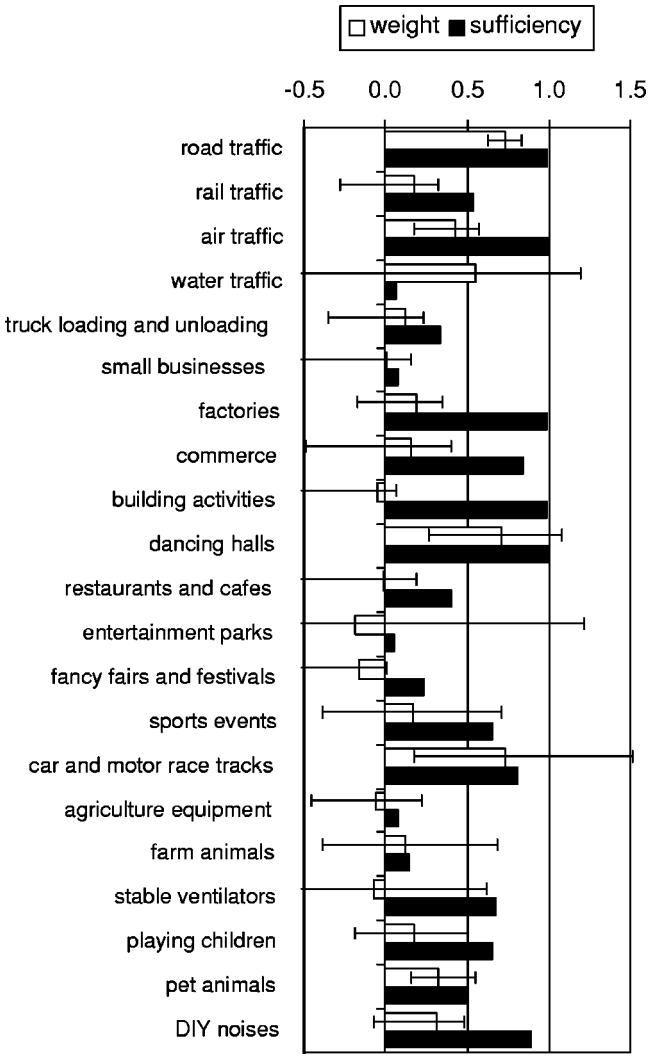

FIG. 8. A comparison of the weights w_s in a linear regression model and the sufficiencies λ in a fuzzy model.

decide to report general noise annoyance if annoyance by one of the sources is high, based on many aspects of the sound. One of them may be the temporal axes, including on-time when occurring, frequency of occurrence, and time of day when occurring. It is not unreasonable to assume that this decision also depends on the magnitude of the effect, hence λ_L.

D. Changing the frame of reference

Adding sufficiency is not the only way the fuzzy model can be made source dependent. Rating a particular characteristic of an object or a situation always involves a frame of reference. For rating general noise annoyance, this can be the universe of all imaginable degrees of annoyance that noise can cause. There is no particular reason for the frame of reference for rating road traffic noise, for example, to be the same. The difference in the frame of reference is not as obvious as when rating the height of people or buildings, but it is nevertheless not necessarily negligible.

In fuzzy rule bases the frame of reference can be different in the antecedent and the consequent of a rule. This can lead to a different universe U_s and U_t for defining the fuzzy sets representing the vocabulary used in the antecedent and consequent. Including a change in the frame of reference will lead to new verbal description of rules. For example, a rule may read ''If rail traffic noise annoyance is *extreme*, then general annoyance is *strong*.'' Using the five-word vocabulary, subtle changes caused by the different frame of reference cannot accurately be described. Modifiers can solve this problem. The example could then read ''If rail traffic noise annoyance is *extreme*, then general annoyance is *somewhat less than extreme*.'' Several mathematical models for modifiers were developed.[24] In this work a shift modifier is used. Using this approximation, the membership function $L_{sl,i}(u)$ for ''*somewhat less than* L_i'' becomes $L_{sl,i}(u)=L_i(u-a)$, where a is a suitable constant. It is a straightforward generalization to make a dependent on the source since the size of the change in frame of reference can depend on the source. The a_s can then be subject to an optimization comparable to the optimization of λ_s.

It turns out that the performance of a model based on a change of the frame of reference alone is not significantly better than the strongest component model. This failure is attributed to a lack of increase in uncertainty in the contribution of annoyance by unimportant sources to A_t. This feature is implicitly present in the sufficiency-based approach.

E. Analysis of the remaining prediction error

The fuzzy rule based model predicts general annoyance correctly based on the knowledge of the reported annoyance for individual sources for about 60% of the subjects (including a weighting factor for the occurrence in the database). In this section the nonpredicted part is analyzed for its dependence on other variables.

Some of the sources that subjects have in mind when rating their general noise annoyance, may not figure in the list subsequently presented to them. The questionnaire therefore contained an open question allowing respondents to describe other sources or activities. A distribution over the difference between the predicted and reported general annoyance (categories labeled from 1 to 5) is constructed after selecting those people that did and did not mention sources not in the list presented to them. Figure 9 shows that underestimates of general noise annoyance are more frequent in the group of subjects that mention other sources, as could be expected. However, the difference is less than expected. This may be due to the poor description people usually give. From this description it is not always clear whether they are giving more details on a source they think they have seen in the list or whether they consider the source not to be covered by the list (e.g., if fire trucks are mentioned, are they already included in the evaluation of road traffic noise?).

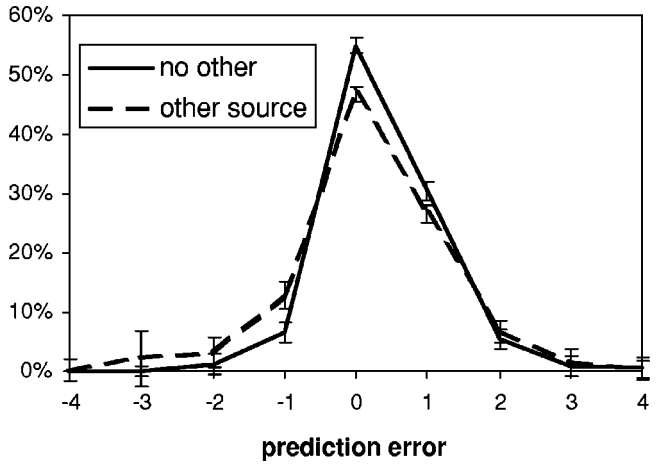

FIG. 9. A comparison of the distribution of the subjects over the prediction error between the cases where additional sources are mentioned and those where no additional sources are mentioned.

The ideas developed in this work consider the cognitive process involved in deriving a general noise annoyance rating. This process may be influenced by a number of personal factors. In the questionnaire there are three variables that can be included in the analysis: age, gender, education. Figure 10 compares the distribution over the prediction error of different age groups. Only the extreme curves are highlighted. The fuzzy model clearly overpredicts general annoyance ratings more often for young people. Prediction errors are smallest for the age groups around 60 and above 75. This does not imply that these age groups rate general annoyance more

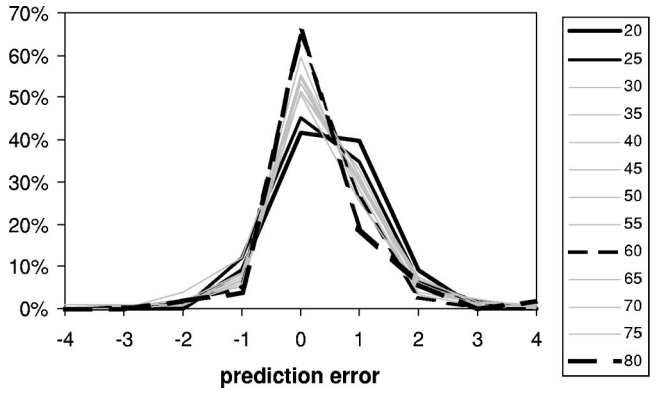

FIG. 10. A comparison of the distribution of the subjects over prediction error for different age categories.

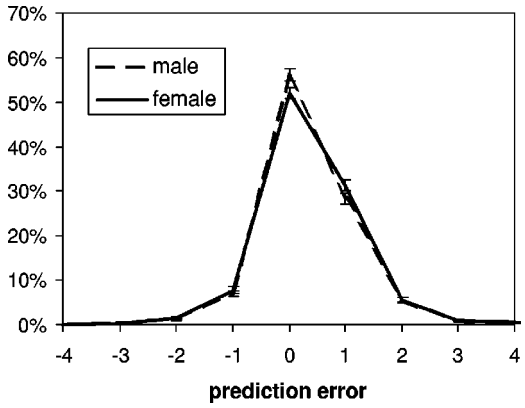

FIG. 11. A comparison of the distribution of male and female subjects over the prediction error.

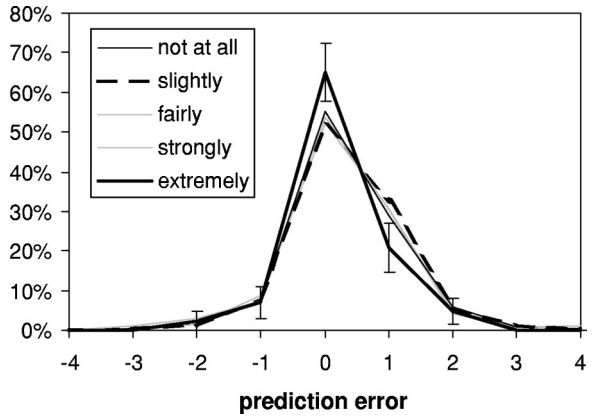

FIG. 12. A comparison of the distribution of the subjects over the prediction error for different levels of annoyance by odor.

consistently since the model contains a number of fitted parameters that make it correspond best to the age group represented most in the database. However, this clearly proves that age has an influence on the process of rating general annoyance based on the annoyance by different sources. From a single observation it cannot be distinguished whether the age describes a change in the cognitive process as people grow older (people aged 20–25 rate differently) or whether it is a generation issue (people born in the 1970s rate differently).

Figure 11 compares the distribution of male and female subjects over prediction error. Overprediction of general noise annoyance is slightly less for male subjects. Although this difference is significant, it remains very small.

The level of education was recorded in eight intervals corresponding to the Belgian school system. Observed differences are not significant. Since age and level of education correlate quite strongly, there may be a partial compensation of higher education by higher age that obscures possible differences, but no conclusive statements in this sense can be made on the basis of the available data.

The influences of the context of the general noise annoyance question in the questionnaire and the precise phrasing of this question, have been pointed out in the literature. In the questionnaire that is used here, the general noise annoyance question is immediately followed by a similar question on odor. Figure 12 shows how the distribution of test subjects over prediction error depends on the rating on the odor question. In case of a rating ''extremely'' on the odor question, the overprediction of general noise annoyance is significantly lower. If interpreted as an effect caused by the closeness of the questions, this would indicate that the extreme answer to the odor annoyance question increases the rating on general noise annoyance. However, it cannot be excluded that the rating on the odor question reveals a personality trait that also influences the cognitive process involved in aggregating the answer to the general noise annoyance question.

VI. DISCUSSION AND CONCLUSIONS

A survey was conducted that included a general noise annoyance rating and a rating of the noise annoyance caused by a selection of sources. The questions were located in the questionnaire in such a way as to minimize direct influences between them and they were formulated in accordance with recently proposed guidelines. To uncover the cognitive process involved in general or global noise annoyance judgment, several models were tested for their performance in predicting the answers given by over 3000 subjects exposed, *in situ*, to various combinations of sound sources.

Classical perceptual models mainly focus on simultaneously occurring noise. As was observed in many previous studies, these models tend to predict annoyance levels that are higher than the levels reported by the test subjects. The strongest component model or dominant source model seems to be the best predictor. This conclusion even holds when two or more sources induce similar levels of annoyance. However, the theoretical background of this model is somewhat thin. When this model is translated to a classical logic form, the cognitive process involved becomes clearer, thus explaining its success. One of the ambitious objectives of fuzzy logic is to mimic human reasoning more closely. Therefore it looks appealing to fuzzify this logic model in an attempt to predict survey results more accurately. If done correctly, it was observed that the fuzzy variant of the logic annoyance accumulation model incorporates a kind of inhibition. Strong annoyance by several sources can lead to extreme general noise annoyance. However, this basic fuzzy model does not perform very well, mainly because the principle of compromise (or accumulation paradox) is enhanced by it.

Two ideas are introduced in the fuzzy annoyance accumulation model to counteract the overestimation of reported general noise annoyance. The first idea is that noise annoyance by a particular source may or may not be sufficient to report general noise annoyance. The sufficiency of a rule in the fuzzy rule base is introduced as a mathematical model to implement this. One of the advantages of this model is that it allows to differentiate between sources and indeed the sufficiency parameter extracted by optimization on a subset of the available data, shows some correspondence to the linear regression coefficients proposed by other authors. Among others, the temporal axes, including on-time when occurring, frequency of occurring, and time of day when occurring may be a reason why people rate the importance of several

TABLE III. Summary of common fuzzy *t*-norm and their associated *t*-conorm and residual implicator.

Name	Norm	Conorm	Residual implicator
Zadeh	$M(x,y)=\min(x,y)$	$M^*(x,y)=\max(x,y)$	$I_M(x,y)=1$ (if $x\leqslant y$); $=y$ (if $x>y$)
Product	$P(x,y)=x.y$	$P^*(x,y)=x+y-x.y$	$I_P(x,y)=1$ (if $x\leqslant y$); $=y/x$ (if $x>y$)
Lukasiewicz	$W(x,y)=\max(0,x+y-1)$	$W^*(x,y)=\min(1,x+y)$	$I_W(x,y)=\min(1,1-x+y)$

sources of annoyance differently in an aggregation task.

The second idea that is proposed to account for the overestimation of general noise annoyance is a change in the frame of reference. It can be argued that rating noise annoyance caused by, for example, the neighbors pet or road traffic on a close highway is done by contrasting it to a slightly different frame of reference. The frame of reference for rating general noise annoyance is different all together. The mathematical model proposed to implement this idea consists in changing the consequent of the rules using modifiers. The simple modifier proposed here shifts the possibility distribution for the linguistic label used in the consequent as a model for saying "*a little bit less than*." Numerically this second approach is heavier than the first one and it turns out that its predictive capabilities are not much higher.

Regardless of the efforts put into predicting a general noise annoyance rating on the basis of the knowledge of noise annoyance caused by several sources, the response of some 40% of the subjects involved in this survey is poorly predicted. By contrasting the remaining prediction error to several variables also included in the questionnaire, some guidelines are obtained for future improvement of the model. Causes of noise annoyance not mentioned in the list of sources and activities or not recognized as such by the subject, account for some of the anomalies. However, the correlation to the response to an open question at the end of the list of sources is much lower than could be expected. In this survey we also found an influence of the answer to the question following the general noise annoyance question, indicating, as some authors have suggested, that the context of the question in the questionnaire may influence the answer. Again, only a very small part of the remaining prediction error is explained by this factor. Finally, the effects of a few demographic variables that may influence the cognitive accumulation process, are considered. Level of education does not show a relation to the remaining prediction error. Young people, on the other hand, seem to rate their general noise annoyance lower even if they report the same levels of annoyance by particular sources. The difference between male and female respondents is small but noticeable.

In summary, we proposed a new view on the process involved in rating general noise annoyance based on a known noise annoyance by individual sources and used fuzzy rules to implement a model for it. This model is slightly, but statistically, significantly better than the classical model that best predicts the results found in our survey, the strongest component model.

APPENDIX: FUZZY OPERATORS

In this article, a fuzzy set A is introduced as a mapping from the universe, U, into the unit interval $[0,1]$, called the membership function, μ_A. The membership function can be seen as an extension of the characteristic function, χ_C, that characterizes a classical (crisp) set C, which is a mapping $U\rightarrow\{0,1\}$. When $\chi_C(u)=1$, then $u\in C$; otherwise when $\chi_C(u)=0$, $u\notin C$. By allowing any value in the unit interval, this "membership value" can gradually transform from not belonging to the set to full membership.[20]

In the same spirit, the classical operations on crisp sets are also extended. A generalization of the intersection operation, which corresponds to the *AND* operation in logic, is known as a triangular norm (also called a *t*-norm). A *t*-norm, T, is a symmetric, associative, increasing $[0,1]\times[0,1]\rightarrow[0,1]$ mapping satisfying $T(1,x)=x$ for every $x\in[0,1]$. Please observe that this mapping coincides with the truth table of the classical *AND* operator. The dual operation of a *t*-norm is called a triangular conorm, or *t*-conorm. A *t*-conorm, S, is defined as a symmetric, associative, increasing $[0,1]\times[0,1]\rightarrow[0,1]$ mapping satisfying $S(0,x)=x$ for every $x\in[0,1]$. A *t*-conorm extends the union operation on sets and the *OR* operator in logic. In fuzzy literature, several choices for norms and conorms exist, Table III shows some common examples, including the original operators proposed by Zadeh. The following ordering can be proven: $W\leqslant P\leqslant M$ (largest norm) $\leqslant M^*$ (smallest conorm) $\leqslant P^*\leqslant W^*$.[25]

Not only the *AND* and *OR* logical operators can be "fuzzified," also the classical implicator can be extended. Among several families of fuzzy implicators that were proposed, the residual implicators are widely used in applications. A residual implicator I_T is defined as $I_T(x,y)=\sup\{\gamma\in[0,1]|T(x,\gamma)\leqslant y\}$, for each x and y in $[0,1]$. Also see Table III for some common incarnations.

[1] B. Berglund, U. Berglund, M. Goldstein, and T. Lindvall, "Loudness (or annoyance) summation of combined community noises," J. Acoust. Soc. Am. **70**, 1628–1634 (1981).

[2] C. A. Powell, "A summation and inhibition model of annoyance response to multiple community noise sources," NASA Technical Paper 1479, 1979.

[3] J. Vos, "Annoyance caused by simultaneous impulse, road traffic and aircraft sounds: A qualitative model," J. Acoust. Soc. Am. **91**, 3330–3345 (1992).

[4] B. Berglund and M. Nilsson, "Empirical issues concerning annoyance models for combined community noises," *Proceedings of Internoise 1997*, Budapest, 1997, pp. 1053–1058.

[5] T. Ronnenbaum, B. Schulte-Fortkamp, and R. Weber, "Synergetic effects of noise from different sources: A literature study," *Proceedings of Internoise 1996*, Liverpool, UK, 1996, pp. 2241–2246.

[6] S. M. Taylor, "A comparison of models to predict annoyance reactions to noise from mixed sources," J. Sound Vib. **81**, 123–138 (1982).

[7] R. F. S. Job and J. Hatfield, "Factors contributing to reported reaction to combined noise sources," *Proceedings of Internoise 2000*, Nice, France, 2000.

[8] B. Schulte-Fortkamp, "Noise from combined sources: How attitudes towards environment and sources influence the assessment," *Proceedings of Internoise 99*, Fort Lauderdale, 1999.

[9] R. F. S. Job, J. Harfield, N. L. Carter, P. Peploe, R. Taylor, and S. Morrell, ''Reaction to combined noise sources: The roles of general and specific noise sensitivity,'' in Ref. 8.
[10] J. Vos, ''On total annoyance caused by different environmental sounds: a review and suggestions for additional research,'' in Ref. 7, IN2000/946.
[11] H. M. Miedema and T. Gjestland, ''A noise metric for multi-source noise environments,'' in Ref. 7, IN2000/125.
[12] R. Guski, U. Felscher-Suhr, and R. Schuemer, ''Measuring retrospective annoyance in field studies: Prerequisites, procedures, and problems,'' *Proceedings of the 137th Meeting of Acoustical Society of America and 2nd Convention of the European Acoustics Association: FORUM ACUSTICUM*, Berlin, Germany, 1999.
[13] J. M. Fields, R. G. De Jong, T. Gjestland *et al.*, ''Standardized general-purpose noise reaction questions for community noise surveys: research and a recommendation,'' J. Sound Vib. **242**, 641–679 (2001).
[14] D. Botteldooren, A. Verkeyn, C. Cornelis, and M. De Cock, ''On the meaning of noise annoyance modifiers,'' Acta Acustica united with Acustica **88**, 239–251 (2002).
[15] M. H. Birnbaum, ''The devil rides again: Correlation as an index of fit,'' Psychol. Bull. **79**, 239–242 (1973).
[16] B. Berglund and M. Nilsson, ''Loudness of combined noises derived from singular and concurrent community noises,'' *Proceedings of the 16th International Congress on Acoustics*, Seattle, WA, 1998.
[17] B. Berglund and M. E. Nilsson, ''Total annoyance and perceptually discernible noise sources,'' in Ref. 7.
[18] S. Hallmann, R. Guski, and R. Schuemer, ''Cognitive processes in global noise annoyance Judgment,'' *Proceedings of Internoise 2001*, Den Haag, The Netherlands, 2001.
[19] A. Verkeyn, M. De Cock, D. Botteldooren, and E. Kerre, ''Generating membership functions for a Noise annoyance model from experimental data,'' in *Soft Computing in Measurement and Information Acquisition*, edited by L. Reznik and V. Kreinovich (Springer-Verlag, Berlin, in press).
[20] L. A. Zadeh, ''Fuzzy sets,'' Information and Control **8**, 338–353 (1965).
[21] D. Dubois and H. Prade, ''Fuzzy sets in approximate reasoning, Part I: Inference with possibility distributions,'' Fuzzy Sets Syst., **40**, 143–202 (1991).
[22] D. Dubois and H. Prade, ''What are fuzzy rules and how to use them,'' Fuzzy Sets Syst., **84**, 169–185 (1996).
[23] E. Tsiporkova and H.-J. Zimmermann, ''Aggregation of compatibility and equality: a new class of similarity measures for fuzzy sets,'' *Proceedings of IPMU—Information Processing and Management of Uncertainty in Knowledge-Based Systems*, 7th International Conference, Paris, France, 1998, pp. 1769–1776.
[24] M. De Cock and E. Kerre, ''The representation of linguistic hedges using fuzzy relational calculus,'' *Proceedings of the Joint 9th IFSA/20th NAFIPS Conference*, Vancouver, Canada, July 2001, pp. 1608–1613.
[25] G. Klir and B. Yuan, *Fuzzy Sets and Fuzzy Logic: Theory and Applications* (Prentice–Hall, Englewood Cliffs, NJ, 1995).

Statistically stable ultrasonic imaging in random media

James G. Berryman[a)]
University of California, Lawrence Livermore National Laboratory, P.O. Box 808 L-200, Livermore, California 94551-9900

Liliana Borcea[b)]
Computational and Applied Mathematics, Rice University, Houston, Texas 77005-1892

George C. Papanicolaou[c)]
Department of Mathematics, Stanford University, Stanford, California 94305

Chrysoula Tsogka[d)]
CNRS/LMA, 31 Chemin Joseph Aiguier, 13402 Marseille Cedex 20, France

(Received 30 January 2002; revised 31 May 2002; accepted 27 June 2002)

Analysis of array data from acoustic scattering in a random medium with a small number of isolated targets is performed in order to image and, thereby, localize the spatial position of each target. Because the host medium has random fluctuations in wave speed, the background medium is itself a source of scattered energy. It is assumed, however, that the targets are sufficiently larger and/or more reflective than the background fluctuations so that a clear distinction can be made between targets and background scatterers. In numerical simulations nonreflective boundary conditions are used so as to isolate the effects of the host randomness from those of the spatial boundaries, which can then be treated in a separate analysis. It is shown that the key to successful imaging is finding statistically stable functionals of the data whose extreme values provide estimates of scatterer locations. The best ones are related to the eigenfunctions and eigenvalues of the array response matrix, just as one might expect from prior work on array data processing in complex scattering media having homogeneous backgrounds. The specific imaging functionals studied include matched-field processing and linear subspace methods, such as MUSIC (MUtiple SIgnal Classification). But statistical stability is not characteristic of the frequency domain, which is often the province of these methods. By transforming back into the time domain after first diagonalizing the array data in the frequency domain, one can take advantage of both the time-domain stability and the frequency-domain orthogonality of the relevant eigenfunctions. [DOI: 10.1121/1.1502266]

PACS numbers: 43.60.Pt, 43.60.Gk, 43.30.Vh [JJM]

I. INTRODUCTION

Imaging in ultrasonics is closely related to recent studies of time-reversal acoustics that have been experiencing a very rapid growth in interest and research activity since the early work of Fink *et al.*,[1] Jackson and Dowling,[2] and Prada and Fink.[3] In particular, a series of review articles[4–9] has appeared recently that, when taken altogether, largely summarizes the current state-of-the-art.

It is important to distinguish *physical* time-reversal and re-emission of the acoustic signals by the array, so as to produce optimal focusing on a target, from *synthetic* time-reversal processing in which the acoustic array data are used to estimate the location of the scatterers. The work of Prada and Fink[10] and Prada *et al.*[11] on the D.O.R.T. method (French acronym for a diagonalization of the array response matrix) has clarified the connection between individual scattering objects and the eignfunctions of the time-reversal operator. Scatterers can be associated directly with eigenfunctions except when they are not well separated or when they are placed in some special, symmetric positions relative to the array.[12] Such degeneracies are, however, not important in random media.

After decomposing the array response matrix using eigenfunctions (this is normally done in the frequency domain), two alternatives are available for us to pursue. Either we can use the eigenfunctions to refocus acoustic energy back onto the scattering target (for purposes either of communication or medical ultrasound treatments—see, for example, Refs. 9 and 13), or we can try to make use of them to localize or form an image of the scatterers' spatial distribution. Both of these applications are relatively straightforward if the background medium is itself homogeneous.[14] But, if the background medium is heterogeneous (i.e., the acoustic wave speed varies randomly with position), then the difficulties rapidly mount for both applications even if there are no additional complications. Such complications might, for example, include (1) near/close boundaries as will commonly occur in wave guides[15,16] (including the ocean bottom and surface for ocean acoustics[17]), (2) drift of the actual acoustic medium itself or just its physical properties due to currents or temperature fluctuations,[18] (3) periodic changes such as

[a)]Electronic mail: berryman1@llnl.gov
[b)]Electronic mail: borcea@caam.rice.edu
[c)]Electronic mail: papanico@math.stanford.edu
[d)]Electronic mail: tsogka@lma.cnrs-mrs.fr

expansion and contraction due to the breathing of a patient while being diagnosed or treated with ultrasound.

Our focus in this paper will be to ignore any additional complications, and concentrate instead on what difficulties are introduced just by the spatial heterogeneity of the acoustic medium, and what can be done with acoustic array data to achieve reliable images or maps of any significant scatterers present in such media. One companion paper[19] addresses the issues of refocusing sound at a target in the presence of a heterogeneous acoustic background with significant multipathing (multiple scattering), and some of the results on imaging presented here are an outgrowth of another companion paper[20] on acoustic imaging in random media.

It is beyond our current scope to review the literature on acoustics in random media, but we will mention a few relevant references. Early work by Keller[21,22] and Karal and Keller[23,24] has shown that the averaged Green's function in random media is a well-behaved quantity and how the effective wave speed and apparent attenuation due to multiple scattering both depend on the statistics of the fluctuating acoustic wave speed. These and many other topics are presented in Ref. 25. Wave front stabilization in complex and especially in layered media has been observed[26] and studied extensively in Refs. 27–33.

There have been many methods of estimating target location using acoustic array data. Some of the most popular ones in recent years have continued to be matched-field processing,[34–38] MUSIC (MUltiple SIgnal Classification),[12,39,40] and other linear subspace methods.[41–43] We will be discussing necessary modifications of these methods here, since the randomness we consider has a different character than that usually envisioned in these traditional analyses of acoustic array data, because it comes from multipathing that is generated by the random medium.

Typical array processing methods assume that a source is located at a great distance from the array, while the propagating medium is homogeneous, so that from the point of view of the array of the target looks like a point source. The incident sound arriving at the array takes the form of a plane-wave having no measurable curvature across the array aperture and, furthermore, has no measurable amplitude variation across that aperture. Array noise has usually been treated as due either to diffuse sources of white noise coming simultaneously from all directions, or to isolated ''noise'' sources having the same types of source characteristics as the targets of interest. Because the applications of interest have often involved passive bearing detection of active sources, most of the methods and their minor variations considered here were first introduced for such passive data collection and processing problems. But, for time-reversal methods, it quickly becomes clear that virtually the same methods—except for some obvious minor technical differences—should be considered for both active and passive arrays.

Time-reversal processing of the array response data is most naturally based from the outset on the Singular Value Decomposition (SVD). This approach is consistent with the concept of real-space time-reversal—involving an iterative procedure that amounts to using the power method for finding the singular vector of the data matrix having the largest singular value. When the full response/transfer matrix has been measured for a multistatic active array, the resulting data matrix can be analyzed directly by SVD to determine not only the singular vector having the largest singular value, but all singular vectors and singular values—simultaneously. There remain some issues about signal-to-noise ratios suggesting that the physical iterative approach of finding these same singular vectors can be preferable to the purely computational alternative both in acoustics[44] and also in other inverse problems.[45] But it is also important to recognize that the SVD of the transfer matrix does not require specialized hardware (any acoustic array can be used to do this), whereas the physical time-reversal approach for ultrasound does require very specialized and often quite expensive hardware. Thus, SVD may have a distinct advantage in some time-reversal imaging applications.

For acoustical imaging purposes, we do not need to propagate the actual time-reversed signal back into the physical random medium, whereas for either communication or target retrofocusing applications, such real-space backpropagation is always required. From this point of view, time-reversal imaging can also be seen as a relatively inexpensive process. The drawback is that imaging is always done using a fictitious medium for the simulated backpropagation that produces these images since the real medium is not known. Its large scale features could be estimated from other information, such as geological data obtained by seismic methods. For example, migration methods[46–48] can be used, where very large arrays—much larger than those we contemplate using here—are required. However, the small-scale random inhomogeneities are not known and cannot be effectively estimated, so the simplest thing to do is ignore them when imaging.

The following results are based in part on another analytical and computational study of time-reversal in random media by the present authors.[20] In the first section, we briefly present the problem to be studied and then elucidate the notation to be used in the following sections. Then, we present a series of examples—in order to compare and contrast the results. Section II focuses on the standard matched-field and MUSIC objective functionals in the frequency domain. These methods do *not* provide statistically stable results and, therefore, are not useful for imaging in media with randomly fluctuating acoustic wave speed and strong multipathing. Section III then shows how these same objective functionals may be transformed into the time domain in order to produce statistically stable and, therefore, useful images that localize the target cross range (or bearing) in a satisfactory manner. Section IV then goes further to show how range information may be obtained from the time-domain arrival data after careful processing and subsequent averaging of multiple copies of the pertinent singular vectors contained in the multistatic array data. Synthetic Aperture Imaging (SAI) is also used to provide another source of comparison to a familiar data processing scheme. Our conclusions are summarized in Sec. V.

II. PROBLEM STATEMENT AND NOTATION

An array has N transducers located at spatial positions $\mathbf{x}_p$, for $p=1,...,N$. When used in active mode, the array probes the unknown acoustic medium containing M small scatterers by emitting pulses and recording the time traces of the back-scattered echoes. We call the resulting data set the multistatic array response (or transfer) matrix $P(t)=(P_{pq}(t))$, where p and q both range over all the array elements. For our simulations, we consider a linear array where two adjacent point transducers are a distance $\lambda/2$ apart, with λ being the carrier (central) wavelength of the probing pulses. Such an arrangement ensures that the collection of transducers behaves like an array having aperture $a=(N-1)\lambda/2$ and not like separate entities, while keeping the interference among the transducers at a minimum.[49] Our goal is to detect and then localize all M of the targets in the random medium, if possible.

The array response matrix $\hat{P}(\omega)$ in the frequency domain is, in our linear acoustics simulations, symmetric but not Hermitian. The singular value decomposition (SVD) of the response matrix is given explicitly by

$$\hat{P}(\omega)=\hat{U}(\omega)\Sigma(\omega)\hat{V}^H(\omega). \tag{1}$$

The eigenvectors of $\hat{P}(\omega)\hat{P}^H(\omega)$ having unit norm, denoted by $\hat{\mathbf{U}}_r(\omega)$, for $r=1,...,N$, are the columns of matrix $\hat{U}(\omega)$. The eigenvalues of $\hat{P}(\omega)\hat{P}^H(\omega)$ are $\sigma_r^2(\omega)$, with $\sigma_r(\omega)$ being the singular values of $\hat{P}(\omega)$ that form the diagonal matrix $\Sigma(\omega)$. The significant singular vectors $\hat{\mathbf{U}}_r(\omega)$ [i.e., those in the range of $\hat{P}(\omega)$] correspond to singular values $\sigma_r(\omega)>0$ for $1\leqslant r\leqslant M$, where M is either the number of targets, or the size of the array (N)—whichever is smaller. For definiteness, we usually assume that the number of targets is smaller than the array size N, so that M is in fact the number of distinguishable targets. In our setup, the left singular vectors $\hat{\mathbf{U}}_r(\omega)$ are the complex conjugates of the right singular vectors $\hat{\mathbf{V}}_r(\omega)$, for $r=1,...,N$. Most physical arrays, however, are not constructed with isotropic point transducers and, furthermore, the amplitude response (especially in transmission mode) does not have to be linear (with strong deviations from linearity generally occurring at both high and very low amplitudes), so measured response matrices are not necessarily symmetric. We assume symmetry here for simplicity, and this is fully consistent with our linear acoustics simulations. All of our analysis nevertheless carries over to the nonsymmetric case.

We denote by $\hat{\mathbf{g}}_0(\mathbf{y}^s,\omega)$ the vector observed at the array for a source located at $\mathbf{y}^s$ in a deterministic medium (i.e., the medium with the wave speed c_0 given by the averaged velocity of the random medium). In our simulations, c_0 is constant but, in general, it could vary in space—assuming prior knowledge of the environment. Then, $\hat{\mathbf{g}}_0(\mathbf{y},\omega)$ is given by

$$\hat{\mathbf{g}}_0(\mathbf{y}^s,\omega)=\begin{pmatrix}\hat{G}_0(\mathbf{y}^s,\mathbf{x}_1,\omega)\\ \hat{G}_0(\mathbf{y}^s,\mathbf{x}_2,\omega)\\ \vdots\\ \hat{G}_0(\mathbf{y}^s,\mathbf{x}_N,\omega)\end{pmatrix}, \tag{2}$$

where $\hat{G}_0(\mathbf{y}^s,\mathbf{x}_j,\omega)$ is the deterministic two-point Green's function, and $\mathbf{x}_j$ is the location of the jth array element.

We also define the projection $\mathcal{P}_N\hat{\mathbf{g}}_0(\mathbf{y},\omega)$ of $\hat{\mathbf{g}}_0(\mathbf{y}^s,\omega)$ onto the null-space of $\hat{P}\hat{P}^H(\omega)$ by

$$\mathcal{P}_N\hat{\mathbf{g}}_0(\mathbf{y}^s,\omega)=\hat{\mathbf{g}}_0(\mathbf{y}^s,\omega)-\sum_{r=1}^{M}[\hat{\mathbf{U}}_r^H(\omega)\hat{\mathbf{g}}_0(\mathbf{y}^s,\omega)]\hat{\mathbf{U}}_r(\omega), \tag{3}$$

for each frequency in the support of the probing pulse $\hat{f}(\omega)$.

Our simulations assume that $\lambda\leqslant\ell\ll a=(N-1)\lambda/2\ll L$, where λ is the central wavelength, ℓ is a characteristic length scale of the inhomogeneity (like a correlation length), a is the array aperture, and L is the approximate distance to the targets from the array. This is the regime where multipathing, or multiple scattering, is significant even when the standard deviation of sound speed fluctuations is only a few percent.

We solve the wave equation in 2D with a numerical method based on the discretization of the mixed velocity-pressure formulation for acoustics. For the spatial discretization we use a new finite element method,[50] which is compatible with mass-lumping techniques (i.e., it leads to explicit time discretization schemes) and for the time discretization we use a centered second order finite difference scheme. In the numerical simulations, we have statistically homogeneous Gaussian random velocity fields generated using a random Fourier series, with constant mean $c_0=1.5$ km/s, and exponential correlation function having correlation length $\ell=0.3$ mm and standard deviation ranging from 1% to 5%. The probing pulse is given by

$$f(t)=-2\pi^2\nu^2\left(t-\frac{1}{\nu}\right)e^{-\pi^2\nu^2[t-(1/\nu)]^2}. \tag{4}$$

The central frequency is $\nu=3$ MHz and $\hat{f}(\omega)$, $(\omega=2\pi\nu)$ is supported over the band of frequencies 0.159–7.958 MHz. The carrier wavelength is $\lambda=0.5$ mm and the aperture of the array is $a=2.5$ mm. Then, the targets, which are soft scatterers, are modeled by small squares. The size of a small target is $\lambda/30\times\lambda/30$, while the size of a larger one is $\lambda/15\times\lambda/15$. Simulations are done on individual realizations, to be consistent with what happens in practice; there is no averaging of results from many realizations here. Furthermore, the same realization is typically used for the tests of all the imaging methods. Whenever the parameters (s and M.F.) (M.F., maximum fluctuations) are fixed, the realization is also fixed; but when the parameters change, the realization necessarily has changed. More details concerning the simulations may be found in Refs. 20 and 50.

We purposely present all the formulas in their most general form in terms of Green's functions. Thus, these formulas are valid either in 2D, as is relevant specifically to our simulations, or in 3D. The comparisons shown here use the Hankel-function fields in free space for the 2D simulations, but these functions would be replaced by point source Green's functions of the form $e^{ikr}/4\pi r$ for realistic data applications in 3D. Due to the high cost of numerically simulating wave propagation in random medium, with significant multipathing, we only did 2D simulations up to now.

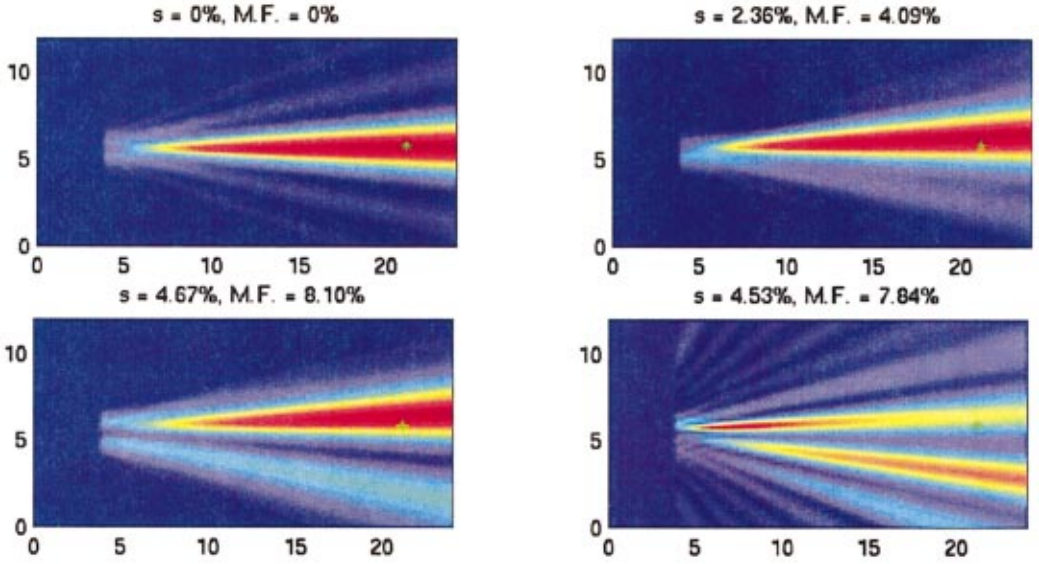

FIG. 1. The matched field central frequency [MF estimate (6)] estimate of the location of one target in random media with different strength of the fluctuations of the sound speed. The exact location of the target is denoted by the green star. The standard deviation s and maximum fluctuations (M.F.) are indicated on the top of each view. The horizontal axis is the range in mm and the vertical axis is the cross range in mm.

III. FREQUENCY DOMAIN METHODS: NOT STATISTICALLY STABLE

Two well-known frequency-domain imaging methods, matched-field processing[34–36,38,51] and MUSIC,[12,39–42,52,53] will be presented next to show how these methods behave in the types of random media we are considering.

A. Matched field–central frequency

For matched-field (MF) processing, we compute

$$\mathcal{G}^{(j)}_{\mathrm{MF}}(\mathbf{y}^s) = |\hat{\mathbf{U}}^H_j(\omega)\hat{\mathbf{g}}_0(\mathbf{y}^s,\omega)|^2, \tag{5}$$

and display the objective functional

$$\mathcal{R}_{\mathrm{MF}}(\mathbf{y}^s) = \sum_{j=1}^{M} \frac{\mathcal{G}^{(j)}_{\mathrm{MF}}(\mathbf{y}^s)}{\max_{\mathbf{y}^s} \mathcal{G}^{(j)}_{\mathrm{MF}}(\mathbf{y}^s)}, \tag{6}$$

for a discrete set of points (usually regularly spaced on a grid which then aids in the ultimate computer display) $\mathbf{y}^s$ in the target domain.

Examples of matched-field processing with one or two targets are displayed in Figs. 1 and 2.

The standard-matched-field (SMF) processing[38] uses a somewhat different functional operating directly on $\hat{P}(\omega)\hat{P}^H(\omega)$. In our notation, the Bartlett-type objective functional of Ref. 38 is

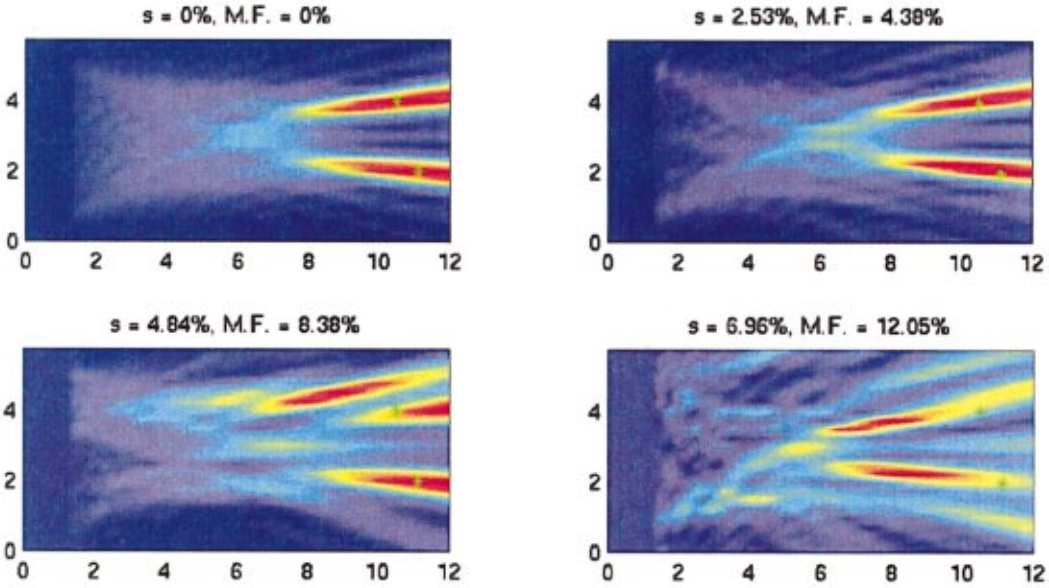

FIG. 2. Similar to Fig. 1 but with two targets.

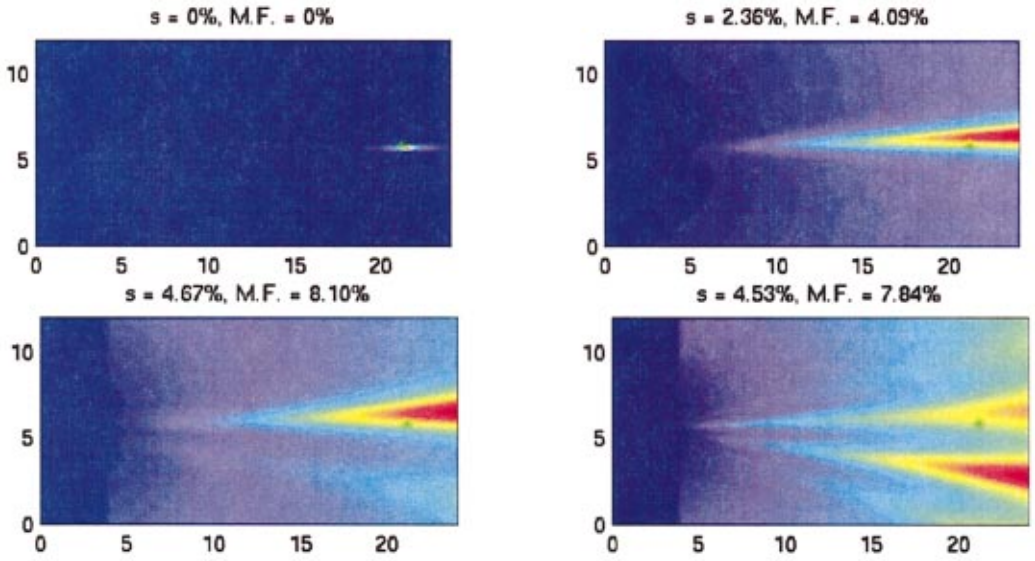

FIG. 3. The MUSIC central frequency estimate [MUSIC estimate (9)] of the location of one target in random media with different strength of the fluctuations of the sound speed. The exact location of the target is denoted by the green star. The standard deviation s and maximum fluctuations (M.F.) are indicated on the top of each view. The horizontal axis is the range in mm and the vertical axis is the cross range in mm.

$$\mathcal{R}_{\mathrm{SMF}}(\mathbf{y}^s)=\sum_{j=1}^{M}\sigma_j^2(\omega)\mathcal{G}_{\mathrm{SMF}}^{(j)}(\mathbf{y}^s), \tag{7}$$

where $\sigma_j^2(\omega)$ is the singular value corresponding to the singular vector $\hat{\mathbf{U}}_j(\omega)$ and

$$\mathcal{G}_{\mathrm{SMF}}^{(j)}(\mathbf{y}^s)=\frac{|\hat{\mathbf{U}}_j^H(\omega)\hat{\mathbf{g}}_0(\mathbf{y}^s,\omega)|^2}{|\hat{\mathbf{g}}_0(\mathbf{y}^s,\omega)|^2}. \tag{8}$$

If there is a small number of targets and these targets do not differ significantly in strength at the central frequency (as is the case in our simulations), then there is no essential difference between the two imaging functionals. If, for example, we want to identify only the strongest scatterer, then we may consider only the first term in either sum, since the singular vectors are ordered according to their corresponding singular values from largest to smallest.

B. MUSIC—central frequency

For the MUSIC algorithm, we compute

$$\mathcal{G}_{\mathrm{MUSIC}}(\mathbf{y}^s)=|\mathcal{P}_N\hat{\mathbf{g}}_0(\mathbf{y}^s,\omega)|^2, \tag{9}$$

with $\mathcal{P}_N\hat{\mathbf{g}}_0(\mathbf{y}^s,\omega)$ defined by (3). We display the objective functional

$$\mathcal{R}_{\mathrm{MUSIC}}(\mathbf{y}^s)=\frac{\min_{\mathbf{y}^s}\mathcal{G}_{\mathrm{MUSIC}}(\mathbf{y}^s)}{\mathcal{G}_{\mathrm{MUSIC}}(\mathbf{y}^s)}, \tag{10}$$

for points $\mathbf{y}^s$ in the target domain.

Examples for MUSIC with one or two targets in homo-

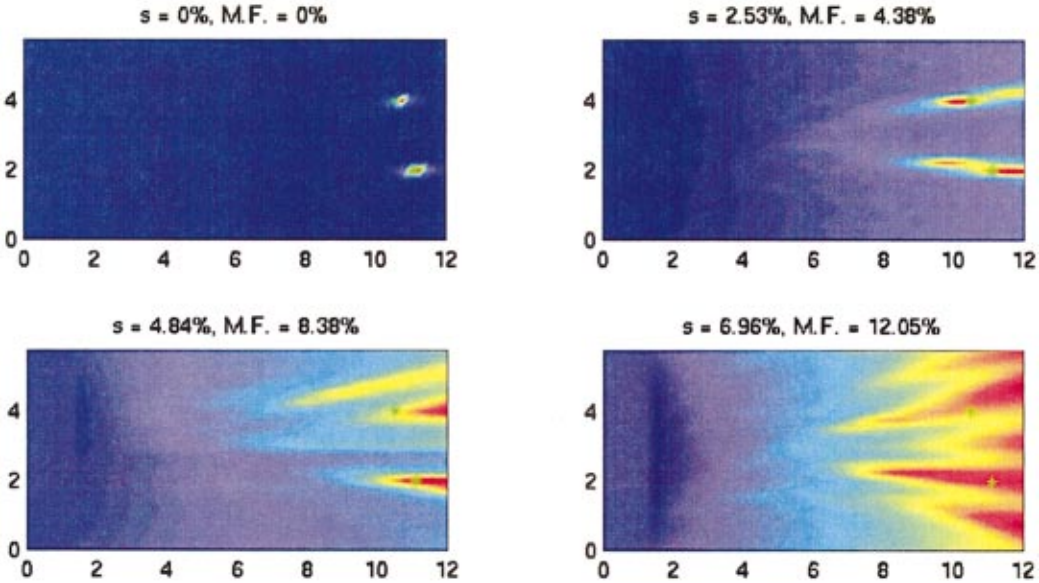

FIG. 4. Similar to Fig. 3 but with two targets.

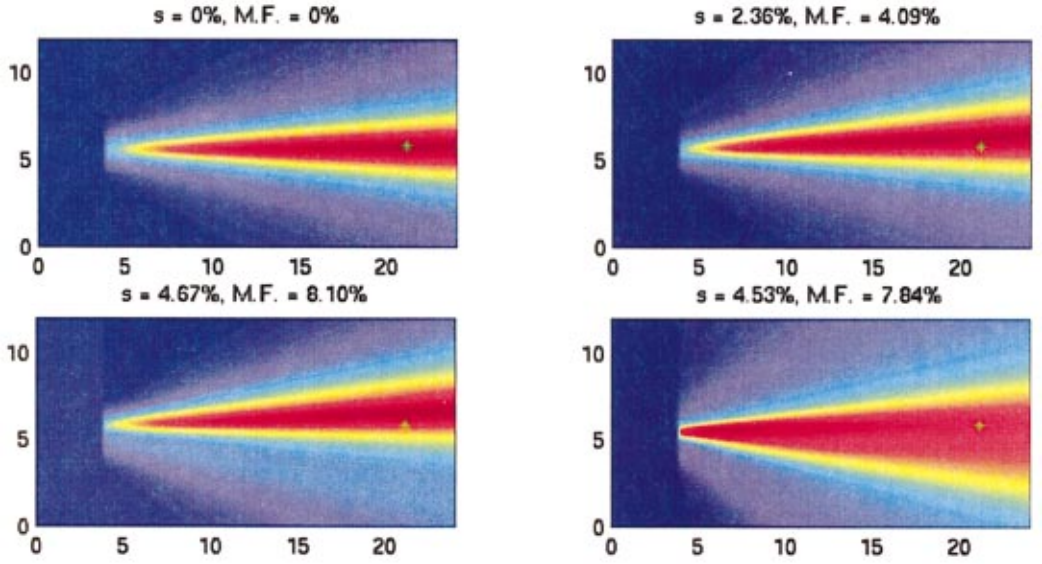

FIG. 5. The matched field time estimate [MF_T estimate (12)] of the location of one target in random media with different strength of the fluctuations of the sound speed. The exact location of the target is denoted by the green star. The standard deviation s and maximum fluctuations (M.F.) are indicated on the top of each view. The horizontal axis is the range in mm and the vertical axis is the cross range in mm.

geneous and random media are displayed in Figs. 3 and 4.

When there is only one target in a homogeneous medium, then there is only one significant eigenvector of the array response matrix and it is proportional to $\hat{\mathbf{g}}_0(\mathbf{y}^t,\omega)$, where $\mathbf{y}^t$ is the target location. It is clear in this case that both the MF and the MUSIC functionals have only a single term which peaks when $\mathbf{y}^s=\mathbf{y}^t$. Similarly, in the case of several targets in a homogeneous medium, the significant eigenvectors are linear combinations of $\hat{\mathbf{g}}_0(\mathbf{y}_j^t,\omega)$, where $\mathbf{y}_j^t$ are the target locations and the functionals will have local maxima at the target locations.

In both of these frequency domain examples, it is clear from the figures that no range information is obtained from these objective functionals in random media, and even the cross-range information is often quite haphazard. Indeed, as the random fluctuations in the velocity increase, there are false peaks and the functionals may not peak at the targets at all. (Note that MUSIC does provide the correct range for the zero variance case.) Lack of statistical stability prevents these imaging approaches from being useful in random media with significant multipathing considered here. When the realization of the random medium is changed, the images obtained typically change also—which is what we mean by the phrase ''lack of statistical stability'' for these methods.

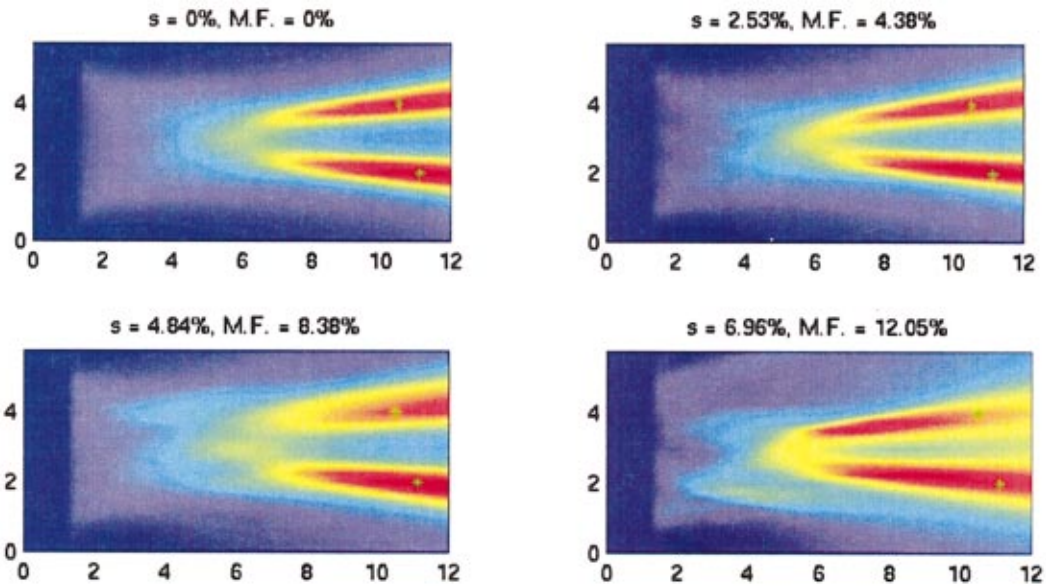

FIG. 6. Similar to Fig. 5 but with two targets.

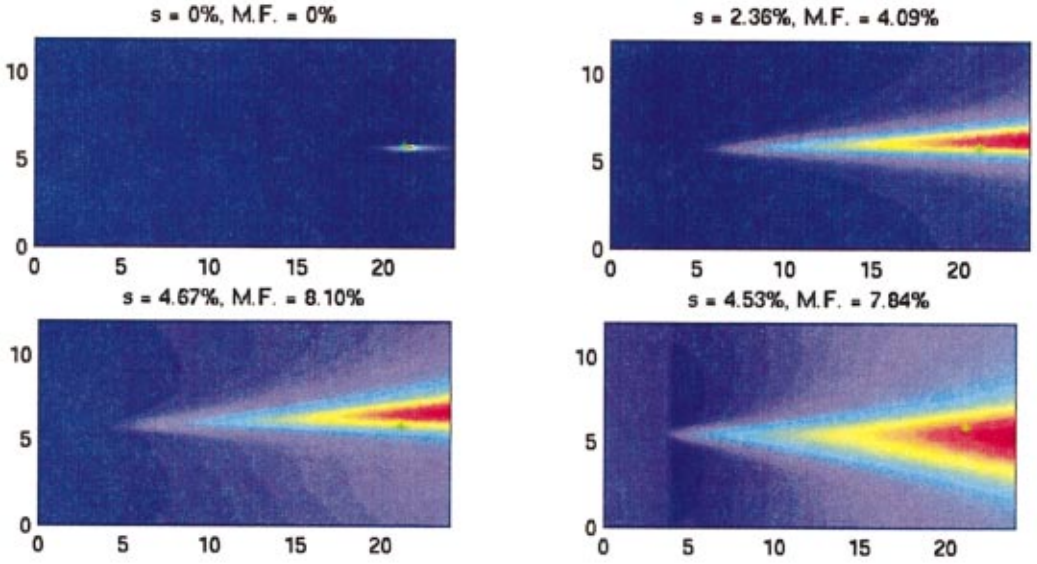

FIG. 7. The DOA estimate [DOA estimate (15)] of the location of one target in random media with different strength of the fluctuations of the sound speed. The exact location of the target is denoted by the green star. The standard deviation s and maximum fluctuations (M.F.) are indicated on the top of each view. The horizontal axis is the range in mm and the vertical axis is the cross range in mm.

IV. STATISTICALLY STABLE TIME DOMAIN METHODS

Next we consider the same two methods of the preceding section, but now we transform back to the time domain to take advantage of the statistical stability that can be gained this way.

A. Matched field in time

For matched-field processing, we compute

$$\mathcal{G}^{(j)}_{\mathrm{MF}_T}(\mathbf{y}^s,t)=\int e^{-i\omega t}\sigma_j(\omega)|\hat{\mathbf{U}}^H_j(\omega)\hat{\mathbf{g}}_0(\mathbf{y}^s,\omega)|^2\,d\omega. \quad (11)$$

Since the factor multiplying $e^{-i\omega t}$ in the integrand is real and nonnegative, this integral clearly takes its maximum value for $t=0$—which is also, therefore, the location of the peak of the corresponding pulse in the time domain. We then display the objective functional

$$\mathcal{R}_{\mathrm{MF}_T}(\mathbf{y}^s)=\sum_{j=1}^{M}\frac{\mathcal{G}^{(j)}_{\mathrm{MF}_T}(\mathbf{y}^s,t=0)}{\max_{\mathbf{y}^s}\mathcal{G}^{(j)}_{\mathrm{MF}_T}(\mathbf{y}^s,t=0)}, \quad (12)$$

for points $\mathbf{y}^s$ in the target domain.

Examples of matched-field processing in the time domain with one or two targets are displayed in Figs. 5 and 6.

B. DOA (time-domain MUSIC)

The next method is a time-domain variant of MUSIC which we will label DOA, because it gives very good esti-

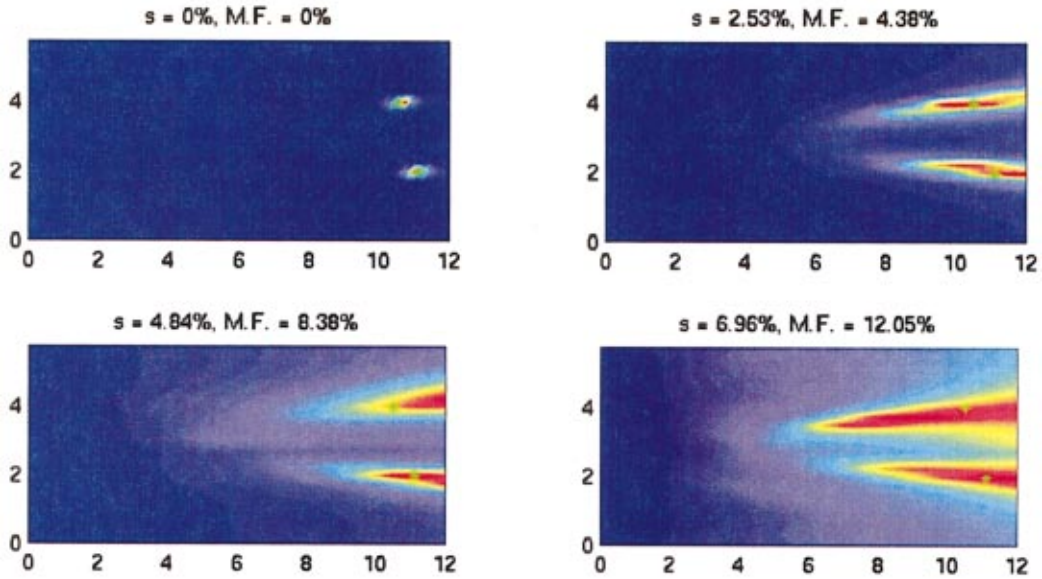

FIG. 8. Similar to Fig. 7 but with two targets.

mates of the direction of arrival. (Note that matched field in time also gives good estimates of the direction of arrival.)

To define a time variant of MUSIC, we first normalize the projection $\mathcal{P}_N\hat{\mathbf{g}}_0(\mathbf{y}^s,\omega)$ [given by (3)] by the singular value $\sigma_j(\omega)$ and then take the inverse Fourier transform to go to the time domain,

$$\mathcal{F}^{(j)}(\mathbf{y}^s,t)=\int e^{-i\omega t}\sigma_j(\omega)\hat{\mathbf{g}}_0(\mathbf{y}^s,\omega)d\omega-\int e^{-i\omega t}\sigma_j(\omega)\times\sum_{r=1}^{M}[\hat{\mathbf{U}}_r^H(\omega)\hat{\mathbf{g}}_0(\mathbf{y}^s,\omega)]\hat{\mathbf{U}}_r(\omega)d\omega. \tag{13}$$

Theoretical analysis shows that the functionals $\mathcal{F}^{(j)}(\mathbf{y}^s,t)$ are statistically stable, i.e., they behave like deterministic quantities, and thus it seems natural to evaluate them at deterministic times (i.e., simple geometrical spreading times). We then form the sum

$$\mathcal{G}^{(j)}(\mathbf{y}^s)=\sum_{p=1}^{N}|\mathcal{F}^{(j)}(\mathbf{y}^s,t_p(\mathbf{y}^s))|^2, \tag{14}$$

and display the objective functional

$$\mathcal{R}_{\mathrm{DOA}}(\mathbf{y}^s)=\sum_{j=1}^{M}\frac{\min_{\mathbf{y}^s}\mathcal{G}^{(j)}(\mathbf{y}^s)}{\mathcal{G}^{(j)}(\mathbf{y}^s)}, \tag{15}$$

for points $\mathbf{y}^s$ in the target domain.

The arrival time $t_p(\mathbf{y}^s)$ is the deterministic travel time from the pth transducer to the search point,

$$t_p(\mathbf{y}^s)=\frac{|\mathbf{x}_p-\mathbf{y}^s|}{c_0}. \tag{16}$$

Examples for time-domain MUSIC with one or two targets are displayed in Figs. 7 and 8.

The cross-range results are now dramatically improved in both methods. Range information is still not to be found here, but the statistical stability of the universal ''comet tails'' is now easily observed. The images shown are for specific realizations, but the results do not change significantly when the underlying realization of the random medium is changed. This fact has been repeatedly shown in our simulations, and is the main characteristic of statistically stable methods.

V. TIME DOMAIN PROCESSING AND RANGE ESTIMATION METHODS

To complete the localization of the targets, we also need an estimate of the range. Good range estimates can be obtained in the near field either from amplitude moveout information or from arrival time information. In the far field, only the arrival time information is useful, and we will concentrate on arrival times in the present analysis.

One commonly used range estimator is Synthetic Aperture Imaging or SAI. Another alternative that arises in the time-reversal approach is the use of arrival time information in the singular vectors. This arrival time information can also be averaged for random media—see Ref. 20—to obtain very stable estimates of arrival times. Both of these methods will now be combined with the time-domain methods of the preceding section to obtain well-localized images of the targets.

A. Matched field in time combined with SAI

The SAI objective function is

$$\mathcal{R}_{\mathrm{SAI}}(\mathbf{y}^s)=\sum_{p=1}^{N}P_{pp}(2t_p(\mathbf{y}^s)). \tag{17}$$

At a search point $\mathbf{y}^s$ in the domain of interest, we compute the deterministic arrival time for diagonal entry $P_{pp}(t)$. That is, the time to go from the pth transducer to the search point $\mathbf{y}^s$ and then come back to the pth transducer. This is twice the arrival time $t_p(\mathbf{y}^s)$ given by (16). Note that the SAI functional gives good range information even in random media (see Ref. 20).

The idea here is to combine the functional SAI which gives good range information with the functional MF_T which provides good cross range resolution in order to get good images. One way of doing this combination is to display

$$\mathcal{R}_{\mathrm{MF}_T-\mathrm{SAI}}(\mathbf{y}^s)=\sum_{j=1}^{M}\frac{\mathcal{G}^{(j)}_{\mathrm{MF}_T-\mathrm{SAI}}(\mathbf{y}^s)}{\max_{\mathbf{y}^s}\mathcal{G}^{(j)}_{\mathrm{MF}_T-\mathrm{SAI}}(\mathbf{y}^s)}, \tag{18}$$

where

$$\mathcal{G}^{(j)}_{\mathrm{MF}_T-\mathrm{SAI}}(\mathbf{y}^s)=\left|\sum_{p=1}^{N}P_{pp}(2t_p(\mathbf{y}^s))\right|\mathcal{G}^{(j)}_{\mathrm{MF}_T}(\mathbf{y}^s,t=0). \tag{19}$$

Examples of time-domain matched-field processing with Synthetic Aperture Imaging as the range estimator for one or two targets are displayed in Figs. 9 and 10. The method is statistically stable and gives good estimates of the target locations.

B. Matched field in time combined with times from averaged singular vectors

We would like to use the singular vectors $\hat{\mathbf{U}}_j(\omega)$ to estimate the travel times from target j to the array. Remark though that the singular vectors $\hat{\mathbf{U}}_j(\omega)$ which are normalized ($\|\hat{\mathbf{U}}_j(\omega)\|=1$) carry an arbitrary, frequency dependent, phase. Because of this $\mathbf{U}_j(t)$ look incoherent in the time domain. We can, however, calculate N, coherent in time, versions of singular vectors by projecting the columns of the response matrix onto them

$$\hat{\mathbf{U}}_j^{(p)}(\omega)=[\hat{\mathbf{U}}_j(\omega)^H\hat{\mathbf{P}}^{(p)}(\omega)]\hat{\mathbf{U}}_j(\omega),\quad p=1,...,N,\quad j=1,...,M. \tag{20}$$

Here $\hat{\mathbf{P}}^{(p)}$ is the pth column of the response matrix $\hat{P}(\omega)$. Clearly $\hat{\mathbf{U}}_j^{(p)}(\omega)$ are singular vectors of $\hat{P}(\omega)$ and carry the phase of its pth column. We use these various versions of the singular vectors to estimate $\tau_p^{(j)}$, for $j=1,...,M$, and $p=1,...,N$, the travel times for target j to the array element p as the minimizers of

$$\min_{\tau_p^{(j)}}\int_0^T\sum_{p=1}^{N}\left|\mathbf{U}_j^{(p)}(t-\tau_p^{(j)})-\frac{1}{N}\sum_{q=1}^{N}\mathbf{U}_j^{(q)}(t-\tau_q^{(j)})\right|^2dt. \tag{21}$$

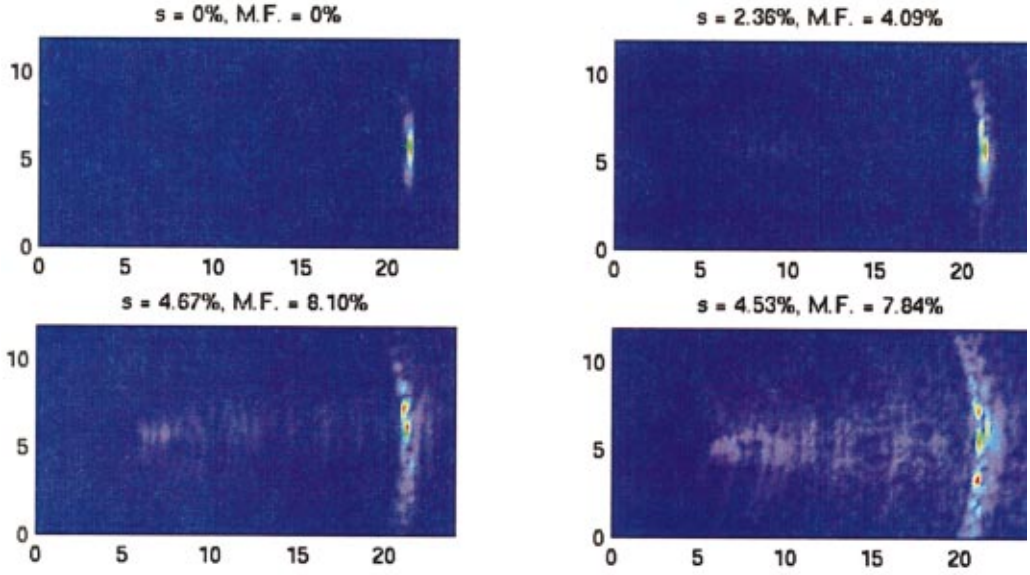

FIG. 9. Combined MF_T and SAI [MF_T−SAI estimate (18)] estimation of the location of one target in random media with different strength of the fluctuations of the sound speed. The exact location of the target is denoted by the green star. The standard deviation s and maximum fluctuations (M.F.) are indicated on the top of each view. The horizontal axis is the range in mm and the vertical axis is the cross range in mm.

The ATSV (Arrival Times from averaged Singular Vectors) functional is defined by

$$\mathcal{R}_{\mathrm{ATSV}}(\mathbf{y}^s)=\sum_{j=1}^{M}\frac{\min_{\mathbf{y}^s}\mathcal{G}^{(j)}_{\mathrm{ATSV}}(\mathbf{y}^s)}{\mathcal{G}^{(j)}_{\mathrm{ATSV}}(\mathbf{y}^s)}, \tag{22}$$

where

$$\mathcal{G}^{(j)}_{\mathrm{ATSV}}(\mathbf{y}^s)=\sum_{p=1}^{N}[\tau_p^{(j)}-2t_p(\mathbf{y}^s)]^2. \tag{23}$$

We combine MF_T with ATSV to obtain

$$\mathcal{R}_{\mathrm{MF}_T-\mathrm{ATSV}}(\mathbf{y}^s)=\sum_{j=1}^{M}\frac{\mathcal{G}^{(j)}_{\mathrm{MF}_T-\mathrm{ATSV}}(\mathbf{y}^s)}{\max_{\mathbf{y}^s}\mathcal{G}^{(j)}_{\mathrm{MF}_T-\mathrm{ATSV}}(\mathbf{y}^s)}, \tag{24}$$

where

$$\mathcal{G}^{(j)}_{\mathrm{MF}_T-\mathrm{ATSV}}(\mathbf{y}^s)=\mathcal{G}^{(j)}_{\mathrm{MF}_T}(\mathbf{y}^s)/\mathcal{G}^{(j)}_{\mathrm{ATSV}}(\mathbf{y}^s). \tag{25}$$

Examples of time-domain matched-field processing with arrival-time estimates from the averaged singular vectors for one or two targets are displayed in Figs. 11 and 12. This method is also statistically stable and gives good estimates of the target locations. The results look somewhat better than those in Figs. 9 and 10, and considerably better for stronger fluctuations.

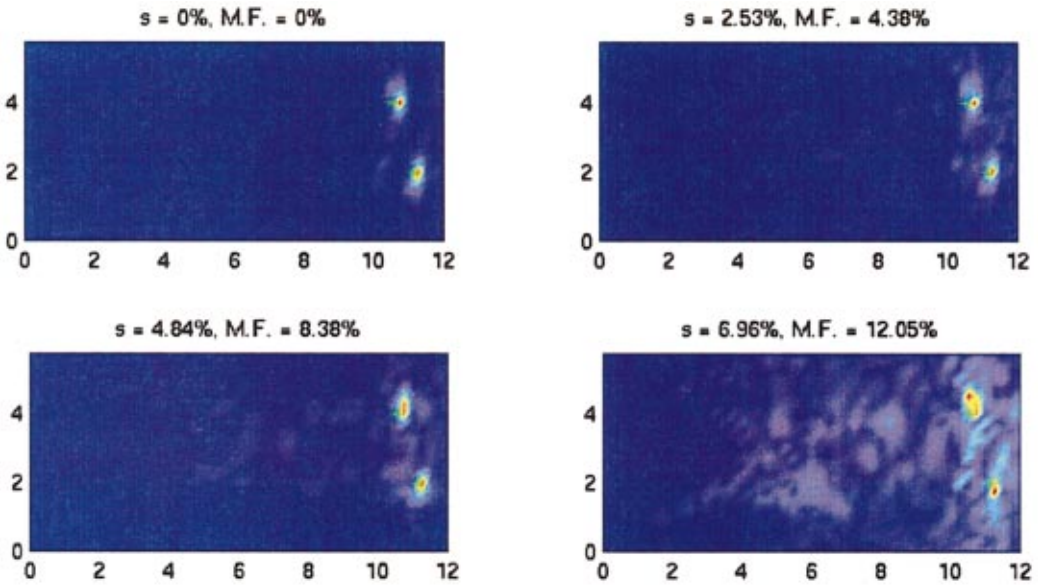

FIG. 10. Similar to Fig. 9 but with two targets.

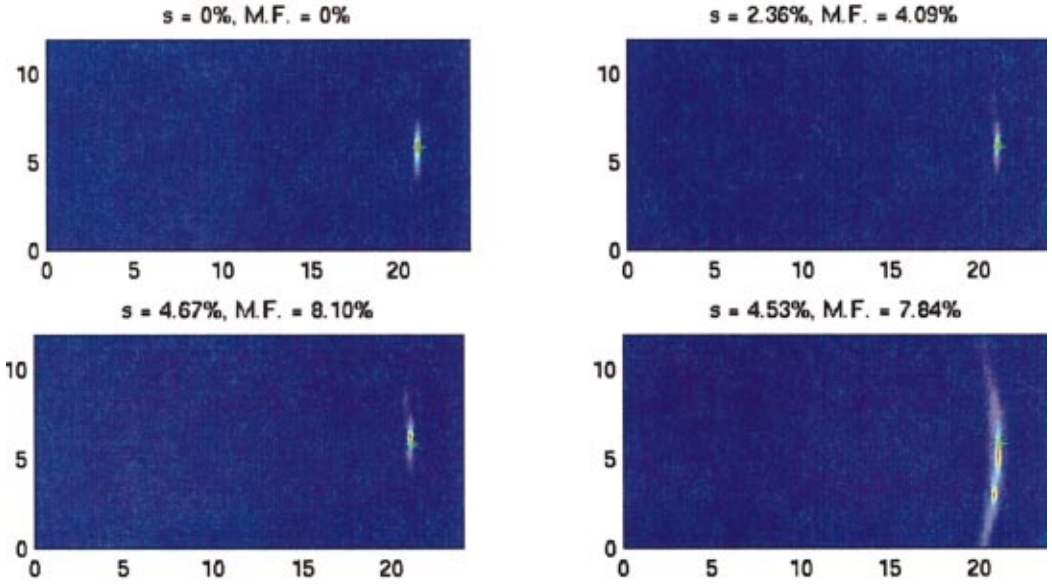

FIG. 11. Combined MF_T and ATSV [MF_T−ATSV estimate (24)] estimation of one target location in random media with different strength of the fluctuations of the sound speed. The exact location of the target is denoted by the green star. The standard deviation s and maximum fluctuations (M.F.) are indicated on the top of each view. The horizontal axis is the range in mm and the vertical axis is the cross range in mm.

C. DOA combined with SAI

The DOA–SAI estimator is

$$\mathcal{R}_{\mathrm{DOA-SAI}}(\mathbf{y}^s)=\sum_{j=1}^{M}\frac{\mathcal{G}^{(j)}_{\mathrm{DOA-SAI}}(\mathbf{y}^s)}{\max_{\mathbf{y}^s}\mathcal{G}^{(j)}_{\mathrm{DOA-SAI}}(\mathbf{y}^s)}, \tag{26}$$

where

$$\mathcal{G}^{(j)}_{\mathrm{DOA-SAI}}(\mathbf{y}^s)=\left|\sum_{p=1}^{N}P_{pp}(2t_p(\mathbf{y}^s))\right| \Big/ \mathcal{G}^{(j)}(\mathbf{y}^s), \tag{27}$$

and $\mathcal{G}^{(j)}(\mathbf{y}^s)$ is given by (14).

Examples of time-domain MUSIC with Synthetic Aperture Imaging estimates as range estimator for one or two targets are displayed in Figs. 13 and 14. This method is also statistically stable and gives good estimates of the target locations.

D. DOA combined with arrival times from averaged singular vectors

For each search point $\mathbf{y}_s$, we compute the objective functional

$$\mathcal{R}_{\mathrm{SAT}}(\mathbf{y}^s)=\sum_{j=1}^{M}\frac{\min_{\mathbf{y}^s}\mathcal{G}^{(j)}_{\mathrm{SAT}}(\mathbf{y}^s)}{\mathcal{G}^{(j)}_{\mathrm{SAT}}(\mathbf{y}^s)}, \tag{28}$$

where

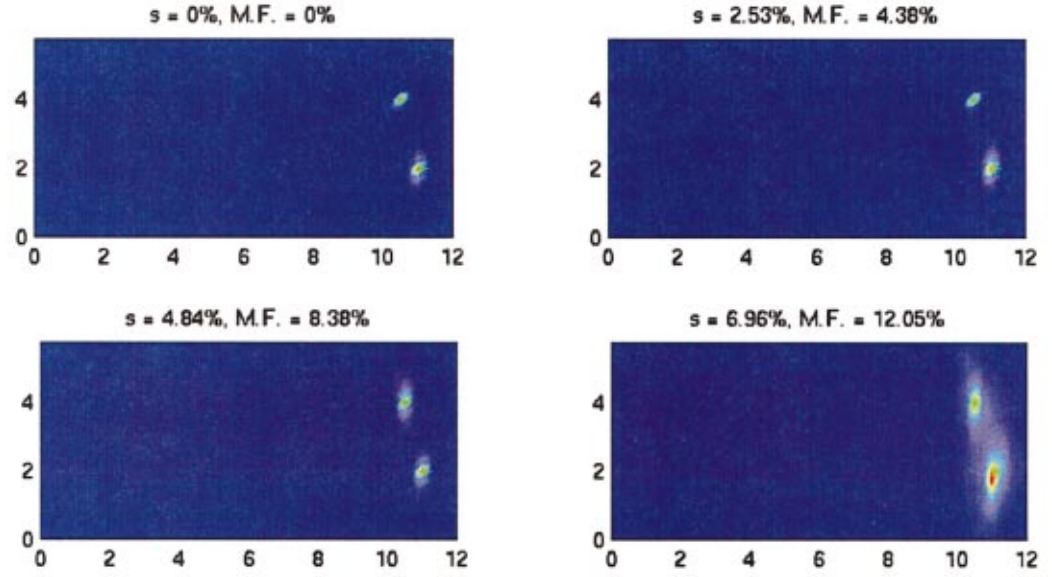

FIG. 12. Similar to Fig. 11 but with two targets.

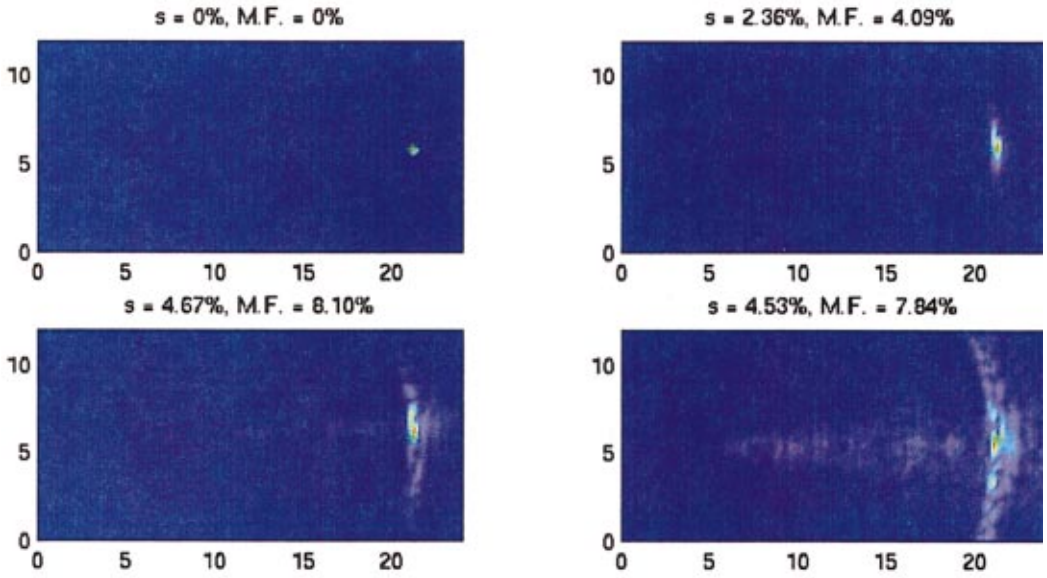

FIG. 13. Combined DOA and SAI [DOA–SAI estimate (26)] estimation of one target location in random media with different strength of the fluctuations of the sound speed. The exact location of the target is denoted by the green star. The standard deviation s and maximum fluctuations (M.F.) are indicated on the top of each view. The horizontal axis is the range in mm and the vertical axis is the cross range in mm.

$$\mathcal{G}^{(j)}_{\mathrm{SAT}}(\mathbf{y}^s) = \sum_{p=1}^{N} |\mathcal{F}^{(j)}(\mathbf{y}^s, t_p(\mathbf{y}^s))|^2 [\tau_p^{(j)} - t_p(\mathbf{y}^s)]^2. \qquad (29)$$

Here $\mathcal{F}^{(j)}(\mathbf{y}^s,t)$ is defined by (13), $t_p(\mathbf{y}^s)$, for $p=1,...,N$, are the deterministic arrival times given by (16) and $\tau_p^{(j)}$, for $p=1,...,N$, and $j=1,...,M$, are the arrival times computed in (21). We call (28) the Subspace Arrival Time (SAT) estimator.

Examples of SAT or time-domain MUSIC with arrival time estimates from the averaged singular vectors for one or two targets are displayed in Figs. 15 and 16. This method is again statistically stable and gives good estimates of the target locations. The results again look somewhat better than those in Figs. 13 and 14. These localization results have apparently degraded the least of all those considered here at the highest values of the random fluctuations.

VI. CONCLUSIONS

For imaging applications in randomly inhomogeneous acoustical media, the foregoing results lead us to the following conclusions: (1) Single frequency methods (including MUSIC and D.O.R.T.) are not statistically stable, and therefore cannot be used without modification in the presence of significant amounts of spatial heterogeneity in the acoustic wave speed distribution. (2) In contrast, time-domain methods are statistically stable for any objective functional having the characteristic that the random Green's functions appear in

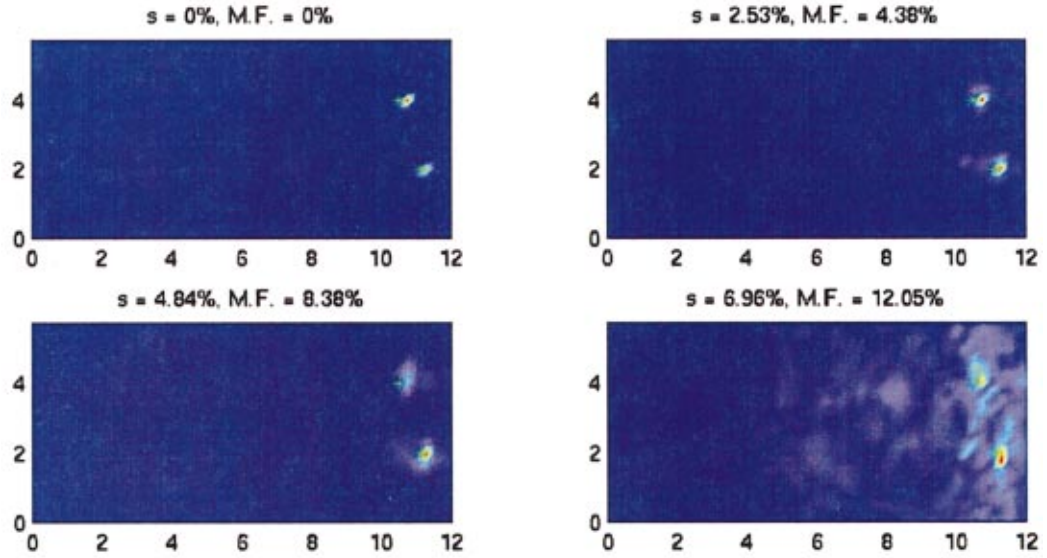

FIG. 14. Same as Fig. 13 with two targets.

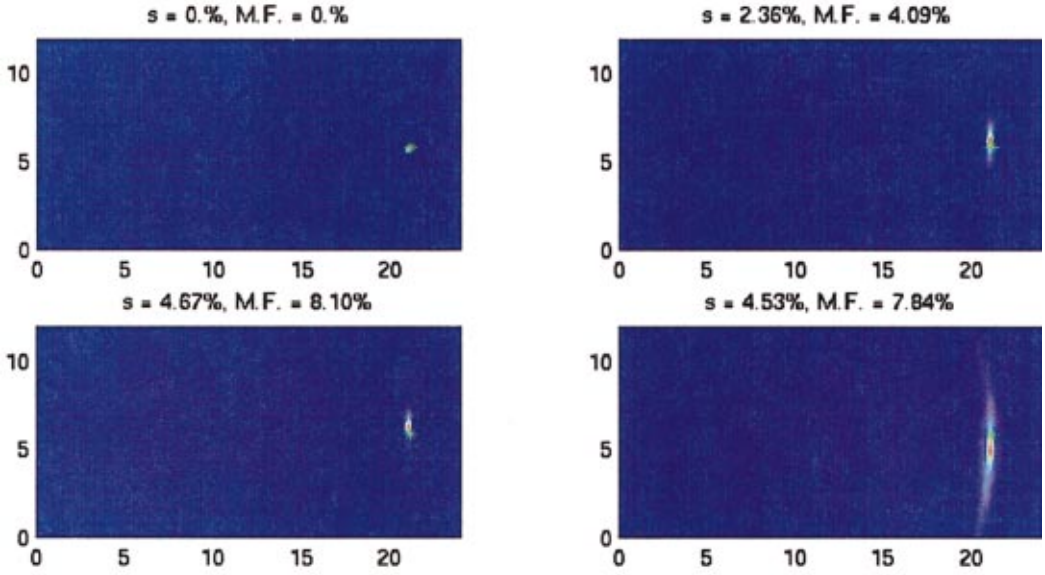

FIG. 15. The SAT estimate [estimate (28)] of one target in random media with different strength of the fluctuations of the sound speed. The exact location of the target is denoted by the green star. The standard deviation s and maximum fluctuations (M.F.) are indicated on the top of each view. The horizontal axis is the range in mm and the vertical axis is the cross range in mm.

Hermitian conjugate pairs of gg^*.[20] This result has been shown here to be true for DOA and Matched Field, and is expected to be true more generally. (Of course, statistical stability is a necessary, but not a sufficient, condition for optimal imaging in random media, so satisfaction of this criterion is not enough in itself.) (3) The DOA estimates seem superior to those of Matched Field, but a careful analysis shows that this is only superficially so because of the quantity chosen for display in these plots. In the homogeneous case, exact calculations show that this superficial difference is just related to shapes (not the locations) of the peaks in each of the objective functionals, and therefore is only a display issue and not fundamental. (4) Both DOA and Matched Field give only cross-range or bearing information. Range information must be obtained separately.

To locate the targets in random media, we need either multiple views (using multiple arrays) so we can triangulate, or we need to extract a direct measure of range from the data. Both arrival time and amplitude moveout (i.e., changes in peak arrival time and amplitude correlated directly with the array element locations) contain sufficient information to extract range. Usefulness of amplitudes is limited by the range itself; if the range is so large that the arrivals appear as planar across the array aperture then only the plane-wave arrival time is useful. In the examples chosen here, we concentrated on arrival time and this information was obtained by combining MF with either SAI or ATSV (arrival times from averaged singular vectors). As anticipated, results obtained after intersection with SAI are not as good as the ones obtained after intersection with ATSV. But the results were shown

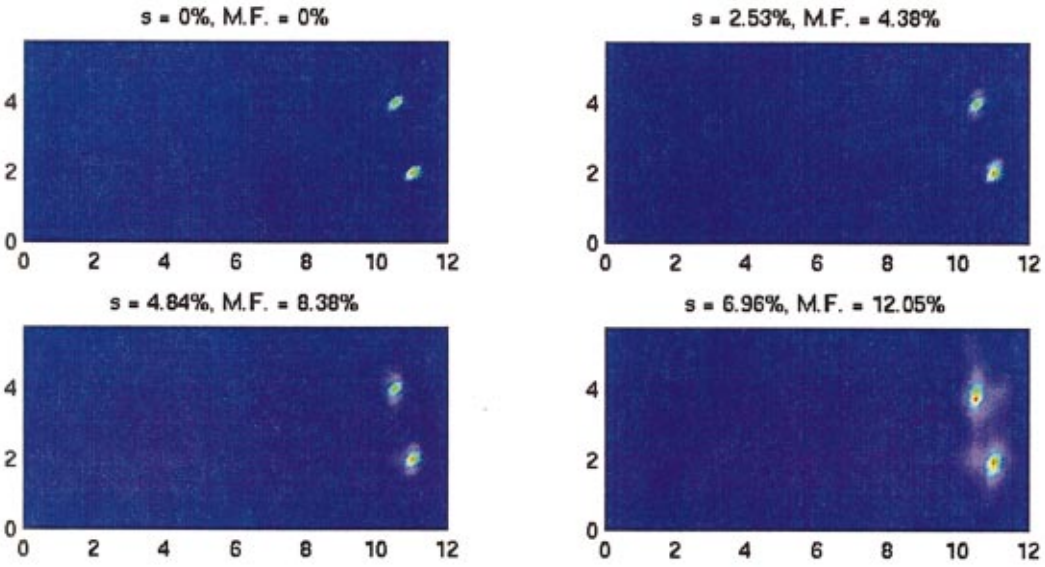

FIG. 16. The SAT estimate as in Fig. 15 for two targets.

nevertheless to be a good compromise because this method does not require a separate arrival time analysis (recall that SAI is not statistically stable[20]).

Our main conclusion is that there is no essential difference in imaging with MF or DOA when either SAI or ATSV are used.

ACKNOWLEDGMENTS

We thank W. A. Kuperman and H. C. Song for helpful leads into the array processing literature. We thank D. H. Chambers for useful comments on the paper. The work of J. G. Berryman was performed under the auspices of the U.S. Department of Energy by the University of California Lawrence Livermore National Laboratory under Contract No. W-7405-ENG-48 and supported specifically by the LLNL Laboratory Directed Research and Development Program and Environmental Management Sciences Program. The work of L. Borcea was partially supported by the National Science Foundation under grants Nos. DMS-9971209 and DMS97-09320, by DOE DE-FG03-00ER25424, and by ONR Grant No. N00014-02-1-0088. The work of G. C. Papanicolaou was supported by grants AFOSR F49620-01-1-0465, NSF DMS-9971972, DOE DE-FG03-00ER25424, and ONR N00014-02-1-0088.

[1] M. Fink, C. Prada, F. Wu, and D. Casserau, ''Self focusing in inhomogeneous media with time reversal acoustic mirrors,'' in *Proc. IEEE Ultrason. Symp. 1989*, edited by B. R. McAvoy (IEEE, New York, 1989), Vol. 2, pp. 681–686.

[2] D. R. Jackson and D. R. Dowling, ''Phase conjugation in underwater acoustics,'' J. Acoust. Soc. Am. **89**, 171–181 (1991).

[3] C. Prada, F. Wu, and M. Fink, ''The iterative time reversal mirror: A solution to self-focusing in the pulse echo mode,'' J. Acoust. Soc. Am. **90**, 1119–1129 (1991).

[4] M. Fink, ''Time reversal acoustics,'' Phys. Today **50**(3), 34–40 (1997).

[5] M. Fink, ''Time-reversed acoustics,'' Sci. Am. **281**, 91–97 (1999).

[6] M. Fink, D. Cassereau, A. Derode, C. Prada, P. Roux, M. Tanter, J.-L. Thomas, and F. Wu, ''Time-reversed acoustics,'' Rep. Prog. Phys. **63**, 1933–1995 (2000).

[7] M. Fink and C. Prada, ''Acoustic time-reversal mirrors,'' Inverse Probl. **17**, R1–R38 (2001).

[8] M. Fink, ''Chaos and time-reversed acoustics,'' Phys. Scr., T **T90**, 268–277 (2001).

[9] G. ter Haar, ''Acoustic surgery,'' Phys. Today **54**(12), 29–34 (Dec. 2001).

[10] C. Prada and M. Fink, ''Eigenmodes of the time reversal operator: A solution to selective focusing in multiple-target media,'' Wave Motion **20**, 151–163 (1994).

[11] C. Prada, S. Manneville, D. Spoliansky, and M. Fink, ''Decomposition of the time reversal operator: Detection and selective focusing on two scatterers,'' J. Acoust. Soc. Am. **99**, 2067–2076 (1996).

[12] H. Lev-Ari and A. J. Devaney, ''The time-reversal technique reinterpreted: Subspace-based signal processing for multi-static target location,'' *IEEE Sensor Array and Multichannel Signal Processing Workshop, Cambridge, MA, March, 2000* (IEEE, NYC, 2000), pp. 509–513.

[13] J.-L. Thomas and M. A. Fink, ''Ultrasonic beam focusing through tissue inhomogeneities with a time reversal mirror: Application to transskull therapy,'' IEEE Trans. Ultrason. Ferroelectr. Freq. Control **43**, 1122–1129 (1996).

[14] T. D. Mast, A. I. Nachman, and R. C. Waag, ''Focusing and imaging using eigenfunctions of the scattering operator,'' J. Acoust. Soc. Am. **102**, 715–725 (1997).

[15] M. Tanter, J.-L. Thomas, and M. Fink, ''Influence of boundary conditions on time-reversal focusing through heterogeneous media,'' Appl. Phys. Lett. **72**, 2511–2513 (1998).

[16] N. Mordant, C. Prada, and M. Fink, ''Highly resolved detection and selective focusing in a waveguide using the D.O.R.T. method,'' J. Acoust. Soc. Am. **105**, 2634–2642 (1999).

[17] W. A. Kuperman, W. S. Hodgkiss, H. C. Song, T. Akal, C. Ferla, and D. R. Jackson, ''Phase conjugation in the ocean: Experimental demonstration of an acoustic time-reversal mirror,'' J. Acoust. Soc. Am. **103**, 25–40 (1998).

[18] C. LeFloch, M. Tanter, and M. Fink, ''Self-defocusing in ultrasonic hyperthermia: Experiment and simulation,'' Appl. Phys. Lett. **74**, 3062–3064 (1999).

[19] P. Blomgren, G. Papanicolaou, and H. Zhao, ''Super-resolution in time-reversal acoustics,'' J. Acoust. Soc. Am. **111**, 230–248 (2002).

[20] L. Borcea, G. C. Papanicolaou, C. Tsogka, and J. G. Berryman, ''Imaging and time reversal in random media,'' Inverse Problems **18**, 1247–1279 (2002).

[21] J. B. Keller, ''Wave propagation in random media, '' *13th Symposium in Applied Mathematics, New York, 1960* (American Mathematical Society, Providence, Rhode Island, 1962), pp. 227–246.

[22] J. B. Keller, ''Stochastic equations and wave propagation in random media,'' *16th Symposium in Applied Mathematics, New York, 1963* (American Mathematical Society, Providence, Rhode Island, 1964), pp. 145–170.

[23] F. C. Karal, Jr. and J. B. Keller, ''Elastic, electromagnetic, and other waves in a random medium,'' J. Math. Phys. **5**, 537–547 (1964).

[24] J. B. Keller and F. C. Karal, Jr., ''Effective dielectric constant, permeability, and conductivity of a random medium and the velocity and attenuation coefficient of coherent waves,'' J. Math. Phys. **7**, 661–670 (1966).

[25] A. Ishimaru, *Wave Propagation and Scattering in Random Media* (Academic, New York, 1978).

[26] R. F. O'Doherty and N. A. Anstey, ''Reflections on amplitudes,'' Geophys. Prospect. **19**, 430–458 (1971).

[27] R. G. Richards and W. Menke, ''The apparent attenuation of a scattering medium,'' Bull. Seismol. Soc. Am. **73**, 1005–1021 (1983).

[28] R. Burridge, G. Papanicolaou, and B. White, ''Statistics of reflected pulses,'' Lect. Notes Math. **1186**, 265–270 (1986).

[29] R. Burridge, G. Papanicolaou, and B. White, ''Statistics for pulse reflection from a randomly layered medium,'' SIAM (Soc. Ind. Appl. Math.) J. Appl. Math. **47**, 146–168 (1987).

[30] R. Burridge, G. Papanicolaou, and B. White, ''One-dimensional wave-propagation in a highly discontinuous medium,'' Wave Motion **10**, 19–44 (1988).

[31] R. Burridge, G. Papanicolaou, P. Sheng, and B. White, ''Probing a random medium with a pulse,'' SIAM (Soc. Ind. Appl. Math.) J. Appl. Math. **49**, 582–607 (1989).

[32] J. F. Clouet and J.-P. Fouque, ''A time reversal method for an acoustical pulse propagating in randomly layered media,'' Wave Motion **25**, 361–368 (1997).

[33] K. Solna and G. Papanicolaou, ''Ray theory for a locally layered random medium,'' Waves Random Media **10**, 151–198 (2000).

[34] H. P. Bucker, ''Use of calculated sound field and matched-field detection to locate sound sources in shallow water,'' J. Acoust. Soc. Am. **59**, 368–373 (1976).

[35] A. B. Baggeroer, W. A. Kuperman, and H. Schmidt, ''Matched field processing: Source localization in correlated noise as an optimum parameter estimation problem,'' J. Acoust. Soc. Am. **83**, 571–587 (1988).

[36] A. B. Baggeroer, W. A. Kuperman, and P. N. Mikhalevsky, ''An overview of matched field methods in ocean acoustics,'' IEEE J. Ocean. Eng. **18**, 401–424 (1993).

[37] J. L. Krolik, ''Matched-field minimum variance beamforming in a random ocean channel,'' J. Acoust. Soc. Am. **92**, 1408–1419 (1992).

[38] F. B. Jensen, W. A. Kuperman, M. B. Porter, and H. Schmidt, *Computational Ocean Acoustics* (AIP Press, New York, 1994).

[39] R. O. Schmidt, ''Multiple emitter location and signal parameter estimation,'' *Proceedings of the RADC Spectrum Estimation Workshop* (Rome Air Development Center, Rome, NY, 1979), pp. 243–258.

[40] R. O. Schmidt, ''Multiple emitter location and signal parameter estimation,'' IEEE Trans. Antennas Propag. **AP-34**, 276–281 (1986).

[41] D. H. Johnson, ''The application of spectral estimation methods to bearing estimation problems,'' Proc. IEEE **70**, 1018–1028 (1982).

[42] D. H. Johnson and S. R. DeGraaf, ''Improving the resolution of bearing in passive sonar arrays by eigenvalue analysis,'' IEEE Trans. Acoust., Speech, Signal Process. **ASSP-30**, 638–647 (1982).

[43] M. Cheney, ''The linear sampling method and the MUSIC algorithm,'' Inverse Probl. **17**, 591–596 (2001).

[44] K. G. Sabra, S. R. Khosla, and D. R. Dowling, ''Broadband time-reversing array retrofocusing in noisy environments,'' J. Acoust. Soc. Am. **111**, 823–830 (2002).

[45] M. Cheney, D. Isaacson, and J. C. Newell, ''Electrical impedance tomography,'' SIAM Rev. **41**, 85–101 (1999).

[46] J. F. Claerbout, *Fundamentals of Geophysical Data Processing with Applications to Petroleum Prospecting* (McGraw-Hill, New York, 1976).
[47] K. Aki and P. G. Richards, *Quantitative Seismology: Theory and Methods* (Freeman, New York, 1980), Vol. II.
[48] N. Bleistein, J. K. Cohen, and J. W. Stockwell, Jr., *Mathematics of Multidimensional Seismic Imaging, Migration, and Inversion* (Springer, New York, 2001).
[49] B. D. Steinberg, *Microwave Imaging with Large Antenna Arrays* (Wiley, New York, 1983).
[50] E. Bécache, P. Joly, and C. Tsogka, ''An analysis of new mixed finite elements for the approximation of wave propagation problems,'' SIAM (Soc. Ind. Appl. Math.) J. Numer. Anal. **37**, 1053–1084 (2000).
[51] G. L. D'Spain, J. J. Murray, W. S. Hodgkiss, N. O. Booth, and P. W. Schey, ''Mirages in shallow water matched field processing,'' J. Acoust. Soc. Am. **105**, 3245–3265 (1999).
[52] P. Stoica and A. Nehoral, ''MUSIC, maximum likelihood, and Cramer-Rao bound,'' IEEE Trans. Acoust., Speech, Signal Process. **17**, 720–741 (1989).
[53] P. Stoica and R. Moses, *Introduction to Spectral Analysis* (Prentice Hall, New York, 1997).

Range-dependent seabed characterization by inversion of acoustic data from a towed receiver array

Martin Siderius[a] and Peter L. Nielsen
SACLANT Undersea Research Centre, Viale San Bartolomeo 400, 19138 La Spezia, Italy

Peter Gerstoft
Marine Physical Laboratory, Scripps Institute of Oceanography, La Jolla, California 92093

(Received 2 April 2001; revised 31 January 2001; accepted 18 February 2002)

The MAPEX2000 experiments were conducted in the Mediterranean Sea in March, 2000 to determine seabed properties using a towed acoustic source and receiver array. Towed systems are advantageous because they are easy to deploy from a ship and the moving platform offers the possibility for estimating spatially variable (range-dependent) seabed properties. In this paper, seabed parameters are determined using a matched-field geoacoustic inversion approach with measured, towed array data. Previous research has successfully applied matched-field geoacoustic inversion techniques to measured acoustic data. However, in nearly all cases the inverted data were collected on moored, vertical receiver arrays. Results here show that seabed parameters can also be extracted by inverting acoustic measurements from a towed array of receivers, and these agree with those inverted using data received simultaneously on a vertical array. These findings imply that a practical technique could be developed to map range-dependent seabed parameters over large areas using a towed acoustic system. An example of such a range-dependent inversion is given using measurements from the MAPEX2000 experiments. [DOI: 10.1121/1.1502264]

PACS numbers: 43.60.Pt, 43.60.Gk, 43.30.Wi, 43.30.Xm [DLB]

I. INTRODUCTION

Sound propagation in shallow waters is known to vary drastically depending on location. Transmission-loss measurements taken around the world, in the frequency band of 0.5–1.5 kHz, show as much as 50 dB variability at 100-km source–receiver separations.[1] This variability can greatly influence the performance of a wide variety of sonar systems, and can be attributed to several environmental factors including surface wave-height conditions, water column sound-speed properties, bathymetry, and seabed type. The seabed often has a strong impact on propagation and its properties are probably the most difficult to obtain. Numerical models can be used to predict sonar system performance, but these rely on good information about the environment (e.g., seabed properties).

In recent years, model-based acoustic inversion techniques have been under development to determine properties of the seabed. Matched-field processing (MFP), geoacoustic inversion is a model-based technique that has been applied successfully in characterizing the seabed for the most important parameters for propagation prediction. This is a remote sensing method that uses down-range acoustic measurements to infer properties of the seabed. Computer simulations are used to model the down-range acoustic response to different seabed types, and efficient search algorithms are applied to find the environment giving an optimal match between modeled and measured data.[2–4] By far, the most common configuration has been a sound source and a vertical line array (VLA) of receivers spanning a large portion of the water column.[5–7] The VLA configuration is sensible as the propagating acoustic field is received at all angles (in the ideal case of $N\times 2D$ propagation with an array spanning the entire water column). In principle, if a towed sound source is used with a moored VLA, large areas could be probed and in some cases range-dependent seabed properties determined.[8] However, as the range increases between source and receiver, variability in the environment can destroy the prediction capability of the matched-field processor due to inaccuracies in the modeling. This variability could be caused by, among other factors, changes in bathymetry, variability in the ocean sound speed, or abrupt changes in the seabed properties. This range dependency can often be extremely difficult to include in the numerical modeling required for the MFP inversion, and may take some range-dependent propagation codes out of their region of numerical accuracy. While some factors like bathymetry might be well known and could be included in the MFP inversion modeling, other factors such as detailed, range-dependent, ocean sound-speed profiles are not likely to be available. For reliable seabed estimates, a geometry with either fixed source or receiver array may be limited to 2 km (or less) separation between the two due only the ocean sound-speed variability.[9] In addition, with either the source or receivers in a fixed location, the inverted bottom properties are averaged over the distance between the two. This is problematic in cases where distinct bottom types impact acoustic propagation in significantly different ways such that the behavior of the field would not be captured

[a]Currently at Science Applications International Corporation, 10260 Campus Point Dr., San Diego, CA 92121.

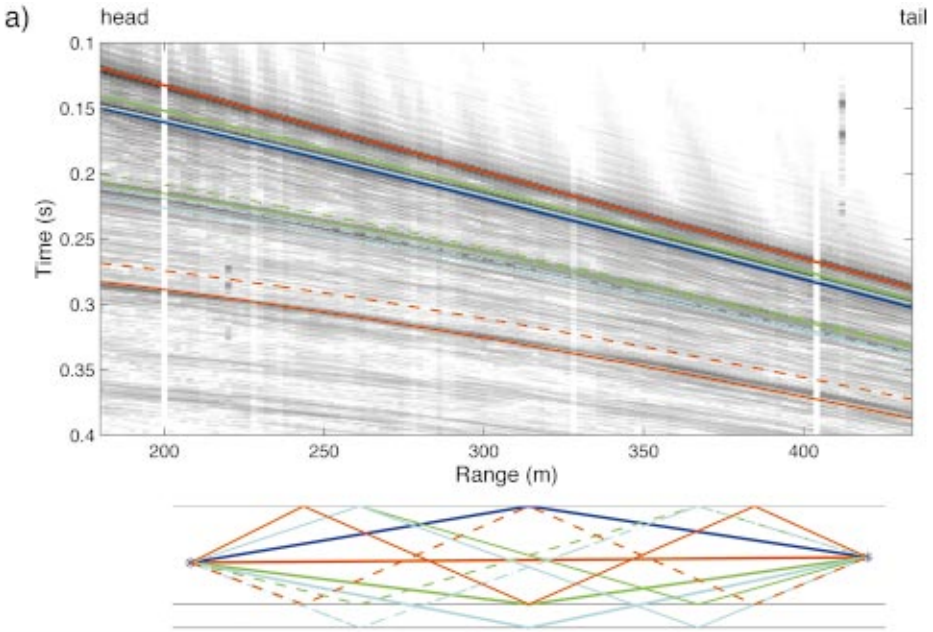

FIG. 1. Measured time series showing arrivals structure (top) and ray diagram to a single receiver (bottom). The ray diagram is based on simple geometric analysis and is color coded to help identify the corresponding arrivals on the measured time-series. The following geometry was used for the ray trace in bottom panel: source depth 72 m, head receiver depth 65 m, tail receiver depth 70 m, water depth 125 m sub-bottom depth 135 m, source-head receiver distance 180 m, and constant sound speed of 1510 m/s.

correctly using averaged seabed properties as input to a propagation model.

In this paper, matched-field geoacoustic inversion is considered using a towed horizontal line array (HLA). An HLA system has several advantages over a VLA including the ease in which it can be deployed from a ship. Since the HLA and towed sound source are kept at short range separations, MFP degradation due to water column sound-speed variability is minimized or eliminated. The requirement for range-dependent modeling in the MFP inversion is also eliminated because the bottom type and bathymetry can usually be assumed constant over the short distance separating source and HLA. Because of the short distance between source and HLA and because both are towed, distinct, range-dependent bottom types can be determined. A disadvantage of the HLA is that it does not span the water column and capture acoustic energy at all propagation angles. The inversion method described in this paper was motivated by the seismic industry where towed, horizontal arrays are commonly used. Examples of a seismic display using HLA measurements are shown in Figs. 1 and 2. In Fig. 1 the acquisition is for source and array at midwater depth with the head of the array about 180 m from the source. In Fig. 2, the source and array are closer to the sea surface. These figures indicate that the data contain information about a variety of propagation angles that have interacted with the bottom. The arrivals in Figs. 1 and 2—other than the direct and surface bounce—have information about the seabed sound speed, attenuation, and layer structure.

The seismic community has established techniques such as coring and wide-angle reflection measurements to determine seabed properties such as sound speed and density.

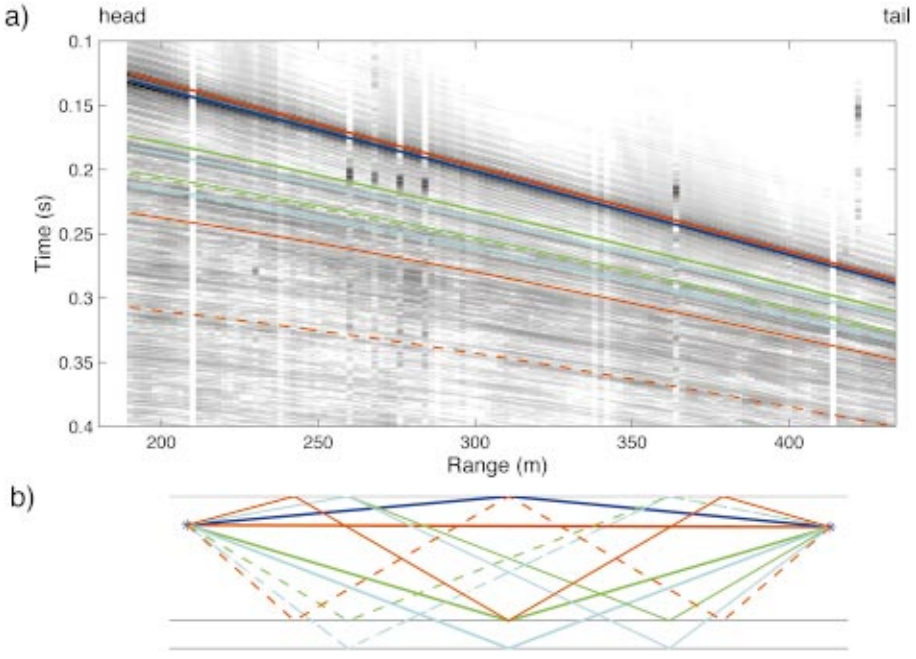

FIG. 2. Measured time series showing arrivals structure (top) and ray diagram to a single receiver (bottom). The ray diagram is based on simple geometric analysis and is color coded to help identify the corresponding arrivals on the measured time-series (bottom). There does not seem to be any arrivals corresponding to the bottom reflection (solid green) in the measured data. In the area for this data collection, the bottom is known to be soft and for shallow angles the reflection coefficient is close to zero. The following geometry was used for the ray trace in bottom panel: source depth 29 m, head receiver depth 30 m, tail receiver depth 31 m, water depth 121 m sub-bottom depth 130 m, source-head receiver distance 185 m, and constant sound speed of 1510 m/s.

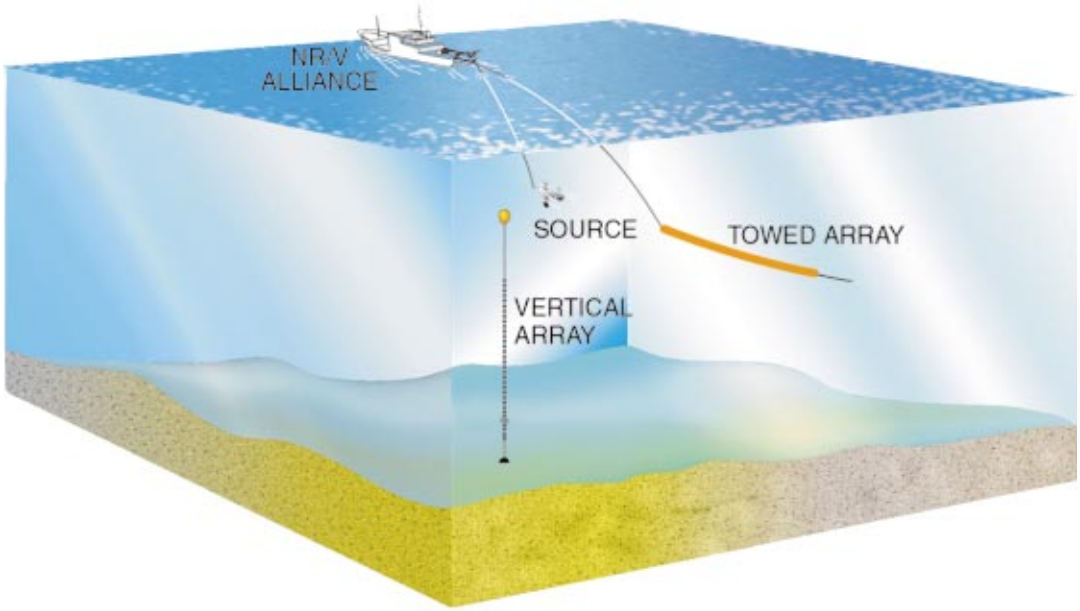

FIG. 3. Experimental geometry for 7 March 2000.

Coring methods are probably the most direct—this attempts to take a pristine sample of the seabed which is then analyzed (i.e., material sound speed is estimated by acoustic travel time measurements through the core). There are several drawbacks to coring as a way to produce quantities for input into numerical propagation models. Coring can typically only sample the top 1–5 m of the seabed. Harder seabeds (including sand) are often difficult (or impossible) to core. Coring is time consuming, requires specialized equipment not available on all ships, and is difficult in high sea states. Wide-angle reflection is another approach for estimating seabed properties. This acoustic technique estimates seabed layer thicknesses and sound speed by taking travel time measurements at different angles from the same reflector (same layer) in the seabed. Recently, using a moored receiver and towed sound source, this method has been extended to include the seabed loss parameter by also measuring seabed, frequency-domain bottom loss.[10] Although VLA, MFP geoacoustic inversions, can be problematic (for practical reasons and in range-dependent environments), this configuration has produced good simulated and experimental results. In particular, when source–receiver separations are small, or the range dependence weak, the VLA geoacoustic inversion can provide excellent seabed parameter estimates. In this paper, a VLA is used on conjunction with a towed HLA as shown in Fig. 3. Although the interest here is to develop a seabed characterization methodology based on an HLA, the VLA is used for comparing inverted seabed parameter estimates. It is important to show consistency between these two configurations as the VLA inversion is probably closest to ''ground-truth'' knowledge of the seabed available. To insure a good quality VLA inversion, the distances between the sound source and VLA are kept short (about 1 km).

In past years, geoacoustic data inversion for seabed properties using horizontal apertures (synthetic or towed arrays) has been proposed.[11,12] Jesus and Caiti[13] and Caiti, Jesus, and Kristensen[14] demonstrated the concept of MFP inversion with a towed array (156-m aperture) using narrowband data. Although broadband data were simulated, the measured data were only based on single frequencies. The feasibility test was successful, but several problems with the method are described in the concluding remarks of Ref. 14. Among the most important difficulties encountered were array shape deformation, low resolvability of the seabed parameters, and balancing the trade-off between computational efficiency and accuracy of the inversion solution. Each of these problem areas is addressed in this paper. Using a broadband signal transmission, the HLA shape is better estimated and the bottom properties are better resolved. Also, here, all geometric parameters (i.e., source and receiver positions and water depth) are included in the inversion process and do not rely completely on nonacoustic sensors. Using deeper tow depths for source and array together with a broadband signal received on a 254-m array provides a larger spread of reflection angles over a greater frequency band, and this additional information allows for an improved inversion. The inversions in this paper use a cost function (equivalent to a frequency-domain matched filter) that takes advantage of the broadband signal. The data inversions considered here use a set of seabed parameters that should minimize parameter coupling and allow for a more detailed description of the seabed than those in previous HLA inversions (i.e., sediment sound speed, layer thickness, attenuation, and subbottom sound speed are included). Finally, inversion of VLA measurements for exactly the same seabed parameters in the same location as for the HLA provides for a good comparison of the results.

In Sec. II of this paper the inversion procedure is described. In Sec. III, a simulation study is presented to illustrate and compare HLA and VLA geoacoustic inversion. A sensitivity study is presented to estimate which parameters might be resolved in the inversions. Section IV describes the

MAPEX2000 experiments and the acoustic data collected for validation of the inversion methods. Section V presents the geoacoustic inversion results using the MAPEX2000 experimental data taken on both a VLA and HLA.

II. INVERSION PROCEDURE

Measurements of acoustic data showing large differences in propagation loss for various locations around the world are indications that acoustics might be used in an inverse scheme to infer properties of the environment. This is the motivation for MFP, geoacoustic inversion. The method is summarized in the following list.

(1) Measure the acoustic field at the site of interest. A signal transmission covering a broad band of frequencies contains more information than that of a single tone and will generally produce better inversion results.[15] In the work considered in this paper, the band 220–800 Hz is considered. Although single hydrophone inversions are possible, arrays of receivers are generally more useful.

(2) Choose a propagation model that is suitable for the experimental conditions. For the HLA configuration considered here, the acoustic source is only a few hundred meters from the hydrophones. Steep angle propagation paths cannot be neglected and a model valid in the near-field must be used. Here, the broadband, complex normal-mode model ORCA[16] is used. This is a layered normal-mode model that includes the continuous spectrum. To demonstrate the robustness of the inversion approach, the parabolic equation method RAM[17] is also used as a propagation model. Other models may be appropriate, including ray theoretic codes that correctly treat the seabed interactions.

(3) Define a geoacoustic model for the site with a set of parameters that can be implemented in the propagation model. Only parameters which influence the down-range acoustic field should be considered. Otherwise, there is little hope that the acoustic fields will contain enough information to invert for those parameter values. Typically, a simplified description of the seabed is required to produce a stable inversion, as parameter coupling may cause an apparent instability.[18] Here, one- and two-sediment layer models overlying an infinite half-space are considered.

(4) Determine a cost function to quantify the agreement between the experimental measurements and the modeled data. Two cost functions based on the Bartlett correlator are used here.[19,20] The first correlates the modeled and measured pressure fields over the array of hydrophones and the magnitudes are summed over frequency as shown in Eq. (1)

$$B_H = \frac{1}{N_F} \sum_{j=1}^{N_F} \frac{|\Sigma_{i=1}^{N_H} p_{ij} q_{ij}^*|^2}{\Sigma_{i=1}^{N_H} |p_{ij}|^2 \Sigma_{i=1}^{N_H} |q_{ij}|^2}. \quad (1)$$

The second cost function is given by Eq. (2). Here, the acoustic field is correlated in frequency with the magnitudes summed over the hydrophone array

$$B_F = \frac{1}{N_H} \sum_{i=1}^{N_H} \frac{|\Sigma_{j=1}^{N_F} p_{ij} q_{ij}^*|^2}{\Sigma_{j=1}^{N_F} |p_{ij}|^2 \Sigma_{j=1}^{N_F} |q_{ij}|^2}. \quad (2)$$

In Eqs. (1) and (2), N_F is the number of frequency components, N_H is the number of hydrophones, and the measured and modeled complex pressure vectors are p_{ij} and q_{ij} (* denotes the complex conjugate operation). Both correlators take on a value of 1 for two identical signals and 0 for completely uncorrelated signals. Equation (1) is a maximum likelihood-derived objective function when the noise is additive and identically distributed on each hydrophone but the noise level may vary across frequencies. For Eq. (2), the noise is assumed identically distributed on each frequency but may vary across hydrophones. There were no obvious differences in the results for simulated data using either Eq. (1) or Eq. (2); however, with the experimental data Eq. (1) performed slightly better on the VLA and Eq. (2) slightly better on the HLA. The reason for this is not completely known, but it may be because the transmitted signal was better equalized to produce a flat spectrum [required for Eq. (2)] than the equalization to produce a flat hydrophone response across the HLA [required if using Eq. (1)]. For all inversions of measured data considered in this paper, Eq. (1) is used with the VLA and Eq. (2) with the HLA.

(5) An efficient algorithm is needed to navigate the enormous search space and find the global minimum to the cost function. This type of large-scale optimization requires a method such as genetic algorithms[4] or simulated annealing.[3] Both methods have been applied to MFP geoacoustic inversions with success. This is a constrained optimization problem with each of the desired inversion parameters bounded by a predetermined search space. In all the inversions considered in this paper (both HLA and VLA), a genetic algorithm search is used with the propagation models ORCA or RAM as implemented in the inversion code SAGA.[21] A total computation of 40 000 forward models was used in the inversion searches.

(6) Estimate the quality (errors) of the inversion. Several possibilities exist for estimating the accuracy of the inverted solution. A simple approach is to plot the cost function value versus corresponding parameter value. In this way, the distribution of high cost function values should cluster near the true parameter value. The character of such plots indicate the sensitivity of each parameter. This is shown with examples in Sec. III. Another important quality check is to examine the *a posteriori* distributions.[4]

A. Reducing the dominance of the direct and surface arrivals

The largest amplitude acoustic arrivals are usually due to the direct and sea-surface paths, yet these paths do not contribute to inversion for bottom properties. These arrivals depend only on the geometry of the experiment (i.e., source and receiver positions) and weakly on the ocean sound speed and sea-surface states. However, failure to account for these arrivals can significantly degrade the quality of the inversion results. One way to overcome allowing these arrivals from dominating the inversion problem would be to filter (or time gate) them. In practice, an automatic procedure to select from received time series only the surface and direct arrivals could be difficult. It can be especially complicated in cases

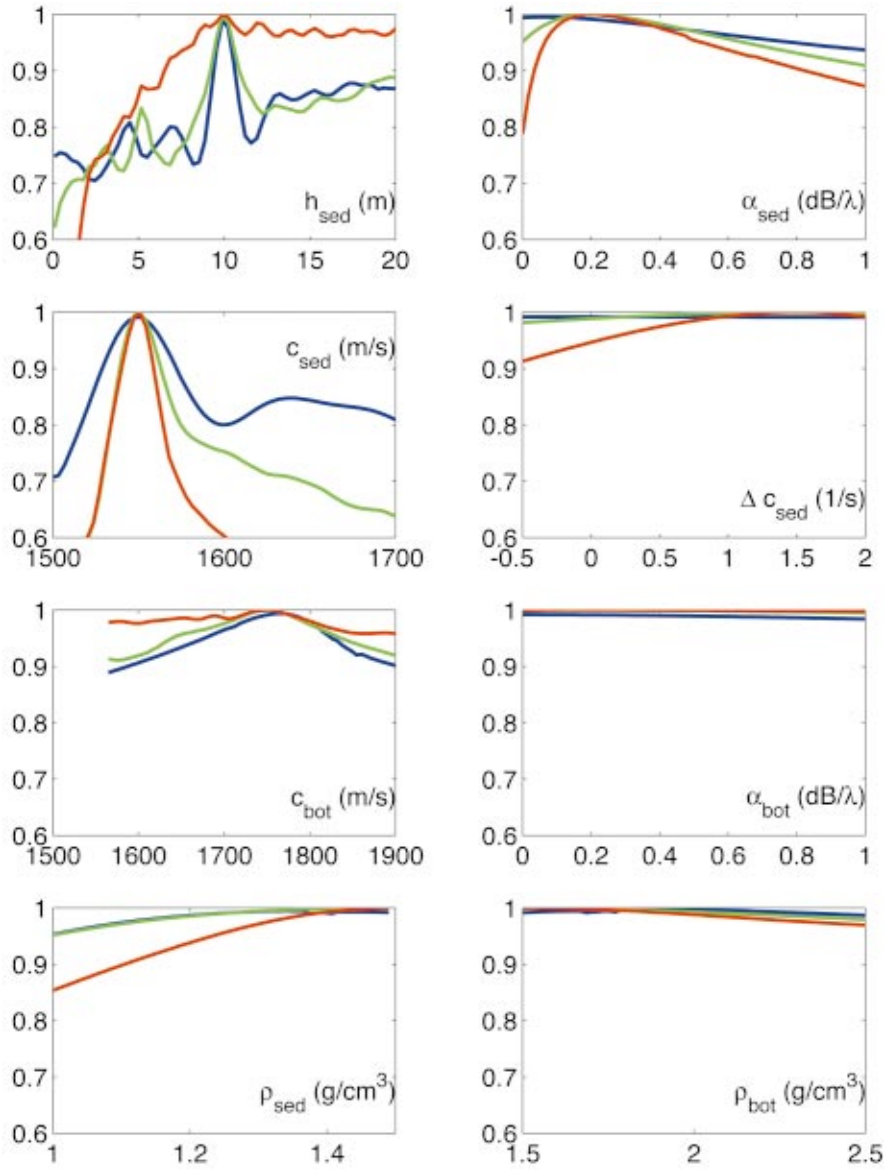

FIG. 4. Cost function evaluated against the reference solution as each seabed parameter takes on all its possible values. While evaluating a parameter, all of the others are held fixed at their known value. The cost function value is given on the *y*-axis and the parameter value on the *x*-axis. The blue curve gives the result for the horizontal array, the green curve for the vertical array moored 1 km from the source and the red curve is for a vertical array moored at 5 km. Reference and test solutions were simulated using ORCA.

when multiple arrivals interfere with each other (see Fig. 1). For instance, with a receiver and source at midwater depth the first surface and first bottom arriving paths will interfere. Nearly the same result as filtering can be accomplished by limiting the search intervals for geometric parameters. In principle, for geoacoustic inversion experiments, the geometry is known through direct measurements such as depth sensors on the towed source and receiver arrays. In practice, there is some slight uncertainty in source and receiver depths and other factors like array shape (e.g., tilt) may not be measured at all. There are also slight errors in the bottom depth measurement from the ship's echo sounder (on the order of 1 m for the MAPEX2000 experiments). Inverting acoustic measurements for source and receiver depths provides a valuable sanity check of the data quality and data processing. Furthermore, it avoids placing too much confidence in depth sensors and provides an estimate for array tilt.

Therefore, a two-step approach is used for the inversions considered in this paper. First, a geometry-only inversion is made, and second, these parameters are ''locked down'' for a full inversion for bottom properties. This is followed by a second inversion for geometric parameters only when using the newly inverted seabed parameters (as a check). This procedure is related to ''focalization''[2] and the subspace approach of Refs. 22 and 23. For the measured data considered in Sec. IV, the geometry-only-inversion results agreed with the direct measurements (within experimental error). Additionally, the geometry-only inversion provided a valuable estimate for array tilt that was not readily available from direct measurements. Although the term locked down is used, the geometric parameters were not fixed at one value during the full inversion for bottom properties. The geometric parameters were allowed to vary by approximately the expected errors in the measurements. This approach is practical, since numerically the search for geometric parameters can be done extremely fast. Note the following normal-mode expression for the pressure field:

$$p(r,z) = \frac{\exp(i\pi/4)}{\rho(z_s)\sqrt{8\pi r}} \sum_{n=1}^{N} \frac{1}{\sqrt{k_{rn}}} \times \Psi_n(0,z_s)\Psi_n(r,z)\exp(ik_{rn}). \quad (3)$$

This assumes a time-harmonic $\exp(-i\omega t)$ point source in a cylindrical geometry positioned at range $r=0$ and depth $z=z_s$ with normal modes, $\Psi_n(z)$, corresponding horizontal wave numbers, k_{rn}, and density, $\rho(z)$.[24] The numerical approach is to compute the normal modes and horizontal wave numbers for one environment and store these in memory. Then, computing new pressure fields to invert for the geometry (i.e., source and receiver positions) requires only a repeat summation of Eq. (3) with new z_s, z, and r. The geometry-only inversion can be done in about 1% of the CPU time for a full inversion. By searching for these geometric parameters first, their search space can be greatly limited when included in the full inversion, which keeps the highly sensitive geometric parameters from dominating the inversion.

III. HORIZONTAL AND VERTICAL ARRAY SEABED CHARACTERIZATION: A SIMULATION STUDY

Much more research has been done using a VLA for matched-field geoacoustic inversion, and there is a good understanding of the sensitivity of both seabed parameters and experiment geometry. With the HLA, these sensitivities are less well known. A good initial discussion on HLA sensitivity can be found in Refs. 13 and 14. Some of the system and geometrical parameters that are expected to impact the inversion are as follows.

(i) *Source and HLA depth*: It is expected that good insonification of the bottom favors towing closer to the seafloor. In practice, this can be difficult due to the danger of accidentally dragging the source or array on the bottom. Safe tow depths are usually determined based on how well the bathymetry of the area is known as well as how quickly equipment can be recovered.

(ii) *Source and HLA separation*: It is also expected that better information will be obtained if the HLA receives from propagation directions around the critical angle. Since the critical angle is usually unknown, it may be difficult to set the ideal source–HLA separation distance.

(iii) *Array length*: For a range-independent environment, longer HLAs should perform better than short ones (since more propagation angles would be received and therefore more information about bottom interactions). However, this has to be balanced by the practical issues such as array motion, more complicated propagation (over longer ranges), and possibly range dependence in the bathymetry or seabed properties.

(iv) *Signal type and bandwidth*: Geoacoustic inversion using VLAs typically shows better performance using broadband rather than narrow-band signals. This is expected to be true also for HLA inversion.

In this section, using simulations, the sensitivity of seabed parameters determined with an HLA inversion method is compared with the sensitivity using a VLA. There are an enormous number of possible combinations of the aforementioned system and geometrical parameters; including all of them in this sensitivity study would confuse the results. Instead, these were fixed at the values used in the MAPEX2000 experiments described in Sec. IV.

TABLE I. Seabed parameters used to generate the reference solution. Parameter labels and search intervals are also shown. Attenuation and density are constant through the sediment and sub-bottom. Sound speeds refer to compressional acoustic waves and attenuation is given in units of decibels per wavelength.

Parameter	Reference value	Search minimum	Search maximum
Sediment thickness: h_{sed} (m)	10	0.1	20
Sediment speed: c_{sed} (m/s)	1550	1450	1700
Attenuation: α (dB/λ)	0.2	0.0	1.0
Density: ρ (g/cm^3)	1.5	1.0	2.5
Sub-bottom speed: c_{bot} (m/s)	1750	c_{sed}	($c_{\text{sed}}+250$)

Seabed sensitivity has a strong dependency on the parametrization used in the propagation modeling. Here, a one-layer geoacoustic model is used (sediment overlying a infinite half-space sub-bottom). Although this may seem overly simplistic, it is unlikely that a more highly resolved bottom could be extracted from these measurements and this inversion method.[9] Further, it is unlikely that a more sophisticated geoacoustic model would significantly change propagation predictions. This is explored further in Sec. V. Numerical simulations are used here to create a known set of data on both an HLA and VLA similar to the MAPEX2000 experimental data.

The first test of sensitivity is to look at each seabed parameter separately. For a selected parameter, the acoustic fields are computed for all values in its search space. Meanwhile, each of the other seabed parameters is held fixed at its known (reference) value. The eight parameters considered and their reference values are: sediment sound speed $c_{\text{sed}}=1550$ m/s, sediment layer thickness $h_{\text{sed}}=10$ m, sediment attenuation $\alpha_{\text{sed}}=0.2$ dB/λ (wavelength), sediment density $\rho_{\text{sed}}=1.5$ g/cm^3, sediment sound-speed gradient $\Delta c_{\text{sed}}=1.5$ 1/s, sub-bottom sound speed $c_{\text{bot}}=1750$ m/s, sub-bottom attenuation $\alpha_{\text{bot}}=0.2$ dB/λ, sub-bottom density $\rho_{\text{bot}}=1.5$ g/cm^3.

Three experimental geometries are considered: (1) HLA with the closest hydrophone 300 m away from the source; (2) VLA at 1-km source–receiver separation, and (3) VLA at 5-km separation. The water depth was taken as 130 m and the source depth was 55 m. The VLA had 48 hydrophones with 2-m spacing spanning the depths 24–118 m. The HLA was at 60 m depth, had 128 hydrophones with 2-m spacing spanning ranges 300–554 m from the source. The cost function was determined using Eq. (1) for both HLA and VLA,

TABLE II. Geometric parameters and search intervals around estimated values for geoacoustic inversions.

Parameter	Search interval
Source range	±5 m
Source depth	±1 m
Array depth	±1 m
Array tilt	±1 m
Bottom depth	±1 m

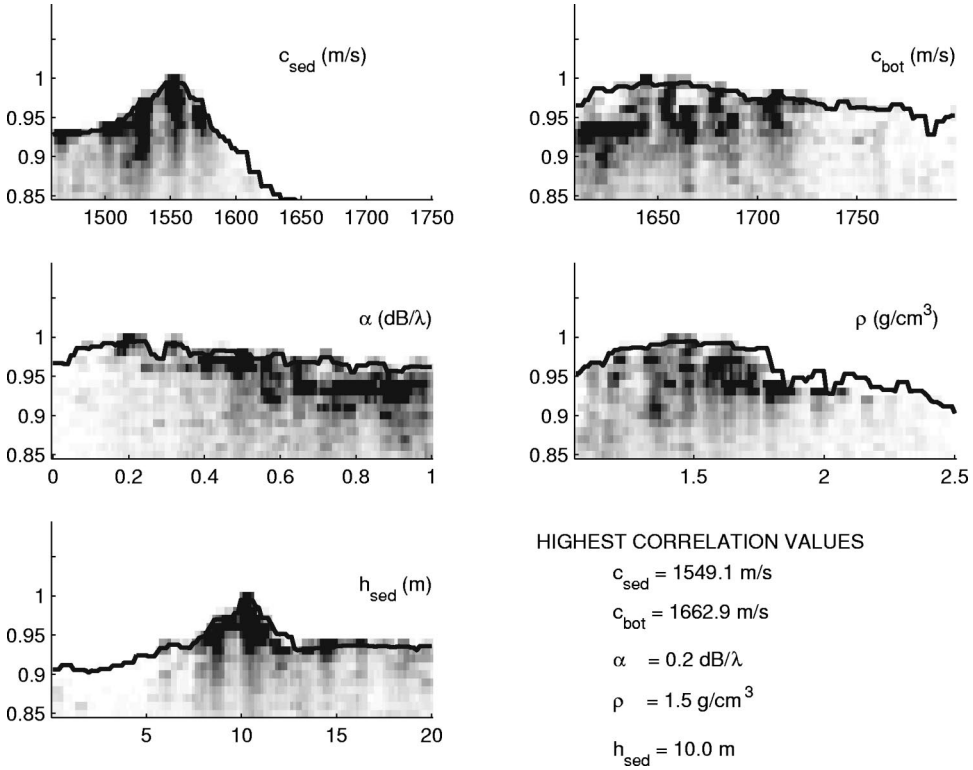

FIG. 5. Simulated data using ORCA: cost function values (along the *y*-axis without dimension) for the HLA at 300 m for each of 40,000 forward models included in the genetic algorithm search. Parameter and their units are indicated in the upper right corners of each panel and the *x*-axis corresponds to the search interval.

and the results for each parameter is given in Fig. 4. From Fig. 4, it can be seen that the VLA at 1 km and the HLA have the greatest sensitivity to h_{sed} and c_{bot}, while the VLA at 5 km is more sensitive to c_{sed} and ρ_{sed}. None of the geometries are sensitive to the sub-bottom attenuation (α_{bot}) or density (ρ_{bot}), and there is only slight sensitivity to sediment sound-speed gradient (Δc_{sed}). A caveat to this sensitivity test is the interdependency of each parameter on the others. For example, the sensitivity to sediment thickness and sub-bottom properties will also depend on the sediment properties (e.g., sound speed and density). That is, the ability to sense the sub-bottom and the interface between the sediment and sub-bottom will depend on the amount of penetration through the sediment. However, this simple sensitivity test provides both an estimate of how the cost function varies in the neighborhood of the true solution and guidelines for choosing param-

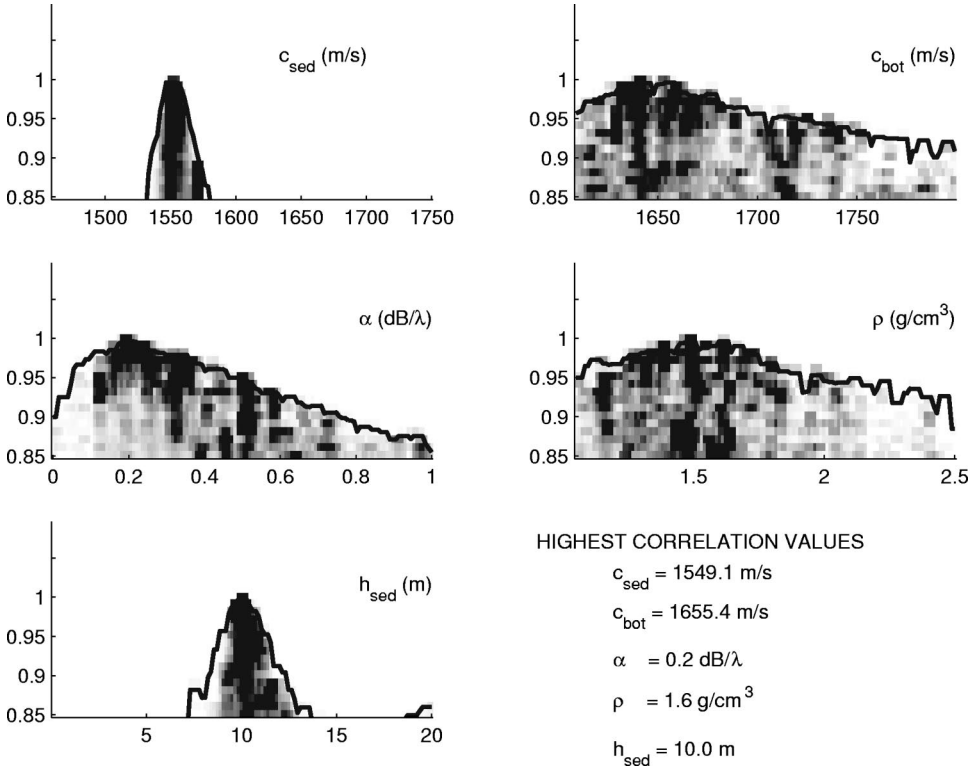

FIG. 6. Simulated data using ORCA: cost function values (along the *y*-axis without dimension) for the VLA at 1 km for each of 40,000 forward models included in the genetic algorithm search. Parameter and their units are indicated in the upper right corners of each panel and the *x*-axis corresponds to the search interval.

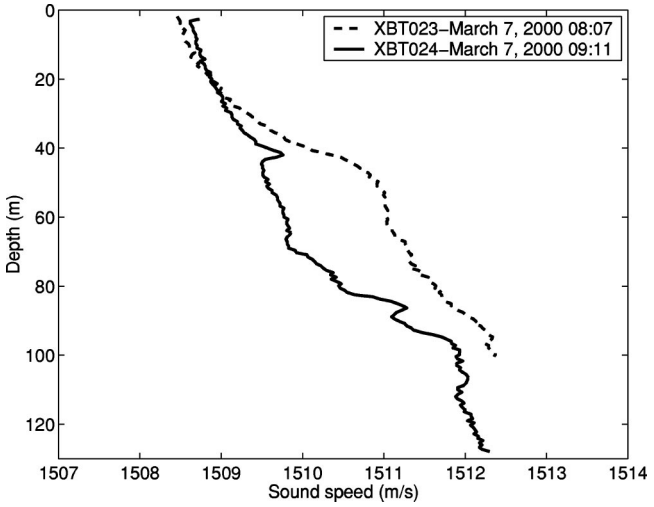

FIG. 7. Sound speed taken from XBT casts at positions 36°32.45′ N and 14°49.20′ E (at 8:07 UTC) 36°27.34′ N and 14°46.47′ E (at 9:11 UTC) on 7 March 2000.

eters. With the given sensitivity curves, the geoacoustic model was refined to include one sediment layer (over a half-space sub-bottom) but to ignore the sediment sound-speed gradient (e.g., constant sediment sound speed with depth) and to limit the model to a single attenuation and density (constant with depth through the sediment and sub-bottom).

A full inversion was performed on the reference solution using each of the three geometries described. The geoacoustic parameters for the simulation and the search intervals for the inversion are given in Table I. The geometrical parameters had small search intervals (the reasons for this are outlined in Sec. II A) and these are given in Table II.

The inversion results are presented in two ways. The set of parameter values corresponding to the single, highest correlation between reference and inverted solutions is given. Then, all the cost function values for each of the 40 000 forward model computations in the inversion are plotted with the corresponding parameter values. As the search algorithm converges, a particular part of the parameter space may be sampled more often than other parts. To give a sense of this sampling, a gray scale is used to indicate how the search algorithm sampled each parameter value. The most heavily sampled parts of the parameter search space appear darkest. These scatter plots reveal parameter sensitivity by showing how the cost function varies as the parameter search space is sampled. In this way, each parameter sensitivity can be judged without the bias imposed by keeping the other parameters fixed. The most likely value for each of the parameters can be interpreted from the peaks in the scatter plots. In Fig. 5 the scatter plot results from the HLA are shown, and in Fig. 6 the results from the VLA at 1 km. The scatter plots results resemble the sensitivity curves from Fig. 4. For both the VLA and HLA geometries, the scatter plots show heavy sampling and a peak at the correct value for each parameter. Figures 5 and 6 indicate higher sensitivity from the VLA, but the bottom properties are still resolved using the HLA.

IV. THE MAPEX2000 EXPERIMENTS

The MAPEX2000 experiments were conducted by the SACLANT Undersea Research Centre and took place on the Malta Plateau (between Italy and Malta) from 22 February to 27 March 2000. The purpose of the experiments described here is to validate the HLA geoacoustic inversion method and compare this with a VLA geoacoustic inversion. The

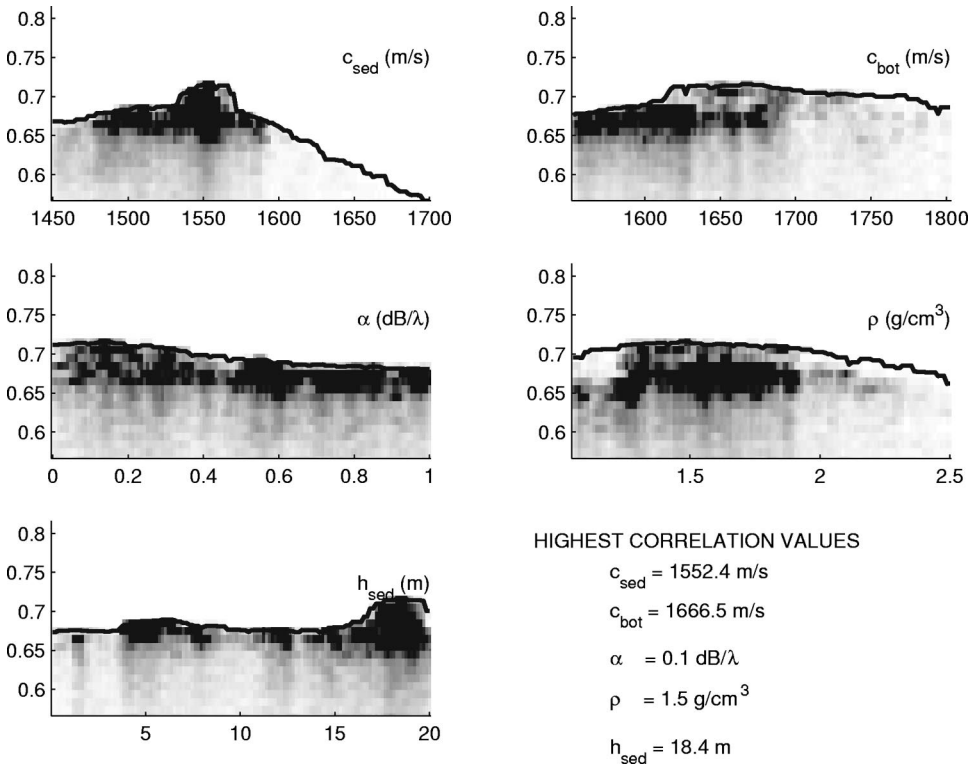

FIG. 8. MAPEX2000 HLA measured data inversion using propagation model ORCA from ping-9:07 on 7 March 2000. Cost function values (along the *y*-axis without dimension) for the HLA for each of 40,000 forward models included in the genetic algorithm search. Parameter and their units are indicated in the upper right corners of each panel and the *x*-axis corresponds to the search interval.

experimental setup showing the moored VLA and towed HLA is shown in Fig. 3. In this article, only the measurements taken on 7 March 2000 are considered.

A. Acoustic data

During the experiments of 7 March 2000, broadband acoustic signals were transmitted using flextensional sources mounted in a tow fish. A sequence consisting of linear frequency-modulated (LFM) sweeps and multitones were repeated every minute. In this paper, only 1-s sweeps from 150–800 Hz are considered. All transmissions were equalized using a programmable signal generator to produce signals having a flat spectrum. Prior to the 7 March 2000 experiments, the radiation patterns were measured from the sources showing no more than 1 dB directionality for the 150–800 Hz band.[25] Therefore, no correction was needed for the source radiation pattern (assumed omnidirectional). The received time series was converted to the frequency domain using a fast Fourier transform. Frequency bins corresponding to 220–800 Hz in 10-Hz increments were used in the inversion for comparison with modeled results.

The HLA is 254 m in total length, and for data considered here, the entire length of the array was used (128 hydrophones spaced at 2 m). Both the array and source were towed from the NRV ALLIANCE at approximately 5 knots. The distance between the sound source and the closest hydrophone on the HLA was about 300 m. The tow depth of the source and HLA varied slightly during the acoustic runs, but generally were maintained at 55–65-m depth. The VLA was deployed at position 36°26.668′ N and 14°46.751′ E and the acoustic data were received on NRV ALLIANCE by radio telemetry. The VLA has 48 equally spaced hydrophones covering 94 m of the water column (spanning depths of 24–118 m). The VLA was bottom moored (the water depth was 130 m) and kept upright using a subsurface float.

B. Oceanographic data

Sound-speed profiles were measured before, during, and after the acoustic experiments. Conductivity, temperature, and depth (CTD) measurements were taken from NRV ALLIANCE before and after each towed source acoustic run. During the acoustic runs, expendable bathythermograph (XBT) probes were deployed from NRV ALLIANCE to measure the ocean temperature profile. The salinity from the CTD casts were used to calculate sound speed from the XBT probes. Typical sound speeds taken from two XBT probes on 7 March 2000 are shown in Fig. 7. The profiles are slightly upward refracting (the typical condition for the experimental area in March), but the overall change in sound speed over depth is only about 4 m/s. For the two geoacoustic inversions considered here, the input sound-speed profile for the acoustic modeling was taken from the derived XBT closest in time to the acoustic transmission.

V. HORIZONTAL AND VERTICAL ARRAY SEABED CHARACTERIZATION: EXPERIMENTAL RESULTS

A 1-s LFM signal (150–800 Hz) was transmitted at 09:07 UTC from ALLIANCE located at 36°26.688′ N and 14°46.230′ E (denoted ping-9:07). This was simultaneously recorded on the HLA and the VLA (the VLA was about 1 km from the source). The same ping was inverted from receptions on the HLA and VLA with exactly the same procedure and search intervals as for the simulations in Sec. III. Equation (2) was used as the cost function for the HLA inversions and Eq. (1) for the VLA. The signal-to-noise ratio was about 20 dB for the data considered here. The scatter plots showing the most likely and highest correlation values for the seabed parameters are shown in Fig. 8 for the HLA and Fig. 9 for the VLA.

Both the HLA and VLA show clustering of the high cost-function values near the global maximum, best-fit solution, and both agree in the values for the seabed parameters that are most sensitive. Although the highest cost-function values (or fitness) are less than they were for the simulations, Figs. 8 and 9 have a 0.25 range on the cost-function axis (y axis) as was shown for the simulations Figs. 5 and 6. Since the signal-to-noise ratio was high, it is likely the lower overall cost function value was caused by a mismatch in the modeling of the experiment geometry, seabed, water column, or sea surface. As with the simulations, the VLA has slightly better sensitivity to the seabed parameters than does the HLA. However, clear values for the seabed parameters are found with the HLA in agreement with the VLA. Both HLA and VLA inversions indicate a dominant sediment layer at about 17–19-m depth.

A comparison of the measured and modeled (using ORCA) acoustic impulse responses are shown in Figs. 10 and 11. Both figures show multipath structure. For both the HLA and VLA, two of the first three strong arrivals contain no information about the seabed as these are direct and surface-bounce arrivals (the second arrival can be due to either the surface or the bottom bounce depending on geometry). Later arrivals have at least one interaction with the seabed. From Fig. 11, the tilt of the VLA can be inferred by the slight difference in direct path arrival times across the array. Using the arrival times along the array, and assuming the direct arrival is a plane wave, the VLA was tilted to give a 6–7-m displacement between the top and bottom hydrophones. Although this can be computed directly, it was left as an unknown and determined in the inversion process which found a value of 7-m VLA displacement (for the full inversion for bottom properties, the VLA tilt search interval was 6–8 m of displacement).

A. Geoacoustic inversion over a range-dependent seabed

The advantages of using a towed array–towed sound source configuration becomes clearer in range-dependent areas. For a fixed VLA like that used in MAPEX2000, only the sound source is mobile to probe the range-dependent environment. However, a VLA MFP inversion introduces modeling problems since the range-dependence needs to be included. The HLA configuration avoids this difficulty as the distance between source and receiver is kept small and range dependence can usually be neglected (slight range dependence such as water-depth changes can often be compensated for by allowing small shifts in source and receiver

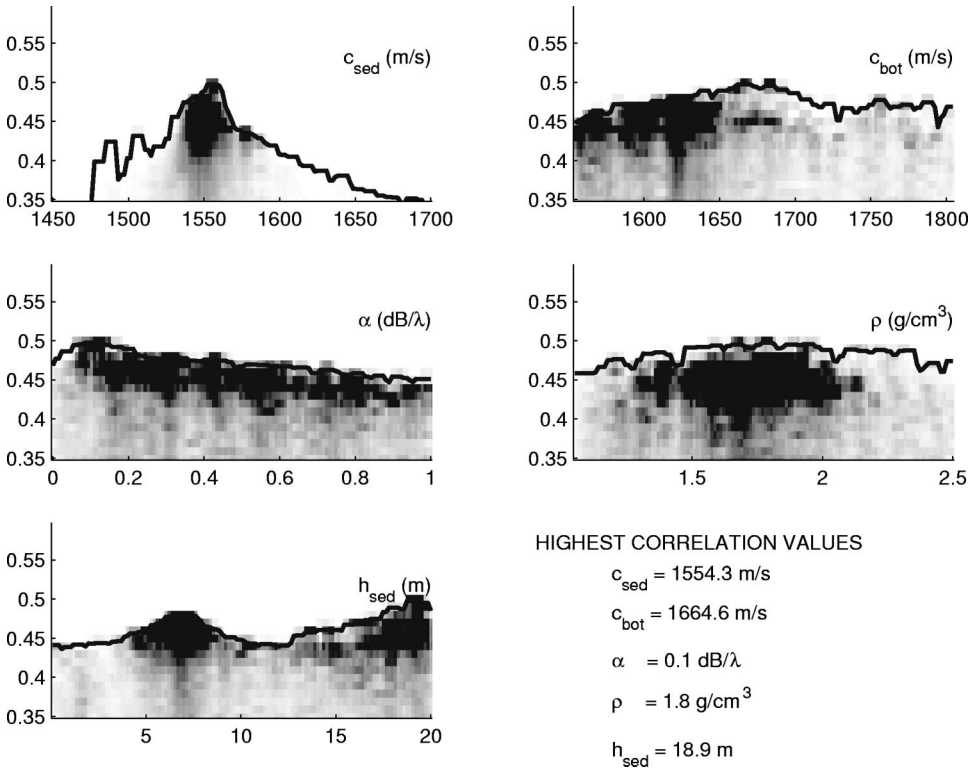

FIG. 9. MAPEX2000 VLA measured data inversion using propagation model ORCA from ping-9:07 on 7 March 2000. Cost function values (along the *y*-axis without dimension) for the VLA for each of 40,000 forward models included in the genetic algorithm search. Parameter and their units are indicated in the upper right corners of each panel and the *x*-axis corresponds to the search interval.

positions[26,27]). A second inversion was carried out for a ping taken at 08:05 UTC from ALLIANCE located at 36°32.580′ N and 14°49.260′ E (denoted ping-8:05). The water depth at the source–HLA location was 99 m and the VLA was still in the same position as for ping-9:07 (in water depth of 130 m). Doing a VLA inversion for ping-8:05 is problematic due only to the bathymetry change of 31 m between the source and VLA locations. Also, there is about 11 km between source and VLA, and range-dependent ocean sound speeds may need to be included. Further, the bottom properties also change along the track between ping-9:07 and ping-8:05. The area near ping-8:05 is characterized by a very soft layer on top of a harder sub-bottom. The HLA seabed inversion results are shown in Fig. 12. The different bottom type near

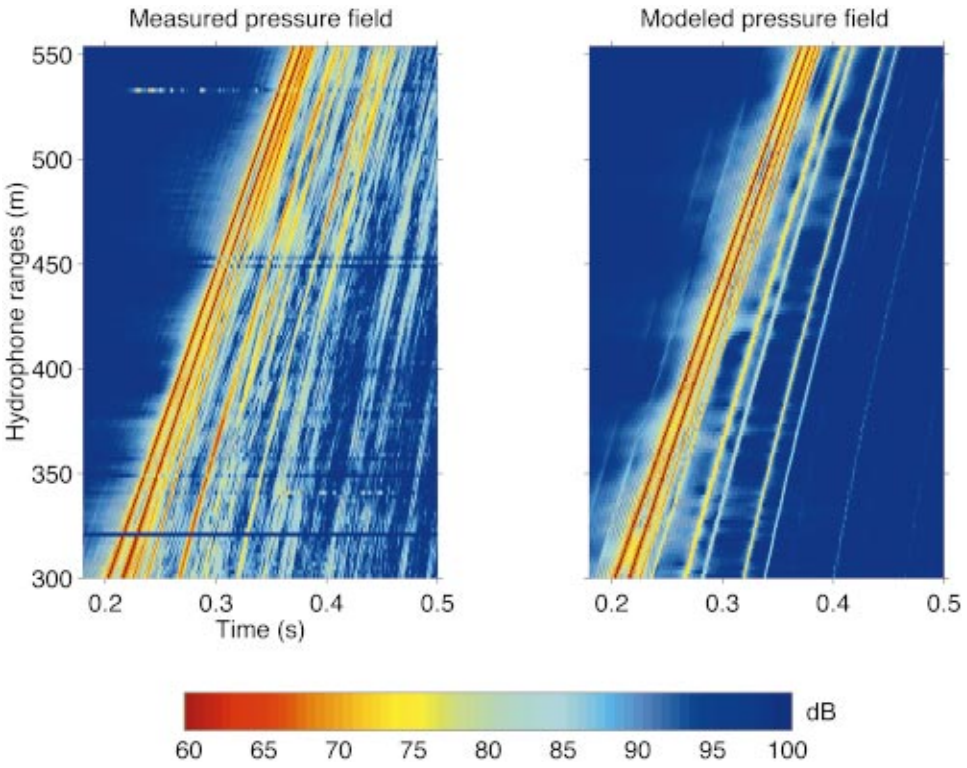

FIG. 10. Measured and modeled band-limited impulse responses for the HLA. The modeled field used the best fit seabed properties from the inversion.

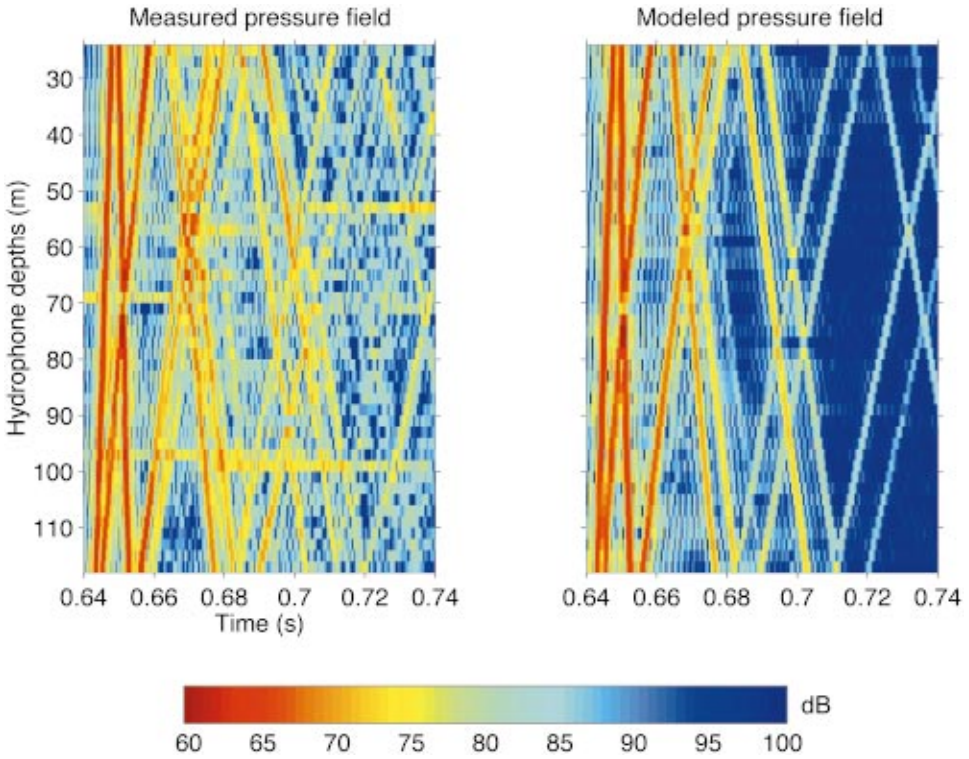

FIG. 11. Measured and modeled band-limited impulse responses for the VLA. The modeled field used the best fit seabed properties from the inversion.

ping-8:05 is evident from the results in Fig. 12. The soft layer is detected and is about 10 m in thickness. The lower sub-bottom speed is also well determined, which is likely because the soft sediment layer allows better acoustic penetration down to the sub-bottom. A VLA inversion was attempted using a range-independent assumption even though the water depth changed along the track by about 31 m. The VLA results showed a very poor cost-function value for the best-fit solution, and none of the geoacoustic parameters was well determined. It is possible that including the range-dependent bathymetry would improve the best-fit cost-function value; however, it would greatly increase computation time and it would remain difficult to interpret the averaged seabed properties found over the 11-km track.

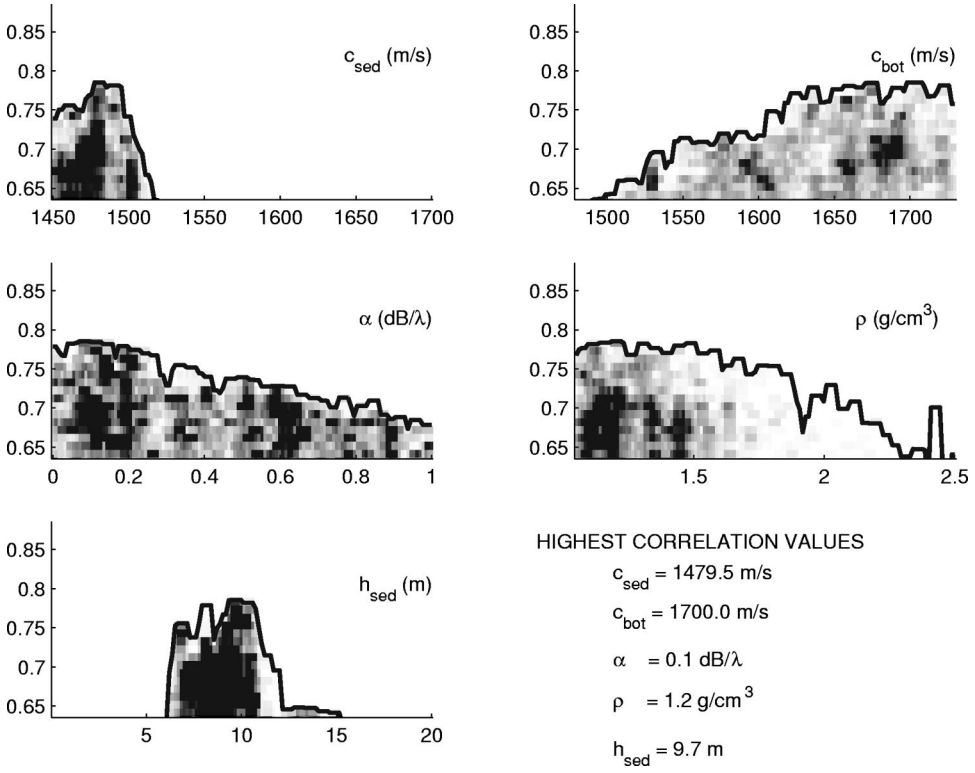

FIG. 12. MAPEX2000 HLA measured data inversion using propagation model ORCA from ping-8:05 on 7 March 2000. Cost function values (along the *y*-axis without dimension) for the HLA for each of 40,000 forward models included in the genetic algorithm search. Parameter and their units are indicated in the upper right corners of each panel and the *x*-axis corresponds to the search interval.

TABLE III. Geoacoustic properties for ping-8:05 using one-layer and two-layer models. Attenuation and density were assumed constant with depth through the sediment.

Parameter	One-layer model	Two-layer model
Sediment-1 thickness: h_{sed1} (m)	9.7	9.3
Sediment-2 thickness: h_{sed2} (m)	⋯	9.5
Sediment-1 speed: c_{sed1} (m/s)	1480	1487
Sediment-2 speed: c_{sed1} (m/s)	⋯	1695
Sub-bottom speed: c_{bot} (m/s)	1700	1763
Attenuation: α (dB/λ)	0.1	0.01
Density: ρ (g/cm^3)	1.2	1.4

A second inversion was made on ping-8:05 using a more sophisticated geoacoustic model that included two sediment layers over an infinite half-space. Within each of the two layers the geoacoustic properties were assumed constant (no gradients). As an additional check, the forward propagation model RAM was used in place of ORCA. The search algorithm and objective function are the same as those already described. The results of the comparison are shown in Table III. The table shows the two inversions produce a similar seabed. The slow layer of about 9–10 m over a faster layer is again well determined. The second layer of the two-layer model has a sound speed nearly the same as the half-space of the one-layer model. Both inversions produce low attenuation and a similar density. The significance of the one-layer and two-layer inversions demonstrates that for these data the method is not particularly sensitive to the propagation model, and that the one-layer model is probably adequate to describe the seabed.

Inversion of the data taken between ping-8:05 and ping-9:07 is useful to show how the inverted seabed properties vary along the track. Inversion results for nine pings along the track, using the two-layer geoacoustic model with propagation model RAM, are shown in Fig. 13. The figure shows the inverted sound speed in the seabed and the inverted layering. As previously noted, for ping-8:05 the two-layer RAM inversion results are very similar to the one-layer ORCA results and the same is true for ping-9:07. For ping-9:07, the two-layer model results indicate nearly the same properties in both layers ($c_{sed1}=1550$ m/s and $c_{sed2}=1563$ m/s), which implies the existence of only one dominant sediment layer. The average speed in both layers of 1557 m/s and combined layer thickness of 19.8 m agrees well with the one-layer ORCA results, giving speed of 1554 m/s and thickness of 18.9 m. There is also a consistency between pings taken near each other (in time and space), and there was a fairly gradual change in the inverted seabed properties moving along the range-dependent track. The slow sediment layer (sound speed less than that in the water column) that was evident from ping-8:05 was apparent in other pings along the track, but this layer gradually became thicker, moving along the track from ping-9:07 to ping-8:05 (Fig. 13).

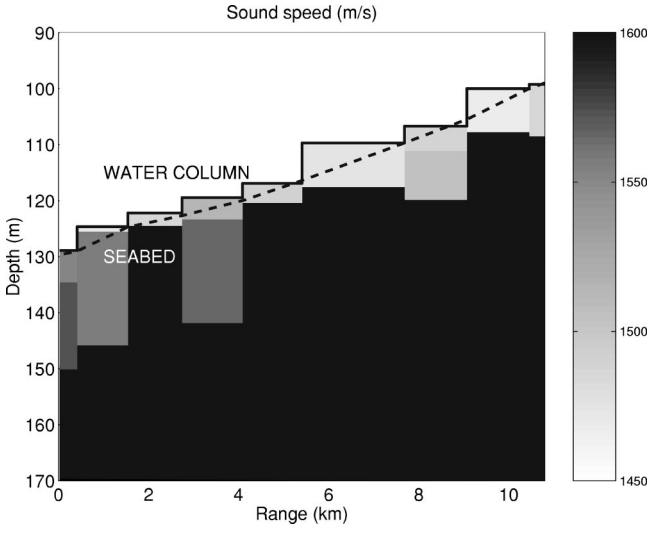

FIG. 13. MAPEX2000 HLA measured data inversion between sites 1 (ping-9:07) and 4 (ping-8:05) on 7 March 2000 using 2-layer geo-acoustic model and propagation model RAM. Layer thickness and sound speed in the sediment are shown. Inverted properties are held constant in range between data points. Solid lines (stair-steps) are indicated at inverted water depth values and measured bathymetry is given by the dashed line.

VI. CONCLUSIONS

Knowing the geoacoustic properties of the seabed is critical for accurate acoustic propagation modeling for sonar performance prediction. This paper describes an inversion method to obtain these geoacoustic parameters using a towed horizontal line array (HLA) of receivers and a broadband sound source. Matched-field processing (MFP) geoacoustic inversion methods have been shown as a promising technique for determining seabed properties, but most of the research has used measurements from a vertical line array (VLA). A towed array has many advantages over the moored, vertical array configuration such as easier deployments and being able to neglect range dependence in the MFP inversion while still mapping range-dependent seabed properties.

An important validation for the HLA inversions presented here is the comparison with the VLA inversion, and results are in good agreement for data taken where the source was near the VLA (where it is expected the VLA inversion will perform best). For an 11-km track the VLA data inversion did not perform well due to the range-dependent environment. Using the HLA data inversion this problem was circumvented, making it possible to determine seabed properties along the entire 11-km track. In this sense, the HLA inversions outperformed the VLA inversions.

Several issues need to be addressed in future research and three main ones are listed here. (1) *Computational*—The computational demands using normal-mode or parabolic equation forward models are still quite high and for practical, real-time seabed estimates a propagation code will be required that is fast, includes all the physics of the seabed interactions, and is valid near the sound source. Ray tracers may offer a good alternative to normal modes or parabolic equation methods for rapidly computing broadband impulse responses. It may be possible to use a ray tracer if the acoustic bottom interactions are treated correctly.[28,29] (2) *Geometry*—The ideal measurement geometry will also need to be determined as it is likely that parameters like array length, tow depths, and signal types will need to be optimized to improve estimates of the seabed properties. (3) *Cost functions*—Cost functions have different sensitivities that de-

pend on array type, signal type, and seabed parameterization. There may be a better set of cost functions (than used here) to improve the performance of HLA inversions.

ACKNOWLEDGMENTS

The authors wish to acknowledge all the members who participated in MAPEX2000. Special thanks to E. Michelozzi as engineering coordinator and P. Boni for managing the data acquisition of data. The authors would also like to gratefully acknowledge the crews of NRV ALLIANCE and ITNS TAVOLARA.

[1] R. J. Urick, *Sound Propagation in the Sea* (Defense Advanced Research Projects Agency, Washington, D.C., 1979).
[2] M. D. Collins and W. A. Kuperman, ''Focalization: Environmental focusing and source localization,'' J. Acoust. Soc. Am. **90**, 1410–1422 (1991).
[3] M. D. Collins, W. A. Kuperman, and H. Schmidt, ''Nonlinear inversion for ocean bottom properties,'' J. Acoust. Soc. Am. **92**, 2770–2783 (1992).
[4] P. Gerstoft, ''Inversion of seismo-acoustic data using genetic algorithms and *a posteriori* probability distributions,'' J. Acoust. Soc. Am. **95**, 770–782 (1994).
[5] D. F. Gingras and P. Gerstoft, ''Inversion for geometric and geoacoustic parameters in shallow water: Experimental results,'' J. Acoust. Soc. Am. **97**, 3589–3598 (1995).
[6] J. P. Hermand and P. Gerstoft, ''Inversion of broadband multi-tone acoustic data from the Yellow Shark summer experiments,'' IEEE J. Ocean. Eng. **21**, No. 4, 324–346 (1996).
[7] N. R. Chapman and A. Tolstoy, ''Special issue: Benchmarking geoacoustic inversion methods,'' J. Comput. Acoust. **6**, No. 1&2, 1–289 (1998).
[8] M. Siderius, M. Snellen, D. Simons, and R. Onken, ''An environmental assessment in the Strait of Sicily: Measurement and analysis techniques for determining bottom and oceanographic properties,'' IEEE J. Ocean. Eng. **25**, No. 3, 364–386 (2000).
[9] M. Siderius, P. Nielsen, J. Sellschopp, M. Snellen, and D. Simons, ''Experimental study of geoacoustic inversion uncertainty due to ocean sound-speed fluctuations,'' J. Acoust. Soc. Am. **110**, 769–781 (2001).
[10] C. Holland and J. Osler, ''High-resolution geoacoustic inversion in shallow water: A joint time- and frequency-domain technique,'' J. Acoust. Soc. Am. **107**, 1263–1279 (2000).
[11] G. V. Frisk and J. F. Lynch, ''Shallow water waveguide characterization using the Hankel transform,'' J. Acoust. Soc. Am. **76**, 205–216 (1984).
[12] W. A. Kuperman, M. F. Werby, K. E. Gilbert, and G. J. Tango, ''Beam forming on bottom-interacting tow-ship noise,'' IEEE J. Ocean. Eng. **10**, No. 3, 290–298 (1985).
[13] S. M. Jesus and A. Caiti, ''Estimating geoacoustic bottom properties from towed array data,'' J. Comput. Acoust. **4**, No. 3, 273–290 (1996).
[14] A. Caiti, S. M. Jesus, and A. Kristensen, ''Geoacoustic seafloor exploration with a towed array in a shallow water area of the Strait of Sicily,'' IEEE J. Ocean. Eng. **21**, No. 4, 355–366 (1996).
[15] G. Haralabus and P. Gerstoft, ''Source localization in shallow water using multi-frequency processing of shot data,'' Technical Report SR-253, SACLANT Undersea Research Centre, La Spezia, Italy, 1996.
[16] E. K. Westwood, C. T. Tindle, and N. R. Chapman, ''A normal mode model for acousto-elastic ocean environments,'' J. Acoust. Soc. Am. **100**, 3631–3645 (1996).
[17] M. D. Collins, ''A split-step Padé solution for parabolic equation method,'' J. Acoust. Soc. Am. **93**, 1736–1742 (1993).
[18] M. Snellen, D. Simons, M. Siderius, J. Sellschopp, and P. Nielsen, ''An evaluation of the accuracy of shallow-water matched-field inversion results,'' J. Acoust. Soc. Am. **109**, 514–527 (2001).
[19] P. Gerstoft and C. F. Mecklenbräuker, ''Ocean acoustic inversion with estimation of *a posteriori* probability distributions,'' J. Acoust. Soc. Am. **104**, 808–819 (1998).
[20] C. F. Mecklenbräuker and P. Gerstoft, ''Objective functions for ocean acoustic inversions derived by likelihood methods,'' J. Comput. Acoust. **8**, 259–270 (2000).
[21] P. Gerstoft, ''SAGA Users Manual 2.0, an inversion software package,'' Technical Report SM-333, SACLANT Undersea Research Centre, La Spezia, Italy, 1997.
[22] P. Ratilal, P. Gerstoft, and J. T. Goh, ''Subspace approach to inversion by genetic algorithms involving multiple frequencies,'' J. Comput. Acoust. **6**, No. 1&2, 99–115 (1998).
[23] M. I. Taroudakis and M. G. Markaki, ''Bottom geoacoustic inversion by matched-field processing—A sensitivity study,'' Inverse Probl. **16**, 1679–1692 (2000).
[24] F. B. Jensen, W. A. Kuperman, M. B. Porter, and Henrik Schmidt, *Computational Ocean Acoustics* (American Institute of Physics, New York, 1994).
[25] L. Troiano, ''Sound source for MAPEX2000,'' Internal memorandum to M. Siderius on sound source calibration for MAPEX2000 experiments, 22 February 2000.
[26] G. L. D'Spain, J. J. Murray, W. S. Hodgkiss, N. O. Booth, and P. W. Schey, ''Mirages in shallow-water matched-field processing,'' J. Acoust. Soc. Am. **105**, 3245–3265 (1999).
[27] C. H. Harrison and M. Siderius, ''Correlations between search parameters in geoacoustic inversion,'' in *Proceedings of the Fifth European Conference on Underwater Acoustics* [European Commission, Rue de la Loi/Wetstraat 200 (SDME 7/85), B-1049 Brussels, 2000], pp. 203–208, Directorate-General for Research.
[28] E. K. Westwood and P. J. Vidmar, ''Eigenray finding and time series simulation in a layered-bottom ocean,'' J. Acoust. Soc. Am. **81**, 912–924 (1987).
[29] E. K. Westwood and C. T. Tindle, ''Shallow-water time series simulation using ray theory,'' J. Acoust. Soc. Am. **81**, 1752–1761 (1987).

Iterative reconstruction algorithm for optoacoustic imaging

G. Paltauf,[a] J. A. Viator, S. A. Prahl, and S. L. Jacques
Oregon Medical Laser Center and Oregon Graduate Institute, Portland, Oregon

(Received 30 October 2000; revised 18 June 2002; accepted 25 June 2002)

Optoacoustic imaging is based on the generation of thermoelastic stress waves by heating an object in an optically heterogeneous medium with a short laser pulse. The stress waves contain information about the distribution of structures with preferential optical absorption. Detection of the waves with an array of broadband ultrasound detectors at the surface of the medium and applying a backprojection algorithm is used to create a map of absorbed energy inside the medium. With conventional reconstruction methods a large number of detector elements and filtering of the signals are necessary to reduce backprojection artifacts. As an alternative this study proposes an iterative procedure. The algorithm is designed to minimize the error between measured signals and signals calculated from the reconstructed image. In experiments using broadband optical ultrasound detectors and in simulations the algorithm was used to obtain three-dimensional images of multiple optoacoustic sources. With signals from a planar array of 3×3 detector elements a significant improvement was observed after about 10 iterations compared to the simple radial backprojection. Compared to conventional methods using filtered backprojection, the iterative method is computationally more intensive but requires less time and instrumentation for signal acquisition.
 [DOI: 10.1121/1.1501898]

PACS numbers: 43.60.Pt, 43.60.Rw, 43.35.Ud [JCB]

I. INTRODUCTION

Optoacoustic or thermoacoustic imaging is a method to localize objects inside an acoustically homogeneous medium that have contrast in the visible, infrared, or microwave range of thee electromagnetic spectrum. It is based on the generation of thermoelastic stress waves as a short pulse from a laser or a microwave source is absorbed by an object in the medium. The contrast for image formation is provided by enhanced heat and stress generation in structures with preferential optical absorption. Compared to conventional ultrasonic pulse-echo imaging, where ultrasound is generated outside the sample and is scattered by acoustical heterogeneities, in optoacoustic imaging the source of pressure waves is the observed target itself. The wavelength of optoacoustic waves depends on size and shape of fluctuations in the distribution of absorbed energy, thus producing a broadband acoustic spectrum that extends over the ultrasonic frequency range, from about 0.1 to 100 MHz. The upper limit is given by $1/t_p$, where t_p is the duration of the exciting pulse. Consequently the resolution limit and at the same time the smallest achievable acoustic wavelength are given by $t_p c$, where c is the speed of sound. Structures larger than this limit fulfill the condition of stress confinement, which states that maximum thermoelastic stress is produced if the heating pulse is shorter than the time the mechanical disturbance needs to escape from a target structure of characteristic size d,

$$t_p \ll t_{\mathrm{ac}} = d/c, \tag{1}$$

where t_{ac} is called the acoustic relaxation time. The pressure waves created in the heated regions propagate to the surface where they are detected with high bandwidth transducers. An image reconstruction method is applied to the signals to create a map of the absorbed energy in the medium. The resulting image is generally not a quantitative reconstruction of a physical property of the material. It rather shows the location of optical absorbers in a similar way as in pulse-echo ultrasound, where acoustical scatterers are located. Only under certain circumstances, such as in the imaging of layered materials with negligible optical scattering, the distribution of the optical absorption coefficient can be reconstructed.

Optoacoustic imaging is applicable to nondestructive testing of materials where the interesting structures have low imaging contrasts for conventional methods like pulse-echo ultrasound but at the same time have high contrast for optical radiation. Sufficient penetration of light to the target structures is also a prerequisite. Since many imaging targets in biological tissue meet these requirements, the optoacoustic method is particularly promising for noninvasive medical imaging. Some structures that are barely seen by established imaging methods employing x rays or ultrasound but exhibit a strong contrast for visible or near infrared light are the increased blood concentration due to neovasculature in breast tumors,[1] vascular abnormalities in skin[2] or inflamed cancerous tissue.[3] Due to the strong scattering of light in tissue, optoacoustic waves are excited by diffusely propagating light. Other than in pure optical imaging, where imaging information comes from diffusely backscattered or transmitted light and the resolution is poor (in the range of 1 cm), in optoacoustic imaging the information about the imaged objects is carried by pressure waves, which are much less scattered than light and are therefore capable of producing images with better resolution (in the range of 1 mm or less). Using multiple wavelengths the spectral information of optical imaging can also be obtained with optoacoustic imaging.

[a]Present address: Institut fuer Experimentalphysik, Karl-Franzens-Universitaet Graz, Universitaetsplatz 5, A-8010 Graz, Austria; electronic mail: guenther.paltauf@kfunigraz.ac.at

The techniques used to transform the information contained in the optoacoustic signals into images depends on the complexity of the target structures. Single, static detectors are used for layered samples.[4–7] More complicated structures can be imaged by scanning a focused acoustic transducer together with the optical source along a line on the surface of an object, creating an image of a two-dimensional section perpendicular to the surface.[7,8] Scanning is, however, limited by the available pulse repetition rate of pulsed lasers, which ranges up to about 100 Hz. To record the amount of data needed for three-dimensional imaging therefore requires parallel detection and processing of optoacoustic signals using ultrasonic transducer arrays. An image of the absorbed light distribution is constructed by backprojecting the acoustic signals among all possible source locations. For a single isotropic detector and a point source these locations lie on the surface of a sphere with the detector in the center. Summation of multiple spheres with their centers at different detector positions generates the reconstruction. If the information contained in the signals about the imaged objects is limited these backprojection spheres (or arcs in a two-dimensional section) tend to remain in the reconstruction, creating image artifacts. The main limitations are the finite number of detector elements and the finite solid angle of detection. Large arrays with plane, curved or hemispherical arrangements of up to 4000 detectors[9,10] or detection principles providing spatially continuous, two-dimensional snapshots of the acoustic pressure distribution in a plane[11,12] have therefore been used to maximize the information that is acquired from the optoacoustic sources. To increase the contrast of interesting structures relative to background absorption and to reduce artifacts, usually a filtering of either the acoustic signals prior to backprojection or of the reconstructed image is performed. High-pass filters reduce the slowly changing signal components caused by background absorption.[1] A method derived from the inverse three-dimensional Radon transform uses backprojection of the temporal derivatives of acoustic pressure signals.[13,14] This method creates full three-dimensional images of the source but needs a high number of detector elements. Filtering methods acting on the reconstructed image use thresholding to remove some of the background or spatial frequency-domain filters to reduce high-frequency backprojection artifacts.[1]

In the present work we propose an alternative concept that reduces artifacts even when signals from only a small number of detectors (e.g., form a 3×3 detector array) are available. This technique increases both contrast and resolution of the reconstructed images, thereby obviating the filtering step used by other techniques. The reconstruction algorithm is iterative and was adapted from algebraic image reconstruction techniques and in particular from the simultaneous iterative reconstruction technique that is used in computer tomography in cases where data sets are noisy and incomplete.[15] The method is also closely related to deconvolution techniques commonly used in fields like spectroscopy[16,17] or microscopy.[18] The basic idea is to treat the image reconstruction as an inverse problem and to minimize the error between the measured acoustic signals and the signals that are calculated with a forward model of optoacoustic sound generation from a reconstructed image. Section II describes the algorithm and the models needed for the forward and the inverse problems. A simulation for a known source distribution and a first experimental reconstruction follow.

II. IMAGE RECONSTRUCTION ALGORITHM

The basic problem of image reconstruction is to invert the forward problem of optoacoustic wave generation and detection. Solution of the forward problem yields pressure-time signals at the element positions in the ultrasonic sensor array, given an initial distribution of absorbed energy in the medium. This distribution is created by absorption of a laser pulse and can be regarded as the source of the pressure wave. In the inverse problem the three-dimensional absorbed energy distribution is sought given a set of acoustic signals at the array positions.

Optoacoustic wave generation is described by the solution of the thermoelastic wave equation.[19,20] Since in soft tissues the optical contrast, which determines the optoacoustic sources, is generally much higher than the small variations of acoustic impedance, an acoustically homogeneous medium is assumed. It is advantageous to use the solution for the velocity potential, which is related to the acoustic pressure by

$$p(\mathbf{r},t) = -\rho \frac{\partial \phi(\mathbf{r},t)}{\partial t}, \tag{2}$$

where ϕ is the velocity potential, ρ the density, p the acoustic pressure, and $\mathbf{r}$ the position of the detector. To model the detection process we use a discrete, matrix-based formulation of the problem that uses a retarded Green's function solution of the thermoelastic wave equation.[13,21] The three-dimensional distribution of volumetric energy density $W(\mathbf{r})$ after absorption of a laser pulse is discretized into a grid of size $N_x\times N_y\times N_z$ and described by a vector $\mathbf{W}$ where each element $W_j (j=1\cdots N_x\times N_y\times N_z)$ contains the average value of the energy density within a volume element of size ΔV at position $\mathbf{r}_j$. A second vector $\boldsymbol{\phi}$ contains the values of the velocity potential measured as a function of time at all positions of the sensor array. The number of measured values ϕ_k is given by the number M of temporal samples in the signal of a single detector, times the number L of detectors in the array. The measurement is described by

$$\boldsymbol{\phi} = \mathbf{AW}$$

or

$$\phi_k = \sum_j A_{kj} W_j$$

with

$$A_{kj} = -\frac{\beta}{4\pi\rho C_p}\frac{\Delta V}{\Delta t}\frac{h_{kj}}{R_{kj}} w_{kj}$$
$$R_{kj} = |\mathbf{r}_k - \mathbf{r}_j|, \quad h_{kj} = \begin{cases} 1 & \text{if } |t_k - R_{kj}/c| < \Delta t/2, \\ 0 & \text{else,} \end{cases} \tag{3}$$

where β is the thermal expansion coefficient, C_p the specific heat capacity at constant pressure, and Δt the time step at which velocity potentials are sampled. The point $\mathbf{r}_k$ is the position of the detector at the kth measurement. The factors w_{kj} contain parameters that describe the detection process. A directional sensitivity of the detectors can be modeled by factors w_{kj} that depend on the angle θ_{kj} between the vector $\mathbf{r}_k - \mathbf{r}_j$ and the normal to the detector plane. According to the definition of h_{kj}, all nonzero elements in a row of **A** belong to volume elements whose centers lie within a spherical shell of radius ct_k and width $c\Delta t$ around $\mathbf{r}_k$. The matrix **A** is extremely sparse and can be quite large (e.g., 1.64×10^5 for typical numbers of $N_x=N_y=N_z=40$, $M=256$ and $L=10$), which precludes a direct matrix inversion. Since most of the elements of **A** are zero a compression can be utilized. First **A** is divided into L submatrices that correspond to single detector positions. Each of these submatrices has only $N_x\times N_y \times N_z$ elements unequal to zero, one per column. This results from the fact that the center of each volume element can only lie within one spherical shell. The nonzero elements are stored in a three-dimensional, $N_x\times N_y\times N_z$ matrix. A second auxiliary matrix of the same size stores the value of k (the row number in the original submatrix of **A**) of each element. To perform the matrix multiplication in Eq. (3), elements of equal k are summed with the help of the auxiliary matrix. The number of elements to be stored is therefore reduced by a factor of $M/2$.

To avoid a loss of information in the modeling of the detection process the spatial increments Δx, Δy, Δz and the time interval Δt have to be matched in a way that the average sound propagation time through a volume element, t_{prop}, is not smaller than Δt. Since the latter is usually predetermined by the sampling interval of the recording instrument the spatial increments are chosen using the inequality

$$\Delta t \leqslant t_{\text{prop}} = \frac{\Delta x + \Delta y + \Delta z}{3c}. \tag{4}$$

Some oversampling (using $\Delta t < t_{\text{prop}}$) increases the accuracy of the calculated signals and is sometimes necessary to limit the size of matrix **A**. However, a calculation with $\Delta t < t_{\text{prop}}$ induces noise (shot noise induced by the arrival of waves from individual volume elements) that can be eliminated by convolving $\boldsymbol{\phi}$ with **g**, a vector containing a Gaussian function with an $1/e$ width corresponding to t_{prop},

$$g_i = \frac{2}{t_{\text{prop}}\sqrt{\pi}} \exp[-(2t_i/t_{\text{prop}})^2]. \tag{5}$$

It has been shown previously that the optoacoustic wave emitted from a small spherical source has a pressure profile given by the time derivative of a Gaussian function.[22] **g** can therefore be regarded as the elementary velocity potential signal that is emitted from a volume element. If the laser pulse duration t_p is longer than t_{prop}, accurate modeling of $\boldsymbol{\phi}$ requires the use of a broader Gaussian function for the convolution, which is done by replacing t_{prop} in Eq. (5) by t_p. Although in practice we first calculated the signals using Eq. (3) and then performed the convolution, we assume for the sake of simplicity the convolution to be integrated in matrix **A** and keep the notation $\boldsymbol{\phi}=\mathbf{AW}$ for the signal generation process (to generate a matrix that includes the convolution a Toeplitz matrix generated from **g** could be multiplied with **A**).

A first-order reconstructed image **I** of the source **W** can be obtained by backprojecting the measured signals $\boldsymbol{\phi}$ into the source volume using a matrix **B**,

$$\mathbf{I} = \boldsymbol{\phi}\mathbf{B}$$

or

$$I_j = \sum_k \phi_k B_{kj}. \tag{6}$$

The backprojection matrix **B** is related to **A**. Different ways to define its elements B_{kj} are possible. The following definition conserves energy, making the sum over all elements of the image vector the same as the sum over the source vector,

$$B_{kj} = \frac{A_{kj}}{L\sum_i A_{ki}^2}. \tag{7}$$

In the resulting image, each volume element is assigned the sum of measured velocity potentials to which it contributed, normalized by $L\sum_i A_{ki}^2$ and weighted with A_{kj}. The sum in the denominator of Eq. (7) takes into account the number of volume elements in each spherical shell. This kind of normalization can cause problem in actual measurements because noise is amplified in image elements that lie on truncated shells near the edges of the source volume. We found that the following definition of B_{kj} gave better results with experimental signals:

$$B_{kj} = -h_{kj}R_{kj}u_{kj}. \tag{8}$$

In this definition the $1/R_{kj}$ attenuation of the optoacoustic generation process is compensated and the backprojection of velocity potentials is weighted with factors u_{kj}. For achieving the best signal to noise ratio in the reconstructed image it has been suggested to set $u_{kj}=w_{kj}$.[9] No normalization with the number of elements is used and consequently no energy conservation is obtained. A separate normalization as described in the following is necessary to achieve energy conservation.

In the above-defined projection the velocity potential measured at a certain time t_k at a certain detector position is smeared over all cells on a spherical shell with radius ct_k. For a detector array with L elements, each point in the source volume is imaged by L spherical shells intersecting at the point location. This has an effect similar to smearing the original with a three-dimensional point spread function. With a small number of array elements this function is strongly dependent on the position in the source volume. Simple filtering operations in frequency domain are therefore not applicable for deconvolution of the reconstructed image. It is obvious that the operation in Eq. (6) is not an inversion of the signal generation process described by matrix **A**. Backprojection can, however, be used to generate reconstructions of optoacoustic sources under two conditions: (1) the data set is sufficiently big, containing signals that are measured from many directions around the source, (2) some kind of filtering

of the signals is used prior to backprojection to improve the image. If the data set is not complete the inverse problem can be solved in an iterative process that is related to a method in computer tomography known as simultaneous iterative reconstruction technique.[15] It is also related to the van Cittert algorithm that was originally used to deconvolve spectra with the response function of the spectrometer.[16,17] The basic idea is to use backprojection to create a first-order image from the measurement $\boldsymbol{\phi}$, calculate new signals $\boldsymbol{\phi}^{(1)}$ from the reconstruction by applying signal generation matrix $\mathbf{A}$ on the image vector, and then add the backprojection of the residual $\boldsymbol{\phi}-\boldsymbol{\phi}^{(1)}$ to the image. Subsequent iterations are described by

$$\begin{aligned}\boldsymbol{\phi}^{(n)}&=\mathbf{KAI}^{(n)},\\ \mathbf{I}^{(n+1)}&=\mathbf{I}^{(n)}+(\boldsymbol{\phi}-\boldsymbol{\phi}^{(n)})\mathbf{B}.\end{aligned} \tag{9}$$

Since the reconstructed energy density has to be positive, a non-negativity constraint is imposed on each new estimate. This means that only positive values are kept in the image and negative values are set to zero. $\mathbf{K}$ is a diagonal matrix that contains for each detector position a normalization coefficient that ensures energy conservation. To derive the coefficient K for a single detector element first a relation between the total absorbed energy Q in the source and the measured velocity potential signal [or acoustic pressure signal with Eq. (2)] is obtained from Eq. (3)

$$Q=\Delta V\sum_j W_j=-\frac{4\pi\rho c C_p}{\beta}\Delta t\sum_k t_k\phi_k. \tag{10}$$

To match $\boldsymbol{\phi}^{(n)}$ energetically with $\boldsymbol{\phi}$, K has to be

$$K=\frac{\sum_k t_k\phi_k}{\sum_k t_k\sum_j A_{kj}I_j^{(n)}}. \tag{11}$$

To obtain a correct value for the total energy from relation (10) requires that all $w_{kj}=1$ and that the detectors are absolutely calibrated. However, even if these requirements are not entirely met the normalization coefficient derived in Eq. (11) will render $\boldsymbol{\phi}$ and $\boldsymbol{\phi}^{(n)}$ comparable in size, which is necessary for calculating the residual. It has to be emphasized that due to different responses of detectors in an array or due to other fluctuations in the measurement the coefficient K can have different values for each detector element. K is therefore an important factor in deriving the correct signals from backprojected images. It has been pointed out that the convergence of the van Cittert algorithm requires suppression of noise.[17] We found that the convolution with $\mathbf{g}$ described in Eq. (5) provides sufficient smoothening of signals to avoid the buildup of noise and to keep the solution converging. Tests with insufficient smoothening, using a shorter integration time than t_{prop}, yielded solutions that diverged after several iterations (not shown).

Iterations start by setting $\mathbf{I}^{(0)}=0$, creating a first estimate $\mathbf{I}^{(1)}$ that is the backprojection of the measured velocity potentials. Since ultrasonic detectors usually measure acoustic pressure, the signals are first converted into velocity potentials by integration. The norm of the residual can be used as a quality measure of the reconstruction and to monitor the improvement achieved by the iterations. The error of the velocity potential after the nth iteration is defined as

$$\text{err}_\phi^{(n)}=\sum_k(\phi_k-\phi_k^{(n)})^2. \tag{12}$$

In the following simulations and experiments, the iterations were stopped if the improvement of the error became smaller than 1% of the initial error, that is

$$\frac{\text{err}_\phi^{(n-1)}-\text{err}_\phi^{(n)}}{\text{err}_\phi^{(1)}}<0.01\,. \tag{13}$$

Using the definition in Eq. (8) for the backprojection matrix, the reconstruction algorithm produces a three-dimensional image in arbitrary units. A normalization by the maximum value is useful for displaying sections of the image and for observing the progress of the iterations. It is also possible to create an absolute image $\mathbf{W}^{(n)}$ in units of absorbed energy density using conservation of energy. Since the volume integral over the reconstructed image has to be equal to the total absorbed energy Q, the images have to be multiplied with a normalization factor

$$\mathbf{W}^{(n)}=\frac{Q}{\Delta V\sum_j I_j^{(n)}}\mathbf{I}^{(n)}. \tag{14}$$

In an experiment the value of Q is obtained from measured signals using Eq. (10). In a simulation it is given by the volume integral over the known source distribution.

III. SIMULATION

We simulated the imaging of two spherical sources using a planar array of 3×3 detectors. The detectors were assumed to be omnidirectional and therefore we set all $w_{kj}=1$. This corresponded to the actual experimental conditions that are described in Sec. IV. Instead of using $u_{kj}=w_{kj}$ we used $u_{kj}=\cos\theta_{kj}$ for the directional weights in the backprojection. The resulting overall weight factors $R_{kj}\cos\theta_{kj}$ are equal to the distance to point $\mathbf{r}_j$ from the detector plane. Backprojection spheres therefore do not reach the detector plane, which slightly decreases the lateral resolution but yields a better convergence of the algorithm compared to isotropic backprojection. The energy density distribution in the sources was given by Gaussian functions with an $1/e$ radius of $a=0.2$ mm,

$$W_j=\exp(-(\mathbf{r}_j-\mathbf{r}_c)^2/a^2), \tag{15}$$

where $\mathbf{r}_c$ is the position of the center. The total source cube had a size of $2\times2\times2$ mm^3 and was divided into a grid of $40\times40\times40$ points. The centers of the two sources (hereafter referred to as ''spheres'') were located at the Cartesian coordinates $\mathbf{r}_{c1}=(1.5,1,0.8)$ mm and $\mathbf{r}_{c2}=(0.5,1,1.3)$ mm. The arrangement of spheres and detector array is schematically shown in Fig. 1. Figure 2 shows one of the velocity potential signals $\boldsymbol{\phi}$ calculated from the original source distribution $\mathbf{W}$, the signal $\boldsymbol{\phi}^{(1)}$ calculated from $\mathbf{I}^{(1)}$ and the residual $\boldsymbol{\phi}-\boldsymbol{\phi}^{(1)}$ that is used to generate the improved estimate $\mathbf{I}^{(2)}$.

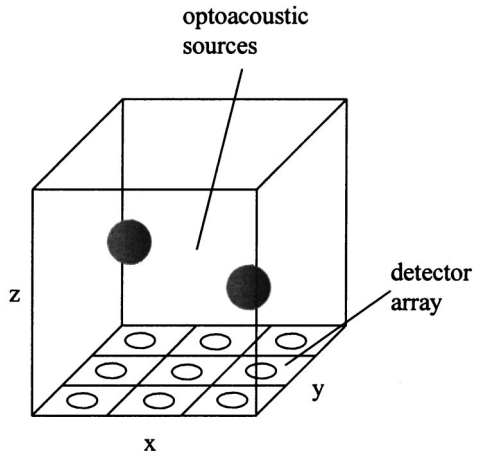

FIG. 1. Geometry of detector array and optoacoustic sources for the simulation.

The resolution of the two sphere signals is diminished in $\boldsymbol{\phi}^{(1)}$, leading to the negative components in the residual. Section images through the centers of the two spheres for the original $\mathbf{W}$, the initial estimate $\mathbf{I}^{(1)}$ and the improved reconstruction after 12 iterations, $\mathbf{I}^{(12)}$ are displayed in Fig. 3. For better comparison of original and reconstruction, all images are normalized by their maximum. The absolute energy density values obtained from Eq. (14) are displayed in the gray level scales. The maximum of $\mathbf{I}^{(1)}$ is only about 5% of the maximum value of $\mathbf{W}$. Furthermore, the source labeled with 1 appears brighter (maximum 0.047) than source 2 (maximum 0.037). The separation of the sources and the accuracy of their relative strengths are clearly improved after 12 iterations. In $\mathbf{I}^{(12)}$ both sources are equally bright with a maximum value of 0.12. Figure 4 displays the error of velocity potentials as a function of the number of iterations. No significant further improvement was achieved after 12 iterations, when the error reached about 40% of its initial value. The fact that the error cannot be further reduced is believed to be due to the small number and plane arrangement of detectors in the array.

The simulation offers the opportunity to quantitatively compare the reconstructed distribution with the known original. This analysis was used to investigate the influence of the

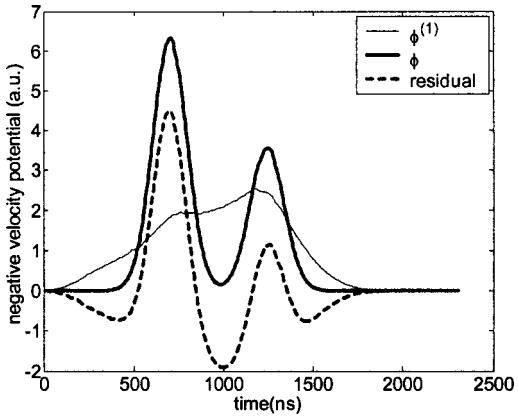

FIG. 2. Simulated velocity potential at one of the nine detector positions. The negative velocity potential is displayed as a function of time. Comparison of the measured signal $\boldsymbol{\phi}$, the signal derived from the first estimate $\boldsymbol{\phi}^{(1)}$ and the residual $\boldsymbol{\phi}-\boldsymbol{\phi}^{(1)}$.

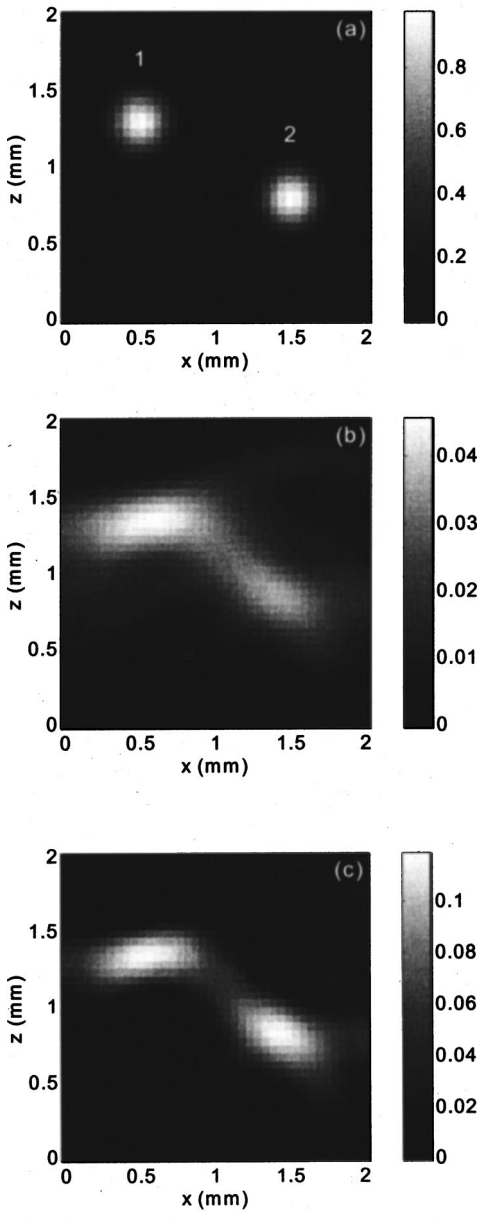

FIG. 3. Simulation of image reconstruction using the iterative algorithm. Displayed is a section through the centers of the spheres at $y=1$ mm. The gray level scales show the values of the reconstruction normalized by the total absorbed energy: (a) original distribution $\mathbf{W}$, (b) first estimate $\mathbf{I}^{(1)}$. Maximum of source 1: 0.047, of source 2: 0.037. (c) Image after 12 iterations $\mathbf{I}^{(12)}$. Maxima of both sources 1 and 2: 0.12.

number of detectors in the array on the quality of the reconstruction. The error of the three-dimensional reconstruction after n iterations can be defined as

$$\mathrm{err}_I^{(n)}=\sum_j (W_j-I_j^{(n)})^2. \tag{16}$$

For a comparison of the shapes of the two distributions, $\mathbf{W}$ and $\mathbf{I}^{(n)}$ are normalized by their maximum value. This corresponds to the visual impression one gets from the section images in Fig. 3, which are normalized in the same way. Alternatively, a comparison of the absolute energy density can be done by replacing $\mathbf{I}^{(n)}$ by $\mathbf{W}^{(n)}$ from Eq. (14). In this simulation, the detectors were always distributed over a square of 2×2 mm^2. The square was divided into a number

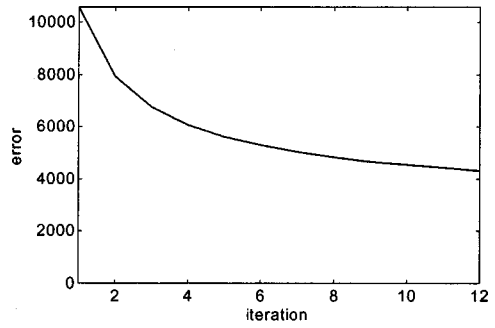

FIG. 4. Errors in the simulation between $\boldsymbol{\phi}$ and $\boldsymbol{\phi}^{(n)}$ as a function of the number of iterations n.

of equal areas according to the number of elements and the detector points were placed in the centers of these areas. Figure 5(a) shows the errors of the reconstruction for the two different normalization methods as a function of the number of array elements. In Fig. 5(b) the mean error of the velocity potential is displayed, also as a function of the number of array elements. The mean error is the value obtained from Eq. (12) divided by the number of array elements, L. All graphs show the final errors after termination of the iterations. Since the radial backprojection is the ideal reconstruction for a single detector, the corresponding error of the velocity potential vanishes. A reconstruction of any three-dimensional object needs at least three detector positions, as indicated by the high errors of the images for 1 and 2 detector elements. The final error of the images decreased until the number of detectors reached 9. There was no significant further improvement when the number of detectors was increased from 9 to 16. The improvement was much more pronounced in the reconstruction that was normalized by its maximum value than in the absolute reconstruction. The final error of the velocity potential was constant for 4, 6, 9, and 16 detector elements. From this analysis it follows that for the reconstruction of simple objects as the two spheres a number of 9 detector elements is sufficient. The use of 16 elements insignificantly improves the reconstruction but almost doubles the computation time.

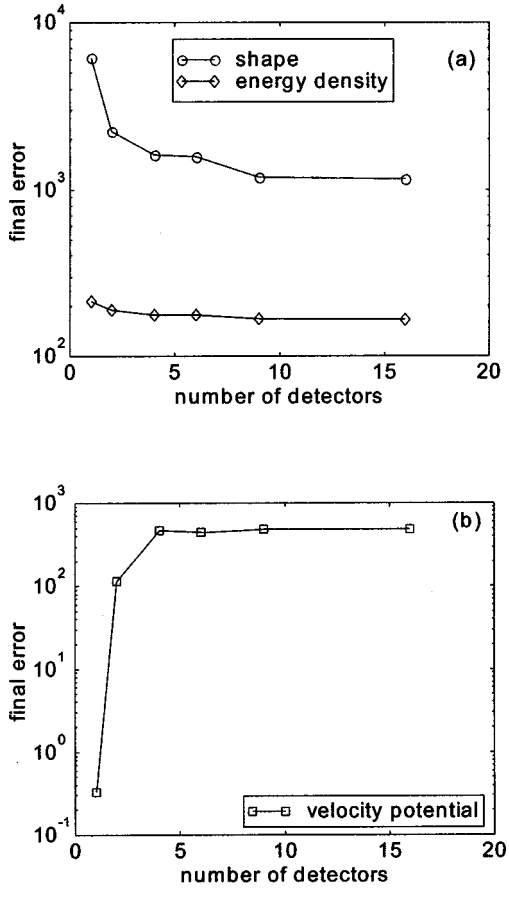

FIG. 5. Final errors in the simulation as a function of the number of detectors in a quadratic array. (a) Error of the reconstructed image. For comparison of shapes both $\mathbf{W}$ and $\mathbf{I}^{(n)}$ are normalized to their maximum. Comparison of energy density is done after normalizing $\mathbf{I}^{(n)}$ using the total absorbed energy. (b) Final error of velocity potential. Errors calculated with Eq. (13) are divided by the number of array elements.

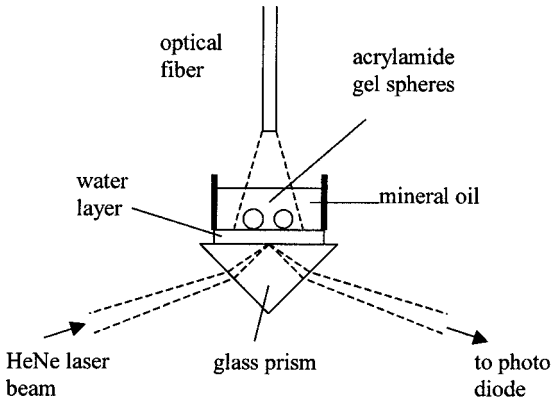

FIG. 6. Experimental setup for the optoacoustic imaging of two absorbing spheres. For detection of the acoustic waves, a focused laser beam is modulated by pressure changes at a glass–water interface.

IV. EXPERIMENT

In an experiment we tested the iterative algorithm for the imaging of two absorbing sources in an optically clear environment. Two spheres made of acrylamide gel with added absorber (Direct Red 81, Sigma Chemical) were placed on a thin plastic film and were surrounded by clear mineral oil (Fig. 6). The absorption coefficient of the gel was $\mu_a = 60\ \mathrm{cm}^{-1}$. The oil prevented the dye from diffusing out of the spheres. The diameters of the spheres were 1.2 and 1.5 mm, respectively, and the distance between the centers was 2.15 mm. A 1-mm-diameter optical fiber was used to irradiate the spheres from above. The laser source was a frequency-doubled, Q-switched Nd:YAG laser operating at a wavelength of 532 nm with a pulse duration of 5 ns. The laser pulse energy was 5 mJ and the laser spot diameter was 4 mm. With an optical absorption depth $1/\mu_a$ of 170 μm both spheres were optically thick, and therefore only a thin layer facing the incident laser pulse was heated. The acoustic signals were recorded with an optical detector described previously.[23] A continuous HeNe probe beam was focused to an elliptical spot with principal diameters of 120 and 250 μm on the interface of a glass prism and a water layer. The layer separated the glass prism from the plastic film carrying the gel spheres and had a thickness of 3 mm. An acoustic wave being incident on the glass surface from the water layer

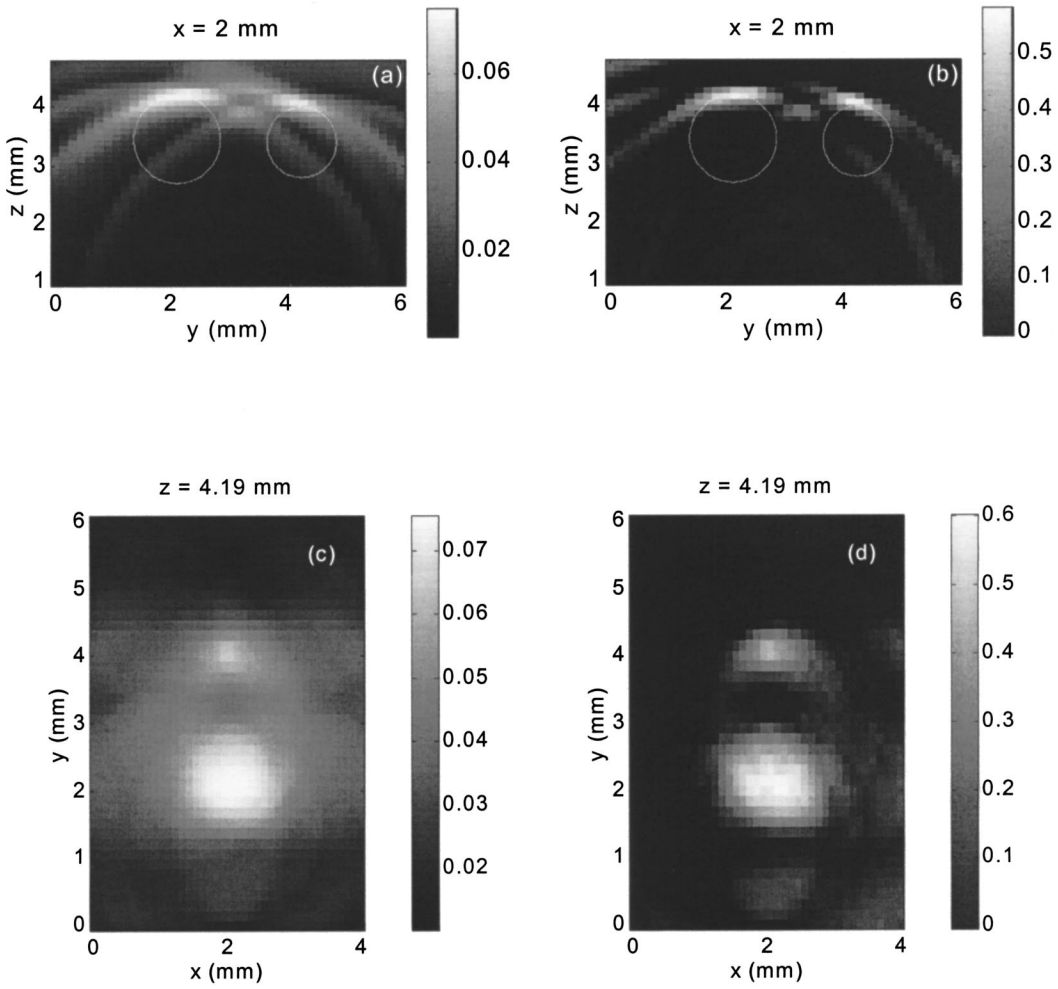

FIG. 7. Experimental image reconstruction. Sections along $y-z$ planes [(a), (b)] and $x-y$ planes [(c), (d)] of the first estimate $\mathbf{I}^{(1)}$ [(a), (c)] and the estimate after 11 iterations, $\mathbf{I}^{(11)}$ [(b), (d)] are displayed. The values of the gray level scales are in J/cm^3. The circles in (a) and (b) indicate the positions of the absorbing spheres.

slightly changed the relative optical refractive index between the two media, thereby varying the Fresnel reflectance of the interface. This caused modulations of the probe beam intensity that were detected with a fast photodiode. The signals from the photodiode were amplified and recorded on a digital storage oscilloscope. Choosing an incident angle of the probe beam slightly smaller than the critical angle of total internal reflection of the glass-water interface maximized the sensitivity of the detector. The undisturbed optical reflectance at the prism–water interface was 0.8. Calibrating the detector using a procedure based on the Fresnel formula and the change of refractive index with pressure, $dn/dp = 1.35 \times 10^{-5}$ bar^{-1} yielded a sensitivity of 0.6% modulation per bar of pressure.[23] The overall sensitivity of the system taking into account the response of the photodiode and the gain of the amplifier was 1 mV/bar. The noise level of averaged signals (over 32 sweeps) was about 20 μV or 20 mbar.

The directivity of an ultrasound detector for pulsed excitation is known to depend on the size of the sensor area, the distance between source and detector and the temporal shape and duration of the signal, which are in turn determined by the shape of the source and the pulse duration of the laser.[9] Unlike a piezoelectric element that is sensitive to the pressure that enters into the piezoelectric material, the optical sensor measures changes of pressures and associated density modulations that occur at the surface of the glass prism. Therefore there is no angle-dependent attenuation of the pressure wave due to acoustic mismatch for the optical sensor and only the integration effect of the obliquely incident wave on the detector plane plays a role. In a separate experiment (not shown) we found that indeed the directional dependence of signal shape and maximum can be readily described by integration effects over the detector area. It turned out that for the experimental signal shapes and within the aperture used for the experiment the optical detector can be regarded as omnidirectional. Consequently we set all weight factors $w_{jk} = 1$, independent of angle. To simulate a detector array, the detector point was scanned over a grid of 3×3 points in a plane, with a grid size of 1 mm in x direction and of 1.5 mm in the y direction.

V. RESULTS

Figure 7 shows two sections of the reconstructed volume (size $4 \times 6 \times 4$ mm^3), one parallel to the $y-z$ plane and one parallel to the $x-y$ plane. The algorithm stopped after 11 iterations. For each plane, the first-order reconstruction, $\mathbf{I}^{(1)}$, and the final reconstructed image, $\mathbf{I}^{(11)}$, are displayed. The

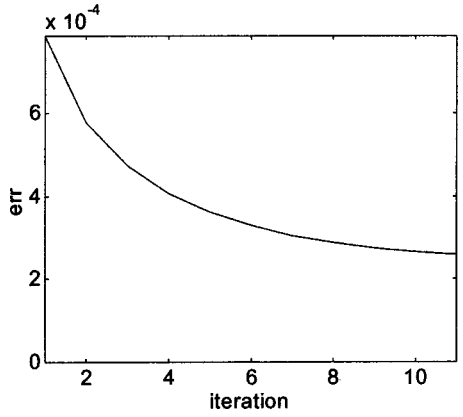

FIG. 8. Experimental image reconstruction: errors between ϕ and $\phi^{(n)}$ as a function of the number of iterations n.

$y-z$ section shows how the backprojection arcs are strongly reduced after 11 iterations. In an $x-y$ section, the backprojection artifacts cause a blur that again nearly disappears in the improved image. The values in the gray level bar are absorbed energy density in units of J/cm^3. They were obtained by normalizing $\mathbf{I}^{(n)}$ using Eq. (14). The total absorbed energy was calculated from the measured acoustic signals using Eq. (10), giving an average value of 1.5 mJ. This is a reasonable value considering that the incident laser pulse energy was 5 mJ and that the cross section of the spheres only partly filled the laser spot. From iteration 1 to iteration 11 the maximum energy density increased by a factor of 8, due to the less spreading of energy over the backprojection spheres and increased concentration in the two sources. The corresponding errors are shown in Fig. 8.

VI. DISCUSSION

An iterative method has been described to reconstruct the distribution of absorbed energy density from thermoelastic pressure signals detected with a transducer array. The minimization of the error between the measured signals and the signals calculated from the reconstructed distribution leads to a self-consistent solution of the optoacoustic imaging problem and an inversion of Eq. (3). All knowledge about the source that is required in the algorithm comes from the measured signals and the condition that the result has to be positive.

During the iterations the artifacts, which appear as backprojection arcs or blur in the two-dimensional sections of $\mathbf{I}^{(1)}$, were markedly reduced. Comparing initial estimates with improved estimates in Figs. 3 and 7 might suggest that similar improvements could be achieved by simple thresholding, where parts of the images are set to zero that are darker than a certain threshold. However, the sources may have different strengths, and thresholding could also remove actual structures together with the artifacts. In addition, as the simulation has shown the one-step backprojection sometimes produces incorrect relative source strengths. Applying a threshold to remove backprojection arcs to the reconstruction in Fig. 3(b) would have emphasized this error. Instead the iterative algorithm was able to correct the reconstruction and to make the brightness of the two sources equal.

The maximum of the absolute source strength was always too low compared to the original. In the simulations the maximum reconstructed energy density increased between $\mathbf{I}^{(1)}$ and $\mathbf{I}^{(11)}$ from about 5% to 12% of the corresponding value in the original distribution $\mathbf{W}$. In the experiment, an eightfold increase of maximum energy density from 0.075 to 0.6 J/cm^3 was observed. This was still too low compared to an estimated value of 2.4 J/cm^3 derived from the experimental parameters using

$$W_{\max}=\frac{Q}{A_{\text{las}}}\mu_a, \tag{17}$$

where A_{las} is the laser spot area of 0.126 cm^2, and the values of laser pulse energy Q and absorption coefficient μ_a are 5 mJ and 60 cm^{-1}, respectively. The reason why the algorithm tends to give too low maximum values is the effect of slight spreading of energy around a reconstructed source on the sum in the denominator of Eq. (14). The energy content in residual artifacts increases the integral and reduces the maximum value of the image.

The error in the velocity potential did not approach zero but rather seemed to converge to a certain constant level. This shows the limit of the algorithm when it is applied to data recorded on a finite size plane array. Backprojection of residual terms in Eq. (9) can only correct the reconstruction from a limited range of directions, leaving artifacts that cannot be corrected at all. The algorithm is expected to be more efficient if spheres from all directions intersect in one image point, that is if the detectors are arranged on a spherical array around the imaged volume. In practical applications, however, this is usually not possible. Applying the algorithm to signals from curved arrays with an increased solid angle of detection compared to a plane array should improve the convergence.

Since all information for the reconstruction comes from the measured signals, the detectors have to be very accurate. The main requirements are sufficiently high bandwidth and the absence of measuring artifacts such as ringing. The optical detector used in this study met these requirements. Another advantage of the optical detector is that it is transparent and can be transilluminated by the laser pulse. This makes it easier to apply laser pulses and to collect the acoustic signals on the same surface of a sample. A drawback is that the sensitivity of optical detection using changes of Fresnel reflection is limited to about 1% modulation per bar.[12] For the acoustic pressure amplitudes recorded in our experiments (in the range of 0.2 bar) this yielded a satisfactory signal to noise ratio. However, if higher sensitivity is needed, piezoelectric detectors should be employed and appropriate filtering of signals incorporated to remove measurement artifacts.[10]

In optoacoustic imaging, the reconstruction problem is always three-dimensional.[14] This is partly caused by the diffuse propagation of the light pulse that excites the thermoelastic wave. It is therefore not possible to limit the generation of signals to a plane as in 2D x-ray computer tomography, where information from only a single, thin section of the sample is projected. Reconstruction of a 2D slice therefore requires collection of information from the whole volume to discriminate sources in the imaged section from

those outside this section. Furthermore, knowing only the source distribution in a cross-sectional plane, it is impossible to solve the optoacoustic wave equation to obtain a set of signals. The algorithm developed in this study can therefore only be applied to the full source volume. This makes the method computationally intensive. Generating or backprojecting a signal from or to a volume of $40\times40\times40$ points took about 6 s on a G4 Power PC (Apple Computer, Inc.). Using 9 detector positions, one full iteration was accomplished in a little less than 2 min and the whole reconstruction using 11 iterations required 22 min.

An important question is the performance of the iterative algorithm in comparison with existing methods. Thermoacoustic images with a quality comparable to x-ray CT have been obtained with hemispherical arrays and microwave pulse sources.[10] Pressure signals from an array of 4000 or more elements are differentiated before backprojection, leading to a reconstruction method similar to the inverse three-dimensional Radon transform. Taking the first derivative of pressure (equivalent to the second derivative of velocity potential) leads to signals that have some similarity to the residuals that are used to improve the first image estimate in the iterative algorithm (Fig. 2). Employing the filtered backprojection to our experimental signals we obtained a reconstruction with an error of the velocity potential of 7.4×10^{-4}, which is lower than 7.8×10^{-4} achieved with backprojection of unfiltered signals but higher than the final error of the iterative algorithm of 2.6×10^{-4}. This shows that the inverse Radon method is not designed to work with a low number of detectors, where the feedback provided by the iterative algorithm has the better correcting effect. Another method of filtered backprojection uses a high pass filter to remove the slowly changing signal from background absorption. This creates new pressure and velocity potential signals that correspond only to small structures with contrast relative to the background.[1] A similar kind of filtering could be useful to process the signals that are used as input for the iterative algorithm, which would then produce a corrected image of only these structures.

VII. CONCLUSION

Iterative reconstruction of three-dimensional optoacoustic images leads to a significant reduction of artifacts, a correction of relative source strengths and an improvement of contrast compared to a single backprojection of velocity potentials. Compared to existing reconstruction techniques for three-dimensional optoacoustic or thermoacoustic imaging that use filtered backprojection of signals and high numbers of detector array elements the iterative method uses a low number of elements and a minimization technique that replaces the filtering step. The method may be useful in imaging applications where only a small number of array elements can be used, for example if the time for signal acquisition and the size of the transducer are limited.

Apart from the optoacoustic imaging problem the proposed reconstruction technique could also be applied to other problems in acoustics where the imaged objects are at the same time sources of acoustic waves. In the theoretical description it is shown how the temporally retarded signals from an acoustic source can be calculated using a set of linear equations. The reconstruction method is based on these equations, however, the way in which sound is generated is not limited to the optoacoustic effect.

ACKNOWLEDGMENT

G.P. was supported by the Austrian Program for Advanced Research and Technology (APART) of the Austrian Academy of Sciences.

[1] V. A. Andreev, A. A. Karabutov, S. V. Solomatin, E. V. Savateeva, V. Aleynikov, Y. V. Zhulina, R. D. Fleming, and A. A. Oraevsky, ''Optoacoustic tomography of breast cancer with arc-array-transducer,'' in *Biomedical Optoacoustics*, edited by A. A. Oraevsky [Proc. SPIE **3916**, 36–47 (2000)].

[2] C. G. A. Hoelen, F. F. M. de Mul, R. Pongers, and A. Dekker, ''Three-dimensional photoacoustic imaging of blood vessels in tissue,'' Opt. Lett. **23**, 648–650 (1998).

[3] S. L. Jacques, J. A. Viator, and G. Paltauf, ''Optoacoustic imaging of tissue blanching during photodynamic therapy of esophageal cancer,'' in *Biomedical Optoacoustics*, edited by A. A. Oraevsky [Proc. SPIE **3916**, 322–330 (2000)].

[4] A. A. Oraevsky, S. L. Jacques, R. O. Esenaliev, and F. K. Tittel, ''Laser-based optoacoustic imaging in biological tissues,'' in *Laser-Tissue Interaction V*, edited by S. L. Jacques [Proc. SPIE **2134A**, 122–128 (1994)].

[5] J. A. Viator, S. L. Jacques, and S. A. Prahl, ''Depth profiling of absorbing soft materials using photoacoustic methods,'' IEEE J. Sel. Top. Quantum Electron. **5**, 989–996 (1999).

[6] A. A. Karabutov, N. B. Podymova, and V. S. Letokhov, ''Time-resolved laser optoacoustic tomography of inhomogeneous media,'' Appl. Phys. B: Lasers Opt. **63**, 545–563 (1996).

[7] G. Paltauf and H. Schmidt-Kloiber, ''Pulsed optoacoustic characterization of layered media,'' J. Appl. Phys. **88**, 1624–1631 (2000).

[8] E. V. Savateeva, A. A. Karabutov, M. Motamedi, B. Bell, R. Johnigan, and A. A. Oraevsky, ''Noninvasive detection and staging of oral cancer *in vivo* with confocal opto-acoustic tomography,'' in Ref. 1, pp. 55–66.

[9] C. G. A. Hoelen and F. F. M. de Mul, ''Image reconstruction for photoacoustic scanning of tissue structures,'' Appl. Opt. **39**, 5872–5883 (2000).

[10] R. A. Kruger, D. R. Reinecke, and G. A. Kruger, ''Thermoacoustic computed tomography,'' Med. Phys. **26**, 1832–1837 (1999).

[11] G. Paltauf, H. Schmidt-Kloiber, K. P. Köstli, and M. Frenz, ''Optical method for two-dimensional ultrasonic detection,'' Appl. Phys. Lett. **75**, 1048–1050 (1999).

[12] G. Paltauf, H. Schmidt-Kloiber, K. P. Koestli, M. Frenz, and H. P. Weber, ''Optoacoustic imaging using two-dimensional ultrasonic detection,'' in Ref. 1, pp. 240–248.

[13] P. Liu, ''Image reconstruction from photoacoustic pressure signals,'' in *Laser-Tissue Interaction VII*, edited by S. L. Jacques [Proc. SPIE **2681**, 285–296 (1996)].

[14] P. Liu, ''The P-transform and photoacoustic image reconstruction,'' Phys. Med. Biol. **43**, 667–674 (1998).

[15] A. C. Kak and M. Slaney, *Principles of Computerized Tomographic Imaging* (IEEE Press, New York, 1988).

[16] P. H. van Cittert, ''Zum einfluβ der spaltbreite auf die intensitätsverteilung in spektrallinien'' (Influence of slit width on the intensity distribution in spectral lines), Z. Phys. **69**, 298–308 (1931).

[17] P. A. Jansson, ''Method for determining the response function of a high-resolution infrared spectrometer,'' J. Opt. Soc. Am. **60**, 184–191 (1970).

[18] D. A. Agard, ''Optical sectioning microscopy: Cellular architecture in three dimensions,'' Annu. Rev. Biophys. Bioeng. **13**, 191–219 (1984).

[19] V. E. Gusev and A. A. Karabutov, *Laser Optoacoustics* (American Institute of Physics, New York, 1993).

[20] G. J. Diebold and T. Sun, ''Properties of photoacoustic waves in one, two, and three dimensions,'' Acustica **80**, 339–351 (1994).

[21] G. Paltauf, H. Schmidt-Kloiber, and M. Frenz, ''Photoacoustic waves excited in liquids by fiber-transmitted laser pulses,'' J. Acoust. Soc. Am. **104**, 890–897 (1998).

[22] C. G. A. Hoelen and F. F. M. de Mul, ''A new approach to photoacoustic signal generation,'' J. Acoust. Soc. Am. **106**, 695–706 (1999).

[23] G. Paltauf and H. Schmidt-Kloiber, ''Measurement of laser-induced acoustic waves with a calibrated optical transducer,'' J. Appl. Phys. **82**, 1525–1531 (1997).

Interpretation of standard distortion product otoacoustic emission measurements in light of the complete parametric response

David M. Mills[a)]
V. M. Bloedel Hearing Research Center, Department of Otolaryngology, Head & Neck Surgery, University of Washington, Seattle, Washington 98195

(Received 13 April 2002; revised 12 June 2002; accepted 13 June 2002)

Emission characteristics (at $2f_1-f_2$) are measured in Mongolian gerbil as a function of the independent variation of all four stimulus parameters, the frequencies (f_1 and f_2) and the intensities (L_1 and L_2) of the two stimulus tones. The main five-dimensional display chosen is a logarithmic grid of frequencies, where for each frequency pair there is a contour map of the emission amplitude as a function of the two stimulus levels. The feature which leads to the greatest complexity in the proper interpretation of emission responses is the widespread presence of ''notches'' in these contour maps. Notches are lines of relative minima in the emission amplitude, and are found at either: (1) constant L_1, but only in regions where $L_1>L_2$; or (2) at constant L_2, only where $L_2 \geqslant L_1$. Notches are not found at any other orientations, and are associated with emission phase shifts of about 180° as the notch line is traversed. These notch characteristics are explained by phase cancellation in a simple cochlear amplifier model in which there is a change, as a function of the stimulus level alone, of relevant characteristics of the cochlear response to a single tone. Only one mechanism of emission generation is required to explain the observed patterns, i.e., there is no need to invoke different ''active'' and ''passive'' mechanisms. Unless properly accounted for, the presence of notches adversely affects all of the standard emission measurements, i.e., all methods which cover a restricted parameter set such as DPgrams, input–output or ''growth'' functions, and frequency ratio functions. Conversely, because the notch location appears approximately invariant in the cochlea, notches potentially make it possible to use certain emission growth functions to estimate forward and reverse middle-ear transfer functions.
[DOI: 10.1121/1.1505021]

PACS numbers: 43.64.Ha, 43.64.Jb, 43.64.Kc [BLM]

I. INTRODUCTION

While increasingly a useful tool for investigating cochlear function, distortion product otoacoustic emissions (DPOAEs) contain an inherent complexity that potentially limits their usefulness. In the simplest case of two-tone measurements, there is a total of four stimulus parameters which can be varied independently. These are the two stimulus frequencies (f_1 and f_2) and the two stimulus levels (L_1 and L_2). The complexity arises because the normal mammalian cochlea is a *strongly* nonlinear system. The response even at fixed stimulus frequencies depends strongly on the stimulus levels and is highly asymmetric with respect to the two levels. The emission is also dependent on the ratio of the two stimulus frequencies, f_2/f_1, and of course varies with the overall stimulus frequency as well (e.g., Mills and Rubel, 1994). A complete characterization of a given cochlea requires measurements over all four stimulus parameters varied independently.

For reasonable intervals in stimulus parameters, a complete parametric characterization can take days. For most investigations, a more limited parameter set must be chosen. Any such choice can be thought of as a sequence of points or lines taken through the complete four-dimensional parameter space. To date, most such choices have been made rather arbitrarily on the basis of convenience or convention, or at best on the basis of preliminary measurements over a limited parameter space. The method or criterion for choosing a restricted set for routine measurements has not been well established. Obviously, the method for choosing must depend on the goal of the measurements. However, even within sets of measurements which have similar goals, the process through which the parameter set should be chosen has not been well established. As a consequence, there are not yet any truly ''standard'' methods of DPOAE measurement.

Examples of the general classes of limited parameter sets that have been chosen follow. The simplest example is the ''DP audiogram'' or ''DPgram'' (e.g., Lonsbury-Martin *et al.*, 1990). This is defined as the emission amplitude (at $2f_1-f_2$) as a function of stimulus frequency for fixed stimulus levels and fixed frequency ratio. The second example, covering more of the parameter space, is a set of input–output, or ''growth'' functions (e.g., Brown, 1987; Lonsbury-Martin *et al.*, 1987). A growth function is defined as a plot of the emission amplitude as a function of stimulus level, with fixed frequencies and a fixed relationship between the two stimulus levels. A *set* of such may, for example, include growth functions over a range of f_2 frequencies. Several different level relationships have been employed, including equal levels, where $L_1=L_2$; and unequal levels where L_1 is

a)Electronic mail: dmmills@u.washington.edu

greater than L_2, e.g., $L_1 = L_2 + 10$ dB (e.g., Whitehead *et al.*, 1995a; stimulus levels in dB SPL). There are other suggested relationships, notably $L_1 = 0.4\ L_2 + 39$ dB (Kummer *et al.*, 1998). Some investigators have included in the general class of growth functions those responses measured when fixing one of the two stimulus levels and varying the other (e.g., Brown, 1987; Shi and Martin, 1997). A third major class is the ''frequency ratio function'' (e.g., Brown and Gaskill, 1990a; Kimberley *et al.*, 1993; Taschenberger *et al.*, 1995). This is defined as a plot of the emission amplitude and phase angle as a function of the frequency ratio, f_2/f_1, with constant stimulus levels. Also held constant is *one* of the frequencies, either f_1, f_2, or an emission frequency, e.g., $2f_1 - f_2$.

Even within these three classes there are a number of choices to be made. For example, for growth functions one must choose a frequency ratio and the relationship between stimulus levels. One general approach is to make preliminary measurements over some part of the parameter space, with the goal of identifying those parameters which give a relative maximum in emission amplitude (in a particular cochlea). This limited parameter set is then used in the investigation (e.g., Faulstich *et al.*, 1996). There are potential problems with this approach. One problem is that of identifying the maximum of a surface over a four-dimensional space when varying only *some* of the dimensions. More problematic for clinical purposes, the fact that the emission is relatively large in the normal case does not establish that those same stimulus parameters are the best choice to measure *changes* in hearing function.

Some studies have addressed this issue by looking at the effect of a given auditory manipulation on different choices of growth function. The unequal-level choice was found to be generally more sensitive than the equal-level choice in several situations, including changes due to noise damage in experimental animals (Wiederhold *et al.*, 1986; Whitehead *et al.*, 1995a), to tone-induced temporary threshold shift in humans (Sutton *et al.*, 1994), and to acute responses to certain ototoxic drugs (Whitehead *et al.*, 1992a; Mills and Rubel, 1994; Shi and Martin, 1997). Of course, these initial parametric studies have generally ignored large parts of the complete parameter space, particularly potential variations with stimulus frequencies and frequency ratios.

Progress has also been made in understanding the relationship between different methods of varying parameters in frequency ratio functions. Model calculations confirmed by observations have provided a useful explanation of relationships between phase gradients measured with the three different methods, i.e., fixed-f_1, fixed-f_2, and fixed emission frequency (e.g., Shera *et al.*, 2000; Tubis *et al.*, 2000). For this reason, the present work does not study the relationship between the three types, and includes only frequency ratio functions for fixed f_2 as representative of all three types. This particular type was chosen because it fits best with the main parametric representation chosen for this study.

While phase gradients with frequency ratio are therefore not a focus of the present study, the interpretation of the *amplitude response* of typical frequency ratio functions remains an active area of investigation and is considered in the context of the complete parametric response. The interpretation of growth function measurements and the best choice of parameters for such measurements also remain an active area of investigation. As will be seen, the interpretation of all DPOAE measurements is confounded by the presence of ''notches'' found throughout the parameter space. Such notches represent sharp decreases in emission amplitude, lines of relative minima along particular parameter coordinates, and are accompanied by rapid changes in the emission phase angle across the line. The behavior of these notches, their locations in parameter space, and their interpretation turn out to be crucial for the interpretation of standard DPOAE measurements.

The present study is intended to extend and complement previous studies which have explored more limited parameter spaces. In particular, this report extends an initial parametric study in gerbil which was limited in frequency by time and equipment limitations (Mills and Rubel, 1994). While space precludes a thorough review, examples of other limited parametric studies include those focused on frequency ratio functions (Fahey and Allen, 1986; Brown and Gaskill, 1990a, b; Lukashkin and Russell, 2001) and those focused on asymmetries with stimulus levels (Wiederhold *et al.*, 1986; Brown, 1987; Gaskill and Brown, 1990; Whitehead *et al.*, 1992a, b, 1995a, b; Hauser and Probst, 1991). While the full parametric response to be reported here generally agrees with responses found in studies over a more limited parameter space, the intent here is to show that the study of the complete parametric response can provide additional, useful perspective on the interpretation of earlier results.

II. METHODS

Subjects were young adult Mongolian gerbils (*Meriones unguiculates*) from Charles River Laboratories (Wilmington, MA). Equipment and procedures were similar to those previously detailed (Mills and Rubel, 1996; Mills and Shepherd, 2001). All animal procedures were approved by the Animal Care Committee of the University of Washington. Briefly, animals were anesthetized with a mixture of ketamine hydrochloride (Ketaject, Phoenix Pharm., 80 mg/kg) and xylazine (Xyla-ject, Phoenix Pharm., 5 mg/kg). Supplements of this mixture at 1/3 the initial dosage were given as needed to maintain a surgical depth of anesthesia throughout. The animal was attached to an adjustable surgical head holder (Kopf) employing a bite bar, and positioned on a heating pad. Animal temperature was maintained at 37 °C by an automatic system monitoring anal temperature. The pinna on the left side was removed, and a small amount of tissue removed over the bulla immediately dorsal-posterior to the ear canal. A small hole was drilled into the bulla and a tube (0.86-mm i.d. by 6.5 cm long) force-fit into the hole. The purpose of the small-diameter tube was to provide static pressure relief for the middle ear while maintaining normal middle-ear function.

A custom coupler (Mills and Rubel, 1996) was advanced under micromanipulator control and sealed to the left ear canal. The coupler included a port for a low-noise microphone (Etymotics ER10B), a port for a probe tube reference

microphone, and two ports for sound delivered through tubing from custom tweeters. Before beginning measurements, a wideband noise signal was generated by one tweeter, and the output of the low-noise microphone was calibrated *in situ* by comparison to the output of the probe tube microphone. The same coupler and calibration were used for DPOAE and auditory brainstem response (ABR) measurements.

One animal was the subject for each initial set of DPOAE measurements at a single f_2 frequency. Grids of emission output as a function of stimulus levels (L_1, L_2) varied independently were measured for a prechosen set of seven stimulus frequency ratios spanning the range from $f_2/f_1 = 1.06$ to 1.59 at approximately logarithmic intervals. Stimulus frequencies, f_2, were chosen at octave intervals from 1 to 32 kHz, a total of six different f_2 frequencies. These choices divided the four dimensional stimulus space into a set of 42 stimulus frequency pairs (f_1, f_2), with a grid of stimulus intensities (L_1, L_2) to be measured at each combination of stimulus frequencies.

Each grid of emission output was obtained by independently varying both stimulus levels at 5-dB intervals. Maximum levels were $L_1 \times L_2 = 80 \times 80$ dB SPL at all f_2 frequencies except at 32 kHz, where maximum levels were 90×90 dB SPL. At most f_2 frequencies, the emission amplitude at each point was measured by synchronous averaging for 4 s, resulting in a total time of about 20 min required to measure each grid. At the frequency extremes, $f_2 = 1$ and 32 kHz, the noise floor was higher and increased integration times were used. For analysis, a contour map of each data grid was constructed. To generate a contour map, an exact square grid was first calculated by extrapolation from the actual values of L_1 and L_2 measured and the emission amplitude was smoothed slightly (using a negative exponential smoothing function with a fourth-order polynomial and a sampling proportion of 0.1–0.2; Sigma Plot 2000, SPSS, Chicago, IL).

To obtain additional information on the phase changes with stimulus frequency ratio, the seven basic grids were supplemented by taking frequency ratio functions for each animal. These plots were obtained by holding the f_2 frequency and stimulus levels fixed and varying the frequency ratio at close intervals (typically 0.02). Frequency ratio functions were measured for a small set of stimulus levels, $L_1 \times L_2$, at the same f_2 as for that animals' contour maps.

To complement maps and functions measured at a given f_2, and to delimit variability, measurements were made in a second group of subjects across f_2 frequency. These measurements included standard emission measurements such as ''DPgrams'' and growth functions, both with $f_2/f_1 = 1.21$. Growth functions were measured with equal levels, $L_1 = L_2$, and unequal levels, with $L_1 = L_2 + 20$ dB. For comparison to the emission growth function thresholds, ABR measurements were also made in the second group. Pin electrodes were inserted subcutaneously, with the positive differential located between the eyes, the negative differential at the base of the neck, and the reference electrode at the left rear leg. Tone pips were used with frequencies chosen to be the same as the f_2 frequencies. Pips had a $\cos^2$ rise and fall time of 1 ms, a total duration of 5 ms, were of alternating polarity, presented at a rate of 31 Hz, and averaged over 1000 presentations. For the 3–4 curves near threshold, two or more ABR measurements were recorded at each stimulus level, so that the threshold could be unambiguously determined within a 5-dB interval. All traces were recorded and thresholds determined offline by visual inspection.

Following measurements in the animal, instrumental noise and distortion levels were estimated by repeating the DPOAE measurements at the same parameter choices, but with the animal replaced by a long tube (3.2-mm i.d. by 5 m). This effectively ''infinite'' tube, of approximately the diameter of the gerbil ear canal, provides a load with an impedance across frequency estimated to be generally equal to or lower than the impedance at the entrance to the gerbil ear canal (Mills and Rubel, 1996). Hence, this measurement provides an upper bound on the possible instrumental distortion present when the animal is measured. In addition, during animal measurements the noise floor was estimated for each stimulus presentation by an appropriate average of the bins next to the emission frequency at $2f_1 - f_2$. Emission amplitudes were included in data analysis only when they were at least 10 dB above noise and instrumental distortion amplitudes (except in Fig. 4, as noted).

III. RESULTS

A. The ''complete'' observed emission distribution

In this report, results are summarized only for the most important and most frequently measured emission component, the cubic distortion tone (CDT) at the frequency $2f_1 - f_2$. Results from a typical grid measurement are displayed in Fig. 1(A). The measurements for each grid consist of a set of emission amplitudes and phases over a grid of points in stimulus level space, for fixed stimulus frequencies. In this example, the frequencies were $f_1 = 6.25$ kHz and $f_2 = 8$ kHz $(f_2/f_1 = 1.28)$. The contour map represents the emission amplitudes versus stimulus levels, with L_1 on the horizontal axis and L_2 on the vertical axis. In this map, a given contour follows a line of constant emission amplitude in the $L_1 \times L_2$ space. To aid in visualization and interpretation of such maps, elevation views are shown along selected planes or cross sections through the contour map, as indicated in panel (A) by dashed lines *B* through *F*.

The contour map is clearly very asymmetric with respect to L_1 and L_2. The line *E*, which cuts the map at $L_1 = L_2$, clearly does not divide the emission distribution in half. In addition, there is a large notch at $L_1 = 70$ dB SPL which extends vertically almost all the way through the distribution, i.e., until it nears the region where $L_2 \approx L_1$. As Fig. 1(C) suggests, over the whole region where $L_2 < L_1$, the shape and location of the notch do not depend at all on the level L_2. For this reason, a notch with this orientation will be referred to as an ''L_1 notch.''

Note the behavior of the emission phase angle shown in the lower part of each elevation view. While the absolute values of the phase angles are not relevant, *relative* changes over a given grid are important. Because stimulus frequencies are not changing in this map, all phase angle changes are due to nonlinear effects. That is, linear parts of a system

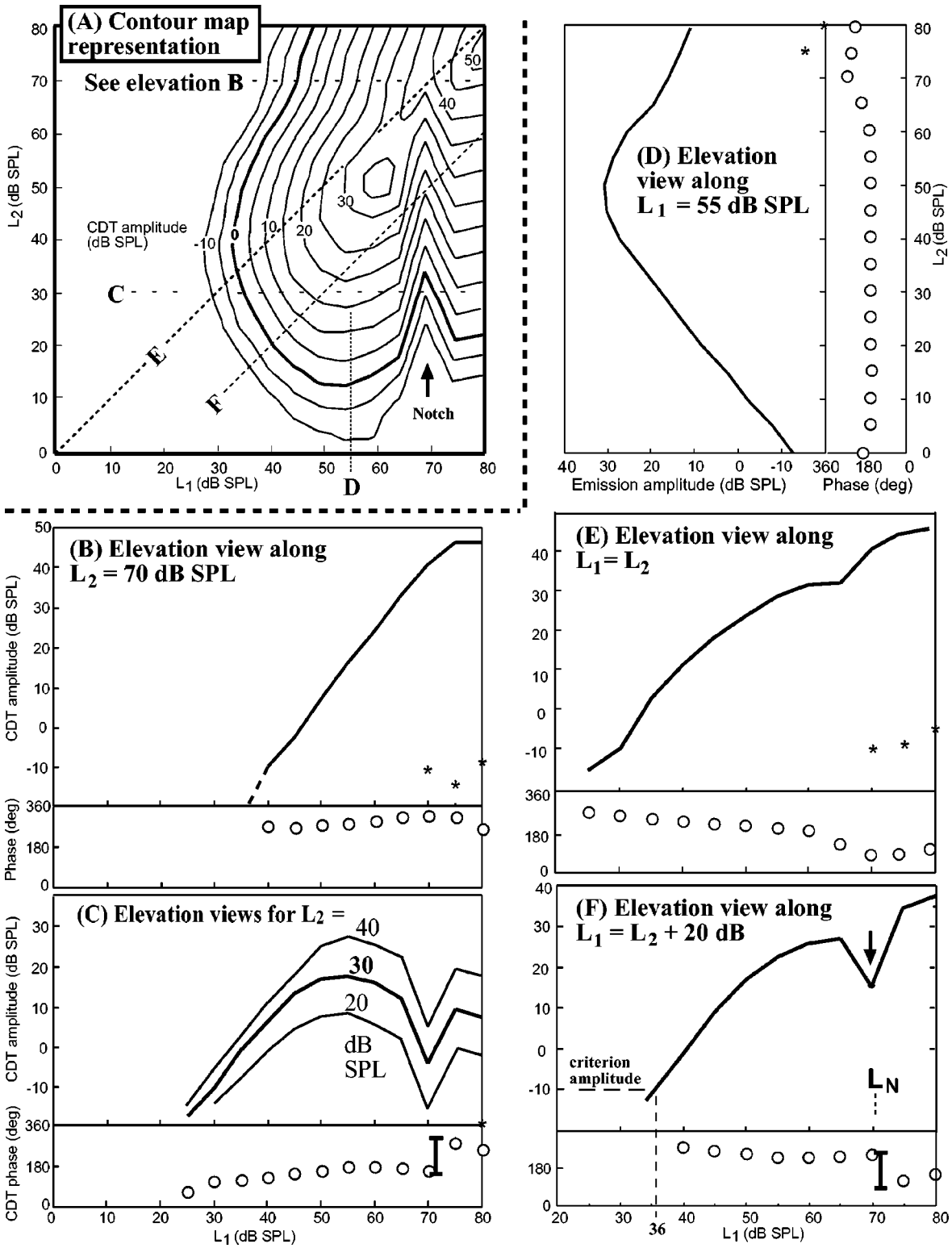

FIG. 1. (A) Upper left is a contour map derived from the measurements over a given grid of stimulus levels, and is a representation of the emission amplitude versus both stimulus levels, L_1 on the horizontal axis and L_2 on the vertical. The line for an emission amplitude of 0 dB SPL is shown in bold on this map and in all subsequent ones, and contours are shown spaced at 5-dB intervals in emission amplitude in all maps. Dashed lines denoted **B** through **F** represent planes cut through the emission distribution, and cross-sectional or ''elevation'' views at these planes are given in the corresponding panels (B)–(F). Most cross-sectional views are oriented so that they share an axis with the main contour view. This was not done with the two 45° cross sections (lower right panels), where (E) represents a growth function along $L_1=L_2$, and (F) represents a growth function along $L_1=L_2+20$ dB. However, the horizontal scales in (E) and (F) are elongated by $\sqrt{2}$ so that the dimensions agree with the distance along the 45° cuts through the contour map (A). In all elevation views, in addition to the amplitude as a function of stimulus level, open circles show the measured emission phase angle. The scale bar represents 180 deg. Elevation view (C) shows amplitude responses for three different L_2 levels as noted, but phase responses are for $L_2=30$ dB SPL only. Note also that the contour maps are smoothed slightly for plotting (see Sec. II). However, the elevation views shown are not smoothed, and represent the raw data used to derive the contour maps. For future use, the emission ''threshold'' amplitude of -10 dB SPL is indicated in (F), with the associated threshold level being $L_1=36$ dB SPL for this example. The notch level, L_N, is also noted, in this case occurring for $L_1=70$ dB SPL. Asterisks in the elevation views represent measured noise and instrumental distortion levels (see Sec. II). Where no asterisks are shown, it means that the values were below -20 dB SPL.

cannot contribute phase changes while varying stimulus levels at fixed frequencies. The behavior shown is typical, in that phase changes are usually small or gradual as the stimulus level is changed, except for particular regions where there is sometimes seen a rapid change or jump in phase angle. Such jumps often total about 180°, and a scale bar of height 180° is shown for comparison.

In general, there is a one-to-one correspondence between notches observed in the contour map amplitude plots and jumps or rapid changes in the associated phase of the emission. For example, there are notches in the cross sections (C) and (F), and corresponding, clearly related jumps in phase. In contrast, for (B), (D), and (E), the notches in the map are avoided and the phase angle changes are more gradual. Because of the general correspondence of rapid phase changes with notches, and otherwise only gradual phase changes, the phase angle responses do not add a lot of independent information to the contour map representation as shown in Fig. 1(A). For the main data summary, therefore, the focus is on the amplitude distribution, with phase information included only when particularly relevant or for illustration.

A complete parametric representation of the normal distribution of emission amplitude is summarized in Fig. 2. This is a five-dimensional representation in which all axes are logarithmic, though not of the same scale. This display presents the variation with the stimulus frequency, f_2, starting at 1 kHz for the top row and increasing in octave intervals to reach 32 kHz for the bottom row. Frequency ratios range from $f_2/f_1=1.06$ to 1.59 from left to right, at approximately logarithmic intervals. This means that the f_1 frequency *decreases* from left to right for each row in this display, as does the $2f_1-f_2$ emission frequency. For each frequency pair, there is a contour map which represents a plot of the emission amplitude as a function of the independent variation of both stimulus levels, L_1 and L_2. The same conventions are used as in Fig. 1(A).

As in Fig. 1, the vertical arrows in Fig. 2 illustrate *some* of the stimulus levels, L_1, where jumps or rapid phase changes were observed in the phase responses (not shown). The horizontal arrows indicate that similar phase changes also can occur at a particular L_2. Note that only some of the phase jumps are indicated in Fig. 2; in general, a phase jump or rapid change was found to occur whenever there was a notch in the amplitude distribution. Note also that over the entire parameter space (Fig. 2), only *two* types of notches were found. These are "L_1 notches," which have their minima along a line of constant stimulus level, L_1, and "L_2 notches," which are aligned along a line of constant L_2.

Note that the sharp notches seen in Figs. 1 and 2 when stimulus levels are changed can potentially intrude when using any other parametric manipulations. For this reason, the conclusions to be drawn from such maps will be deferred until supplemental data have been summarized. These supplemental data include measurements in which the focus is on the variation of amplitude and phase angle with stimulus frequencies. First, however, it is necessary to consider possible effects of bidirectional middle-ear transmission at lower frequencies. This consideration leads to changes in the stimulus levels to be measured as a function of frequency, and has implications for interpretation of results at lower frequencies.

B. Possible effects of middle ear on measured emission patterns

The difference between the maps at $f_2=1$ and 2 kHz (first two rows of Fig. 2) is noteworthy. The maps for $f_2=2$ kHz remain robust for all f_2/f_1, but the emissions for $f_2=1$ kHz become very weak as f_2/f_1 becomes large, i.e., as f_1 becomes small. This abrupt behavior contrasts especially with more gradual changes observed at higher frequencies, i.e., as f_2 goes from 2 to 8 kHz. One possible explanation for this is provided from an examination of the behavioral hearing threshold for the gerbil (Ryan, 1976). The auditory threshold in this animal was found to be relatively flat from 1 to 16 kHz, but it increased at a rate of about 40 dB/decade for frequencies below 1 kHz [see the dashed lines in Fig. 7(A)]. The corner frequency appeared to be about 1 kHz. *Suppose* that the major cause of this rise were due to the gerbil middle ear, and let us ask what would be the effect on the emission maps in Fig. 2. That is, the goal here is to calculate how these maps might look if the middle ear instead were transparent, or, equivalently, if the measurements could be made at the stapes. For demonstration, the calculations will employ the simplest model consistent with the behavioral threshold data: that middle ear effects in the gerbil cause a *bidirectional* decrease in transmission of 40 dB per decade for frequencies below 1 kHz, and no change above. It should be emphasized that it is not being suggested that such a simple model is "correct" or adequate for detailed measurements, only that it is the simplest model one can employ for a first attempt at exploring possible effects of the gerbil middle ear on its observed emission pattern.

First consider the $f_2=1$ kHz maps; an example for $f_2/f_1=1.28$ is shown in Fig. 3. The f_2 frequency is at the middle-ear corner frequency, so there is no correction to be made to any L_2 values. At this frequency ratio, however, the f_1 frequency is at 780 Hz and the inward transmission through the middle ear would be decreased about 5 dB. To make the middle ear transparent, then, the stimulus input scale is first decreased to reflect its effective value at the cochlea by shifting the L_1 scale 5 dB to the right, as shown in the middle panel [Fig. 3(B)]. Next, note that, for the chosen f_1 and f_2, the CDT emission at $2f_1-f_2$ is at a frequency of 560 Hz. The simple model suggests that middle-ear effects would cause about 10-dB attenuation in the outward transmission at this frequency relative to that at 1 kHz. To compensate for the middle-ear effects, then, 10 dB is added to the emission amplitude. In effect, the emission contours are appropriately *relabeled* to compensate for the 10-dB decrease, as done in the right panel. This is the final step of the transformation of the measured contour map to a "compensated" contour map, i.e., the map which presumably would have been measured if the gerbil middle ear were transparent.

To allow for such transformations, the $f_2=1$ kHz grids had to be measured to higher L_1 levels and lower emission amplitudes than for Fig. 2. Data from these additional measurements in another animal and subsequent transformations

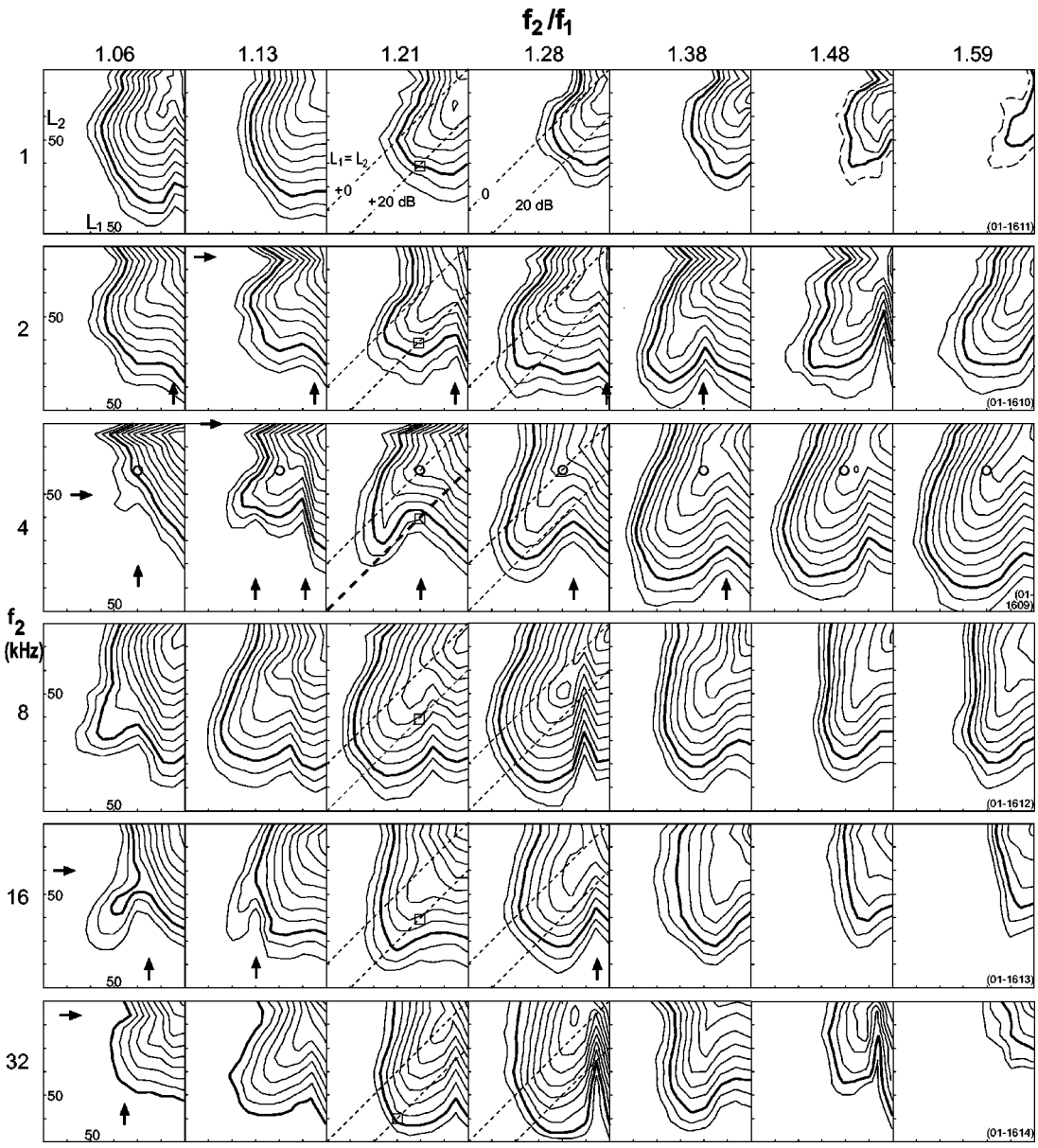

FIG. 2. Complete parametric representation: emission amplitudes measured as a function of the independent variation of all four of the stimulus parameters. As in Fig. 1(A), each contour map illustrates the emission amplitude as a function of the stimulus level L_1 (on the horizontal axis) and the stimulus level L_2 (on the vertical axis). In all panels, the bold contour line represents an emission amplitude of 0 dB SPL, and contours are shown at 5-dB intervals. Maps have been trimmed at lower stimulus levels to minimize white space, but the axes are the same across each row of maps. The ticks at 50 dB SPL are identified in the left column. The points for which $L_1 \times L_2 = 60 \times 40$ dB SPL also are noted by open squares in the column for $f_2/f_1 = 1.21$. In all contour maps, the upper right corner is at $L_1 = L_2$. This is equal to 80 dB SPL except at 32 kHz, where the grids go to 90 dB SPL in both stimulus levels. For reference, dashed lines (at 45°) for growth functions with $L_1 = L_2$ and with $L_1 = L_2 + 20$ dB are also shown in two columns. Also, in the 4-kHz row, the open circles indicate the level pair $L_1 = L_2 = 60$ dB SPL. The lowest contour plotted in most maps is at -10 dB SPL, except at the extremes of frequency, where the increase in noise floor prevented measurements to these levels. The arrows indicate *some* of the regions where the emission phase angle showed a jump or rapid change of about 180 deg.

are summarized in Fig. 4. This figure also includes transformations of the $f_2 = 2$ kHz maps. For these maps, since the f_1 frequencies were all between 1 and 2 kHz, no stimulus levels needed to be transformed, and it was possible to use the same animal as in Fig. 2. The emission amplitude alone was adjusted, and only for the three maps on the right for which the emission frequency, $2f_1 - f_2$, was below 1 kHz.

Overall, the emission patterns estimated for a ''transparent'' middle ear change relatively little as a function of frequency (Fig. 4 compared to Fig. 2). Further discussion is deferred to the summary of results.

C. Frequency ratio functions

For each subject in Fig. 2, i.e., for each row representing a given f_2 frequency, frequency ratio functions were also measured at the same f_2. These are measures for a given $L_1 \times L_2$ at relatively close spacing in the f_2/f_1 frequency ratio. Close steps are required so that phase variations can be unambiguously unwrapped. A number of frequency ratio functions were taken for each subject, typically at 10-dB intervals in $L_1 \times L_2$, for levels of 60 dB SPL and below. One set of such functions is illustrated in Fig. 5 for the stimulus

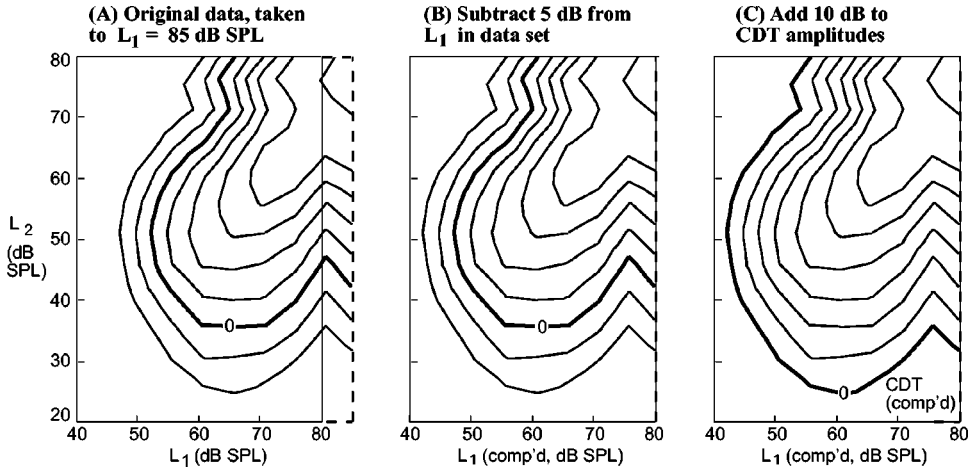

FIG. 3. Illustration of data transformations which can be made to contour maps to approximately compensate for possible middle-ear effects. The left contour map (A) represents the measured emission amplitude in the ear canal for $f_2=1$ kHz and $f_2/f_1=1.28$. In this animal, unlike the animal in Fig. 2, emissions were measured to stimulus levels of $L_1=85$ dB SPL. Panel (B) illustrates the transformation in L_1 stimulus level by 5 dB and panel (C) illustrates the transformation in emission amplitude by 10 dB to approximately account for middle-ear effects. Values were rounded for this illustration: the actual amounts from the model used to construct Fig. 4 were 4.3 and 8.6 dB, respectively.

levels $L_1\times L_2=60\times 60$ dB SPL. The location of this stimulus level is indicated by the open circles in Fig. 2 (shown in the row for $f_2=4$ kHz only) and in Fig. 4(C). For $f_2=1$ kHz, measurements were also made at the ''compensated'' stimulus levels ''60''$\times 60$ dB SPL, indicated in Fig. 4(A) by the open circles. As discussed above, the compensated levels are taken for progressively higher L_1 levels as the frequency ratio increases. In Fig. 5, to illustrate typical emission amplitude corrections for middle-ear effects, the measured emission amplitude (thin line) was increased as indicated (heavy line) in the amount of 40 dB/decade for *all* $2f_1-f_2$ frequencies below 1 kHz.

In the representation in Fig. 5, the horizontal axis is a linear scale and equal to stimulus frequency f_1/f_2 but in the

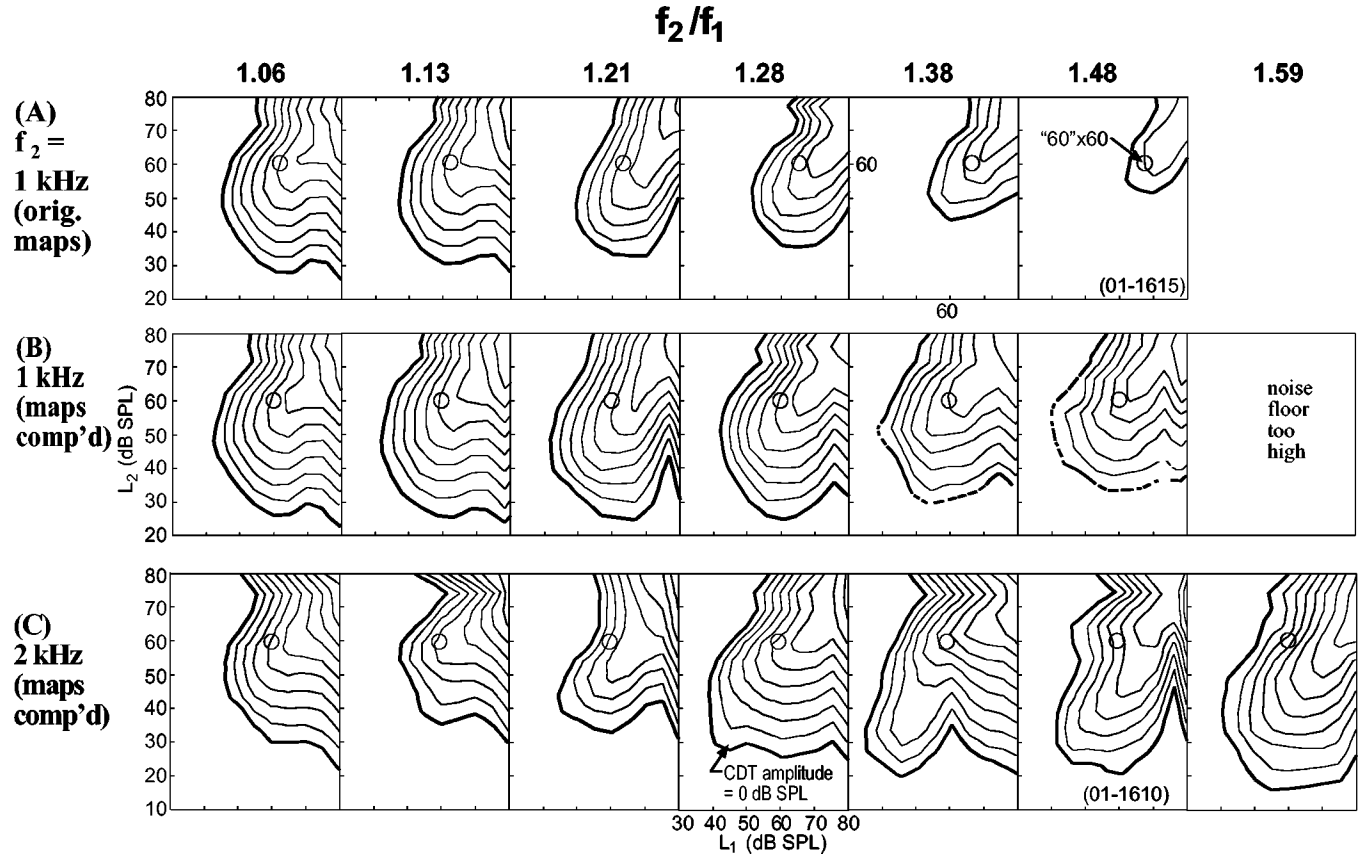

FIG. 4. Transformation of measured contour maps for $f_2=1$ and 2 kHz to account for possible effects of the middle ear. In all maps, the lowest contour level (thick line) represents an emission of 0 dB SPL, and lines are shown at 5-dB intervals. The 1-kHz data are from the same animal as Fig. 3, and the 2-kHz data from the same animal as Fig. 2. For best comparison with the compensated maps, the 1-kHz maps are presented exactly as are the 1-kHz maps in Fig. 2, i.e., only to a fixed $L_1=80$ dB SPL in the ear canal and down to a specific measured value of the emission amplitude, in this case 0 dB SPL. Measurements were actually made to higher L_1 and to much lower emission amplitudes, to allow for the subsequent transformations. The middle row (B) shows the effect on the observed 1-kHz maps of correcting for middle-ear function as illustrated in Fig. 3. For reference, the open circles in (A) and (B) indicate the location of the *compensated* level $L_1\times L_2=$''60''$\times 60$ dB SPL, and in (C) open circles indicate the level $L_1\times L_2=60\times 60$ dB SPL. Dashed contour lines indicate uncertainty due to noise or instrumental distortion. At $f_2=1$ kHz with $f_2/f_1=1.59$, even with integration times of 24 s, the noise floor at the emission frequency of 260 Hz was too high to make measurements sensitive enough to allow compensation, so this map was omitted.

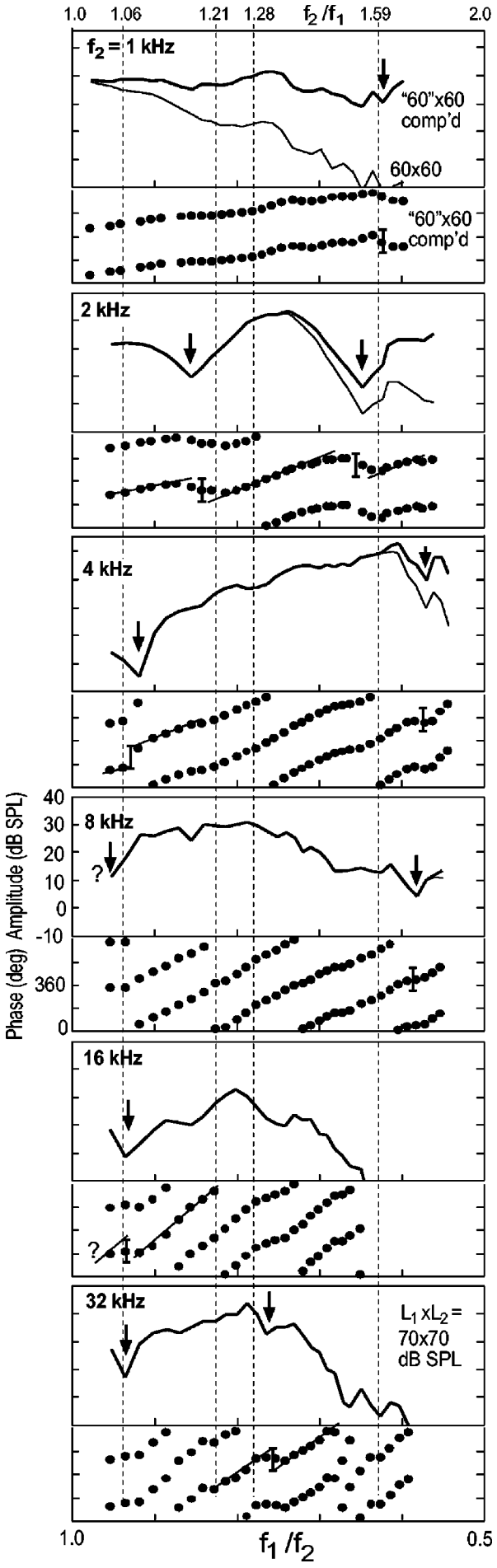

FIG. 5. Plots of emission amplitude versus frequency ratio f_2/f_1, i.e., ''frequency ratio functions,'' which for this study were measured for fixed f_2 frequencies and correspond to a given row in Fig. 2, and were for the same subjects (except the 1-kHz animal was the same as Figs. 3 and 4). Same layout as Fig. 2, in that from top to bottom are results for f_2 frequencies at octave intervals, and frequency ratio, f_2/f_1, increases from right to left. At each f_2 frequency, the vertical axis is the emission amplitude, scale shown in the panel for $f_2=8$ kHz. The horizontal axis is f_1/f_2 and is a linear scale (at bottom). The corresponding ratios f_2/f_1 are noted on the top of the figure. Dashed vertical lines reference some of the ratios for which contour maps are shown in Figs. 1–4. Stimulus levels were fixed at $L_1 \times L_2 = 60 \times 60$ dB SPL unless otherwise noted. In addition, a special compensated stimulus level was measured for $f_2 = 1$ kHz, where L_2 was fixed at 60 dB SPL but L_1 was increased proportionally at larger f_2/f_1 to account for middle-ear transmission effects [actual levels employed are indicated by open circles in Fig. 4(A)]. Also, because of the higher noise floor at 32 kHz, the level $L_1 \times L_2 = 70 \times 70$ dB SPL was chosen for display. Phase angles are repeated at 360-deg intervals for clarity. The scale bar represents 180 deg, and indicates possible locations of rapid phase changes, or ''jumps.'' The vertical arrows above point to possible or probable ''notches'' in the amplitude function. As noted, phase angles shown for 1 kHz were from the measurements with compensated levels (of L_1).

reverse direction. This is done so that low f_2/f_1 values (near unity) lie to the left in Fig. 5 as they do in Fig. 2. The linear frequency scale (in f_1) is used rather than logarithmic as in other displays, because a constant slope in the phase angle versus the frequency f_1 represents a constant phase gradient or group velocity. In this representation, a phase angle increasing from left to right corresponds to a positive group velocity. The scale bar in the phase plots is 180°, and is located, for comparison, in places where there appear to be anomalous changes in phase. The arrows indicate associated notches in the frequency ratio function.

The phase changes associated with notches are less clear in Fig. 5 than in Fig. 1. This is obviously because there are intrinsic phase changes associated with the group delay in the frequency ratio response function, but there are no similar phase gradients intrinsic to growth functions. Therefore, the vertical bars in Fig. 5 only indicate some places where there *may* be rapid phase changes associated with phase cancellation effects. The relationship of the notches identified with different methods of varying parameters is discussed in the summary of the results.

D. DPgrams

Another common method of measuring emission responses within a (very) restricted parameter set is the ''DPgram.'' This is defined as a plot of emission amplitude versus f_2 frequency holding the stimulus levels and the frequency ratio constant. A typical response is shown in Fig. 6. This plot is for a frequency ratio of $f_2/f_1=1.21$, with $L_1\times L_2=60\times 60$ dB SPL in the upper part (A) and with $L_1\times L_2=60\times 40$ dB SPL below (B). The horizontal axis is the stimulus frequency, f_2. Emission amplitudes are shown as the bold line and the phase angles as the filled circles. No compensation was done for possible middle-ear effects in this display.

DPgrams

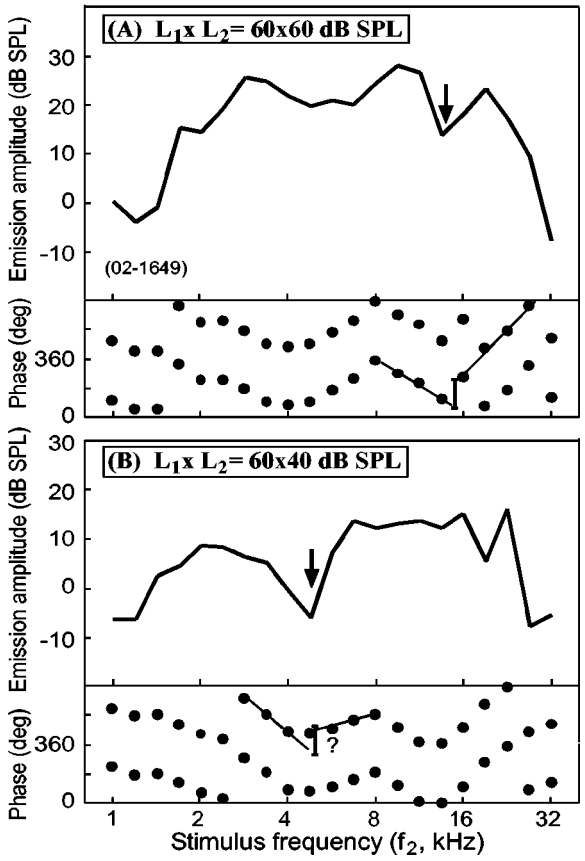

FIG. 6. Typical DP grams, plots of emission amplitude as a function of f_2 frequency, with fixed frequency ratio and fixed stimulus levels. Measurements were made at 1/4-octave intervals in f_2. Stimulus and emission levels were those measured in the ear canal, i.e., they were not compensated for middle-ear effects. The line shows the DPgram amplitude and the filled circles below represent the emission phase response, repeated at 360-deg intervals. The scale bar represents 180 deg. Arrows denote some probable notch locations.

E. Emission growth and threshold functions

As noted in the Introduction, for routine measurements it is obviously necessary to choose a subset of the entire parameter space. DPgrams are fast and generally suitable for screening purposes, but sample only a very limited part of the stimulus parameter space. For general use, the next step up in complexity has typically been the use of growth functions, plots of emission amplitude with fixed frequency and level ratios. Two common choices of level ratio are illustrated in Figs. 1 and 2, for comparison to the overall map of emission amplitude. These are equal level ratios, where $L_1=L_2$, and unequal levels, with $L_1=L_2+20$ dB. These were chosen for this study to span the range of level ratios most often used. Examples of these growth functions are noted in Fig. 2 for frequency ratios in the usual range, i.e., for f_2/f_1 from 1.2 to 1.3.

An obvious advantage for the main display format chosen for this study is that any growth function simply represents a cross section or elevation view along a line in a stimulus level grid (e.g., 45° dashed lines in Fig. 2). A given animal was measured to contribute one row, i.e., one f_2 value, of Fig. 2. To complement and support these data, measurements of growth functions were taken in additional animals at fixed frequency ratio but across f_2 frequency, i.e., by sampling one column of Fig. 2. Emission threshold measures were constructed from these growth functions, as defined in Fig. 1(F), and compared with ABR threshold measures in the same animals. An example is shown in Fig. 7.

F. Summary of results

A review of all data obtained in this study leads to the conclusions summarized below, with interpretations of these results deferred to the next section.

(i) For any combination of stimulus frequencies, the normal intensity distribution is usually highly asymmetric as a function of the stimulus levels. This can be seen most easily by looking at the lines $L_1=L_2$ drawn in typical contour maps; by far, most of the measurable emission occurs in the region ''below'' this line, i.e., where $L_1>L_2$. The exception occurs when the frequency f_1 becomes close to f_2, that is, as f_2/f_1 tends to one. Mathematically, of course, as the two frequencies tend to equality the intensity distribution

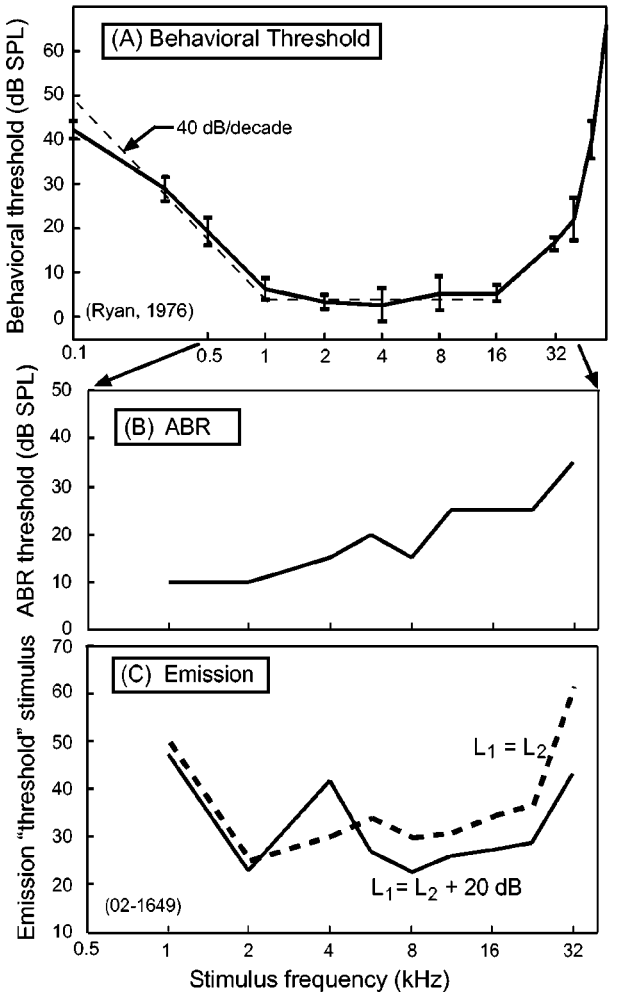

FIG. 7. Frequency-threshold functions for gerbil. (A) The top graph summarizes the normal adult behavioral threshold determined by Ryan (1974). Vertical bars are standard errors. Dashed lines indicate the simple middle-ear model discussed in the text. (B) ABR threshold response for an individual animal, same one as in Fig. 6. (C) Emission threshold measures for the same animal, for criterion emission amplitude equal to −10 dB SPL. Dashed line is for equal level, $L_1=L_2$, and the solid line is for unequal levels, with $L_1=L_2+20$ dB. For comparison between these choices, the mean stimulus amplitude $(L_1+L_2)/2$, is plotted on the vertical axis. No corrections for possible middle-ear effects were made to any of these threshold determinations. Note that the horizontal axes in (B) and (C) represent only a segment of the frequency span in (A), as noted by the arrows.

must tend to symmetry with respect to L_1 and L_2. Such a trend is clearly seen in the left columns in Fig. 2.

(ii) There are very frequently observed *notches* in the emission amplitude as a function of the stimulus parameters. As seen in Fig. 2, for example, there are "L_1 notches" representing a sharp decrease in the emission intensity as a function of L_1, occurring at a given L_1 across a large range in L_2. Note that the variation in the apparent sharpness of the notch between maps in Figs. 1–4 is not necessarily significant, because the apparent sharpness of the notch depends partly on the exact choice of stimulus levels relative to the actual location of the minimum in amplitude. (In this study, all data collection for contour maps and growth functions used a 5-dB spacing in both stimulus levels.) The *location* of the notch is potentially significant, however, and even more significant is the fact that in a given map there is essentially no variation in the L_1 notch location or shape as L_2 is varied. An example of this was shown in Fig. 1(C), and this conclusion has been verified by extensive examination of the raw data. Reflecting this, Fig. 2 shows that the contour maps fitted to the observed data always give purely "vertical" L_1 notches, or purely "horizontal" L_2 notches.

(iii) The L_1 notches usually disappear when the stimulus level L_2 becomes comparable to L_1. That is, L_1 notches are never found where $L_2 \gg L_1$. In addition to the L_1 notches noted in Fig. 2, there are also frequently found "L_2 notches." Some examples of these are indicated by horizontal arrows in Fig. 2. The L_2 notches have very similar characteristics to the L_1 notches, and all conclusions for L_1 notches apply to L_2 notches with indices interchanged. For example, L_2 notches are never found where $L_1 \gg L_2$. Notches are *never* found at orientations other than these two in stimulus level plots.

(iv) As the ratio f_2/f_1 decreases (given row in Fig. 2), both L_1 and L_2 notches typically are found to occur at smaller stimulus levels. This "movement" can result in a weakness in emissions in low stimulus level regions for small f_2/f_1. At $f_2=4$ and 16 kHz, for example, the low stimulus level emission almost vanishes as L_1 and L_2 notches appear to "converge" when f_2/f_1 becomes close to unity (Fig. 2, arrows, leftmost maps). This has obvious consequences for frequency ratio functions, discussed below. For moderate f_2/f_1, however, the notch movement seems typically gradual, with the notch stimulus levels typically increasing slowly with increasing f_2/f_1. Note that the L_1 notch for $f_2=1$ kHz (Fig. 2, top row) is found to be more consistent with those at other f_2 frequencies when middle ear effects are approximately accounted for [Fig. 4(B)].

(v) When a notch is observed in *any* emission amplitude representation, the emission phase angle is typically observed to have a jump or rapid change as the relevant parameter is moved through the notch region (Figs. 1, 5, and 6). The jump or total change in phase angle is often near 180°. The phase change is more obvious in growth function plots (Fig. 1) or indeed in any plots where stimulus frequencies are constant. This is evidently the case because in such a representation there are *no* phase angle changes added by the linear part of the system. No matter in what display the notches are observed, however, notches in amplitude appear to be associated with rapid phase changes. Clearly, no matter how the parameters are varied, a minimum in one map at a certain set of parameters is the *same* minimum found in any other map at the same set of parameters. However, the rapidity of the observed phase changes and the sharpness of the

notch depend on the specific cut taken, i.e., depend on the direction followed through the parameter space.

(vi) Consider typical displays where stimulus levels are fixed but frequencies are changed, such as frequency ratio functions (Fig. 5) and DPgrams (Fig. 6). Notches observed in these displays may be identified with *either* L_1 or L_2 notches as seen in contour maps. There is a simple rule to determine which is the most likely identification. For stimulus levels chosen so that $L_1 > L_2$, a notch observed in a frequency function will usually be associated with an L_1 notch in the contour map (e.g., ''vertical'' notches near the location of the open squares in Fig. 2 at some f_2 frequencies). If the stimulus levels are equal, $L_1 = L_2$, or unequal with $L_2 > L_1$, the phase cancellation observed in any frequency response will usually be identified with an L_2 notch in maps like Fig. 2 (e.g., ''horizontal'' notches near open circles in Figs. 2–4). This is simply because L_1 notches typically appear only in regions where $L_2 < L_1$, and L_2 notches are typically seen only in regions where $L_2 \geqslant L_1$, as illustrated in Figs. 2–4. Of course, because effective levels of stimuli at the inner ear depend on middle-ear transmission, relationships between levels becomes less certain as f_2/f_1 increases, particularly for frequencies over which the middle-ear transmission is changing rapidly. In such cases, the comparison should be made for stimulus levels referred to the stapes, as in the transformations in Figs. 3 and 4. In all cases, care is required in identifying notches found when using equal-level stimuli, as these potentially could be either L_1 or L_2 notches (Fig. 2).

(vii) In the DPgram [Fig. 6(B)], the notch seen near 4 kHz is very clearly associated with a deep L_1 notch seen in the 4-kHz contour map near the open square in Fig. 2. It is *not* due to an elevation of hearing threshold near 4 kHz in this animal. This conclusion is supported in general by behavioral thresholds in gerbil [Fig. 7(A)], and, in particular, by ABR thresholds measured in the same animal [Fig. 7(B)]. Note also that the phase angle changes in the DPgrams seen in Fig. 6, while compatible with 180° shifts at notches, appear more difficult to consistently interpret than those in the growth function displays.

(viii) In the growth functions, those for the unequal case, $L_1 = L_2 + 20$ dB, appear to be slightly stronger than those for the equal case, $L_1 = L_2$, at the same mean stimulus level, i.e., when compared using the values $(L_1 + L_2)/2$. That is, the emission ''threshold'' is relatively lower (Fig. 7), at least for frequencies at 8 kHz and above. The notable exception is near $f_2 = 4$ kHz, where the leftward shift (to lower L_1) of the L_1 notch makes the emission relatively weaker for the unequal case growth function. That is, this notch is located near the open square in the 4-kHz map in Fig. 2, and it shows up as an anomalous increase in emission threshold in the associated frequency threshold curve in another subject (Fig. 7). Obviously, this is the same L_1 notch that interferes with the DPgram at 60×40 dB SPL in the same subject (Fig. 6).

(ix) Both amplitude and phase as a function of frequency ratio are complicated by the presence of notches. For example, in the equal-level frequency ratio functions (Fig. 5) the two minima in the 2-kHz function (arrows) appear to be associated with an L_2 notch in the relevant maps which ''moves'' in and out of the location of the relevant stimulus point [Fig. 4(C), open circles]. Also, notches on the left side of the curves for f_2 of 4 to 32 kHz seem particularly important in determining the characteristic shape of the frequency ratio function. In addition, if the decrease in emission amplitude attributed to middle-ear effects is corrected for (thick lines in Fig. 5), there is little evidence that the frequency ratio function has a general ''bandpass'' effect. Put another way, except for the effects of notches and middle ear, the emission amplitude pattern is nearly independent of frequency ratio at moderate stimulus levels (Figs. 4 and 5). The remaining exception is a modest ''low-pass'' effect observed, i.e., there is a gradual decrease of emission amplitude with increasing frequency ratio. However, this decrease is only seen for f_2 frequencies above 8 kHz and only at relatively large f_2/f_1 ratios.

The notches noted in all representations in this study have been discussed at length, because it appears that their presence is responsible for many problems in the interpretation of emission data, as discussed below.

IV. INTERPRETATION

A. Middle-ear forward- and reverse-transfer functions

A simple model for forward transfer though the gerbil middle ear was derived from its known behavioral response [Fig. 7(A)]. It was further assumed that the reverse transfer function was similar to the forward. With these two assumptions, the contour maps observed (Fig. 2) were transformed into those which would have been observed if the middle ear were transparent (Fig. 4). It can be seen that the transformed maps for $f_2 = 1$ kHz [Fig. 4(B)] change much less with frequency ratio than did the originals [Figs. 2 and 4(A)].

Recently, Keefe (2002) has taken the opposite approach with growth function data for the human ear. Making the *assumption* that the emission pattern is frequency invariant, the shapes of forward- and reverse-transfer middle ear functions were derived by transforming observed growth functions. The shapes of the two transfer functions so derived were found to be similar.

Note that the approach taken by Keefe (2002) did not specifically utilize the idea that the notch location itself might be invariant. Suppose that it could, in fact, be shown that the location of the notches (in stimulus level space) depended primarily on the stimulus levels as measured at the stapes, at least when measured at a given frequency ratio, f_2/f_1. It has already been shown, of course, that the location of the notch is essentially independent of the stimulus level ratio, L_1/L_2, the implications of which are discussed further

below. Suppose further that the emission amplitude was shown to be similarly invariant when referred to the stapes, i.e., with stimulus levels constant also as referred to the stapes. In short, suppose that the emission pattern was relatively constant with a transparent middle ear, at least at a given frequency ratio, f_2/f_1. In this case, the shapes of both the middle-ear forward- and reverse-transfer functions can be estimated from the observed emission patterns.

To do this, the shape of the forward-transfer function is first determined by taking a particular set of growth functions. Assume, for simplicity, that the frequency ratio to be used is equal to a half octave, so that $f_2/f_1=1.41$. For each choice of f_2, hold L_2 constant and step L_1 in relatively short intervals (1–2.5 dB) to securely locate the L_1 notch level; call it L_{1N}. The values of L_2 chosen are relatively unimportant, but should be chosen high enough to give good emission amplitude (and adequate signal to noise) for L_1 values flanking the notch region, but still low enough that it is assured that the f_1 response remains dominant in this region. A satisfactory response would be similar to the growth functions shown in Fig. 1(C), except that somewhat shorter L_1 stimulus intervals would be preferred for increased accuracy. For this example, L_{1N} is about 70 dB SPL at the frequency of $f_1=6.25$ kHz. Similar growth functions would be measured for all f_2 at half-octave intervals, say, over the frequency range of interest. On the assumption that the notch level is invariant at the cochlea, the values of L_{1N} determined as a function of frequency f_1 give directly the shape of the forward-transfer function as a ''threshold function,'' $L_{1N}(f)$, in dB SPL.

Now, given the shape of the forward-transfer function, the set of stimulus levels that needs to be applied at the ear canal to give constant values referred *to the stapes* can be calculated. Such invariant levels are used to measure the shape of the reverse transfer function as follows. Suppose one wishes to consistently apply an L_1 that is 20 dB lower than the notch level at the stapes, for example, as this is a choice that makes sense from the emission maps (Figs. 2–4). The appropriate stimulus level to be applied in the ear canal at the frequency, f_1, is given directly by $L_1=[L_N(f_1)-20\ \text{dB}]$. Suppose one also wanted the simultaneously applied L_2 to be consistently 20 dB less than the f_1 signal, *both referred to the stapes*. The value to be applied in the ear canal is then $L_2=[L_N(f_2)-40]$. Note the frequency to be used in the forward-transfer function is f_2 in this case. Obviously, the reason for choosing half-octave steps in f_2 and for the frequency ratio, f_2/f_1, in this illustration is to make it simple to fill in the forward-transfer function so that it can be used for both f_1 and f_2 frequencies. The shape of the reverse-transfer function is then given directly by measuring the amplitude of the emission as the stimulus levels are appropriately varied with the applied frequencies. The relevant frequency of the reverse function would be, of course, the emission frequency at $2f_1-f_2=0.41f_2$.

Of course, using notches is possible only if measurable notches can be found in the subject's emission pattern [as in Fig. 1(C)]. If not, the method of Keefe (2002) might be attempted, where the overall shapes of the emission amplitude function would be matched. However, finding and using L_1 notches is potentially more accurate, precisely because the location of the L_1 notch does not depend on the stimulus level L_2, eliminating one source of variability.

B. Interpretation of notches

Notches in the emission amplitude are found throughout the parameter space. Their characteristics are clearest in the contour maps of Figs. 1–4, because in each map, the stimulus frequencies are fixed. Uniformly, in this representation notches appear to occur in a line which either runs horizontally (along constant L_2) or vertically (along constant L_1). Uniformly, there are associated jumps in the emission phase of about 180 deg when a sharp notch is traversed at right angles to the minimum line. It has long been argued that characteristics of the notch suggest that ''phase cancellation'' is responsible (Brown, 1987). It has further been shown that the detailed relationship of notch depth and phase change can be explained by a simple model of phase cancellation (Mills and Rubel, 1994). In this model, the total emission is assumed to be the sum of two different ''components'' which have an intrinsic phase difference, and the relative amplitudes of the two components are assumed to vary differentially as a function of stimulus parameters. If the phase difference between the two components is exactly 180°, the sum of the two components will be zero at those parameter values where the two have the same amplitude. On each side of such a minimum, the observed phase in the total emission will be that of the component which has the largest amplitude on that side. For phase differences near 180°, in other words, there will be a very deep minimum (measured in dB), and across the minimum there will be an abrupt jump in phase of 180° in the total emission. For smaller differences in phase, of course, the minimum will be less deep and the phase change more gradual. Such a phase cancellation model accounts well for the detailed variation observed with different intrinsic phase differences (Mills and Rubel, 1994; Mills, 1997, 1998).

Phase cancellation agrees so well with observations that it is the generally accepted explanation. However, phase cancellation by itself does not explain why there should be only two *orientations* of notches observed in the maps of Figs. 2–4. That is, there are only observed notches along lines with L_1 constant or L_2 constant, and no notches at any other orientation and no notches for which the orientation changes continuously across the contour map, i.e., no notches which curve in stimulus level space (except for the trivial case where there is a right angle or sharp turn where L_1 and L_2 notches ''intersect''). The L_1 notches, occurring along lines of constant L_1, typically occur only in regions where $L_1>L_2$. The L_2 notches usually occur only in regions where $L_2>L_1$. To understand this peculiar behavior requires understanding these specific characteristics in terms of cochlear mechanics.

Consider only L_1 or ''vertical'' notches as seen in Fig. 2; arguments for the other orientation follow by interchanging indices. The ''vertical'' extension of these notches demonstrates that the behavior occurs for a given L_1 independent of L_2, as long as $L_1>L_2$. That is, the notch must essentially depend on the behavior of the cochlear response to the fre-

quency f_1 *independent* of its response to f_2, for stimulus conditions where the f_1 wave is dominant. The notch behavior, in other words, must actually follow from a consideration of the *change* in characteristics with stimulus level *for the response to a single tone*. Note that this important conclusion follows logically from the observations (Fig. 2) without dependence on any particular model of the cochlea.

Of course, as is well known from basilar-membrane measurements (e.g., Sellick *et al.*, 1982; Ruggero and Rich, 1991), there *is* a pronounced change in the shape of the basilar-membrane amplitude response as the stimulus level changes. The response to a single tone at low stimulus levels is sharply peaked, and at high stimulus levels is much broader. The reason for the change of shape is attributed to saturation of the cochlear amplifier. Further, it seems reasonable to assume that, even if there were two frequencies present in the stimulus, the change of shape of the dominant traveling wave should occur at approximately the same stimulus level of the *dominant* wave. It is exactly this kind of change, a change in the response to a single tone that occurs with stimulus level only (with frequency fixed) that the emission observations demand.

However, an additional assumption is required to explain the origin of a notch in the *emission* pattern. This assumption is that, associated with the change in shape of the traveling wave, there is a change in a *relevant* phase angle. Such a phase angle change may occur only in one part of the overall region which produces the emission, of course. There might be, for example, a difference in the phase of the outer hair cell response in regions where the cochlear amplifier is not saturated, compared to regions where it is. The phase of the outer hair cell transduction channel response would be the relevant phase assuming the outer hair cells predominantly generate the emission. Because it involves saturation of the dominant wave, such a phase transition is likely to be robust. That is, the change should occur at about the same stimulus level in the presence of another stimulus at a different frequency, provided the second stimulus remains relatively weak. The observed notch behavior then follows.

The presence of the two orientations of notches, and only these two, was noted earlier as an emergent property of a simple model of the cochlear amplifier [see Fig. 5(A) in Mills, 1997]. This model assumes that all the emission from the cochlea arises from a single mechanism, but that when summed, emissions from slightly different parts of the emission-generating region of the cochlea can have different phase angles. The model includes the effects of saturation of the cochlear amplifier in determining the shapes of both traveling waves and their interaction with each other, i.e., two-tone suppression. As long as the f_2 wave is relatively weak, the f_1 wave will have a sharp peak at low L_1 stimulus levels and most of the emission will come from the rising side of the sharp peak (Mills, 1997). The sharp peak occurs precisely because, at this stimulus level, the cochlear amplifier does not become fully saturated. At high L_1 stimulus levels, in contrast, most of the emission will come from a broadened f_1 peak. All or most of the broadened peak will have a different phase angle than the sharp peak; the peak is broad, after all, precisely because at this stimulus level the cochlear amplifier is saturated over most of the response. As long as the f_2 wave is relatively weak compared to the f_1 wave, the change in f_1 wave characteristics will occur at *the same* L_1 *level*. Therefore, the notch, if one occurs, will occur at the same L_1 level for all L_2 levels and hence will be "vertical." Of course, the notch will be sharpest if the difference in angle at the place of summation turns out to be about 180°, and will be weaker otherwise. When the levels are of the opposite strength, i.e., when $L_2 > L_1$, all the same arguments apply but with an interchange of indices. Any notches must be L_2 notches in this case.

C. Interpretation of frequency ratio functions

The discovery of the amplitude response of the frequency ratio function has been the subject of considerable study and controversy. The behavior which drew most attention was that it appeared that there was typically a decrease observed in the amplitude of the frequency ratio function as the two frequencies become close. A decrease was found to occur for all orders of the odd, lower frequency distortion products (e.g., $2f_1-f_2$, $3f_1-2f_2$, etc). Strikingly, the decrease was found to occur as a function of the individual emission frequencies, not of the frequency ratio. Further, it was noted that the same decrease did not occur in distortion tones detected psychoacoustically. It was suggested that the decrease was due to the effect of a "second filter," e.g., in the micromechanics of the outer hair cell–tectorial membrane subsystem (Brown and Gaskill, 1990a; Allen and Fahey, 1993).

However, this interpretation is not well supported by the complete parametric response. First, note that for f_2 frequencies of 1 and 2 kHz, there is *no* observed decrease in emission amplitude at *any* stimulus levels as $f_2/f_1 \rightarrow 1$ (Fig. 2). For higher f_2 frequencies, there *is* an observed decrease in emission amplitude as $f_2/f_1 \rightarrow 1$, but only at lower stimulus levels. In all cases, however, the observed decrease appears to be associated with notches which have "moved" into this stimulus parameter region. At $f_2 = 4$ kHz, for example, phase angle responses (jumps indicated by arrows in Fig. 2) confirm that the L_1 and L_2 notches have "converged." This convergence appears to lead to a remarkably weak distribution in the low stimulus level region at the lowest frequency ratio ($f_2/f_1 = 1.06$) used for contour maps. However, the supplemental measurements for very small f_2/f_1 ratios (Fig. 5) suggest that, once this ratio is traversed, the emission amplitude recovers again. That is, even for low stimulus levels the decrease seen at low f_2/f_1 is only temporary; and recovers as $f_2/f_1 \rightarrow 1$. Further, the maps in Fig. 2 demonstrate that at high stimulus levels in *either* L_1 or L_2 (along the right side or top of the contour maps) there is no general decrease in emission amplitude as $f_2/f_1 \rightarrow 1$ for any f_2 frequency.

For Mongolian gerbil, therefore, it can be concluded that there is generally no decrease of emission amplitude with decreasing stimulus frequency ratio, as $f_2/f_1 \rightarrow 1$. When there appears to be, the decrease is actually associated with the existence of a notch, or phase cancellation, over a small region of parameter space. These results in gerbil agree with recent parametric studies in guinea pig by Lukashkin and Russell (2001), who also summarize evidence that a similar

explanation may apply to observed human responses. It appears that this is likely to be a general result: The observed decrease of emission amplitude as the frequency ratio tends to unity is generally due to the presence of a notch at the relevant parameters. As evidence of this, Lukashkin and Russell (2001) note that when the frequency ratio moves even closer to 1, the emission amplitude typically increases again (as in Fig. 5).

The presence of the phase cancellation is also associated with ''nonlinearities'' in the phase gradient (Fig. 5, vertical bars). Such rapid phase changes are often observed but usually avoided or ignored by those seeking to measure phase gradients.

Finally, the distributions shown in Figs. 2–5 also weaken the case for a general roll-off of emission amplitude with *increasing* frequency ratio, f_2/f_1. At least for f_2 frequencies from 1 to 4 kHz, the observed roll-off essentially disappears when putative middle-ear effects are included (Fig. 4; bold lines, Fig. 5). That is, the typically observed roll-off at low frequencies with high f_2/f_1 appears to be largely due, not to an increased separation of the two traveling wave patterns on the basilar membrane, but to the increased difficulty of the emission getting out through the middle ear as its frequency decreases. Note that this kind of frequency roll-off depends on the emission frequency itself, not the stimulus frequency ratio. Middle-ear effects therefore would cause the same roll-off in all orders of the emission in accordance with the frequency of the emission component, not the frequency ratio. This agrees with the observations.

Recent studies of frequency ratio functions in gerbils detailed complex responses as a function of stimulus level and f_2 frequency (Faulstich and Kössl, 2000). Changes in phase gradient patterns at low compared to high f_2 frequencies were attributed to the existence of multiple DPOAE sources, possibly associated with intrinsic changes in cochlear mechanics at frequencies below 2 kHz. However, only stimulus levels with $L_1=L_2+10$ dB were considered. Further, the results reported were completely consistent with ''components'' separated by notches as identified here. One can, of course, get the impression of multiple sources through looking at measurements at specific $L_1\times L_2$ (Fig. 5). However, if one looks at the emission response over the entire parametric space (Figs. 2–4), one concludes that there are no important differences in emission characteristics as a function of stimulus levels across f_2 frequency, at least not from 1 to 4 kHz. This is especially true if probable middle-ear effects are included (Figs. 4 and 5). Note also that only the emission *amplitudes* have been ''corrected'' for middle-ear effects in the frequency response functions (Fig. 5). Assuming the rise in auditory threshold below 1 kHz [Fig. 7(A)] is due to middle-ear changes, there would also be additional phase changes caused by middle-ear transmission which contribute to measured phase gradients at all emission frequencies below 1 kHz. Addition of such a shift could contribute to the appearance of a change in phase gradients at low frequencies.

D. Interpretation of growth functions

Growth functions have been widely used, e.g., for detailed investigation of cochlear function across frequency in comparative studies (e.g., Brown, 1987; Kössl, 1992; Manley *et al.*, 1993; Mills and Shepherd, 2001), as well as studies of the effects of ototoxic insult (e.g., Brown *et al.*, 1989; Mills *et al.*, 1993). Typically, the investigator makes a choice of stimulus frequency ratio f_2/f_1 somewhere between 1.2 and 1.3, and chooses a rule for the stimulus level relationship. Many early studies used the $L_1=L_2$ rule by default or for simplicity, but later studies have more often used unequal ratios, in particular, $L_1=L_2+10$ dB. Overall, there are a bewildering number of studies with different parameter choices, and of studies employing different methods and experimental manipulations with the goal of making a rational choice among parameters to be used.

It is not the intention of this study to attempt to completely resolve the many important issues raised. Rather, this study proposes only to use the complete parametric response to refine the interpretation of the typical growth function response.

First, consider the interpretation of typical growth functions as seen in Figs. 1(E) and (F). The general shape of these functions has led to the suggestion that the total emission was a sum of two different components, one predominant at low stimulus levels and the other component at high stimulus levels. The differing vulnerability of these two components to certain manipulations led to the suggestion that there could be different *mechanisms* of generation in the cochlea, e.g., ''active'' and ''passive'' mechanisms (Rosowski *et al.*, 1984; Brown, 1987; Johnstone *et al.*, 1990; Norton and Rubel, 1990; Whitehead *et al.*, 1990, 1992a, b; Mills and Rubel, 1994).

There are a number of emerging reasons for arguing that there is probably only one mechanism that is producing the DPOAE emission, at least in mammals under most conditions. First, the appearance of different components, including different phase gradients, does not necessarily imply that there are two different mechanisms, as noted above. Rather, there could be only one mechanism but emissions could arise from ''different places'' along the organ of Corti (Lonsbury-Martin *et al.*, 1987; Mills, 1997). Further, the extremely consistent relationship between the two components, such as demonstrated in Figs. 2–4, argues that only one mechanism must be at work. That is, if there really were two completely different mechanisms, why is the relationship between them observed to be so consistent? If the emission arose from different processes one would expect that, between subjects, the active mechanism would be relatively stronger or weaker than the passive, so that, for example, the notch location would vary among subjects much more than it does.

Finally, if the observed characteristics can be shown to result from a single mechanism, parsimony suggests that it is the more useful explanation. In the simple model discussed above (Mills, 1997, 1998), for example, the emission was assumed to arise from only one mechanism. The impression of two components arises solely because the emissions generated in *slightly* different cochlear regions have different phase angles when summed. The basic unity of the emissions

at all stimulus levels can also be demonstrated by their graded vulnerability to acoustic insult (e.g., Mom *et al.*, 2001).

One other complication should be discussed. This involves DPOAE models or cochleae which also include ''reflection'' effects. Reflection models consider the possibility that, in addition to the normal backward-propagating emission, waves at the distortion frequency also propagate apically from the generation site, are amplified and then can ''reflect'' at their cochlear place. The reflected wave subsequently combines with the usual backward-propagated emission (Stover *et al.*, 1999; Shera and Guinan, 1999; Talmadge *et al.*, 1999; Konrad-Martin *et al.*, 2001). This combination can also create level-dependent notches depending on the phase relationship between the two waves. However, this complication is not important in the gerbil. The gerbil two-tone emission amplitude is insensitive to a third tone added near the emission frequency (Mills, 2000). In any case, even in the reflection model, there is only one mechanism and one region posited for the actual DPOAE *generation*.

From the point of view of the complete parametric response, the impression of two different components in typical growth functions is a simple consequence of the presence of a region of phase cancellation in the summed emission. If the line through stimulus space taken for the growth function passes across a region of phase cancellation, it will result in a growth function with a relative minimum. Otherwise, it will not (Fig. 1).

It is apparent that DPOAEs would be a more consistent and useful measure if it were possible to account for the presence of such notches in measurements, while still using necessarily limited parameter sets. For example, notches observed due to *reflection* at the emission frequency place can be eliminated by adding a suppressor tone at a frequency just above the emission frequency (Heitmann *et al.*, 1998). However, reflection notches are of different origin than the ones in Fig. 2, which appear to be due to components *intrinsic* to the generation process and much more intimately tied together. As noted above, the appearance of two components, and of the notch, is actually tied to a change in the behavior of the *response to a single tone* as a function of stimulus level. This conclusion suggests that it is probably impossible to suppress these notches by adding a third, weak tone, though this should be verified experimentally. The observations (Fig. 2) suggest that it is also impossible to avoid such notches in general by simply changing the frequency ratio. An examination of the complete parametric response (Fig. 2) suggests that it *might* be possible in a specific animal to choose a line which avoids a sharp decrease, and which still went through regions of high emission amplitude. However, this would require knowing in advance the complete emission pattern from the animal!

It appears impossible to set up a rule or procedure which completely avoids the effects of notches in the emission pattern. Rather, it seems preferable to plan measurements so that these notches can be securely identified when they occur, and to improve interpretations of emission measurements by taking their presence, nature, and meaning into account.

ACKNOWLEDGMENTS

Thanks to Brandon Warren for equipment and computational support, to Natalie Hardie and Rob Shepherd for ABR tutelage, and to Ed Rubel for useful discussions. Support for this research was provided by Grants DC 04077 and DC 04661 from the National Institute for Deafness and Other Communication Disorders, National Institutes of Health.

Allen, J. B., and Fahey, P. F. (**1993**). ''A second cochlear-frequency map that correlates distortion product and neural tuning measurements,'' J. Acoust. Soc. Am. **94**, 809–816.

Brown, A. M. (**1987**). ''Acoustic distortion from rodent ears: A comparison of responses from rats, guinea pigs, and gerbils,'' Hear. Res. **31**, 25–38.

Brown, A. M., and Gaskill, S. A. (**1990a**). ''Can basilar membrane tuning be inferred from distortion measurement?'' in *The Mechanics and Biophysics of Hearing: Proceedings of a Conference held at the University of Wisconsin, Madison, WI, 25–29 June 1990*, edited by P. Dallos, C. D. Geisler, J. W. Mathews, M. A. Ruggero, and C. R. Steele (Springer, New York), pp. 164–169.

Brown, A. M., and Gaskill, S. A. (**1990b**). ''Measurement of acoustic distortion reveals underlying similarities between human and rodent mechanical responses,'' J. Acoust. Soc. Am. **88**, 840–849.

Brown, A. M., McDowell, B., and Forge, A. (**1989**). ''Acoustic distortion products can be used to monitor the effects of chronic gentamicin treatment,'' Hear. Res. **42**, 143–156.

Fahey, P. F., and Allen, J. B. (**1986**). ''Characterization of the cubic intermodulation distortion products in the cat external auditory meatus,'' in *Peripheral Auditory Mechanisms: Proceedings of a Conference held at Boston University, Boston, MA, 13–16 August 1985*, edited by J. B. Allen, J. L. Hall, A. Hubbard, S. T. Neely, and A. Tubis (Springer, New York), pp. 314–321.

Faulstich, M., and Kössl, M. (**2000**). ''Evidence for multiple DPOAE components based upon group delay of the 2 f_1-f_2 distortion in the gerbil,'' Hear. Res. **140**, 99–110.

Faulstich, M., Kössl, M., and Reimer, K. (**1996**). ''Analysis of nonlinear cochlear mechanics in the marsupial *Monodelphis domestica:* Ancestral and modern mammalian features,'' Hear. Res. **94**, 47–53.

Gaskill, S. A., and Brown, A. M. (**1990**). ''The behavior of the acoustic distortion product, 2 f_1-f_2, from the human ear and its relation to auditory sensitivity,'' J. Acoust. Soc. Am. **88**, 821–839.

Hauser, R., and Probst, R. (**1991**). ''The influence of systemic primary-tone level variation L_2-L_1 on the acoustic distortion product emission 2 f_1-f_2 in normal human ears,'' J. Acoust. Soc. Am. **89**, 280–286.

Heitmann, J., Waldmann, B., Schnitzler, H.-U., Plinkert, P. K., and Zenner, H.-P. (**1998**). ''Suppression of distortion product otoacoustic emissions (DPOAE) near 2 f_1-f_2 removes DP-gram fine structure—Evidence for a secondary generator,'' J. Acoust. Soc. Am. **103**, 1527–1531.

Johnstone, B. M., Gleich, B., Mavadat, N., McAlpine, D., and Kapadia, S. (**1990**). ''Some properties of the cubic distortion tone emission in the guinea pig,'' Adv. Audiology **7**, 57–62.

Keefe, D. H. (**2002**). ''Spectral shapes of forward and reverse transfer functions between ear canal and cochlea estimated using DPOAE input/output functions,'' J. Acoust. Soc. Am. **111**, 249–260.

Kimberley, B. P., Brown, D. K., and Eggermont, J. J. (**1993**). ''Measuring human cochlear traveling wave delay using distortion product emission phase responses,'' J. Acoust. Soc. Am. **94**, 1343–1350.

Konrad-Martin, D., Neely, S. T., Keefe, D. H., Dorn, P. A., and Gorga, M. P. (**2001**). ''Sources of distortion product otoacoustic emissions revealed by suppression experiments and inverse fast Fourier transforms in normal ears,'' J. Acoust. Soc. Am. **109**, 2862–2879.

Kössl, M. (**1992**). ''High frequency distortion products from the ears of two bat species, *Magaderma lyra* and *Corollia perspicillata*,'' Hear. Res. **60**, 156–164.

Kummer, P., Janssen, T., and Arnold, W. (**1998**). ''The level and growth behavior of the 2 f_1-f_2 distortion product otoacoustic emission and its relationship to auditory sensitivity in normal hearing and cochlear hearing loss,'' J. Acoust. Soc. Am. **103**, 3431–3444.

Lonsbury-Martin, B. L., Harris, F. P., Stagner, B. B., Hawkins, M. D., and Martin, G. K. (**1990**). ''Distortion product emissions in humans. I. Basic properties in normally hearing subjects,'' Ann. Otol. Rhinol. Laryngol. Suppl. **99**, 3–14.

Lonsbury-Martin, B. L., Martin, G. K., Probst, R., and Coats, A. C. (**1987**). ''Acoustic distortion products in rabbit ear canal. I. Basic features and physiological vulnerability,'' Hear. Res. **28**, 173–189.

Lukashkin, A. N., and Russell, I. J. (**2001**). ''Origin of the bell-like dependence of the DPOAE amplitude on primary frequency ratio,'' J. Acoust. Soc. Am. **110**, 3097–3106.

Manley, G. A., Köppl, C., and Johnstone, B. M. (**1993**). ''Distortion-product otoacoustic emissions in the bobtail lizard I. General characteristics,'' J. Acoust. Soc. Am. **93**, 2820–2833.

Mills, D. M. (**1997**). ''Interpretation of distortion product otoacoustic emission measurements. I. Two stimulus tones,'' J. Acoust. Soc. Am. **102**, 413–429.

Mills, D. M. (**1998**). ''Origin and implications of two components in distortion product otoacoustic emissions'' in *Otoacoustic Emissions: Basic Science and Clinical Applications*, edited by C. I. Berlin (Singular, San Diego), pp. 85–104.

Mills, D. M. (**2000**). ''Frequency responses of two- and three-tone distortion product otoacoustic emissions in Mongolian gerbil,'' J. Acoust. Soc. Am. **107**, 2586–2602.

Mills, D. M., Norton, S. J., and Rubel, E. W. (**1993**). ''Vulnerability and adaptation of distortion product otoacoustic emissions to endocochlear potential variation,'' J. Acoust. Soc. Am. **94**, 2108–2122.

Mills, D. M., and Rubel, E. W. (**1994**). ''Variation of distortion product otoacoustic emissions with furosemide injection,'' Hear. Res. **77**, 183–199.

Mills, D. M., and Rubel, E. W. (**1996**). ''Development of the cochlear amplifier,'' J. Acoust. Soc. Am. **100**, 428–441.

Mills, D. M., and Shepherd, R. K. (**2001**). ''Distortion product otoacoustic emission and auditory brainstem responses in the echidna (*Tachyglossus aculeatus*),'' JARO **2**, 130–146.

Mom, T., Bonfils, P., Gilain, L., and Avan, P. (**2001**). ''Origin of cubic difference tones generated by high-intensity stimuli: Effect of ischemia and auditory fatigue on the gerbil cochlea,'' J. Acoust. Soc. Am. **110**, 1477–1488.

Norton, S. J., and Rubel, E. W. (**1990**). ''Active and passive ADP components in mammalian and avian ears,'' in *The Mechanics and Biophysics of Hearing: Proceedings of a Conference held at the University of Wisconsin, Madison, WI, 25–29 June 1990*, edited by P. Dallos, C. D. Geisler, J. W. Mathews, M. A. Ruggero, and C. R. Steele (Springer, New York), pp. 219–227.

Rosowski, J. J., Peake, W. T., and White, J. R. (**1984**). ''Cochlear nonlinearities inferred from two-tone distortion products in the ear canal of the alligator lizard,'' Hear. Res. **13**, 141–158.

Ruggero, M. A., and Rich, N. C. (**1991**). ''Furosemide alters organ of Corti mechanics: Evidence for feedback of outer hair cells upon the basilar membrane,'' J. Neurosci. **11**, 1057–1067.

Ryan, A., (1976) ''Hearing sensitivity of the mongolian gerbil, *Meriones unguiculatis,*'' *J. Acoust. Soc. Am.* **59**, 1222–1226.

Sellick, P. M., Patuzzi, R., and Johnstone, B. M. (**1982**). ''Measurement of basilar membrane motion in the guinea pig using the Mossbauer technique,'' J. Acoust. Soc. Am. **72**, 131–141.

Shera, C. A., and Guinan, J. J. (**1999**). ''Evoked otoacoustic emissions arise by two fundamentally different mechanisms: A taxonomy for mammalian OAEs,'' J. Acoust. Soc. Am. **105**, 782–798.

Shera, C. A., Talmadge, C. L., and Tubis, A. (**2000**). ''Interrelations among distortion-product phase-gradient delays: Their connection to scaling symmetry and its breaking,'' J. Acoust. Soc. Am. **108**, 2933–2948.

Shi, Y.-B., and Martin, W. H. (**1997**). ''ABR and DPOAE detection of cochlear damage by gentamicin,'' J. Basic Clin. Physiol. Pharmacol. **8**, 141–155.

Stover, L. J., Neely, S. T., and Gorga, M. P. (**1999**). ''Cochlear generation of intermodulation distortion revealed by DPOAE frequency functions in normal and impaired ears,'' J. Acoust. Soc. Am. **106**, 2669–2678.

Sutton, L. A., Lonsbury-Martin, B. L., Martin, G. K., and Whitehead, M. L. (**1994**). ''Sensitivity of distortion-product otoacoustic emissions in humans to tonal over-exposure: Time course of recovery and effects of lowering L_2,'' Hear. Res. **75**, 161–174.

Talmadge, C. L., Long, G. R., Tubis, A., and Dhar, S. (**1999**). ''Experimental confirmation of the two-source interference model for the fine structure of distortion product otoacoustic emissions,'' J. Acoust. Soc. Am. **105**, 275–292.

Taschenberger, G., Gallo, L., and Manley, G. A. (**1995**). ''Filtering of distortion-product otoacoustic emissions in the inner ear of birds and lizards,'' Hear. Res. **91**, 87–92.

Tubis, A., Talmadge, C. L., Tong, C., and Dhar, S. (**2000**). ''On the relationships between the fixed-f_1, fixed f_2, and fixed ratio phase derivatives of the 2 f_1-f_2 distortion product otoacoustic emission,'' J. Acoust. Soc. Am. **108**, 1772–1785.

Whitehead, M. L., Lonsbury-Martin, B. L., and Martin, G. K. (**1990**). ''Actively and passively generated acoustic distortion at 2 f_1-f_2 in rabbits,'' in *The Mechanics and Biophysics of Hearing: Proceedings of a Conference held at the University of Wisconsin, Madison, WI, 25–29 June 1990*, edited by P. Dallos, C. D. Geisler, J. W. Mathews, M. A. Ruggero, and C. R. Steele (Springer, New York), pp. 243–250.

Whitehead, M. L., Lonsbury-Martin, B. L., and Martin, G. K. (**1992a**). ''Evidence for two discrete sources of 2 f_1-f_2 distortion-product otoacoustic emission in rabbit. I. Differential dependence on stimulus parameters,'' J. Acoust. Soc. Am. **91**, 1587–1607.

Whitehead, M. L., Lonsbury-Martin, B. L., and Martin, G. K. (**1992b**). ''Evidence for two discrete sources of 2 f_1-f_2 distortion product otoacoustic emission in rabbit. II. Differential physiological vulnerability,'' J. Acoust. Soc. Am. **92**, 2662–2682.

Whitehead, M. L., McCoy, M. J., Lonsbury-Martin, B. L., and Martin, G. K. (**1995a**). ''Dependence of distortion-product otoacoustic emissions on primary levels in normal and impaired ears. I. Effects of decreasing L_2 below L_1,'' J. Acoust. Soc. Am. **97**, 2346–2358.

Whitehead, M. L., Stagner, B. B., McCoy, M. J., Lonsbury-Martin, B. L., and Martin, G. K. (**1995b**). ''Dependence of distortion-product otoacoustic emissions on primary levels in normal and impaired ears. II. Asymmetry in L_1, L_2 space,'' J. Acoust. Soc. Am. **97**, 2359–2377.

Wiederhold, M. L., Mahoney, J. W., and Kellog, D. L. (**1986**). ''Acoustic overstimulation reduces 2 f_1-f_2 cochlear emissions at all levels in the cat,'' in *Peripheral Auditory Mechanisms: Proceedings of a Conference held at Boston University, Boston, MA, 13–16 August 1985*, edited by J. B. Allen, J. L. Hall, A. Hubbard, S. T. Neely, and A. Tubis (Springer, New York), pp. 322–329.

Modifications of a single saturating non-linearity account for post-onset changes in $2f_1-f_2$ distortion product otoacoustic emission

Andrei N. Lukashkin[a] and Ian J. Russell
School of Biological Sciences, University of Sussex, Falmer, Brighton BN1 9QG, United Kingdom

(Received 6 March 2002; revised 26 June 2002; accepted 30 June 2002)

$2f_1-f_2$ distortion product otoacoustic emissions (DPOAEs) were recorded from guinea pigs. DPOAEs showed complex time dependence at the onset of stimulation. The DPOAE, measured during the first 500 ms, can either decrease or increase at the onset depending on both the frequencies and levels of the primary tones. These changes are closely associated with amplitude minima (notches) of the DPOAE I/O functions. These notches are characteristic of DPOAE growth functions measured from guinea pigs for primary tones of 50–60-dB sound-pressure level (SPL). Apparent changes in the DPOAE amplitude occur because the notch shifts to higher levels of the primaries during the onset of stimulation. This shift of the notch to higher levels increases for lower f_2/f_1 ratios but does not exceed about 2 dB. DPOAE amplitude increases for a constant level of the primaries if the onset emission is situated at the low-level, falling slope of the notch. If the onset DPOAE is located on the high-level, rising slope of the notch, then the upward shift of the notch causes the emission either to decrease monotonically, or to decrease initially and then increase. By establishing that the $2f_1-f_2$ onset changes reflect a shift in the growth-function notch, it is possible to predict the temporal behavior of DPOAEs in the two-dimensional space of the amplitude of the primaries and for their different frequency ratios.
[DOI: 10.1121/1.1502903]

PACS numbers: 43.64.Jb, 43.64.Bt, 43.64.Kc [BLM]

I. INTRODUCTION

DPOAEs recorded from the ears of mammals depend in a complex way on the levels and frequencies of the primary tones and vary with time during prolonged stimulation. Studies by Brown (1988), Whitehead *et al.* (1991), Kirk and Johnstone (1993), Kujawa *et al.* (1995), and Lowe and Robertson (1995), all reported time-dependent changes in the magnitude of the f_2-f_1 component of the DPOAE. These changes occur over a period of several minutes from the onset of delivering the primary stimulus tones (f_1 and f_2) to the ipsilateral ear. However, similar time-dependent changes were not detected in the magnitude of the $2f_1-f_2$ component (but see Puel and Rebillard, 1990). More recently, Liberman *et al.* (1996) reported changes in the $2f_1-f_2$ component on a much shorter time scale of a few hundred milliseconds following the onset of stimulation. Liberman *et al.* (1996) noted that the time constant of these relatively fast onset changes is similar to the time constant of efferent mediated effects recorded at different levels of the auditory system (Desmedt, 1962; Fex, 1967; Wiederhold and Kiang, 1970; Gifford and Guinan, 1987; Warren and Liberman, 1989). These relatively fast post-onset changes in the DPOAE are considerably reduced following section of the olivocochlear nerve bundle (OCB) (Liberman *et al.*, 1996; Kujawa and Liberman, 2001). An intriguing feature of the post-onset changes is their bidirectionality. The DPOAE amplitude can either decrease or increase after the onset depending on both the frequencies and intensities of the primary tones. Kim *et al.* (2001) has also reported biphasic post-onset changes, when a rapid reduction in DPOAE amplitude is followed by DPOAE growth. The post-onset changes in DPOAE have been observed for a relatively narrow range of stimulus parameters. Kujawa and Liberman (2001) reported that these changes are closely associated with amplitude minima (notches) routinely observed at the DPOAE I/O functions. They speculated that the OCB activation affected interaction between the multiple components of the DPOAE, which produced an amplitude notch due to phase cancellation between them. However, local notches in the growth functions of the distortion component can be observed at the output of a single saturating nonlinearity (Weiss and Leong, 1985; Lukashkin and Russell, 1998, 1999). This genesis of the notch explains the specific DPOAE behavior seen for various experimental procedures (Fahey *et al.*, 2000; Lukashkin and Russell, 2001; Lukashkin *et al.*, 2002).

In the current study we investigate the origin of the post-onset changes of the $2f_1-f_2$ DPOAE frequency component. We show that the post-onset DPOAE changes reflect an upward shift of the notch in their growth function to higher levels of the primaries during prolonged stimulation. If the level of the generated emission was far from the notch in the DPOAE growth function, then time-dependent, post-onset changes in the DPOAE were not observed during a stimulus of 512 ms in duration. On the basis of this, we were able to unambiguously predict the DPOAE temporal behavior in the two-dimensional space of the levels of the two primaries, and for their different frequency ratios. The predictions are based upon a hypothesis that the notch in the

[a]Electronic mail: a.lukashkin@sussex.ac.uk

DPOAE growth functions arises due to nonmonotonic behavior of distortion components at the output of a single saturating nonlinearity (Weiss and Leong, 1985; Lukashkin and Russell, 1998, 1999). We suggest that temporal changes in the DPOAE are likely to reflect time-dependent changes in the mechanical input to the outer hair cells (OHCs), possibly as a consequence of mechanical changes in the OHCs themselves.

II. METHODS

Pigmented guinea pigs (250–350 g) were anesthesized with the neurolept anesthetic technique (0.06 mg/kg body weight atropine sulphate s.c., 30 mg/kg pentobarbitone i.p., 250 μl/kg Hypnorm i.m.). Additional injections of Hypnorm were given every 40 min. Additional doses of pentobarbitone were administered as needed to maintain a nonreflexive state. The heart rate was monitored with a pair of skin electrodes placed on both sides of the thorax. The animals were tracheotomized and artificially respired, and their core temperature was maintained at 38 °C with a heating blanket and head holder. The middle-ear cavity of the ear used for the DPOAE measurements was open to equilibrate air pressure on the both sides of the tympanic membrane (Zheng *et al.*, 1997). Strychnine in concentration 1 mg/kg b.w. was injected intravenously. Skin above a vein used for injection was dissected and strychnine was injected under visual control to insure successful infusion. Measurements of the DPOAE growth functions were begun within 5 min of the injection and lasted for a further 25 min. Pilot experiments (Lukashkin and Russell, unpublished data, 2002) showed that strychnine in the concentrations 1 mg/kg b.w. completely blocked the suppressive effect of electrical stimulation of the medial olivocochlear (MOC) efferents on the auditory nerve's compound action potential in guinea pigs during the 25 min it took to collect the data.

Sound was delivered to the tympanic membrane by a closed acoustic system comprising two Bruel & Kjaer 4134 $\frac{1}{2}$-in. microphones for delivering tones and a single Bruel & Kjaer 4133 $\frac{1}{2}$-in. microphone for monitoring sound pressure at the tympanum. The microphones were coupled to the ear canal via 1-cm-long, 4-mm diameter tubes to a conical speculum, the 1-mm-diameter opening of which was placed about 1 mm from the tympanum. The closed sound system was calibrated *in situ* for frequencies between 1 and 50 kHz. Known sound-pressure levels were expressed in dB SPL *re*: 2×10^{-5} Pa. White noise for acoustical calibration and tone sequences for auditory stimulation were synthesised by a Data Translation 3010 board and delivered to the microphones through low-pass filters (100-kHz cutoff frequency). Signals from the measuring amplifier were digitized using the same board and averaged in the time domain. The maximum level of the system distortion measured with an artificial ear cavity for the highest levels of primaries used in this study ($L_1=L_2+10$ dB$=75$ dB SPL) was 70 dB below the primary level. Experimental control, data acquisition, and data analysis were performed using a PC with programs written in TESTPOINT (CEC, Bellerica, MA).

The following experimental procedures were used.

(i) DPOAE-grams. Responses to 50 tone bursts of 20.48-ms duration with 50-ms interval between them were averaged in the time domain. Tone sequences were synthesized and data were sampled at 200 kHz. Every tone burst was windowed with a raised cosine of 2-ms duration. Amplitudes and phase angles of the spectral peaks were obtained by performing an FFT on a time-domain-averaged signal using the first 2048 points after the initial 2 ms to avoid the influence of the signal windowing. This procedure was used to obtain DPOAE-grams (f_2 was swept, f_2/f_1 ratio was constant, levels L_1 and L_2 of the primaries were constant, L_2 was 10 dB below L_1) for low-level primaries. DPOAE-grams were recorded on a regular basis during experiment to confirm that the animals were in a stable physiological condition. Data collected from an animal were not used if DPOAE levels dropped by more than 5 dB at the f_2 frequencies used for the other procedures.

(ii) Post-onset changes. Longer tone bursts of 512 ms with 3-s interval between them were used to study post-onset changes of the DPOAE. Tone sequences were synthesized and data were sampled at 100 kHz in this case. Every tone burst was windowed with a raised cosine of 2-ms duration. Hence, the initial and final 2 ms of the response were excluded from data analysis to avoid influence of the signal windowing. The 512-ms tone bursts limited time-domain averaging to only ten responses with the result that the data were relatively noisy (see Sec III), but the duration of each experiment was minimized. During data analysis a temporal window 2048 points in length (i.e., 20.48 ms of duration) was slid along the 512-ms response in increments of 5 ms. Amplitudes and phase angles of the spectral peaks were obtained by performing an FFT of this temporal window. The moment of time that corresponded to the starting point of the temporal window was considered as the time when the amplitude and phase angle of the DPOAE were calculated. The sliding window technique was used to find the DPOAE growth during the simultaneous increase of L_1 and L_2 (L_2 was 10 dB below L_1) or during the increase of L_1 while L_2 was kept constant. The last procedure was utilized to reconstruct the DPOAE behavior in the $L_1\times L_2$ parameter space.

All procedures involving animals were performed in accordance with UK Home Office regulations.

III. RESULTS

A. Shift of the amplitude notch at stimulus onset

Amplitude alterations of the DPOAE at the $2f_1-f_2$ frequency were associated with an amplitude minimum (notch) in all guinea pigs in this study. This notch is routinely observed in the DPOAE response for intermediate level primaries within the frequency range used in this study. Systematic changes in the amplitude of the DPOAE were not observed

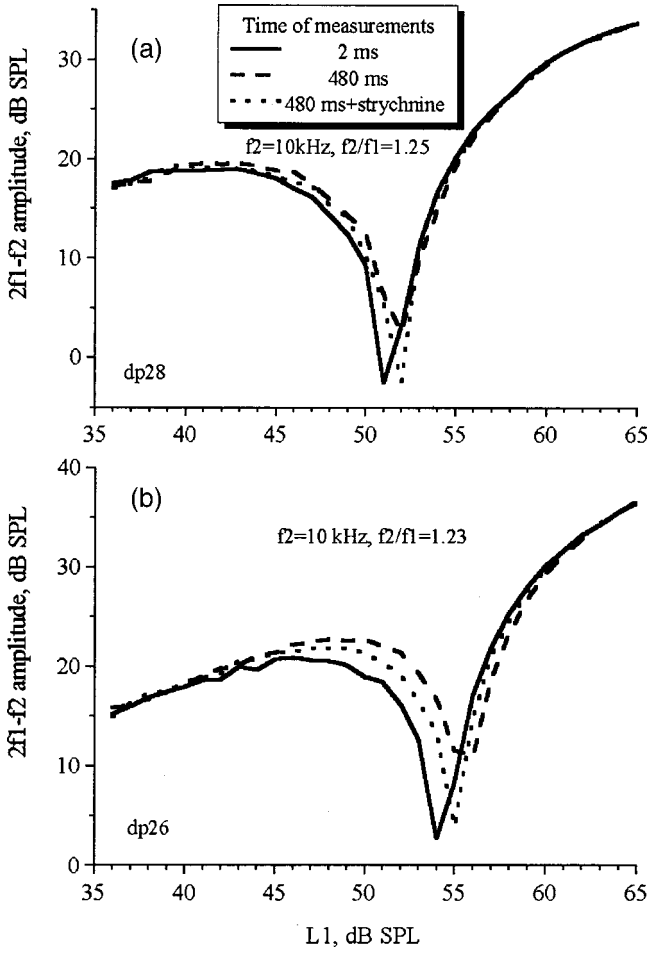

FIG. 1. Time dependence of the position of the amplitude notch for the $2f_1-f_2$ frequency component of the DPOAE before and after intravenous injection of strychnine (1 mg/kg b.w.). Data for two animals are presented. Solid line shows DPOAE response at the beginning of the prolonged acoustical stimulation. This response does not change after the injection of strychnine. Dashed and dotted curves represent the DPOAE responses in the 480 ms following the onset of the stimulation before and after the injection, respectively. f_2 and f_2/f_1 are indicated within each panel. L_1 step is 1 dB. L_2 is 10 dB below L_1.

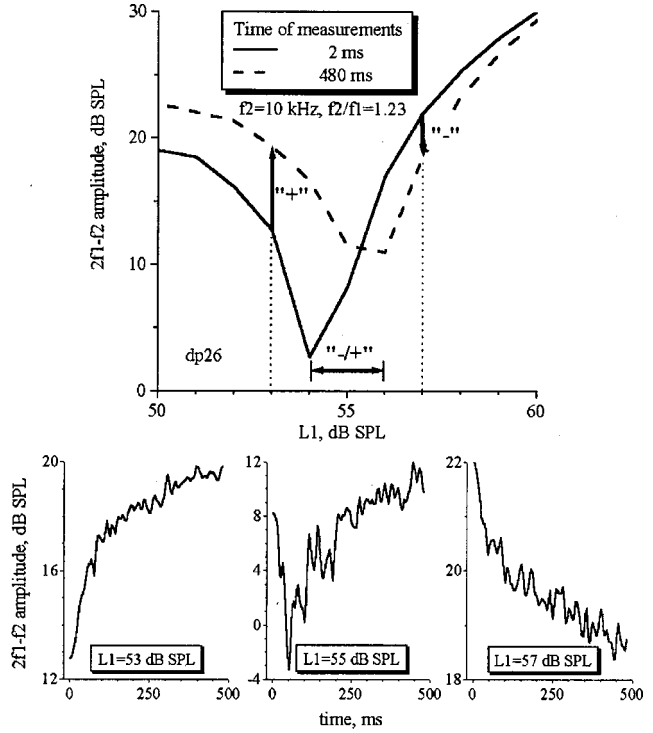

FIG. 2. Dependence of the post-onset changes of the DPOAE on the levels of the primaries. Top panel shows the response presented in Fig. 1(b) in the vicinity of the amplitude notch. Vertical arrows indicate changes of the DPOAE amplitude for particular pairs of the primary levels; $L_1/L_2=53/43$ dB SPL (left arrow) and $L_1/L_2=57/47$ dB SPL (right arrow). Temporal courses of these changes are shown in the bottom left and right panels, respectively. Middle panel of the bottom row shows biphasic time dependence of the DPOAE for the L_1 range indicated by the horizontal arrow in the top panel. L_1 is indicated within each of the bottom panels. The other notations are the same as in Fig. 1.

during the onset of prolonged tone bursts for DPOAE levels that were not affected by the notch, for example, when the DPOAE was generated by low-level (as low as $L_1/L_2=20/10$ dB SPL) or high-level (up to $L_1/L_2=75/65$ dB SPL) primaries.

Sliding window analysis revealed that the notch gradually shifts upwards with time in that higher levels of the primaries elicit it at successive periods in time following the onset of the tone bursts (Fig. 1). This displacement of the notch position is usually completed within the period of the 512-ms tone burst, but may continue beyond it (Fig. 2). The shift becomes significantly smaller (Fig. 1, dotted lines) after intravenous injection of strychnine, which is known to block the action of the OCB (Desmedt and Monaco, 1961). Strychnine in the concentrations used in this study completely blocked the suppressive effect of electrical stimulation of the MOC efferents on the auditory nerve's compound action potential in guinea pigs (Lukashkin and Russell, unpublished data, 2002). Therefore, the observed shift of the notch is at least partially mediated by the activity of the MOC efferents.

Inspection of the curves in Fig. 1 reveals that relatively small shifts (1–1.5 dB) of the notch position along the L_1 axis induce far greater changes in the level of the DPOAE observed for the same level of the primaries. The magnitude of the DPOAE changes depends on the sharpness of the notch and the position of the DPOAE level relative to that of the notch. The sharper the notch and the closer the DPOAE level to the tip of the notch, the stronger are the observed changes in the DPOAE. Correspondingly, sharper notches are observed near the optimum frequency ratio of the primaries that generate emissions at the maximum amplitude. In all animals recorded, the shift of the left, low-level slope of the notch is more pronounced than the analogous shift of the high-level slope. This difference causes the notch to become narrower and seemingly shallower. This apparent reduction in the depth of the notch does not take place when the initial notch is sharp, i.e., when the ratio is optimal. An apparent reduction in the depth of the notch is seen because the discrete steps of 1 dB, which are used in this study to increment the primary levels, are too large to resolve the new position of the amplitude minimum. A shifted notch as deep, or even deeper, than that at the onset of stimulation can be observed [see Fig. 1(a) and below] when the shifted position of the minimum falls close to the level of a primary pair used for DPOAE stimulation.

This single shift of the amplitude notch also explains all

three types of the $2f_1-f_2$ changes (increase, decrease, and biphasic variations), which have been documented at the onset of prolonged stimulation (Liberman *et al.*, 1996; Sun and Kim, 1999; Kim *et al.*, 2001; Kujawa and Liberman, 2001). Figure 2 shows a fragment of the curves from Fig. 1(b) in the vicinity of the notch. An increase in the DPOAE is observed for levels of primaries generating emission on the left slope of *the initial notch* (solid line). The left upward-pointing vertical arrow (Fig. 2, top panel) specifies this increase of the amplitude for a particular level of primaries (Fig. 2, bottom left panel). In contrast, the DPOAE decreases for levels of primaries generating emission on the right slope of *the steady-state notch* (dashed line). The right downward-pointing vertical arrow (Fig. 2, top panel) indicates the DPOAE decrease for a specific level of primaries (Fig. 2, bottom right panel). A biphasic DPOAE response (i.e., a decrease followed by an increase) takes place for any primary levels generating DPOAE between initial and steady-state notch positions (Fig. 2, bottom middle panel). This range of primaries is indicated in Fig. 2, top panel, by a horizontal double-headed arrow. It is worth noting that post-onset changes of DPOAE described in this section are observed for optimum f_2/f_1 ratios, when the notch is sharp and its shift is well pronounced. The biphasic response may be absent if the stimulus parameters are not optimal so that the notch is shallow, or hard to resolve, when the time-dependent shift of the notch is small (see below).

B. Dependence of DPOAE post-onset changes on the ratio of the primary frequencies

The notch in the DPOAE I/O function was produced at lower levels by pairs of primaries with lower f_2/f_1 frequency ratios than by those with higher f_2/f_1 ratios (Lukashkin and Russell, 2001). This is to be expected because of the increase of the f_1 amplitude in the f_2 place for lower f_2/f_1 ratios. Thus, one can expect different polarities of the post-onset changes in the DPOAE amplitudes for primaries of the same level, but of different f_2/f_1 ratios, because the initial position of the notch is different in these cases. This is illustrated in Fig. 3(a), where a primary pair $L_1/L_2=56/46$ dB SPL generates DPOAEs on the left, falling slope of the notch when their frequency ratio $f_2/f_1=1.26$. However, primaries of the same levels generate DPOAEs on the right, rising slope when f_2/f_1 ratio is decreased to 1.24. As a result of this different mapping of the DPOAE relative to the notch, post-onset changes of the DPOAE amplitude for the two f_2/f_1 ratios are opposite in direction [Fig. 3(b)]; emissions increases with time from onset for $f_2/f_1=1.26$ and decrease when $f_2/f_1=1.24$.

The magnitude of the post-onset shift of the notch also depends on the f_2/f_1 ratio. Larger f_2/f_1 ratios produced a smaller shift in all five guinea pigs in which this dependence was studied. A representative example of this effect is shown in Fig. 4. The larger shift of the tip of the notch for smaller f_2/f_1 ratios was associated with a greater shift of the left, falling slope of the notch and a post-onset elevation in the level of the notch [Fig. 4(a)]. As a result of this elevation of the shallow notch, biphasic post-onset changes in the DPOAE response were hardly observed. Biphasic responses

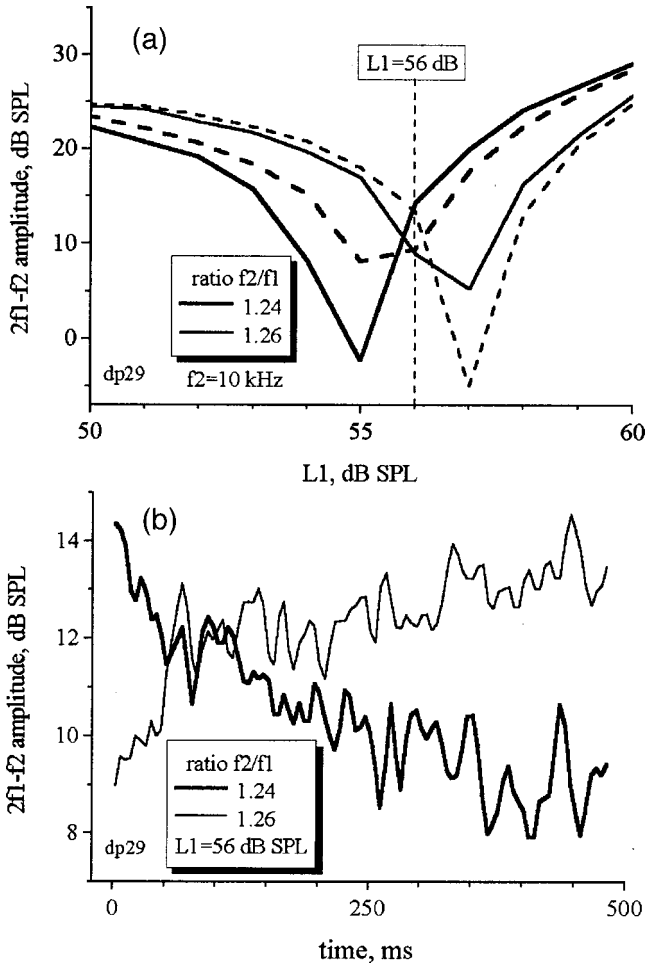

FIG. 3. Dependence of the post-onset changes of the $2f_1-f_2$ component on the ratio of the primary frequencies. Thick and thin curves show responses for f_2/f_1 of 1.24 and 1.26, respectively. f_2 is 10 kHz. L_2 is 10 dB below L_1. (a) Dependence of the initial and steady-state notch position on the f_2/f_1 ratio. (b) Temporal changes of the DPOAE for the same level of the primaries $L_1/L_2=56/46$ dB SPL but for different f_2/f_1 ratios. The dashed line at the top panel indicates corresponding intersection of the growth function. The other notations are the same as in Fig. 1.

were not observed for larger f_2/f_1 ratios because the level shift of the notch was very small and below the 1-dB resolution of our experiments [Fig. 4(b)]. Therefore, a sizable biphasic response could be recorded only for a relatively narrow range of f_2/f_1 ratios, which produced DPOAEs of near-maximum amplitude with a well-pronounced local minimum in their growth functions.

C. Dependence of DPOAE post-onset changes in primary-levels space

The DPOAE amplitude notch forms a distinctive pattern in the two-dimensional space of the primary levels $L_1\times L_2$. Namely, when measured in the $L_1\times L_2$ parameter space, the $2f_1-f_2$ DPOAE component shows notches, which occur when the level of one of the primaries is varied with the other one kept constant [Fig. 5, 6(a)]. Mills (1997) brought this experimental observation to general attention, and Lukashkin and Russell (1999) offered an explanation for it. The explanation is consistent with the idea that the notch is generated as a consequence of nonmonotonic behavior in the

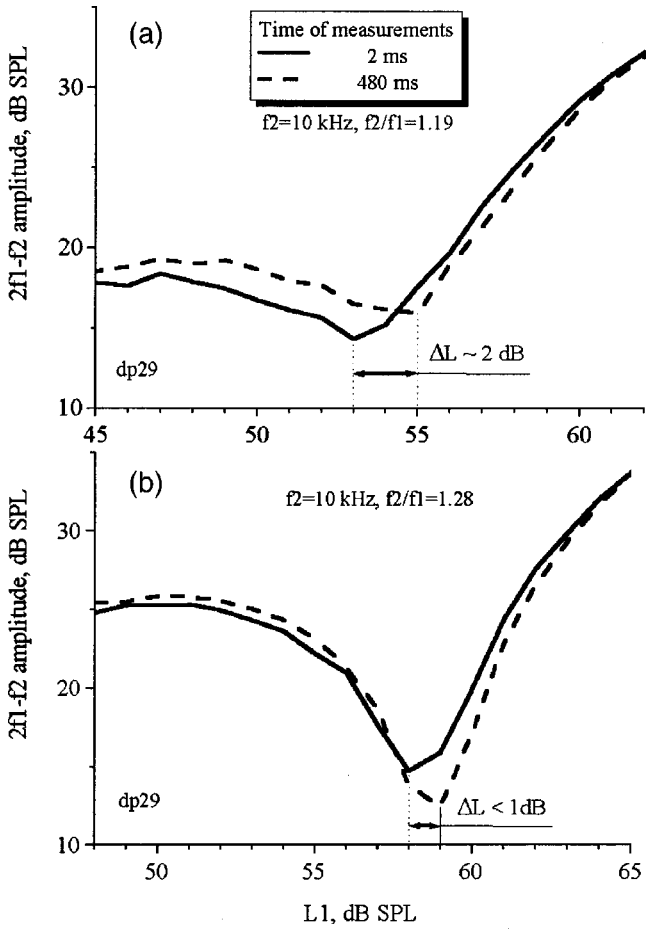

FIG. 4. Magnitude of the shift of the amplitude notch depends on the ratio of the primary frequencies. Horizontal arrows show corresponding differences, ΔL, in initial and steady-state position of the notch. $f_2=10$ kHz and is the same for both panels. f_2/f_1 is indicated within each panel. L_1 step is 1 dB. L_2 is 10 dB below L_1. The other notations are the same as in Fig. 1.

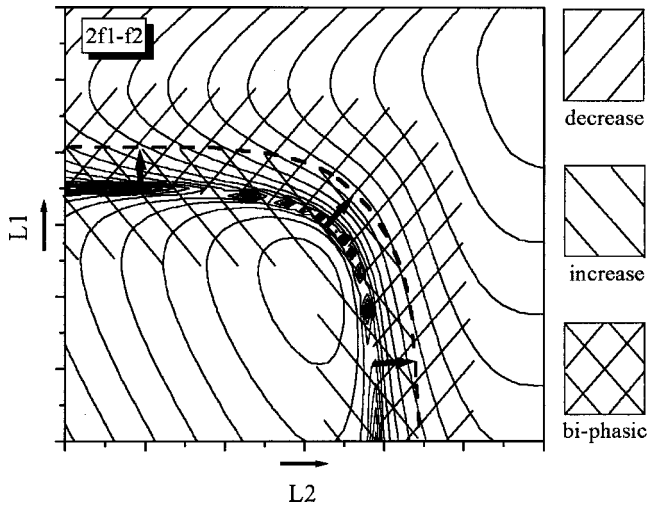

FIG. 5. Hypothetical zones with different post-onset changes of the $2f_1-f_2$ frequency component in the $L_1\times L_2$ plane (modification of Fig. 2, bottom right, from Lukashkin and Russell, 1999). Different hatching indicates these zones. Initial position of the amplitude notch is shown by the isoresponse lines. Thick arrows indicate post-onset shift of the notch and dashed line shows its steady-state position. Axes are given in arbitrary units. Arrows near the axis symbols point in the direction of growth of the primary levels. See the main text for further explanations.

distortion at the output of a saturating nonlinearity. On the basis of the studies reported here, a few regions with different DPOAE post-stimulus changes can be predicted in the $L_1\times L_2$ plane (Fig. 5). In this figure a dashed line indicates a hypothetical steady-state position of the notch, when the notch is observed at higher primary levels. It is anticipated that post-onset changes of the DPOAE should not be seen in two areas of the plane well below the initial and well above the steady-state position of the notch (nonhatched regions in Fig. 5). It is predicted that post-onset decreases in DPOAE should occur in the right-hatched area above and to the right of the initial notch position. A left-hatched region of the $L_1\times L_2$ plane in Fig. 5, situated below and to the left of the steady-state position of the notch, denotes the primary levels for which increases in the $2f_1-f_2$ DPOAE should occur. Overlap of the last two areas (double-hatched zone, Fig. 5) forms a region where both an initial decrease followed by an increase of the DPOAE should be seen.

The experimentally measured $2f_1-f_2$ DPOAE pattern in the $L_1\times L_2$ plane [Fig. 6(a)] resembles the theoretically predicted distribution of the emission amplitudes (Fig. 5). However, one major difference exists, namely, the amplitude notch becomes shallow when it is parallel to the L_1 axis, in other words when $L_2>L_1-5$ dB. In agreement with results presented in Sec. III B, biphasic post-onset responses are not apparent in the vicinity of the shallow notches. However, biphasic post-onset changes in the DPOAE can be seen for primary levels that generate emissions just above the sharp notch, which is located parallel to the L_2 axis. Post-onset changes of the DPOAE are also in agreement with theoretical predictions for the remaining regions of the $L_1\times L_2$ plane (compare Figs. 5 and 6). The post-onset DPOAE amplitude does not change for primary levels that generate emissions that are not affected by the notch (points 1, 4, 7, and 10 in Fig. 6). However, the post-onset DPOAE amplitude grows (points 3, 5, and 8) or declines (points 2, 6, and 9) for levels of the primaries that generate emissions on the falling or rising slopes of the notch, respectively.

IV. DISCUSSION

In this paper we have shown that the post-onset changes in amplitude of the $2f_1-f_2$ DPOAE frequency component that occur during prolonged acoustic stimulation of the guinea pig cochlea reflect a shift in the notch of the $2f_1-f_2$ growth function so that, with increasing time of stimulation, the notch occurs at higher levels of the primaries. Only $2f_1-f_2$ DPOAEs that are generated at levels close to that of the notch show post-onset changes. If the DPOAE level is far from the notch in its growth function, i.e., the levels of the primaries are more than about 10 dB higher or lower than those at the tip of the notch, then post-onset changes in the DPOAE were not observed. Stability of the $2f_1-f_2$ component generated by low- and high-level primaries and variability of the midlevel $2f_1-f_2$ emission has also been reported during electrical stimulation of the OCB (Siegel and Kim, 1982). Similar shift of the notch and absence of the $2f_1-f_2$ level alterations in the region outside the notch have also been observed in gerbil (Manfred Kössl, personal communi-

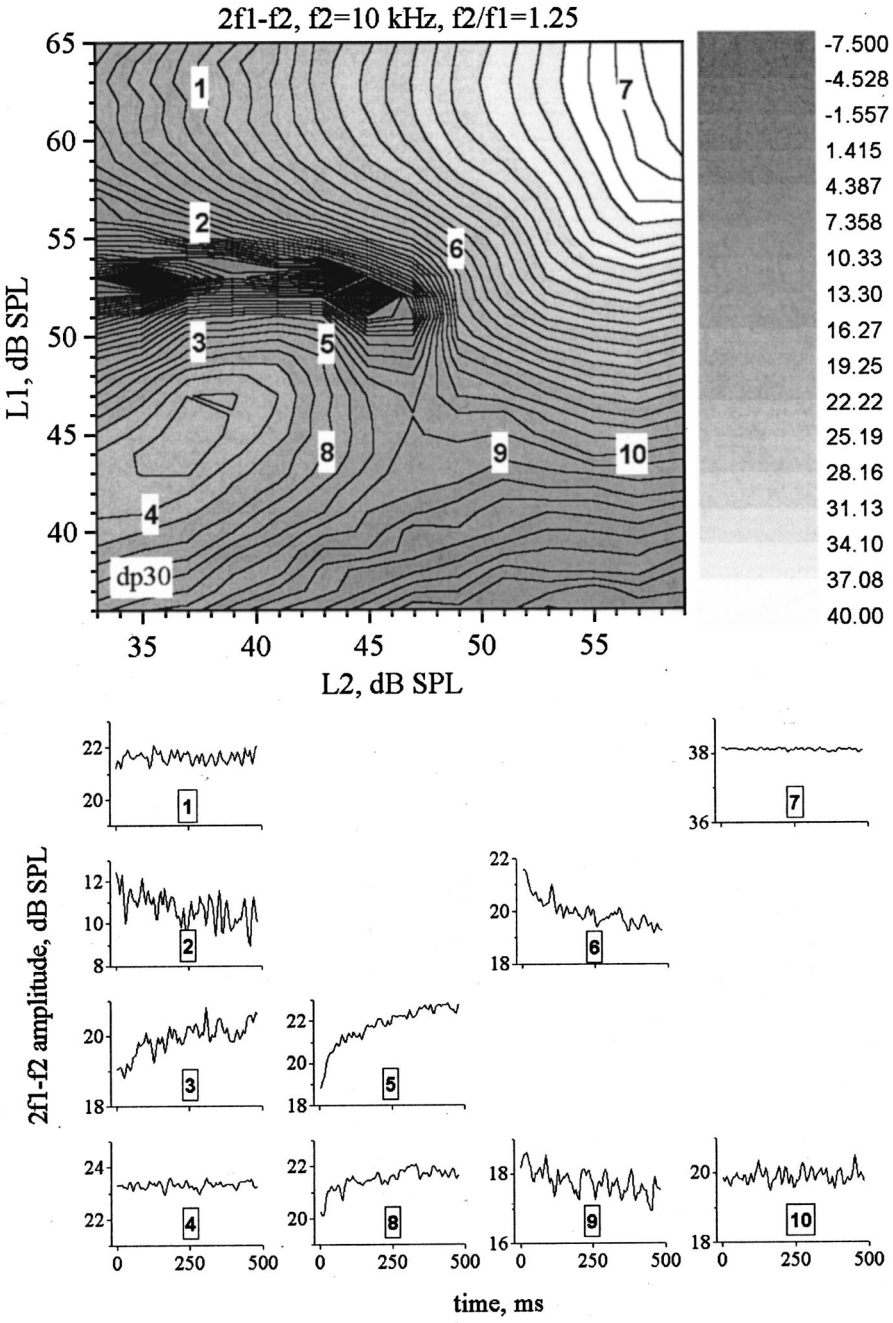

FIG. 6. Distribution of the 2 f_1-f_2 amplitude in the plane of the primary levels. The 2 f_1-f_2 amplitude is measured 2 ms after the onset of the stimulating tone burst. Numbers on the top plane show specific points for which post-onset changes are shown at the bottom of the figure. The isoresponse lines are 1 dB apart. The gray-scale chart on the right shows the corresponding amplitude of the 2 f_1-f_2 component in dB SPL. f_2 and f_2/f_1 are indicated above the top panel. L_1 and L_2 steps are 1 and 2 dB, respectively.

cation, 2002). Hence, it is likely that all post-stimulus alterations of the 2 f_1-f_2 component that have been described to date (Liberman *et al.*, 1996; Sun and Kim, 1999; Kim *et al.*, 2001; Kujawa and Liberman, 2001) originate in the upward shift of the amplitude notch that is reported here. It is, therefore, difficult to make any quantitative comparisons between these data. Indeed, the current study shows that the magnitude of the DPOAE alterations depends considerably on the specific position of the DPOAE in the vicinity of its local minimum. Thus, variations in the magnitude of the effect in the different studies can be explained simply by different positioning of the DPOAE in the vicinity of the notch. Accordingly, the magnitude of the DPOAE changes is not the most suitable parameter to characterize the post-onset changes in 2 f_1-f_2 DPOAE. The *shift of the notch minimum* (see, for example, Fig. 4) provides a more objective and comparable parameter, and hence is a better characteristic of the process. Another suggestion relates to the usage of the term ''adaptation'' which has been utilized to describe the post-onset changes. It is obvious from the current study that the properties of the post-onset process do not resemble those normally associated with physiological adaptation, and the usage of this term seems to be inappropriate.

By establishing that the origin of the post-stimulus changes of the DPOAE is associated with a shift of the amplitude notch, we are able to predict the temporal behavior of the DPOAE for different levels of the primaries and for their different frequency ratios. It should be re-emphasized that our predictions of the notch position (Figs. 3, 5, 6) are based upon a hypothesis that the occurrence of the notch is due to nonmonotonic behavior of distortion components at the output of a single saturating nonlinearity (Weiss and Leong,

1985; Lukashkin and Russell, 1998, 1999). This single-source hypothesis, which contrasts with proposals that the notch is due to phase cancellation between several sources, has received recent experimental support (Fahey *et al.*, 2000; Lukashkin and Russell, 2001; Mom *et al.*, 2001; Lukashkin *et al.*, 2002). It is worth noting that the distinctive pattern of the notch in the two-dimensional space of the primary levels is not unique to guinea pigs. Similar positions of the notch in the $L_1 \times L_2$ plane have been observed in rabbits, gerbils, and mice (Whitehead *et al.*, 1992; Mills and Rubel, 1994; Mills, 1997; Parham, 1997). Therefore, it is likely that the specific predictions from the current study on the direction of the post-stimulus changes of the DPOAE amplitude can be extended, at least, to these other mammalian species. It should be noted that monotonic growth of the DPOAE I/O functions is frequently recorded from humans (Whitehead, 1998). In the absence of the notch and, therefore, associated alterations of the DPOAE, small but significant post-stimulus changes of the human DPOAE (Kim *et al.*, 2001) seem to indicate real changes in emission level and not simply a shift of the notch. However, Kim *et al.* (2001) specifically emphasized that they observed amplitude notches accompanied by a phase change of 70°–80° in the DPOAE level functions of humans. Therefore, a shift of the notch could be the basis for the post-stimulus changes of the DPOAE even in the experiments cited by Kim *et al.* (2001). However, this speculation requires further investigation because notches in the human DPOAE might have an origin which is different from that in rodents. Nonmonotonicities seen in the human DPOAE are associated with fine structure (He and Schmiedt, 1993, 1997), which is absent in rodents (Whitehead, 1998). Thus, different origins of the notches in rodent and human DPOAEs might implicate different mechanisms for post-onset changes in DPOAEs recorded from rodent and human ears.

It is beyond the scope of the current work to establish mechanisms underlying the reported shift of the amplitude notch. However, it seems likely that the post-onset changes in DPOAE are due, at least in part, to an efferent effect, because the changes can be partially blocked by intravenous levels of strychnine (Fig. 1) that normally completely suppress the effects of electrical OCB activation on the cochlea's mechanical and neural responses to tones (Lukaskin and Russell, unpublished, 2002). Possibly the residual post-onset changes are due to efferent effects that are strychnine insensitive (Kirk and Johnstone, 1993). There are two main causes which can lead to a change of the notch position after activation of the MOC efferent system. First, a change in DPOAE amplitude can be a consequence of a decline in active cochlear feedback. Similar multidirectional alterations of the DPOAE amplitude (both increases and decreases) were observed following furosemide treatment (Lukashkin *et al.*, 2002). Hence, it is plausible to suggest that the upward shift of the notch, described in the current study, occurs because of a reduction in electromechanical feedback from the OHCs as a consequence of ipsilateral OCB activation. A reduction in the DPOAE caused by low-level primaries is also observed if the shift of the notch is a consequence of a decrease in cochlear feedback (Lukashkin *et al.*, 2002). However, the current study shows that the DPOAE generated by the low-level primaries remains constant during the post-stimulus shift of the notch (Fig. 1). This observation may indicate that the response of the laterally activated OCB efferents at low SPLs is not sufficient to cause a measurable decrease in DPOAE amplitude.

Another hypothetical cause of the observed shift of the notch might be a temporal change of the DPOAE producing nonlinearity. It has been reported that OCB activation modifies nonlinear currents through the OHC mechanoelectrical transducer (Patuzzi and Rajan, 1990). At the same time, the OHC mechanoelectrical transducer is likely to be the strongest nonlinearity of the auditory periphery (Patuzzi *et al.*, 1989; Santos-Sacchi, 1993) that is responsible for the DPOAE generation, and the operating point of the nonlinearity is situated above its point of inflection in the basal turn of the mammalian cochlea (Frank and Kössl, 1996; Lukashkin and Russell, 1998). Theoretical analysis of the behavior of the amplitude notch in I/O functions of the distortion products at the output of a saturating nonlinearity shows that the position of the notch depends strongly on the position of the operating point of the nonlinearity (Lukashkin and Russell, 1998, 1999). An upward shift of the amplitude notch would be observed during an upward bias of the operating point further away from the point of inflection. An upward shift of the notch corresponds to displacement of the OHC hair bundles in the positive direction and to an increase in the steady-state transducer conductance. It is plausible to suggest that the steady-state displacement of the hair bundle is due to the relative displacement of the cochlear structures via the hyperpolarization and static elongation of the OHCs due to activation of the efferent neurones. The OHC elongation might lead to displacement of the OHC hair bundle in the positive direction if the basilar membrane and reticular lamina could move independently (Mammano and Ashmore, 1993). In this case the OHC elongation might cause a counterdirectional movement of the basilar membrane towards the scala tympany and the reticular lamina towards the scala vestibuli. Indeed, intracellular injection of negative current into OHCs *in situ* causes an upward shift of the operating point of the OHC receptor potential (Russell and Kössl, 1991). This shift was proposed to occur because elongation of the OHCs caused the hair bundles to be displaced in the excitatory direction. Furthermore, such a shift in the operating point of the OHC receptor potential following electrical stimulation of the OCB was proposed to be a means by which the cochlear amplifier was attenuated, with a consequent reduction in tone-evoked BM displacements (Murugasu and Russell, 1996).

ACKNOWLEDGMENTS

This work was supported by a grant from the Wellcome Trust.

Brown, A. M. (**1988**). "Continuous low level sound alters cochlear mechanics: An efferent effect?" Hear. Res. **34**, 27–38.

Desmedt, J. E. (**1962**). "Auditory-evoked potentials from cochlea to cortex as influenced by activation of the efferent olivocochlear bundle," J. Acoust. Soc. Am. **34**, 1478–1496.

Desmedt, J. E., and Monaco, P. (**1961**). "Mode of action of the efferent olivocochlear bundle on the inner ear," Nature (London) **192**, 1263–1265.

Fahey, P. F., Stagner, B. B., Lonsbury-Martin, B. L., and Martin, G. K. (**2000**). ''Nonlinear interactions that could explain distortion product interference response areas,'' J. Acoust. Soc. Am. **108**, 1786–1802.
Fex, J. (**1967**). ''Efferent inhibition in the cochlea related to hair-cell dc activity: Study of postsynaptic activity of the crossed olivocochlear fibers in the cat,'' J. Acoust. Soc. Am. **41**, 666–675.
Frank, G., and Kössl, M. (**1996**). ''The acoustic two tone distortions $2f1-f2$ and $f2-f1$ and their possible relation to changes in the gain and the operating point of the cochlear amplifier,'' Hear. Res. **98**, 104–115.
Gifford, M. L., and Guinan, J. J., Jr. (**1987**). ''Effect of electrical stimulation of medial olivocochlear neurons on ipsilateral and contralateral cochlear responses,'' Hear. Res. **29**, 179–194.
He, N., and Schmiedt, R. A. (**1993**). ''Fine structure of the $2f_1-f_2$ acoustic distortion product: Changes with primary level,'' J. Acoust. Soc. Am. **94**, 2659–2669.
He, N., and Schmiedt, R. A. (**1997**). ''Fine structure of the $2f_1-f_2$ acoustic distortion product: Effects of primary levels and frequency ratios,'' J. Acoust. Soc. Am. **101**, 3554–3565.
Kim, D. O., Dorn, P. A., Neely, S. T., and Gorga, M. P. (**2001**). ''Adaptation of distortion product otoacoustic emission in humans,'' JARO **2**, 31–40.
Kirk, D. L., and Johnstone, B. M. (**1993**). ''Modulation of f_2-f_1: Evidence for a GABA-ergic efferent system in apical cochlea of the guinea pig,'' Hear. Res. **67**, 20–34.
Kujawa, S. G., Fallon, M., and Bobbin, R. P. (**1995**). ''Time-varying alterations in the f_2-f_1 DPOAE response to continuous primary stimulation. I. Response characterization and contribution of the olivocochlear efferents,'' Hear. Res. **85**, 142–154.
Kujawa, S. G., and Liberman, M. C. (**2001**). ''Effect of olivocochlear feedback on distortion product otoacoustic emission,'' JARO **2**, 268–278.
Liberman, M. C., Puria, S., and Guinan, J. J., Jr. (**1996**). ''The ipsilaterally evoked olivocochlear reflex causes rapid adaptation of the $2f_1-f_2$ distortion product otoacoustic emission,'' J. Acoust. Soc. Am. **99**, 3572–3584.
Lowe, M., and Robertson, D. (**1995**). ''The behavior of the f_2-f_1 acoustic distortion product: Lack of effect of brainstem lesions in anesthetized guinea pigs,'' Hear. Res. **83**, 133–141.
Lukashkin, A. N., and Russell, I. J. (**1998**). ''A descriptive model of the receptor potential nonlinearities generated by the hair cell mechanoelectrical transducer,'' J. Acoust. Soc. Am. **103**, 973–980.
Lukashkin, A. N., and Russell, I. J. (**1999**). ''Analysis of the f_2-f_1 and $2f_1-f_2$ distortion components generated by the hair cell mechanoelectrical transducer: Dependence on the amplitudes of the primaries and feedback gain,'' J. Acoust. Soc. Am. **106**, 2661–2668.
Lukashkin, A. N., and Russell, I. J. (**2001**). ''Origin of the bell-like dependence of the DPOAE amplitude on primary frequency ratio,'' J. Acoust. Soc. Am. **110**, 3097–3106.
Lukashkin, A. N., and Russell, I. J. (2002) (unpublished).
Lukashkin, A. N., Lukashkina, V. A., and Russell, I. J. (**2002**). ''One source for distortion product otoacoustic emissions generated by low- and high-level primaries,'' J. Acoust. Soc. Am. **111**, 2740–2748.
Mammano, F., and Ashmore, J. F. (**1993**). ''Reverse transduction measured in the isolated cochlea by laser Michelson interferometry,'' Nature (London) **365**, 838–841.
Mills, D. M. (**1997**). ''Interpretation of distortion product otoacoustic emission measurements. I. Two stimulus tones,'' J. Acoust. Soc. Am. **102**, 413–429.
Mills, D. M., and Rubel, E. W. (**1994**). ''Variation of distortion product otoacoustic emission with furosemide injection,'' Hear. Res. **77**, 183–199.
Mom, T., Bonfils, P., Gilain, L., and Avan, P. (**2001**). ''Origin of cubic difference tones generated by high-intensity stimuli: Effect of ischemia and auditory fatigue on the gerbil cochlea,'' J. Acoust. Soc. Am. **110**, 1477–1488.
Murugasu, E., and Russell, I. J. (**1996**). ''The effect of efferent stimulation on basilar membrane displacement in the basal turn of the guinea pig cochlea,'' J. Neurosci. **16**, 325–332.
Parham, K. (**1997**). ''Distortion product otoacoustic emissions in the C57BL/6J mouse model of age-related hearing loss,'' Hear. Res. **112**, 216–234.
Patuzzi, R. B., Yates, G. K., and Johnstone, B. M. (**1989**). ''Outer hair cell receptor current and sensorineural hearing loss,'' Hear. Res. **42**, 47–72.
Patuzzi, R., and Rajan, R. (**1990**). ''Does electrical stimulation of the crossed olivo-cochlear bundle produce movement of the organ of Corti?'' Hear. Res. **45**, 15–32.
Puel, J.-L., and Rebillard, G. (**1990**). ''Effect of contralateral sound stimulation on the distortion product $2F_1-F_2$: Evidence that the medial efferent system is involved,'' J. Acoust. Soc. Am. **87**, 1630–1635.
Russell, I. J., and Kössl, M. (**1991**). ''The voltage responses of hair cells in the basal turn of the guinea-pig cochlea,'' J. Physiol. (London) **435**, 493–511.
Santos-Sacchi, J. (**1993**). ''Harmonics of outer hair cell motility,'' Biophys. J. **65**, 2217–2227.
Siegel, J. H., and Kim, D. O. (**1982**). ''Efferent neural control of cochlear mechanics? Olivocochlear bundle stimulation affect cochlear biomechanical nonlinearity,'' Hear. Res. **6**, 171–182.
Sun, X. M., and Kim, D. O. (**1999**). ''Adaptation of distortion product otoacoustic emission in young-adult and old CBA and C57 mice,'' J. Acoust. Soc. Am. **105**, 3399–3409.
Warren, E. H., and Liberman, M. C. (**1989**). ''Effect of contralateral sound on auditory-nerve responses. I. Contribution of cochlear efferents,'' Hear. Res. **37**, 89–104.
Weiss, T. F., and Leong, R. (**1985**). ''A model for signal transmission in an car having hair cells with free-standing stereocilia. IV. Mechanoelectric transduction stage,'' Hear. Res. **20**, 175–195.
Whitehead, M. L. (**1998**). ''Comment on 'Interpretation of distortion product otoacoustic emission measurements. I. Two stimulus tones [J. Acoust. Soc. Am. **102**, 413–429 (1997)],' '' J. Acoust. Soc. Am. **103**, 2740–2742.
Whitehead, M. L., Lonsbury-Martin, B. L., and Martin, G. K. (**1991**). ''Slow variation of the amplitude of acoustic distortion at f_2-f_1 in awake rabbits,'' Hear. Res. **51**, 293–300.
Whitehead, M. L., Lonsbury-Martin, B. L., and Martin, G. K. (**1992**). ''Evidence for two discrete sources of $2f_1-f_2$ distortion-product otoacoustic emission in rabbit. II. Differential physiological vulnerability,'' J. Acoust. Soc. Am. **92**, 2662–2682.
Wiederhold, M. L., and Kiang, N. Y. S. (**1970**). ''Effect of electric stimulation of the crossed olivocochlear bundle on single auditory-nerve fibers in the cat,'' J. Acoust. Soc. Am. **48**, 950–965.
Zheng, Y. L., Ohyama, K., Hozawa, K., Wada, H., and Takasaka, T. (**1997**). ''Effect of anesthetic agents and middle ear pressure application on distortion product otoacoustic emissions in the gerbil,'' Hear. Res. **112**, 167–174.

Place specificity of multiple auditory steady-state responses

Anthony T. Herdman
School of Audiology and Speech Sciences, The University of British Columbia, 5804 Fairview Avenue, Vancouver, British Columbia V6T 1Z3, Canada

Terence W. Picton
Rotman Research Institute, Baycrest Centre for Geriatric Care, University of Toronto, 3560 Bathurst Street, Toronto, Ontario M6A 2E1, Canada

David R. Stapells[a)]
School of Audiology and Speech Sciences, The University of British Columbia, 5804 Fairview Avenue, Vancouver, British Columbia V6T 1Z3, Canada

(Received 14 September 2001; accepted for publication 15 July 2002)

Auditory steady-state responses (ASSRs) were elicited by simultaneously presenting multiple AM (amplitude-modulated) tones with carrier frequencies of 500, 1000, 2000, and 4000 Hz and modulation frequencies of 77, 85, 93, and 102 Hz, respectively. Responses were also evoked by separately presenting single 500- or 2000-Hz AM tones. The objectives of this study were (i) to determine the cochlear place specificity of single and multiple ASSRs using high-pass noise masking and derived-band responses, and (ii) to determine if there were any differences between single- and multiple-stimulus conditions. For all carrier frequencies, derived-band ASSRs for 1-octave-wide derived bands ranging in center frequency from 0.25 to 8 kHz had maximum amplitudes within a $\frac{1}{2}$ octave of the carrier frequency. For simultaneously presented AM tones of 500, 1000, 2000, and 4000 Hz, bandwidths for the function of derived-band ASSR amplitude by derived-band center frequency were 476, 737, 1177, and 3039 Hz, respectively. There were no significant differences when compared to bandwidths of 486 and 1371 for ASSRs to AM tones of 500 or 2000 Hz presented separately. Results indicate that ASSRs to moderately intense stimuli (60 dB SPL) reflect activation of reasonably narrow cochlear regions, regardless of presenting AM tones simultaneously or separately. [DOI: 10.1121/1.1506367]

PACS numbers: 43.64.Qh, 43.64.Ri [LHC]

I. INTRODUCTION

A continuing goal of evoked potential audiometry is to develop a technique that will quickly and accurately estimate hearing thresholds in individuals who cannot reliably respond behaviorally. Auditory steady-state responses (ASSRs) may theoretically be recorded more quickly and recognized more objectively than the more widely accepted auditory brainstem response (ABR) (Herdman and Stapells, 2001; Lins *et al.*, 1996; Rance *et al.*, 1998; Rickards *et al.*, 1994). In addition, ASSRs may provide a more frequency-specific assessment of hearing than the ABR because the amplitude-modulated (AM) tones used to elicit ASSRs have a narrower spectrum than the brief tones used to elicit the ABRs (Hartmann, 1997).

To establish a frequency-specific threshold in humans, two criteria must be met. The first criterion—acoustic specificity—requires the acoustic energy of the stimulus to have minimal spectral splatter and to be centered at the frequency of interest (Stapells, Picton, and Durieux-Smith, 1994; Stapells *et al.*, 1985). Limiting the spectral splatter lessens the activation of responses by frequencies other than the frequency of interest. A classic problem involving reduced acoustic specificity is when a brief, high-frequency tone burst is heard by an individual with a severe high-frequency hearing loss and near-normal hearing at lower frequencies. The hearing (and thus the ABR) may be mediated by the lower-frequency energy in a brief, high-frequency tone burst (Picton *et al.*, 1979). Acoustic specificity is measured by analyzing the spectrum of the stimulus. The AM stimuli used to evoke the ASSRs are acoustically very frequency specific. Sinusoidally amplitude-modulated tones have an acoustic spectrum with three peaks of energy, one centered at the carrier frequency and two side bands at the carrier frequency plus/minus the modulation frequency (Hartmann, 1997).

The second criterion—cochlear place specificity—requires that the cochlear activation occurs at the location on the basilar membrane where continuous pure tones of that frequency have their maximal activation (Starr and Don, 1988). A large spread of activation to other regions of the basilar membrane will make it difficult to determine which cochlear place is producing the response. A classic problem involving reduced place specificity occurs when a low-frequency tone is still heard by an individual with no functioning hair cells beyond the first turn of the cochlea. The response is initiated through regions of the cochlea that respond best to higher-frequency tones. Place specificity may be measured by analyzing the extent of the cochlea that is activated by the stimulus using high-pass noise (HPN) masking to isolate responding regions of the cochlea (Teas, Eld-

[a)]Author to whom correspondence should be addressed; electronic mail: stapells@audiospeech.ubc.ca

ridge, and Davis, 1962). Presenting HPN masking at different cutoff frequencies together with stimuli may be used to limit the cochlea's response. Subtractions can then determine ''derived responses'' that reflect the activation of the cochlear regions between the two cutoff frequencies of the HPN (Don, Eggermont, and Brackmann, 1979; Eggermont, Spoor, and Odenthal, 1976; Nousak and Stapells, 1992; Oates and Stapells, 1997b; Ponton, Don, and Eggermont, 1992; Stapells *et al.*, 1994).

Place specificity of ASSRs to AM tones is still under investigation. Early ASSR studies, using AM tones modulated between 40–50 Hz, revealed good place specificity by estimating behavioral thresholds in hearing-impaired individuals and by using high-pass noise masking techniques (Griffiths and Chambers, 1991; Kuwada, Batra, and Maher, 1986). Although these results seemed promising for using ASSRs in a clinical setting, the 40-Hz response was found to be inconsistent and unreliable in infants (Aoyagi *et al.*, 1993; Maurizi *et al.*, 1990; Stapells *et al.*, 1988; Suzuki and Kobayashi, 1984). Modulating AM tones between 70–110 Hz can evoke stable ASSRs in infants and adults, whether sleeping or awake (Aoyagi *et al.*, 1993; Cohen, Rickards, and Clark, 1991; Levi, Folsom, and Dobie, 1993; Lins *et al.*, 1995; Rickards *et al.*, 1994). Results from studies comparing behavioral and ASSR thresholds in individuals with different configurations and magnitudes of hearing impairments have shown correlations of 0.69 and 0.99 between these measures (Aoyagi *et al.*, 1994; Lins *et al.*, 1996; Picton *et al.*, 1998; Rance *et al.*, 1998). However, the extent of the place specificity has not been quantified. Thus, it is important that the place specificity of the 70–110-Hz ASSR be assessed by means of masking.

Results from a two-tone masking study by John and colleagues (John *et al.*, 1998) suggest that a 1000-Hz AM tone (60 dB SPL) modulated at 80 Hz activates the basilar membrane within a $\frac{1}{2}$ octave on either side of the stimulus carrier frequency. These data warrant further investigation using other carrier frequencies and noise-masking techniques.

This paper investigates place specificity for the single- and multiple-ASSR methods using derived responses. We obtained amplitudes for ASSRs to single AM tones and to multiple (four) AM tones presented at 60 dB SPL in high-pass filtered noise masking with cutoff frequencies at $\frac{1}{2}$-octave steps (ranging from 0.25 to 16.0 kHz). Amplitudes for 1-octave-wide derived bands for each stimulus frequency were calculated, providing amplitude profiles as a function of derived-band center frequency. Bandwidths and center frequencies (CFs) were determined for each derived-band amplitude profile. By examining these measures, we are able to demonstrate the place specificity for ASSRs and to investigate whether differences exist between ASSRs to single-and multiple-stimulus or between different carrier frequencies.

II. METHODS

A. Subjects

Nine adults (4 females) volunteered for this study. Their ages ranged from 18 to 30 years (mean age 21 years). Normal middle-ear compliance and reflexes were confirmed for all participants at each test session using tympanometry and ipsilateral acoustic-reflex measures. All participants had pure-tone behavioral thresholds of 15 dB HL (ANSI, 1996) or better for octave frequencies between 500 and 4000 Hz.

B. Stimuli

The stimuli were sinusoidal AM tones that were generated and presented by the MASTER system (John and Picton, 2000). Parameters for these stimuli are based on those previously reported (Herdman and Stapells, 2001; Lins *et al.*, 1996). AM tones were presented to a test ear (chosen randomly between right and left ears for each subject) through ER-3A insert earphones. AM tones had carrier frequencies (f_c) of 500, 1000, 2000, and 4000 Hz that were 100% amplitude modulated at frequencies of 77.148, 84.961, 92.773, and 100.586 Hz, respectively. These modulation frequencies (f_m) were used to obtain an integer number of cycles for the f_m in an EEG recording section (of 1.024 seconds).

AM tones were presented to the subject under two conditions: (1) Single: AM tones of 500 or 2000 Hz were presented separately to the test ear; and (2) Multiple: simultaneous presentation of four AM tones (500, 1000, 2000, and 4000 Hz) to the test ear.

The intensity of the AM tones was 60 dB SPL (49–53 dB nHL; Herdman and Stapells, 2001), calibrated for each tone separately. The intensity of the combined stimulus was 66 dB SPL.

C. High-pass noise masking

All stimuli were combined with ipsilateral HPN. Broadband white noise was generated (Tucker Davis Technologies WG1) and then high-pass filtered (96 dB/octave slope; Wavetek model 852 filter) using cutoff frequencies at $\frac{1}{2}$-octave steps: 0.25, 0.354, 0.5, 0.707, 1.0, 1.41, 2.0, 2.83, 4.0, 5.66, 8.0, 11.31, and 16.0 kHz. The HPN cutoff frequency of 16.0 kHz was used to provide response measures in a ''non-masked'' condition. This was done to account for possible effects of broadband noise leaking through the filter (Oates and Stapells, 1997a) and to keep the filter in the stimulus/masker setup for all conditions. All $\frac{1}{2}$-octave HPN cutoff frequencies between 0.25 and 16.0 kHz were used in the multiple-stimulus condition. Different HPN cutoff frequencies were used for the single presentations of 500- and 2000-Hz tones. HPN cutoff frequencies were between 0.25 and 4.0 kHz for the single 500-Hz AM tone presentation, and between 0.5 and 8.0 kHz for the single 2000-Hz AM tone presentation. These cutoff frequencies were chosen to obtain results for at least one octave below and two octaves above the stimulus carrier frequency.

The intensity of the broadband noise was adjusted for each subject to a level just sufficient to mask ASSRs for all carrier frequencies in both conditions. Behavioral masking levels were established first by asking subjects to identify AM tones presented for 1 s while broadband noise was continually delivered ipsilaterally. The intensity of the broadband noise was increased by 2 dB SPL for correct response trials, then decreased by 1 dB SPL for no response trials. The behavioral masking level for each condition was at the noise

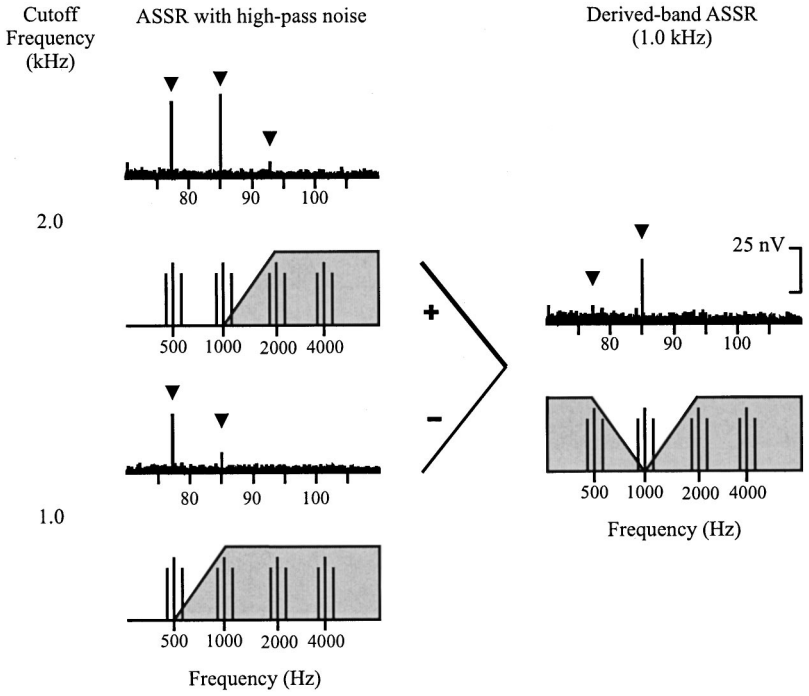

FIG. 1. HPN/DR technique. The upper traces depict the EEG amplitude spectrum for multiple ASSRs to AM tones of 500, 1000, 2000, and 4000 Hz. Statistically significant ($p<0.01$) ASSRs are designated by arrowheads. These responses correspond to the acoustic line spectra of the AM tones which are presented directly below each EEG spectrum. This may be illustrated in such a manner because the modulation frequency (at which neurons respond) increases with carrier frequency. In addition to the AM tone spectra, HPN masking is depicted as the gray box that has a cutoff frequency at 2 kHz for the upper left graph and 1 kHz for the lower left graph. Subtraction of these two responses in the time domain yields a derived band with a center frequency of 1 kHz (lower right acoustic spectra) and the corresponding EEG spectrum for the multiple derived-band ASSR depicted above.

intensity for which the participant indicated no more than one correct response out of five, with at least three out of five correct responses 1 dB lower. The mean (± 1 standard deviation) behavioral masking level for the 60-dB SPL stimuli was 80 ± 2 dB SPL. The highest level of behavioral masking just needed to mask any stimulus (including the multiple-stimulus condition) was used as a starting intensity for determining the broadband noise level required to mask ASSRs. In order to determine the physiological (ASSR) masking levels for each subject, the broadband noise was increased using 2-dB steps for ''response present'' recordings and decreased using 1-dB steps for ''no-response'' recordings. ASSR masking levels were determined as the lowest broadband noise intensity that just sufficiently masked all ASSRs for all conditions. The mean ASSR masking level was 82 ± 2 dB SPL.

D. Derived-band auditory steady-state responses

Derived-band ASSRs were obtained by subtracting ASSRs with HPN masking from ASSRs with HPN masking that had a cutoff frequency 1 octave higher (Don *et al.*, 1979; Eggermont, 1976). Subtractions were performed on the time-domain waveforms (rather than frequency spectra) and the results transformed into the frequency domain. This was simpler than performing subtraction in the frequency domain, which would require vector arithmetic to consider both the amplitude and phase of a response. The schematic in Fig. 1 shows the frequency spectra of the subtraction of ASSR time-domain averages. ASSRs to multiple AM tones in 1.0-kHz HPN masking were subtracted from ASSRs to multiple AM tones in 2.0-kHz HPN masking in order to obtain derived-band ASSRs in a derived band centered at 1.0 kHz (i.e., representing contributions from cochlear regions with characteristic frequencies between 1.0 and 2.0 kHz). The figure shows only the amplitude spectra of the responses because these are the most informative, and shows only those portions of the spectra near the response frequencies. The design of the study was fortuitous in that the modulation (at which the brain responds) increased as the carrier frequency increased. This is not a requirement, but it does allow the brain response to be lined up in the figure above the acoustic spectra for the AM tones. Note that the frequency axis is different between EEG and acoustic spectra. Obtaining the acoustic response area for the derived-band procedure was done by subtracting the unmasked part of the 1-kHz HPN response from the masked part of the 2-kHz HPN response. The response area is conceptually similar to that obtained with notched noise, with one important exception: the derived-response method shows substantially less of the ''upward spread of masking'' seen with notched noise (Picton *et al.*, 1979). Note, the derived-band subtraction technique will increase the background residual noise by the square root of 2 compared to the HPN averages. Sufficient averaging was performed to adjust for this factor.

Half-octave-wide derived bands were not utilized because these narrower derived bands result in very low signal-to-noise levels and thus highly variable response amplitudes across subjects. This has previously been shown by Oates and Stapells (1997b). Derived responses were therefore calculated for one-octave-wide bands with center frequencies separated by $\frac{1}{2}$-octave intervals. The derived-band center frequency was designated as the lower HPN cutoff frequency in the subtraction procedure. There is some controversy concerning the designation of the center frequency of the derived band (discussed in detail by Oates and Stapells, 1997b). Several earlier studies chose the lower HPN cutoff frequency as the center frequency based on subtractions of HPN acoustic spectra (Don and Eggermont, 1978; Don *et al.*, 1979; Eggermont and Don, 1980; Oates and Stapells, 1997b; Nousak and Stapells, 1992). Results from a recent within-band masking study in our lab (Stapells and So, 1999) indicate that the center frequency of the derived band is close to

the lower HPN cutoff frequency. This result is due to the finite slope of the filter, and would only be applicable to 1-octave-wide derived bands and similar filter slopes.

Derived-band ASSR amplitudes were determined for each derived-band center frequency in each condition to obtain amplitude profiles. Amplitude profiles were used to calculate the bandwidth and the center frequencies (CFs) for the derived-band ASSRs. Bandwidth at 50% (or −6 dB; $BW_{6\,dB}$) of the maximal derived-band ASSR was determined for each subject's amplitude profile and then averaged across subjects. To compare the width of the $BW_{6\,dB}$ across carrier frequency, two types of transformations were used. The first transformation was conversion into an octave scale, given by the following equation:

$$\mathrm{BW(octaves)} = \log_2(\mathrm{HF} \div \mathrm{LF}), \tag{1}$$

where HF is high-frequency edge (in Hz) and LF is the low-frequency edge (in Hz) of the amplitude profile at 50% maximal peak derived-band ASSR amplitude. For example, a bandwidth of 1 octave centered at 1000 Hz would have a low-frequency edge equal to 707 Hz and a high-frequency edge of 1414 Hz, giving an linear bandwidth of 707 Hz. The second transformation of the $BW_{6\,dB}$ was conversion into a $Q_{6\,dB}$ measurement, given by

$$Q_{6\ dB} = BW_{6\ dB} \div \text{carrier frequency} \tag{2}$$

(Hartmann, 1997).

Derived-band center frequencies were calculated as the geometric mean of the low- and high-frequency edges at 50% maximal amplitude on the amplitude profiles, given by

$$\text{center frequency} = \sqrt{\mathrm{LF} \times \mathrm{HF}}. \tag{3}$$

Center frequencies (CFs) were compared between stimuli of different carrier frequencies as a percent of stimulus carrier frequency or as octaves from the carrier frequency, given by

$$\%\mathrm{CF} = 100\% \times (\mathrm{CF} \div \text{carrier frequency}), \tag{4}$$

$$\mathrm{CF(octaves)} = \log_2(\mathrm{CF} \div \text{carrier frequency}). \tag{5}$$

E. Procedure

For each subject, this study consisted of three recording sessions, each requiring 2–3 h, for a total of 6–9 h. An exception was one participant who completed the study in one overnight session of 7 h. During behavioral measures, participants relaxed in a comfortable reclining chair in a double-walled sound-attenuated booth. During ASSR measures, participants slept or relaxed in the same recliner and booth. Background acoustic noise levels of the booth, which were below the recommended maximum ambient noise levels for audiometric threshold testing using insert earphones (ANSI, 1999), were 12, 10, 10, and 12 dB SPL for 1-octave-wide bands centered at 0.5, 1, 2, and 4 kHz, respectively.

F. Evoked potentials

ASSR data were collected from recording electrodes at the vertex (Cz) and on the back of the neck, in the midsagittal plane just below the hairline. A forehead placement was used for the ground electrode. Interelectrode impedances were less than 3 kOhms at 10 Hz. The EEG was filtered using a bandpass of 30 to 250 Hz (12 dB/octave), amplified 80 000 times, and AD-converted at a rate of 500 Hz. An EEG recording sweep contained 16 sections of 1.024 s each. Sections contaminated by muscle or movement artifacts (i.e., having voltages exceeding $\pm 40\ \mu$V) were rejected from averaging. EEG recordings ranged from 6 to 48 sweeps per condition by HPN cutoff frequency, taking approximately 2 to 14 min per recording.

For online analysis, fast Fourier transform (FFT) converted ASSR average time-domain waveforms into the frequency domain. The FFT resolution was 0.061 Hz, spanning from 0 to 250 Hz. Amplitudes were measured from baseline to peak. Relative ASSR amplitudes were calculated as percentages of an individual's ''nonmasked'' ASSR amplitude (i.e., 16-kHz HPN masker). These were then averaged across subjects to obtain mean relative amplitudes. Additionally, grand mean waveforms were obtained by averaging the time-domain waveforms across all subjects and then transforming this grand average into the frequency domain. This procedure takes into account the phases of the individual responses, and was used to determine if only averaging individuals' amplitudes was valid. ASSRs were determined as ''response present'' or ''no response'' by comparing the amplitude at f_m and the average amplitude of the background noise in 60 adjacent spectral frequencies on either side of f_c (Dobie and Wilson, 1996; Lins *et al.*, 1995; Zurek, 1992). A response was considered present when the F ratio of the signal to noise was significant at p values <0.01. A no response required averaging of the EEG until a level of average background noise amplitude was less than 8.5 nanovolts (nV) *and* $p > 0.20$. Nonsignificant response amplitudes were given a value equal to the average background noise amplitude in adjacent frequencies (i.e., residual noise).

G. Statistical analysis

For statistical analyses, the HPN cutoff frequencies and derived-band center frequencies were normalized to the stimulus carrier frequency. For example, an HPN cutoff frequency or a derived-band center frequency of 1 kHz was classified as ''plus 1 octave'' for the 500-Hz AM tone and ''minus 1 octave'' for the 2000-Hz AM tone. This allowed for comparisons of results across all carrier frequencies.

Three-way repeated-measures analyses of variance (ANOVA) were used to analyze ASSR or derived-band ASSR relative amplitudes across two conditions (single and multiple), two carrier frequencies (500 and 2000 Hz), and six normalized HPN cutoff frequencies (−1.0, −0.5, 0.0, 0.5, 1.0, and 1.5 octaves) or five normalized derived-band center frequencies (−1.0, −0.5, 0.0, 0.5, and 1.0 octaves). Two-way repeated-measures ANOVAs were used to analyze ASSR or derived-band ASSR relative amplitudes for the multiple-stimulus condition across four carrier frequencies (500, 1000, 2000, and 4000 Hz) and six normalized HPN cutoff frequencies (−1.0, −0.5, 0.0, 0.5, 1.0, and 1.5 octaves) or five normalized derived-band center frequencies (−1.0, −0.5, 0.0, 0.5, and 1.0 octaves). One-way repeated-measures ANOVAs were used to analyze $Q_{6\,dB}$ or %CF across four carrier frequencies (500, 1000, 2000, and 4000

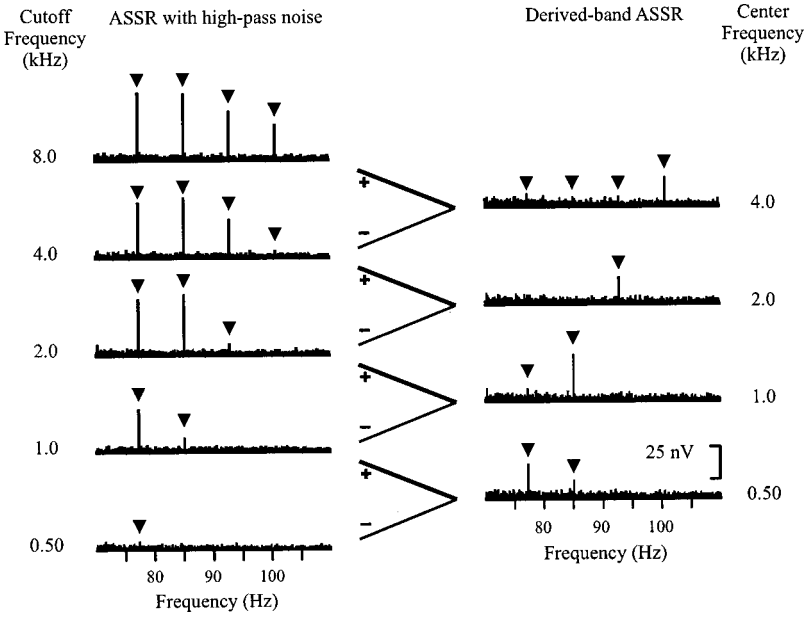

FIG. 2. Grand mean EEG spectra for the multiple-stimulus condition. On the left are EEG spectra for multiple ASSRs in the presence HPN with cutoff frequencies ranging from 0.5 to 8.0 kHz (designated on the far left). Statistically significant ($p<0.01$) ASSRs are designated by arrowheads. On the right are shown derived-band ASSRs for one-octave derived bands obtained by sequential subtraction of the ASSR in the presence of HPN.

Hz) in the multiple-stimulus condition. Two-way repeated-measures ANOVAs were used to analyze $Q_{6\,dB}$ or %CF across two conditions (single and multiple) and two carrier frequencies (500 and 2000 Hz). Huynh–Feldt epsilon correction factors for degrees of freedom were used when appropriate. Results of these ANOVAs were considered significant if $p<0.01$. Newman–Keuls *post hoc* comparisons were performed only for significant main effects and interactions. Results of the *post hoc* tests were considered significant if $p<0.05$.

III. RESULTS

A. Multiple-stimulus condition

Figure 2 shows the grand-mean amplitude spectra for ASSRs to multiple AM tones in HPN masking and for derived-band ASSRs. When the HPN cutoff frequency changed from 8.0 to 4.0 kHz, ASSRs to 500-, 1000-, 2000-, and 4000-Hz AM tones decreased by 10 (19%), 5 (10%), 8 (22%), and 23 nV (82%), respectively. These attenuations were reflected in the derived band centered at 4.0 kHz, such that there were significant ($p<0.01$) derived-band ASSRs with amplitudes of 10, 8, 8, and 23 nV for the 500-, 1000-, 2000-, and 4000-Hz AM tones, respectively. Lowering the HPN cutoff frequency from 4.0 to 2.0 kHz resulted in a 21-nV (72%) attenuation of the grand-mean ASSRs to the 2000-Hz AM tone modulated at 93 Hz, whereas the largest change in grand-mean ASSR amplitude for the other AM tones was 1 nV. The differences in these grand-mean ASSR amplitudes between the two HPN conditions was revealed in the derived band centered at 2.0 kHz, such that the only significant derived-band ASSR was to the 2000-Hz AM tone (21 nV). Lowering of the HPN cutoff frequency from 2.0 to 1.0 kHz resulted in grand-mean ASSR amplitude reductions of 10 (23%), 35 (74%), 6 (75%), and 0 nV (0%) for the 500-, 1000-, 2000-, and 4000-Hz AM tones. The corresponding derived band centered at 1.0 kHz had significant responses only to 500- and 1000-Hz AM tones (10 and 37 nV, respectively). Similar grand-mean amplitude attenuation and derived-response patterns were seen for other HPN cutoff frequencies, except that there were significant responses in derived bands centered at 4.0 to 8.0 kHz (not shown) for all AM tones.

1. HPN masking

Figure 3 depicts the average of individual ASSR relative amplitudes, plotted as a function of HPN cutoff frequency (in

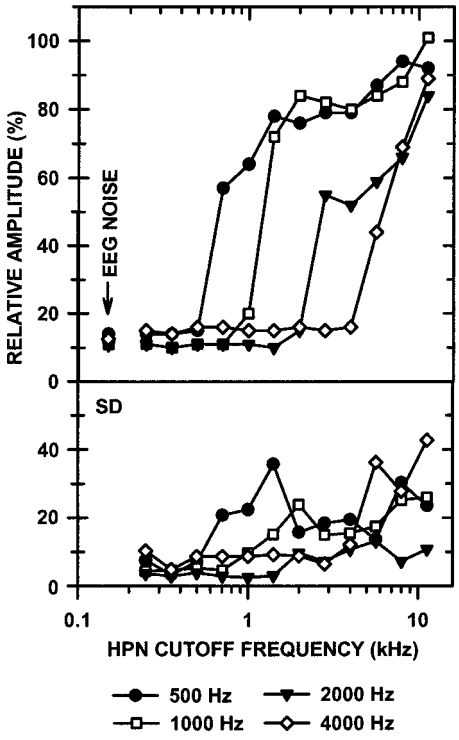

FIG. 3. Mean and standard deviation (s.d.; lower panel) of relative amplitudes (% of ''nonmasked'') for ASSRs to 60 dB SPL AM tones of 500, 1000, 2000, and 4000 Hz recorded in HPN masking for the multiple-stimulus condition. Mean estimates of the noise floor (% of ''nonmasked'') with respect to stimulus carrier frequency are designated at the HPN cutoff frequency of 0.150 kHz.

TABLE I. Comparison of ASSRs to multiple (four) stimuli at different carrier frequencies. Results of two-way repeated measures ANOVAs for ASSRs in HPN and derived-band ASSR.

Effect	ASSR in HPN				Derived-band ASSR			
	df	F	ε[a]	p[b]	df	F	ε	p
Carrier frequency[c]	3, 24	1.92	0.8	0.168	3, 24	2.65	0.42	0.13
HPN[d] or CF[e]	5, 40	109	0.5	<0.001[f]	4, 32	30.5	1	<0.001[f]
Carrier frequency x HPN or CF	15, 120	3.86	0.4	0.004[f]	12, 96	2.19	0.5	0.061

[a]Huynh–Feldt epsilon correction factor for degrees of freedom.
[b]Probability reflects corrected degrees of freedom.
[c]Carrier frequency: 500, 1000, 2000, and 4000 Hz.
[d]High-pass noise cutoff frequency normalized to carrier frequency: −1.0, −0.5, 0, 0.5, 1.0, and 1.5 octaves from stimulus frequency.
[e]Derived-band center frequency normalized to carrier frequency: −1.0, −0.5, 0, 0.5, and 1.0 octaves from stimulus frequency.
[f]Significant ($p<0.01$).

$\frac{1}{2}$-octave steps) obtained in the multiple-stimulus condition. Mean (± standard deviation) nonmasked ASSR amplitudes for multiple AM tones of 500, 1000, 2000, and 4000 Hz were 65 ± 33, 68 ± 24, 60 ± 16, and 45 ± 17 nV, respectively. Looking across AM tones, the means of individual ASSR amplitudes for HPN cutoff frequencies greater than the carrier frequency were reduced by 0 to 48% from nonmasked ASSRs. For HPN cutoff frequencies at and below the carrier frequency, means of individual amplitudes were attenuated by at least 80% from nonmasked ASSR amplitudes and typically fell to the EEG residual noise floor (plotted at 0.15 kHz) within the first $\frac{1}{2}$ octave of the stimulus frequency.

To identify any differential masking effects across carrier frequencies, HPN cutoff frequencies were normalized to the stimulus carrier frequency. Overall, there were no significant differences between carrier frequencies, as shown by ANOVA results in Table I (left half). However, ASSR relative amplitudes in response to 2000-Hz AM tones were significantly lower than responses to 1000- and 4000-Hz AM tones, for cutoff frequencies greater than $\frac{1}{2}$ octave above the carrier frequency (*post hoc* analyses of the significant carrier frequency by HPN interaction are shown in Table I). When collapsed across carrier frequency, ASSR relative amplitudes for HPN cutoff frequencies above the carrier frequency were significantly larger than amplitudes for HPN cutoff frequencies at and below the carrier frequency (significant HPN effect, Table I).

2. Derived-band ASSR

Figure 4 illustrates the place specificity as determined by the derived-band response technique for the multiple-stimulus ASSR. The maxima of the mean of individual ASSR relative amplitudes for the derived-band ASSR profiles ranged from 55% to 70% of ''nonmasked'' ASSR amplitudes. These maxima occurred in derived-bands at or $\frac{1}{2}$ octave below the carrier frequency. Mean amplitudes for derived-bands one-octave below the carrier frequency are not different from the noise. The response amplitudes for derived bands one octave above the carrier frequency are greater than the noise floor for the 500- and 4000-Hz stimuli. Mean amplitude profiles for the 1000- and 2000-Hz stimuli do not show this asymmetry in amplitude profiles.

No significant differences in derived-band ASSR amplitude profiles occurred between carrier frequencies (500 to 4000 Hz) when derived-band center frequencies were normalized to octaves above and below the carrier frequency (carrier frequency effect and interaction, Table I). A significant main effect of derived-band center frequency (Table I) was caused by the expected peak-like shape of the amplitude profile. *Post hoc* tests revealed that amplitudes for derived-band center frequencies at and $\frac{1}{2}$ octave below the carrier frequency were significantly larger than those at other derived-band frequencies.

Place specificity for the multiple-stimulus condition was

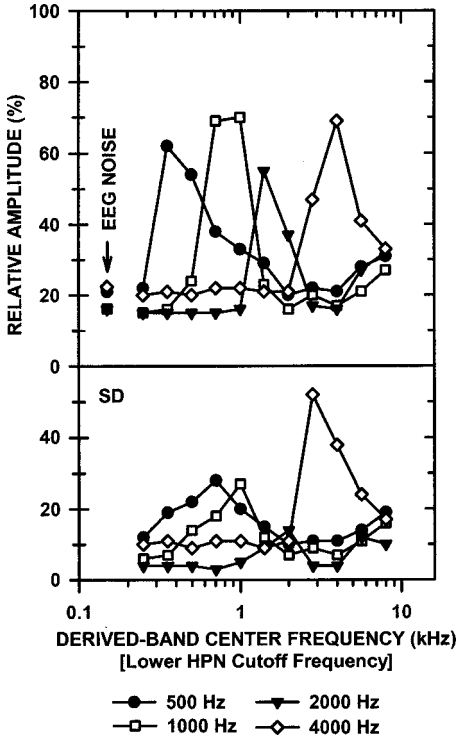

FIG. 4. Mean and standard deviation (s.d.; lower panel) of relative amplitudes (% of ''nonmasked'') for one-octave-wide derived-band ASSRs to 60 dB SPL AM tones of 500, 1000, 2000, and 4000 Hz for the multiple-stimulus condition. Mean estimates of the noise floor (% of ''nonmasked'') with respect to stimulus carrier frequency are designated at the derived-band center frequency of 0.150 kHz.

TABLE II. Measurements for derived-band multiple-stimulus ASSRs (means and standard deviations).

Measure	AM tone carrier frequency			
	500 Hz	1000 Hz	2000 Hz	4000 Hz
$BW_{6\,dB}$ (Hz)	476±220	737±226	1177±324	3039±890
(Octaves)[a]	1.21±0.30	1.19±0.27	1.02±0.21	1.03±0.28
CF (Hz)	555±253	858±98	1602±118	4185±703
(Octaves)[b]	0.05±0.53	−0.23±0.16	−0.32±0.11	0.05±0.23
$Q_{6\,dB}$	1.23±0.32	1.23±0.29	1.44±0.34	1.47±0.44
% CF (%)	111±51	86±10	80±6	105±18

[a]Octave scale for $BW_{6\,dB}$.
[b]Octaves from carrier frequency.

evaluated by calculating the $BW_{6\,dB}$, CF, $Q_{6\,dB}$, and %CFs for derived-band ASSR amplitude profiles (Table II). Amplitude profiles for all carrier frequencies had $BW_{6\,dB}$ approximately one-octave wide and CFs within $\frac{1}{4}$ octave of the stimulus frequency. One-way ANOVAs revealed no significant differences across carrier frequencies for $Q_{6\,dB}$ or for %CF ($p=0.28$ and $p=0.13$, respectively).

B. Single- versus multiple-stimulus condition

Figure 5 shows the grand mean amplitude spectra for ASSRs to *single* 500-Hz AM tones (modulated at 77 Hz) in HPN masking and for the corresponding derived-band-ASSRs. The derived band centered at 2.0 kHz had a 13-nV ASSR to a 500-Hz AM tone, which is more than twice the difference (6 nV) in ASSR amplitudes between the two corresponding HPN cutoff frequencies of 2.0 and 4.0 kHz. The derived band centered at 1.0 kHz showed there was a small, yet significant, 9-nV ASSR to a 500-Hz AM tone. This is inconsistent with only a 1-nV difference between ASSR amplitudes of 27 and 26 nV for ASSR in HPN with cutoff frequencies of 2.0 and 1.0 kHz, respectively. The derived band centered at 0.5 kHz had a 24-nV ASSR to a 500-Hz AM tone, which corresponded to the amplitude reduction when the HPN cutoff frequency was lowered from 1.0 to 0.5 kHz. No change in ASSR amplitude to a 500-Hz AM tone occurred when the HPN cutoff frequency decreased from 0.5 to 0.25 kHz. The corresponding derived band centered at 0.25 kHz showed a nonsignificant ASSR to a 500-Hz AM tone.

Figure 6 shows the grand mean amplitude spectra for ASSRs to *single* 2000-Hz AM tones, modulated at 93 Hz, in HPN masking and for the corresponding derived-band ASSRs. The ASSR amplitude to the 2000-Hz AM tone was reduced by 11 nV (50%) when the HPN cutoff frequency decreased from 8.0 to 4.0 kHz. This amplitude reduction was revealed by the small but significant derived-band ASSR (12 nV) in the derived band centered at 4.0 kHz. Lowering of the HPN cutoff frequency 4.0 to 2.0 kHz resulted in an additional 10-nV (90%) reduction in ASSR amplitude. This reduction was reflected by a significant derived-band ASSR of 11 nV for the derived band centered at 2.0 kHz. Further lowering of the HPN cutoff frequency resulted in no more than a 2-nV change in amplitude, and the corresponding derived bands revealed nonsignificant ASSRs.

1. HPN masking

Figure 7 shows a comparison of the mean of individual ASSR relative amplitudes between single- and multiple-

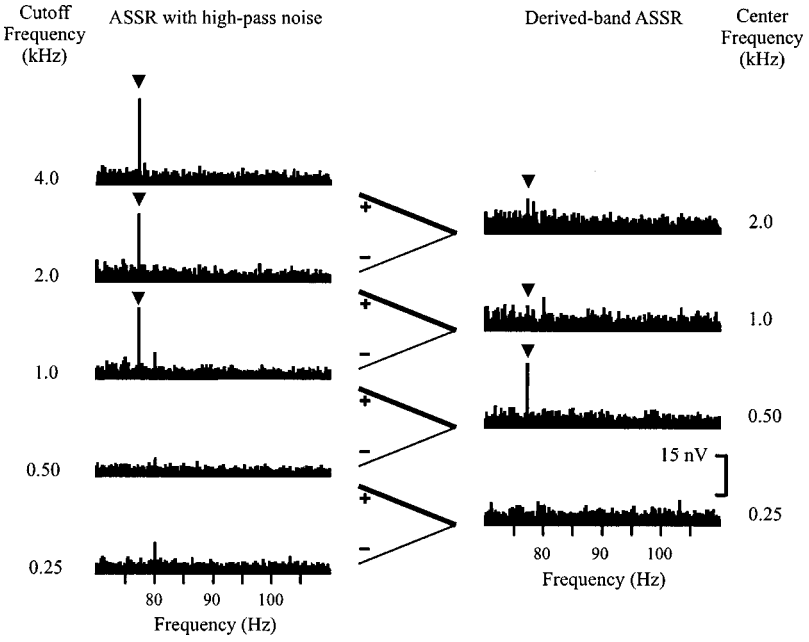

FIG. 5. Grand mean EEG spectra for the single 500-Hz AM tone condition. On the left are EEG spectra for an ASSR evoked by a 500-Hz AM tone in the presence of HPN with cutoff frequencies ranging from 0.25 to 4.0 kHz (designated on the far left). Statistically significant ($p<0.01$) ASSR are designated by arrowheads. On the right are shown derived-band ASSRs for one-octave derived bands obtained by sequential subtraction of the ASSR in the presence of HPN.

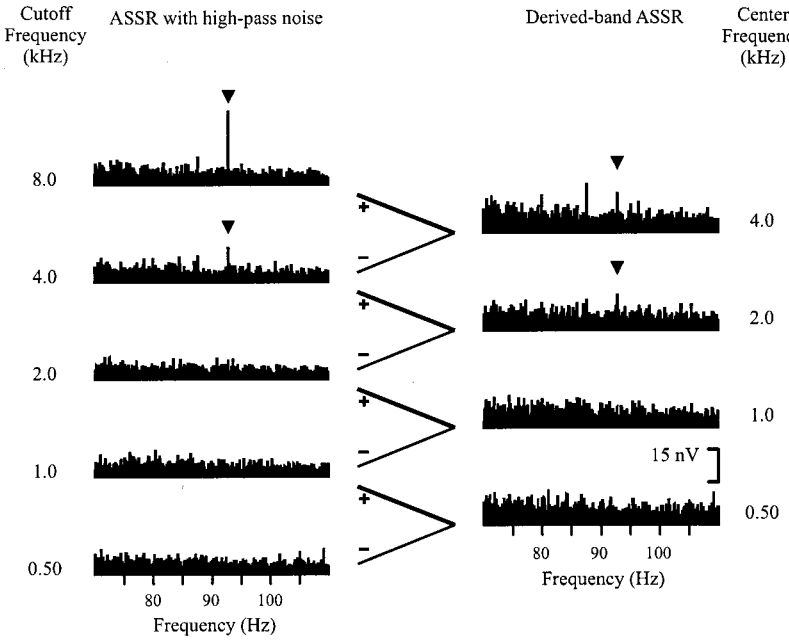

FIG. 6. Grand mean EEG spectra for the single 2000-Hz AM tone condition. On the left are EEG spectra for an ASSR evoked by a 2000-Hz AM tone in the presence of HPN with cutoff frequencies ranging from 0.5 to 8.0 kHz (designated on the far left). Statistically significant ($p<0.01$) ASSR are designated by arrowheads. On the right are shown derived-band ASSRs for one-octave derived bands obtained by sequential subtraction of the ASSR in the presence of HPN.

stimulus conditions, plotted as a function of HPN cutoff frequency (in $\frac{1}{2}$-octave steps). Mean ($\pm$standard deviation) nonmasked ASSR amplitudes for single AM tones of 500 and 2000 Hz were 72 ± 56 and 58 ± 20 nV, respectively. This figure shows that the HPN amplitude profiles were similar between single- and multiple-stimulus conditions. However, there are somewhat larger amplitudes (on average) at some HPN cutoff frequencies for the single-stimulus compared to the multiple-stimulus condition.

Results from a three-way ANOVA on the HPN data, however, indicated no significant differences for relative ASSR amplitude between single- and multiple-stimulus conditions, as well as no significant interactions involving condition (Table III). There was no significant effect of carrier frequency; however, there was an interaction of carrier frequency by HPN cutoff frequency (Table III). *Post hoc* analyses revealed that ASSR amplitudes for HPN cutoff frequencies greater than $\frac{1}{2}$ octave from the carrier frequency were significantly larger for 500-Hz than for 2000-Hz AM tones. As expected, there was a significant effect of HPN cutoff frequency when averaged across conditions and carrier frequencies (Table III). *Post hoc* analyses uncovered that ASSR amplitudes for HPN cutoff frequencies $\frac{1}{2}$ octave and greater than the carrier frequency were larger than those for HPN cutoff frequencies less than and equal to the carrier frequency.

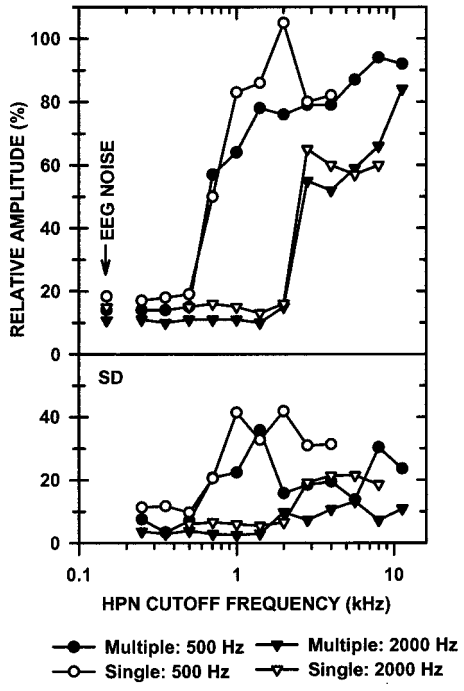

FIG. 7. Mean and standard deviation (s.d.; lower panel) of relative amplitudes (% of ''nonmasked'') for ASSRs to 60 dB SPL AM tones of 500 and 2000 Hz recorded in HPN masking for single- and multiple-stimulus conditions. Mean estimates of the noise floor (% of ''nonmasked'') with respect to stimulus carrier frequency and condition are designated at the HPN cutoff frequency of 0.150 kHz.

2. Derived-band ASSR

Means of individual ASSR relative amplitudes for 1-octave-wide derived bands, obtained in $\frac{1}{2}$-octave steps, were compared between single- and multiple-stimulus conditions (Fig. 8). Amplitude profiles for the 500- and 2000-Hz AM tones were similar between conditions, except that the peaks of the amplitude profile for the 500-Hz AM tone were at derived-band center frequencies of 0.5 and 0.354 kHz for the single- and multiple-stimulus conditions, respectively. Additionally, there were larger relative amplitudes for the single 500-Hz AM tone at derived-band center frequencies from 0.5 to 2 kHz compared to the multiple-stimulus condition. For the 2000-Hz AM tone, there were larger relative amplitudes at derived-band center frequencies from 1.41 to 4 kHz for the single-stimulus condition compared to the multiple-stimulus condition. However, despite these apparent differences in means, they did not reach significance (Table III). Furthermore, there were no significant interactions involving condition. *Post hoc* analyses of the expected significant main effect of derived-band center frequency revealed

TABLE III. Comparison of ASSRs for single- and multiple-stimulus conditions. Results of three-way repeated measures ANOVAs for ASSR in HPN and derived-band ASSR.

	ASSR in HPN				Derived-band ASSR			
Effect	df	F	ε[a]	p[b]	df	F	ε	p
Condition[c]	1, 8	1.05	1	0.336	1, 8	3.24	1	0.11
Carrier frequency[d]	1, 8	2.83	1	0.131	1, 8	2.81	1	0.132
HPN[e] or CF[f]	5, 40	243.5	0.67	<0.001[g]	4, 32	35.09	0.415	<0.001[g]
Condition x Carrier frequency	1, 8	0.02	1	0.884	1, 8	0.09	1	0.768
Condition x HPN or CF	5, 40	0.69	0.53	0.553	4, 32	2.69	0.523	0.095
Carrier frequency x HPN or CF	5, 40	8.87	0.68	<0.001[g]	4, 32	4	1	0.010[g]
Condition x Carrier frequency x HPN or CF	5, 40	1.31	0.71	0.291	4, 32	0.82	0.547	0.468

[a]Huynh–Feldt epsilon correction factor for degrees of freedom.
[b]Probability reflects corrected degrees of freedom.
[c]Condition: single versus multiple stimuli.
[d]Carrier frequency: 500 vs 2000 Hz.
[e]High-pass noise cutoff frequency normalized to carrier frequency: −1.0, −0.5, 0, 0.5, 1.0, and 1.5 octaves from stimulus frequency.
[f]Derived-band center frequency normalized to carrier frequency: −1.0, −0.5, 0, 0.5, 1.0 octaves from stimulus frequency.
[g]Significant ($p<0.01$).

that derived-band ASSR relative amplitudes were significantly larger for derived-band center frequencies at and $\frac{1}{2}$ octave below the carrier frequency compared to derived-band center frequencies greater than and equal to $\frac{1}{2}$ octave above, as well as one-octave below the carrier frequency ($p<0.025$). There was no carrier frequency effect (Table III). However, there was a significant interaction between carrier frequency and derived-band center frequency. *Post hoc* analyses revealed significantly larger derived-band ASSRs to the 500-Hz than 2000-Hz AM tone for derived-band center frequencies equal to and $\frac{1}{2}$ octave greater than their respective carrier frequencies ($p<0.002$).

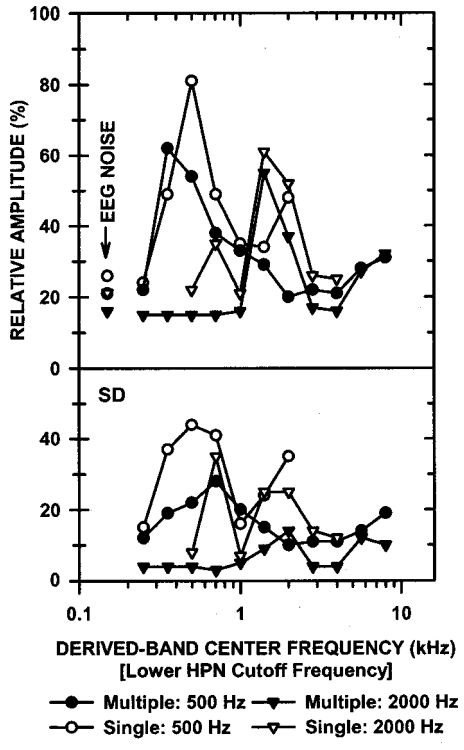

FIG. 8. Mean and standard deviation (s.d.; lower panel) of relative amplitudes (% of ''nonmasked'') for one-octave-wide derived-band ASSRs to 60 dB SPL AM tones of 500 and 2000 Hz for the single- and multiple-stimulus conditions. Mean estimates of the noise floor (% of ''nonmasked'') with respect to stimulus carrier frequency are designated at the derived-band center frequency of 0.150 kHz.

For the single-stimulus condition, mean values of $BW_{6\,dB}$ were approximately one-octave wide and mean CFs were generally within $\frac{1}{4}$ octave of the carrier frequency (see Table IV). These results were not different from measures of place specificity for the multiple-stimulus condition, as revealed by two-way repeated-measures ANOVA. There was no significant difference in $Q_{6\,dB}$ or %CF between conditions (single versus multiple), between carrier frequency (500 versus 2000 Hz), and no condition by carrier frequency interactions.

IV. DISCUSSION

The frequency specificity of an auditory-evoked potential, such as the ASSR, can be subdivided into three aspects: acoustic specificity of the stimulus, cochlear place specificity, and frequency specificity of central auditory neurons. These will be discussed below in greater detail regarding the multiple and single ASSRs.

A. Acoustic specificity of the stimulus

A stimulus' acoustic specificity is identified as the amount of spectral splatter around the nominal frequency (Durrant, 1983). The amount of spectral splatter of a stimulus is dependent on duration, rise/fall times, gating, transfer function of the transducer, and resonant properties of the acoustic coupler (Burkard, 1984; Durrant, 1983; Harris, 1978; Nuttall, 1981). It is important when estimating a hear-

TABLE IV. Measurements for derived-band single- and multiple-stimulus ASSRs (means and standard deviations).

	AM tone carrier frequency			
	500 Hz		2000 Hz	
Measure	Single[a]	Multiple[b]	Single	Multiple
$BW_{6\,dB}$ (Hz)	486±193	476±220	1371±512	1177±324
(Octaves)[c]	1.20±0.35	1.21±0.30	1.11±0.28	1.02±0.21
CF (HZ)	558±128	555±253	1691±210	1602±118
(Octaves)[d]	0.13±0.29	0.05±0.53	−0.25±0.18	−0.32±0.11
$Q_{6\,dB}$	1.25±0.35	1.23±0.32	1.32±0.29	1.44±0.34
% CF (%)	112±26	111±51	85±11	80±6

[a]Single-stimulus condition.
[b]Multiple-stimulus condition.
[c]Octave scale for $BW_{6\,dB}$.
[d]Octaves from carrier frequency.

ing threshold for a specific frequency to limit the amount of spectral splatter so as to limit activation of the cochlear regions which have characteristic frequencies away from the nominal stimulus frequency. If there is a large amount of spectral splatter, additional frequencies may be used by the auditory system to produce a response. Thus, thresholds for the frequency of interest would be underestimated.

Because the brief tones required for the ABR need to have rapid onsets and short durations, their spectra show considerable spectral splatter (Hartmann, 1997). Brief tones typically used to evoke ABRs thus have sidelobes that may activate cochlear regions away from the frequency of interest. When using high-intensity brief tones to elicit ABRs, it may be necessary to add notched-noise masking to limit sidelobe activation of the cochlea (Picton, 1991; Picton *et al.*, 1979; Stapells and Oates, 1997; Stapells *et al.*, 1994; Stapells *et al.*, 1990; Stapells *et al.*, 1985). Unlike brief tones, the spectral splatter for long-duration AM tones is confined to three spectral peaks, one peak at the carrier frequency and two side peaks at a frequency of plus/minus 1 modulation frequency from the carrier frequency. The spectral spread for AM tones modulated between 77–101 Hz ranges from 154–202 Hz at minus 6 dB from peak amplitude and is centered around the carrier frequency. This suggests that AM tones would be preferable over brief tones for use in estimating hearing thresholds. However, acoustic spectral splatter is only one aspect of frequency specificity for the ASSR. Place specificity and neuronal specificity also play important roles when using evoked potentials to estimate hearing thresholds.

B. Cochlear place specificity

Due to basilar-membrane mechanics, the frequency components of a stimulus may not activate only discrete regions of the cochlea with characteristic frequencies specific to the stimulus' spectral components. Both upward and downward spread of activation exists in the cochlea. Albeit, there is greater upward spread of excitation whereby low-frequency stimuli of moderate-to-high intensities can cause appreciable displacement of the basal regions of the cochlea that have characteristic frequencies above the spectral components in the stimulus (Dallos, 1996). Because regions away from the frequency of interest are being activated, this spread of activation may also contribute to an underestimation of hearing thresholds, as would spectral splatter discussed above. Increasing the intensity of the stimulus results in greater spread of activation within the cochlea due both to upward spread of activation and to more-intense acoustic sidelobes that exceed the thresholds at these frequencies. Thus, it is important to identify the extent of the spread of activation or place specificity for moderate-to-high-intensity stimuli. A *caveat* to the present study is that only moderately intense (60 dB SPL) tones were used. Presenting higher intensity AM tones would require higher levels of masking, which would have exceeded our safety limits.

1. Place specificity of multiple ASSRs

Results from this study show good place specificity for the multiple-ASSR method. Significant reductions in relative amplitudes for HPN cutoff frequencies above $\frac{1}{2}$ octave from the carrier frequency suggest some upward spread of excitation. However, the largest reduction in ASSR relative amplitudes is when the HPN cutoff frequency is lowered from $\frac{1}{2}$ octave above the carrier frequency to the carrier frequency. This large differential in masking suggests that large contributions to responses are from cochlear regions with characteristic frequencies between the stimulus frequency and $\frac{1}{2}$ octave above. These results are analogous to data reported in a HPN study of tone-evoked ABR and MLR (Oates and Stapells, 1997a). Oates and Stapells (1997a) reported significant decreases in ABR wave $V-V'$ and MLR wave $Na-Pa$ when HPN cutoff frequencies were lowered from $\frac{1}{2}$ octave above (707 or 2830 Hz) the stimulus frequency to the stimulus frequency (500 or 2000 Hz). Thus, HPN data for ASSR show similar place specificity to those of the ABR and MLR.

In contrast to HPN data, the derived-band response method delineates both high- and low-frequency sides of the cochlear regions that contribute to ASSRs. Derived-band ASSR results reveal reasonably narrow activation of the cochlea for all carrier frequencies. An upward spread of activation can be seen for the 500- and 4000-Hz mean amplitude profiles (Fig. 4) in that there is a shallower sloping function for the high-frequency sides of the profiles than the steep-sloping function for the low-frequency side. This asymmetry

suggests that the stimulus activates regions basal to the characteristic frequency as well as regions with characteristic frequencies equal to the stimulus frequency. Regions more than $\frac{1}{2}$ octave apical to the stimulus frequency are less activated by the stimulus as compared to basal regions greater than $\frac{1}{2}$ octave from the nominal stimulus frequency. Visual observations may suggest that there is a difference in place specificity between stimuli. However, this noticeable difference is not significant, as indicated by the lack of interaction between carrier frequency and derived-band ASSRs. Furthermore, mean $BW_{6\,dB}$ results demonstrate that ASSRs to AM tones predominantly reflect activation of cochlear regions with characteristic frequencies from approximately $\frac{1}{2}$ octave below to $\frac{1}{2}$ octave above the carrier frequency, with no difference between carrier frequency. This good place specificity of ASSRs is in agreement with that reported by John *et al.* (1998). Using AM tones of various carrier frequencies to mask ASSRs to a 60-dB SPL, 1000-Hz AM tone modulated at 80.9 Hz, John and colleagues reported significant reductions in ASSR amplitudes when the masker AM tone was within $\frac{1}{2}$ octave of the 1000-Hz AM tone. Reduction in ASSR amplitudes shown by John *et al.* may be due to a demodulation of the response to the AM tone by the addition of a masking tone, instead of the suggested direct masking, as pointed out by Bernstein (1994). That is, a pure tone presented simultaneously with an AM tone can significantly reduce the amplitude of the energy at the modulation frequency (Bernstein, 1994). Results from the present study, which show that there is a significant masking within $\frac{1}{2}$ octave of the carrier frequency, however, support the claim of direct masking made by John *et al.* (1998). Moreover, other carrier frequencies (500-, 2000-, and 4000-Hz) also showed good place specificity, as indicated by results from the present study.

For derived bands centered at 5.66 and 8 kHz, response amplitudes are significantly greater than the noise floor for all stimuli (Fig. 4). This result was not expected for AM tones of 500 to 2000 Hz because the derived-band amplitude profile dips to nonsignificant ASSR amplitudes (i.e., to the EEG noise floor) and then rises to significant responses in the derived bands centered at 5.66 and 8.0 kHz. This contradicts the cochlear traveling wave envelopes that do not show this increase in response amplitude for high-frequency regions to these lower frequency stimuli, as is seen in Fig. 4. One possible explanation for this result is that the HPN responses used to calculate the derived-bands (e.g., 8- and 4-kHz responses) have greater differences in phase as compared to lower HPN conditions (i.e., below 2 kHz). Thus, the subtraction of the HPN conditions (8- and 4-kHz responses) with phase differences that are largely out of phase with each other could create large derived-band amplitudes, whereas phase discrepancy for the lower HPN responses are largely in phase. Another possible explanation for an increase in ASSR amplitudes for derived bands at the above 4 kHz is that as the HPN cutoff frequency is increased there is a possible ''release from masking'' of responses in these high-frequency derived-band regions. Consider that all frequency stimuli produce a small amplitude response from cochlear regions above 4 kHz. Also, consider that HPN masking levels used in this study are sufficient to fully mask out all ASSRs, including the ones in derived bands centered at 5.66 and 8 kHz. The HPN masking level might not be sufficient to mask responses from the 8-kHz region and above as compared to the broadband masker. This effect may be explained by assuming that the broadband masking also involves suppression mechanisms in addition to ''line-busy'' effects (Delgutte, 1996). When the HPN cutoff frequency is increased (i.e., less masking of the lower-frequency cochlear regions), there might be less suppression of neurons responding to high-frequency cochlear regions by the less active lower-frequency cochlear regions that are now unmasked. Stapells *et al.* (1985) observed similar phenomena in notched-noised masking of click ABRs. They revealed a waveform earlier in latency than expected when a notch of 0.5 kHz was introduced in the broadband masker. Considering its latency, this earlier wave was suggested to originate in the basal portion of the cochlea and was a result of a release from masking when the notched was introduced. Further investigation into this issue is needed.

Grand-mean data consider the phase of the derived-band ASSRs by averaging the time-domain waveforms of all subjects and then transforming it into the frequency domain; in contrast, mean relative derived-band ASSR amplitudes obtained from individuals do not. The results show that the grand-mean amplitudes (Figs. 2, 5, and 6) are somewhat smaller than the mean relative derived-band ASSR amplitudes (Figs. 4 and 8). This discrepancy is a result of phase variability between subjects because averaging ASSRs that have different phases will result in deconstruction of the time-domain waveform. Although there is some inconsistency in the magnitude of the mean derived-band ASSRs, the amplitude profiles between grand-mean amplitudes and mean amplitudes of individuals are very similar. Both show peak amplitudes at the stimulus frequency and largely diminished responses an octave away. Thus, calculating the amplitude profiles by averaging individual amplitudes seems to be a valid method for determining measures of place specificity.

2. Place specificity of single- versus multiple-ASSR

Another key issue being tested in this study was the possibility of masking within the multiple-stimulus condition. That is, does the presence of the lower-frequency stimuli cause masking of the ASSR to higher-frequency stimuli? Results of the present study indicate no significant differences in measures of place specificity of the ASSR whether AM tones are presented separately or simultaneously. When compared across conditions, HPN data for AM tones of 500 and 2000 Hz show the same decrease in ASSR amplitudes as the HPN cutoff frequency decreases from $\frac{1}{2}$ octave above to the carrier frequency. Comparing between conditions, ASSR amplitudes are greater, on average, for the single-stimulus than the multiple-stimulus condition at HPN cutoff frequencies of 1 to 2 octaves (500 Hz) and 1 to 1.5 octaves above the carrier frequency. These differences may suggest that addition of other AM tones can cause attenuation of response amplitudes. However, differences did not reach significance between single- and multiple-stimulus conditions and suggests that interactions

TABLE V. Measurements for derived-band multiple-stimulus ASSRs and ABRs/MLRs (means, standard deviations, and sample size) and t-test comparisons between ASSR and ABR/MLR.

	Tone carrier frequency					
	500 Hz			2000 Hz		
Measure	ASSR[a]	ABR[b]	MLR[b]	ASSR	ABR	MLR
$BW_{6\,dB}$ (Hz)	481±201	648±182	632±123	1274±427	1726±525	1355±427
Sample size	9	12	12	9	12	12
t-score[c]	···	1.99	2.14	···	2.11	0.65
df	···	19	19	···	19	18
p-value	···	0.061	0.046	···	0.048	0.650

[a]Averaged results across single- and multiple-stimulus conditions.
[b]Results for 53- and 52-dB nHL brief-tones (exact Blackman gated) of 500 and 2000 Hz, respectively (Oates and Stapells, 1997b).
[c]Comparison of means between ASSR-ABR and ASSR-MLR.
df=degrees of freedom calculated for independent samples (Howell, 1997, pp. 192).

between stimuli, such as masking, do not appear to occur when simultaneously presenting multiple (four) AM tones that have carrier frequencies an octave apart. Thus, the multiple-ASSR technique would provide an advantage of being able to assess multiple place-specific thresholds in less time as compared to single-stimulus methods. This has also been shown for multiple-stimulus techniques used to evoke transient ABRs (Hoke *et al.*, 1991).

Comparing ASSRs in HPN masking between carrier frequencies, however, showed that amplitudes are significantly diminished for 2000-Hz compared to 500-Hz AM tones. This difference can also be seen in ABR and MLR data reported by Oates and Stapells (1997a). This trend is supported by behavioral results showing that detection of a 2000-Hz stimulus is more affected by masking noise than detection of a 500-Hz tone (Reed and Bilger, 1973).

Analyses of derived-band ASSR amplitude profiles between conditions further confirms that place specificity is not significantly different between multiple- and single-ASSR methods. There were differences, though statistically nonsignificant, between the peak amplitudes of the derived-band profiles. For the 500-Hz AM tone in the multiple-stimulus condition, the peak amplitude is smaller and shifted more apically than in the single-stimulus condition. Also, there are smaller derived-band relative amplitudes at the carrier frequency and above for the 2000-Hz AM tone in the multiple-stimulus condition, as compared to the single-stimulus condition. These results may support the hypothesis that there are indeed interactions between stimuli that affect the derived-band profiles. These differences, however, are not substantial.

3. General comments

For some carrier frequencies, the peak of the derived-band amplitude profiles are $\frac{1}{2}$ octave below the stimulus frequency (e.g., 500 Hz for the multiple-stimulus condition; Fig. 4) or the derived-band ASSR center frequencies are below the stimulus frequency (e.g., 1000 and 2000 Hz; Table II). These observations may suggest that it would be more appropriate to designate the derived-band center frequency as the higher HPN cutoff frequency in the subtraction procedure. However, this would also shift the peaks and center frequencies for the other stimulus frequencies (e.g., 4000 Hz) by $\frac{1}{2}$ octave. In doing this the center frequency for the 4000-Hz AM tone (multiple-stimulus condition) would be 5918 Hz (i.e., 1918 Hz from the stimulus frequency), which is quite different from the more respectable 4185 Hz (i.e., 185 Hz from the stimulus frequency). Data from the present study, therefore, provide more support to specifying the derived-band center frequency as the lower HPN cutoff frequency.

Derived-band ASSR amplitude profiles from this study look similar to derived responses for ABRs and MLRs (Oates and Stapells, 1997b). This comparable place specificity indicates that the high acoustic specificity for AM tones does not directly translate into better place specificity of the ASSRs. For instance, a 1000-Hz AM tone modulated at 85 Hz has an acoustic bandwidth of 170 Hz, whereas the corresponding ASSR to the 1000-Hz AM tone reflects responses from a bandwidth of 737 Hz.

Average $BW_{6\,dB}$ values for the ASSRs, and for ABRs and MLRs to 500- and 2000-Hz tones (Oates and Stapells, 1997b), shown in Table V, reveal similar degrees of place specificity across the different methods. Several of the statistical comparisons using Student t-tests with unequal sample sizes (Howell, 1997), show a better specificity for the ASSR technique with *p* values between 0.01 and 0.10 (see Table V). These differences would be compatible with the increased acoustic specificity of AM tones over the brief tones. Nevertheless, the differences in bandwidths between ABRs/MLRs and ASSRs are small and may not be that meaningful in clinical situations. Further research is needed in patients with steeply sloping hearing losses.

C. Frequency specificity of central auditory neurons

In addition to acoustic specificity and place specificity, the tuning curves of the neurons generating the ASSRs should be considered when discussing the frequency specificity of the auditory-evoked potentials. The cochlea processes sound like a bank of filters centered at different frequencies. In a normal cochlea responding to single tones, the narrow tuning of one of these cochlear filters is directly translated to the primary auditory neurons which innervate a particular cochlear place. Thus, the tuning curves of the auditory-nerve fibers are essentially the same as the activation patterns of the basilar membrane (Pickles, 1988). Some

central neurons preserve the specificity of these primary afferent tuning curves because they are mostly activated by fibers coming from the same cochlear place (i.e., from the same cochlear filter). Other neurons are activated by converging afferent fibers with a range of characteristic frequencies and thus show broader tuning curves (Rhode and Greenberg, 1992). Our results suggest that the central neurons generating ASSRs at modulation frequencies of 75–105 Hz (believed to be within the brainstem; Mauer and Döring, 1999; Herdman *et al.*, 2001) have a frequency specificity broader than that of primary auditory neurons. This suggests that these neurons integrate frequency information over a range of cochlear filters surrounding the carrier frequency of the stimulus.

Most studies of frequency specificity do not use multiple simultaneous stimuli. Processes such as suppression and lateral inhibition may alter the neuronal specificity of the responses when multiple stimuli occur together. The results of the present study suggest that these processes do not significantly affect the responses. However, this lack of effect may be related to the one-octave separation of the carrier frequencies and the moderate intensity level. At higher intensities, significant interactions between all stimuli may occur (John *et al.*, 1998). Even at moderate intensities, there may be some attenuation of the lower-frequency responses by concomitant high-frequency sounds (John *et al.*, 1998; Dolphin and Mountain, 1993). The effects may be quite complex when multiple stimuli are presented to pathological ears. Further research is warranted.

V. CONCLUSIONS

Multiple- and single-ASSR methods exhibit good place specificity. Results indicate that ASSRs reflect activation of narrow regions of the cochlea by AM tones modulated between 70–110 Hz presented at 60 dB SPL. This specificity is as good as or slightly better than that obtained with the transient evoked potentials (ABRs/MLRs) elicited by brief tones. Such differences are not clinically significant and do not seem to provide the ASSR technique with the advantage of a more frequency-specific estimate of hearing thresholds than ABR or MLR methods. Both are equally good.

Place specificity is not altered when multiple (four) stimuli are presented simultaneously, therefore showing that multiple AM tones are processed similarly within the cochlea as compared to single AM tones. Additionally, there is no evidence for the masking of high-frequency stimuli by low-frequency tones presented at 60 dB SPL and one-octave apart, in normal-hearing adults. Given that place specificity is not significantly different between multiple-and single-stimulus conditions, it is clear that the multiple ASSR technique has a considerable advantage of using multiple stimuli to dramatically reduce recording time.

ACKNOWLEDGMENTS

Grants from the Canadian Institutes of Health Research (Picton, Stapells, and John) and the Natural Sciences and Engineering Research Council of Canada (Stapells) supported this research. Anthony Herdman was supported by a Ph.D. Studentship from the Canadian Institutes of Health Research.

ANSI (**1996**). ANSI S3.6-1996, ''Specifications for Audiometers'' (American National Standards Institute, New York).

ANSI (**1999**). ANSI S3.1-1999, ''Maximum Permissible Ambient Noise Levels for Audiometric Test Rooms'' (American National Standards Institute, New York).

Aoyagi, M., Kiren, T., Furuse, H., Fuse, T., Suzuki, Y., Yokota, M., and Koike, Y. (**1994**). ''Pure-tone threshold prediction by 80-Hz amplitude-modulation following response,'' Acta Oto-Laryngol., Suppl. **Suppl. 511**, 7–14.

Aoyagi, M., Kiren, T., Kim, Y., Suzuki, Y., Fuse, T., and Koike, Y. (**1993**). ''Optimal modulation frequency for amplitude-modulation following response in young children during sleep,'' Hear. Res. **65**, 253–261.

Bernstein, L. R. (**1994**). ''Comment on 'The envelope following response (EFR) in the Mongolian gerbil to sinusoidally amplitude-modulated signals in the presence of simultaneously gated pure tones' '' [J. Acoust. Soc. Am. **94**, 3215–3226 (1993)], J. Acoust. Soc. Am. **96**, 1189–1190.

Burkard, R. (**1984**). ''Sound pressure level measurement and spectral analysis of brief acoustic transients,'' Electroencephalogr. Clin. Neurophysiol. **57**, 83–91.

Cohen, L. T., Rickards, F. W., and Clark, G. M. (**1991**). ''A comparison of steady-state evoked potentials to modulated tones in awake and sleeping humans,'' J. Acoust. Soc. Am. **90**, 2467–2479.

Dallos, P. (**1996**). ''Overview: Cochlear neurobiology,'' in *The Cochlea*, edited by P. Dallos, A. N. Popper, and R. R. Fay (Springer, New York), pp. 1–43.

Delgutte, (**1996**). ''Physiological models for basic auditory percepts,'' in *The Cochlea*, edited by P. Dallos, A. N. Popper, and R. R. Fay (Springer, New York), pp. 157–220.

Dobie, R. A., and Wilson, M. J. (**1996**). ''A comparison of *t* test, *F* test, and coherence methods of detecting steady-state auditory-evoked potentials, distortion-product otoacoustic emissions, or other sinusoids,'' J. Acoust. Soc. Am. **100**, 2236–2246.

Dolphin, W. F., and Mountain, D. C. (**1993**). ''The envelope following response (EFR) in the Mongolian gerbil to sinusoidally amplitude-modulated signals in the presence of simultaneously gated pure tones,'' J. Acoust. Soc. Am. **94**, 3215–3226.

Don, M., and Eggermont, J. J. (**1978**). ''Analysis of the click-evoked brainstem potentials in man using high-pass noise masking,'' J. Acoust. Soc. Am. **63**, 1084–1092.

Don, M., Eggermont, J. J., and Brackmann, D. E. (**1979**). ''Reconstruction of the audiogram using brainstem responses and high-pass noise masking,'' Ann. Otol. Rhinol. Laryngol. Suppl. **57**(3 Pt 2), 1–20.

Durrant, J. D. (**1983**). ''Fundamentals of sound generation,'' in *Bases of Auditory Brain-Stem Evoked Responses*, edited by E. J. Moore (Grune & Stratton, New York), pp. 15–49.

Eggermont, J. J. (**1976**). ''Electrocochleography,'' in *Handbook of Sensory Physiology*, edited by W. D. Keidel and W. D. Neff (Springer, New York), pp. 625–704.

Eggermont, J. J., and Don, M. (**1980**). ''Analysis of the click-evoked brainstem potentials in humans using high-pass noise masking. II. Effect of click intensity,'' J. Acoust. Soc. Am. **68**, 1671–1675.

Eggermont, J. J., Spoor, A., and Odenthal, D. W. (**1976**). ''Frequency specificity of tone-burst electrocochleography,'' in *Electrocochleography*, edited by R. J. Ruben, C. Elberling, and G. Salomon (University Park, Baltimore), pp. 215–246.

Griffiths, S. K., and Chambers, R. D. (**1991**). ''The amplitude modulation-following response as an audiometric tool,'' Ear Hear. **12**(4), 235–241.

Harris, F. J. (**1978**). ''On the use of windows for harmonic analysis with the discrete Fourier transform,'' Proceedings of the Institute of Electrical and Electronic Engineers **66**, 51–83.

Hartmann, W. M. (**1997**). *Signals, Sound, and Sensation* (American Institute of Physics, Woodbury, NY).

Herdman, A. T., and Stapells, A. T. (**2001**). ''Thresholds determined using the monotic and dichotic multiple auditory steady-state response technique in normal-hearing subjects,'' Scand. Audiol. **30**, 41–49.

Herdman, A. T., Lins, O., Van Roon, P., Stapells, D. R., Scherg, M., and Picton, T. W. (**2001**). ''Generators of auditory steady-state responses,'' International Evoked Response Audiometry Study Group XVII Biennial Symposium Abstracts, Vancouver, July, p. 115.

Hoke, M., Pantev, C., Ansa, L., Lutkenhoner, B., and Herrmann, E. (**1991**). ''A time-saving BERA technique for frequency-specific assessment of the auditory threshold through tone-pulse series stimulation (TOPSTIM) with simultaneous gliding high-pass noise masking (GHINOMA),'' Acta Oto-Laryngol., Suppl. **482**, 45–56.

Howell, D. C. (**1997**). *Statistical Methods for Psychology* (Wadsworth, Belmont, CA).

John, M. S., Lins, O. G., Boucher, B. L., and Picton, T. W. (**1998**). ''Multiple auditory steady-state responses (MASTER): Stimulus and recording parameters,'' Audiology **37**, 59–82.

John, M. S., and Picton, T. W. (**2000**). ''MASTER: A Windows program for recording multiple auditory steady-state responses,'' Comput. Methods Programs Biomed. **61**(2), 125–150.

Kuwada, S., Batra, R., and Maher, V. L. (**1986**). ''Scalp potentials of normal and hearing-impaired subjects in response to sinusoidally amplitude-modulated tones,'' Hear. Res. **21**, 179–192.

Levi, E. C., Folsom, R. C., and Dobie, R. A. (**1993**). ''Amplitude-modulation following response (AMFR): Effects of modulation rate, carrier frequency, age, and state,'' Hear. Res. **68**, 42–52.

Lins, O. G., Picton, P. E., Picton, T. W., Champagne, S. C., and Durieux-Smith, A. (**1995**). ''Auditory steady-state responses to tones amplitude-modulated at 80–110 Hz,'' J. Acoust. Soc. Am. **97**, 3051–3063.

Lins, O. G., Picton, T. W., Boucher, B. L., Durieux-Smith, A., Champagne, S. C., Moran, L. M., Perez-Abalo, M. C., Martin, V., and Savio, G. (**1996**). ''Frequency-specific audiometry using steady-state responses,'' Ear Hear. **17**, 81–96.

Mauer, G., and Döring, W. H. (**1999**). ''Generators of amplitude modulation following response (AMFR),'' International Evoked Response Audiometry Study Group XVII Biennial Symposium Abstracts, Tromsø, May–June.

Maurizi, M., Almadori, G., Paludetti, G., Ottaviani, F., Rosignoli, M., and Luciano, R. (**1990**). ''40-Hz steady-state response in newborns and in children,'' Audiology **29**, 322–328.

Nousak, J. K., and Stapells, D. R. (**1992**). ''Frequency specificity of the auditory brain stem response to bone-conducted tones in infants and adults,'' Ear Hear. **13**, 87–95.

Nuttall, A. H. (**1981**). ''Some windows with very good sidelobe behavior,'' IEEE Trans. Acoust., Speech, Signal Process. **29**, 84–91.

Oates, P., and Stapells, D. R. (**1997a**). ''Frequency specificity of the human auditory brainstem and middle latency responses to brief tones. I. High-pass noise masking,'' J. Acoust. Soc. Am. **102**, 3597–3608.

Oates, P., and Stapells, D. R. (**1997b**). ''Frequency specificity of the human auditory brainstem and middle latency responses to brief tones. II. Derived response analyses,'' J. Acoust. Soc. Am. **102**, 3609–3619.

Pickles, J. (**1988**). *An Introduction to the Physiology of Hearing* (Academic, San Diego), Chap. 5, pp. 112–162.

Picton, T. W. (**1991**). ''Clinical usefulness of auditory evoked potentials: A critical evaluation,'' J. Speech-Language Pathol. Audiol. **15**, 3–29.

Picton, T. W., Durieux-Smith, A., Champagne, S. C., Whittingham, J., Moran, L. M., Giguère, C., and Beauregard, Y. (**1998**). ''Objective evaluation of aided thresholds using auditory steady-state responses,'' J. Am. Acad. Audiol **9**, 315–331.

Picton, T. W., Ouellette, J., Hamel, G., and Smith, A. D. (**1979**). ''Brainstem evoked potentials to tonepips in notched noise,'' J. Otolaryngol. **8**, 289–314.

Ponton, C. W., Don, M., and Eggermont, J. J. (**1992**). ''Place-specific derived cochlear microphonics from human ears,'' Scand. Audiol. **21**, 131–141.

Rance, G., Dowell, R. C., Rickards, F. W., Beer, D. E., and Clark, G. M. (**1998**). ''Steady-state evoked potential and behavioral hearing thresholds in a group of children with absent click-evoked auditory brain stem response,'' Ear Hear. **19**, 48–61.

Reed, C. M., and Bilger, R. C. (**1973**). ''A comparative study of S/N and E/No,'' J. Acoust. Soc. Am. **53**, 1039–1045.

Rhode, W. S., and Greenberg, S. (**1992**). ''Physiology of the cochlear nuclei,'' in *The Mammalian Auditory Pathway: Neurophysiology*, edited by A. N. Popper and R. R. Fay (Springer-Verlag, New York), pp. 94–152.

Rickards, F. W., Tan, L. E., Cohen, L. T., Wilson, O. J., Drew, J. H., and Clark, G. M. (**1994**). ''Auditory steady-state evoked potentials in newborns,'' Br. J. Audiol. **28**, 327–337.

Stapells, D. R., Galambos, R., Costello, J. A., and Makeig, S. (**1988**). ''Inconsistency of auditory middle latency and steady-state responses in infants,'' Electroencephalogr. Clin. Neurophysiol. **71**, 289–295.

Stapells, D. R., and Oates, P. (**1997**). ''Estimation of the pure-tone audiogram by the auditory brainstem response: A review,'' Audiol. Neuro-Otol. **2**, 257–280.

Stapells, D. R., Picton, T. W., and Durieux-Smith, A. (**1994**). ''Electrophysiologic measures of frequency-specific auditory function,'' in *Principles and Applications in Auditory Evoked Potentials*, edited by J. T. Jacobson (Allyn and Bacon, Needham Heights, MA), pp. 251–283.

Stapells, D. R., Picton, T. W., Durieux-Smith, A., Edwards, C. G., and Moran, L. M. (**1990**). ''Thresholds for short-latency auditory evoked potentials to tones in notched noise in normal-hearing and hearing-impaired subjects,'' Audiology **29**, 262–274.

Stapells, D. R., Picton, T. W., Pérez-Abalo, M., Read, D., and Smith, A. (**1985**). ''Frequency specificity in evoked potential audiometry,'' in *The Auditory Brainstem Response*, edited by J. T. Jacobson (College-Hill, San Diego), pp. 147–177.

Stapells, D. R., and So, M. R. (**1999**). ''High-pass noise masked/derived-band auditory brainstem responses: Cochlear contributions determined by narrow-band maskers,'' XVI Biennial Symposium of the International Evoked Response Audiometry Study Group, Norway, 30 May–3 June, p. 15.

Starr, A., and Don, M. (**1988**). ''Brain potentials evoked by acoustic stimuli,'' in *Human Event-Related Potentials, EEG Handbook*, edited by T. W. Picton (Elsevier, Amsterdam), Revised series, Vol. 3, pp. 97–157.

Suzuki, T., and Kobayashi, K. (**1984**). ''An evaluation of 40-Hz event-related potentials in young children,'' Audiology **23**, 599–604.

Teas, D. C., Eldridge, D. H., and Davis, H. (**1962**). ''Cochlear responses to acoustic transients: An interpretation of whole-nerve action potentials,'' J. Acoust. Soc. Am. **34**, 1438–1459.

Zurek, P. M. (**1992**). ''Detectability of transient and sinusoidal otoacoustic emissions,'' Ear Hear. **13**, 30–310.

Contribution of spectral cues to human sound localization

Erno H. A. Langendijk[a] and Adelbert W. Bronkhorst
TNO Human Factors Research Institute, P.O. Box 23, 3769 ZG Soesterberg, The Netherlands

(Received 14 December 2000; revised 27 June 2002; accepted 27 June 2002)

The contribution of spectral cues to human sound localization was investigated by removing cues in $\frac{1}{2}$-, 1- or 2-octave bands in the frequency range above 4 kHz. Localization responses were given by placing an acoustic pointer at the same apparent position as a virtual target. The pointer was generated by filtering a 100-ms harmonic complex with equalized head-related transfer functions (HRTFs). Listeners controlled the pointer via a hand-held stick that rotated about a fixed point. In the baseline condition, the target, a 200-ms noise burst, was filtered with the same HRTFs as the pointer. In other conditions, the spectral information within a certain frequency band was removed by replacing the directional transfer function within this band with the average transfer of this band. Analysis of the data showed that removing cues in $\frac{1}{2}$-octave bands did not affect localization, whereas for the 2-octave band correct localization was virtually impossible. The results obtained for the 1-octave bands indicate that up–down cues are located mainly in the 6–12-kHz band, and front–back cues in the 8–16-kHz band. The interindividual spread in response patterns suggests that different listeners use different localization cues. The response patterns in the median plane can be predicted using a model based on spectral comparison of directional transfer functions for target and response directions. © *2002 Acoustical Society of America.* [DOI: 10.1121/1.1501901]

PACS numbers: 43.66.Ba, 43.66.Pn, 43.66.Qp [LRB]

I. INTRODUCTION

Although the auditory system is not topographically organized at the sensory level, it can nevertheless resolve sound source locations implicitly from the acoustic signals at both ears. In order to determine the lateral angle of a sound source, the auditory system relies on cues such as the interaural differences in time and intensity (e.g., Blauert, 1997). In the median plane, however, these binaural cues are virtually absent and, although they may still be perceptually relevant, for example for externalization of sounds, they are probably not used for sound localization (Morimoto and Nomachi, 1982). In fact, also with respect to locations outside the median plane, the interaural differences are approximately constant within an entire cone of positions, the so-called ''cone of confusion'' (Woodworth, 1938). It is now acknowledged that the folds of the pinnae perform a direction-dependent filtering of the incoming sound, providing additional (spectral) cues essential for localizing sources on these cones (e.g., Blauert, 1997). It is, however, still unclear what these spectral cues are.

The studies that have tried to clarify the role of spectral cues in human sound localization can be broadly divided into three categories. In one group of studies, an analysis was performed of the so-called head-related transfer functions (HRTFs), which describe the acoustical transfer from a loudspeaker in the free field to the eardrum. For example, Shaw (1982) measured HRTFs in ten subjects and found that in eight of his subjects a spectral minimum systematically moved along the frequency axis as a function of source elevation. In the case of two other listeners, however, the minimum varied in level but not in frequency. Han (1994), who measured HRTFs using a dummy head, suggested that not the notch-minimum but the low-frequency slope of the notch code's elevation and additional peaks and dips serve as secondary cues. Blauert (1969/1970) and Middlebrooks *et al.* (1989), on the other hand, emphasized the existence of peaks instead of dips in the HRTFs. Given the diversity of possible cues that can be derived from the HRTFs and given the considerable intersubject variability, it is unlikely that HRTF analysis alone will identify the spectral cues that are actually used by the auditory system.

A second group of studies attempted to elucidate the role of spectral cues in localization experiments by using band-limited signals as stimuli. Blauert (1969/1970), for example, reported that in the case of $\frac{1}{3}$-octave bandpass noise presented on the median plane, localization judgments were highly dependent on center frequency, but not on sound source position. Similar observations were made for off-median plane positions (Morimoto and Aokata, 1984). Hebrank and Wright (1974) extended Blauert's approach using various types of band-limited noise; they found that increments in frontal elevation are signaled by an increase in the lower cutoff frequency of a 1-octave notch. The results of these studies were, however, obtained by averaging localization data across listeners, i.e., while ignoring individual differences in spectral cues. An exception is the study of Middlebrooks (1992), who used individual DTFs to predict localization performance for narrow-band stimuli. In the case of all these studies, however, it is uncertain if cues derived from band-limited signals can explain localization of broadband sounds.

In a third group of studies localization of broadband sounds was studied while spectral cues were distorted. This can be accomplished in a number of ways, for example, by filling parts of the pinnae with putty (Gardner and Gardner, 1973; Musicant and Butler, 1984; Oldfield and Parker, 1984;

[a]Present address: Philips Research, Prof. Holstlaan 4, 5656 AA, Eindhoven, The Netherlands. Electronic mail: erno.langendijk@philips.com

Hofman and van Opstal, 1998a) or by covering them with blocks (Gardner and Gardner, 1973). Although it was found that deformation of the pinnae distorted the localization percept, identification of spectral cues was difficult because these techniques do not allow precise and systematic control of the acoustic signal arriving at the eardrum.

In the current study, an alternative approach is presented, which is based on headphone presentation of virtual sounds (Wightman and Kistler, 1989a). With this technique virtual sources can be generated that cannot be discriminated from real sources (Zahorik *et al.*, 1995; Langendijk and Bronkhorst, 2000). This technique allows well-defined modifications of the HRTF in any frequency band, and is therefore expected to be more powerful than pinna deformation, which alters the external-ear response over the entire frequency range.

A few recent studies have already demonstrated the power of using virtual auditory displays as a scientific tool for investigating the role of spectral cues in human sound localization. Wenzel *et al.* (1993), for example, showed that the use of nonindividualized HRTFs degrades localization performance. Asano *et al.* (1990) and Kulkarni and Colburn (1999) found that frequency-domain smoothing of HRTFs at high frequencies (above 2–3 kHz) does not affect localization performance as long as the major features are preserved. A similar conclusion can be drawn from two other studies that showed that the spatial features of the HRTFs can be modeled as a linear combination of five (Kistler and Wightman, 1992) to seven (Langendijk and Bronkhorst, 1997) principal components. Unfortunately, principal component analysis does not provide a meaningful interpretation of spectral cues (except for the first component which codes the interaural intensity difference).

In the present study, the influence of spectral cues on sound localization was investigated by removing possible cues from single frequency bands varying in bandwidth and center frequency. Localization was investigated using sources in the median plane and the right hemisphere. Responses were given with a virtual acoustic pointer: a virtual sound source whose position can be controlled via a hand-held stick. Listeners gave their responses by placing the acoustic pointer at the same apparent position as a virtual target. It was shown in an earlier study (Langendijk and Bronkhorst, 1997) that this method is more sensitive than giving verbal coordinates of the perceived sound direction (e.g., Wightman and Kistler, 1989b). The results were analyzed in order to identify the frequency bands containing up–down and front–back cues. A model of sound localization was developed that used individual HRTFs to predict the listeners' response patterns for target sources in the median plane.

II. METHOD

A. Listeners

Eight listeners (five male and three female) with normal hearing (hearing loss $\leqslant$20 dB at octave frequencies between 250 and 8000 Hz) participated in the experiment. All the listeners had previous experience in sound localization experiments. The two authors, who were also subjects (P1 and P8), had extensive experience in such experiments

B. Stimulus and response

The procedures for measuring HRTFs and for generating virtual sound sources are very similar to those described in Bronkhorst (1995) and Langendijk and Bronkhorst (2000). In short, in each ear, the tip of an 80-mm-long probe tube connected to a Sennheiser KE 4-211 microphone was placed close to the listener's eardrum. HRTFs were recorded for 976 loudspeaker positions roughly evenly spaced (about 5.6 degrees angular resolution) on a sphere with a 1.14-m radius. Positions had elevations between −56.25 and 90 degrees and a 360-degree azimuth range. During the measurements, the position and orientation of the listener's head were monitored using a Polhemus head tracker. Transfer functions of Sennheiser HD 520 headphones were measured immediately after the HRTF measurements with the probe tubes left in place and with the headphones carefully placed over the ears. Virtual sources were synthesized by real-time filtering the stimulus with 512-points FIR filters at a 50-kHz sampling rate. The filters (one for each ear and each direction) were minimum-phase approximations of individually measured HRTFs. Each filter was shifted in the time domain with a delay estimated on the basis of the measured HRTF and a reference measurement at the center position of the head (by taking the maximum of the cross correlation of the two impulse responses). The headphone compensation (equalization) was realized by dividing the HRTFs by the individual (left and right) headphone transfer functions in the frequency domain. Filtering was performed on a PC board with a DSP32C processor and two 16-bit AD/DA channels (50 kHz/channel).

Target stimuli were bursts of 200-ms Gaussian noise bandpass filtered between 200 Hz and 16 kHz with 10-ms cosine square on- and off-set ramps. Twenty-five files with noise bursts were stored on a hard-disc of a PC; on each presentation a file was chosen at random, played via a DA converter (Tucker Davis Technologies, DD1) and fed into the DSP-board for real-time filtering. The stimuli were presented via the Sennheiser headphones at an A-weighted level of approximately 65 dB.

The listeners gave a response by pointing a virtual acoustic pointer (VAP) at the position at which they had heard the target stimulus. The pointer was a 100-ms harmonic complex (fundamental frequency 210 Hz; 71 equal amplitude components) generated by a virtual sound source using equalized head-related transfer functions (HRTFs) as described above. The listeners controlled the position of the pointer via a hand-held stick that rotated about a fixed point. The azimuth and elevation of the stick were coded as voltages and were recorded in a PC using a board with 12-bit A/D converters (Lab-PC, National Instruments). The stick was placed in front of the listener, about 30 cm above the seat of the chair with the base (lower metal part) pointing straight up. The stick was calibrated so that when it was horizontal and pointing directly ahead, (azimuth, elevation) was equal to (0 degrees, 0 degrees). The coordinate system

of the stick consequently coincided with that of the listener except for a vector translation from the point of rotation of the stick to the center of the head.

In the present study the magnitude spectra of the HRTFs (H_i) were considered in terms of dB [$20\log_{10}(|H_i|)$] and each HRTF was treated as the sum of two functions: the average transfer function (ATF) and the directional transfer function (DTF). The ATF contained nondirectional components of the HRTFs such as the ear canal resonance and was calculated by averaging the HRTFs across all 976 positions for each ear of each listener. The DTFs were calculated by subtracting the ATF from the HRTFs. Note that the definition of DTF is slightly different from that used by Middlebrooks (Middlebrooks and Green, 1990; Middlebrooks, 1999a), who took the root-mean-square (rms) of the HRTFs to calculate the average transfer function.

In the experiment spectral cues in specific frequency bands were removed by replacing the corresponding part of the DTF by its average value for that band. The modification was performed separately for the left and right ears. There are two important aspects to take into consideration regarding this procedure. First, the modified frequency bands in the experimental conditions are on a logarithmic frequency scale, while the features in the DTF are approximately even-spaced on a linear frequency scale. This means that more features are captured in the high-frequency bands. The choice of using logarithmic scaling is based on the intention to study only perceptually relevant details. Second, when cues are about the size of the frequency band or when the band contains a large peak or deep dip that affects the level of the entire band, the cues are not effectively removed. In other words, the procedure is most effective in removing ''local'' spectral cues, such as peaks, dips, and slopes which extend over a frequency range smaller than the modified frequency band.

C. Design

There were nine experimental conditions. In the baseline condition, no spectral cues were removed from the DTFs. In the 2-octave condition, spectral cues were removed from the 4–16-kHz frequency band. In the three 1-octave conditions, referred to as the low, middle, and high 1-octave conditions, spectral cues were removed from 4–8, 5.7–11.3, and 8–16 kHz, respectively. In the low, middle-low, middle-high, and high $\frac{1}{2}$-octave conditions spectral cues were removed from 4–5.7, 5.7–8, 8–11.3, and 11.3–16 kHz, respectively. Figure 1 illustrates how the left-ear DTF of one of the listeners for the direction (azimuth, elevation) is (0 degrees, −56 degrees) changes when spectral cues are removed from the eight frequency bands.

Selection of the target positions was based on their lateral angle and elevation. These are defined as the angle between the vector from the center of a sphere to a position on this sphere and the median vertical plane and the horizontal plane, respectively. Target positions were taken near the intersections of equal lateral angle contours (at 0, 30, and 60 degrees) and equal elevation contours (at −60, −30, 0, 30, 60, and 90 degrees). This resulted in a total of 23 target positions evenly distributed in the right hemisphere. Figure 2

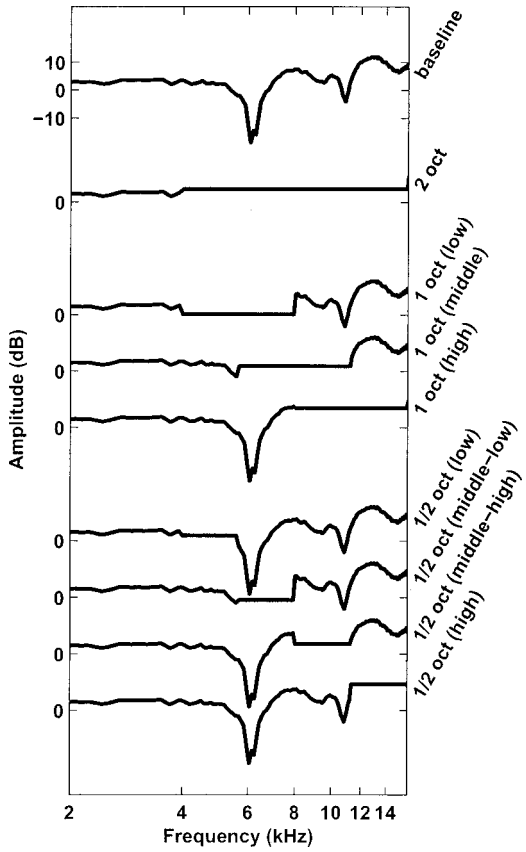

FIG. 1. Example of the effect of the removal of spectral cues from the left ear DTF for one listener for one direction (0°, −56°) for each condition. From top to bottom: Baseline, 2-octave, 1-octave (low, middle, high), and $\frac{1}{2}$-octave (low, middle-low, middle-high, high) conditions.

shows a frontal view of the target positions on a sphere. Because a unique description of a point on the lateral angle contour requires both an elevation and an indication to discriminate front and rear, an additional angle α was defined to describe the position on this lateral angle contour. At frontal positions the angle α was equal to the elevation, while at rear positions the angle was obtained by subtracting the elevation from 180 degrees. In the manuscript, elevation refers to both

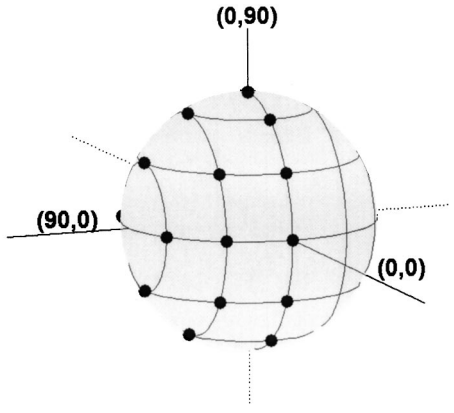

FIG. 2. Target positions viewed from the front. Frontal and rear positions are mirror-symmetric with respect to the lateral-vertical plane. Targets were located in the median plane ($n=11$) and in two planes parallel to the median plane that cut the horizontal plane at 30° ($n=8$) and 60° ($n=4$) azimuth, respectively. The three planes are referred to as the vertical planes with a lateral angle of 0°, 30°, and 60°, respectively.

frontal and rear positions, unless otherwise indicated.

The presentation order of conditions and target positions was as follows. A block of trials started with the baseline condition. Next, the remaining eight conditions were presented according to an 8×8 Latin square design. Finally, the block was completed with a repetition of the baseline condition. Within each condition, the 23 target positions were presented in random order. Each block, consisting of 230 trials, was repeated five times.

The experiment was carried out in a sound-proof booth. The listeners were seated on a chair and were instructed to keep their heads up with their eyes closed. To familiarize them with the pointing task they were first asked to participate in several hundred trials using stimuli created with the original (unprocessed) HRTFs. This took about 10 to 20 min. The experiment took less than 2 h, including 5–10-min breaks after each block of trials. A block of trials could be finished within 10–15 min.

III. RESULTS

The results of the study will be presented in three sections. In the first section, the raw localization data will be presented and the type of localization errors that were made will be described. In the second section, an analysis of variance will be applied to the elevation errors and the percentages of front–back confusions (responses in a hemisphere—front or rear—different from that of the target), providing information concerning the presence of up–down and front–back cues in certain frequency bands across all the listeners. In the third section, a model will be described that is able to predict individual response patterns in the median plane.

A. Raw data

Illustrations of the response patterns discussed below, localization judgments for all target positions, obtained from two listeners (P8 and P6) in all conditions, are displayed in Figs. 3 and 4, respectively. The panels in different columns show data obtained for targets in vertical planes with lateral angles of 0, 30, and 60 degrees, respectively. In different rows they show the data obtained for the different conditions. In each panel, localization judgments have been plotted as a function of target angle, with the size of each disc representing the number of judgments in a 30-degree-wide interval. Note that the target/response angle for front positions is equal to the elevation and that for rear positions it was obtained by subtracting the elevation from 180 degrees.

As expected, listeners were accurate in localizing most targets in the baseline condition. The greatest errors (in elevation) were made for positions with elevations of about 60 degrees or more and for rear positions above the horizontal plane. Percentages of front–back confusions were relatively low and confusions occurred in general more frequently for positions close to the lateral-vertical plane (the vertical plane going through the ears, as opposed to the median-vertical plane going between the ears) with elevations above the horizontal plane. In the case of some listeners, confusions also occurred for front target positions with elevations below the horizontal plane (see the data for P8 in Fig. 3). The results are in agreement with those of previous studies (Wightman and Kistler, 1989b; Makous and Middlebrooks, 1990; Carlile *et al.*, 1997).

In the 2-octave condition, localization performance was very poor in the case of all listeners except listener P8, whose performance in judging the elevation was fair, but who localized almost all the targets in the rear and above the horizontal plane. The localization judgments of the other listeners were restricted to one or two response regions. In the case of listener P6, for example, this response region was in the front around -45 degrees elevation. The majority of most listeners' responses were in the rear, one listener (P6) responded mainly to the front, and in the case of one listener front–back discrimination was somewhat better than chance performance but all responses were close to the horizontal plane.

In the 1-octave conditions a substantial decrease in localization performance was on the whole observed for the middle and high frequency bands and only a mild effect for the low frequency band. Response patterns varied considerably across listeners and conditions. For example, in the low 1-octave condition most judgments of listener P8 concerning targets below the horizontal plane were in the horizontal plane and front–back confusions were recorded only for one position (0 degrees, -56 degrees). In the high 1-octave condition, on the other hand, this listener perceived almost all median plane targets in the rear. In the middle 1-octave condition, front–back confusions were recorded for this listener for about half of the frontal median plane targets and his elevation percept was disturbed with respect to most target locations. The removal of cues in the low 1-octave condition had virtually no effect on listener P6. This was also the case with respect to targets in the frontal median plane in the middle 1-octave condition. With respect to targets in the rear, however, both elevation and front-back percepts were significantly disturbed in this condition. In the high 1-octave condition, this listener's elevation judgments were disturbed both in the front and in the rear, but the scatter of his responses was not as prominent as in the middle 1-octave condition. Front–back confusions were recorded for all target locations in the rear, as in the middle 1-octave condition.

In general, none of the $\frac{1}{2}$-octave conditions had a great effect on target localization, except in some specific cases. For example, the localization responses of listener P8 in the middle-low condition were compressed in elevation (i.e., closer to the horizontal plane than the targets) and in the middle-high condition almost all targets below the frontal horizontal plane were perceived in the rear and elevation was somewhat compressed.

B. Analysis of variance

In order to separate the effects of condition and target position, a repeated measures analysis of variance (ANOVA) was performed of the elevation error and the percentage of front–back errors. Elevation errors were calculated by taking the absolute difference between target and response elevation, with elevation being the angle with respect to the horizontal plane (i.e., irrespective of front–back location). In the case of front–back errors, the variable of interest was the

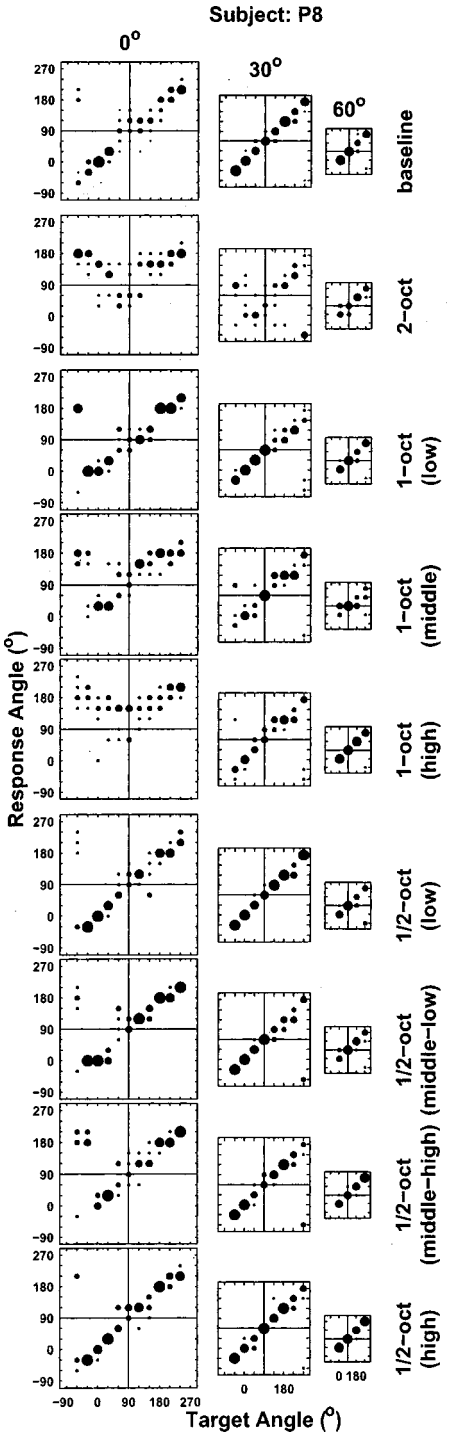

FIG. 3. Localization judgments of listener P8 for all targets and all conditions. The panels in the different columns show the data obtained for targets in vertical planes with lateral angles of 0°, 30°, and 60°, respectively. In the different rows, they show the data obtained in the different conditions. In each panel, localization judgments are plotted as a function of target angle, and the size of each disc represents the number of judgments in a 30° wide interval. The smallest discs represent one judgment, the largest discs represent ten judgments in the baseline condition and five judgments in the other conditions. For positions in front of the listener the target/response angle is equal to elevation, but for positions behind the listener it was obtained by subtracting the elevations from 180°. The vertical and horizontal lines represent the angles that separate frontal from rear positions for targets and responses, respectively. Note that for positions in the vertical planes with a lateral angle of 30°(60°) the target/response angles between 60°(30°) and 120°(150°) and between −60° (−30°) and 240° (210°) do not exist. Therefore, they are ''collapsed'' onto the horizontal and vertical lines. This explains the smaller size of those panels.

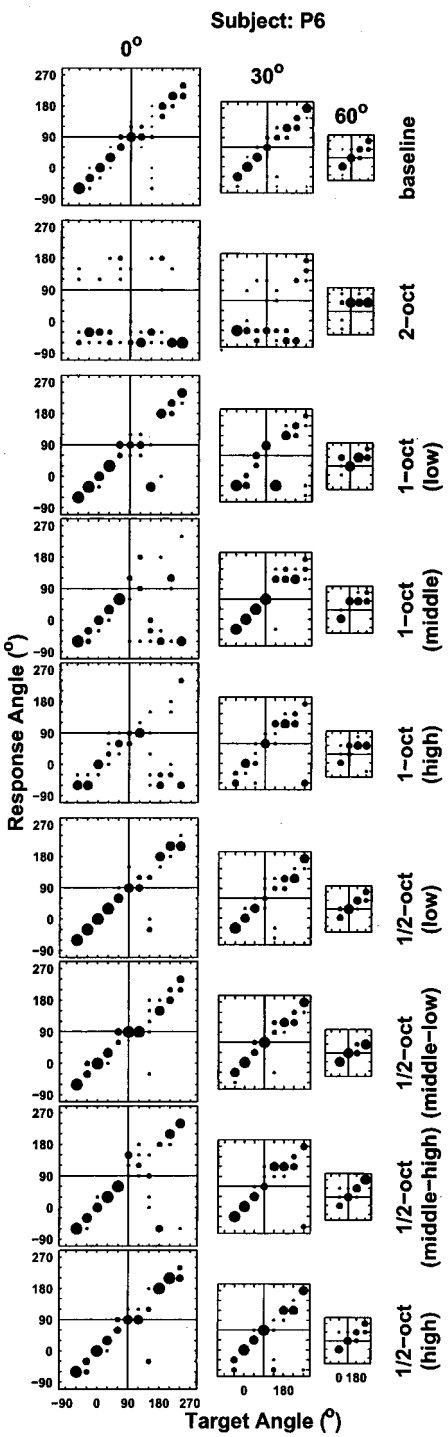

FIG. 4. Same as Fig. 3, but now showing the data of listener P6.

number of responses in a hemisphere (front or rear) different from that of the target divided by the total number of target presentations. Targets in the lateral-vertical plane were excluded from the front–back analysis. Both types of errors were averaged across the five repetitions of each pair of condition and target position. The outcome of the ANOVA showed that all main effects and interactions were significant ($p<0.01$) for both types of error.

Figure 5 shows the elevation error for each condition collapsed across target positions and listeners. A Tukey HSD *posthoc* analysis showed that the 2-octave condition and the

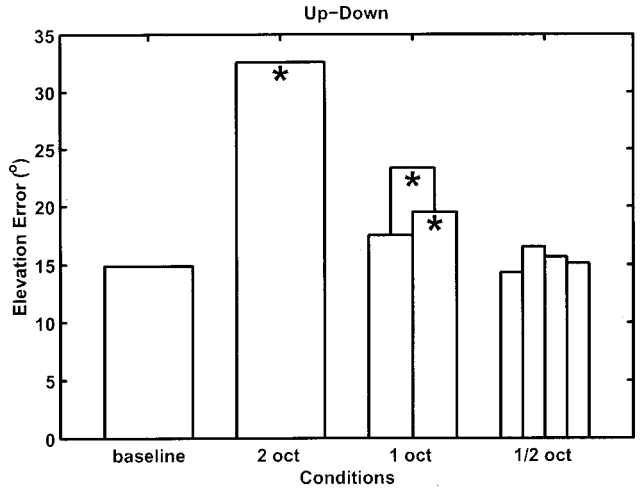

FIG. 5. Elevation error in the baseline condition and the other conditions collapsed across listeners and target positions. The width of a bar and the relative position between bars in one condition represents the bandwidth and the relative center frequency of the band in each of the conditions. The * marks conditions significantly different ($p<0.05$) from the baseline condition.

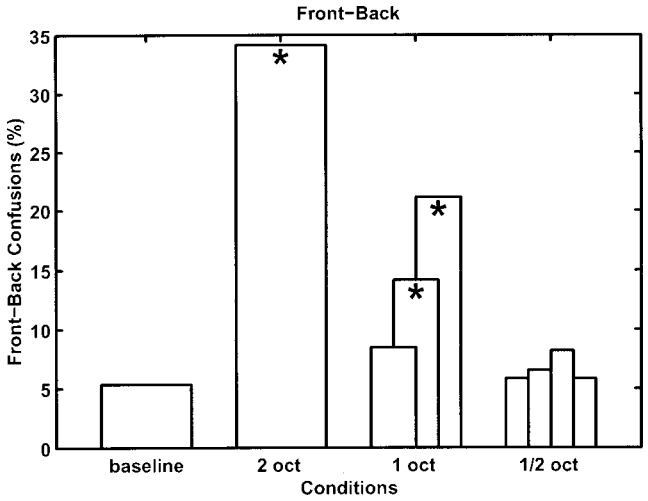

FIG. 6. Percentage of front–back errors in the baseline condition and the other conditions collapsed across listeners and target positions. All the other conventions are as in Fig. 5.

middle and high 1-octave conditions were significantly different ($p<0.01$) from the baseline condition. All three conditions were also significantly different ($p<0.05$) from each other. The results obtained in the $\frac{1}{2}$-octave conditions were not significantly different from those obtained in the baseline condition ($p>0.1$). The mean elevation error was greatest in the 2-octave condition; it is only somewhat smaller than the mean error of 40 degrees that would have been obtained if listeners had always responded in the direction (0 degrees, 0 degrees). The fact that the elevation error is significantly greater in the middle 1-octave condition than in the other 1-octave conditions suggests that the up–down cues were most prominent in this frequency region.

The percentage of front–back confusions collapsed across target positions and listeners is shown in Fig. 6. The 2-octave condition and the middle and high 1-octave conditions were significantly different ($p<0.01$) from the baseline condition, as was tested with a Tukey HSD *posthoc* analysis, and each of them was also significantly different ($p<0.05$) from the other. Differences between the $\frac{1}{2}$-octave conditions and the baseline condition were not significant ($p>0.1$). As with the elevation errors, the mean error was significantly greater in one of the 1-octave conditions—in this case the high 1-octave band—than in the others. This indicates that the front–back cues were located mainly in this band.

Because the results obtained for certain target positions in this analysis appeared to be clustered, a second repeated-measures ANOVA was performed, in which targets were divided into different groups for each type of error. For the elevation error there were three groups: down, middle, and up with target elevations -60 and -30 degrees, 0 and 30 degrees, 60 and 90 degrees, respectively. For the percentage of front–back errors there were two groups: front and back (as before, targets in the lateral-vertical plane were ignored in the front–back analysis). All main effects and interactions were significant ($p<0.01$) for both types of errors, except for the main effect of position for the front-back error.

Table I shows the results obtained for both types of errors collapsed across listeners (first nine columns) and collapsed across listeners and conditions (last column). The data in the last column indicate that it was more difficult to localize targets in the up region than in the middle region. The obtained results for the two-way interaction between condition and target region indicate that the elevation errors in the down regions in the middle-1-octave and 2-octave conditions were significantly greater ($p<0.01$) than in the corresponding baseline condition. With respect to the up region this was only the case in the 2-octave condition. The percentage of front–back errors recorded at frontal positions increased by factors of 3 and 5 ($p<0.01$) in the high-1-octave and 2-octave conditions, respectively, with respect to the corresponding baseline condition. All other conditions were not significantly different from the corresponding baseline condition.

In order to investigate individual differences in front–back and elevation errors, the listeners were treated as a random factor in an ANOVA with condition and target region as other main effects. The outcome of the analysis showed that all main effects and the two-way interaction between listener and target region were significant ($p<0.01$) for both types of error. Across listeners the mean elevation errors were between 15 and 26 degrees and the mean front–back error rates between 5% and 22%. The two-way interaction recorded for the front–back error was caused by one listener who confused rear target positions, whereas all the others confused frontal target positions. The interaction recorded for the elevation errors was due to the fact that two listeners made greater elevation errors in the up region than in the down region, whereas the others made similar errors in these regions. The two-way interaction between listener and condition was not significant for both types of error ($p>0.4$). This indicates that the mean errors in the different conditions were similar across listeners. However, as noted above, the response patterns did show considerable variation (see, for example, Figs. 3 and 4).

TABLE I. Elevation errors for sources in the down, middle and up regions (top three rows) and percentages of front–back errors in the back and front regions (bottom two rows) in all conditions collapsed across listeners. The last column shows the average across conditions and listeners. The various 1- and $\frac{1}{2}$-octave conditions have been labeled L(ow), M(iddle), H(igh), M(iddle)-L(ow), M(iddle)-H(igh). The results printed in **boldface** (in first nine columns only) are significantly different ($p<0.01$) from those obtained in the corresponding baseline condition (i.e., when results are compared within rows). The underlined results are significantly different ($p<0.01$) from those obtained in the middle region (top three) or the back region (bottom two-rows) when results are compared within conditions (i.e., within columns). Significant differences were tested in a Tukey HSD *posthoc* analysis.

	Condition									
			1-oct			$\frac{1}{2}$-oct				
Region	Baseline	2-oct	L	M	H	L	M-L	M-H	H	Mean
Down	14°	**38**°	19°	**29**°	21°	14°	18°	15°	14°	20°
Middle	14°	23°	14°	17°	16°	13°	14°	13°	15°	16°
Up	19°	**47**°	23°	29°	27°	19°	21°	23°	18°	25°
Back	2%	16%	6%	14%	11%	3%	3%	8%	3%	7%
Front	8%	**52**%	11%	14%	**31**%	9%	10%	8%	8%	17%

C. Model

1. Description

A model was developed that predicts the individual response patterns on the basis of the frequency spectrum of the signal presented to the listener and the individually measured directional transfer functions. The model, which is similar to that described in a number of previous studies (Middlebrooks, 1992; Zakarauskas and Cynader, 1993; Hofman and Van Opstal, 1998b; Langendijk *et al.*, 2001), assumes that the auditory system compares the spectrum of the signal arriving at the eardrums with a set of stored spectral templates associated with particular sound source directions. The direction in which the template is most similar to the input spectrum will have the highest chance of being perceived.

In the model, the templates are represented by the individually measured DTFs. The DTFs, with cues removed according to each condition, were used as the input spectra. In the implementation of the model, a limited number of parameters are introduced. The first parameter (BW) concerns the representation of the DTFs; DTFs were averaged in $\frac{1}{3}$-, $\frac{1}{6}$-, $\frac{1}{12}$-, or $\frac{1}{24}$-octave bands.

The second parameter (DO) was inspired by a study by Zakarauskas and Cynader (1993), who stated that taking the second-order derivative of the DTF with respect to frequency would allow more accurate localization estimates; in the present study the zeroth-, first-, or second-order derivative of the DTFs was taken. The third parameter (CP) is related to the implementation of the comparison process; the measure of similarity between two DTFs was determined either by the cross-correlation coefficient (as in Middlebrooks, 1992) or by the standard deviation of the difference (the square root of the variance; as in Middlebrooks, 1999b). The outcomes obtained for both measures were transformed to probabilities between 0 and 1. In the case of the cross-correlation coefficient this was done simply by adding 1 and then dividing by 2. In the case of the standard deviation, values could range from 0 to infinity. Somewhat arbitrarily a Gaussian function (the normal probability density function with mean 0 and standard deviation S, introducing a fourth parameter) was applied to realize the transformation. This function implies that outcomes of the comparison process between 0 and $S/2$ acquire a probability near 1, whereas for outcomes larger than $S/2$ the probability decreases rapidly with an increasing S. Because model performance dropped significantly at S values outside the range 0.5–4, optimum performance was determined within this range. For each input spectrum the probabilities of all the templates were first averaged across both ears and then normalized to one. This resulted in a probability density function (pdf) for the response distribution for each target position in each condition.

The performance of the model was investigated for all combinations of the parameter settings. For simplicity, only median plane positions were considered in the analysis. Model performance was quantified using maximum likelihood statistics (McCullagh and Nelder, 1989). The likelihood statistic (L) was calculated as follows:

$$L=\sum_{i=1}^{N} -2\log_e(p_i), \tag{1}$$

where p_i is the value of the pdf at the position of response i and N is the number of responses in one condition ($=11$ targets$\times 5$ repetitions). Note that for the parameter values for which L is minimized the model is most likely to be true. Optimum parameter settings were found for BW$=\frac{1}{6}$ octave, DO$=0$, CP$=$standard deviation, and $S=2$. The analysis revealed that the effect of BW was relatively small. Taking the first- or second-order derivative, however, led to a substantial decrease in model performance. This was also the case when the cross-correlation coefficient was taken as a similarity measure, instead of the standard deviation. Model performance was about the same for $S=1$ and 2, but decreased substantially when $S=0.5$ or 4 was taken.

2. Validation: Probability density functions

The first five panels of Fig. 7 show the pdfs for the optimum parameter settings for 53 positions in the median plane for one listener (P6) in a subset of the conditions together with the actual responses (○) to the 11 target positions. In each panel, each column represents a single pdf for all

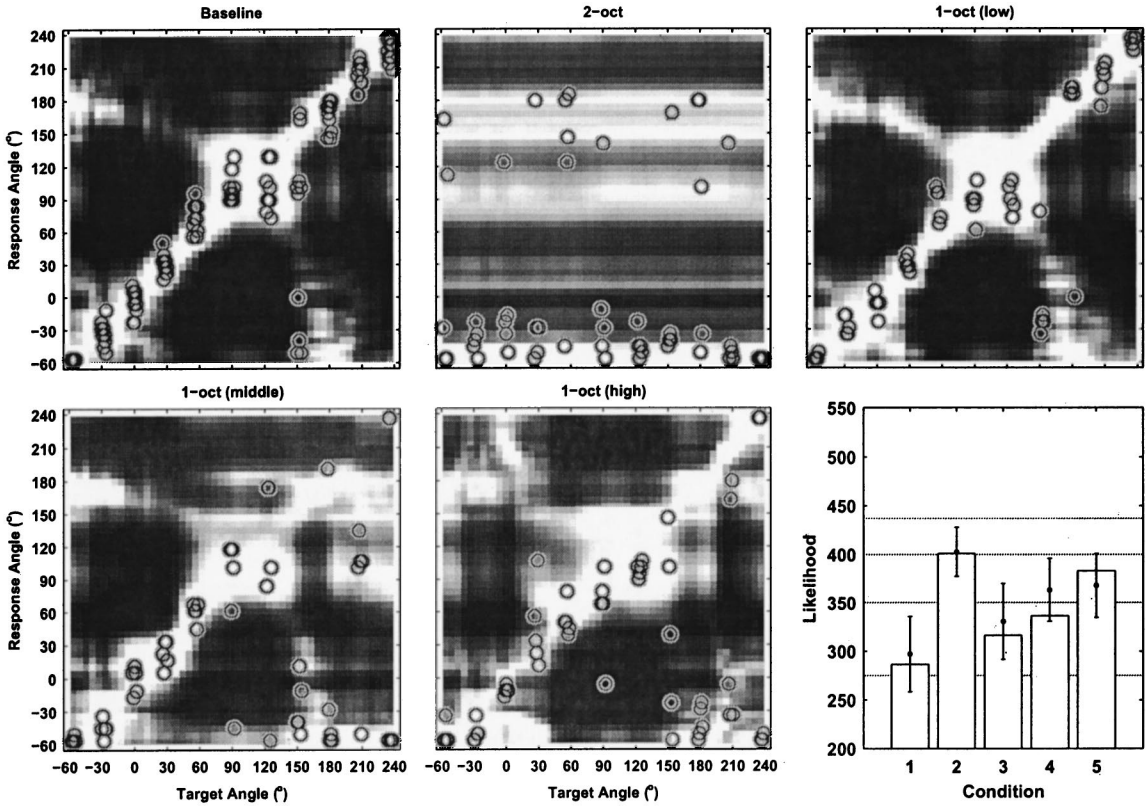

FIG. 7. Probability density function (pdf) and actual responses (◦) for one listener (P6) as a function of target position. Each column represents a single pdf for all possible response locations (53) for one target location. The shading of each cell codes the probability density (light/dark is high/low probability, respectively). Responses have been ''jittered'' horizontally over ±2° for clarity. The first five panels show the results obtained in different conditions. The results obtained in the low, middle-low and high $\frac{1}{2}$-octave conditions are not shown, but the response patterns and the pdfs were very similar to those in the baseline condition. The last panel shows the likelihood statistic of the model for the actual responses in each condition (bars), the average and the 99% confidence interval of the expected likelihood (dots and bars, respectively) and the likelihoods for a flat response distribution and a tri-, bi- and unimodal response distribution (horizontal lines from top to bottom, respectively). See the text for details.

possible response locations (53) for one target location. The shading of each cell codes the probability (light/dark is high/low probability, respectively). Similar plots showing the results obtained for two other listeners are shown in Figs. 8 and 9.

In the baseline condition the model predicts, as expected, that the highest probability for the responses is at the target position (i.e., on the diagonal). It also predicts that the response distribution is broader for target positions around 90 degrees elevation and that front–back confusions might occur.

In the 2-octave condition the model predictions were quite remarkable; either one or two positions were predicted irrespective of the target position. These positions could be very different across listeners, but, in general, they coincided with the listeners' response positions (except those of one listener).

Predictions for the low 1-octave condition were not much different from those for the baseline condition. In the middle and high 1-octave conditions, on the other hand, the model predictions were quite different from those in the baseline and they also differed from each other. In the middle 1-octave condition, the model predicted localization errors for positions in the rear below the horizontal plane for all listeners. For some listeners the model also predicted errors for the low-front positions and occasionally for rear and frontal positions above the horizontal plane. In general, the model in these cases predicted that listeners would give a response near the horizontal plane and that front–back confusions were more likely to occur than in the baseline condition, but not as likely as in the high 1-octave condition. The model also predicted that in the case of a front–back confusion, the elevation error would, in general, be greater than in the case of a response in the correct hemisphere. Figures 7–9 illustrate these general features, but also show that some model predictions can differ substantially across listeners for certain target positions.

In the $\frac{1}{2}$-octave conditions the model predictions were not much different from those in the baseline condition (and they have therefore been omitted in the figures).

In the case of the majority of the listeners (see Figs. 7 and 8 as typical examples) the model seems to predict localization performance in all conditions quite accurately. Responses generally fell in regions with a high predicted probability, even in the 2-octave condition.

3. Validation: Likelihood statistics

In order to quantify model performance and to interpret the results, three different types of likelihood statistics were calculated for each listener for each condition. The first statistic is the actual likelihood, which was calculated on the

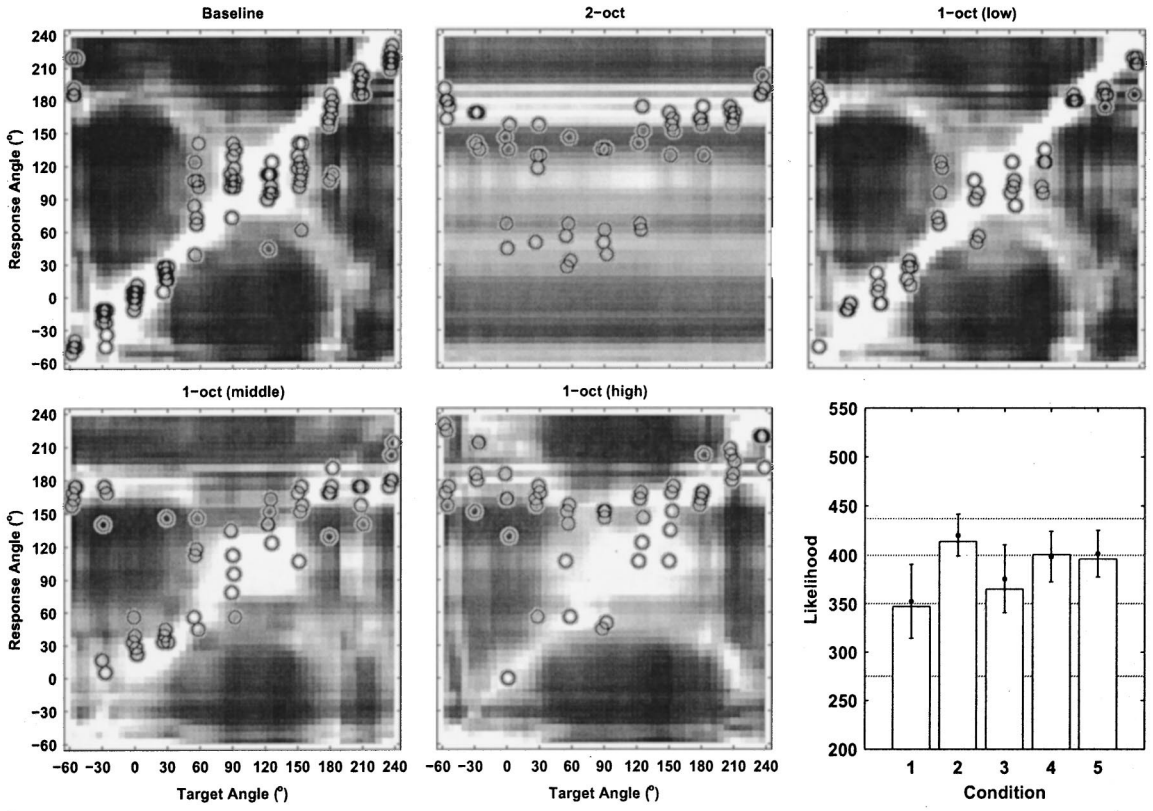

FIG. 8. Same as Fig. 7, but now showing the data of listener P8.

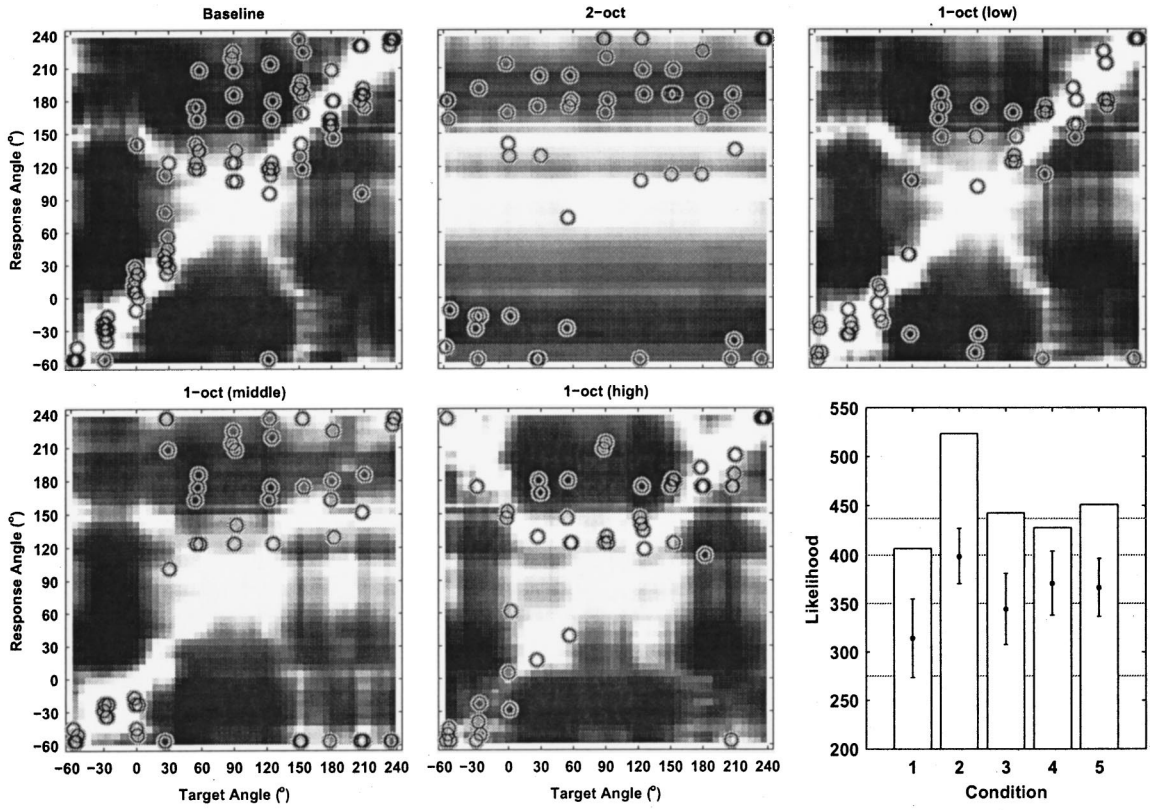

FIG. 9. Same as Fig. 7, but now showing the data of listener P3.

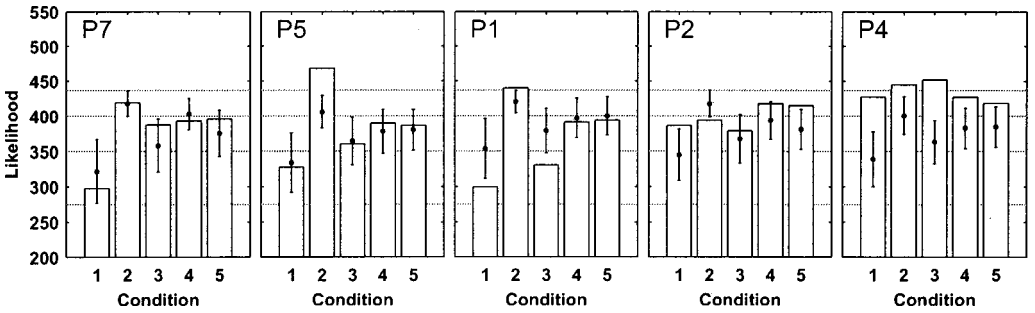

FIG. 10. Likelihood plots of listeners P1, P2, P4, P5, and P7, respectively.

basis of the actual responses and the pdfs generated from the listener's individual DTFs (as described above). The second statistic—the expected likelihood—was calculated using the same individual pdfs, but instead of taking the actual responses, responses (five for each target) were drawn randomly according to the pdf for the target concerned. The procedure was repeated a hundred times and the average and 99% confidence intervals of the expected likelihood were calculated. The third statistic is the likelihood corresponding to responses drawn from either a single Gaussian distribution or a sum of two or three Gaussian distributions (bi- and trimodal distributions).

The single Gaussian distribution had a mean at the target position and a sigma of 17 degrees (which is the average standard deviation of the elevation error in the baseline condition across listeners and target positions, with front–back confusions removed from the data). Because likelihoods were averaged across target positions, the Gaussian likelihood was calculated only for one position (target at 0 degrees elevation). In the case of the bimodal distribution, a pdf was generated from the sum of two Gaussian distributions with means 0 and 180 degrees and sigmas of 17 degrees. In the case of the trimodal distribution, a pdf was generated from the sum of three Gaussian distributions with means of 0, 90, and 180 degrees and sigmas of 17 degrees. An additional likelihood value was calculated using a uniform chance distribution $[L=-110\log(1/53)=437]$, in order to estimate the upper limit of the likelihood for chance performance. Note that all likelihoods described here are independent of condition.

The likelihoods of the various Gaussian distributions can be interpreted as follows. In the case of a listener who is not making front–back confusions, the actual likelihood statistic is expected to be close to the unimodal likelihood. In the case of a listener who makes front–back confusions for about half of the responses, the likelihood is expected to be close to the bimodal likelihood. Of course, the likelihoods of the various Gaussian distributions give only one interpretation of the likelihood values, focused on uni-, bi-, and trimodality. A similar increase in likelihood can be obtained by increasing the sigmas of the distributions. Therefore, the values of the likelihoods of the Gaussian distributions should not be seen as exact values.

Before the results of the likelihood statistics can be analyzed three important aspects must be taken into consideration: (1) If two models are tested with the same localization data, then the model with the lower likelihood statistic is the better model. (2) The likelihood of the model for the actual data should fall within the 99% confidence interval of the expected likelihood. (3) Better localization performance corresponds, in general, to lower values of the likelihood statistic.

The results of the likelihood statistics are shown in the sixth panel of Figs. 7–9, for listeners P6, P8, and P3, respectively, and in Fig. 10 for the other listeners. The bars show the likelihood of the model for the actual responses obtained in the five selected conditions. The dots and error bars represent the average and confidence intervals of the expected likelihood, respectively. The horizontal lines show the likelihood of the Gaussian distributions for the uni-, bi-, and trimodal distributions and for the flat distribution, respectively.

The results of the likelihood analysis show that in the case of four listeners (P5–P8) the likelihoods of the actual responses fall within the 99% confidence interval of the expected likelihood for all conditions (except the 2-octave condition in the case of listener P5). These data provide direct quantitative support of what was already observed in visual inspection of the pdfs and the actual responses in Figs. 7 and 8: namely, that the model does seem to predict the actual response locations. In the case of two listeners (P1 and P2), the likelihoods are within or just outside the 99% confidence regions. In the case of listener P1, the responses in the baseline and low 1-octave conditions were more accurate than those predicted by the model, which could have been due to this listener's extensive experience in localization experiments.

In the case of the remaining two listeners (P3 and P4) the model predictions and the data did not agree. The results obtained for one of these listeners, P3, are shown in Fig. 9. Note that performance was already relatively poor in the baseline condition and that there were frequent responses in regions with low predicted probabilities in all conditions. However, when only target positions which could be correctly localized in the baseline condition (for example, the frontal target positions below 60 degrees) are considered, the responses and predictions agreed well in the other conditions, too. Similar results were obtained for the other listener (P4) with deviating response likelihoods. The fact that pdfs obtained for these listeners in the baseline condition are not much different from those obtained for the other listeners with better localization performance (compare, for example, the pdfs in the baseline condition in Figs. 7–9) suggests that their DTFs contained sufficient spectral cues, but that they were not able to access and/or use this information.

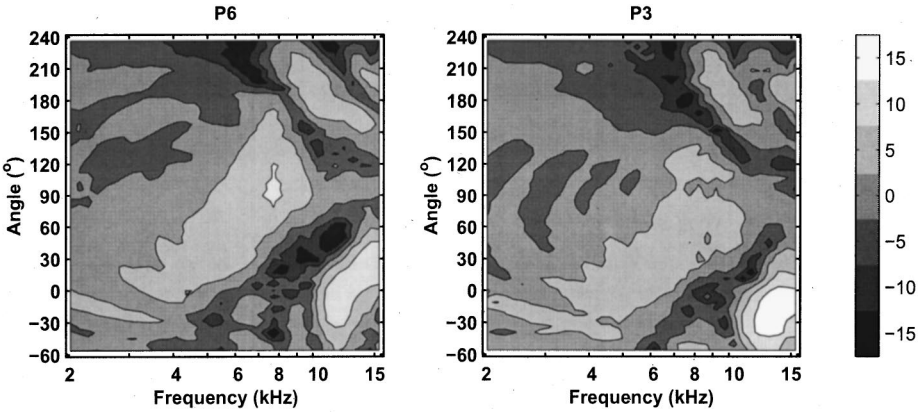

FIG. 11. Left-ear DTFs of two listeners (P6 and P3) plotted as a function of the angle in the median plane. Note that for positions in front of the listener the angle is equal to the elevation, but for positions behind the listener it was obtained by subtracting the elevations from 180°. Gray shading codes the amplitude (dB) of the DTF according to the bar on the right.

The likelihoods for the baseline condition obtained for listeners whose data agreed with the model predictions are, in general, between the unimodal and bimodal reference likelihoods. This is in accordance with the observation that the model predicts that most responses should fall near the target location, but that some will occur near the (front–back) confused target location. Note that a higher likelihood value may be due to bimodality or to an increase in the scatter of the responses around the target location; in both cases the number of likely response locations increases. Visual inspection of the pdfs suggests that bimodality occurred mainly for the lower elevations (below 30 degrees) and increase in response scatter for the higher elevations (above 60 degrees). The likelihoods for the 1-octave conditions were all above those for the baseline condition and in general near the bimodal reference (low 1-octave condition) or between the bimodal and trimodal reference (middle and high 1-octave conditions). Likelihood values were highest for the 2-octave condition, in general near and above the trimodal reference. The likelihood values for the $\frac{1}{2}$-octave conditions were close to those for the baseline condition.

IV. DISCUSSION

The results of the present experiment show that the spectral cues in the 4–16-kHz frequency band are essential for correctly localizing broadband sounds. The results of the 1-octave conditions suggest that the most important up–down cues are present in the middle 1-octave band (5.7–11.3 kHz) and that front–back cues are coded mainly in the high 1-octave band (8–16 kHz). Differences in individual response patterns suggest that within these bands listeners used different localization cues. The model presented in this article can predict, with some limitations, the individual response patterns in the median plane.

Because of the experimental design, localization cues were disturbed within a specific localization band, while cues that act over a larger frequency resolution (i.e., wider bandwidth) than the affected band remained intact. For example, if the auditory system has a slope detector that uses the amplitude difference between two adjacent $\frac{1}{2}$-octave bands as a localization cue, then this cue would be substantially disturbed in the 1-octave condition, but much less or not at all in the $\frac{1}{2}$-octave condition. A reduction in localization performance in a certain condition implies that there is a cue in that disturbed band. The absence of any reduction in localization performance suggests that there is no cue in the disturbed frequency band or that localization cues outside the affected band outweigh the disrupted information in the affected band. In either case, there was no potent cue entirely within the modified band.

A. Localization cues

A detailed analysis of the individual DTFs revealed that for frontal and rear positions with the same elevation the DTFs are quite similar in the middle 1-octave band, but very distinct in the high 1-octave band. The major difference is a prominent peak in the high 1-octave band for positions in the front that is very small or absent in the rear. The most probable elevation cue, located in the middle 1-octave band, is a spectral notch with a center frequency that increases as a function of elevation. Another cue for high elevations could be the existence of a large peak in the middle 1-octave band. These general observations can be verified, for example, in the left and right panels of Fig. 11 showing the left-ear DTF amplitude (coded in gray) as a function of frequency and the median-plane angle (α) in the case of subjects P6 and P3, respectively.

Apart from these general features, some individual differences can also be observed. For example, in the regions with low amplitudes (dark gray), the left ear DTF of listener P6 (left panel Fig. 11) has three small notches in the frequency range from 4 to 11 kHz for −60 degrees (frontal) elevation which merge to a single large notch for 0 degrees elevation with increasing elevation. When elevation increases further to 90 degrees, the center frequency of this notch increases from 8 to 15 kHz. For rear positions there are two notches with center frequencies at 6 and 11 kHz that both increase about 1 octave in frequency per 120 degree elevation increase. There seems to have been similar cues for listener P3 (right panel Fig. 11), with the following exceptions: (1) for frontal positions below the horizontal plane there were two rather than three notches, (2) some of the center frequencies of the notches occurred at different frequencies, and (3) the widths of the notches seemed to be narrower.

Although the elevation notch seems to be a prominent and unambiguous cue that has also been identified as such in previous studies (Shaw, 1974; Hebrank and Wright, 1974;

Han, 1994; Watkins, 1978), the results from the $\frac{1}{2}$-octave condition do not support that such a narrow notch would be a localization cue. Because the notch is, in general, smaller than $\frac{1}{2}$ an octave, it must have been distorted quite heavily, but localization was not affected in the $\frac{1}{2}$-octave conditions. As stated previously, this could have been a result of the fact that cues at other frequencies than the distorted band could have been used. Another explanation that would be in line with a study from Rakerd and Hartman (1999) is that localization in the median plane is mediated by broadly tuned features of the spectrum. After all, a distortion of such a notch in the $\frac{1}{2}$-octave condition results in a broad local minimum of the DTF at the center frequency of the notch.

For the same reason, it is unlikely that slope detectors (for slopes within $\frac{1}{2}$ an octave), such as suggested by some authors (Hebrank and Wright, 1974; Han, 1994), serve as cues. Hebrank and Wright also suggested that the high elevations are coded by a $\frac{1}{4}$-octave peak between 7 and 9 kHz. Such a cue would also have been disturbed seriously in the middle-high $\frac{1}{2}$-octave condition. The discrepancy might be attributable to the fact that Hebrank and Wright used band-limited signals introducing severe distortions of the available cues, whereas in the present study a relatively mild distortion of the available cues was used only at specific frequencies, leaving the available cues at other frequencies intact.

Evidence for the predominance of front–back cues in the high 1-octave band was also provided by Bronkhorst (1995), who showed that the percentage of front–back confusions with respect to broadband stimuli increased substantially when the low-pass cutoff frequency was reduced from 16 to 7 kHz, whereas the increase in up–down errors was relatively small. Inspection of the individual DTFs of our subjects (see Fig. 11 for two of them) revealed a pronounced peak in the high 1-octave band for all frontal positions and a smaller or no peak at all in the case of rear positions. The potential importance of this feature for front–back discrimination was already suggested by Hebrank and Wright (1974).

The analysis of the DTFs revealed that the most prominent up–down and front–back cues could be identified in the middle and high 1-octave bands, respectively. Yet, the localization data shows that removing spectral cues in the middle 1-octave band not only disturbs up–down discrimination, but also front–back discrimination. Similarly, removing cues in the high 1-octave band disturbs not only front–back discrimination, but also up–down discrimination. It could be that in the analysis of the DTFs some spectral features were overlooked, but it is more likely that because the middle and high 1-octave bands partly overlap that the front–back errors in the middle 1-octave condition and the up–down errors in the high 1-octave condition were a result of distorting front–back and up–down cues, respectively, in the overlapping frequency range (i.e., 8–11.5 kHz). In that case, we do not agree with the conclusion from Hebrank and Wright (1974) that the prominent dip in the middle 1-octave band could serve as a front cue.

In some studies (Blauert, 1969/1970; Asano *et al.*, 1990) the existence of low-frequency cues (below 4 kHz) has been suggested. Although no such cues were manipulated in the present experiment, the results obtained for the 2-octave condition provide an estimate of the maximum amount of information present in the frequency region below 4 kHz. Given that the performance in this condition was not much above chance, it can be tentatively concluded that low-frequency cues have only a minor effect.

The interaction between condition and listener was not significant with respect to either the elevation error or the front–back error, but the response patterns sometimes varied considerably between listeners and conditions. These results agree with what was found in detailed investigations of the individual DTFs in the present study, namely that the primary notch in the middle 1-octave band and the frontal peak in the high 1-octave band existed for all listeners, but the exact frequencies of these cues and their specific spectral shape (width and magnitude) were different across listeners. There were also secondary peaks and dips that were different across listeners. These results are in agreement with those of previous localization studies that emphasized individual differences in localization cues (Shaw, 1982; Wenzel *et al.*, 1993; Middlebrooks, 1999b).

B. Localization process

Most models presented in the literature assume that the auditory system has some knowledge of the directional filtering of the outer ear. Blauert (1969/1970), for example, suggested that the auditory system derives locations on the cone of confusion from the signal energy in specific frequency bands (''directional bands''). Hebrank and Wright (1974), on the other hand, argued that steep slopes in the HRTFs determine the sound location. However, to our knowledge, these concepts have never been implemented in a model that can be used to predict localization of broadband sounds. Watkins (1978) presented a model in which the sound source location is decoded in a spectral-pattern recognition process, in which a best-fitting comb-filter pattern is determined. This model could predict his own localization data for comb-filter stimuli, and data of Hebrank and Wright (1974) for high-, low- and bandpass filtered stimuli. The model could not, however, distinguish between front and rear positions.

Middlebrooks proposed that the auditory system has knowledge of the directional filters of the pinnae themselves and showed that such a simple model, in which the sound direction is determined by the best-fitting directional filter, can predict localization data of both broadband (Middlebrooks, 1999b) and narrow-band (Middlebrooks, 1992) stimuli for positions all around the listener. Since then a number of other studies have proposed similar models for predicting localization of single sound sources (Hofman and Van Opstal, 1998b; Janko *et al.*, 1995; Chung *et al.*, 2000) and multiple sound sources (Langendijk *et al.*, 2001) on the basis of this principle.

In the present study, a number of variations on Middlebrook's model were tested against the actual localization data and a maximum likelihood procedure was used to measure model performance. The advantage of using this procedure is that it does not impose any constraints on the shape of the response distribution (which may have multiple modes that could be narrow or broad). For example, in a previous study

(Watkins, 1978) only a single position was predicted as the response location (which coincided with the position for which the pdf reaches its maximum). The present study, on the other hand considers the output of the model as a probability density function in which any position is a possible candidate for a response, but some positions are more likely to trigger a response than others. This approach has similarities with that used by Middlebrooks (1992) who ranked the predicted positions according to the outcome of the model in order to measure model performance.

Analysis of the performance of the model revealed that taking the first- or second-order derivative with respect to the frequency bins of the DTF (parameter DO) led to a decrease in performance relative to not taking a derivative. This is a surprising outcome because Zakarauskas and Cynader (1993) showed that, in theory, the processing of spectral cues would in that case be more robust with respect to variations in the stimulus spectrum. However, these authors did not test their hypothesis against actual localization data, and our data suggest that the auditory system does not use this more optimum strategy.

Two listeners in the present experiment were unable to localize sounds correctly in the baseline condition for a subset of the positions. This is not uncommon in sound localization research (Bronkhorst, 1995; Middlebrooks, 1999b; Wightman and Kistler, 1989b). Four possible explanations can be given of which the last is the most likely. (1) Wightman and Kistler (Wightman and Kistler, 1989b) suggested that the inability of one of their listeners to localize correctly resulted from the absence of prominent binaural disparity cues (interaural spectral differences), however, no such evidence was found in the present study and Morimoto and Nomachi (1982) showed that the removal of binaural disparity cues hardly affects localization accuracy. (2) The HRTFs of two listeners did not possess any localization cues. Yet, in the present study, both the model predictions of the response distribution and the detailed investigation of the HRTFs indicate that sufficient (monaural) localization cues were available for all the listeners tested. (3) The observed differences in performance between listeners could be that errors were introduced by our procedure for generating virtual sounds, which affected some listeners more than others. However, the two listeners who performed poorly in the present experiment also performed below average in free-field localization tests carried out with the same listeners in a separate study. (4) The most likely explanation seems to be that that these two listeners failed to learn how to map the available cues to the correct position. It would be interesting to investigate whether poor localizers can be trained to become good localizers or whether there is a serious deficit in their auditory systems that prevents them from ever becoming good localizers.

APPENDIX: MODEL EQUATIONS

The templates ($\tilde{X}$) and the input spectra ($\tilde{Y}$) of the model were averaged in 1/n-octave bands (parameter BW) using

$$X_{1/n}(j)=\sqrt{\frac{1}{N(j)}\sum_{i=n(j)}^{n(j+1)-1}X(i)^2}, \tag{A1}$$

where $n(j)$ is the first bin in the jth 1/n-octave band and $N(j)$ the number of bins in that band $[N(j)=n(j+1)-1-n(j)]$.

Taking the first-(X') and second-(X'') order derivative (DO) with respect to frequency was accomplished with

$$X'(j)=X(j+1)-X(j), \tag{A2}$$

$$X''(j)=X'(j+1)-X'(j). \tag{A3}$$

The probabilities (P) for the cross-correlation coefficient method (XCC) were calculated using

$$P=\frac{\mathrm{XCC}+1}{2}, \tag{A4}$$

$$\mathrm{XCC}=\frac{C(X,Y)}{\sqrt{C(X,X)C(Y,Y)}}, \tag{A5}$$

$$C(X,Y)=\frac{1}{N-1}\sum_{i=1}^{N}(X_i-\overline{X})(Y_i-\overline{Y}). \tag{A6}$$

In the standard deviation method (STD), which uses a normal probability density function (f) to transform to probabilities, the following equations are used:

$$P=f(\mathrm{STD},S,0), \tag{A7}$$

$$\mathrm{STD}=\sqrt{\frac{1}{N}\sum_{i=1}^{N}(Z_i-\overline{Z})^2}, \tag{A8}$$

$$f(x,\sigma,\mu)=\frac{1}{\sigma\sqrt{2\pi}}e^{-(1/2)((x-\mu)/\sigma)^2}, \tag{A9}$$

where S is a free parameter, $Z=X-Y$, and $\overline{X}$, $\overline{Y}$, $\overline{Z}$ are the averages across all 1/n-octave bands of X, Y, Z, respectively.

Finally, the probability vectors P for each target position were normalized to unity across the 53 possible response positions.

Asano, F., Suzuki, Y., and Sone, T. (**1990**). ''Role of spectral cues in median plane localization,'' J. Acoust. Soc. Am. **88**, 159–168.

Blauert, J. (**1969/70**). ''Sound localization in the median plane,'' Acustica **22**, 205–213.

Blauert, J. (**1997**). *Spatial Hearing* (MIT, Cambridge, MA).

Bronkhorst, A. W. (**1995**). ''Localization of real and virtual sound sources,'' J. Acoust. Soc. Am. **98**, 2542–2553.

Carlile, S., Leong, P., and Hyams, S. (**1997**). ''The nature and distribution of errors in sound localization by human listeners,'' Hear. Res. **114**, 179–196.

Chung, W., Carlile, S., and Leong, P. (**2000**). ''A performance adequate computational model for auditory localization,'' J. Acoust. Soc. Am. **107**, 432–445.

Gardner, M. B., and Gardner, R. S. (**1973**). ''Problem of localizing in the median plane: Effect of pinnae cavity occlusion,'' J. Acoust. Soc. Am. **53**, 400–408.

Han, H. L. (**1994**). ''Measuring a dummy head in search of pinna cues,'' J. Audio Eng. Soc. **42**, 15–37.

Hebrank, J., and Wright, D. (**1974**). ''Spectral cues used in the localization of sound sources on the median plane,'' J. Acoust. Soc. Am. **56**, 1829–1834.

Hofman, P. M., and Van Opstal, A. J. (**1998a**). ''Relearning sound localization with new ears,'' Nat. Neurosci. **1**, 417–421.
Hofman, P. M., and Van Opstal, A. J. (**1998b**). ''Spectro-temporal factors in two-dimensional human sound localization,'' J. Acoust. Soc. Am. **103**, 2634–2648.
Janko, J. A., Anderson, T. R., and Gilkey, R. H. (**1995**). ''Using neural networks to evaluate the viability of monaural and interaural cues for sound localization,'' in *Binaural and Spatial Hearing in Real and Virtual Environments*, edited by R. H. Gilkey and T. R. Anderson, (Erlbaum, Hillsdale, NJ) pp. 557–570.
Kistler, D. J., and Wightman, F. L. (**1992**). ''A model of head-related transfer functions based on principal components analysis and minimum-phase reconstruction,'' J. Acoust. Soc. Am. **91**, 1637–1647.
Kulkarni, A., and Colburn, H. S. (**1999**). ''Role of spectral detail in sound-source localization,'' Nature (London) **396**, 747–749.
Langendijk, E. H. A., and Bronkhorst, A. W. (**1997**). ''Collecting localization responses with a virtual acoustic pointer,'' J. Acoust. Soc. Am. **101**, 3106.
Langendijk, E. H. A., and Bronkhorst, A. W. (**2000**). ''Fidelity of 3D-sound reproduction using a virtual auditory display,'' J. Acoust. Soc. Am. **107**, 528–537.
Langendijk, E. H. A., Kistler, D. J., and Wightman, F. L. (**2001**). ''Sound localization in the presence of one or two distracters,'' J. Acoust. Soc. Am. **109**, 2123–2134.
Makous, J., and Middlebrooks, J. (**1990**). ''Two-dimensional sound localization by human listeners,'' J. Acoust. Soc. Am. **87**, 2188–2200.
McCullagh, P., and Nelder, J. A. (**1989**). *Generalized Linear Models* (Chapman and Hall, London).
Middlebrooks, J. (**1992**). ''Narrow-band sound localization related to external ear acoustics,'' J. Acoust. Soc. Am. **92**, 2607–2624.
Middlebrooks, J. C. (**1999a**). ''Individual differences in external-ear transfer function reduced by scaling in frequency,'' J. Acoust. Soc. Am. **106**, 1480–1492.
Middlebrooks, J. C. (**1999b**). ''Virtual localization improved by scaling nonindividualized external-ear tranfer functions in frequency,'' J. Acoust. Soc. Am. **106**, 1493–1509.
Middlebrooks, J., and Green, D. (**1990**). ''Directional dependence of interaural envelope delays,'' J. Acoust. Soc. Am. **87**, 2149–2162.
Middlebrooks, J., Makous, J. C., and Green, D. M. (**1989**). ''Directional sensitivity of sound-pressure levels in the human ear canal,'' J. Acoust. Soc. Am. **86**, 89–107.
Morimoto, M., and Aokata, H. (**1984**). ''Localization cues of sound sources in the upper hemisphere,'' J. Acoust. Soc. Jpn. (E) **5**(3), 165–173.
Morimoto, M., and Nomachi, K. (**1982**). ''Binaural disparity cues in median-plane localization,'' J. Acoust. Soc. Jpn. (E) **3**(2), 99–103.
Musicant, A. D., and Butler, R. A. (**1984**). ''The psychophysical basis of monaural localization,'' Hear. Res. **14**, 185–190.
Oldfield, S., and Parker, S. (**1984**). ''Acuity of sound localization: a topography of auditory space. II. Pinna cues absent,'' Perception **13**, 601–617.
Rakerd, B., Hartman, W. M., and McCaskey, T. L. (**1999**). ''Identification and localization of sound sources in the median saggital plane,'' J. Acoust. Soc. Am. **106**, 2812–2820.
Shaw, E. (**1974**). ''Transformation of sound pressure level from the free field to the eardrum in the horizontal plane,'' J. Acoust. Soc. Am. **56**, 1848–1861.
Shaw, E. A. G. (**1982**). *Localization of Sound: Theory and Applications* (Amphora, Groton, CT), pp. 30–41.
Watkins, A. J. (**1978**). ''Psychoacoustical aspects of synthesized vertical locale cues,'' J. Acoust. Soc. Am. **63**, 1152–1165.
Wenzel, E. M., Arruda, M., Kistler, D. J., and Wightman, F. L. (**1993**). ''Localization using nonindividualized head-related transfer functions,'' J. Acoust. Soc. Am. **94**, 111–123.
Wightman, F. L., and Kistler, D. J. (**1989a**). ''Headphone simulation of free-field listening. I: Stimulus synthesis,'' J. Acoust. Soc. Am. **85**, 858–867.
Wightman, F. L., and Kistler, D. J. (**1989b**). ''Headphone simulation of free-field listening. II: Psychophysical validation,'' J. Acoust. Soc. Am. **85**, 868–878.
Woodworth, R. (**1938**). *Experimental Psychology* (Holt, New York).
Zahorik, P., Wightman, F. L., and Kistler, D. J. (**1995**). ''On the discriminability of virtual and real sound sources,'' in *Proceedings of the ASSP (IEEE) Workshop on Applications of Signal Processing on Audio and Acoustics* (IEEE, New York).
Zakarauskas, P., and Cynader, M. S. (**1993**). ''A computational theory of spectral cue localization,'' J. Acoust. Soc. Am. **94**, 1323–1331.

An adaptive procedure for categorical loudness scaling

Thomas Brand and Volker Hohmann
Medizinische Physik, Carl-von-Ossietzky Universität Oldenburg, D-26111 Oldenburg, Germany

(Received 4 May 2001; revised 4 February 2002; accepted 27 June 2002)

In this study, an adaptive procedure for categorical loudness scaling is introduced and evaluated. The procedure adjusts the presentation levels to the subject's individual auditory dynamic range without employing any premeasurement and presents levels in randomized order. The procedure has been named ''Oldenburg—ACALOS'' (Oldenburg—Adaptive CAtegorical LOudness Scaling). It was evaluated using repeated measurements with ten subjects with normal hearing and ten subjects with sensorineural hearing impairment. The results of this investigation revealed that the adaptive procedure provides greater reliability, while being more time efficient than a reference procedure that uses constant stimuli. © *2002 Acoustical Society of America.* [DOI: 10.1121/1.1502902]

PACS numbers: 43.66.Cb, 43.66.Yw [MRL]

I. INTRODUCTION

Loudness functions are used for the diagnosis of loudness recruitment in clinical audiology (e.g., Allen *et al.*, 1990; Hellmann and Meiselman, 1993; Kießling *et al.*, 1993; Kießling, 1995; Hohmann and Kollmeier, 1995; Launer *et al.*, 1996) and for determining the input/output characteristics of hearing aids with automatic gain control (e.g., Pascoe, 1978; Geller and Margiolis, 1984; Hellbrück and Moser, 1985; Margiolis, 1985; Moore *et al.*, 1992; Kießling *et al.*, 1996). In this study an optimized adaptive procedure for the assessment of loudness functions is introduced and evaluated that uses the method of categorical loudness scaling.

The classical, number-based procedures to measure loudness functions, such as the ''ratio scale'' procedure (e.g., Stevens, 1957) or the different kinds of magnitude estimation and magnitude production (e.g., Hellman and Zwislocki, 1963; Hellmann and Meiselman, 1993), require some training and are somewhat difficult to handle in audiology. Furthermore, in audiology, one is often interested in the question of how loud a stimulus is perceived in terms of ''soft'' and ''loud'' rather than in the ratios of loudness of different stimuli. The categorical loudness scaling method (e.g., Pascoe, 1978; Heller, 1985; Allen *et al.*, 1990; Hohmann and Kollmeier, 1995) applies these loudness categories.

Pure-tone audiometry determines the limits of the auditory dynamic range. Different listeners, however, may show different loudness functions, even if they have similar auditory dynamic ranges (e.g., Brand and Hohmann, 2001). Categorical loudness scaling procedures determine loudness functions at their limits but also at moderate levels, which are more relevant for daily life situations. However, hearing-aid fitting is mostly based on the pure-tone audiogram. The same holds for the prescriptive rules used for hearing-aid fitting (McCandless and Lyregaard, 1983; Byrne and Dillon, 1986; Berger *et al.*, 1988; Cornelisse *et al.*, 1995; Killion, 1996). These rules predict the loudness growth based on the threshold. Loudness scaling is rarely used in clinics because the measurement time is long compared to pure-tone audiometry. Furthermore, according to Elberling (1999) as well as Wesselkamp *et al.* (2001), the extra effort of categorical loudness scaling is not worthwhile, because no additional information for the hearing-aid fitting process is provided. Thus, it seems unclear to what extent loudness scaling is useful for hearing-aid fitting. This should be investigated in further clinical studies. In any case, if loudness scaling is used, the procedure should be as efficient and reliable as possible. Therefore, an approach for an optimized procedure for categorical loudness scaling is introduced and evaluated in this study.

An efficient loudness scaling procedure has to ensure that the number of inaudible stimuli is small, because they do not produce any loudness ratings. Furthermore, harmful levels have to be avoided. The stimuli should be evenly distributed within the limits of the individual auditory dynamic range to reduce bias effects (Parducci and Perret, 1971; Montgomery, 1975). The different categorical loudness scaling procedures available today (e.g., Pascoe, 1978; Heller, 1985; Allen *et al.*, 1990; Elberling and Nielsen, 1993; Hohmann and Kollmeier, 1995; Ricketts and Bentler, 1996; Cox *et al.*, 1997; Rasmussen *et al.*, 1998; Keidser *et al.*, 1999) fulfill these demands either by using a premeasurement phase, which roughly determines the individual auditory dynamic range before the actual data collecting phase begins, or by using iterated ascending level sequences which stop when the uncomfortable level is reached. To our knowledge, there is no procedure which omits the premeasurement and which randomizes levels at the same time.

The use of a premeasurement phase (e.g., Heller, 1985; Allen *et al.*, 1990; Elberling and Nielsen, 1993; Hohmann and Kollmeier, 1995; Ricketts and Bentler, 1996; Rasmussen *et al.*, 1998) has the advantage that the stimulus levels in the data collection phase can be randomized to reduce biases. However, we observed that the upper limit of the auditory dynamic range was often underestimated by the premeasurement phase that we used before the constant stimuli procedure described below. This premeasurement phase employed an ascending level sequence which was perceived as being threatening by the listeners. As a consequence, no loud or very loud stimuli occurred in the subsequent data collection phase. In such cases, significant biases have to be expected, because loudness ratings depend on the range of presentation

levels (e.g., Teightsoonian, 1973; Marks and Warner, 1991; Gabriel, 1996) and many subjects systematically shift their response criterion to cover the dynamic range of stimuli using the entire scale (Poulton, 1989). One possibility to solve this problem would be to use a premeasurement phase which determines the upper limit of the auditory dynamic range without employing sequences with ascending levels. This could be done manually, for example. However, such an approach would result in an even greater time commitment. In any case, a premeasurement phase is inefficient since it produces no data.

Using iterated ascending level sequences, which stop when the rating ''too loud'' is given (e.g., Pascoe, 1978; Cox *et al.*, 1997; Keidser *et al.*, 1999), has the advantage that the highest stimulus level is adapted to the subjects auditory dynamic range in each ascending iteration. This is useful if the subject changes their criterion for too loud during the measurement. On the other hand, ascending level sequences cause significant biases of loudness function estimates and the results deviate significantly from those of randomly selected level sequences (e.g., Gabriel, 1996; Jenstad *et al.*, 1997). Parducci and Perret (1971) found that randomized levels avoid a cumulation of biases.[1]

The Oldenburg—ACALOS (Adaptive CAtegorical LOudness Scaling) procedure tries to combine the advantages of randomized levels (which have so far only been realized by procedures using a premeasurement phase) and of the omission of the premeasurement phase (which has so far only been realized by procedures using ascending level sequences). The procedure iteratively adapts the level range to the subject's responses. It is based on the constant stimuli version of the Oldenburg loudness scaling procedure, which uses a premeasurement consisting of an ascending level sequence (Hohmann and Kollmeier, 1995). This prior version is a typical representantative of categorical loudness scaling procedures with premeasurement and subsequent data collection using randomized levels. It has been used by Hohmann and Kollmeier (1995), Launer (1995), Albani *et al.* (1997), and Brand and Hohmann (2001). Very similar procedures have been used by Kießling *et al.* (1993, 1997). We use the constant stimuli procedure as a reference procedure in this study.

Most adaptive procedures in psychoacoustics converge to a certain given target values in the response domain to achieve maximum accuracy of threshold estimates (e.g., Taylor and Creelman, 1967; Levitt, 1971; Campbell, 1974). Such procedures were also used in loudness comparison methods, usually in randomly interleaved sequences of trials (e.g., Jesteadt, 1980; Buus *et al.*, 1999). A somewhat different approach was used in the ScalAdapt procedure (Kießling *et al.*, 1996) which aims to set hearing-aid parameters by converging to a fixed target loudness only, without estimating the loudness function completely. For diagnostical purposes, we did not follow this approach in this study. Converging to specific targets might cause significant response biases due to range and context effects (e.g., Poulton, 1989).

The rationale of this study was to evaluate to what extent the adaptive procedure fulfills the following demands:

(1) The stimulus spacing should be equal in the subject's loudness domain (Parducci and Perret, 1971; Poulton, 1989).
(2) The whole individual auditory dynamic range should be employed in order to reduce range equalizing biases.
(3) The number of presentation levels outside the auditory dynamic range should be reduced in order to yield more efficiency.
(4) The order of stimulus levels should be randomized.

The hypothesis which we wanted to test in this study was whether the adaptive procedure is able to generate the desired level distribution and to yield an efficient estimate of the loudness function, and whether its results deviate from the results obtained with the constant stimuli procedure. This was tested with repeated measurements with ten normal-hearing subjects and ten subjects with hearing impairment.

II. METHOD

A. Subjects and measurement program

Ten normal-hearing subjects (5 male, 5 female; aged 24–57 years; median 28 years) and ten subjects with hearing impairment (6 male, 4 female; aged 22–76 years; median 58 years) participated in the experiment. The hearing threshold of the normal-hearing subjects was lower than 15 dB HL at the standard audiometric frequencies from 125 Hz to 8 kHz. At 1 kHz the thresholds were in the range of −15 to 10 dB HL. The hearing thresholds were measured manually using a KIND DA 930 audiometer with Telephonics TDH 39P headphones. Each hearing threshold level was measured using at least two reversals of the presentation level. The step size was 5 dB. Three of the normal-hearing subjects were members of the research group. The other subjects had no prior experience in psychoacoustical experiments and were paid on an hourly basis. The subjects with hearing impairment showed sensorineural hearing losses of different degrees. Their hearing thresholds ranged from 15 to 85 dB HL at 500 Hz and from 15 to 95 dB HL at 4 kHz. At 1 kHz the range was 20 to 85 dB HL. They had never performed loudness scaling prior to the experiment. Ten runs of both the constant stimuli and the adaptive procedures were completed by each subject. Five repetitions with the same ear and procedure were performed in a block. Then, ear and/or procedure was changed. The sequence of blocks was randomized between subjects.

B. Response scale

Both constant stimuli and adaptive procedures used the response scale shown in Fig. 1. It consisted of 11 response alternatives. Five categories were titled ''sehr leise'' (''very soft''), ''leise'' (''soft''), ''mittel'' (''medium''), ''laut'' (''loud''), and ''sehr laut'' (''very loud'') and corresponded to 5, 15, 25, 35, and 45 cu (categorical units) as shown on the left side of Fig. 1. These categories had been chosen as they are common language expressions related to loudness. The category ''medium'' was chosen because it is not related to

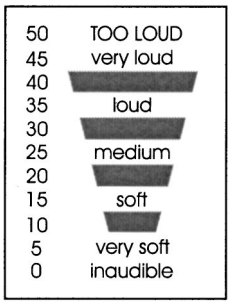

FIG. 1. Category scale with 11 response alternatives used by the subjects to rate the loudness. The numbers on the left side indicate the categorical units (cu) which are used for data storage and analysis. They were not visible to the subjects.

another perceptual dimension like, for example, ''comfortable.'' Four unnamed response alternatives were used to increase the total number of response alternatives. They were indicated with horizontal bars and corresponded to 10, 20, 30, and 40 cu. The limiting categories are titled ''unhörbar'' (''inaudible'') and ''ZU LAUT'' (''TOO LOUD'') corresponding to 0 and 50 cu. The total number of 11 response alternatives is a compromise between precision and usability in clinical diagnostics (Brand, 2000). The level assigned to a given loudness category x is termed the ''categorical loudness level'' L_x. L_{25}, for example, is the level corresponding to medium. Prior to testing, each listener was instructed verbally by the experimenter (see Appendix B). During the instructions, the response box was demonstrated and any questions were answered.

C. Constant stimuli procedure

The constant stimuli version of the Oldenburg loudness scaling procedure (Hohmann and Kollmeier, 1995) included two parts. First, the auditory dynamic range of the listener was estimated. In the second part, the loudness function was assessed in the predetermined auditory dynamic range.

The first part used an ascending stimulus level sequence beginning at 0 dB HL with a step size of 5 dB. The listener's task was to press the response button as soon as the stimulus was audible. Then, the level was further increased in 15-dB steps up to 85 dB HL and in 5-dB steps beyond 85 dB HL. The listener was then asked to press another response button as soon as the stimulus was perceived as too loud. In order to avoid harmful sounds, the sequence stopped at 115 dB HL if the listener had not pressed the response button by then.

In the second part of the procedure, two stimuli were presented at seven levels distributed equidistantly on a dB scale within the predetermined auditory dynamic range. The listener rated the loudness using the scale described above. The stimuli were presented in a pseudorandom order such that the maximum difference between successive levels was smaller than half of the dynamic range of the sequence. In this way, context effects, due to the tendency of many subjects to rate the current stimulus relatively to the previous stimulus, should be reduced. The pseudorandom sequences were constrained to have an increasing tendency.

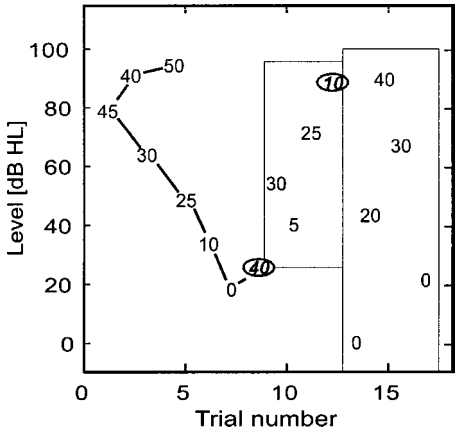

FIG. 2. Example of a run produced by the adaptive procedure. The responses are indicated with numbers between 0 (inaudible) and 50 (too loud). The numbers that are marked with ellipses indicate obvious outliers in the response statistics. The abscissa indicates the trial number. The ordinate indicates the presentation level. Those presentation levels which belong to the same iteration of the adaptive procedure are combined by rectangles. The upper and lower limits of the rectangles correspond to the limits of the estimated auditory dynamic range per iteration.

D. Adaptive procedure

The adaptive procedure also consisted of two phases, which was not obvious to the subject, because he/she rated the loudness in both phases. The auditory dynamic range of the subject was roughly estimated in the first phase. More data were collected in the second phase. In this phase, the dynamic range, in which the stimuli were presented, was re-estimated twice.

The first phase started with a stimulus at 80 dB HL. When this was inaudible or too loud, the level was changed in 15-dB steps until a response between inaudible and too loud was given. Thereafter, two interleaved sequences of stimuli began. During the first sequence, the level was increased in 10-dB steps until 90 dB HL, then in 5-dB steps, until the response too loud was given or the maximum level of 115 dB HL was reached. The limitation of the highest presentation level was necessary to prevent the listener from experiencing harmful sounds. In the second sequence, the stimulus level was decreased in 15-dB steps, until it was inaudible. Then it was increased in 5-dB steps until it was audible again. The descending sequence ended when 0 dB HL was reached to be consistent with the constant stimuli procedure, which was also limited to the same minimal presentation level.

In the second phase it was assumed that the final levels of the two interleaved sequences in the first phase corresponded to the categorical loudness values L_5 (very soft) and L_{50} (too loud). The four categorical loudness levels L_{15}, L_{25}, L_{35}, and L_{45} were estimated by linear interpolation and presented in randomized order. Then, a linear function was fitted to the results of all previous trials[2] (including those of the first phase) using a modified least-squares fit (see below) and five levels L_5, L_{15}, L_{25}, L_{35}, and L_{45} were estimated and presented in random order. This process of ''estimating and presenting'' can be iterated several times. Two iterations were performed in this study. Figure 2 gives a sketch of the adaptive procedure with two iterations.

During the procedure described above, the listener was protected against harmful loud stimuli by the constraint that in any case, the level was limited to maximally 5 dB above the last level which was rated as too loud before.[3]

It can be shown using Monte Carlo simulations that the adaptive procedure generates an even distribution of stimulus levels within the auditory dynamic range of the subject (Brand, 2000), provided that the loudness function of the subject is linear. However, many subjects do not fulfill this prerequisite.

E. Model function and fitting

On completion of a run using either the constant stimuli or adaptive procedure, the following model function was fitted to the data:[4]

$$F(L)=\begin{cases} 25+m_{\mathrm{lo}}(L-L_{\mathrm{cut}}) & \text{for } L\leqslant L_{15}, \\ \mathrm{bez}(L,L_{\mathrm{cut}},L_{15},L_{35}) & \text{for } L_{15}<L<L_{35}, \\ 25+m_{\mathrm{hi}}(L-L_{\mathrm{cut}}) & \text{for } L\geqslant L_{35}. \end{cases} \quad (1)$$

It consisted of two linear parts with independent slope values m_{lo} and m_{hi}. The two parts intersected at the level L_{cut}. The transition region between the levels L_{15} (soft) and L_{35} (loud) was smoothed, using a Bezier fit denoted with $\mathrm{bez}(L,L_{\mathrm{cut}},L_{15},L_{35})$. The exact form of the Bezier smoothing is given in Appendix A.[5] This model function provided the best fit to experimental data on the shape of loudness functions from categorical scaling compared to ten other common model loudness functions (Brand, 2000).

The model function $F(L)$ was fitted to the data $R_i(L_i)$ using a modified least-squares fit, that is, by minimizing $\Sigma_i\Delta_i^2$. The distance Δ_i between model function and data was defined as

$$\Delta_i=\begin{cases} 0 & \text{for } F(L_i)<0 \ \wedge \ R_i(L_i)=0, \\ 0 & \text{for } F(L_i)>50 \ \wedge \ R_i(L_i)=50, \\ R_i(L_i)-F(L_i) & \text{otherwise.} \end{cases} \quad (2)$$

This definition of Δ_i takes into account that ceiling effects, which are due to the limited response scale, decrease the variability of loudness ratings of both inaudible and extremely loud sounds.

F. Stimulus and apparatus

A one-third-octave band of noise was used (center frequency 1 kHz, duration 2 s, sampling rate 44.1 kHz, windowed with 100-ms $\cos^2$ ramps). During each trial, the noise was presented twice with a silent interstimulus interval of 1 s duration.

A personal computer with a coprocessor board (Ariel DSP 32C) with 16-bit stereo AD–DA converters was used to control the experiment including stimulus presentation and recording of the subject's responses. The stimulus levels were adjusted by a computer-controlled custom-designed audiometer. Signals were presented monaurally to the subjects using Sennheiser HDA 200 headphones. The headphones were calibrated using a B&K 4153 artificial ear, a B&K 4134 microphone, and a B&K 2510 measuring amplifier. A correction factor of -0.7 dB was introduced to compensate for the frequency response at 1 kHz of the headphones on the artificial ear. The subjects were seated in a sound-insulated booth. Their task was to rate the loudness of each stimulus presented using an Epson EHT 10S handheld computer with an LCD touchscreen showing the response scale.

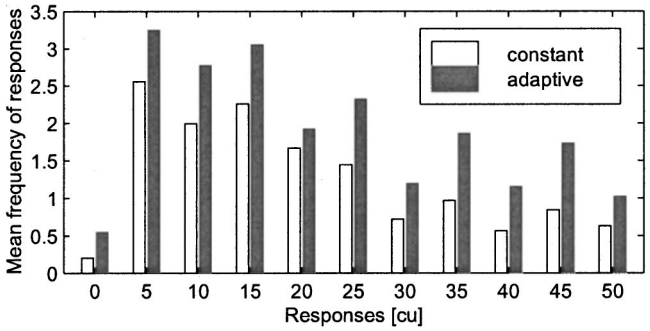

FIG. 3. Mean frequency of the different response alternatives per run for the normal-hearing subjects for both constant stimuli and adaptive procedure.

III. RESULTS

A. Limits of auditory dynamic range

One demand on the loudness scaling procedure was that the level range should cover the whole auditory dynamic range of the subject. The occurrence of the ratings inaudible and/or very soft indicates that the lower limit of the auditory dynamic range had been reached. At least one occurrence of such a response was found in 95% of the runs using the constant stimuli procedure and in 100% of the runs using the adaptive procedure.

In 29% of the runs using the constant stimuli procedure, the premeasurement phase ended with a too-low estimate of the UCL, that is, none of the responses very loud or too loud occurred. This problem occurred for 20% of the measurements with the subjects with normal hearing and for 37% of the measurements with the subjects with hearing impairment. Using the adaptive procedure, the uncomfortable level was not reached only in those cases where it exceeded the maximum allowed level of 115 dB HL. This occurred in 9% of the runs with normal-hearing subjects and in 10% of the runs with subjects with hearing impairment.

B. Distribution of responses

Figure 3 shows the mean frequency distribution of the responses per run for the normal-hearing subjects using both procedures. The adaptive procedure needed on average 20.9 trials per run, whereas the constant stimuli procedure always needed 14 trials per run. Since the premeasurement phase was omitted in the adaptive procedure, both procedures took about the same measurement time. As the minimal stimulus level (0 dB HL for both procedures) was audible for many of the normal-hearing subjects, the frequency of inaudible responses is lower compared to other responses.

The mean response frequencies shown in Fig. 3 are not evenly distributed but decrease with increasing loudness in both procedures. This is consistent with the fact that the loudness function of a 1-kHz narrow-band signal usually has an increasing slope for normal-hearing subjects (see Sec.

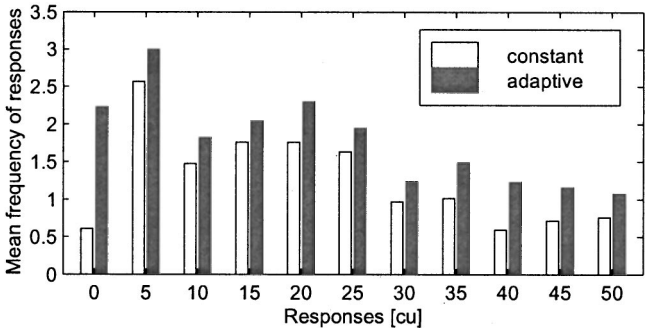

FIG. 4. Mean frequency of response alternatives per run for the subjects with hearing impairment for both constant stimuli and adaptive procedure.

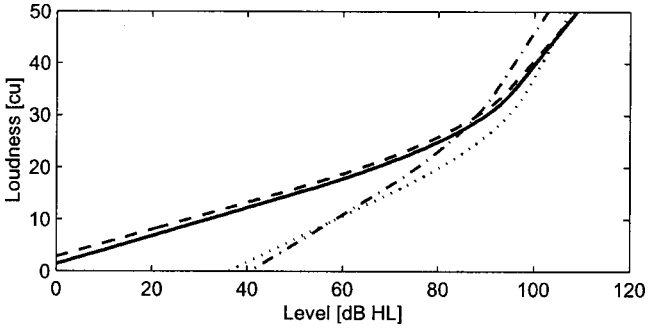

FIG. 5. Loudness functions with the median parameters displayed in Table I. Normal-hearing subjects with adaptive procedure (solid), normal-hearing subjects with constant stimuli procedure (dashed), subjects with hearing impairment with adaptive procedure (dotted), subjects with hearing impairment with constant stimuli procedure (dash-dotted).

III C). Hence, the level range related to loudness values below 25 cu is wider than the level range for loudness values above 25 cu. This means that more stimuli were presented in the lower than in the upper loudness range, since both procedures generated equally distributed stimulus levels on a dB scale. The response frequency shows a somewhat larger relative decrease with level for the constant stimuli than for the adaptive procedure. This is consistent with the fact that in the constant stimuli procedure more cases occurred in which no stimuli were presented near the uncomfortable level compared to the adaptive procedure.

The frequencies of the named response alternatives (5, 15, 25, 35, and 45 cu) tend to be larger than the frequencies of the respective neighboring unnamed response alternatives (10, 20, 30, and 40 cu) for both procedures. A similar effect was found by Keidser *et al.* (1999), who used a scale with 5 labeled and 18 not labeled response alternatives.

Figure 4 shows the mean response frequencies per run for the subjects with hearing impairment. Here, the adaptive procedure generated on average 19.5 trials per run. The response frequencies decreased with increasing loudness at a lower rate than for the normal-hearing subjects (Fig. 3). This is consistent with the more linear loudness functions found for subjects with hearing impairment (see Sec. III C). The decrease was more pronounced in the constant stimuli than in the adaptive procedure. Again, this is consistent with the fact that in the constant stimuli procedure more cases occurred in which no stimuli were presented near the uncomfortable level. The tendency to choose the named response alternatives more frequently is not as obvious as for the normal-hearing subjects.

C. Loudness function estimates

Table I shows the median values of the estimated loudness function parameters for both groups of subjects and both procedures. For each ear, the median values of the parameter estimates were calculated across all ten runs with a given procedure. The median values from these values across all ears (normal-hearing and hearing-impaired, respectively) are displayed in Table I.

TABLE I. Median values of the estimated loudness function parameters for both normal-hearing subjects (NH) and subjects with hearing impairment (HI) obtained by both adaptive and constant stimuli procedures.

	Median (L_{25}) [dB]	Median (m_{lo}) [cu/dB]	Median (m_{hi}) [cu/dB]
NH (adaptive)	80.3	0.27	1.17
NH (constant)	78.1	0.26	1.06
HI (adaptive)	88.6	0.44	1.70
HI (constant)	82.6	0.56	1.42

The adaptive procedure generated higher L_{25} estimates than the constant stimuli procedure for both groups of subjects. This difference was relatively large (about 7 dB) for the subjects with hearing impairment. The adaptive procedure estimated a stronger increase of slope with level (i.e., the ratio of m_{hi} to m_{lo} is larger) compared to the constant stimuli procedure. Figure 5 shows loudness functions with the parameters displayed in Table I.

Figure 6 shows the mean intraindividual standard deviation of the L_x estimate (the ''categorical loudness level'' L_x denotes the level which is related to the loudness categories x). The adaptive procedure yielded 20% to 50% smaller standard deviations than the constant stimuli procedure for both groups of subjects.

IV. DISCUSSION

The Oldenburg—ACALOS procedure introduced here differed from the original constant stimuli procedure (Hohmann and Kollmeier, 1995) in two points: It used an adaptive stimulus placement and it used a nonlinear model loudness

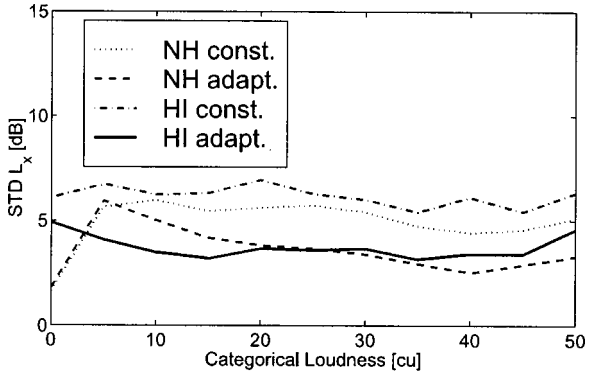

FIG. 6. Intraindividual standard deviations of L_x estimates for normal-hearing (NH) and subjects with hearing impairment (HI) with the adaptive and the constant stimuli procedure.

function.[4] Both modifications together led to a better test–retest reliability of the loudness function estimate. Using the adaptive procedure, the standard deviations of the estimates of the categorical loudness levels L_x amounted to 4–5 dB for both groups of subjects (Fig. 6). These values are equal to or slightly smaller than those generated by the NAL-ACLS procedure (Keidser *et al.*, 1999). While the NAL-ACLS needs 60 trials, the adaptive Oldenburg loudness scaling procedure needs about 20 trials, making the latter much more efficient. The LGOB procedure generated within-subject standard deviations of 2.9 dB in normal-hearing subjects using 45 trials plus premeasurement phase (Allen *et al.*, 1990). Under the assumption that the standard deviations decrease with $1/\sqrt{n}$ with increasing number of trials n, this would correspond to 4.3 dB using 20 trials. Hence, the efficiency of the LGOB procedure is comparable to that of the adaptive Oldenburg procedure. However, the LGOB procedure requires a premeasurement phase which is restructured in the adaptive Oldenburg procedure to allow the data to be included in the final estimate. This makes the adaptive Oldenburg procedure slightly more efficient. Rasmussen *et al.* (1998) used an average of 123 trials per frequency and generated intrasubject intersession standard deviations of 4–8 dB with a maximum at medium levels. Robinson and Gatehouse (1996) used 64 trials and generated intraindividual intersession standard deviations which decreased from 7 to 2.8 dB with increasing level. However, the intersession standard deviations of Rasmussen *et al.* and Robinson and Gate-house cannot be compared directly to the intrasession standard deviations of this study, because the subjects had less possibility to refer to their previous ratings in the case of intersession measurements.

The adaptive procedure determines the level related to each loudness category with a test–retest reliability which is comparable to the reliability of the assessment of hearing thresholds by clinical pure-tone audiometry. Accurate pure-tone audiometry procedures, however, are able to yield better reliability when the number of trials used is comparable to the adaptive loudness scaling procedure. Jervall and Arlinger (1986) found a test–retest standard deviation between 2 and 3 dB at 1 kHz with a manual procedure using a 2-dB step size, which required on average five crossings of the threshold. Using a 5-dB step size, they found a test–retest standard deviation between 3 and 4.3 dB, which required on average four threshold crossings. However, the ACALOS procedure provides information not only on the limits of the auditory dynamic range, but also on the shape of the loudness functions. In a subsequent clinical study, it should be investigated whether this additional information is useful for diagnostics of hearing impairment and for hearing-aid fitting. Whereas it can be assumed that the shape of the individual loudness functions can provide information for differential diagnostics, its use for hearing-aid fitting is questionable (Elberling, 1999). Elberling states that the variance of the inverse slope of the loudness function is constant across subjects, and that categorical loudness scaling cannot provide additional information about the required gain and compression ratio of the hearing aid. However, this statement was derived under the assumption that the threshold estimate has no error, which is not realistic. It also holds only if loudness functions are assumed to be linear, which is not consistent with the nonlinear loudness functions found in categorical loudness scaling. In a clinical study, it should therefore be investigated whether the ACALOS procedure provides additional information that cannot be predicted from the pure-tone audiogram using prescriptive rules for hearing aid fitting (McCandless and Lyregaard, 1983; Byrne and Dillon, 1986; Berger *et al.*, 1988; Cornelisse *et al.*, 1995; Killion, 1996). We assume that valuable information can be provided, because we found quite different shapes of loudness functions even for subjects who show similar limits of their auditory dynamic range (Brand and Hohmann, 2001). Furthermore, it has to be taken into account that prescriptive rules cause an additional error of about 7 dB for the uncomfortable level (Pascoe, 1988) which has to be added to the error of the threshold estimate, whereas the ACALOS procedure yields a total standard deviation of 4–5 dB.

However, one main problem still remains with the application of categorical loudness scaling to hearing-aid fitting: the large variance of loudness functions across normal-hearing subjects, which makes it difficult to quantify the target loudness function (Elberling, 1999).

The constant stimuli and the adaptive procedures differed between their loudness function estimates, although they used the same model loudness function. The loudness functions estimated by the adaptive procedure tended to have larger L_{25} values (see Fig. 5). The estimates of m_{hi} were increased using the adaptive procedure compared to the constant stimuli procedure for the subjects with hearing impairment. The differences between the procedures may be due to context effects caused by the differences between stimulus placements.

(1) The adaptive procedure generated a slightly smaller stimulus spacing than the constant stimuli procedure. The stimulus spacing affects loudness function estimates (Parducci and Wedell, 1989; Poulton, 1989).
(2) The adaptive procedure always began with a presentation level of 80 dB HL. The constant stimuli procedure presented level sequences which tended to increase. Since the initial level of the adaptive procedure tended to be louder for subjects with normal hearing than for subjects with hearing impairment, we believe that the larger differences between procedures for the subjects with impaired hearing may be explained by an anchoring effect of the first stimulus.
(3) The premeasurement phase of the constant stimuli procedure often led to a stimulus level distribution which did not cover the whole auditory dynamic range (especially for the subjects with impaired hearing). This caused a bias, because subjects tend to use the whole response scale. Usually, the adaptive procedure better covers the whole auditory dynamic range.

The adaptive loudness scaling procedure introduced here appears to be efficient and accurate. However, it is still capable of being improved.

(1) The minimum stimulus level should not be limited to 0

dB HL. This would allow coverage also of the full auditory dynamic range of normal-hearing subjects with lower hearing thresholds.

(2) The number of iterations in the second part of the adaptive procedure can easily be extended to increase measuring accuracy. While two iterations were used in this study, three iterations might increase the usability for clinical audiometry and hearing-aid fitting.

(3) Some normal-hearing subjects have reported that the restriction to 11 response alternatives forced them to respond less accurately than they could, especially at soft levels. Scales with more response alternatives, for example the scale of the Würzburg loudness scaling procedure (Heller, 1985) with more than 50 response alternatives and the scale by Keidser *et al.* (1999) with 23 response alternatives, would possibly increase the measuring accuracy. However, some subjects may be puzzled by too many response alternatives.

(4) In order to yield unbiased estimates of the loudness functions, Parducci and Perret (1971) as well as Poulton (1989) recommended to distribute the stimulus levels uniformly on the loudness scale. Unfortunately, such a distribution is currently rarely achieved in our case, since the procedure is optimized for a dB scale, and the relation between level and loudness is often nonlinear, that is, the loudness function shows an increasing slope with increasing level. A solution would be to use a nonlinear model for the loudness function during the actual experiment. This would allow equalizing the responses to a uniform distribution in the remainder of the run. However, more trials would then be required for a stable estimate of the nonlinear model function. We assume that a first valid estimate would be possible after the first block of the second phase of the adaptive procedure.

(5) The average measurement time per trial $T \approx 12$ s is very long compared to other procedures [e.g., $T < 8$ s (Allen *et al.*, 1990), $T < 6$ s (Ricketts and Bentler, 1996), $T \approx 3$ s (Rasmussen *et al.*, 1998)]. T can be reduced by about 6 s by reducing the stimulus to a single presentation of a 1-s noise and by shortening the time interval between response and next presentation.

V. CONCLUSIONS

The Oldenburg—ACALOS (Adaptive CAtegorical LOudness Scaling) procedure estimates the levels related to each loudness category with an intraindividual standard deviation of 4–5 dB using a total number of about 20 trials. The stimulus levels are presented in a pseudorandom order. No premeasurement is necessary. The adaptive version is more efficient than other procedures.

ACKNOWLEDGMENTS

We are very grateful to Birger Kollmeier for his substantial support and contribution to this work. We would like to thank Birgitta Gabriel, Kerstin Sommer, and Anita Gorges for performing the measurements. Thanks are also due to Glenis Long as well as two anonymous reviewers for very helpful comments on an earlier version of this manuscript. We also thank Andrew J. Oxenham for very helpful comments on this manuscript. This study was supported by BMBF and by the CEC supporting action NATASHA.

APPENDIX A: BEZIER SMOOTHING

The Bezier smoothing between 15 and 35 cu is given by

$$\mathrm{bez}(L, L_{\mathrm{cut}}, L_{15}, L_{35}) = y_0 + y_1 \cdot t + y_2 \cdot t^2, \tag{A1}$$

with

$$t(L) = \begin{cases} -\dfrac{x_1}{2x_2} - \sqrt{\dfrac{L - x_0}{x_2} + \dfrac{x_1^2}{4x_2^2}} & \text{for } \dfrac{y_k - y_a}{x_k - x_a} < \dfrac{y_k - y_b}{x_k - x_b} \\ -\dfrac{x_1}{2x_2} + \sqrt{\dfrac{L - x_0}{x_2} + \dfrac{x_1^2}{4x_2^2}} & \text{for } \dfrac{y_k - y_a}{x_k - x_a} > \dfrac{y_k - y_b}{x_k - x_b} \end{cases},$$

and with

$$x_0 = L_{15}, \quad y_0 = 15,$$

$$x_1 = 2 \cdot L_{\mathrm{cut}} - 2 \cdot L_{15}, \quad y_1 = 2 \cdot 25 - 2 \cdot 15,$$

$$x_2 = L_{15} - 2 \cdot L_{\mathrm{cut}} + L_{35} \text{ and } y_2 = 15 - 2 \cdot 25 + 35.$$

The inverse of Eq. (A1) is given by

$$\mathrm{bez}^{-1}(F, L_{\mathrm{cut}}, L_{15}, L_{35}) = x_2 \cdot \left(t + \frac{x_1}{2x_2} \right)^2 - \frac{x_1^2}{4x_2^2} + x_0, \tag{A2}$$

with

$$t = \frac{y}{y_1} - \frac{y_0}{y_1},$$

and with x_0, x_1, x_2, y_0, y_1, and y_2 as defined above.

Equation (A2) can be used to calculate, e.g., the L_{25} parameter [$L_{25} = \mathrm{bez}^{-1}(25, L_{\mathrm{cut}}, L_{15}, L_{35})$].

APPENDIX B: INSTRUCTION

In this experiment, we ask you to judge the loudness of sounds.

Sounds will be presented to you via headphones. After each sound presentation, a response scale will appear on the response box. Please indicate how loud you have perceived the sound on this scale after each presentation. You have the response alternatives ''inaudible,'' ''very soft,'' ''medium,'' ''loud,'' ''very loud,'' and ''too loud.'' You can also choose the intermediate steps indicated by black bars.

Please indicate your response by touching the corresponding field. If you have perceived the sound, e.g., as loud, please touch the word loud. If you have perceived the sound, e.g., between very soft and soft, please touch the bar between very soft and soft. If the response scale appears and you have not heard anything, please touch the field inaudible. There are no right or wrong answers. What matters is how you perceived the sound.

As soon as you gave your response, the response scale will disappear and the next sound will be presented.

Do you have any questions?

[1]Loudness functions derived from categorical loudness scaling differ from those derived from other methods such as magnitude estimation because

response scale and task are totally different. This is not meant when we use the phrase ''bias.''

[2]The phrase ''trial'' is used for the presentation and rating of a single stimulus in contrast to ''run,'' which means all presentations of a certain stimulus at different levels.

[3]It may seem inappropriate to present a stimulus with a higher level than a stimulus which was previously rated as too loud. However, experimental findings from the constant stimuli procedure have indicated that many subjects shift their criterion for too loud upwardly during the run. Note that the adaptive procedure demands a stimulus which is louder than a stimulus previously rated as too loud only in those cases in which the preceding too loud rating was inconsistent with the majority of the remaining responses.

[4]The original version of the constant stimuli procedure (Hohmann and Kollmeier, 1995) used a linear model function with a variable offset for low levels.

[5]Because of the smoothing in the medium range, the L_{cut} parameter in Eq. (1) does not represent the medium loudness level L_{25} but rather the level where the two linear parts would intersect without smoothing. L_{25} is always specified in this study, because it is easier to interpret than L_{cut}.

Albani, S., Brand, T., Gabriel, B., Hohmann, V., and Kollmeier, B. (**1997**). ''Referenzdaten der Oldenburger Hörflächenskalierung,'' in *Hörflächenskalierung, Buchreihe Audiologische Akustik*, edited by B. Kollmeier (Median, Heidelberg), pp. 18–22.

Allen, J. B., Hall, J. L., and Jeng, P. S. (**1990**). ''Loudness growth in 1/2-octave bands (LGOB)—A procedure for the assessment of loudness,'' J. Acoust. Soc. Am. **88**, 745–753.

Berger, K. W., Hagberg, E. N., and Rane, R. L. (**1988**). *Prescription of Hearing Aids: Rationale, Procedure and Results*, 5th ed. (Herald, Kent, OH).

Brand, T. (**2000**). ''Analysis and Optimization of Psychophysical Procedures in Audiology,'' Ph.D. thesis, BIS, University of Oldenburg, Germany.

Brand, T., and Hohmann, V. (**2001**). ''Effect of hearing loss, centre frequency, and bandwidth on the shape of loudness functions in categorical loudness scaling,'' Audiology **40(2)**, 92–103.

Buus, S., Florentine, M., and Poulsen, T. (**1999**). ''Temporal integration of loudness in listeners with hearing losses of primarily cochlear origin,'' J. Acoust. Soc. Am. **105**, 3464–3480.

Byrne, D., and Dillon, H. (**1986**). ''The National Acoustic Laboratories' (NAL) new procedure for selecting the gain and frequency response of a hearing aid,'' Ear Hear. **7**, 257–265.

Campbell, R. A. (**1974**). ''Modifications to the BUDTIF procedure,'' J. Acoust. Soc. Am. Suppl. 1 **56**, S57.

Cornelisse, L. E., Seewald, R. C., and Jamieson, D. G. (**1995**). ''The input/output formula: A theoretical approach to the fitting of personal amplification devices,'' J. Acoust. Soc. Am. **97**, 1854–1864.

Cox, R. M., Alexander, G. C., Taylor, I. M., and Gray, G. A. (**1997**). ''The contour test of loudness perception,'' Ear Hear. **18**(5), 389–400.

Elberling, C. (**1999**). ''Loudness scaling revisited,'' J. Am. Acad. Audiol. **10**, 248–260.

Elberling, C., and Nielsen, C. (**1993**). ''The dynamics of speech and the auditory dynamic range in sensorineural hearing impairment,'' in Recent Developments in Hearing Instrument Technology—15th Danavox Symposium, edited by J. Beilin and G. R. Jensen, pp. 99–133.

Gabriel, B. (**1996**). ''Equal-loudness Level Contours: Procedures, Factors and Models,'' Ph.D. thesis, Universität Oldenburg.

Geller, D., and Margiolis, R. H. (**1984**). ''Magnitude estimation of loudness. I. Application to hearing aid selection,'' J. Speech Hear. Res. **27**, 20–27.

Hellbrück, J., and Moser, L. M. (**1985**). ''Hörgeräte-Audiometrie: Ein computerunterstütztes psychologisches Verfahren zur Hörgeräteanpassung,'' Psychologische Beiträge **27**, 494–508.

Heller, O. (**1985**). ''Hörfeldaudiometrie mit dem Verfahren der Kategorienunterteilung (KU),'' Psychologische Beiträge **27**, 478–493.

Hellman, R. P., and Zwislocki, J. (**1963**). ''Monaural loudness function at 1000 cps and interaural summation,'' J. Acoust. Soc. Am. **35**, 856–865.

Hellmann, R. P., and Meiselman, C. H. (**1993**). ''Rate of loudness growth for pure tones in normal and impaired hearing,'' J. Acoust. Soc. Am. **93**, 966–975.

Hohmann, V., and Kollmeier, B. (**1995**). ''Weiterentwicklung und klinischer Einsatz der Hörfeldskalierung,'' Audiologische Akustik **34**, 48–59.

Jenstad, L. M., Cornelisse, L. E., and Seewald, R. C. (**1997**). ''Effects of test procedure on individual loudness functions,'' Ear Hear. **18**, 401–408.

Jervall, L., and Arlinger, S. (**1986**). ''A comparison of 2-dB and 5-dB step size in pure-tone audiometry,'' Scand. Audiol. **15**, 51–56.

Jesteadt, W. (**1980**). ''An adaptive procedure for subjective judgments,'' Percept. Psychophys. **28**, 85–88.

Keidser, G., Seymour, J., Dillon, H., Grant, F., and Byrne, D. (**1999**). ''An efficient, adaptive method of measuring loudness growth functions,'' Scand. Audiol. **28**, 3–14.

Kießling, J. (**1995**). ''Loudness growth in sensorineural hearing loss—Consequences for hearing aid design and fitting,'' Audiologische Akustik **34**(2), 82–89 (in German).

Kießling, J., Pfreimer, C., and Dyrlund, O. (**1997**). ''Clinical evaluation of three different loudness scaling protocols,'' Scand. Audiol. **26**, 117–121.

Kießling, J., Schubert, M., and Archut, A. (**1996**). ''Adaptive fitting of hearing instruments by category loudness scaling (ScalAdapt),'' Scand. Audiol. **25**, 153–160.

Kießling, J., Steffens, T., and Wagner, I. (**1993**). ''On the clinical application of loudness scaling,'' Audiologische Akustik **32**(4), 100–115 (in German).

Killion, M. C. (**1996**). ''Talking hair cells: What they have to say about hearing aids,'' in Hair Cells and Hearing Aids, edited by C. I. Berlin, pp. 125–172.

Launer, S. (**1995**). ''Loudness Perception in Listeners with Sensorineural Hearing Impairment,'' Ph.D. thesis, Universität Oldenburg.

Launer, S., Hohmann, V., and Kollmeier, B. (**1996**). ''Modeling loudness growth and loudness summation in hearing-impaired listeners,'' in *Modeling Sensorineural Hearing Loss*, edited by W. Jesteadt (Erlbaum, Hillsdale, NJ), pp. 175–185.

Levitt, H. (**1971**). ''Transformed up–down methods in psychoacoustics,'' J. Acoust. Soc. Am. **49**, 467–477.

Margiolis, R. H. (**1985**). ''Magnitude estimation of loudness. III. Performance of selected hearing aid users,'' J. Speech Hear. Res. **28**, 411–420.

Marks, L. E., and Warner, E. (**1991**). ''Slippery context effect and critical bands,'' J. Exp. Psychol. **17**, 986–996.

McCandless, G. A., and Lyregaard, P. E. (**1983**). ''Prescription of gain/output (POGO) for hearing aids.,'' Hearing Instruments **34**(1), 16–21.

Montgomery, H. (**1975**). ''Direct estimation: Effect of methodological factors on scale type,'' Scand. J. Psychol. **16**, 19–29.

Moore, B. C. J., Johnson, J. Seloover, Clark, T. M., and Pluvinage, V. (**1992**). ''Evaluation of a dual-channel full dynamic range compression system for people with sensorineural hearing loss,'' Ear Hear. **13**(5), 349–370.

Parducci, A., and Perret, L. F. (**1971**). ''Category rating scales: Effect of relative spacing and frequency of stimulus values,'' J. Exp. Psychol. Monograph **89**, 427–452.

Parducci, A., and Wedell, D. H. (**1989**). ''The category effect with rating scales: Number of categories, number of stimuli and method of presentation,'' J. Exp. Psychol. Hum. Percept. Perform. **12**(4), 496–516.

Pascoe, D. P. (**1978**). ''An approach to hearing aid selection,'' Hearing Instruments **29**, 12–16.

Pascoe, D. P. (**1988**). ''Clinical measurements of the auditory dynamic range and their relation to formulas for hearing aid gain,'' in Hearing Aid Fitting, 13th Danavox Symposium, edited by J. H. Jensen, pp. 129–152.

Poulton, E. C. (**1989**). *Bias in Quantifying Judgements* (Erlbaum, Hillsdale, NJ).

Rasmussen, A. N., Olsen, S. Ø., Borgkvist, B. V., and Nielsen, L. H. (**1998**). ''Long-term test–retest reliability of category loudness scaling in normal-hearing subjects using pure-tone stimuli,'' Scand. Audiol. **27**, 161–167.

Ricketts, T. A., and Bentler, R. A. (**1996**). ''The effect of test signal type and bandwidth on the categorical scaling of loudness,'' J. Acoust. Soc. Am. **99**, 2281–2287.

Robinson, K., and Gatehouse, S. (**1996**). ''Test–retest reliability of loudness scaling,'' Ear Hear. **17**, 120–123.

Stevens, S. S. (**1957**). ''On the psychophysical law,'' Psychol. Rev. **64**, 153–181.

Taylor, M. M., and Creelman, C. D. (**1967**). ''PEST: Efficient estimates on probability functions,'' J. Acoust. Soc. Am. **41**, 782–787.

Teightsoonian, R. (**1973**). ''Range effects in psychophysical scaling and a review of Stevens' law,'' Am. J. Psychol. **86**, 3–27.

Wesselkamp, M., Marolf-Hackl, S., and Kiessling, J. (**2001**). ''Comparison of two digital hearing instrument fitting strategies,'' Scand. Audiol. **30**, Suppl. 52, 73–75.

Lateralization and detection of pulse trains with alternating interaural time delays

Uma Balakrishnan[a] and Richard L. Freyman
Department of Communication Disorders, University of Massachusetts, Amherst, Massachusetts 01003

(Received 7 September 2000; revised 9 July 2002; accepted 9 July 2002)

The effect of onset interaural time differences (ITDs) on lateralization and detection was investigated for broadband pulse trains 250 ms long with a binaural fundamental frequency of 250 Hz. Within each train, ITDs of successive binaural pulse pairs alternated between two of three values (0 μs, 500 μs left-leading, and 500 μs right-leading) or were invariant. For the alternating conditions, the experimental manipulation was the choice of which of two ITDs was presented first (i.e., at stimulus onset). Lateralization, which was estimated using a broadband noise pointer with a listener adjustable interaural delay, was determined largely by the onset ITD. However, detection thresholds for the signals in left-leading or diotic continuous broadband noise were not affected by where the signals were lateralized. A quantitative analysis suggested that binaural masked thresholds for the pulse trains were well accounted for by the level and phase of harmonic components at 500 and 750 Hz. Detection thresholds obtained for brief stimuli (two binaural pulse or noise burst pairs) were also independent of which of two ITDs was presented first. The control of lateralization by onset cues appears to be based on mechanisms not essential for binaural detection. © *2002 Acoustical Society of America.* [DOI: 10.1121/1.1504859]

PACS numbers: 43.66.Dc, 43.66.Pn, 43.66.Qp [LRB]

I. INTRODUCTION

When a signal is presented binaurally within a continuous broadband masker, the threshold of the signal is improved when the interaural time delay of the signal differs from that of the masker. This masking level difference (or MLD) can be as large as 15 dB for low-frequency signals. An associated phenomenon is that the signal and masker are lateralized in different intracranial positions. Exactly how these two phenomena are related, i.e., whether release from masking depends upon lateralization, or whether they arise from common mechanisms, has been the subject of both experimental and theoretical exploration spanning several decades [see Durlach and Colburn (1978) for a review of the early work].

As an example of research demonstrating a relation between lateralization and detection, Hafter *et al.* (1969) showed that if the interaural delay imposed on a signal is different from that of a masker, the reduction in signal threshold could be predicted by the extent of laterality of the signal relative to that of a diotic masker. On the other hand, Bernstein and Trahiotis (1997) showed that removing lateralization as a basis for comparison of signal and nonsignal intervals, by roving the masker's interaural differences, had little effect on binaural signal detectability. Also, it has been known for a long time that, under at least some MLD conditions (e.g., diotic broadband noise, with a monaural 500-Hz signal delivered to either ear) listeners can detect the signal at S-N ratios at least 4–6 dB lower than those required for accurate left-versus-right lateralization (Egan and Benson, 1966).

It seems that the relation between release from masking and lateralization is not one of absolute dependence. However, this does not mean that the two phenomena do not share a common basis. Lateralization theories of binaural hearing (Webster, 1951; Jeffress, 1972), in their more recent versions (Stern and Shear, 1996; Stern and Trahiotis, 1997), assume that masking level differences and lateralization are based on different features of the same internal display of interaural differences.

The experiments presented here are also concerned with the relation between lateralization and binaural detection, but deal specifically with stimuli whose perceived lateral position is determined by interaural onset cues. Stated simply, we wondered whether the precedence effect, which operates strongly for lateralization, also operates for binaural detection. In a seminal paper that rekindled much of the current interest in the precedence effect, Yost and Soderquist (1984) replicated and extended the original findings of Wallach *et al.* (1949). A basic summary of their results is that the ITD of the first of two binaural pairs of pulses contributes considerably more to lateralization than the ITD of the second pair, provided that there is only a short interval of time between the two pairs. Of the greatest interest here was the final experiment conducted by Yost and Soderquist (1984), which showed that the first pulse pair also contributed more to signal detectability in the presence of a continuous diotic masker than did the second pair. When a time delay was imposed on the first pulse pair, but the second pulse pair was diotic, signal detection improved relative to conditions in which the first pair was diotic and the second was dichotic. This effect of the order of ITDs on signal threshold suggests that the mechanisms responsible for the precedence effect in lateralization also affect binaural detection, supporting the idea of a link between lateralization and detection for these stimuli.

Like many stimuli used in studies of the precedence effect, the signals used by Yost and Soderquist (1984) were

[a]Electronic mail: ubalakris@wcsu.k12.vt.us

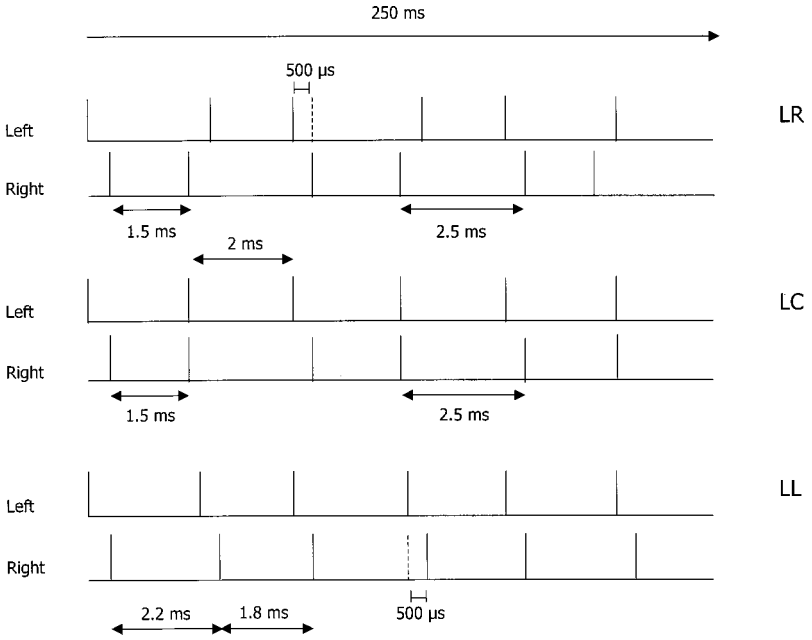

FIG. 1. Three of the nine binaural broadband pulse trains of 250-ms duration. The first 10 ms of the trains are shown. Pulse trains LR (top panel) and RL (not shown) had 500-μs time leads alternating left and right. Trains LC (middle panel) and three others not shown (CL, RC, and CR) had alternating dichotic and diotic pulse pairs. Signals LL (bottom panel), RR, and CC (not shown) had consistent interaural time cues. Interpulse intervals for these last three signals were staggered around 2 ms to vary between 1.8 and 2.2 ms so that their binaural fundamental frequency matched that of the other six trains with alternating interaural time leads.

very short, consisting of two pairs of pulses only 1 ms apart. The purpose of the current study was to explore the potential influence of the precedence effect on binaural detection for longer stimuli. The present stimuli consisted of 250-ms-long trains of binaural pulses in which consecutive pairs of pulses alternated between two values of ITD. Essentially, these stimuli simply repeated the two-pair sequence used by Wallach *et al.* (1949) and Yost and Soderquist (1984) over 250 ms. The lateralization of such alternating pulse trains is strongly determined by the ITD imposed on the very first pair of pulses (Freyman *et al.*, 1997). Our question was whether the mechanisms responsible for this strong onset dominance on lateralization of these trains would also influence binaural detection, as they seem to in the results of Yost and Soderquist (1984) for brief stimuli. In addition to binaural detection, lateralization measures were also obtained, so that both types of data could be compared within the same subjects. Following the experiments with the long trains, the pulse trains were truncated to just two pairs of pulses to evaluate the influence of the precedence effect on the detection of these shortened stimuli.

II. EXPERIMENT I: LATERALIZATION AND DETECTION OF PULSE TRAINS

This experiment compared lateralization and masked binaural detection of nine different pulse trains of 250-ms duration. Six of the nine trains were composed of repeated pairs of pulses whose ITD alternated between two values. The other three had consistent ITDs throughout the train.

A. Method

1. Subjects

Listeners were four young adults in the age range 21–35 years with air conduction thresholds $\leqslant$15 dB HL (*re*: ANSI, 1989) at 0.25, 0.5, 1, 2, 4, and 6 kHz. Subjects listened in a sound-treated booth (IAC 1640), seated in front of an Apple II computer that they used to record their responses.

2. Stimuli

Three sets of stimuli are described: the ''targets'' or pulse trains, the pointer stimulus used for lateralization, and the maskers. All three were generated on a microcomputer. The pulse trains were 250 ms long and consisted of 125 binaural pairs of digitally generated rectangular pulses. The sampling rate was 20 kHz and pulse duration was 50 μs (one sampling interval), as generated by a D/A converter. Three different ITDs were used: left or right lead of 500 μs and center (0 μs) to create a total of nine trains. Three of these had consistent ITDs through their duration, and the other six had ITDs alternating between two of the three values. The interpulse interval (IPI) was 2 ms measured binaurally from the onset of one pulse pair to the onset of the next. This IPI was selected because it was found to elicit a strong effect of onset ITD by Freyman *et al.* (1997).

Figure 1 shows three of the nine trains used in the experiments. As shown, pulse pairs in train LR (top of Fig. 1) alternated between left-lead (-500 μs) and right-lead ($+500$ μs) with the initial pair leading left. Train RL (not shown) had initial ITD leading to the right with the next ITD left leading, and the alternation continued in this way through the duration of the train. For train LC (middle of Fig. 1), ITDs alternated between -500 and 0 μs (C) with the initial time lead to the left. In train CL (not shown) the initial pulse pair was diotic and the next pulse pair was left leading, with the alternation continuing in that order throughout the signal. Two other diotic–dichotic alternating pulse trains, RC and CR (not shown), were similar to LC and CL with 0 μs alternating with $+500$ μs. The bottom trace of Fig. 1 shows the nonalternating pulse train LL for which all time leads were -500 μs. Not shown are two other nonalternating trains CC (0 μs) and RR ($+500$ μs).

As can be seen from Fig. 1, for LR and RL, monaural IPIs alternated between 1.5 and 2.5 ms, resulting in a fundamental frequency of 250 Hz in each ear. Spectral analysis revealed that these two pulse trains had energy at all har-

monic multiples of the fundamental with the exception of 1 kHz and odd integer multiples of 1 kHz. For LC, CL, RC, and CR the alternation of diotic and dichotic pulse pairs resulted in a 500-Hz fundamental frequency in one ear and a 250-Hz fundamental frequency in the other.[1] For these six trains with alternating ITDs the ''binaural'' fundamental frequency was 250 Hz. To match this frequency, the IPI for the three trains with consistent ITDs was slightly staggered around 2 ms and alternated between 1.8 and 2.2 ms (see Fig. 1).

The trains were presented from a two-channel 16-bit D/A converter (TD2 QDA2). The analog output of the D/A converter was low-pass filtered at 8500 Hz (TTE 1390), attenuated (Charybdis), impedance transformed, and delivered over a matched set of earphones (TDH-39) mounted on MX-41/AR supra-aural cushions. The output of the earphones was measured through a 6 cm^3 coupler on a sound level meter (General Radio 1565-B) set on ''C'' weighing and fast response mode as the stimuli were played without interruption by the host computer. The trains were presented at 50 dBC for the lateralization experiments.

The pointer stimulus was a binaurally correlated Gaussian distributed white noise burst of 50-ms duration with a 5-ms rise/fall time. The listener controlled the whole waveform interaural delay of the stimulus. The range of available ITDs was $+800$ μs (right) to -800 μs (left). The sampling rate of 50 kHz used for generating and presenting the noise burst allowed for adjustments of the variable ITD in 20 μs steps. The pointer was low-pass filtered at 8.5 kHz, calibrated, and presented as described for the targets and delivered at 42 dBC.

For the detection experiment, the probes were the same nine pulse train targets described above. The masker was a continuous, digitally generated white noise created by constructing sequences of independent Gaussian distributed numbers. A single token of noise 7 s in duration was duplicated in two channels to make interaurally correlated diotic and dichotic binaural noise maskers. For the dichotic masker a time lead to the left ear of 500 μs was imposed. The noise tokens were then repeated without pause, low-pass filtered at 8.5 kHz, and taped on a digital audio recorder (Sony DAT 75ES) to create continuous recordings of the diotic and dichotic maskers. Each masker was attenuated (TTE PA3), added to the probe via a passive mixer, impedance transformed, and delivered to the subjects through the earphones. The overall masker level for the set of experiments to be described was 54 dBC.

3. Procedures

a. Lateralization. The protocol used for the lateralization experiments was similar to that used by Freyman *et al.* (1997). Listeners adjusted the ITD of the pointer until its intracranial image matched that of the target by rotating the knob of a five-turn potentiometer. The voltage generated by the potentiometer was digitized and a corresponding ITD value was applied to the pointer by software. Lateralization was estimated by the ITD value of the pointer chosen by the listeners to match the target's lateral position. While the estimation was indirect, it was based on the assumption of a linear relation between extent of lateralization and ITD in the range approximately ± 630 μs as suggested by Blauert (1997, p. 144). For purposes of computing the arithmetic mean of the pointer ITDs across trials, the assumption of linearity was extended to ± 800 μs. Within a given trial the target and the pointer alternated, with each being presented three times successively at a rate of two presentations per second. The alternation continued indefinitely as the subject rotated the knob of the potentiometer to position the pointer at the intracranial location of the target. While the alternation was automatic, subjects could listen to the pointer or target alone repeatedly, or interrupt the presentation of both. No time limit was placed on the subjects for making a match. Subjects indicated their choice of a match by pressing a key on the response computer. After a match was made, the next target was presented. Within each block, the order of targets was random. Prior to the presentation of each target, the ITD of the pointer was randomly reassigned to eliminate any bias with respect to the rotations of the dial of the potentiometer. Subjects matched all nine targets in a single listening ''block.'' Generally, the entire block of nine targets was completed in about 5 to 7 min. Each subject listened to six blocks of the nine targets to yield six matches per target. Because one of the subjects' (S3's) initial matches had shown a great deal of scatter, and differed substantially from the other subjects' data for some conditions, a second complete set of matches was obtained from her. As it turned out, the means of the matches for all nine trains were similar between the first and second sets of data, but the scatter was considerably diminished in the second set. The results displayed in the figures are for the second set of matches.

b. Detection. The subjects' task was to detect the probe signals in the presence of the continuous masker. A four-interval forced-choice paradigm was used in which the signal was presented in one randomly selected interval. The beginning of each trial was marked by a warning message on a response computer screen followed by four light bars appearing on the screen successively to mark the four intervals, each of which was 500-ms long. Subjects responded by pressing one of four keys on a keyboard. Feedback was provided following subject responses by flashing of the light bar corresponding to the interval in which the probe occurred. An adaptive tracking method with a two-down, one-up stepping rule was used to track the 70.7% correct point on the psychometric function (Levitt, 1971). The initial step size was 8 dB and halved with each successive reversal to stabilize at 2 dB. For each probe, the probe level was tracked over ten reversals and the probe threshold was computed as the arithmetic mean of the last six reversals expressed in dB. The nine probes were presented in a listening block, which was completed by the subject in a single listening session with a short break after the fifth adaptive track. Each subject completed three such listening blocks. The three thresholds thus obtained were averaged to determine the final threshold for each probe. Prior to the first listening session, subjects were familiarized with the task, with a practice run consisting of one probe. The practice probe was randomly selected across subjects. All subjects were able to do this task without difficulty and no further practice was given.

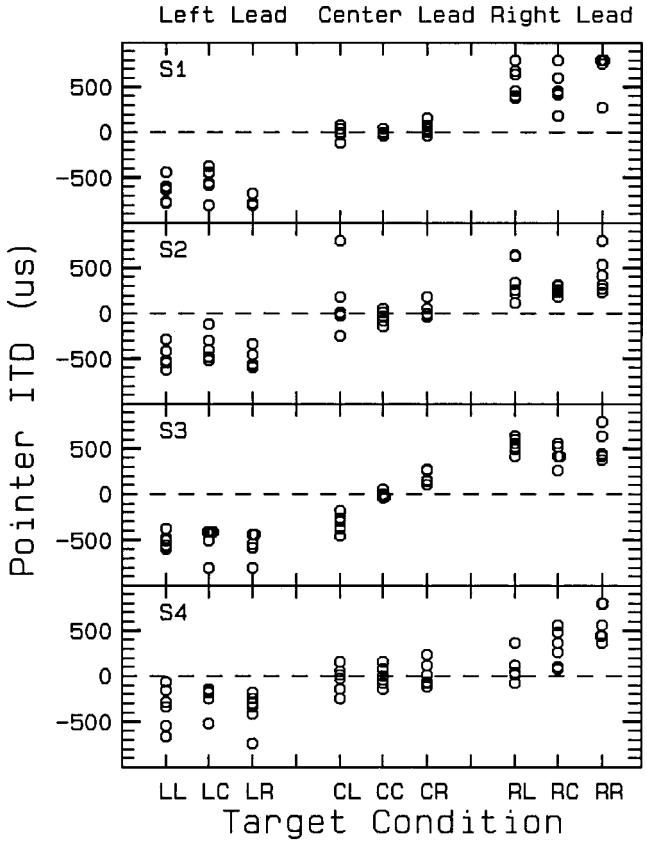

FIG. 2. Pointer adjustments for each of six matches for the nine targets for four subjects. Negative values on the ordinate indicate lateralization to the left, and positive to the right. See text for explanation.

B. Results

1. Lateralization

a. Pointer adjustments. Figure 2 displays all six matches made by the four subjects for each of the nine targets. The abscissa is arranged to group targets with the same onset ITD but which differ from one another in their ongoing ITD configurations. The ordinate indicates pointer ITD in microseconds. Negative values are arbitrarily assigned to denote left-leading pointer ITDs and positive values indicate right-leading ITDs. The general dependence of lateralization on onset ITD is evident. For example, the three left-onset targets were lateralized to the left even though their ongoing ITDs were different. Similarly, lateralization of the center-leading and right-leading targets was largely controlled by the initial ITD. While the influence of the onset ITD was robust, there were some exceptions to the general trend as shown by subject S2's matches to the targets RL and RC, S3's matches to CL, and subject S4's matches to RC and RL. In these cases, the onset ITD had less influence on lateralization. Although there was often considerable variability across the six matches for each condition, this cannot be completely attributable to the alternation of ITD. For example, S4's matches to LL and S2's matches to RR show wide scatter even though there the ITDs were invariant. Nevertheless, these two targets were always matched by subjects on the appropriate side of midline.

Using correlation analysis, Saberi (1996) showed that while the first ITD of a binaural pulse train with randomly varying ITDs contributes the most to lateralization, the ITDs of later pulses also contribute. The variations in our pointer matches suggest that the relative influence of onset and ongoing ITDs on lateralization was not homogeneous across subjects or conditions. We also note that there may be asymmetry between ears for some subjects as shown in the difference in responses to left-leading versus right-leading targets (see S4's responses). Freyman *et al.* (1997) also showed some asymmetry in two of their three subjects for the comparable condition (LR vs RL at 2 ms IPI). Despite the variability and asymmetry, the bulk of the data from the two studies demonstrates a powerful effect of the onset ITD within a train of alternating binaural pulse pairs.

b. Calculation of c. Shinn-Cunningham *et al.* (1993) quantified the degree to which onsets controlled lateralization by computing the statistic *c*, which was defined as the relative weighting of the first ITD in a brief binaural pair of lead-lag stimuli presented over headphones. Although our signals were much longer than the brief stimuli used in their original analysis, we sought to quantify the relative contribution of the first ITD for our stimuli using the same metric. The values were obtained from their Equation 2,

$$c=(\alpha-\tau_2)/(\tau_1-\tau_2),$$

where α was the pointer ITD that matched the target's lateral image, and τ_1 and τ_2 were the nominal leading and trailing ITDs, respectively. We defined τ_1 as the first ITD and τ_2 as the second ITD in our alternating trains. The mean values of *c* derived from the subjects' pointer matches for the six alternating targets were 0.82 for LC, 1.05 for LR, 0.89 for CL, 0.86 for CR, 0.75 for RC, and 0.89 for RL. Most of these are well within the range estimated by Shinn-Cunningham *et al.* for data from several studies. Thus, the strength of the precedence effect for these long trains appears to be consistent with that reported for brief stimuli.

A second calculation of *c* was made to factor out any listener bias in the use of the acoustic pointer. To accomplish this, the two nominal ITD values of the alternating trains were replaced by the subjects' pointer ITD matches for the nonalternating signals with the corresponding ITD. For example, in the case of LR, instead of using -500 and 500 us as τ_1 and τ_2, the actual pointer matches by each subject for LL and RR were substituted. For LC, the pointer matches for LL and CC were used as τ_1 and τ_2. The variable α, of course, was the subject's pointer match for the signal with alternating ITD. The set of mean values of *c* derived in this fashion were 0.82 for LC, 1.04 for LR, 0.93 for CL, 0.89 for CR, 0.68 for RC, and 0.87 for RL. These values agree quite closely with those shown above for the computation using the nominal values of τ_1 and τ_2.

c. Consideration of peripheral auditory models. Attempts have been made recently to understand several aspects of the precedence effect through mostly peripheral auditory analyses (e.g., Tollin and Henning, 1999; Hartung and Trahiotis, 2001), or through a combination of a binaural temporal window and a post-onset weighting mechanism (Akeroyd and Bernstein, 2001). While none of these models was intended to explain the lateralization of the type of stimuli used here, any of them might successfully do so if it was

assumed that lateralization was determined in the early part of the pulse train, and was maintained throughout the ambiguous pulse train through higher level processes. The goal of the model, then, would be to explain lateralization at the beginning of the train. We thought that it would be useful to apply the type of analysis described by Hartung and Trahiotis (2001) to our signals.

Hartung and Trahiotis (2001) processed pairs of precedence-type binaural transients through a bank of gammatone filters and the hair cell processing model of Meddis *et al.* (1990). The filterbank consisted of 14 filters whose center frequencies ranged from 244.7 to 1690 Hz and were spaced by their respective equivalent-rectangular bandwidths (ERB) (Glasberg and Moore, 1990). The output of each filter was fed to the Meddis *et al.* (1990) hair cell model which rectified, low-pass filtered, and compressed the input signal. The cross-correlation products of the outputs of the two ears from the hair cell model were summed across frequency channels with equal weighting assigned to each channel for values of τ in the range -1500 to 1500 μs incremented in 10-μs steps. The location of the peak in the cross correlation as a function of τ was used to predict precedence data for several previous experiments that had used brief pairs of clicks. To accommodate the longer impulse response of the narrower (lower frequency) filters, the cross correlation was computed over a filtered signal duration of 30 ms.

We applied the same model to our signals. The peripheral filtering process incorporated the inner ear hair cell model described by Meddis *et al.* (1990) using the default parameters listed in Fig. 1 of that paper. The model was implemented in Matlab using code made available by the Helsinki University of Technology. The hair cell processing was applied to the output of a bank of 14 filters whose center frequencies were separated by their respective ERBs. The center frequencies ranged from 244.7 to 1702.1 Hz. Cross correlations of the outputs of the hair cell model at the two ears were obtained for each center frequency over the same range of τ used by Hartung and Trahiotis with the difference that τ incremented in 50-μs steps because our signals were sampled at 20 kHz. As in Hartung and Trahiotis (2001), the unweighted values of cross correlation for each τ were averaged across the 14 center frequencies. In preliminary testing of our signals with the inner hair cell model, it became apparent that the choice of the input level (rms) had some bearing on the relative height of the cross correlation peaks. Therefore, the signals were processed at two input levels, 70 and 50 dB SPL.

Cross correlations of the outputs of the hair cell model were computed over rectangular windows of varying duration beginning at stimulus onset. An illustrative set of functions for the stimulus LR at 70 dB SPL is shown in Fig. 3 for window durations of 5, 10, 20, 30, 50, and 100 ms and the full signal duration ('F'). The correlations are normalized to the amplitude of the highest peak for each function. For all the signals with alternating ITDs, the major peak of the cross-correlation function occurred at the first ITD in the alternating sequence (within the 50-μs resolution offered by the sampling rate). There was typically a second bump in the function that corresponded to the second delay in the signal.

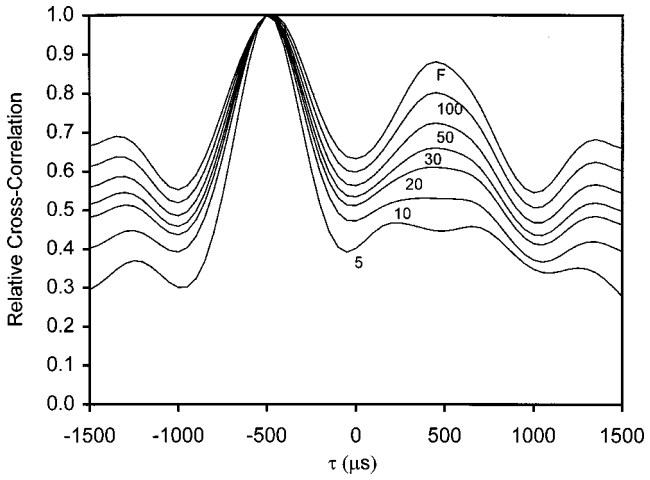

FIG. 3. Cross-correlation functions for signal LR obtained using a 14-filter gammatone filterbank and the hair cell processing model of Meddis *et al.* (1990). Cross correlation averaged across frequency is shown for various rectangular window durations beginning at stimulus onset. Window durations were 5, 10, 20, 30, 50, and 100 ms, as well as the full signal duration "F." Cross correlation was normalized to the highest peak for each function.

This peak became more defined and its relative amplitude increased as window duration increased. Hartung and Trahiotis (2001) suggested that adaptation resulting from dynamic compression in the hair cell model explained the larger contribution of the initial delay to the cross-correlation function for two brief binaural stimulus pairs. It is interesting that even when averaged over the full signal duration of 250 ms, adaptation in the hair cell model is sufficient to show a modest advantage for the initial interaural delay.

Understanding how such multiply peaked functions might be interpreted by the central auditory system requires further assumptions and modeling. At first glance, it is not clear as to which features of the cross correlation might be salient to judgments of laterality. One possibility is that when multiple and unequal peaks occur, the auditory system picks the one that is highest. Because the highest peak for each signal corresponded to the nominal ITD of the initial delay, this hypothesis predicts complete domination of lateralization by the initial ITD, that is, a c of 1.0. It so happens that the c's computed from our data for LR were very close to 1.0. However, while the functions for the other alternating signals (not shown) also showed peaks at the initial ITD, values of c ranged well below 1.0, implying some contribution from the second ITD.

Another hypothesis that incorporates the contribution of the second ITD is that the lateralized image is formed by weighting the two strongest peaks according to their relative heights. For the 5-ms function depicted in Fig. 3, the amplitude of the peak at $+500$ μs is 44.61% of that at -500 μs. This relative weighting of τ_1 and τ_2 occurs when c is 0.69. Using these same assumptions, the predicted c values are also 0.69 for RL, LC, and RC, and slightly higher (0.74) for CR and CL. For an input level of 50 dB SPL (the stimulus level used in the experiment) the predicted values were 0.62 for LR and RL, 0.61 for LC and RC, and 0.68 for CL and CR. These values are all below the c values for the data. Thus, even with the shortest window of 5 ms, the strength of

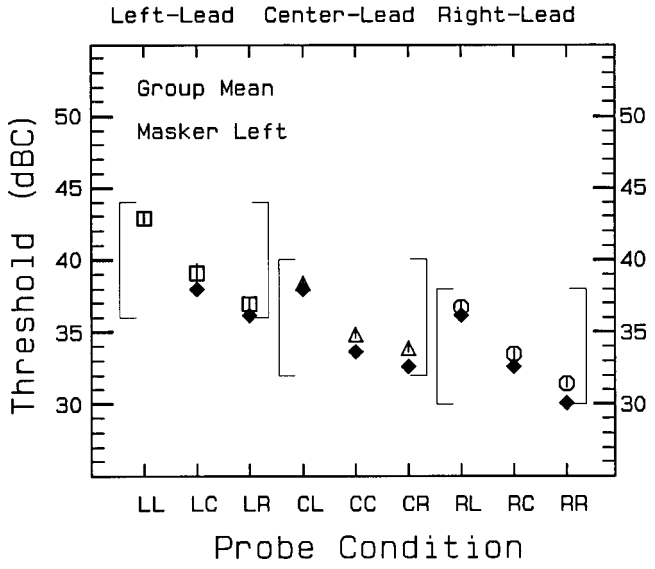

FIG. 4. Group mean masked detection thresholds and ± one standard error for the same pulse trains used in the lateralization experiment. The broadband masker was left-leading (−500 μs). Targets with the same onset ITD are enclosed in brackets for ease of viewing. The filled diamonds display the predicted thresholds obtained from the analysis shown Table II using Colburn and Durlach's data (1965) and described in the text.

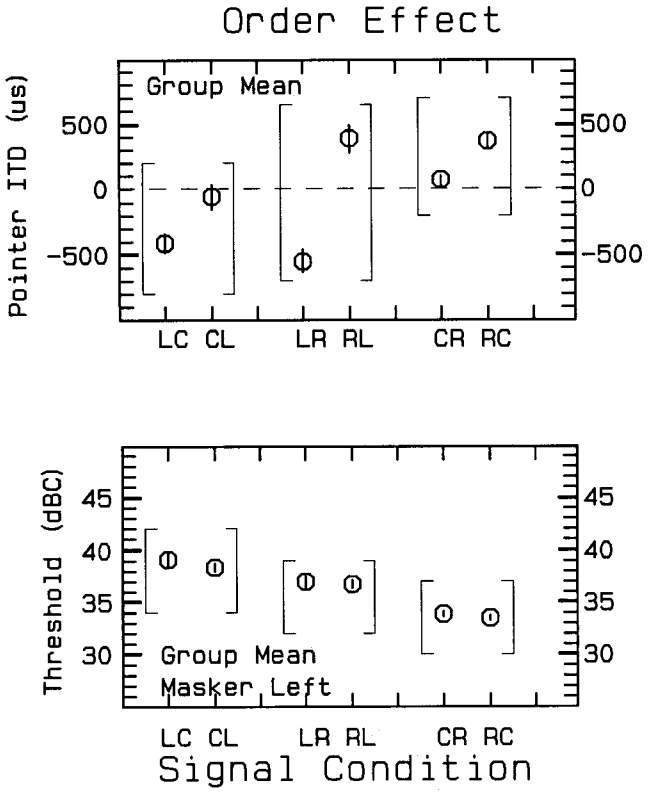

FIG. 5. Group mean pointer adjustments (top panel) and detection thresholds (bottom panel) replotted for the six pulse trains with alternating time leads. Brackets enclose trains with opposing orders of ITDs.

the precedence effect is underestimated by the assumption of proportional weighting of the major peaks. However, a common trend in both the predictions and the *c* values from the data is that *c* is larger when the initial ITD is more central (i.e., CL and CR had higher *c*'s than LC and RC).

The underestimation of the strength of the precedence effect through this model might result from a number of factors. Clearly suspect is the assumption that lateralization results from the proportional weighting of the peaks according to their height. Additional factors relevant to the estimation of the precedence effect in this model are the (possible) weighting assigned to the definition and sharpness of the peaks, the role of multiple peaks (we only considered two), and the interactions that may take place between these diverse elements of the cross-correlation function. It could also be the case that the critical elements for determining lateralization shift depending on listening conditions. There is also the issue of the temporal width and shape of the window used to compute and analyze the cross correlation. Finally, it is worth restating that the output of the cross-correlation functions, the relative height of the peaks, and ultimately the predicted *c* are highly dependent on the input level supplied to the hair cell model.

2. Detection

a. Results. Figure 4 displays group mean detection thresholds (open symbols) for the −500 μs (left-leading) masker. (The filled diamonds will be discussed later.) We chose to display the group mean data rather than individual thresholds because detection thresholds were consistent across subjects as indicated by the small standard errors (0.27–0.5 dB). The ordinate displays threshold in dB SPL and the abscissa indicates the nine probe conditions which are grouped the same way as for the lateralization experiments, i.e., according to their onset ITD. Thresholds were clearly dependent on both alternating ITDs, not just the onset. Highest thresholds occurred for the nonalternating probe LL, which had the same ITD as the masker. Thresholds improved in an orderly manner as one or both of the ITDs in the train were increasingly removed from that of the masker. After LL, the next highest thresholds were for LC and CL, followed in order by LR and RL, CC, CR and RC, and finally RR. Masking level difference (MLD), measured as the difference between thresholds for LL and the other probes, reached a maximum of 11.45 dB for probe RR, which had a simple delay in opposition to that of the masker. This maximum MLD is consistent with data reported by other investigators for low-frequency pure tones in a broadband masker (see Durlach and Colburn, 1978, p. 432).

The primary question in comparing lateralization and detection of these pulse trains was whether the ITD of the first pulse pair, which largely determined the perceived lateral position of these signals, also largely determined the masked detection thresholds. Here the answer was unequivocally no. This result, implicit in Fig. 4, is illustrated more clearly in Fig. 5, which contrasts group mean lateralization data with the replotted detection data from Fig. 4 for the six targets with opposing orders of ITDs. The top panel displays lateralization of the six targets while detection thresholds for the same are plotted in the bottom panel. The data clearly demonstrate that while onsets influenced perceived lateral position, they did not influence the detection thresholds of the signals to any meaningful degree.

Figure 6 displays group mean thresholds for the probes

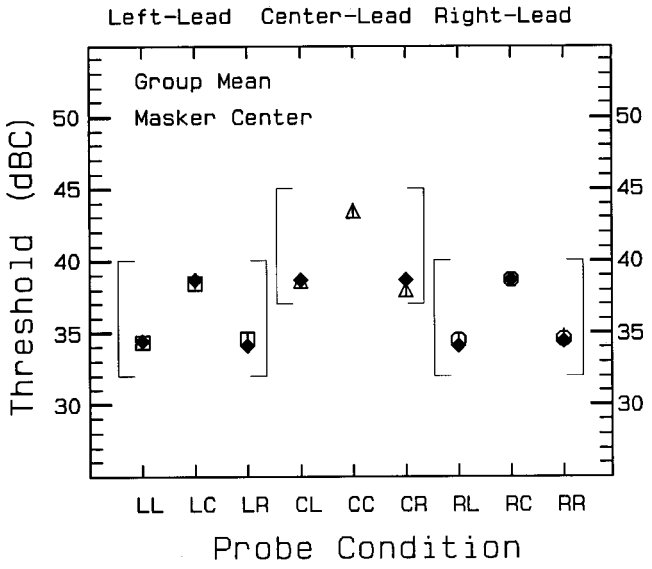

FIG. 6. Group mean detection thresholds for the nine pulse trains in the presence of a diotic masker. Targets with the same onset ITD are enclosed in brackets for ease of viewing. Filled diamonds represent predicted thresholds as in Fig. 4.

for the four subjects in the diotic masker. (Again, the filled diamonds will be discussed later.) As with the lateralized masker, there was no effect of onset ITD for thresholds. MLDs simply increased as one or both ITDs in the probes shifted away from that of the masker. As was to be expected, the highest thresholds occurred for the diotic probe, CC. The lowest thresholds occurred for the probes where neither of the ITDs was diotic, namely, for LL, LR, RR, and RL. Maximum MLDs averaged approximately 9 dB, which was slightly less than the 11 dB MLD seen for the lateralized masker.

b. Quantitative analysis. As stated above, a simple consideration of both ITDs of the pulse trains in relation to the ITD of the masker predicts the correct ordering of the thresholds across the probes for each masker. However, the extant literature on MLDs does not provide a *quantitative* understanding of the thresholds based on this type of broadband analysis. To develop such predictions, we made the assumption that because of the short interpulse intervals and rapid alternation in ITD, the signals could effectively be treated as complex tones with stationary, frequency-dependent interaural phase and interaural level differences. Relative thresholds among the probes were predicted by considering the expected MLDs for each of the frequency components as well as the signal-to-noise (S-N) ratio of the component as estimated at the output of a bank of auditory filters.

To compute the S-N ratios, both signals and maskers were passed separately through a simulation of auditory filtering. This was modeled by Matlab implementation (Slaney, 1993) of a bank of 240 gammatone filters spaced equally on an equivalent rectangular bandwidth (ERB) scale over the range of 250 to 10,000 Hz. The dense spacing of the filters created center frequencies (CFs) that were usually within a few Hz of the harmonic frequencies of the probe signals (multiples of 250 Hz). In a few test cases, the CFs were shifted to match the harmonic frequencies exactly, but this did not alter the outputs of the filters significantly. S-N ratio was determined as the difference in dB between the probe and masker at the output of the filters. ILDs were computed as the difference in S-N ratio between the two ears. Interaural phase differences (IPDs) were derived from 8192 point FFTs of the probes. The IPDs for the left leading masker were computed for an interaural delay of 500 μs at each frequency.

Spectral analysis had shown that the amplitude of the components was relatively flat across a broad frequency range with some local variation across adjacent harmonics. As a result of the widening of the filters with increasing CF, which effectively admitted more noise into the filter, the S-N ratios were best in the low frequencies, specifically 250, 500, and 750 Hz, for all of the probes. Because these frequencies are also associated with large MLDs (see Colburn and Durlach, 1965), they were considered for prediction of thresholds.

For each masker, thresholds were predicted for eight of the probes relative to a ninth baseline probe, which was defined as the one whose interaural differences matched those of the masker (i.e., probe LL with the left leading masker and CC with the diotic masker). In the baseline condition, S-N ratio alone was assumed to determine threshold. For the other eight conditions, S-N ratio and interaural differences in level and phase were used to predict the threshold. For simplicity, we assumed that the masked threshold for a given probe was determined by the one spectral component with the best or lowest predicted threshold. For all nine probes in the left leading masker and seven of the nine probes in the diotic masker, the 500-Hz component predicted the lowest threshold. For the two probes LR and RL, when the masker was diotic, the lowest threshold was predicted for the 750-Hz component. Examination of the masked thresholds for the 250-Hz component at the masker overall level we used suggested that this component would be below the threshold of audibility. For this reason, this frequency was ignored in the prediction of thresholds.

Table I shows S-N ratios for the two ears along with IPD at 500 and 750 Hz for the nine probes. The relative S-N ratio for each probe at both frequencies was normalized to that for LL at 500 Hz. Negative values of IPD represent left lead and positive values, right. For probes LC/CL, and RC/CR, there was a binaural component at 500 Hz and only a monaural component at 750 Hz. Thus, for these four probes, the only measurable IPD was at 500 Hz. The dashed lines in Table I denote the ear with no signal energy at 750 Hz and where no IPD could be calculated.

Table II shows the steps through which relative thresholds were predicted for each probe in relation to the baseline probe. The top half of the table shows the predictions when the masker was left leading, the bottom half for the diotic masker.

For each masker, the top row displays the probe conditions with the progression of ITDs from left-most to right-most. The second row displays the IPD of the probe relative to that of the masker. For example, at 500 Hz the IPD of probe LL was 0 degrees relative to that of the left leading masker, but -90 degrees relative to the diotic masker.

TABLE I. S-N ratios for the two ears along with IPD at 500 and 750 Hz for the nine probes. The relative S-N ratio for each probe at both frequencies was normalized to that for LL at 500 Hz. Negative values of IPD represent left lead and positive values, right. For probes LC/CL, and RC/CR, there was a binaural component at 500 Hz; at 750 Hz there was only a monaural component. Thus, for these probes, the only measurable IPD was at 500 Hz. The dashed lines indicate the ear that received no signal energy at 750 Hz and where no IPD could be calculated. See text for details.

Frequency	LL	LC/CL	LR/RL	CC	RC/CR	RR
500 Hz						
S-N Left	0	−2.46	−2.46	0.12	0.55	0.01
S-N Right	0	0.55	−2.46	0.12	−2.46	0.01
IPD	−90	−45	0	0	45	90
750 Hz						
S-N Left	−6.39	−1.23	−1.23	−7.37	···	−6.37
S-N Right	−6.39	···	−1.23	−7.37	−1.23	−6.37
IPD	−135	···	180	0	···	135

The third row displays MLD data for a 500-Hz tone from Colburn and Durlach (1965, Table I, Method 1) for IPDs in the range 0–180 degrees. This study was selected because it also incorporated the effect of interaural level differences (ILDs) on MLD. We used Colburn and Durlach's data to predict our thresholds for both the lateralized and diotic maskers, although their thresholds were obtained for a diotic masker only. The two probe conditions where Colburn and Durlach's (1965) data were not used were for LR and RL when the masker was diotic. The IPD and associated MLD for these conditions are shown with asterisks in the table. For these, IPD at 500 Hz was the same as that of the masker (0 degrees), whereas IPD at 750 Hz was 180 degrees. Because the S-N ratio at 750 Hz was also 1 dB better than that at 500 Hz, the lowest predicted thresholds were obtained at 750 Hz. Because Colburn and Durlach's data were obtained only at 500 Hz, we decided to obtain our own MLDs for three new normal-hearing subjects for pure tone probes at 750 Hz in the NoSo and NoSπ conditions. The procedures were similar to those used in experiment 1 with the exception that the masker was adapted with the 750-Hz probe held constant at 41 dBC. The averaged MLDs were used to predict thresholds for LR and RL for the diotic masker condition. We also collected MLDs for a 500-Hz pure tone to verify that our data were consistent with those reported in the literature.

The fourth row in Table II displays adjustments to MLD made for probes CL, LC, CR, and RC, which had ILDs of 3 dB. For these, the reductions in MLD were estimated by interpolation from Colburn and Durlach's (1965, Table I) data on the effect of ILD on MLD. Specifically, the MLDs for ILD conditions of +6 and −6 dB were averaged and subtracted from the MLDs for the 0 dB ILD condition. The resulting value was divided in half because our signals had ILDs of only 3 dB. The fifth row displays S-N ratio, normalized to the baseline probe for each masker (LL for masker left, and CC for masker center). For the case where there were ILDs, the S-N ratio in the better ear was incorporated into our calculations of MLD. The sixth row displays the predicted reduction in threshold relative to the baseline condition (sum of rows 3, 4, and 5).

The filled diamonds in Figs. 4 and 6 display the predicted thresholds obtained from the analysis shown in Table II. Predicted probe thresholds for the left leading masker (Fig. 4) were derived by subtracting the values in row 6 of Table II (top half) from the threshold for LL. Predicted thresholds for the diotic masker (shown in Fig. 6) were derived by subtracting the values in row 6 (bottom half) from the threshold for CC. As can be seen, subjects' mean thresholds agree well with the predictions. Thus, the findings support our assumptions that the pulse trains are treated by the auditory system as tonal complexes, and that the detection of these stimuli is based on a single harmonic component at which the combination of S-N ratio and MLD provides the lowest threshold. This is not to suggest that integration across channels never occurs. Indeed, especially where the predicted thresholds for two or more frequency components are close, summation might be expected. For the probes in this experiment, there was always a single component that yielded a substantially lower prediction than the others. This could explain why the actual obtained thresholds agreed with the prediction based on a single frequency component.

TABLE II. Predictions of thresholds for each probe in relation to the baseline probe. The top half of the table shows the predictions when the masker was left-leading, the bottom half for the diotic masker. C&D 1965 refers to Colburn and Durlach's (1965) data for a 500-Hz probe. The asterisks indicate data collected at 750 Hz for our subjects. See text for detailed explanation.

	LL	LC/CL	LR/RL	CC	CR/RC	RR
Masker left						
IPD *re*: Masker (deg.)	0	45	90	90	135	180
C&D 1965 MLDs (dB)	0	5.1	9.15	9.15	11.2	12.7
Adjust for ILD (dB)		−0.75			−1.45	
S-N ratio (dB) better ear	0	0.55	−2.46	0.12	0.55	0.1
Prediction (dB)	0	4.9	6.69	9.27	10.3	12.8
Masker center						
IPD *re*: Masker (deg.)	−90	−45	180 (750 Hz)*	0	45	90
C&D 1965 MLDs (dB)	9.15	5.1	10.74*	0	5.1	9.15
Adjust for ILD (dB)		−0.75			−0.75	
S-N ratio (dB) better ear	−0.12	0.43	−1.35	0	0.43	−0.11
Prediction (dB)	9.03	4.78	9.39	0	4.78	9.04

TABLE III. Group mean masker level thresholds in dBC and one standard error (in parentheses) for 50 μs two-pulse pair stimuli. Row 1: left-leading masker (ITD=−500 μs), OAL=56 dBC. Row 2: diotic masker, OAL=56 dBC. Row 3: diotic masker, OAL 77=dBC.

CC	LL	LC	CL	LR	RL	CR	RC	RR
31.50 (0.25)	34.67 (0.26)	33.42 (0.30)	33.53 (0.20)	33.33 (0.28)	32.61 (0.57)	31.81 (0.37)	31.45 (0.26)	30.36 (0.44)
34.28 (0.07)	31.03 (0.61)	33.20 (0.17)	34.03 (0.12)	31.83 (0.32)	31.55 (0.30)	33.39 (0.48)	32.95 (0.31)	30.97 (0.28)
54.31 (1.31)	50.39 (0.64)	52.81 (1.05)	53.64 (0.97)	51.83 (1.00)	51.06 (0.56)	53.61 (1.11)	53.03 (0.73)	50.00 (0.34)

III. EXPERIMENT II: MLDs FOR BRIEF BINAURAL PULSES AND NOISE BURSTS

The data reported thus far indicate that, whereas the lateralization of pulse trains with alternating ITDs is dominated by the first ITD, the binaural masked detection thresholds of these stimuli are not dominated by the onset ITD. Instead, threshold is determined by the steady-state monaural and interaural characteristics of the signals in relation to those of the masker. The disparity between the dominance of onset ITD in lateralization and the lack of contribution of the onset in detection is different from data reported by Yost and Soderquist (1984) for stimuli consisting of two binaural pairs of pulses. In the brief stimuli used by Yost and Soderquist, the energy in the first pulse pair was half of the total energy in the entire signal and, so, under MLD conditions, the precedence effect could operate. For the long trains used in experiment I, the energy in the first pulse pair was negligible relative to that in the succeeding train of 124 pulse pairs. This could provide a reasonable explanation for the differences in the data obtained by them for brief pairs of pulses and by us for the longer pulse trains. To determine whether in fact duration was the critical difference between the two studies, we truncated our signals to create comparable brief stimuli.

A. Truncated pulse trains from experiment I

The nine pulse trains used in experiment I were truncated so that only the first two pairs of pulses of each train remained. The ITD configuration and interpulse intervals were the same as those used for the long trains. The same four subjects who listened to the long trains also listened to these nine probes. The procedures associated with the experiment were identical to those described in experiment I. Initially, the same two masker conditions used in experiment I were run (masker ITD of 0 and −500 μs, with masker overall level fixed at 56 dBC). The first two rows of Table III show group mean thresholds for the two maskers along with one standard error in parentheses. Threshold variability across subjects was negligible as can be seen by inspecting the standard errors. For both maskers, MLDs were quite small for these short probes. For example, for the 0-μs ITD masker (row 2), the maximum difference in thresholds, that between CC and RR or LL, was about 3.3 dB. By contrast, the range was about 9 dB for the longer probes used in experiment I (Fig. 6). For the probes with two different ITDs, there is little evidence that the order of ITDs was important. Again, for the diotic masker (row 2), mean probe thresholds for the paired probes CR versus RC and CL versus LC varied by less than 1 dB. However, with the total MLD so compressed, it might be difficult to demonstrate any marked effect of ITD order. Because it is known that MLDs become larger at higher masker levels (e.g., Yost, 1985), the same experiment with the brief stimuli described above was rerun with the diotic noise masker where the overall level was increased by 21 dB to 77 dBC. Listeners were the same four subjects who participated in the previous experiments. Group mean thresholds are shown in the third row of Table III. Again, threshold variability across subjects was small. Relative to the lower-level masker, a slight increase in maximum MLD is evident in the threshold difference between CC and LL or CC and RR (about 4 dB). The range of MLDs was still compressed and the effect of ITD order was less than 1 dB as shown by the difference in thresholds for the probe pairs CR versus RC, and CL versus LC.

B. Yost and Soderquist (1984) type stimuli

Using brief stimuli similar to those described in the above section, Yost and Soderquist (1984) had shown that the ITD of the first of two pulse pairs had a stronger effect on masked detection thresholds than the second. Because our data (Table III) did not show a substantial effect of ITD order, a second set of experiments was run with new subjects and with stimuli and procedures more closely matching the conditions used by Yost and Soderquist. The probes were 100-μs pulse pairs with interpulse intervals of 1 ms with ITDs of 0 and 600 μs, values that represented the maximum ITD range used by Yost and Soderquist in their detection experiment. Only right time leads (+600 μs) were used because none of the previous data had shown evidence of asymmetries in detection thresholds. Four probe ITD configurations were selected: CC (Yost and Soderquist's IAT1 =IAT2=0 condition), RR (IAT1=IAT2=600), RC (IAT1 =600, IAT2=0), and CR (IAT1=0, IAT2=600). For comparison, we obtained thresholds for two other probes, R (single dichotic pulse pair with ITD of 600 μs) and C (single diotic pulse pair). The masker was a diotic Gaussian noise. Signals and masker were generated at a sampling rate of 20 kHz and low-pass filtered at 5 kHz (TDT PF1).

Five new normal-hearing subjects (three college-age students and the two authors) listened via earphones in a 2-AFC experimental protocol with the probe level fixed and masker level adapted to determine masked threshold. The probe lev-

TABLE IV. Group mean masker levels at signal threshold in dBC and one standard error (in parentheses) for 100-μs pulses (row 1) and 1-ms-long noise burst pairs (row 2). The four columns on the left show data for two-pulse or two-burst pair signals. Columns 5 and 6 show data for single-pulse or single-burst stimuli. The right-leading ITD was 600 μs.

Probe condition	CC	CR	RC	RR	C	R
100-μs pulses	73.17 (0.20)	76.71 (0.37)	77.01 (0.69)	77.99 (0.73)	71.60 (0.31)	77.02 (0.65)
1-ms frozen noise bursts	71.55 (0.20)	75.45 (0.60)	75.78 (0.44)	79.93 (0.54)	69.72 (0.67)	76.22 (1.05)

els of 37 dBC were set to yield masker presentation levels over an adaptive track which were in the range used by Yost and Soderquist, an overall level of about 75 dBC (38 dBC spectrum level). This was also the starting level for each adaptive track. A two-down one-up stepping rule was used with a step size of 1 dB. The total number of reversals was 12 with the masker level at signal threshold determined as the arithmetic mean of the last nine level reversals. All of the procedures described are identical to those used by Yost and Soderquist (1984) with the possible exception of the starting SPL of the adaptive track, which was unspecified in that paper. One intentional departure from their procedures was a modification to the adaptive tracking suggested by Trahiotis *et al.* (1990) to maximize attention to binaural cues at near threshold levels, particularly when cues for detection might be changing during adaptive tracking. Specifically, the change involved presentation of two trials at each masker level, even when the subject's response to the first trial was a ''miss.'' This offered the subject a second opportunity to hear the probe at the same near-threshold masker level where an incorrect response occurred, although the second trial did not otherwise affect the progression of the adaptive tracking and was not counted toward the computation of the masker level at signal threshold. Our objective in using this procedure was to maximize listeners' detection performance in dichotic conditions, thereby helping to create the widest possible range of thresholds.

Table IV, first row, shows the mean masker levels required to just mask each of four probes along with one standard error, entered in parentheses. Maximum group mean difference in detection thresholds (comparison of masker levels for CC versus RR) was marginally higher than that seen for the 50-μs pulses used in Sec. III A (Table I), at about 4.82 dB, but less than the approximately 6 dB reported for two subjects by Yost and Soderquist (1984). As with the data shown in Table III, the effect of the order of ITDs was practically nonexistent. For probe RC masker level thresholds were about 1 dB less than those for RR, similar to the results obtained by Yost and Soderquist (1984). For probe CR, on the other hand, masker level at threshold for our subjects was very similar to that obtained for RC. For the equivalent condition, Yost and Soderquist found masker levels to be about 3 dB lower and close to the CC condition. The right-most two cells of Table IV, first row, show mean masker levels for the dichotic and diotic single pulse-pair probes. As can be seen from a comparison of RR versus R and CC versus C, there was a slight increase in the masker levels needed to mask the two pulse-pair probes. However, MLDs for the single-pulse probes were similar to those for the two-pulse probes, with the group mean MLD at 5.42 dB (C minus R). It is also worth noting that masker levels at threshold for CR and RC are very close to that for R alone, suggesting that the contribution of the diotic ITD in the CR and RC probes was negligible.

C. Noise burst stimuli

In this section we report data obtained for brief stimuli designed to produce a larger range of MLDs, which might reveal ITD order effects previously unobservable for our pulse pairs. The stimuli were two pairs of binaural white noise bursts. Each burst was 1 ms in duration. The same sample of noise was used both within and between burst pairs, and across intervals, trials, runs, and subjects.[2] Pilot data revealed that the magnitude of MLDs varied across 1-ms noise-burst tokens, presumably because of the details of the low-frequency spectrum. The selected token produced a relatively large MLD in the single burst pair condition, and thereby allowed for a more robust evaluation of onset ITD effects in two burst pair conditions of listening. The ITD configurations and filter conditions for the noise burst probes were the same as those used in Sec. III B. The interburst interval (IBI) was 2 ms measured from the onset of the leading burst of the first burst pair to the onset of the leading burst of the second burst pair. This meant that the IBI was the same in each ear for the probes CC and RR with nonalternating ITDs. For the probes with the alternating ITDs, CR and RC, the IBI was 2 ms in the right ear, and 1.6 ms and 400 μs, respectively, in the left ear.

Subjects listened to the probes with the noise masker adapted, using the same experimental protocol described in Sec. III B, with the exception that the initial step size was 4 dB. This step size was halved to 2 dB after the first reversal, and then again to 1 dB after the second reversal to remain at that value for the rest of the run. This choice was made to eliminate unnecessary trials at the beginning of the adaptive track before approaching threshold levels.

Results for four subjects are reported in Table IV, row 2. Maximum mean masker level difference was about 8.4 dB, substantially higher than that obtained for the pulses (first row of Table IV). However, the effect of the order of ITDs still remained negligible; that is, masker levels at probe threshold for RC and CR were virtually the same. In the right-most two cells of row 2, group mean masker levels for single dichotic and diotic noise burst pairs are shown. Comparison of the masker levels at threshold for RC and CR with

that of R alone suggests that there was no additional contribution of the diotic noise burst pair to detection and that masker levels were driven by the dichotic burst pair alone. As with the pulse probes, addition of an identical second noise burst pair increased overall masker levels required for threshold detectability (i.e., RR relative to R and CC relative to C).

IV. DISCUSSION

The primary question asked in this paper was whether the onset cues that dominated lateralization would also influence binaural detection thresholds. Our findings show that binaural masking level differences are independent of onset cues even when those cues cause signals in quiet to be lateralized to a different intracranial position from that of the masker. Specifically, for the trains with alternating ITDs across successive pulse pairs, the ITD that occurred first in the alternation strongly affected lateralization but had no measurable effect on detection.

Some investigators (for example, Buell *et al.*, 1991) have suggested that onset cues would be more important for lateralization when the steady-state portion of a signal contains interaural ambiguities. Perhaps our stimuli were lateralized so strongly with the onset because of the ambiguities contained in their steady-state structure. Following the work of Hartmann and Rakerd (1989), Freyman *et al.* (1997) showed that the continuous spectrum broadband transient energy in the onset, coupled to the sparse spectral density of the steady-state portions of tonal complexes, increased the potency of the onset. Even though our signals were made up of a series of transients, the short 2-ms interpulse interval and the rapidity of the alternation of ITDs in relation to the sluggishness of the binaural auditory system (Grantham and Wightman, 1978) might have caused the binaural auditory system to process these stimuli as complex tones with an abrupt onset and ambiguous ongoing interaural cues. These factors could account for the strong onset dominance seen for our trains.

Control of lateralization by onset cues may result at least partially from peripheral auditory processes. Hartung and Trahiotis (2001) demonstrated that adaptation in a model of hair cell processing, in combination with a cross correlation analysis, was sufficient to explain several characteristics of the precedence effect for pairs of binaural transients. As shown in Fig. 3 of the current paper, the same model showed diminishing dominance of the cross-correlation peak corresponding to the first of two alternating ITDs as increasingly longer segments were included in the analysis. However, the output of the model still produces an approximately 14% higher cross-correlation peak corresponding to the initial ITD than second ITD even when it is applied to the entire stimulus duration. How the central auditory system might deal with multiple cross-correlation peaks of unequal height or what might be the appropriate analysis time window have not yet been fully considered in our treatment of the model.

It seems clear that the mechanisms that mediate lateralization and detection are different, at least when the lateralization is controlled by interaural cues at stimulus onset. Lateralization appears to be largely dependent on increased weighting of early arriving binaural information within a signal, whereas detection thresholds are determined by the information available over the duration of the entire signal. Specifically, differences in thresholds among our complex stimuli were highly predictable by considering the S-N ratios and interaural differences of individual frequency components in the complex, and relating these to MLDs for sinusoids available in the literature. Thus, the internal binaural representation on which masked binaural detection is based is apparently not influenced by interaural onset delays.

Yost and Soderquist (1984) obtained a different result from the lateralization versus detection comparison for brief stimuli consisting of only two pulse pairs. In that case, both detection and lateralization were influenced strongly by the ITD of the pulse pair that was presented first. These results agree nicely with conceptualizations of the precedence effect that propose a brief period of post-onset insensitivity to directional information, possibly ascribable to inhibitory mechanisms (Zurek, 1980, 1987; Lindemann, 1986). If post-onset inhibition weakens binaural cues and their contribution to lateralization, it makes sense that they would also be unavailable for detection. However, the results of experiment II in the current study showed little or no effect of the order of ITDs for brief stimuli. This was true for truncated versions of our own pulse trains, for stimuli and conditions designed to closely replicate a subset of Yost and Soderquist's (1984) conditions, and for stimuli consisting of two binaural noise burst pairs.

The primary difference in the data of the two studies is that, in the presence of diotic noise, our subjects had better relative thresholds when a diotic stimulus pair preceded a dichotic pair than Yost and Soderquist's (1984) listeners did (our CR condition versus their IAT1=0, IAT2=600 μs). They had shown little release from masking in that condition, whereas our subjects performed essentially as if the diotic pair was not present. That is, the diotic–dichotic and the dichotic–diotic thresholds were not only virtually identical to one another, but also highly similar to the thresholds for the dichotic stimuli when presented alone. This is a logical result if one considers the thresholds of the individual pulse pairs to be relevant to the threshold of the two-pair composite. As shown in the top row of Table IV, the masker level needed to mask the dichotic pair alone (R) was 5 dB higher than the diotic pair alone (C). It is difficult to appreciate how the diotic pair, presented at -5 dB relative to its 71% threshold in a diotic masker, could influence the audibility of the dichotic pair presented in the same noise.

The reasons for the differences between the current results and those of Yost and Soderquist (1984) are not clear to us. It is possible that specific differences between the way that the experiments were conducted contributed to the differences in the outcome. Our adaptive track began with the masker at 75 dBC, a level near the eventual mean threshold for the CR stimulus and at which the diotic pair, if presented alone, was already 2 dB below threshold. The starting level used by Yost and Soderquist (1984) was unspecified. Other factors such as the initial step size, and our use of a second presentation after a miss, might also have influenced the results.

In summary, the mechanisms responsible for onset dominance in lateralization of 250-ms pulse trains do not appear to influence their internal representation in a manner that affects the detectability of the stimuli under binaural masking conditions. Our data for brief pairs of pulses and noise bursts reveal a similar result and are different from what some of the previous literature indicates (Yost and Soderquist, 1984). The factors that contributed to the differences in results between the two studies are, at the moment, unclear to us. Further research may allow us to identify the common and disparate binaural mechanisms that mediate lateralization and binaural detection.

ACKNOWLEDGMENTS

The authors would like to thank the subjects who participated in these experiments, and Kuan Chung Huei, Shih Chai Shiang, and Jayanta Dey for their assistance with software and hardware used for the experiments. The research reported here was part of the doctoral dissertation of the first author. This research was supported by a grant from the National Institute of Deafness and other Communicative Disorders (DC01645). The authors would also like to thank Dr. Leslie Bernstein, Associate Editor, for comments and suggestions, which, we believe, have greatly improved this paper.

[1]The difference in monaural fundamental frequency produced a complex pattern of interaural level differences for pulse trains LC, RC, CR, and CL. For example, considering trains LC and CL in the frequencies 2000 Hz and below, the left ear signal contained harmonic components at 500, 1000, 1500, and 2000 Hz, while the right ear signal contained components at 250, 500, 750, 1250, 1500, 1750, and 2000 Hz. Thus there were monaural components in the left ear at 1 kHz and monaural components in the right ear at 250, 750, 1250, and 1750 Hz. Predictably, RC and CR were mirror images of LC and CL.

[2]The burst token of 20 points (50 μs/point) had the following integer values: −51, −442, 738, 926, 633, −99, 369, 545, 830, 266, −206, −419, −377, 35, 167, −219, −56, 363, −17, −66.

Akeyrod, M. A., and Bernstein, L. R. (**2001**). ''The variation across time of sensitivity to interaural disparities: behavioral measurements and quantitative analyses,'' J. Acoust. Soc. Am. **110**, 2516–2526.

ANSI (**1989**). ANSI S3.6-1989, ''Specifications for audiometers'' (American National Standards Institute, New York).

Bernstein, L. R., and Trahiotis, C. (**1997**). ''The effects of randomizing values of interaural disparities on binaural detection and on discrimination of interaural correlation,'' J. Acoust. Soc. Am. **102**, 1113–1120.

Blauert, J. (**1997**). *Spatial Hearing* (MIT, Cambridge, MA).

Buell, T. N., Trahiotis, C., and Bernstein, L. R. (**1991**). ''Lateralization of low-frequency tones: Relative potency of gating and ongoing interaural delays,'' J. Acoust. Soc. Am. **90**, 3077–3085.

Colburn, H. S., and Durlach, N. I. (**1965**). ''Time-intensity relations in binaural unmasking,'' J. Acoust. Soc. Am. **38**, 93–103.

Durlach, N. I., and Colburn, H. S. (**1978**). ''Binaural phenomena,'' in *Handbook of Perception, Vol. IV* (Academic Press, New York).

Egan, J. P., and Benson, W. (**1966**). ''Lateralization of a weak signal presented with correlated and with uncorrelated noise,'' J. Acoust. Soc. Am. **40**, 20–26.

Freyman, R. L., Zurek, P. M., Balakrishnan, U., and Chiang, Y. C. (**1997**). ''Onset dominance in lateralization,'' J. Acoust. Soc. Am. **101**, 1649–1659.

Glasberg, B. R., and Moore, B. C. J. (**1990**). ''Derivation of auditory filter shapes from notched-noise data,'' Hear. Res. **47**, 103–138.

Grantham, W. D., and Wightman, F. L. (**1978**). ''Detectability of varying interaural temporal differences,'' J. Acoust. Soc. Am. **63**, 511–523.

Hafter, E. R., Bourbon, W. T., Blocker, A. S., and Tucker, A. (**1969**). ''A direct comparison between lateralization and detection under conditions of antiphasic masking,'' J. Acoust. Soc. Am. **46**, 1452–1457.

Hartmann, W. M., and Rakerd, B. (**1989**). ''Localization of sound in rooms IV: The Franssen effect,'' J. Acoust. Soc. Am. **86**, 1366–1373.

Hartung, K., and Trahiotis, C. (**2001**). ''Peripheral auditory processing and investigations of the ''precedence effect'' which utilize successive transient stimuli,'' J. Acoust. Soc. Am. **110**, 1505–1513.

Jeffress, L. A. (**1972**). ''Binaural Signal Detection: Vector Theory,'' in *Foundations of Modern Auditory Theory, Vol. II*, edited by J. V. Tobias (Academic, New York), pp. 351–369.

Levitt, H. (**1971**). ''Transformed Up-Down Methods in Psychoacoustics,'' J. Acoust. Soc. Am. **49**, 467–477.

Lindemann, W. (**1986**). ''Extension of a binaural cross-correlation model by contralateral inhibition. II. The law of the first wave front,'' J. Acoust. Soc. Am. **80**, 1623–1630.

Meddis, R., Hewitt, M. J., and Shackleton, T. M. (**1990**). ''Implementation details of a computational model of the inner hair-cell/auditory nerve synapse,'' J. Acoust. Soc. Am. **87**, 1813–1816.

Saberi, K. (**1996**). ''Observer weighting of interaural delays in filtered impulses,'' Percept. Psychophys. **58**, 1037–1046.

Shinn-Cunningham, B. G., Zurek, P. M., and Durlach, N. I. (**1993**). ''Adjustment and discrimination measurements of the precedence effect,'' J. Acoust. Soc. Am. **93**, 2923–2932.

Slaney, M. (**1993**). ''An efficient implementation of the Patterson Holdsworth auditory filter bank,'' Apple Computer Technical Report #35.

Stern, R. M., and Shear, G. D. (**1996**). ''Lateralization and detection of low-frequency binaural stimuli: Effects of distribution of internal delay,'' J. Acoust. Soc. Am. **100**, 2278–2288.

Stern, R. M., and Trahiotis, C. (**1997**). ''Models of Binaural Perception,'' in *Binaural and Spatial Hearing in Real and Virtual Environments*, edited by R. H. Gilkey and T. B. Anderson (Lawrence Erlbaum, Hillsdale, NJ).

Tollin, D. J., and Henning, G. B. (**1999**). ''Some aspects of the lateralization of echoed sound in man. II. The role of stimulus spectrum,'' J. Acoust. Soc. Am. **105**, 838–849.

Trahiotis, C., Bernstein, L. R., Buell, T. N., and Specktor, Z. (**1990**). ''On the use of adaptive procedures in binaural,'' J. Acoust. Soc. Am. **87**, 1359–1361.

Wallach, H., Newman, E. B., and Rosenzweig, M. R. (**1949**). ''The Precedence Effect in Sound Localization,'' Am. J. Psychol. **52**, 315–336.

Webster, F. A. (**1951**). ''The influence of interaural phase on masked thresholds. I. The role of time-deviation,'' J. Acoust. Soc. Am. **23**, 452–462.

Yost, W. A. (**1985**). ''Click stimuli do produce masking level differences, sometimes,'' J. Acoust. Soc. Am. **77**, 2191–2192.

Yost, W. A., and Soderquist, D. R. (**1984**). ''The precedence effect: Revisited,'' J. Acoust. Soc. Am. **76**, 1377–1383.

Zurek, P. M. (**1980**). ''The precedence effect and its possible role in the avoidance of interaural ambiguities,'' J. Acoust. Soc. Am. **67**, 952–964.

Zurek, P. M. (**1987**). ''The Precedence Effect,'' in *Directional Hearing*, edited by W. A. Yost and G. Gourevitch (Springer-Verlag, New York), pp. 85–105.

Detection of static and dynamic changes in interaural correlation

Susan E. Boehnke[a] and Susan E. Hall
Department of Psychology, Dalhousie University, Halifax, Nova Scotia B3H 4J1, Canada

Torsten Marquardt
Department of Physiology, University College London, Gower Street, London WC1E 6BT, United Kingdom

(Received 7 March 2002; revised 8 July 2002; accepted 8 July 2002)

This study examines the relation between a static and a dynamic measure of interaural correlation discrimination: (1) the just noticeable difference (JND) in interaural correlation and (2) the minimum detectable duration of a fixed interaural correlation change embedded within a single noise-burst of a given reference correlation. For the first task, JNDs were obtained from reference interaural correlations of +1, −1, and from 0 interaural correlation in either the positive or negative direction. For the dynamic task, duration thresholds were obtained for a brief target noise of +1, −1, and 0 interaural correlation embedded in reference marker noise of +1, −1, and 0 interaural correlation. Performance with a reference interaural correlation of +1 was significantly better than with a reference correlation of −1. Similarly, when the reference noise was interaurally uncorrelated, discrimination was significantly better for a target correlation change towards +1 than towards −1. Thus, for both static and dynamic tasks, interaural correlation discrimination in the positive range was significantly better than in the negative range. Using the two measures, the length of a binaural temporal window was estimated. Its equivalent rectangular duration (ERD) was approximately 86 ms and independent of the interaural correlation configuration. © *2002 Acoustical Society of America.* [DOI: 10.1121/1.1504857]

PACS numbers: 43.66.Mk, 43.66.Pn, 43.66.Rq [LRB]

I. INTRODUCTION

The interaural correlation (''ρ'') of a dichotic noise stimulus is a measure of the similarity of the waveforms presented to the left and right ears. If the waveforms presented to each ear are identical (diotic or ''correlated,'' $\rho = +1$), the resulting perception is of a compact sound source whose location can be specified precisely at the center of ''intracranial'' space. Reducing the interaural correlation, for example by adding independent noise to either channel, widens the perceptual image and makes it more diffuse. When noises from fully independent sources are presented to each ear (''uncorrelated,'' $\rho = 0$), the resulting perception is that of a diffuse sound that fills the head, but may have two dominant sources near the ears (see Blauert and Lindemann, 1986). When identical noises are presented to each ear and the waveform at one ear is inverted, the stimulus becomes interaurally ''negatively correlated'' ($\rho = -1$). There are no formal reports on the perception of negatively correlated noise. It has been described as two relatively compact sources near the ears (see Hirsh, 1948), although a few of our listeners reported one dominant blurred image displaced laterally. It is occasionally described by listeners as unpleasant or irritating. In this paper, the terms ''correlated,'' ''negatively correlated,'' and ''uncorrelated'' refer to interaural correlations of +1, −1, and 0, respectively. Following mathematical convention, any change towards −1 will be considered a decrease and any change towards +1 will be considered an increase in interaural correlation. Note, however, that while shifts towards −1 will be referred to as a decrease, the noises presented to each ear have maximal independence at zero correlation.

There has been a renewed interest in examining human sensitivity to interaural correlation, particularly with respect to its relation to the binaural masking level difference (e.g., Durlach *et al.*, 1986) and dichotic pitches (Culling *et al.*, 1998a, b). Recently, Culling *et al.* (2001) reported a study on the discriminability of different positive interaural correlations of a subband of noise within a correlated broadband noise. Their results were similar in form to those first reported by Pollack and Trittipoe (1959a) who manipulated the correlation of the entire spectrum. Specifically, discrimination was very fine for decreases in interaural correlation from a reference of $+1 (\Delta\rho = 0.02-0.04)$, progressively degraded with decreases in the reference value, and was worst ($\Delta\rho = 0.3-0.5$) for an uncorrelated reference (Pollack and Trittipoe, 1959a, b; Gabriel and Colburn, 1981; Koehnke *et al.*, 1986; Jain *et al.*, 1991; Bernstein and Trahiotis, 1992; Culling *et al.*, 2001).

The binaural system is unable to follow rapid changes in interaural correlation, as evidenced by the relative difficulty listeners have in detecting or discriminating dynamic changes in interaural disparities (e.g., Grantham and Wightman, 1978, 1979). This ''binaural sluggishness'' has been characterized in terms of a ''binaural temporal window''—a moving-average filter that integrates binaural information over time according to some weighting function. Several studies have attempted to determine the shape and equivalent rectangular duration (ERD) of the window (e.g., Kollmeier and Gilkey, 1990; Culling and Summerfield, 1998; Bernstein

[a]Electronic mail: sboehnke@is2.dal.ca

et al., 2001). In an attempt to measure the ERD but not the window shape, Akeroyd and Summerfield (1999) recently examined detection of dynamic changes in interaural correlation in an experiment described as a binaural analog of gap detection. In monaural temporal gap detection, the parameter of change is intensity (Moore *et al.*, 1988); in the binaural analog, the parameter of change is the interaural correlation. The ''gap'' was represented by uncorrelated noise embedded in correlated noise markers. This stimulus can be described as a sequence of three contiguous noises in which the first and last (markers) are of interaural correlation X, and the center (target) noise is of interaural correlation Y, i.e., $X/Y/X$. At either ear alone a continuous noise is heard through the duration of the stimulus. The analogy assumes that there is a decrease in activity in the binaural temporal window's output specifically during the uncorrelated Y noise, similar to that effected in the output of a monaural temporal window by a decrease in intensity (a gap). It follows that as the Y noise decreases in duration it contributes less weight to the smoothed output (Akeroyd and Summerfield, 1999). This means that the effective change in interaural correlation is less than that specified by the stimulus. The minimum detectable target duration is thus a measure of the ability to detect a short departure from the marker's interaural correlation. For stimulus conditions in which noises of different bandwidths and center frequencies were used, Akeroyd and Summerfield (1999) found that a binaural temporal window model could predict the binaural gap thresholds obtained in the $+1/0/+1$ configuration by knowing the subject's interaural correlation discrimination acuity for the same stimulus conditions, i.e., their JND (''just noticeable difference'') from a reference of $+1$. Akeroyd and Summerfield (1999) estimated the equivalent rectangular duration (ERD) of the binaural temporal window to be about 140–210 ms depending on the model employed. This is much longer than the analogously defined Gaussian-shaped monaural temporal window [e.g., Moore *et al.*, 1988, 27 ms (corrected value, see Akeroyd and Summerfield, 1999)]. While useful as an analogy, the term ''binaural gap detection'' limits the implied possibilities of the paradigm. Since the ''gap'' could in theory be an increase or decrease in interaural correlation from a reference noise of any given correlation value, the task might provide a more general way to probe the detectability of interaural correlation changes. In purely stimulus terms, the general paradigm is analogous to increment- and decrement-duration detection in the intensity domain, of which gap detection is a single case. For clarity, the ''binaural gap'' paradigm might be more generally construed, and will be referred to in this report, as ''interaural correlation change-interval'' (ICCI) detection.

Another task that uses the full range of interaural correlation is the binaural masking level difference or BMLD. Like ICCI detection, the BMLD has been linked to interaural correlation discrimination (e.g., Durlach *et al.*, 1986; Koehnke *et al.*, 1986; Jain *et al.*, 1991; Culling *et al.*, 2001). The BMLD is the binaural advantage in detecting a signal (S) in noise (N) when the interaural configuration of the signal [e.g., correlated (o), negatively correlated (π), uncorrelated (u)] differs from that of the masking noise, as compared typically to the condition in which both the signal and noise are presented diotically. At present, the correspondence between the BMLD and correlation discrimination has only been made clear for cases of correlation discrimination from positive reference values, such as the NoSπ condition (Durlach *et al.*, 1986; Culling *et al.*, 2001). In light of a relation among the interaural correlation JND, and both ICCI detection and the BMLD, one might make predictions for different ICCI-detection and correlation-discrimination conditions based on what is known about the BMLD under analogous configurations. For instance, the BMLD is largest for NoSπ, and is several dB less for the NπSo condition (Hirsh, 1948); one would therefore predict better interaural correlation discrimination from a reference of $+1$ than from a reference of -1. See Table I for an overview of corresponding BMLD, ICCI-detection, and JND tasks. Note that these predictions would be expected to hold only to the degree that the BMLD can be conceived in terms of correlation discrimination, a correspondence that is good, but not complete (Durlach *et al.*, 1986).

The present study examined the relation between performance on the interaural correlation JND and the ICCI-detection tasks. Thresholds were obtained for all $X/Y/X$ configurations of correlated, negatively correlated, and uncorrelated wideband noise. JNDs for interaural correlation were obtained from corresponding reference interaural correlations (ρ_{ref}) of $+1$, -1, and 0 in the positive (0+) or negative (0−) direction (see Table I). JNDs from $\rho_{\text{ref}}=+1$ and -1 should be related to performance in the 1/0/1 and $-1/0/-1$ conditions, respectively. JNDs from $\rho_{\text{ref}}=0$ in the positive and negative directions should be related to performance in the 0/1/0 and $0/-1/0$ conditions, respectively. In order to determine whether the two data sets were related by the same binaural temporal window, we used the ''ρ_w'' model to estimate the window length for each related pair of JND and ICCI-detection conditions. The model is described in detail by Akeroyd and Summerfield (1999), and follows the strategy of Grantham and Wightman (1979), Kollmeier and Gilkey (1990), and Culling and Summerfield (1998).

II. METHODS

A. Listeners

Data for the ICCI-detection conditions were collected from eight subjects (five female) ranging in age from 20 to 35 years, and included the three authors. Five of those listeners (including the first two authors) also participated in the correlation discrimination (JND) experiment. Listeners SB, SH, and JH were highly experienced in a variety of auditory temporal processing tasks; TM, DR, and MC had participated in a few other psychoacoustical tasks; and listeners BV and RO were relatively inexperienced. All had normal audiograms from 250 Hz to 8 kHz. In both the ICCI-detection and the JND tasks, listeners completed many practice runs of each condition until thresholds stabilized, and the mean threshold for each condition was taken from the last three threshold determinations. Subjects were always provided with visual feedback.

TABLE I. Relation among the binaural masking level difference, interaural correlation change interval (ICCI) detection, and interaural correlation discrimination (JND) for various interaural configurations. Higher scores on the BMLD task indicate better performance while lower scores on the dynamic (ICCI) and static (JND) interaural correlation tasks indicate better performance. BMLD data taken Moore (1997) and Durlach and Colburn (1978). Binaural temporal change detection and correlation JND values are from the present study.

	BMLD(dB) Nρ Sρ	Interaural correlation change-interval (ICCI) detection	Correlation JND	
			Reference (ρ)	Comparison
Signal causes decorrelation from +1	$N_{+1}S_{-1}$ (NoSπ) 15 dB	1/−1/1 1.48 ms	+1	$\Delta\rho = -0.045$
	$N_{+1}S_{0}$ (NoS90°) 6 dB[a]	1/0/1 2.40 ms		
Signal causes decorrelation from −1	$N_{-1}S_{+1}$ (NπSo) 13 dB	−1/1/−1 3.98 ms	−1	$\Delta\rho = +0.086$
	$N_{-1}S_{0}$ (NπS90°) 4 dB[a]	−1/0/−1 7.60 ms		
Signal causes a change in correlation from 0	$N_{0}S_{+1}$ (NuSo) 4 dB	0/1/0 21.01 ms	0	$\Delta\rho = +0.32$
	$N_{0}S_{-1}$ (NuSπ) 3 dB	0/−1/0 42.88 ms	0	$\Delta\rho = -0.46$

[a]The comparison of uncorrelated noise, as used in our experiments, with a tone with an interaural phase difference of 90 degrees, as used in this BMLD condition, is not entirely correct. Two uncorrelated noises originate from independent sources, i.e., have a *coherence* of zero. The phase shift introduced to the tone does result in an interaural correlation of 0, but it retains of *coherence* of 1. However, for illustrative purposes only, the values for the NoS90° and NπS90° conditions reported in Durlach and Colburn (1978) are displayed.

B. Dynamic changes in interaural correlation—The interaural correlation change-interval (ICCI)-detection task

There were six $X/Y/X$ configurations tested for detecting a dynamic change in correlation. These are illustrated schematically in Fig. 1. Stimuli were created using Matlab software (The Mathworks) and presented at a sampling frequency of 44 100 Hz at 16-bit amplitude quantization on the audio processor of an Apple PowerMacintosh 8600. The stimuli were constructed by concatenating three independent noise bursts (0–22 050 Hz), and the total stimulus was shaped with 10-ms rise and fall times. For each stimulus presentation new noises were generated. The total stimulus duration was fixed at 500 ms; thus, the marker durations increased as the target noise decreased adaptively. Stimuli were presented to subjects at a comfortable listening level (70 dB SPL) over AudioTechnica ATH-M40fs Precision Studiophones, while they were seated in a sound-attenuating booth.

Thresholds for detecting the target (Y) noise were measured using a two-interval, two-alternative forced-choice task and a three-down, one-up adaptive method, estimating the 79.4% point on the psychometric function (Levitt, 1971). On each trial, listeners were presented, in random order, with a standard stimulus consisting of noise of correlation X and a test stimulus in the $X/Y/X$ configuration. The task was to indicate whether the test stimulus was in the first or second interval. The initial Y-noise duration was set well above detection threshold for a given stimulus condition (10–70 ms). Until the first incorrect response, the center noise duration was decreased by a factor of 1.2 for each step. Subsequently, the target (Y) noise duration was increased by a factor of 1.2 after each incorrect response, or decreased by a factor of 1.2 after three consecutive correct responses. Each adaptive staircase continued for eight reversals and the geometric mean of the target noise durations for the last six reversals was defined as the ICCI-detection threshold.

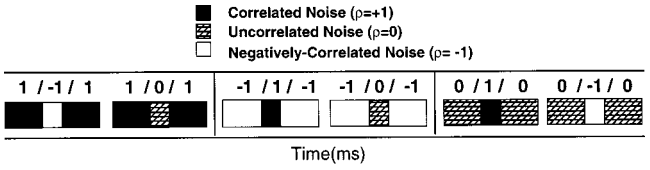

FIG. 1. Schematic of the interaural correlation change interval (ICCI) detection conditions. The stimuli are a contiguous sequence of three broadband noises of X and Y correlation of equivalent intensity, in the configuration $X/Y/X$. The interaural correlation is represented by the black (correlated, $\rho=1$), hatched (uncorrelated, $\rho=0$), and white (negatively correlated, $\rho=-1$) sections. In the 2AFC task, detection is of the presence of Y noise.

C. Discrimination of static changes in interaural correlation (JND)

The general experimental details were the same as above, except for the following. The just noticeable difference (JND) for the reduction in interaural correlation from a reference of $\rho_{\text{ref}}=+1.0$ and $\rho_{\text{ref}}=0$, and for an increase in interaural correlation from $\rho_{\text{ref}}=-1$ and $\rho_{\text{ref}}=0$, was determined. The stimuli were wideband noises of 400-ms duration (10-ms rise/fall times) with a fixed value of interaural correlation. Reference stimuli (the standard) were noise bursts with an interaural correlation of 1, −1, or 0. The interaural correlation of the test stimuli was controlled by mixing two independent Gaussian noises, one interaurally correlated ($N_{+1},\rho=1$) and the other negatively correlated (N_{-1},ρ

$=-1$), as described in Eq. (1) (see van der Heijden and Trahiotis, 1997 for further details). In this equation N_{+1} is the power of the interaurally correlated noise, N_{-1} is the power of the negatively correlated noise, and N_p is the power of the sum:

$$N_\rho = \tfrac{1}{2}(1+\rho)N_{+1} + \tfrac{1}{2}(1-\rho)N_{-1}. \quad (1)$$

JNDs were measured using a four-interval, two-alternative forced-choice task and a three-down, one-up adaptive method, estimating the 79.4% point on the psychometric function (Levitt, 1971). On each trial, the first and last intervals had the correlation of the reference stimulus. The test stimulus was randomly located in the second or third position. The task of the listener was to indicate which of the middle two noise bursts was of discrepant correlation. For JNDs from $\rho_{\text{ref}}=+1$ and -1, the initial interaural correlations of the test stimulus were $+0.5$ and -0.5, respectively, and the correlation was changed towards the reference correlation with correct responses. For JNDs from a $\rho_{\text{ref}}=0$, the initial correlation of the test stimulus was either $+1.0$ or -1.0 and was changed with correct responses towards 0. The same three-down, one-up adaptive procedure as described in Sec. II B was used to determine the threshold using a step size factor of 1.2 based on the difference between the test interaural correlation and the reference interaural correlation.

III. RESULTS

A. Interaural correlation change interval (ICCI)-detection thresholds

Thresholds for the duration of a noise of interaural correlation Y were obtained from eight listeners for each of the $X/Y/X$ conditions. These are plotted on a log scale in Fig. 2(a). Individual subject means and standard errors (based on the final three observations collected) for each condition are presented in the main graph, and the group means for each condition are presented in the inset graph. There are two important trends in the data. Targets embedded in correlated or negatively correlated markers (1/−1/1 and 1/0/1, or −1/1/−1 and −1/0/−1) were generally more easily detected than targets embedded in uncorrelated markers (0/1/0 or 0/−1/0). That is, it was easier to detect a brief change in correlation from markers of $\rho=\pm 1$ than from markers of $\rho=0$.

Second, detection performance of listeners was better when detection of the change was executed in the positive range of interaural correlation than in the negative range. The mean thresholds for detecting uncorrelated noise amid correlated or negatively correlated markers, 1/0/1 and −1/0/−1, were 2.34 and 7.43 ms, respectively, a difference which was statistically significant [$F(1,7)=13.42$, $p<0.01$].[1] For larger changes in correlation, 1/−1/1 and −1/1/−1, the mean thresholds across listeners were 1.43 and 3.91 ms, respectively. A repeated measures ANOVA indicated that this difference in thresholds was also statistically significant [$F(1,7)=7.5$, $p<0.03$]. These conditions are analogous to the first pair (1/0/1 and −1/0/−1), but the change in correlation is twice the magnitude of change caused by an uncorrelated Y noise (e.g., a correlation change of 1.0 for 1/0/1 vs 2.0 for 1/−1/1) for a given duration. As a consequence, a shorter duration of Y would be required for the smeared window output to reach the threshold for correlation discrimination. That is, the mixing of negatively correlated noise with correlated noise within the temporal window has twice the decorrelating effect as the mixing uncorrelated and correlated noise. The benefit in performance seen with a doubling of the correlation change of the target, however, was proportionately greater for negatively correlated markers (49% decrease in threshold) than for positively correlated markers

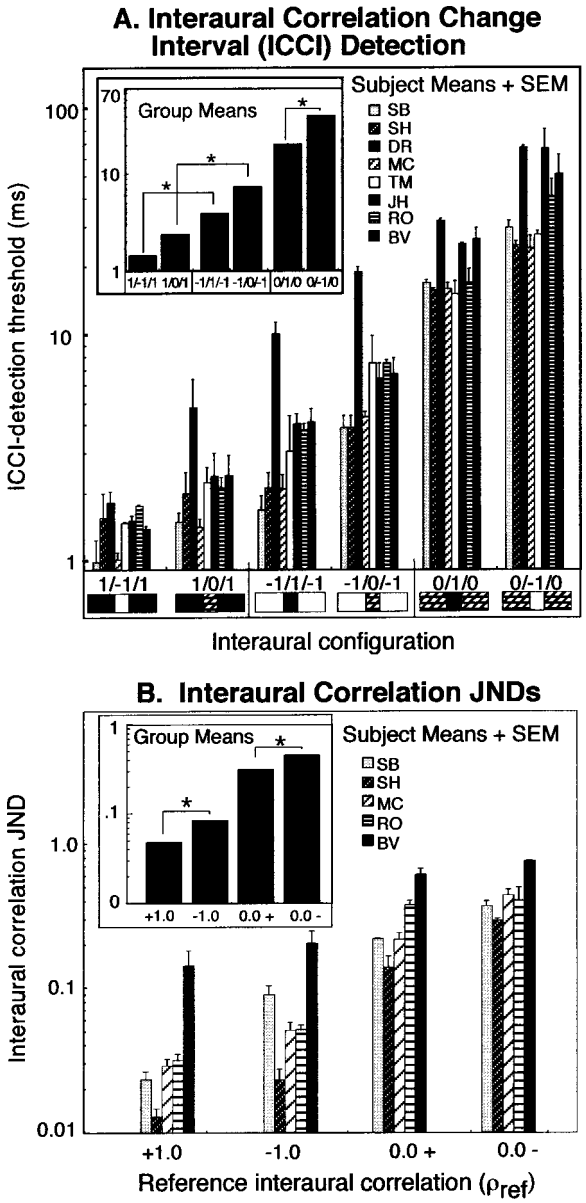

FIG. 2. (a) Duration thresholds (ms) for a dynamic measure of interaural correlation sensitivity—the interaural correlation change interval (ICCI) detection task (see Fig. 1 for schematic of stimuli). Individual subject means with standard errors for the six interaural configurations (see text) are presented in the main graph, and the group means are presented in the inset graph. (b) Interaural correlation JNDs. Individual subject means with standard errors are presented in the main graph for four conditions—the just noticeable decrease in interaural correlation from references of 1 and −1, and a just noticeable increase in correlation from $\rho_{\text{ref}}=0$, in either a positive or negative direction (see text). Group means are presented in the inset graph. In both (a) and (b) asterisks indicate that the difference between the specified bars was statistically significant ($p<0.05$).

(29% decrease). A repeated measures ANOVA with two factors—the interaural correlation of the markers ($\rho=+1$ or -1) and the size of correlation change caused by the target (correlation change of 1.0 or 2.0)—resulted in a significant interaction [$F(1,7)=22.35$, $p<0.01$]. This interaction indicates that the benefit of a larger correlation change was significantly greater for increases in correlation from -1 than for decreases from $+1$.

Finally, detection of a correlated noise amid uncorrelated markers was relatively poor, particularly if the *Y* noise was negatively correlated. The mean thresholds for the 0/1/0 and 0/−1/0 conditions were 20.57 and 41.45 ms, respectively. These results show that the detection of changes in interaural correlation from zero was also significantly asymmetric in the positive and negative range of interaural correlations [$F(1,7)=22.5$, $p<0.01$].

B. Interaural correlation JNDs

The interaural-correlation JNDs are shown in Fig. 2(b). Results from five individual listeners are plotted in the main graph with standard errors based on their three final threshold determinations. Group mean data are presented in the inset graph. JNDs for every listener were consistently best for $\rho_{\text{ref}}=+1$ with a mean of 0.048. The mean JND for $\rho_{\text{ref}}=-1$ was 0.084. A repeated measures ANOVA indicated that this asymmetry was statistically significant [$F(1,4)=9.5$, $p<0.05$]. JNDs for $\rho_{\text{ref}}=0$ were poorer in general and more variable across subjects. The mean JND for an increase in correlation towards $+1$ was 0.31, while that for a decrease in correlation toward -1 was 0.45. Again, this asymmetry was statistically significant [$F(1,4)=19.6$, $p=0.01$].

C. Equivalent rectangular duration of the binaural temporal window

We wondered whether the processing mechanism limiting performance on all these tasks could be characterized as sharing the same binaural temporal window ERD. If this were the case, the duration of the binaural temporal window measured would be independent of the interaural configuration used. In order to calculate an estimate of this binaural temporal window ERD for each subject and configuration, we used the "ρ_w" model [see Akeroyd and Summerfield, 1999, Eqs. (3)–(6)]. Following the strategy employed by others (Grantham and Wightman, 1978; Kollmeier and Gilkey, 1990; Culling and Summerfield, 1998), this model measures the interaural correlation directly on the stimulus waveform. The temporal window used in the model is symmetric, and has a Gaussian shape. The model assumes that the ICCI is detected if the change in the output of the temporal window during the *X*/*Y*/*X* stimulus exceeds the JND for the corresponding change in interaural correlation.

In Fig. 3, the ICCI-detection thresholds (durations of *Y* noise in ms) are plotted against the corresponding correlation JND for each subject (see Akeroyd and Summerfield, 1999, Fig. 10). Superimposed on these data are lines that represent predicted relations between ICCI-detection threshold and JNDs, based on different binaural temporal window ERDs.

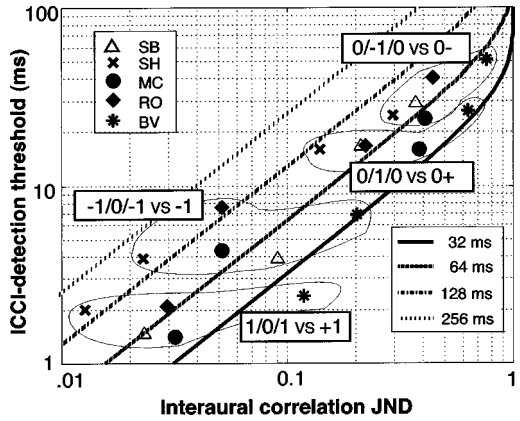

FIG. 3. The relation between the dynamic measure of interaural correlation sensitivity (ICCI detection) and the static measure (JND) can be explained via a temporal window that smears temporal changes in interaural correlation. The data points show the experimental measurements from each subject from Figs. 2(a) and (b). Interaural correlation JNDs are plotted against the ICCI-detection threshold (ms) for related configurations. Superimposed on these points are lines which represent a binaural temporal window length (ERD) calculated using the "ρ_w" model (see Akeroyd and Summerfield, 1999, Fig. 10). A binaural temporal window with a fixed duration (ERD in ms as per the legend) can explain all JND and ICCI threshold pairs that fall along a single line. The location of the data points for different conditions shifts upward along these lines for the conditions with poorer thresholds. This linear shift demonstrates that changes in acuity are correlated for the static and dynamic tasks, and thus the window ERD remains relatively constant across conditions. The lines calculated by the model are based on a change in correlation of 1 (e.g., +1 to 0). A different set of lines would be generated if the change in correlation was 2 (e.g., +1 to −1). It is for this reason that the data for the 1/−1/1 and −1/1/−1 conditions are not plotted here. The actual ERDs for all conditions are reported in Fig. 4.

ICCI and JND pairs that fall along a given line can be explained by a binaural temporal window with a duration corresponding to the ERD represented by that line. The location of the data points moves upwards along these lines for the conditions with poorer thresholds, indicating that the performance for different interaural configurations is correlated for both the static and dynamic tasks, and, thus, for a given listener the window ERD remains relatively constant across configurations. The lines representing the different ERDs in this figure are generated only for changes in correlation with a magnitude of 1.0 (e.g., +1 to 0). It is for this reason that the 1/−1/1 and −1/1/−1 conditions, for which the magnitude of change in correlation is twice the size (2.0), are not plotted in Fig. 3. If the lines of equal ERD were plotted for a correlation change of 2.0, they would be shifted downward because the model predicts that the ICCI-detection thresholds would be approximately half the size for the same JND values.

Figure 4 shows the actual individual ERDs calculated for each condition, including the conditions where the *X* and *Y* noise are of opposite correlation, 1/−1/1 and −1/1/−1. These were also generated using the "ρ_w" model. Although individual listeners' ERDs vary somewhat across condition, there appears to be greater variability across listeners. There was no significant difference in the mean ERD, collapsed across listeners, obtained for different conditions [$F(4,20)=1.4$, $p>0.26$]. The grand mean ERD across listener and conditions was 86 ms, with a standard deviation of 52.7 ms.

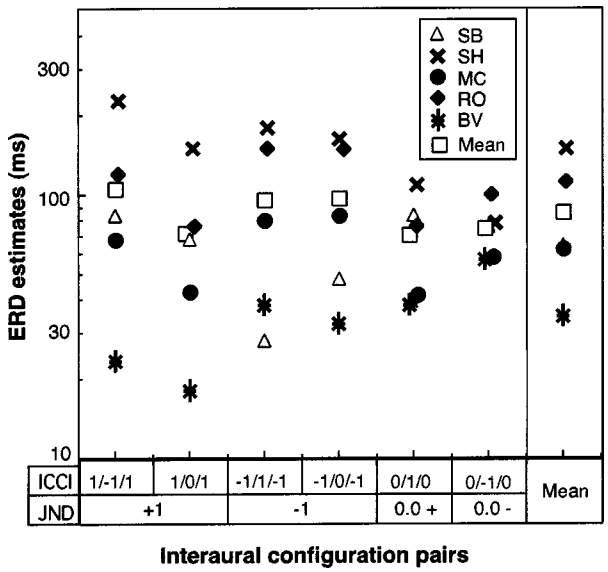

FIG. 4. Binaural temporal window ERD estimations (ms) for individual subjects and the grand mean ERD for each interaural configuration (open squares). The ICCI detection and JND conditions used to generate the window estimate are labeled on the *x* axis. The "ρ_w" model was used to estimate the binaural window ERD required to explain the ICCI-detection threshold based on the subject's JND. While ERDs are variable across listeners, there is less variability across condition for a given listener.

IV. DISCUSSION

The purpose of this study was to examine static (JND) and dynamic (ICCI detection) interaural correlation sensitivity under a variety of interaural configurations using wideband noise. Results for both tasks followed the same dependence on interaural configuration—the lowest thresholds were for discrimination of a change in interaural correlation from ± 1, and the highest were for a change in correlation from 0. The results replicate those of other investigators for the positive range (Pollack and Trittipoe, 1959a, b; Gabriel and Colburn, 1981; Koehnke *et al.*, 1986; Jain *et al.*, 1991; Culling *et al.*, 2001). However, they are the only data for the negative range of which we are aware other than an informal mention by Pollack and Trittipoe (1959a). The second major result is that interaural correlation sensitivity (dynamic or static) is more acute in the positive than in the negative range. Specifically, discrimination of a change in interaural correlation from a reference of $+1$ was significantly more acute than from -1, and discrimination of increases in correlation from a reference of 0 toward $+1$ were significantly more acute than a decrease towards -1.

A. Interaural correlation sensitivity for $\rho_{ref}=+1$

Interaural correlation sensitivity is most acute from a reference of $+1$, and this acuity is probably what underlies the maximal release from masking in the classic NoSπ BMLD condition (see Sec. III D). The JNDs for a departure in correlation from a reference of $+1$ ($\Delta\rho=0.045$) observed in this study were close to values previously reported for broadband noise (e.g., Pollock and Trittipoe, 1959a: $\Delta\rho=0.04$; Gabriel and Colburn, 1981: $\Delta\rho=0.03$; Koehnke *et al.*, 1986: $\Delta\rho=0.02$; Akeroyd and Summerfield, 1999: $\Delta\rho=0.023$). Gabriel and Colburn (1981) also described a bandwidth dependence on the JND from a reference interaural correlation of $+1$, such that acuity degrades with increasing bandwidth. Consistent with this effect, our thresholds for wideband noise are slightly higher than those obtained by Gabriel and Colburn for their widest band of noise (4.5 kHz, $\Delta\rho=0.02-0.03$). Interestingly, bandwidth effects act in the opposite direction for interaural correlation JND from uncorrelated noise references (Gabriel and Colburn, 1981), i.e., performance improves with bandwidth.

The absolute values of thresholds in the 1/0/1 configuration were consistently lower (<3 ms in 7/8 listeners) than the 5 ms mean observed by Akeroyd and Summerfield (1999) for their widest stimulus bandwidth (100–500 Hz). This may indicate that performance remains stable, or continues to improve with increases in bandwidth in the ICCI-detection task, akin to bandwidth effects in monaural gap detection (e.g., Fitzgibbons, 1983). This is contrary to the bandwidth effect observed for the JND from $+1$, in which acuity tends to degrade with increasing bandwidth (Gabriel and Colburn, 1981).

In the dynamic task (ICCI detection), performance improved with greater distance in correlation of the target noise from marker noise of $+1$ interaural correlation. A change to -1 (i.e., $1/-1/1$) resulted in $\sim$30% lower thresholds than a change to 0 (i.e., 1/0/1).

B. Interaural correlation sensitivity for $\rho_{ref}=-1$

Sensitivity to interaural correlation changes from a reference of -1 was found to be relatively acute, but significantly worse than performance from a reference of $+1$. This is inconsistent with the study on interaural correlation sensitivity by Pollack and Trittipoe (1959a), in which they reported that "extensive informal tests" with negative reference correlations "yielded results that were indistinguishable from results with positive correlations" (p. 1251). The reason for this discrepancy is not clear, though it may be related to the difference in methodology. Comparisons between the two studies are difficult because Pollack and Trittipoe did not describe their method. It may be that our use of a staircase procedure was more sensitive, which may be reflected in the lower mean thresholds we obtained in the positive range, at least from uncorrelated references. Similar to the results with reference correlation of $+1$, performance for the $-1/1/-1$ condition was better than for the $-1/0/-1$ condition. This benefit, with a doubling of the interaural correlation change from negatively correlated markers ($\sim$50%), was significantly greater than that observed for correlated markers ($\sim$30%).

C. Interaural correlation sensitivity for $\rho_{ref}=0$

JNDs for an increase in correlation from $\rho_{ref}=0$ ($\Delta\rho=0.31$) are consistent with previous reports (range: $\Delta\rho=0.3$ to 0.5, Pollack and Trittipoe, 1959a; Gabriel and Colburn, 1981; Koehnke *et al.*, 1986; Jain *et al.*, 1991; Culling *et al.*, 2001). They match well with Gabriel and Colburn's value ($\Delta\rho=0.3$) for their widest stimulus bandwidth (4.5 kHz), but are somewhat lower than that obtained by Pollack and Trittipoe (1959a) for wideband noise (0.44). A new result

was that discrimination of an increase in correlation towards $+1$ ($\Delta\rho = 0.31$) was better than discrimination of a decrease towards -1 ($\Delta\rho = 0.45$), a condition for which we have found no comparable data reported. This was consistent with the pattern of data we obtained for ICCI detection, in which the duration required for detection of an increase in correlation from uncorrelated markers (0/1/0, 20.57 ms) was lower than that required for detection of a decrease in correlation (0/−1/0: 41.45 ms). Therefore, the correspondence in performance on the dynamic and static tasks holds for uncorrelated references, as observed for references of $\rho = \pm 1$.

Pollack and Trittipoe (1959a) made the reasonable suggestion that the poorer sensitivity at lower reference correlations was the result of the increased sampling variance for correlations near 0 (also see Gabriel and Colburn, 1981), that is, that performance would be degraded as a result of the increased trial-to-trial variation in correlation of the stimuli as the nominal correlation approaches 0. However, this explanation would predict equal performance in the positively and negatively correlated direction, as there is no difference in the sampling variance in the two configurations.

D. Interaural correlation sensitivity and masking level differences (BMLD)

Both dynamic and static measures of sensitivity to departures of correlation from a negatively correlated reference were poorer than those observed from a positively correlated reference. The asymmetry in performance is consistent with the difference in binaural masking level difference (BMLD) (see Table I). For example, it is well known that the largest BMLD (~15 dB) occurs for the NoSπ condition, which corresponds to the JND for $\rho_{\text{ref}} = +1$. The NπSo condition, which corresponds to the JND from $\rho_{\text{ref}} = -1$, provides less masking release (~13 dB) (Moore, 1997). This asymmetry in correlation discrimination from positive and negative references is thus consistent with the prevailing theory that performance on BMLD and correlation discrimination tasks may be limited by the same mechanism (e.g., Durlach *et al.*, 1986; Koehnke *et al.*, 1986; Jain *et al.*, 1991; Culling *et al.*, 2001). Models which explain the difference between the NoSπ and NπSo BMLD conditions (and by extension the JND from $\rho_{\text{ref}} = +1$ and -1, respectively) traditionally require the postulation of coincidence detector neurons with a distribution of internal delays centered on zero interaural difference. In the NoSπ condition, the decorrelation of the noise by the antiphasic signal is assumed to be most salient in neurons with near equal internal delays, the density of which is proposed to be maximal. Neurons most highly activated by the negatively correlated noise in the NπSo condition have greater internal delay differences. There are fewer of these neurons available, which would make detection of the decorrelation (decrease in activity) in the NπSo condition worse than in the NoSπ condition (Jeffress *et al.*, 1956; Colburn, 1977). An alternative explanation is that the phase-delayed masker noise (Nπ) is not perfectly compensated, except at center frequency, by the optimal internal delay. Thus, the noise cannot be cancelled entirely by a time delay, as proposed by, for example, the equalization/cancellation model of Durlach (1978). And in other models (e.g., Colburn, 1977), the decorrelation in the optimum ITD channel effected by the signal must be detected in comparison to a representation of the phase-delayed masker noise that is already less than unity. All these explanations would similarly predict the observed difference in the correlation JND between references of $+1$ and -1. However, they assume that for a given frequency band there is an array of coincidence-detecting neurons with a wide range of different internal axonal delays that can compensate for large interaural time differences. The physiological validity of such a required distribution of internal delays has been called into question (McAlpine *et al.*, 2001; Brand *et al.*, 2002).

Given that the asymmetry in performance on the tasks using markers or references of $+1$ and -1 seemed to follow the patterning of data in BMLD conditions, we wondered whether the asymmetry from an uncorrelated reference might also follow BMLD patterns for uncorrelated noises. Reports usually show a small BMLD (~2–5 dB) for uncorrelated noise with either a correlated signal (NuSo) or a negatively correlated signal (NuSπ) (Hirsh, 1948; Blodgett *et al.*, 1958; Robinson and Jeffress, 1963; Langford and Jeffress, 1964). However, reports of a *difference* in the BMLD for a negatively correlated (Sπ) and correlated signal (So) in uncorrelated masking noise (Nu) have been conflicting. There is either no reliable difference, or the NuSo condition provides approximately 1 dB more masking release than the NuSπ condition (Blodgett *et al.*, 1958; Robinson and Jeffress, 1963; Langford and Jeffress, 1964). Apparently, there may be no relation between the BMLD and correlation discrimination for conditions where the reference noise is uncorrelated (see Durlach *et al.*, 1986). In these BMLD conditions, monaural cues contribute to detection of the signal as the sound pressure level at each ear is significantly increased in the frequency band containing the signal. The observed BMLD in the Nu condition can be accounted for by having two independent chances to detect the signal monaurally in the uncorrelated noises at each ear (Langford and Jeffress, 1964; Durlach *et al.*, 1986; Jain *et al.*, 1991). The monaural account is further bolstered by the fact that NuSo thresholds show the same frequency dependence as monaural conditions (Durlach and Colburn, 1978). In contrast, the noise stimuli used in the correlation discrimination tasks do not contain any monaural cues (no change in level) and detection must be mediated solely by binaural processes. The asymmetry observed in the correlation JND predicts that the binaural cues would be stronger for the NuSo than the NuSπ conditions. The fact that a difference is not consistently observed in the BMLD measures for these conditions empirically suggests that the available monaural cues override the binaural ones.

E. Evidence for an asymmetry in positive and negative correlation space

In summary, there are a number of lines of evidence from this study which suggest the existence of an asymmetry in acuity for interaural correlation in the positive and negative range. First, while interaural correlation sensitivity was most acute from unity (positive or negative), sensitivity was significantly more acute from $+1$ compared with -1. Corre-

lation sensitivity was generally poor from an uncorrelated reference. However, it was significantly poorer if the change is made towards more negative than towards more positive correlations. Finally, in the ICCI-detection task, there was a significantly greater benefit with the increasing size of correlation change, when that change was in the positive direction. Specifically, thresholds in the $1/-1/1$ condition were $\sim$30% more acute than in the 1/0/1 conditions, while thresholds in the $-1/1/-1$ condition were $\sim$50% more acute than in the $-1/0/-1$ condition. It is yet to be determined if this benefit for increases in correlation holds for reference correlations other than unity. The asymmetry in performance from references of $+1$ and -1 is consistent with the asymmetry observed NoSπ and NπSo BMLD conditions, thus providing further evidence that the BMLD might be explained in terms of interaural correlation discrimination.

The observed asymmetry might reflect an asymmetry in the internal neural representation of negatively and positively correlated noises. The internal representation of uncorrelated noise might not be half-way on some continuum between the representation of negatively and positively correlated noise, but may be closer to the representation of negatively correlated noise. That is, the gradient in internal representation between negatively correlated and uncorrelated noise is smaller than the gradient between uncorrelated and positively correlated noise.

F. The representation of interaural correlation

An interaural correlation change is represented differently in different binaural coincidence detecting neurons, depending on their internal delay and type of binaural input. In the example of a change from correlated to uncorrelated noise (1/0/1), the activity in a binaural channel sensitive to correlated noise would briefly decrease. This decrease would represent the reduction in intensity of the positively correlated component of the uncorrelated noise [see Eq. (1)]. In contrast, there would be a brief increase in activity in a channel that does not respond to correlated noise, but is strongly activated by negatively correlated noise. This increase would represent the intensity of just the negatively correlated component of the uncorrelated noise. Activity in these channels would change inversely when the interaural correlation is changed: they form an opponent channel pair. Thus, in contrast to a monaural intensity change, for example, any correlation change, regardless of its direction, results in both an increase and a decrease in activity as cues for detection. Although the absolute change in activity may be equal in both channels, the proportional change in activity would differ. That is, the percentage decrease in the activity of the channel maximally activated by the reference noise would be less than the percentage increase in activity in the channel minimally activated by the reference noise. This might suggest that the brief increase in activity in the minimally activated channel would be a more salient cue for detection of the interaural correlation change.

The neurophysiological basis for binaural channels selectively activated by positively or negatively correlated stimuli might lie in binaurally innervated neurons with small and large axonal delay differences between predominantly excitatory inputs from each ear, as postulated in the classical Jeffress model (Jeffress, 1948). A channel with equal axonal travel time from both ears would be most sensitive to correlated noise and far less responsive to negatively correlated noise. However, if the difference in axonal travel time from the ears is equivalent to half the period of the characteristic frequency of the neuron, the response to correlated noise will be minimal and the neuron would be most sensitive to negatively correlated noise. As an alternative to an implementation using axonal delays, these opponent channels might be comprised of the ''peak-type'' and ''trough-type'' neurons which are maximally sensitive to positive and negative interaural correlation of noise, respectively (Shackleton *et al.*, 2002; Fitzpatrick *et al.*, 2002). ''Peak-type'' neurons are coincidence detectors receiving predominantly excitatory, phase-locked inputs from each ear. ''Trough-type'' neurons receive phase locked excitation from one ear and phase-locked inhibition from the other. For this reason they are most responsive when the phase-locked inputs from each ear arrive out of phase, that is, when the signal is interaurally negatively correlated.

G. Binaural temporal windows

Our mean binaural temporal window ERD (86 ms) is within the same general range as found previously (e.g., Grantham and Wightman, 1979, 44–243 ms; Culling and Summerfield, 1998, 97 ms; Akeroyd and Summerfield, 1999, 40–400 ms), and larger than the reported values for the analogous Gaussian monaural temporal window [e.g., Moore *et al.*, 1988, 27 ms (corrected value, see Akeroyd and Summerfield, 1999)]. Subjects differed in their pattern across configuration, but not in any consistent way, and there was no significant difference between the mean ERDs obtained for the different interaural configurations. The mean threshold reported here of 86 ms is significantly shorter than that reported by Akeroyd and Summerfield (1999) using the same methods and model (210 ms). According to the ''ρ_w'' model, the reason for this could either be higher JND values or shorter ICCI-detection thresholds in our experiments. The JNDs reported here for $\rho_{\text{ref}}=+1$ (with the exception of listener BKV) were not substantially larger than those reported by Akeroyd and Summerfield (1999) for their widest bandwidth (100–500 Hz). However, our ICCI-detection thresholds were far lower for (2.34 vs 5.3 ms), despite similar methods. A major difference in both experiments is the bandwidth of the stimuli used. Akeroyd and Summerfield (1999) used exclusively low-pass filtered stimuli with a cutoff frequency of 500 Hz. One possibility is that frequency components above 500 Hz contribute to ICCI-detection performance but not to static correlation discrimination. In fact, static correlation discrimination has a tendency to degrade with increased bandwidth (Gabriel and Colburn, 1981). The ''ρ_w'' model would then predict a dependency of the ERD on lower cutoff frequency. A detailed examination of the bandwidth and frequency dependence of the two tasks in the same listeners would be required to determine whether our lower temporal window ERDs were the result of the wider bandwidth used, or simply that our listeners fell in the lower end of the population ERD range.

The method employed here for estimating the binaural temporal window (after Akeroyd and Summerfield, 1999) provided an efficient way to compare the window ERD for the different binaural configurations tested. The method also has the advantage that it exclusively probes the binaural system. However, it does not provide for estimation of the window shape. Other methods, such as those which use BMLD-like stimuli distributed in time (i.e., No noise followed by a $S\pi$ signal) have provided estimations of the shape of the window (e.g., Kollmeier and Gilkey, 1990; Culling and Summerfield, 1998; Holube *et al.*, 1998). These studies have revealed a symmetric double-sided exponential or rounded exponential weighting function with a duration between 40 and 200+ ms depending on the listener and the task parameters (see Holube *et al.*, 1998). This ERD range is similar to that estimated in this study using the "ρ_w" model. More recently, Bernstein *et al.* (2001) estimated the binaural temporal window using a task similar in form to that used here; however, detection was of a change in lateralization by ITD of a brief correlated noise embedded in correlated or uncorrelated markers. Their data was best accounted for by a window with two time constants: a very short one that was heavily weighted at the temporal midpoint and a second one that was 14 ms. This might suggest that the binaural system exploits different temporal windows for tasks probing different aspects of binaural temporal processing (i.e., changes in ITD vs changes in interaural correlation) (Kollmeier and Gilkey, 1990; Bernstein *et al.*, 2001).

H. Limitations and future directions

Conclusions from this study are limited to broadband noise stimuli, and extreme references correlations (± 1 and 0). It remains to be determined if the asymmetry that we observed can be observed for other reference values, although this might be a way to determine the temporal window shape. Future studies are also required to show whether the asymmetry holds for correlation discrimination at various noise bandwidths and center frequencies, and in fringed correlation discrimination (Jain *et al.*, 1991). This latter configuration mimics the BMLD task for a narrow-band signal. The change in correlation occurs only in a narrow frequency band fringed by noise of a reference correlation, but the energy in the frequency band used for detection remains constant. We expect that detection of a decorrelation in a band surrounded by a positively correlated fringe would be better than in a negatively correlated fringe.

V. CONCLUSIONS

(1) Static and dynamic measures of interaural correlation follow the same general pattern of dependence on interaural configuration.
(2) There is an asymmetry in performance of both static and dynamic measures of interaural correlation sensitivity in the positive and the negative range in that correlation sensitivity is more acute in the positive range.
(3) The mean binaural temporal window equivalent rectangular duration (ERD) was relatively constant across interaural configuration, although individual listeners ERD patterns varied in unique ways. Listeners also differed in their mean individual window length. The mean ERD was 86 ms.

ACKNOWLEDGMENTS

Special thanks to Dennis P. Phillips who supported the research with a grant from NSERC of Canada, and provided helpful suggestions on the manuscript. Thanks also to M. Akeroyd, two anonymous reviewers, and D. McAlpine for helpful suggestions that greatly improved the manuscript, and to C. Trahiotis for kindly sending a copy of *The MLD: A Collection of Seminal Papers* to SB. Finally, sincere thanks to L. Bernstein for superb editorial guidance and suggestions. SB is grateful for scholarship support from NSERC of Canada and the I. W. Killam Trust. TM's visit to Canada was supported by a Bogue Fellowship from the Department of Physiology at University College London.

[1]It should be noted that the shorter the duration of the two independent noise bursts presented to each ear, the greater the variability of their interaural correlation. Thus, for the target durations near threshold in the 1/0/1 and $-1/0/-1$ configurations, our uncorrelated noises are unlikely to be truly uncorrelated. Across multiple repetitions, the average of the normalized correlation between the waveforms should approximate zero. However, this is not true at high frequencies where envelopes convey the information. The minimum normalized correlation for independent noise envelopes is approximately +0.78 (van de Par and Kohlrausch, 1995). Logically, if this was contributing to our results, it would predict equal performance on the $-1/0/-1$ (envelope correlation: $+1/0.78/+1$) and 1/0/1 task (envelope correlation: $+1/0.78/+1$), which was not observed. To test the impact of information conveyed at high frequencies directly, listeners SB and SE repeated all ICCI-detection conditions with low-pass filtered stimuli ($f_{LP} = 800$ Hz). Thresholds for the 1/0/1 (SB:1.96; SH: 1.7) and $-1/0/-1$ (SB:3.27; SH:6.62) conditions were within 1 ms of the listeners' wideband noise results. Thresholds for the 0/1/0 (SB:26.5; SH:20.95) and $0/-1/0$ (SB:34.66; SH:32.54) conditions were slightly higher, but within range, of their values for wideband noise.

Akeroyd, M. A., and Summerfield, A. Q. (**1999**). "A binaural analog of gap detection," J. Acoust. Soc. Am. **105**, 2807–2820.

Bernstein, L. R., and Trahiotis, C. (**1992**). "Discrimination of interaural envelope correlation and its relation to binaural unmasking at high frequencies," J. Acoust. Soc. Am. **91**, 306–316.

Bernstein, L. R., Trahiotis, C., Akeroyd, M. A., and Hartung, K. (**2001**). "Sensitivity to brief changes of interaural time and interaural intensity," J. Acoust. Soc. Am. **109**, 1604–1615.

Blauert, J., and Lindemann, W. (**1986**). "Spatial mapping of intracranial auditory events for various degrees of interaural coherence," J. Acoust. Soc. Am. **79**, 806–813.

Blodgett, H. C., Jeffress, L. A., and Taylor, R. W. (**1958**). "Relation of masked threshold to signal duration for various interaural phase combinations," Am. J. Psychol. **71**, 283–290.

Brand, A., Behrend, O., Marquardt, T., McAlpine, D., and Grothe, B. (**2002**). "Precise inhibition is essential for microsecond interaural time difference coding," Nature (London) **417**, 543–547.

Colburn, H. S. (**1977**). "Theory of binaural interaction based on auditory nerve data. II. Detection of tones in noise," J. Acoust. Soc. Am. **61**, 525–533.

Culling, J. F., and Summerfield, Q. (**1998**). "Measurements of the binaural temporal window using a detection task," J. Acoust. Soc. Am. **103**, 3540–3553.

Culling, J. F., Colburn, H. S., and Spurchise, M. (**2001**). "Interaural correlation sensitivity," J. Acoust. Soc. Am. **110**, 1020–1029.

Culling, J. F., Summerfield, A. Q., and Marshall, D. H. (**1998a**). "Dichotic pitches as illusions of binaural unmasking. I. Huggins' pitch and the 'binaural edge pitch,' " J. Acoust. Soc. Am. **103**, 3509–3526.

Culling, J. F., Marshall, D. H., and Summerfield, A. Q. (**1998b**). "Dichotic pitches as illusions of binaural unmasking. II. The Fourcin pitch and the dichotic repetition pitch," J. Acoust. Soc. Am. **103**, 3527–3539.

Durlach, N. I. (**1978**). ''Binaural signal detection: Equalization and Cancellation theory,'' in *Foundations of Modern Auditory Theory*, edited by J. V. Tobias (Academic, New York).
Durlach, N. I., and Colburn, H. S. (**1978**). ''Binaural phenomena,'' in *Handbook of Perception: Hearing*, edited by E. C. Carterette and M. P. Friedman (Academic, New York), Chap. 10.
Durlach, N. I., Gabriel, K. J., Colburn, H. S., and Trahiotis, C. (**1986**). ''Interaural correlation discrimination: II. Relation to binaural unmasking,'' J. Acoust. Soc. Am. **79**, 1548–1557.
Fitzgibbons, P. J. (**1983**). ''Temporal gap detection in noise as a function of frequency, bandwidth and level,'' J. Acoust. Soc. Am. **74**, 67–72.
Fitzpatrick, D. C., Ebert, C. S., Pollock, H. W., Pearson, J. M., and Crocker, W. D. (**2002**). ''Responses of auditory cortical neurons sensitive to interaural time differences (ITDs) to changes in interaural correlation,'' in Abstracts of the 25th MidWinter Meeting of the Association for Research in Otolaryngology, Abst. #46.
Gabriel, K. J., and Colburn, H. S. (**1981**). ''Interaural correlation discrimination: I. Bandwidth and level dependence,'' J. Acoust. Soc. Am. **69**, 1394–1401.
Grantham, D. W., and Wightman, F. L. (**1978**). ''Detectability of varying interaural temporal differences,'' J. Acoust. Soc. Am. **63**, 511–523.
Grantham, D. W., and Wightman, F. L. (**1979**). ''Detectability of a pulsed tone in the presence of a masker with time-varying interaural correlation,'' J. Acoust. Soc. Am. **65**, 1509–1517.
Hirsh, I. (**1948**). ''The influence of interaural phase on interaural summation and inhibition,'' J. Acoust. Soc. Am. **20**, 536–544.
Holube, I., Kinkel, M., and Kollmeier, B. (**1998**). ''Binaural and monaural auditory filter bandwidths and time constants in probe tone detection experiments,'' J. Acoust. Soc. Am. **104**, 2412–2425.
Jain, M., Gallagher, D. T., Koehnke, J., and Colburn, H. S. (**1991**). ''Fringed correlation discrimination and binaural detection,'' J. Acoust. Soc. Am. **90**, 1918–1926.
Jeffress, L. A. (**1948**). ''A place theory of sound localization,'' J. Comp. Physiol. Psychol. **41**, 35–39.
Jeffress, L. A., Blodgett, H. C., Sandel, T. T., and Wood III, C. L. (**1956**). ''Masking of tonal signals,'' J. Acoust. Soc. Am. **28**, 416–426.
Koehnke, J., Colburn, H. S., and Durlach, N. I. (**1986**). ''Performance in several binaural-interaction experiments,'' J. Acoust. Soc. Am. **79**, 1558–1562.
Kollmeier, B., and Gilkey, R. H. (**1990**). ''Binaural forward and backward masking: evidence for sluggishness in binaural detection,'' J. Acoust. Soc. Am. **87**, 1709–1719.
Langford, T. L., and Jeffress, L. A. (**1964**). ''Effect of noise cross correlation on binaural signal detection,'' J. Acoust. Soc. Am. **36**, 1455–1458.
Levitt, H. (**1971**). ''Transformed up-down methods in psychoacoustics,'' J. Acoust. Soc. Am. **49**, 467–477.
McAlpine, D., Jiang, D., and Palmer, A. R. (**2001**). ''A neural code for low-frequency sound localisation in mammals,'' Nat. Neurosci. **4**, 396–401.
Moore, B. C. J. (**1997**). *An Introduction in the Psychology of Hearing: 4th edition* (Academic, New York), p. 238, Table 6.1.
Moore, B. C. J., Glasberg, B. R., Plack, C. J., and Biswas, A. K. (**1988**). ''The shape of the ear's temporal window,'' J. Acoust. Soc. Am. **83**, 1102–1116.
Pollack, I., and Trittipoe, W. J. (**1959a**). ''Binaural listening and interaural noise cross correlation,'' J. Acoust. Soc. Am. **31**, 1250–1252.
Pollack, I., and Trittipoe, W. J. (**1959b**). ''Interaural noise correlation: Examination of the variables,'' J. Acoust. Soc. Am. **31**, 1616–1618.
Robinson, D. E., and Jeffress, L. A. (**1963**). ''Effect of varying the interaural noise correlation on the detectability of tonal signals,'' J. Acoust. Soc. Am. **35**, 1947–1952.
Shackleton, T. M., Arnott, R. H., and Palmer, A. R. (**2002**). ''Interaural correlation functions in the inferior colliculus of the guinea pig,'' in Abstracts of the 25th MidWinter Meeting of the Association for Research in Otolaryngology, Abst. #48.
van der Heijden, M., and Trahiotis, C. (**1997**). ''A new way to account for binaural detection as a function of interaural noise correlation,'' J. Acoust. Soc. Am. **101**, 1019–1022.
van de Par, S., and Kohlrausch, A. (**1995**). ''Analytical expressions for the envelope correlation of certain narrow-band stimuli,'' J. Acoust. Soc. Am. **98**, 3157–3169.

Economy of effort in different speaking conditions. I. A preliminary study of intersubject differences and modeling issues

Joseph S. Perkell,[a] Majid Zandipour, Melanie L. Matthies,[b] and Harlan Lane[c]
Speech Communication Group, Research Laboratory of Electronics, Massachusetts Institute of Technology, Cambridge, Massachusetts 02139

(Received 6 March 1998; revised 8 June 2002; accepted 16 July 2002)

This study explores the hypothesis that clear speech is produced with greater ''articulatory effort'' than normal speech. Kinematic and acoustic data were gathered from seven subjects as they pronounced multiple repetitions of utterances in different speaking conditions, including normal, fast, clear, and slow. Data were analyzed within a framework based on a dynamical model of single-axis frictionless movements, in which peak movement speed is used as a relative measure of articulatory effort (Nelson, 1983). There were differences in peak movement speed, distance and duration among the conditions and among the speakers. Three speakers produced the ''clear'' condition utterances with movements that had larger distances and durations than those for ''normal'' utterances. Analyses of the data within a peak speed, distance, duration ''performance space'' indicated increased effort (reflected in greater peak speed) in the clear condition for the three speakers, in support of the hypothesis. The remaining four speakers used other combinations of parameters to produce the clear condition. The validity of the simple dynamical model for analyzing these complex movements was considered by examining several additional parameters. Some movement characteristics differed from those required for the model-based analysis, presumably because the articulators are complicated structurally and interact with one another mechanically. More refined tests of control strategies for different speaking styles will depend on future analyses of more complicated movements with more realistic models. [DOI: 10.1121/1.1506369]

PACS numbers: 43.70.Aj, 43.60.Bk [AL]

I. INTRODUCTION

In order to improve models of speech motor control, it is important to characterize the various constraints under which speech production operates. The requirement for intelligibility imposes constraints on the acoustic characteristics of the signal that are related to clarity (cf. Picheny *et al.*, 1986; Moon and Lindblom, 1994; Moon, 1991). Clarity constraints may vary according to environmental conditions that require the speaker to use different styles—such as speaking clearly in a noisy environment or when the listener has a hearing loss. In comparison to normal (citation or casual) speech, clear speech has been shown to be characterized by greater intelligibility, greater intensity (by 3–5 dB in vowel nuclei), longer sound segments, an expanded vowel space, tighter acoustic clustering within vowel categories, greater distinctiveness of VOT between voiced and voiceless stop consonants and released word-final stops (cf. Picheny *et al.*, 1986; Moon and Lindblom, 1994; Moon, 1991). Such clear speech might be produced with movements that are larger, slower, more precise, and possibly more effortful. Lindblom (1990) has hypothesized that there is a trade-off between clarity and economy of effort that occurs with changes in speaking styles: clear speech should be produced with greater articulatory effort than normal speech. In the current study we test the hypothesis that speakers will exert more effort when asked to speak clearly than when they speak normally. We test this hypothesis by examining a relative measure of effort in the production of speech movements in various speaking conditions. For this purpose, we define ''economy of effort'' as a strategy in which the motor control system attempts to minimize the physical ''cost'' of making articulatory movements. Economy of effort appears to be a characteristic of movement in general, and it is a principle that guides speech movement planning in the control model of Guenther (Guenther, 1995; Guenther *et al.*, 1998; Perkell *et al.*, 2000).

To compare a measure of articulatory effort across different speaking conditions, the study uses peak movement speed, which is an approximation based on a cost optimization analysis of a dynamical model of single-axis frictionless movements (Nelson, 1983). A second objective of this study is to consider the extent to which such a simple model may be valid for analyzing complicated speech movements.

II. BACKGROUND

In the first study that directly addressed this issue, Adams (1990) reported on tongue-blade opening movements for the word ''tad'' as produced in casual and clear conditions by five speakers. ''The clear speech condition was associated with longer movement durations and larger maximum dis-

[a]Also at the Department of Brain and Cognitive Sciences, MIT and the Department of Cognitive and Neural Systems, Boston University. Electronic mail: perkell@speech.mit.edu
[b]Also at the Department of Communication Disorders, Boston University.
[c]Also at the Department of Psychology, Northeastern University.

placement and peak velocity values relative to the casual condition in some subjects.'' (p. iii). In order to develop a rationale for a more thorough investigation that includes an analysis of articulatory effort, it is helpful to consider observations of articulatory kinematics that have been made in studies of other factors, such as speaking rate, speech tempo, stress, and vowel quantity.

In the Kuehn and Moll (1976) kinematic study of speaking rate, it was found that in order to increase speaking rate, some speakers increased articulatory velocities and produced little articulatory undershoot, while others did not increase velocities and produced more articulatory undershoot. There were positive relationships across subjects between both articulatory velocity and movement displacement and the size of the articulators, possibly reflecting a generally observed linear relationship between peak velocity and distance (cf. Ostry *et al.*, 1987; Ostry and Munhall, 1985; Linville, 1982; Vatikiotis-Bateson and Fletcher, 1992; Flanagan *et al.*, 1990). Sonoda and Nakakido (1986) studied the effect of speaking rate on jaw movements. Similarly to Kuehn and Moll, they observed that the increase in speaking rate was produced either with an increase in velocity and little change in distance (i.e., no undershoot) or with relatively constant velocity and a decrease in movement distance (undershoot).

In a kinematic study of tempo and prosody, Edwards *et al.* (1991) found that two of four subjects, in complying with ''slow speech'' instructions, decreased the velocity of a phrase-final mandible closing gesture, while the other two delayed the onset of the closing gesture without decreasing velocity. The latter two subjects had generally longer syllable durations than the former two. As an explanation for these findings, Edwards *et al.* (1991) hypothesized a lower limit on velocity that may be physiologically based or perceptually based (to preserve phonetic identity).

To help make inferences about articulatory effort and the control mechanisms that underlie kinematic observations, some investigators (cf. Munhall *et al.*, 1985; Ostry and Munhall, 1985; Hertrich and Ackermann, 1997) have adopted principles from a cost optimization analysis of single-axis movements of an undamped, linear, mass-spring model (Nelson, 1983). According to this analysis, *peak velocity* can be used as a *relative measure of the physical cost* of performing skilled movements.

Nelson's (1983) analysis shows that minimization of energy or of jerk (the third derivative of displacement vs time) produces in each case a profile of movement velocity versus time similar to the pattern that results from an undamped linear mass-spring system with constant stiffness, in which velocity vs time for a single movement looks similar to the positive half of a sinusoid function. Figure 1(a), from Nelson (1983), shows velocity profiles for minimum energy (*E*), minimum jerk (*J*), and constant stiffness (*K*), all three of which look similar to those observed from speech movements. The peak velocity of the movement of the linear spring model is related to movement distance and time constraints by $V=\pi D/2T$ (where $V=$peak velocity, $D=$distance, and $T=$time). Peak velocity is also equivalent to the impulse cost measure (time integral of the magnitude of the force per unit mass) in Nelson's analysis. Even though a minimum-impulse solution produces a trapezoidally shaped velocity profile [*V*, in Fig. 1(a)] that is less like those of speech movements, it is possible to use peak velocity as a measure of *relative* effort, because all of the minimum-cost solutions produce similarly shaped cost functions, shown in Fig. 1(b) (when percent cost is plotted as a function of movement time—from Nelson, 1983). As Nelson points out, a single criterion is ''generally insufficient to encompass what we mean by optimum'' (p. 140), and skilled movements reflect a compromise or trade off among competing objectives, one of which, in the case of speech, is producing an intelligible sound sequence. As explained below, the current study

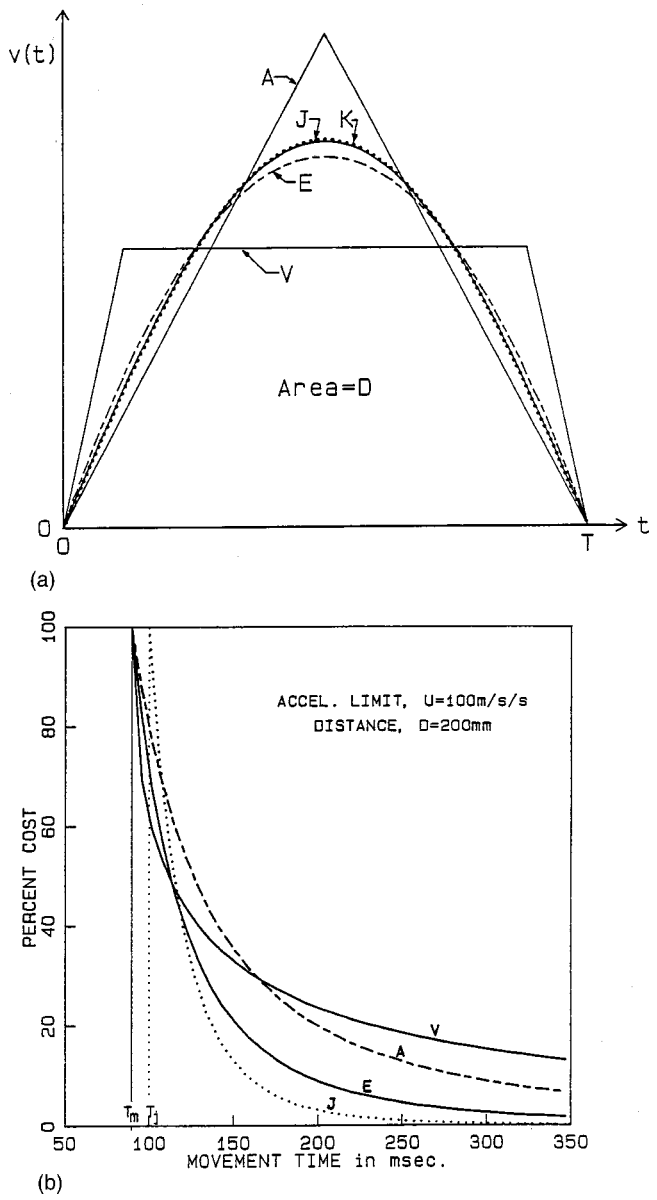

FIG. 1. (a) Comparison of velocity patterns of a single-axis, frictionless system for the same movement time and distance that are optimum with respect to five different objectives: *A*, minimum peak acceleration (solid line); *E*, minimum energy (dashed line); *J*, minimum jerk (solid); *K*, constant stiffness (dotted); and *V*, minimum peak velocity; or impulse (solid) (Fig. 3 in Nelson, 1983). (b) Curves of minimum percent cost as a function of movement time for fixed distance, *D*, and acceleration limit *U*. *V*, peak velocity (impulse) cost; *A*, peak acceleration cost; *E*, energy cost; and *J*, jerk cost (Fig. 6 in Nelson, 1983).

is of nearly linear two-dimensional movements, so we use peak movement speed (the tangential velocity maximum) as a relative measure of effort. We also examine additional parameters to investigate other aspects of the movements.

The ratio of peak velocity to average velocity, $c = V/V_a$ (where V_a = average velocity, D/T), provides an index of velocity profile shape (Nelson, 1983; Ostry and Munhall, 1985). To some extent, the velocity profile shape (as indexed by the value of c) can reflect the selection of a particular cost optimization criterion (e.g., energy, jerk, impulse). For model velocity profiles that are symmetrical (equal durations of acceleration and deceleration phases), unimodal (smooth, with one acceleration peak in the first half of the movement and one deceleration peak in the second half) and have velocity values of zero at movement beginning and end, a value of $c = 1.0$ would correspond to a rectangular profile and a value of 2.0 would correspond to a triangular profile [profile (A) in Fig. 1(a)]. A rectangular profile would be produced by an acceleration impulse at movement beginning and a deceleration impulse of equal magnitude at movement end. A triangular profile would be produced by an acceleration pulse for half of the movement followed by a deceleration pulse of equal magnitude for the second half of the movement. Thus, these two profiles represent theoretical, physically unrealizable limits; many actual movements may fall between the two patterns. On the other hand, if actual movements have velocity profiles that do not meet the above criteria (unimodal, symmetrical, and zero velocity at movement beginning and end), values of c can exceed 2.0.

Another parameter, the ratio of peak velocity to distance, has been considered to reflect actuator ''stiffness,'' if the system can be represented by a second-order damped dynamical model (cf. Nelson, 1983; Ostry *et al.*, 1983; Ostry and Munhall, 1985).[1] The level of stiffness may be thought of as a relative index of the level of muscle activity that is used to produce a movement.

In the above-referenced rate and clarity study (Adams, 1990), normal and faster-than-normal speech was produced with unimodal velocity profiles, while the slower-than-normal speech had multipeaked (i.e., less smooth) velocity profiles. Values of c were found to decrease with increases in speaking rate; they approached $\pi/2$ (1.57), the value that is characteristic of the sinusoidal velocity profile of the frictionless mass-spring model.

Hertrich and Ackermann (1997) measured acoustic and labial kinematic variables in a study of vowel quantity in German. They found intersubject differences for several measures, and interactions among the measures. The results included: distinct linear peak velocity-distance relationships for each quantity class, an influence of vowel quantity on the scaling of velocity and amplitude in oral opening movements, more peaked velocity profiles for long than short vowels, and differential effects of vowel quantity on the symmetry of velocity profiles in opening versus closing movements. Values of parameter c were consistently greater than $\pi/2$. Closing gestures were characterized as fast and ballistic, and opening gestures were more sensitive to phonetic timing. Among other things, Hertrich and Ackermann concluded that durational information was conveyed more consistently by acoustic results than by movement durations.

In sum, previous studies of articulatory kinematics invariably have found intersubject differences. They also have shown systematic relations among movement parameters, such as velocity versus distance, that are characteristic of other types of movements and may be used to make some inferences about aspects of the underlying control. According to a cost analysis of uniaxial frictionless movements, peak velocity may be used as a relative index of effort. The ratio of peak velocity to distance may be used to indicate relative levels of muscle stiffness underlying the movements. The ratio of peak velocity to average velocity (c) can also reflect relative effort, but only if the movements being compared have smooth, symmetrical velocity profiles and have the same duration. On the other hand, if movements are not smooth or symmetrical (i.e., have acceleration and deceleration phases of different durations) and they have relatively high values of c (approaching and exceeding 2.0), the simple modeling framework may not be an entirely suitable tool of analysis.

III. METHODS

Based on the preceding background, a study was conducted of measures of effort and other movement characteristics in six speaking conditions, using data from utterances elicited from seven subjects in those conditions.

A. Subjects, speech materials, and data acquisition

The subjects were seven young adult speakers of American English without speech or hearing deficits or pronounced regional dialect, three females and four males.

The subjects read short sentences containing CVC ''test'' words in six different speech conditions. Utterances were of the form ''say C_1VC_2 again,'' where C_1VC_2 is ''bob,'' ''dod'' or ''gog,'' with stress on the CVC word. The three test words were selected to investigate the effect of articulator (lower lip, tongue blade, tongue body) on the movements. (It is acknowledged that the movements of all three articulators are influenced by mandible movements: the lower lip is the most influenced and the tongue body is the least influenced. However, these influences of the mandible are not examined in the current study.) Both the opening movement toward the V_1 target and the closing movement toward C_2 were examined to investigate the effect of movement type.[2] *Normal* speech was elicited by asking the subjects to pronounce the utterances at a ''conversational'' pace. *Fast* speech was elicited by asking the subjects to pronounce the utterances at what they perceived as twice their normal rate. *Slow* speech was elicited by asking the subjects to pronounce the utterances at what they perceived as half their normal rate. *Clear* speech was elicited by telling the subjects that someone in the next room was checking their pronunciation and they would be rewarded according to the number of utterances pronounced correctly. (Speaking louder was discouraged; articulating clearly was encouraged.) A *rapid + clear* condition rewarded the subjects for a combination of brevity and number of correctly pronounced tokens. Finally, in a casual condition, called ''*informal*,'' subjects were

shown a number of 4×4 matrices (one at a time), with each cell containing a test word and a number (1–4), and the columns labeled $A-D$. The subject was asked to tell a listener how to number a similar (un-numbered) matrix by saying, for example, ''One is the 'bob' in *A*, the 'dod' in *C*, the 'gog' in *D*.... Two is the gog in *B*, the dod in *D*,...[etc.].'' In this condition the subject was not rewarded for clarity and was told not to worry about mistakes; the resulting utterances were judged informally to be quite casual in nature.

There were 15 repetitions of each utterance in each condition. Utterances containing the three CVC words were interspersed randomly with repetitions of utterances containing other CVC words and alternative stress patterns that were designed to explore the acoustic and kinematic effects of stress, vowel quality, and consonant place and manner of articulation (not covered in the current report). The full corpus included approximately 1400 utterances and took approximately 45 minutes to produce.

Recordings were made of the acoustic signal and displacement versus time signals from small (5 mm long $\times$2.5 mm diam) coils placed in the midsagittal plane on the lips, tongue and mandible, as transduced by an ElectroMagnetic Midsagittal Articulometer (EMMA) system (Perkell *et al.*, 1992). The transducer coils were mounted with adhesive on the vermilion border of the upper lip (UL) and lower lip (LL), the gingival papilla between the two lower central incisors, the tongue body dorsum about 5 cm from the tip (called tongue back, TB), and the tongue blade about 1 cm from the tip (called tongue front, TF). Additional transducers, on the bridge of the nose and upper incisor, were used as a maxillary frame of reference to define the coordinate system of movements of the other transducers. A directional microphone was suspended 14 inches from the subject's mouth. Utterance materials were presented, 10 items at a time, on sheets of paper hanging in front of the subject. After a short period of adaptation, the presence of the transducers was judged aurally to have a negligible effect on the subjects' utterances.

B. Signal processing, data extraction, and data analysis

Each channel of movement signal was digitized at 312.5 samples per second (aggregate rate for 32 channels, 10 kHz), and the speech signal was sampled at 10 kHz after being low-pass filtered at 4.5 kHz. During the subsequent signal processing, articulator x (horizontal) and y (vertical) displacements in the midsagittal plane were calculated from the EMMA output voltages (see Perkell *et al.*, 1992). The displacement signal was low-pass filtered with an FIR filter that began to roll off at 13 Hz and was greater than 60 dB down at 22 Hz. Then, velocity and acceleration in the x and y directions were computed by differentiating the low-pass filtered displacement vs time signals with a backward difference approximation (computing the difference between adjacent values divided by the time step, 3.2 ms). Following differentiation, the resulting velocity and acceleration signals were low-pass filtered with an FIR filter that began to roll off at 38 Hz and was greater than 60 dB down at 47 Hz.

To check the validity of the EMMA data and look for long-term trends that could include fatigue effects, we examined time-series plots of the x and y values and the EMMA misalignment correction index (Perkell *et al.*, 1992) for each transducer, extracted at the time of the beginning of each token. We also examined midsagittal $x-y$ plots of the same data. Abrupt changes and long-term drift in the time series and outlying points in the $x-y$ display were few in number; they were noted and the corresponding data were removed from subsequent analyses.

Figure 2 illustrates the data extraction procedures; it shows signals for a portion of the utterance ''Say gog again,'' spoken in the normal condition. The acoustic signal [panel (A) of Fig. 2] was labeled manually in two stages: (1) identification of the tokens and (2) marking of three acoustic events: the beginning of C_1 (C_1beg), the release burst for C_1 (C_1rel), and the beginning of C_2 (C_2beg), the same as the end of the vowel. The labeling process included the automatic extraction of vowel duration and SPL (measured from the midvowel RMS amplitude, relative to a calibration signal).

Panel (C) of Fig. 2 shows the $x-y$ trajectory of a transducer coil on the tongue body for the utterance. Data were extracted from the C_1–V opening (between 3 and 4 on the trajectory) and the V–C_2 closing (between 4 and 5) movements in each of the CVC words (the carrier word *say* was not analyzed). As exemplified in the figure, the movement paths were slightly curved; however, for the current purposes, it is assumed that to a first approximation, such movements can be analyzed according to the model of single-axis movements discussed above. In order to adapt the analysis framework described in the background to slightly curved, two-dimensional (2D) movements, it is assumed that *peak speed* and *distance along the path of the 2D* movements correspond respectively to *peak velocity* and *distance of single-axis movements*.

Movement speed was computed according to the formula

$$\text{Speed}=\sqrt{v_x^2+v_y^2},$$

where $v_x=dx/dt$ and $v_y=dy/dt$. The magnitude of the acceleration signal was computed according to

$$\text{Acceleration magnitude}=\sqrt{(dv_x/dt)^2+(dv_y/dt)^2}.$$

Data were extracted algorithmically from movements of the tongue body transducer for the word ''gog,'' the tongue front transducer for ''dod'' and the lower lip transducer for ''bob.'' Movement events were identified algorithmically in the speed versus time traces, as exemplified in panel (B) of Fig. 2 for the tongue-body transducer. The vertical arrows indicate the times of the labeled acoustic events [shown in part (A)]; the asterisks show the algorithmically identified velocity peaks for the movements; and the numbered circles along the bottom axis show the algorithmically identified times of tongue movement beginning (3 and 4) and end (2, 4, and 5). [Events 2–5 are also indicated on the $x-y$ trajectory in Panel (C).] As explained below, three movements are marked in the figure with symbols; however, only the second and third movements are analyzed and discussed.

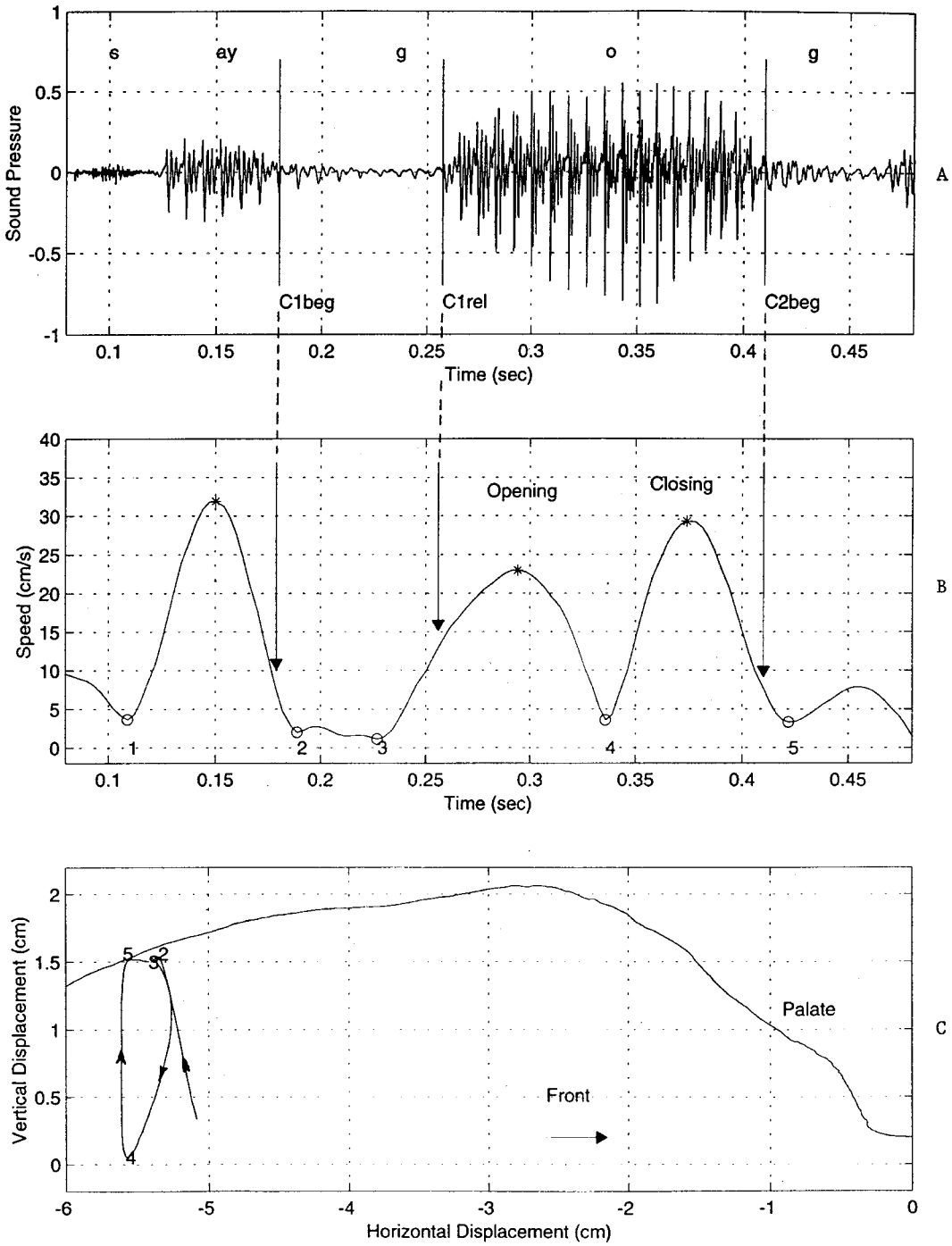

FIG. 2. (A) The acoustic signal for part of the utterance "say gog..." in the normal speaking condition. (B) Speed versus time for a transducer on the tongue body. The vertical arrows indicate the times of the acoustic events; the asterisks show algorithmically identified velocity peaks for the opening and closing movements, and the numbered circles along the bottom axis show the algorithmically identified times of movement beginning and end. (C) The $x-y$ trajectory for the tongue body transducer.

To identify each movement, its speed peak was found in relation to a nearby acoustic event; then movement beginning and end points were identified as the minima immediately preceding and following the peak. By definition, this approach yielded one speed peak per movement. In some cases, the end of one movement was the same event as the beginning of the next. This is illustrated in panel (B) by the circle numbered 4, which is at the end of the opening movement and at the beginning of the closing movement. In other cases the two events were different: the end of the closing movement for C_1 (shown by circle 2) occurs prior to the beginning of the opening movement for the vowel (circle 3). The time interval between events 2 and 3 is called an "intermovement interval." It contains small, low-speed movements of the transducer that occur during consonant closure. Although an example is not shown in the figure, intermovement intervals also occurred at maximum vowel opening, when the articulator paused briefly between the opening and closing movements. Both types of intermovement intervals

(during C_1 closure and during maximum V opening) occurred more often at low speaking rates. Since speed includes x and y components of velocity, it almost never reaches a zero value (cf. Mooshammer, Hoole, and Kühnert, 1995).

From examining a number of $x-y$ trajectories marked as in panel (C), Fig. 2, it was inferred that the end of the closing movement for the preceding consonant, C_1 (event 2), corresponded approximately to the time that the tongue body or blade collided with the hard palate (or the two lips collided with one another). The beginning of the opening movement for the vowel (event 3) corresponded approximately to when the articulators were breaking contact at consonant release.

As the algorithm was being run, it displayed each speed trace with decisions marked on the computer screen [similar to panel (B) in Fig. 2, but with 16 tokens to a screen]. Visual inspection revealed ubiquitous nonzero speed values at movement beginning and end points and frequent intermovement intervals, as mentioned above. There were also some more variable traces for which the algorithm failed; therefore, the experimenter observed every decision and noted the tokens in which the extraction was not successful. Those tokens were later eliminated from further analysis. [The original data extraction also included the C_1 closing movement, between circles 1 and 2 in Fig. 2(B). Because of context-related variability in this movement, it is not included in the current report. However, a failure to correctly extract data from any of the three movements was cause for rejection of a token.] Usually, 13 to 15 of the 15 tokens in each condition were analyzed successfully; the minimum was nine.[3]

The following parameters were extracted and calculated for each opening and closing movement:

(1) movement duration,
(2) distance along the $x-y$ path,
(3) peak speed (maximum speed reached during a movement)—a relative measure of effort,
(4) peak speed/distance—a relative index of the ''stiffness'' of underlying muscle contraction,
(5) c = peak speed/average speed, where average speed = distance/duration,
(6) number of peaks in the acceleration magnitude signal—an index of the lack of movement smoothness,
(7) symmetry of the speed profile, measured by the percentage of the movement duration spent in acceleration (where 50% represents true symmetry),
(8) movement curvature ratio (distance along the actual trajectory/straight-line distance between the movement end points).

To investigate the main hypothesis, clear-condition speech is produced with greater effort than normal-condition speech, the data were analyzed for each subject individually in the following ways.

(1) Six three-way repeated-measures ANOVAs were performed for each subject. In each ANOVA, the main effects tested were for speech condition (clear versus normal), movement (opening versus closing), and articulator (tongue back, tongue front, and lower lip) and their interactions. The six dependent variables were acoustic vowel duration, SPL, and the first four movement parameters listed above.

In order to compare the strengths of the main effects in the ANOVAs, it was necessary to correct the values of F for their variable degrees of freedom. In general, the numerical value of a test of significance reflects the product of the size of the effect and the size of the study. Specifically, we used the measure eta-square (Young, 1993): $F=(\eta^2/1-\eta^2)*$ (df error/df means)

(2) The mean values are compared in bar plots, with significant differences indicated by showing the values of $\eta^2\times 100$, which indicates the percentage of variance accounted for in the comparison.

(3) Data from all of the conditions are examined graphically in a peak speed, distance, duration ''performance space,'' in which bounding parameter values are determined by the above-mentioned second-order model (Nelson, 1983; Nelson *et al.*, 1984).

To explore the validity of using the undamped linear spring model, values of movement parameters 5–8 (above), as well as occurrences of intermovement intervals are considered in relation to the model's underlying assumptions.

IV. RESULTS

The main focus of this study is the difference in kinematic parameters between normal and clear speech. These differences are analyzed most extensively and are then compared with kinematic parameters from other speech conditions in a more limited analysis.

A. Differences between the clear and normal speech conditions, opening and closing movements and articulator

The top half of Fig. 3 is a plot of mean values of vowel acoustic duration (in seconds) for the seven subjects, comparing the clear condition (unfilled bars) with the normal condition (shaded bars). The error bars show one standard error about the mean. The data for each bar are averaged across all repetitions of the tokens in the condition for the three test words, bob, dod, and gog. For each significant main effect in the ANOVA ($p\leqslant 0.05$), the percentage of variance accounted for by the effect is shown above the pair of bars. The range of mean duration values across subjects and conditions is about 0.11 s to 0.22 s. The figure shows that for subjects 1, 2, 3, 6, and 7, the clear condition vowels were significantly longer than in the normal condition.

The bottom half of Fig. 3 shows mean values of SPL (in dB), plotted in the same way as in the top half of the figure. The range of means across subjects and conditions is about 68 to 77 dB. The figure shows that subject 5 spoke with more volume in the clear condition (in spite of the instruction to avoid speaking louder). Subjects 1 and 3 actually spoke more softly in the clear condition (perhaps because of the instruction to avoid speaking louder).

Mean peak speed values ranged from about 14 to 35 cm/s. The top panel of Fig. 4 shows mean peak speed (in cm/s) for the clear versus normal condition, averaged across movement and articulator and plotted as in Fig. 3. It shows

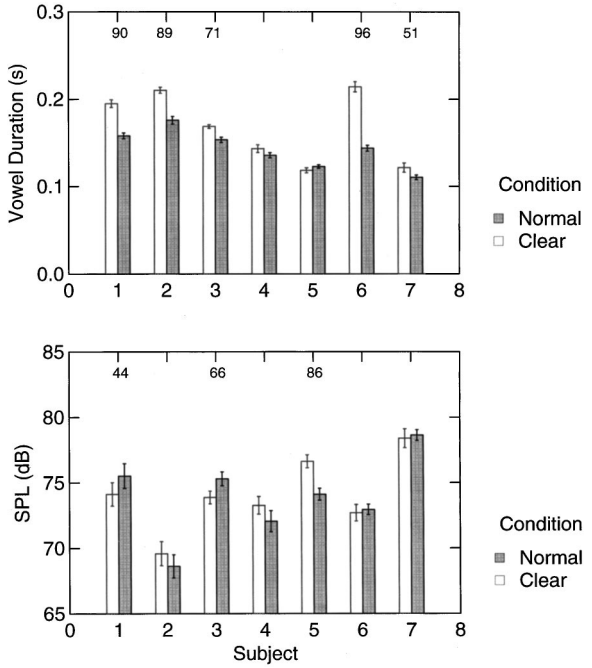

FIG. 3. Top half: Mean values of vowel duration (in seconds) for the seven subjects, comparing the clear condition (unfilled bars) with the normal condition (shaded bars). The error bars show one standard error about the mean. The data for each bar are averaged across movement and articulator. For each significant main effect in the ANOVA ($p \leq 0.05$), the percentage of variance accounted for by the effect is shown above the pair of bars. Bottom half: Mean values of SPL (in dB), plotted in the same way as in the top half.

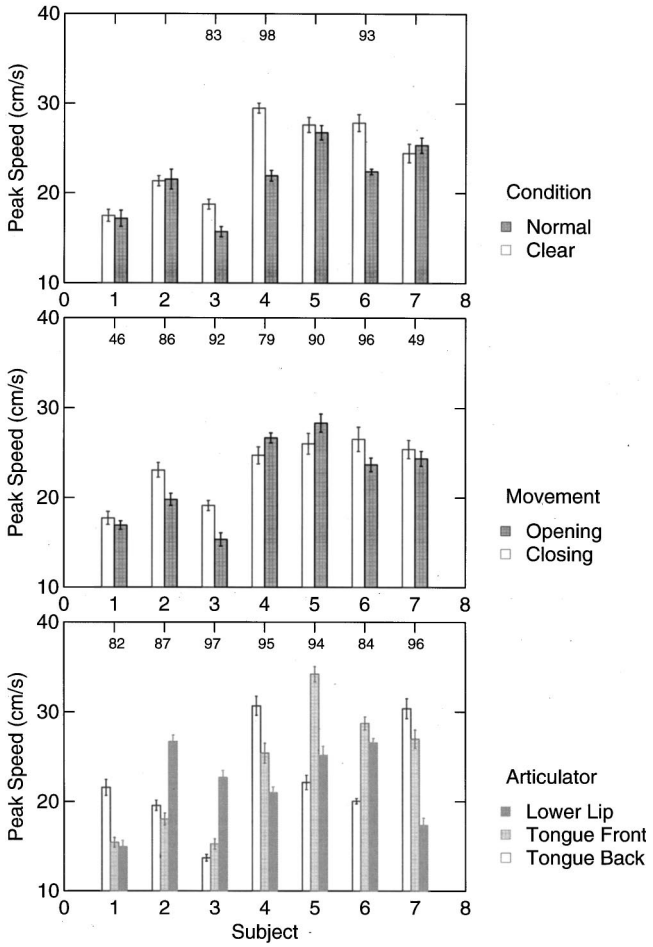

FIG. 4. Top panel: Mean peak speed (in cm/s) for the clear versus normal condition, averaged across movement and articulator and plotted as in Fig. 3. Middle panel: mean peak speed values for opening (shaded bars) versus closing (clear bars) movements, averaged across condition and articulator. Bottom panel: Mean peak speed values for the lower lip (dark bars), tongue front (light bars), and tongue back (clear bars) averaged across condition and movement type.

that subjects 3, 4, and 6 used faster movements in the clear than in the normal condition. The middle panel shows mean peak speed values for opening (shaded bars) vs closing (clear bars) movements, averaged across condition and articulator. It shows that subjects 1, 2, 3, 6, and 7 had faster closing than opening movements and subjects 4 and 5 had faster opening than closing movements. The bottom panel compares mean speed values for the lower lip (dark bars), tongue front (light bars), and tongue back (clear bars) averaged across condition and movement type. It shows that tongue back movements were fastest for subjects 1, 4, and 7; tongue front movements were fastest for subjects 5 and 6 and lip movements were fastest for subjects 2 and 3.

Figure 5 shows mean values of movement duration (s), plotted in the same way as in Fig. 3. Movement duration means ranged from about 0.07 s to 0.17 s. The top panel shows that subjects 2, 3, 4, 6, and 7 produced the clear condition with longer duration movements than the normal condition and subject 5 produced the clear condition with slightly shorter movements than the normal condition. The middle panel shows that opening movements were longer than closing movements for all the subjects, and the bottom panel shows intersubject differences in the ordering of movement duration by articulator.

Figure 6 shows mean values of movement distance (cm), plotted as in Fig. 4. Mean values of distance ranged from about 1 to 2 cm. The top panel shows that subjects 3, 4, and 6 produced the clear condition with larger movements than the normal condition. The middle panel shows that all subjects used larger opening than closing movements, and the bottom panel shows subject-specific differences in the ordering of distance by articulator. Although each C_1VC_2 is symmetric, the movement paths for C_1V and VC_2 are different and do not overlap [e.g., Fig. 2(C)]. This is presumably due to the anatomical arrangement of the different muscle groups that are used for opening and closing movements, as well as some muscle interaction (co-contraction). For example, during the production of the CVC, ''gog,'' the anterior genioglossus and hyoglossus muscles depress the tongue body for the opening movement and the styloglossus, posterior genioglossus and mylohyoid muscles raise the tongue body for the closing movement toward the hard palate (Maeda and Honda, 1994). Based on the anatomy and modeling work (Perkell, 1996), the directions of the resultant force vectors for the tongue lowering and tongue raising muscle groups cannot be equal and opposite to one another over the courses of the lowering and raising movements. Velar consonants, as illustrated in Fig. 2(C), are almost always produced with some sliding contact in which the tongue body moves in the anterior direction (Mooshammer *et al.*, 1995). A comparison of the bottom panels in Figs. 4 (peak speed) and 6 shows that the ordering of peak speed by articulator parallels that of

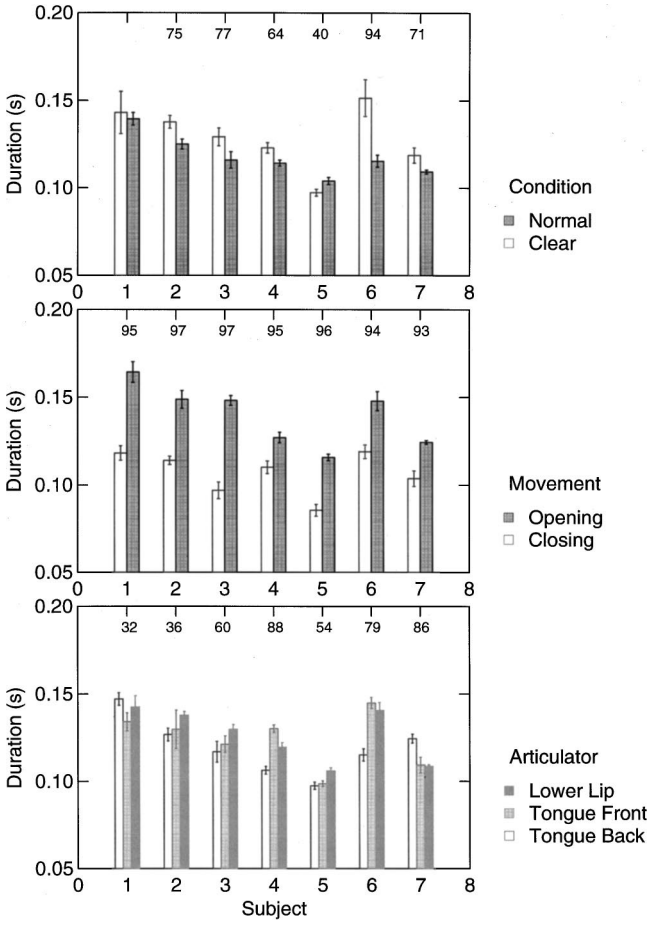

FIG. 5. Top panel: Mean values of movement duration (s), plotted as in Fig. 4. Middle panel: Mean durations for opening (shaded bars) versus closing (clear bars) movements, averaged across condition and articulator. Bottom panel: Mean durations for the lower lip (dark bars), tongue front (light bars), and tongue back (clear bars) averaged across condition and movement type.

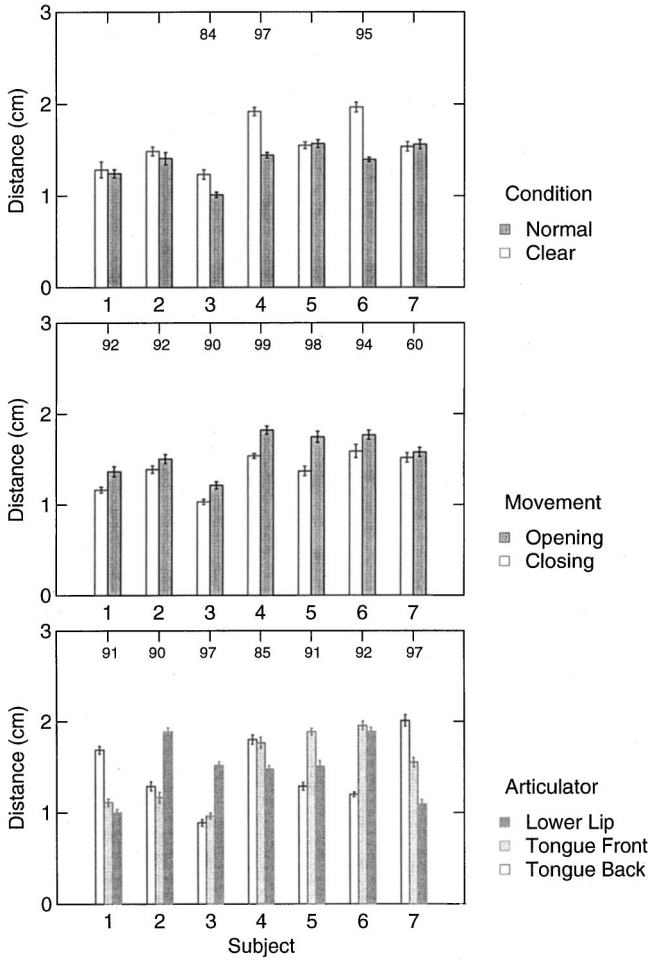

FIG. 6. Top panel: Mean values of movement distance (cm), plotted as in Fig. 4. Middle panel: Mean distances for opening (shaded bars) versus closing (clear bars) movements, averaged across condition and articulator. Bottom panel: Mean distances for the lower lip (dark bars), tongue front (light bars), and tongue back (clear bars) averaged across condition and movement type.

movement distance for the different subjects, reflecting the commonly found linear relationship between velocity and distance.

Figure 7 shows mean values of peak speed/distance (s^{-1}), a relative indicator of muscle stiffness, plotted as in Fig. 4. The top panel indicates that subjects 2, 6, and 7 used less muscle stiffness in the clear than the normal condition although the effect was strong only for subject 6. The middle panel shows that muscle stiffness was greater for closing than opening movements for all the subjects, and bottom panel shows intersubject differences in the ordering of stiffness by articulator.

Table I summarizes the observations made from Figs. 3–7 about the differences between the clear and normal conditions. It shows the percent of variance accounted for by significant main effects in the ANOVAs, in which the clear condition had greater mean parameter values than the normal condition. The rows correspond to: peak speed, movement duration, movement distance, peak speed/distance, vowel duration and SPL. The columns correspond to subjects. Percentage values of 80 or higher are shown in boldface. For cases in which the mean parameter value was greater in the normal than in the clear condition, the percent value is enclosed in braces; all but one of these main effects were relatively weak. The table shows that for the clear condition, Subjects 3, 4, and 6 increased peak speed, movement duration and movement distance (also see Adams, 1990). It is likely that the co-occurrence of changes in these three parameters reflects the commonly found relations among pairs of these parameters (see Background). Subject 6 had the largest number of significant parameter changes, including the only strongly significant change in peak speed/distance, a decrease in the clear condition. Subjects 1, 2, and 7 mainly employed longer vowel duration for the clear condition and subjects 2 and 7 also lowered peak speed/distance slightly. Subject 5 increased SPL. Thus, there were substantial differences among the speakers in the way they produced the test utterances in the clear condition compared to the normal condition.

B. Examination of data from additional conditions in a peak speed, distance, duration performance space

In order to gain further insight into whether the above observations reflect increased effort in the clear condition for subjects 3, 4, and 6, and to compare the normal and clear

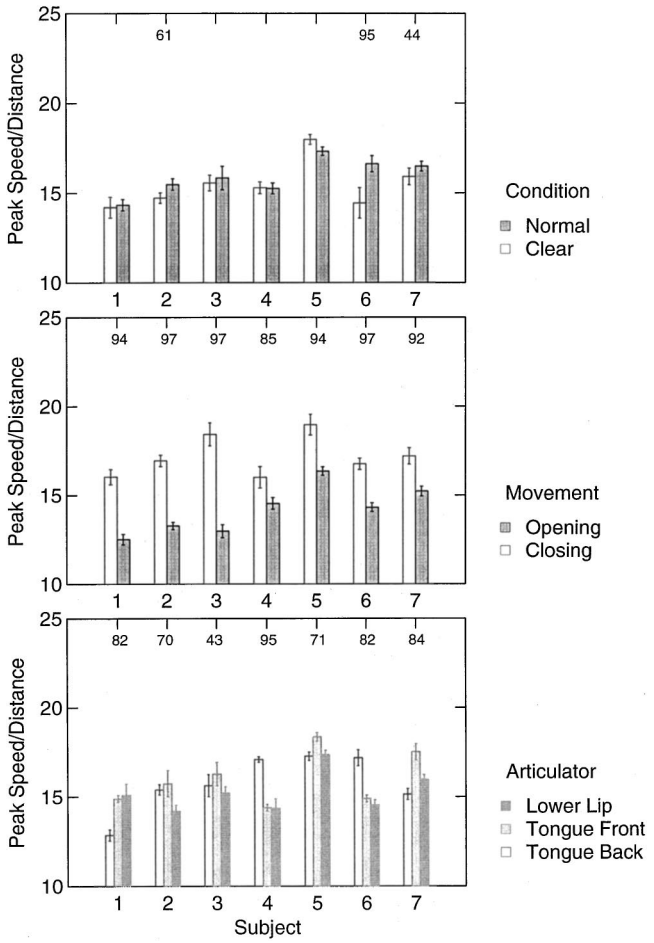

FIG. 7. Top panel: Mean values of peak speed/distance, plotted as in Fig. 4. Middle panel: Mean values of peak speed/distance for opening (shaded bars) versus closing (clear bars) movements, averaged across condition and articulator. Bottom panel: Mean values of peak speed/distance for the lower lip (dark bars), tongue front (light bars), and tongue back (clear bars) averaged across condition and movement type.

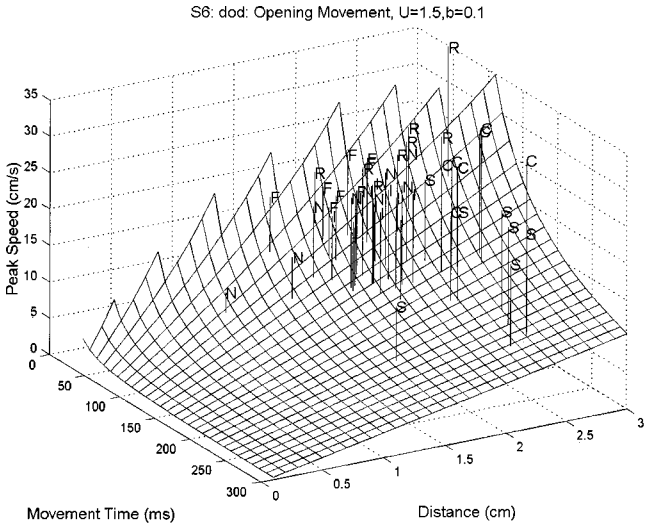

FIG. 8. Values of peak speed, distance and duration for tongue blade opening movements for subject 6. Each symbol represents a single movement; different symbols identify data from the speech conditions: *N* for normal, *C* for clear, *S* for slow, *F* for fast, *R* for rapid+clear, and *I* for informal. The concave surface represents a minimum ''effort'' (peak speed) bound for a one-dimensional, frictionless dynamical model with an acceleration limit of 1.5 g.

conditions with the other speech conditions, the data are examined in a peak speed, distance, duration ''performance space.''

Figure 8 plots peak speed, distance and duration for tongue blade opening movements for subject 6. Each symbol in the plot represents a single movement; different symbols identify data from the speech conditions: *N* for normal, *C* for clear, *S* for slow, *F* for fast, *R* for rapid+clear, and *I* for informal. (Each data value lies at the lower left corner of the symbol.) The concave surface represents a limiting bound for movements of the one-dimensional, frictionless dynamical system with an acceleration limit of 1.5 g;[4] optimized to minimize the impulse cost (Nelson, 1983). Parameter values that define the surface are calculated according to the equation that describes minimum-impulse movements:

$$V_m = (TU/2) - \sqrt{(TU/2)^2 - DU},$$

where T and D are the movement duration and distance respectively, and U is the maximum acceleration limit [Eq. (10), p. 138; Nelson, 1983]. As U increases, the height of the surface decreases. A value of 1.5 g for U is adequate to include speech movements with the highest acceleration values measured in the current study (see also Nelson *et al.*, 1984). All actual data points must lie above the bounding surface because they cannot be frictionless and generally are not of the minimum-impulse form.

For slow-condition movements, there is little change of distance with a change in duration (time); however, for faster movements in the other conditions, the data are distributed in a roughly linear fashion above a ''knee'' in the bounding surface, beyond which the effort gradient begins to increase sharply. According to Nelson (1983, p. 142), if ''movements can be characterized as having an economy of effort as well as time, they should be located above the knee region of this surface, where a reasonable trade-off between effort and time is possible.''

TABLE I. Percent of variance accounted for by significant effects in ANOVAs ($p \leq 0.05$).

Effect (boldface: %≥80)		Subject						
Clear>Normal {opposite}		**1**	**2**	**3**	**4**	**5**	**6**	**7**
Peak speed	(Fig. 4)			**83**	**98**		**93**	
Movement duration	(Fig. 5)		75	77	64	{40}	**94**	71
Movement distance	(Fig. 6)			**84**	**97**		**95**	
Peak speed/distance	(Fig. 7)		{61}				**{95}**	{44}
Vowel duration	(Fig. 3)	**90**	**89**	71			**96**	51
SPL	(Fig. 3)	{44}		{66}		**86**		

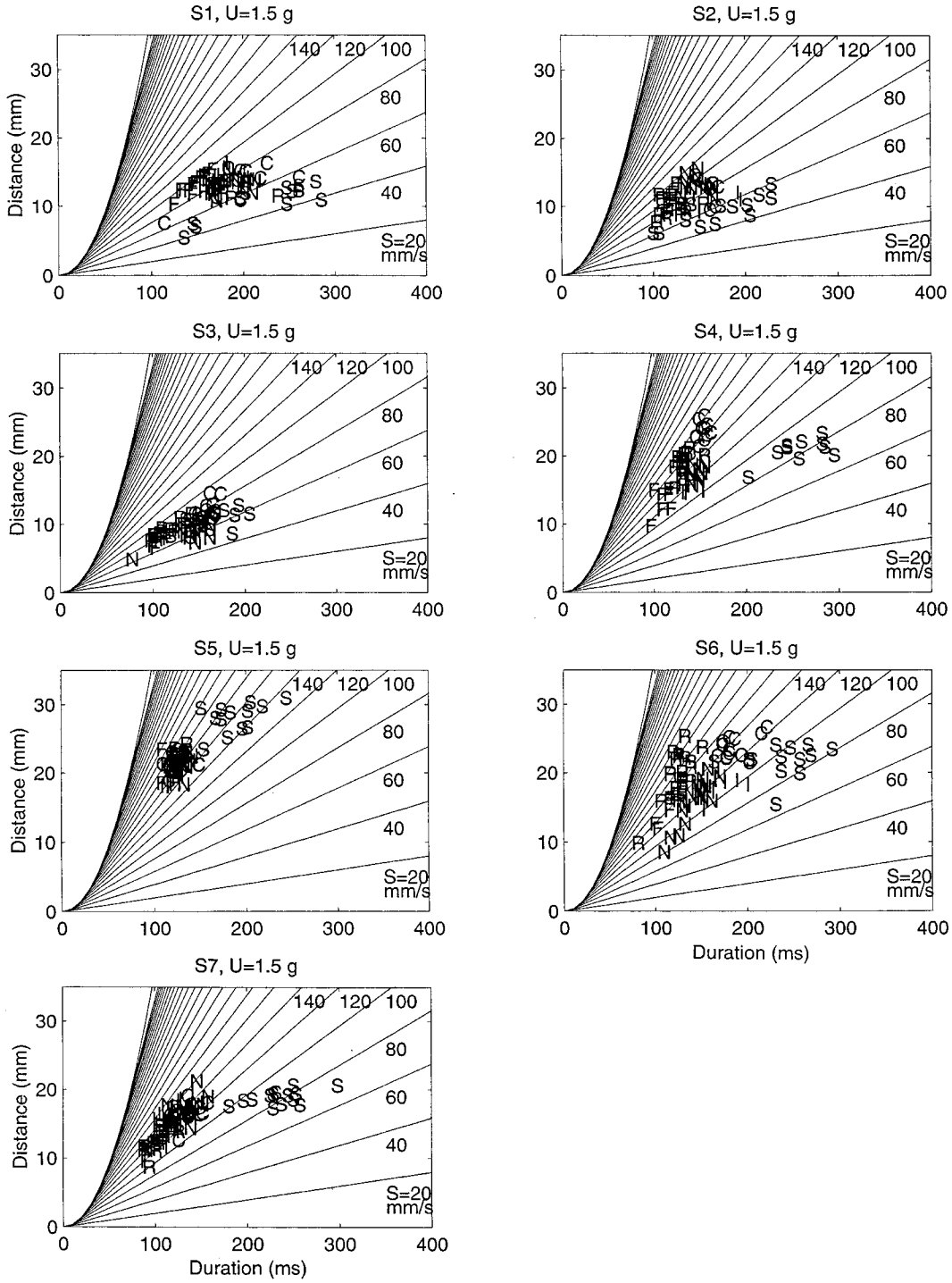

FIG. 9. Distance versus duration plots of tongue-front (blade) opening movements for the seven subjects in ''top-down'' views of the 3D performance space shown in Fig. 8. In each plot the solid curve on the left represents a theoretical minimum-time (maximum acceleration) limit of 1.5 g. The straight lines radiating from the minimum time limit show ''iso-effort'' (iso-peak speed) contours that represent the height of the bounding surface in Fig. 8.

Figure 9 shows distance vs duration plots of tongue-front (blade) opening movements for the seven subjects. These are ''top-down'' views of the 3D minimum-impulse-cost performance space that is exemplified in Fig. 8. In each plot the solid curve on the left represents a theoretical minimum-time (maximum acceleration) limit of 1.5 g. It corresponds to a top-down view of the left edge of the 3D surface where the surface becomes virtually vertical. The minimum-time solution is defined by

$$T_{\min} = 2\sqrt{D/U}.$$

The straight lines radiating from the minimum time limit show ''iso-effort'' (iso-peak speed) contours that represent the intersection of the bounding surface shown in Fig. 8 with a horizontal plane at different heights (values of peak speed). Corresponding to the increasing height of the surface in Fig. 8, these iso-effort contours show a gradient that increases sharply as the minimum-time bound is approached, reflecting

increasingly larger levels of effort. Actual movement points have to lie to the right of the bound. In general, the slow condition data (*S*) lie in separate groups to the right of the other data, indicating the longest durations. Compared to the other data, the slow condition data also appear to show less variation in distance with variation in duration. Post-hoc planned contrasts showed significant differences between the slow condition data and all of the other conditions grouped together for almost every parameter and subject. In addition, the slow movements had approximately twice as many acceleration peaks as the other movements, i.e., they were less smooth than the other movements (also see Weineke *et al.*, 1987).

Movements in the other conditions have shorter durations; their data tend to be distributed along a bounding iso-peak-speed (effort) contour, the level of which differs among the subjects. Along the contour, movement duration tends to vary linearly with movement distance. The level of the limiting peak speed contour shown in Fig. 9 ranges from a low of 60–80 mm/s for subjects 3, 1, and 2 to a high of about 180 mm/s for subjects 5 and 4, with subjects 6 and 7 falling in between. There is a great deal of overlap among the data from the different conditions, except for slow.

Such plots were similar in form for the other articulators and for closing movements (not shown), although the data values differed somewhat (as demonstrated above in Sec. IV A).

Figure 10 shows the same kind of plots for tongue front opening movements as in Fig. 9, but the data for each condition are represented by a single symbol at the centroid of the distribution for the condition. A convex hull shows the outer limits of all of the underlying individual data points. The overall amount of variation in the data differs among the subjects; subject 6's data have about twice the range of distance and duration as subject 3's data. For subjects 3, 4, and 6, the centroid of the clear condition data (*C*) lies at a somewhat higher iso-effort level than the normal condition data (*N*). This result is consistent with the observations in Sec. IV A of higher values of peak speed, duration, distance and parameter *c* for these subjects. For all except subject 3, the centroid of the slow condition data lies at a lower iso-effort level than the other data. For all except subject 5, the centroids for the fast (*F*) and/or rapid+clear (*R*) data lie furthest to the lower left of the plots; however there are only two examples in which iso-effort levels are obviously higher for the *F* or *R* centroids than for the other conditions (*F* for subject 1, *R* for subject 6). Consistent with the observations made in Sec. IV A, subject 5's movement data do not differ among conditions aside from the slow condition.

Table II summarizes observations from plots like Fig. 10 for all three articulators and opening and closing movements. A + sign indicates that the clear condition centroid was at least one iso-effort level (20 mm/s) higher than the normal condition centroid. A + in parentheses indicates that the clear condition was about one-half an iso-effort level (10 mm/s) higher than the normal condition centroid. The table shows that the observations made from Fig. 10 for tongue front opening movements are largely representative of the data for the other articulators and closing movements, with subject 4 showing the most consistent effects across movement type and articulator.

C. Movement characteristics that differ from assumptions of the model

As observed above for subjects 3, 4, and 6, the pattern of differences for the acoustic and kinematic measures is generally consistent with the hypothesis that movements in the clear condition (with respect to the normal condition) are characterized by higher peak speed, indicating greater effort. The movements for these subjects also have longer movement durations and greater movement distances. However, since the measures are made from 2D movements of points on very complicated 3D structures that are interacting mechanically with one another, it is necessary to be cautious about the use of a measure of effort that is based on a relatively simple model. As is shown below, further analyses of the movements indicate that a number of them fail to meet criteria that are assumed by the model. Specifically (a) many movements are not smooth (with simple acceleration and deceleration phases), (b) their velocity profiles are not symmetrical (with equal amounts of time spent in acceleration and deceleration), and (c) as discussed above, their paths are not straight. These factors are examined in the following analyses, with the exclusion of data from the ''informal'' condition (which was not produced by one subject) or the ''slow'' condition (in which movements had about twice as many acceleration peaks as in any of the other conditions).

To indicate movement smoothness, Fig. 11 shows the distribution of the number of peaks in the acceleration magnitude signal (representing both acceleration and deceleration phases of the movements). Data from all seven subjects for opening and closing movements are grouped together. Smoother movements have lower numbers of acceleration peaks. About 60% of the movements have two acceleration magnitude peaks, which is expected for smooth movements with single acceleration and deceleration phases and is assumed by the model. About 12% of the movements have only one acceleration magnitude peak. These occurred primarily in the fast and rapid+clear conditions, most likely because the acceleration peak responsible for the acceleration phase occurred just before the algorithmically identified movement beginning. The remaining 28% of the movements had more than two acceleration magnitude peaks, which were related to small inflections in the movement and velocity signals. Similar plots were examined by subject, condition, and movement type. The distribution shapes differed only slightly among the subjects; the clear condition had a somewhat larger proportion of movements with more than two acceleration magnitude peaks than the normal, fast or rapid+clear conditions; and opening movements showed a somewhat larger proportion of movements with more than two peaks than closing movements. In sum, a significant number of movements (even excluding slow movements) were not entirely smooth, contrary to one of the assumptions of the undamped linear spring model.

To examine the symmetry of the movement speed profiles, Fig. 12 shows the distribution of values of a measure of symmetry of the speed trace, the amount of time spent in

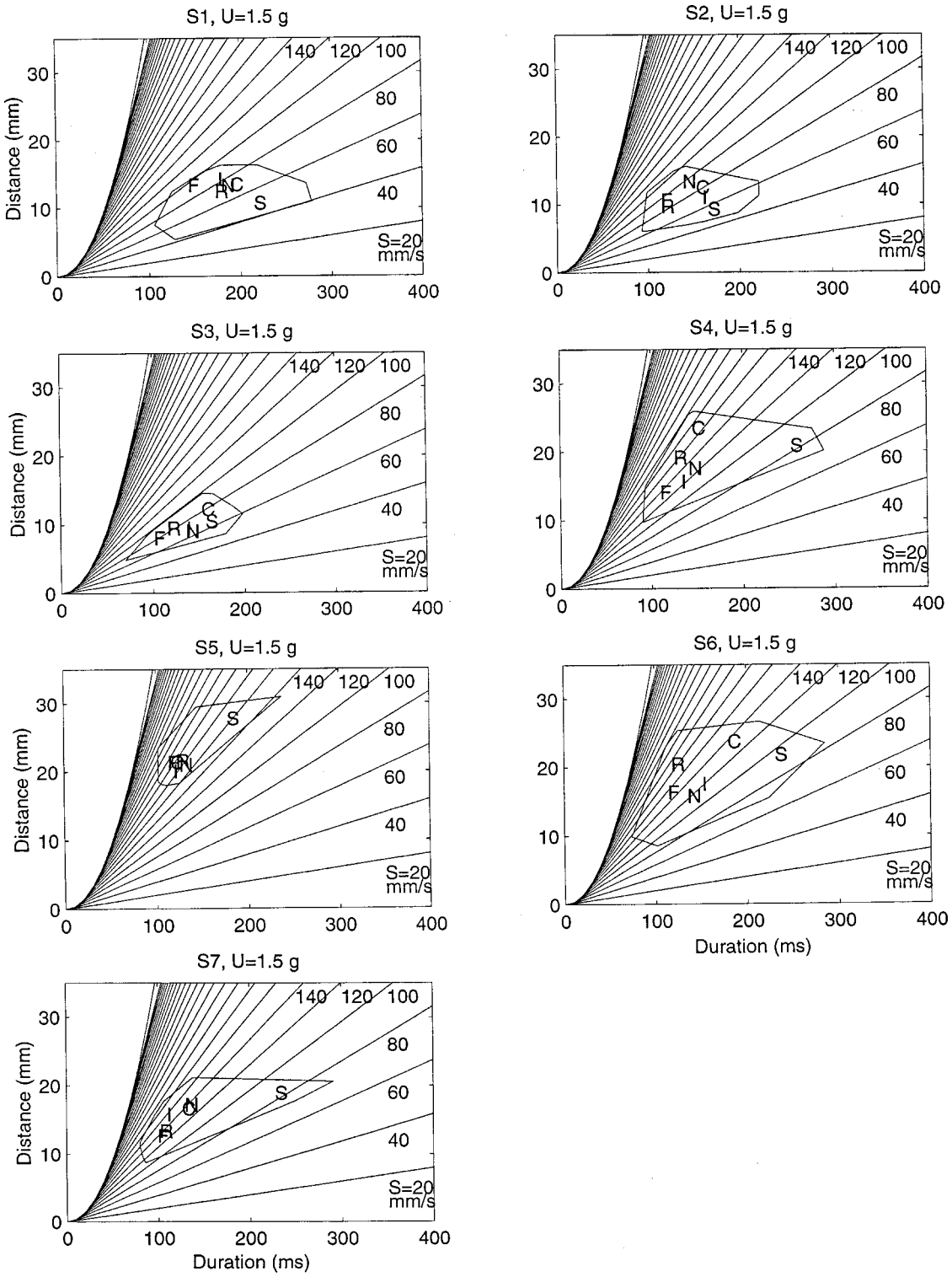

FIG. 10. Distance versus duration plots of tongue-front (blade) opening movements for the seven subjects, as in Fig. 9, with the data for each condition represented by a single symbol at the centroid of the distribution for the condition. A convex hull shows the outer limits of all of the underlying individual data points.

acceleration as a percentage of the movement duration, for both opening and closing movements. The distribution is quite broad, with substantial numbers of movements occurring in bins that span the range from 38% to 70%. Although movements in the fast condition were more symmetrical than in other conditions, this result indicates that most of the speed profiles were far from symmetrical.

The occurrence of an inter-movement interval preceding a vowel opening movement indicates that the identified beginning of the opening movement corresponded to the breaking of articulatory contact, rather than the actual onset of the underlying opening gesture. Among the 840 opening movements in the normal, clear, fast and rapid+clear conditions, 171 were preceded by intermovement intervals. In other

TABLE II. Cases in which iso-effort for clear is greater than for normal.

Articulator	Movement	Subject 1	2	3	4	5	6	7
Tongue	closing	+	(+)	(+)	(+)		(+)	
Back	opening		(+)		+			
Tongue	closing			+	+		+	
Front	opening			(+)	+		+	
Lower lip	closing			+	+			
	opening				+	(+)	+	

words, for 20% of the tokens (excluding slow), the measured characteristics of the opening movement must have been influenced by articulatory contact during the preceding consonant. It is very likely that the actual beginning of the opening movement occurs during the closure and is obscured by it. Consistent with these observations, Löfqvist and Gracco (1997) speculate that the spatial target for movements involving articulatory contact is at a virtual location beyond the place of contact. (Also see Westbury and Hashi, 1997.)

Movement curvature was quantified with the ''curvature ratio,'' the ratio of the integrated distance along the movement path to the straight-line distance between the two movement end points. While most of the movements followed relatively straight paths, with curvature ratios less than 1.1, 17% of the movements (281 of 1680) had ratios greater than 1.1, ranging up to about 1.4.

Consistent with the preceding observations, across the normal and clear data sets for all seven subjects, mean values of parameter *c* ranged from about 1.6 to 2.2. The occurrence of values approaching and exceeding 2.0 is a further indication that at least some of the movements do not meet the model's assumptions. Other studies have also reported values of *c* that exceed 2.0 (cf. Adams *et al.*, 1993; Shaiman *et al.*, 1997), possibly for the same reasons.

These results indicate that a significant proportion of the movements do not strictly meet the criteria required for making inferences about underlying control and articulatory effort from a kinematic analysis based on the linear, frictionless mass-spring model.

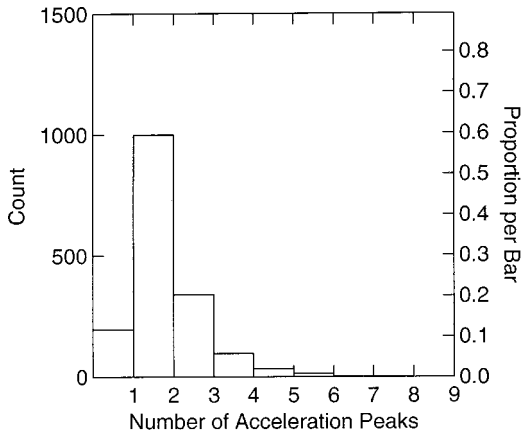

FIG. 11. The distribution of the number of peaks in the acceleration magnitude signal for the movements including all the speech conditions except ''informal'' and ''slow.''

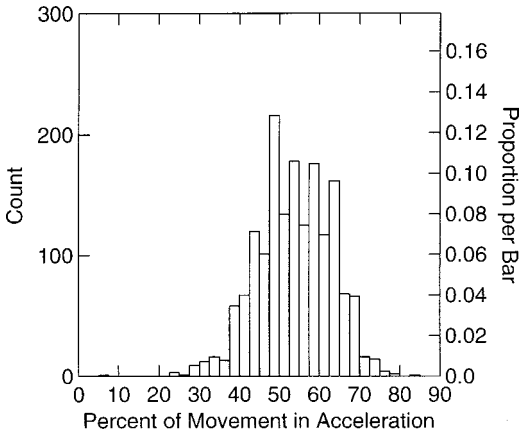

FIG. 12. The distribution of values of a measure of symmetry of the speed trace, the amount of time spent in acceleration as a percentage of the movement duration. Opening and closing movements from all subjects in all conditions but ''informal'' and ''slow'' are included.

V. SUMMARY AND CONCLUSIONS

Three of the seven speakers (subjects 3, 4, and 6) responded in an expected way to the instructions. In the clear condition they used higher peak speeds, longer movement durations and greater distances. The performance space analysis indicated that these three subjects used increased effort (peak speed) in the clear condition. The data from these three *S*'s therefore, support the hypothesis that clear speech is produced with greater effort than normal speech. On the other hand, subjects 1, 2, and 7 mainly used vowel duration increases for the clear condition, and subject 5 mainly used an SPL increase. Changes in peak speed/distance (an indirect index of relative stiffness of underlying muscle contraction) were less consistent and the three significant ones were in the negative direction.

A consistent outcome was that slow-condition movements are very different from those elicited in the other conditions. According to the performance space analysis, they are produced with less effort because their longer durations are not accompanied by proportionally larger distances. They are also less smooth than movements in the other conditions. These results are consistent with others (cf. Adams, 1990) and indicate that such slow movements may be un-natural for normal speakers (Weineke *et al.*, 1987). The lack of smoothness of slow movements may reflect some physiological lower limit, although such an idea would require further investigation.

It has been speculated that articulator size would influence articulatory kinematics (see review in Perkell, 1997). For example, it might be expected that movements of the tongue body would be slower than those of the much smaller tongue blade. Contrary to this speculation, there was intersubject variation in which articulator showed the highest values of peak speed, movement duration, distance, peak speed/distance and parameter *c*. It is possible that these subject by parameter interactions for articulator are conditioned primarily by subject differences in distances moved by the tongue body, tongue blade and lips. Such differences may be due to habit, as appears to be the case for readily observed cross-speaker differences in the range of vertical mandible move-

ments during speech. They may also be due to anatomy. For example, the amount of vertical tongue displacement differentiating nonlow vowels from one another can depend on the ratio of palatal height to width (Perkell, 1979). As mentioned in the introduction, Kuehn and Moll (1976) found positive relationships across subjects between both articulatory velocity and movement displacement and the size of the articulators. In the current study, the observed similar patterning of peak speed and movement distance across subject and articulator would follow from an approximately linear relation between speed and distance.

The finding that consonant-closing movements uniformly have shorter durations and higher values of peak speed/distance than vowel opening movements is consistent with the result of Hertrich and Ackermann (1997) and their suggestion that the closing movements may be more ballistic in nature. However, there are intersubject differences in whether peak speed is higher for opening or for closing movements. These findings need to be explored further in future studies.

Further generalizations from the data are hampered by intersubject differences and the fact that movement characteristics were somewhat different from those assumed by the underlying model. As mentioned above, the lip and especially the tongue movement data come from single points on the surfaces of anatomically complicated structures that are composed mostly of muscle and are interacting mechanically with other structures. The model was used originally to analyze movements of the jaw (Nelson, 1983), which is a solid, relatively massive articulator and is therefore the articulator that is most subject to dynamic constraints and effort costs. It also has a relatively clear principal axis of motion. The following companion paper (Perkell and Zandipour, 2002) represents an initial step in examining the influence of the mandible on the kinematics of the other articulators. Another complicating factor is the occurrence of inter-movement intervals, some of which are due to articulatory contact. We suggest that the complexity of articulatory structures and their physical interactions, as exemplified by contact, make it difficult to precisely quantify some important movement characteristics with current techniques and analyses.

Several additional factors could underlie the individual differences in the results. There could be differences in the way the subjects interpreted the instructions and they could differ in the way they produce and/or perceive the acoustic correlates of clear speech. An important issue, to be addressed in future work, is the manner and extent to which each subject produced acoustic correlates of clarity. The subjects could also differ in their motor performance limits. The following companion study explores this idea, but the results do not resolve the issue.

It appears that more adequate tests of control strategies for different speaking styles will depend upon further developments in the physiological–biomechanical modeling of more complicated movements with more realistic boundary conditions. Physiological–biomechanical simulations could help to quantify the effects of articulatory contact and relative amounts of energy flow in the musculature. Such work should lead to more accurate measures of physical articulatory effort, which would make it possible to determine the limitations of using simple dynamical models. When more accurate effort measures are made, it may be found that physical cost is too simple a concept to account for changes in speaking style, and it may be necessary consider ideas such as motor programming complexity and psychological factors as well. Future work should also include thorough investigations of the sources of individual differences and studies of the clarity-related acoustic characteristics of the utterances and their intelligibility in the different speaking conditions. Ultimately, as suggested by Hertrich and Ackermann (1997), it may be found that the most invariant aspects of different speaking styles are in their acoustic or perceptual results.

ACKNOWLEDGMENTS

This work was supported by research Grant No. 5 R01 DC01925 from the National Institute on Deafness and Other Communication Disorders, National Institutes of Health. We are very grateful to Winston Nelson for his valuable comments, to Hermann Ackermann, Ingo Hertrich, Anders Löfqvist, David Ostry, and Gary Weismer for their helpful reviews, and to Gareth Coote, Brandy Karl, and especially Erik Strand and Jennell Vick for their help with data extraction.

[1]This measure of actuator ''stiffness'' corresponds to the square root of the stiffness factor, k, in Nelson, 1983 [Eqs. (12) and (13), p. 139 and Appendix E]. It also relates to the natural frequency of simple harmonic motion, $\omega_n = 2\pi/\tau$, where τ is the duration of a complete cycle, $\tau = 2\,\mathrm{T}$.

[2]Although the data are examined for the effects of articulator and movement type, these effects are not the primary focus of this study. They will be dealt with in more depth in subsequent analyses of additional materials from the corpus.

[3]The experiment originally included an eighth subject. His movement speeds were higher than for any of the other subjects; however, his displacement and velocity profiles were very irregular, varying so much from one token to the next that they could not be analyzed with the algorithm.

[4]$1\ \mathrm{g} = 9.806\ \mathrm{m/s^2}$, the acceleration due to gravity.

Adams, S. G. (**1990**). ''Rate and clarity of speech: An x-ray microbeam study,'' Ph.D. thesis, University of Wisconsin, Madison.

Adams, S. G., Weismer, G., and Kent, R. D. (**1993**). ''Speaking rate and speech movement velocity profiles,'' J. Speech Hear. Res. **36**, 41–54.

Edwards, J., Beckman, M. E., and Fletcher, J. (**1991**). ''The articulatory phonetics of final lengthening,'' J. Acoust. Soc. Am. **89**, 369–382.

Flanagan, J. R., Ostry, D. J., and Feldman, A. G. (**1990**). ''Control of human jaw and multi-joint arm movements,'' in *Cerebral Control of Speech and Limb Movements*, edited by G. E. Hammond (North-Holland, Elsevier Science Publishers, Amsterdam), pp. 29–57.

Guenther, F. H. (**1995**). ''Speech sound acquisition, coarticulation, and rate effects in a neural network model of speech production,'' Psychol. Rev. **102**, 594–621.

Guenther, F. H., Hampson, M., and Johnson, D. (**1998**). ''A theoretical investigation of reference frames for the planning of speech movements,'' Psychol. Rev. **105**, 611–633.

Hertrich, I., and Ackermann, H. (**1997**). ''Articulatory control of phonological vowel length contrasts: Kinematic analysis of labial gestures,'' J. Acoust. Soc. Am. **102**, 523–536.

Kuehn, D. P., and Moll, K. L. (**1976**). ''A cineradiographic study of vc and cv articulatory velocities,'' J. Phonetics **4**, 303–320.

Lindblom, B. (**1990**). ''Explaining phonetic variation: A sketch of the H & H theory,'' in *Speech Production and Speech Modeling*, edited by W. J. Hardcastle and A. Marchal (Kluwer, Dordrecht), pp. 403–440.

Linville, R. N. (**1982**). ''Temporal aspects of articulation: Some implications for speech motor control of stereotyped productions,'' Ph.D. thesis, University of Iowa, Department of Speech Pathology and Audiology.
Löfqvist, A., and Gracco, V. (**1997**). ''Lip and jaw kinematics in bilabial stop consonant production,'' J. Speech Lang. Hear. Res. **40**, 877–893.
Maeda, S., and Honda, K. (**1994**). ''From EMG to formant patterns of vowels: The implication of vowel spaces,'' Phonetica **51**, 17–29.
Moon, S.-J. (**1991**). ''An acoustic and perceptual study of undershoot in clear and citation-form speech,'' PERILUS XIV, University of Stockholm, Institute of Linguistics, pp. 153–156.
Moon, S.-J., and Lindblom, B. (**1994**). ''Interaction between duration, context, and speaking style in English stressed vowels,'' J. Acoust. Soc. Am. **96**, 40–55.
Mooshammer, C., Hoole, P., and Kühnert, B. (**1995**). ''On loops,'' J. Phonetics **23**, 3–21.
Munhall, K. G., Ostry, D., and Parush, A. (**1985**). ''Characteristics of velocity profiles of speech movements,'' J. Exp. Psychol. **11**, 457–474.
Nelson, W. L. (**1983**). ''Physical principles for economies of skilled movements,'' Biol. Cybern. **46**, 135–147.
Nelson, W. L., Perkell, J. S., and Westbury, J. R. (**1984**). ''Mandible movements during increasingly rapid articulations of single syllables: Preliminary observations.'' J. Acoust. Soc. Am. **75**, 945–951.
Ostry, D., Keller, E., and Parush, A. (**1983**). ''Similarities in the control of speech articulators and the limbs: Kinematics of tongue dorsum movement is speech,'' J. Exp. Psychol. **9**, 141–147.
Ostry, D., and Munhall, K. G. (**1985**). ''Control rate and duration of speech movements,'' J. Acoust. Soc. Am. **77**, 640–648.
Ostry, D. J., Cooke, J. D., and Munhall, K. G. (**1987**). ''Velocity curves of human arm and speech movements,'' Exp. Brain Res. **68**, 37–46.
Perkell, J. S. (**1979**). ''On the nature of distinctive features: Implications of a preliminary vowel production study,'' in *Frontiers of Speech Communication Research*, edited by B. Lindblom and S. Ohman (Academic, London), pp. 365–480.
Perkell, J. S. (**1996**). ''Properties of the tongue help to define vowel categories: hypotheses based on physiologically oriented modeling,'' J. Phonetics **24**, 3–22.
Perkell, J. S. (**1997**). ''Articulatory processes,'' in *The Handbook of Phonetic Sciences*, edited by W. Hardcastle and J. Laver (Blackwell, Oxford), pp. 333–370.
Perkell, J. S., Cohen, M. H., Svirsky, M., Matthies, M., Garabieta, I., and Jackson, M. (**1992**). ''Electro-magnetic midsagittal articulometer (EMMA) systems for transducing speech articulatory movements,'' J. Acoust. Soc. Am. **92**, 3078–3096.
Perkell, J. S., Guenther, F. H., Lane, H., Matthies, M. L., Perrier, P., Vick, J., Wilhelms-Tricarico, R., and Zandipour, M. (**2000**). ''A theory of speech motor control and supporting data from speakers with normal hearing and with profound hearing loss,'' J. Phonetics **28**, 233–372.
Perkell, J. S., and Zandipour, M. (**2002**). ''Economy of effort in different speaking conditions. II. Kinematic performance spaces for cyclical and speech movements,'' J. Acoust. Soc. Am. **112**, 1642–1651.
Picheny, M. A., Durlach, N. I., and Braida, L. D. (**1986**). ''Speaking clearly for the hard of hearing II: Acoustic characteristics of clear and conversational speech,'' Speech Hear. Res. **29**, 434–446.
Shaiman, S., Adams, S. G., and Kimelman, M. D. Z. (**1997**). ''Velocity profiles of lip protrusion across changes in speaking rate,'' J. Speech Lang. Hear. Res. **40**, 144–158.
Sonoda, Y., and Nakakido, K. (**1986**). ''Effect of Speaking Rate on Jaw Movements in Vowel Sequence,'' J. Acoust. Soc. Jpn. (E) **7**, 5–12.
Vatikiotis-Bateson, E., and Fletcher, J. (**1992**). ''Articulatory correlates of linguistically contrastive events: Where are they?'' in *Speech Perception, Production and Linguistic Structure*, edited by Y. Tohkura, E. Vatikiotis-Bateson, and Y. Sagisaka (IOS, Amsterdam), pp. 341–358.
Weineke, G., Janssen, P., and Belderbos, H. (**1987**). ''The influence of speaking rate on the duration of jaw movements,'' J. Phonetics **15**, 111–126.
Westbury, J., and Hashi, M. (**1997**). ''Lip-pellet positions during vowels and labial consonants,'' J. Phonetics **25**, 405–419.
Young, M. A. (**1993**). ''Supplementing tests of statistical significance: Variation accounted for,'' J. Speech Lang. Hear. Res. **36**, 644–656.

Economy of effort in different speaking conditions. II. Kinematic performance spaces for cyclical and speech movements

Joseph S. Perkell[a] and Majid Zandipour
Speech Communication Group, Research Laboratory of Electronics, Massachusetts Institute of Technology, Cambridge, Massachusetts 02139

(Received 6 March 1998; revised 8 June 2002; accepted 16 July 2002)

This study was designed to test the hypothesis that the kinematic manipulations used by speakers in different speaking conditions are influenced by kinematic performance limits. A range of kinematic parameter values was elicited by having seven subjects produce cyclical CV movements of lips, tongue blade and tongue dorsum (/bɑ/, /dɑ/, /gɑ/), at rates ranging from 1 to 6 Hz. The resulting measures were used to establish speaker- and articulator-specific kinematic performance spaces, defined by movement duration, displacement and peak speed. These data were compared with speech movement data produced by the subjects in several different speaking conditions in the companion study (Perkell *et al.*, 2002). The amount of overlap of the speech data and cyclical data varied across speakers, from almost no overlap to complete overlap. Generally, for a given movement duration, speech movements were larger than cyclical movements, indicating that the speech movements were faster and were produced with greater effort, according to the performance space analysis. It was hypothesized that the cyclical movements of the tongue and lips were slower than the speech movements because they were more constrained by (coupled to) the relatively massive mandible. To test this hypothesis, a comparison was made of cyclical movements in maxillary versus mandibular frames of reference. The results indicate that the cyclical movements were not strongly constrained by mandible movements. The overall results generally indicate that the cyclical task did not succeed in defining the upper limits of kinematic performance spaces within which the speech data were confined. Thus, the hypothesis that performance limits influence speech kinematics could not be tested effectively. The differences between the speech and cyclical movements may be due to other factors, such as differences in speakers' ''skill'' with the two types of movement, or the size of the movements—the speech movements were larger, probably because of a well-defined target for the primary, stressed vowel.
[DOI: 10.1121/1.1506368]

PACS numbers: 43.70.Aj, 43.60.Bk [AL]

I. INTRODUCTION

The companion paper (Perkell *et al.*, 2002) reports on a study of economy of effort in different speaking conditions. For that study, kinematic and acoustic measures were made of opening and closing movements of the lower lip, tongue blade and tongue body for the utterances ''bob,'' ''dod,'' and ''gog,'' respectively. The utterances were spoken in carrier phrases in different elicitation conditions (including normal and clear) by seven speakers. The results showed interspeaker differences in motor strategies for implementing the different speaking conditions. In comparison to the normal condition, three speakers produced the utterances in the clear condition with larger, longer duration movements that involved greater effort—according to an analysis based on a simple dynamical model (Nelson, 1983). Three other speakers mainly increased vowel duration and the seventh speaker increased sound level.

There are several possible reasons for the interspeaker differences. The purpose of the current study was to test the hypothesis that such differences are due to differences in motor performance capabilities. This study uses cyclical speechlike movements at different rates and compares their parameter values with those from the speech movements. The cyclical data are used to determine kinematic performance limits in a space defined by movement distance, peak speed and duration, with the idea that speech movement parameters might be constrained to occur within those limits. A comparison of the speech movement data from Perkell *et al.* (2002) with the cyclical movement data in the current study shows differences between the two types of movements. Therefore, a secondary goal of this study is to explore one of several possible reasons for those differences, the role of the mandible.

II. BACKGROUND

It is generally believed that the biomechanical properties of the articulators impose dynamical constraints that determine preferred and maximum possible rates of articulatory movement (see review in Perkell, 1997). For example, recent modeling and experimental work has provided a preliminary quantitative illustration of how the filtering action of the peripheral biomechanics and low-level control mechanisms may account for differences in observed mandibular move-

[a]Also at the Department of Brain and Cognitive Sciences, MIT and the Department of Cognitive and Neural Systems, Boston University. Electronic mail: perkell@speech.mit.edu

ments that otherwise might have been attributed to central commands (cf. Ostry *et al.*, 1996; Laboissière *et al.*, 1996; Perrier *et al.*, 1996).

As described in Perkell *et al.* (2002), to help make inferences about the control mechanisms that underlie kinematic behavior, some investigators have adopted principles from a control analysis of single-axis movements of an undamped, mass-spring model (Nelson, 1983; Munhall *et al.*, 1985; Nelson *et al.*, 1984; Ostry and Munhall, 1985; see Hertrich and Ackermann, 1997, for a useful review). In Nelson's analysis, peak movement velocity (speed in the current studies) can be considered to be a measure of effort. Perkell *et al.* (2002) also investigated another parameter, the ratio of peak speed to distance, which has been considered to reflect actuator ''stiffness,'' if the system can be represented by a second-order dynamical model (cf. Ostry *et al.*, 1983; Ostry and Munhall, 1985). The level of stiffness may be thought of as a relative index of the level of muscle activity that is used to produce a movement.

In an earlier study of cyclical movements by Westbury and Dembowski (1993), 30 subjects produced strings of the syllable /pʌ/, /tʌ/, and /kʌ/ at their maximum possible repetition rate. Across speakers and syllable types (/pʌ/, /tʌ/ and /kʌ/), the maximum possible rate ranged from 4.1 to 8.7 Hz, with little difference among articulators. The speakers' strategies ranged between two extremes: moving all of the articulators, including the mandible, and moving only the primary articulator. Across articulators, posterior tongue points moved the most and the fastest; increasingly anterior points moved correspondingly slower. There was a strong covariance of movement distance and speed, but no relation between range of movement and cycle rate. In general, there were a number of differences among speakers.

In measures of increasingly rapid, repetitive, speechlike and nonspeech mandible movements from three speakers, Nelson *et al.* (1984) found large intersubject differences in maximum distance, duration, peak velocity and acceleration of speech movements. Detailed analyses of distance and duration data from one subject indicated that movements with durations of 100 ms or less might have been constrained by dynamical limits. Longer duration movements appeared not to be constrained in this way. These results led to the hypothesis that different speakers may have different performance limits, which are partly constrained by articulatory dynamics. The current study extends the approach of Nelson *et al.* (1984).

III. METHODS

In the current study, we examine intersubject differences in the relation between repetitive movements and speech movements from Perkell *et al.* (2002).

The data were gathered from the same subjects in the same recording sessions as those described by Perkell *et al.* (2002). Briefly, as illustrated in Fig. 1, movements were recorded of EMMA transducer coils placed with adhesive on the tongue body (about 5 cm back from the tip, labeled TD, for ''tongue dorsum'' in Fig. 1), tongue blade (about 1 cm back from the tip, TB in Fig. 1), and on the vermillion borders of the upper and lower lips (UL and LL). Two fixed

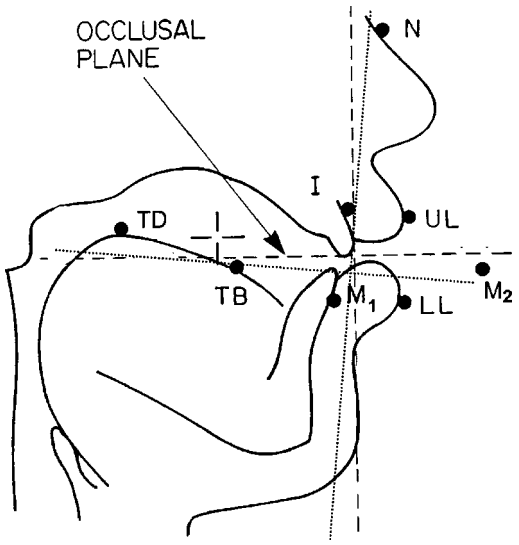

FIG. 1. A schematic illustration of transducer coil placements and the maxilla- and mandible-based coordinate systems. The transducer coils are represented by filled circles, labeled N (nose), I (upper incisors), TD (tongue dorsum), TB (tongue blade), UL (upper lip), LL (lower lip), M_1 (mandibular, mounted on the lower central interincisor papilla), and M_2 (mandibular, mounted on a jaw clip that was attached to the mandible). The maxilla-based coordinate system is illustrated by dashed lines; the mandible based system, by dotted lines. See text for details.

transducers, on the bridge of the nose (N) and the gingival papilla between the upper central incisors (I), were used as a maxillary frame of reference (Perkell *et al.*, 1992).

In order to study mandible movements in more detail, we used two mandibular EMMA transducer coils, for capturing the mandible's rotational and translational sagittal-plane degrees of freedom (cf. Westbury, 1988; Edwards and Harris, 1990; Vatikiotis-Bateson and Ostry, 1995). One of the mandibular transducer coils, labeled M_1 in Fig. 1, was mounted as usual, on the gingival papilla between the lower central incisors. To hold a second coil at a sufficiently large distance from the first one, we fabricated a ''jaw extension,'' based on a dental cast of each subject's mandible. The extension consisted of a small stainless steel bar that was bent to run along the buccal aspect of the subject's gingival mucosa in the molar and premolar region on the left side. It was made to pass out of the corner of the mouth and turn toward the midline to form a small platform in the midsagittal plane about 2 cm in front of the lips. The second transducer, labeled M_2 in Fig. 1 was mounted on the platform. The bar was shaped carefully to minimize interference with labial movements. In order to hold the bar firmly to the mandible, its intraoral portion was embedded in a custom-made clip. The clip was fabricated from dental acrylic and orthodontic (spring) wire so that it fit snugly over the molar and premolar teeth and gingival mucosa without interfering with speech articulations.

Thus the data are analyzed in two midsagittal frames of reference, maxillary (as in Perkell *et al.*, 2002) and mandibular. These are illustrated schematically in Fig. 1. For the maxillary reference frame (dashed axes in Fig. 1), the *x* axis was established parallel to the occlusal plane, determined by briefly recording the positions of two transducer coils that

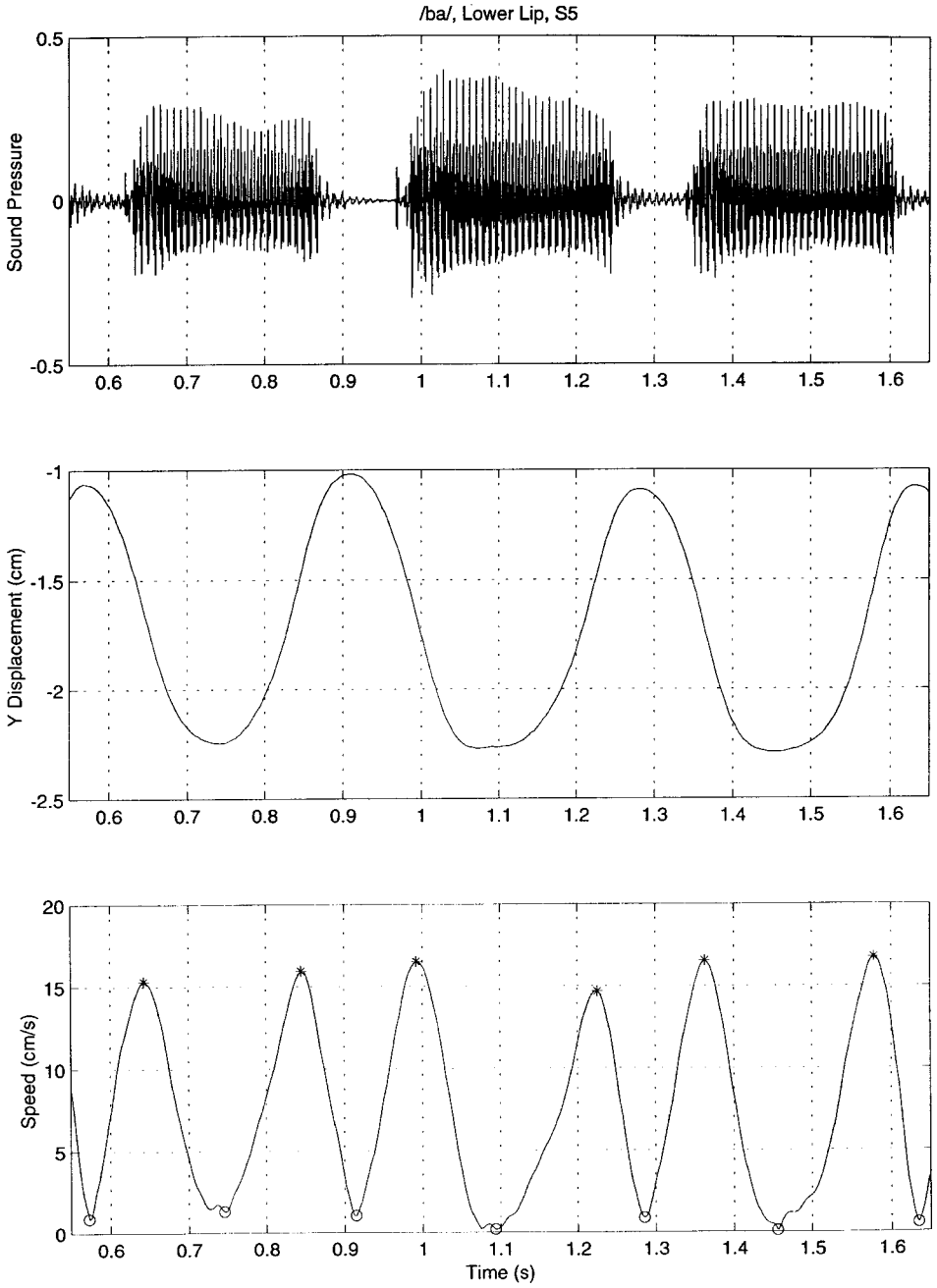

FIG. 2. The acoustic signal (top panel), vertical displacement (middle panel), and speed (bottom panel) signals versus time for lower lip movements (in the maxillary reference frame) for three /bɑ/ syllables produced at a 3 Hz repetition rate by subject 5. The asterisks indicate peak speed events and the circles indicate movement beginning and end events.

are attached to a plastic bite plate that the subject holds lightly between the upper and lower teeth. The origin is the location of a point just anterior to the edges of the upper central incisors (the anterior coil on the bite plate). The *y* (vertical) axis passes through the origin and is perpendicular to the *x* axis. Positive *x* values are in the anterior direction. For the mandibular reference frame, the *x* axis is parallel to the occlusal plane when the teeth are closed on the bite plane; the *y* axis is perpendicular to the *x* axis. As schematized by the dotted axes in Fig. 1, the mandibular reference frame translates and rotates according to the movements of the two mandibular transducer coils. Unless stated otherwise, the movement data described below are in the *maxillary* reference frame.

For this study, the subject was presented with a periodic auditory stimulus from a metronome at 1, 2, 3, 4, 5, and 6 times per second (with rates arranged in semirandom order). At each rate, the subject pronounced a smooth, continuous string of approximately 8–10 syllables: /bɑbɑbɑ.../ or /dɑdɑdɑ.../ or /gɑgɑgɑ.../, keeping time with the stimulus signal as well as possible.

Signal processing was the same as is described in Perkell *et al.* (2002), except that the kinematic signal values were computed in both the maxillary and mandibular frames of reference. To calculate signal values in the mandibular frame of reference, for each frame of data, the signal processing calculated the amount of translation and rotation of the mandible relative to the maxilla-based coordinate system. Then, each *x* and *y* value for the LL, TD, and TB transducers was transformed into the mandibular coordinate system.

Figure 2 shows the acoustic signal, vertical displacement, and speed signals versus time for lower lip movements (in the maxillary reference frame) for three /bɑ/ syllables

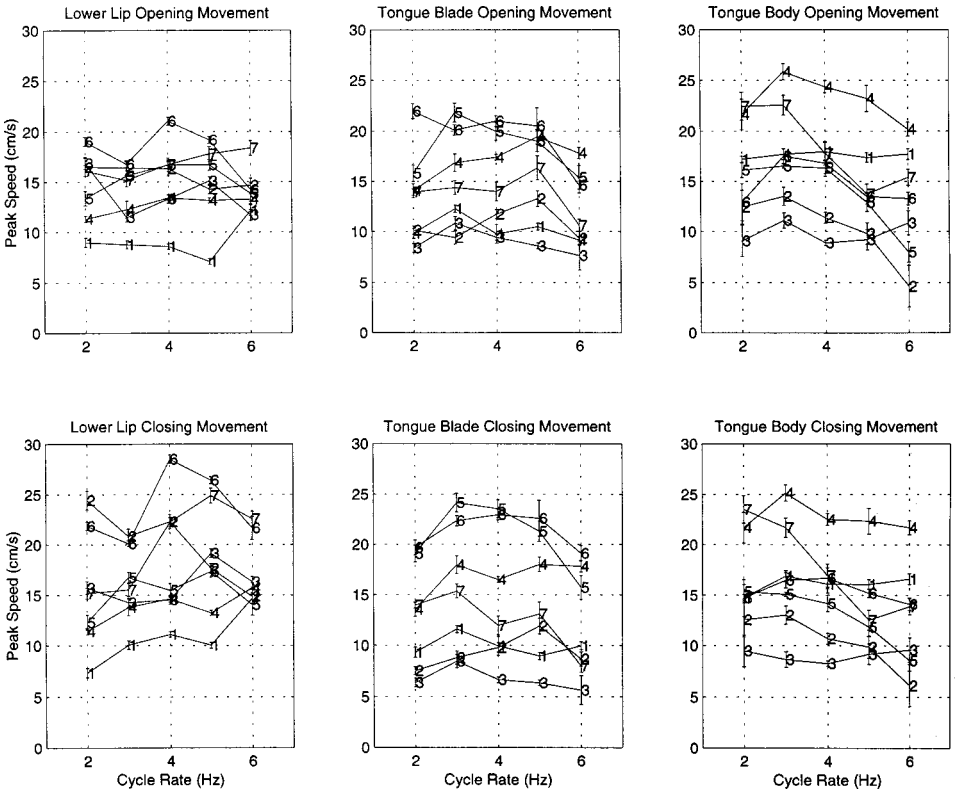

FIG. 3. Mean values of peak speed (cm/s) for opening and closing movements (upper and lower rows) as a function of cycle rate (from 2 to 6 Hz) of the lower lip, tongue blade, and tongue dorsum (columns, from left to right). Values for each subject are connected by a solid line and identified with the subject number; the error bars show ±1 standard error about the mean.

produced at a 3 Hz repetition rate by subject 5. Because of the cyclical nature of the task, the opening and closing movements were delineated somewhat differently from the speech movements in the preceding study (Perkell *et al.*, 2002). For the cyclical task, the beginning and end times of individual opening and closing movements were defined by local minima in the speed trace, marked by circles in the figure. Even when there were multiple local minima at a time of maximum opening or closure (as shown for the end of the opening movements at about 0.74, 1.1, and 1.45 s), the end of one movement and beginning of the next was always defined as the same event: the local minimum with the lowest value. There is always one major local maximum, the speed peak, and there can be one or more small local maxima around the movement beginning and/or end (as shown around 0.73, 1.09, and 1.47 s).[1] For each movement, the peak speed event is marked by an asterisk in the figure. It is evident from irregularities in the speed profile that the movement durations are not completely uniform from cycle to cycle, despite the rhythmical nature of the task.

As described in Perkell *et al.* (2002), the following parameters were extracted from the kinematic signals:

(1) movement duration,
(2) distance along the $x-y$ path,
(3) peak speed (maximum speed reached during a movement)—a relative measure of effort,
(4) peak speed/distance—a relative index of the stiffness of underlying muscle contraction.

IV. RESULTS

The six panels in Fig. 3 show mean values of peak speed (cm/s) for opening and closing movements (upper and lower rows) as a function of cycle rate (from 2 to 6 Hz) of the lower lip, tongue blade, and tongue body (columns, from left to right). In each panel, values for each subject are connected by a solid line and identified with the subject number; the error bars show 1 standard error about the mean. Across the data set, the mean values range between 5 and 29 cm/s. The shapes of the functions vary considerably among subjects, articulator and movement type (opening/closing). There are some examples of generally decreasing speed with increasing rate (e.g., tongue body opening and closing movements for subjects 2 and 7) and some examples of a peak at an intermediate rate (e.g., tongue blade opening and closing movements for subject 5). However, many of the functions show little or no regular pattern.

The six panels in Fig. 4 show (from left to right) mean values of movement distance (cm), duration (s) and peak speed/distance (s^{-1}) or lower lip opening and closing movements (upper and lower rows), plotted as in Fig. 3. In general, movement distance and duration decrease with cycle rate, as expected. Mean values of distance ranged between 0.5 and 2 cm and mean values of duration ranged between 0.07 and 0.35 s. Peak speed/distance means increased with cycle rate, ranging from 10 to 25 s^{-1}, indicating increased stiffness of underlying muscle contraction with increasing rate. This is consistent qualitatively with the characteristics of the undamped linear spring model in Nelson (1983).

These patterns were similar for the tongue blade and body (not shown).

In order to gain some insight into underlying dynamical constraints, values of peak speed, distance, and duration are examined in a 3D performance space (Nelson, 1983; Nelson *et al.*, 1984; Perkell *et al.*, 2002). Figure 5 plots cyclical movement data for lower lip opening movements for subject

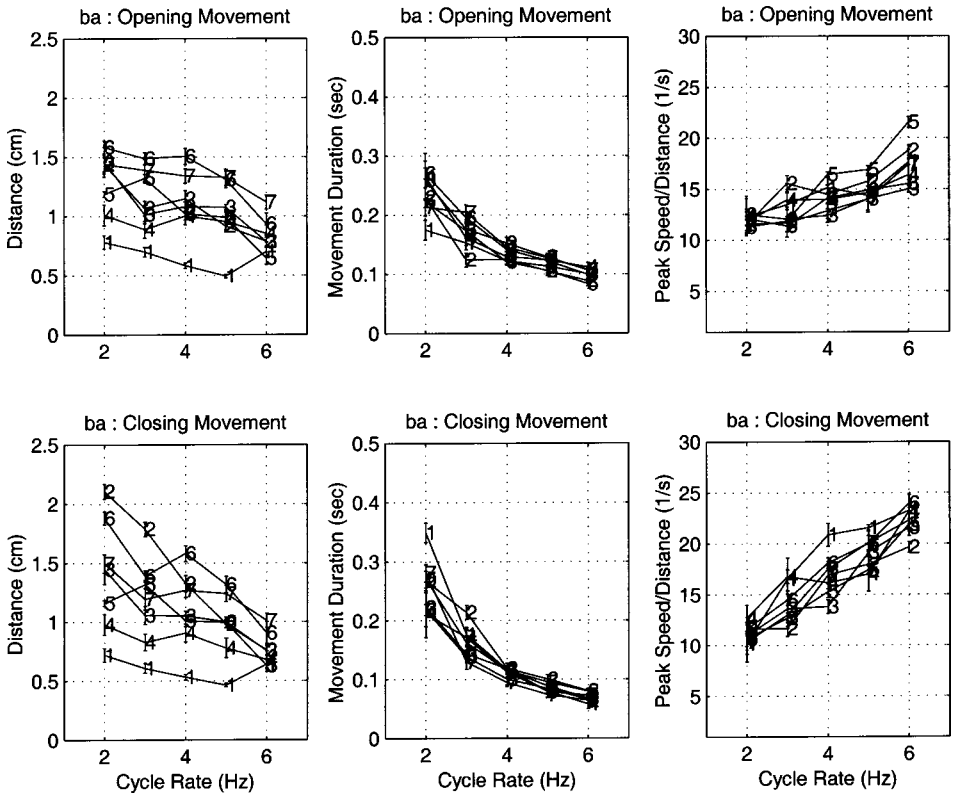

FIG. 4. Mean values of movement distance (cm), duration (s), and peak speed/distance for lower lip-opening and -closing movements (upper and lower rows), plotted as in Fig. 3.

5. The location of (the lower left-hand corner of) each number in the plot indicates the value of peak speed, distance and duration for a single movement that was produced at the cyclical rate corresponding to the number, for rates at 2 to 6 Hz. The concave surface represents a minimum-impulse-cost bound for a one-dimensional, frictionless dynamical model with an acceleration limit of 1.5 g (Nelson, 1983; Perkell *et al.*, 2002). For the current studies, according to the minimum-impulse-cost optimization, peak speed is considered to be a relative measure of effort, and all actual data points must lie above the bounding surface (for more details, see Perkell *et al.*, 2002). In the plot, all but one of the cyclical data points from 6 to 4 Hz lie roughly along a distance vs time line that is located above a ''knee'' in the surface, beyond which the effort gradient increases rapidly as movement time decreases. At lower cycle rates (3 and 2 Hz), the data move away from the knee, and distance does not increase consistently with increasing movement time. Thus, at higher rates, the movement kinematics seem to be limited by a steep gradient in the effort that would be required to increase or maintain distance while decreasing time.[2]

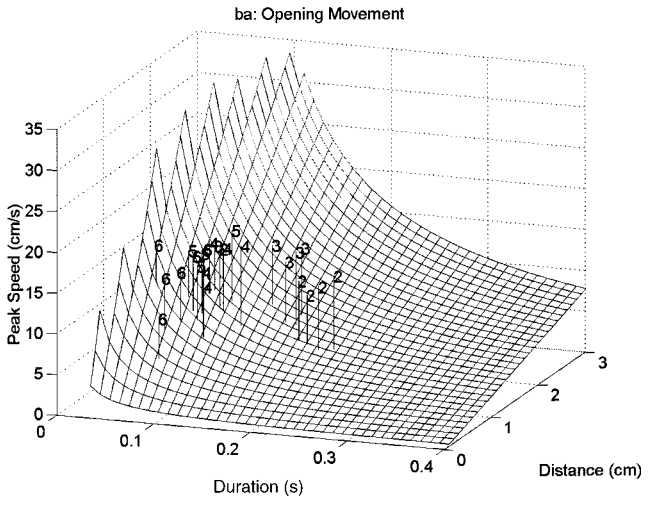

FIG. 5. Cyclical movement data for lower lip-opening movements for subject 5. Each number represents a single movement at cyclical rates from 2 to 6 Hz. The concave surface represents a minimum-impulse-cost (peak speed) bound for a one-dimensional, frictionless dynamical model with an acceleration limit of 1.5 g.

Figure 6 shows distance versus duration plots of lower lip-opening movements for the seven subjects. These are ''top-down'' views of the 3D performance space that is exemplified in Fig. 5. In each plot, the solid curve at the left represents a theoretical minimum-time limit (that corresponds to a maximum acceleration of 1.5 g). The straight lines radiating from the minimum time (maximum acceleration) limit show iso-effort (iso-peak speed) contours that represent the height of the bounding surface shown in Fig. 5. (For more detail, see Perkell *et al.*, 2002.) Although the locations and amount of scatter of the data in these plots differ from one subject to the next, they all exhibit approximately the same trend. Slower, lower-cycle-rate movements, at 2 and 3 Hz, are distributed in time with little corresponding change in distance. As movement time decreases with increasing cycle rate, most of the higher-rate points cluster approximately along one of the iso-effort contours, indicating that the movements are being constrained by effort limits. The limiting contour value differs across subjects, ranging from a low value of about 80 mm/s for subject 4 to an upper value of about 160 mm/s for subject 7. Examination of the same kind of plots for the other articulators (from the syllable strings /dadada.../ and /gagaga.../, not shown) and for closing movements revealed a generally similar pattern,

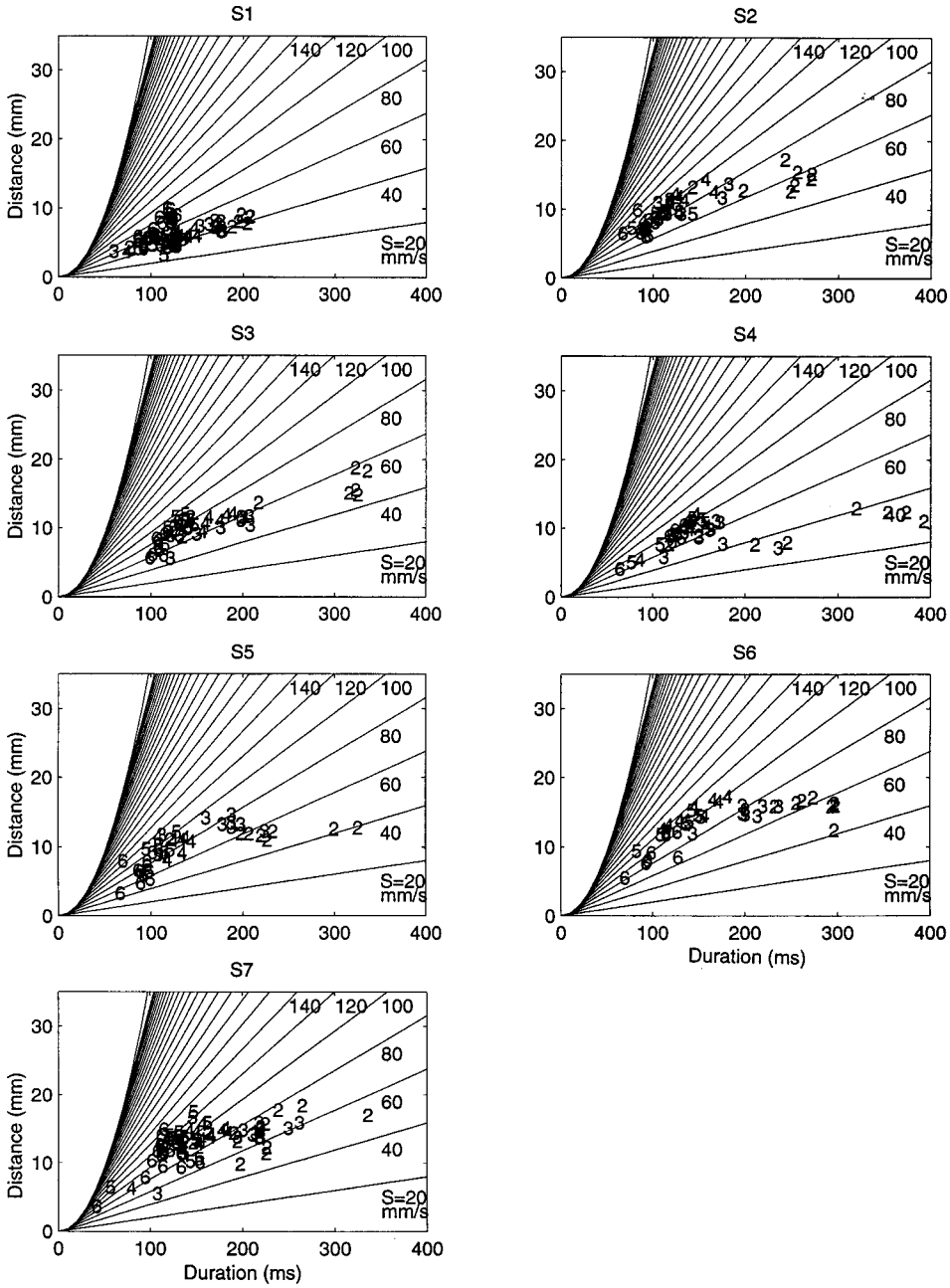

FIG. 6. Distance versus duration plots of lower lip-opening movements for the seven subjects. In each plot, the solid curve represents a theoretical minimum-time (maximum acceleration) limit of 1.5 g. The straight lines radiating from the minimum time limit show "iso-effort" (iso-peak speed) contours that represent the height of the bounding surface shown in Fig. 5.

showing reduced distance as time approaches the minimal time limit. There were some differences in values of the limiting contour among the subjects, articulators and movement type, but these did not demonstrate any particularly revealing pattern.

Figure 7 compares data from the lip-opening speech movements (from Perkell *et al.,* 2002) with the lip-opening cyclical movements for each of the seven subjects. The coordinates are the same as in Fig. 5: distance (mm) along the vertical axis and duration (ms) along the horizontal axis. The scales are also the same. The centroid of the group of values at each cyclical rate is indicated by a single number. A dashed line corresponding to a convex hull encloses all of the data points for the cyclical data. The plot also shows data for the speech opening movements of the lower lip (from the study described by Perkell *et al.,* 2002). The centroid of values for each of the speech conditions is indicated by a letter (Fast, Rapid+clear, Normal, Slow, Clear and Informal). A solid convex hull encloses all of the data points for the speech movement data. The amount of overlap of the two data types varies from none for subject 5 to complete overlap for subject 7. Many centroids of the speech condition data occur at higher values of distance and at higher effort level contours than the cyclical data (except for subject 7). For the most part, the shortest duration movements for the speech and cyclical tasks have a duration of about 100 ms. The higher effort levels for the speech movements seem to be related to the fact that the speech movements are larger (cover greater distances). Approximately similar patterns were observed in the plots for the other articulators and for closing movements. In all these plots there were differences across speakers, articulators and movements (closing vs opening).

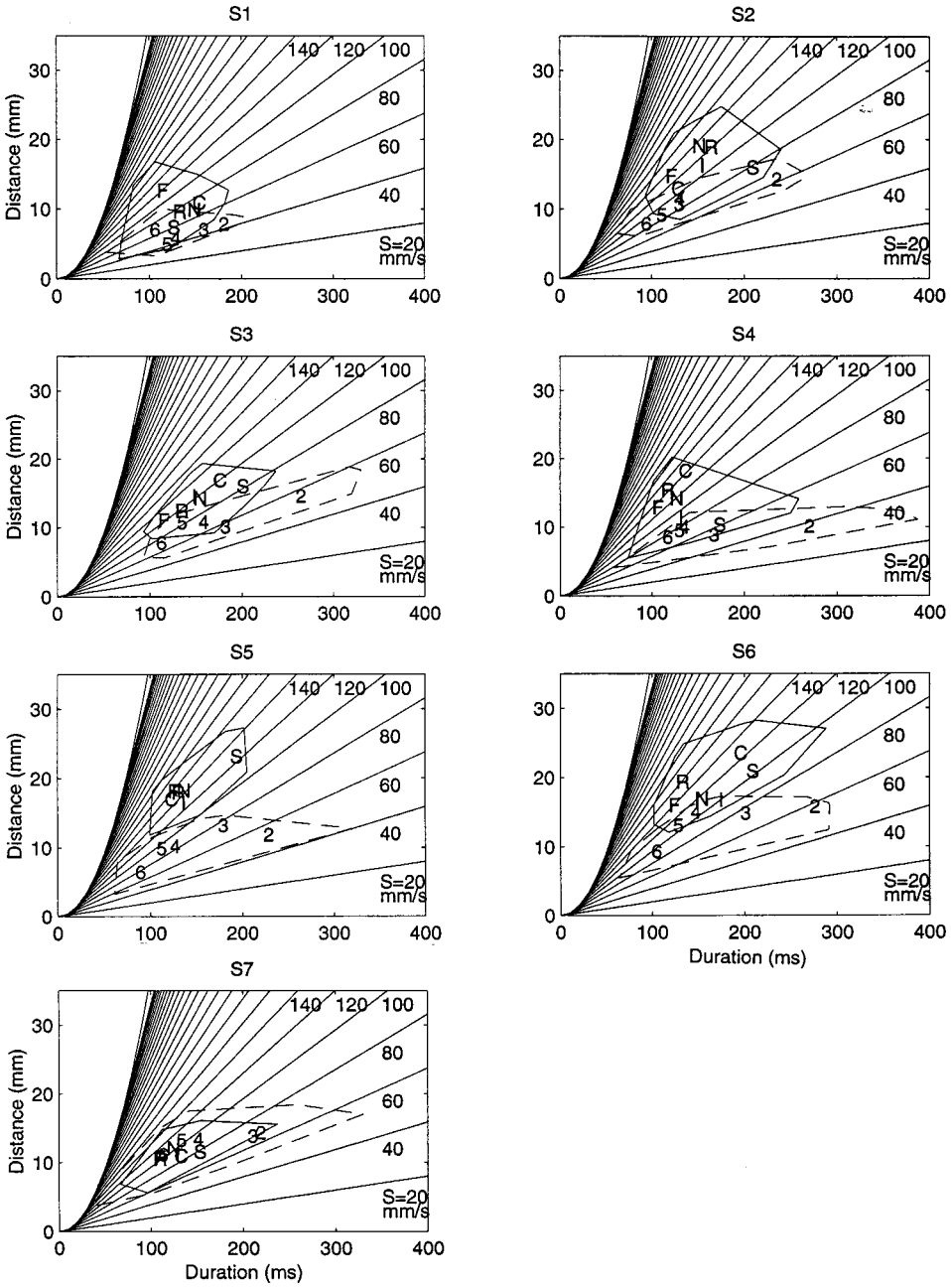

FIG. 7. A comparison of movement distance (mm) versus duration (ms) data from the lip-opening speech movements with the lip-opening cyclical movements. Each panel corresponds to the data from one of the subjects. The center of the group of values at each cyclical rate is indicated by a single number. A dashed line corresponding to a convex hull that encloses all of the data points for the cyclical data. The center of values obtained for each of six speech conditions is indicated by a letter (Fast, Rapid+clear, Normal, Slow, Clear and Informal, Perkell *et al.*, 2002). A solid convex hull encloses all of the data points for the speech movement data.

It is evident from Fig. 7 that the cyclical task did not define the outer limits of kinematic performance for the speakers. A combination of several factors may account for this result. As mentioned just above, one factor seems to be that the speech movements are larger than the cyclical movements. Another contributing factor may be that the cyclical movements are more constrained than the speech movements by virtue of being more ''coupled'' to movements of the relatively massive mandible, and this effect differs among the speakers. This hypothesis is examined in the next figure.

Figure 8 shows an example of subject 4's $x-y$ trajectories at the 4 Hz cyclical rate. The left-hand column of panels shows trajectories plotted in the mandible-based coordinate system. The right-hand column shows the same trajectories, but plotted in the maxilla-based coordinate system. The top two panels show trajectories from the syllable string /bɑbɑbɑ.../; the middle panels show trajectories for the syllable string /dɑdɑdɑ.../; and the bottom panels show trajectories from the syllable string /gɑgɑgɑ.../. In each of the left-hand panels, the leftmost trajectory is from the tongue-dorsum (TD) transducer; the center trajectory is from the tongue blade (TB) transducer and the upper and lower trajectories on the right are from the upper (UL) and lower lip (LL) transducers. The plots in the right column also show trajectories for the lower incisor (LI) movements (of the mandible), which of course do not show in the mandible-based plots on the left. The same kinds of plots were examined for all seven subjects and for cycle rates of 2, 4, and 6 Hz.

Inspection of all of the subjects' plots indicated that the size of subject 4's LI trajectories represented an approximate median with respect to the other subjects. The trajectories for subjects 1, 2, and 3 were similar in size or slightly smaller, and the trajectories for subjects 5, 6, and 7 were slightly

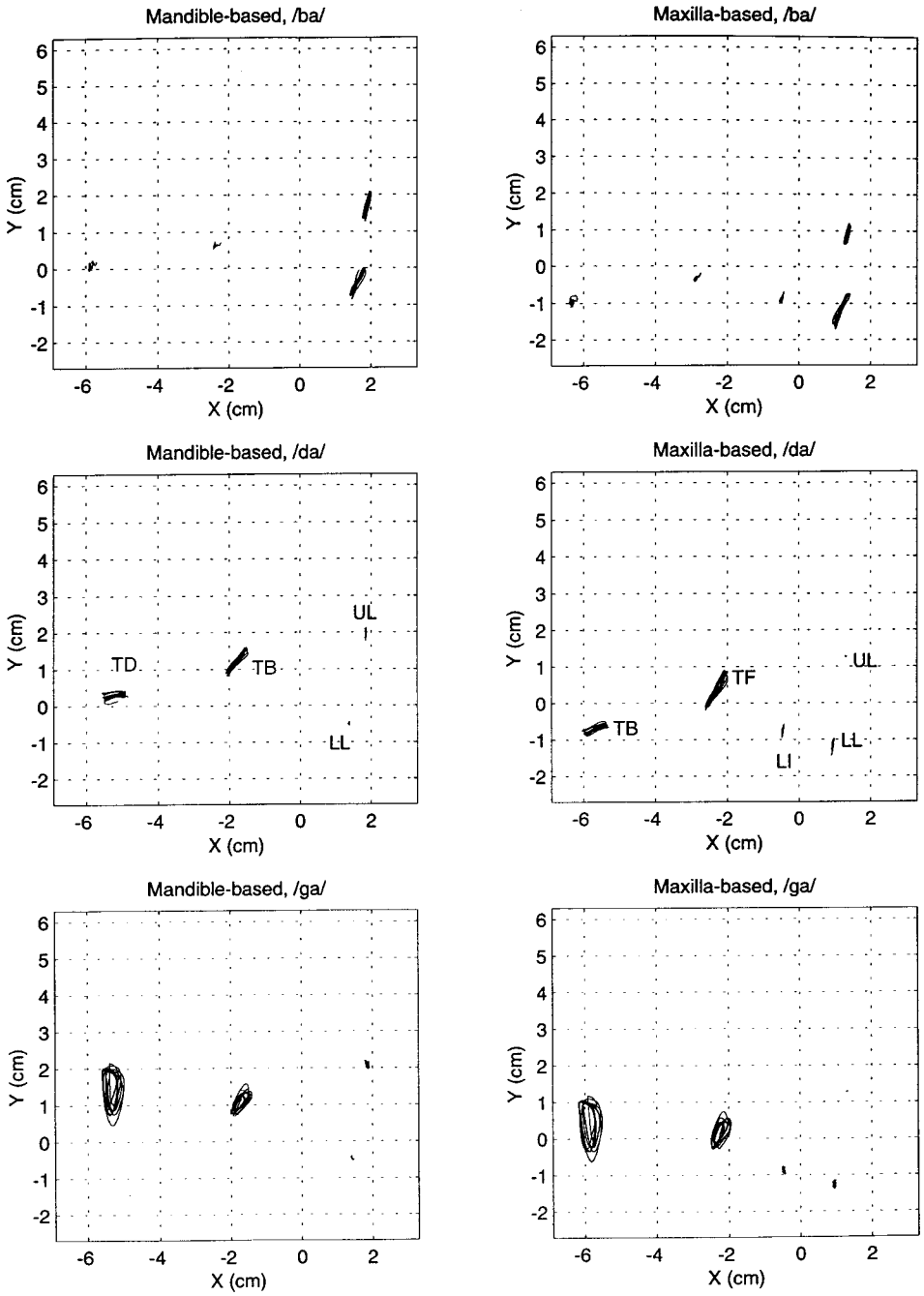

FIG. 8. An example of subject 4's $x-y$ trajectories at the 4 Hz cyclical rate. The left-hand column of panels shows trajectories calculated in the mandible-based coordinate system. The right-hand column shows the same trajectories, but calculated in the maxilla-based coordinate system. The top two panels show trajectories from the syllable string /bɑbɑbɑ/; the middle panels show trajectories for the syllable string /dɑdɑdɑ.../; and the bottom panels show trajectories from the syllable string /gɑgɑgɑ.../. In each panel, the leftmost trajectory is from the tongue-dorsum (TD) transducer; the center trajectory is from the tongue blade (TB) transducer and the upper and lower trajectories on the right are from the upper (UL) and lower lip (LL) transducers. The plots in the right column also show trajectories for the lower incisor (LI) movements (of the mandible).

larger. Although there were some slight differences in the appearance of the trajectories at the other two cycle rates and across the subjects, the pattern shown in Fig. 8 is quite representative. In general, the tongue and lower lip movement trajectories in the two frames of reference (comparing the columns) are very similar to one another. In the maxillary reference frame (right column), the mandible movement (LI) trajectories are considerably smaller than the LL trajectories for the /bɑ.../ movements (top row), the TF trajectories for the /dɑ.../ movements (middle row) and the TB trajectories for the /gɑ.../ movements (bottom row).

The panels in Fig. 9 plot mean values of opening movement size for the seven subjects. The bars in each panel compare the mean size of lower lip (LL, for /bɑ/), tongue front (TF, for /dɑ/) and tongue back (TB, for /gɑ/) opening movements with their associated mandible (Man) opening movements for the same syllable strings at three cycle rates: 2 (black bars), 4 (clear bars), and 6 (gray bars) Hz. In general, the mandible movements are a fraction of the size of the corresponding tongue and lip movements, although the size of the fraction varies somewhat. The tongue body movements have larger distances than the lower lip and tongue blade (TF) movements for subjects 1, 4, 5, and 7 (also see Westbury and Dembowski, 1993), especially at the lower cycle rates, but the other subjects do not exhibit this pattern. (To some extent, the larger distances of the tongue movements are due to their curved paths and the fact that distance is calculated along the path.) Consistent with Fig. 4, there is a tendency for movement size to decrease with rate. A plot for closing movements had the same general features.

Thus it appears that the cyclical movements were accomplished largely with the primary articulator, and gener-

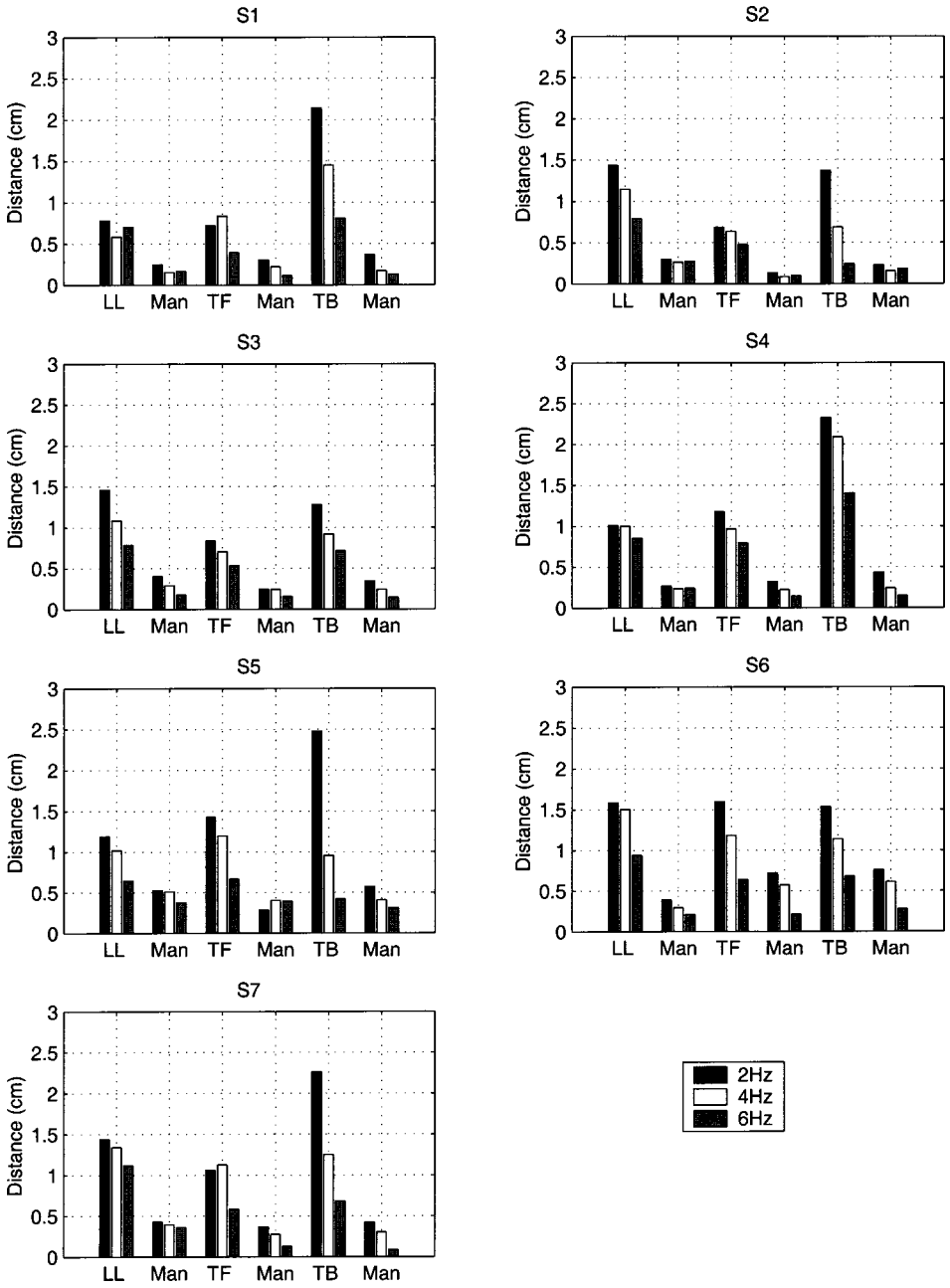

FIG. 9. Mean values of opening movement size for the seven subjects. The bars in each panel compare the mean size of lower lip (LL—for bɑ/), tongue front (TF—for /dɑ/), and tongue back (TB—for /gɑ/) opening movements with their associated mandible (Man) opening movements at three cycle rates: 2 (black bars), 4 (clear bars), and 6 (gray bars) Hz.

ally without much participation of the mandible. These observations agree with those of Westbury and Dembowski (1993). They indicate that the subjects' strategy seems to have been to largely ''decouple'' the primary articulator movements from the mandible in order to make it possible to accomplish the cyclical task.

V. DISCUSSION AND CONCLUSIONS

The observations made above indicate that lower kinematic performance values for the cyclical movements (with respect to the speech movements) are not explained by the constraining effect of the relatively massive mandible.

One possible contribution to the differences between the speech and cyclical movements is that the speech movements are biomechanically different and are controlled differently from the cyclical movements. A CVC word in sentence context does not require the same kind of carefully timed and controlled sequence of reversals that is inherent in a rhythmic repetition task. A likely and important contribution to the differences between movements in the two types of tasks is reflected in the generally larger size of the speech movements at any given movement duration (discussion of Fig. 7, above). In the speech task, the target vowel /ɑ/ is purposefully stressed, whereas the cyclical task did not include such a constraint. It is very likely that the vowel is significantly reduced at higher cycle rates in the repetition task. We plan to test this hypothesis in future work that will include acoustic measurements, along with kinematic measurements of primary articulator movements for unstressed productions of the CVC word and measures of mandible movements for both stressed and unstressed CVC utterances in the speech task.

Finally, it is also possible that the speech movements are much more practiced than the cyclical movements; that is,

the speech movements are ''skilled'' and the cyclical movements are not. This idea is more difficult to address quantitatively.

ACKNOWLEDGMENTS

This work was supported by research Grant No. 5 R01 DC01925 from the National Institute on Deafness and Other Communication Disorders, National Institutes of Health. We are very grateful to Winston Nelson for his valuable comments and to Hermann Ackermann, Ingo Hertrich, Anders Löfqvist, David Ostry, and Gary Weismer for their helpful reviews.

[1]With the approach of Perkell *et al.* (2002) for delimiting speech movements, the small local maxima of speed at movement beginning and end times would, by definition, occur during ''intermovement intervals,'' which were not included in the speech movement durations in that study. This difference between the cyclical and speech movements in methods for identifying movement beginning and end events produces a slight bias toward longer movement durations among the cyclical movements that have multiple local minima in the speed traces. However, these differences are small and are confined to the longer-duration, lower-rate movements. The differences have no impact on any of the observations made about relations between the speech and cyclical movements.

[2]The movement durations are variable at each rate, especially at 2 and 3 Hz, partly because of the way the movement beginning and end times were identified algorithmically, as noted above. The 1 Hz data were far to the right, beyond the duration limit of the plot. They are not considered in the analysis.

Edwards, J., and Harris, K. S. (**1990**). ''Rotation and translation of the jaw during speech,'' J. Speech Hear. Res. **33**, 550–562.

Hertrich, I., and Ackermann, H. (**1997**). ''Articulatory control of phonological vowel length contrasts: Kinematic analysis of labial gestures,'' J. Acoust. Soc. Am. **102**, 523–536.

Laboissière, R., Ostry, D. J., and Feldman, A. G. (**1996**). ''The control of multi-muscle systems: human jaw and hyoid movements,'' Biol. Cybern. **74**, 373–384.

Munhall, K. G., Ostry, D., and Parush, A. (**1985**). ''Characteristics of velocity profiles of speech Movements,'' J. Exp. Psychol. **11**, 457–474.

Nelson, W. L. (**1983**). ''Physical principles for economies of skilled movements,'' Biol. Cybern. **46**, 135–147.

Nelson, W. L., Perkell, J. S., and Westbury, J. R. (**1984**). ''Mandible movements during increasingly rapid articulations of single syllables: Preliminary observations,'' J. Acoust. Soc. Am. **75**, 945–951.

Ostry, D. J., Gribble, P. L., and Gracco, V. L. (**1996**). ''Coarticulation of jaw movements in speech production: Is context sensitivity in speech kinematics centrally planned?,'' J. Neurosci. **16**, 1570–1579.

Ostry, D., Keller, E., and Parush, A. (**1983**). ''Similarities in the control of speech articulators and the limbs: Kinematics of tongue dorsum movement is speech,'' J. Exp. Psychol. **9**, 141–147.

Ostry, D., and Munhall, K. G. (**1985**). ''Control rate and duration of speech movements,'' J. Acoust. Soc. Am. **77**, 640–648.

Perkell, J. S. (**1997**). ''Articulatory processes,'' in *The Handbook of Phonetic Sciences*, edited by W. Hardcastle and J. Laver (Blackwell, New York), pp. 333–370.

Perkell, J. S., Cohen, M. H., Svirsky, M., Matthies, M., Garabieta, I., and Jackson, M. (**1992**). ''Electro-magnetic midsagittal articulometer (EMMA) systems for transducing speech articulatory movements,'' J. Acoust. Soc. Am. **92**, 3078–3096.

Perkell, J., Zandipour, M., Matthies, M., and Lane, H. (**2002**). ''Clarity versus economy of effort in speech production. I. A preliminary study of inter-subject differences and modeling issues,'' J. Acoust. Soc. Am. **112**, 1627–1641.

Perrier, P., Lœvenbruck, H., and Payan, Y. (**1996**). ''Control of tongue movements in speech: The Equilibrium Point hypothesis perspective,'' J. Phonetics **24**, 53–75.

Vatikiotis-Bateson, E., and Ostry, D. J. (**1995**). ''An analysis of the dimensionality of jaw motion in speech,'' J. Phonetics **23**, 101–117.

Westbury, J. R. (**1988**). ''Mandible and hyoid bone movements during speech,'' J. Speech Hear. Res. **31**, 405–416.

Westbury, J. R., and Dembowski, J. (**1993**). ''Articulatory kinematics of normal diadochokinetic performance,'' Annual Bulletin, No. 27, Research Institute of Logopedics and Phoniatrics, University of Tokyo, pp. 13–36.

Experimental verification of the quasi-steady approximation for aerodynamic sound generation by pulsating jets in tubes

Zhaoyan Zhang, Luc Mongeau, and Steven H. Frankel
School of Mechanical Engineering, Purdue University, West Lafayette, Indiana 47907

(Received 17 October 2001; revised 28 May 2002; accepted 15 July 2002)

Voice production involves sound generation by a confined jet flow through an orifice (the glottis) with a time-varying area. Predictive models of speech production are usually based on the so-called quasi-steady approximation. The flow rate through the time-varying orifice is assumed to be the same as a sequence of steady flows through stationary orifices for wall geometries and flow boundary conditions that instantaneously match those of the dynamic, nonstationary problem. Either the flow rate or the pressure drop can then be used to calculate the radiated sound using conventional acoustic radiation models. The quasi-steady approximation allows complex unsteady flows to be modeled as steady flows, which is more cost effective. It has been verified for pulsating open jet flows. The quasi-steady approximation, however, has not yet been rigorously validated for the full range of flows encountered in voice production. To further investigate the range of validity of the quasi-steady approximation for voice production applications, a dynamic mechanical model of the larynx was designed and built. The model dimensions approximated those of human vocal folds. Airflow was supplied by a pressurized, quiet air storage facility and modulated by a driven rubber orifice. The acoustic pressure of waves radiated upstream and downstream of the orifice was measured, along with the orifice area and other time-averaged flow variables. Calculated and measured radiated acoustic pressures were compared. A good agreement was obtained over a range of operating frequencies, flow rates, and orifice shapes, confirming the validity of the quasi-steady approximation for a class of relevant pulsating jet flows.
[DOI: 10.1121/1.1506159]

PACS numbers: 43.70.Aj, 43.28.Ra [AL]

LIST OF SYMBOLS

A_g	glottal area (m^2)
A_t	tube cross-sectional area (m^2)
c	speed of sound (m/s)
C_d	dimensionless orifice discharge coefficient
d_t	tube inner diameter (m)
f	frequency (Hz)
G	Green's function
H	Heaviside function
k	wave number (m^{-1})
L	distance from the orifice (m)
P_{ij}	pressure stress tensor (Pa)
p	total pressure (Pa)
p'	unsteady pressure (Pa)
Q	instantaneous flow rate (m^3/s)
Q_0	mean flow rate (m^3/s)
R	reflection coefficient
Re	Reynolds number $Q_0 d_t / A_t \nu$
T_{ij}	Lighthill stress tensor
U	flow velocity (m/s)
U_c	centerline velocity (m/s)
u'	acoustic particle velocity (m/s)
v	orifice wall velocity (m/s)
Z_g	glottal impedance (Pa m^{-3}s)
Δp	instantaneous pressure drop across the orifice (Pa)
Δp_0	mean pressure drop across the orifice (Pa)
ρ_0	ambient density (kg/m^3)
ω	angular frequency (rad/s)
ν	kinematic viscosity (m/s^2)
σ_{ij}	viscous stress tensor

Subscripts

up	upstream
dn	downstream
0	time-averaged
c	centerline

I. INTRODUCTION

A good understanding of voice production is essential for many applications in speech sciences. For example, some physiological models for speech synthesis and recognition are based on articulatory parameters to model the speech production process (Gupta and Schroeter, 1993). Such physiological models of speech production may someday assist surgeons to predict the possible consequences of phonosurgery, or guide surgeons in the clinic. They may also allow more realistic speech synthesis and more effective speech recognition algorithms to be developed.

The basic mechanism of phonation is well understood, as described by Wegel (1930), Flanagan (1965), Titze (1973, 1974), and others. Airflow is expelled out from the lungs by contraction of the rib cage. Air flows through the bronchi, the trachea, and the vocal folds where it is modulated by the flow-induced vibrations of the vocal folds. A pulsating jet

flow is discharged into the supraglottal region, exciting acoustic waves within the vocal tract. The vibration of the glottis is driven by the periodic changes in the pressure gradient across the vocal folds. When the vocal folds are fully closed, the pressure on the upstream side is increased, and, after it reaches a threshold, forces the folds to open. As air flows out, the pressure gradient is decreased and the vocal folds are brought back together by the combination of a lower static pressure and elastic forces in the tissue. The cycle then repeats. The frequency of the vocal folds' oscillations determines the voice's pitch.

In the widely used source–filter model of speech production, the flow through the vocal folds is modeled as an ideal sound source, and the vocal tract acts as an acoustic filter (Flanagan, 1965). The source term is characterized by a nonlinear "glottal impedance," $Z_g(t)$, which is defined as the ratio of the transglottal pressure drop to the volume flow rate through the glottis. The characteristics of the acoustic filter depend on the instantaneous configuration of the vocal tract, such as the position of the tongue, teeth, lips, and velum. The glottal impedance is essential to the source–filter model. It is a time-varying quantity determined by many factors, including geometry, as well as inflow (subglottal) and outflow (supraglottal) boundary conditions. A detailed understanding of the flow field is required to calculate the glottal impedance from first principles.

The flows involved in the production of speech are essentially three-dimensional and turbulent (Alipour *et al.*, 1995). Three-dimensional simulations are needed to fully capture the detailed flow and acoustic fields. Recently, Zhao (2000) performed direct numerical simulations to investigate the sound production mechanisms in confined axisymmetric jet flows through modulated orifices. However, because the pulsating jet flows involve turbulence and flow separation and the glottal geometry is complex, it is prohibitively expensive to directly calculate the three-dimensional details of the flow and the acoustic fields simultaneously using computational methods.

The quasi-steady approximation is often made to simplify fluid flow analysis. It is assumed that the flow through a time-varying orifice can be simulated by a sequence of steady flows through orifices with the same geometry and boundary conditions as the time-varying orifice at specific time values. It is assumed that intrinsically unsteady effects related to flow acceleration or hysteresis can be neglected. The quasi-steady approximation allows the modeling of speech production as a sequence of steady flows, which are much easier to simulate than unsteady flows. The instantaneous glottal impedance can also be approximated by glottal impedances obtained directly from measurements using static physical models. The pressure–flow relationship in static physical models was studied first by Wegel (1930) and van den Berg *et al.* (1957), and empirical expressions were obtained for the glottal impedance. Many studies of static configurations, both experimental and computational, have since been reported (see, for example, Scherer *et al.*, 1983; Guo *et al.*, 1993).

Although it is widely used in speech-related applications, the quasi-steady approximation has not been thoroughly validated experimentally. The range of validity of the assumption is unknown for phonation (McGowan, 1993). Attempts have been made to investigate the flow field of confined jets flow through steady and pulsating orifices. Shadle *et al.* (1987) studied jet flow through a mechanically modulated orifice with a time-varying area. However, their studies were limited to flow visualization and static impedance measurements. So *et al.* (1987) investigated the near-field behavior of gas jets in a long tube. Iguchi *et al.* (1990) compared the properties of steady and pulsating confined jets through an orifice with constant area, and reported a difference in flow characteristics between acceleration phase and deceleration phase. Deviations from the quasi-steady approximation were observed also in the study of pulsating confined hydraulic jets by Diebold *et al.* (1990). Pelorson *et al.* (1994) and Pelorson (2001) have investigated flow separation phenomena and pressure–flow relationship for both steady and unsteady flows through constrictions in a duct. They showed that the pressure and flow velocity in unsteady flow predicted using the quasi-steady approximation was accurate, except for short instants prior to orifice closure and opening.

Mongeau *et al.* (1997) used a driven dynamic mechanical model in order to investigate the validity of the quasi-steady approximation for an open jet configuration. There was no tube downstream of the modulated rubber orifice. Furthermore, only one orifice shape, with convergent walls, was considered. The same question for confined pulsating jets, however, has not yet been addressed. In voicing, the geometry of the constriction between vocal folds varies during one cycle. The shape of the modulated orifice can be in turn divergent, straight, or convergent. This could induce significant changes in the flow dynamics, and may challenge the legitimacy of the quasi-steady approximation. The present study was aimed at extending the verification of the quasi-steady approximation for confined jet-flow configurations, and a few orifice geometries that are generically similar to the glottis during voicing.

II. THEORETICAL BACKGROUND

An idealization of the human larynx and the vocal tract as shown in Fig. 1(a). Air flows at low speed through an orifice in a rigid circular uniform tube.

A. Steady-state pressure–flow relationship

Consider first the case for which the orifice area does not change with time. For Reynolds numbers typical of phonation, the flow upstream and within the glottis is mostly laminar. Since the flow velocity is much smaller than the speed of sound, it is reasonable to assume an incompressible flow relation. Bernoulli's equation for a steady flow, along a streamline through the center of the orifice, yields

$$p_{\mathrm{up}} - p_{\mathrm{dn}} = \tfrac{1}{2}\rho_0 U_c^2, \tag{1}$$

where p_{up} and p_{dn} are the upstream and downstream pressure, respectively, ρ_0 is the ambient density, and U_c is the centerline flow velocity within the orifice. The volumetric flow rate could be obtained by integrating the axial velocity

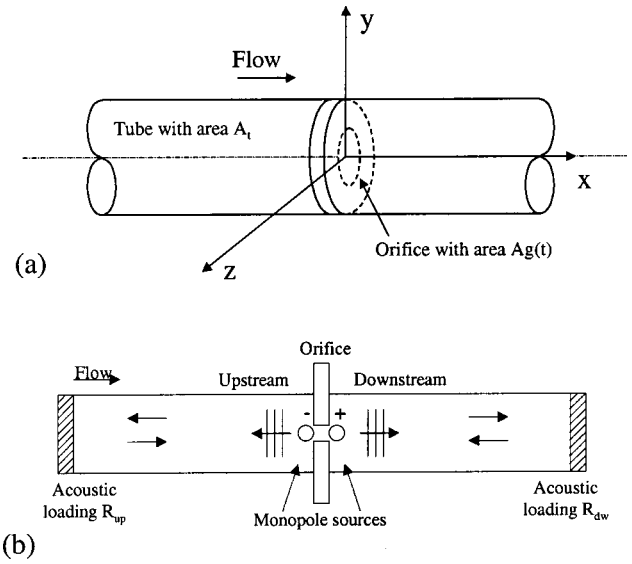

FIG. 1. (a) The coordinate system used in the model; (b) Acoustical representation of the physical model.

within the orifice over a plane normal to the tube axis (here the x axis)

$$Q=\int\int_{A_g} U(y,z)\cdot n_x dA_g, \tag{2}$$

where A_g is the orifice area. Due to the influence of viscosity near the walls, the flow velocity is not uniform over the cross section of the orifice. The orifice discharge coefficient is defined as

$$C_d=\frac{Q}{U_c A_g}. \tag{3}$$

Equation (2) can be rewritten in the following form, also known as Bernoulli's obstruction theory:

$$Q=C_d A_g U_c. \tag{4}$$

The orifice coefficient allows the effects of viscosity, of turbulence on the mean flow, of flow separation, and of orifice geometry to be accounted for. This parameter may be easily calculated from measured values of the pressure differential across the orifice, and the volumetric flow rate. Equations (1)–(4) provide the so-called steady pressure–flow relations which are the basis for quasi-steady models.

B. Quasi-steady approximation

If the quasi-steady approximation is valid, Eqs. (1) and (4) are then valid also for unsteady flow, with the variables in the equations representing the instantaneous values. For unsteady flow, the instantaneous pressure gradient across the orifice $\Delta p(t)$ can be decomposed into two components: a time-averaged pressure gradient Δp_0 and a time-varying component $(p'_{up}-p'_{dn})$. By substitution, Eq. (1) can be rewritten as

$$\Delta p(t)=\Delta p_0+p'_{up}(0^-,t)-p'_{dn}(0^+,t)=\tfrac{1}{2}\rho_0 U_c^2. \tag{5}$$

This formulation neglects intrinsically unsteady phenomena altogether. The unsteady form of Bernoulli's equation includes an additional flow acceleration term, i.e., the time derivative of the velocity potential. One might expect this term to contribute whenever large flow accelerations occur, such as when the glottis opens. Vortical structures shed by the orifice wall motion could persist over a significant period of time. They are convected at a rather low velocity (approximately one-half the centerline flow velocity), and thus they could alter the boundary condition downstream in the dynamic problem. The formation of a leading vortex (see, for example, Zhao *et al.*, 2000a) when the orifice impulsively transitions from a completely closed configuration (no flow through the orifice at all) to a fully developed jet is also an inherently unsteady phenomenon which would not appear in a steady flow. Whether or not these effects contribute significantly to sound radiation is the main question addressed in this study.

C. Acoustic source model

Strictly speaking, three major sound generation mechanisms contribute to the radiated sound, as explained in details by Zhao (2000) and Zhao *et al.* (2001b): (1) a quadrupole source related to kinetic energy fluctuations of the flow downstream of the orifice; (2) a monopole source due to the mass of the volume of air displaced by the motion of the orifice walls; and (3) a dipole source due to the unsteady axial forces exerted by the walls on the fluid. For conditions typical of human voice production, the dipole source is dominant among the three sound-generation mechanisms (more information about the formal acoustic analogy solution for this problem is provided in the Appendix). The dipole source radiates sound waves that are equal in magnitude and opposite in sign propagating upstream and downstream of the orifice.

Assuming low-frequency planar waves radiated in both directions from the orifice, one can always idealize the source region as a moving piston. Considering an observer located in the far field on either side of the piston, the piston can be modeled either as an equivalent monopole source or an equivalent dipole. The vocal-fold dimensions are small in comparison with the wavelengths of interest. The two segments of tissue are 1.0 to 1.5 cm in length for females, 1.8 to 2.2 cm for males, and 2 to 3 mm in thickness. For this study, the source region was idealized as two ideal, acoustically compact, one-dimensional equivalent monopoles. The pulsating flow radiates sound both downstream and upstream, with the corresponding monopole sources having equal strength and opposite (180°) phase [Fig. 1(b)]. Note again that these equivalent monopole sources are not the same as the classical ''displacement flow'' monopole according to Lighthill's acoustic analogy (an intrinsically nonstationary effect since its strength increases linearly with frequency). The equivalent monopole source strength includes all sound-generation mechanisms within the source region, believed to be dominantly dipole-like [see Eq. (A5)]. The reason for choosing a monopole rather than a dipole was to allow indirect verification of the quasi-steady assumption, as clarified in Sec. II E.

D. Sound wave reflections in tubes

Reflections occur as plane waves propagate through finite-length ducts. The influence of reflections can be modeled theoretically by adding image sources whose strength is determined from the acoustic loading at the end of each duct. The upstream and downstream sides of the orifice are considered separately, as illustrated in Fig. 1(b). Each system has its own monopole source located at the orifice. Each monopole source radiates into a rigid tube with a termination characterized by a reflection coefficient R. Plane-wave propagation is assumed considering the small tube diameter and the low fundamental frequency (below 200 Hz) of the orifice oscillations. The acoustic pressure p' both upstream and downstream can then be expressed as (Pierce, 1989)

$$p'(x,t) = \int B(x,\omega)\{e^{j(\omega t - k(L-x))} + R \cdot e^{j(\omega t + k(L-x))}\} d\omega, \tag{6}$$

where $B(x,\omega)$ is a function of position and frequency to be determined, x is the distance along the tube from the orifice, L is the tube length or the distance of the microphone from the source location, and ω and k are the angular frequency and wave number, respectively.

Using the one-dimensional equivalent monopole source model, the unsteady velocity at the source end is related to the unsteady flow rate through

$$u'_{\mathrm{up}}(0,t) = \int \frac{B_{\mathrm{up}}(0,\omega)}{\rho_0 c}\{e^{j(\omega t - kL)} - R \cdot e^{j(\omega t + kL)}\} d\omega = -\frac{1}{A_t}\{Q(t) - Q_0\}, \tag{7}$$

$$u'_{\mathrm{dn}}(0,t) = \int \frac{B_{\mathrm{dn}}(0,\omega)}{\rho_0 c}\{e^{j(\omega t - kL)} - R \cdot e^{j(\omega t + kL)}\} d\omega = \frac{1}{A_t}\{Q(t) - Q_0\}, \tag{8}$$

where u'_{up} and u'_{dn} are acoustic velocities in the upstream and downstream tubes, respectively, c is the speed of sound, A_t is the cross-section tube area, and Q_0 the time-averaged volumetric flow rate. The subtraction of Q_0 from the instantaneous flow rate inside the parenthesis is to remove the nonzero mean component of the particle velocities.

E. Verification procedure

The easiest way to verify predictions based on quasi-steady models would be to simultaneously measure transglottal pressure and flow rate for static and dynamic configurations. Unfortunately, the measurement of the instantaneous flow rate for the dynamic problem was not possible due to hardware limitations. An indirect method using radiated sound data and empirical static pressure–flow data was used instead. One advantage of this ''inverse filtering'' approach is that only the features of the flow that are responsible for sound radiation are accounted for. Any ''near-field'' effect (which would not contribute to speech production anyway) is automatically ignored. For this reason, it is advantageous to measure sound pressure away from the orifice. This, however, necessitates a deconvolution of the reflected waves and an iterative method of solution.

The procedure for the verification of the quasi-steady assumption is as follows. The upstream or downstream acoustic pressure was obtained by solving Eqs. (4), (5), (6), (7), and (8) simultaneously. First, initial values were selected for the upstream and downstream acoustic pressure, denoted by $p'^{1}_{\mathrm{up}}(0,t)$ and $p'^{1}_{\mathrm{dn}}(0,t)$, respectively. These were then substituted into Eq. (5) and U_c was obtained from the known (directly measured) Δp_0. The instantaneous flow rate, $Q(t)$, was then calculated from U_c and measured C_d and $A_g(t)$ values using Eq. (4). With $Q(t)$, $u'_{\mathrm{up}}(0,t)$, and $B_{\mathrm{up}}(0,\omega)$ calculated using Eq. (7), $p'^{i+1}_{\mathrm{up}}(0,t)$ was then determined using Eq. (6), where the superscript $i+1$ means the input for the $i+1$ iteration. The value of $p'^{i+1}_{\mathrm{dn}}(0,t)$ was determined in the same way using Eqs. (6) and (8). The quantity $p'^{i+1}_{\mathrm{up}}(0,t)$ was compared to its value at the previous iteration, $p'^{i}_{\mathrm{up}}(0,t)$. If the maximum difference was larger than a predetermined threshold value, i.e., $|\max[p'^{i+1}_{\mathrm{up}}(0,t) - p'^{i}_{\mathrm{up}}(0,t)]| > \varepsilon$, the iterations continued with $p'^{i+1}_{\mathrm{up}}(0,t)$ and $p'^{i+1}_{\mathrm{dn}}(0,t)$ as the input for the next iteration. Otherwise, the iterative process was stopped and $p'^{i+1}_{\mathrm{up}}(0,t)$ and $p'^{i+1}_{\mathrm{dn}}(0,t)$ yielded the final value for $p'_{\mathrm{up}}(0,t)$ and $p'^{i+1}_{\mathrm{dn}}(0,t)$, respectively.

To ensure numerical convergence, the acoustic pressure was filtered such that only the first few harmonic frequency components were retained. Frequency components above about 600 Hz were ignored. The filtering process was carried out in the frequency domain, every time Eq. (6), (7), or (8) was solved. Finally, $p'_{\mathrm{up}}(L,t)$ and $p'_{\mathrm{dn}}(L,t)$ were calculated using Eq. (6) for comparisons with experimental data.

This scheme relies on static pressure–flow relations in order to calculate the radiated sound pressure in the dynamic problem. Any shortcoming of the static relations would result in differences between the predicted and the directly measured radiated sound pressure, implying a failure of the quasi-steady approximation.

III. EXPERIMENTAL APPARATUS

A schematic of the experimental apparatus is shown in Fig. 2(a). A rubber orifice plate was built to simulate the human vocal-fold geometry, and acted as a constriction to the airflow. Three different orifice geometries (straight, convergent, and divergent) (Fig. 3) were used in the experiments. The orifice plates were molded using a liquid rubber with a room temperature vulcanized catalyst. During molding, two metallic driving rods were inserted within the rubber substrate such that they protruded from each side. These two rods were connected to an eccentric and a shaft entrained by an electric motor. Their movements were synchronized such that they moved in phase. The orifice was forced to open and close periodically at the desired frequency, adjusting the rotational frequency of the motor. Complete closure (with no leakage) was enforced over one portion of the cycle in all cases. The background mechanical noise generated by the motor and other moving parts was measured with the air supply turned off. This so-called ''background'' pressure signal actually included the displacement flow sound related to

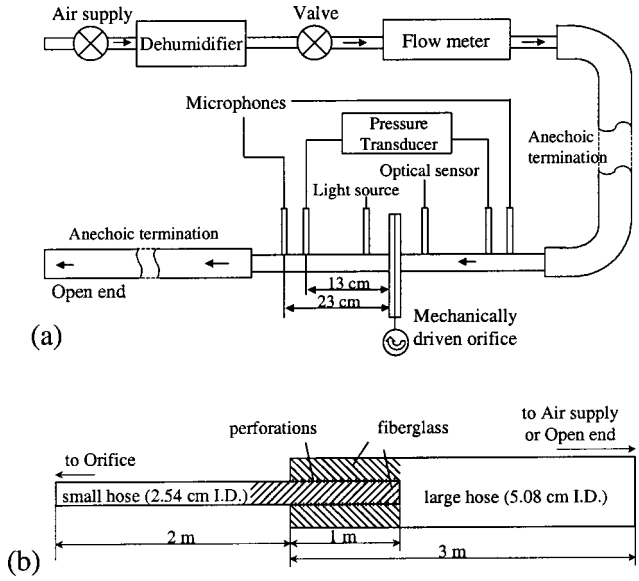

FIG. 2. Schematic of (a) experimental apparatus; (b) anechoic terminations.

the opening and closing of the orifice, which could not be distinguished from the mechanical noise. The amplitude of the background mechanical noise was found to be small compared with the sound generated by the pulsating flow inside the tube. The pressure signals associated with the measured background noise were nevertheless subtracted from measured sound pressures in the presence of airflow, with proper phase reference to the motion of the orifice. This procedure did not affect the signals significantly, as discussed later.

The orifice plate was inserted between two aluminum plates, which hosted the ends of the intake and discharge hoses. Two anechoic terminations were connected to the orifice plate on both sides to reduce possible reflections from either the air supply or the open end. Each anechoic termination was made of two overlapping sections of corrugated, rubber hoses with different inner diameters [Fig. 2(b)]. The smaller hose, having a 2.54-cm inner diameter, was connected directly to one aluminum plate at one end. Near the other end, the smaller hose was perforated and wrapped using fiberglass over a 1-m-long section. This end section was then inserted into a larger rubber hose with a 5.08-cm inner diameter. The junction was sealed to avoid any flow leakage.

The anechoic terminations were designed to minimize sound reflections from the upstream and downstream ends of the tubes. To evaluate their performance, the anechoic terminations (from the second microphone location) were treated as equivalent two-pole black box elements. The reflection factor was measured using the well-known two-microphone method (Seybert *et al.*, 1977). Microphones (B&K 4938), 6 mm in diameter, were mounted on each anechoic termination tube both upstream and downstream of the orifice, with one microphone mounted 13 cm from the orifice and another 23 cm from the orifice. The results are shown in Fig. 4. The measured reflection factor magnitudes of both upstream and downstream anechoic terminations vary between about 0.2 and 0.3 over most of the frequency range. The reflection factor is much larger at low frequency. Further reduction of the reflection factor at low frequency is very difficult with passive methods. The effects of reflection were suppressed using the convolution method discussed in Sec. II D.

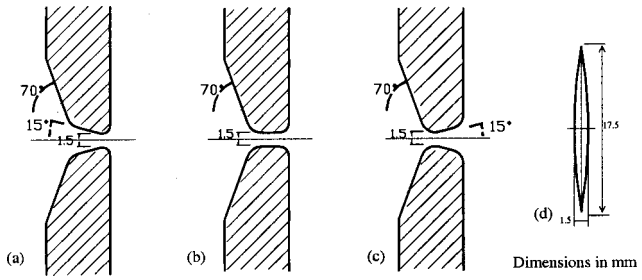

FIG. 3. Cross section of the three orifice passages: (a) convergent; (b) straight; and (c) divergent. The flow direction is from left to right. (d) elevation of the orifice showing the frontal opening area.

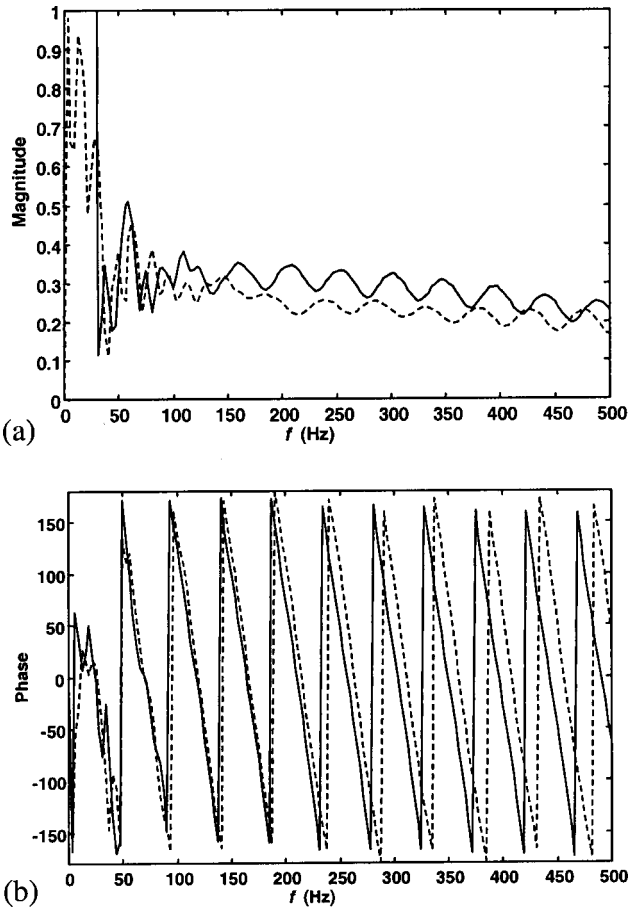

FIG. 4. Reflection factors of the upstream and downstream anechoic terminations. (a) magnitude; (b) phase. ———: upstream; – –: downstream.

To accurately measure the orifice area function, a photoelectric sensor and a light source were installed on opposite sides of the orifice, mounted on the tube walls. The photoelectric sensor signal was calibrated for different orifice openings, using the following approach. A picture of the orifice was made, with a scale placed close to the orifice opening. Numbers of pixels within the orifice opening and within the scale (the area of which was known *a priori*) were then counted using image-processing software. Their ratio is the ratio of the area of the orifice and that of the scale. The value of the orifice area was then calculated. The process was re-

peated nine times for nine different orifice openings. A linear relation between the output electric signal from the light sensor and the orifice area was found. A linear regression (with coefficient of determination $R^2=0.987$) between the light sensor output and the orifice area was obtained for subsequent data processing.

The volumetric flow rate was measured using a precision mass-flow meter (Baratron type 558A). The time-averaged pressure gradient across the orifice was measured using a pressure gauge (Baratron type 220C). The output signals from the microphones and the light sensor were acquired at a sampling rate of 16 384 Hz, using a HP356XA data acquisition system, and saved for subsequent analysis.

IV. RESULTS

The experiments were performed for three different orifice geometries, and mean pressure drops across the orifice of 6-, 9-, and 12-cm H_2O. The upstream and downstream acoustic pressures were recorded together with the mean flow rate through the orifice and the instantaneous orifice area. The experiments were performed at four different frequencies: 70, 80, 100, and 120 Hz. The experimental results for the convergent orifice geometry are discussed first.

A. Steady-state pressure–flow relationship

Steady pressure–flow relationships were obtained. The mean pressure drop across the orifice and the mean volume flow rate through the orifice were measured. The orifice discharge coefficients were then calculated from Eq. (3) and plotted against the Reynolds number, which is defined here based on the inner diameter of the smaller rubber hose d_t ($d_t=2.54$ cm)

$$\mathrm{Re}=\frac{Q_0 d_t}{A_t \nu}, \tag{9}$$

where ν is the kinematic viscosity. The results are shown in Fig. 5 for $\Delta p_0=12$ cm H_2O, and a convergent orifice geometry.

The orifice discharge coefficient increases with the Reynolds number for low Reynolds number flows. At higher Reynolds number, as the flow becomes more turbulent, the orifice discharge coefficient appears to asymptote to a value around 0.86. The pressure–flow relation was found to be repeatable. The effects of the orifice area A_g on the orifice discharge coefficient were found to be negligible (Mongeau *et al.*, 1997). A constant orifice discharge coefficient value of 0.86 was used in the predictions of the acoustic pressure for the convergent orifice (and a similar procedure was followed for the other shapes).

B. Orifice area

The orifice area during one cycle was measured using the photoelectric sensor. Figure 6 shows the orifice area at three different frequencies (80, 100, and 120 Hz), with $\Delta p_0=12$-cm H_2O and a convergent orifice geometry. The maximum orifice area function varied slightly for different frequencies. It generally increased over time during any test. This was most probably due to orifice deformation during the experiments. The duty cycle varied slightly with the orifice geometry. For the same geometry, the duty cycle remained nearly the same for different frequencies. The duty cycle was about 0.6 for the convergent orifice.

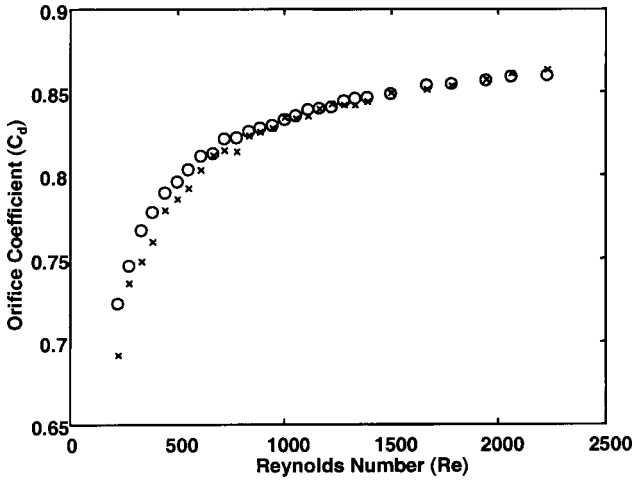

FIG. 5. Static pressure–flow relationship for the fully opened convergent orifice. The orifice discharge coefficient defined by Eq. (3) is plotted against the Reynolds number. Two sets of pressure-flow data were measured, before and after the experiments. xxx: before experiments; ooo: after experiments.

C. Unsteady flow measurements: Acoustic pressure and source volume velocity

Figure 7 shows the unsteady pressures measured upstream and downstream of the convergent orifice, with $f=80$ Hz, $\Delta p_0=12$-cm H_2O. The downstream unsteady pressure signal was multiplied by -1 to facilitate comparisons between upstream and downstream waveforms. Also shown in Fig. 7 are the upstream and downstream background noises measured in the absence of flow with the motor running at the same frequency. These are much smaller than the unsteady pressures with flow. This confirms that the displacement flow, which is included in the background noise, is negligible compared with the dipole contributions. The data were not corrected for the influence of reflections

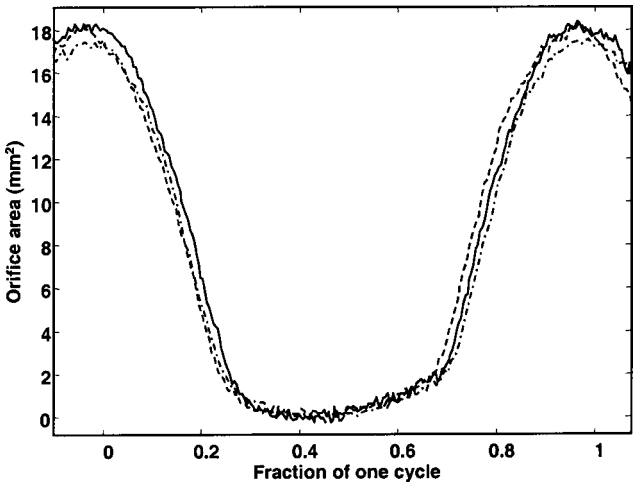

FIG. 6. Typical orifice area function during one cycle. $\Delta p_0=12$-cm H_2O, and convergent orifice geometry. ———: 80 Hz; – –: 100 Hz; — · — · —: 120 Hz.

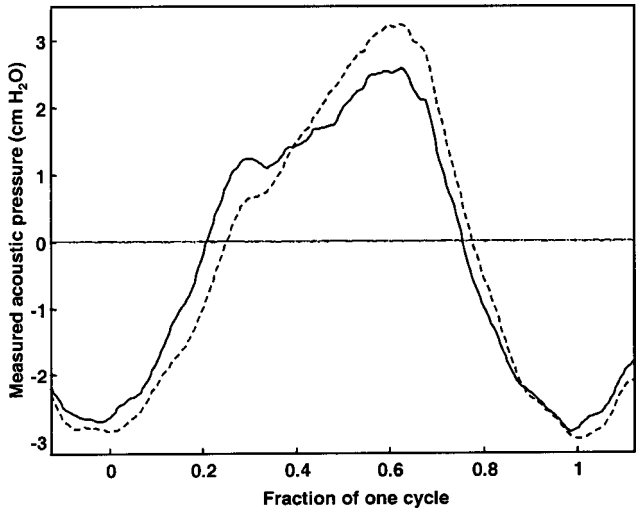

FIG. 7. The measured upstream and downstream unsteady pressure in the convergent orifice case. $f=80$ Hz, $\Delta p_0=12$-cm H_2O. ———: upstream; — —: downstream $\times(-1)$; – –: upstream background noise; --: downstream background noise.

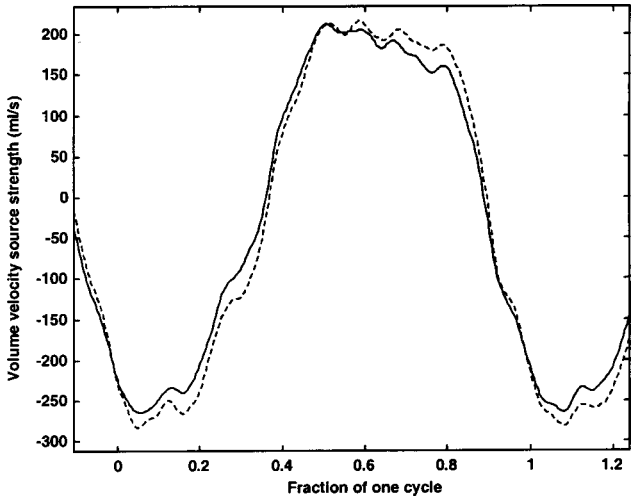

FIG. 8. Volume velocity source strength at the origin calculated based on the measured sound pressure and the reflection coefficient measured simultaneously at the same experiments. $f=80$ Hz, $\Delta p_0=12$-cm H_2O, and convergent orifice geometry. ——: upstream; – –: downstream $\times(-1)$.

off the tube ends in this case. Despite a slight phase difference, the upstream unsteady pressure is nearly perfectly 180° out of phase with the downstream unsteady pressure. The upstream unsteady pressure is generally out of phase with the orifice area (Fig. 6), while the downstream unsteady pressure is in phase with the orifice area, although both acoustic signatures have a slightly different shape from the orifice area function. This is consistent with the postulated dipole source model described in Sec. II.

The relative difference between the upstream and downstream measured sound pressure is quantified by a relative difference factor defined as

$$\Delta_p=\frac{\max(|(-p_{\mathrm{dn}})-p_{\mathrm{up}}|)}{\max(|p_{\mathrm{up}}|)}. \tag{10}$$

This error factor (11.95%) takes into account the possible differences in both the magnitude and the phase of the pressure signals.

The differences in the magnitude and phase between the upstream and downstream sound pressure here are primarily due to reflections from the tube ends at low frequency. As stated before, the upstream and downstream terminations can be modeled as two separate acoustic systems. These two acoustic systems should be excited by the same source strength amplitude according to the equivalent monopole source model. However, the reflection factors R vary with frequency and are different from each other (as shown in Fig. 4). Therefore, the unsteady pressures in these two acoustic systems, due to different standing wave patterns, are different.

Volume velocity sources originating at the orifice for the two acoustic systems should be more representative of source strength than the far-field pressure signals. The velocity source strength is defined as the acoustic volume flow rate at the location of the orifice. There are two volume velocity sources, one upstream and one downstream, each corresponding to one of the two acoustic systems. The source volume velocities can be calculated using Eq. (7) and Eq. (8), based on the measured sound pressure and the reflection coefficient of the corresponding anechoic termination. Figure 8 shows the comparison between the upstream and downstream source volume velocities obtained using the unsteady pressure data of Fig. 7. Again, the downstream velocity source was multiplied by -1 for comparison. The upstream velocity source has the same shape and magnitude as the downstream velocity source, 180° out of phase. Compared with unsteady pressure data, the source volume velocity waveform is more closely matched to the orifice area function. This high correlation confirms that the source of the measured unsteady pressure is mostly the dipole source due to pulsating airflow through the orifice rather than displacement flow due to orifice oscillations.

The relative difference between the upstream and downstream source volume velocities, evaluated as in Eq. (10), was 2.93% for this case. The upstream and downstream source volume velocities were in good agreement for all operating conditions. The relative difference for the volume velocity source strengths (2.93%) is smaller than that for the pressure (11.95%), which is expected as the effects of reflection were eliminated.

The same observations were made for other driving frequencies and mean pressure drops. The upstream and downstream source volume velocities were consistently found to be almost equal in strength and opposite in phase.

D. Quasi-steady model predictions

The upstream unsteady pressure was predicted following the method described in Sec. I E. The predicted upstream unsteady pressure is compared to the measured upstream unsteady pressure in Fig. 9. The frequency was 80 Hz, the mean pressure drop 12-cm H_2O, and the mean flow rate 221 ml/s. A constant convergent orifice discharge coefficient of 0.86 was used. The prediction, based on the quasi-steady approximation, agrees very well with the experimental data. The measured unsteady pressure waveform was successfully reconstructed from the orifice area function, including the

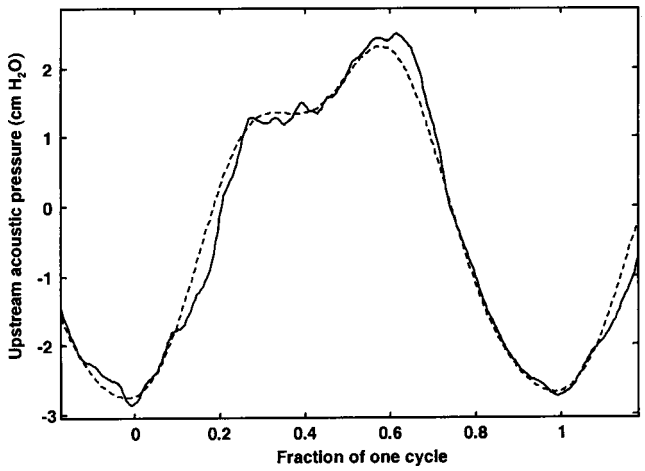

FIG. 9. Comparison between the measured upstream sound pressure and that predicted from the monopole source model and quasi-steady approximation. $f=80$ Hz, $\Delta p_0=12$-cm H_2O, and convergent orifice geometry. ———: measured; – –: predicted.

effects of reflections. The relative difference between the measured and predicted upstream sound pressure for different operating conditions, quantified by a relative error factor, was about 3.43%.

There are several possible causes for the discrepancies between the predictions and the measured data. In the predictions, the high-frequency components were discarded to ensure convergence of the iterative method. Evidently, high-frequency components are missing in the predictions. Second, as discussed before, the contributions of turbulence to both the dipole and quadrupole sources were neglected in this study. The model therefore could not capture their contributions, which are generally small and occur mostly at high frequency. The experimental determination of the reflection factors of the two anechoic terminations R is also a significant source of error. The reflection factors play an important role in the prediction procedure, and any error in this quantity is amplified by the iteration process.

The mean flow rate can be calculated from Eq. (4), with the centerline velocity U_c calculated from Eq. (5). The relative difference between the measured and predicted mean volumetric flows was about 2.58%, which was deemed acceptable.

A similar agreement was also obtained for the other operating conditions at different driving frequencies and mean pressure drops in the comparisons between the measured and predicted unsteady pressures and mean flow rates. At 100 Hz, the relative differences between the measured and predicted upstream acoustic pressure were less than 7.20%; the relative differences between the measured and predicted mean volumetric flow rates were less than 5.69%. At 120 Hz, the relative differences were less than 3.90% between the measured and predicted acoustic pressure, and less than 5.09% between the measured and predicted mean volumetric flow rates.

V. DISCUSSION

A. Influence of orifice geometry

The same measurements were repeated for straight and divergent orifice geometries at different operating conditions. The upstream and downstream unsteady pressures were measured, and the volume velocity of the source was deconvolved from the pressure data. The unsteady pressure was predicted based on the quasi-steady approximation and the equivalent monopole source model, and then compared to the experimental data. Typical results are shown in Fig. 10 and Fig. 11 for straight and divergent orifice geometries, respectively.

Good agreements between source volume velocities (within 3.5%), between measured and predicted pressures (within 7%), and between mean flow rate (within 8%) were obtained both for the straight and divergent orifice geometry cases. The effects of orifice geometry on the quasi-steady behavior were insignificant.

B. Influence of mean pressure drop

The influence of the mean pressure drop on sound production is governed by Bernoulli's equation. The amplitude of the generated sound should increase as the square root of the mean pressure drop [Eqs. (1), (4), and (8)]. Figure 12 shows the dimensionless volume velocity source strength for mean pressure drops of 6-, 9-, 12-cm H_2O. The data shown are for 120 Hz and the straight orifice geometry. The source volume velocity was nondimensionlized using the square root of the mean pressure drop across the orifice. The good collapse of the data also justifies the application of Bernoulli's obstruction theory for steady flow, on which the quasi-steady approximation lies. The slight discrepancy is believed to be due to experimental errors.

C. Influence of frequency

According to the quasi-steady approximation, frequency should have no effect on the sound pressure if the effects of acoustic loading are neglected. The presence of reflections, however, causes a frequency dependent acoustic loading. This colors the acoustic signatures, both upstream and downstream, as shown in Fig. 13(a). In contrast, the source volume velocity should be less dependent, if not independent, of frequency. Figure 13(b) shows the velocity sources at different frequencies, with the mean pressure drop across the orifice kept at 12-cm H_2O (for the straight orifice geometry). The figure shows a reduced dependence of the velocity source strength on the frequency, as expected. The discrepancies are believed to be due mostly, to errors in the reflected wave deconvolution process.

D. Unsteady effects and acoustical resonance

The quasi-steady approximation neglects the effects of flow acceleration and deceleration. These effects might be important at the short instants prior to orifice abrupt closure and opening, at which the derivative of the flow velocity is very large. Bernoulli's equation may not be valid for these

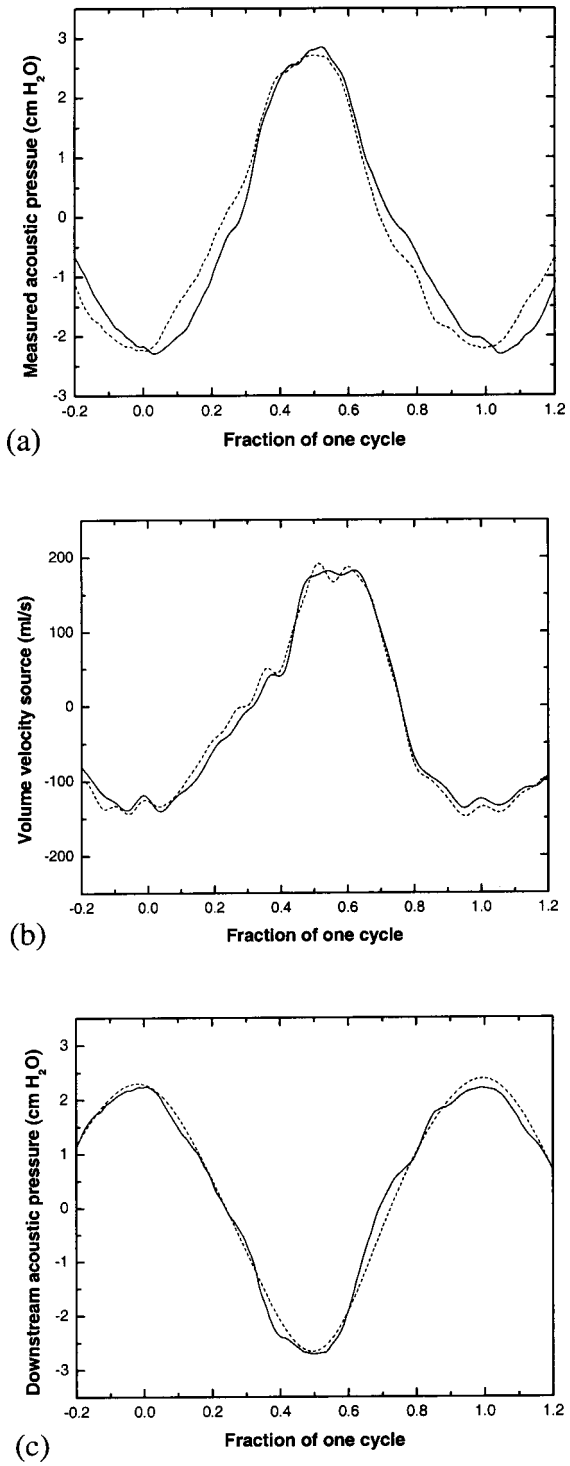

FIG. 10. Experimental results and analysis for straight orifice geometry. $f=120$ Hz, $\Delta p_0=12$-cm H_2O. (a) measured unsteady pressure upstream and downstream of the orifice, with the downstream unsteady pressure multiplied by minus 1 for convenient comparison. ——: upstream; — —: downstream $\times(-1)$. (b) calculated volume velocity source strength, both upstream and downstream. The downstream is again multiplied by minus 1. ——: upstream; — —: downstream $\times(-1)$. (c) comparison between the measured and predicted downstream acoustic pressure. ——: measured; — —: predicted.

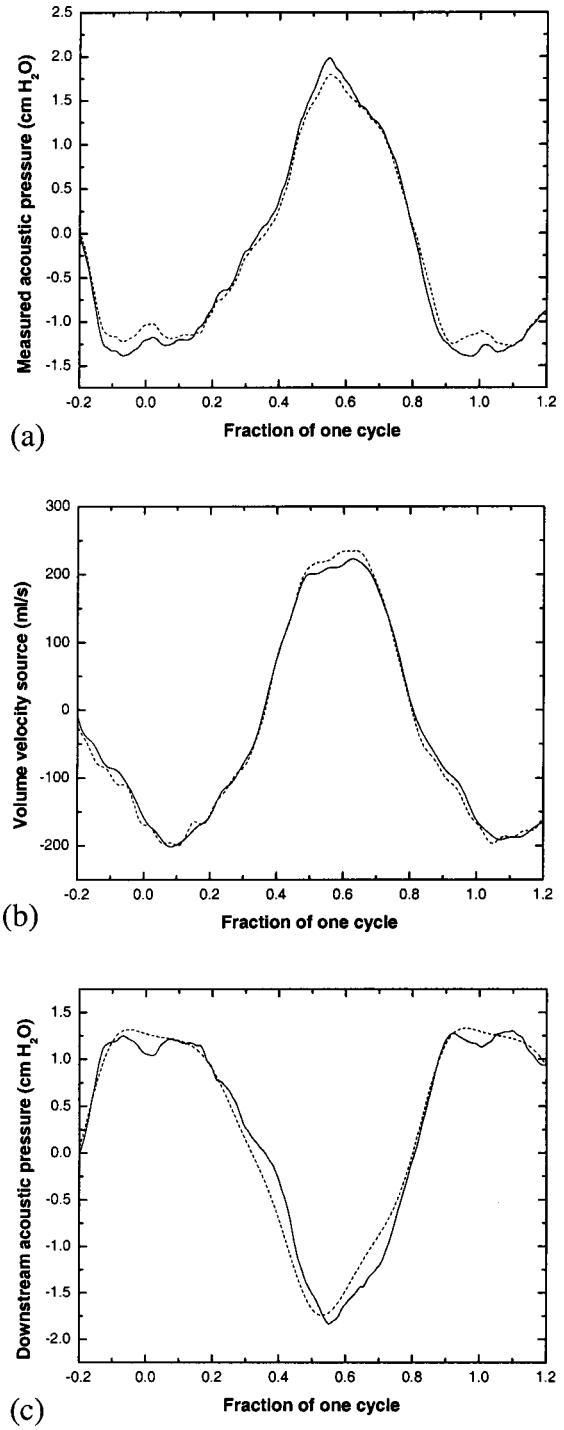

FIG. 11. Experimental results and analysis for divergent orifice geometry. $f=100$ Hz, $\Delta p_0=12$-cm H_2O. (a) measured unsteady pressure upstream and downstream of the orifice, with the downstream unsteady pressure multiplied by minus 1. ——: upstream; — —: downstream $\times(-1)$. (b) volume velocity source strength, both upstream and downstream, with the downstream curve again multiplied by minus 1. ——: upstream; — —: downstream $\times(-1)$. (c) comparison between the measured and predicted downstream unsteady pressure. ——: measured; — —: predicted.

short instants, and viscous effects and acoustic near field must be accounted for to accurately model the flow and sound radiation (Mongeau *et al.*, 1997).

Another situation at which deviations from the quasi-steady behavior may be significant is when the orifice is driven at the formant frequency. Although acoustic effects and source behavior are generally considered to be independent, they are in many ways coupled by a nonlinear relationship between instantaneous transglottal pressure and flow rate. It is anticipated that for frequencies corresponding to

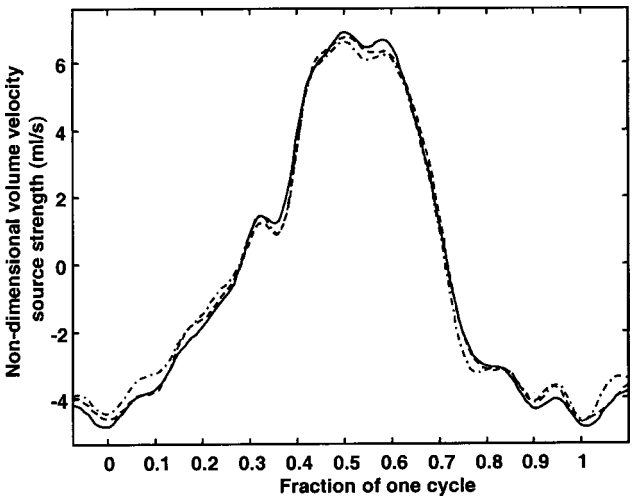

FIG. 12. Volume velocity source strengths at 120 Hz for three different mean pressure drops (6-, 9-, 12-cm H_2O), and straight orifice geometry. The volume velocity source strength is scaled by the square root of the mean pressure drop. ——: 12-cm H_2O; — —: 9-cm H_2O; ---: 6-cm H_2O.

the resonance frequencies of the subglottal tube, there will be a pressure node at the location of the glottis. The transglottal pressure therefore should vanish, or even become negative. It is possible that at resonance some reverse flow might then occur during parts of one glottal cycle, severely distorting the pulsating jet flow behavior. The comparative magnitude of the dipole and monopole contributions may therefore be different. This will be the object of future work.

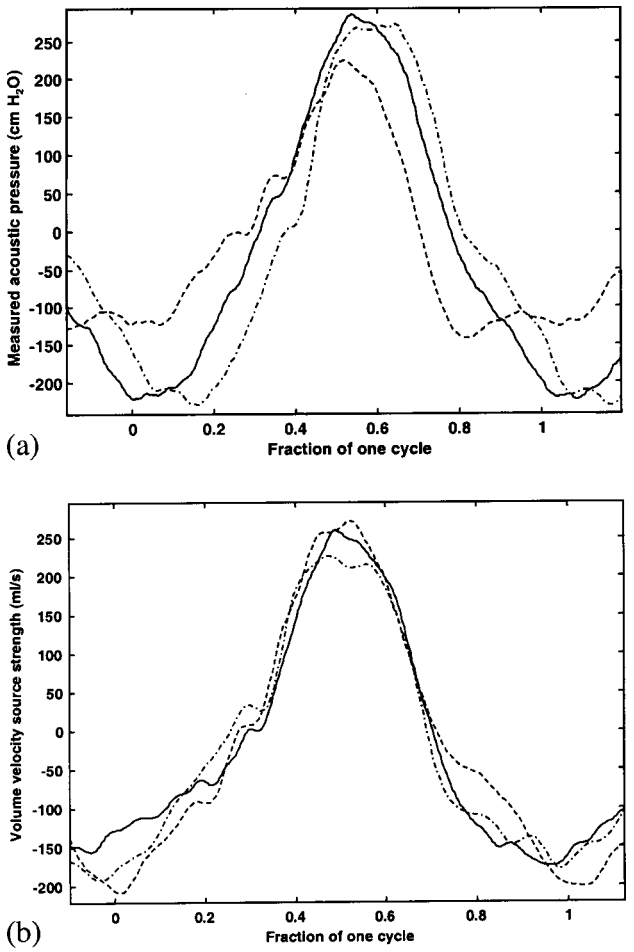

FIG. 13. Volume velocity source strengths for different frequencies. Δp_0 = 12-cm H_2O, convergent orifice geometry. (a) measured sound-pressure data. (b) corresponding volume velocity source strength. ——: 70 Hz; — —: 100 Hz; ---: 120 Hz.

VI. CONCLUSION

The quasi-steady approximation was validated for the tonal component of sound generated by pulsating confined jets. Experiments were performed over the fundamental frequency range extending from 70 to 120 Hz. The radiated unsteady pressure predicted using the quasi-steady approximation and a one-dimensional sound radiation model was found to be in good agreement with experimental data. This implies that monopole and quadrupole components are negligible compared with dipole source mechanisms in pulsating flows (as in voiced sound production), at least at frequencies below a few kilohertz. The orifice oscillation frequency was found to have little effect on dipole sound source strength. Different orifice geometries (straight, convergent, and divergent orifices) simulating the glottis at three different stages during phonation were investigated. The effects of orifice geometry on the quasi-steady behavior of dipole sound generation in unsteady flow were insignificant.

ACKNOWLEDGMENTS

This study was supported by Research Grant No. 5 RO1 DC03577-04 from the National Institute of Deafness and Other Communication Disorders, National Institutes of Health.

APPENDIX: SOUND SOURCES IN SPEECH PRODUCTION

The sound generation mechanisms in confined flows through oscillating orifices may be described theoretically using the Ffowcs Williams–Hawkings (FWH) equation (Ffowcs Williams and Hawkings, 1969). To define the different domains of interest, a detailed view of the presumed source region (around the orifice) is shown in Fig. 14. The fixed cylindrical control volume V' consists of the orifice section, together with the upstream and downstream tubes, including the deformable part of the orifice walls. The source region V includes only the gas within the orifice, and it has a moving boundary. Ideal planar acoustic waves are assumed upstream and downstream of the source region. An observer, or ''virtual microphone,'' is placed in the acoustic far field inside the control volume V', but outside the source region V. The observer can be on either side of the orifice. The

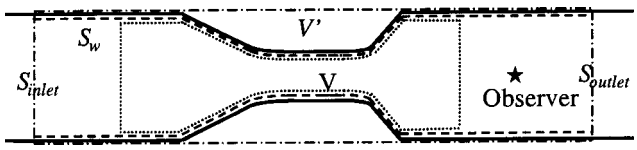

FIG. 14. Integral domains and surfaces for the application of the Ffowcs Williams–Hawkings equation.

surface delimiting the position of the walls is denoted by S_w, with the normal unit vector pointing into the fluid. The FWH equation is

$$\left\{\frac{\partial^2}{\partial\tau^2}-c_0^2\nabla^2\right\}[H(S)\rho'] = \frac{\partial^2}{\partial y_i\partial y_j}[T_{ij}H(S)]-\frac{\partial}{\partial y_i}[F_i\delta(S)]+\frac{\partial}{\partial\tau}[Q\delta(S)], \tag{A1}$$

where $H(S)$ is the Heaviside function, $\delta(S)$ is the Dirac function, and $S(y,\tau)$ is a function describing the geometry of the wall boundary. It is assumed that $S>0$ in the flow region, $S<0$ outside the flow region, and $S=0$ on the boundary. The quantities on the right-hand side of the equation are given by

$$T_{ij}=\rho u_i u_j+\delta_{ij}(p_0+p'-c_0^2\rho')-\sigma_{ij}, \tag{A2}$$

$$F_i[p\,\delta_{ij}-\sigma_{ij}+\rho u_i(u_j-v_j)]\frac{\partial S}{\partial y_j}, \tag{A3}$$

$$Q=[\rho_0 v_i+\rho(u_i-v_i)]\frac{\partial S}{\partial y_i}, \tag{A4}$$

where v_j is the wall velocity, σ_{ij} is the viscous stress tensor, and $\rho'=\rho-\rho_0$ is the fluctuating density.

Assuming a no-slip condition on the wall boundary, and adiabatic compression and rarefaction, the solution to the FWH equation for one-dimensional plane wave propagation in a duct may be written as

$$\begin{aligned} p'(x,t)=&\frac{1}{2A_0c_0}\frac{\partial}{\partial t}\int_V[\rho u_1^2-\sigma_{11}]_{t*}dV && \text{(I)}\\ &-\frac{1}{2A_0}\int_{S_w}[p'\delta_{1j}-\sigma_{1j}]_{t*}n_j \\ &\times\text{sign}(x_1-y_1)dS && \text{(II)}\\ &-\frac{1}{2A_0}\int_{S_w}[\rho_0c_0v_j]_{t*}n_j\,dS && \text{(III)}\\ &+\frac{1}{2A_0}\int_{S_{\text{inlet}}}[c_0^2\rho'+\rho c_0u_1]_{t*}dS && \text{(IV)}\\ &+\frac{1}{2A_0}\int_{S_{\text{outlet}}}[c_0^2\rho'-\rho c_0u_1]_{t*}dS, && \text{(V)} \end{aligned} \tag{A5}$$

where n_j is a unit normal vector directed outwards the flow region, **x** and **y** are the observer and source positions, respectively, $t^*=t-|x_1-y_1|/c_0$ is the retarded time, and V is the source region.

Contributions from four types of sources may be identified. Term I is a quadrupole source related to the turbulent flow and viscous stress inside the tube, specifically the kinetic energy of the fluctuating flow motion along the direction of wave propagation. Term I may be comparatively large when the flow is turbulent. Term II is a dipole source due to the unsteady forces exerted by the walls onto the fluids. The viscous stress components in both terms I and II may be ignored (Zhao, 2001b). Term III is a monopole source due to the motion of the orifice walls. It is sometimes referred to as a "displacement flow." Terms IV and V are monopole sources enforced at the inlet and outlet boundaries. Since the inlet and outlet boundaries are located in the acoustic region, these two monopole sources are image sound sources arising from the interactions between radiated sound waves with the outer boundaries of the domain V'. If the tubes were perfectly anechoically terminated, there would be no reflection from both the inlet and outlet, and terms IV and V would vanish. In the case of imperfect anechoic termination they can be accounted for using a convolution method, as discussed in Sec. II D.

Turbulence may contribute to sound generation, specifically through terms I and II. Term I is the Reynolds stress in the direction of wave propagation. The fluctuating pressure due to turbulence contributes to term II as well. The turbulence-generated sound is mostly of high frequency, and is important to speech quality. However, its magnitude is much smaller than the sound generated by tonal source components. It may therefore be neglected as a first approximation. The contribution of turbulence was the object of a separate study (Zhang *et al.*, 2002).

Based on the above assumptions, Eq. (A5) shows that unsteady flow and orifice wall motion give rise to two types of sound-generation mechanisms. The monopole source, term III, is induced entirely by the oscillation of the orifice wall. Its magnitude increases with orifice velocity, and therefore increases with oscillation frequency. The dipole contribution, term II, is due to the net unsteady force exerted by the walls onto the fluid in the direction of sound wave propagation. It is governed by the pressure drop (or Bernoulli head loss) across the orifice induced largely by the unsteady flow through the orifice, with a very small contribution from the acceleration of the walls. Recent numerical studies of comparable flows (Zhao, 2000; Zhao *et al.*, 2000a, 2000b, 2001a, 2001b) showed that when there is no externally imposed unsteady flow, both the quadrupole term and the dipole term are negligible compared with term III, the monopole source. When an externally imposed unsteady flow is present, however, the dipole source becomes significantly large, as the fluctuating pressure on the walls increases. The monopole source strength was found to increase with the orifice oscillation frequency, while the dipole source contribution remained nearly unchanged as the frequency was varied (Zhang *et al.*, 2001). Therefore, at low frequencies and for an externally imposed unsteady flow, the dipole source dominates, and most of the energy of the radiated sound comes from the unsteady flow contribution in the dipole term. The effects of wall motion are significant only at high frequencies.

In human speech, where unsteady airflow is present, the typical value of fluctuating velocity in glottis is of the order of 40 m/s, and the associated pressure drops are of the order $\frac{1}{2}\rho_0U_c^2\sim 1$ kPa. This value is much larger than the velocity of the vocal-fold walls, which is of the order of 0.1 m/s (for a pitch frequency about 100 Hz and a 2-mm vocal-fold displacement). For planar waves, $p'=\rho_0c_0u'$ and the monopole source pressures ($\sim$45 Pa) are negligible in this case. Therefore, the dipole source is dominant, at least at low frequencies.

Alipour, F., and Scherer, R. C. (**1995**). ''Pulsatile airflow during phonation: An excised larynx model,'' J. Acoust. Soc. Am. **97**, 1241–1248.
Diebold, B., Delouche, A., Dumee, PH., Guglielmi, J.-P., Delouche, P., and Peronneau, P. (**1990**). ''*In vitro* analysis of a model of intracardiac jet: Analysis of the central core of axisymmetric jets,'' J. Biomech. **23**, No. 1, 35–44.
Ffowcs Williams, J. E., and Hawkings, D. L. (**1969**). ''Sound generation by turbulence and surfaces in arbitrary motion,'' Philos. Trans. R. Soc. London, Ser. A **264**, 321–342.
Flanagan, J. L. (**1965**). *Speech Analysis, Synthesis, and Perception* (Springer, Berlin).
Guo, C. G., and Scherer, R. C. (**1993**). ''Finite element simulation of glottal flow and pressure,'' J. Acoust. Soc. Am. **94**, 688–700.
Gupta, S. K., and Schroeter, J. (**1993**). ''Pitch-synchronous frame-by-frame and segment-based articulatory analysis by synthesis,'' J. Acoust. Soc. Am. **94**, 2517–2530.
Iguchi, M., Yamazaki, H., Yamada, E., and Morita, Z. (**1990**). ''Velocity and turbulence intensity in a pulsating jet through a sudden expansion,'' Trans. Jpn. Soc. Mech. Eng. **56**, 1659–1664.
McGowan, R. S. (**1993**). ''The quasisteady approximation in speech production,'' J. Acoust. Soc. Am. **94**, 3011–3013.
Mongeau, L., Franchek, N., Coker, C. H., and Kubli, R. A. (**1997**). ''Characteristics of a pulsating jet through a small modulated orifice, with application to voice production,'' J. Acoust. Soc. Am. **102**, 1121–1133.
Pelorson, X. (**2001**). ''On the meaning and accuracy of the pressure-flow technique to determine constrictions within the vocal tract,'' Speech Commun. **35**, 179–190.
Pelorson, X., Hirschberg, A., van Hassel, R. R., Wijnands, A. P. J., and Auregan, Y. (**1994**). ''Theoretical and experimental study of quasi-steady flow separation within the glottis during phonation. Application to a modified two-mass model,'' J. Acoust. Soc. Am. **96**, 3416–3431.
Pierce, A. D. (**1989**). *Acoustics: An Introduction to its Physical Principles and Applications* (American Institute of Physics, New York).
Scherer, R. C., Titze, I. R., and Curtis, J. F. (**1983**). ''Pressure-flow relationships in two models of the larynx having rectangular glottal shapes,'' J. Acoust. Soc. Am. **73**, 668–676.
Seybert, A. F., and Ross, D. F. (**1977**). ''Experimental determination of acoustic properties using a two-microphone random-excitation technique,'' J. Acoust. Soc. Am. **61**, 1362–1370.
Shadle, C. H., Elliott, S. J., and Nelson, P. A. (**1987**). ''Visualization of the air flowing through a dynamic model of the vocal folds,'' ISVR Technical Report 154.
So, R. M. C., Ahmed, S. A., and Yu, M. H. (**1987**). ''The near-field behavior of turbulent gas jets in a long confinement,'' Exp. Fluids **5**, 2–10.
Titze, I. R. (**1973**). ''The human vocal cords: A mathematical model. I,'' Phonetica **28**, 128–170.
Titze, I. R. (**1974**). ''The human vocal cords: A mathematical model. II,'' Phonetica **29**, 1–21.
van den Berg, J. W., Zantema, J. T., and Doomenbal, P. (**1957**). ''On the air resistance and the Bernoulli effect of the human larynx,'' J. Acoust. Soc. Am. **29**, 626–631.
Wegel, R. L. (**1930**). ''Theory of vibration of the larynx,'' Bell Syst. Tech. J. **9**, 207–227.
Zhang, C., Zhao, W., Frankel, S. H., and Mongeau, L. (**2001**). ''Computational aeroacoustics of phonation: Effect of subglottal pressure, glottal oscillation frequency, and ventricular folds,'' J. Acoust. Soc. Am. **109**, 2412.
Zhang, Z., Mongeau, L., and Frankel, S. H. (**2002**). ''Broadband sound generation by confined turbulent jets,'' J. Acoust. Soc. Am. **112**, 677–689.
Zhao, W. (**2000**). ''A numerical investigation of sound radiated from subsonic jets with application to human phonation,'' Ph.D. thesis, Purdue University, West Lafayette, Indiana.
Zhao, W., Frankel, S. H., and Mongeau, L. (**2000a**). ''Effects of trailing jet instability on vortex ring formation,'' Phys. Fluids **12**, No. 3, 589–596.
Zhao, W., Frankel, S. H., and Mongeau, L. (**2000b**). ''Effects of spatial filtering on sound radiation from a subsonic axisymmetric jet,'' AIAA J. **38**, No. 11, 2032–2039.
Zhao, W., Frankel, S. H., and Mongeau, L. (**2001a**). ''Large eddy simulation of sound radiation from subsonic turbulent Jets,'' AIAA J. **39**, No. 8, 1469–1477.
Zhao, W., Frankel, S. H., and Mongeau, L. (**2001b**). ''Numerical simulations of sound from confined pulsating axisymmetric jets,'' AIAA J. **39**, No. 10, 1868–1874.

Perceptual learning following changes in the frequency-to-electrode assignment with the Nucleus-22 cochlear implant

Qian-Jie Fu,[a] Robert V. Shannon, and John J. Galvin III
Department of Auditory Implants and Perception, House Ear Institute, 2100 West Third Street, Los Angeles, California 90057

(Received 30 September 1999; accepted for publication 25 June 2002)

The goal of the present study was to investigate the time course of adaptation by experienced cochlear implant users to a shifted frequency-to-electrode assignment in their speech processors. Speech recognition performance of three Nucleus-22 cochlear implant users was measured over a 3-month period, during which the implant listeners continuously wore ''experimental'' speech processors that were purposely shifted by 2–4 mm in terms of the frequency-to-electrode assignment relative to their normal processor. Baseline speech performance was measured with each subject's clinically assigned speech processor just prior to implementation of the experimental processor. Baseline speech performance was measured again after the 3-month test period, immediately following the reinstallation of the clinically assigned processor settings. Speech performance with the experimental processor was measured four times during the first week, and weekly thereafter over the 3-month period. Results showed that the experimental processor produced significantly lower performance on all measures of speech recognition immediately following implementation. Over the 3-month test period, consonant and HINT sentence recognition with the experimental processors gradually approached a performance level comparable to but still significantly below the baseline and postexperiment measures made with the clinically assigned processor. However, vowel and TIMIT sentence recognition with the experimental processors remained far below the level of the baseline measures even at the end of the 3-month experimental period. There was no significant change in performance with the clinically assigned processor before or after fitting with the experimental processor. The results suggest that a long-time exposure to a new pattern of stimulation may not be able to compensate for the deficit in performance caused by a 2–4-mm shift in the tonotopic location of stimulation, at least within a 3-month period. [DOI: 10.1121/1.1502901]

PACS numbers: 43.71.Es, 43.71.Ky, 43.66.Ts [DOS]

I. INTRODUCTION

The cochlear implant (CI) is an auditory prosthetic device capable of restoring hearing sensation to profoundly deaf individuals. To provide optimal performance for each patient, modern CI speech processors provide control over the many parameters of electrical stimulation delivered to the cochlea. Results from previous studies have shown significant effects of several parameters in the signal processing (e.g., number of electrodes, frequency-to-electrode assignment) on speech performance in CI listeners (Fishman *et al.*, 1997; Fu and Shannon, 1998, 1999a, b, c; Fu *et al.*, 1998; Lawson *et al.*, 1999; Skinner *et al.*, 1995). However, many of these studies were ''acute'' measures, where subjects had either no time or limited time to adapt to the new patterns of electrical stimulation produced by changes in the speech processor parameters.

It seems plausible that CI listeners will adapt to some degree with long-term exposure to electrically stimulated speech patterns. Many studies have examined the change in performance over time in ''naive'' or newly implanted CI users; these CI users have had to adapt to the differences between their previous experience with normal acoustic hearing and the pattern of activation produced by electrical stimulation. These studies showed that most gains in performance occur in the first 3 months of use (Spivak *et al.*, 1987; Waltzman *et al.*, 1986; George *et al.*, 1995; Gray *et al.*, 1995; Loeb and Kessler, 1995). However, continued improvement has been observed over longer periods of time for some CI users (Tyler *et al.*, 1997).

The effects of learning have also been studied with implant recipients who, although already experienced with the implant device, have had to adapt to new electrical stimulation patterns provided by updated speech processors, speech processing strategies, and/or clinical fitting systems. For most subjects, significant and rapid improvement was observed during the first 3 to 6 months, with little to no improvement observed beyond 6 months (Wilson *et al.*, 1991; Shallop and McGinn-Brunelli, 1995; Dorman and Loizou, 1997; Pelizzone *et al.*, 1999). In general, the learning patterns were similar whether subjects were naive listeners adapting to the new sensory patterns of a cochlear implant or experienced implant users adapting to changes in the speech processor.

The learning capabilities of CI users may alleviate some of the acute effects on speech performance caused by parametric variations of the speech processor. Parametric changes that improve the representation of speech cues may result in

[a]Electronic mail: qfu@hei.org

 0001-4966/2002/112(4)/1664/11/$19.00

an immediate improvement in speech recognition, while changes that degrade the representation of speech cues may produce a temporary deficit in recognition that may be accommodated over time as a CI user becomes more familiar with the new electrical patterns. Thus, it is quite possible that detrimental effects of parametric changes to the speech processor observed in ''acute'' studies may be less significant over time as a CI listener becomes more experienced with the new processor parameters. Previous studies have indeed observed some adaptation to parametric manipulations of the speech processor. One typical example involves adaptation to tonotopically shifted speech processors, in which the frequency-to-electrode assignment was shifted relative to the normal acoustic frequency-to-place mapping. Fu and Shannon (1999a, b) demonstrated that speech performance of CI users was highly dependent on a well-matched (relative to normal) frequency-to-electrode assignment; a tonotopic shift in the frequency-to-electrode assignment resulted in immediate and significant drops in speech performance. However, Rosen *et al.* (1999) observed a rapid accommodation by normal-hearing (NH) subjects listening to frequency-shifted speech via 4-band noise vocoder. They found that speech recognition immediately dropped almost to chance level when the carrier bands were shifted basally by 6.5 mm relative to the analysis bands (1.3–2.9 octaves, depending on frequency). However, after only 3 h of training, the deficit in performance with the shifted speech processor was reduced by half.

Fu and Shannon (1999a, b) also found that CI listeners might at least partly accommodate to the new patterns of speech sounds, even after long-term exposure to their everyday speech processor. In those studies, two hypotheses were proposed to explain how listeners might learn to recognize electrically stimulated speech patterns: tonotopic-matching and accommodation. In the tonotopic-matching hypothesis, the best speech recognition performance is achieved when the frequency information delivered to an electrode is matched to the normal characteristic frequency of the neurons stimulated by that electrode. This mapping is defined as the normal acoustic map. Under the accommodation hypothesis, speech recognition improves over time as the listener gains experience with the spectral information delivered to each electrode by the speech processor. Even if the spectral information is delivered to the ''wrong'' tonotopic location with respect to the normal acoustic map, the listener gradually adapts to the altered pattern (Rosen *et al.*, 1999). This mapping is called the adapted electric map.

While CI users may adapt somewhat to altered speech patterns produced by a less-than-optimal frequency-to-electrode assignment, some issues remain to be addressed regarding listeners' accommodation to spectral mismatches. One issue involves the degree to which learning can compensate for deficits in performance caused by a spectral mismatch. Posen *et al.* (1993) found that, even after considerable training with spectrally altered stimuli, performance with spectrally shifted speech never achieved the baseline levels for unshifted speech stimuli. Rosen *et al.* (1999) reported that, while performance improved with training, NH subjects listening to frequency-shifted speech via 4-band noise vocoder performed below the baseline scores measured with matched analysis and carrier bands. Fu and Shannon (1999a) also measured vowel recognition scores as a function of the analysis filters in both CI users and NH subjects listening to similarly degraded speech. The results showed that the performance functions (percent correct versus tonotopic shift) of CI listeners exhibited a peak well below that of NH subjects listening to similarly degraded speech. However, the overall shape of the functions was similar between the two groups, suggesting that both groups were similarly affected by the tonotopic shift; CI performance was simply shifted downward. Fu and Shannon hypothesized that the difference in peak performance was due to CI users' difficulty in accommodating completely to the tonotopic shift. In general, it is unclear whether CI listeners can completely adapt to spectrally altered speech patterns. The normal ''internal'' representations of speech—which may be defined as the abstract pattern representation unique to phonemes and are derived from life-long experience with the peripheral neural patterns of speech sounds—cannot be completely displaced.

Another issue affecting CI listeners' ability to accommodate spectral mismatches involves the time course over which most learning takes place. In the above-mentioned Rosen *et al.* (1999) study, NH subjects listening to spectrally degraded speech improved from chance-level performance to 50% of the baseline measures within 3 h. Many of the aforementioned studies that tracked performance immediately after implantation found continued significant improvement over the first 6-month period.

The limiting factor of CI users' ability to accommodate new speech patterns may also depend on the input acoustic patterns. While parametric changes in the spectral and temporal resolution of a speech processor may have immediate beneficial or detrimental effects that CI users' may accommodate, the degree and time course of accommodation may ultimately depend on the spectro-temporal resolution of the speech processor. Speech processing strategies that improve the resolution of the input acoustic pattern have shown marked improvements in performance in those patients who switched to the updated processors (Dorman and Loizou, 1997; Pelizzone *et al.*, 1999; Wilson *et al.*, 1991). Skinner *et al.* (1995) found that six out of seven Nucleus-22 implant patients using the SPEAK strategy performed better in vowel tests with frequency allocation Table 7 (120–8600 Hz) than with frequency Table 9 (150–10 832 Hz). In the SPEAK strategy, the frequency allocation tables determine the frequency-to-electrode assignment. Skinner *et al.* argued that Table 7 assigned more electrodes to important frequency regions below 1 kHz, thereby improving vowel recognition. These results suggest that the peak performance or degree of adaptation to spectrally shifted speech may depend on both the degree of mismatch and the resolution of the shifted speech. If implant users have ''infinite'' plasticity, frequency allocations with better spectral resolution (within the speech range) would most likely provide the best performance. However, for severe spectral mismatches, the learning potential may be limited and/or the learning process may be very slow; the benefit of improved spectral resolution may not

TABLE I. Subject information for three Nucleus-22 cochlear implant listeners who participated in the present study. Frequency table refers to the frequency allocation used by the listener in their clinically assigned processor. Insertion depth is reported as the number of stiffening rings outside the round window from the surgical report. A full insertion would be 0 rings out.

Subject	Age	Gender	Cause of deafness	Duration of use	Insertion depth	Frequency table
N3	55	M	Trauma	6 years	3 rings out	7
N4	39	M	Trauma	4 years	4 rings out	9
N7	54	M	Unknown	4 years	0 rings out	9

offset the disadvantage caused by the mismatch, resulting in poor performance.

In summary, adaptation to an altered frequency-to-electrode mapping does not preclude or reduce the relative importance of the various speech processor parameters. However, it is necessary to evaluate the long-term effects of parametric variations on speech performance, especially for those parameters that have a dramatic effect on performance in ''acute'' studies. The goal of this study is to determine whether this parameter's detrimental effect on speech recognition would persist, or whether the listeners would rapidly adapt to the frequency-shifted representation of speech information through their cochlear implants. We hypothesize that the time course and completeness of the accommodation to a shift or distortion in the tonotopic pattern of speech depends on the degree of the shift or distortion. Mild shifts or distortions might result in a rapid and complete accommodation, which more severe shifts or distortions might result in long-term and incomplete accommodation.

II. METHODS

A. Subjects

Three postlingually deafened adults using the Nucleus-22 implant device participated in this study. All had at least 4 years experience using the SPEAK speech processing strategy and all were native speakers of American English. The SPEAK strategy used in the Nucleus-22 processor divides an input acoustic signal into 20 frequency bands, extracts the amplitude envelope from all 20 bands, and then stimulates the electrodes corresponding to the 6 to 10 bands containing the maximum amplitudes (Seligman and McDermott, 1995). The frequency allocation table specifies the frequency range covered by the speech processor and the frequency ranges assigned to each electrode. All implant subjects had 20 active electrodes available for use. Two subjects (N4 and N7) used frequency allocation Table 9 (150–10 823 Hz) in their clinically assigned processor and one subject (N3) used frequency allocation Table 7 (120 Hz–8658 Hz). All participants had extensive experience in speech recognition experiments and were highly familiar with the tasks used in this experiment. Table I contains relevant information for the three subjects and Table II lists cutoff frequencies of frequency allocation Tables 1, 7, and 9.

B. Experimental speech processor mapping

In the Nucleus-22 implant device, the MAP consists of the psychophysical parameters for each individual patient stored in the memory of the speech processor; it is used to accommodate perceptual differences between patients and compensates for differences between electrodes within the same patient. The MAP determines how acoustic information is transformed into the patterns of electric stimulation. A primary function of the MAP is to translate the spectral information found in the incoming acoustic signal into stimulation of the appropriate electrodes. During the clinical fitting, frequency ranges are assigned to the electrodes. The experimental speech processor was implemented in each subject's Spectra 22 speech processor (i.e., hardware device) by assigning frequency allocation Table 1 (frequency range: 75–5411 Hz), thereby shifting the filterbank analysis bands one octave lower for subjects N4 and N7, and 0.68 octave lower for subject N3. In all cases, 20-electrode processors were used; threshold and maximum comfort levels (T- and C- levels) for each electrode as well as the optimal microphone sensitivity were remeasured for each subject prior to the experiment using the clinical fitting system. Subjects volunteered to wear the experimental processor as their ''everyday'' map continuously for a 3-month period, allowing them to experience the new processor in a variety of settings outside the laboratory environment.

C. Test materials

Speech recognition was assessed using four sets of test materials, including two closed-set identification tasks and two open-set recognition tasks. The two closed-set identification tasks included multitalker vowel and consonant identification. Vowel recognition was assessed in a 12-alternative identification paradigm for 12 phonemes, including 10 monophthongs (/i ɪ ɛ æ u ʊ ɑ ʌ ɔ ɝ/) and 2 diphthongs (/o e/), presented in an /h/-vowel-/d/ context (heed, hid, head, had, who'd, hood, hod, hud, hawed, heard, hoed, hayed). The tokens for these closed-set tests were digitized natural productions from 5 men, 5 women, and 5 children, drawn from speech samples collected by Hillenbrand *et al.* (1995). Consonant recognition was assessed in a 16-alternative identification paradigm for the consonants /b d g p t k l m n f s ʃ v z θ dʒ/, presented in an /a/-consonant-/a/ context. Three speakers (1 male, 2 female) produced two exemplars of each consonant. All consonant tokens were recorded at the House Ear Institute.

Two open-set recognition tasks included two sentence tests. Recognition of words in sentences was measured using the Hearing in Noise Test (HINT) sentences (Nilsson *et al.*, 1994) and the DARPA TIMIT acoustic–phonetic continuous

TABLE II. Cutoff frequencies are assigned to each electrode for experimental (Table 1) and clinically assigned (Tables 7 and 9) speech processors. CF0 represents the lower cutoff and CF1 represents the upper cutoff to the most apical electrode in the array. Numbers in the table for CF2–CF20 represents the upper cutoff of the frequency band assigned to successively more basal electrodes.

	Table 1	Table 7	Table 9
CF0	75	120	150
CF1	175	280	350
CF2	275	440	550
CF3	375	600	750
CF4	475	760	950
CF5	575	920	1150
CF6	675	1080	1350
CF7	775	1240	1550
CF8	884	1414	1768
CF9	1015	1624	2031
CF10	1166	1866	2333
CF11	1340	2144	2680
CF12	1539	2463	3079
CF13	1785	2856	3571
CF14	2092	3347	4184
CF15	2451	3922	4903
CF16	2872	4595	5744
CF17	3365	5384	6730
CF18	3942	6308	7885
CF19	4619	7390	9238
CF20	5411	8658	10823

speech corpus (Garofolo *et al.*, 1993). The sentences were of low to moderate difficulty for the HINT materials and of moderate to extreme difficulty for the TIMIT materials.

D. Procedures

Speech recognition with the experimental processor was tested immediately at the time of fitting, then 1, 2, and 4 days after fitting, and weekly thereafter, until the end of the 3-month test period. Speech intelligibility tests using subjects' ''everyday'' speech processor were administered immediately before fitting with the ''experimental'' processor and again immediately after the 3-month experimental period, with no readjustment period.

Each test block included 180 tokens (12 vowels $\times$15 talkers) for vowel identification and 192 tokens (16 consonants$\times$3 talkers$\times$2 exemplars$\times$2 repeats) for consonant identification. On each trial, a stimulus token was chosen randomly, without replacement, and presented to the subject. Following presentation of each token, the subject responded by pressing one of 12 buttons in the vowel test or one of 16 buttons in the consonant test, each marked with one of the possible responses. The response buttons were labeled in an /h/-vowel-/d/ context for the vowel recognition task and /a/-consonant-/a/ context for the consonant recognition task. No feedback was provided to the subjects.

For HINT sentence recognition, a list was chosen pseudorandomly from among 26 lists, and sentences were chosen randomly, without replacement, from the 10 sentences within that list. For TIMIT sentence recognition, a list was chosen pseudorandomly from among 50 lists, and sentences were again chosen randomly, without replacement, from the 20 sentences within that list. The subject responded by repeating the sentence as accurately as possible. Two different sets of 10 HINT sentences and three different sets of 20 TIMIT sentences were used for each testing session. Individual data points represent two runs for both vowel and consonant identification, two runs for HINT sentence recognition (20 sentences), and three runs for TIMIT sentence recognition (60 sentences). No feedback was provided, and subjects were instructed to guess if they were not sure, although they were cautioned not to provide the same response for each guess. Note that TIMIT sentence recognition was not measured for subject N4 because the test materials were not available at that time.

To avoid any differences in performance between subjects due to differences between the headset microphones, all speech tokens were presented via Cochlear's Audio Input Selector (AIS) device; the gain of the AIS was set to maximum. All speech stimuli were presented at a comfortable loudness level and all stimuli were equated in terms of long-term root-mean-square (rms) level.

III. RESULTS

Table III shows the pretesting baseline performance and postexperiment control measures for multitalker vowel and consonant identification, HINT sentence recognition, and TIMIT sentence recognition. The pretest baseline performance was measured immediately before implementing the experimental processor. For this baseline measure, subjects used their everyday clinically assigned SPEAK processors. The postexperiment control performance was measured immediately after reimplementing the clinically assigned SPEAK processors, with no period of adjustment. A Student's t-test on the group scores showed that the postexperiment scores were not significantly different from the preexperiment baseline measures for all speech recognition measures.

Figure 1 shows the individual scores for vowel and consonant phoneme recognition as a function of time. In each panel, the initial three filled symbols represent scores mea-

TABLE III. Pretest baseline and postexperiment control performance for the three subjects with their clinically assigned speech processors. The speech tests were presented at 70 dB SPL.

	Vowels(%)		Consonant(%)		HINT(%)		TIMIT(%)	
Subject	Pre-	Post-	Pre-	Post-	Pre-	Post-	Pre-	Post-
N3	69.5	66.4	74.2	70.3	96.2	96.1	58.9	59.2
N4	81.1	83.6	78.1	84.9	100	100	n/a	n/a
N7	64.5	67.8	70.1	71.1	100	99.0	63.2	62.0
Mean	**71.7**	**72.6**	**74.1**	**75.4**	**98.7**	**98.4**	**61.1**	**60.6**

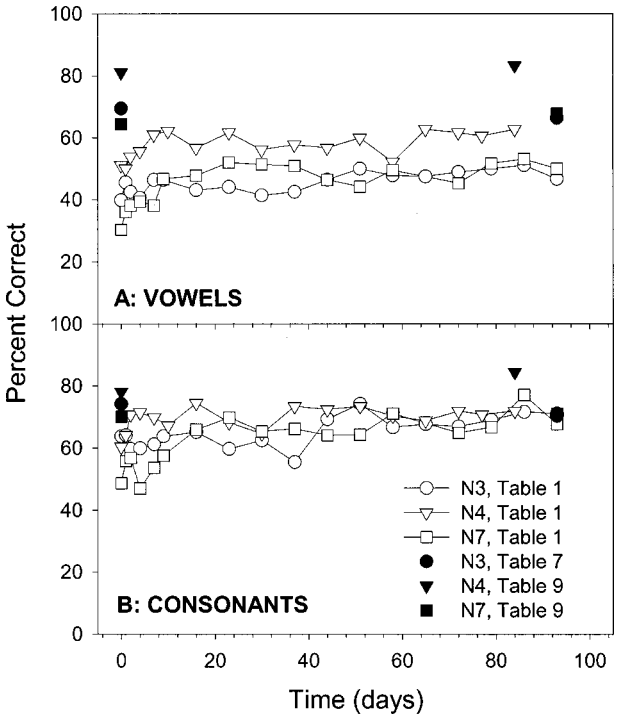

FIG. 1. Vowel and consonant recognition scores as a function of time (postfitting) for the three subjects. The open symbols represent the scores measured with the experimental processor and the filled symbols represent the scores measured with the clinical processor.

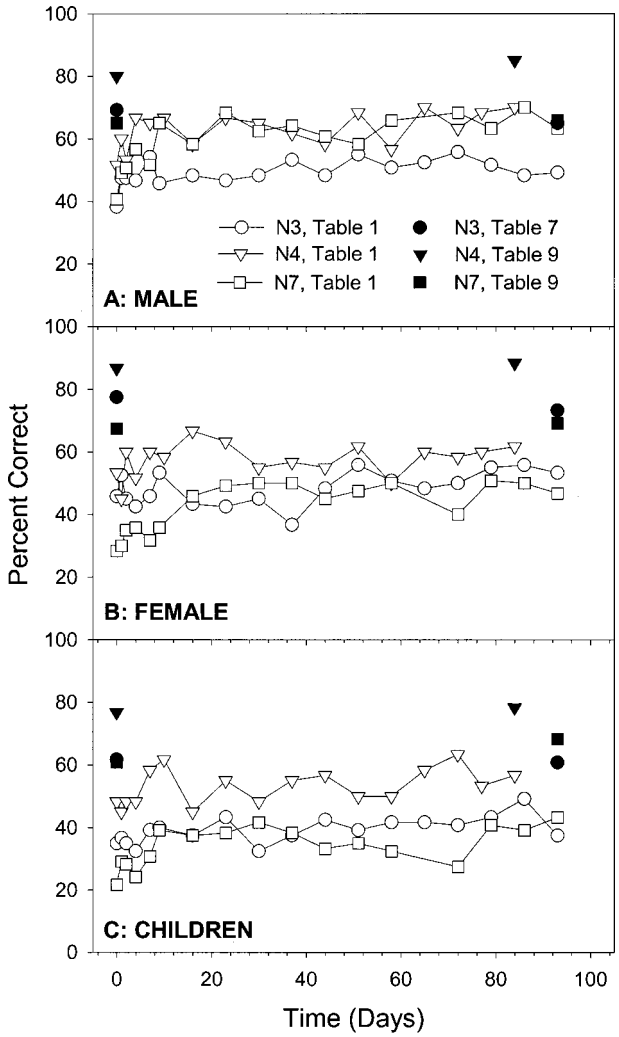

FIG. 2. Vowel recognition scores of male, female, and child talkers as a function of time (postfitting) for the three subjects. The open symbols represent the scores measured with the experimental processor and the filled symbols represent the scores measured with the clinical processor.

sured with the clinical processor just before implementation of the experimental processor. The final three filled symbols represent measurements taken with the clinical processor immediately after reinstallation at the end of the 3-month experimental period. Multitalker vowel identification (top panel) dropped dramatically immediately after implementing the experimental processor; the drop in performance ranged from 29.8 to 34.3 percentage points across listeners, with a mean drop of 31.6 percentage points. The mean deficit gradually reduced to 20.7 percentage points during the first week, after which little significant improvement was observed. An analysis of the variance in these mean deficit scores showed no significant improvement after day 58 [$F(1,5)=2.78$, $p=0.17$], and the asymptotic performance with the experimental speech processor remained significantly lower than the baseline performance ($p<0.001$).

For multitalker consonant identification (bottom panel), a mean drop in performance of only 15.9 percentage points was observed immediately after implementing the experimental processor. The mean deficit reduced to about 10 percentage points after 9 days, and 5 percentage points after 44 days. An analysis of the variance in these mean deficit scores showed no significant improvement after day 44 [$F(1,7)=0.96$, $p=0.36$]. As with vowel recognition, consonant recognition performance with the experimental speech processor remained significantly lower than the baseline performance with the clinically assigned speech processor ($p<0.001$).

Figure 2 shows an analysis of the vowel recognition scores from Fig. 1 according to talker gender. For male talkers (top panel), mean performance dropped 27.8 percentage points immediately postfitting. The mean deficit quickly reduced to 14.7 percentage points after only 3 days of exposure to the experimental processor, then gradually reduced to about 10 percentage points after 3 months of exposure. However, an analysis of the variance in these mean deficit scores showed no significant improvement after day 22 [$F(1,10)=3.24$, $p=0.11$]. A Student's t-test on deficit scores further showed that subject N7 achieved an asymptotic performance level similar to the baseline score measured with his clinically assigned speech processor ($p>0.05$). For female talkers (middle panel), mean performance dropped 34.7 percentage points immediately postfitting; female vowel identification scores remained about 22 percentage points lower than the prefitting baseline performance, even after 3 months of exposure to the experimental processor. An analysis of the variance in these mean deficit scores showed no significant improvement after day 44 [$F(1,7)=2.21$, $p=0.19$]. Similarly, the mean drop in vowel identification for child talkers (bottom panel) reduced from 31.4 percentage points immediately postfitting to about 20 percentage points

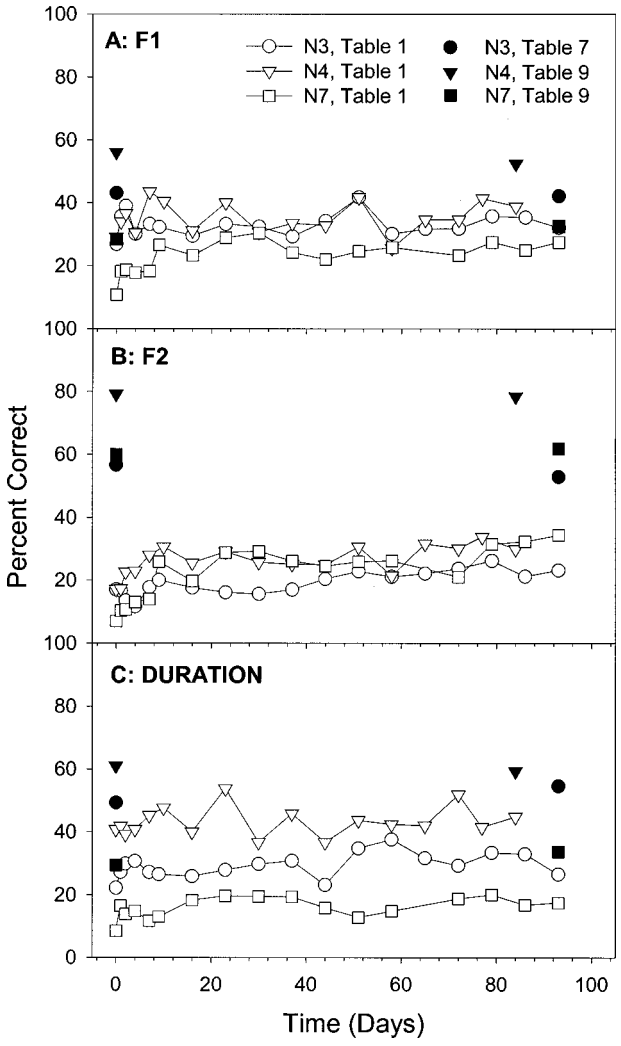

FIG. 3. Vowel information received according to the features of first and second formants ($F1$ and $F2$) and vowel duration, as a function of time (postfitting) for the three subjects. The open symbols represent the scores measured with the experimental processor and the filled symbols represent the scores measured with the clinical processor.

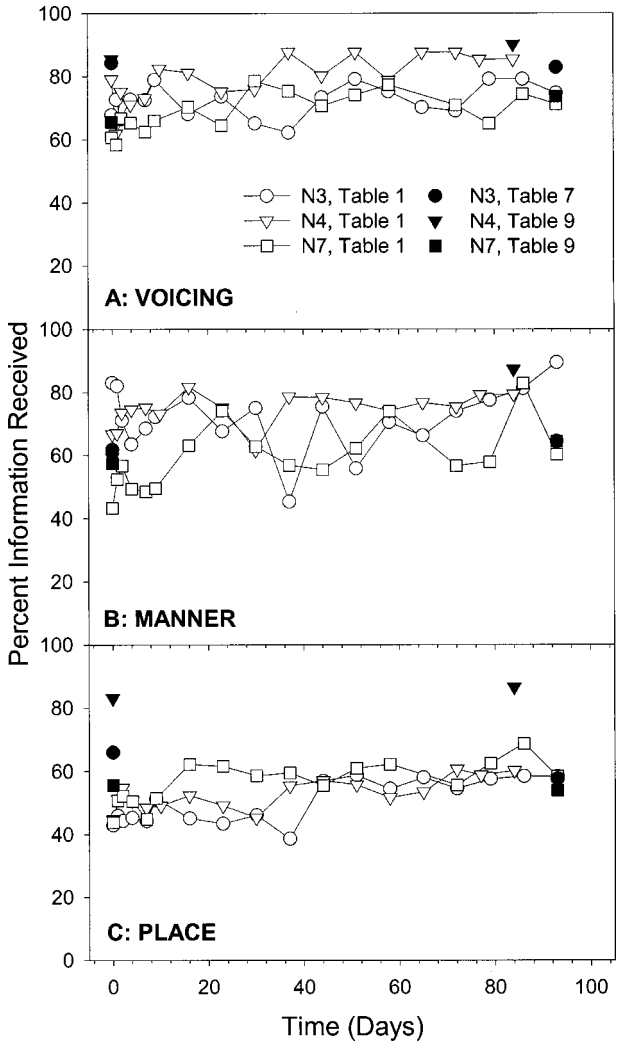

FIG. 4. Consonant information received on the production-based features of voicing, manner, and place as a function of time (postfitting) for the three subjects. The open symbols represent the scores measured with the experimental processor and the filled symbols represent the scores measured with the clinical processor.

after 7 days of exposure, after which no further improvement was observed [$F(1,13)=1.94$, $p=0.19$].

Figure 3 presents further analysis of the vowel recognition scores from Fig. 1 according to the following vowel features (Skinner *et al.*, 1996): duration, tongue height ($F1$), and tongue position ($F2$). Tongue height is associated with the acoustic frequency (Hz) of the vowel first formant ($F1$), and the tongue position, from the front to back of the oral cavity, is associated with the distance between the second ($F2$) and first formant ($F1$). For $F1$ information received (top panel), the mean drop in performance was 20.2 percentage points immediately postfitting. After 1 day of exposure to the experimental processor, the deficit in $F1$ information received reduced to 13.2 percentage points, after which no significant improvement was observed [$F(1,16)=1.62$, $p=0.22$]. Asymptotic performance with the experimental speech processor remained significantly lower than the baseline performance ($p<0.001$). In terms of $F2$ information received (middle panel), mean performance dropped more than 50 percentage points immediately postfitting. The amount of $F2$ information received gradually improved over time and the mean deficit reduced to about 35 percentage points after 3 months of exposure to the experimental processor. An analysis of the variance in these mean deficit scores showed no significant improvement after day 51 [$F(1,6)=4.25$, $p=0.09$] and the asymptotic performance with the experimental speech processor remained significantly lower than baseline performance ($p<0.001$). For vowel duration information received (bottom panel), a mean deficit of 22.7 percentage points was observed immediately postfitting. An analysis of the variance in these mean deficit scores showed no significant improvement after day 2 [$F(1,16)=4.06$, $p=0.06$]; asymptotic performance with the experimental speech processor remained significantly lower than baseline performance with the clinically assigned speech processor ($p<0.001$).

Figure 4 presents a feature analysis of the consonant recognition scores shown in Fig. 1 as a function of time, according to the production-based categories of voicing, manner, and place of articulation (Miller and Nicely, 1955).

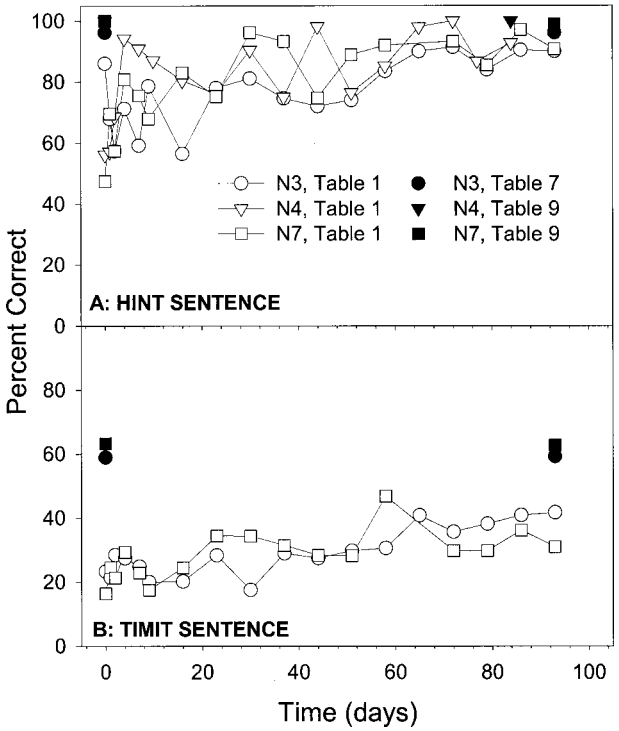

FIG. 5. HINT and TIMIT sentence recognition scores as a function of time (postfitting) for the three subjects. The open symbols represent the scores measured with the experimental processor and the filled symbols represent the scores measured with the clinical processor.

In terms of voicing information received (top panel), mean performance dropped 9.2 percentage points immediately post-fitting. There was no significant improvement after 1 month of exposure [$F(1,9)=3.27$, $p=0.11$]; however, asymptotic performance with the experimental processor was not significantly lower than the clinically assigned processor ($p=0.07$). A large intersubject variation was observed. Subject N7 actually demonstrated slightly higher reception of voicing information when using frequency Table 1, while subject N3 remained slightly lower. A significantly different recognition pattern was observed in the reception of manner cues (middle panel). Manner reception actually improved by 5 percentage points immediately postfitting; after 3 months, mean scores were 15 percentage points higher than the initial baseline performance. However, postexperiment control measures made immediately after reimplementing the clinically assigned processor were also 15 percentage points higher than the baseline performance, suggesting that listeners improved in identification of manner cues simply from exposure to the testing. In terms of consonant place information received (bottom panel), mean scores were 24.4 percentage points lower than the baseline scores immediately postfitting. The performance deficit gradually reduced to about 9 percentage points after 3 months of exposure to the new processor. An analysis of the variance in these on mean deficit scores showed no significant improvement after day 44 [$F(1,7)=4.46$, $p=0.08$]; here, asymptotic performance with the experimental speech processor remained significantly lower than the baseline performance with the clinically assigned speech processor ($p<0.001$).

Figure 5 shows individual scores for HINT and TIMIT sentence recognition as a function of time. For HINT sentence recognition (top panel), a mean drop of 35.6 percentage points was observed immediately following implementation of the new speech processor. The deficit reduced to about 20 percentage points after 1 week of exposure to the new processor and to about 10 percentage points 1 month later, after which no improvement was observed [$F(1,9)=3.92$, $p=0.08$]. Asymptotic performance with the experimental speech processor remained significantly lower than baseline performance ($p<0.001$). For TIMIT sentence recognition (bottom panel), a mean drop in performance of 41.2 percentage points was observed immediately postfitting with the experimental processor. Note that only two subjects' data are available (TIMIT recognition scores were not measured in subject N4 because the test materials were not available at that time). The mean deficit for TIMIT sentences reduced to about 27 percentage points after 37 days of exposure to the new speech processor, after which no improvement was observed [$F(1,8)=4.42$, $p=0.07$]. Again, asymptotic performance with the experimental speech processor remained significantly lower than baseline performance with the clinically assigned speech processor ($p<0.001$).

IV. DISCUSSION

The data from the present study show that all subjects exhibited significantly better speech recognition scores after 3 months of exposure to the experimental speech processor than those measured immediately postfitting, consistent with results from the previous learning studies (Wilson *et al.*, 1991; Shallop and McGinn-Brunelli, 1995; Dorman and Loizou, 1997; Pelizzone *et al.*, 1999), indicating that all subjects were capable of learning the spectrally distorted patterns caused by a shifted frequency-to-electrode assignment. However, subjects were not able to completely accommodate to the new speech patterns. After 3 months of daily use, performance with most test materials remained significantly lower than levels measured with the clinically assigned processor.

A. Time course and performance variability

The recovery function shown in the learning curves seems to have been highly dependent on the speech test materials. The amount of adaptation and the rate of recovery were remarkably different for the four speech recognition measures. For example, the mean performance deficits in vowel and consonant recognition were comparable immediately postfitting. Mean vowel recognition remained 20 percentage points lower than the pretest baseline measures after 3 months of exposure (Fig. 1, top). On the other hand, mean consonant scores after 3 months were only about 4 percentage points lower than the pretest baseline measures. For subject N7, consonant recognition gradually reached a performance level similar to the baseline measures. One explanation for this difference might be that the temporal patterns (important for consonant recognition) were much less affected by the mismatched frequency-to-electrode assignment than the spectral patterns (important for vowel rec ognition). A similar disparity in the learning curve was also observed between the HINT and TIMIT sentence materials.

However, the difference in sentence recognition might best be explained by performance ceiling effects associated with the easy HINT sentences.

In addition to being highly dependent on test materials, the learning curves also demonstrated high intersubject and intrasubject variability. For example, subject N7 showed the largest performance deficit in vowel and consonant recognition immediately postfitting, but showed the least performance deficit after 3 months of daily use. In terms of intrasubject variability, speech performance varied significantly from day to day, or week to week. This variability was also somewhat dependent on the speech test materials. For example, the consonant recognition performance of subjects N3 and N4, after significantly improving during the first 2 months of exposure to the experimental processor, actually appeared to slightly deteriorate during the last month of the test period. Similarly, subject N7's performance in TIMIT sentence recognition appeared to drop during the last month of testing, despite continually improving during the first 2 months of exposure to the experimental processor. Overall, performance at the end of the test period was significantly better than that measured at the early stages of learning for all subjects and all test materials. The variation across trials was relatively small for vowel and consonant identification, but high for sentence recognition. This may be due in part to the variability within the acoustic stimuli that comprised the speech test materials. Although all speech materials were equated for long-term rms level, there is much less amplitude variation in the phoneme sets than found in the sentence sets, which can vary greatly within and across sentences. The sentence sets also vary more in terms of overall linguistic complexity than the phoneme sets.

B. Familiarization and adaptation periods

Despite the high variation across subjects and trials for all test materials, the learning curves can be characterized by two distinct periods, which we term familiarization and adaptation. For most measures, performance improved significantly during the first several days or weeks, after which a relatively slow improvement or no improvement was observed. In this initial period, because the new patterns of electric stimulation were very different from previous patterns to which the implant listeners were accustomed, subjects were forced to ''familiarize'' themselves with the characteristics of these new patterns. The familiarization process might be compared to the experience of adjusting to someone who speaks with a heavy accent; word recognition might be relatively poor at first, but after a short time, recognition can improve considerably. This familiarization process was also reflected in the speech quality reported by these subjects. All subjects reported that speech sounded ''really strange'' immediately after implementing the experimental processor. However, the ''strange''-sounding speech was reported as sounding much more ''natural'' after only several days of exposure. This recovery of natural-sounding speech possibly indicated that the familiarization period was over.

Following the familiarization process was a period of longer-term adaptation. In this period, although the speech had achieved a natural sound quality, the spectral patterns delivered to the electrodes remained dramatically different from those of the clinically assigned processor. While the relative tonotopic distribution of excitation may have been similar between the clinical and the experimental processors, the speech patterns were being delivered to a more basal distribution of electrodes. In their everyday use of the experimental processors, subjects had to adapt to the new patterns of speech sounds by use of feedback from the talker or other means (such as lipreading). The adaptation process was relatively slow when compared to the familiarization process.

C. Spectral resolution and spectral mismatch

Skinner *et al.* (1995) found that frequency allocation Table 7 provided better vowel recognition than the clinically recommended Table 9 for several CI listeners. They speculated that vowel recognition improved due to the fact that Table 7 provided more analysis bands in the speech frequency range, thus improving spectral resolution in this frequency range. Svirsky and Meyer (1997) provided a mathematical model that predicted vowel recognition, given a frequency allocation and fundamental auditory resolution of an implant listener. The model also predicted improved performance with Table 7 because Table 7 maps a more restricted frequency range (although one that covers the relevant speech spectrum) onto more electrodes than Table 9, expanding the cochlear representation and thus providing better discrimination for formant frequencies. Based on this hypothesis, frequency allocation Table 1, used in the present experimental processors, expands the key speech frequency range even more in terms of cochlear distance and, given an implant listener with ''unlimited'' neural plasticity, could have resulted in even higher levels of vowel perception. However, the data from the present study clearly demonstrated that, even after 3 months of daily use, speech recognition with most test materials remained significantly lower than the performance levels measured with the ''everyday'' clinically assigned processor. Recently, Svirsky *et al.* (2001) developed a mathematical model of speech perception by cochlear implant users (the MPI model) to estimate the maximum vowel identification scores that could be obtained from cochlear implant users, based on their measured electrode discrimination abilities. They found that seven out of eight subjects initially performed significantly worse than the maximum estimates (or ''psychophysical ceilings'') provided by the MPI model. However, all subjects reached these ceilings after a few months of experience with their cochlear implants. They suggest that, when the spectral mismatch is not too pronounced, users of cochlear implants may be able to adapt to it.

These results suggest that there is probably a limited range of spectral shifting over which alternate representations may be learned (at least in a 3-month period). The best-matched frequency region may only tolerate limited distortion to a given spectral pattern, beyond which even extended learning may not be sufficient to accommodate radically shifted spectral patterns. Fu and Shannon (1999a, b) proposed two hypotheses—tonotopic matching and accommodation—to explain how CI listeners might develop ''internal'' representations of electrically stimulated speech

patterns. In the tonotopic-matching hypothesis, the best speech performance is achieved when the acoustic frequency information is delivered to an electrode that stimulates neurons in the correct cochlear location for that frequency. Even though the best speech recognition occurs with tonotopic matching, there is a range (~3 mm) of frequency-to-electrode mismatch that can be tolerated without compromising speech perception. Fu and Shannon suggest that this ±3-mm tolerance is due to the central pattern recognition accommodating to the normal variation across talkers, from low-pitched males to high-pitched children. Although the precise location of the electrodes along the longitudinal axis of the scala tympani is difficult to determine accurately (Ketten *et al.*, 1998; Skinner *et al.*, 1994), an estimation of the location can be obtained from Greenwood's (1990) formula based on the reported insertion depth of the electrode array. Some degree of spectral mismatch is unavoidable because of the limited electrode insertion depth and the spacing of electrodes along the array. Some of the variation in performance across cochlear implant listeners may be due to the relative location of the electrodes and frequency assignments relative to the normal acoustic map. CI listeners whose map is within 3 mm of the acoustic map may be able to adapt relatively quickly to the pattern of information provided by the implant. CI listeners whose map is more than 3 mm from the acoustic map might have low performance and long adaptation times. The present results show incomplete adaptation to a map that was intentionally misadjusted even after 3 months of daily use.

Under the accommodation hypothesis, speech recognition improves over time as the listener gains experience with the spectral information delivered to each electrode by the speech processor. Even if the spectral information is delivered to the ''wrong'' tonotopic location with respect to the normal acoustic map, the listener gradually adapts to the altered pattern (Rosen *et al.*, 1999), which then becomes the ''internal'' representation for that person. This mapping is called the adapted electric map. Previous ''acute'' studies suggest that implant listeners do adapt to the frequency-to-electrode map in their processor over time, as illustrated by the fact that subjects who have dramatically different electrode insertion depths use similar frequency-to-electrode assignments to obtain the best performance (Fu and Shannon, 1999a, b). In the present study, subject N3 used frequency allocation Table 7 in his everyday clinically assigned speech processor, while subjects N4 and N7 used Table 9. Thus, the shift toward Table 1 in the experimental processors was less severe for subject N3 (0.68 octave, compared to 1 octave for N4 and N7). However, subject N3 showed as much, if not more of a performance deficit than the other subjects, immediately after implementing the shifted experimental processor. At the end of the 3-month test period, N3 exhibited a similar degree of accommodation as the other two subjects, both in terms of overall performance and in rate of improvement. The relative shifts from the adapted electric map (Table 7 to Table 1 versus Table 9 to Table 1) may not have been large enough to produce any marked differences in performance.

The data from the present study also indicate the strong contribution of tonotopic matching to speech performance. If speech performance was limited by the adapted electric map, subjects with different electrode insertion depths should have shown similar improvement over time. Although the general pattern of the learning curve was similar across these three subjects, some intersubject differences indicate that speech performance might have been affected by the degree of tonotopic mismatch. As shown in Table I, subject N7 had a full insertion depth, while subjects N3 and N4 had 3 and 4 rings out, respectively; therefore, the location of electrode array was 2.25 to 3 mm deeper for subject N7 than for the other subjects. According to the tonotopic-matching hypothesis, frequency allocation Table 1 should provide less of a mismatch between the acoustic information and the electrode locations for subject N7 than for subjects N3 and N4. The results did show that the deficit between the asymptotic performance with the experimental processor and the pretesting baseline performance was smaller for subject N7 than for subjects N3 and N4 in most measures. A clear example is shown in the vowel scores of male talkers (see Fig. 3, top). Thus, it is possible that the degree of tonotopic mismatch might affect how completely CI users were able to accommodate the frequency-shifted experimental processor during the 3-month period.

D. Baseline performance versus postexperiment measures

It was somewhat surprising that there was no significant difference between the pretest baseline performance and the postexperiment control performance measured with the clinical processor (see Table II). Subjects were able to improve their performance by adapting to the new patterns of electric stimulation of the experimental processor, yet also maintained the performance levels achieved with the previous patterns of stimulation delivered by the clinically assigned processor. This result raises the question of how learning and adaptation affect well-ingrained internal representations of frequency space. Does the new map of internal frequency space supplant the previously learned map, or can two maps coexist? If there can be only one map at a time and the experience with the experimental MAP had gradually shifted the internal representation of frequency space, then we would expect a reduction in performance when subjects were returned to the original clinically assigned map. But, the fact that there was no significant performance drop immediately following the reinstallation of the clinical processor suggests that the internal representation had not been significantly reshaped, or that multiple maps can coexist. The improvement in speech performance observed with the experimental processor may have caused only a temporary shift in the internal representation of frequency space, or only mildly influenced the internal map. As a new internal representation becomes established, it is possible that the previous map is not ''erased,'' but that both maps exist with differing saliencies. As more experience with the new representation is gained, that new representation may become dominant and the old representation may gradually weaken. It is also possible that once an internal representation were sufficiently ''ingrained'' it might not weaken from disuse.

Clearly, 3 months was not enough time to either fully modify the old internal representation or establish equivalent performance with a new internal representation. Over a longer (perhaps much longer) time course these CI users may have been able to either establish the new internal representations or access both new and old representations with relative ease. It is possible that postlingually deafened implant patients start to establish an alternate representation when they first begin to experience electrical stimulation immediately after implantation. The new patterns of stimulation are learned in comparison to the existing patterns learned during their previous experience with normal hearing. Once established, the patterns produced by electrical stimulation become the new templates against which parametric changes in the speech processor are compared, which in turn are always compared to the speech patterns that were experienced in normal hearing. Recent results with children (Eisenberg *et al.*, 2000) suggests that in a normal-hearing child the original learning process can take more than 7 years to establish. If this is the case, then establishing a secondary template as an adult might take an equally long time, especially if the new pattern is sufficiently different from the original acoustic pattern.

E. Clinical implications

The data from the present study and from previous acute studies of frequency shifting experiments indicate that the interaction between the normal acoustic map and the adapted electric map will significantly affect speech performance in CI listeners. Although CI users may be capable of adapting to any pattern of electric stimulation, the peak level of performance and the adaptation period may depend on how well matched the frequency allocation of the device is to the original acoustic map. A severe spectral mismatch may result in a lower asymptotic level of performance as well as a longer accommodation period. One might expect that designing a filterbank of analysis bands that was well matched to the location of the electrode array for each patient might solve this problem. And, while it is probably true that a frequency allocation based on the normal acoustic map might require a relatively short accommodation period, such an allocation, especially for implant users with shallower insertion depths, might result in a loss of important low-frequency speech information, which cannot be restored by accommodation. The frequency range of the acoustic signal would be more severely restricted than for the clinically recommended frequency allocation range. In such a case, a frequency allocation assignment with a wider overall frequency range and better spectral resolution might provide better performance, despite the spectral mismatch between some analysis and carrier bands.

In a cochlear implant it should also be considered that it is the neurons that define the normal acoustic location, not necessarily the electrode location in the scala tympani. The nerves activated by an electrode might not be exactly adjacent to the electrode's cochlear location, due to the degeneration of peripheral neural processes, current flow pathways, and the geometry of the spiral ganglion in the modiolus. In any case, the trade-off between a tonotopically matched mapping, electrode insertion depth, and adaptation should be carefully considered in the initial fitting of a cochlear implant speech processor.

V. SUMMARY AND CONCLUSIONS

Three Nucleus-22 cochlear implant listeners voluntarily wore a speech processor for a period of 3 months that was purposely shifted in terms of frequency-to-electrode assignment. Results showed that, immediately postfitting, the speech processor with the altered frequency-to-electrode assignment produced significantly lower performance in all measures of speech recognition. Over a 3-month period, recognition scores of consonants and HINT sentences with the experimental processor gradually approached a performance level comparable to the baseline and postexperiment measures made with the clinically assigned processor. In contrast, recognition scores of vowels and TIMIT sentences remained far below the pretest baseline performance for all subjects at the end of the 3-month training period. Postexperiment control measures made immediately following the reinstallation of the clinically assigned processor were not significantly different from the baseline measures made with the clinical processor just prior to the experiment, suggesting that the internal representation of frequency space (spectral patterns) had not been reshaped by 3-months experience with a shifted frequency-to-electrode assignment.

ACKNOWLEDGMENTS

We appreciate the efforts of the three cochlear implant listeners for their tireless and heroic participation in the current experiments. We wish to thank Professor James Hillenbrand for allowing us to use the multitalker vowel test materials. We are grateful to Mario Svirsky and three anonymous reviewers for useful suggestions on an earlier draft of this paper. The research was supported by Grant No. R03-DC-03861 and Contract No. N01-DC-92100 from NIDCD.

Dorman, M. F., and Loizou, P. C. (**1997**). ''Changes in speech intelligibility as a function of time and signal processing strategy for an Ineraid patient fitted with continuous interleaved sampling (CIS) processors,'' Ear Hear. **18**, 147–155.

Eisenberg, L., Shannon, R. V., Martinez, A. S., Wygonski, J., and Boothroyd, A. (**2000**). ''Speech recognition with reduced spectral cues as a function of age,'' J. Acoust. Soc. Am. **107**, 2704–2710.

Fishman, K., Shannon, R. V., and Slattery, W. H. (**1997**). ''Speech recognition as a function of the number of electrodes used in the SPEAK cochlear implant speech processor,'' J. Speech Hear. Res. **40**, 1201–1215.

Fu, Q.-J., and Shannon, R. V. (**1998**). ''Effects of amplitude nonlinearity on phoneme recognition by cochlear implant users and normal-hearing listeners,'' J. Acoust. Soc. Am. **104**, 2570–2577.

Fu, Q.-J., Shannon, R. V., and Wang, X. (**1998**). ''Effects of noise and number of channels on vowel and consonant recognition: Acoustic and electric hearing,'' J. Acoust. Soc. Am. **104**, 3586–3596.

Fu, Q.-J., and Shannon, R. V. (**1999a**). ''Recognition of spectrally degraded and frequency-shifted vowels in acoustic and electric hearing,'' J. Acoust. Soc. Am. **105**, 1889–1900.

Fu, Q.-J., and Shannon, R. V. (**1999b**). ''Effects of electrode configuration and frequency allocation on vowel recognition with the Nucleus-22 cochlear implant,'' Ear Hear. **20**, 332–344.

Fu, Q.-J., and Shannon, R. V. (**1999c**). ''Effect of acoustic dynamic range on phoneme recognition in quiet and noise by cochlear implant listeners,'' J. Acoust. Soc. Am. **106**, L65–L70.

Garofolo, J. S., Lamel, L. F., Fisher, W. M., Fiscus, J. G., Pallett, D. S., and Dahlgren, N. L. (**1993**). ''The DARPA TIMIT Acoustic-Phonetic Continuous Speech Corpus CDROM,'' NTIS order number PB91-100354.

George, C. R., Cafarelli, D., Sheridan, C., and Haacke, N. (**1995**). ''Preliminary findings of the new Spectra 22 speech processor with first-time cochlear implant users,'' Ann. Otol. Rhinol. Laryngol. Suppl. **166**, 272–275.

Gray, R. F., Quinn, S. J., Court, I., Vanat, Z., and Baguley, D. M. (**1995**). ''Patient performance over eighteen months with the Ineraid intracochlear implant,'' Ann. Otol. Rhinol. Laryngol. Suppl. **166**, 275–277.

Greenwood, D. D. (**1990**). ''A cochlear frequency-position function for several species—29 years later,'' J. Acoust. Soc. Am. **87**, 2592–2605.

Hillenbrand, J., Getty, L., Clark, M., and Wheeler, K. (**1995**). ''Acoustic characteristics of American English vowels,'' J. Acoust. Soc. Am. **97**, 3099–3111.

Ketten, D. R., Skinner, M. W., Wang, G., Vannier, M. W., Gates, G. A., and Neely, J. G. (**1998**). ''*In vivo* measures of cochlear length and insertion depth of nucleus cochlear implant electrode arrays,'' Ann. Otol. Rhinol. Laryngol. Suppl. **175**, 1–16.

Lawson, D., Wilson, B., and Zerbi, M. (**1999**). ''Speech processors for auditory prostheses,'' Second Quarterly Progress Report, NIDCD Contract N01-DC-8-2105, Neural Prosthesis Program, Bethesda, MD.

Loeb, G. E., and Kessler, D. K. (**1995**). ''Speech recognition performance over time with the Clarion cochlear prosthesis,'' Ann. Otol. Rhinol. Laryngol. Suppl. **166**, 290–292.

Miller, and Nicely (**1995**). ''An analysis of perpetual confusions among some English consonants,'' J. Acoust. Soc. Am. **27**, 338–352.

Nilsson, M., Soli, S. D., and Sullivan, J. A. (**1994**). ''Development of the Hearing in Noise Test for the measurement of speech reception thresholds in quiet and in noise,'' J. Acoust. Soc. Am. **95**, 1085–1099.

Pelizzone, M., Cosendai, G., and Tinembart, J. (**1999**). ''Within-patient longitudinal speech reception measures with continuous interleaved sampling processors for Ineraid implanted subjects,'' Ear Hear. **20**, 228–237.

Posen, M. P., Reed, C. M., and Braida, L. D. (**1993**). ''Intelligibility of frequency-lowered speech produced by a channel vocoder,'' J. Rehabil. Res. Dev. **30**, 26–38.

Rosen, S., Faulkner, A., and Wilkinson, L. (**1999**). ''Adaptation by normal listeners to upward spectral shifts of speech: Implications for cochlear implants,'' J. Acoust. Soc. Am. **106**, 3629–3636.

Seligman, P. M., and McDermott, H. J. (**1995**). ''Architecture of the Spectra-22 speech processor,'' Ann. Otol. Rhinol. Laryngol. **104** Suppl. 166, 139–141.

Shallop, J. K., and McGinn-Bruncllli, T. (**1995**). ''Speech recognition performance over time with the Spectra 22 speech processor,'' Ann. Otol. Rhinol. Laryngol. Suppl. **166**, 306–307.

Skinner, M. W., Ketten, D. R., Vannier, M. W., Gates, G. A., Yoffie, R. L., and Kalander, W. A. (**1994**). ''Determination of the position of Nucleus cochlear implant electrodes in the inner ear,'' Am. J. Otol. **15**, 644–651.

Skinner, M. W., Holden, L. K., and Holden, T. A. (**1995**). ''Effect of frequency boundary assignment on speech recognition with the SPEAK speech-coding strategy,'' Ann. Otol. Rhinol. Laryngol. Suppl. **166**, 307–311.

Skinner, M. W., Fourakis, M. S., Holden, T. A., Holden, L. K., and Demorest, M. E. (**1996**). ''Identification of speech by cochlear implant recipients with the Multipeak (MPEAK) and Spectral Peak (SPEAK) speech coding strategies. I. Vowels,'' Ear Hear. **17**, 182–197.

Spivak, L. G., Shapiro, W. H., Waltzman, S. B., and Cohen, N. L. (**1987**). ''Cochlear implant performance as a function of time,'' American Speech-Language Association Convention, New Orleans, November 1987.

Svirsky, M. A., and Meyer, T. A. (**1997**). ''A mathematical model of vowel perception by cochlear implantees who use the SPEAK stimulation strategy,'' Association for Research in Otolaryngol., St. Petersburg, FL, 1997.

Svirsky, M. A., Silveira, A., Suarez, H., Neuburger, H., Lai, T. T., and Simmons, P. M. (**2001**). ''Auditory learning and adaptation after cochlear implantation: A preliminary study of discrimination and labeling of vowel sounds by cochlear implant users,'' Acta Oto-Laryngol. **121**, 262–265.

Tyler, R., Parkinson, A. J., Woodworth, G. G., Lowder, M. W., and Gantz, B. J. (**1997**). ''Performance over time of adult patients using the Ineraid or Nucleus cochlear implant,'' J. Acoust. Soc. Am. **102**, 508–522.

Waltzman, S. B., Cohen, N. L., and Shapiro, W. H. (**1986**). ''Long-term effects of multichannel cochlear implant usage,'' Laryngoscope **96**, 1083–1087.

Wilson, B. S., Finley, C. C., Lawson, D. T., Wolford, R. D., Eddington, D. K., and Rabinowitz, W. M. (**1991**). ''New levels of speech recognition with cochlear implants,'' Nature (London) **352**, 236–238.

Benefits of amplification for speech recognition in background noise

Christopher W. Turner and Belinda A. Henry
Department of Speech Pathology and Audiology, University of Iowa, Iowa City, Iowa 52242

(Received 29 January 2002; accepted for publication 12 July 2002)

The purpose of the present study was to examine the benefits of providing audible speech to listeners with sensorineural hearing loss when the speech is presented in a background noise. Previous studies have shown that when listeners have a severe hearing loss in the higher frequencies, providing audible speech (in a quiet background) to these higher frequencies usually results in no improvement in speech recognition. In the present experiments, speech was presented in a background of multitalker babble to listeners with various severities of hearing loss. The signal was low-pass filtered at numerous cutoff frequencies and speech recognition was measured as additional high-frequency speech information was provided to the hearing-impaired listeners. It was found in all cases, regardless of hearing loss or frequency range, that providing audible speech resulted in an increase in recognition score. The change in recognition as the cutoff frequency was increased, along with the amount of audible speech information in each condition (articulation index), was used to calculate the ''efficiency'' of providing audible speech. Efficiencies were positive for all degrees of hearing loss. However, the gains in recognition were small, and the maximum score obtained by an listener was low, due to the noise background. An analysis of error patterns showed that due to the limited speech audibility in a noise background, even severely impaired listeners used additional speech audibility in the high frequencies to improve their perception of the ''easier'' features of speech including voicing. [DOI: 10.1121/1.1506158]

PACS numbers: 43.71.Ky, 43.71.Gv, 43.66.Sr [KRK]

I. INTRODUCTION

There have been a considerable number of recent studies suggesting that the benefits of providing audible speech to listeners with sensorineural hearing loss (as is done by a hearing aid), has limitations. For example, Ching *et al.* (1998) and Hogan and Turner (1998) showed that providing bands of high-frequency speech at audible levels for severe hearing losses often resulted in no increase or even a decrease in speech recognition for some patients. This trend was evident for speech information above approximately 2500–3000 Hz. Turner and Cummings (1999), Skinner (1980), and Rankovic (1991) provided similar evidence that maximizing the amount of audible speech was not always the most beneficial strategy for patients with sensorineural hearing loss. On the other hand, Ching *et al.* (1998) and Turner and Brus (2001) demonstrated that for lower-frequency regions of the speech range, amplifying speech to audible levels consistently provided benefit to all patients.

This linking of a limited benefit for amplification to the degree of hearing loss implies that the degree and type of cochlear damage is an important factor in determining whether audible speech will be beneficial or not. A number of authors (e.g., Van Tasell, 1993; Turner, 1999; Turner and Cummings, 1999; Turner and Brus, 2001; Vickers *et al.*, 2001) hypothesized that these severe hearing losses indicate damage to the inner hair cells. Vickers *et al.* (2001) have also shown limited benefits of amplification and suspected that this occurs when speech is presented to ''dead regions'' of the cochlea. Such damage could interfere with the perception of speech, particularly with the place of articulation feature of speech, which is carried to a large extent by the higher-frequency regions of speech.

All of the above-mentioned studies looked at the recognition of speech in quiet (i.e., no background noise). In the present study we extended this line of research to the situation where speech is presented in a background noise that has a spectrum similar to the speech. The present study determined the ability of hearing-impaired listeners, with a range of hearing loss degrees and configurations, to extract speech information from the audible portion of the speech signal when listening in background noise. At the outset of this study, we quite expected that our results would lead to conclusions similar to the previous research. Since it is well known that listeners with sensorineural hearing loss often have difficulty understanding speech in noisy backgrounds (even when they may do quite well in quiet), our expectations were that the benefits of amplification would again be zero or even negative in some situations (severe loss and high frequencies), perhaps even to a greater extent than in the previous research which measured speech recognition in quiet. However, our original predictions were not realized. In contrast, we found that amplification of speech in a background noise always provided some benefit for listeners with hearing loss, regardless of the degree of hearing loss and/or the frequency region of speech. Although these gains in speech recognition were for the most part small, this contrary finding does provide additional insights into the speech recognition abilities of listeners with sensorineural hearing impairment. It also can serve as a caution in accepting the con-

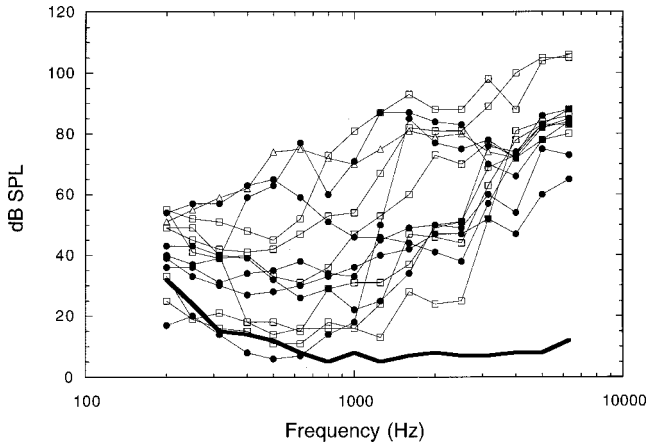

FIG. 1. The pure-tone sensitivity thresholds for the normal-hearing and hearing-impaired subjects in this study. The heavy solid line represents the average thresholds of the normal-hearing subjects. The lighter lines with individual symbols show the thresholds of the hearing-impaired listeners.

clusions of the previous research in too sweeping of a manner.

II. METHODS

A. Subjects

Five normal-hearing listeners and 13 listeners with sensorineural hearing loss were recruited for this study. The normal-hearing subjects had pure-tone sensitivity thresholds better than 20 dB HL (ANSI, 1996) at all octave test frequencies from 250 to 8000 Hz. The 13 listeners with sensorineural hearing loss were specifically recruited to yield a sampling of various degrees of sensorineural hearing loss across the frequency range. The pure-tone thresholds for these subjects are displayed in Fig. 1. The bold line shows the average thresholds for the group of normal-hearing subjects. Each of the lines with symbols represents the thresholds for an individual hearing-impaired subject. All subjects were native speakers of American English. All of the hearing-impaired listeners had bilateral hearing losses and the better ear of each was used for all testing.

B. Stimuli

Pure-tone thresholds were measured at the center frequencies of one-third-octave bands from 200 to 8000 Hz for calculations of speech audibility using the articulation index (AI). Test tones were 500 ms in duration with 25-ms rise–fall times. All testing (thresholds and speech recognition) was done in a sound booth using Sennheiser HD 25-SP supra-aural headphones. All sound levels reported in these experiments are referenced to the levels developed by these headphones in the NBS-9A coupler.

The speech recognition testing in this experiment used the same materials as in our previous studies (Hogan and Turner, 1998; Turner and Brus, 2001). The 12 lists of the Nonsense Syllable Test (NST, UCLA version) were used to measure consonant recognition. These consonants are well-suited to subsequent error pattern analysis. Each of the 12 lists consisted of 21 or 22 consonants presented with a fixed talker (male or female), consonant position (initial or final), and vowel context. One hundred randomly chosen stimuli were presented from each list; thus, a data point for an individual subject in a particular listening condition was based upon 1200 trials. All speech tokens were stored digitally and presented under computer control (Macintosh G4) through a 16-bit digital-to-analog converter (Audiomedia III, Digidesign, Inc.) at a sampling rate of 44.1 kHz with a built-in antialiasing filter set to 20 kHz. For the hearing-impaired subjects, the speech materials were presented through an analog high-pass emphasis spectrum shaper (Altec-Lansing 1753). Several versions of high-pass shaping were employed, as well as a range of presentation levels, chosen to accommodate the variation in hearing-loss configurations across subjects. The high-pass shaping provided from 15–30 dB of relative gain for frequencies above 1000 Hz.

C. Procedures

Pure-tone thresholds were measured using a computer-controlled adaptive procedure that varied tone levels via a Tucker-Davis programmable attenuator (model PATT). A one-up, two-down, four-alternative forced-choice procedure was employed using 2-dB steps and the threshold was taken as the average of the final 8 of 13 reversals of the procedure.

For speech testing, the consonant phonemes were displayed as labeled buttons on a touchscreen (MicroTouch). The subjects were instructed to respond following the presentation of each token by touching the corresponding button on the touchscreen. All subjects first participated in several practice sessions in which they were given feedback and learned to associate the various tokens with the correct consonant response button. For these conditions, speech was presented in a wideband condition (low-pass filtered at 9000 Hz) with no background noise present. Normal-hearing listeners heard the speech at 70 dB SPL without high-pass shaping. The subjects with hearing loss listened to the speech through one of the spectrum shapers, which was chosen on an individual basis, in an attempt to maximize the frequency range for which speech could be made audible. An appropriate presentation level of the speech was also determined at this time by asking the subject to choose the level that ''provided the most information about the speech sounds yet was not uncomfortably loud.'' The chosen spectral level of speech for each subject was then used for a series of low-pass filtered conditions, described below. For several of the more severely hearing-impaired listeners, speech recognition was also obtained at one additional higher speech presentation level in a further attempt to provide maximum speech audibility at the highest frequencies.

Each subject's recognition score for the NST materials was then measured for the broadband condition without background noise. No trial-by-trial feedback was given to the subject for this testing, or for any subsequent testing. The recognition scores in quiet for all the normal-hearing subjects was at least 96%; for the hearing-impaired subjects the mean recognition scores in quiet were 65% (range 51 to 77%).

The background noise was a multitalker babble consisting of both male and female voices played continuously from a compact disk recording throughout each testing session. It

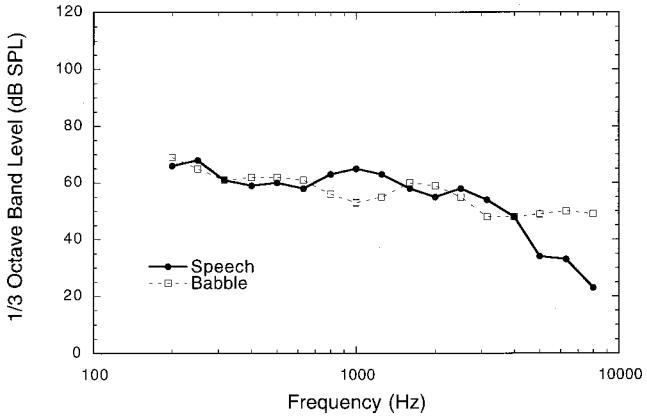

FIG. 2. The long-term average spectra of the NST speech lists and the multitalker babble. For this figure the signals were presented at equal overall sound-pressure levels and were not presented through the spectrum shaper.

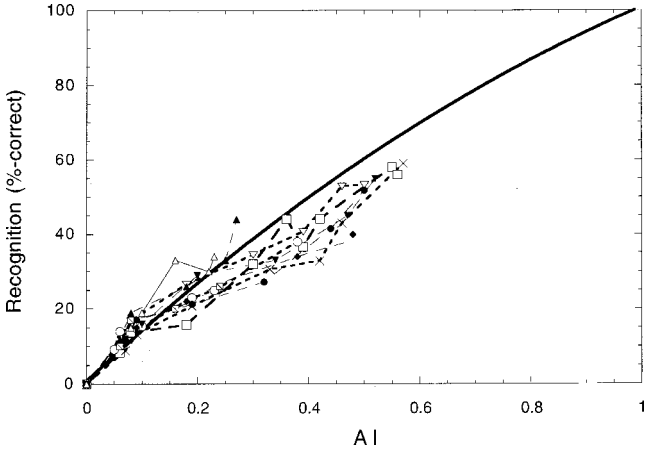

FIG. 3. Recognition in percent correct as a function of the amount of audible speech information (AI) for all subjects. The solid line represents a curve fitted to the normal-hearing subjects's data. The individual lighter lines with symbols represent individual hearing-impaired subjects' data.

was attenuated and mixed with the speech channel prior to any spectrum shaping. Figure 2 displays the long-term spectra of both the concatenated NST stimuli (with no silent spots between tokens) and the babble, as measured at the output of the headphones. For each subject, an appropriate level of background noise was then chosen during some additional pilot testing and was then used for the remainder of the speech recognition testing. Our goal in setting the background noise level was to reduce the subjects' scores in the noise to be approximately two-thirds of their score in quiet, thus providing a consistent reduction of score across subjects. For example, if a subject's score in quiet was 60%, the level of the background noise was chosen to yield a recognition score of approximately 40%. For the normal-hearing listeners, a signal-to-babble ratio of +4 dB provided the appropriate decrease in recognition, and was used for all normal-hearing subjects. The average signal-to-babble ratio for the hearing-impaired subjects was +9 dB (range +4 to +14 dB).

Speech plus background noise was presented to each subject under seven low-pass filtering conditions. The low-pass filter cutoffs were 350, 560, 900, 1400, 2250, 3500, and 5600 Hz, as well as the broadband (9000 Hz) condition. A Kemo (VBF8.04) filter with slopes of 30 dB/octave was used. The order of filter conditions was randomly ordered for each subject.

III. RESULTS

A. Data analysis

The data were analyzed using a method identical to that used in our previous studies (Hogan and Turner, 1998; Turner and Brus, 2001), and the reader is referred to those studies for a more detailed description of the procedures. For each filter cutoff condition, a final recognition score based upon the average of the 12 lists was obtained. A value of articulation index (AI) or speech intelligibility index (SII) was calculated for each listening condition for each subject (ANSI, 1969, R1997) using the subjects' pure-tone thresholds, and the presentation levels of the filtered speech and background noise in that condition. The one-third-octave band AI method using the frequency-importance function for these NST materials was employed. The calculated AI is a value between 0.0 and 1.0 representing the proportion of speech formation available to the listener. Data analysis using the earlier (1969) version is presented in this report; however, we also performed the analysis using the newer version (R1997) and the conclusions are essentially the same. The data were plotted as speech recognition in percent-correct) as a function of the degree of audible speech information (AI). The raw data (percent correct as a function of AI) for all hearing-impaired listeners are displayed in Fig. 3, along with the average articulation function for the normal-hearing listeners. The data for all the normal-hearing listeners were pooled and fit with a second-order polynomial to serve as a reference. The data of the normal-hearing subjects in this study were essentially identical to the normal-hearing subjects of Turner and Brus (2001). In general, all the functions for hearing-impaired subjects show increases in recognition as AI increases.

A second-order polynomial function was also fit to each individual hearing-impaired subject's data. See Fig. 4 for two

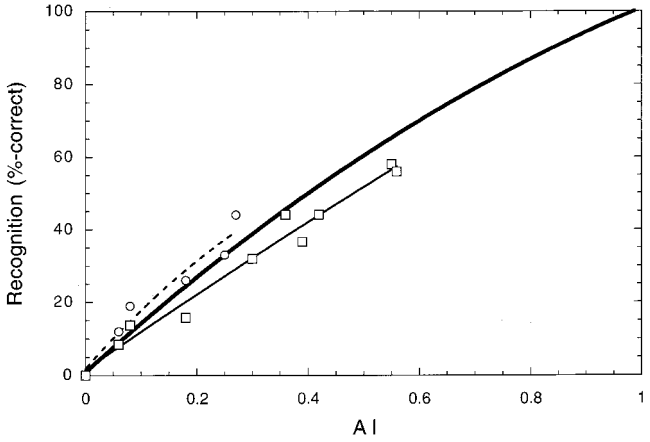

FIG. 4. The articulation functions for the normal-hearing subjects and also for two of the hearing-impaired subjects. The heavy solid line is the fitted curve to the data of the normal-hearing subjects. The two symbol types display the data from the two hearing-impaired subjects. The lighter lines are the fitted curves for those two hearing-impaired subjects.

examples. The dark solid line of Fig. 4 represents the fitted articulation function of the normal-hearing subjects in this study. As the low-pass filter cutoff was increased to 3500 Hz and above, not all hearing-impaired subjects obtained an increase in their calculated audible speech information (AI), particularly if their pure-tone sensitivity thresholds were highly elevated for those higher frequencies (for example, the subject represented by the open circles in Fig. 4). Those data points were not included in this figure or the data analysis. And, the curve fit was based upon fewer than seven data points. For other subjects, as mentioned previously, consonant recognition was measured at an additional higher presentation level, yielding additional data points (for example, the open squares of Fig. 4).

As in our previous studies, the question asked was ''For a given increment of audible speech information presented to a hearing-impaired subject, how will the change in that subject's speech recognition compare to that of a normal-hearing subject receiving the same increment of audible speech information?'' In order to quantify this, we again used the measure of ''efficiency,'' which is simply the ratio of the hearing-impaired listener's recognition improvement to the normal-hearing listener's improvement, measured at the same AI value on each subject's articulation function. All measures of efficiency were calculated from the subjects' fitted curves, as in our previous studies. An efficiency of 1.0 means that for this increment of speech audibility, the listener used the newly audible speech just as well as a normal-hearing listener would. An efficiency of 0.0 means that the listener received no benefit from the audible speech.

The subjects' pure-tone thresholds were known for each one-third-octave band test frequency, allowing one to relate the efficiency for each increment of audible speech to the degree of hearing loss present at the frequencies of the increment. These sensitivity thresholds could then be compared to the values of a large group of normal-hearing listeners who were measured with the same Sennheiser HD-25SP headphones (Hogan and Turner, 1998), to yield the degree of hearing loss. Our increments of speech audibility, obtained by increasing the low-pass cutoff frequency of the filtered speech, were 2 one-third-octave bands wide. For our measure of the degree of hearing loss, the sensitivity threshold was taken as the average of the two bands.

In Fig. 5, the efficiencies of all hearing-impaired subjects for all frequencies are displayed as function of the degree of hearing loss. In every case, for hearing losses up to 90 dB HL, the calculated efficiency was positive, indicating that providing additional audible speech to patients with all degrees of hearing loss provides benefits in speech recognition for speech presented in a background noise.

Of particular interest here are the efficiencies for the higher-frequency regions of speech. Several previous studies, as mentioned above, found negative or zero benefits of audible speech (under quiet listening conditions) for higher-frequency regions of speech when the hearing loss was severe. In Fig. 6, the calculated efficiencies for the speech bands of 2250–3500 Hz and also for 3500–5600 Hz are plotted separately, thus indicating the benefits of audible speech for frequencies of 2250 Hz and above. No data were

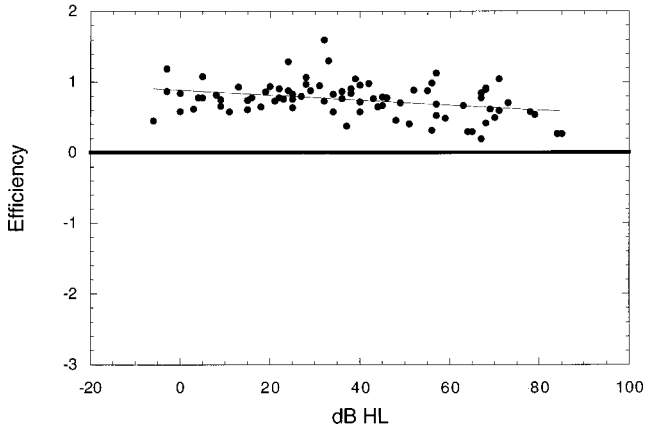

FIG. 5. The efficiency of audible speech for recognition plotted as function of the degree of hearing loss. All subjects and all conditions are shown in this figure. The degree of hearing loss is expressed as the difference between the pure-tone thresholds of normal-hearing subjects and the pure-tone threshold of the hearing-impaired subject.

available for the speech band of 5600–9000 Hz, as audible speech could not be provided to any of the hearing-impaired listeners for that frequency range without exceeding uncomfortable loudnesses for the subjects. As expected from the previous figure, all efficiencies are positive. When linear regression lines are fit to the data points of these higher frequencies, the extrapolated intersections with a value of zero efficiency are over 110 dB HL in each case, further suggesting that providing audible speech to any degree of hearing loss does provide benefits for speech recognition in a background noise.

IV. DISCUSSION

In the present study, it was shown that for listening to speech in a substantial background noise, all hearing-impaired listeners obtained benefit from amplified audible speech regardless of the degree of hearing loss. This finding held true even for the higher-frequency regions of the speech spectrum. This appears to be in contrast to the conclusions of the previous research Ching *et al.* (1998) and Hogan and Turner (1998), as well as others. The primary difference between the present study and these previous ones is that

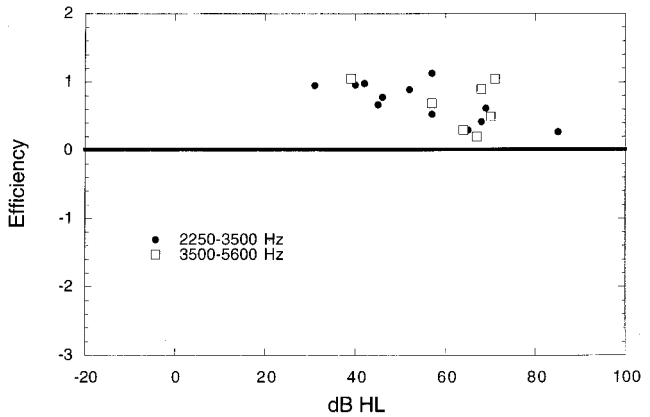

FIG. 6. The efficiency of audible speech for recognition plotted as a function of the degree of hearing loss. In this figure, only the data for low-pass filter cutoff frequencies of 3500 and 5600 Hz are shown.

speech recognition was measured in a background noise, and the previous work measured speech in a quiet background. Thus, our original hypotheses were not confirmed; the benefits of amplified speech in a background noise were not zero or negative for high frequencies and severe hearing loss. We had also hypothesized that these deficits would be more severe in noise backgrounds than in the previously measured effects in quiet; this certainly was not the case.

An examination of the raw data of the present study, as well as that of previous studies, provides a possible explanation for the present results. In the study of Hogan and Turner (1998), the hearing-impaired subjects obtained speech recognition scores ranging from 40% to 90% in the broadest bandwidth conditions, and it was typical for the presented speech (with no background noise present) to yield maximum AI values ranging from approximately 0.6 to 0.8 in these conditions. In other words, in the previous research, the majority of the speech signal was audible to the hearing-impaired listeners. In the present study, due to the spectrally similar background noise, the hearing-impaired subjects' speech recognition scores ranged from 24% to 55% in the broadest bandwidth conditions, and the speech signal was much less audible, with maximum AI values ranging from 0.23 to 0.62 (see Fig. 3). Thus, the earlier studies were measuring the ability of hearing-impaired listeners using the higher frequencies of speech to increase their speech recognition scores above values that were already rather high, presumably looking at their ability to recognize the remaining ''most difficult'' features and phonemes of speech. In the present study the additional high-frequency audible speech added was used by the hearing-impaired subjects to increase rather low recognition scores in every case. The noise background allowed these subjects only a small fraction of the possible audible speech in the lower-frequency conditions. As higher-frequency regions were made audible to these subjects, they presumably used the additional audible speech to increase recognition of ''easier'' features and phonemes of speech.

One way to look at which types of speech features were being recognized by the subjects is to look at their perception of the commonly used distinctive features of speech such as voicing, manner, and place of articulation. For each hearing-impaired subject, the raw response matrices for speech recognition for each condition were analyzed using the FIX analysis program (Department of Phonetics and Linguistics, University College of London), which provides the relative information transmitted (RTI) measure of the transmission of these distinctive features of speech. This program is based upon the ''sequential information analysis'' described by Wang and Bilger (1973). The information transmitted was calculated iteratively, holding the order of analysis fixed as voicing, then manner, followed by place. In the three panels of Fig. 7, the RTI for voicing, manner, and place are displayed as a function of audible speech information (AI) for three of the hearing-impaired subjects. The trends seen in the data of these three subjects are similar to that in the other subjects' data. As one moves from the left to the right on each graph, additional high frequencies of speech have been made audible to the listener. For each subject, the values for

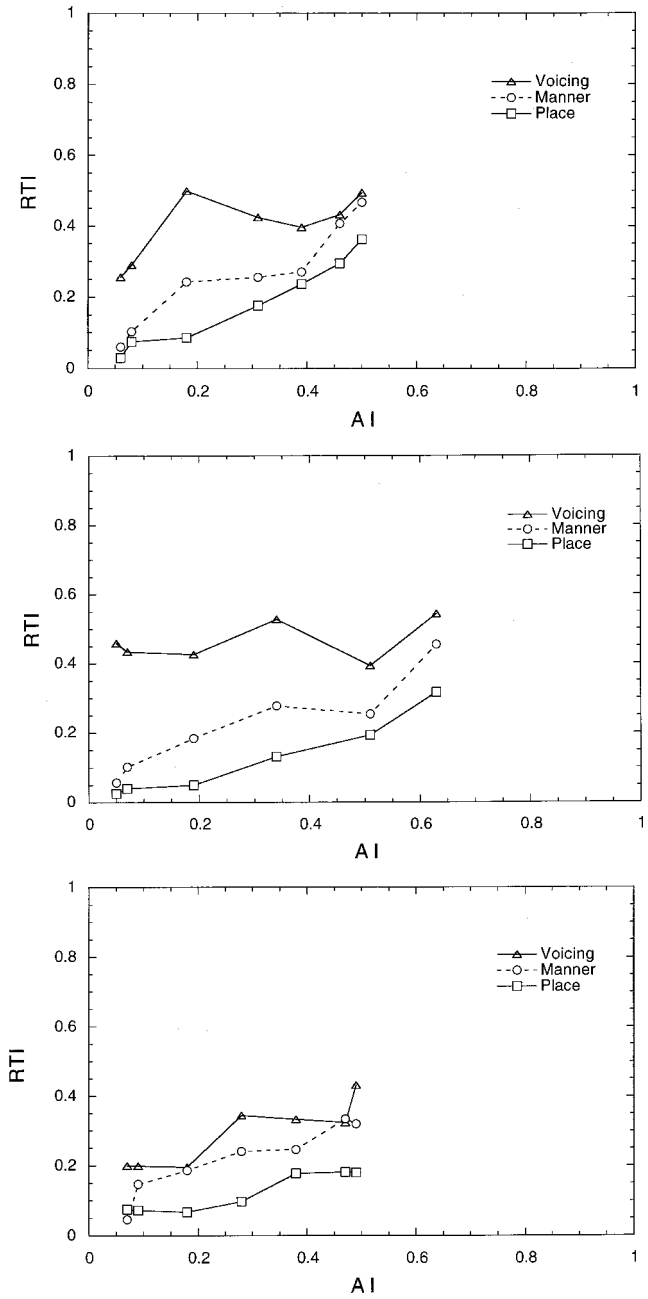

FIG. 7. The relative information transmitted (RTI) of the individual features of speech (voicing, manner, and place) is plotted as function for AI for three hearing-impaired subjects. Each panel corresponds to an individual subject.

voicing and manner are generally increasing even as speech is added up to 5600 Hz (the rightmost data point). And, in all three of the subjects, perception of the place of articulation feature is also increasing. In every instance, the RTI for any of the three features of speech reaches a maximum of 0.6 or less. In other words, even at the widest bandwidth condition the hearing-impaired subjects had plenty of speech cues remaining in which to show improvement. The fact that voicing cues are available across a wide bandwidth of speech has been shown by Grant and Walden (1996). Under quiet conditions, most listeners can get these same voicing cues from low-frequency regions of speech. In background noise, all frequency regions are used. The features of manner and place, which are usually associated with higher-frequency

regions, also increased as listening bandwidth was increased. The results of the present study suggest that there are some easier cues for manner and even place that can be perceived by listeners with even severe hearing loss in the higher-frequency regions. This pattern of results is different from the feature analyses observed in previous research (speech in quiet) such as Vickers *et al.* (2001), where RTI for voicing and manner were often at 0.8 or above for wideband speech recognition. In these cases, only the more difficult cues of speech remained for the hearing-impaired listener to receive from increasing audibility at high frequencies, and apparently severe hearing loss can degrade the transmission of these remaining difficult speech cues.

It should be noted that the recognition gains these hearing-impaired subjects showed in response to the additional high-frequency bands of speech were usually not large (often on the order of 5% or less). These gains in speech recognition were also usually less than would be expected from normal-hearing listeners receiving equivalent increments in speech audibility, which further supports the idea that a hearing aid does not fully restore speech understanding for these patients. The small gains were also consistent with the small increments of AI that were added in these conditions (due to the presence of background noise and hearing loss). Although these subjects did not complain of uncomfortable loudness in these experimental conditions, listening to amplified speech and noise at these levels in everyday life may not be as acceptable. Thus, the clinical utility of providing large amounts of high-frequency gain should be viewed somewhat cautiously, despite the numerical conclusions of the present study.

In summary, the present study revealed that when the cues of speech are severely limited by background noise, providing audible speech via amplification showed positive benefit in all cases. Adding high-frequency audible speech in the presence of a relatively intense background noise was beneficial in all cases, regardless of the degree of hearing loss. In this case, when speech audibility is so limited, even the easier cues of speech remain elusive to the listener, and any small increase in speech audibility is put to good use.

ACKNOWLEDGMENTS

This research was funded in part by a grant from the National Institute of Deafness and other Communicative Disorders (1R01 DC00377). Many thanks to Hope Jones, Melanie Buhr, Courtney Burke, Ann Torkelson, Kristine Melis, and Arik Wald for their assistance on this project.

ANSI (**1969**). ANSI S3.5-1969, ''American National Standard: Methods for the Calculation of the Articulation Index'' (American National Standards Institute, New York).

ANSI (**1996**). ANSI S3.66-1996, ''American National Standard: Specifications for Audiometers'' (American National Standards Institute, New York).

ANSI (**R1997**), ANSI S3.6-1997, ''American National Standard: Methods for the Calculation of the Articulation Index'' (American National Standards Institute, New York).

Ching, T., Dillon, H., and Byrne, D. (**1998**). ''Speech recognition of hearing-impaired listeners: Predictions from audibility and the limited role of high-frequency amplification,'' J. Acoust. Soc. Am. **103**, 1128–1140.

Grant, K. W., and Walden, B. E. (**1996**). ''Evaluating the articulation index for auditory-visual consonant recognition,'' J. Acoust. Soc. Am. **100**, 2415–2424.

Hogan, C., and Turner, C. W. (**1998**). ''High-frequency amplification: Benefits for hearing-impaired listeners,'' J. Acoust. Soc. Am. **104**, 432–441.

Rankovic, C. M. (**1991**). ''An application of the Articulation Index to hearing-aid fitting,'' J. Speech Hear. Res. **27**, 391–402.

Skinner, M. W. (**1980**). ''Speech intelligibility in noise-induced hearing loss: Effects of high-frequency compensation,'' J. Acoust. Soc. Am. **67**, 306–317.

Turner, C. W. (**1999**). ''The limits of high-frequency amplification,'' Hear. J. **52**, 10–14.

Turner, C. W., and Brus, S. (**2001**). ''Providing low- and mid-frequency speech information to listeners with sensorineural hearing loss,'' J. Acoust. Soc. Am. **109**, 2999–3006.

Turner, C. W., and Cummings, K. J. (**1999**). ''Speech audibility for listeners with high-frequency hearing loss,'' Am. J. Audiol. **8**, 47–56.

Van Tasell, D. J. (**1993**). ''Hearing loss, speech and hearing aids,'' J. Speech Hear. Res. **36**, 228–244.

Vickers, D. A., Moore, B. C. J., and Baer, T. (**2001**). ''Effects of low-pass filtering on the intelligibility of speech in quiet for people with and without dead regions at high frequencies,'' J. Acoust. Soc. Am. **110**, 1164–1175.

Wang, M. D., and Bilger, R. C. (**1973**). ''Consonant recognition in noise, a study of perceptual confusions,'' J. Acoust. Soc. Am. **54**, 1248–1266.

Acoustical analysis and model-based sound synthesis of the kantele[a)]

Cumhur Erkut[b)] and Matti Karjalainen
Laboratory of Acoustics and Audio Signal Processing, Helsinki University of Technology, Espoo, Finland

Patty Huang
Center for Computer Research in Music and Acoustics, Stanford University, Stanford, California 94305-8180

Vesa Välimäki[c)]
Laboratory of Acoustics and Audio Signal Processing, Helsinki University of Technology, Espoo, Finland

(Received 3 January 2002; revised 3 July 2002; accepted 3 July 2002)

The five-string Finnish kantele is a traditional folk music instrument that has unique structural features, resulting in a sound of bright and reverberant timbre. This article presents an analysis of the sound generation principles in the kantele, based on measurements and analytical formulation. The most characteristic features of the unique timbre are caused by the bridgeless string termination around a tuning pin at one end and the knotted termination around a supporting bar at the other end. These result in prominent second-order nonlinearity and strong beating of harmonics, respectively. A computational model of the instrument is also formulated and the algorithm is made efficient for real-time synthesis to simulate these features of the instrument timbre. © *2002 Acoustical Society of America.* [DOI: 10.1121/1.1504858]

PACS numbers: 43.75.Gh, 43.75.Wx [NHF]

I. INTRODUCTION

The *kantele*[1] refers to a group of plucked string instruments that have been common in traditional folk music in Finland, its neighboring region in Northwest Russia, and the Baltic states.[2,3] The instrument and its variations are called the *kannel* in Estonia, the *kanklės* in Lithuania, the *kokle* in Latvia, and the *gusli* in Russia.[2] They belong to the family of zithers. The five-string Finnish kantele has a significant role in Finnish folklore as the instrument of rune singers, and in Finnish mythology, especially in the Kalevala, the collection of ancient Finnish runes.[4] It is estimated that the origins of the kantele are more than 1000 years old.

The traditional Finnish kantele has five strings and a body made of a single piece of wood. The traditional instrument illustrated in Fig. 1 is hollowed out at the top and the opening is covered by a top plate with a sound hole (X-shaped in this model). Strings are terminated at the wider end around wooden tuning pegs. At the other end the strings are attached with a knotted termination around the *varras*, a bar typically made of metal, in a U-shaped raised body structure (the *ponsi*).

At the end of 18th century the instrument started an evolution to new forms. The body of the kantele was eventually constructed of separate plates instead of a single piece of wood, and the wooden tuning pegs were replaced by metallic tuning pins. This type of the instrument is the focus of the present study. To be able to play more complex music the kantele was made larger and equipped with more strings—for example, 9 to 15 strings. For compatibility with concert music, a *concert kantele* has been developed since the 1920's to contain up to 45 strings, with a range of about five octaves. The challenge of playing in different keys and with chromatic notes was solved by including a lever mechanism, similar to that of a concert harp, for rapid change of tuning.

The kantele has a characteristic sound that is bright and reverberant.[5] Only recently, acoustical studies have been carried out on the instrument to reveal the features that make the unique sound. In a previous work,[6] based on measurements and signal analysis, specific properties of string terminations were reported as prominent sources of the characteristic kantele tone. A recent study focused on the body vibrations of a general class of the Baltic psalteries.[7]

The objective of the present article is to give a systematic and thorough presentation of the instrument, showing the

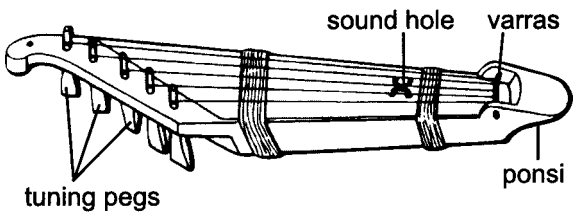

FIG. 1. A Finnish traditional five-string kantele made by hollowing out the top of a single wood block and covering it with a top plate. The strings are attached, without a bridge, to the tuning pegs at the left-hand side and to a bar at the right-hand side. After Sadie (Ref. 2).

[a)]Portions of this work were presented in "Analysis, modeling, and real-time sound synthesis of kantele, a traditional Finnish string instrument," Proceedings of IEEE International Conference on Acoustics, Speech, and Signal Processing, Minneapolis, MN, April 1993, and "Nonlinear modeling and synthesis of the kantele—A traditional Finnish string instrument," Proceedings of International Computer Music Conference, Beijing, China, October 1999.

[b)]Electronic mail: cumhur.erkut@hut.fi

[c)]Part of the work done while at Tampere University of Technology, Pori School of Technology and Economics, Pori, Finland.

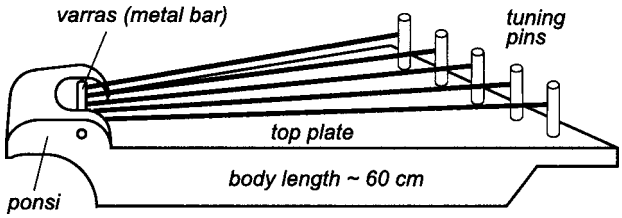

FIG. 2. Structure of a five-string kantele used in most experiments of this study. The body is made hollow from the bottom and left open. After Karjalainen *et al.* (Ref. 6).

behavior of kantele strings, body, and sound radiation. This article starts with a structural description of an open-body kantele, as well as playing techniques and tuning of the instrument in Sec. II. Section III presents an acoustical analysis of the instrument. The terminations of the strings deserve special attention since they introduce strong beating and nonlinear effects to the sound. The nonlinear vibrations of the kantele strings are of exceptional importance in producing the resulting timbre. The properties of body vibrations as a response to the driving forces on the strings are demonstrated. In Sec. IV, a computationally efficient sound synthesis algorithm is presented. The algorithm captures the most essential properties of the kantele sound, and allows for the synthesis of kantele tones in real time.

II. DESCRIPTION OF THE INSTRUMENT

A. Construction and tuning

Our study focuses on a present-day version of the traditional five-string kantele, illustrated in Fig. 2. The body is hollowed open at the bottom and thus there is no need for a sound hole. This model was used due to its structural simplicity.

The five metal strings are of equal diameter (0.35 mm) with lengths ranging from 32.5 to 47.8 cm. At the narrower end of the kantele the strings are wound once around the varras and knotted as shown in Fig. 3. At the opposite end the metal tuning pins are screwed directly into the soundboard that is the top plate of the body, and the strings are terminated directly around the pins without a bridge (Fig. 4). Such terminations are unique structural features of the instrument.

The five-string kantele is tuned to a diatonic scale, and the third string can be tuned to a major third, minor third, or somewhere in between. The tuning of the lowest string is

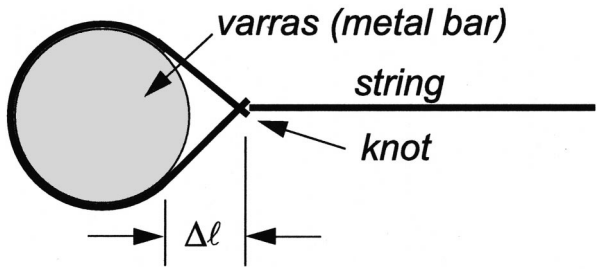

FIG. 3. String with a knot termination around the varras (metal bar). Effective string lengths differ by Δl for different vibration directions. After Karjalainen *et al.* (Ref. 6).

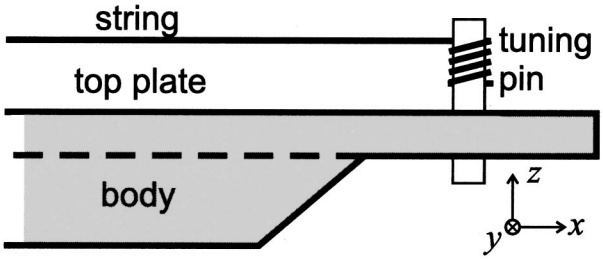

FIG. 4. String termination around a tuning pin without a bridge. A reference coordinate system is indicated at the bottom part of the figure. After Karjalainen *et al.* (Ref. 6).

typically near D_4 (294 Hz), although transposition of several semitones (up or down) is also common. In our experiments, the lowest string has been tuned to $E\flat_4$ (311 Hz).

B. Playing techniques

The five-string kantele is played across one's lap or on a table, with the shortest string closest to the player. There are regional and personal variations in playing technique, but the most common traditional way is to interleave fingers of left and right hands, with one finger for each string and the right thumb playing the highest string. A string is plucked upwards so that all other strings remain free to vibrate. This makes a reverberant sound. Damping of strings or plucking horizontally so that the finger damps the next string can be used in modern playing. Another technique that yields an even brighter sound is to strike a string by fingernail. These techniques can also be combined. Playing can consist of a melody line, accompaniment, or both, although in traditional playing there was often no clear distinction between them.

III. ACOUSTICAL ANALYSIS OF THE KANTELE

A. Observations of kantele tones

Figure 5 shows the amplitude envelope trajectories of the first three harmonics of (a) a softly plucked and (b) a strongly plucked kantele tone. The measurements were carried out in an anechoic chamber, where the microphone

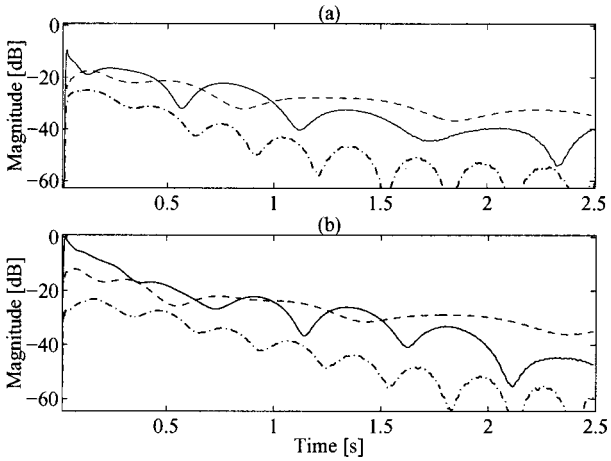

FIG. 5. Envelope trajectories of kantele tones. The first harmonic is shown with a dashed line, the second with a solid line, and the third with a dash-dotted line. (a) A softly plucked tone and (b) a strongly plucked tone. The plucking point is the midpoint of the third string.

(B&K 4145) was fixed at a distance of 1 meter above the top plate of the instrument. The plucking point is the midpoint of the third string so that, according to the linear theory of string vibration, even harmonics should be absent.[8]

The first noticeable feature of the kantele tones in Fig. 5 is a strong beating of harmonics. This phenomenon is explained in Sec. III B. Another feature is the presence and dominance of the second harmonic. The initial magnitude of the second harmonic is approximately 10 dB higher in the case of a strong pluck in Fig. 5(b), compared to that of the soft pluck in Fig. 5(a). The generation and the amplitude dependence of the second harmonic indicate a nonlinear mechanism, which is the subject of Sec. III C. Section III D presents the formulation of a nonlinear longitudinal force component, and Sec. III E derives an analysis method. In Sec. III F we demonstrate by measurements how the body of the instrument responds to the forces applied on a tuning pin. Within the same section, we also briefly discuss the properties of the body of the traditional kantele, as well as the energy transfer between the strings.

Throughout the discussion we use the following convention to refer to three orthogonal vibration directions. A rectangular reference coordinate system is shown in Fig. 4. The x axis is along the strings so that the varras is at $x=0$ and a tuning pin is at $x=L$. The y axis is parallel to the top plate, and the z axis is in the direction of the normal to the top plate. The *longitudinal*, *horizontal*, and *vertical* directions are aligned with the unit vectors of the x, y, and z axes, respectively. When we refer to a vibration in the plane spanned by horizontal and vertical unit vectors, we use the term *transverse*.

B. Analysis of the beating

The observed beating in Fig. 5 is essentially a result of the knotted termination at the varras. This termination dictates two different effective string lengths, one for the vertical and another for the horizontal vibration, with a length difference of Δl (see Fig. 3). For the vertical polarization, the knot is the termination point, whereas for the horizontal polarization, the contact point to the varras is the termination point.[6,7] As a consequence, the vertical and horizontal fundamentals have a constant frequency difference Δf_0 that creates the beats.

To verify this explanation, we used a modified kantele,[9] where the string is terminated without a knot, but otherwise the construction is identical to that of the regular kantele. Figure 6 shows the first three harmonic envelopes extracted from (a) regular and (b) knotless kantele tones of the same frequency ($f_0=415$ Hz). In the knotless design the beating vanishes, confirming our explanation.

The frequency difference of the two transverse polarizations is related to the length difference Δl by

$$\Delta f_0 = f_{0,z} - f_{0,y} = \frac{c}{2l} - \frac{c}{(2l+\Delta l)} = \frac{\Delta l}{l} f_{0,y}, \tag{1}$$

where l is the effective length of the string between the tuning pin and the knot (see Fig. 3), $c=\sqrt{T/\rho}$ is the transverse propagation speed determined in terms of the string tension T and the linear mass density ρ, and Δl is the difference of the effective string length for different polarizations. The frequency difference can also be confirmed experimentally by analyzing the amplitude envelope of the first harmonic of recorded kantele tones and by extracting the beating frequency by fitting a sine wave using the nonlinear least-squares method.[10] To avoid confusion, we refer to the extracted fundamental frequency difference as $\Delta f_{0,\mathrm{ex}}$.

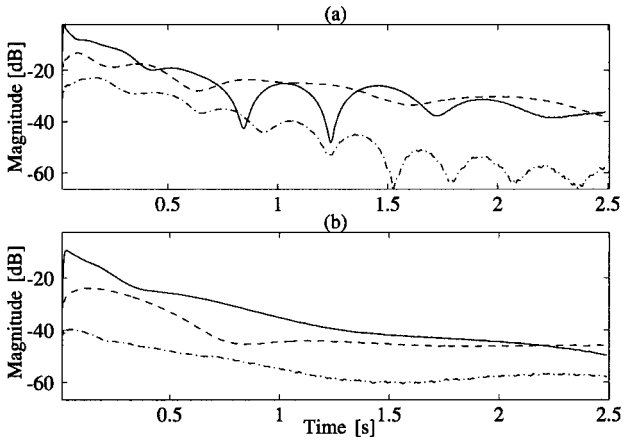

FIG. 6. Envelope trajectories of tones from a normal (a) and a modified (b) kantele. The first harmonic is shown with a dashed line, the second with a solid line, and the third with a dash-dotted line. The plucking strength is medium and the plucking point is the midpoint of the third string. The strong beating does not appear in the knotless kantele.

Figure 7 presents an example where the linear trend and mean of the envelope of the first harmonic have been removed on a logarithmic (dB) scale in order to compensate the natural decay of the harmonic, and a sine wave has been fitted to the available data above the noise level. We observed experimentally that the plucking direction slightly alters the beating pattern. Note that, because of nonlinear coupling between different polarizations, the string exhibits an elliptical vibration pattern shortly after the initial pluck, regardless of the initial excitation direction.[11] Therefore, we use an average of two cases, a horizontal and a vertical pluck. We noticed that this method yields a good estimate of

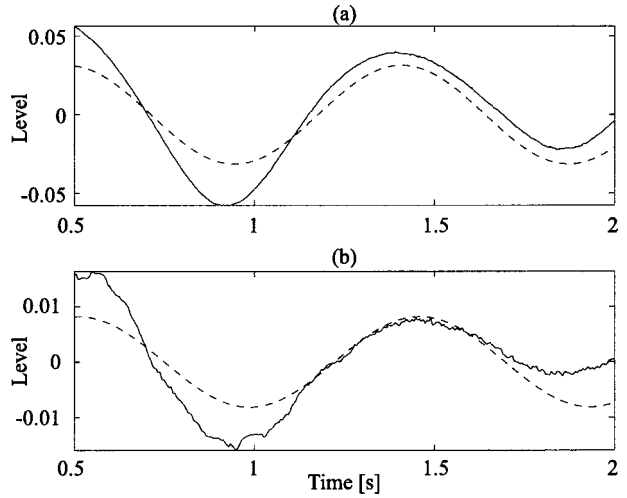

FIG. 7. Beating of the first harmonic (solid line) in a kantele tone plucked horizontally (a) and vertically (b), with a nonlinear least-squares sine wave fit (dashed line).

TABLE I. The fundamental frequencies $f_{0,y}$ of the horizontal polarizations, the frequency differences Δf_0 according to Eq. (1), and the extracted frequency differences $\Delta f_{0,ex}$ for the five strings of the kantele. All quantities are given in hertz.

String	#1	#2	#3	#4	#5
$f_{0,y}$	465.2	414.5	391.3	354.5	314.3
Δf_0	1.50	1.28	1.10	0.95	0.76
$\Delta f_{0,ex}$	1.30	1.04	1.07	0.97	0.77

the difference in the fundamental frequency of vibration of the two polarizations.

Table I shows the fundamental frequencies of horizontal polarizations for the five strings of the kantele and the frequency differences Δf_0, obtained by inserting the measured length l and the effective length difference Δl for each string into Eq. (1). The extracted frequency differences $\Delta f_{0,ex}$ are obtained by the sine-fitting method described above. Δf_0 and $\Delta f_{0,ex}$ are in qualitative agreement. The differences are caused by the imaginary part of the input admittance at the tuning pin,[12] and by the nonlinearities discussed in the next section.

C. Tension modulation nonlinearity

Unlike an ideal flexible string, a real string, such as a kantele string, is linear to the first-order approximation only. Reformulation of the wave equation to include these second-order terms has a relatively long history (see Ref. 13 for a review). The major cause of nonlinearities is that any small transverse displacement of the string makes a second-order change in its length and therefore in its tension. By assuming fixed boundary conditions and using an excitation force of a frequency close to that of the first mode of the string, the tension modulation is shown both analytically and experimentally to cause a fundamental frequency descent,[14,15] a whirling motion,[16–18] coupling between different modes and directions,[12,15,19] and amplitude jumps.[11,20]

Legge and Fletcher showed that the generation of missing modes in a musical instrument is only possible when a realistic model of the termination at the bridge is taken into account.[12] However, they concluded that with a termination similar to that of a bridgeless kantele, the nonlinearities cannot provide subsequent excitation of any of the missing even harmonics, if the string is initially plucked near its center. Moreover, according to their theory, even in case of a termination by a guitar-like bridge, the unexcited modes should exhibit a slow build-up (typically around 100 ms). The behavior of the second harmonic in Figs. 5 and 6—specifically, the observed rapid onset with a high initial level—is not consistent with their conclusion.

This inconsistency is clarified by noting the structural differences between the kantele and other plucked-string instruments. In most string instruments, the bridge is the usual termination point of the strings at one end, and it is relatively rigid in the longitudinal direction.[8] An important function of the bridge is to transmit the transverse forces of the string to the body of the instrument, and hence the longitudinal force component is usually filtered out. A plucked-string body is typically not responsive to the longitudinal forces below 1 kHz.[21]

In the kantele, the tuning pins are not rigid in the longitudinal direction and transmit any longitudinal force efficiently to the body. As will be demonstrated in the following, nonlinear mechanisms caused by the tension modulation create a longitudinal force component, called the *tension modulation driving force*,[22] or TMDF for short, which accounts for the instantaneous onset and high initial amplitude of the second harmonic in Figs. 5 and 6.

A similar mechanism has been observed in an acoustical guitar, an orchestral harp, and a piano.[23] The partials thus generated are termed as *phantom partials*, and it has been concluded that any plucked-string or struck-string instrument that is susceptible to longitudinal string forces could produce phantom partials. The phantom partials are observed between 1–3 kHz. Measurement results indicate that the kantele body is susceptible to the longitudinal TMDF. The TMDF has a significant effect on the lowest partials, thus on the timbre, as will be demonstrated in the following.

D. TMDF formulation

In order to obtain the TMDF exerted on a tuning pin, we ignore the effective length difference in transverse directions discussed in Sec. III B and rely on the knotless kantele analysis data. Moreover, the string is taken to be linearly elastic, the inharmonicity caused by string stiffness (dispersion) is assumed negligible, and the cross-sectional area of the string (and hence its density) is taken to be constant during the vibration.

For steel strings, the transverse propagation speed is usually smaller than 10% of the longitudinal propagation speed. This practically means that the first longitudinal component of the string vibration has a frequency higher than the tenth transverse harmonic. However, here we focus on the lowest harmonics of the kantele tones. This fact justifies why we assume that TMDF is the only longitudinal force component acting on a tuning pin and neglect the effects of longitudinal wave propagation. Note that the same argument has also been used in several analytical treatments of nonlinear string vibrations.[12,16]

Under these assumptions, elongation of the string l_{dev} may be expressed as the deviation from the nominal string length L

$$l_{\mathrm{dev}} = \int_0^L \left[1 + \left(\frac{\partial y}{\partial x} \right)^2 + \left(\frac{\partial z}{\partial x} \right)^2 \right]^{1/2} dx - L$$

$$\approx \int_0^L \frac{1}{2} \left[\left(\frac{\partial y}{\partial x} \right)^2 + \left(\frac{\partial z}{\partial x} \right)^2 \right] dx, \tag{2}$$

where x, y, and z denote the spatial variables (see Fig. 4) along the longitudinal, horizontal, and vertical directions, respectively, and the approximation is obtained by neglecting all but the first terms of Taylor series expansion of the slopes. If the supports are rigid, the tension yields

$$T = T_0 + ES \frac{l_{\mathrm{dev}}}{L}, \tag{3}$$

where T_0 is the nominal tension of the string in rest, E is Young's elastic modulus of string material, and S is the cross-sectional area of the string. It is customary[8,15] to define the longitudinal force exerted on the pin as

$$F_x(T) \approx -T|_{x=L} = -\left(T_0 + ES\frac{l_{\text{dev}}}{L} \right). \tag{4}$$

Equation (4) is the analytical expression of TMDF. The negative sign indicates that the force is pulling the tuning pin towards the center of the instrument. There is a similar TMDF component acting on the varras at $x=0$ with a positive sign.

The eigenfunctions for the lossy wave equation in the two transverse directions are exponentially decaying sinusoids with amplitudes $a_{y,m}$ and $a_{z,n}$, where m and n indicate the harmonic numbers for the horizontal direction y and vertical direction z, respectively. The Fourier coefficients $a_{y,m}$ and $a_{z,n}$ have the physical dimension of meters. Inserting the eigenfunctions in Eq. (4) and neglecting terms of fourth- and higher order in $a_{y,m}/L$ and $a_{z,n}/L$, TMDF can be approximated as

$$F_x(T) \approx -T_0 - \frac{\pi^2 ES}{8L^2} \times \left\{ \sum_m m^2 a_{y,m}^2 [1-\cos(2\omega_{y,m}t+\phi_{y,m})] e^{-2t/\tau_{y,m}} + \sum_n n^2 a_{z,n}^2 [1-\cos(2\omega_{z,n}t+\phi_{z,n})] e^{-2t/\tau_{z,n}} \right\}, \tag{5}$$

where ω, ϕ, and τ are the frequency, initial phase, and time constant of the decay, respectively, corresponding to a particular mode.

Equation (5) suggests that each transverse harmonic contributes to the TMDF with two exponentially decaying components within the square brackets. The first terms do not oscillate, and they are the primary cause of the fundamental frequency descent.[14,15] As will be shown later, the fundamental frequency descent in kantele tones can be used to extract information for the nonlinear behavior.[24] The oscillatory terms have twice the frequency and one half the decay times of the corresponding harmonics.

Given an initial displacement consisting of odd harmonics only, according to Eq. (5), the TMDF components that have twice the fundamental frequency are generated solely by the first harmonic of each polarization. Figure 8 illustrates the TMDF acting on the tuning pin in the absence of the vertical component. The top part of the figure depicts the horizontal fundamental y_1 of unity amplitude ($a_{y,1}=1$) that decays with its characteristic rate. The resulting TMDF pulls the tuning pin towards the center of the instrument twice during one period of the fundamental, and decays twice as fast.

In particular, if the initial displacement consists only of a single-polarization fundamental (e.g., in the y direction), and if the constant tension T_0 is suppressed, the time-varying part of Eq. (5) becomes

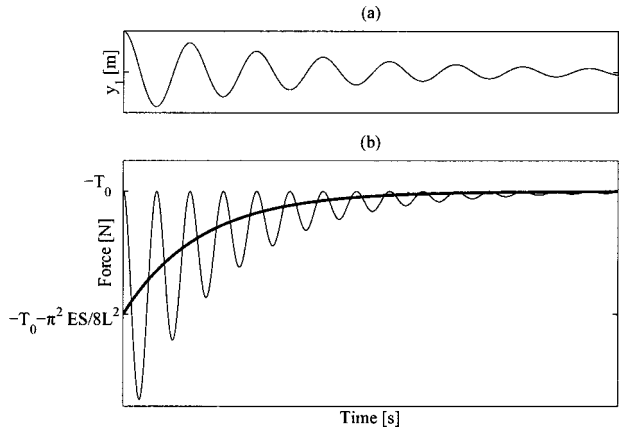

FIG. 8. The illustration of the TMDF for a single polarization case. (a) The exponentially decaying fundamental y_1 of unity amplitude. (b) The corresponding TMDF. The thick line is the component that causes the fundamental frequency descent, and the thin curve is the oscillatory component.

$$F_x(t) = -\frac{\pi^2 ES}{8L^2}(a_{y,1}^2 e^{-2t/\tau_{y,1}})(1-\cos(2\omega_{y,1}t+\phi_{y,1})). \tag{6}$$

Equation (6) is essentially the same in form with the dimensionless nonlinear mixing force given in Ref. 23 [see Eq. (3) in the reference]. It also suggests that $F_x(t)$ may be related to the dilated eigenfunction $y_1(x,2t)$ by appropriate scaling and phase shifting. This property may be utilized as an analysis procedure. We present such an analysis procedure in the next subsection.

The kantele responds as a passive, linear system to the forces applied on its tuning pins. Therefore, some part of the TMDF is transmitted to the body, some part of it is reflected, and the rest is dissipated. We first concentrate on reflection.

The frequency difference of transverse and longitudinal modes, as stated in the previous section, indicates that the reflected TMDF component cannot be efficiently coupled to a longitudinal mode. It may, however, generate a transverse mode. The famous experiment of Melde demonstrates the possibility of the missing transverse mode generation by driving a string from one end in the longitudinal direction.[20] A recent study[25] shows that the three-dimensional admittance matrix of a musical instrument may interchange energy between longitudinal and transverse directions. This property is proved to be important in nonlinear generation of missing modes.[12]

If the TMDF is coupled back to the string by either mechanism, a generated transverse second harmonic should exhibit a build-up onset until the coupled energy is balanced by internal losses. After the balance instant, the second harmonic should decay with a characteristic rate that is independent of the first harmonic and governed only by the string and body properties. The tuning pin velocity measurements in transverse directions indicate the existence of such a component. However, the velocity magnitude of the generated transverse harmonic is typically 20 dB lower than the magnitude of the first harmonic. In terms of the forces, this difference is roughly 30 dB. We therefore conclude that the instantaneous onset and high initial amplitude of the second harmonic in Figs. 5 and 6 are caused by the TMDF compo-

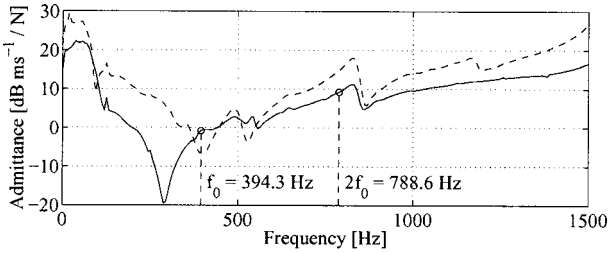

FIG. 9. The magnitude of the admittance measured in the longitudinal (solid) and horizontal (dashed) directions. The admittance values in the longitudinal direction corresponding to the first and second harmonics are indicated with small circles.

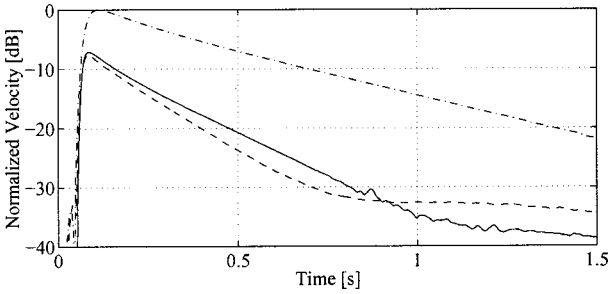

FIG. 10. The extracted velocity magnitude envelopes of the first harmonic (dash-dotted) and the second harmonic (dashed). The calculated second harmonic generated by the TMDF is represented by a solid curve. The measurements were carried out on a modified kantele.

nent that is transmitted to the body and in turn radiated. Next, we discuss an analysis procedure to verify this explanation.

E. TMDF analysis

Consider Eq. (5) for $m=n=1$ and $a_{y,1}=a_{z,1}=a_1$. The equality of the initial amplitudes can be assured by deflecting the string along bisection of the transverse unit vectors (see Fig. 4). In this case, the oscillatory part of the TMDF yields

$$F_{\mathrm{osc}}=2(a_1)^2\frac{\pi^2 ES}{8L^2}\,\xi(2t), \tag{7}$$

where $\xi(2t)$ is the normalized first harmonic that can be extracted from a velocity measurement using a bandpass filter, and then by dilating the filtered signal by a factor of 2. The dilation can simply be carried out by downsampling. The TMDF component thus calculated can be filtered with a premeasured input admittance function of the tuning pin and converted to the longitudinal velocity. The measured and calculated magnitude envelopes of the second harmonics are then compared. Similarly, the first harmonic can be extracted from a recorded tone, and the calculated TMDF component can be converted to the sound pressure by filtering it with the longitudinal body response.

The details of an experiment, in which the third string of the kantele was tuned to $f_0=394$ Hz, are described below. In the experiment, we used velocity data. The length of the string is 0.4015 m, and its diameter is 0.35 mm. The elastic modulus of the particular string is not known; therefore, we referred to literature for typical elastic moduli for steel strings of musical instruments[8] and assumed that $E=2\times10^9$ N/m^2.

The longitudinal input admittance function has been obtained by exciting the tuning pin with an impulse hammer and measuring its velocity with a laser vibrometer. For accuracy, 200 individual hits were averaged. The measured longitudinal admittance around $2f_0$ is shown in Fig. 9 together with the horizontal admittance function. The admittance values corresponding to the first and second harmonics of the third kantele string are also indicated in the figure.

The string has been displaced with a finger by $a_1=2$ mm at its midpoint along the bisection of the transverse unit vectors, and then released. The vibrations of the tuning pin are measured with a laser vibrometer. The first and the second harmonics are extracted from the measured signal using two fourth-order bandpass Butterworth filters with the center frequencies f_0 and $2f_0$, respectively. The passband of the filters has been set wider than the fundamental frequency descent, and the phase delays introduced by the filters have been compensated. The extracted first and second harmonics are represented in Fig. 10 by dash-dotted and dashed curves, respectively.

The velocity of the second harmonic is calculated as follows. The extracted first harmonic is normalized, downsampled by 2, and scaled by $2a_1^2\pi^2(ES/8L^2)=0.0236$, according to Eq. (7). The oscillatory TMDF term thus calculated is filtered by the measured longitudinal admittance function shown in Fig. 9. The resulting velocity magnitude envelope is represented by a solid curve in Fig. 10.

The calculated and measured velocities are found to be in quantitative agreement up to $t=0.75$ s. At this instance the magnitude of the second harmonic is approximately 20 dB less than its initial level. From this instance on, another decay rate that is in the vicinity of the transverse second harmonic is observed. The magnitude difference roughly corresponds to the difference between the transmitted and reflected TMDF components, both discussed in the previous subsection. Similar results have been obtained when the recorded tones are analyzed instead of the velocity measurements. In all measurements, the instance at which the transmitted and reflected TMDF components become comparable in magnitude varies between $t=0.5$ and $t=1$ s.

The assumption about the rigid terminations dictates that the admittance and consequently the velocity at the tuning pin should vanish. However, as Fig. 9 reveals, the tuning pin in practice has a nonvanishing velocity. In order to resolve this conflict, we may correct the eigenfrequencies and the damping coefficients in Eq. (5) using perturbation calculations.[26] However, these perturbations are not crucial for a qualitative description of the nonlinear phenomena of the kantele, as may be justified from Fig. 10.

F. Contribution of the body

The discussion so far explains the generation of the second harmonic in a kantele tone, but it does not account for the high initial magnitude of this component [see Fig. 6(b)]. This difference may be explained by the body responses to tuning peg impulse excitation in three orthogonal directions, as shown in Fig. 11. The measurements were carried out in

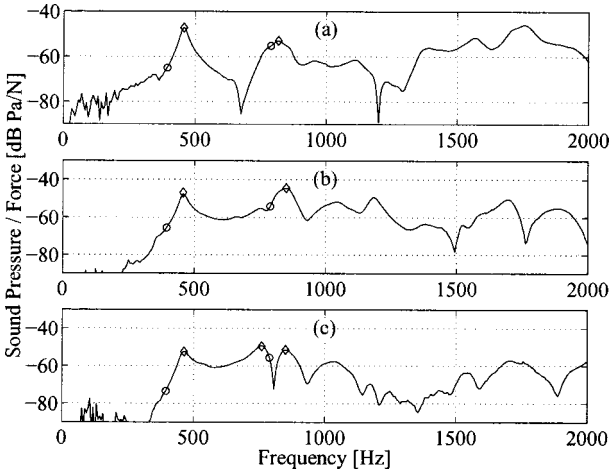

FIG. 11. Sound radiation from the kantele body as a response to (a) vertical; (b) horizontal; and (c) longitudinal driving forces at the third tuning pin. The low-frequency peaks of the radiation functions are indicated by diamonds, whereas the frequencies of the fundamental ($f_0 = 394.3$ Hz) and second harmonic of the attached string are indicated by circles.

an anechoic chamber. The instrument was held as the player would hold it in a typical performance, i.e., on his/her lap. The tuning pins were struck with an impulse hammer (PCB 086C02), and the response was recorded with a microphone (B&K 4145), fixed at a distance of 1 m. For accuracy, magnitude responses of 200 individual hits were averaged for each direction. Only the low-frequency response is given in the figure. The resonances of the body are represented by diamonds, and the frequencies of the first and second harmonic are indicated with circles.

The lowest resonances occur at 457 Hz for both the vertical and horizontal responses, and at 463 Hz for the longitudinal response. Note that four strings of the kantele are tuned below these frequencies (cf. Table I), unlike the other Baltic psalteries that have typically two or three resonances within the tuning range.[7] Other resonances can be observed at 817 and 850 Hz for vertical and horizontal directions, respectively. The peak at 850 Hz is also present in the longitudinal response, among a closely spaced peak at 758 Hz. The magnitude levels corresponding to the fundamental frequency ($f_0 = 394.3$ Hz) are about 20 dB lower compared to the lowest resonance for all responses, indicating that the first harmonic is not efficiently radiated. The second harmonic, on the other hand, is coupled to strong body resonances for each direction, and therefore it is radiated efficiently. Note that the levels corresponding to the second harmonics are comparable in each direction. A strong coupling to a body resonance decreases the decay times of the corresponding harmonics.[26] This may explain why the measured second harmonic decays slightly faster than the calculated one in Fig. 10.

For the sake of completeness, we also present a brief summary of the measurements we conducted on the traditional kantele that has a sound hole (see Fig. 1). In a typical playing condition, i.e., when the instrument is played on the lap of the player, the back-plate resonances are partially damped out. At the low-frequency end, the sound hole essentially couples the lowest soundboard resonance and the cavity resonance, as in the case of the guitar.[27] Figure 12 presents the response of the traditional kantele to the vertical excitation force applied to its third tuning peg in a typical playing condition. The lowest coupled resonance occurs around 522 Hz, where the air flow into the kantele is in the opposite direction of the soundboard vibration. In the second resonance, which is at 732 Hz, the soundboard vibration and the air flow have the same direction.

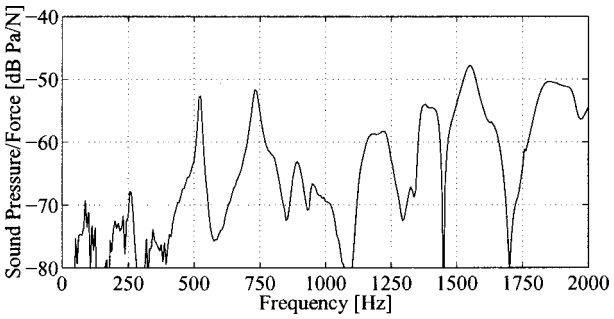

FIG. 12. Sound radiation from the kantele body with a sound hole, as a response to a vertical excitation force at the middle tuning peg.

In every multiple-string instrument, some portion of an individual string's energy is fed to the other strings by various coupling mechanisms. This phenomenon, in which a string vibrates without any direct excitation but is driven only by vibrations of other strings, is called *sympathetic vibration*. Despite the perceptual importance of sympathetic vibrations, there are relatively few analytical treatments of their mechanism,[26,28] and these treatments usually focus on two strings coupled to the body through a common bridge. However, kantele strings are coupled to the body at one end by individual tuning pins, and at the other by the varras. Altogether, they constitute a system where the resonance characteristics of five strings, five tuning pins, a common body, and a metal bar should be simultaneously taken into account. An analytical treatment of such a system is a challenging task. We chose a simpler approach to examine the total amount of energy transferred from one string to all the others.

We plucked each kantele string in an anechoic room and recorded the total response (with other strings free to vibrate) with a microphone (B&K 4145) fixed at a distance of 1 m. After 2 s, we damped the plucked string with a piece of cotton, and kept on recording the sympathetic vibrations of the other strings. The short-time Fourier transform (STFT) of the analysis data allowed us to specify the damping instance precisely. We calculated rms energy within 500 ms before and after the damping point, averaging 50-ms segments. Repeating this procedure eight times for each string, we obtained the average energy levels just before and after the damping instant. This experiment shows that the energy transfer is most pronounced between the fifth and the first string, followed by the fifth and the third, the fourth and second, and the third and the first strings. Note that all these pairs constitute simple harmonic relationships. These results may be incorporated in the synthesis model, which is the topic of the next section.

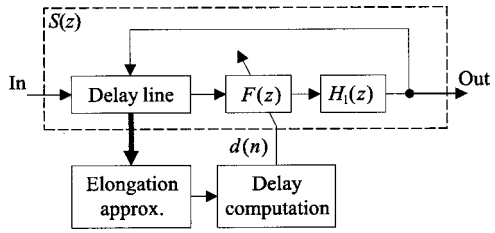

FIG. 13. Computational model $S(z)$ of a vibrating string (the dashed box) where elongation caused by string vibration affects the loop delay through modulation of the delay parameter $d(n)$ of the fractional delay filter $F(z)$. The input signal is an array of sample values that is inserted into the delay line and that corresponds to the initial string slope.

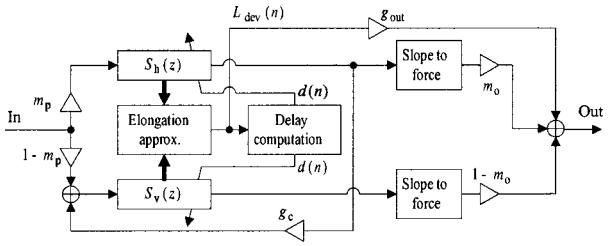

FIG. 14. Dual-mode string model which accounts for the tension modulation. Blocks $S_h(z)$ and $S_v(z)$ are identical with the model shown in Fig. 13.

IV. SOUND SYNTHESIS OF THE KANTELE

Even in the earliest studies on nonlinear string vibrations, numerical procedures have been proposed in addition to the more rigorous analytical treatment, since their results are easier to interpret.[14] Model-based sound synthesizers that capture the essentials of the sound production mechanisms of various sound sources are currently being used to test and verify the underlying hypotheses and assumptions.[29]

In this section, a synthesis model for the kantele is proposed. The suggested model is based on the principles of digital waveguide modeling.[30] In an earlier work, kantele tones were synthesized with a linear digital waveguide string model that had an instantaneous nonlinearity at its output.[6] However, in our current synthesis method,[24] the nonlinearity is realized with time-varying signal-dependent elements. The method is based on a recently developed technique to account for the effects of tension modulation caused by variable string displacement.[13,31] Our aim has been to develop a sound synthesis algorithm that would be sufficiently simple to run in real time, but that would still faithfully reproduce all the peculiar phenomena of the kantele sound described in Sec. III of this paper. In the following, we refer to transverse directions with their explicit names in the formulas to avoid confusion between the vertical spatial variable (see Fig. 4) and the standard DSP unit delay operator z^{-1}.

A. Computational model for a nonlinear string with two polarizations of vibration

Figure 13 shows the block diagram of the nonlinear string model where the tension modulation is incorporated.[13,31] The digital delay line and the fractional delay filter $F(z)$ together implement the delay that corresponds to the fundamental period of the synthesized sound. Filter $F(z)$ can be implemented using Lagrange interpolation,[32] for example. We prefer the FIR Lagrange interpolators to all-pass filters since they have less transient artifacts during parameter updates, despite the losses they introduce at high frequencies.

The filter $H_1(z)$ is called the loop filter, and it is a one-pole filter that implements the frequency-dependent losses of the string[33,34]

$$H_1(z) = g_1 \frac{1+a_1}{1+a_1 z^{-1}}. \tag{8}$$

Tension modulation is realized using a signal-dependent fractional delay filter. This requires computation of the elongation of the string,[13,24] which is approximated as a squared sum of the string slope $\partial y/\partial x$. Integration with respect to time converts the instantaneous elongation estimate into deviation of the delay parameter.[13,31] The model of Fig. 13 can simulate nonlinear transverse string vibration in one polarization of the string (vertical or horizontal).

The model structure for each kantele string consists of two parallel string models, one for each polarization, as depicted in Fig. 14, where $S_h(z)$ and $S_v(z)$ are identical to the model $S(z)$ of Fig. 13.[24] As suggested in previous works, the delay line lengths of the two models must be slightly different to generate beats in the synthetic tone.[33–35] Notice that the output signal of the horizontal string model leaks to the input of the vertical one (scaled by multiplying coefficient g_c in Fig. 14), as suggested in Ref. 35, so that a revolving polarization is obtained but the system remains stable regardless of the value of the coupling coefficient g_c. While the overall recursive system cannot be guaranteed to remain stable when parameter values of $F(z)$ are time varying, in practice we have not encountered stability problems. It appears that the transient response time of $F(z)$ is faster than the modulation period. Moreover, the losses introduced by $F(z)$ and $H_1(z)$ reduce the Q values of resonances.

The mixing coefficient m_p distributes the initial pluck signal between the horizontal and vertical polarizations, whereas m_o adjusts the contribution of each string to the output signal. Both mixing coefficients have values between 0 and 1.

The total tension of the string, which controls the fractional delay filters in the model of Fig. 14, is approximated by accounting for signals propagating in both waveguide models. In the dual-polarization vibration, the elongation of the string is given by Eq. (2). In the digital waveguide formulation, Eq. (2) is expressed as

$$\begin{aligned} L_{\mathrm{dev}}(n) &= \sum_{k=0}^{\hat{L}_{\mathrm{nom}}-1} \sqrt{1+s_h^2(n,k)+s_v^2(n,k)} - \hat{L}_{\mathrm{nom}} \\ &\approx \frac{1}{2} \sum_{k=0}^{\hat{L}_{\mathrm{nom}}-1} s_h^2(n,k)+s_v^2(n,k), \end{aligned} \tag{9}$$

where $\hat{L}_{\mathrm{nom}}$ is the integer-valued length of the delay line, and $s_h(n,k)$ and $s_v(n,k)$ are the horizontal and vertical slope waves, corresponding to $\partial y/\partial x$ and $\partial z/\partial x$ in Eq. (2), respectively. The instantaneous deviation $L_{\mathrm{dev}}(n)$ needs to be integrated along the string length to obtain the overall deviation, which accounts for the change in wave propagation speed.

The integration is approximated with a digital one-pole filter

$$I(z)=g_{\mathrm{p}}\frac{1+a_{\mathrm{p}}}{1+a_{\mathrm{p}}z^{-1}}, \tag{10}$$

where the coefficient values are chosen to be $a_{\mathrm{p}}=1/\hat{L}_{\mathrm{nom}}$ and $g_{\mathrm{p}}=-(1+A)/2$. This choice of coefficient value a_{p} yields a window length equivalent to that of a running average of $\hat{L}_{\mathrm{nom}}$ points, i.e., the nominal length of the delay lines in the string model. Parameter A is the modulation depth related to the string properties and the nominal tension. It can be either calculated from the measured physical quantities of the string, or estimated from the recorded tones, as will be shown below.

The output signal of the one-pole filter is the time-varying delay parameter $d(n)$, which is used to adjust the fractional delay filters in the string models. The direct signal path in Fig. 14 from the elongation estimation block to the output implements the oscillatory term of the TMDF given in Eq. (4) by the selection $g_{\mathrm{out}}=T_0A/L$. For sound synthesis purposes g_{out} may also be used as a parameter to alter the synthetic timbre. Since the synthetic wave variables in the digital waveguides are slope waves, they need to be converted to force waves before the output sum. The force at the tuning pin end may be approximated by[13]

$$f(n,\hat{L}_{\mathrm{nom}})=c_{\mathrm{nom}}s(n,\hat{L}_{\mathrm{nom}}) \tag{11}$$

for each polarization, where c_{nom} is the nominal transverse wave propagation speed.

B. Parameter estimation and synthesis examples

The nonlinear digital waveguide model of the kantele can produce the features of the instrument only if it is properly calibrated. The parameters of the model may be estimated using formerly proposed techniques for the linear part of the system,[34] plus techniques to extract the delay line lengths of the two polarizations and to estimate the appropriate tension modulation parameter A.[13] The use of the latter two methods is described below.

The calculated or experimentally extracted fundamental frequency difference, discussed in Sec. III B, can be directly converted to the delay line length of $S_{\mathrm{h}}(z)$ and $S_{\mathrm{v}}(z)$. Recall that

$$L_{\mathrm{h}}=\hat{L}_{\mathrm{nom,h}}+L_{\mathrm{frac,h}}=\frac{f_{\mathrm{s}}}{2f_{0,\mathrm{y}}} \tag{12}$$

is the delay length of $S_{\mathrm{h}}(z)$, and a similar expression gives the delay length of $S_{\mathrm{v}}(z)$. The difference of the delay line lengths for both polarizations usually manifests itself in the fractional part, so that the $\hat{L}_{\mathrm{nom,h}}=\hat{L}_{\mathrm{nom,v}}$ for the first four strings, as can be seen from Table II. The fractional parts are given relative to the sampling interval $T=1/f_{\mathrm{s}}$. For example $L_{\mathrm{frac,h}}=0.98$ corresponds to $0.98T=22.22$ microseconds of delay.

There are several ways to obtain the tension modulation parameter A. This parameter can be calculated from the elastic modulus E, the cross-sectional area S, and the nominal tension T_0 of the string if such data are available.[13] Alternatively, it can be estimated from the fundamental frequency descent of a recorded tone. An example of variation of the fundamental frequency is given in Fig. 15, where the second string has been initially displaced 4.0 mm at its midpoint, and then released. The maximum fundamental frequency here is $f_{0,\max}=424.9$ Hz, and the nominal value is $f_{0,\mathrm{nom}}=409$ Hz. Note that, according to a recent study,[36] the overall f_0 variation of 15.9 Hz is well above the perception threshold, and thus clearly audible.

TABLE II. Integer and fractional parts of the delay line lengths for both polarizations. The sampling frequency is $f_{\mathrm{s}}=44\,100$ Hz. All quantities are given relative to the sampling interval $T=1/f_{\mathrm{s}}$.

String	#1	#2	#3	#4	#5
$\hat{L}_{\mathrm{nom}}$	47	53	56	62	69
$L_{\mathrm{frac,v}}$	0.27	0.06	0.19	0.03	0.98
$L_{\mathrm{frac,h}}$	0.40	0.20	0.35	0.20	1.16

An approximation formula for the A parameter that simulates the observed descent is readily available.[13] Here, we extract the modulation depth by minimizing the mean-square error between the frequency trajectories of the recorded and synthesized tones. In the synthesis model, the fundamental frequency is $f_{0,\mathrm{nom}}=409$ Hz. The loop filter coefficients [see Eq. (8)] are $g_{1,\mathrm{h}}=0.9946$ and $a_{1,\mathrm{h}}=-0.0106$ for the horizontal polarization, and $g_{1,\mathrm{v}}=0.9972$ and $a_{1,\mathrm{v}}=-0.0232$ for the vertical polarization. The coupling coefficient is set to a very small value $g_{\mathrm{c}}=0.0005$, and the input and output mixing parameters are $m_{\mathrm{p}}=0.55$ and $m_{\mathrm{o}}=0.44$, respectively. In Fig. 15, the variation of the fundamental frequency of this synthetic tone is presented with a dashed line. The best match in the mean-square sense is obtained with $A=3876.3$.

The parameter A thus specified, a final example demonstrates that the dual-mode kantele string model can simulate all the essential features of a kantele tone discussed in Sec. III. In this example, the fundamental frequency is set close to that of the third string, i.e., $f_0=393.75$ Hz. Note that this value corresponds to an integer delay line length of 56 samples when the sampling frequency is $f_{\mathrm{s}}=44\,100$ Hz. However, the delay line length difference in both polarizations is preserved in accordance with Table II.

The loop filter coefficients $g_{1,\mathrm{h}}=0.9937$, $g_{1,\mathrm{v}}=0.9983$, $a_{1,\mathrm{h}}=-0.0086$, and $a_{1,\mathrm{v}}=-0.0232$ provide similar decay times to the extracted decay times of the original kantele tone (see Fig. 10). As in the previous example, $g_{\mathrm{c}}=0.0005$, $m_{\mathrm{p}}=0.55$, and $m_{\mathrm{o}}=0.44$. The TMDF coefficient is deter-

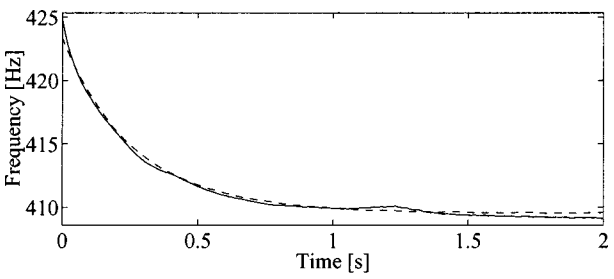

FIG. 15. Variation of the fundamental frequency in a kantele tone (obtained from the modified kantele) resulting from a fortissimo pluck (solid line) and a synthetic tone (dashed line).

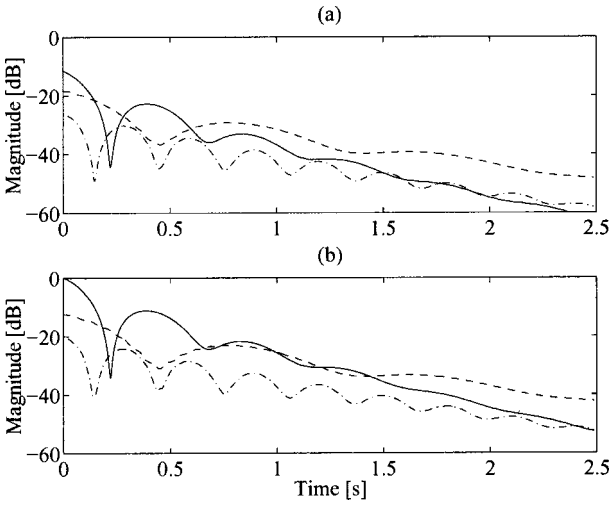

FIG. 16. Envelope trajectories of synthetic kantele tones. The first harmonic is shown with a dashed line, the second one with a solid line, and the third one with a dash-dotted line. (a) A softly plucked tone and (b) a strongly plucked tone. The plucking point is the midpoint of the string. The synthetic tone captures the most important features of a kantele tone as shown in Fig. 5.

mined by using typical values for musical steel strings, and set to $g_{\text{out}}=823$. A softly plucked and a strongly plucked tone are simulated by setting the initial deflection of the string to 1 and 2 mm, respectively. Figure 16 shows the amplitude envelope trajectories of (a) the softly plucked and (b) the strongly plucked synthetic kantele tones.[5]

A comparison between the synthetic and measured kantele tones (cf. Fig. 5) indicates that the model captures the most important features of a kantele tone, i.e., the beating of the harmonics, and the nonlinear generation and rapid onset of the second harmonic. The differences between the magnitudes of the measured and synthetic harmonics may be explained by noting that the model output shown in Fig. 16 is the composite force at the tuning pin, whereas Fig. 6 represents the radiated sound. It has been shown in Sec. III F that the body causes a filtering effect that inserts an additional 10-dB difference between the first and second harmonic. There are also perceptual differences between the synthetic and measured kantele tones. The parameter estimation method described here is entirely physical. Better results may be obtained if the research results on the perceptual aspects of the pitch glides[36] could be included in the parameter estimation procedure.

The simulations can be extended by incorporating a model of the kantele body based on the measurement data presented in Sec. III F. A body filter should be considered, since the *commuted synthesis method*[37,38] that is based on the linearity and time invariance of the whole system cannot be utilized in the nonlinear kantele model. Various filtering techniques for body modeling are readily available.[39–42] A body model might improve the perceptual match between the real and synthetic tones. However, the main purpose of the model presented in this paper is to verify and test the causes and effects of the nonlinear phenomena in the kantele tones, and the improvement in the synthesis quality is left for future work.

V. CONCLUSIONS

In this paper the kantele, a traditional Finnish folk music instrument, has been analyzed. The historical and structural properties of the kantele have been briefly overviewed. Two peculiar features of the kantele sound, i.e., the beating of the harmonics and the dominance and generation of the second harmonic, have been described in terms of the physical mechanisms. The cause and effect of the tension modulation driving force (TMDF) have been experimentally demonstrated, and its analytical approximation is presented. Unlike many other stringed instruments, the kantele has been shown to be susceptible to the TMDF.

A more detailed analysis could include various coupling mechanisms between the strings, their terminations (tuning pins and the varras), and the body, and could account for nonlinear coupling of different polarizations or generation of higher harmonics by the transverse components of the forces caused by the tension modulation. However, in this work the unique features of the bridgeless kantele have been found to be related to beating and to the TMDF, and a detailed analysis of other phenomena is left for future research.

The proposed synthesis model, which is based on the principles of digital waveguides and on a nonlinear string model that incorporates tension modulation, has been shown to capture the essential nonlinear properties of the kantele tones. Synthetic sounds produced by the model are in accordance with both the measurements and the analytical approximations. In the present time, the synthesis model includes only the fundamental properties of the real instrument. With increasing computational power, soon it will be feasible to directly incorporate the measured admittance and radiation functions within the sound source models. Then, the correspondence between the real and synthetic instrument could be more striking. Nevertheless, as demonstrated in the paper, even a simple model mimics the essential characteristics of the instrument, and the synthetic sound it produces can be used to verify the underlying assumptions and explanations. The real and synthetic sound examples of the kantele are available via the Worldwide Web.[5]

ACKNOWLEDGMENTS

This research was conducted within the project ''Sound Source Models—Analysis, Synthesis, and Coding'' financed by the Academy of Finland. The work of C. Erkut has been supported by the Jenny and Antti Wihuri Foundation. The authors would like to thank Dr. Arja Kastinen and Mr. Rauno Nieminen for providing valuable information about the history, form, and function of the instrument.

[1] Pronounced *'kän·te·le*.

[2] *The New Grove Dictionary of Musical Instruments*, edited by S. Sadie (MacMillan, London, 1984), pp. 358–359.

[3] I. Oramo, I. Hämäläinen, K. Virtamo, K. Aho, and M. Elfving, *Suuri musiikkiti-etosanakirja* (Music encyclopedia, in Finnish) (Weilin and Göös, Keuruu, Finland, 1990), pp. 168–171.

[4] *New Larousse Encyclopedia of Mythology*, edited by F. Guirand (Hamlyn, London, U.K., 1986), Chap. 9.

[5] Recorded sound examples are available at: http://www.acoustics.hut.fi/publications/papers/jasa-kantele/index.html

[6] M. Karjalainen, J. Backman, and J. Pölkki, ''Analysis, modeling, and

real-time sound synthesis of the kantele, a traditional Finnish string instrument,'' in Proc. IEEE Int. Conf. Acoust. Speech Signal Processing (Minneapolis, MN, 1993), pp. 229–232.
[7] A. Peekna and T. D. Rossing, ''The acoustics of baltic psaltery,'' in Proceedings of the International Symposium on Musical Acoustics (ISMA) (Perugia, Italy, 2001), pp. 437–442.
[8] N. H. Fletcher and T. D. Rossing, *The Physics of Musical Instruments* (Springer, New York, 1998), 2nd ed.
[9] Special thanks are due to ''Ikaalisten soitinrakentajat,'' who manufactured this special instrument.
[10] P. Stoica and R. Moses, *Introduction to Spectral Analysis* (Prentice-Hall, Upper Saddle River, NJ, 1997), pp. 146–151.
[11] R. J. Hanson, J. M. Anderson, and H. K. Macomber, ''Measurements of nonlinear effects in a driven vibrating wire,'' J. Acoust. Soc. Am. **96**, 1549–1556 (1994).
[12] K. A. Legge and N. H. Fletcher, ''Nonlinear generation of missing modes on a vibrating string,'' J. Acoust. Soc. Am. **76**, 5–12 (1984).
[13] T. Tolonen, V. Välimäki, and M. Karjalainen, ''Modeling of tension modulation nonlinearity in plucked strings,'' IEEE Trans. Speech Audio Process. **8**, 300–310 (2000).
[14] G. F. Carrier, ''On the non-linear vibration problem of the elastic string,'' Q. Appl. Math. **3**, 157–165 (1945).
[15] C. Valette, ''The mechanics of vibrating strings,'' in *Mechanics of Musical Instruments*, edited by A. Hirschberg, J. Kergomard, and G. Weinreich (Springer, New York, 1995), pp. 116–183.
[16] G. V. Anand, ''Large-amplitude damped free vibration of a stretched string,'' J. Acoust. Soc. Am. **45**, 1089–1096 (1969).
[17] J. W. Miles, ''Resonant, nonplanar motion of a stretched string,'' J. Acoust. Soc. Am. **75**, 1505–1510 (1984).
[18] C. E. Gough, ''The nonlinear free vibration of a damped elastic string,'' J. Acoust. Soc. Am. **75**, 1770–1776 (1984).
[19] Z. C. Feng, ''Does nonlinear intermodal coupling occur in a vibrating stretched string?,'' J. Sound Vib. **182**, 809–812 (1995).
[20] N. Tufillaro, ''Nonlinear and chaotic string vibrations,'' Am. J. Phys. **30**, 408–414 (1989).
[21] B. E. Richardson, ''String instruments: Plucked,'' in *Encyclopedia of Acoustics*, edited by M. J. Crocker (Wiley, New York, 1997), Vol. 4, pp. 1627–1634.
[22] T. Tolonen, C. Erkut, V. Välimäki, and M. Karjalainen, ''Simulation of plucked strings exhibiting tension modulation driving force,'' in Proc. Int. Comput. Music Conf. (Beijing, China, 1999), pp. 5–8.
[23] H. A. Conklin, ''Generation of partials due to nonlinear mixing in a stringed instrument,'' J. Acoust. Soc. Am. **105**, 536–545 (1999).
[24] V. Välimäki, M. Karjalainen, T. Tolonen, and C. Erkut, ''Nonlinear modeling and synthesis of the kantele—A traditional Finnish string instrument,'' in Proc. Int. Comput. Music Conf. (Beijing, China, 1999), pp. 220–223.
[25] X. Boutillon and G. Weinreich, ''Three-dimensional mechanical admittance: Theory and new measurement method applied to the violin bridge,'' J. Acoust. Soc. Am. **105**, 3524–3533 (1999).
[26] C. E. Gough, ''The theory of string resonances on musical instruments,'' Acustica **49**, 124–141 (1981).
[27] O. Christensen and B. B. Vistisen, ''Simple model for low-frequency guitar function,'' J. Acoust. Soc. Am. **68**, 758–766 (1980).
[28] G. Weinreich, ''Coupled piano strings,'' J. Acoust. Soc. Am. **62**, 1474–1484 (1977).
[29] G. Essl and P. R. Cook, ''Measurements and efficient simulations of bowed bars,'' J. Acoust. Soc. Am. **108**, 379–388 (2000).
[30] J. O. Smith, ''Physical modeling using digital waveguides,'' Comput. Music J. **16**, 74–91 (1992).
[31] V. Välimäki, T. Tolonen, and M. Karjalainen, ''Plucked-string synthesis algorithms with tension modulation nonlinearity,'' in Proc. IEEE Int. Conf. Acoust. Speech Signal Processing (Phoenix, AZ, 1999), pp. 977–980.
[32] T. Laakso, V. Välimäki, M. Karjalainen, and U. K. Laine, ''Splitting the unit delay-tools for fractional delay filter design,'' IEEE Signal Process. Mag. **13**, 30–60 (1996).
[33] D. A. Jaffe and J. O. Smith, ''Extensions of the Karplus–Strong plucked-string algorithm,'' Comput. Music J. **7**, 56–69 (1983).
[34] V. Välimäki, J. Huopaniemi, M. Karjalainen, and Z. Jánosy, ''Physical modeling of plucked string instruments with application to real-time sound synthesis,'' J. Audio Eng. Soc. **44**, 331–353 (1996).
[35] M. Karjalainen, V. Välimäki, and T. Tolonen, ''Plucked-string models: From the Karplus–Strong algorithm to digital waveguides and beyond,'' Comput. Music J. **22**, 17–32 (1998).
[36] H. Järveläinen and V. Välimäki, ''Audibility of initial pitch glides in string instrument sounds,'' in Proc. Int. Comput. Music Conf. (Havana, Cuba, 2001).
[37] J. O. Smith, ''Efficient synthesis of stringed musical instruments,'' in Proc. Int. Comput. Music Conf. (Tokyo, Japan, 1993), pp. 64–71.
[38] M. Karjalainen, V. Välimäki, and Z. Jánosy, ''Towards high-quality sound synthesis of the guitar and string instruments,'' in Proc. Int. Comput. Music Conf. (Tokyo, Japan, 1993), pp. 56–63.
[39] K. Bradley, M. H. Cheng, and V. L. Stonick, ''Automated analysis and computationally efficient synthesis of acoustic guitar strings and body,'' in Proc. IEEE Workshop of Applications of Signal Processing to Audio and Acoustics (New Paltz, NY, 1995), pp. 238–241.
[40] M. Karjalainen and J. O. Smith, ''Body modeling techniques for string instrument synthesis,'' in Proc. Int. Comput. Music Conf. (Hong Kong, 1996), pp. 232–239.
[41] P. R. Cook and D. Trueman, ''NBody: Interactive multidirectional musical instrument body radiation simulators, and a database of measured impulse responses,'' in Proc. Int. Comput. Music Conf. (Ann Arbor, MI, 1998), pp. 353–356.
[42] M. Karjalainen, V. Välimäki, H. Penttinen, and H. Saastamoinen, ''DSP equalization of electret film pickup for the acoustic guitar,'' J. Audio Eng. Soc. **48**, 1183–1193 (2000).

Linking the sounds of dolphins to their locations and behavior using video and multichannel acoustic recordings

Rebecca E. Thomas[a)]
Biology Department, Woods Hole Oceanographic Institution, Woods Hole, Massachusetts 02543

Kurt M. Fristrup
Bioacoustics Research Program, Cornell Laboratory of Ornithology, Ithaca, New York 14850

Peter L. Tyack
Biology Department, Woods Hole Oceanographic Institution, Woods Hole, Massachusetts 02543

(Received 1 May 2002; revised 3 May 2002; accepted 22 May 2002)

It is difficult to attribute underwater animal sounds to the individuals producing them. This paper presents a system developed to solve this problem for dolphins by linking acoustic locations of the sounds of captive bottlenose dolphins with an overhead video image. A time-delay beamforming algorithm localized dolphin sounds obtained from an array of hydrophones dispersed around a lagoon. The localized positions of vocalizing dolphins were projected onto video images. The performance of the system was measured for artificial calibration signals as well as for dolphin sounds. The performance of the system for calibration signals was analyzed in terms of acoustic localization error, video projection error, and combined acoustic localization and video error. The 95% confidence bounds for these were 1.5, 2.1, and 2.1 m, respectively. Performance of the system was analyzed for three types of dolphin sounds: echolocation clicks, whistles, and burst-pulsed sounds. The mean errors for these were 0.8, 1.3, and 1.3 m, respectively. The 95% confidence bound for all vocalizations was 2.8 m, roughly the length of an adult bottlenose dolphin. This system represents a significant advance for studying the function of vocalizations of marine animals in relation to their context, as the sounds can be identified to the vocalizing dolphin and linked to its concurrent behavior. [DOI: 10.1121/1.1494805]

PACS numbers: 43.80.Ka, 43.30.Sf, 43.80.Jz [WA]

I. INTRODUCTION

Studies of animal communication and social behavior ideally use methods where signals and actions can be associated with individuals. Only under these conditions can one fully study social interactions involving signal and response. Studies of marine mammal acoustic repertoires have been hampered by the difficulty of identifying which animal produces each sound. Marine mammals generally do not open their mouths when they vocalize[1] underwater, nor do they regularly release bubbles. Humans cannot routinely use their auditory capabilities to localize underwater sounds directly. However, these technical difficulties need not inhibit research on marine mammal acoustic behavior. Acoustic communication is especially important for these species, because they are often out of sight of each other, but can remain in acoustic contact at long ranges.

Several solutions have been proposed and used to solve the problem of identifying the vocalizing animal, including isolating animals (Lilly and Miller, 1961; Caldwell *et al.*, 1990; Sayigh *et al.*, 1990), attaching tags to animals (Evans and Sutherland, 1963; Tyack, 1991; Tyack and Recchia 1991; Nowacek *et al.*, 1998), and identifying the vocalizing animal using bubblestreams (Dahlheim and Awbrey, 1982; McCowan, 1995; McCowan and Reiss, 1995; Herzing, 1996). These methods have produced valuable results, but in the case of isolation or tags can yield biased data by altering the behavior of the animal. Bubblestream emissions occur relatively rarely (Caldwell *et al.*, 1990; Fripp, 1999), and themselves may function as a behavioral display. Also, sounds produced with bubblestreams may not be a random subsample of all the sounds emitted (Fripp, 1999).

Methods to locate the source of a sound and to link this acoustic location to visual images promise the ability to obtain unbiased results without modifying the behavior of the study animals. However, the first part of this method, acoustic localization, has proven difficult to achieve for marine mammals, and few implementations have been linked to visual data to allow identification of the vocalizer. Linear arrays for sound beamforming and dispersed arrays for localization are widely used techniques for determining the location or direction of a sound source. Beamforming using towed linear arrays is often suitable for field work at sea with free-ranging animals, because the array can be easily towed while maintaining fixed distances between hydrophones. When the length of the array is small relative to the distance to the sound source, only the bearing to the source is obtained. This bearing indicates angle relative to the line of the array, so the locus of possible locations is a cone. With careful positioning of the array relative to the animals, focal follows of single animals can be performed. For example, Miller and Tyack (1998) followed free-ranging killer whales while beamforming their calls using a small towed array.

Dispersed array localization has been used more often

a)Electronic mail: rthomas@whoi.edu

than linear beamforming to study cetacean sounds. Watkins and Schevill (1972) used a drifting three-dimensional array to determine $x-y$ positions of finback whales, right whales, and white-beaked dolphins. Although the technique used passive acoustic localization, they needed to produce intermittent pings to determine hydrophone locations. The calibration pings can interfere with the behavior being observed; they had the effect of temporarily halting sperm whale sound production (Watkins and Shevill, 1975).

Clark *et al.* (1986) used a fixed array to study bowhead whales during their spring migration off Pt. Barrow, Alaska. Placing the hydrophones at fixed locations in the ice eliminated the need for intermittent pings. Spiesberger and Fristrup (1990) developed a method combining passive localization of vocalizing animals with acoustic tomography. Their technique allowed for localization of vocalizing animals in addition to construction of maps of sound speed and wind (or current) fields. However, their technique has yet to be implemented in its entirety for marine mammals. Freitag and Tyack (1993) demonstrated the feasibility of acoustic localization of bottlenose dolphin sounds in a captive environment. Although successful, their study demonstrated that reverberation presents a problem for localization in captive environments, and they did not attempt to link acoustic locations to visual. Janik (2000) demonstrated the feasibility of a two-dimensional acoustic localization system for determining positions of vocalizing bottlenose dolphins in the wild. Reverberation did not appear to be a significant problem in this study, most likely due to the fact that the fixed array was located in a large channel rather than in a reverberant captive pool.

A few methods have endeavored to combine acoustic location or bearing data with concurrent video recordings to obtain the identity of a vocalizing animal. Dudzinski *et al.* (1995) developed a video/acoustic system for underwater recording of dolphin interactions. Analysis of the data used a human observer to aurally determine if the sound came from the right, left, or center of the system, but did not allow for pinpointing the sound source on the video image. Brensing *et al.* (2001) designed a system of two pairs of closely spaced hydrophones to localize dolphins within a pool. They had a video component to the system, but did not show video overlay.

Few, if any, studies have been able to link the locations of sounds to a detailed record of behavior. The technique presented here projects acoustic localization results onto a video recording of dolphin behavior. An observer watching the video can see behaviors happening, hear the concurrent vocalizations, and also see on the screen which individual produced the vocalization. Having a record of which animal produced which sound, and what it was doing when it produced the sound, is important for understanding the function of communicative sounds. The identity of the calling animal can be determined, and the behavioral context of the sound can be revisited. A number of research directions that require knowledge of the identity of the vocalizing animal can be explored, as well as data archived for future reference and reanalysis.

The focus of this study was not a demonstration of the merits of a particular localization algorithm, but a demonstration that acoustic localization data can be combined with video analysis methods to successfully associate dolphin sounds with the individuals that produce them. Video recordings have long been used to supplement visual observations, and to provide an archival record of behavior. The capacity to augment the video imagery and soundtrack with a visual indication of the animal producing each sound magnifies the scientific and archival value of these recordings. Acoustic localization software provided by the Cornell Bioacoustics Research Program was used here because it was available for this study and easily adapted to its needs. Any other localization package that yielded equivalent or better localization accuracy could be substituted in its place, without substantially affecting the conclusions of this work.

II. METHODS

A. Study site

This research was performed at Dolphin Quest Bermuda's interim facility at the Maritime Museum in the Naval Dockyards on Ireland Island, Bermuda in the fall of 1999. At this time, the dolphins' social group was composed of two mother–calf pairs, a juvenile male and a juvenile female, for a total of six animals. The lagoon facility measured roughly 30 meters by 45 meters. The sides of the lagoon were composed of irregular limestone bricks, covered with algae and other organisms. The ramparts of the Naval Dockyards directly abutted the lagoon on one side. Eight hydrophones were placed around three sides of the lagoon, and the video camera was placed on the rampart next to the lagoon, approximately 9 m high (Fig. 1). The lagoon was connected to the ocean via a short channel with a gate on the lagoon side, allowing the water level in the lagoon to change with the local tides. The temperature of the seawater at a depth of approximately 0.5 m was recorded each day of observation from a mercury thermometer. The speed of sound was calculated from temperature and salinity from standard equations (Urick, 1982). Because salinity and depth have less significant effects than temperature, salinity was assumed to be constant at 36.6 ppt, and the pressure effect on the speed of sound was assumed to be nil, the same as assuming a depth of 0 m for the path from the animal in the shallow lagoon to the hydrophone.

B. Acoustic localization

Eight hydrophones (High Tech Inc. HTI-94-SSQ) were placed around three of the four sides of the lagoon. The fourth side of the lagoon directly abutted the ramparts of the Dockyard fort, with no convenient spot to anchor a hydrophone. An eight-channel TASCAM DA-88 multitrack recorder digitally sampled signals simultaneously from all the hydrophones and then saved the digitized signals to tape. The TASCAM DA-88 sampled at 48 kHz and had a flat frequency response (± 0.5 dB) from 20 Hz to 20 kHz. The frequency response of the hydrophones was 2 Hz to 30 kHz, so the recorded signals were frequency limited by the

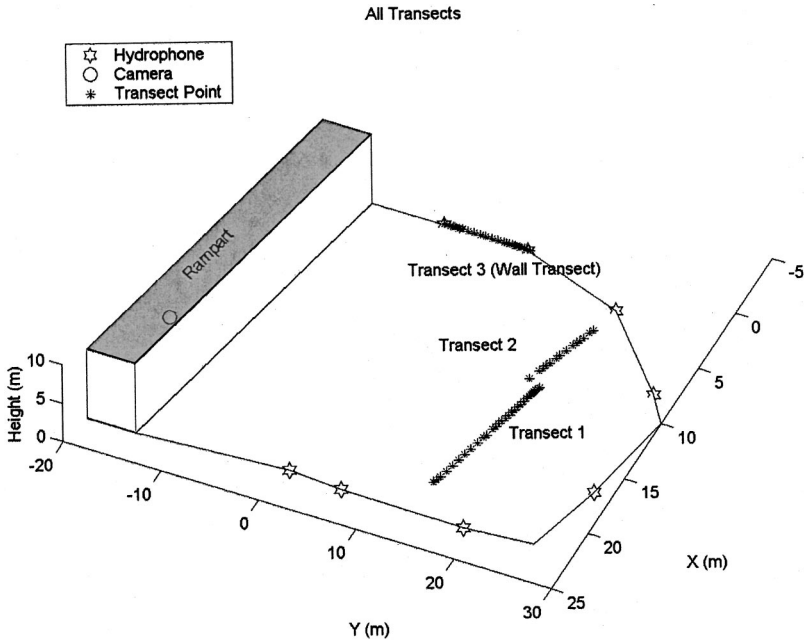

FIG. 1. Schematic of the lagoon with locations of the camera, hydrophones, and transect points.

TASCAM recorders to the range of 20 Hz to 20 kHz. Eight channels of 1-s data (Microsoft wave format) occupied 0.73 Mb of disk space.

1. Data acquisition

The digital data on tape were transferred directly to a computer running Microsoft Windows using the ''Translator Plus'' digital audio format converter (Spectral Inc., Woodinville, WA) and STUDIO TRACKS XP software.

2. Signal selection process

A suite of MATLAB (MathWorks, Natick, MA) programs was used for performing the various aspects of signal selection. An automated energy detector was used to detect, extract, and save sounds above a preset energy threshold (modified from Fripp *et al.*, 1997). This enabled more extensive screening of the multichannel data than would be feasible using people to screen sounds, while taking advantage of human judgment to edit the relatively compact set of detections. The operator viewed eight-channel spectrograms of the extracted sound cuts. The operator would discard the cut if it contained only noise or if the dolphin vocalization was excessively contaminated by transient signals (e.g., snapping shrimp clicks). Otherwise, the operator would highlight the sounds in time and frequency. These time and frequency parameters were saved for the localization step.

3. Localization algorithm

A brief summary of the algorithm used in this study is provided here, but any acoustic localization algorithm that provided comparable results could be substituted. The algorithm chose points in space and calculated the time delays between phones that would result if the sound came from that point in space. The value of each cross-correlation function at the corresponding time delay was determined. The sum of the cross-correlation values is proportional to the beamformed energy corresponding to the designated point, and the search algorithm looked for the point that maximized the summed correlation values. [See Johnson and Dudgeon (1993) for a detailed description of beamforming.] This contrasts to alternative schemes in which the time delays associated with the peaks of each cross-correlation function are taken, and a least-squares fit is performed to obtain a location estimate from these time delays (Spiesberger and Fristrup, 1990). The beamforming algorithm produces accurate locations in acoustic scenarios (overlapping sound transients, multipath) that can present difficulties for algorithms based on peak picking. Details of the algorithm used in this study can be found in Fristrup and Dunsmore (unpublished).

As the lagoon was not very deep, the localization was performed only in the x and y dimensions. A typical localization of a dolphin vocalization took about 22 s on a Pentium III 700 MHz computer. The algorithm gave two outputs: the $x-y$ localization coordinates and a term that quantified the quality of the localization. A heuristic threshold for localization quality was implemented to remove outliers caused by poor localization quality.

4. Calibration of acoustic localization system: Locations of hydrophones

Precise hydrophone locations are needed for accurate localization. Approximate interhydrophone distances were measured using a tape measure to obtain approximate hydrophone positions. To obtain more precise locations, a calibration signal set was played at each hydrophone (ostensibly yielding a time delay of 0 for that hydrophone). The calibration signal set consisted of a set of five pseudorandom sequences and a set of four upsweeps (4–7 kHz). The pseudorandom sequences, also known as Barker codes (Barker, 1953), are binary sequences with good autocorrelation properties; autocorrelated Barker codes have high main lobes and low sidelobes. The sequence used for this study was an 11-bit Barker code (1,−1,1,1,−1,1,1,1,−1,−1,−1), set so each

bit lasted a little over 0.01 s, with the total 11-bit sequence lasting about 0.125 s, or 1/8 s. The upsweeps each lasted about 1 s.

Received calibration signals were saved as multichannel sound cuts. Localization was performed on each sound cut to obtain a series of estimates of hydrophone locations. Interphone time delays were calculated from these estimated locations and also saved. Outlier localizations were removed, yielding a set of localizations and corresponding sets of calculated time delays for each of the eight hydrophones. The time delays were converted into distances using the speed of sound, yielding eight sets of interhydrophone distances. These sets were condensed into the matrix $\mathbf{D_{exp}}$. The matrix $\mathbf{D_{exp}}$ is an 8×8 matrix of interhydrophone distances. To determine the best-fit $x-y$ positions that would yield these distances, a multidimensional unconstrained nonlinear minimization [Nelder-Mead (Press *et al.*, 1992)] was performed in MATLAB. This type of minimization requires no assumptions about the function to be minimized. The function to be minimized was $\|\mathbf{D_{pos}}-\mathbf{D_{exp}}\|$, minimizing over $\mathbf{D_{pos}}$. $\mathbf{D_{pos}}$ is the set of interposition distances between a set of eight $x-y$ positions. The $\mathbf{D_{pos}}$ which minimizes $\|\mathbf{D_{pos}}-\mathbf{D_{exp}}\|$ should be the distances between the correct hydrophone positions. In the minimization, $\mathbf{D_{pos}}$ was initialized as the set of distances between the tape-measured hydrophone positions. For reference in the real world, one hydrophone was arbitrarily set to (0,0), and the x coordinate of an adjacent hydrophone set to 0. The rest of the hydrophone coordinates were calculated from these two hydrophones and the best-fit $\mathbf{D_{pos}}$ resulting from the minimization.

5. Calibration of the acoustic localization system: Accuracy and precision

In order to determine the accuracy of the acoustic localization system, calibration transects were performed along a dock that separated the lagoon into two parts as well as along a side wall of the lagoon (Fig. 1). The same calibration signal as used for calibrating the hydrophone locations was played at set locations along three transect lines, transect 1, transect 2, and transect 3. The lines were measured using a tape measure. The error was calculated as the distance from mean localized position to actual position (calculated using tape measured lines).

C. Video system

The video camera was placed at a height of approximately 9 m, on the side of the lagoon abutting the ramparts. The camera was placed in approximately the same position each day. A wide-angle lens (KVC-05 0.5 x) and polarizing filter were attached to the 3 ccd digital video camcorder (SONY TRV-900) used for recording video. At the beginning of each recording session, the timestamps on the video and audio recorders were synchronized to a digital chronometer. Once the camera was in place for the day, it was not moved. Video recordings were later imported into a PC computer using a DVRaptor card and ADOBE PREMIERE software.

There are two parts to calibrating a camera image. The first is the intrinsic calibration, in which the internal geometric and optical workings of the camera are calibrated. As long as the focal length of the lens is kept constant, the intrinsic parameters will not vary with recording of different images. The second part of calibrating a camera image is the extrinsic calibration. In this calibration, parameters such as the distance to objects in the world frame coordinate system, rotation, etc. are calibrated. For our system we always used the same configuration of lenses, filters, and zoom; therefore, the intrinsic calibration only needed to be performed once. The camera was installed each morning and then not moved for the day, so the extrinsic calibration needed to be performed once for each day of observation. A camera calibration toolbox for MATLAB obtained from Cal-Tech (Bouguet, 2000) was used for both the intrinsic and extrinsic calibrations. The projection feature of the calibration toolbox transformed the real-world coordinates of localizations into video space.

1. Intrinsic calibration

The camera calibration toolbox included a checkerboard that we attached to stiff matting board. The checkerboard was videotaped and 20 images representing a diversity of video angles and distances were used for the intrinsic calibration. The toolbox, with some initial user input, automatically finds the corners of the checkerboard boxes and performs the intrinsic calibration. Parameters from this calibration were saved in a file for later use.

2. Extrinsic calibration

After solving for the intrinsic parameters, the extrinsic parameters were calculated by relating known points in the world coordinate system with their pixel analogs in the video image. Video frame pixel coordinates were obtained by plotting the image in MATLAB and using the mouse to click on locations in the image. We chose five easily recognizable locations to be used for daily calibration. The daily calibration yielded the extrinsic calibration parameters for that day.

One way of measuring the error of the video imaging system is in terms of the projection error, which is the difference between the actual position and the projected position. Using a tape measure we determined the world coordinates at 100 set locations around the lagoon (videotaped on 1 November 1999). The real world positions of these coordinates were termed $\mathbf{X_{ti}}$ (in meters). These positions were projected (from the extrinsic parameters calculated from the five specified points) into video frame coordinates. We called these projected coordinates $\mathbf{x_{ti}}$ (in pixels). From the video image we determined the pixel location of the $\mathbf{X_{ti}}$ coordinates by plotting the image in MATLAB and using the mouse to click on each location in the video frame. We termed these video frame coordinates $\mathbf{x_{mi}}$. We backprojected $\mathbf{x_{mi}}$ to real-world coordinates, $\mathbf{X_{mi}}$ (in meters) for comparison with $\mathbf{X_{ti}}$. The projection error in terms of real-world coordinates is calculated as $\mathbf{E_i}=\mathbf{X_{ti}}-\mathbf{X_{mi}}$. The error in terms of pixels is $\mathbf{e_i}=\mathbf{x_{ti}}-\mathbf{x_{mi}}$.

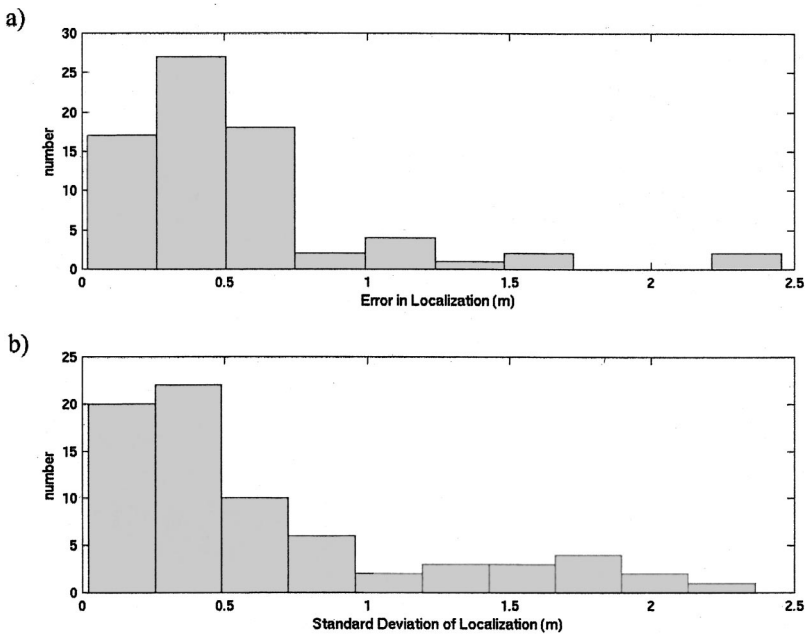

FIG. 2. Histograms of error and standard deviation of the acoustic localization system.

D. Method for fusion of acoustic localization and video imaging

Projected sound-source positions derived from acoustic localization were plotted in MATLAB against a blue background and exported as numbered picture files. The localizations were projected onto the water's surface, taking into account daily tidal fluctuations. The tidal height was assumed to not change significantly over each 2-h observation period. The picture files were imported into ADOBE PREMIERE as an animated video clip. The video sequence from the same time sequence as the localizations was also imported. The video sequence and animated video clip were overlaid, setting the blue background in the animated localization clip to transparent. This results in the localized positions appearing as bull's-eyes on the video clip [see Fig. 7(a) in Sec. III].

A set of sound playbacks across the lagoon (transect 1) was videotaped to compare positions obtained from both acoustic localization and video imaging. Pixel positions of the acoustic source were measured directly from the video images by clicking the mouse on the position of the source where the cable exited the water. The difference in localized position and video frame position was calculated for each playback location to obtain the error of the overall localization/video system for calibration sounds.

Dolphin localization: A set of 222 sounds from dolphins swimming freely in the lagoon was localized. Of the subset of these sounds that could be localized to a dolphin or a group of dolphins, ten sounds of each of three sound types were randomly chosen. The three sound types were echolocation clicks, burst-pulsed sounds, and whistles. For each vocalization, the error was calculated as the distance between the localized position and the nearest dolphin. When possible, the blowhole was used as the reference point for the dolphin. If more than one dolphin was in the immediate area, the error was calculated as the distance between the localized position and the mean position of the two nearest dolphins. Instances when more than two dolphins were in the immediate area were not used.

III. RESULTS

This paper presents the results of a combined acoustic localization and video imaging system. The results are broken down into three categories: acoustic localization results, video imaging results, and combined acoustic localization and video imaging results. The results of the combined system are broken down into two categories: results from the artificial sound source, and results from dolphins.

A. Error of acoustic localization system

The error and standard deviation of the acoustic localization system were determined by comparing known source playback locations along the transect lines to the correspond-

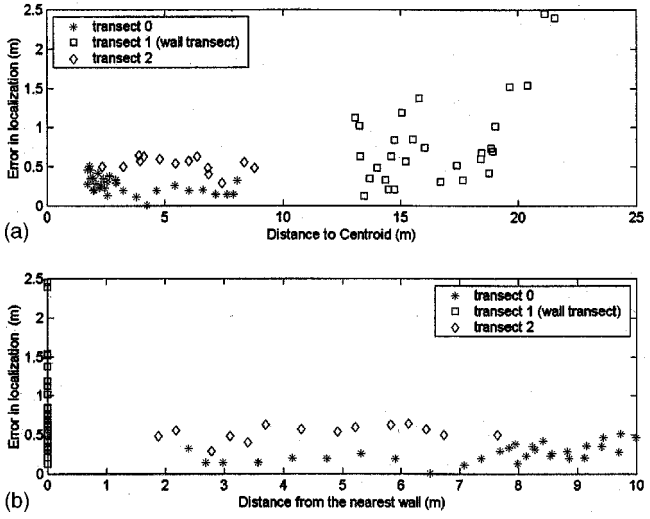

FIG. 3. (a) Error in localization plotted versus distance from source position to centroid of array. (b) Error in localization plotted versus distance from nearest wall.

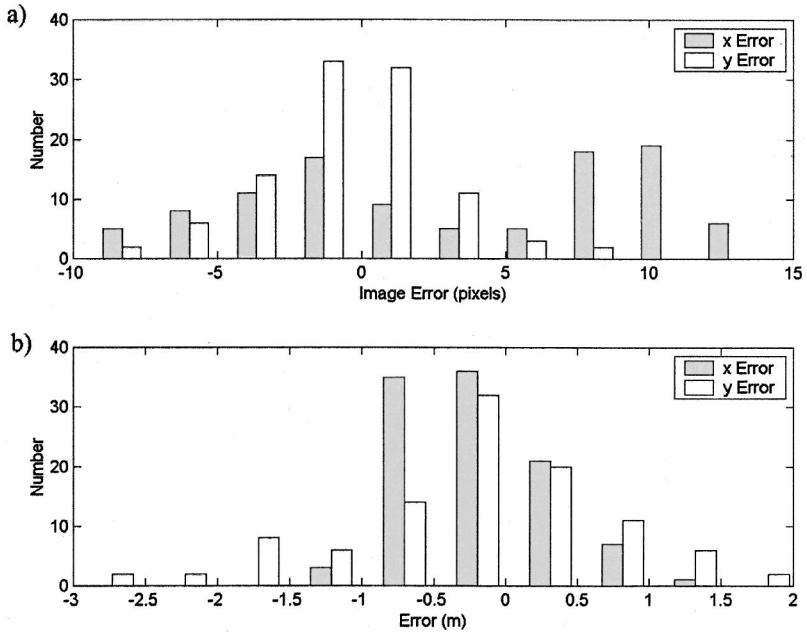

FIG. 4. (a) Histogram of projection error of the video system in terms of pixels. The video frame is 480×720 pixels. (b) Histogram of the projection error in terms of real-world coordinates (m).

ing positions calculated from acoustic localization. The histograms of error and standard deviation are shown in Fig. 2.

The localization error was less than 1.5 m for 95% of the measurements (mean error=0.54 meters). Thus, the accuracy of the localization system can be thought of as being better than 1.5 m. The mean standard deviation was 0.64 m. Thus, the precision of localization can be thought of as being two standard deviations, or 1.28 m.

Figure 3 presents the error as a function of distance from the centroid of the array as well as of distance from the nearest wall. The error appeared to increase both with increasing distance from the centroid of the array as well as with decreasing distance to the nearest wall.

B. Error of video imaging system

The histogram of the video projection error in terms of pixels is shown in Fig. 4(a). The size of each video image in pixels was 480×720. Of the error in the *x* dimension, 95% was less than 11.6 pixels. This was less than 1.6% percent of the image size in the *x* dimension. Of the error in the *y* dimension, 95% was less than 6.4 pixels, which was less than 1.3% of the image size in the *y* dimension. The mean error was 6.0 pixels in the *x* dimension and 2.4 pixels in the *y* dimension.

The projection error was also calculated in terms of real-world coordinates. The histogram of this error is shown in Fig. 4(b). For ease of visualization, the projection error in terms of real-world coordinates is plotted at the location of each coordinate in Fig. 5. Of the projection error, 95% was less than 0.9 m in the *x* axis, and 2.0 m in the *y* axis. The mean projection error was 0.5 m in the *x* axis and 0.7 m in the *y* axis. The overall 2D projection error was less than 2.1 m for 95% of the measurements. The mean 2D projection error was 0.9 m.

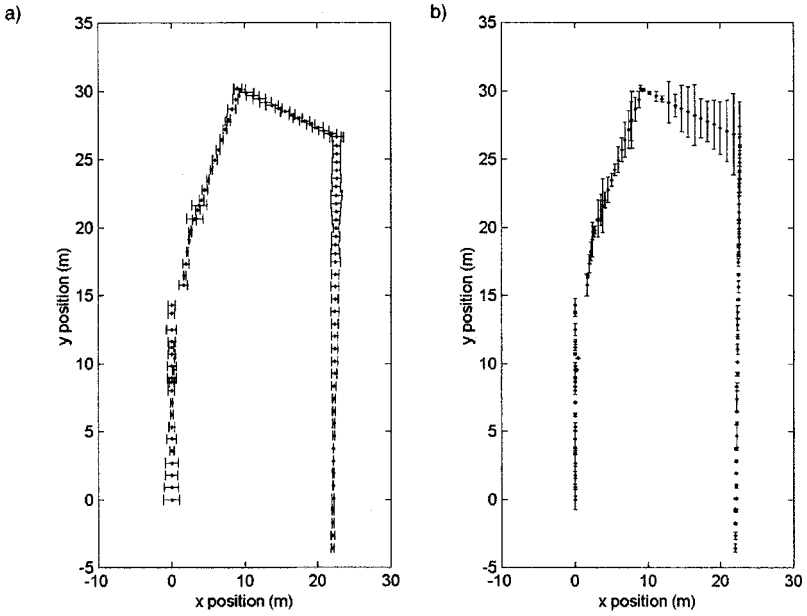

FIG. 5. Projection error in terms of real-world coordinates. (a) The error in the *x* dimension at each *x*–*y* position is plotted as an error bar centered at that position. (b) The error in the *y* dimension at each *x*–*y* position is plotted as an error bar centered at that position.

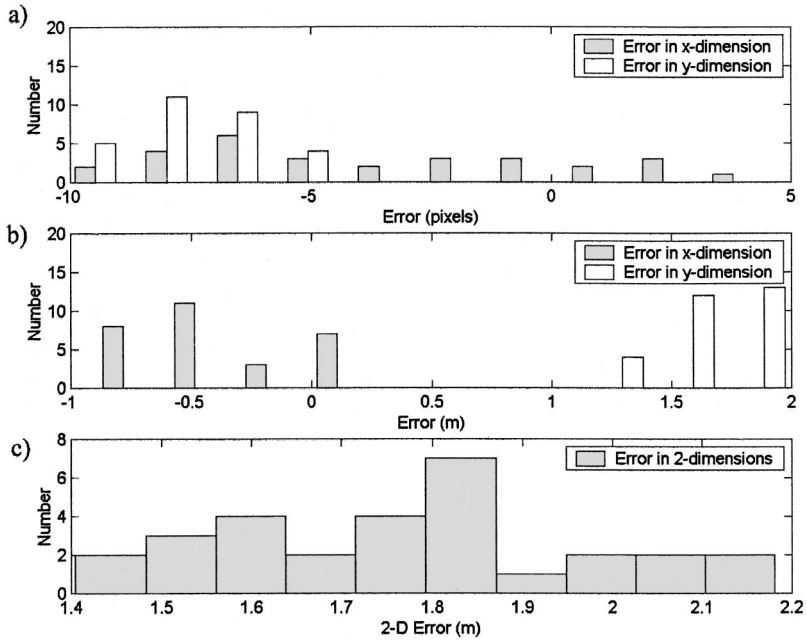

FIG. 6. (a) Difference in calculated pixel position of the acoustic source using acoustic localization and video imaging. (b) Difference in meters of calculated position of the acoustic source using acoustic localization and video imaging. (c) 2D error (m) between the calculated position of the acoustic source using acoustic localization and video imaging.

C. Synthesis of acoustic localization and video

1. Artificial sound source

Video recordings were performed during acoustic calibration transect 1 across the center of the lagoon (shown in Fig. 1). This allowed direct comparison of the projected positions obtained by acoustic localization to positions obtained directly from video images. Figure 6 presents histograms of the error between localized positions and video frame positions in terms of both pixel and real-world coordinates. Of the error measurements in the *x* and *y* axes, 95% were less than 10.0 and 9.8 pixels, respectively [Fig. 6(a)]. In real-world coordinates this corresponds to errors less than 0.9 and 2.0 m, respectively [Fig. 6(b)]. The mean errors in the *x* and *y* axes were 4.7 and 7.5 pixels, respectively. In real-world coordinates this corresponds to mean errors of 0.4 and 1.7 m in the *x* and *y* axes, respectively. The 2D error between the localized and video frame positions was less than 2.1 m for 95% of the measurements [Fig. 6(c)]. The mean 2D error was 1.8 m.

2. Dolphin sounds

The final set of results reports the error of the system with the dolphins as the sound source, matching localized sounds with the video images of the vocalizing dolphins. An example of matching a localized vocalization to a dolphin is shown in Fig. 7(a), with the spectrogram of the localized echolocation click shown in Fig. 7(b). The *x* axis, *y* axis, and 2D results from the comparisons of localized positions to video frame positions are shown for each of the three sound types in Table I. The means were calculated for each sound type as well as over all three sound types: 95% of the errors were less than 0.8 m in the *x* dimension, 2.5 m in the *y* dimension, and 2.9 m in the combined dimensions (2D). The

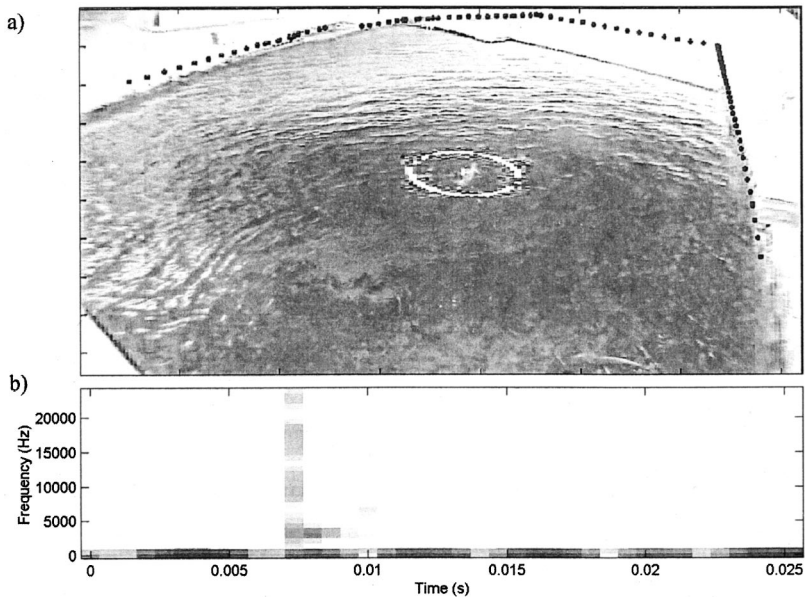

FIG. 7. Example localization of a dolphin vocalization. (a) The bull's-eye overlaid onto the video image shows the localized position of the vocalizing dolphin. (b) Spectrogram of the vocalization (echolocation click) that was used for the localization. Only frequencies above 10 000 Hz were used for this particular localization.

TABLE I. Mean error between localized and video frame positions for each of three vocalization types, the mean error over all three vocalization types, and the 95% error limit over all three vocalization types.

	X Dimension (m)	*Y* Dimension (m)	2D (m)
Burst pulsed sounds	0.33	1.29	1.34
Echolocation clicks	0.52	0.65	0.83
Whistles	0.34	1.24	1.28
Overall mean	0.40	1.06	1.13
95% error limit	0.75	2.52	2.91

mean error of echolocation clicks appears to be lower than that of the other two sound types. However, the difference in error between the sound types cannot be considered to be statistically significant (ANOVA, $p=0.068$).

In addition to determining the errors between localized positions and video frame positions of vocalizing dolphins, the percent of localized sounds that could be attributed to a dolphin or a group of dolphins was also calculated (Table II). When only one dolphin was in the immediate vicinity of the localization (no other dolphins were within 1.5 m), the vocalization was determined to be from that individual. In some cases, more than one dolphin could be seen within 1.5 m of the localized position. In these instances the vocalization could only be identified as coming from that group of dolphins. In other cases it could not be determined that a dolphin was in the area. However, since in some areas the video image did not extend to the bottom of the lagoon, there were occasions when a dolphin was believed to be in the area, but the presence of the dolphin could not be confirmed. A dolphin might be believed to be in the area if the path between the dolphin's previous and following surfacings crossed the area around the localized position.

IV. DISCUSSION

The localization error of 95% of the measurements from the calibration signals was less than 1.5 m. This is less than the average length of an adult bottlenose dolphin (1.9–3.9 m, (Read *et al.*, 1993). The precision (2 standard deviations) of the localization of the calibration signals was 1.28 m. In this sense, we should be able to distinguish sound sources that are greater than 1.28 m apart. The error was not constant at all points within the array, but was larger near the wall of the lagoon (Fig. 3). This trend was observed primarily in transect 3. The other transects showed no trend of increasing error with either decreasing distance from the wall or increasing distance from the centroid of the array. These transect points along the wall were also the points furthest from the centroid. Therefore, it was not possible to rigorously separate the effects of decreasing distance from the wall and increasing distance from the centroid. However, the tight linkage between error greater than about 0.75 m and proximity to the wall suggests that the wall may have been the main factor. Reflections of sound off the wall can confuse the localization algorithm. This problem with multipath is common among localization algorithms (e.g., Freitag and Tyack, 1993; discussion in Spiesberger and Fristrup, 1990; Spiesberger, 1999). Confusion is likely to be greatest when the sound originates near the wall and the reflected sound cannot be isolated from the direct path. There are several practical ways to reduce this problem. Localized positions from reflected sounds will appear to come from outside the lagoon, which we know is not possible. Setting more detailed search boundaries for the algorithm might alleviate this problem. Another solution would be to keep the dolphins away from the walls, which in this setting was not practical. Spiesberger (1998, 1999, 2000) presents an algorithm that can deal with some aspects of multipath.

TABLE II. Number and percentage of localized vocalizations that could be attributed to a dolphin or group of dolphins.

	Number (Total=222)	Percentage
Cannot determine if dolphin in area:		
No reason to believe there is a dolphin:	8	3.6%
Reason to believe there is a dolphin:	27	12.2%
Can identify to group of dolphins:	101	45.5%
Can identify to individual dolphin:	86	38.7%

The error of the video system was measured in terms of pixels [Fig. 4(a)] and then projected into meters [Fig. 4(b)]. The absolute pixel error appeared to be the greatest in the *x* axis. However, the errors in terms of percentage of image size were similar for both the *x* and *y* axes. When the error of the video system was projected into meters, the error was greater in the *y* dimension. Error in the *y* dimension appeared to increase with increasing *y* position (Fig. 5), which was also increasing distance from the camera. The lagoon was longer in the *y* dimension than in the *x* dimension, so fitting more of the *y* axis into the image resulted in lower resolution and greater error at the limits. This skewed distribution of error could be improved by placing the video camera higher and at less of an angle to the lagoon (e.g., suspend the camera from an overhead position, as in Nowacek *et al.*, 2000). Another feature of Fig. 4(a) is the bimodality of the *x* error. Due to practical considerations of accessibility to different parts of the lagoon, the *x* axis was sampled more heavily at the extremes than at the middle. If one side were better calibrated at the expense of the other side, it would result in the observed bimodality of the *x* error.

The error of the overall system (Fig. 6) must take into account the errors of both the acoustic localization and video projection components. The 95% error bound calculated from the combined acoustic localization and video transect was 2.1 m. A comparison of this error bound to the 2.1-m error bound for the video calibrations and the 1.5-m error bound from the acoustic transects suggests that the video component of the system dominates the error.

Although the transects using calibration sounds from a mechanical source demonstrate that the system ostensibly had an error less than 2.1 m, the true test of the system is with sounds from the dolphins. The 95% error bound for the dolphin vocalizations was 2.9 m, roughly the length of an adult dolphin's body. The errors in video position and localized position of dolphin sounds were worse than those from calibration sounds from a mechanical source. This was probably due to a combination of several factors. The first factor

has to do with the calibration signal itself. The Barker codes and frequency upsweeps used for calibration were specifically designed to be easily locatable, while dolphin sounds may or may not be. In addition, many of the dolphin sounds may have lower signal-to-noise ratios than the calibration sounds, making localizations more susceptible to contamination from ambient noise, such as snapping shrimp clicks. Another factor was the movement of the dolphin while vocalizing, which may result in smearing of the localization. Also, if the synchronization between the acoustic localization and the video imaging is not perfect, rapid movements of the dolphin will result in an increased discrepancy between the localized position and the position on the video image. The third factor concerned the limited visibility of the water column. For the dolphin sounds, most of the matches between the localizations and the dolphin image on the video were to whatever portion of the dolphin's anatomy was visible. Since dolphins can be up 4 m long, using a portion of the anatomy far from the head could cause significant error. In addition, although the operator attempted to keep track of all the dolphins in the pool, it is possible that limited visibility may have resulted in an ID mismatch.

This system of acoustic localization using a fixed array combined with elevated video imaging has several benefits. The elevated video enables increased visibility into the water column, along with possibilities of more detailed behavior analyses. The localization component enables matching of the vocalization to concurrent behavior. Another advantage of this system is that it is not necessary that the human observers be near the animals under observation. This may be important as the animals were fed by human trainers, and the presence of any humans may interrupt the dolphins' normal social routine. The system could be used in a wide variety of captive situations, as long as the appropriate localization and video information could be obtained. Use of the system in reverberant captive environments may be limited by the localization algorithm used. The primary disadvantage of this system is that fixed arrays and elevated video cameras can be difficult to implement in ocean situations with free-ranging dolphins. Possibilities for implementation include placing fixed hydrophone arrays and video equipment in a bay or channel which is frequented by wild animals (Janik, 2000). A smaller system could possibly be implemented off of a boat using a towed array and video system on a tethered blimp [combining the systems described by Miller and Tyack (1998) and Nowacek *et al.* (2000)]. Obtaining error results for these situations would be facilitated by further theoretical work on the algorithm.

There are several avenues for improvement of the system. Increased resolution would enable identification of the vocalizing dolphin when dolphins are closer together. The video projection error appears to be the dominant source of error. However, since the video calibration error was sometimes over 10 pixels, the solution is probably not to increase image resolution. In one sense, this level of video error is not inherent to the system, and the results could probably be easily improved by superior camera placement and improved camera calibration. Placing the camera over the lagoon would reduce the error in at least one dimension. Using more than 5 points to perform daily calibrations, as well as using points spaced more evenly in the image, would probably increase accuracy of the calibration as well. Reducing this video error would be a relatively easy way to increase resolution of the entire system.

Increasing resolution of the acoustic localization system would also be helpful. Use of even slightly incorrect hydrophone positions can cause significant errors in localization. Thus, any method of improving calibration of hydrophone positions would likely decrease localization error. Placing the source a known distance from each hydrophone instead of directly adjacent to each hydrophone might avoid possible hydrophone overloading, near-field effects, as well as strong reverberation effects from the wall next to each hydrophone. Also, the localization algorithm could be improved to reduce its sensitivity to reverberation. Use of a sampling rate higher than 48 kHz could improve the resolution of the system. Although data storage might become more of an issue, more of the higher-frequency energy in echolocation clicks and burst pulsed sounds would be captured.

V. CONCLUDING REMARKS

The combination of acoustic localization and video sampling techniques allows us to link dolphin sounds with the identity of the vocalizing dolphin. If the behavior of the vocalizing dolphin is known, either from the video record or from more detailed real-time behavioral sampling, sounds can be linked to the contexts under which they were made. This is very important if we desire to ascertain the functions of vocalizations. Possible uses of this system include studying numerous aspects of the social contexts and behavioral function of vocal behavior as well as purely acoustic aspects of sounds under normal social conditions (e.g., directionality). There exist several avenues for improvement of the system. However, many new and interesting questions about marine mammal behavior can be asked and answered with the current resolution. For instance, echolocation behavior of foraging animals could be studied, capturing the behavior of the echolocating dolphin, and possibly its prey as well, on video. The system might help resolve the current debate on the existence of signature whistles in normally socializing bottlenose dolphins (McCowan and Reiss, 1995, 2001) by providing unbiased data sets of whistles identified to individual. The system might also help in testing the hypothesis that animals use cues in signal directionality for pod cohesion and communication (Lammers, 2001; Miller, 2002).

ACKNOWLEDGMENTS

The authors would like to thank DolphinQuest Bermuda and its kind and helpful staff for use of the facility, for their efforts on behalf of the project, and for their flexibility and incredible support. The Bermuda Maritime Museum was also very helpful and understanding of research needs and schedules. Stephanie Watwood was indispensable for data collection in the field, and deserves extra gratitude for her tireless efforts. Thanks to Kathy Dunsmore for assistance in development and writing of the localization algorithm. Thanks to Jay Wheeler, Amy Apprill, and Eli Woolery for assistance

with data collection. The manuscript was improved by revisions made by Michael Casso, John Buck, John Leonard, Amy Samuels, and three anonymous reviewers. Funding was provided by the Waikoloa Marine Life fund, Grant No. IBN-9975523 from the National Science Foundation, a graduate student fellowship for R. Thomas from the National Science Foundation, and an Ocean Ventures Fund Grant for R. Thomas from the Woods Hole Oceanographic Institution. This is Woods Hole Oceanographic Institution Contribution Number 10444.

[1]We follow the usage of Tyack and Miller (2002; section 6.2.2) calling ''vocalizations'' any sounds produced by specializations of the respiratory tract. We do not mean to imply that all sounds called vocalizations are made by the larynx.

Barker, R. H. (**1953**). ''Group synchronizing of binary digital systems,'' in *Communication Theory*, edited by W. Jackson (Butterworth, London), pp. 273–287.

Bouguet, J. (**2000**). http://www.vision.caltech.edu/bouguetj/calib_doc/

Brensing, K., Linke, K., and Todt, D. (**2001**). ''Sound source location by difference of phase, on a hydrophone array with small dimensions,'' J. Acoust. Soc. Am. **109**, 430–433.

Caldwell, M. C., Caldwell, D. K., and Tyack, P. L. (**1990**). ''A review of the signature whistle hypothesis for the Atlantic bottlenose dolphin, *Tursiops truncatus*,'' in *The Bottlenose Dolphin: Recent Progress in Research*, edited by S. Leatherwood and R. R. Reeves (Academic, San Diego), pp. 199–234.

Clark, C. W., Ellison, W. T., and Beeman, K. (**1986**). ''A preliminary account of the acoustic study conducted during the 1985 spring bowhead whale, *Balaena mysticetus*, migration off Pt. Barrow, Alaska,'' Rep. Int. Whaling Comm. SD/39/PS8: 311–316.

Dahlheim, M. E., and Awbrey, F. (**1982**). ''A classification and comparison of sounds of captive killer whales (*Orcinus orca*),'' J. Acoust. Soc. Am. **72**, 661–670.

Dudzinski, K. M., Clark, C. W., and Wursig, B. (**1995**). ''A mobile video/acoustic system for simultaneous underwater recording of dolphin interactions,'' Aquat. Mammals **21.3**, 187–193.

Evans, W. E., and Sutherland, W. W. (**1963**). ''Potential for telemetry in studies of aquatic animal communication,'' in *Bio-telemetry*, edited by L. E. Slater (Pergamon, Oxford), pp. 217–224.

Freitag, L., and Tyack, P. L. (**1993**). ''Passive acoustic localization of the Atlantic bottlenose dolphin using whistles and clicks,'' J. Acoust. Soc. Am. **93**, 2197–2205.

Fripp, D., Tyack, P., Johnson, M., and Thomas, R. (**1997**). ''An integrated approach to the quantitative analysis of dolphin whistles,'' 32nd Annual Meeting of the Animal Behavior Society, College Park, Maryland.

Fripp, D. R. (**1999**). ''Techniques for studying vocal learning in bottlenose dolphins, *Tursiops truncatus*,'' Ph.D. dissertation, MIT/WHOI Joint Ph.D. Program 99-02, Woods Hole, MA.

Fristrup, and Dunsmore (unpublished). ''A robust algorithm for localizing animal sounds''.

Herzing, D. L. (**1996**). ''Sounds and associated underwater behavior of free-ranging Atlantic spotted dolphins, *Stenella frontalis*, and bottlenose dolphins, *Tursiops truncatus*,'' Aquat. Mammals **22**, 61–79.

Janik, V. M. (**2000**). ''A two-dimensional acoustic localization system for marine mammals,'' Marine Mammal Sci. **16**, 437–447.

Johnson, D. H., and Dudgeon, D. E. (**1993**). *Array Signal Processing: Concepts and Techniques* (Simon and Schuster, New York), pp. 111–198.

Lammers, M. O., and Au, W. W. L. (**2001**). ''Directionality and the occurrence of social acoustic signals in traveling pods of Hawaiian spinner dolphins (*Stenella longirostris*),'' 14th Biennial Conference on the Biology of Marine Mammals, Vancouver B.C., Canada, 30 November 2001.

Lilly, J. C., and Miller, A. M. (**1961**). ''Sounds emitted by the bottlenose dolphin,'' Science **133**, 1689–1693.

MathWorks (**1984–1999**). MATLAB 5.3.1, Natick, MA, The MathWorks, Inc.

McCowan, B. (**1995**). ''A new quantitative technique for categorizing whistles using simulated signals and whistles from captive bottlenose dolphins (Delphinidae, *Tursiops truncatus*),'' Ethology **100**, 177–193.

McCowan, B., and Reiss, D. (**1995**). ''Quantitative comparison of whistle repertoires from captive adult bottlenose dolphins (Delphinidae: *Tursiops truncatus*): A re-evaluation of the signature whistle hypothesis,'' Ethology **100**, 193–209.

McCowan, B., and Reiss, D. (**2001**). ''The fallacy of signature whistles in bottlenose dolphins: A comparative perspective of 'signature information' in animal vocalizations,'' Anim. Behav. **62**, 1151–1162.

Miller, P. J., and Tyack, P. L. (**1998**). ''A small towed beamforming array to identify vocalizing resident killer whales (*Orcinus orca*) concurrent with focal behavioral observations,'' Deep-Sea Res., Part II **45**, 1389–1405.

Miller, P. J. O. (**2002**). ''Mixed-directionality of killer whale stereotyped calls: a direction of movement cue?'' Behav. Ecol. Sociobiol. **52**, 262–270.

Nowacek, D. P., Tyack, P. L., Wells, R. S., and Johnson, M. P. (**1998**). ''An onboard acoustic data logger to record biosonar of free-ranging bottlenose dolphins,'' J. Acoust. Soc. Am. **103**, 2908.

Nowacek, D., Wells, R. S., and Tyack, P. L. (**2000**). ''A platform for continuous behavioral and acoustic observations of free-ranging marine mammals: Overhead video combined with underwater audio,'' Marine Mammal Sci. **17**, 191–199.

Press, W. H., Teukolsky, S. A., Vetterling, W. T., and Flannery, B. P. (**1992**). *Numerical Recipes in C* (Cambridge University Press, Cambridge, UK), pp. 408–412.

Read, A., Wells, R., Hohn, A., and Scott, M. (**1993**). ''Patterns of growth in wild bottle-nosed dolphins, *Tursiops truncatus*,'' J. Zool. **231**, 107–123.

Sayigh, L. S., Tyack, P. L., Wells, R. S., and Scott, M. D. (**1990**). ''Signature whistles of free-ranging bottlenose dolphins *Tursiops truncatus*: Stability and mother-offspring comparisons,'' Behav. Ecol. Sociobiol. **26**, 247–260.

Spiesberger, J., and Fristrup, K. (**1990**). ''Passive localization of calling animals and sensing of their acoustic environment using acoustic tomography,'' Am. Nat. **125**, 107–153.

Spiesberger, J. L. (**1998**). ''Linking auto- and cross-correlation functions with correlation equations: Application to estimating the relative travel times and amplitudes of multipath,'' J. Acoust. Soc. Am. **104**, 300–312.

Spiesberger, J. L. (**1999**). ''Locating animals from their sounds and tomography of the atmosphere: Experimental demonstration,'' J. Acoust. Soc. Am. **106**, 837–846.

Spiesberger, J. L. (**2000**). ''Finding the right cross-correlation peak for locating sounds in multipath environments with a fourth-moment function,'' J. Acoust. Soc. Am. **108**, 1349–1352.

Tyack, P. (**1991**). ''Use of a telemetry device to identify which dolphin produces a sound,'' in *Dolphin Societies*, edited by K. Pryor and K. S. Norris (University of California Press, Berkeley), pp. 319–344.

Tyack, P. L., and Recchia, C. A. (**1991**). ''A datalogger to identify vocalizing dolphins,'' J. Acoust. Soc. Am. **90**, 1668–1671.

Tyack, P. L., and Miller, E. H. (**2002**). ''Vocal anatomy, acoustic communication, and echolocation in marine mammals,'' in *Marine Mammal Biology: An Evolutionary Approach*, edited by A. R. Hoelzel (Blackwell Scientific, Oxford, England), pp. 142–184.

Urick, R. J. (**1982**). *Sound Propagation in the Sea* (Peninsula, Los Altos, CA), pp. 4–6.

Watkins, W. A., and Schevill, W. E. (**1972**). ''Sound source location by arrival-times on a non-rigid three-dimensional hydrophone array,'' Deep-Sea Res. Oceanogr. Abstr. **19**, 691–706.

Watkins, W. A., and Shevill, W. E. (**1975**). ''Sperm whale (*Physeter catodon*) react to pingers,'' Deep-Sea Res. Oceanogr. Abstr. **22**, 123–129.

Discrimination of amplitude-modulated synthetic echo trains by an echolocating bottlenose dolphin

Lois A. Dankiewicz
Science Applications International Corporation, 3990 Old Town Avenue, Suite 208A, San Diego, California 92110

David A. Helweg and Patrick W. Moore[a)]
Space and Naval Warfare Systems Center, 53560 Hull Street, San Diego, California 92152

Justine M. Zafran
Science Applications International Corporation, 3990 Old Town Avenue, Suite 105A, San Diego, California 92110

(Received 31 January 2002; revised 7 June 2002; accepted 9 July 2002)

Bottlenose dolphins (*Tursiops truncatus*) have an acute ability to use target echoes to judge attributes such as size, shape, and material composition. Most target recognition studies have focused on features associated with individual echoes as opposed to information conveyed across echo sequences (feature envelope of the multi-echo train). One feature of aspect-dependent targets is an amplitude modulation (AM) across the return echoes in the echo train created by relative movement of the target and dolphin. The current study examined whether dolphins could discriminate targets with different AM envelopes. ''Electronic echoes'' triggered by a dolphin's outgoing echolocation clicks were manipulated to create sinusoidal envelopes with varying AM rate and depth. Echo trains were equated for energy, requiring the dolphin to extract and retain information from multiple echoes in order to detect and report the presence of AM. The dolphin discriminated amplitude-modulated echo trains from those that were not modulated. AM depth thresholds were approximately 0.8 dB, similar to other published amplitude limens. Decreasing the rate of modulation from approximately 16 to 2 cycles per second did not affect the dolphin's AM depth sensitivity. The results support multiple-echo processing in bottlenose dolphin echolocation. This capability provides additional theoretical justification for exploring synthetic aperture sonar concepts in models of animal echolocation that potentially support theories postulating formation of images as an ultimate means for target identification.
[DOI: 10.1121/1.1504856]

PACS numbers: 43.80.Lb, 43.66.Gf [WA]

I. INTRODUCTION

The basic requirement for any man-made or biological underwater sonar system is to detect a signal, usually an echo, in the surrounding noisy sea. For the dolphin, this detection is accomplished in part by extensively adapted auditory neural systems about which the functional capabilities are not yet fully understood. The exquisite biological sonar system of the bottlenose dolphin (*Tursiops truncatus*) is a prime example of evolutionary adaptation for use in shallow water, cluttered, high noise, and extremely reverberant environments such as bays, estuaries, and near-shore waterways. Although this capability has evolved over the past 50 million years, the discovery of dolphin echolocation is comparatively new, dating back to the late 1940s (Busnel and Fish, 1980). Since then, research conducted under rigorous experimental conditions has demonstrated that dolphins have an acute ability to judge from returning target echoes whether that target is hollow or solid, how thick it is, and to judge attributes such as size, shape, and material composition (Au, 1993; Busnel and Fish, 1980; Helweg *et al.*, 1996; Nachtigall and Moore, 1988; Thomas and Kastelein, 1990).

Although many previous studies have addressed the basic question of what acoustic features are used by the dolphin in biosonar target recognition, most have focused on features associated with *individual* echoes returning from ensonified targets. This approach disregards information that may be conveyed across dynamic or static features of echo sequences (echo train), or multi-echo integration. Floyd (1980) provided the first application of signal detection theory to multiple observations (Swets *et al.*, 1988) in dolphin echolocation. He provided three models of echo detection in noise that contrasted coherent summation, noncoherent summation, and independent evaluation processes. In contrast to Floyd's detection models, the current study examines whether dolphins are capable of using changes in echo amplitude over the course of multiple echoes (echo envelope) to discriminate targets.

Traditionally, the amplitude modulation (AM) of echo envelopes most often has been discussed with reference to the effects of insect wing beats on the envelope of individual bat echolocation calls (Busnel and Fish, 1980; Nachtigall and Moore, 1988). A bottlenose dolphin echolocation click is ba-

[a)]Author to whom correspondence should be addressed: Code 23501, Space and Naval Warfare Systems Center, San Diego, 53560 Hull Street, San Diego, CA 92152. Electronic mail: pmoore@spawar.navy.mil

sically too brief to sustain much AM, but the return echo contains multiple highlights. The energy contained in the highlights may be integrated, enhancing the dolphin's echo detection performance (Vel'min and Dubrovskiy, 1976; Moore *et al.*, 1984). In contrast, some information about object shape can be carried by the AM of an echo *train*, but discrimination of objects based on the amplitude envelope of the echo train has not been reported. Several theories include the assumption that dolphins are sensitive to systematic changes across multiple echoes. In a computational model of dolphin echo signal processing designed to account for the observation that dolphins usually emit multiple clicks during biosonar research tasks, combination, or fusion, of multiple echoes resulted in improved echo categorization (Moore *et al.*, 1991; Roitblat *et al.*, 1991). Altes *et al.* (1998, 2001) produced synthetic aperture sonarlike images by combining echoes from objects ensonified at multiple orientations with dolphin clicks, providing a theoretical foundation for speculation that dolphins form images of objects using information gathered through echolocation (Harley *et al.*, 1996; Herman *et al.*, 1998).

Multi-echo integration is analogous to the use of sequential aspect changes for discriminating between objects or identifying orientation of aspect-dependent objects. One acoustic feature of echoes from aspect-dependent targets is the AM of the return echoes in a train, which can be a function of the changing orientation of the target relative to the dolphin. Multi-echo integration capability would render a dolphin able to discriminate an amplitude-modulated echo train from one of constant amplitude, while total energy is held constant. Sensitivity to the AM of multiple echoes has not been directly measured, however. A previous study has shown an echolocating dolphin to be capable of detecting a 1-dB difference in target strength upon comparing return echoes from stationary targets (Evans, 1973). Physiological evidence from evoked-potential recording from inferior colliculus (Bullock *et al.*, 1968), and behavioral results from both free-field threshold tests of absolute hearing ability (Johnson, 1967) and interaural measures (Moore *et al.*, 1995), all have demonstrated sensitivity to amplitude changes as low as 1 dB. These results suggest that a dolphin capable of multi-echo integration may be similarly sensitive to the AM of echo sequences.

The current study was designed to test the hypothesis that echolocating dolphins can detect changes in amplitude of an envelope formed by multiple echoes and to examine limits of such ability. Testing was accomplished using electronic echoes generated interactively by computer as a dolphin emitted echolocation clicks. The use of electronic echoes permitted strict experimental control over the stimulus features available to the dolphin, since control of the features would not have been possible using physical targets. This is the first study of amplitude sensitivity in the ''active'' auditory system. From a biomimetic, signal processing standpoint, this work has application to understanding if and how one should go about ''fusing'' multi-aspect information.

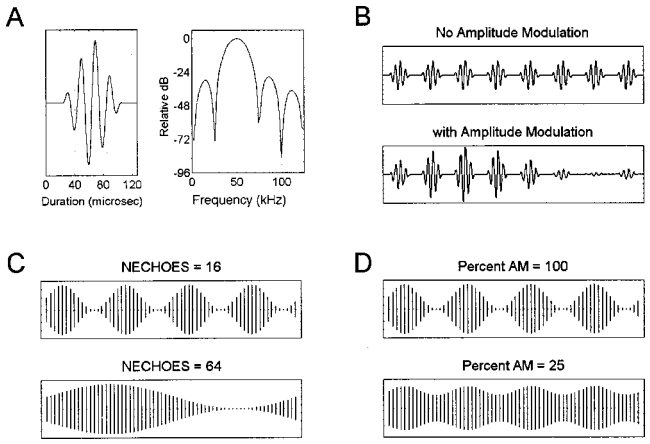

FIG. 1. (A) Enlargement of a single stimulus pulse (left) and its spectrum (right). (B) Examples of a GO and NO-GO stimulus used in the experiment. Each stimulus was comprised of multiple echoes over which amplitude was constant (NO-GO) or modulated (GO). (C) Comparison of two GO stimuli that have equal %AM, but differ in number of echoes (NECHOES=16 and 64 shown). The rate at which the envelope of the GO stimulus was modulated was a function of the number of echoes used to define it. Each vertical line represents a single synthetic echo. (D) Envelope contour was determined by % AM, the difference between echoes of highest and lowest amplitudes. The NECHOES is 16 in this portion of the figure.

II. METHODS

A. Subject

The subject of this study was a 17-year-old female bottlenose dolphin, ''CAS.'' CAS was housed with two companion dolphins in enclosures located in San Diego Bay at the Space and Naval Warfare Systems Center facilities. Experimental sessions were conducted in an enclosure that was inaccessible to the other animals. The subject's hearing was recently evaluated as normal by a comprehensive audiometric assessment (Brill *et al.*, 2001).

B. Synthetic echo stimuli

Each trial consisted of a series of synthetic echoes triggered by the dolphin's outgoing echolocation clicks, with one synthetic echo generated per click emitted by the dolphin. In both AM and no-AM trial type conditions [Fig. 1(B)], individual echoes were triangle-windowed 50-kHz pulses, 128 μs in duration. The stimuli were used to test specific experimental parameters and were not intended to mimic echoes from real objects in a naturalistic setting. The analytic waveform and spectrum are illustrated in Fig. 1(A). Digital waveforms were corrected for the transducer's measured transmit response prior to analog conversion. Calibration measurements confirmed good match between desired and analytic spectra.

Ambient noise in San Diego Bay was approximately 80 dB *re*: 1 μPa^2/Hz above 1 kHz, so a consistent noise floor was created by the addition of 95 dB SPL of white noise to all synthetic echoes used in the experiment. The bandwidth for rms noise power was estimated using Q derived from critical band measures of the bottlenose dolphin receiver. Q was approximately 2.2 for signals with center frequency of 60 kHz (Au and Moore, 1990). The synthetic signals used in

this study had center frequency of 50 kHz, thus the 95 dB SPL white noise floor was set using an estimated bandwidth of approximately 22.72 kHz.

To prevent the dolphin from attempting to solve the discrimination using only the first synthetic echo of each trial, the starting phase of the AM sinusoid was randomized by drawing from a Gaussian distribution with mean of 90 (± 5) degrees. This manipulation equated the starting amplitude of the first echoes of the no-AM and AM echo trains.

Two aspects of the amplitude envelope modulation contour were varied in this study—depth of modulation and the rate at which the modulated contour changed. The depth of AM in the GO stimulus envelope was manipulated by varying notch depth, defined as %AM [Fig. 1(D)]. The amplitude of the NO-GO synthetic echo trains was constant, and GO synthetic echo amplitudes varied depending on %AM. The source level was held constant at 133 dB SPL *re*: 1 μPa for all NO-GO echoes, except during training. GO stimulus echo trains had equivalent source level on average, with individual echo levels ranging between 0 and 139 dB (depending on the %AM value) prior to the addition of white noise.

Assessment of CAS's sensitivity to AM as a function of time was examined by requiring the AM to cycle through a complete period over a predetermined number of echoes (NECHOES; 4, 8, 16, 32, or 64) [Fig. 1(C)]. Greater amplitude differences between successive echoes were therefore necessary at NECHOES=4 ($|\Delta dB|=0.32$; %AM=100) than at NECHOES=64 ($|\Delta dB|=0.02$; %AM=100). Thus, the highest AM rate was associated with NECHOES of 4, and the lowest with 64. Furthermore, AM envelopes were briefest for the NECHOES=4 condition and longest for NECHOES=64. Although echo presentation pace was partly determined by the animal since her clicks triggered synthetic echo delivery, the equipment was designed to simulate a 6-m range by limiting the interecho interval so that echoes could not be triggered any faster than 8 ms apart. Thus, at higher levels of NECHOES, the full range of AM information was delivered over a longer period due to the inter-echo interval restriction.

Percent AM can be equated with a minimum amplitude difference detectable by the dolphin. Total energy was held constant across the echo train, thus the dolphin could not simply solve the discrimination by cumulative energy differences that would otherwise emerge across the echo train. Two measures of %AM therefore could be derived—the amplitude difference between adjacent echoes (a pairwise comparison) or the overall amplitude difference (max-min echo amplitudes) (Fig. 2). The former relationship makes the fewest memory assumptions, assuming a sliding memory register only two echoes deep. The latter assumes a deeper memory register (fill the register then make the max versus min comparison). We converted %AM to minimum amplitude difference using the latter relationship, which provides the most conservative (less sensitive) estimate.

C. Apparatus

An electronic Synthetic Echo System (SES) was assembled for the purpose of detecting the dolphin's echolocation clicks and delivering the corresponding synthetic echoes. System onset, experimental variables (%AM, NECHOES), trial type (GO, NO-GO), and response logging were controlled using a LabView Virtual Instrument driver with a National Instruments PCI MIO-16E-1 multifunction board hosted on a Pentium PC. The digital synthetic echoes were combined with white noise, and the resultant signals stored to RAM prior to each trial.

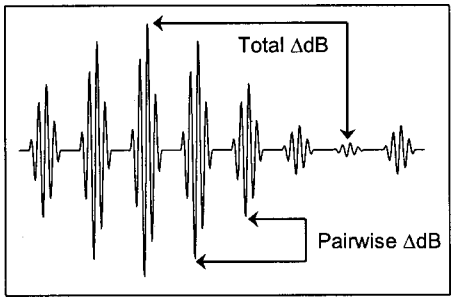

FIG. 2. Relationship between %AM of the echo train envelope and potential measures of amplitude limens.

An apparatus was constructed for animal and hydrophone placement during sessions. The subject's hoop station was situated 1.35 m below the water surface and 0.48 m away from an acoustically opaque shield. Shield removal indicated start-of-trial, and CAS's clicks were then detected by a Reson TC4013 omnidirectional broadband hydrophone located 0.64 m from her melon. The analog input data were bandpass filtered (3–300 kHz), amplified (54 dB of gain; Stanford Research Systems SR 560 filter/amplifier), and then passed to the multifunction board. Every emitted click exceeding 170 dB *re*: 1 μPa triggered the analog output of a synthetic echo by the SES. Analog echoes were filtered and amplified (10–200 kHz, 20 dB of gain) using a DL Electronics 4302 filter/amplifier, and projected by a second Reson TC4013 hydrophone located 1.35 m from CAS's melon. A 6.0-m range was simulated by inserting a delay of 8.0 ms between the triggering click and output of the echo, thereby providing a consistent focal point for the animal. Surface reflections were eliminated by a floating mat comprised of nylon bristles located at the surface between the dolphin and the Reson transducers. The system was calibrated by transmitting the synthetic echoes from the Reson TC4013 transducer and receiving them on a calibrated ITC 6030 omnidirectional hydrophone located at the dolphin's position in the hoop station.

D. Session procedure

Each trial began with the dolphin placing her rostrum on an inter-trial station located at the water surface, facing a trainer. Upon receipt of a hand cue from the trainer, CAS submerged and positioned her head in the test station hoop. The trainer raised the shield out of her echolocation pathway as a computer operator engaged the synthetic echo electronics. A 4.0-s trial period ensued, during which time the subject could echolocate *ad libitum*. A synthetic echo was produced for every click received. The subject was required to back out of the stationing hoop and touch a nearby paddle (GO response) to report an AM synthetic echo train and required to remain in the hoop for 4.0 s (NO-GO response) to report a

no-AM echo train. A miss was recorded if the animal performed a NO-GO response for the AM condition, and a false alarm recorded if a GO response was made to a no-AM stimulus. Correct responses were reinforced with a secondary (1-s 5-kHz tone) and a primary (approximately three fish) reinforcer. Incorrect responses were not reinforced. Trials were arranged in blocks of ten, with an equal number of GO and NO-GO trials presented per block. Trial type sequencing was determined by a Gellermann series (Gellermann, 1933) modified so that successive trials within a block were controlled (0.5 first order conditional probability of a GO trial following a NO-GO, or vice versa). Sessions began with an easily discriminable ten-trial block to assess subject motivation. The session was suspended temporarily if performance was below 80%. One data session was conducted per day.

E. Training and experimental phases

1. Training

In order to train CAS to perform the appropriate responses for both stimulus types, the stimuli were initially varied in both overall energy and envelope modulation. CAS was first exposed to the GO stimulus only (modulated envelope, %AM=100 and NECHOES=4) and learned to perform the appropriate corresponding paddle-press response (three to four sessions). During these sessions, on approximately half of the trials, no synthetic echoes were delivered and the NO-GO response was reinforced. Over the next 20 sessions, the NO-GO stimulus echoes (no-AM) were introduced at a source level of 118 dB SPL and increased by 3.0 dB every 10–50 trials until the total energy equaled that of the GO stimulus (133 dB SPL). Once signal energy was equated, envelope modulation alone provided the only feature upon which discrimination was possible. Successful completion of this phase of training established CAS's ability to discriminate between modulated and unmodulated echo trains and prepared her for tests in which the AM depth and rate were changed.

2. Threshold titration

All sessions in which %AM was systematically adjusted to measure CAS's threshold followed a titration method similar to the up/down staircase as reported by Moore and Schusterman (1987). Sessions began with the AM parameter held constant and at an easily discriminable level. If the initial ten-trial block was successful (performance $\geqslant$80%), %AM was then decreased in 2% increments for every GO stimulus trial until an incorrect response to a GO stimulus was given. Adjustments to %AM for all subsequent GO stimulus trials were then made in 1% increments. The %AM was increased after a miss and decreased after a correct GO response. Adjustments to %AM were never contingent on NO-GO stimulus trial responses. A reversal was defined as an instance in which the %AM adjustment changed directions (reversed), with the first reversal of every session occurring on the first incorrect GO stimulus trial. A session ended after ten reversals had been collected. The %AM threshold estimate was defined as the mean of the %AM reversal values, which corresponds to a 50% correct discrimination performance.

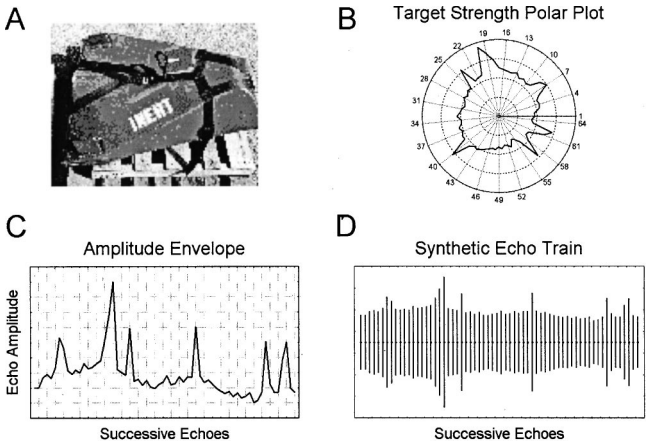

FIG. 3. Derivation of the amplitude envelope from the ROCKAN mine simulator. A photograph of the ROCKAN simulator on a palette is shown in (A), and (B) is the polar plot of the free-field target strength measured for the object (measured at the Applied Research Laboratory, University of Texas at Austin—Lake Travis test facility). (C) illustrates the amplitude profile when the polar data are unwrapped. (D) illustrates the amplitude variation in the synthetic echo train when the envelope is applied to a 64-echo train.

3. Testing

Testing was conducted in four stages.

a. Stage 1: NECHOES. The first measure was a preliminary assessment of CAS's AM discrimination ability at all NECHOES levels. Only one level was utilized per session. With %AM held constant at 100, performance was bracketed in one to three 20-trial (approx.) sessions, first at NECHOES=8, followed by 16, 32, and lastly 64.

b. Stage 2: Percent AM. With NECHOES held constant at 8, %AM was titrated down to threshold level. Five sessions were conducted overall, the last two of which were ten-reversal threshold sessions. CAS's performance at ''NECHOES'' and ''%AM'' assessment phases provided estimates of her performance boundaries at these stages. Thus, detailed testing could be initiated using stimulus values closer to her estimated thresholds.

c. Stage 3: NECHOES & %AM. Systematic testing of CAS's discrimination ability of the depth and rate of an AM echo train was conducted whereby %AM was titrated at each NECHOES level in two threshold sessions. Sessions in which NECHOES=16 were conducted first, followed by sessions at 32, then 64. Bracketing threshold sessions (two to three) were conducted at each NECHOES level before experimental data was collected.

d. Stage 4: Envelope modulation. Five 40-trial sessions were performed in which the GO stimulus AM was derived using scaled acoustic backscatter from a ROCKAN mine simulator, an object roughly shaped like a triangular wedge [see Fig. 3(A)]. This phase investigated whether CAS was able to detect AM echo trains using the amplitude envelope from the mine simulator. NECHOES and %AM were held constant at 64 and 100, respectively. The polar plot of relative target strength from the real world object is presented in

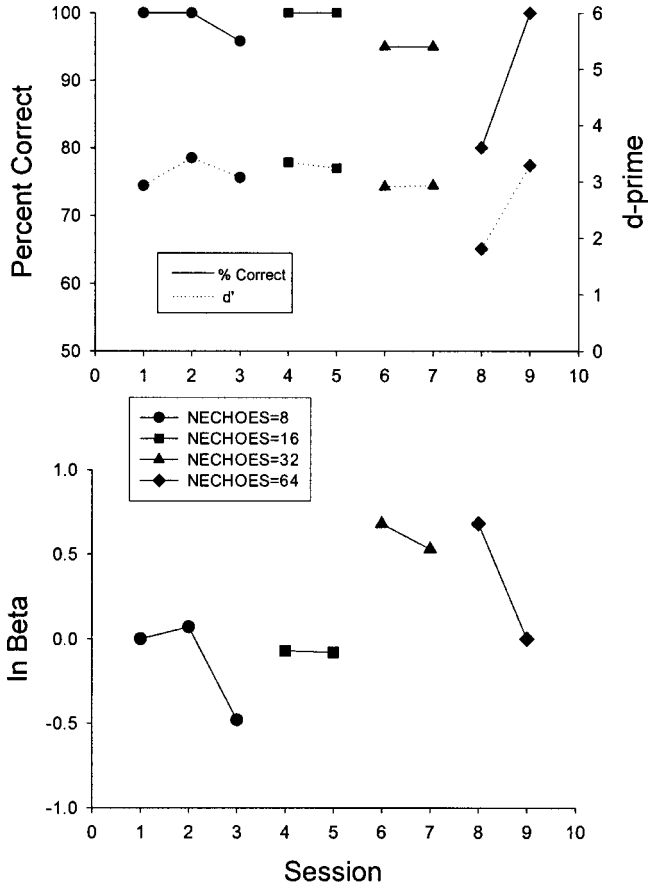

FIG. 4. Stage 1 preliminary AM rate assessment: Behavioral performance results at different AM rate levels (NECHOES=8, 16, 32, and 64) while %AM was held constant at 100 are shown. Percent correct performance (%) and sensitivity (d') results are presented in the top graph, and response bias [$\ln(\beta)$] in the bottom (20-trial sessions).

Fig. 3(B), and the 64-point extracted test envelope modulation function is presented in Figs. 3(C) and (D).

F. Data analysis

Behavioral results from stages 1 and 4 (NECHOES; envelope modulation) were evaluated using the theory of signal detection (TSD) (Green and Swets, 1988). Both the subject's signal detection sensitivity (d') and response bias (β), reported as $\ln(\beta)$, were computed in these instances since signal parameters (AM depth and rate) were not varied during a session. Results from stages 2 and 3 were evaluated by estimating thresholds using the mean of the titration reversals (50% correct discrimination performance).

III. RESULTS

A. Number of echoes (NECHOES)

Sessions in which NECHOES varied while %AM was held constant at 100 (Stage 1) are shown in Fig. 4. Percent correct performance and signal detection characteristics (d';β) are plotted as a function of NECHOES. CAS's ability to discriminate AM trials from no-AM trials remained at or above 80% correct for all levels of NECHOES. Choice performance and sensitivity (d') were equally strong at NECHOES=8, 16, and 32, but the increase in β at NECHOES=32 shows that CAS became conservative in her

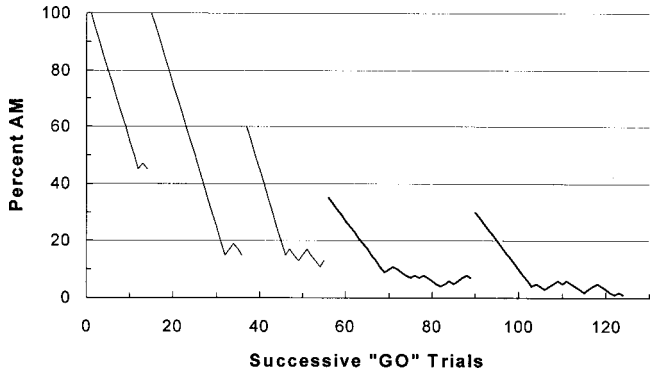

FIG. 5. Stage 2 initial %AM titration data: Percent AM values by trial during training sessions ($n=3$) and subsequent threshold estimates ($n=2$) (NECHOES=8 for all) are shown. Only AM trials (GO condition) are represented, and sessions are presented from left to right in the order they were conducted.

responding, possibly indicating a shift in her response strategy as the NECHOES were increased. CAS had poorer discrimination performance during the initial NECHOES=64 session, as evidenced by the low sensitivity value (d') and higher β. This performance decrement was resolved by the second session, suggesting a growing familiarization with the stimulus at NECHOES=64. The β values across sessions show a slight tendency toward more liberal responding in the subsequent sessions of each NECHOES level. Taken together, these results suggest that the subject tended to be conservative in her responding when first introduced to a new NECHOES level, but demonstrated a clear ability to discriminate the AM stimuli as NECHOES was manipulated.

B. Initial %AM titrations

Titration results of the first five sessions in which %AM varied and NECHOES were held constant at 8 (Stage 2) are presented in Fig. 5. All AM trials are shown, with reversals depicted by the point at which the line changes direction. These trials are represented graphically in the order they were conducted across the five sessions. The first three sessions clearly illustrate CAS's learning of the %AM manipulation task, with performance nearly asymptotic after session 3. In the first session, initial exposure to the test stimulus culminated in only three reversals with a mean of 45%AM. The two subsequent sessions consisted of two and five reversals, respectively, with an average value of 17%AM at both session's reversal points. Finally, two ten-reversal threshold sessions were conducted, yielding first a 7.3%AM threshold, then a 3.9% threshold. The subject's ability to discriminate %AM improved with each session, and performance reached asymptote by the fifth session. These results indicate that the subject was able to discriminate very small amplitude modulations at NECHOES=8.

C. NECHOES and %AM

Threshold estimates for the %AM obtained at NECHOES=8, 16, 32, and 64 are shown in Fig. 6. The two sessions reported for NECHOES=8 are the same two threshold sessions describe in the previous section (initial %AM titrations). Thresholds were calculated using the 50% correct

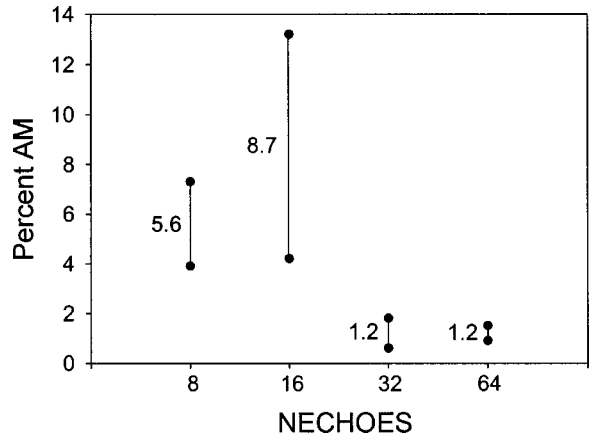

FIG. 6. Stage 3 threshold testing: Behavioral performance results on two %AM titration sessions (threshold estimates) at each AM rate (NECHOES=8, 16, 32, and 64) are shown. Thresholds are denoted by single points, with a line added to depict the range. The means of every threshold pair are adjacent to each line. NECHOES=8 data were taken from the two ten-reversal threshold sessions conducted in stage 2.

discrimination performance (mean reversal value for each session), and false alarm rates ranged from 0.01 to 0.40, with a mean value of 0.25. For each NECHOES level, two ten-reversal thresholds are plotted and the corresponding mean value noted. The animal's overall performance shows improvement in discrimination ability across sessions irrespective of the increase in NECHOES.

D. Object envelope simulation

Five 40-trial, minelike envelope discrimination sessions were conducted in which NECHOES=64 and %AM=100 for all sessions. Testing discrimination ability as opposed to measuring thresholds of that ability was the goal of this phase. The subject performed at 97% correct on four of the sessions and 100% on the other. The mean d' was 3.66 (sd =0.14) and mean $\ln\beta$ equaled 0.24 (sd=0.48), indicating that her discrimination performance was stable across sessions (Table I). These results show that CAS had little difficulty discriminating the irregular AM envelope associated with the minelike object.

IV. DISCUSSION

The major finding of this study was that an echolocating dolphin was able to discriminate amplitude-modulated (AM) echo trains from those that were not modulated, and that ability persisted as both rate and depth of AM were manipulated. Discrimination accuracy was maintained as rate of envelope modulation decreased. As AM depth was reduced, discrimination thresholds stayed consistently low, indicating a high degree of sensitivity to changes in the amplitude envelope of an echo train. Furthermore, decreasing the rate of modulation did not adversely affect this sensitivity to reductions in AM depth. These results provide data in support of the hypothesis that dolphins may recognize targets using features compiled across multiple echoes (envelope of an echo train). Further empirical support was offered by the finding that when successive echo amplitudes rose and fell irregularly, as real-world objects do, the echo train was easily distinguishable from a non-modulating echo train, as evidenced by a nearly perfect discrimination performance by the dolphin.

TABLE I. Percent correct performance and signal detection characteristics for each envelope simulation session (Stage 4, $n=20$ trials per session).

Session	% Correct	d'	$\ln(\beta)$
1	100	3.91	0.02
2	97	3.60	0.57
3	97	3.60	0.57
4	97	3.60	0.57
5	97	3.57	−0.51

The *average* of all AM thresholds was approximately 4.2% AM, which corresponds to an 0.8-dB total variation in amplitude (maximum − minimum) across the sequence of echoes. The largest difference between any two successive echoes at the slowest modulation rate (NECHOES=64) was approximately 0.02 dB. It does not seem likely, therefore, that the dolphin could have used this two-echo amplitude difference (cf. Dubrovskiy *et al.*, 1978) to accomplish AM discrimination. Past research has demonstrated amplitude discrimination limens no lower than about 1 dB (Bullock *et al.*, 1968; Evans, 1973; Johnson, 1967; Moore *et al.*, 1995). The %AM threshold of 4.2% (0.8 dB) of this study is consistent with the other amplitude discrimination limens, supporting speculation that the dolphin's echo memory register is more than two echoes deep and may be substantially deeper, given CAS's high performance with 64-echo trains.

We can speculate about the amplitude modulation rates experienced by the dolphin in this study. The minimum inter-echo interval was 8 ms, corresponding to a maximum rate of 125 echoes per second. At NECHOES=8, a full AM cycle occurred in approximately 64 ms, or an AM rate of approximately 15.6 echoes per second. At NECHOES=64, a full AM cycle occurred in 512 ms, or an AM rate of approximately 1.9 echoes per second. These rates are the maximum that the dolphin could have experienced (see Murchison, 1980; Penner, 1988).

The dolphin's ability to discriminate amplitude-modulated echo trains is not explained by the energy integration mechanism that underlies detection of single echoes in noise (Moore *et al.*, 1984; Vel'min and Dubrovskiy, 1976; Au *et al.*, 1988). Within echoes, inter-highlight intervals tend to be measured in tens of microseconds. In contrast, the synthetic echoes used in this study were separated by a minimum of 8 ms, which is orders of magnitude greater than the 265-μs energy integration window (Moore *et al.*, 1984; Vel'min and Dubrovskiy, 1976; Au *et al.*, 1988). Thus, any information used by the animal to distinguish one echo train type from another was based solely on an ability to extract and retain information from successive echoes in order to arrive at a decision regarding the varying amplitude characteristics of the train. The ability to garner information from the combination of multiple echoes—in addition to individual within-echo highlights—would serve to heighten detection and classification performance for objects encountered in the environment, as computational models have demonstrated (Floyd, 1980; Moore *et al.*, 1991; Roitblat

et al., 1991, 1993). The results provide theoretical justification for exploring the application of synthetic aperture sonar concepts in multi-echo models of animal echolocation (e.g., Altes *et al.*, 1998, 2001), which has ramifications for mental imagery theories that postulate formation of object images as an ultimate means for their identification (Harley *et al.*, 1996; Herman *et al.*, 1998). Future studies on dolphin biosonar capabilities should therefore examine aspects of information processing from complex echo trains as well as individual echoes.

Because echo trains are comprised of multiple echoes, the dolphin necessarily received more than one echo per trial. Prior research has shown that stimulus detectability can be enhanced in humans when multiple observations are allowed (see Floyd, 1980; Swets *et al.*, 1988; Green and Swets, 1988 for review). Those studies were designed to elucidate the possible mechanisms by which detection occurs as opposed to measuring the degree of detection enhancement. The classical interpretation of multiple observations and their implication on results of the current study are not considered applicable as this study did not utilize noise-only trials (no signal present) as a detection task would require, and no attempt was made to address the theory *a priori*. The potential contribution of this phenomenon to multiple echo integration capabilities in the dolphin could provide an interesting basis for further study.

In conclusion, the results reported here provide additional support for multiple-echo processing in bottlenose dolphin echolocation, and this, in turn, provides additional theoretical justification for exploring the application of synthetic aperture sonar concepts in models of animal echolocation. Future studies should seek to provide explicit evidence of multi-echo fusion, and to test for coherent echo integration processes that underlie algorithmic-based synthetic aperture sonar imaging processing use in traditional signal processing approaches.

ACKNOWLEDGMENTS

This study was made possible in part thanks to sponsorship by Dr. Randy Jacobson (ONR321TS Project WX20056). The behavioral data collection team (Tricia Kamolnick, Jennifer Briar, and Wendi Fellner) helped the dolphin maintain her focus through the study. We thank Dr. David Kastak, Dr. Dorian Houser, and Dr. Randy Brill for their thoughtful reviews of the manuscript.

Altes, R. A., Helweg, D. A., and Moore, P. W. (**2001**). ''Biologically inspired synthetic aperture sonar,'' SSC San Diego Technical Report, 1848, DTIS.

Altes, R. A., Moore, P. W. B., and Helweg, D. A. (**1998**). ''Tomographic image reconstruction of MCM targets using synthetic dolphin signals,'' SPAWARSYSCEN, San Diego Technical Document, 2993, DTIS.

Au, W. W. L. (**1993**). *The Sonar of Dolphins* (Springer-Verlag, New York), Chap. 9, pp. 177–215.

Au, W. W. L., and Moore, P. W. B. (**1990**). ''Critical ratio and critical bandwidth for the Atlantic Bottlenose dolphin,'' J. Acoust. Soc. Am. **88**, 1635–1638.

Au, W. W. L., Moore, P. W. B., and Pawloski, D. A. (**1988**). ''Detection of complex echoes in noise by an echolocating dolphin,'' J. Acoust. Soc. Am. **83**, 662–668.

Brill, R. L., Moore, P. W. B., and Dankiewicz, L. A. (**2001**). ''Assessment of dolphin (*Tursiops truncatus*) auditory sensitivity and hearing loss using jawphones,'' J. Acoust. Soc. Am. **109**, 1717–1722.

Bullock, T. H., Grinnel, A. D., Ikezono, E., Kameda, K., Katsuki, Y., Nomoto, M., Sato, O., Suga, N., and Yanagisawa, K. (**1968**). ''Electrophysiological studies of the central auditory mechanisms in cetaceans,'' Z. Vergl. Physiol. **59**, 117–156.

Busnel, R.-G., and Fish, J. F. (eds.) (**1980**). *Animal Sonar Systems* (Plenum, New York).

Dubrovskiy, N. A., Krasnov, P. S., and Titov, A. A. (**1978**). ''Auditory discrimination of acoustic stimuli with different phase structures in a bottlenose dolphin,'' in *Marine Mammals*, pp. 114–115.

Evans, W. E. (**1973**). ''Echolocation by marine delphinids and one species of freshwater dolphin,'' J. Acoust. Soc. Am. **54**, 191–199.

Floyd, R. W. (**1980**). ''Models of cetacean signal processing,'' *Animal Sonar Systems*, edited by R.-G. Busnel and J. F. Fish (Plenum, New York), pp. 615–623.

Gellermann, L. W. (**1933**). ''Chance orders of alternating stimuli in visual discrimination experiments,'' J. Gen. Psychol. **42**, 206–208.

Green, D. M., and Swets, J. A. (**1988**). *Signal Detection Theory and Psychophysics* (Peninsula, Los Altos, CA).

Harley, H. E., Roitblat, H. L., and Nachtigall, P. E. (**1996**). ''Object representation in the bottlenose dolphin (*Tursiops truncatus*): Integration of visual and echoic information,'' J. Exp. Psychol. Anim. Behav. Process. **22**(2), 164–174.

Helweg, D. A., Roitblat, H. L., Nachtigall, P. E., and Hautus, M. J. (**1996**). ''Recognition of three-dimensional aspect-dependent objects by an echolocating bottlenosed dolphin,'' J. Exp. Psychol. Anim. Behav. Process. **22**, 19–31.

Herman, L. M., Pack, A. A., and Hoffmann-Kuhnt, M. (**1998**). ''Seeing through sound: dolphins (*Tursiops truncatus*) perceive the spatial structure of objects through echolocation,'' J. Comp. Psychol. **112**(3), 292–305.

Johnson, C. S. (**1967**). ''Sound detection thresholds in marine mammals,'' in *Marine BioAcoustics, Vol. II*, edited by W. N. Tavolga (Pergamon, New York), pp. 247–260.

Moore, P. W. B., Hall, R. W., Friedl, W. A., and Nachtigall, P. E. (**1984**). ''The critical interval in dolphin echolocation: What is it?'' J. Acoust. Soc. Am. **76**, 314–317.

Moore, P. W. B., Pawloski, D. A., and Dankiewicz, L. (**1995**). ''Interaural time and intensity difference thresholds in the Bottlenose dolphin (*Tursiops truncatus*),'' in *Sensory Systems of Aquatic Mammals*, edited by R. A. Kastelein, J. A. Thomas, and P. E. Nachtigall (De Spil, The Netherlands), pp. 11–23.

Moore, P. W. B., Roitblat, H. L., Penner, R. H., and Nachtigall, P. E. (**1991**). ''Recognizing successive dolphin echoes with an Integrator Gateway Network,'' Neural Networks **4**, 701–709.

Moore, P. W. B., and Schusterman, R. J. (**1987**). ''Audiometric assessment of Northern fur seals, *Callorhinus ursinus*,'' Marine Mammal Sci. **3**, 31–53.

Murchison, A. E. (**1980**). ''Detection range and range resolution of echolocating bottlenose porpoise,'' in *Animal Sonar Systems*, edited by R.-G. Busnel and J. F. Fish (Plenum, New York), pp. 43–70.

Nachtigall, P. E., and Moore, P. W. B. (eds.) (**1988**). *Animal Sonar: Processes and Performance* (Plenum, New York).

Penner, R. H. (**1988**). ''Attention and detection in dolphin echolocation,'' in *Animal Sonar: Processes and Performance*, edited by P. E. Nachtigall and P. W. B. Moore (Plenum, New York), pp. 707–713.

Roitblat, H. L., Moore, P. W. B., Helweg, D. A., and Nachtigall, P. E. (**1993**). ''Representation and processing of acoustic information in a biomimetic neural network,'' in *From Animals to Animats 2: Simulation of Adaptive Behavior*, edited by J.-A. Meyer, S. W. Wilson, and H. L. Roitblat (MIT, Cambridge, MA), pp. 90–99.

Roitblat, H. L., Moore, P. W. B., Nachtigall, P. E., and Penner, R. H. (**1991**). ''Natural dolphin echo recognition using an Integrator Gateway Network,'' Adv. Neural Inform. Process. Syst. **3**, 273–281.

Swets, J. A., Shipley, E. F., McKey, M. J., and Green, D. M. (**1988**). ''Multiple observations of signals in noise,'' in *Signal Detection and Recognition by Human Observers*, edited by J. A. Swets (Peninsula, Los Altos, CA), pp. 201–220.

Thomas, J. A., and Kastelein, R. A. (eds.) (**1990**). *Sensory Abilities of Cetacans: Laboratory and Field Evidence* (Plenum, New York).

Vel'min, V. A., and Dubrovskiy, N. A. (**1976**). ''The critical interval of active hearing in dolphins,'' Sov. Phys. Acoust. **2**, 351–352.